IBIC 2017

INTERNATIONAL BEAM INSTRUMENTATION CONFERENCE

20-24 August 2017

Hosted by the
Facility for Rare Isotope Beams

Grand Rapids, Michigan
Amway Grand Plaza Hotel

Topics

- Opening and Closing Sessions
- Overview and Commissioning
- BPMs and Beam Stability
- Time-Resolved Diagnostics and Synchronization
- Beam Loss Detection and Machine Protection
- Beam Profile Monitors
- Machine Parameter Measurements

Program Committee

Ayhan Aydin, Ankara University
Willem Blokland, SNS
Mark Boland, ASLS
John Byrd, LBL
Nathan Eddy, FNAL
Mario Ferianis, Sincrotrone Trieste
Alan Fisher, SLAC
David Gassner, BNL
Ubaldo Iriso, ALBA
Andreas Jansson, ESS
Rhodri Jones, CERN
Kevin Jordan, JLAB
Dinakar Kanjilal, IUAC
Yongbin Leng, SSRF
Steve Lidia (IBIC17 Chair), FRIB
Zhengzheng Liu (Scientific Chair), FRIB
Sergio Marques, LNLS
Toshiyuki Mitsuhashi, KEK
James Sedillo, LANL
Kay Wittenburg, DESY
Junhui Yue, IHEP

MICHIGAN STATE UNIVERSITY

INTERNATIONAL BEAM INSTRUMENTATION CONFERENCE | IBIC 2017
20-24 August 2017 Grand Rapids, Michigan, USA

FRIB

Dear Colleagues,

On behalf of the organizing committee, I am pleased to welcome you to Grand Rapids, Michigan, USA, for the 2017 International Beam Instrumentation Conference (IBIC 17).

IBIC is a fruitful and successful gathering of the world's beam instrumentation community and it reflects the maturity of international collaboration in the field of beam instrumentation for accelerators. IBIC is dedicated to exploring the physics and engineering challenges of beam diagnostic and measurement techniques for particle accelerators worldwide. The conference program will include tutorials on selected topics, invited and selected talks, as well as poster sessions. An industrial exhibition and a tour to the Facility for Rare Isotope Beams (FRIB) will also be included.

IBIC 17 is hosted by the Facility for Rare Isotope Beams (FRIB) which is scheduled for completion in 2022. FRIB will be a scientific user facility for the Office of Nuclear Physics in the U.S. Department of Energy Office of Science (DOE-SC) and is funded by the DOE-SC, Michigan State University (MSU) and the State of Michigan. Supporting the mission of the Office of Nuclear Physics in the DOE-SC, FRIB will enable scientists to make discoveries about the properties of rare isotopes, nuclear astrophysics, fundamental interactions, and applications for society, including in medicine, homeland security, and industry.

The venue is the Amway Grand Hotel and Conference Center, voted “Best Service” (Meeting/Event Venue) by Michigan Meetings + Events Magazine in 2016, in the heart of the city and surrounded by a wide offering of hotels and restaurants.

Grand Rapids, the second largest city in Michigan, is located on the Grand River about 30 miles east of Lake Michigan. Grand Rapids is known for its industry and more recently for the arts.

We look forward to welcoming you to Grand Rapids, Michigan.

Steve Lidia, IBIC 17 Conference Chair

IBIC 2017 Committees

Scientific Programme Committee

Ayhan Aydin, Ankara University
Scott Baily, LANL
Willem Blokland, SNS
Mark Boland, ASLS
John Byrd, LBL
Nathan Eddy, FNAL
Mario Ferianis, ELETTRA
Alan Fisher, SLAC
Dave Gassner, BNL
Ubaldo Iriso, ALBA
Andreas Jansson, ESS
Rhodri Jones, CERN
Kevin Jordan, JLab
Dinakar Kanjilal, India
Yongbin Leng, SINAP
Steven Lidia, FRIB (IBIC17 chair)
Zhengzheng Liu, FRIB (PC Chair)
Sergio Marques, LNLS
Toshiyuki Mitsuhashi, KEK
Kay Wittenburg, DESY
Junhui Yue, IHEP/Lanzhou

Local Organizing Committee

Steven Lidia, FRIB **(Chair)**
Zhengzheng Liu, FRIB **(SPC Chair)**
Scott Cogan, FRIB
Gerlind Kiupel, FRIB
Dylan Maxwell, FRIB
Amy McCausey, FRIB
Rebecca Shane, FRIB

JACoW Editorial Team

Evelyn Akers, JLab
Isidre Costa, ALBA-CELLS
Amy McCausey, FRIB
Maggie Montes-Loera, SLAC
Maria Power, ANL
Volker RW Schaa, GSI
Rebecca Shane, FRIB

JACoW External Help

Matt Arena, FNAL (SPMS Support)
Anthony Cuffe, JLab (JACoW File Server)
Volker RW Schaa, GSI (JACoW Scripts)

Contents

ISBN: 978-3-95450-192-2 doi:10.18429/JACoW-IBIC2017-MO1AB1

FRIB PROJECT STATUS AND BEAM INSTRUMENTATION CHALLENGES*

J. Wei#, H. Ao, S. Beher, N. Bultman, F. Casagrande, J. Chen, S. Cogan, C. Compton, L. Dalesio, K. Davidson, A. Facco[1], F. Feyzi, V. Ganni, A. Ganshyn, P. Gibson, T. Glasmacher, L. Hodges, K. Holland, H.-C. Hseuh[2], A. Hussain, M. Ikegami, S. Jones, R.E. Laxdal[3], S. Lidia, G. Machicoane, I. Malloch, F. Marti, S. Miller, D. Morris, J. Nolen[4], P. Ostroumov, J. Popielarski, L. Popielarski, E. Pozdeyev, T. Russo, K. Saito, S. Stanley, H. Tatsumoto, R. Webber, T. Xu, Y. Yamazaki, Facility for Rare Isotope Beams, Michigan State University, East Lansing, MI, USA
K. Dixon, M. Wiseman, Thomas Jefferson National Laboratory, Newport News, VA, USA
M. Kelly, Argonne National Laboratory, Argonne, IL, USA
K. Hosoyama, KEK, Tsukuba, Japan
S. Prestemon, Lawrence Berkeley National Laboratory, Berkeley, CA, USA
A. Aleksandrov, Oak Ridge National Laboratory, Oak Ridge, TN, USA
N. Eddy, Fermi National Accelerator Laboratory, Batavia, IL, USA
[1] also at INFN - Laboratori Nazionali di Legnaro, Legnaro (Padova), Italy
[2] also at Brookhaven National Laboratory, Upton, NY, USA
[3] also at TRIUMF, Vancouver, Canada
[4] also at Argonne National Laboratory, Argonne, IL, USA

Abstract

With an average beam power two orders of magnitude higher than operating heavy-ion facilities, the Facility for Rare Isotope Beams (FRIB) stands at the power frontier of the accelerator family. This paper summarizes the status of design, technology development, construction, commissioning, as well as path to operations and upgrades. We highlight beam instrumentation challenges including machine protection of high-power heavy-ion beams and complications of multi-charge-state and multi-ion-species accelerations.

INTRODUCTION

During the past decades, accelerator-based neutron-generating facilities, such as SNS [1], J-PARC [2], PSI [3], and LANSCE [4], advanced the frontier of proton beam power to the 1 MW level, as shown in Fig. 1. FRIB is designed to advance the power frontier for heavy ions by more than two orders of magnitude, to 400 kW [5].

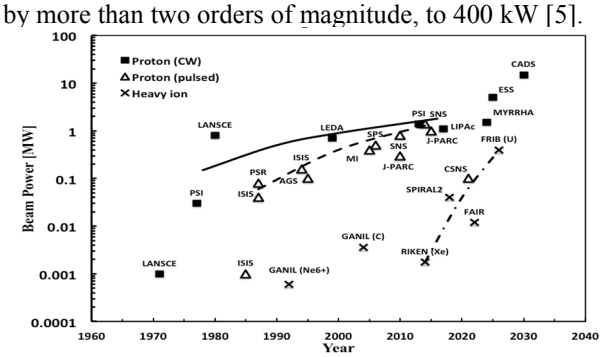

Figure 1: Achieved and planned average beam power on target for proton and heavy ion facilities.

*Work supported by the U.S. Department of Energy Office of Science under Cooperative Agreement DE-SC0000661 and the National Science Foundation under Cooperative Agreement PHY-1102511.
#wei@frib.msu.edu

The FRIB driver accelerator is designed to accelerate all stable ions to energies >200 MeV/u with a beam power on the target of up to 400 kW (Table 1). The driver accelerator consists of a 46 m long Front End [6] containing electron-cyclotron-resonance (ECR) ion sources and a room temperature RFQ followed by a 472 m long SRF linac with quarter-wave-resonators (QWR) of β_0=0.041 and 0.085 and half-wave-resonators (HWR) of β_0=0.29 and 0.53 in a folded layout to facilitate charge stripping and beam collimation and to accommodate the limited real estate footprint in the center of the MSU campus (Fig. 2). Up to 400 kW of the primary beam is focused down to a spot size of 1 mm in diameter striking the production target for rare isotope production. Following the low-loss design philosophy [7], the design average uncontrolled beam loss is below 1 W/m. For heavy ions like uranium at low energies, activation and radiation shielding is of less concern; the 1 W/m limit addresses concerns in damage on superconducting cavity surfaces and in cryogenic heat load [5].

Table 1: FRIB Driver Accelerator Baseline Parameters

Parameter	Value	Unit
Primary beam ion species	H to ^{238}U	
Beam kinetic energy on target	> 200	MeV/u
Maximum beam power on target	400	kW
Macropulse duty factor	100	%
Beam current on target (^{238}U)	0.7	emA
Beam radius on target (90%)	0.5	mm
Driver linac beam-path length	517	m
Average uncontrolled beam loss	< 1	W/m

ISBN: 978-3-95450-192-2 doi:10.18429/JACoW-IBIC2017-MO1AB1

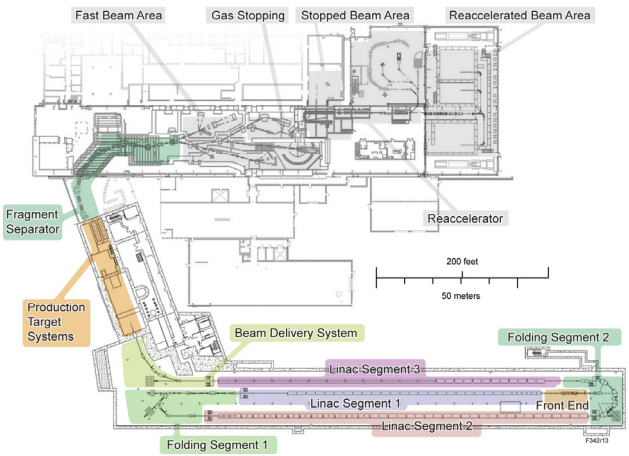

Figure 2: Schematic layout of the FRIB driver accelerator, target, and fragment separator (colored areas) and existing infrastructure (gray).

CONSTRUCTION STATUS

FRIB long-lead procurements were launched since 2012, two years before start of accelerator construction. They include the high power ECR source, the RFQ, niobium material for SRF cavities, pre-production cavities, the 4.5 K refrigeration "cold box", and cryogenic distribution.

Since 2013, we started major in-house production infrastructure preparation. The 2500 m^2 "SRF Highbay" at MSU houses areas for material inspection, cavity coordinate measurements and alignment checks, vacuum furnace degassing, parts cleaning, chemical etching, high-pressure water rinsing, SRF coupler conditioning, cavity dewar testing, cold mass assembly, and cryomodule testing. This facility, together with the cryomodule assembly area and the machine shop, supports the production throughput of testing five cavities per week and one cryomodule per month.

During the three years since the start of accelerator technical construction in 2014, FRIB accelerator construction is about 76% complete measured by earned-value project controls. About 65% of the total $303M accelerator construction is for material and work-for-others contracts, and about 35% is for in-house labor. About 94% of baselined major procurements (orders above $50k) have been either spent or committed. In-house work focuses on design, prototyping, system requirements and interface definition, contract statement-of-work and acceptance criteria listing development, vendor technical management, in-house fabrication, installation, testing, and commissioning. Major in-house work includes SRF cavity process and certification, cryomodule assembly, 2 K coldbox and cryogenic pieces.

Accelerator installation (Fig. 3) started before the beneficial occupancy date (BOD). The accelerator commissioning is divided into 8 steps, following the beam trajectory starting from the Front End. Each step of commissioning is contingent upon a successful accelerator readiness review (ARR). Each ARR is preceded by several device readiness reviews (DRR) of subsystems.

Figure 3: FRIB tunnel showing the lower LEBT and RFQ fully installed, and first QWR cryomodules aligned.

The first DRR was conducted in October 2016 allowing the operation of the FRIB room temperature ECR ion source [8]. Upon completion of the third DRR, the Ar beam produced from the ECR ion source was transmitted to the end of Low Energy Beam Transport (LEBT), as shown in Figs. 4 and 5. Presently, the RFQ is being conditioned in preparation for the Front End beam commissioning (ARR01) by September 2017 [6]. Commissioning of the β_0=0.041 superconducting RF section (ARR02) is planned for May 2018 upon completion of the 4.5 K cryogenic system (Fig. 6) [9].

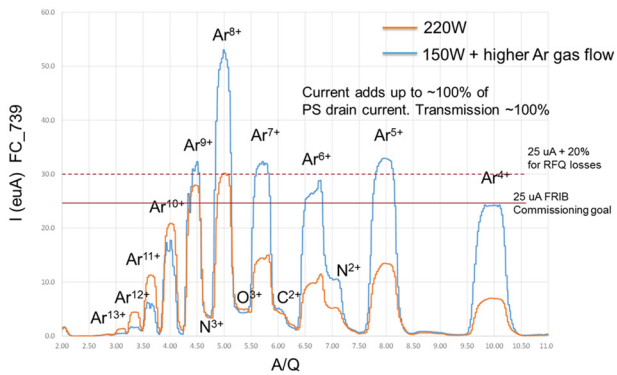

Figure 4: Mass-to-charge (A/Q) scan of Argon ion beam after two weeks of integrated tests showing current recorded on the Faraday Cup (FC_739).

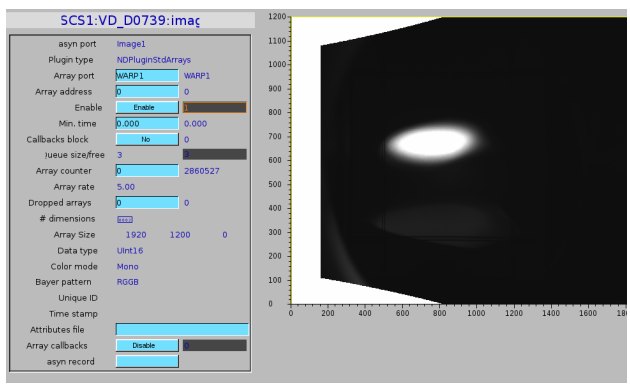

Figure 5: Image of the Ar ion beam on the diagnostics viewer plate near the end of FRIB LEBT.

ISBN: 978-3-95450-192-2 doi:10.18429/JACoW-IBIC2017-MO1AB1

Figure 6: 4.5 K coldbox installed in the FRIB cryogenics building [9]. The Floating Pressure Process – Ganni Cycle [10] is implemented to provide efficient adaptation to the actual loads.

Major accelerator R&D and subsystem prototyping are completed. These systems include integrated cryogenics, "bottom-up" cryomodules of low-β cavities and solenoids, charge stripping, and machine protection for high-power, low-energy heavy ion beams.

Integrated Cryogenics and SRF Cryomodule

An integrated design of the cryogenic refrigeration, distribution, and cryomodule systems is key to efficient SRF operations [9, 10]. The prototype distribution module and cryomodule have been successfully cold-tested together for both 4.5 K and 2 K operations. Integrated test with the 4.5 K cryogenic system at the upper-level cryogenic building (Fig. 6), the cryogenic transfer line from the refrigerator to the tunnel, the modular cryogenic distribution sections inside the tunnel, and the β_0=0.041 SRF cryomodules is planned before the ARR02 beam commissioning in May 2018.

To facilitate efficient assembly, simplify alignment, and allow U-tube cryogenic connections for maintainability, FRIB adopted an innovative bottom-up cryomodule design with the resonators and solenoids supported from the bottom [11, 12], as shown in Fig. 7. The cryogenic headers are suspended from the top for vibration isolation. By July 2017, all types of production QWR and HWR cavities in such "bottom-up" configurations are successfully validated.

Liquid Lithium Charge Stripping

FRIB uses a liquid lithium film moving at a speed of ~50 m/s. Tests with a proton beam produced by the LEDA source demonstrated that power depositions similar to the FRIB uranium beams are achievable without destroying the film [13]. In April 2017, the electromagnetic pump was successfully tested for lithium circulation. The production charge stripper along with the safety system will be fabricated by March 2018, as shown in Fig. 8.

Figure 7: Pre-production β_0=0.53 cryomodule under assembly, with 8 SRF cavities operating at 2 K and a solenoid operating at 4.5 K temperature, respectively.

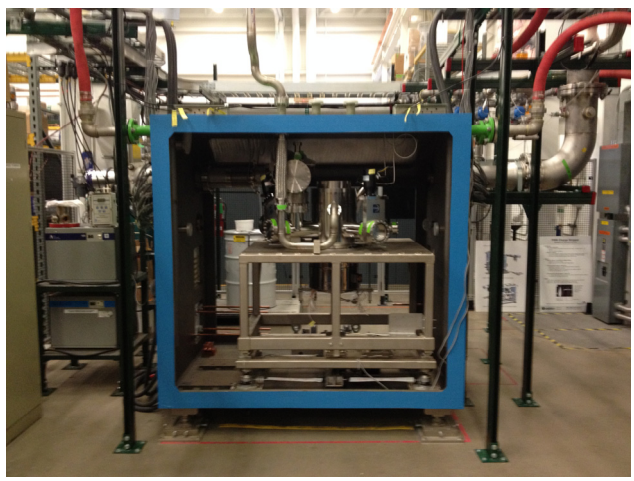

Figure 8: Liquid lithium charge stripper under assembly. The charge stripper assembly is contained in a sealed vessel that can be instantly filled with Ar gas. This vessel is a "credited engineered control" for hazard mitigation.

BEAM INSTRUMENTATION CHALLENGES

This section lists some examples of challenges in FRIB accelerator beam instrumentation and diagnostics.

Multi-layered Machine Protection

Machine protection is challenging for FRIB's intense low-energy heavy ion beams due to the low detection sensitivity and high power concentration in a short range. FRIB adopts multi-time scale and multi-layer approaches (Table 2). The fast protection system (FPS) is required to mitigate beam loss within 35 μs (10 μs for detection, 10 μs for controls processing, 5 μs for inhibit action, and 10 μs for beam clearing) to prevent damage to beam line components [14]. Primary detection methods include Low-level RF (LLRF) monitoring, differential beam current monitoring, halo monitor rings for high-sensitivity loss

ISBN: 978-3-95450-192-2 doi:10.18429/JACoW-IBIC2017-MO1AB1

detection (Fig. 9), and current-monitoring modules for critical magnet power supply inhibition. The fast beam inhibit is achieved by independently disabling both the upper and lower 90° electrostatic bends in the LEBT. Addition mitigation at a slower time scale is to disable the ECR ion source high voltage.

Table 2: Machine Protection for the FRIB Driver Linac

Mode	Time	Detection	Mitigation
FPS	~35 µs	LLRF controller Dipole current monitor Differential BCM Ion chamber monitor Halo monitor ring Fast neutron detector	LEBT bend electro-static deflector
RPS (1)	~100 ms	Vacuum status Cryomodule status Non-dipole PS Quench signal	As above; ECR source HV
RPS (2)	>1 s	Thermo-sensor Cryo. heater power	As above

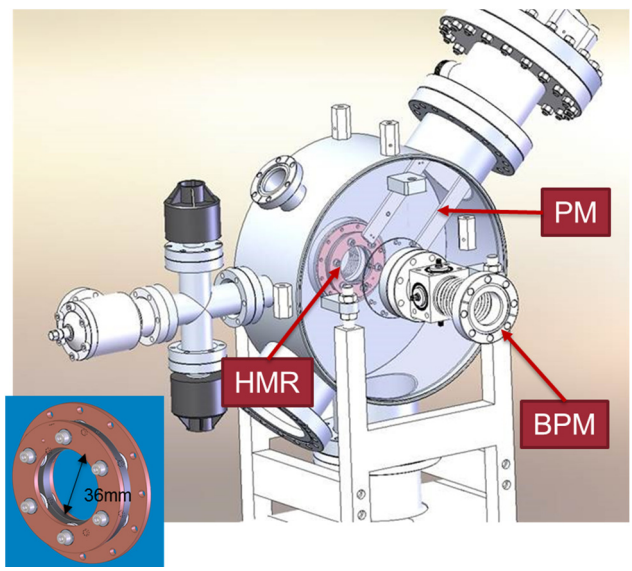

Figure 9: Room-temperature diagnostics section containing beam position (BPM) and profile (PM) monitors and halo monitoring ring (HMR, insert).

Low-loss Detection for SRF Performance

The machine protection system needs to function not only at a fast time scale to stop acute beam loss, but also at slow time scales to mitigate small, chronic beam loss (Table 2). Experience at SNS indicates correlation between chronic beam loss and performance degradation of the SRF cavities. Figure 10 shows the thermometry sensors installed in the cryomodule to detect beam loss at 1 W/m level at a response time scale of seconds.

Multi-charge-state, Multi-Species Diagnostics

To reach the design high beam intensity, FRIB driver linac simultaneously accelerates up to five charge states ($^{238}U^{76+}$, $^{238}U^{77+}$, $^{238}U^{78+}$, $^{238}U^{79+}$, $^{238}U^{80+}$) with a momentum spread of ~±2.6%. FRIB upgrade requires simultaneous acceleration of both heavy and light ions (e.g. $^{238}U^{79+}$, H_3^+). Beam instrumentation must accommodate wide momentum aperture in particular at the high-dispersion folding segments (Fig. 11) and residual dispersion under normal and fault conditions, and ensure tightly focused beam spot (~ 1 mm) at locations of charge stripper and the production target.

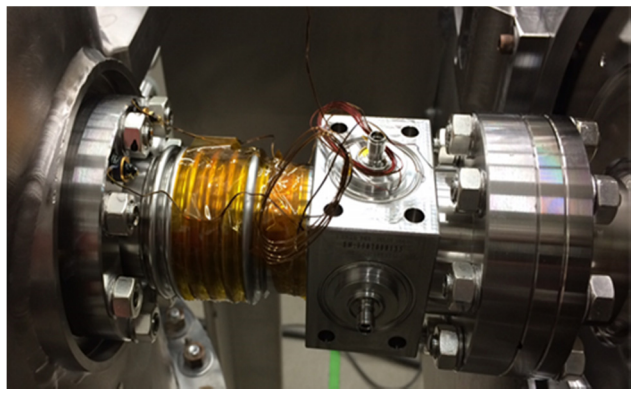

Figure 10: Cold BPM and thermometry sensors (resistance temperature detectors, RTDs) installed along the beam line in the FRIB SRF cryomodule.

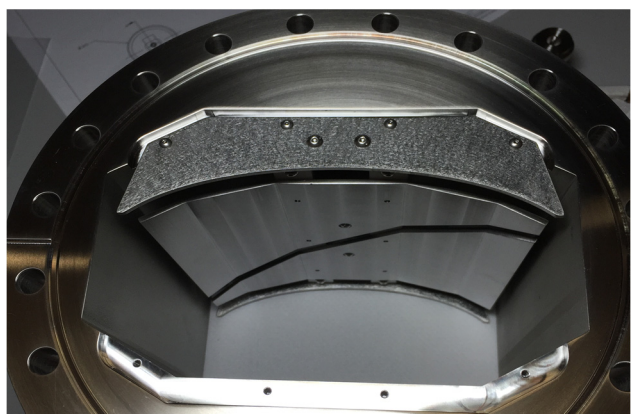

Figure 11: Elliptical beam position monitor for multi-charge state beam in Folding Segment dispersive section. The 150 mm wide horizontal aperture accommodates up to five uranium beam charge states over 80 mm spread.

High-power Charge Selection and Scraping

Charge selection requires up to several tens of kW of heavy ion beams of unwanted charge states to be scraped at energy near 18 MeV/u. Rotating scrapers of graphite discs, a scaled-down version of the FRIB production target [15], will be used to withstand the power.

Target Beam Position Monitoring

Beam instrumentation must withstand the high radiation environment near the production target monitoring the 400 kW heavy ion beam focusing onto a spot of 1 mm diameter

ISBN: 978-3-95450-192-2 doi:10.18429/JACoW-IBIC2017-MO1AB1

striking the production target [15]. Figure 12 shows the radiation-cooled, multi-slice graphite target of 30 cm diameter that rotates at 5000 rpm. Target diagnostics include optical thermal imaging and beam position monitoring. Shielding is carefully designed to block the "back shine" from the target ensuring proper operation of accelerator magnets and diagnostics for beam delivery.

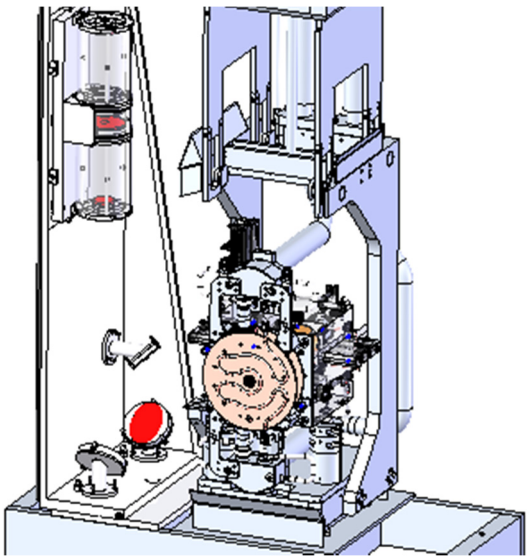

Figure 12: Schematics of the production target insert. The thermal imaging optics is located on the left side.

Folded Accelerator Geometry Complications

The folded accelerator lattice causes radiation cross-talk issue from high-energy linac sections that confound low-energy beam loss measurements. Local shielding is likely needed to raise signal-to-noise ratio in low-energy section of the driver linac. Sensitive loss monitors will be used during tuning of the low energy section upon staged beam commissioning and diagnose.

Beam Structure and Dynamic Range

Both continuous-wave (CW) and pulsed beams are to be accelerated in the linac. The CW beam is notched with beam gaps of 50 μs at 100 Hz to facilitate diagnostics. Beam instrumentation is designed to function over wide intensity and charge-state range from 50 eμA and 50 μs beam pulses during commissioning to full intensity (e.g. 700 eμA ^{238}U) CW beams [16].

User Cycle Flexibility

Table 3 shows user requested operational weeks per year during commissioning and initial operations [17]. The linac must be easily tuneable to allow fast user cycle change. The ion source is located at surface level with adequate instrumentation in the LEBT (Fig. 13) to allow easy maintenance and fast tuning.

Table 3: User Requested Operational Weeks Per Year for Various Types of Primary Beams Upon Operation Start

Beam type	Needed date	Weeks/year
^{36}Ar, ^{86}Kr	Commissioning	As needed
^{238}U	Starting year 1	12
^{48}Ca	Starting year 1	7
^{78}Kr	Starting year 1	3
^{124}Xe	Starting year 1	2
^{18}O, ^{16}O	Starting year 1	2
^{82}Se	Starting year 2	6
^{92}Mo	Starting year 2	3
^{58}Ni, ^{22}Ne, ^{64}Ni	Starting year 2	3

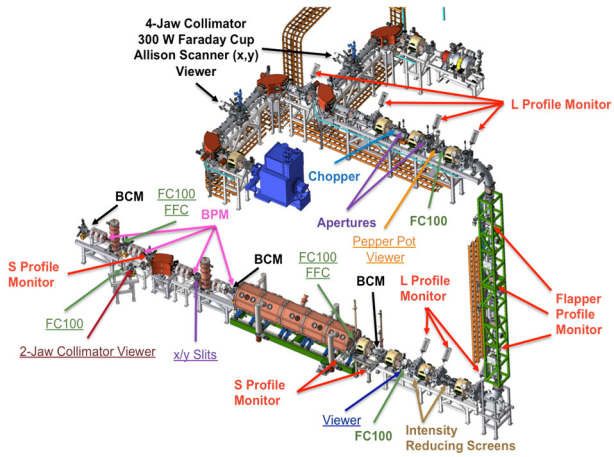

Figure 13: Front End beam instrumentation and diagnostics containing 12 types of 49 devices, as partly listed in Table 3.

Automated Tuning for Machine Availability

As a national user facility with over 1400 registered users, FRIB accelerator must operate with high availability (~ 90%) and reliability. Automated lattice tuning assisted by virtual accelerator modelling is being developed taking advantage of flexibility of the SRF linac. Table 4 shows the main diagnostics devices to be installed in the linac to facilitate operational availability [16]. In addition to permanently installed devices, a temporary diagnostics station is being prepared for staged beam commissioning starting from the first SRF linac section. As shown in Fig. 14, this temporary station contains two timing calibrated beam position monitors, a wire scanner, a Silicon detector, a bunch length monitor, halo monitor rings, and a beam current monitor.

ISBN: 978-3-95450-192-2 doi:10.18429/JACoW-IBIC2017-MO1AB1

Table 4: Main Permanently Installed Diagnostic Devices (560 in total) Located in the Front End (FE), Linear Segments 1, 2, and 3 (LS), and Folding Segments and Beam Delivery Segment (FS) of the FRIB Driver Linac

Device	FE	LS	FS	Total
Position monitor, BPM	4	103	43	150
Current monitor, ACCT	3		9	12
Current monitor, DCCT	1			1
Loss monitor, halo ring		17		17
Loss monitor, ion chamber		15	32	47
Loss monitor, neutron detector	1	22	1	24
Loss monitor, thermometry		192	48	240
Profile monitors	14	6	22	42
Bunch shape monitor			1	1
Allison emittance scanner	2			2
Pepper pot emittance meter	1			1
Faraday Cup; fast Faraday Cup	7, 2			9
Viewer plate	5			5
Selecting slits, 300 W	5			5
Collimation aperture, 100 W	2			2
Intensity reducing screen	2			2

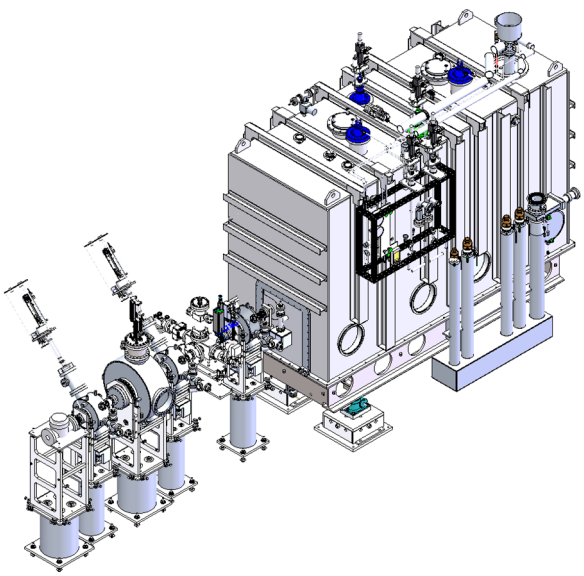

Figure 14: The temporary diagnostics station to be used for staged beam commissioning of the SRF linac containing two timing calibrated beam position monitors, a wire scanner, a Silicon detector, a bunch length monitor, halo monitor rings, and a beam current monitor.

TEAM AND COLLABORATIONS

FRIB accelerator is fortunate to attract many excellent technical leaders and subject matter experts worldwide with cultural background of more than 20 countries. At the peak of construction, a total of about 160 full-time-equivalent staff manage technical aspects of the procurements and perform in-house work. Efforts are made to form FRIB culture with project discipline, resource sharing (Fig. 15), and rigorous peer reviews.

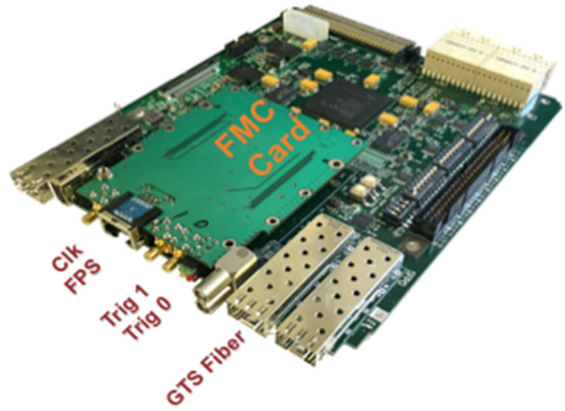

Figure 15: The FRIB general-purpose digital board (FGPDB) shared by several systems, including machine protection, controls, diagnostics, and low-level RF.

FRIB accelerator systems design and construction have been facilitated under work-for-others agreements with many DOE-SC national laboratories including ANL, BNL, FNAL, JLab, LANL, LBNL, ORNL, and SLAC, and in collaboration with institutes worldwide including BINP, KEK, IHEP, IMP, INFN, INR, RIKEN, TRIUMF, and Tsinghua University. The cryogenic system is developed in collaboration with JLab. The recent experience gained from design of the cryogenic system for the JLab 12 GeV upgrade is used in the design of both the refrigerator cold box and the compression system. The liquid lithium charge stripping system is developed in collaboration with ANL. BNL collaborated on the development of the alternative helium gas stripper. The SRF development benefited greatly from the expertise of the low-β SRF community. FRIB has been collaborating with INFN on resonator development and with ANL on RF coupler and tuner development, and is assisted by JLAB on cryomodule design, by KEK on superconducting solenoids, and by FNAL and JLab on cavity treatments. FRIB is collaborating with LBNL on the development of VENUS-type ECR ion sources.

Experienced industrial suppliers worldwide have been assisting FRIB accelerator construction following established procurement processes.

FUTURE PERSPECTIVE

Following beam commissioning of the FRIB Front End, early operation is expected to start in 2018 with ECR ion source user program developments. As rest of the accelerator is built and installed, project construction completion (CD-4) is expected in 2022.

After reaching the project CD-4 milestone for routine operations as a user facility, we expect to steadily increase the beam power and raise the machine availability, reliability and tuneability to the full design capability in 4 years. Beam power ramp up consists of three elements: fine-tuning of components dedicated for high power beam operation, including the high power ion source, liquid lithium charge stripper, and high power charge selector;

ISBN: 978-3-95450-192-2 doi:10.18429/JACoW-IBIC2017-MO1AB1

tuning for multi-charge-state beam acceleration; and beam quality improvement, including beam loss mitigation.

Science-driven upgrade plans include doubling the linac output energy by filling the vacant slots in the linac tunnel with β_0=0.65 cryomodules, simultaneous heavy ion and light ion acceleration, an ISOL (Isotope Separation On-Line) option for rare isotope production, and storage rings for rare isotopes. Design studies and prototyping efforts for the energy upgrade have been launched.

ACKNOWLEDGMENTS

We thank the FRIB Accelerator Systems Advisory Committee for their valuable guidance, colleagues who participated in FRIB accelerator peer reviews including G. Ambrosio, J. Anderson, D. Arenius, W. Barletta, G. Bauer, G. Biallas, J. Bisognano, S. Bousson, S. Caspi, M. Champion, M. Crofford, C. Cullen, D. Curry, R. Cutler, G. Decker, J. Delayen, J. Delong, G. Dodson, H. Edwards, J. Error, J. Fuerst, F. Kornegay, K. Kurukawa, J. Galambos, J. Galayda, G. Gassner, P. Ghoshal, J. Gilpatrick, C. Ginsburg, S. Gourlay, M. Harrison, S. Hartman, S. Henderson, G. Hoffstaetter, J. Hogan, S. Holmes, M. Howell, R. Kersevan, A. Hodgkinson, N. Holtkamp, H. Horiike, C. Hovater, H. Imao, R. Janssens, R. Keller, J. Kelley, P. Kelley, J. Kerby, A. Klebaner, J. Knobloch, R. Lambiase, M. Lamm, Y. Li, C. LoCocq, C. Luongo, K. Mahoney, J. Mammosser, T. Mann, W. Meng, N. Mokhov, Y. Momozaki, G. Murdoch, W. Norum, H. Okuno, S. Ozaki, R. Pardo, S. Peggs, R. Petkus, C. Pearson, F. Pellemoine, T. Peterson, C. Piller, J. Power, T. Powers, J. Preble, J. Price, D. Raparia, J. Rathke, A. Ratti, T. Roser, M. Ross, R. Ruland, J. Sandberg, R. Schmidt, W.J. Schneider, D. Schrage, I. Silverman, K. Smith, J. Sondericker, W. Soyars, C. Spencer, R. Stanek, M. Stettler, W.C. Stone, J. Stovall, H. Strong, S. Sharma, Y. Than, J. Theilacker, Y. Tian, J. Tuozzolo, V. Verzilov, R. Vondrasek, P. Wanderer, P. Wright, H. Xu, L. Young, and A. Zaltsman, and colleagues who advised and collaborated with the FRIB team including A. Burrill, A.C. Crawford, K. Davis, X. Guan, P. He, Y. He, A. Hutton, S.H. Kim, P. Kneisel, R. Ma, K. Macha, G. Maler, E.A. McEwen, S. Prestemon, J. Qiang, T. Reilly, R. Talman, J. Vincent, X.W. Wang, J. Xia, Q.Z. Xing. The FRIB accelerator design is executed by a dedicated team in the FRIB Accelerator Systems Division with close collaboration with the Experimental Systems Division headed by G. Bollen, the Conventional Facility Division headed by B. Bull, the Chief Engineer's team headed by D. Stout, with support from the FRIB project controls, procurement, and ES&H teams, and from NSCL and MSU.

REFERENCES

[1] J. Galambos, in *Proc. PAC'13*, Pasadena, 2013, p. 1443.
[2] K. Hasegawa *et al.,* in *Proc. IPAC'13*, Shanghai, 2013, p. 3830.
[3] M. Seidel *et al.,* in *Proc. IPAC'10*, Kyoto, 2010, p. 1309.
[4] R.W. Garnett *et al.,* in *Proc. PAC'11*, New York, 2011, p. 2107.
[5] J. Wei *et al.,* in *Proc. LINAC'12*, Tel-Aviv, 2012, p. 417.
[6] E. Pozdeyev *et al.*, in *Proc. PAC'13*, Pasadena, 2013, p. 734.
[7] J. Wei, *Rev. Mod. Phys.* 75, 2003, p.1383.
[8] G. Machicoane *et al.*, in *Proc. PAC'09*, Vancouver, 2009, p. 432
[9] F. Casagrande, presented at IPAC'15, Richmond, 2015, Talk THYB1.
[10] V. Ganni *et al.*, *CEC-ICMC 59*, 323 (2013).
[11] T. Xu *et al.,* in *Proc. LINAC'16*, East Lansing, 2016, p. 673.
[12] A. Facco *et al.*, *Proc. IPAC'12*, New Orleans, 2012, p. 61.
[13] J. Nolen *et al.,* FRIB Report FRIB-T30705-TD000450, 2013.
[14] M. Ikegami, in *Proc. IPAC'15*, Richmond, 2015, p.2418.
[15] F. Pellemoine, *Nucl. Instrum. Meth.* B317, 369 (2013).
[16] S. Lidia *et al.*, in *Proc. IBIC '15*, Melbourne, 2015, p. 226.
[17] T. Glasmacher, presented at LINAC'16, East Lansing, 2016, Paper FR3A02.

ISBN: 978-3-95450-192-2 doi:10.18429/JACoW-IBIC2017-MO2AB2

OVERVIEW AND STATUS OF DIAGNOSTICS FOR THE ESS PROJECT

T. J. Shea*, R. Baron, B. Cheymol, C. Derrez, T. Grandsaert, A. Jansson, H. Hassanzadegan, I. Dolenc-Kittelmann, H. Kocevor, S. Molloy, C. Thomas
European Spallation Source, Lund, Sweden
E. Adli, U. Oslo, Oslo, Norway
M. Poggi, INFN, Legnaro, Italy
M. Ferianis, Sincrotrone Trieste, Trieste, Italy
I. Bustinduy, ESS Bilbao, Bilbao, Spain
P. Aden, STFC, Daresbury, UK
T. Papaevangenlou, J. Marroncle, L. Segui, CEA, Saclay, France
S. Vilcins, DESY, Hamburg, Germany
A. J. Johannson, LTH, Lund, Sweden

Abstract

The European Spallation Source, now under construction in Lund, Sweden, aims to be the world's most powerful pulsed neutron scattering facility. Driving the neutron source is a 5 MW superconducting proton linear accelerator operating at 4 percent beam duty factor and 14 Hz repetition rate. Nineteen partner institutions from across Europe are working with the Accelerator Division in Lund to design and construct the accelerator. The suite of accelerator instrumentation consists of over 20 unique system types developed by over 20 partners and collaborators. Although the organizational complexity presents challenges, it also provides the vast capabilities required to achieve the technical goals. At this time, the beam instrumentation team is in transition, completing the design phase while scaling up to the deployment phase. Commissioning of the ion source has commenced in Catania, preparations for installation on the Lund site are ramping up, and basic R&D on target instrumentation continues. Beam commissioning results from the systems immediately following the ion source will be presented, along with technical highlights and status of the many remaining instrumentation systems.

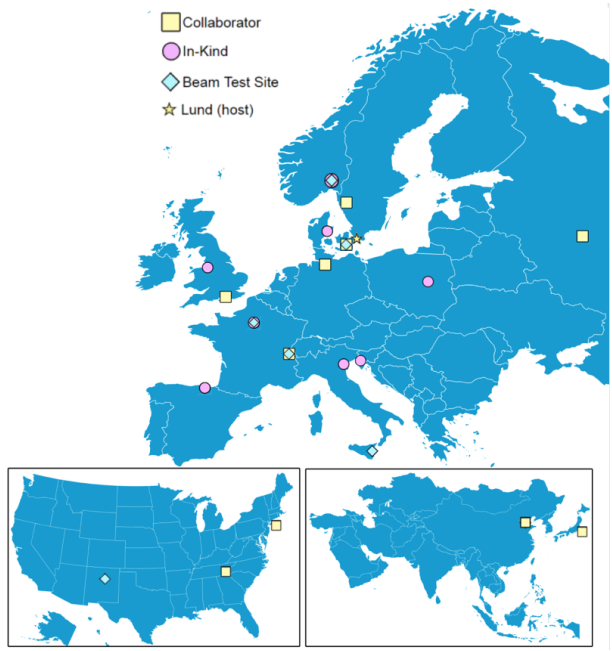

Figure 1: Map of In-kind partners, collaborators, and test sites.

OVERVIEW

The Project Organization

Like the ESS project itself, the beam diagnostics project is executed by an international partnership. Figure 1 illustrates the breadth of this organization, consisting of in-kind contributors from partner countries, collaborators that participate via memorandum or contract, and finally, several institutes that provide beam test facilities. From this partnership of over 20 institutions, all designs, components and completed systems are eventually delivered to the host facility, ESS in Lund, Sweden.

The Diagnostic Suite

As itemized in Table 1, the beam diagnostics team will deliver a comprehensive suite of instrumentation that supports commissioning and operations of the ESS accelerator. Reading from left to right in the table, the devices are deployed in the 75 keV transport line (LEBT) following the ion source, in the normal-conducting section ending with the drift tube linac (DTL), in the superconducting section ending with the high beta linac (HBL), and finally in the transport lines to the tuning dump and the target.

MEASUREMENT CAPABILITIES

The diagnostic systems provide three categories of measurement, the first being beam accounting. Throughout the machine, various diagnostic devices measure the beam current and where it is lost, starting from constituents of beam extracted from the ion source, then the proton current and losses throughout the accelerator, and finally the beam leaving aperture in the region of the tuning dump and the target.

* thomas.shea@esss.se

ISBN: 978-3-95450-192-2 doi:10.18429/JACoW-IBIC2017-MO2AB2

Table 1: Inventory of Diagnostics Throughout the ESS Machine

System	LEBT	RFQ	MEBT	DTL	Spk	MBL	HBL	HEBT	A2T	DumpL	TOTAL
Position	0	0	7	15	14	9	21	16	12	4	98
Ionization profile	0	0	0	0	1	3	1	0	0	0	5
Fluorescence profile	1	0	2	0	0	0	0	0	1	0	4
Ionization chamber	0	0	0	5	52	36	84	49	37	6	269
Neutron detector	0	0	5	11	14	4	0	1	0	0	35
Wire scanner	0	0	3	0	3	3	1	3	1	0	14
Bunch Shape	0	0	1	0	1	1	0	0	0	0	3
Faraday cup	1	0	1	2	0	0	0	0	0	0	4
Current monitor	1	1	4	5	0	1	1	2	3	2	20
Emittance	1	0	1	0	0	0	0	0	0	0	2
Aperture monitor	0	0	0	0	0	0	0	0	3	1	4
Doppler	1	0	0	0	0	0	0	0	0	0	1
Multi-wire grid	0	0	0	0	0	0	0	0	1	0	1

With beam accounted for, instrumentation from the other two categories, centroid measurements and distribution measurements provide a more detailed characterization of the beam properties.

Beam Accounting

Doppler System The Doppler system measures the species fraction with a non-intercepting technique based on neutralization of ion beam particles passing through the residual gas [1–3]. It was used for the characterization of the high intensity beams at ATP and LEDA [4], on the LEBT lines at SILHI, IFMIF and ESS [5], and also for the characterization of neutral beams in tokamaks [6]. The instrument is composed of a high sensitivity and high resolution spectrometer[1], a 25 m long fiber bundle in a round end to linear end configuration, and an optimized lens coupling assembly matching the geometry imposed by the viewport of the vacuum tank. Through the viewport, the spectrometer acquires a spectrum of the beam luminescence at 14 Hz, triggered by the machine timing system. Each spectrum is analyzed to deliver a species fraction measurement.

The instrument has been delivered and commissioned on the ESS source at INFN in Catania. It met the design performance, and by adjusting the spectrometer exposure and the trigger delay, it performs not only single shot measurements, but also intra-pulse measurements. The details of the measurement performance have been published elsewhere [7], and a typical spectrum is presented in Figure 2.

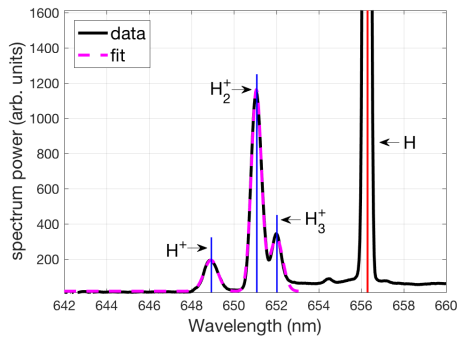

Figure 2: Typical spectrum from the Doppler system showing the Balmer α ray and Doppler shifted rays of H, H_2 and H_3. The vertical lines are positioned using the Doppler shift equation, the mass and energy of the species, and the geometrical angle of observation.

Beam Current Monitors The Beam Current Monitor (BCM) system in total consists of 20 sensors: 18 AC Current Transformers and 1 Fast Current Transformer all from Bergoz, as well as one specially instrumented position monitor electrode that is planned for bunched beam current measurements downstream of the MEBT chopper. Most of the sensors will be provided by the ESS in-kind partners as integral parts of the different linac sections. As with most other diagnostic systems, the BCM electronics is based on the MicroTCA.4 platform, and in this case will include a Struck SIS8300-KU as the digitizer. An external, custom front-end unit provides a calibrator, a remote sanity check, signal conditioning and a redundant power module [8]. Signal processing functions, implemented on a Field Programmable Gate Array (FPGA), provide machine protection and beam monitoring functions and has been developed together with DESY and Cosylab. It is currently being tested and verified at ESS. An AC Current Transformer and an early version of the MTCA-based electronics were deployed in Catania to measure the current of the 75 kV ion source power supply. Although not a direct measurement of extracted proton beam current, the results in Figure 3 demonstrate that the system can meet performance requirements in an accelerator environment.

Like the other systems responsible for machine protection, the BCM system must provide low latency. To keep latency

[1] Shamrock500i with a cooled CCD camera Newton 920, from ANDOR

ISBN: 978-3-95450-192-2 doi:10.18429/JACoW-IBIC2017-MO2AB2

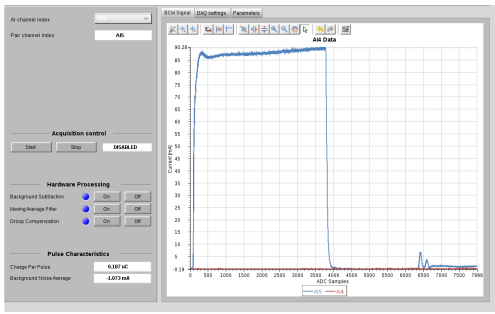

Figure 3: Current of the power supply extracting a beam pulse from the ESS ion source.

below 2 µs, the system uses fast ADCs running at 88 MSa/s, FPGA-based processing, short cables and fast analog electronics. The ADC data is low-pass filtered and decimated in the FPGA, thus resulting in a sample rate of 11 MSa/s with the advantage of reducing noise and data traffic on the network, and without compromising the useful bandwidth of 1 MHz. Also, data at the full sample rate is buffered in local memory for test and data-on-demand purposes. Future improvements include an optical link for differential current measurement over large distances, automatic setting of the machine protection parameters based on the machine state, and automatic calibration.

Faraday Cups The Faraday cups primarily provide destinations for the beam in the normal conducting linac during start up and tuning operations. Particularly at low energies, they also measure the current with reasonable accuracy. The LEBT Faraday cup was fully commissioned in late 2016, and this Faraday cup is the only one able to handle the full ESS beam duty factor. PANTECHNIK designed and constructed this Faraday cup based on ESS specifications. The other Faraday cups are able to withstand a small fraction of the beam power and will be used more as beam stops. ESS-Bilbao has designed the MEBT Faraday cup and began the fabrication process in mid-2017. At the time that this paper was written, the two other Faraday cups located in the DTL are still under design at ESS.

Beam Loss Monitors Loss of even a small fraction of the intense ESS beam could result in significant radiation and destruction of accelerator equipment. The Beam Loss Monitor (BLM) systems are the only diagnostics capable of detecting the smallest fraction of beam loss, approaching parts per million, that could activate machine components and prevent hands-on maintenance. Two types of detectors will be deployed, each providing unique capabilities. The first type is an ionization chamber (ICBLM) that provides a simple and proven detector, but lacks the ability to discriminate against background from the accelerating structures. The second type is a neutron detector (nBLM) of higher complexity, but with the ability to discriminate between neutrons produced by loss of even low energy protons, and photons produced by field emission in the cavities. Monte Carlo simulations are used to optimize the locations of the detectors, such that coverage and redundancy are provided for machine protection purposes, and spatial resolution is provided for diagnostic purposes [9].

The ICBLM detectors are parallel-plate gas ionization chambers developed by CERN for LHC and manufactured and tested at the Institute for High Energy Physics, Protvino, Russia. They are chosen for the ESS linear accelerator due to their fast response, stable gain, robustness against aging, large dynamic range (about 8 decades), and the low required maintenance. The ICBLM detector is very sturdy, its radiation resistance is very good.

As shown in Table 1, ICBLM detectors are located throughout the accelerator, and the total quantity is high enough to afford some redundancy. Adjustable mounts will allow refinement of the layout based upon initial operational experience. 285 detectors were received at ESS in July 2017 and are now under reception and calibration tests [10].

The baseline for the ICBLM readout electronics is an 8-channel, 20-bit commercial-off-the-shelf picoammeter in MTCA format. Its full-scale ranges of 500 µA and 10 mA, together with a 300 kHz input bandwidth ensure it fulfills ESS requirements. A complete evaluation of this readout solution is being performed by the Beam Diagnostics team in Lund and Figure 4 depicts an example of the test results. An alternative solution involving a custom acquisition crate equipped with the latest CERN BLEDP prototype is being evaluated. Two BLEDP acquisition cards have been received at ESS, featuring an advanced current-to-frequency converter covering the 10 pA to 30 mA range. To support testing in the ESS controls environment, a readout has been implemented with an FPGA-based platform in MTCA. A double width AMC HV power supply in MTCA format is being evaluated as well, giving a complete ICBLM system prototype. The final ICBLM system layout will be fixed in early 2018, and at the same time, the corresponding selection of the electronics will be made based on the evaluation results.

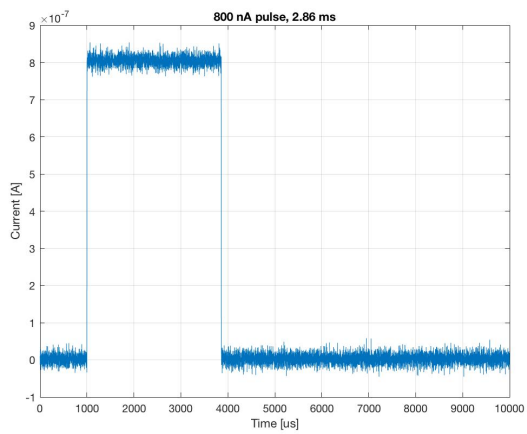

Figure 4: A test pulse corresponding to the smallest beam loss rate that the ICBLM system must measure. The signal was acquired by prototype current readout electronics.

ISBN: 978-3-95450-192-2 doi:10.18429/JACoW-IBIC2017-MO2AB2

The nBLM detectors are based on Micromegas devices specially designed to be sensitive to fast neutrons and insensitive to low energy photons. In addition, the detectors will be as insensitive as possible to thermal neutrons. The nBLM system will complement the ICBLM systems, being optimized to operate in the low energy region of the accelerator, where almost none of the charged particles escape the vacuum envelope. The Micromegas detectors will be equipped with appropriate neutron-to-charge converters and absorbers to fulfill these requirements. Two detection techniques will be implemented: the fast detector relies on proton recoils produced by the elastic scattering of a neutron in a hydrogen-rich converter, and the slow detector uses a Boron-10 converter that moderates the neutrons first to increase the efficiency. A 3D model of the detector package is shown in Figure 5.

A total of 42 fast detectors and 42 slow detectors will be delivered from CEA-Saclay to Lund by April 2019. The layout is still being refined, with a focus on providing complete coverage in the low energy end of the linac, plus several additional channels for development purposes in the high energy end. Using ESS loss scenarios as input [9,11], Monte Carlo simulations performed with GEANT4 show that the detectors give a multiple counts within 1 µs when low energy protons are lost at a low level of 0.01 W/m. At high loss levels, the system will experience pileup and eventually transition from event mode to current mode readout. The CEA-Saclay team has commenced laboratory testing of the first prototypes and in Fall 2017, they will begin testing at different radiation facilities to study response in high radiation environments with different source particles. The final design of the detectors, the electronics and the control system will be completed by May 2018 and the foreseen installation and commissioning will start by the end of 2018.

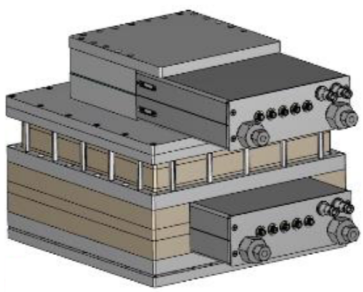

Figure 5: The neutron detector package, showing the fast detector on top and the slow detector surrounded by its polyethylene moderator below.

Aperture Monitors The Aperture Monitors measure the portion of the beam current that exits the physical aperture. They are used for tuning as well as for machine protection. The instrument detects the prompt current induced by the proton beam as it passes through metallic plates, and the slower temperature rise of low-mass temperature sensors that surround the aperture. There are 4 Aperture Monitors in the accelerator: one in front of the tuning Dump, two in the target station, and one at the final beam waist located about 20 meters upstream of the target. The first 3 are fixed in transverse position and consist of 16 Nickel plates and 12 thermal sensors surrounding the aperture. The 4th one consists of 4 movable plates and thermal sensors that can be adjusted to intercept only the halo of the focussed beam. The current induced in the plates is measured with a 300 kHz bandwidth, while the signal from the thermal sensors is constrained by thermal mass to much lower bandwidth.

Centroid Measurements

Once beam current is accounted for, the single particle understanding of the machine is verified and refined through 3D measurements of the bunch centroid, including phase and transverse position. The primary system for these measurements, and the only one distributed throughout the accelerator is the Beam Position Monitor (BPM) system. In addition, a few additional systems provide centroid measurements at locations that lack BPMs.

Beam Position Monitors The ESS linac will be instrumented with 98 BPMs, the majority of which are designed to have their peak spectral response at the beam bunching frequency. In the sections of the linac where the accelerating RF is also at the bunching frequency, the BPM receivers are tuned to the 2nd harmonic. The MEBT and the DTL BPM electrodes are shorted striplines, with those in the DTL tanks being embedded inside drift tubes. Throughout the remainder of the linac, the electrodes are buttons.

The electronics design is based on the same commercial MicroTCA.4 digitizer that is used in the BCM system, complemented by a commercial transition module and also a custom RF Front-End chassis for RF filtering, calibration and gain adjustment. The electronics can be tuned to 352 MHz or 704 MHz by selecting the proper bandpass filters and analog down-conversion local oscillator frequency.

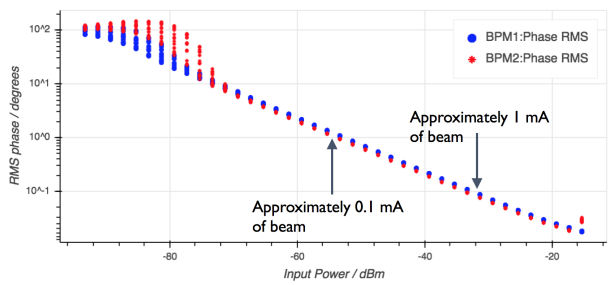

Figure 6: BPM electronics prototype results showing measured RMS phase over a range of input power.

Figure 6 shows the most recent results from a test of the prototype electronics. Performance is characterized over the range of input power expected for the ESS linac. The input power was swept over this very wide range, and the RMS of phase and other parameters for a 2 MHz readout signal bandwidth were recorded. This demonstrates that the performance meets requirements for measuring beam phase

ISBN: 978-3-95450-192-2 doi:10.18429/JACoW-IBIC2017-MO2AB2

with respect to the Phase Reference Line (0.1 degrees RMS at nominal beam parameters).

Additional centroid measurements All of the of the systems described in the next section also provide centroid measurements, but a few merit special attention because of their unique capability or location. In the LEBT, there is no RF structure that provides a signal to the BPM system, so the Non-invasive Profile Monitors measure the transverse position. In the target station, the Grid and the Imaging systems support centering of the beam footprint.

Distribution Measurements

Beyond the centroid measurements, distribution measurements deliver the next level of detail about proton beam properties. In most cases, the cost of obtaining this detail is the need to perform invasive measurements, typically during special modes of operation that limit beam duty factor. Some systems allow measurements during full duty factor operation by employing inherently non-invasive techniques (Non-invasive Profile Monitor), by employing invasive techniques for brief periods of time (fast wire scanners), or by operating on or in a structure designed to receive the full beam current (Grid and Imaging systems).

Emittance Measurement Units Two Emittance Measurement Units (EMU) will be installed in the ESS linac. The first one is an Allison scanner in the LEBT, and is already installed and commissioned at the ion source test stand located at INFN-LNS in Catania. This EMU is able to measure the full beam power at the exit of the ion source with a time resolution of 1 µs. A time-resolved measurement result is shown in Figure 7. The second EMU will be installed in the MEBT, and it is based on slit and grid system built at ESS-Bilbao. A design concept has been analyzed and performance of the device has been predicted [12].

Bunch Shape Monitors The bunch length will be measured in the MEBT, at the transition between the warm and cold linac, and within the cold linac by utilizing 3 Bunch Shape Monitors designed and constructed by INR. The resolution of the instrument is 0.5 degrees.

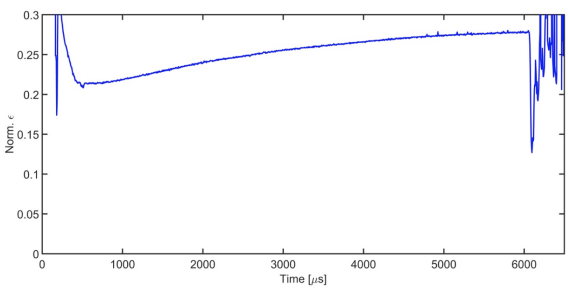

Figure 7: Time-resolved emittance of 75 keV beam measured directly after the ion source in Catania.

Invasive Profile Monitors: Wire Scanners and Grid In normal-conducting and superconducting sections of the ESS linac, 11 wire scanner systems will be installed, and for all of them, the profiles will be reconstructed by measuring the secondary emission signal from the wire. In addition, the wire scanners installed in the elliptical sections and downstream will be equipped with a scintillator in order to measure the shower created by the interaction of the beam with the wire [13, 14]. The operation of the wire scanner is limited by the thermal load on the wire, so the beam duty cycle must be reduced to preserve the wire integrity. Measurement at full beam power will be possible by using 3 fast wire scanner stations in the transport line that follows the linac. The simulation results shown in Figure 8 demonstrate that peak wire temperature stays below the melting point of carbon throughout a scan of the proton beams expected in this section of the machine. The design and fabrication of these fast wire scanners is done at CERN and the readout system will be similar to that of the other wire scanners.

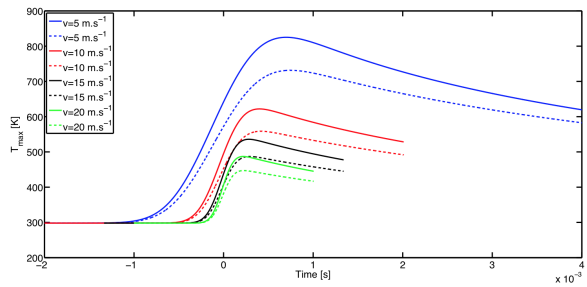

Figure 8: Simulation of wire peak temperature during a scan at 560 MeV (solid line) and 2000 MeV (dashed line) for different wire velocities.

In the target station, a multi-wire grid system is being designed at ESS, with support of collaborators from cADS, J-Parc, and SNS. The main function of the Grid is to provide two 1D profiles of the beam on target. The grid is fixed in position within the diagnostics plug in the the target monolith. Unlike the wire scanners upstream, this device only intercepts a reduced-density beam that has been prepared for delivery to the target by expansion and/or rastering. With the wire temperature moderated by the low beam current density and the resulting radiation shielded by the target monoilith, this device can measure full duty-factor beam.

Non-invasive Profile Monitors Non-invasive Profile Monitors (NPM) are designed to measure beam profiles of long pulses when the wire scanners cannot be used. For pulses at full peak current, this includes pulse lengths from 50 µs to 3 ms. There are two types of NPMs designed for the ESS. One is the Beam Induced Fluorescence (BIF) monitor based on imaging the beam-induced fluorescence of the residual gas, and the other is an Ionization Profile Monitor (IPM) based on collecting charge from beam induced ionization of the residual gas. The BIF is designed and constructed at ESS, whereas the IPM is designed and constructed by CEA-Saclay as an in-kind contribution. The first

ISBN: 978-3-95450-192-2 doi:10.18429/JACoW-IBIC2017-MO2AB2

BIF system has been delivered for the LEBT, and is waiting for commissioning with beam [15], and the IPM prototypes are being prepared for testing in Saclay.

Imaging Imaging systems produce a 2D map of the beam's transverse current distribution on the Target and the Tuning Dump [16] and are a key component of the beam-on-target instrumentation suite [17]. They are the only instruments capable of directly measuring with the required precision the beam current footprint on Target during production. They are also sensitive enough to detect unrastered short pulses for system calibration and beam tuning purposes. There are two imaging systems in the target area, one looking at the target wheel, and one looking at the Proton Beam Window. They are redundant, but also can be used to measure the beam divergence. Fiducials at the object plane allow geometric calibration of the beam measurement, and also allow measurement of the target wheel position with respect to the neutron moderator position. An additional imaging system measures beam as it approaches the tuning dump.

Many challenges have to be overcome to deliver these imaging systems, primarily due to the radiation environment. The source for imaging the protons is a luminescent material, coated on beam-intercepting components. This material must be luminescent at the high temperature induced by the primary beam and secondary particles from the target, and it has to remain luminescent for the lifetime of the device, i.e. 5 years for the target wheel and 2 years for the proton beam window. In addition, and particularly for the moving target wheel, the luminescence decay time should be shorter than 10 μs in order to provide a still image of the beam [18]. Studies are being carried out in order to downselect the best candidate materials. These studies include long irradiation campaigns. This first one that has started recently, is an irradiation of 2 kinds of materials, chromium alumina and yttria, at Brookhaven National Laboratory's BLIP facility, under the RaDIATE collaboration [19]. After a series of post irradiation examinations, these materials will be qualified in proton beams at DTU and at higher energy facilities available at LANL and J-PARC.

Optics design is also affected by the target environment. The radiation shielding requirements mandate a small numerical aperture for the optical system, limiting not only the transmission, but also placing severe constraints on position and size of the optical elements. In addition, the radiation from the target will heat the first optical elements, potentially disrupting the image quality. It may also induce chemical reactions that can affect the reflectance of the mirror. For instance, a water and air leak, common in high power target stations, can lead to formation of acids that will rapidly attack and damage the surface of the mirrors. Downselection of optical component material and coating is proceeding with a goal of mitigating these issues. An optical design has already been simulated and prototyped at University of Olso as shown in Figure 9.

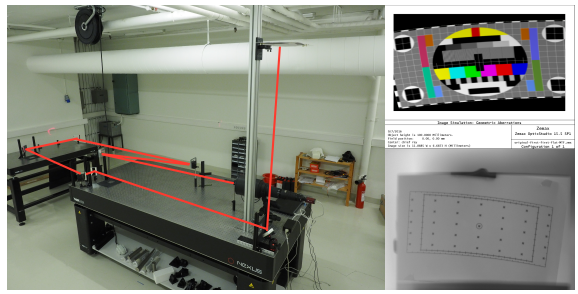

Figure 9: Prototype of the optical system at the University of Oslo. The image target is shown on the bottom right, and the Zemax simulation on the top right. The agreement shows that the performance in design and in reality are matched.

PROTECTION STRATEGY

Several beam diagnostic systems provide input to the beam interlock system, reporting potentially damaging beam conditions before damage occurs. With a processing latency on the order of microseconds, these diagnostic systems calculate the response of machine components to primary protons and secondary particles, producing a scaler value called damage potential. When this value exceeds a predetermined threshold, the beam interlock system can suppress beam production within microseconds to tens of microseconds. To achieve this performance and the required availability, these protection functions are implemented in field programmable gate arrays. Two general classes of damaging conditions are detected by the appropriate diagnostic devices: beam loss in the linac, and errant beam properties at destinations.

Beam Loss in the Linac

The BCM, nBLM, and ICBLM systems measure beam loss in the linac. All three are capable of detecting peak current losses that exceed 2% of the nominal 62.5 mA peak current. Below this level, errors could dominate the current difference reported by the BCM system, yet some accelerator components can still be damaged by an integrated loss exceeding about one μC within the diffusion time constant. Therefore, the nBLM and ICBLM provide exclusive coverage for low level losses over a pulse or even multiple pulses.

Over much longer time scales, an average loss limit of 1 W/m should lead to acceptable activation levels in the accelerator tunnel and acceptable lifetime of radiation sensitive components. Temporarily, machine studies and other activities could produce elevated losses, and these would be managed by an activation plan and monitored by the nBLM and ICBLM systems.

Utilization of multiple signals communicated over low-latency links will provide additional robustness and protection capability. Protection functions that combine signals from multiple beam loss detectors can increase immunity to anomalous single-channel errors like sparks, and reduce sensitivity to the spatial distribution of the lost beam. Time-of-flight measurements by the BPM system can detect beam

ISBN: 978-3-95450-192-2 doi:10.18429/JACoW-IBIC2017-MO2AB2

energy deviations before they exceed the acceptance of the accelerator. For some failures, like RF faults that occur during a beam pulse, the beam production could be suppressed *prior* to beam loss.

Beam Properties at Destinations

Properly tuned, the ESS accelerator transports beam with low loss to one of several intended destinations, from insertable Faraday cups, to the fixed tuning dump and finally, to the target station. These destinations vary in their beam handling capabilities, and a suite of diverse and redundant instrumentation systems assure that beam properties do not exceed specified limits [20]. A combination of the two imaging systems and multiwire Grid protect the target station from high current density that could overheat the beam windows or the target elements. Just upstream of the tuning dump, an imaging system provides similar protection. At both of these locations, aperture monitors protect against energy deposition in the vacuum envelope and shielding just upstream of the target and dump.

When beam enters a section of accelerator that has not been verified, the destination must be assumed to be anywhere in this section, including the most sensitive components. Even after tuning and verification of a section, the ultimate destination might only be configured to absorb a limited charge per pulse and average beam current. From start up with initial test pulses through operations with fully verified beam transport, the BCM system in the low energy end of the linac will verify that beam pulse parameters are consistent with intentions.

OUTLOOK

During 2017, beam measurements at CEA-Saclay and ion source commissioning in Catania provided valuable experience and demonstrated that the initial BCM, Doppler, Emittance, and Faraday cup systems achieved their performance requirements. In early 2018, these same systems will be deployed in Lund, Sweden to measure the first proton beam at the ESS site. In 2019, most types of diagnostic systems will be deployed and commissioning of bunched beam will commence.

ACKNOWLEDGMENTS

The ESS beam diagnostics team gratefully acknowledges INFN colleagues in Catania for designing and commissioning the ion source and LEBT, which provided beam for the commissioning of the initial diagnostic systems. Every diagnostic system depends on technology and service provided by the ESS Integrated Control System division, is integrated into the accelerator with the help of the ESS Linac Group, and benefits from the clear requirements provided by the ESS Beam Physics section.

REFERENCES

[1] L. Philpot, R. Hugues, and C. Fan, "Spectra induced by 200keV proton impact on nitrogen," *Physical Review*, vol. 123, no. 6, 1961.

[2] M. S. D. Jong and N. Rowlands, "Proton beam diagnostics using optical spectroscopy," *Nucl. Instrum. Methods Phys. Res. B*, vol. 10, pp. 822–824, 1985.

[3] G. Bolme, L. Hansborough, T. Hardek, D. Hodgkins, E. Meyer, C. Rose, J. D. Schneider, J. D. Sherman, H. V. Smith Jr., M. Stettler, R. R. Stevens Jr., M. Thuot, T. Zaugg, A. Arvin, A. S. Bolt, M. Richards, J. Kamperschroer, P. Balleyguier, and R. Ferdinand, "A DC proton injector for use in high-current CW linacs," in *Proc. EPAC'98*, pp. 1424–1426, 1998.

[4] J. H. Kamperschroer, J. D. Sherman, T. J. Zaugg, A. H. Arvin, A. S. Bolt, and M. C. Richards, "Doppler-shift proton fraction measurement on a CW proton injector," in *Proc. LINAC'98*, Chicago, IL, USA, pp. 511–513, 1998.

[5] F. Senée, G. Adroit, R. Gobin, B. Pottin, and O. Tuske, "Beam species fraction measurement using doppler shift method with Fujikura fiberscope for IFMIF-Eveda injector," in *Proc. DIPAC'11*, (Hamburg), pp. 407–409, 2011.

[6] R. Uhlemann, R. S. Hemsworth, G. Wang, and H. Euringer, "Hydrogen and deuterium ion species mix and injected neutral beam power fractions of the TEXTOR-PINIs for 20-60 kV determined by Doppler shift spectroscopy," *Review of Scientific Instruments*, vol. 64, no. 4, pp. 974–982, 1993.

[7] C. Thomas *et al.*, "Development and commissioning of the Doppler-shift unit for the measurement of the ion species fractions and beam energy of the ESS proton source," in *Proc. of International Particle Accelerator Conference (IPAC'17)*, Copenhagen, Denmark, pp. 936–938, May 2017.

[8] H. Hassanzadegan, M. Donna, A. Jansson, H. Kocevar, T. Shea, and M. Werner, "Implementation issues and first results of the ESS beam current monitor system," in *Proc. of International Particle Accelerator Conference (IPAC'17)*, Copenhagen, Denmark, pp. 745–747, May 2017.

[9] I. Dolenc Kittelmann and T. Shea, "Simulations and detector technologies for the beam loss monitoring system at the ESS linac," in *Proc. 57th ICFA Advanced Beam Dynamics Workshop on High-Intensity and High-Brightness Hadron Beams (HB'16)*, Malmö, Sweden, July 3-8, 2016, pp. 553–558, 2016.

[10] V. Grishin, B. Dehning, A. Koshelev, A. Larionov, V. Seleznev, and M. Sleptsov, "Ionization chambers as beam loss monitors for ESS linear accelerator," in *Proc. of International Beam Instrumentation Conference (IBIC'17)*, Grand Rapids, Michigan, 2017.

[11] M. Eshraqi, R. De Prisco, R. Miyamoto, and Y. I. Levinsen, "Preliminary study of the possible failure modes of the components of the ESS linac," Tech. Rep. ESS-0031413, ESS, 2015.

[12] B. Cheymol and A. Ponton, "Accuracy determination of the ESS MEBT emittance measurements," in *Proc. of 27th Linear Accelerator Conference (LINAC'14)*, Geneva, Switzerland, August 31-September 5, 2014, TUPP039, 2014.

[13] B. Cheymol, "Effect of beam losses on wire scanner scintillator readout, hypothesis and preliminary results," in

ISBN: 978-3-95450-192-2 doi:10.18429/JACoW-IBIC2017-MO2AB2

Proc. of 57th ICFA Advanced Beam Dynamics Workshop on High-Intensity and High-Brightness Hadron Beams (HB'16), Malmö, Sweden, July 3-8, 2016, pp. 216–220, 2016.

[14] B. Cheymol, "Scintillator detectors for the ESS high energy wire scanner," in *Proc. of 57th ICFA Advanced Beam Dynamics Workshop on High-Intensity and High-Brightness Hadron Beams (HB'16)*, Malmö, Sweden, July 3-8, 2016, pp. 232–236, 2016.

[15] C. Thomas *et al.*, "Design and implementation of non-invasive profile monitors for the ESS LEBT," in *Proc. of International Beam Instrumentation Conference (IBIC'16)*, Barcelona, Spain, Sept. 13-18, 2016, no. 5, pp. 552–555, February 2017.

[16] E. Adli *et al.*, "The ESS target proton beam imaging system as in-kind contribution," in *Proc. of International Particle Accelerator Conference (IPAC'17)*, Copenhagen, Denmark, International Particle Accelerator Conference, pp. 3422–3425, May 2017.

[17] T. Shea, C. Böhme, B. Cheymol, S. Gallimore, H. Hassanzadegan, E. Pitcher, and H. D. Thomsen, "Proton beam measurement strategy for the 5 MW European Spallation Source target," in *Proc. IBIC'13*, TUPC02, Oxford, UK, 2013.

[18] C. Thomas *et al.*, "Preliminary measurement on potential luminescent coating material for the ESS target imaging systems," in *Proc. of International Beam Instrumentation Conference (IBIC'16)*, Barcelona, Spain, Sept. 13-18, 2016, pp. 560–563, 2017.

[19] K. Ammigan *et al.*, "The RaDIATE high-energy proton materials irradiation experiment at h brookhaven linac isotope producer facility," in *Proc. of International Particle Accelerator Conference (IPAC'17)*, Copenhagen, Denmark, pp. 3593–3596, May 2017.

[20] T. J. Shea, L. Coney, R. Linander, A. Jansson, E. J. Pitcher, A. Nordt, C. Thomas, and H. D. Thomsen, "Instrumentation and machine protection strategy for the ESS target station," in *International Collaboration of Advanced Neutron Sources ICANS XXI*, Mito, Japan, 2014.

ISBN: 978-3-95450-192-2 doi:10.18429/JACoW-IBIC2017-MO2AB3

SESAME STORAGE RING DIAGNOSTICS AND COMMISSIONING

H. Al-Mohammad, K. Manukyan, SESAME, Allan, Jordan

Abstract

SESAME Storage Ring is a 2.5 GeV Synchrotron Light Source in Allan, Jordan. The commissioning of the Storage Ring has been done in spring 2017. The storage ring is equipped with 64 BPMs whereas 48 connected to Libera-Brilliance+, three fluorescent screens, one FCT, one DCCT, four BLMs, two Bunch by Bunch kickers and one Synchrotron Radiation Monitor. This paper gives an overview of the Diagnostics elements and our experience during the commissioning.

INTRODUCTION

The SESAME Storage Ring (SR) shown in Fig. 1 is a 2.5 GeV Light Source of 133.2 m circumference composed of 8 DBA cells with dispersion in all straight sections (8*4.4 m and 8*2.4 m), offers a maximum capacity of 25 beamlines [1]. The RF system consists of four 500 MHz ELETTRA cavities powered by four 80 kW Solid State Amplifiers [2]. A 800 MeV Booster Synchrotron (original from BESSY I) injects the beam into the SR with 1 Hz repetition frequency. The SR main parameters are listed in Table 1.

Table 1: Storage Ring Main Parameters

Energy (GeV)	2.5
Circumference (m)	133.2
RF Frequency (MHz)	499.654
Repetition freq.(Hz)	1
Betatron tunes Q_X / Q_Y	7.23 / 6.19
Horizontal emittance ε_x (nm.rad)	26
Momentum compaction factor	0.0083
Circulating Current(mA)	250
Energy loss per turn (keV)	603

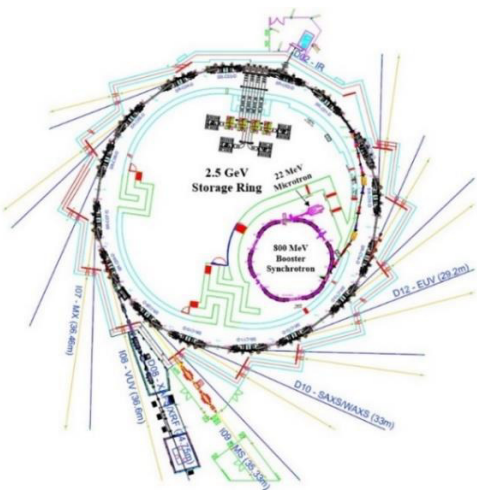

Figure 1: SESAME Facility.

Commissioning of the Microtron had been done in 2012, commission of the Booster in 2014 and of the SR in 2017. Throughout the commissioning, the Diagnostics components are key elements to check SR performance a set of equipment's are installed in the machine in order to measure electron beam current, transverse shape, position inside the vacuum chamber and orbit, tune, chromaticity and emittance. In the following, we present the different diagnostics elements installed in the SR and our experience during the commissioning.

BPM SYSTEM

There are 64 button type beam position monitor (BPM) in SR, which are distributed around the ring as 4 BPMs/cell, two of them flanking the bending magnet and two at beginning and end of the straight sections, 48 of them are connected to Libera Brilliance + [3] and one BPM is connected to a Spectrum Analyser. The BPMs are connected to the Libera B+ by low attenuation RF cables with different lengths (20 m-45 m). 8 Libera B+ units are equipped with GDX (Gigabit Data eXchange) module for FOFB which will be done by using 32 BPM, 4 GDX modules are donated from Instrumentation Technologies as a support to SESAME project. For early stage of the commissioning (first turn(s)), the BPMs could not be used for indication of beam position, due to the low beam intensity, but ADC buffer data and sum signal were used to indicate the passage of the beam. The signal of BPM1 for the first turns is shown in Fig. 2 exemplarily. Once a beam of about mA was stored, transverse beam position could be evaluated and orbit correction was done via SVD method using initially the theoretical and later the measured response matrix. By doing beam based alignment and tuning RF frequency it was possible to correct horizontal orbit to 0.3mm and to 0.17 mm rms, as shown in Fig. 3 [1] then BPMs can be calibrated in positon relative to magnet centres.

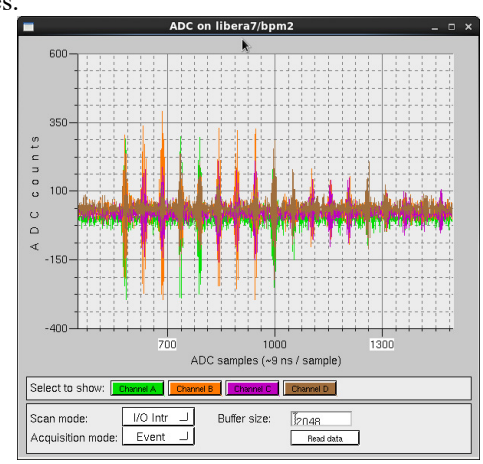

Figure 2: ADC Buffer Data for Few Turns in SR.

ISBN: 978-3-95450-192-2 doi:10.18429/JACoW-IBIC2017-MO2AB3

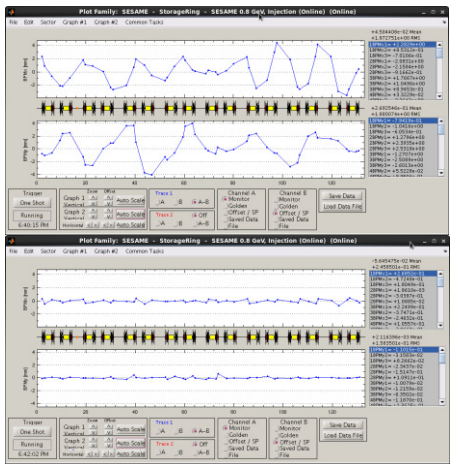

Figure 3: Uncorrected (up) and Corrected closed orbit on Same Scale (down).

TUNE MEASUREMENT

Turn-by-turn data were used to determine both the horizontal and vertical tune by FFT analysis. While the horizontal tune could easily being determined from the injection kick from the beginning, determine the vertical tune measurement was critical at low beam intensity and could only be achieved with a vertical offset of the injected beam. With higher beam intensities both tunes could then be determined from the injection kick or by beam shaker. The injection kicker with reduced strength is further used during ramping of the beam from 0.8 to 2.5 GeV and at 2.5 GeV operation to determine the tunes. Figure 4 shows turn-by-turn data and FFT analysis from BPM1 exemplarily, and same tunes measured by spectrum analyser.

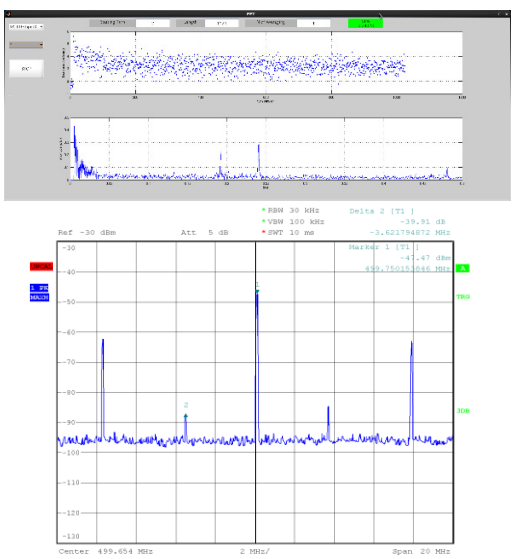

Figure 4: Turn-by-turn data and vertical and horizontal tune (up) and same tunes measured by spectrum analyser picked up by another BPM.

FLORESCENT SCREENS

Florescent Screens (FS) are very useful in the early stage of the commissioning. Four in air FS are installed in the Transfer Line 2 (TL_2) which connects the Booster to the SR. These FS are vertical mounted, pneumatic actuated type with Aluminium Oxide screen material and monitored by Basler CCD camera and Kowa Lenses. In the SR three FS are installed with same specification as in TL_2 but mounted in horizontal direction. The first screen behind the SR injection septum is controlled by stepper motor to see either the injected or the full turn beam. Further screens are installed in cell 6 and 10, by this configuration one FS is in each 1/3 of the ring. Figure 5 shows the FSs installed in TL_2 and SR and Fig. 6 shows the 1st full turn beam in 11th of Jan 2017.

Figure 5: FS installed in TL_2 (left) and motorized one in SR injection section (right).

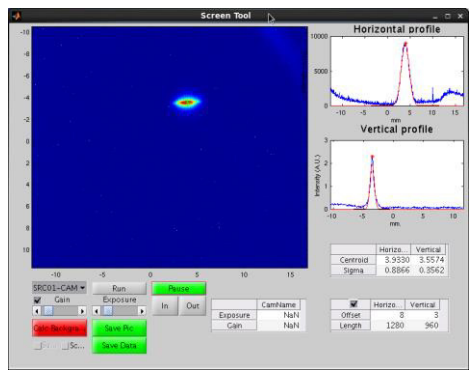

Figure 6: 1st full turn beam on FS in injection section.

FCT AND DCCT

In Transfer line 2 (TL_2) a fast current transformer (FCT) from Bergoz Instrumentation [4] is installed which has a sensitivity of 2.5 V/A, it has a standard CF40 ceramic break with a simple bypass shield, the FCT is directly connected to an oscilloscope (Tektronix DPO5104B) by coax-ial cable (TWS240-FR). Figure 7 shows the output of this FCT.

In the SR one FCT and one DCCT from Bergoz are installed beside each other sharing same ceramic break and outside shield as shown in Fig. 8. The ceramic break is a standard curricular CF150 with 22.8 mm length. In order to preserve the impedance for the beam and have a specific capacitance value for the FCT we designed a beam shield having the same shape as the standard vacuum chamber with overlapping lips as break. These lips will form in

ISBN: 978-3-95450-192-2 doi:10.18429/JACoW-IBIC2017-MO2AB3

parallel capacitance to ceramic break capacitance so it modifies the total capacitance of the gap. The outer shield is designed to have 2 thin sheets of μ-Metal and soft iron outer layer to improve the shielding from external EMI and RFI.

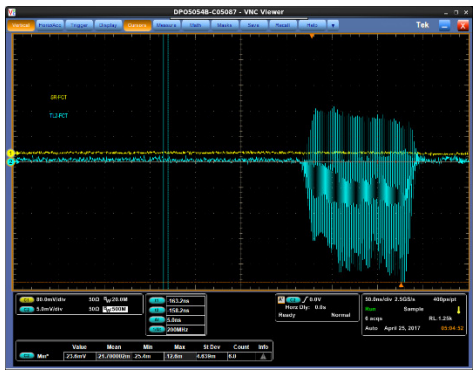

Figure 7: Beam Pulse in TL_2 FCT.

FCT and DCCT assembly are installed in cell 2 in the ring, the FCT is connected directly to Tektronix DPO5104B scope by TWS240-FR coaxial cable while the DCCT connected to Agilent 34410A 6 ½ digit digital multi-meter which is connected via Ethernet connection to EPICS control system. The temperature of the core is fine with the current that we achieved and no need for cooling. Figure 9 shows the first few turns in the SR picked up by FCT.

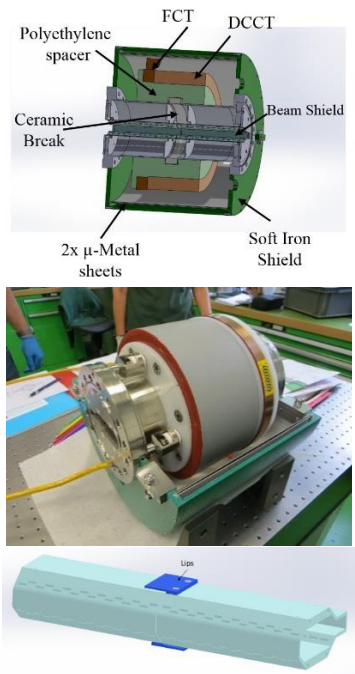

Figure 8: SR FCT and DCCT Assembly in 3D (up) and after assembly (middle) and Beam Shield with the Lips (down).

Figure 9: 1st few turns in the SR by FCT (Left) and DCCT Current.

SRM

There is one synchrotron radiation monitor in the SR which is located in cell 14. SRM used to measure transversal beam size in the ring and monitor transverse instabilities. The challenge here to measure both planes on same SRM, the vertical resolution is limited due to diffraction caused by a crotch absorber in the vacuum chamber. To overcome the diffraction limit and to be able to measure the vertical beam size a double slit was installed to allow interferometry measurements.

Figure 10 shows the layout of the SRM. To measure horizontal beam size a direct imaging method were used. At these stages of the commissioning and operation the complete SRM system including the optical component installed inside the tunnel. So all calibration and optimizing optical lenses and other components were done in the lab.

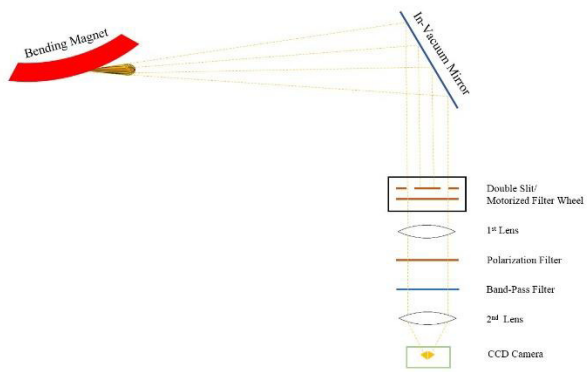

Figure 10: SRM Layout. The radiation produced at the bending magnet BM14 is directed towards the optical beam line using in-vacuum mirror. The distance from the source point to the optical system is 4.5 m.

The vertical beam size can be calculated using interferometry, the measurement principle is explained in detail in Ref. [5]. In summary, it is based on the interferogram produced by monochromatic and polarized synchrotron light

ISBN: 978-3-95450-192-2 doi:10.18429/JACoW-IBIC2017-MO2AB3

after passing through a double slit. When these two beamlets are focused into a CCD camera, the electron beam size can be inferred from the visibility of the interferogram, which indicates the complex degree of spatial coherence of the photons [6].

According to Equation 1 by determination of the visibility V of an interference pattern the visibility is the normalized intensity difference between maximum and minimum values of the corresponding interferometry.

$$\sigma_y = \frac{\lambda R}{\pi D} \cdot \sqrt{\frac{1}{2} \cdot \ln\left(\frac{1}{V}\right)} \quad (1)$$

Where λ is wavelength, D is the slit separation and the R is the distance between source point and slit. The calibration where done in the lab, sector start where used to calculate the resolution of optical system (40 µm) and camera calibration factor. The optical components are from Thorlabs [7], a motorized filter wheel (MFW) is installed with six natural density filter and controlled remotely to give us a high dynamic range of measurement and to reduce the light intensity in order to protect the CCD chip of the camera. This MFW used also to make a slit scan inside the tunnel by install a multi slit (with different D) instead of filters to commission the interferometry with the real beam, by this way the best separation between double slit will be known and then implement it in the system for long term then install the filters back again. A polarization filter installed in order to prevent the two polarizations of the synchrotron light from cancelling each other. And since interferometry with synchrotron light requires monochromatic light, a narrow-band band-pass filter has to be implemented in the system [8]. Figure 11 shows the 1st light seen on the camera at injection energy, this photo was taken before few hours of submission of this paper, so the system still under commissioning and need optimization.

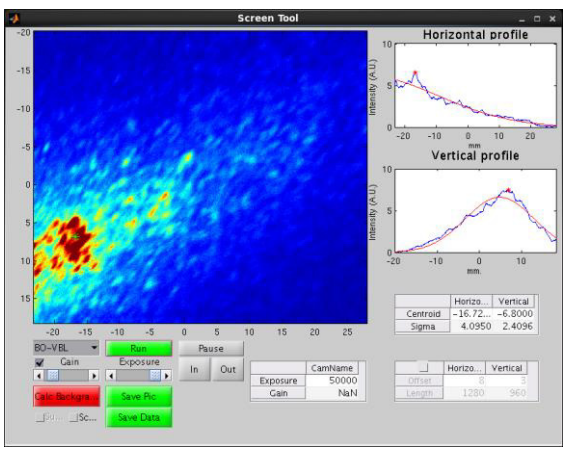

Figure 11: 1st result of SRM at 800MeV which taken before few hours of submission time of this paper, the system need more optimization, alignment and study.

BLM

Four Beam Loss Detectors (BLD) installed inside the tunnel and connected to one Beam Loss Monitor (BLM) installed in the diagnostic rack, this BLM can connect up to 4 BLD at same time, The BLM and one BLD are donated from Instrumentation Technologies to support SESAME project. The BLD are Photo-Multiplier Tube (PMT) type it will detect the visible light photon at its photo-cathode, and the emitted electron will be amplified inside this PMT and an electric current impulse will be created at its anode and this anode's output signal will be transported over a cable to the electronics signal acquisition system. The scintillator rod and the PMT are housed together in a dedicated single, light weight, Aluminium tube structure. This housing maintains the PMT and the rod in a stable and optimum position (for the optical coupling) and has two lids at either end. It is conceived such to make possible an easy, simple and reliable assembly of the components while providing light-tight shielding against ambient light and suitable cable passages [9].

The BLDs are installed in four cells in the machine, two before injection section and two after. Since the cables of these BLD are long (50m) we will move them to other cells and make a round to see the losses in the whole machine. Figure 12 shows the results from these BLDs, it gives us an indication of the big loses in cell 2 (CH-D) compared to the others.

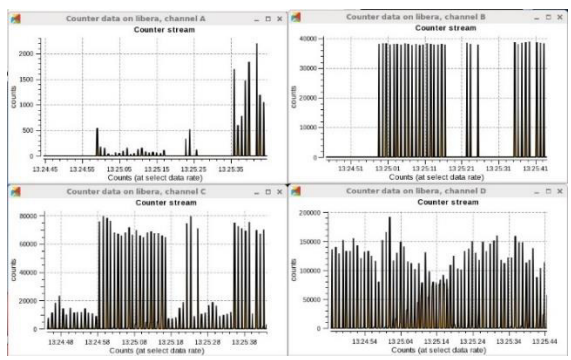

Figure 12: BLDs counts results, channels A,B,C and D are the detectors installed in cells 15,16,1,2 respectively.

ACKNOWLEDGEMENT

The authors would like to thank Instrumentation Technologies for donating four GDX modules and one Beam Loss Monitors and one Beam Loss Detector for SESAME. Also for all SESAME staff who contributed in this achievement through discussions, suggestions and installation. We are grateful for the support from the entire groups especially vacuum group and special thanks to M. Al-Najdawi (vacuum engineer) for his support in design and installation of the diagnostics system and to diagnostics trainees (A. Khasawneh, R. Al-Omar and M. Momani) at the time of the installation and construction for their contribution in designing, implementation, calibration and installation of subsystems.

ISBN: 978-3-95450-192-2 doi:10.18429/JACoW-IBIC2017-MO2AB3

REFERENCES

[1] M. Attal, E. Huttel, K. Manukyan *et al* "Commissioning of SESAME storage ring" *Proc. of IPAC'17*, Copenhagen, Demark.

[2] D. Foudeh, E. Huttel, N. Sawai, "The RF system of the sesame storage ring", *Proc. of IPAC'17*, Copenhagen, Demark.

[3] Instrumentation Technologies, http://www.i-tech.si

[4] Bergoz Instrumentation, http://www.bergoz.com

[5] T. Mitsuhashi "Recent trends in beam size measurements using the spatial coherence of visible synchrotron radiation", *Proc. of IPAC'15*, Richmond, VA, USA

[6] U. Iriso, L. Torino "First transverse beam size measurements using interferometry at ALBA" *Proc. of IBIC'13*, Oxford,UK.

[7] Thorlabs, http://www.thorlabs.de

[8] Michael Holz "Determination of the transversal electron beam size at the ANKA storage ring" Master Thesis, Electrical Engineering Dept., Hochschule Karlsruhe Technik und Wirtschaft, Germany, 2014.

[9] K. Bertus, P. Leban "Prototype results with complete beam loss monitor system optimized for synchrotron light sources", *Proc. of IPAC'15*, Richmond, VA, USA

ISBN: 978-3-95450-192-2 doi:10.18429/JACoW-IBIC2017-MO3AB1

CHARACTERIZING THE COUPLED BUNCH DRIVING TERMS IN A STORAGE RING *

Katherine C. Harkay†, Tim Berenc, Louis Emery, Ulrich Wienands, ANL, Argonne, IL, USA
Dmitry Teytelman, Dimtel, Inc., San Jose, CA, USA
John Byrd, LBNL, Berkeley, CA, USA
Rohan Dowd, Australian Synchrotron, Clayton, Australia

Abstract

Stable operation of a modern high current storage rings requires attention to the sources of coupling impedance. Methods ranging from EM modeling to bench and beam measurements are routinely used to characterize accelerator components. The beam-based method presented here complements existing approaches, and allows precise measurements and identification of narrowband resonances in structures such as RF cavities or in-vacuum undulators. We combine the well-established approach of characterizing eigenvalues of coupled-bunch instabilities with modern high-throughput data acquisition tools and automatic analysis methods. By sequentially exciting low-amplitude oscillation of individual modes below the instability threshold and observing open-loop damping, we automatically map the eigenvalues of all even-fill eigenmodes. Repeating the measurements while changing operating conditions, such as cavity temperatures or undulator gaps, provides a detailed mapping of the impedance source. These measurements are used to extract impedance parameters as well as to optimize accelerator settings. Experimental results from the Advanced Photon Source and other accelerators illustrate the technique.

INTRODUCTION

In this paper we present a beam-based method for measuring narrowband coupling impedances in a storage ring. Such narrow resonant modes, typically parasitic modes in vacuum structures or higher-order modes (HOMs) in RF cavities, can potentially excite severe coupled-bunch instabilities. Precise characterization of these resonances is important for optimizing the operation of existing machines as well as for planning of upgrades.

MEASUREMENT METHOD

Instabilities and Impedances

In order to characterize the coupling impedances we measure the eigenvalues of the even-fill eigenmodes (EFEMs). Modal eigenvalue Λ_l defines the open-loop trajectory $A_l e^{\Lambda_l t}$ of EFEM l. The real part of the eigenvalue determines the modal growth or damping rate and the imaginary part — the oscillation frequency. In the longitudinal plane, the eigenvalues are described by the following relation:

$$\Lambda_l = \Lambda_0 + \frac{\pi\alpha e f_{\rm rf}^2 I_0}{E_0 h\omega_s} Z^{\parallel\rm eff}(l\omega_0 + \omega_s), \qquad (1)$$

where $\Lambda_0 = -\lambda_{\rm rad} + i\omega_s$ is the unperturbed eigenvalue, $Z^{\parallel\rm eff}$ is the effective impedance, related to the physical impedance as follows:

$$Z^{\parallel\rm eff}(\omega) = \sum_{p=-\infty}^{\infty} \frac{p\omega_{\rm rf} + \omega}{\omega_{\rm rf}} Z^{\parallel}(p\omega_{\rm rf} + \omega) \qquad (2)$$

In the transverse plane we have [1]:

$$\Lambda_l = (-\lambda_{\rm rad}^{\perp} + i\omega_\beta) - \frac{cef_{\rm rev} I_0}{2\omega_\beta E_0} Z^{\perp\rm eff}(l\omega_0 + \omega_\beta) \qquad (3)$$

$$Z^{\perp\rm eff}(\omega) = \sum_{p=-\infty}^{\infty} Z^{\perp}(p\omega_{\rm rf} + \omega), \qquad (4)$$

where c is the speed of light and ω_β is the betatron frequency. The transverse impedance, unlike longitudinal, does not scale with frequency when aliasing to $Z^{\perp\rm eff}$.

Modal eigenvalues sample machine impedances at synchrotron or betatron sidebands of many revolution harmonics. To characterize the resonant modes we need a way to tune their frequencies. For higher order modes in RF cavities the typical method for tuning the HOMs is to change the cavity temperature. Mechanisms to change the geometry of the structure provide another way of tuning the resonances. These include cavity tuners, in-vacuum undulators (IVUs) with movable jaws, and others.

A measurement of complex eigenvalues as a function of a tuning parameter characterizes the aliased effective impedance $Z^{\rm eff}(\omega)$. In order to reconstruct the original HOM resonance additional information is required. Aliased impedance measurement defines, with the resolution of the RF frequency, where in the spectrum the true impedance might be located. One way to localize the impedance is to compare these frequencies to the known HOM spectra, from simulations or bench measurements. If the structure in question has RF probes, it can be investigated with beam to resolve various resonances. In this case, a single-bunch fill pattern is normally used to generate a comb of revolution frequency harmonics extending beyond the beam pipe cut-off frequency.

To summarize, by scanning a resonant mode and measuring EFEM eigenvalues we can extract the response as a function of the scanning parameter. In order to translate that information to the modal frequency and bandwidth we need

* Work at supported by U. S. Department of Energy, Office of Science, under Contract No. DE-AC02-06CH11357.
† harkay@aps.anl.gov

ISBN: 978-3-95450-192-2 doi:10.18429/JACoW-IBIC2017-MO3AB1

two pieces of information — the conversion factor/function between the scanning parameter and HOM frequency and the original unaliased frequency of the HOM. In some situations we can obtain the conversion factor by observing the effect of the single HOM on multiple EFEMs. As the Advanced Photon Source (APS) measurements demonstrate, when the resonances have very high Q, their tuning can be extracted from the eigenvalue shifts of closely spaced synchrotron sidebands with $2f_s$ separation. In the transverse plane, closest sidebands are spaced by twice the fractional betatron tune[1]. In other situations, tuning sensitivity can be high enough to move the mode across several revolution harmonics, thus providing a convenient calibration — this is the approach taken in the Australian Synchrotron measurements.

Unfortunately, there is no universal recipe for extracting impedance parameters. In each case, a unique combination of impedance sources, accelerator parameters, and physically accessible controls and measurement signals determines what can and cannot be characterized. Thus, experimenters should be ready to improvise and to adapt the measurement to the machine.

Experimental Setup

Our method is based on the transient drive/damp measurement. In this measurement, a bunch-by-bunch feedback system is configured to excite a single eigenmode with sinusoidal output. Upon a software trigger, the excitation is turned off and the evolution of the eigenmode is recorded in the open loop configuration. The drive/damp measurement dates from the mid-1990s [2], [3, page 47]. In general, this measurement can be performed both below and above the instability threshold. Since the feedback is turned off for all EFEMs, it is easier to perform the measurements under the threshold. Above the instability threshold, unstable modes grow exponentially, limiting the maximum allowable time in the open-loop state. This limit interferes with measurements of slowly damping EFEMs.

An important advantage of the drive/damp measurement over the traditional grow/damp measurement performed above the instability threshold is that any eigenmode can be probed at will. As discussed below, measurements of stable eigenmodes shifted to faster damping by the HOMs are important for proper characterization of unaliased impedances.

While the measurement technique was first utilized in the early 1990s, recent advances in real-time data acquisition capabilities and online/offline analysis have pushed the method to a qualitatively new state. Modern diagnostic systems allow measurement of more than one or two modes —an arbitrary subset or even all eigenmodes can be quickly scanned. This extension of the approach was first developed at Diamond Light Source [4] and has been since used at multiple accelerators around the world.

With a large number of eigenmodes to probe, efficient data acquisition is critical. THe feedback processor used in these experiments (iGp12) captures 20–35 ms of beam motion every 500 ms. The repetition rate is limited by the internal memory readout bandwidth of 320 Mbps. Using a custom mode scan tool we streamed these acquisitions to a control computer. The mode scan tool steps the drive excitation frequency through a range of eigenmodes, specified by the user, and captures a desired number of measurements for each mode.

Data sets, captured as described in the previous section, are automatically processed by our custom Matlab tools to extract the modal eigenvalues (growth or damping rates and oscillation frequencies). The traditional approach to analyzing bunch-by-bunch data is to transform signals from bunch to EFEM basis [5]. Such analysis is powerful, since it extracts all the eigenmodes, but is computationally intensive. If, however, we are only interested in a single eigenmode, a much more efficient approach is available. In this method, we select the appropriate single detection frequency for the eigenmode in question[2], mix the beam signal with the complex exponential reference signal $e^{i\omega t}$, and lowpass filter the result. This process shifts the desired mode to baseband and lowpass filtering selects only that eigenmode. THe resulting complex trajectory is then fitted with a complex exponential to estimate the growth/damping rate and the oscillation frequency. For a detailed discussion of the eigenvalue estimation method refer to [3, pages 48–54].

Limitations

We would be remiss not to discuss the limitations of the technique described here. As discussed earlier, measuring EFEM eigenvalues under the instability threshold allows the experimenter to extend the feedback-off period as far as needed, in order to resolve very long damping times. At the same time, the eigenvalue shift from a given impedance scales linearly with beam current, thus limiting sensitivity to smaller impedances.

Another important limitation is due to the fact that we characterize the impedances by measuring eigenvalue shifts. If the unperturbed eigenvalue Λ_0 changes from measurement to measurement, it limits the smallest resolvable shifts. This effect is most pronounced in the transverse plane, specifically, in the EFEM frequency measurements.

EXPERIMENTAL RESULTS

In this work we present results of three experimental measurements at three different accelerators: longitudinal at MAX IV 3 GeV ring, vertical at the Australian Synchrotron (AS), and longitudinal at the Advanced Photon Source (APS). The measurements are arranged in increasing order of sophistication in the experimental technique. At MAX IV, measurements of a single eigenmode were performed above the instability threshold. This approach is conceptually identical to the work presented in [6]. In the AS studies, a group of vertical EFEMs was measured both below and above the threshold. Finally, at the APS, complete modal scans

[1] Closest spacing is $2\omega_\beta - \omega_{\rm rev}$ for $\omega_\beta > \omega_{\rm rev}/2$.

[2] Upper or lower synchrotron sideband of the appropriate revolution harmonic.

ISBN: 978-3-95450-192-2 doi:10.18429/JACoW-IBIC2017-MO3AB1

Table 1: MAX IV Parameters

Parameter description	Value
Beam energy	3 GeV
Beam current	500 mA
Number of bunches	176
Nominal RF frequency	100 MHz
Harmonic number	176
Synchrotron frequency	680 Hz
Radiation damping time	25 ms

Table 2: AS Parameters

Parameter description	Value
Beam energy	3 GeV
Beam current	200 mA
Number of bunches	300
Nominal RF frequency	499.654 MHz
Harmonic number	360
Vertical tune	5.216

below the instability threshold were used to identify and characterize multiple longitudinal HOMs in RF cavities.

MAX IV 3 GeV

Relevant parameters of the MAX IV 3 GeV ring are summarized in Table 1. The goal of longitudinal instability studies in MAX IV was to optimize cavity temperatures for minimum growth rates. Before temperature optimization the longitudinal instability threshold was 3 mA. With an low shunt impedance improvised kicker [7], reduction of growth rates was necessary to extend the control range of the longitudinal feedback.

Figure 1 shows the result of a temperature scan of the main RF cavity 20, with the eigenvalues of mode 167 responding to the temperature changes. In order to quantify

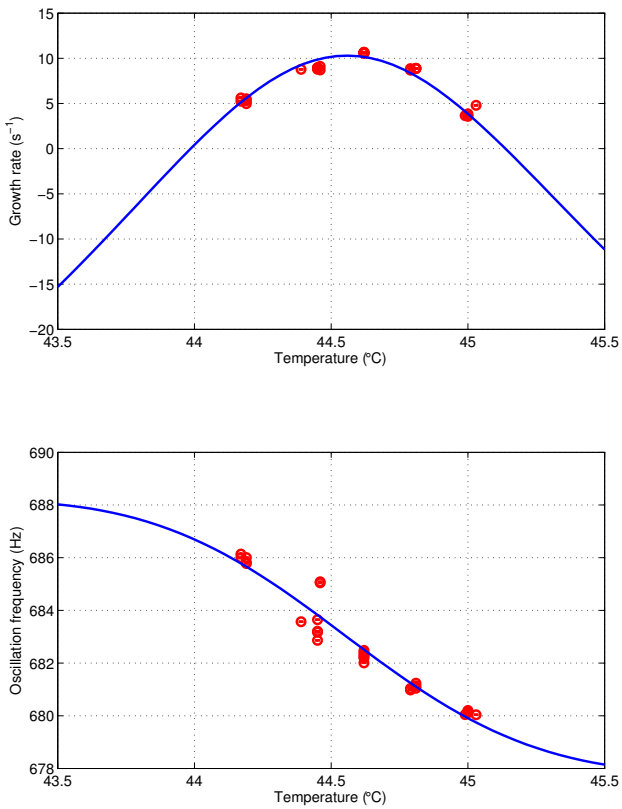

Figure 1: Mode 167 eigenvalues and the resonant fit.

the effective impedance we fit a resonant mode response to the measurements.

The most straightforward analysis technique is to fit resonant responses to the measured modal eigenvalues using temperature as a substitute for frequency. At each temperature T the eigenvalue can be calculated using the following five-parameter form:

$$\lambda = \frac{i\lambda_{\max} T T_{\mathrm{bw}}}{T_0^2 + iTT_{\mathrm{bw}} - T^2} + \lambda_0 + i\omega_s^0 \tag{5}$$

where T_0 is the temperature where peak growth rate $\lambda_{\max}$ is reached, T_{bw} is the resonant bandwidth, λ_0 is baseline growth rate[3] and ω_s^0 is the base modal frequency[4].

After similar temperature scans were performed on all main and harmonic RF cavities, we adjusted the cavity temperatures to minimize the growth rates, increasing the longitudinal instability threshold from 3 to 17 mA.

Australian Synchrotron

In the Australian Synchrotron, fast vertical growth rates are observed, driven by the IVUs. When the IVU gaps are open, vertical instabilities are dominated by the resistive wall. When the gaps are closed, however, much faster instabilities occur. The growth rates of these instabilities depend strongly on the gap position. Figure 2 shows the growth rates for mode 359 (−1, resistive wall) and 222–224 as a function of IVU05 gap setting. As the gap is reduced, the resonant mode crosses the lower betatron sideband of 222$^{\mathrm{nd}}$ revolution harmonic, then 223$^{\mathrm{rd}}$ and 224$^{\mathrm{th}}$. Of course, these can be baseband harmonics or harmonics above any multiple of the RF frequency.

Fitting resonant responses to the growth rates of individual modes we generate the plot shown in Fig. 3, this time using the IVU gap as a substitute for frequency. Spacing of the peaks for the neighboring modes corresponds to the resonance shifting by ω_{rev} and provides a convenient way to calibrate our scanning parameter. Two distances agree within 3% and give us the tuning coefficient of 4.8 MHz mm^{-1}. Fitted bandwidths range from 75 to 78 µm or 360–374 kHz. The fits show that the shunt impedance increases as the undulator jaws get closer to the beam.

[3] Radiation damping rate is expected here, unless constant impedances due to cavities in other regions are shifting the eigenvalue.

[4] Should be the zero current synchrotron frequency without other impedances affecting the eigenmode.

ISBN: 978-3-95450-192-2 doi:10.18429/JACoW-IBIC2017-MO3AB1

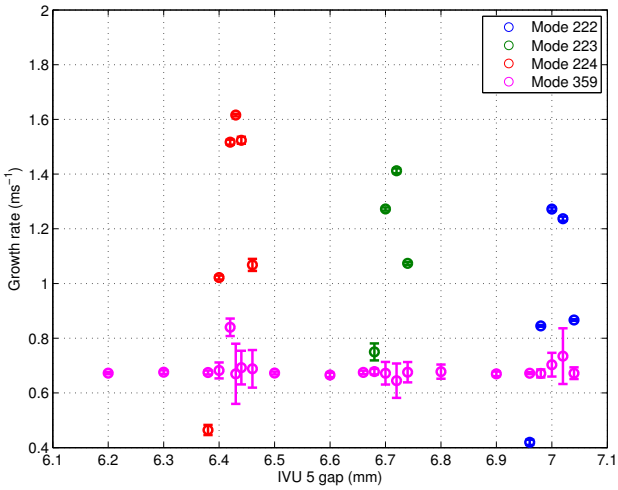

Figure 2: Vertical growth rates vs. IVU05 gap setting.

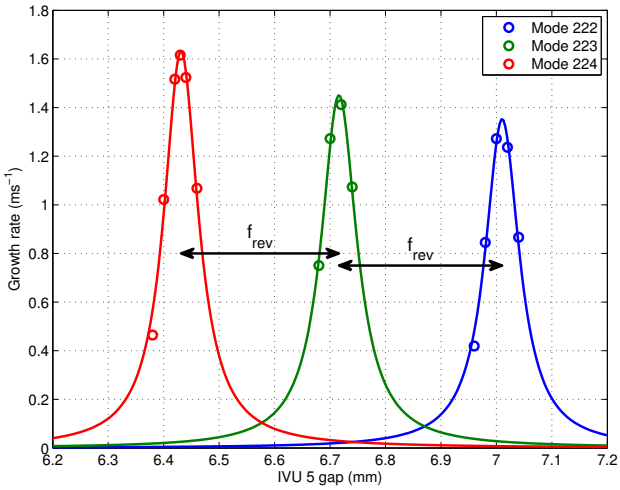

Figure 3: Vertical growth rates and resonant mode fits.

Unlike cavity HOM tuning, IVU jaws do have to travel through the resonant region, so the instability cannot be fully avoided. At the same time, these measurements can be used in operation to select more stable positions and to add stability when the resonant mode crosses the betatron sideband[5].

A numerical study of resonant modes in IVU05 was done using HFSS [8]. Table 3 compares calculated and measured parameters. In general, we see good agreement between these, taking into consideration the fact that HFSS model assumed ideal electrical conductivities for all materials and, therefore, under-estimated the bandwidth.

[5] Additional stabilization can come from the increased bunch-by-bunch feedback gain or from raised chromaticity. Both of these have negative side effects and are best kept lower in steady state operation.

Table 3: Comparison of Measured and Modeled Parameters for the IVU05 Mode 3

Parameter description	Measurement	Model
Tuning sensitivity, MHz mm^{-1}	4.79	4.81
Bandwidth, kHz	360–374	239
CF @ 6 mm gap, MHz	186.4	194.4

Advanced Photon Source

Setup Accelerator parameters, relevant to the APS measurements, are provided in Table 4. Since the Advanced Photon Source is not equipped with a longitudinal bunch-by-bunch feedback system, an improvised setup was created. A conventional front-end was used to detect the phase of the sum signal of a button position monitor relative to the 4th harmonic of the RF frequency. In the absence of a wideband longitudinal kicker we used an improvised kicker consisting of two transverse striplines driven common mode. The longitudinal shunt impedance of such a kicker has $\sin^2(\frac{\omega l}{2c})$ dependence on frequency [9]. For the APS striplines peak response occurs near $f_{\rm rf}/2$. Since nominal fill pattern populates every 4th RF bucket, we used the back-end shaper in iGp12 [10] to apply an inverted kick to the RF bucket following the bucket where the true kick was applied. The resulting modulation upconverts the kick to $f_{\rm rf}/2$, placing the kick signal near the peak of the stripline kicker's shunt impedance.

In our experiments we used two main types of streaming configurations:

- Four acquisition per mode, modes 1–323, roughly 11 minutes scan time;
- Ten acquisitions per mode, a subset of 48 modes, 4 minutes scan time.

The first measurement configuration covered all possible eigenmodes except the lowest frequency mode (mode 0). Based on several complete scans we have identified a subset of EFEMs with strong driving terms. These eigenmodes were then measured in more detail.

Individual measurements Figure 4 illustrates the time-domain evolution of two eigenmodes in a drive/damp measurement. Mode 36 was driven by the bunch-by-bunch feedback system to the initial level of 0.025° and decays exponentially in the 34 ms transient. At the same time, mode 0 is continuously excited by wideband and narrowband spectral

Table 4: APS Parameters

Parameter description	Value
Beam energy	7 GeV
Beam current	100 mA
Number of bunches	324
Nominal RF frequency	352 MHz
Harmonic number	1296
Synchrotron frequency	2.22 kHz
Radiation damping time	4.82 ms

ISBN: 978-3-95450-192-2 doi:10.18429/JACoW-IBIC2017-MO3AB1

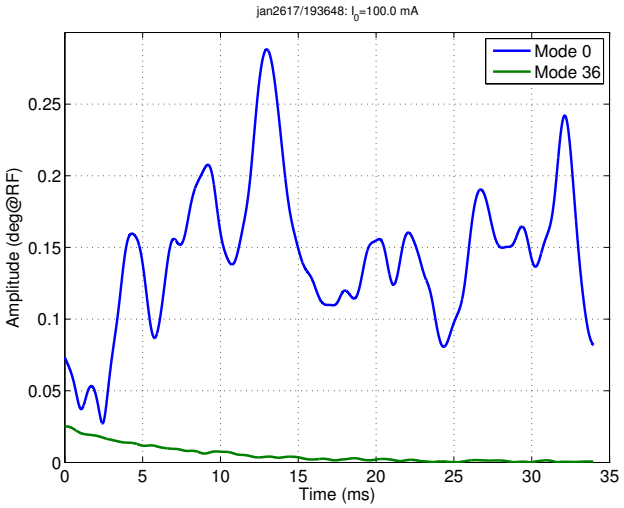

Figure 4: Time domain evolution of modes 0 (driven by RF disturbances) and 36 (excited by the LFB) in a drive/damp measurement at 100 mA.

components in the vicinity of the RF frequency to a much higher 0.14° average amplitude.

This significant difference between the externally driven motion of mode 0 and the achievable amplitudes of other modes points to the important machine setup requirement for these measurements. High degree of fill pattern uniformity is critical for successful measurements of this type. Variation in bunch currents multiplies the modal spectrum, producing a convolution in the frequency domain. Such convolution projects some of the motion of mode 0 to other modes, dramatically raising the measurement noise floor. Since the noise floor is typically on the order of 1.3 millidegrees, even small coupling from 140 millidegrees of mode 0 can compromise the signal of interest. The fill pattern uniformity requirement drops somewhat when a true longitudinal kicker is available, since much higher amplitudes can be reached.

Results of a single scan are shown in Fig. 5. The mode spectrum is folded around half the harmonic number h, to plot mirror modes l and $h-l$ (also denoted as $-l$) at the same point. The reason for that is that the coupling impedance function $Z(\omega)$ is hermitian, that is $Z(\omega) = Z^*(\omega)$ where * connotes complex conjugate [3, page 12]. As a result, eigenmodes l and $-l$ are driven by $Z(\omega)$ and $-Z^*(\omega)$, leading to identical imaginary part shifts (tune shifts) and opposing real part shifts (growth/damping rates). In such a presentation, narrowband resonances produce clearly visible shifts for pairs of modes, especially noticeable for modes 36, 151, and −95.

In order to tune the cavity HOMs we used cavity temperature control. In the APS, one can adjust cavity temperatures in sectors, with four cavities per sector. Both sector setpoint and individual cavity temperatures were recorded. Comparison of individual cavity temperatures to the setpoint shows a linear relationship in all cases. Thus, fitting and analysis

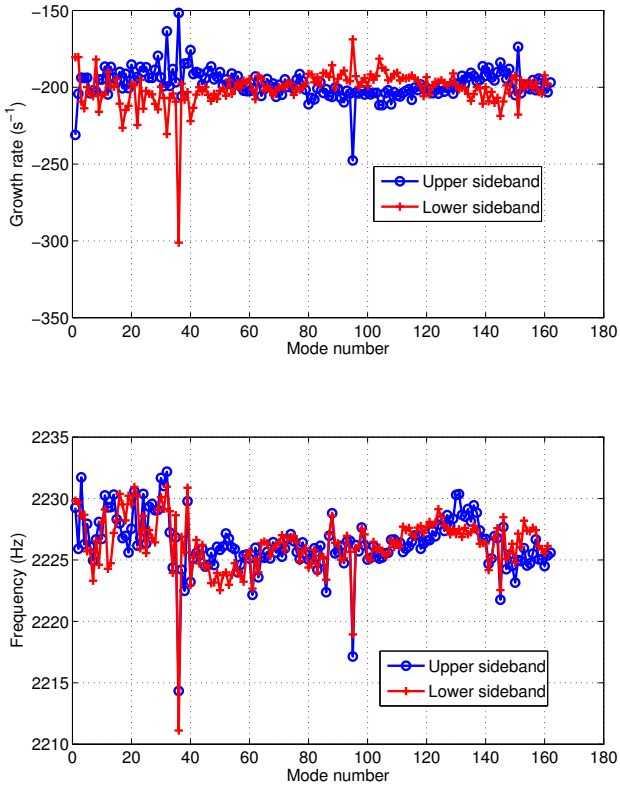

Figure 5: All mode scan at 76 mA. Modes 32, 36, 40, -95, 151 are clearly driven by narrowband resonances.

here were done relative to the sector setpoint rather than the temperature measurements of individual cavities.

HOM parameter fitting A set of modal scans taken at different temperature setpoints characterizes the dependence of all modal eigenvalues on that temperature. Many EFEMs do not respond to the temperature change. For those modes with significant eigenvalue shifts away from Λ_0, lack of response suggests the driving impedance is in a different RF sector. Mode −95 seen in Fig. 5 falls in that group. Later measurements showed that this mode is driven by cavity 4 in Sector 40. For modes without significant shifts from Λ_0, either there is no significant driving impedance or the resonant mode is tuned too far away from the relevant synchrotron sideband. Figure 6 shows the results of the temperature variation study in Sector 36. Eigenvalues of two modes, 36 and −36, are plotted versus temperature setpoint. The temperature scan was done at a beam current of 76 mA to keep the beam under the instability threshold. As Fig. 6 shows, mode 36 gets very close to the instability threshold at 82.5 °F.

The relationship between resonant frequency and temperature is assumed to be linear in the small temperature range explored in the experiment. For each HOM, we define

$$\omega_r(T) = \omega_{\mathrm{sb}} + K_T(T - T_0) \qquad (6)$$

Here ω_{sb} is the synchrotron sideband of the revolution harmonic to which the mode is tuned at temperature T_0.

ISBN: 978-3-95450-192-2 doi:10.18429/JACoW-IBIC2017-MO3AB1

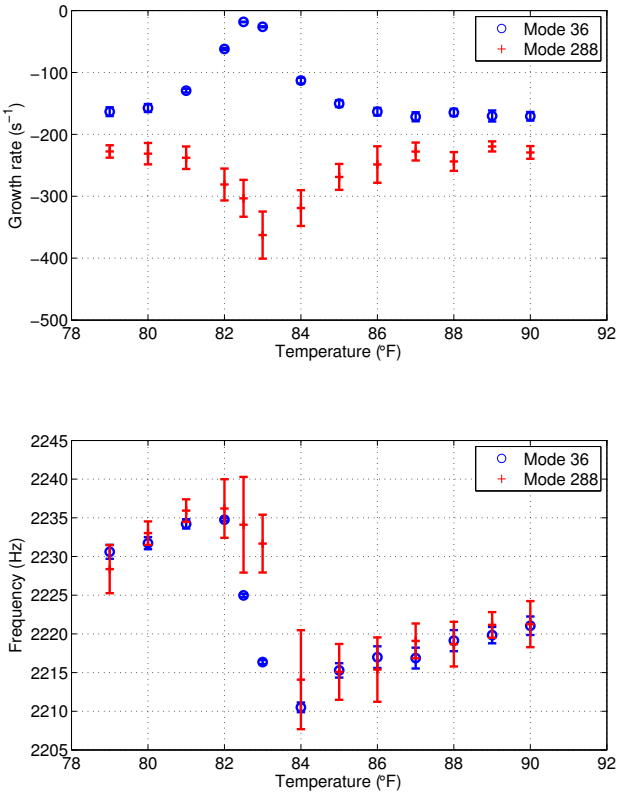

Figure 6: Modes 36 and 288(−36) are sampling the same HOM impedance.

If we examine Fig. 6 carefully, we find a clear shift between peak growth rates for modes 36 and −36. Equations 1 and 2 help explain the asymmetry between positive and negative modes. That asymmetry is due to the fact that the positive mode samples the HOM impedance at $N\omega_{\mathrm{rf}} + M\omega_{\mathrm{rev}} + \omega_s$ while the negative mode reacts to the impedance at $-N\omega_{\mathrm{rf}} - M\omega_{\mathrm{rev}} + \omega_s$. As noted earlier, impedance function is hermitian, thus the negative mode is effectively sampling at $N\omega_{\mathrm{rf}} + M\omega_{\mathrm{rev}} - \omega_s$. Therefore, a separation of $2\omega_s$ can be used to extract the HOM temperature tuning sensitivity if the mode is narrow enough. From the plot, the difference between the two peaks is roughly 0.75 °F. That corresponds to $2f_s$ shift in the impedance center frequency, or 4.45 kHz. Dividing the two numbers we get the tuning sensitivity $K_T \approx 5.9$ kHz/°F.

Figure 7 shows the results of simultaneously fitting both modes 36 and −36. The estimated shunt impedance and Q are fairly close to the URMEL model predictions of 1.67 MΩ and 41,000, respectively. Extracted tuning sensitivity of 6.3 kHz/°F is in agreement with our rough estimate. Our earlier assumption of the linear relationship between temperature and HOM frequency is confirmed by the good agreement between measured and fitted eigenvalues.

Figure 8 illustrates one of the practical applications of this measurement. Plotting the fits to all the HOMs observed during the scan versus sector setpoint temperature gives us an easy way to optimize the operating temperature. Within

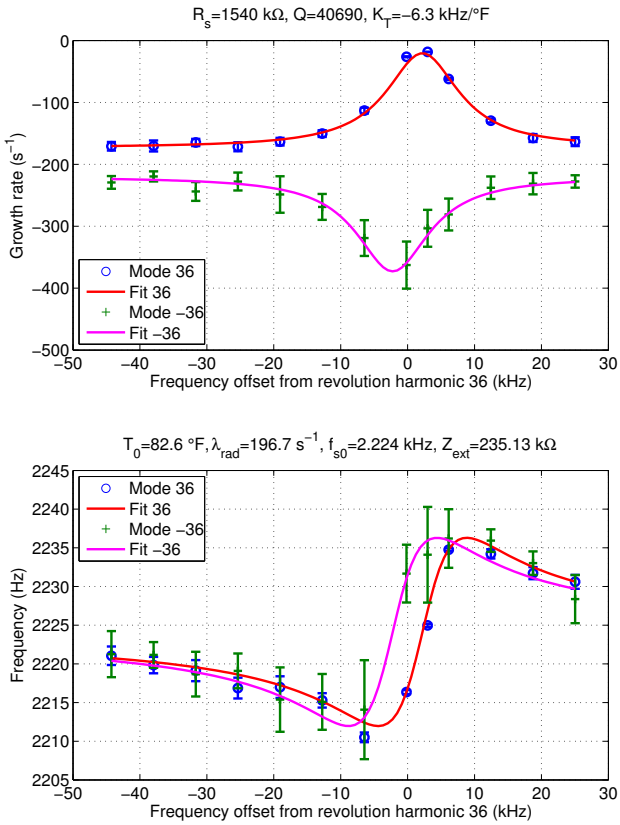

Figure 7: Fitting HOM response to both modes 36 and −36 extracts the temperature coefficient of the resonant mode. With known source frequency around 537 MHz the HOM is fully parameterized.

the practically achievable range of setpoints from 80 to 90 °F minimum growth rate point is 87 °F. Since some variation of temperatures around the setpoint is to be expected, 86 °F is a slightly better practical choice.

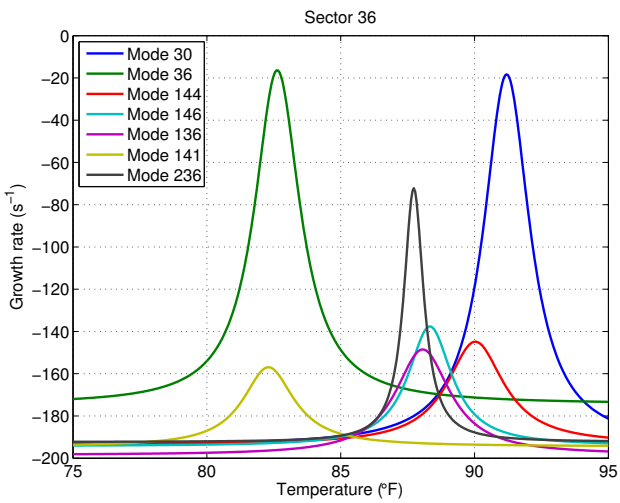

Figure 8: Growth rates due to all the HOMs observed in sector 36 at 74 mA.

ISBN: 978-3-95450-192-2 doi:10.18429/JACoW-IBIC2017-MO3AB1

Table 5: Rough identification of the HOMs

HOM frequency, MHz	537	918	1207
Cavity	Mode number		
S36C2	30	136	-98
S40C4	31	138	-95
S40C3	32	139	-92
S38C2	32	139	-91
S36C1	34	141	-88
S40C1	34	142	-86
S40C2	35	143	-83
S36C4	36	144	-82
S38C1	36	145	-80
S36C3	38	146	-77
S37C3	39	149	-72
S38C4	39	150	-71
S38C3	40	151	-69
S37C2	43	153	-63
S37C1	43	154	-61
S37C4	44	155	-59

After the APS upgrade (APS-U), the ring circumference will change slightly. As a result, to predict the minimum achievable growth rates with individual cavity temperature adjustments, we need to match the measured modes with the individual cavities. Table 5 provides a rough identification guide for three dominant HOMs in the APS cavities. This guide is generated as follows. With a single bunch in the ring to create a comb of revolution frequency harmonics, we examined individual cavity HOM probes, and for each mode recorded the revolution harmonic with the highest beam-induced power. Based on Table 5 we assign measured modes to individual cavities. For example, mode 36 measured during the Sector 36 temperature scan is assigned to cavity 4 in that sector. Resonance parameters, extracted from the fitting process, are then used to predict the APS-U growth rates at different cavity temperatures.

SUMMARY

New fourth-generation storage-ring based light sources are moving to beam parameters that make these accelerators more sensitive to driving impedances. In the longitudinal plane the sensitivity is enhanced by low synchrotron frequencies, with growth rates scaling as $1/\omega_s$. Transversely, this higher sensitivity comes about from the very low vertical emittances, with low emittance beams being more sensitive to residual dipole oscillations. Operation of bunch-by-bunch feedback systems at high loop gains, required to suppress fast growth rates, leads to higher residual motion amplitudes.

Precise characterization of resonant impedances becomes, therefore, more important for operational optimization, machine upgrades, and resonance mitigation. Beam-based techniques provide a powerful tool set for identifying and quantifying such resonances. Using multiple even-fill eigenmodes to sample the resonance we can extract shunt impedance, quality factor, center frequency (CF), and tuning sensitivity. In combination with modeling and single-bunch probing the effective impedances can be "unaliased".

These measurements can help provide much needed information prior to the installation of new insertion devices, changes in operating points, or major upgrades.

ACKNOWLEDGMENTS

For the studies at the Advanced Photon Source, special thanks to Nick Sereno, Ali Nassiri, and APS Controls and Operations staff. For the studies at the Australian Synchrotron we would like to thank Mark Atkinson, Mark Boland, Greg LeBlanc, Eugene Tan, Operations staff Louise Hearder and Madeleine Chalmers. Special thanks to Andrew Starritt and Andraz Pozar for software support. Thanks to Åke Andersson, David Olsson, Galina Skripka, Pedro Tavares, and MAX IV staff for their help with the measurements at the MAX IV 3 GeV ring.

REFERENCES

[1] S. Khan, *Collective phenomena in synchrotron radiation sources: Prediction, diagnostics, countermeasures*. Berlin: Springer, 2006.

[2] D. Teytelman *et al.*, "Accelerator diagnostic techniques using time-domain data from a bunch-by-bunch longitudinal feedback system," in *DIPAC 97: beam diagnostics and instrumentation for particle accelerators: Proceedings*, (Frascati (Rome) Italy), pp. 3–5, Laboratori Nazionali di Frascati: SIS–Pubblicazioni, 1997.

[3] D. Teytelman, *Architectures and algorithms for control and diagnostics of coupled-bunch instabilities in circular accelerators*. PhD thesis, Stanford University, 2003. SLAC-R-633.

[4] G. Rehm, M. Abbott, and A. Morgan, "New features and measurements using the upgraded transverse multibunch feedback at Diamond," in *Proceedings, 3rd International Beam Instrumentation Conference (IBIC2014) : Monterey, California, USA, September 14–18, 2014*, pp. 696–699, 2014.

[5] S. Prabhakar *et al.*, "Observation and modal analysis of coupled-bunch longitudinal instabilities via a digital feedback control system," *Part. Accel.*, vol. 57, p. 175, 1997.

[6] D. Teytelman, J. Fox, S. Prabhakar, and J. M. Byrd, "Characterization of longitudinal impedances in storage rings via multibunch effects," *Phys. Rev. ST Accel. Beams*, vol. 4, p. 112801, 2001.

[7] D. Olsson, L. Malmgren, and K. Åhnberg, "Design and implementation of stripline feedback kickers in the MAX IV 3 GeV storage ring," in *Proceedings, 8th International Particle Accelerator Conference (IPAC 2017): Copenhagen, Denmark, May 14-19, 2017*, pp. 4285–4288, 2017.

[8] J. Chi and D. Pelz, "Investigation of instability modes in 2-meter long in-vacuum undulator at the Australian Synchrotron," internal report, Australian Synchrotron, 2016.

[9] G. Lambertson, "Dynamic devices: Pickups and kickers," *AIP Conf. Proc.*, vol. 153, pp. 1413–1442, 1987.

[10] D. Teytelman, "Optimization of bunch-to-bunch isolation in instability feedback systems," in *Proceedings, 2nd International Beam Instrumentation Conference (IBIC2013): Oxford, United Kingdom, September 16–19, 2013*, pp. 116–119, 2013.

ISBN: 978-3-95450-192-2 doi:10.18429/JACoW-IBIC2017-MO3AB2

REVIEW OF BEAM-BASED TECHNIQUES OF IMPEDANCE MEASUREMENT*

V. Smaluk†, Brookhaven National Laboratory, Upton, USA

Abstract

Knowledge of a vacuum chamber impedance is necessary to estimate limitations of particle beam intensity. For new accelerator projects, minimization of the impedance is a mandatory requirement. The impedance budgets are computed during the machine design. Beam-based measurements of the impedance are usually carried out at the beginning of the machine commissioning. Comparisons of the impedance computations and measurements often show significant discrepancies, a factor of two or even more is not something unusual. Since the accuracy of impedance computations is not sufficient, the beam-based measurements are important to estimate the machine impedance and to predict stability conditions for high-intensity particle beams.

WAKEFIELDS AND IMPEDANCES

The beam intensity in storage rings is usually limited by its interaction with electromagnetic fields induced in a vacuum chamber by the beam itself (wakefields). The beam-wakefield interaction is described in terms of wake functions defined as normalized integrals of the Lorentz forces that act on a test particle moving behind a leading particle which excites the wakefields. The velocity of both particles is $\mathbf{v}$ ($|\mathbf{v}| = c$). To analyze the beam stability in most practical cases, it is enough to consider only monopole longitudinal $W_\parallel$ and dipole transverse $\mathbf{W}_\perp$ wake functions. The longitudinal wake function is [1]:

$$W_\parallel(\tau) = -\frac{1}{q}\int_{-\infty}^{\infty} E_z(t,\tau)\ \mathrm{d}t\ , \qquad (1)$$

where q is the charge of leading particle, $\tau = s/c$, s is the distance between the leading and the trailing particles, c is the speed of light. The transverse wake function is defined similarly to the longitudinal one but the integral is normalized by the dipole moment qr of the leading particle; $\mathbf{W}_\perp$ is a vector with horizontal and vertical components:

$$\mathbf{W}_\perp(\tau) = -\frac{1}{q\,r}\int_{-\infty}^{\infty} [\mathbf{E}(t,\tau) + \mathbf{v}\times\mathbf{B}(t,\tau)]_\perp\ \mathrm{d}t\ . \qquad (2)$$

The longitudinal and transverse wake functions are related to each other by the Panofsky-Venzel theorem [1, 2].

For a beam with arbitrary charge distribution, its interaction with wakefields is described by the wake potential:

$$V(\tau) = \int_0^{\infty} W(t)\lambda(\tau - t)\mathrm{d}t\ , \qquad (3)$$

where $\lambda(t)$ is the longitudinal charge density normalized as $\int_{-\infty}^{\infty}\lambda(t)\mathrm{d}t = 1$.

* Work supported by DOE under contract DE-SC0012704
† vsmalyuk@bnl.gov

In the frequency domain, each part of the vacuum chamber is represented by a frequency-dependent longitudinal $Z_\parallel$ and transverse $Z_\perp$ impedances defined as Fourier transforms of the corresponding wake functions. For any vacuum chamber component, the impedance can be approximated by a set of equivalent resonators plus the resistive-wall impedance. The beam interaction with the narrowband impedance and with the broadband one can be analyzed separately. We can assert that the narrowband impedance leads to the bunch-by-bunch interaction and can result in multi-bunch instabilities, whereas the broadband impedance leads to the intra-bunch particle interaction and can cause single-bunch instabilities.

Computation of the impedance budget is an essential part of accelerator design. The impedance of a vacuum chamber is computed by element-wise wakefield simulations using 3D finite-difference simulation codes solving Maxwell equations with the boundary conditions determined by the chamber geometry. The fields are excited by a bunched beam with pre-defined charge distribution. The code output is a wake potential (3) and the impedance is calculated as $Z(\omega) = \tilde{V}(\omega)/\tilde{\lambda}(\omega)$, where $\tilde{V}$ and $\tilde{\lambda}$ are the Fourier transforms of the wake potential and of the longitudinal charge density, respectively. So the bandwidth of the impedance derived from the simulated wake potential is limited by the bunch spectrum width which is inversely proportional to the bunch length defined for the simulation. The mesh size of the solver is very important, it should be small enough to get reliable results for a given bunch spectrum. For a typical bunch length of few millimeters, full 3D simulation of wakefields in a big and complex structure is quite difficult.

Beam-based measurement of the impedance is an important part of a machine commissioning. Comparisons of impedance computations and beam-based measurements show significant discrepancies for many machines, a factor of two or even more. There are many publications describing thorough calculations of impedance budgets and finally the total impedance is multiplied by a "safety factor" of two. Some accelerator facilities have not achieved their design beam currents because the collective effects nave not been predicted correctly at the design stage. Since the accuracy of impedance computations is not sufficient, the beam-based measurements are important to estimate the machine impedance and to predict stability conditions for high-intensity particle beams.

LONGITUDINAL BROADBAND IMPEDANCE

For the longitudinal broadband impedance, the measurable single-bunch effects are: current-dependent bunch lengthening, synchronous phase shift, and energy spread

ISBN: 978-3-95450-192-2 doi:10.18429/JACoW-IBIC2017-MO3AB2

growth due to microwave instability. These effects are dependent on integral parameters combining the impedance and the bunch power spectrum: the effective impedance and the loss factor. If the bunch length is much shorter than the ring average radius, the normalized effective impedance $(Z_\parallel/n)_{\rm eff}$ is defined as

$$\left(\frac{Z_\parallel}{n}\right)_{\rm eff} = \frac{\int_{-\infty}^{\infty} Z_\parallel(\omega)\frac{\omega_0}{\omega}h(\omega)\mathrm{d}\omega}{\int_{-\infty}^{\infty} h(\omega)\mathrm{d}\omega}\,, \qquad (4)$$

where $Z_\parallel(\omega)$ is the frequency-dependent longitudinal impedance, $n = \omega/\omega_0$ is the revolution harmonic number, $\omega_0 = 2\pi f_0$ is the revolution frequency, $h(\omega) = \tilde{\lambda}(\omega)\tilde{\lambda}^*(\omega)$ is the bunch power spectrum, $\tilde{\lambda}(\omega)$ is the Fourier transform of the longitudinal charge density $\lambda(t)$. For a Gaussian bunch, $h(\omega) = e^{-\omega^2\sigma_t^2}$, where $\sigma_t = \sigma_z/c$, σ_z is the bunch length. If the low-frequency longitudinal impedance is assumed to be inductive, the normalized impedance $Z_\parallel/n$ is frequency-independent.

The loss factor $k_\parallel$ determines the coherent loss $\Delta E = k_\parallel q^2$ of the beam energy caused by the beam-impedance interaction; q is the bunch charge. The loss factor can be expressed in terms of the wake potential $V_\parallel$ or of the impedance $Z_\parallel$:

$$k_\parallel = \int_{-\infty}^{\infty} V_\parallel(t)\,\lambda(t)\mathrm{d}t = \frac{1}{2\pi}\int_{-\infty}^{\infty} Z_\parallel(\omega)\,h(\omega)\mathrm{d}\omega\,. \qquad (5)$$

If the bunch is not very short (few millimeters is a typical bunch length for electron/positron storage rings), the measurable single-bunch effects resulted from the beam interaction with a complex impedance produced by computer simulations can be described with reasonable accuracy using a simple broadband resonator model. For longer bunches, even the simplest inductive model is acceptable.

The longitudinal broadband impedance can be estimated by direct measurement of the bunch profile as a function of beam intensity using a streak-camera or a dissector tube, or by indirect measurement of the bunch length using the bunch spectrum width from a button-type pickup electrode.

Interaction of a beam with a broadband impedance deforms the longitudinal bunch profile $\lambda(t)$. A zero-intensity bunch profile $\lambda_0(t)$ is Gaussian. Below the microwave instability threshold, $\lambda(t)$ as a function of the bunch current $I_b = qf_0$ can be described by the Haissinski equation [3]:

$$\lambda(t) = K\lambda_0(t)\exp\left(-\frac{\alpha I_b}{\omega_s^2\sigma_0^2 E/e}\int_{-\infty}^{t} S(t+\tau)\lambda(\tau)\mathrm{d}\tau\right), \qquad (6)$$

where $S(t) = \int_0^t W_\parallel(\tau)\mathrm{d}\tau$, α is the momentum compaction, ω_s is the synchrotron frequency, E is the beam energy. The normalizing factor K is determined by the condition $\int_{-\infty}^{\infty}\lambda(t)\mathrm{d}t = 1$. The Haissinski equation can be solved numerically for a certain impedance model (e.g. broadband resonator) and the model parameters can be find by fitting the measured bunch profile with the equation solution [4]. The intensity-dependent bunch lengthening ($\alpha > 0$) can be approximately described by a cubic equation [5]:

$$\left(\frac{\sigma_t}{\sigma_{t0}}\right)^3 - \frac{\sigma_t}{\sigma_{t0}} = \frac{I_b\,\alpha}{\sqrt{2\pi}\,\nu_s^2\,(\omega_0\sigma_{t0})^3\,E/e}\,\mathrm{Im}\left(\frac{Z_\parallel}{n}\right)_{\rm eff}\,, \qquad (7)$$

where $\nu_s = \omega_s/\omega_0$ is the synchrotron tune, σ_{t0} is the r.m.s. bunch length at zero intensity.

Above the microwave instability threshold, the longitudinal beam dynamics is characterized by the intensity-dependent energy spread growth and a turbulent bunch lengthening. The relative energy spread $\delta \equiv \sigma_E/E$ can be estimated from a measured r.m.s. horizontal size σ_x determined by the combination of betatron and synchrotron contributions: $\sigma_x^2 = \beta_x\varepsilon_x + (\eta_x\delta)^2$, where β_x is the beta function, ε_x is the emittance, η_x is the dispersion. The transverse beam size is usually measured by a visible light monitor or a pin-hole X-ray camera located in a dispersive section. The beam dynamics above the threshold is very complex, and comprehensive numerical simulations are needed to fit the measured intensity-dependent energy spread with the model impedance.

Note, it is practically impossible to find the microwave instability threshold from the measured bunch lengthening although it is clearly visible on a graph of the measured intensity-dependent energy spread [6], this is also confirmed by numerical simulations [7]. Thus, formula (7) could be useful to fit the bunch lengthening even if the beam current exceeds the microwave instability threshold.

The loss factor can be estimated from the measured intensity-dependent shift $\Delta\phi_s$ of the beam synchronous phase. This phase shift is caused by the coherent energy loss, which is compensated in the accelerating RF cavities every beam turn, as well as the energy loss caused by synchrotron radiation. The formula of synchronous phase shift is derived from the energy balance of the beam:

$$\Delta\phi_s = \frac{I_b k_\parallel}{f_0 V_{\rm RF}\cos\phi_{s0}}\,, \qquad (8)$$

where $V_{\rm RF}$ is the RF voltage, ϕ_{s0} is the synchronous phase at zero current. The loss factor $k_\parallel$ depends on the bunch length growing with the beam current, so the phase shift as a function of the beam current is non-linear. For a low-current beam, we can neglect the bunch lengthening and, with this approximation, the phase shift $\Delta\phi_s$ can be assumed proportional to the zero-current loss factor.

The current-dependent shift of synchronous phase can be measured directly using synchrotron light diagnostics (streak-camera, dissector tube) or RF system diagnostics. To reduce the systematic error resulted from the drift or jitter of the diagnostic instruments, the two-bunch technique is useful. The longitudinal profiles of two bunches are measured simultaneously, one bunch has variable intensity, whereas the other bunch with a fixed intensity is the reference, so the systematic error caused by the instrument drift is eliminated.

The other technique is based on measurement of the closed orbit distortion caused by the coherent energy loss [8]. If the dispersion and its derivative is zero in the accelerating

ISBN: 978-3-95450-192-2 doi:10.18429/JACoW-IBIC2017-MO3AB2

RF cavities, the orbit deviation can be assumed proportional to the dispersion $\eta(s)$. The loss factor $k_\parallel$ can be estimated by measuring the orbit distortion $\Delta x(s)$ as a function of the beam current variation ΔI_b [9]:

$$k_\parallel = \frac{f_0}{\Delta I_b}\,\frac{E}{e}\,\frac{\Delta x(s)}{\eta(s)}\,. \tag{9}$$

If the RF cavities are located in several places, this method can be used to measure the longitudinal loss factor of a section between the cavities. High-precision beam position monitors (BPMs) are now a standard component of beam diagnostics, so the beam orbit can be measured precisely [10].

TRANSVERSE BROADBAND IMPEDANCE

For the transverse broadband impedance, the measurable effects are current-dependent shift of betatron frequencies and rise/damping time of the chromatic head-tail effect. Similar to the longitudinal case, these effects are dependent on integral parameters combining the impedance and the bunch spectrum: transverse effective impedance $Z_{\perp\mathrm{eff}}$ and dipole kick factor $k_\perp$. If the bunch length is much shorter than the ring average radius, the effective impedance is defined as

$$Z_{\perp\mathrm{eff}} = \frac{\int_{-\infty}^{\infty} Z_\perp(\omega) h(\omega-\omega_\xi)\mathrm{d}\omega}{\int_{-\infty}^{\infty} h(\omega-\omega_\xi)\mathrm{d}\omega}\,, \tag{10}$$

where $Z_\perp(\omega)$ is the frequency-dependent transverse impedance, $\omega_\xi = \xi\omega_0/\alpha$, $\xi = d\nu_\beta/(dE/E)$ is the chromaticity, $\omega_\beta = \nu_\beta\omega_0$ is the betatron frequency.

The transverse dipole kick $\Delta x'$ caused by the beam-impedance interaction is

$$\Delta x' = \frac{q}{E/e} k_\perp x\,, \tag{11}$$

where x is the beam transverse offset, $k_\perp$ is the kick factor

$$k_\perp = \int_{-\infty}^{\infty} V_\perp(t)\,\lambda(t)\mathrm{d}t = \frac{1}{2\pi}\int_{-\infty}^{\infty} Z_\perp(\omega)\,h(\omega)\mathrm{d}\omega\,. \tag{12}$$

If the bunch is not very short, the transverse single-bunch effects can be analyzed using the simplified impedance models such as broadband resonator or pure inductive impedance for longer bunches, similarly to the longitudinal impedance.

Interaction of a bunched beam with the broadband impedance results in the transverse mode coupling [11]. If the chromaticity is zero, a fast head-tail instability occurs above the threshold beam current when the coherent (0-th) mode is coupled with the lowest (−1-st) head-tail mode. If the chromaticity is non-zero, the coherent mode damps upon the positive chromaticity and becomes unstable when the latter is negative, and the higher-order head-tail modes behave oppositely. The rise/damping rates decrease rapidly with the mode number, so only few lowest modes are essential and the eigenmode analysis is efficient. The complex frequency Ω_l of l-th head-tail mode can be found solving the eigenvalue problem [11], $\mathrm{Re}\Omega_l$ is the intensity-dependent shift of the mode frequency, $\mathrm{Im}\Omega_l$ is the rise/damping rate.

For the coherent mode, the intensity-dependent tune shift $\Delta\nu_\beta$ and the chromatic damping rate τ_ξ^{-1} can be obtained by spectral analysis of beam oscillations measured by a turn-by-turn BPM. The impedance model parameters are estimated by fitting the measured data with a solution of the eigenvalue problem [4]. If the frequency shift of 0-th mode is small compared with the synchrotron frequency ω_s, the linear approximations [11] for $\Delta\nu_\beta$ and τ_ξ^{-1} are applicable:

$$\Delta\nu_\beta = -\frac{I_b}{2\omega_0 E/e}\sum_i \beta_i k_{\perp i}\,,\quad \tau_\xi^{-1} = \frac{I_b\xi\omega_0}{2\pi\alpha E/e}\sum_i \beta_i \mathrm{Re}Z_{\perp i}\,. \tag{13}$$

Here the summation is over the whole ring, β_i is the amplitude betatron function at the location of i-th local impedance.

LOCAL IMPEDANCE

A local transverse impedance acts on the beam as a defocusing quadrupole, strength of which depends on the beam intensity. The wakefield kick (11) is proportional to the beam charge and its transverse offset at the impedance location.

Measurement of the intensity-dependent betatron phase advance $\mu(s)$ along the ring allows determining the contributions of different sections of the vacuum chamber into the coherent shift of betatron tune. In such a way, one can obtain the azimuthal distribution of the transverse impedance [9].

$$\Delta\mu(s) = -\frac{\Delta I_p}{8\pi CE/e}\int_0^s \beta(\zeta)\,\mathrm{Im}Z_\perp(\zeta)\,\mathrm{d}\zeta\,, \tag{14}$$

where I_p is the peak bunch current ($I_p = \frac{\sqrt{2\pi}}{\omega_0\sigma_t} I_b$ for a Gaussian bunch), C is the ring circumference. Accuracy of this technique is determined by the turn-by-turn resolution of the BPMs, the signals of which are used to calculate the betatron phase. Typically, the intensity-dependent change of the BPM-to-BPM phase advance is rather small, so this technique requires very good turn-by-turn BPM resolution.

The orbit bump method [12, 13] is more sensitive because the BPMs are used in the narrowband orbit mode rather than in the broadband turn-by-turn mode and the noise is much smaller. This method is based on the measurement of a wave-like orbit distortion created by the local wakefield kick (11). If a local orbit bump is created at the impedance location s_0 , the intensity-dependent orbit distortion is:

$$\Delta x(s) = \frac{\Delta q}{E/e} k_\perp x_0 \frac{\sqrt{\beta(s)\beta(s_0)}}{2\sin\pi\nu_\beta}\cos\left(|\mu(s)-\mu(s_0)| - \pi\nu_\beta\right)\,, \tag{15}$$

where x_0 is the orbit bump height. This wave-like orbit distortion can be measured using BPMs, and the wave amplitude is proportional to the kick factor at the bump location. For better accuracy, the systematic error caused by intensity-dependent behavior of the BPM electronics is also measured and then subtracted.

Rapid evolution of BPM electronics allows us to improve much the method accuracy. Now we can measure the orbit distortion of the order of several micrometers [14] compared to the 100-micrometer orbit distortion measured at the very

ISBN: 978-3-95450-192-2 doi:10.18429/JACoW-IBIC2017-MO3AB2

beginning of the bump method development [12]. Further improvement looks problematic because of the systematic errors caused by hysteresis effects of orbit correctors and by the orbit drifts during the measurement.

A technique, which significantly improves the accuracy of the bump method has been recently developed and tested [15]. This technique is based on an AC orbit bump created by sine-wave excitation of four fast correctors adjacent to the section, impedance of which is measured. The narrowband sine-wave signals provide better signal-to-noise ratio. Use of fast correctors eliminates the systematic error caused by hysteresis. The error caused by orbit drifts is also suppressed because the measured signal is not affected by the orbit motion outside the excitation frequency range. The resolution is good enough to measure the orbit distortion of the order of 0.1 μm, which is an order of magnitude smaller than the sensitivity of the conventional bump method.

To measure the impedance of a vacuum chamber component with variable geometry such as beam scrapers or in-vacuum undulators, both orbit and turn-by-turn techniques are effective [10, 16]. Using the reference bunch technique and precise BPMs, a contribution of the movable element to the total betatron tune shift can be accurately measured.

TRANSVERSE NARROWBAND IMPEDANCE

The transverse coupled-bunch instability (CBI) is driven by long-range wakefields (narrowband impedance), usually by trapped modes in cavity-like strictures in the vacuum chamber and by resistive-wall impedance. For M equally-spaced rigid bunches, the complex frequency shift $\Delta\Omega = \Omega - \omega_\beta$ of the n-th CBI mode is [11]:

$$\Delta\Omega_n = -\frac{i}{4\pi}\frac{\omega_0\beta}{E/e}MI_b\sum_{p=-\infty}^{\infty} Z_\perp\left((pM+n)\omega_0+\omega_\beta\right), \quad (16)$$

The frequency shift and rise/damping rate are equal to $\mathrm{Re}\Delta\Omega$ and $\mathrm{Im}\Delta\Omega$, respectively.

Using a transverse multi-bunch feedback system, we can individually excite each CBI mode, then stop the excitation and measure free oscillations (damped or anti-damped) [17]. The model of narrowband transverse impedance includes the resistive-wall impedance [18] and a set of narrowband resonators representing the trapped modes. The parameters of the impedance model are estimated by fitting the measured rise/damping rates of each mode with the values calculated using formula (16). Comparison of the model resonators fitting the measured data with the impedance computed by wakefield simulations is helpful to identify the sources of the resonances.

CONCLUSION

The beam-based measurements are important to estimate the machine impedance and to predict stability conditions for a high-intensity particle beam because the accuracy of impedance budget computations is not sufficient. Comparisons of the impedance computations and beam-based measurements show significant discrepancies for many machines, a factor of two or even more. Integral parameters combining the impedance and the bunch spectrum can be measured: effective impedance, longitudinal loss factor and transverse kick factor. For the longitudinal broadband impedance, the measurable effects are: bunch lengthening, synchronous phase shift, dispersive orbit distortion, and energy spread growth above the microwave instability threshold. These effects can be measured using streak cameras, dissector tubes, RF system diagnostics, BPMs, pin-hole X-ray cameras and synchrotron light monitors. For the transverse broadband impedance, the measurable effects are: coherent betatron tune shift, chromatic head-tail damping, and intensity-dependent orbit distortion. To measure these effects, turn-by-turn BPMs are used. The transverse narrowband impedance can be analyzed using the modal rise/damping times of the transverse coupled-bunch instability measured by bunch-by-bunch feedback systems.

REFERENCES

[1] B.W. Zotter, S.A. Kheifets, *Impedances and Wakes in High-Energy Particle Accelerato*. World Scientific, 1998.
[2] W.K.H. Panofsky, W.A. Wenzel, et al., Rev. Sci. Instrum., vol. 27 (1956), p. 967.
[3] J. Haissinski, Nuovo Cimento vol. 18B, No. 1 (1973).
[4] V. Smaluk, I. Martin, R. Fielder, R. Bartolini, Phys. Rev. ST Accel. Beams. Vol. 18, 064401 (2015).
[5] B. Zotter, *Potential-Well Bunch Lengthening*, CERN SPS/81-14 (DI). Geneva, 1981.
[6] Y.-C. Chae et al, *Measurement of the Longitudinal Microwave Instability in the APS Storage Ring*, in Proc. of PAC'01. Chicago, 2001.
[7] A. Blednykh et al, *A Numerical Study of the Microwave Instability at APS*, in Proc. of NA-PAC'16. Chicago, 2001.
[8] J.P. Koutchouk, *Trajectory and closed orbit correction*, CERN LEP-TH/89-2. Geneva, 1989.
[9] D. Brandt et al, *Measurement of Impedance Distribution and Instability Threshold in LEP*, in Proc. of PAC'95. Dallas, 1995, p. 570.
[10] E. Karantzoulis, V. Smaluk, L. Tosi, Phys. Rev. ST Accel. Beams. Vol. 6, 030703 (2003).
[11] A. Chao, *Physics of Collective Beam Instabilities*. Wiley, 1993.
[12] V. Kiselev, V. Smaluk, *Experimental Study of Impedances and Instabilities at the VEPP-4M Storage Ring*, in Proc. of EPAC'98. Stockholm, 1998.
[13] V. Kiselev, V. Smaluk, Nucl. Instr. and Meth. A 525 (2004), pp. 433–438.
[14] V. Smaluk et al, Phys. Rev. ST Accel. Beams. Vol. 17, 074402 (2014).
[15] V. Smaluk, X. Yang, A. Blednykh, Y. Tian, K. Ha, Nucl. Instr. and Meth. A 871 (2017) pp. 59–62.
[16] B. Podobedov et al, *Novel Accelerator Physics Measurements Enabled by NSLS-II RF BPM Receivers*, in Proc. of IBIC'16. Barcelona, 2016.
[17] R. Bartolini et al, *Analysis of Multi-bunch Instabilities at the Diamond Storage Ring*, in Proc. of IPAC'16. Busan, 2016.
[18] R.L. Gluckstern, J. van Zeijts, B. Zotter, Phys. Rev. E vol. 47 No. 1 (1993), pp. 656–663.

ISBN: 978-3-95450-192-2 doi:10.18429/JACoW-IBIC2017-MO3AB3

BEAM DIAGNOSTIC CHALLENGES FOR FACET-II*

S. Z. Green†, M. J. Hogan, N. Lipkowitz, B. O'Shea, G. White, V. Yakimenko, G. Yocky
SLAC National Accelerator Laboratory, Menlo Park, CA 94025, USA

Abstract

FACET-II, the Facility for Advanced Accelerator Experimental Tests II, is a new accelerator R&D test facility to be constructed at SLAC. It will provide high-energy, high-density electron and positron beams to advance the development of beam driven plasma wakefield acceleration and support a broad range of experiments. The FACET-II beams are expected to have 10 GeV energy, contain 2 nC of charge, have a transverse normalized emittance of 7 microns, be compressed to about 1 micron long and focused to about 6 micron wide at the interaction point. The nominal peak current is 20 kA and is expected to fluctuate up to 200 kA. Most experiments desire complete knowledge of the incoming beam parameters on a pulse-to-pulse basis. However, the extreme beam densities and strong fields of the beam current will destroy any diagnostics intercepting the beam in a single shot and impose unique challenges for beam diagnostics. Moreover, non-intercepting diagnostics are desirable to provide feedback for machine setup and characterization. We need to look beyond conventional diagnostics to seek new solutions for measurements of the high charge, small beam size, short bunch length, and low emittance.

INTRODUCTION

FACET-II, the Facility for Advanced Accelerator Experimental Tests II, is a new accelerator research and development test facility to be constructed at SLAC National Accelerator Laboratory. It's an upgrade of the FACET User Facility that delivered 20 GeV electron and positron beams for experimental programs from April 2012 to April 2016. Experiments at FACET produced high impact results on efficient acceleration of electrons and positrons in plasma. Highlights of these results include mono-energetic electron acceleration, high efficiency electron acceleration [1] and the first high-gradient positron plasma wakefield acceleration (PWFA) [2].

In April 2016, the Linac Coherent Light Source-II (LCLS-II) began construction for the second phase of SLAC's x-ray laser in the first kilometer (Sectors 0 to 10) of the SLAC Linac that previously housed the first half of the FACET accelerator. This represented an opportunity to rebuild and upgrade FACET. FACET-II will occupy the second kilometer of the SLAC Linac from Sectors 10 to 20 and use existing experimental infrastructure in Sector 20 (S20). A schematic layout of FACET-II relative to LCLS and LCLS-II is shown in Fig. 1. FACET-II will operate as a national user facility with experimental programs between 2019 and 2026.

FACET-II will continue to support advanced accelerator PWFA experiments. PWFA research priorities at FACET-II include emittance preservation with efficient acceleration, high brightness beam generation and characterization, positron acceleration, and staging studies. High-gradient high-efficiency acceleration was demonstrated at FACET and will be used to benchmark FACET-II. Full pump depletion of the drive beam and preservation of emittance at the micron level are planned as the first high impact experiments. Emittance preservation at the 10's of nm level is necessary for collider applications. Ultra-high brightness plasma injectors may lead to first applications of PWFA technology and allow the study of emittance preservation at this level. The delivery of positron beams to FACET-II will enable the only positron capability in the world for PWFA research. The emphasis will be to develop techniques for positron acceleration in PWFA stages. An independent witness injector will be added to FACET-II at a later stage as an Accelerator Improvement Project (AIP) to enable studies of high transformer ratio and staging challenges such as timing and alignment.

FACET-II ACCELERATOR

The goal of FACET-II is not only to restore beam capabilities for experimental programs but also to provide beams with greatly improved quality. A schematic of the FACET-II electron and positron systems is shown in Fig. 2. The FACET-II accelerator begins with the radio frequency (RF) photocathode gun and injection system at Sector 10 (S10) that enable delivery of low emittance beams. The 4.3 MeV electron beam goes through the first accelerating section L0 and reaches 134 MeV when injected into the linac for further acceleration through L1, L2, and L3 in Sectors 11–19. Three compression stages BC11, BC14 and BC20 are required to achieve the desired bunch length for compressed electron beams to be delivered to the experimental area in Sector 20 (S20). The design of the injector complex up to BC11 is based on the LCLS S20 injector.

Beam Dynamics

The FACET-II beams were modeled and tested with the 6D particle tracking models *IMPACT-T* [3] and *Lucretia* [4]. Simulation of the injector uses *IMPACT-T* which includes three dimensional space charge effect and is the simulation tool used for LCLS and LCLS-II. The rest of the FACET-II beam dynamics modeling was performed with *Lucretia* for tracking that includes effects of incoherent synchrotron radiation (ISR), coherent synchrotron radiation (CSR), longitudinal and transverse wakefields in structures, and longitudinal space charge. This Matlab-based toolbox was benchmarked against other tracking engines in the context of Linear Col-

* Work supported by DOE Contract DE-AC02-76SF00515
† selina@slac.stanford.edu

ISBN: 978-3-95450-192-2 doi:10.18429/JACoW-IBIC2017-MO3AB3

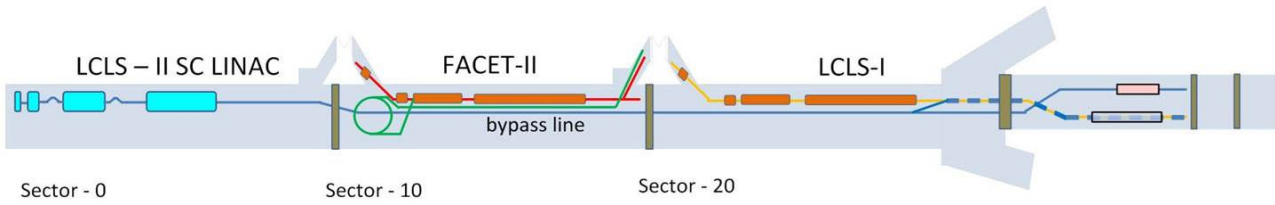

Figure 1: A schematic layout of FACET-II.

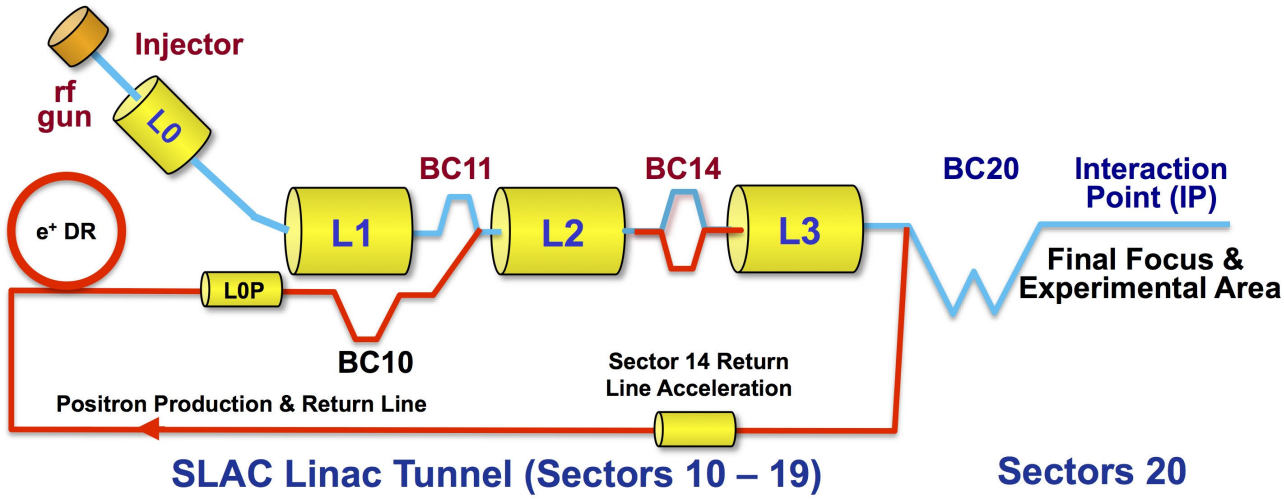

Figure 2: A schematic of the FACET-II electron and positron systems showing the injector, linac, bunch compressors, damping ring, and experimental area.

lider design and FACET. The FACET-II beams were designed and optimized based on these simulation studies to achieve the goals of the experimental programs.

The FACET-II nominal electron beam parameters and their operational ranges are shown in Table 1. Since the diagnostics for electrons and positrons are essentially the same and electrons in FACET-II have more extreme values, only the electron beam parameters are listed. The beam energy of 10 GeV is set by the linac length available for acceleration. The rest of the parameters are mainly driven by the need of the PWFA programs as they have the most demanding requirements and is a priority for the user program. With an upgrade of the BC20 optics, the peak current can reach up to 200 kA.

Table 1: FACET-II Electron Beam Design Parameters and Their Operational Ranges

Parameter	Baseline Design	Range
Final Energy [GeV]	10.0	4.0–13.5
Charge per pulse [nC]	2	0.7–5
Repetition Rate [Hz]	30	1–30
Normalized transverse emittance at S19 $\gamma\epsilon_{x,y}$ [µm–rad]	4.4, 3.2	3–6
Spot Size at IP $\sigma_{x,y}$ [µm]	18, 12	6–20
Min. bunch length σ_z (rms) [µm]	1.8	1.5–20
Max. peak current I_{pk} [kA]	72	10–130
Min. energy spread (rms) [%]	1.4	0.4–1.6
Max. ave. e^- beam power [kW] (10 GeV, 5 nC, 30 Hz)	1.5	0.1–4.2

ACCELERATOR DIAGNOSTICS

Beam diagnostics are essential to the operation of the accelerator as they provide controls, monitoring and tuning as well as optimization of the beam for experiments. Non-intercepting diagnostics are needed to provide feedback to the machine. FACET-II will re-use existing FACET electron beam diagnostics where possible or will adapt existing designs used at LCLS and FACET. The most useful LCLS injector diagnostics are reproduced for the FACET-II injector to provide to the linac a beam of known charge, arrival time, bunch length and distribution, energy, energy spread and distribution, as well as projected and sliced transverse emittance. Other critical diagnostics are located in or after the Bunch Compressors for longitudinal phase space and transverse profile diagnostics. In particular, at each bunch compressor, there will be Transverse RF Deflecting Cavities (TCAV) and a relative Bunch Length Monitor, a YAG screen for measuring energy spread, a wire scanner for transverse beam size and emittance measurement, as well as Beam Position Monitors.

ISBN: 978-3-95450-192-2 doi:10.18429/JACoW-IBIC2017-MO3AB3

Beam Position and Charge Monitors

Beam Position Monitors (BPMs) are the primary diagnostic for monitoring, feedback and tuning. They will be installed in every focusing magnet and key dispersive locations throughout the linac.

Resonant toroid current transformers with calibration winding are used in Toroids to measure the beam charge. Toroids in FACET-II monitor total beam charge at boundaries of functional areas. In particular, a toroid will be in place upstream and downstream of each bunch compressor. Matlab and python scripts regulate beam parameters at individual key locations for energy and orbit stabilization feedback.

Longitudinal Profile Diagnostics

A transverse deflecting cavity (TCAV) operating in conjunction with a profile monitor or wire scanner downstream can be used to measure bunch length and distribution. It is self-calibrating since the RF frequency is well known, however it is invasive to the beam and the same pulse cannot be used for downstream experiments. Relative Bunch Length Monitors (BLEN) such as coherent edge radiation monitor and wall gap monitor are non-destructive and provide pulse-by-pulse bunch length monitoring, but require calibration from a TCAV. A wall gap monitor with ceramic gap and diode will be used as a relative bunch length monitor in the injector system since the frequency is smaller than 300 GHz and peak current is lower than 300 A. A simple ceramic gap radiates into waveguide-coupled diodes (30 GHz to 60 GHz) for bunch length of 0.5 mm to 5 mm before injection into the linac. In BC11 and BC14, a coherent edge radiation monitor consisting of a mirror and pyrometer will be used since frequency will become greater than 300 GHz and peak current will be higher than 300 A. This type of pyroelectric bunch length monitor provides a relative bunch length diagnostic and works well for finding and maintaining peak compression.

Transverse Profile Diagnostics

Profile monitors are the most efficient and intuitive transverse diagnostics available. The Profile Monitors based on Optical Transition Radiation (OTR) are useful for imaging high energy and focused beams with the advantage of being able to see the entire beam profile. However, coherent effects influencing the beam profile have been observed in LCLS [5] due to microbunched structures at optical wavelengths. Strong Coherent Optical Transition Radiation (COTR) is a problem for compressed bunches and is expected at FACET-II for OTR Profile Monitors. The strong COTR from compressed bunches will saturate the OTR screens. Therefore, the wire scanners after BC11 will be used instead of OTR profile monitor for focused beams. There are ways to mitigate this COTR effect, such as screen tilt and fast camera gating, but these approaches have not yet been tested. Since wire scanners have more straightforward calibration in comparison to OTRs, they remain a reliable way to measure beam size for the linac. Wirescanners installed after each bunch compressor can also provide multi-profile emittance measurements to ensure emittance preservation across the linac-Bunch Compressor system.

EXPERIMENTAL DIAGNOSTICS

FACET-II will inherit and improve FACET's diagnostics at the experimental area in S20. Diagnostics that are available to use in place or to be improved upon will be described first, and then concepts for novel beam diagnostics to meet the challenges presented at FACET-II will be discussed.

Energy Spectrum

One of the most useful devices proven for both experiments and beam tuning is the so-called SYAG Profile Monitor in S20. A chicane in a plane of large horizontal dispersion deflects the beam vertically. X-rays from the resulting stripe of synchrotron radiation are intercepted by an off axis scintillator crystal made of Cerium doped Yttrium Aluminum Garnet (Ce:YAG). The X-ray intensity is proportional to the beam intensity giving a measurement of the beam energy spectrum and thus the energy spread can be measured on a shot-to-shot basis without being invasive to the beam.

Longitudinal Profile Diagnostics

Three different methods (TCAV, THz Michelson Interferometer, and Electro-Optic Sampling) of measuring the longitudinal beam profile were tested at FACET. The X-band TCAV provides a resolution of about 10 µm for bunch length measurement in a single shot, but it is destructive to the beam and the measurements are subject to chromatic distortions in the transport optics. The THz Michelson Interferometer, measurements require a scan of many shots and thus represents and average measurement with a resolution of about 5 µm. The Electro-Optic Sampling (EOS) system provides a measurement with resolution of 10 µm in a single shot. The EOS is subject to distortion from laser fluctuations and is challenging to set up. The last two methods are both non-destructive to the beam. The EOS studies performed at FACET were able to measure two-bunch separation of 122 µm with 10 µm resolution that can be improved further [6]. The EOS method appears to be the best of the three available options for longitudinal diagnostics. Nevertheless, FACET-II needs better resolution for the sub-micron beam and there were numerous improvements identified to increase resolution with the EOS as well as to optimize the system for more robust signals.

Another possibility for longitudinal beam profile diagnostics is the Attoscope scheme [7] that was tested at the Brookhaven National Laboratory Accelerator Test Facility early this year with results qualitatively supportive of simulations [8]. This diagnostic method could be developed and evaluated further to test at FACET-II.

ISBN: 978-3-95450-192-2 doi:10.18429/JACoW-IBIC2017-MO3AB3

Transverse Profile Diagnostics

The OTR foils and wires used in profile monitors located near the FACET IP were very susceptible to damage from the high peak current (10 kA) beam at focus. FACET-II will maintain both OTR profile monitors and wire scanners in the experimental area. The use of multi-screen OTR ladders and multi-wire fork wire scanners [9] away from beam waist will help to mitigate damage.

Emittance Measurements

One of the main goals for FACET-II is to demonstrate emittance preservation with low emittance PWFA beams. Therefore, reliable low-emittance measurement techniques are required.

Emittance measurement with a quad scan in a dispersed region can be studied and improved further for FACET-II emittance preservation [6] with normalized emittance down to a few micrometers.

Diagnostics for Extreme Beams

The FACET-II beams will be compressed to about 1 micron long and focused to about 6 micron wide at the interaction point (IP) for experiments in S20. The peak current will be up to 200 kA with emittance of 7 micron–rad. The surface temperature rise by image currents due to single bunch heating [10] is proportional to $(\frac{Q}{\sigma_z})^2 \frac{f^2(\sigma_y/\sigma_x)}{\sigma_x \sigma_y}$. Based on calculations and experience from FACET, the extreme beam densities and strong field of the beam current at FACET-II will destroy any diagnostics intercepting the beam in a single shot and thus impose unique challenges of beam diagnostics. Conventional diagnostics such as those used for operation of the machine as mentioned in the previous section cannot be used in the IP area if any material from the device intercepts the beam. Moreover, most experiments desire complete knowledge of the incoming beam parameters on a pulse-to-pulse basis. Therefore, the key is to develop diagnostics that are non-invasive and provide single-shot measurements. Some of the experimental diagnostics challenges were explored and discussed [6,9] based on experience from FACET. The unprecedented beams at FACET-II provide exciting diagnostic challenges for the accelerator community. A few concepts for novel beam diagnostics are discussed next.

Edge Radiation Interference Interference of dipole edge radiation [11] can be used to monitor for beam divergence as illustrated in the setup in Fig. 3. The visibility of the fringe resulting from the interference depends on beam divergence and emittance. Therefore, the emittance of the electron or positron beams can be determined by the intensity distribution of the edge radiation in this interference scheme that results in fringes of the light intensity. This method was tested with a beam of 60 MeV with emittance of ~1 μm at the Brookhaven National Laboratory Accelerator Test Facility. The edge radiation interferometry is a possibility for measuring low emittance beams and requires further study and development for beams with similar parameters as FACET-II.

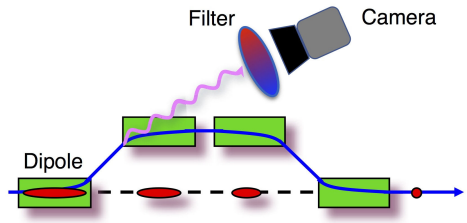

Figure 3: A potential setup for edge radiation from two dipoles.

Betatron Radiation Betatron radiation was emitted by electrons oscillating around the propagation axis due to the constant focusing force in the ion cavity of beam-driven plasma accelerators as illustrated in Fig. 4. There was a proposal [12] to set up a betatron radiation double differential spectrum (DDS) at FACET-II to recover the beam emittance. A bent crystal disperses the betatron radiation where the line-width of the radiation is proportional to the beam emittance. The rms line-width gives emittance through spread in K redshifts, assuming Gaussian betatron amplitude distributions. This method requires detectors for photons with energy in the keV and MeV range further downstream of the plasma accelerator.

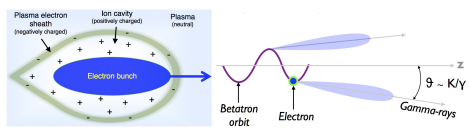

Figure 4: Illustration of betatron radiation from a beam-driven plasma accelerator.

Quadrant EOS The PWFA program at FACET-II will use two closely spaced bunches for experiments. This can be both electron or positron bunches, or a positron witness bunch after an electron drive beam, separated by about 150 μm. Traditional BPMs cannot resolve two beams within this short distance. To study positron witness acceleration in an electron wake as one of the PWFA experiments, the use of quadrant Electro-Optic Sampling (EOS) to measure the position of two beams in space and time will be pursued. This method takes a probe laser from the existing high power 800 nm Ti:Sa laser system that FACET-II inherits from FACET for laser ionized preformed plasma experiments [13]. The Coulomb field from the electron or positron bunch induces birefringence in the EO crystal(s) which could be a single crystal with a hole for beams to pass through or four crystals surrounding the electron/positron beams arranged in a quadrant pattern as shown in Fig. 5. A short, wide laser pulse intersecting the crystal receives polarization rotation. The e-beam profile decoded from polarization pattern is imprinted on the laser [14]. Cameras can

ISBN: 978-3-95450-192-2 doi:10.18429/JACoW-IBIC2017-MO3AB3

be set up to image the EO crystal and be analyzed to provide transverse position that is correlated with time. This type of setup will give both temporal and spatial information for the beams where phase shift occurs depending on where the beam offset is. The spectrally encoded EOS with imaging spectrometer enables non-destructive measurement of r-t beam correlations [15]. The goal is to measure correlations along the ~1 ps long bunch pairs. If testing is successful, this quadrant EOS method will be able to provide powerful single-shot longitudinal and transverse diagnostics.

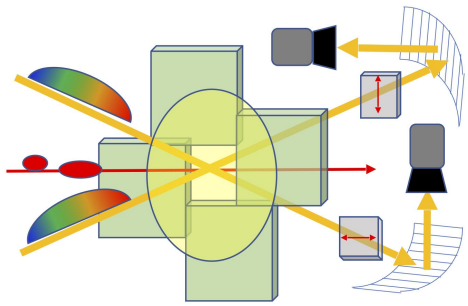

Figure 5: A setup for quadrant EOS with imaging spectrometer.

Bunch Length Monitor in a Gas Cell A gas cell setup could be used to measure bunches of about 3 fs to 30 fs long. Figure 6 is a conceptual illustration of a setup with a gas cell. A laser light resonantly pumps gas to reach an excited state. Its relaxation to intermediate state is triggered by the beam field. The emission rate from intermediate to ground state depends on the temporal spectrum of the beam field. The temperature of the gas affects what wavelength will trigger the transition to the intermediate and relaxed state. Therefore, one can detect gas transitions to characterize pulse length [16].

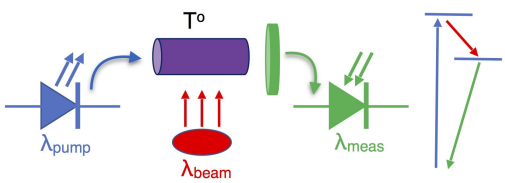

Figure 6: A bunch length monitor with gas cell.

CONCLUSION

FACET-II will deliver high-quality, high-density beams of electrons and positrons for advanced accelerator research. Diagnostics for operation of the injector and accelerator are well developed and based on proven designs at LCLS and FACET. The much higher-intensity electron beams from the photocathode gun pose greater challenges. FACET-II will need even more robust diagnostics when operating with very high peak currents. Conventional diagnostics are unable to measure the small beam size, short bunch length, and low emittance to meet the experimental needs in the IP area. Therefore, new diagnostic methods need to be developed in conjunction with the User Community. Operating as a national user facility, FACET-II welcomes users to submit proposals to develop and test novel diagnostics at the FACET-II beamline. Successful development and implementation of non-invasive, single-shot diagnostics will enable the next generation of experiments to access new regimes with FACET-II's unique capabilities.

ACKNOWLEDGMENT

We would like to thank the FACET Operations team and experimental groups (E-200, E-201, E-206, E-210, and E-224) that contributed to shared diagnostics and committed to continue improving diagnostics for FACET-II.

REFERENCES

[1] M. Litos *et al.*, "High-efficiency acceleration of an electron beam in a plasma wakefield accelerator," *Nature*, vol. 515, p. 7525, 2014.

[2] S. Corde *et al.*, "Multi-gigaelectronvolt acceleration of positrons in a self-loaded plasma wakefield," *Nature*, vol. 524, p. 7566, 2015.

[3] J. Quiang *et al.*, "Three-dimensional quasistatic model for high brightness beam dynamics simulation," *Phys. Rev. ST Accel. Beams* 9, p. 044204, 2006.

[4] P. Tenenbaum, SLAC-PUB-11215, 2005. http://www.slac.stanford.edu/accel/ilc/codes/Lucretia/.

[5] P. Krejcik, "Diagnostic Challenges at LCLS-II and Lessons Learned from LCLS-I at SLAC", presented at the Int. Beam Instrumentation Conf. (IBIC'17), Grand Rapids, Michigan, USA, August 2017, this conference.

[6] M. Hogan, "2016 FACET-II Science Workshop Summary Report," SLAC-R-1078, 2017. http://www-public.slac.stanford.edu/scidoc/docMeta.aspx?slacPubNumber=slac-r-1078.

[7] G. Andonian *et al.*, "Longitudinal profile diagnostic scheme with subfemtosecond resolution for high-brightness electron beams", *Phys. Rev. ST Accel. Beams* 14, p. 072802, 2011.

[8] G. Andonian, private communication, 2017.

[9] C. Clarke *et al.*, "Diagnostics challenges for FACET-II," in *Proc. 4th Int. Beam Instrumentation Conf. (IBIC'15)*, Melbourne, Australia, September 2015, paper MOPB075, pp. 238–242.

[10] X. E. Lin and D.H. Whittum, "Image Current Heating on a Metal Surface," *Phys. Rev. ST Accel. Beams*, 3, p. 101001, 2000.

[11] O.V. Chubar, Ph.D. thesis, 1990.

[12] J. Rosenzweig, 2016 FACET-II Science Workshop.

[13] S.Z. Green *et al.*, "Laser ionized preformed plasma at FACET", *Plasma Physics and Controlled Fusion*, 56, p. 084011, 2014.

[14] A. L. Cavalieri *et al.*, *Phys. Rev. Lett.* 94, p. 114801, 2005.

[15] V. Yakimenko, private communication, 2017.

[16] M. Zolotorev, private communication.

ISBN: 978-3-95450-192-2 doi:10.18429/JACoW-IBIC2017-MOPCC01

ADVANCES IN DIAGNOSTICS FOR MEDICAL ACCELERATORS*

C.P. Welsch†, University of Liverpool and Cockcroft Institute, UK

Abstract

The Optimization of Medical Accelerators (OMA) is the aim of a new pan-European project. As one of the largest initiatives of its kind, OMA joins more than 30 universities, research centers and clinical facilities with industry partners to address the challenges in treatment facility design and optimization, numerical simulations for the development of advanced treatment schemes, and beam imaging and treatment monitoring. This paper starts with an overview of the project's research into beam diagnostics and imaging. It then presents specific research outcomes from investigations into applying detector technologies originally developed for high energy physics experiments (VELO and Medipix) for medical applications; identification of optimum detector configurations and materials for high resolution spectrometers for proton therapy and radiography; ultra-low-charge beam current monitors. Finally, it summarizes the interdisciplinary training program that OMA provides to its 15 Fellows, as well as the wider medical accelerator community.

INTRODUCTION

In 1946 R.R. Wilson introduced the idea of using heavy charged particles in cancer therapy. In his seminal paper [1] he pointed out the distinct difference in depth dose profile between photons and heavy charged particles: While photons deposit their energy along the beam path in an exponentially decreasing manner, heavy charged particles like protons and ions show little interaction when they first enter the target and deposit the dominant portion of their energy only close to the end of their range. This leads to an inverse dose profile, exhibiting a well-defined peak of energy deposition (the Bragg Peak). The depth of the Bragg Peak in the target can be selected precisely by choosing the initial energy of the particles. This allows for a significant reduction of dose delivered outside the primary target volume and leads to substantial sparing of normal tissue and nearby organs at risk. The field of particle therapy has steadily developed over the last 6 decades, first in physics laboratories, and starting in the late 90's in dedicated clinical installations. By March 2013 about 110,000 people had received treatment with particle beams, the vast majority having been treated with protons and around 15,000 patients with heavier ions (helium, carbon, neon, and argon). The latter are considered superior in specific applications since they not only display an increase in physical dose in the Bragg peak, but also an enhanced relative biological efficiency (RBE) as compared to protons and photons. This could make ions the preferred choice for treating radio-resistant tumors and tumors very close to critical organs. Proton- and ion therapy is now spreading rapidly to the clinical realm. There are currently 43 particle therapy facilities in operation around the world and many more are in the proposal and design stage. The most advanced work has been performed in Japan and Germany, where a strong effort has been mounted to study the clinical use of carbon ions. Research in Europe, particularly at GSI, Germany and PSI, Switzerland must be considered outstanding. Initial work concentrated predominantly on cancers in the head and neck region using the excellent precision of carbon ions to treat these cancers very successfully [2]. Also, intensive research on the biological effectiveness of carbon ions in clinical situations was carried out and experiments, as well as Monte Carlo based models including biological effectiveness in the treatment planning process were realized [3]. This work has directly led to the establishing of the Heavy Ion Treatment center HIT in Heidelberg, Germany [4]. HIT started patient treatment in November 2009 and continues basic research on carbon ion therapy in parallel to patient treatments. Several other centers offering carbon ion and proton therapy are under construction or in different stages of development across Europe, e.g. five proton therapy centers are being built in the UK, one more has been commissioned in Marburg, Germany and the Medaustron facility has also started patient treatment recently. The OMA network presently consists of 14 beneficiary partners (three from industry, six universities, three research centers and 2 clinical facilities), as well as of 17 associated and adjunct partners, 8 of which are from industry.

RESEARCH

Continuing research into the optimization of medical accelerators is urgently required to assure the best possible cancer care for patients and this is one of the central aims of OMA [5]. The network's main scientific and technological objectives are split into three closely interlinked work packages (WPs):

- Development of novel beam imaging and diagnostics systems;
- Studies into treatment optimization including innovative schemes for beam delivery and enhanced biological and physical models in Monte Carlo codes;
- R&D into clinical facility design and optimization to ensure optimum patient treatment along with maximum efficiency.

The following paragraphs give three examples of R&D results already obtained by Fellows in the OMA diagnostics work package.

LHCb VELO as an Online Beam Monitor

A non-invasive beam current monitor based on the multi-strip LHCb Vertex Locator (VELO) silicon detector has been developed at the Cockcroft Institute/University of

*This project has received funding from the European Union's Horizon 2020 research and innovation programme under the Marie Skłodowska-Curie grant agreement No 675265.

†c.p.welsch@liverpool.ac.uk

ISBN: 978-3-95450-192-2 doi:10.18429/JACoW-IBIC2017-MOPCC01

Liverpool and first tests have been carried out at the treatment beam line at the Clatterbridge Cancer Centre (CCC), UK. Originally, the VELO detector was designed to track vertices in the LHCb experiment at CERN [6], but first feasibility tests performed at the CCC treatment beam line back in 2010 demonstrated the possibility of non–intrusive beam monitoring. The initial measurements consisted of data taken at several points along the beam line and gave high count rate, high resolution results. It is now planned to relate the proton 'halo' region hit rate, as measured by the VELO detector, with absolute beam current value, determined by a purpose-built Faraday cup. An illustration of the setup is shown in Fig. 1. More details about the design of the monitor are included in [7].

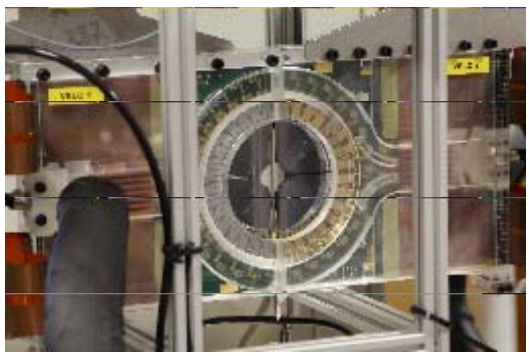

Figure 1: Photograph of the VELO detector that will be used as online beam monitor for quality assurance.

VELO is an example of a silicon micro-strip detector positioned around the experiments interaction region. Using two types of strip geometries the radial and azimuthal coordinates of traversing particles are measured. VELO provides precise measurements of track coordinates which are used to reconstruct the primary collision vertex as well as displaced secondary vertices that are characteristic of B-meson decays. It is hence a promising technology for non-invasive real-time beam monitoring applications. Jacinta Yap is an OMA Fellow based at the University of Liverpool/Cockcroft Institute**.** She works closely with QUASAR Group member Roland Schnuerer and both will further the understanding of VELO as an online beam monitor in medical accelerators. Their initial work has focused on building a deeper understanding of the detector's signal linearity through laser-based measurements in a dedicated lab setup. This was then linked to results obtained from measurements with beam [8]. In a next step, Monte Carlo simulations will be used to reproduce and optimize beam transport at CCC. Results will then be benchmarked against experimental data obtained in additional experimental studies.

Proton Energy and Range Measurement

The goal of the project of Laurent Kelleter is the transfer of specific technology developed for high energy physics experiments at UCL for use in making precision measurements at clinical proton beam therapy (PBT) facilities. This research programme has grown out of the efforts to support the new proton beam therapy centres in the UK, but strong international collaborations have been forged — particularly with OMA partners — that provide wider opportunities for use of the detectors under development. This project seeks to address a number of challenges in providing effective treatment with proton therapy. Chief amongst these is to improve the systems used for patient imaging. Traditional treatment planning with photons requires multiple patient CT images to build up an effective diagnostic image for patient planning, both before the start of treatment and between fractions, to allow changes in the tumour volume to be monitored. However, the increased localisation of proton dose delivery requires a corresponding increase in imaging resolution, exposing the limits of traditional CT imaging. In addition, X-ray CT images do not provide information on the proton-specific absorption characteristics of tissue surrounding the treatment volume.

An alternative is to use protons for imaging: an energy is chosen such that the protons do not stop within the body of the patient but pass through to be detected. Using the same proton beam for both imaging and treatment ensures the patient does not have to be moved between imaging and treatment: in addition, the anatomical information acquired from the imaging does not have to be adjusted from a different imaging modality. A conceptual proton Computed Tomography (pCT) system consists of a series of tracking layers upstream and downstream of the patient, with some method of measuring the final energy of the diagnostic protons.

Figure 2: SuperNEMO OM, showing bare plastic scintillator block (left) and wrapped block with PMT (right).

Preliminary simulations of the detector response were carried out in GEANT4. These showed the anticipated response of the SuperNEMO [9] Optical Module (OM) shown in Fig. 2 in response to the 60 MeV clinical proton beam at the Clatterbridge Cancer Centre (CCC), the only clinical proton therapy facility currently operating in the UK. These simulations indicated a stopping distance remarkably close to that of water — 30.2 mm for PVT plastic as opposed to 30.5 mm in water — supporting the suggestion that the plastic scintillator could replace other water-equivalent materials (such as PMMA plastic) when making a WEPL measurement. The simulations also indicated an energy resolution of 0.6% σ at 60 MeV, below the target resolution of 1% σ. These simulations have since been

ISBN: 978-3-95450-192-2 doi:10.18429/JACoW-IBIC2017-MOPCC01

confirmed in measurements at CCC. More measurements have also been taken at CCC to better understand the results. In addition, OMA partner Medaustron provided the opportunity for the UCL group to make first energy resolution measurements with their calorimeter at energies between 60 MeV and 252 MeV for the first time. Results are being analysed and look very promising.

Measurement of Ultra-Low Charges

Beam current is the basic quantity of a charged particle beam. Beam current is the first check of accelerator functionality and has to be determined in an absolute manner. It is also important for transmission measurements and to prevent for beam losses [10]. However, due to many varieties of accelerator, this becomes a challenging task from beam diagnostic perspective. Beam current is an intermediary for measuring beam lifetime in storage rings, superconducting linacs and ERLs [11]. For the PROSCAN facility at Paul Scherrer Institut (PSI), interceptive ionization chambers or secondary emission detectors have been used for beam current measurement in the past. However, these degrade the beam quality due to multiple scattering or energy losses. Since this implies a strict regulation of the use of these diagnostic devices during therapy, non-interceptive monitors of the beam current would be highly advantageous for online control. OMA Fellow Sudharsan Srinivasan is in the process of developing a reentrant cavity current monitor. This device works on the principle of an ordinary resonant circuit which consists of an inductor and a capacitor in parallel. Its fundamental mode resonant frequency 145.7 MHz was designed to match the 2nd harmonic of the beam pulse repetition rate, 72.85 MHz.

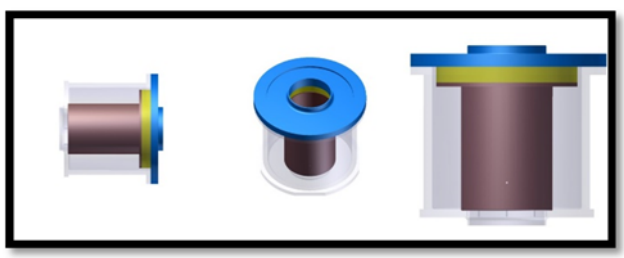

Figure 3: ANSYS HFSS model of the RF current monitor being designed at PSI.

Initial design studies with ANSYS HFSS (High Frequency Structural Simulator) yielded a parametric model which allowed to analyze the monitor properties in detail, see Fig. 3. A prototype is currently being built and will be used for experimental studies in the near future.

TRAINING

The fundamental core of the OMA training is a dedicated cutting-edge research project for each Fellow at their host institution. The network is then used to provide opportunities for secondments and experience at another institution. All Fellows will be in post for 36 months and most of them are registered into a PhD program. This local training will be complemented by a series of network-wide events that include external participation. All OMA Fellows joined a researcher skills training at the University of Liverpool in April 2017. This week-long School included for example sessions on project management, presentation skills, communication of research outcomes to diverse audiences, as well as IP rights and knowledge transfer. As an introduction to the field of medical accelerators all recruited OMA Fellows took part in an international School on the Optimization of Medical Accelerators. This was held at the CNAO Centre in Pavia, Italy in June 2017 and covered beam physics, instrumentation R&D and charged particle beam simulations level [12]. More than 70 researchers participated in this event. A Monte Carlo School will be held in November 2017 in Munich and an international School on the Optimization of Medical Accelerators at an advanced level will be held in 2019. Three 2-day Topical Workshops covering two scientific WPs at a time will also be organized. These will cover 'Facility Design Optimization for Patient Treatment', 'Diagnostics for Beam and Patient Monitoring', and 'Accelerator Design & Diagnostics'. Topical Workshops will be held from early in 2018 and will be announced via the project website [5]. A three-day International Conference will be hosted by the national accelerator center (CNA) in Seville, Spain in the final year of OMA. It will promote all research outcomes and enable the Fellows to engage with other university groups and private companies. The conference will also present an opportunity for follow-up activities between the OMA partners and participating scientists from outside the network and thus serve as a career platform for all Fellows. A Symposium on 28 June 2019 on Accelerators for Science and Society will be organized at the Liverpool Convention Center as a finale to the outreach activities undertaken during the course of the network. This will present the main project findings in an understandable way for the general public, emphasizing applications of the technologies concerned.

SUMMARY AND OUTLOOK

In this paper, a general overview of the OMA project, along with selected initial research from the diagnostics and instrumentation work package was given. A brief overview of the broad and interdisciplinary training program was also given. Many more training events are now setup for the OMA Fellows and the wider medical accelerators community and detailed information will be made available via the project website and the quarterly OMA newsletter.

REFERENCES

[1] M. R. Wilson; *Radiology* 47 (1946) 498-491.

[2] D. Schulz-Ertner, *et al.*, *Int. J. Rad. Onc. Biol. Phys.*, 58, (2004), pp. 631–640 and G. Kraft, *Progr. in Particle and Nuclear Physics* 46 (2001).

[3] M. Krämer, *et al.*, *Phys. Med. Biol.* 45 3299 (2000) and T. Elsässer, *et al.*, *Int. J Rad. Onc. Biol. Phys.* 78 (2010), p. 1177–1183.

[4] S.E. Combs, *et al.*, *Radiotherapy and Oncology* 95 (2010), p. 41-44.

[5] OMA Project, http://www.oma-project.eu

ISBN: 978-3-95450-192-2 doi:10.18429/JACoW-IBIC2017-MOPCC01

[6] LHCb VELO Technical Design Report, CERN/LHCC 2001-0011, LHCb TDR 5, Geneva.

[7] T. Cybulski, "Non-invasive Beam Monitor for Medical Accelerators", *PhD thesis*, Liverpool (2017).

[8] R. Schnuerer, J. Yap, *et al.*, "Non-invasive online beam monitor using LHCb VELO", in *Proc. IPAC'17*, Copenhagen, Denmark, May 2017, paper THPVA136.

[9] R. Arnold *et al.*, Eur. Phys. J. C 70, 927 43 (2010).

[10] P. Forck, "Pick-Ups for bunched beams," JUAS Archamps, p. 6.

[11] J. C. Denard, "Beam Current Monitors," Notes Work. Accel. Instrumentation, BNL, October, 1989, no. 1, pp. 141–155, 1990.

[12] OMA School on Medical Accelerators, https://indico.cern.ch/event/595518/

ISBN: 978-3-95450-192-2 doi:10.18429/JACoW-IBIC2017-MOPCC03

A METHOD OF LOCAL IMPEDANCE MEASUREMENT BY SINE-WAVE BEAM EXCITATION *

V. Smaluk†, X. Yang, A. Blednykh, Y. Tian, K. Ha, Brookhaven National Laboratory, Upton, USA

Abstract

We have developed and tested a technique, which significantly improves the accuracy of the orbit bump method of local impedance measurement. This technique is based on in-phase sine-wave (AC) excitation of four fast correctors adjacent to the vacuum chamber section, impedance of which is measured. The narrow-band sine-wave signals provide better signal-to-noise ratio. Use of fast correctors to the beam excitation eliminates the systematic error caused by hysteresis. The systematic error caused by orbit drift is also suppressed because the measured signal is not affected by the orbit motion outside the excitation frequency range. The measurement technique is described and the result of experimental testing carried out at NSLS-II is presented.

INTRODUCTION

The beam intensity in storage rings is limited by collective effects of beam dynamics resulting from the interaction of a particle beam with electromagnetic fields induced in a vacuum chamber by the beam itself. This interaction can result in serious troubles affecting accelerator performance such as overheating of vacuum chamber components or instability of the beam motion.

The beam-impedance interaction manifests itself in several effects, which can be measured quite precisely using modern beam diagnostic instruments and measurement techniques. So the impedance can be measured experimentally using beam- based techniques. For the longitudinal broadband impedance, the measurable effects are current-dependent bunch lengthening, synchronous phase shift, and energy spread growth due to microwave instability. For the transverse broadband impedance, the measurable effects are current-dependent shift of betatron tunes and rising/damping time of chromatic head-tail interaction.

The impedance distribution along the ring is not uniform and beam-based measurement of local impedance is a subject of importance for accelerator physicists. For example, low-gap light-generating insertion devices make significant contributions to the total impedance of a light sources. Thus, measurement of impedances of already installed insertion devices is helpful to predict the impedance evolution of light sources while installing new insertion devices.

* Work supported by DOE under contract DE-SC0012704
† vsmalyuk@bnl.gov

ORBIT BUMP METHOD

The interaction of a bunched beam with the transverse broadband impedance is characterized by the kick factor:

$$k_\perp = \frac{1}{2\pi}\int_{-\infty}^{\infty} Z_\perp(\omega)\, h(\omega)\mathrm{d}\omega\,, \qquad (1)$$

where $Z_\perp(\omega)$ is the frequency-dependent transverse impedance; $h(\omega) = \tilde{\lambda}(\omega)\tilde{\lambda}^*(\omega)$ is the bunch power spectrum; $\tilde{\lambda}(\omega) = \int_{-\infty}^{\infty} \lambda(t)e^{-i\omega t}\mathrm{d}t$ is the Fourier transform of the bunch longitudinal density $\lambda(t)$ normalized as $\int_{-\infty}^{\infty} \lambda(t)\mathrm{d}t = 1$. A transverse dipole kick $\Delta x'$ caused by the beam-impedance interaction is

$$\Delta x' = \frac{q}{E/e}k_\perp x\,, \qquad (2)$$

where $q = Ne$ is the beam charge, N is the number of particles, x is the beam transverse offset, E is the beam energy, e is the electron charge.

A local transverse impedance acts on the beam as a defocusing quadrupole, strength of which depends on the beam intensity. The orbit bump method [1, 2] is based on the measurement of a wave-like orbit distortion created by the wakefield kick $\Delta x'$ (2) proportional to the beam charge and its transverse position at the impedance location. If a local orbit bump is created at the impedance location, the intensity-dependent orbit distortion is:

$$\Delta x(s) = \frac{\Delta q}{E/e}k_\perp x_0 \frac{\sqrt{\beta(s)\beta(s_0)}}{2\sin\pi\nu_\beta}\cos\left(|\mu(s)-\mu(s_0)|-\pi\nu_\beta\right)\,, \qquad (3)$$

where x_0 is the orbit bump height, s_0 is the impedance location, Δq is the bunch charge variation, ν_β is the betatron tune, β is the beta function, and μ is the betatron phase advance. This wave-like orbit distortion can be measured using beam position monitors, and the wave amplitude is proportional to the kick factor at the bump location. To reduce the systematic error caused by intensity-dependent behavior of the BPM electronics, this error is also measured and then subtracted.

The orbit bump method is more sensitive than the method [3] based on the measurement of intensity-dependent betatron phase advance along the ring because the beam position monitors (BPMs) are used in the narrowband orbit mode rather than in the broadband turn-by-turn mode, and the noise is much smaller.

Evolution of BPM electronics resulted in great improvement of the bump method accuracy from 20 – 40 μm at the very beginning of the method development [4] to

ISBN: 978-3-95450-192-2 doi:10.18429/JACoW-IBIC2017-MOPCC03

0.2 – 0.5 μm) in the resent measurements [5]. Two examples of the measured intensity-dependent orbit distortions with the fitting functions (3) are shown in Fig. 1 (VEPP-4M, 1998) and Fig. 2 (Diamond Light Source, 2014).

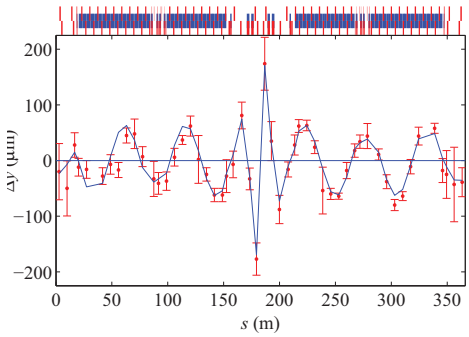

Figure 1: Intensity-dependent orbit distortion (VEPP-4M collider, 1998).

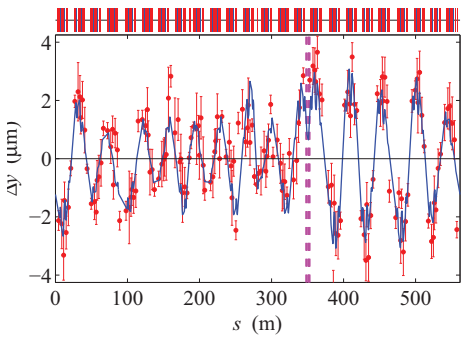

Figure 2: Intensity-dependent orbit distortion (Diamond Light Source, 2014).

Further improvement looks problematic because of the systematic errors caused by hysteresis effects of correctors and by the orbit drifts along the measurement.

AC BUMP TECHNIQUE

To improve the bump method accuracy, we propose a technique based on excitation of an AC orbit bump by use of fast orbit correctors [6]. The fast correctors are working in a bandwidth up to hundreds Hertz and they are typically installed at synchrotron light sources for fast orbit feedbacks. Recent developments of lattice correction techniques using an orbit response matrix measured by sine-wave excitation of the fast correctors show that the AC orbit can be measured with a precision of the order of 0.02 μm [7, 8].

The proposed technique has been tested at NSLS-II by measuring the vertical kick factor of a variable-gap in-vacuum undulator. Four fast correctors located nearby the undulator are selected as shown in Figure 3. The undulator is located in the center of the straight section, the fast correctors are marked as FC, the beam position monitors are marked as BPM, the beta functions are also shown.

To create the AC orbit bump, these four correctors are excited simultaneously by a sine-wave driving signal. Proper excitation amplitudes for the correctors are obtained by scaling the driving signal with the factors pre-calculated using

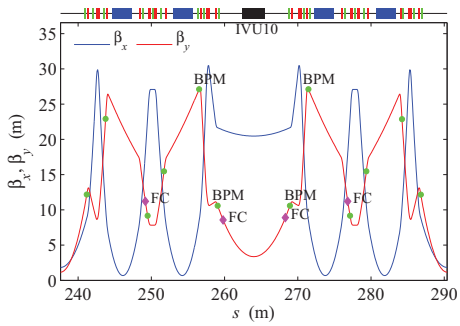

Figure 3: Beta functions and positions of BPMs and fast correctors in the NSLS-II Cell 10. The undulator is located in the center of the section.

the model lattice. The same driving signal is used as a reference for synchronous detection of the beam oscillations measured by BPMs. Figure 4 shows an example of single-BPM data together with the reference signal.

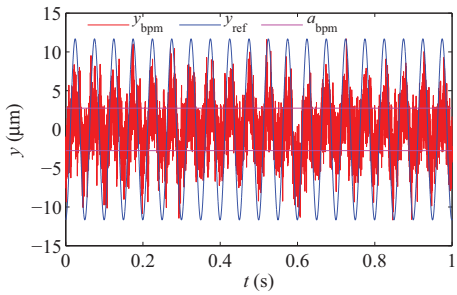

Figure 4: Beam oscillations measured by a BPM and the reference signal.

If the bump is perfectly matched, the beam oscillates between the outer two correctors and the orbit outside the bump is not perturbed. In reality, a residual orbit perturbation outside the bump is caused by the lattice model imperfections. An example of the measured AC orbit bump in comparison with the ideal (simulated) one is shown in Figure 5. The orbit perturbation outside the bump is a source of a systematic error, but it does not exceed 5% for this example.

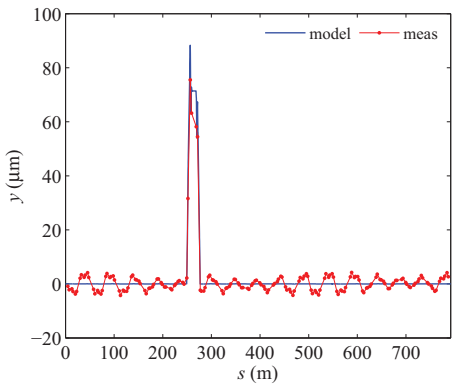

Figure 5: Measured (red) and simulated (blue) AC orbit bumps.

To measure the kick factor of a vacuum chamber section, the AC bump is created in that section and the orbit oscillation is measured by all BPMs as a function of the beam

ISBN: 978-3-95450-192-2 doi:10.18429/JACoW-IBIC2017-MOPCC03

charge variation Δq. The intensity-dependent orbit distortion Δx at the location of each BPM is a difference of the oscillation amplitudes measured by the BPM at different beam charge.

EXPERIMENTAL RESULTS

To test the AC bump technique, the vertical kick factor of a variable-gap in-vacuum undulator has been measured in two cases: closed gap of 6 mm (maximal impedance) and open gap of 25 mm (minimal impedance).

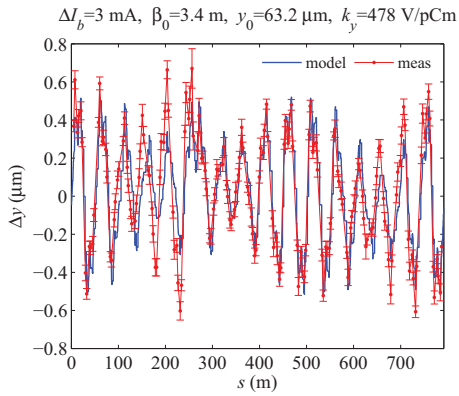

Figure 6: Measured (red dots) and model (blue line) AC orbit distortion. The undulator gap is 6 mm.

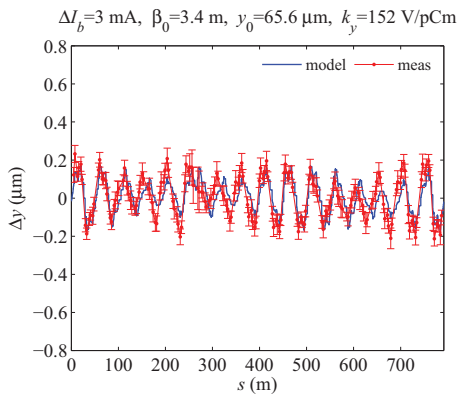

Figure 7: Measured (red dots) and model (blue line) AC orbit distortion. The undulator gap is 25 mm.

The fast correctors were excited by a sine-wave drive signal with the frequency of 20 Hz. The maximal kick angle of the NSLS-II fast corrector is limited by its power supply and can not exceed 15 μrad. The beam oscillation is measured simultaneously by 180 button-type BPMs with the sampling frequency of 10 kHz [9]. The measured noise power spectral density of NSLS-II BPMs is about 0.03 $\mu m/\sqrt{Hz}$. The BPM data were measured during $T = 10$ s, therefore the bandwidth is $\delta f = 1/T = 0.1$ Hz [8] and the noise-limited resolution is about 0.01 μm.

The AC orbit was measured at two values of the beam current: 2 mA and 5 mA (the beam charge was 5.3 nC and 13.2 nC, respectively). The measured AC orbit distortions (3) are shown in Figure 6 and Figure 7. The error bars represent r.m.s. deviation of 10 measurements. As one can see, the measurement resolution is good enough to measure the orbit distortion of the order of 0.1 μm. The kick factor k_y is obtained by fitting the model orbit distortion (3) with the measured data using k_y as a fit parameter.

CONCLUSION

For local impedance measurement, a fast and precise technique based on excitation of an AC orbit bump using fast orbit correctors has been developed and tested at NSLS-II. The results have demonstrated that the measurement resolution is good enough to measure the orbit distortion of the order of 0.1 μm, which is an order of magnitude smaller than the sensitivity of the conventional bump method.

REFERENCES

[1] V. Kiselev, V. Smaluk, "A Method for Measurement of Transverse Impedance Distribution along Storage Ring", in *Proc. of 4th European Workshop on Diagnostics for Particle Accelerators*, Chester, 1999 (PT19).

[2] V. Kiselev, V. Smaluk, "Measurement of Local Impedance by an Orbit Bump Method", *Nucl. Instr. and Meth.*, A 525 (2004).

[3] D. Brandt *et al.*, "Measurement of Impedance Distribution and Instability Threshold in LEP", in *Proc. of PAC-95*. Dallas, 1995, p. 570.

[4] V.Kiselev, V.Smaluk, "Experimental Study of Impedances and Instabilities at the VEPP-4M Storage Ring", in *Proc. of EPAC-98*, Stockholm (IOP, Bristol, 1998), pp. 1005–1007.

[5] V. Smaluk, R. Bartolini, R. Fielder, G. Rehm, A. Blednykh, "Coupling impedance of an in-vacuum undulator: Measurement, simulation, and analytical estimation", *Phys. Rev. ST Accel. Beams.*, Vol. 17, 074402 (2014).

[6] V. Smaluk, X. Yang, A. Blednykh, Y. Tian, K. Ha, "AC orbit bump method of local impedance measurement", *Nucl. Instr. and Meth.*, A 871 (2017) pp. 59–62.

[7] I.P.S. Martin *et al.*, "A Fast Optics Correction for the Diamond Storage Ring", in *Proc. of IPAC 14*, Dresden, 2014 (TUPRI083).

[8] X. Yang, V. Smaluk, L.H. Yu, Y. Tian, K. Ha, "Fast and precise technique for magnet lattice correction via sine-wave excitation of fast correctors", *Phys. Rev. Accel. Beams.*, Vol. 20, 054001 (2017).

[9] K.Vetter *et al.*, "NSLS-II RF Beam Position Monitor Update", *in Proc. of BIW 12*, Newport News, VA, USA, 2012 (WECP02).

ISBN: 978-3-95450-192-2 doi:10.18429/JACoW-IBIC2017-MOPCC04

SIMULATION OF BEAM-BEAM TUNE SPREAD MEASUREMENT WITH BEAM TRANSFER FUNCTION IN RHIC*

Y. Luo†, W. Fischer, X. Gu
Brookhaven National Laboratory, Upton, NY, USA

Abstract

Head-on beam-beam compensation had been successfully implemented routinely in the 2015 polarized proton operation in the Relativistic Heavy Ion Collider at Brookhaven National Laboratory. Two electron lenses have been used to reduce the incoherent beam-beam tune spread to allow a larger proton bunch intensity and therefore a higher luminosity. Beam transfer function was used to determine the beam-beam incoherent tune spread. In this article, we carry out numeric simulations to compare the tune spreads derived from tune histogram and the beam transfer function. Then we present the experimental beam transfer function measurements and extract the tune spreads due to beam-beam interaction and electron lens. Experimental results show that the electron lens reduced the beam-beam tune spread.

INTRODUCTION

The luminosity is limited by the beam-beam interaction in the polarized proton operation operation in the Relativistic Heavy Ion Collider (RHIC) at Brookhaven National Laboratory. To have good beam and polarization lifetimes, the working point is constrained between 2/3 and 7/10 in the tune space. To minimize the head-on beam-beam tune spread and to compensate the nonlinear beam-beam resonance driving terms, two electron lenses (e-lenses) have been installed in RHIC, one for each ring. In 2015, head-on beam-beam compensation had been implemented routinely for the first time in the RHIC 100 GeV polarized proton operation [1–3]. With beam-beam compensation, both the peak and integrated luminosities had been doubled comparing to the previous energy proton operation in 2012.

In the article, we present a fast and efficient way to experimentally determine the incoherent beam-beam tune shift with beam transfer function (BTF) measurement. We first carry out numerical simulations to compare the tune spreads from the BTF calculation and from the tun histogram and the beam-beam parameter. Then we present the BTF measurements during electron current scans without and with beam-beam interaction. The tune spreads introduced by the e-lens are extracted. The experimental results show that the e-lens reduced the beam-beam tune spread.

NUMERICAL SIMULATION

We developed both weak-strong and strong-strong beam-beam codes to numerically calculate BTF and tune histogram [4]. The advantage of weak-strong code is that the particles can be tracked element-by-element through the ring and all the lattice nonlinearities can be included. In the RHIC operation, coherent beam-beam modes can only be detected with external excitation. In the following, we will use the weak-strong beam-beam interaction model. The proton bunch is represented by macro-particles while the other beam by a rigid Gaussian charge distribution. The e-lens is modeled as 4 segments with each one represented by a drift – a 4-d beam-beam kick – a drift.

In one test, the 2015 100 GeV blue ring lattice is used. The lattice tunes are set to (0.69, 0.685). To minimize the tune spread from the chromatic effect, the linear chromaticities are set to (0, 0). The proton bunches collide at IP6 and IP8. The e-lens is switched off. The proton bunch intensity is scanned up to 2.0×10^{11} or a total beam-beam parameter of -0.02.

Figure 1 shows the calculated imaginary part of BTF and the tune histogram with a beam-beam parameter of -0.01. The imaginary part of BTF is wider than that directly calculated tune histogram since BTF is related to the amplitudes of particles. In the following, to compare the width of tune spreads derived from the imaginary part of BTF and the tune histogram, we define the tune spread as the full width of 10% maximum [5]. We choose the full width of 10% maximum other than the well-known full width of half maximum (FWHM) because the former is close to the full span of the tune distribution, and also 10% maximum is a practical choice for experimental BTF measurements to overcome the noise floor.

Figure 2 shows the correlation between the tune spreads derived from the imaginary part of BTF and tune histogram. The horizontal and vertical axises are the tune spreads from the tune histogram and BTF respectively. The tune spread derived from BTF can be fitted linearly with that from the tune histogram, although the tune spread from BTF is about 8% larger than that from the tune histogram in this test. We also found that both the tune spreads from BTF and from the tune histogram can be fitted linearly with the beam-beam parameter, too. They are about half of the beam-beam parameter within a relative error of 12%.

The linear correlations between the tune spreads from the imaginary part of BTF and the tune histogram and the beam-beam parameter provide us a fast and convenient way to estimate the tune spread experimentally based on the high signal-to-noise BTF measurement.

* Work supported by Brookhaven Science Associates, LLC under Contract No. DE-AC02-98CH10886 with the U.S. Department of Energy.
† yluo@bnl.gov

ISBN: 978-3-95450-192-2 doi:10.18429/JACoW-IBIC2017-MOPCC04

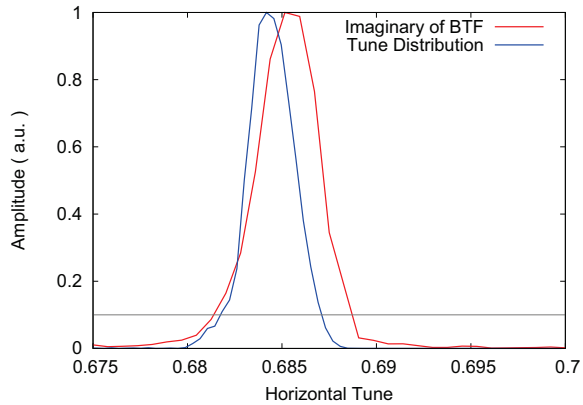

Figure 1: Simulated tune histogram and imaginary part of BTF with a beam-beam parameter of -0.01.

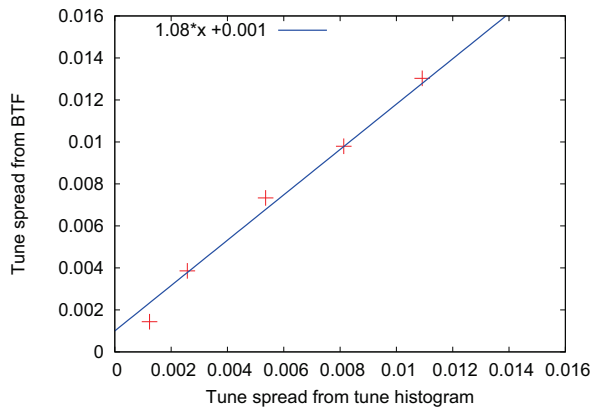

Figure 2: Correlation between the tune spreads derived from BTF and tune histogram.

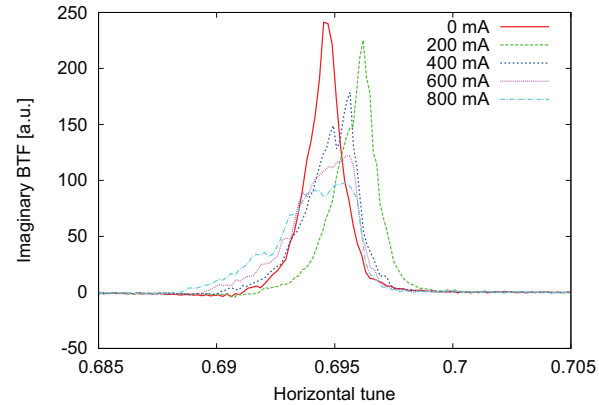

Figure 3: Measured imaginary parts of BTF without beam-beam interaction.

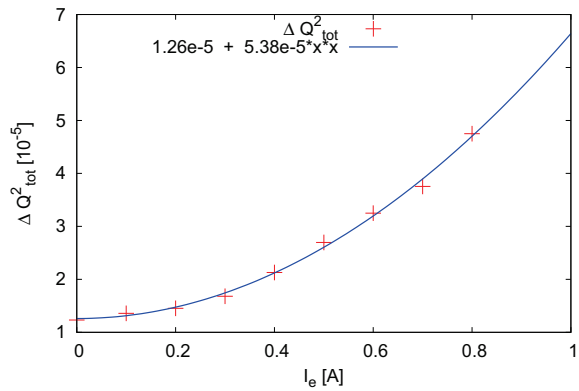

Figure 4: The total tune spread fitted with the electron current according to Eq. (1).

MEASUREMENT RESULTS

Without Beam-beam

Figure 3 shows the measured imaginary BTFs of the proton beam in the Yellow ring during the 2015 100 GeV proton-proton operation. During this experiment, there was no beam-beam interaction. The electron current of the e-lens was scanned from 0 up to 800 mA with a step size of 100 mA. The electron beam size in the interaction region is 0.74 mm, while the proton beam size was 0.60 mm at the same location.

For RHIC, without beam-beam interaction, the main source of tune spread is from the chromatic effect. Since the tune spread generated from the chromatic effect and the tune spread generated from the e-lens are uncorrelated, we have

$$\Delta Q_{tot}^2 = \Delta Q_{resid}^2 + \Delta Q_{elens}^2, \quad (1)$$

where ΔQ_{tot}, ΔQ_{resid}, and ΔQ_{elens} are the total tune spread, and the residual tune spread, and the tune spread contributed by the e-lens. If the electron beam shape and size were well maintained during the electron beam current scan, the tune spread from the electron lens should be proportional to the electron current I_e. Therefore,

$$\Delta Q_{tot}^2 = \Delta Q_{resid}^2 + (k * I_{elens})^2, \quad (2)$$

where k is an unknown constant.

Figure 4 shows ΔQ_{tot}^2 as a function of I_{elens} . ΔQ_{tot}^2 can be fitted very well according to Eq. (1). After knowing ΔQ_{resid}^2, we extract the tune spread contributed by the electron lens ΔQ_{elens} and fit them to a linear function of electron current. Figure 5 shows the result. The tune spread from the e-lens is $\Delta Q_{elens}/\Delta I_e$= 0.0072/A. The incoherent tune shift from the e-lens can be numerically calculated based on the electron beam 's size and current. For 1000 mA electron current, the incoherent tune shift from the e-lens is 0.011.

With Beam-beam

In the proton-Aluminum ion collision, the proton beam's tunes are (0.695, 0.685) while the Aluminum ion beam's tunes are around (0.235, 0.225). There is no coherent beam-beam interaction. In this experiment, we scanned the electron current from 0 up to 1030 mA with proton-Alumimum ion collisions at IP6 and IP8. The total beam-beam parameter from the proton-Alumimum ion collision is about -0.014.

ISBN: 978-3-95450-192-2 doi:10.18429/JACoW-IBIC2017-MOPCC04

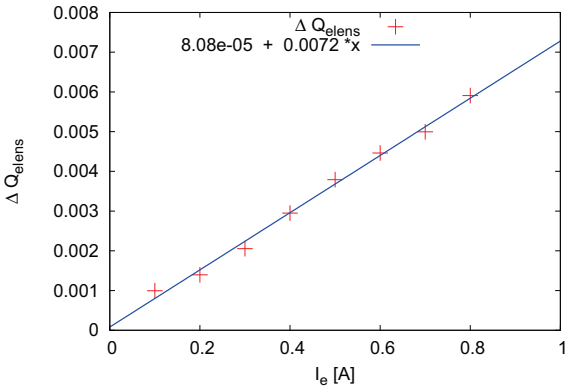

Figure 5: The tune spread from e-lens linearly fitted with the electron current.

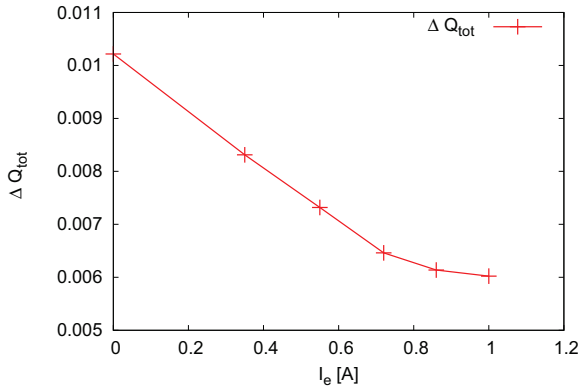

Figure 6: Measured total BTF tune spreads with beam-beam interaction.

The electron bunch size was 0.65 mm. The proton beam size at the e-lens was about 0.60 mm.

Figure 6 shows the measured BTF tune spreads versus the electron current. The total tune spread drops fast at the beginning with a small electron current. Then it drops much slower after the electron current reached 750 mA. A minimum of the total tune spread was reached around 1000 mA. When both the tune spreads from beam-beam interaction and electron lens appear, the total tune spread is given by

$$\Delta Q_{tot}^2 = \Delta Q_{resid}^2 + (\Delta Q_{p\text{-}Al} + \Delta Q_{elens})^2, \quad (3)$$

where $\Delta Q_{p\text{-}Al}$ is the beam-beam tune spread contributed by the proton-Aluminum ion collision. Note that $\Delta Q_{p\text{-}Al}$ and ΔQ_{elens} have different signs. For simplicity, we define $\Delta Q_{p\text{-}Al} + \Delta Q_{elens}$ as the 'beam-beam like' tune spread.

Again we assume that ΔQ_{elens} is proportional to the electron current. Then we have

$$\Delta Q_{tot}^2 = \Delta Q_{resid}^2 + (\Delta Q_{p\text{-}Al} + k * I_{elens})^2, \quad (4)$$

The measured ΔQ_{tot} can be fitted very well with Eq. (4). Knowing ΔQ_{resid}, we further fit the beam-beam like tune spread as a linear function of the electron current. Figure 7 shows the results.

With zero electron current, the total beam-beam like tune spread is solely from the beam-beam interaction $\Delta Q_{p\text{-}Al}$, which is about 0.0083. The tune spread due to the e-lens increases linearly with the electron current with a different sign to $\Delta Q_{p\text{-}Al}$. The slope of the fitting line shows that $\Delta Q_{elens}/\Delta I_e$= 0.0073/A. When the electron current reaches about 1100 mA, the e-lens almost completely compensates the beam-beam tune spread. Therefore the total measured tune spread reached its minimum. The minimum is actually the residual tune spread ΔQ_{resid} from the nonlinear lattice. The lattice tune spread can not be compensated by the e-lens. If we continue increasing the electron current, the total tune spread is expected to grow, which is confirmed by off-line numerical simulation.

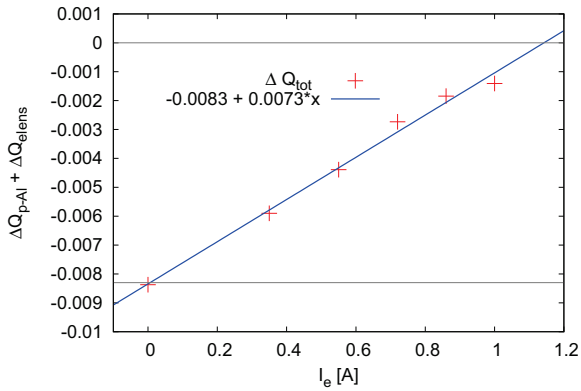

Figure 7: Beam-beam like tune spread linearly fitted with with electron current.

SUMMARY

In this article, we carried out numeric simulations to compare the tune spreads derived from BTF and tune histogram and a linear correlation between them is found, although the tune spread from BTF is slightly larger than that from tune histogram. Both tune spreads also linearly scale with the beam-beam parameter. We extracted the tune spreads from BTF measurements without and with beam-beam interaction. The tune spread from e-lens is a linear function of electron current. Simulations reproduced the similar tune spreads per 1 A. Experimental results show that the beam-beam tune spread could be compensated by the e-lens.

REFERENCES

[1] W. Fischer, X. Gu, *et al.*, *Phys. Rev. Lett.* 115, 264801 (2015).

[2] W. Fischer *et al.*, submitted to *Phys. Rev. Accel. Beams* (2017).

[3] X. Gu *et al.*, *Phys. Rev. Accel. Beams* 20, 023501 (2017).

[4] Y. Luo, *Nucl. Instrum. and Methods* A 801, pp. 95-103 (2015).

[5] P. Gorgen, O. Boine-Frankenheim, and W. Fischer, *Nucl. Instrum. and Methods* A 777, pp. 43-53 (2015).

ISBN: 978-3-95450-192-2 doi:10.18429/JACoW-IBIC2017-MOPCC05

MEASURING BEAM ENERGY WITH SOLENOID*

I. Pinayev†, D. Kayran, V.N. Litvinenko, G. Wang, BNL, Upton, NY 11973, U.S.A.

Abstract

We have developed a method of measuring electron beam energy based on the measurement of the Larmor angle. In this paper, we describe the experimental set-up and obtained results.

INTRODUCTION

Measuring energy of the electron beam with few MeV energy is a challenging task. Conventional approach utilizing energy spectrometer has a disadvantage of low magnetic field in a bending magnet, which is hard to measure accurately and it is affected by the residual magnetic fields. Electron beam is also sensitive to the stray magnetic fields. Time-of-flight technique requires precise measurement of arrival time because the velocity variation is inversely proportional to the square of the relativistic factor.

Low-energy beamlines usually implement solenoids for the focusing of the beam (the usage of the quadrupoles is limited due the same reasons as for the spectrometer dipole). The solenoids are rotating the plane of the betatron oscillations [1] and the rotation angle is directly proportional to the axial field integral, which is usually known with high accuracy, and inversely proportional to the beam rigidity.

The electron beam energy is found from the change in the response matrix with varying excitation current of the solenoid.

MEASUREMENT TECHNIQUE

The transfer matrix of a hard edge solenoid can be represented as multiplication of the rotation matrix M_{rot} and focusing matrix M_f:

$$\begin{pmatrix} \tilde{x} \\ \tilde{x}' \\ \tilde{y} \\ \tilde{y}' \end{pmatrix} = M_{rot} M_f \begin{pmatrix} x \\ x' \\ y \\ y' \end{pmatrix} \quad (1)$$

where rotation matrix is:

$$M_{rot} = \begin{pmatrix} cos\theta & 0 & sin\theta & 0 \\ 0 & cos\theta & 0 & sin\theta \\ -sin\theta & 0 & cos\theta & 0 \\ 0 & -sin\theta & 0 & cos\theta \end{pmatrix} \quad (2)$$

and $\theta = \int eB_{\parallel}(s)/2p\, ds$, where e is electron charge, p is its momentum, and $B_{\parallel}(s)$ is axial field. The focusing matrix can be calculated from the following equation:

$$M_f = \begin{pmatrix} cos\theta & sin\theta/k & 0 & 0 \\ -ksin\theta & cos\theta & 0 & 0 \\ 0 & 0 & cos\theta & sin\theta/k \\ 0 & 0 & -ksin\theta & cos\theta \end{pmatrix} \quad (3)$$

where k is $eB_{\parallel}(s)/2p$.

The real solenoid can be represented as series of hard edge solenoids with different magnetic fields. Because rotation and focusing matrices commute and focusing matrix does not mix horizontal and vertical plane the Larmor angle will be sum of the rotation angles for the parts of solenoid and Eq. 2 is valid for any solenoid.

In our experiment, we steered the electron beam with a trim located prior a solenoid and measured the tilt of the beam trajectory in the X-Y plane (see Fig. 1).

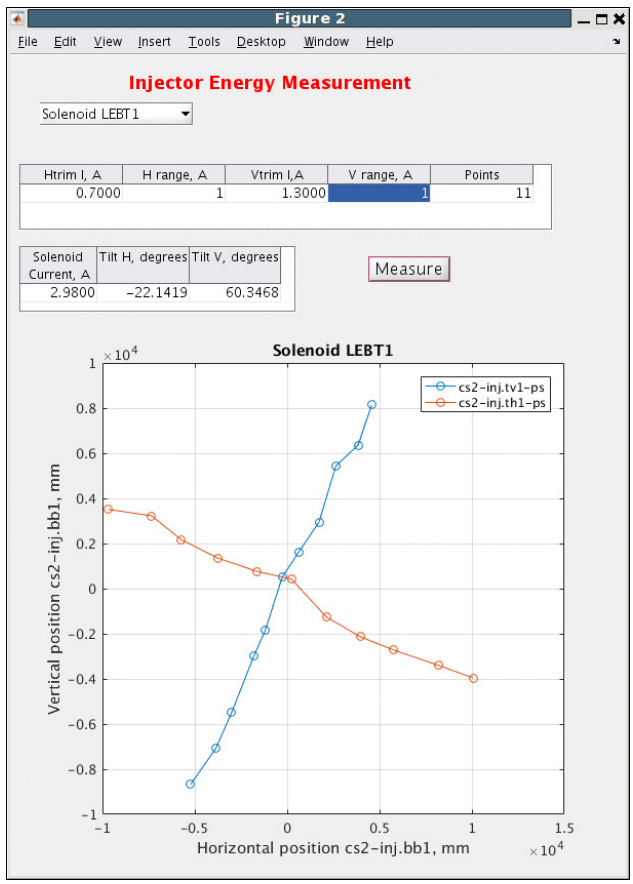

Figure 1: First scan of the orbit tilt in the X-Y plane caused by solenoid's rotation of the orbit. Measured beam position is in microns.

The measurements were performed using an automated MATLAB script. Operator can choose the solenoid (with corresponding beam position monitor (BPM) and trim),

* Work supported by the US Department of Energy under contract No. DE-SC0012704
† pinayev@bnl.gov

ISBN: 978-3-95450-192-2 doi:10.18429/JACoW-IBIC2017-MOPCC05

its current, number of points and trim current range.

First successful attempt was performed on March 24, 2017 (shown in Fig. 1). Two scans with different solenoid settings were done to account for the roll angles of a trim and a BPM. Both vertical and horizontal trims were utilized for the measurement (shown in different color).

The next step improvement was incorporation of two solenoids settings in the same script. For this purpose each trim has individual setting for the middle pf the scan to compensate steering by solenoid and range to account possible reduction in aperture. With this feature the measurement became fully automated. The interface of the upgraded script is shown in Fig. 2.

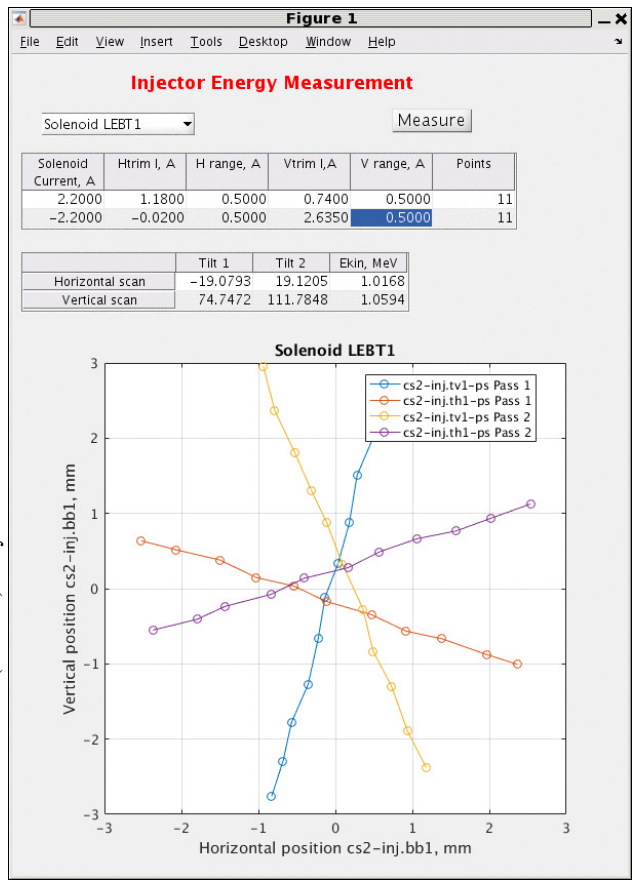

Figure 2: Interface of the MATLAB script with two solenoid settings. There are two lines per setting: one for the horizontal trim and another for the vertical trim.

The script was started being used routinely for the monitoring of the beam energy in the injector beamline and some deficiencies were found. Firstly, the noise in the BPM affected the accuracy of the measurement. Secondly, we observed substantially different tilts changes (up to 30%) for the vertical and horizontal trims, especially with large orbit excursions. We suspected that it was nonlinearity of the BPM response. To overcome these difficulties, we decided to use profile monitor to measure beam position.

This allowed significantly improve reproducibility of the measurements and suppress noise in the beam position measurements. The interface for the profile monitor based script is shown in Fig. 3. The improvements are obvious: the points are located on the straight line and tilt change is close for vertical and horizontal trims.

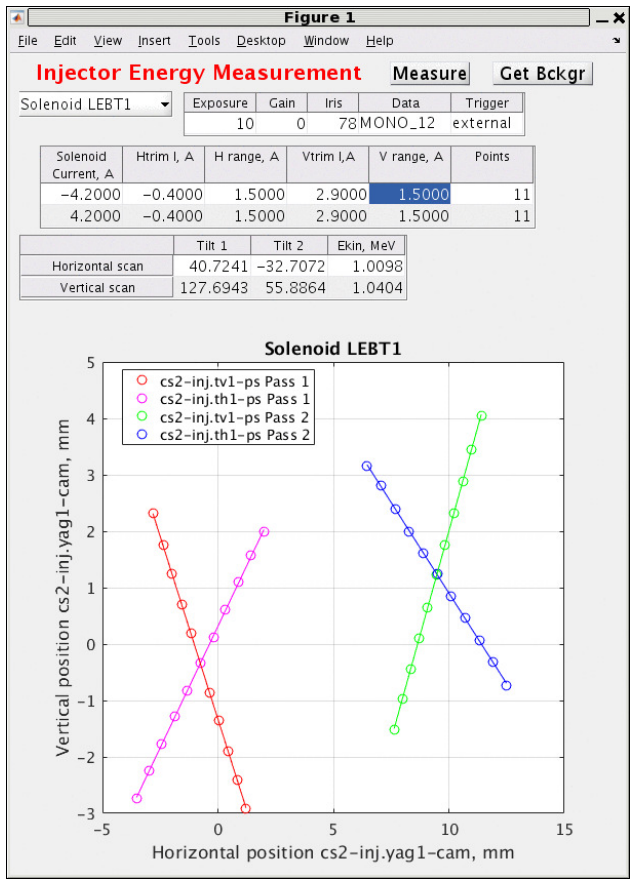

Figure 3: Scan with profile monitor as position measurement device.

The usage of the profile monitor allowed to tightly focus the beam and perform measurement with low charge, where BPMs have significant noise.

Another advantage of the proposed method is insensitivity to the energy spread. We have used it to measure and phase bunching cavities (see Fig. 4).

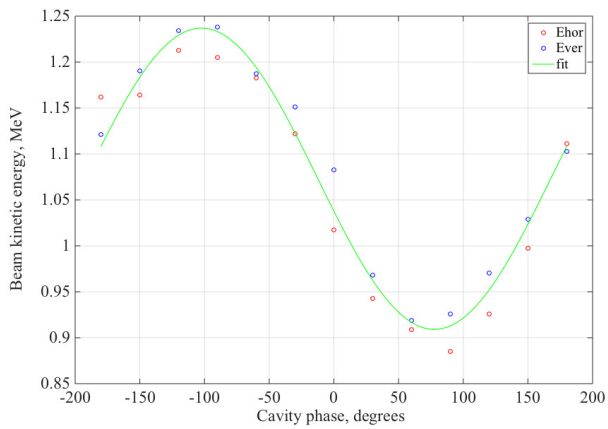

Figure 4: Measurement of the buncher cavities voltage and phase. Beam energy from the gun is 1.073 MeV and buncher voltage is 164 kV.

The maximal induced energy spread of the measurement shown in Fig. 4 was about 4%. Nevertheless, the

ISBN: 978-3-95450-192-2 doi:10.18429/JACoW-IBIC2017-MOPCC05

obtained data have a good fit allowing straightforward calculation of the cavity voltage and phase.

For the guns with photocathodes one can employ the scanning of the laser spot on the cathode to provide beam motion instead of the using the trims. This measurement can be combined with quantum efficiency map scan of the cathode surface.

CONCLUSION

We have developed a method of measuring energy utilizing measurement of the solenoid Larmor angle. It is robust and applicable for very low charges. It is also insensitive to the energy spread of the beam. The device is rather compact and utilizes elements readily available.

REFERENCES

[1] S.Y. Lee, "Linear Coupling", in ***Accelerator Physics***, World Scientific, 1999

ISBN: 978-3-95450-192-2 doi:10.18429/JACoW-IBIC2017-MOPCC06

BEAM BASED ALIGNMENT OF SOLENOID*

I. Pinayev†, Y. Jing, D. Kayran, V.N. Litvinenko, I. Petrushina, K. Shih, G. Wang,
BNL, Upton, NY 11973, U.S.A.

Abstract

In this paper, we present the procedure and experimental results of measuring electron beam position and angle relative to the solenoid axis.

INTRODUCTION

Preserving low emittance of the beam in the transport line require good alignment of the beam trajectory with axis of the focusing element [1]. Axis of a quadrupole can be easily found either buy using array of the Hall probes or vibrating wire measurements [2, 3]. Location of the solenoid axis is much less straightforward due to quadratic dependence of file on the deviation from axis. Situation becomes more complicated because beam coming through a center but with angle with respect to the axis is also deflected by solenoid. Therefore, method of determining beam trajectory vs. solenoid axis with beam itself becomes a necessity.

In [1] the solenoid current was scanned and downstream beam position was recorded. The obtained data were fit using the transfer matrix of solenoid calculated by a special script [4].

We utilize similar approach but since we do not have overlapping magnetic and electrical fields the transfer matrix can be calculated from the magnetic measurement data and beam energy. We also generalized the method to an arbitrary transfer function between solenoid and beam position monitor.

METHODE DESCRIPTION

Calculation of Solenoid Transfer Function

The transfer function of a hard edge solenoid (uniform field of certain length) is well known [5]:

$$\begin{pmatrix} \tilde{x} \\ \tilde{x}' \\ \tilde{y} \\ \tilde{y}' \end{pmatrix} = M_{rot} M_f \begin{pmatrix} x \\ x' \\ y \\ y' \end{pmatrix} \quad (1)$$

where rotation matrix is:

$$M_{rot} = \begin{pmatrix} cos\theta & 0 & sin\theta & 0 \\ 0 & cos\theta & 0 & sin\theta \\ -sin\theta & 0 & cos\theta & 0 \\ 0 & -sin\theta & 0 & cos\theta \end{pmatrix} \quad (2)$$

and $\theta = \int eB_{\parallel}(s)/2p\, ds$, where e is electron charge, p is its momentum, and $B_{\parallel}(s)$ is axial field. The focusing matrix can be calculated from the following equation:

$$M_f = \begin{pmatrix} cos\theta & sin\theta/k & 0 & 0 \\ -ksin\theta & cos\theta & 0 & 0 \\ 0 & 0 & cos\theta & sin\theta/k \\ 0 & 0 & -ksin\theta & cos\theta \end{pmatrix} \quad (3)$$

where k is $eB_{\parallel}(s)/2p$.

The real solenoid can be represented as series of hard edge solenoids with different magnetic fields.

The rotation of beam trajectory was utilized for beam energy measurement.

Transfer Matrix Calculation

We treated focusing elements as infinitesimally short, separated by known drift space. In this case transfer matrix from the solenoid under test to BPM can be found as:

$$M_{tr} = M_{driftBPM} \prod \left(M_{foci} M_{drifti} \right) M_{sol} \quad (4)$$

where $M_{driftBPM}$ is matrix o drift space between the last focusing element and beam position monitor (BPM) used for position observation, M_{foc} is matrix of the focusing element (either solenoid or quadrupole), and M_{sol} is matrix of the solenoid being scanned.

Transfer matrix of the solenoid was calculated using the magnetic measurement data:

$$M_{sol} = M_{drift2} \prod \left(M_{rot} M_f \right) M_{drift1} \quad (5)$$

where M_{drift1} and M_{drift2} are transfer matrices of drifts with negative length transporting beam from the solenoid center to the start of the data and from the end of the data to the solenoid center, respectively.

Data Processing

For each solenoid current the transfer matrix was calculated according to the Eq. (4). Then two *4×N* matrices $\boldsymbol{R}_x$ and $\boldsymbol{R}_y$ were formed:

$$X = \begin{bmatrix} x_1 \\ \cdots \\ x_N \end{bmatrix} = R_x \begin{bmatrix} x_0 \\ x'_o \\ y_0 \\ y'_0 \end{bmatrix} \quad (6)$$

$$Y = \begin{bmatrix} y_1 \\ \cdots \\ y_N \end{bmatrix} = R_y \begin{bmatrix} x_0 \\ x'_o \\ y_0 \\ y'_0 \end{bmatrix} \quad (7)$$

where *X* and *Y* are *1×N* vectors of recorded positions, and vector *W,* appearing on the right side, has offsets and angles of the beam with respect to solenoid axis (X and Y are also relative to this axis). The matrices are formed

* Work supported by the US Department of Energy under contract No. DE-SC0012704
† pinayev@bnl.gov

ISBN: 978-3-95450-192-2 doi:10.18429/JACoW-IBIC2017-MOPCC06

from the respective elements of transfer matrix corresponding to the solenoid current.

$$R_x = \begin{pmatrix} M_{tr11\,1} & M_{tr12\,1} & M_{tr13\,1} & M_{tr14\,1} \\ M_{tr11\,2} & M_{tr12\,2} & M_{tr13\,2} & M_{tr14\,2} \\ \cdots & \cdots & \cdots & \cdots \\ M_{tr11\,N} & M_{tr12\,N} & M_{tr13\,N} & M_{tr14\,N} \end{pmatrix} \quad (8)$$

$$R_y = \begin{pmatrix} M_{tr31\,1} & M_{tr32\,1} & M_{tr33\,1} & M_{tr34\,1} \\ M_{tr31\,2} & M_{tr32\,2} & M_{tr33\,2} & M_{tr34\,2} \\ \cdots & \cdots & \cdots & \cdots \\ M_{tr31\,N} & M_{tr32\,N} & M_{tr33\,N} & M_{tr34\,N} \end{pmatrix} \quad (9)$$

We need to find values for the right-hand vector W minimizing deviations from the observed values $\delta X = X - R_x W$ and $\delta Y = Y - R_y W$.

$$\sum_{i=1}^{N}(\delta x_i^2 + \delta y_i^2) = \delta X^T \delta X + \delta Y^T \delta Y \quad (10)$$

Minimum of the Eq. (10) is reached when its partial derivatives over W are equal zero or in the vector form

$$\left(R_x^T R_x + R_y^T R_y\right) \cdot W - R_x^T X - R_y^T Y = 0 \quad (11)$$

or

$$W = \left(R_x^T R_x + R_y^T R_y\right)^{-1}\left(R_x^T X - R_y^T Y\right) \quad (12)$$

Actual readings have offsets due to the misalignments, BPM errors, deflection of the beam during transport. To account for these offsets, we employed two methods. In the first one of the measurement was chosen as reference and data were processed in the incremental form $X = X - \check{x}_m$ and $Y = Y - y_m$. The matrices were modified accord-ingly. Such approach was used during the first measurements but it artificially assigns too much weight for one set of data. Therefore, we decided to include into the W two offsets

$$W = \begin{bmatrix} x_0 \\ x'_0 \\ y_0 \\ y'_0 \\ x_{offs} \\ y_{offs} \end{bmatrix} \quad (13)$$

$$R_x = \begin{pmatrix} M_{11\,1} & M_{12\,1} & M_{13\,1} & M_{14\,1} & 1 & 0 \\ M_{11\,2} & M_{12\,2} & M_{13\,2} & M_{14\,2} & 1 & 0 \\ \cdots & \cdots & \cdots & \cdots & & \\ M_{11\,N} & M_{12\,N} & M_{13\,N} & M_{14\,N} & 1 & 0 \end{pmatrix} \quad (14)$$

$$R_y = \begin{pmatrix} M_{31\,1} & M_{32\,1} & M_{33\,1} & M_{34\,1} & 0 & 1 \\ M_{31\,2} & M_{32\,2} & M_{33\,2} & M_{34\,2} & 0 & 1 \\ \cdots & \cdots & \cdots & \cdots & & \\ M_{31\,N} & M_{32\,N} & M_{33\,N} & M_{34\,N} & 0 & 1 \end{pmatrix} \quad (15)$$

The offsets correspond to the expected beam position if beam is injected directly on the solenoid axis.

EXPERIMENTAL RESULTS

For the real-time application, we developed a MATLAB script. Initially we used the first approach (no calculation of the offsets) and part of GUI is shown in Fig. 1. The script was setting the solenoid current, waited for the predefined period to the end of the transient process and measured beam position. At the end of the scan fit was performed and data were displayed.

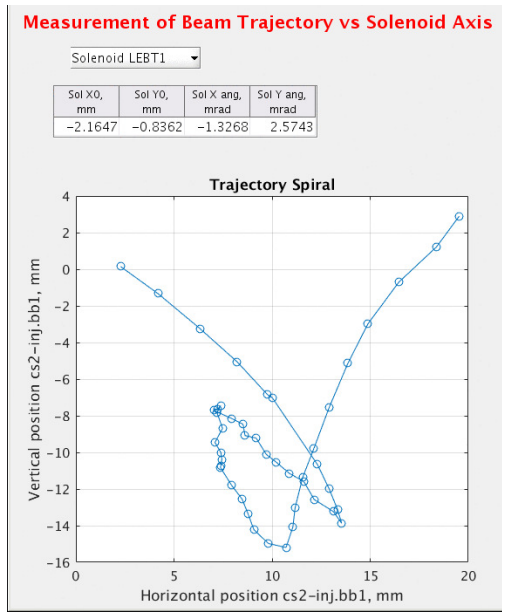

Figure 1: Partial view of a MATLAB GUI for performing solenoid beam based alignment. Not show ae controls for the number of points and scan range.

We tested the accuracy of the procedure by changing the incoming angle of the beam with a horizontal trim in front of the solenoid. The results of the test are shown in Table 1. As one can see the agreement is very good. The effect on the vertical plane is most likely due to the roll of the trim.

Table 1: Results of the Procedure Test with Beam

I_{trim}, A	Bend Angle, mrad	X', mrad	Y', mrad
-2.6	10.1	0.23	4.09
0.0	0.0	-10.59	3.29
1.0	-3.9	-14.69	3.05

After the verification, the procedure was routinely used for orbit measurement and correction. The data of the scan were saved for the later analysis.

Later we have developed script for the analysis of the saved using the second method with fitting of BPM offsets. The results of the analyses are shown in Fig. 2. The measurements were performed at another accelerator with much lower beam energy.

ISBN: 978-3-95450-192-2 doi:10.18429/JACoW-IBIC2017-MOPCC06

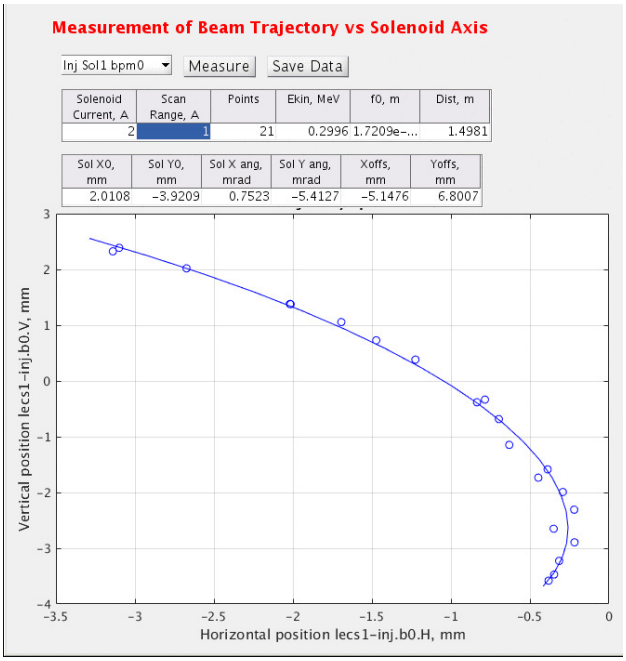

Figure 2: The results of beam based alignment with fitting of the BPM offset.

CONCLUSIONS

We have developed method of the beam based alignment of a solenoid in generalized beam transport line with multiple focusing elements. The method requires knowledge of the axial field of solenoid and beam energy.

The method was tested experimentally on two accelerators and three types of solenoids, and successfully used for the routine measurement of beam position and angle in solenoids.

REFERENCES

[1] C. Gulliford *et al*., "Demonstration of low emittance in the Cornell energy recovery linac injector prototype," Phys. Rev. ST Accel. Beams 16, 073401 (2013)

[2] S. Sanfilippo, "Hall probes: physics and application to magnetometry," in *Proc. CERN Accelerator School: Specialized course on Magnets*, CERN-2010-004, Bruges, Belgium, June 2009.

[3] A. Temnykh, "Vibrating Wire Field-measuring Technique," in *Proc. 10th Int. Magnet Measurement Workshop*, Batavia, IL, U.S.A. October 1997.

[4] C. Gulliford and I. Bazarov, "New method for generating linear transfer matrices through combined RF and solenoid fields," Phys. Rev. ST Accel. Beams 15, 024002 (2012)

[5] S.Y. Lee, "Linear Coupling," in *Accelerator Physics*, World Scientific, 1999, pp. 169-182.

ISBN: 978-3-95450-192-2 doi:10.18429/JACoW-IBIC2017-MOPCC07

DIAGNOSTICS OF ELBE SRF GUN - STATUS AND FUTURE DESIGN

P. Lu, A. Arnold, P. Murcek, J. Teichert, H. Vennekate, R. Xiang, HZDR, Dresden, Germany

Abstract

Since 2015, Mg photocathodes have been applied for the ELBE SRF gun. In 2016, user experiments with a bunch charge of 100 pC and beam transport experiments with 200 pC have been performed. Beams diagnose methods are presented in this article, mainly including measurements of transverse emittance and bunch length. Measurements and corresponding simulations show that the operation parameters of the SRF gun significantly affects the beam quality. A gun lab has been proposed to run as an analog optimizer aiming to explore the potentials of the SRF gun. With the experience of former beam diagnostics, the design of a diagnostics beamline for the future gun lab is described. The purpose is to rebuild phase space projections, either transversely or longitudinally, in a short time scale of several seconds to support analog optimizations for multiple operation parameters.

INTRODUCTION

The concept of SRF (Superconducting Radio Frequency) gun was first proposed in 1988 at the University of Wuppertal [1] and realized in 2002 at HZDR (Helmholtz Zentrum Dresden Rossendorf) [2]. To achieve CW beams with good quality and high bunch charge has always been motivating SRF gun projects. However, the development of SRF guns is still challenged by the processing of cavities, the performance of photocathodes and their lifetime, as well as the risk of cavity contamination [3]. In spite of these challenges, since 2015 an SRF gun has been operating with a magnesium cathode and a 4 MeV, 100 kHz electron beam with the bunch charge up to 200 pC was available in 2016.

As proof of principle, a 100 pC beam was applied in ELBE (superconducting Electron Linac for beams with high Brilliance and low Emittance) for neutron time-of-flight experiments and generation of THz radiation. The beam with the maximum bunch charge of 200 pC was transported in the main beamline of ELBE with negligible beam loss. The energy, energy spread, beam profile and transverse emittance of the beam were measured in a dedicated diagnostics after the SRF gun. The bunch length and slice emittance were measured with the ELBE accelerator modules.

In addition to the design of gun cavity, several operation parameters dominate the beam quality. In general, the phase difference between the RF and the driving laser determines the orientation in the longitudinal phase space; The distance from the cathode surface to the entrance of cavity sets up a trade-off between bunch length and transverse emittance; The transverse size of the laser could be optimized for balancing thermal emittance and space-charge-induced emittance; Moreover, a longer laser pulse reduces the space charge effect but introduces longitudinal nonlinearity to the electron bunch. The working point of all these parameters should be optimized according to a specific requirement.

A new gun lab has been proposed to support the research and development of SRF guns. It will be separated from the ELBE accelerators and therefore offer more experimental time for the gun. The gun lab will consist of an SRF gun and a diagnostics beamline. The beam diagnostics include energy measurement and distribution measurement in both transverse and longitudinal phase spaces. Among them the phase space diagnostics are required to be fast (in 10 seconds) so that gun parameters can be analog and automatically optimized. Longitudinal phase space diagnostics will be probably realized by a transverse deflecting cavity which is possible of single bunch measurement. For transverse phase space diagnostics, different setups based on one dimensional scanning are discussed in the following sections.

CURRENT DIAGNOSTICS BEAMLINE

A diagnostics beamline is connected directly behind the SRF gun at ELBE. Its setup is shown in Figure 1. A Faraday cup is installed to measure the total current. After that three quadrupoles focus the beam for further transport, followed by Screen-station 2 and 3 for beam observation and slit-scan emittance measurement. A 180° horizontal dipole (C-bend) is installed following Screen-station 3 for energy and energy spread measurement, which images the input beam reversely. The distance from its entrance to Screen-station 4 is the same as the distance from its exit to Screen-station 5, as shown in Figure 1. Therefore, projections of a monoenergetic beam on both screens should be the same.

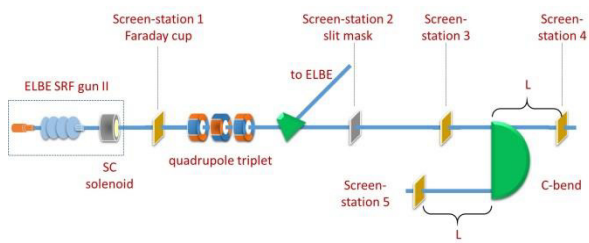

Figure 1: The diagnostics beamline of ELBE SRF gun.

The principle of distribution measurement in transverse phase space is shown in Figure 2. A slit mask is installed at the position of Screen-station 2. It is vertically moveable with a horizontal slit, which has the dimension of 10 mm × 0.1 mm. Screen 3 is located 77 cm after the slit mask to record the sampled beamlet, with the screen installed at 45° to the beam. The scanning step is usually set to 0.1 mm, which is the width of the slit, and thus the entire beam is sampled. The exposure time of the camera should be adjusted to avoid saturation on a normally used YAG (Yttrium Aluminium Garnet) screen for every beamlet. In case of single pulse saturation at high energy

ISBN: 978-3-95450-192-2 doi:10.18429/JACoW-IBIC2017-MOPCC07

and high bunch charge, an OTR (Optical Transition Radiation) screen is also installed as a backup.

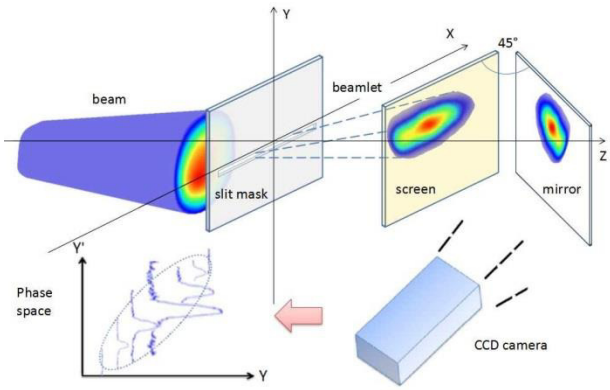

Figure 2: The setup of the slit-scan based distribution measurement in transverse phase space.

It is also necessary to observe the beam in advance at the same position of the slit mask to make sure the entire beam can be sampled by the slit. Therefore, a YAG screens and an OTR screen are installed in Screen-station 2. A calibration screen with coordinates is installed in Screen-station 3 to calibrate beamlet images. The setup of Screen-station 2 and 3 is shown in Figure 3.

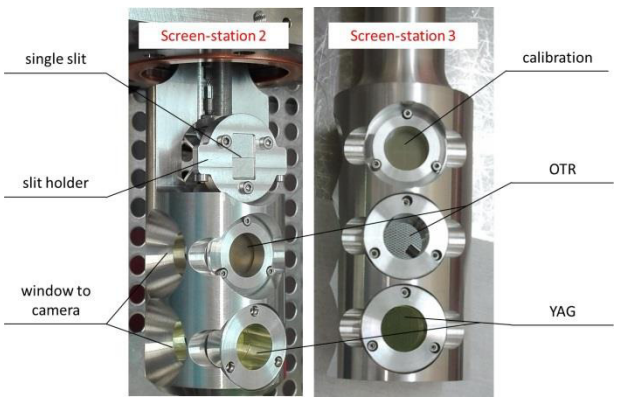

Figure 3: The structure of Screen-station 2 and 3.

The measured transverse phase space distribution can be used further to calculate the rms transverse emittance, with an error less than 15% [4]. The measurement time is over 10 mins, mainly due to the radiation limitation on the slit mask which limits the frequency of macro pulses, and the beam instability which requires more than one image at one position.

CURRENT BUNCH LENGTH AND SLICE EMITTANCE MEASUREMENT

The current diagnostics beamline of ELBE SRF gun is not capable of time resolved measurement. ELBE Linacs have been applied to support it. One of the cavities is used to accelerate the electron bunch at the zero-phase (zero energy gain), which is supposed to quasi-linearly chirp the bunch. In this way the temporal distribution of the bunch is transferred to energy distribution, which can be further transferred to transverse coordinate distribution by a dipole. The longitudinal distribution and bunch length can be calculated from the image of the bunch behind the dipole. This measurement works only if the energy chirp of the bunch before entering the cavity is much smaller than that from the cavity. The setup of this bunch length measurement is indicated in Figure 4.

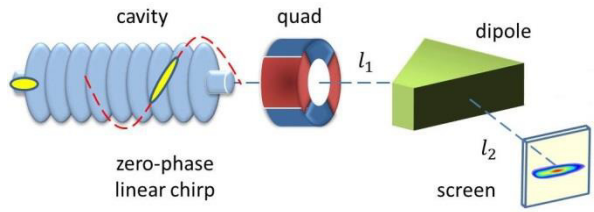

Figure 4: Indication of bunch length and slice emittance measurement at ELBE.

The quadrupole in Figure 4 is used for slice emittance measurement. On the screen, the temporal slices of the bunch have been resolved. The vertical size of each slice is slightly or not affected by the dipole. By scanning the quadrupole and measuring the vertical size of each slice, the emittance of each slice can be calculated applying the well-known method of "quadrupole scan emittance measurement" [5]. The application at ELBE and examples of measurements can be found in Reference [6]. In this measurement, the transverse size-variation of slices due to the quadrupole limits the resolution of slices.

Both the above bunch length and slice emittance measurements are not performed directly to the SRF gun, but assuming that the temporal structure of the bunch maintains from the gun exit to the linac cavity. This is not true for high bunch charges. In this case, complex front to end simulations [4] are necessary to evaluate the measurement. Direct time resolved diagnostics of the SRF gun is highly demanded for optimizing operation parameters.

BEAM DIANOSTICS DESIGN FOR THE NEW GUN LAB

A gun lab has been planned to be built up, separated from the ELBE accelerator, focusing on optimizing the gun itself. Improvements of the gun cavity and photocathode are not included in this article, instead, the design of a dedicated diagnostics beamline will be presented in the following.

The new diagnostics beamline should be able to provide energy measurement and phase space measurements. All measurements are preferred to have a short time scale in ten seconds, resulting in 10^5 parameter combinations are possible to be measured in one-day operation. From the past experiences, the energy measurement will be realized with the same method using a C-bend as shown in Figure 1. When the beam energy changes according to any operation parameter, the current of the dipole should be automatically fed back from the movement of the beam projection on the screen behind the dipole. 10 s is quite relaxed for this procedure.

ISBN: 978-3-95450-192-2 doi:10.18429/JACoW-IBIC2017-MOPCC07

The transverse emittance measurement using the current slit-scan method takes 10 mins which is significantly longer than the desired 10 s. As described, two reasons are dominating the measurement time: beam loss limitation and beam instability. The current macro pulse for beam diagnostics has the minimum duration of 5 ms, realized by a mechanical shutter of the driving laser. Shorter macro pulse will not maintain the same quality of the CW beam for now. For the future new gun lab, better shutters will be applied and the macro pulse length will be mainly limited by the beam loading which is around 0.5 s. A minimum duration of 1 ps is realistic. In this case a frequency of 10 Hz for the macro pulse is possible, and 100 positions of the beam (typical diameter 10 mm) can be measured in 10 s, which is adequate for measuring its emittance.

This measurement time of ten seconds will be enlarged if several images have to be taken at a same position. However, for the purpose of scanning parameter spaces to find the working point, beam instability could be tolerated and a fast processing of measured data is enough to fit the trend of emittance in the parameter space. More accurate measurements can be done around the working point candidate from the fitted trend.

Till now, every measurement parameter has been assumed ideal and the measurement time is right at the limit of 10 s. In the new gun lab the beam loss on the sampling slit could be more tolerable, for example, to apply water cooling slit mask. That means the frequency of the Macro pulse might be one magnitude higher, to 100 Hz, requiring the movement speed of the water cooled slit mask to be more than 10 mm (20 mm considering acceleration/deceleration) per second. The stability of this movement speed in vacuum can be challenging.

Another approach, which will cancel the challenge from scanning the slit, is to scan the beam instead, as already realized in Connell University [7]. A pair of steering magnets are installed in front of the slit mask with opposite fields. The beam through the magnet pair has a horizontal kick and keeps the distribution in transverse phase space. By scanning the beam position, the slit can also sample the beam completely, which is equivalent of scanning the slit. The advantage of this method is the faster scanning speed and the absence of mechanical movement. However, proper design and commissioning of the magnet pair to keep the beam quality undisturbed will also take more effort.

In the emittance measurement described in Reference [7], after the sampled beamlet, there is another group of magnet pair and slit to scan the beamlet. Particles are separated both by position and angle. A Faraday cup is installed to measure the sub-beamlet, which corresponds to the signal on each pixel line if a camera is used. The advantage of the Faraday cup is its higher dynamic range compared to a camera, which will be more universal to scan multiple operation parameters without adjusting the system. With two times of beam scanning, the realized measurement time is 10 s [7]. All three possible setups of transverse emittance measurement are shown in Figure 5.

The comparison of these three setups is summarized in Table 1. The term of "drift space" in the table means a distance in the order of 1 m to resolve the distribution by either position or angle. Such a distance is necessary between the 2 steering magnets and between the slit and screen.

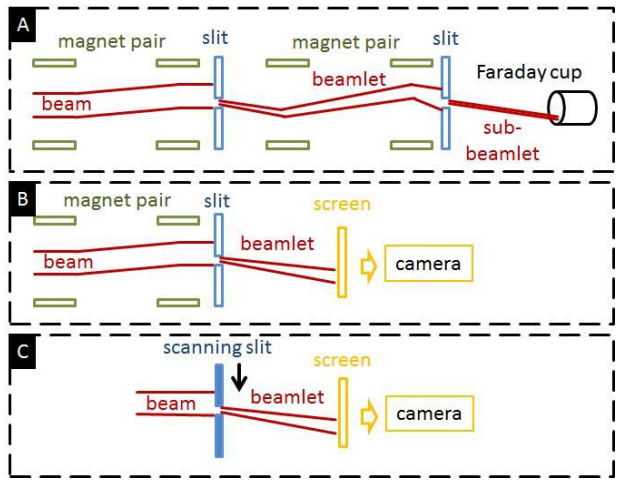

Figure 5: Three possible setups of emittance measurement for the future gun lab.

Table 1: Summary of Different EmittanceMeasurements

setup	A	B	C
magnet pair	2	1	0
slit	2	1	1, movable
Farady cup	1	0	0
screen & camera	0	1	1
measurement time	10 s	1 s	1 to10 s
drift space	~ 2 * 1 m	~ 2 * 1 m	~ 1 m
dynamic range	10^5 to 10^6	10^3	10^3

For diagnostics in the longitudinal phase space, single-bunch-based measurement with a deflecting cavity is preferred [8]. The desired measurement time of 10 s is very relaxed even for averaging with multiple bunches. The longitudinal distribution of an electron beam will be deflected to a transverse direction, e.g. vertical, where the bunch length could be calculated simply using a transverse screen.

If a horizontal bending magnet is applied afterwards, the energy distribution could also be resolved and the longitudinal phase space will be directly projected on a transverse screen after the magnet. The dimension of the system and the parameters of the deflecting cavity should be closely designed, while in this article only simple estimations are made. In general, a measurement range of 50 ps within the ±30° of the deflecting RF field requires the cavity frequency around 3 GHz; A deflected beam with an vertical angle of 15 mrad is desired, indicating that the distance from the exit of deflecting cavity to the screen

ISBN: 978-3-95450-192-2 doi:10.18429/JACoW-IBIC2017-MOPCC07

should be less than 1.6 meters if a 2 inch diameter screen is applied. In between, a 180° bending magnet should be included. From the measurement of the longitudinal phase space, energy spread, bunch length and the uncorrelated energy spread could be calculated, which can be used to evaluate the multiple parameter scanning. Similarly, only rough and systematic results are required to reveal the trend. More accurate measurements can be made around the fitted peak point of the trend.

CONCLUSION

The current beam diagnostics of the SRF gun at ELBE provides vigorous experiences for the design of a new gun lab, aiming to optimize multiple operation parameters in a short time scale, e.g., 24 hours. A measurement time of 10 s is set to be a design target. Energy and the longitudinal phase space measurements are expected to be faster than 10 s for each point, however, transverse emittance measurement is challenging. Three different setups are compared which are all possible to provide a measurement time within 10 seconds. The same setup as the current measurement using a movable slit and a camera is still preferred to better utilize the accumulated experience. More calculations will be followed up to determine details of the diagnostics beamline for the gun lab.

ACKNOWLEDGEMENT

We would like to thank the whole ELBE team for their help and assistance with this project. The work is supported by the European Community under the FP7 programme (EuCARD-2, contract number 312453, and LA3NET, contract number 289191) and by the German Federal Ministry of Education and Research (BMBF) grant 05K12CR1.

REFERENCES

[1] H. Chaloupka et al., "A proposed superconducting photoemission source of high brightness", *Nucl. Instrum. Methods Phys. Res., Sect. A,* vol. 285, issues 1–2, Dec. 1989, pp. 327-332.

[2] D. Janssen et al., "First operation of a superconducting RF-gun", *Nucl. Instrum. Methods Phys. Res., Sect. A,* vol 507, issues 1–2, Jul. 2003, pp. 314-317.

[3] H. Vennekate, "Emittance compensation for SRF photo injectors", *Ph.D. thesis,* Dresden University of Technology, 2017.

[4] P. Lu, "Optimization of an SRF Gun for high bunch charge applications at ELBE", *Ph.D. thesis,* Dresden University of Technology, 2016.

[5] A. Mostacci et al., "Chromatic effects in quadrupole scan emittance measurements", *Phys. Rev. ST Accel. Beams,* vol. 15, p. 082802, Aug. 2012.

[6] J. Rudolph, "Instruments and techniques for analysing the time-resolved transverse phase space distribution of high-brightness electron beams", *Ph. D. thesis,* der Universität Rostock, 2012.

[7] C. Gulliford et. al., "Demonstration of low emittance in the Cornell energy recovery linac injector prototype", *Phys. Rev. ST Accel. Beams,* vol. 16, p. 073401, Jul. 2013.

[8] H. Huck et al., "First results of commissioning of the PITZ transverse deflecting structure", in *Proc. FEL'15*, Daejeon, Korea, Aug. 2015, paper MOP039, pp. 110-114.

ISBN: 978-3-95450-192-2 doi:10.18429/JACoW-IBIC2017-MOPCC08

TIME-OF-FLIGHT MEASUREMENTS AND ANALYSIS OF THE LONGITUDINAL DISPERSION AT THE S-DALINAC*

T. Bahlo†, F. Schließmann‡, M. Arnold, J. Pforr, N. Pietralla
Institut für Kernphysik, Darmstadt, Germany

Abstract

The Superconducting Darmstadt Linear Accelerator S-DALINAC is capable of accelerating electrons to kinetic energies of up to 130 MeV. Due to its three recirculating beamlines the 30 MeV main linac can be used up to four times. The electron beam is recirculated non-isochronously with a distinct longitudinal dispersion to conserve the energy spread of the injector accelerator. Time-of-flight measurements at the beamline connecting injector and main linac will be presented, showing a non-linear dependency on the energy. This effect can be reproduced by simulations using *elegant* [1] and are caused by traversing accelerating cavities with a small transversal displacement and a small angular deviation. Adjusting the magnetic parameters of the beamline compensates this effect. Besides the first recirculation beamline does not provide enough degrees of freedom to set the desired longitudinal dispersion for the non-isochronous recirculation mode. This has to be compensated in succeeding recirculation beamlines or by installation of additional magnets at the first recirculation beamline. Possible beamline modifications and time-of-flight measurements representing the longitudinal dispersion will be presented.

S-DALINAC

The S-DALINAC [2], shown in Fig. 1, is a superconducting, recirculating linear electron accelerator providing kinetic energies of up to 130 MeV. Due to its three recirculation beamlines the main accelerator can be used up to four times in order to reach the design energy. By using a non-isochronous recirculation mode the energy spread of the beam provided by the superconducting injector linac can be conserved over several recirculations. To use this mode a destinct momentum deviation within the electron bunch has to be introduced and a matching longitudinal dispersion R_{56} has to be implemented by quadrupole magnets. The momentum deviation can be introduced by accelerating off-crest with a phase offset of Φ_S.

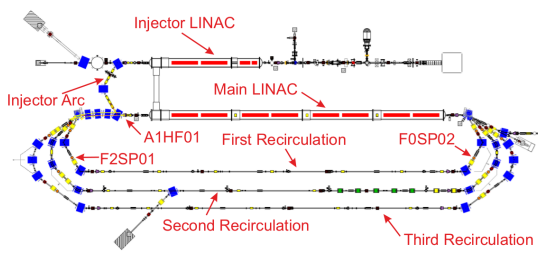

Figure 1: Floorplan of the S-DALINAC. Relevant devices are highlighted.

DETERMINING THE OPERATING POINT

Since the setup of the S-DALINAC has been upgraded from two to three recirculation beamlines [3] a new operating point for the non-isochronouly recirculated mode had to be found. A operating point consists of all quantities influencing longitudinal beam dynamics. Off-crest-acceleration introduces a quasi-proportional energy deviation in respect to the reference particle within a electron bunch since the longitudinal bunch length is short in comparison to one RF period [4]. The slope of this energy deviation can be characterized by the slope of the energy gain ΔE of each particle

$$\Delta E = \hat{E}_z \cos\left(2\pi \cdot f_{\mathrm{RF}} \cdot t + \Phi_S\right)$$

with the maximum energy gain $\hat{E}_z$, the RF frequency f_{RF}, the time t and the synchrotronphase Φ_S. The longitudinal position of an electron in respect to the reference particle can be manipulated by the longitudinal dispersion R_{56} of the beamline, which is associated with the 6×6 beam transport matrix R. This matrix describes the tracking of the particle vector $\vec{x}(s)$ at position s_1 to position s_2:

$$\vec{x}(s_2) = R \cdot \vec{x}(s_1).$$

Assuming all longitudinally coupling components of R to be zero the longitudinal position Δl relative to the reference particle can be expressed by

$$\Delta l = R_{56} \cdot \frac{\Delta p}{p_0}$$

and the optimal operating point using the (I)njector, the (F)irst, (S)econd, and (T)hird recirculation can be calculated:

Φ_S	$R_{56,\mathrm{I}}$	$R_{56,\mathrm{F}}$	$R_{56,\mathrm{S}}$	$R_{56,\mathrm{T}}$
−5.8°	0.21 m	0.2 m	0 m	0.54 m

Several states of the longitudinal phase space for acceleration using all recirculations are plotted in Fig. 2.

Requirements for Optimal Beam Tuning

As mentioned above the electron beam should fulfill specific properties when entering a cavity. Especially the correct alignment of the longitudinal phase space ellipse is crucial for an optimal acceleration process. This is ensured if the longitudinal dispersion outside the cavity is only influenced

* funded by DFG through RTG 2128, INST163/383-1/FUGG and INST163/384-1/FUGG.
† tbahlo@ikp.tu-darmstadt.de
‡ fschliessmann@ikp.tu-darmstadt.de

ISBN: 978-3-95450-192-2 doi:10.18429/JACoW-IBIC2017-MOPCC08

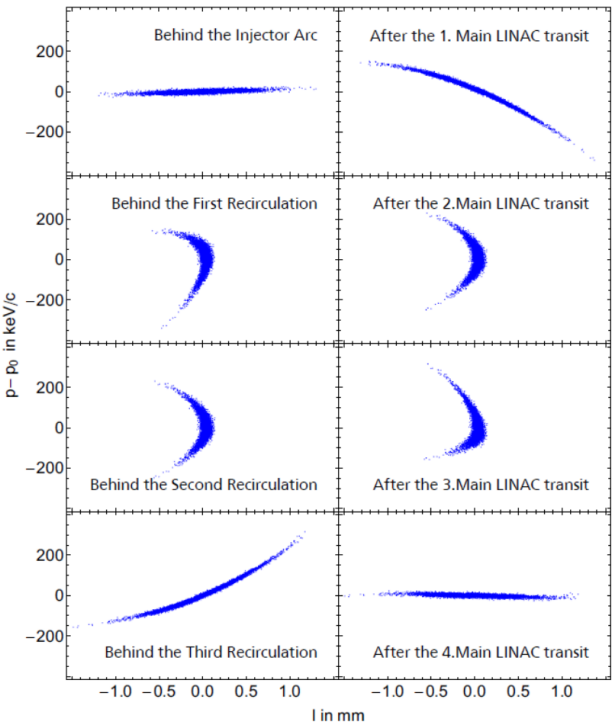

Figure 2: Simulated behavior of the longitudinal phase space at the optimal operating point using all recirculations [5].

by the R_{56} parameter. Therefore the parameters R_{51}, R_{52}, R_{53}, R_{54} as well as the parameters R_{16}, R_{26}, R_{36}, R_{46} have to be zero. It can be shown that most of those parameters vanish simultaneously for the beamline of the S-DALINAC [6] leaving only the parameters R_{16}, R_{26} and R_{56} to be set manually, by adjusting the quadrupole magnets in the injector and all recirculation arcs. The recirculation beamlines of the S-DALINAC consist of two 180° bending arcs and a straight section, that should only be used for pure transversal focussing of the beam. As mentioned before R_{16} and R_{26} should be zero individually at the end of each arc and along with the desired R_{56} five degrees of freedom per recirculation are required.

Upgrade Options for the First Recirculation

Since the first recirculation beamline only includes two quadrupole magnets per 180° arc the neccessary amount of degrees of freedom to arbitrarily choose R_{56} is not available. To achieve the desired parameter value the straight beamline has to be used to manipulate the other transport parameters as well so that the straight beamline can not be used for transversal focussing only. To improve this situation it is desireable to increase the amount of degrees of freedom in the recirculation arcs. This can be achieved by installing additional quadrupole magnets. Due to restricted spacial conditions within the arcs this can only be achieved by replacing existing elements. Until now there are two sextupole magnets named "F0SP01" and "F2SP01" (see Fig. 1) formerly used for beam-break-up experiments that are not in use any more and could be replaced by quadrupole magnets of the same longitudinal length. Alternatively some steerer dipole magnets could be replaced eliminating valuable possibilities to adjust the electron beam within the arcs. Also the installation of combined function magnets is currently taken into account.

MEASUREMENT OF LONGITUDINAL DISPERSION R_{56}

By changing the momentum of the center of the electron beam a phase shift can be introduced. For ultra relativistic particles this phase shift is approximately proportional to Δl since the speed deviation within a bunch is negligable. This leads to the relation

$$\Delta\Phi_{\text{beam}} \approx 360° \cdot \frac{f}{c} \cdot \Delta l = 360° \cdot \frac{f}{c} \cdot R_{56} \cdot \frac{\Delta p}{p_0}$$

The momentum of the beam can be manipulated by changing the amplitude of a accelerator cavity within the momentum acceptance of the respective recirulation arc. By measuring the resulting phase shift the longitudinal dispersion can be calculated.

Phase Measurement Devices

To measure the beam phase at the S-DALINAC RF monitors are used. These devices consist of a stainless-steel pillbox cavity tuned to the RF frequency of the beam. The beam traverses the monitor resonantly exciting electromagnetic fields inside that are measured using RF antennas as shown in Fig. 3. While the time resolution is not sufficient

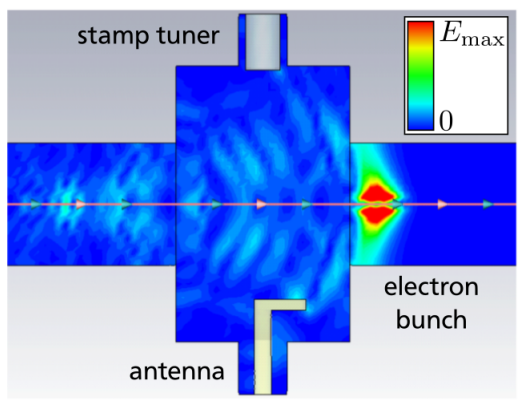

Figure 3: Schematic cross-section of a RF monitor used to measure the beam phase.

to measure the phase of each bunch individually the mean beam phase can be extracted due to the used continuous-wave mode of the S-DALINAC. With these devices phase measurements with a resolution of less than 0.2° are possible assuming the beam current to be greater than approximately 500 nA.

Measurements in the Injector Arc

Measurements at the injector arc using the RF monitor A1HF01 to aquire data (see Fig. 1) for three different val-

ISBN: 978-3-95450-192-2 doi:10.18429/JACoW-IBIC2017-MOPCC08

ues of R_{56} are shown in Fig. 4. During this measurement

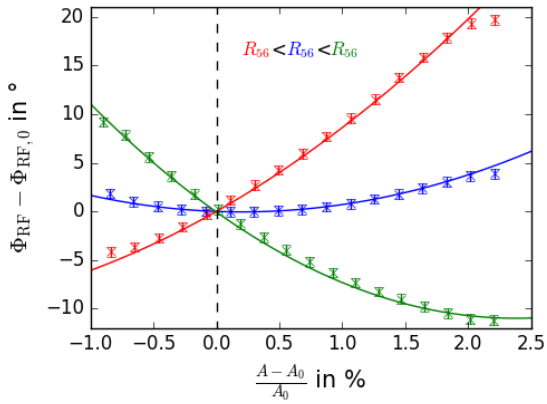

Figure 4: Measured phase shifts behind the injector arc as a function of the relative change in amplitude of the last accelerator cavity for different values of R_{56} measured by RF monitor A1HF01 [5].

the amplitude of the last injector cavity has been varied to change the beam momentum. For small variations from the desired amplitude A_0 the phase response is nearly linear while for bigger changes a parabolic dependency is visible. This shape is a result of two effects. The total path length of the center of the bunch increases, because the electron bunch with momentum mismatch is not traveling through the arc on the designed orbit. This effect already leads to a parabolic shape as can be seen in the simulation results shown in Fig. 5. But as shown, the effect on the phase

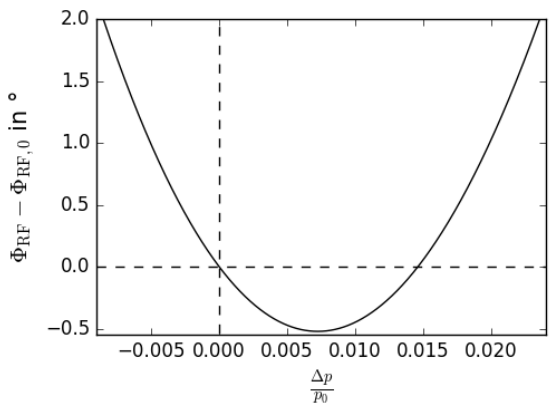

Figure 5: Simulated behavior of the bunch phase behind the injector arc depending on the initial momentum [5].

shift caused by the absolute value of the momentum only is smaller than the measured behavior. A combined change in transversal displacement and angular deviation while changing the amplitude of the accelerating cavity is the reason for the big phase shift, since a transversal displacement and an angular deviation at the entrance of the accelerating cavity lead to a modified transversal displacement and an angular deviation at the exit of this cavity, depending on the acceleration field. The influence of these quantities on the phase shift can be seen in Figs. 5 and 6. To check this dependency

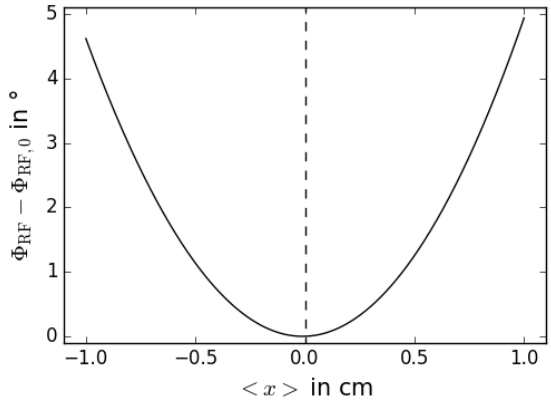

Figure 6: Simulated behavior of the bunch phase behind the injector arc depending on the initial horizontal displacement [5].

a separate measurement has been performed at which the accelerating cavity has been traversed with different entrance displacements. Figure 7 shows the comparison between the measurement and the simulated behavior. Taking into ac-

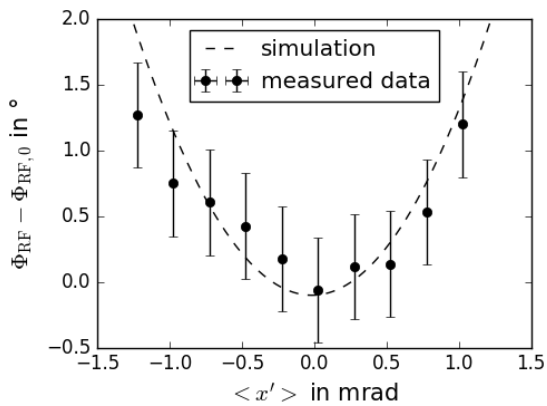

Figure 7: Comparison of the simulated horizontal angular deviation dependency and the measured dependency created by changing the beam position at the entrance of the injector arc using a dipole magnet [5].

count both these effects leads to a simulated behavior which is consistent with the measurement data of Fig. 4.

CONCLUSION

To use a non-isochronous recirculation mode at the S-DALINAC it is neccessary to accelerate off-crest and use a particular longitudinal dispersion R_{56} to conserve the energy spread of the injector accelerator. The first recirculation beamline does not provide enough degrees of freedom to arbitrarily adjust this parameter due to a lack of quadrupole magnets. Proposals for the installation of additional quadrupole magnets replacing existing sextupole or

ISBN: 978-3-95450-192-2 doi:10.18429/JACoW-IBIC2017-MOPCC08

steerer magnets in the first recirculation arcs are currently being evaluated. Several time-of-flight measurements have been performed to determine the actual longitudinal dispersion of the 180° bending arcs showing a non-linear phase shift. These parabolic dependencies can be explained by non-linear increases of the traveled distance depending on the transversal displacement and angular deviation at the entrance of the arc and the momentum variations artificially induced to measure the longitudinal dispersion.

REFERENCES

[1] M. Borland, "elegant: A Flexible SDDS-Compliant Code for Accelerator Simulation," *Advanced Photon Source* LS-287, September 2000.

[2] A. Richter *et al.*, "Operational Experience at the S-DALINAC," In *Proc. of EPAC 1996*, 96, 110–114. IOP Publishing, 1996.

[3] M. Arnold, "Auslegung, Planung und Aufbau einer dritten Rezirkulation mit ERL-Modus für den S-DALINAC," Dissertation (2017), D17, TU Darmstadt.

[4] H. Herminghaus, "On the inherent stability of non-isochronous recirculating accelerators," *Nucl. Instr. and Meth.* A 314 (1992) 209.

[5] F. Schließmann, Master Thesis in preparation, TU Darmstadt.

[6] R. Eichhorn, "Optimierung des Strahltransportsystems und experimentelle Umsetzung verschiedener Methoden zur Gütemessung am S-DALINAC," Dissertation (1999), D17, TU Darmstadt.

ISBN: 978-3-95450-192-2 doi:10.18429/JACoW-IBIC2017-MOPCC11

DIAGNOSTICS FOR TRANSVERSE COUPLED BUNCH INSTABILITIES AT ALBA

U. Iriso, A. Olmos, A. A. Nosych, and L. Torino
ALBA-CELLS, Cerdanyola del Vallés, Spain

Abstract

Transverse Couple Bunch Instabilities (TCBI) have been identified at ALBA as one of the main beam current limitations since its early commissioning in 2011. In these last years, we have developed several diagnostics tools that allow us a better characterization of these instabilities. The Synchrotron Radiation Interferometry has been equipped with a Fast Gated Camera (FGC) to measure the bunch-by-bunch beam size evolution, which, in combination with the diagnostics tools of the Transverse Multibunch Feedback system, provides us with a fruitful insight of these phenomena. This paper describes these diagnostics tools, and as an example, compares the emittance and tune evolution switching on/off some of the vacuum pumps at the Storage Ring.

INTRODUCTION

Beam current limitations have been observed at ALBA since its early commissioning in 2011. They are mainly related with Transverse Coupled Bunch Instabilities (TCBI), which appear above certain current thresholds and they could be cured by increasing the beam chromaticity. The origin of these beam instabilities is mainly related with the Geometrical and Resistive Wall impedances [1], although the influence of ion effects due to large pressures inside the chamber is not ruled out. In these phenomena, the perturbing field produced by a given bunch affects the subsequent bunches and therefore, bunch-by-bunch (BbB) instrumentation is required to obtain reliable diagnostics of these effects.

During these last years, we have developed two bunch-by-bunch instruments that provide us with a better insight into these effects. First, we have equipped our visible light interferometry [2] with a Fast Gated Camera with gating times as short as 2 ns [3], which provides a bunch-by-bunch emittance monitor. Second, we have set-up into operation our Transverse Multi-Bunch Feedback [4], which allows tune measurements to be performed also on a BbB basis. With these instruments, we have performed several experiments switching on/off the vacuum pumps in different sectors of the storage ring in order to evaluate the influence of ion effects on these beam instabilities. This paper reviews this BbB instrumentation and shows the results of these beam experiments.

BEAM SIZE MONITOR

In addition to the X-ray pinhole camera, since 2013 ALBA has been developing a beam size monitor using the Synchrotron Radiation Interferometry (SRI) with visible light [5–7]. Imaging with the X-ray pinhole has two main timing limitations: a)the YAG:Ce screen decay time is typically in the order of 100 ns [8]; and b) the minimum CCD exposure time (around 100 µs). This is obviously too much for ALBA's storage ring, where the bucket length is 2 ns. Since the SRI uses visible light (not X-rays), only the latter one affects the SRI. This can be circunvented by using a FGC with gatings as short as 2 ns.

The general principle of FGCs is as follows: when the light impinges on the photo-cathode of an image intensifier, photo-electrons are emitted and guided through a Multi-Channel Plate by an electric field. A high potential (whose duration can be as short as 2 ns) is applied across the MCP to accelerate and multiply the primary electrons. The final electron avalanche reaches a phosphor screen, whose light is read by a CCD.

The main FGC limitation stems from the space-charge effects produced when the electrons exit the photo-cathode, which enlarges the inteferograms fringes and so the measured beam size is larger. Figure 1 shows interferograms produced by a standard CCD (left) and two types of FGC: the Hamamatsu II C9546 (middle) and the Andor iStar 334T (right). Compared with the CCD camera, the visibility produced by FGCs is lower due to space charge effects, hence the measured beam size is larger. A thorough explanation, as well as a comparison for different cameras is shown in [3].

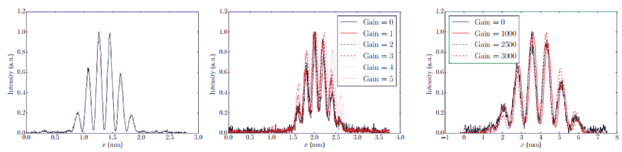

(a) Standard CCD (b) Image Intensifier C9546-01 (c) FGC iStar 334T

Figure 1: Comparison of interferograms produced by a standard CCD camera (left) and two types of FGC. The lower visibility (with higher valleys) is due to space charge effects, and increases the measured beam size.

Nevertheless, this beam size enlargement can be calibrated using the beam itself: we measure the beam size with both the standard CCD and the FGC by changing the beam coupling in a controlled way. This shows a linear relation (see Fig. 2), which we use to calibrate the FGC measurements. Our SRI system is equiped with the Andor FGC camera.

Figure 3 shows the measured bunch-by-bunch beam size with 130 mA in routine operation at ALBA. The calibrated beam size is consistent with the theoretical one. Nevertheless, the resulting size oscillates due to bunch-by-bunch shot noise, which explains the large error bars in Fig. 2. Due to low amount of light, the bunch size is not obtained from a single shot (i.e. single bunch passage), but rather by integrating the light produced by many (typically ~100) passages, for which the gating and trigger are carefully synchronized.

ISBN: 978-3-95450-192-2 doi:10.18429/JACoW-IBIC2017-MOPCC11

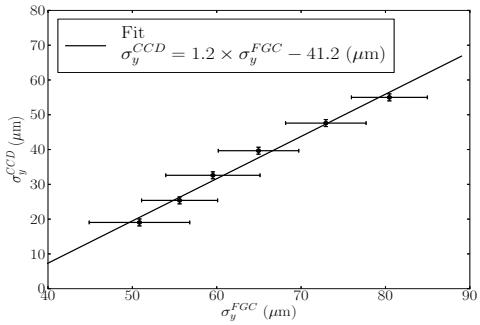

Figure 2: Resulting beam size, measured by the FGC for different couplings versus the same measurement done with a standard CCD.

After the inteferogram of bunch N is obtained, the process is repeated for bunch N+1, until all 448 buckets are scanned. In total, the scan is performed in ~5 min. More details are shown in [3].

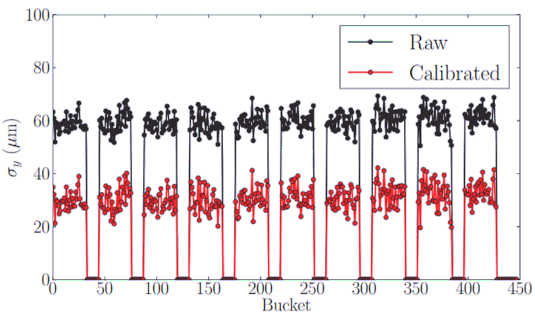

Figure 3: Measured BbB beam size with the ALBA filling pattern: 10 trains, with 32 bunches/train spaced by 12 empty buckets. The final gap is larger (20 buckets).

TUNE MONITOR

With the commissioning of the Transverse Multi-Bunch Feedback (TMBF) in 2015 [4], ALBA is able to measure the tune on a BbB basis. This can be done in two ways. The first one, which we call the *Post-Mortem Analysis*, consists of exciting all bunches at once and getting their position oscillations also at the same time using the *Post-Mortem buffer*. This time frame can be as big as 100k turns, so the precision obtained in this method is 1e-5.

The second one, which we call the *Bunch Scan Analysis*, is to excite and measure the beam position of a single bunch, then move to the following bunch, and repeat the process for all bunches in the filling pattern. Compared with the previous one, this method is significantly slower (in the order of 15 min for the 448 bunches) and is affected by the power supplies jitter, which amounts to 2e-4 (see [9]). This becomes a main limitation in measurements of this kind.

Figure 4 shows an example of tune measurement obtained over 320 bunches, when the machine is filled with 200 mA. For the *Post Mortem Analysis* (top histogram), the tune spread (σ_Q=1e-5) is only limited by the number of acquired turns; while for the *Bunch Scan Method* (bottom histogram) the tune spread is limited by the jitter of power supplies (measured σ_Q=3e-4).

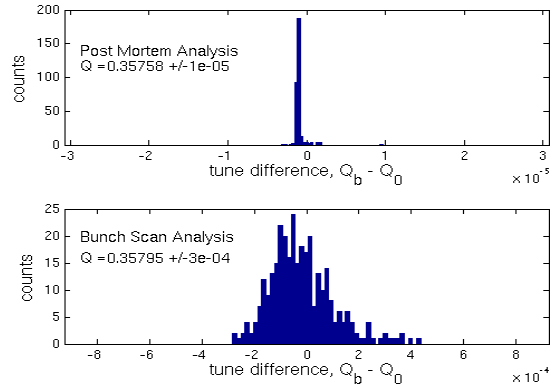

Figure 4: Bunch-by-bunch tune using the *Post Mortem Analysis* (top) and the *Bunch Scan Method* (bottom).

RESULTS WITH PRESSURE BUMPS

In order to investigate the vacuum pressure influence in the CBIs observed at ALBA, we did an experiment in which we switched off the vacuum ion pumps in almost half of the SR (7 sectors out of 16). The NEG coating and cartridges were still active, so the pressure rose only by about 1 order of magnitude. Figure 5 compares the pressure profile as measured by the Cold Cathode Gauges (CCG) in the SR with the pumps on/off. The points below 1e-11 bar indicate a malfunctioning of the CCG.

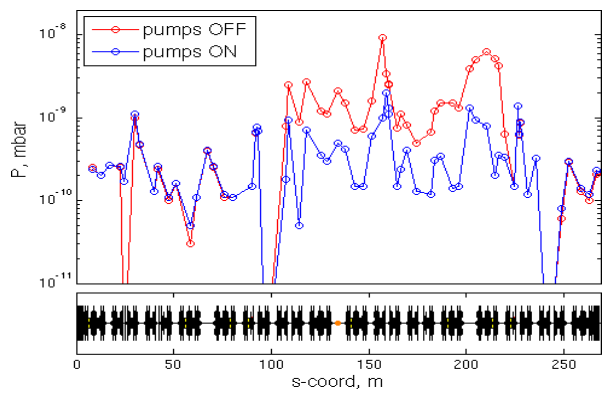

Figure 5: Normal vacuum pressure profile (in blue, with pumps on), compared with the pressure profile (red trace) when the pumps in Sectors S07 - S13 are switched off.

Figure 6 shows the horizontal (blue trace) and vertical (black dots) beam size evolution as measured by the X-ray pinhole camera while this experiment takes place. In this experiment, the pumps are switched off at $t = 0$, and the vertical chromaticity is set to ξ_v=0. The current injection is halted everytime there is a vertical beam blow up. At this point, we take measurements of the tune and bunch-by-bunch beam size; later we cure the instability by increasing the chromaticity (for example, at $t = 1000$ s or $t = 3000$ s). Next, the injection is resumed until a new threshold is reached, and the process is repeated. Finally, we reach 150 mA with a vertical chromaticity of ξ_v=4.4, and no instability is seen. At this point, we switch on the ion pumps ($t \sim 4500$ s), and note that the vertical beam size reaches a smaller equilibrium (from 33 to 28 µm).

ISBN: 978-3-95450-192-2 doi:10.18429/JACoW-IBIC2017-MOPCC11

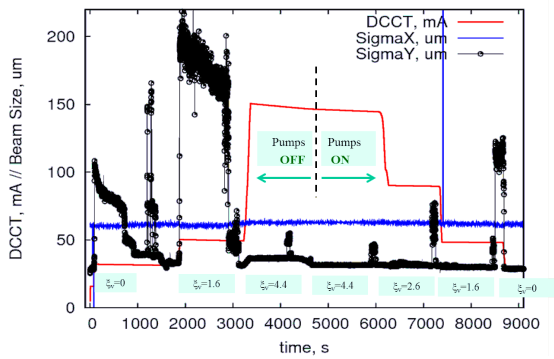

Figure 6: Evolution of DCCT, together with the hor and ver beam size, while switching the ion pumps OFF/ON. The ver chromaticity (ξ_v) is changed during the experiment.

Figure 7 compares the vertical bunch-by-bunch beam size with the pumps on/off for two different currents. For chromaticity ξ_v=2.6, the instability threshold is found at 90 mA with the pumps off, while the beam is stable with the pumps on. This clearly indicates that the presence of ions decreases the expected instability thresholds. Furthermore, the bunch size monitors allow measuring the TCBI rise time (150 bunches, orange dots). On the other hand, there is no significant difference in the bunch-by-bunch comparison for the pumps on and off for a 150 mA beam (even though the pinhole camera shows a vertical beam size difference of 4 µm). On one side, this is related with the resolution given by the FGC camera, which is quite large due to the above-mentioned space charge effects. This could also be an indication that this is not related to Fast Beam Ion Instabilities, but rather to an ion trapping effect.

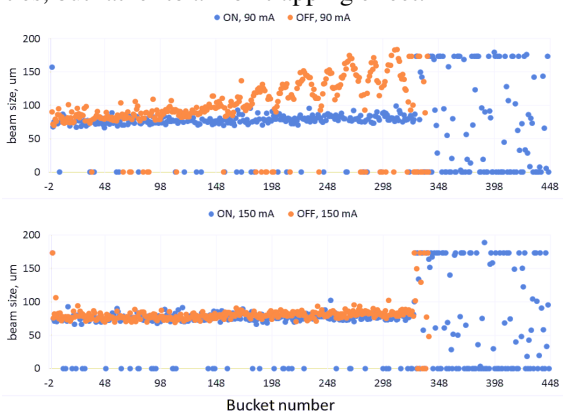

Figure 7: Vertical beam size along the bunches for 90 mA and ξ_v=2.6 (top) and 150 mA with ξ_v=4.4 (bottom) with pumps on/off.

Since the Post-Mortem Analysis needs to coherently excite all bunches at the same time, this could affect the TCBI itself. Therefore, for this experiment we decide to use the *Bunch Scan Analysis* method. Figure 8 (top) shows the measured detuning per bunch when the machine is filled with 150 mA in 320 consecutive bunches (bottom plot). Although small, the detuning with the pumps off is smaller than with the pumps on (from 1.5e-7 to 5e-7/bunch). This is arguably related with the larger presence of ions when the pumps are switched off, since the ions act as a focusing force. This can be used to infer the ion cloud density, and we are currently investigating it.

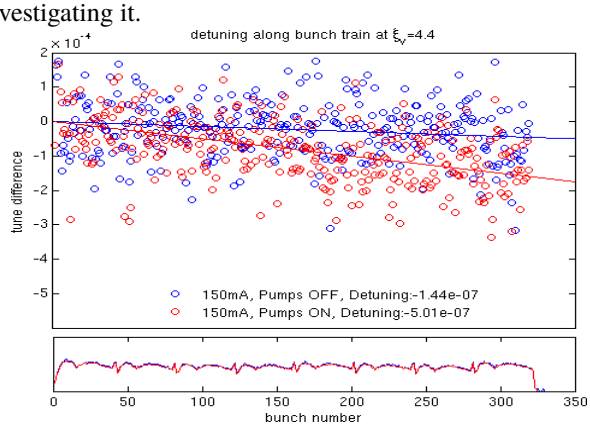

Figure 8: Tune difference along the bunch train wrt tune at bunch 0, with ion pumps on/off. The bottom plot shows the measured filling pattern for both cases.

CONCLUSIONS

ALBA is now equipped with both a BbB beam size and a tune monitor. The BbB size measurements are performed using a FGC that allows gating times as short as 2 ns. Unfortunately, the resolution is limited by the space charge effects produced in the FGC. Nevertheless, qualitative measurements of relative BbB size changes allow to measure the instability rise times with bucket-time resolution. The BbB tune monitor relies on the TMBF electronics described in [4] and can perform two types of tune measurements: using a single bunch excitation/measurement, and using a coherent beam excitation on all bunches, analyzing the position oscillations of the Post-Mortem buffer.

An experiment with switching on/off the vacuum pumps have shown that indeed, the instabilities thresholds are significantly reduced with higher pressure. The BbB beam size monitors showed that the instability rise times are in the order of 150 buckets (for 90 mA and ξ_v=2.6). The BbB tune monitor showed that the detuning with pumps off is smaller, and we are currently investigating if this is consistent with an ion cloud focusing effect.

ACKNOWLEDGEMENTS

We are indebted to R. Monge and the Vacuum Group for their assistance during the pressure bumps experiments.

REFERENCES

[1] T.F. Guenzel and U. Iriso, "Revision of the Impedance Model for the Interpretation of the Single Bunch Measurements at ALBA", in *Proc. of IPAC'15*, Richmond, VA USA, paper MOPJE026, 2015.

[2] L. Torino and U. Iriso, "Transverse beam profile reconstruction using synchrotron radiation interferometry", *Phys. Rev. Accel. Beams* 19, 122801, 2016.

[3] L. Torino, Phd Thesis, ALBA Accelerator Internal Report, ACDIV-2017-02 (2017). https://intranet.cells.

ISBN: 978-3-95450-192-2 doi:10.18429/JACoW-IBIC2017-MOPCC11

es/Divisions/Accelerators/publications/ACDIV-2017-02.pdf

[4] A. Olmos, U. Iriso, J. Moldes, F. Perez, M. Abbott, G. Rehm, and I. Uzun, "Integration of the Diamond Transverse Multibunch Feedback System at ALBA", in *Proc. of IBIC'15*, Melbourne, Australia, paper TUPB046, 2015.

[5] U. Iriso, L. Torino and T. Mitsuhashi, "First Steps Towards a Fast Orbit Feedback at ALBA", in *Proc. IBIC'13*, Oxford, UK, paper WEPC22, 2013.

[6] L. Torino, U. Iriso, and T.M. Mitsuhashi, "Beam Size Measurements using Synchrotron Radiation Interferometry at ALBA", in *Proc. of IBIC'14*, Monterey, CA, USA, paper TUPF23, 2014.

[7] L. Torino and U. Iriso, "Limitations and Solutions of Beam Size Measurements via Interferometry at ALBA", in *Proc. IBIC'15*, Melbourne, Australia, paper TUPB049, 2015.

[8] U. Iriso, M. Alvarez, F. Fernandez, F. Perez, and A. Olmos, "Diagnostics during the ALBA Storage Ring Commissioning", in *Proc. DIPAC'11*, Hamburg, Germany, paper TUOA02, 2011.

[9] M. Carla, G. Benedetti, T. Guenzel, U. Iriso, and Z. Marti, "Local transverse coupling impedance measurements in a synchrotron light source from turn-by-turn acquisitions", *Phys. Rev. Accel. Beams* 19, 121002 (2016).

ISBN: 978-3-95450-192-2 doi:10.18429/JACoW-IBIC2017-MOPCC12

UPGRADE OF BPMS AND SRMS FOR THE BTS TRANSFER LINE AT ALBA

U. Iriso, M. Alvarez, G. Benedetti, A. A. Nosych, A. Olmos, X. Rodriguez
ALBA-CELLS, Barcelona, Spain

Abstract

The beam position and size of the electron beam in the ALBA Booster-To-Storage (BTS) transfer line are monitored using Beam Position Monitors (BPMs) and Synchrotron Radiation Monitors (SRMs). However, their performance was not fully optimized and the beam trajectory in the transfer line was not properly controlled. Consequently, the transfer efficiency in the BTS has been fluctuating since day one, so more studies and precise beam measurements were critically needed to optimize it. Firstly, the SRMs mechanics and automation were significantly improved to provide a more robust optics alignment. Secondly, BPM electronics have been upgraded for single-pass beam detection, showing a factor 10 better position resolution than the former units. Both SRMs and BPMs are now routinely used to keep transmission efficiency along the BTS above 90%.

INTRODUCTION

ALBA's booster and storage ring have a concentric layout with a short (~15 m) transfer line between them. Following the extraction elements (kicker, dipole and septum), the BTS consists of 2 dipoles (in blue in Fig. 1), 7 quads (in purple) and 3 H/V correctors. It follows into an injection section consisting of 2 kicker pairs (in yellow) and a septum (in green) in between them. The booster ramps up the energy of a 0.2 nC Linac charge from 110 MeV to 3 GeV and fires at a 3.125 Hz rate. The BTS diagnostics are quite numerous: 4 BPMs (red crosses), 3 SRMs (yellow stars), 3 FSOTRs and 2 FCTs.

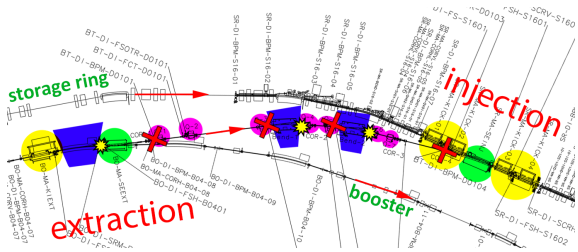

Figure 1: Layout of booster-to-storage transfer line of ALBA.

The injection efficiency measured from the Booster to the Storage Ring has been, for a long time, maximized by scanning mostly the pulsed elements and the BTS last pair of correctors, without paying much attention to the electron beam trajectory in the BTS. This worked reasonably well when we were operating the accelerators in decay mode, injecting only two times per day with the Front Ends (FE) closed. Nevertheless, once we had moved to top-up operation, the instabilities of the injector became an issue since the injection times could be significantly extended and disturb some beamline experiments.

In order to improve and stabilize the injection efficiency, we first performed a beam alignment campaign based on the FSOTRs. This already improved the injection efficiency stability. Nevertheless, since these components are beam destructive elements, we decided to work on the non-destructive instrumentation (SRMs and BPMs) in order to improve the diagnostics and provide a real-time monitoring tool during routine operation. These should not only provide a better understanding of the transmission oscillations, but also should help in finding more stable beam trajectories. This paper describes the improvements in the SRMs and BPMs, and shows the results obtained with them.

SRM UPGRADE

As a non-destructive diagnostic tool, the SRM uses the synchrotron radiation produced when the electron beam traverses a bending magnet. The visible light is guided away by a 45° mirror into the CCD optics, producing a transverse beam image in real-time. The diffraction limit does not significantly affect the beam imaging in the BTS, since the beam size is in the order of ~(200, 100) µm.

There are 3 locations of SRMs in the transfer line [1, 2]. One is placed after a booster dipole in between the extraction elements, and two more SRMs are located after each dipole in the BTS. The SRM setup and optics are all identical: a telephoto zoom lens (Sigma 70-300 mm) is used with a commercial CCD (Basler scA1300-32gm). Each is focused at 1.5 m distance to a source point in the center of the corresponding upstream dipole. Even though the set-up is the same as the one working since day-one in the Booster [3], the SRMs in the BTS did not properly function due to problems with alignment and low visibility, and consequently, the BTS-SRM system received a major upgrade taking care of its a) mechanical stability and b) centering on beam.

Initially, the SRM optics were lightly attached to the girder (Fig. 2, left), and its alignment relied on the viewport. However, in this configuration the SRM weight was partially supported in the viewport as well, thus risking bending it downwards. Moreover, any manipulation of the optics would mean losing any reference of the CCD position with respect to the viewport. Instead, the new generation of ALBA's SRM supports have been designed to be firmly clamped to the girder (Fig. 2, right), allowing independent mechanical adjustment of its optics without forcing the viewport. On the contrary, the viewport is now a stable reference for SRM optics alignment.

ISBN: 978-3-95450-192-2 doi:10.18429/JACoW-IBIC2017-MOPCC12

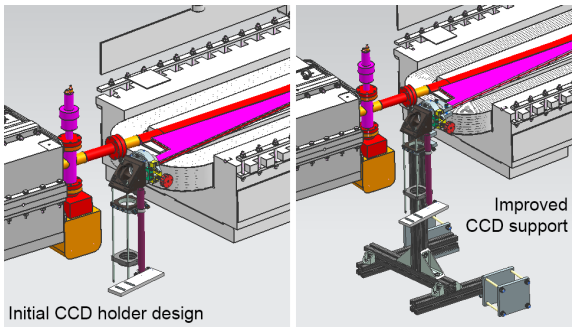

Figure 2: Initial (left) and a heavier redesigned (right) mechanical support of BTS SRMs, allowing stable viewport position.

The alignment of SRMs was done by “looking" for beam manually by stopping the beam and entering the tunnel in between the attempts to tune the mirror angular adjustment screws at minimal zoom of the objective. After both beam spots in SRMs were found, the zoom was increased for more resolution and the internal iris of the objective is set to fully open. Figure 3 shows the beam image of the two SRMs in the BTS after the alignment process had been performed.

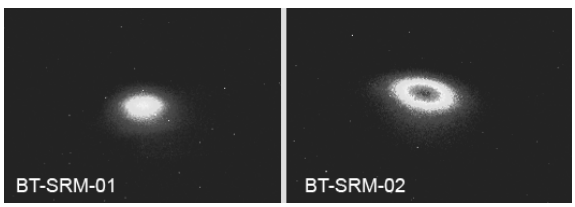

Figure 3: Transfered beam as seen by two SRMs in the transfer line.

BPM UPGRADE

The BTS BPMs are based on button-type feedthroughs, directly welded on the round vacuum chamber. The signals from four buttons are delivered to the processing electronics via long RF coax cables (near 40 meters). BPM signals were formerly digitized and processed by standard Libera Brilliance modules from Instrumentation Technologies [4]. These electronics were meant to take data from multi-turn BPMs, where the beam passes continuously and the acquisition and processing times can be relaxed, leading to acceptable functionality in decay mode. However, ALBA’s operation in top-up requires very low charge beams from the injector, leading to beam currents in the order of tenth of µA through the BTS.

Hence, the combination of very low charge beams, long RF cables and long integration time of electronics had significantly degraded the position resolution of BTS BPMs.

In order to improve their position measurement, the new Libera Spark EL [4] electronics were tested. Such electronics are designed to cope with single pass beams and are based on time definition of the processing window when the beam passes through the BPM. This improves the resolution because the contribution of no-beam signal to position calculation is reduced. Various tests have been done at ALBA with Sparks electronics, both in the BTS transfer line and also in the LINAC exit.

Figure 4 shows the Libera’s difference of position calculation for a BTS BPM during top-up reinjections using a pure 50 µA single bunch beam. Here, the position calculation improves by a factor 10 (std) by using the Spark units wrt the former Brilliance one.

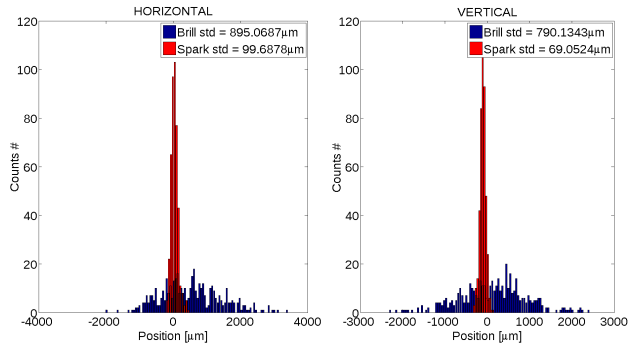

Figure 4: Spark-Brilliance comparison for BTS BPMs on a 50 µA single bunch beam.

APPLICATION IN ROUTINE OPERATION

In the booster, the displacement of an extracted beam with respect to the stored one can be measured at the SRM placed in the booster dipole between the kicker and the extraction septum. With a proper adjustment of time delay and integrating the signal of the CCD camera over the last turns before the extraction, an image with both the stored and the extracted beam is observed (see Fig. 5), and so the distance between them can be set to the design value using the extraction kicker. Next, the extraction kick angle is crosschecked with the fluorescent screen in front of the septum.

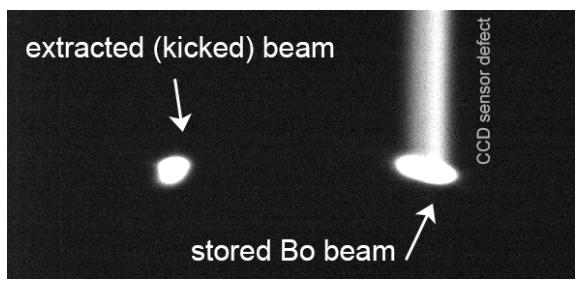

Figure 5: SRM placed in the booster dipole embedded between the extraction kicker and the septum. The separation between the stored beam (the spot at the center of the screen) and the extracted beam (displaced on the left) can be directly monitored and adjusted to the nominal value.

A high-level software has been developed in order to track the beam position along the BO extraction and BTS trajectory. This has become very useful to detect displacements of the beam at the entrance of the first dipole of BTS, and

ISBN: 978-3-95450-192-2 doi:10.18429/JACoW-IBIC2017-MOPCC12

has provided a diagnostic tool for the operators to compensate those displacements by changing the setting of the BO extraction septum.

Figure 6 shows the BTS efficiency (green trace), the beam position at the booster SRM, and the first SRM1 in the BTS (red and black lines, respectively) during 6 h of routine operation with top-up injections occurring every 20 minutes. The beam is displaced at the first SRM when the injection efficiency drops from 90 to 60%.

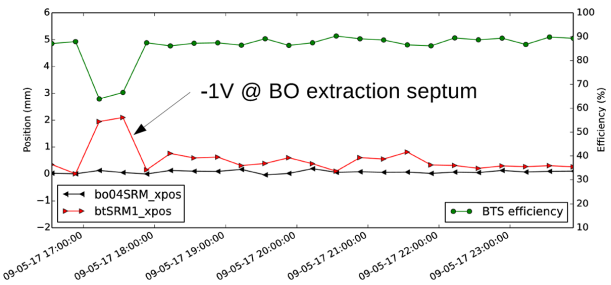

Figure 6: Beam position at BO extraction, BTS entrance and the injection efficiency during 6 h of top-up operation. The efficiency is recovered by bringing back the beam position at the BTS entrance by tuning the extraction septum.

Since the position of the extracted beam stays stable at the booster SRM (between the extraction kicker and septum), the operator reacts decreasing the BO extraction septum setting to recover the previous position at the first SRM. The injection efficiency is immediately recovered in the following top-up injection once the beam displacement is compensated. At the time of this example, the new BPM electronics were not yet commissioned and so we cannot show the BPM data of this incidence.

After the BTS improvement campaign, we conclude that the most probable sources of injection efficiency oscillations are the pulsed elements of BO extraction and SR injection. The effect of BO orbit oscillations (which displaces the beam at the extraction kicker entrance in the order of 100 µm peak-to-peak) is still under study. Currently the Pulsed Magnets group are also monitoring the read-back of the pulsed elements. They had detected drifts and sudden steps in the SR injection septum pulse amplitude, which have been identified as one of the sources of the injection efficiency oscillations.

CONCLUSION

The SRMs and BPMs systems in the BTS transfer line have been improved during 2016 and despite the single pass of low charge beams, they offer a reliable tool to control the beam trajectory. The BPMs have been equipped with the Sparks electronics, providing a factor 10 better resolution in the beam position. Furthermore, the new mechanical design of the SRMs provide a robust and repeatable position system that allowed a proper beam imaging centering, and allow a continuous monitoring of top-up injections. As a result, the fluctuations in the top-up transmission efficiency in the BTS transfer line is reduced, and on average it increased from about 60 to 90% (see blue dots in Fig. 7).

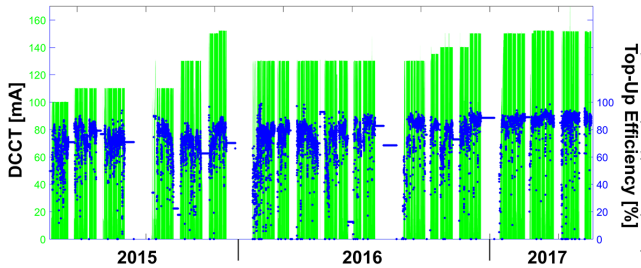

Figure 7: Injection efficiency evolution in BTS, correlated with beam current over time.

ACKNOWLEDGMENTS

We would like to thank M. Pont for fruitful discussions, and triggering the need to improve the BTS transmission efficiency; and N. Ayala for setting-up the required instrumentation to monitor the pulsed elements during machine development shifts.

REFERENCES

[1] U. Iriso and F. Perez, "Synchrotron radiation monitors at ALBA", in *Proc. EPAC2006*, paper THPLS056.

[2] U. Iriso, A. Olmos, and F. Perez, "Electron beam diagnostics for the ALBA light source", in *Proc. DIPAC2007*, paper MOD1A03.

[3] U. Iriso and G. Benedetti, "Beam size and emittance measurements during the ALBA Booster ramp", in *Proc. IPAC2013*, paper TUPWO041.

[4] http://www.i-tech.si/

ISBN: 978-3-95450-192-2 doi:10.18429/JACoW-IBIC2017-MOPCC13

BEAM ENERGY MEASUREMENTS WITH AN OPTICAL TRANSITION RADIATION FOR THE ELI-NP COMPTON GAMMA SOURCE

M. Marongiu*[1], A. Giribono[1], A. Mostacci[1], L. Palumbo[1], M. Pompili, Sapienza University, Rome, Italy
E. Chiadroni, F. Cioeta, G. Di Pirro, G. Franzini, V.Shpakov, A. Stella, C. Vaccarezza, A. Variola
LNF-INFN, Frascati, Italy
D. Cortis, INFN, Rome, Italy
A. Cianchi, Università di Roma II Tor Vergata, Rome, Italy
[1]also at INFN, Rome, Italy

Abstract

A high brightness electron LINAC is being built in the Compton Gamma Source at the ELI Nuclear Physics facility in Romania. To achieve the design luminosity, a train of 32 bunches, 16 ns spaced, with a nominal charge of 250 pC will collide with the laser beam in the interaction point at two electron beam energies, namely 280 MeV and 720 MeV. Electron beam spot size is measured with optical transition radiation (OTR) profile monitors. The paper deals with the possibility of using the OTR monitors to measure also beam energy along the machine; such measurements may help monitoring the accelerating sections performances, especially when the whole bunch train is being accelerated. We discuss the measurement principle, the expected accuracy and the main characteristic of the optical line to retrieve the angular distribution of the emitted radiation.

INTRODUCTION

The Gamma Beam Source [1] (GBS) machine is an advanced source of up to ≈20 MeV Gamma Rays based on Compton back-scattering, i.e. collision of an intense high power laser beam and a high brightness electron beam with maximum kinetic energy of about 740 MeV. The Linac will provide trains of bunches in each RF pulse, spaced by the same time interval needed to recirculate the laser pulse in a properly conceived and designed laser recirculator, in such a way that the same laser pulse will collide with all the electron bunches in the RF pulse, before being dumped. The final optimization foresees trains of 32 electron bunches separated by 16 ns, distributed along a 0.5 µs RF pulse, with a repetition rate of 100 Hz.

The goal of this paper is to verify the possibility of implement an energy measurement technique based on the OTR and to study its expected accuracy; furthermore, the main characteristics of the optical line will be discussed.

In a typical monitor setup, the beam is imaged via OTR or YAG screen using standard lens optics, and the recorded intensity profile is a measure of the particle beam spot [2]. In conjunction with other accelerator components, it will also be possible to perform various measurements on the beam, namely: its energy and energy spread (with a dipole or corrector magnet), bunch length [3] (with a RF deflector), Twiss parameters [4] (by means of quadrupole scan) or in general 6D characterization on bunch phase space [5]. Such technique is common in conventional [6] and unconventional [7, 8] high brightness LINACs.

The optical acquisition system is constituted by the CCD camera "Basler scout A640-70gm" or by the "Hamamatsu Orca-Fash4" with a macro lens. A movable slide is used to place the lens plus camera system closer or farer from the OTR target; such distance is between 60 cm and 130 cm from the OTR target due to mechanical and geometric constraints. In order to avoid possible damage of the optics devices due to the radiation emitted by the beam, a 45° mirror is placed at 40 cm from the target leading to a minimum distance achievable of 60 cm; since the beam pipe is placed 1.5 m from the floor, the maximum distance is instead 130 cm.

OTR RADIATION

Optical Transition Radiation (OTR) monitors are widely used for profile measurements at LINACs. The radiation is emitted when a charged particle beam crosses the boundary between two media with different optical properties [9], here vacuum and a thin reflecting screen (silicon). For beam diagnostic purposes the visible part of the radiation is used; the recorded intensity profile is a measure of the particle beam spot. Advantages of OTR are the instantaneous emission process enabling fast single shot measurements, and the good linearity (neglecting coherent effects). Disadvantages are that the process of radiation generation is invasive, i.e. a screen has to be inserted in the beam path, and that the radiation intensity is much lower in comparison to scintillation screens.

ENERGY MEASUREMENT

Another advantage of the OTR is the possibility to measure the beam energy by means of observation of its angular distribution (see Figures 1 and 2); this can be expressed by the well known formula 1.

$$\frac{dI^2}{d\omega d\Omega} = \frac{e^2}{4\pi^3 c\epsilon_0} \frac{\sin^2\theta}{\left(\frac{1}{\gamma^2} + \sin^2\theta\right)^2} R(\omega,\theta) \qquad (1)$$

Where $R(\omega,\theta)$ is the reflectivity of the screen; the peak of intensity is at $\theta = 1/\gamma$.

Due to the beam divergence, the angular distribution of the whole beam will be different from 0 at the center (see

* marco.marongiu@uniroma1.it

ISBN: 978-3-95450-192-2 doi:10.18429/JACoW-IBIC2017-MOPCC13

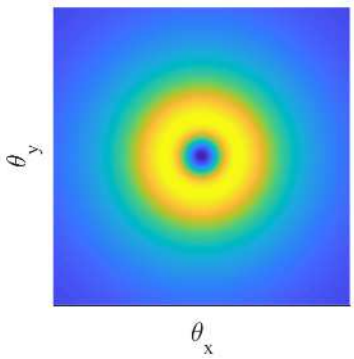

Figure 1: OTR angular distribution of a single electron.

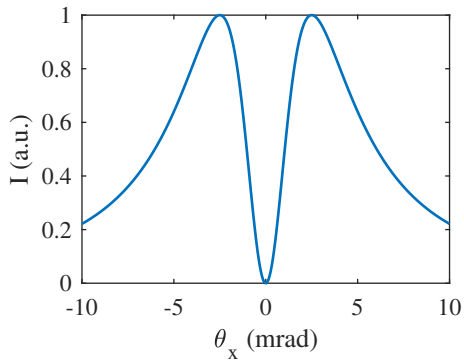

Figure 2: Horizontal profile of the OTR angular distribution of a single electron.

Figure 3); the ratio between the minimum and the maximum intensity is related to the beam divergence. A parameter called visibility can be defined as in Equation (2): the beam divergence measure with the OTR angular distribution can be reliably done if the visibility parameter is greater or equal 0.1 [10] (in analogy with the contrast function). Since the visibility increase with the beam energy, one can also estimate the minimum measurable divergence for a given energy [10].

$$V = \frac{I_{max} - I_{min}}{I_{max} + I_{min}} \tag{2}$$

The presence of OTR screen after each accelerating structure make possible to measure the energy gain of the structure; and, in a multi-bunch configuration, the energy jitter shot to shot if the energy resolution is high enough. These are very interesting features, especially during the commissioning stage of the machine.

OPTICAL LINE

In order to acquire the OTR angular distribution, the distance between the lens and the CCD must be equal to the focal length (f) of the lens; the choice of f determines the dimension Δ of the pixel. Indeed, Δ is given by the physical dimension of the pixel (i.e. 6.5 µm for the Hamamatsu) divided by the focal length. Therefore, f defines the resolution and the field of view of the acquisition; typically, the field of view is in the range $\theta \in [-3/\gamma, 3/\gamma]$, while the resolution must be high enough to distinguish the two peaks and the minimum. For instance, using the Hamamatsu camera ($2048x2048$ pixels) with a 180 mm lens, one obtains a Δ equal to 36 µrad and a field of view of 74 mrad.

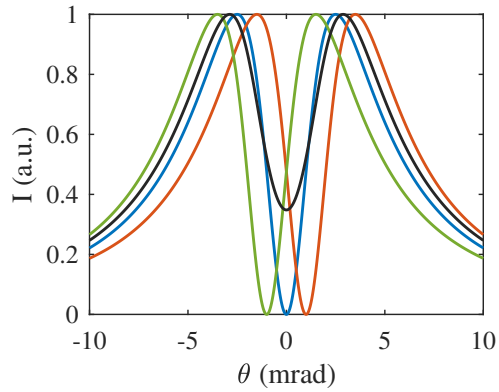

Figure 3: OTR angular distribution for 3 different values of divergence (the blue line represents the 0 divergence, the red one the case of 1 mrad, and the green line the case of −1 mrad) and their sum (black line). All the 4 curves are normalized to their maximum value.

An important parameter to evaluate is the measurement accuracy: one can express it as a function of the number of pixels between the two peaks (N_{px}). This number is proportional to $2/\gamma$: applying the uncertainty propagation rules, the absolute uncertainty reads:

$$\sigma_\gamma = \sqrt{\left(\frac{\partial\gamma}{\partial\theta_1}\right)^2 \sigma_\theta^2 + \left(\frac{\partial\gamma}{\partial\theta_2}\right)^2 \sigma_\theta^2} = \sqrt{\frac{8}{(\theta_1 - \theta_2)^2}\sigma_\theta^2}$$
$$= \frac{2\sqrt{2}}{(\theta_1 - \theta_2)^2}\sigma_\theta = \frac{\sqrt{2}\gamma}{N_{px}\Delta}\sigma_\theta \tag{3}$$

Where σ_θ is the uncertainty of the position of the peak; the latter can be written as the quadrature sum of the position uncertainty and the fit uncertainty:

$$\sigma_\theta^2 = \frac{\Delta^2}{12} + \sigma_{fit}^2 = \frac{\Delta^2}{12}\left(1 + \frac{12\sigma_{fit}^2}{\Delta^2}\right) \tag{4}$$

Therefore, a bigger focal length reduces the value of Δ and increase the value N_{px}, having a positive effect on the relative uncertainty of the energy measurement. However, if the focal length is increased too much, the tails of the angular distribution are cut out by the optic system, eventually compromising the goodness of the fit. Moreover, when the energy increase, the peaks become closer to each other (N_{px} decreases), but the signal to noise ratio increases and therefore, the goodness of the fit. Hence, if it is required a high resolution measurement of the energy and its shot to shot variation, the optic system must be designed specifically for the energy of interest, at the expense of the flexibility.

Another parameter that must be taken into account is the distance between the OTR target and the lens. This is important in order to quantify the amount of radiation that

ISBN: 978-3-95450-192-2 doi:10.18429/JACoW-IBIC2017-MOPCC13

reaches the camera; but it is not a free parameter of the system, due to the geometry and to radiation protection issues of the machine. Moreover, the lens can introduce chromatic aberrations which must be taken into account. In order to estimate the amount of radiation that can be generated by the OTR target and collected by the optic system, one can derive from the Equation (1) the following [11]:

$$n_g(\lambda_1, \lambda_2) = \frac{Q}{e} \frac{\alpha \ln(4\gamma^2 - 1)}{\pi} \ln\left(\frac{\lambda_2}{\lambda_1}\right) \tag{5}$$

Where n_g is the number of photons generated by the OTR as a function of the bandwidth, the beam charge Q and the beam energy. The number of photons that actually are collected by the optic system are related also to the collecting angle $\phi = \arctan(0.5D/a)$, where D is the lens diameter and a is the distance between the lens and the target (as shown by Equation (6)).

$$n_c(Q, \phi, \lambda_1, \lambda_2) = \frac{\alpha}{\pi} \frac{Q}{e} \ln\left(\frac{\lambda_2}{\lambda_1}\right) \left[\ln\left(1 + 4\gamma^2 \tan^2 \frac{\phi}{2}\right) + \right.$$
$$\left. + \frac{\cos\phi}{1 + \gamma^2 \sin^2 \phi} - 1\right] \tag{6}$$

The ratio between the collected photons and the generated photons gives the collecting efficiency of the optic system (see Figure 4). In order to obtain an efficiency of 70%, considering the ELI-GBS geometry and an energy of 150 MeV, a 300 mm lens must be put at a distance 50 cm from the OTR screen ($\theta = 0.3$ rad); different lenses at different distances gives a 70% efficiency.

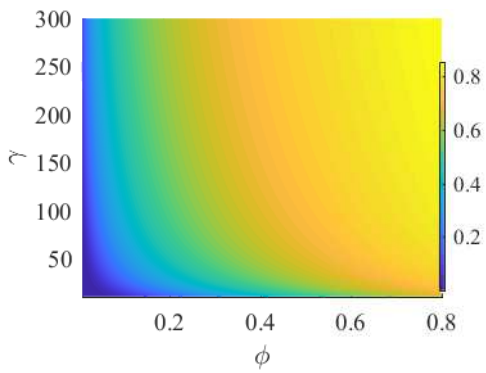

Figure 4: Collecting efficiency of a single lens optic system not taking into account the transmissivity of the lens.

Due to geometry constraints and to radiation protection of the optic system, it may not possible to get too close to the OTR screen; this issue can be solved using a telescope. A simple scheme is based on a single lens system with focal length f at distance p from the OTR screen; it will replicate the source at a distance q from the lens equals to $pf/(f-p)$. For instance, a $1:1$ replica gives $p = q = 2f$; in this way, the CCD and the relative electronics can be put at $4f$ distance farer. Another type of telescope is the so called "4f correlator": in this case a lens is put at a distance f from the OTR screen, and a second lens is put at a distance p in order to have its backward focal plane superimposed to the forward one of the first lens. The source is replicated at the forward focal plane of the second lens: the distance gain this time is $2f_1 + 2f_2$. Analytically, the first lens perform a Fourier transformation of the source, while the second lens does the inverse transformation.

However, one should add lenses to the system only if strictly necessary; indeed, each lens adds a chromatic aberration contribution that could compromise the measurement. This effect can be reduce with, for instance, an achromatic doublet or by introducing some frequency filtering in the Fourier plane of the "4f correlator"; however, due to the transmissivity of the lenses and to the fact that the number of photons collected by the optic system are related to the observation bandwidth (see Equation (6)), this techniques reduce the amount of radiation collected.

The Equation (1) applies in the case of far field approximation: this is possible as long as the distance between the lens and the OTR screen is greater then the quantity $\gamma^2\lambda$ (in the GBS case, this limit value is around 4.5 cm for an energy of 150 MeV). If this condition is not satisfied, the near field approach must be used; in this case an analytical analysis became too complex, and a numerical study (i.e. with Zemax) of the optic system is preferred.

CONCLUSION

The OTR could be a very useful diagnostic tool in order to measure the transverse characteristics of the beam and, observing the angular distribution, the energy .

Due to the fact that the OTR screen are placed all along the machine (24 screen), a distributed energy measurement can be performed; the energy jitter shot to shot can also be evaluated. These measurements are particularly useful during the commissioning stage of the machine. As it has been shown, however, a compromise between the flexibility in the energy range and the necessary accuracy need to be done.

Furthermore, the design of the optic line has been discussed in the far field approximation. Numerical analysis are foreseen in order to study the near field case and evaluate all the possible setups.

REFERENCES

[1] A. Bacci *et al.*, "Electron linac design to drive bright Compton back-scattering gamma-ray sources," *Journal of Applied Physics*, vol. 113, no. 19, p. 194508, 2013.

[2] M. Marongiu *et al.*, "Thermal behavior of the optical transition radiation screens for the eli-np compton gamma source," *Nuclear Instruments and Methods in Physics Research Section A: Accelerators, Spectrometers, Detectors and Associated Equipment*, 2016. [Online]. Available: 10.1016/j.nima.2016.07.040

[3] D. Filippetto *et al.*, "Phase space analysis of velocity bunched beams," *Physical Review Special Topics-Accelerators and Beams*, vol. 14, no. 9, p. 092804, 2011.

ISBN: 978-3-95450-192-2 doi:10.18429/JACoW-IBIC2017-MOPCC13

[4] A. Mostacci *et al.*, "Chromatic effects in quadrupole scan emittance measurements," *Physical Review Special Topics-Accelerators and Beams*, vol. 15, no. 8, p. 082802, 2012.

[5] A. Cianchi *et al.*, "Six-dimensional measurements of trains of high brightness electron bunches," *Physical Review Special Topics-Accelerators and Beams*, vol. 18, no. 8, p. 082804, 2015.

[6] D. Alesini *et al.*, "Status of the sparc project," *Nuclear Instruments and Methods in Physics Research Section A: Accelerators, Spectrometers, Detectors and Associated Equipment*, vol. 528, no. 1, pp. 586–590, 2004.

[7] P. Antici *et al.*, "Laser-driven electron beamlines generated by coupling laser-plasma sources with conventional transport systems," *Journal of Applied Physics*, vol. 112, no. 4, p. 044902, 2012.

[8] A. R. Rossi *et al.*, "The external-injection experiment at the sparc_lab facility," *Nuclear Instruments and Methods in Physics Research Section A: Accelerators, Spectrometers, Detectors and Associated Equipment*, vol. 740, pp. 60–66, 2014.

[9] V. Ginsburg *et al.*, "Radiation of a uniformly moving electron due to its transition from one medium into another," *Zhurnal eksperimentalnoi i teoreticheskoi fiziki*, vol. 16, no. 1, pp. 15–28, 1946.

[10] A. Cianchi *et al.*, "Transverse emittance diagnostics for high brightness electron beams," *Nuclear Instruments and Methods in Physics Research Section A: Accelerators, Spectrometers, Detectors and Associated Equipment*, 2016.

[11] B. Yang, "A design report for the optical transition radiation imager for the lcls undulator," SLAC National Accelerator Laboratory (SLAC), Tech. Rep., 2010.

ISBN: 978-3-95450-192-2 doi:10.18429/JACoW-IBIC2017-MOPCC14

PHYSICS MODEL OF AN ALLISON PHASE-SPACE SCANNER, WITH APPLICATION TO THE FRIB FRONT END*

Chun Yan Jonathan Wong†, National Superconducting Cyclotron Laboratory, East Lansing, USA
Scott Cogan, Yue Hao, Steven Lidia, Steven M. Lund, Tomofumi Maruta‡, Diego Omitto,
Peter Ostroumov, Eduard Pozdeyev, Haitao Ren, Rebecca Shane, Takashi Yoshimoto, Qiang Zhao
Facility for Rare Isotope Beams, East Lansing, USA

Abstract

We study Allison-type phase-space scanners by extending analytic models to include two important geometric features that are conventionally omitted, namely asymmetric slit-plate to dipole-plate gaps at the two ends and finite slit-plate thickness. Their effects can be significant for high-resolution Allison scanners and lead to two corrections in the measurement data relative to more idealized descriptions: 1) a change in the voltage-to-angle conversion relation, and 2) a data point weight compensation factor. These findings are corroborated by numerically integrated single-particle trajectories in a realistic 2D field map of the device. The improved model was applied to the Allison scanner used to measure a 12 keV/u heavy-ion beam in the front-end of the Facility for Rare Isotope Beams (FRIB) at Michigan State University. Preliminary measurements show that the improved model results in significant ($\gtrsim$10%) modifications to beam moments, thus rendering the corrections important for accurate phase-space characterizations.

INTRODUCTION

Allison scanners [1] are widely used to efficiently measure slit-transmitted phase-space projections of low-energy beams. An Allison scanner (see Fig. 1) consists of an entrance slit-plate (slit width s), an aligned exit slit-plate (slit width s) with an integrated Faraday cup, and a bipolar-biased electric dipole (voltage V_0) placed between the two slits. The scanner is translated mechanically (typically in steps) to change the slit position, and the dipole voltage V_0 is varied to select transmittable angles by varying the bending strength. For a particular coordinate and dipole voltage, the scanner samples a point in the beam phase-space. The density of the point is taken to be proportional to the current collected at the Faraday cup.

Idealized analytic formulas relating Allison scanner geometry and voltages to phase-space measures were derived in Refs. [1,2]. These idealized results assume thin slit-plates, an ideal (no-fringe) dipole field, and a symmetric geometry. This paper extends idealized model results by considering two additional geometric features that can lead to significant corrections: 1) asymmetric slit-plate to dipole-plate gaps at the two ends, and 2) finite slit-plate thickness.

* Work supported by the U.S. DOE Office of Science under Cooperative Agreement DE-SC0000661 and the NSF under Grant No. PHY-1102511.
† wong@nscl.msu.edu
‡ On leave from KEK/J-PARC

Asymmetry commonly arises, probably unintentionally, in Allison scanners because relief cuts on thick entrance- and exit-plates have been made in the same direction [3,4]. This asymmetry is also present in the FRIB Allison scanner where relief cuts on both plates face the incoming beam as shown in Fig. 1. Due to this issue, the effective slit-plate to dipole-plate gap on the exit end is more than double that on the entrance end. We find such asymmetries significantly impact angle selection calibration with V_0.

Slit-plate thickness can be neglected when it is much smaller than the slit width. This idealization can break down as Allison scanners decrease slit widths to improve resolution. Recent examples include slit widths of $s \leq 100\,\mu$m planned at GSI FAIR [5] and $s = 38\,\mu$m implemented at TRIUMF [6]. Fig. 1 details the slit plate presently employed in the FRIB scanner where $s = 60\,\mu$m and the effective (not including irrelevant thickness spanning the 30° relief cut) plate-thickness is 254 µm. This approximately 4 : 1 aspect ratio is effectively a small channel, which can scrape particles that would have passed through a slit-plate with no thickness.

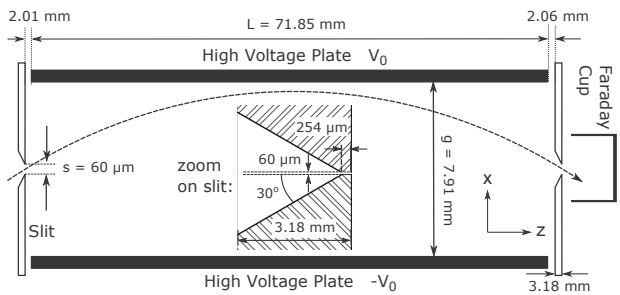

Figure 1: FRIB Allison scanner geometry.

ANALYTIC MODEL

Four geometric models of an Allison scanner are presented in Fig. 2. The models cover combinations of symmetric/asymmetric end-plate to slit-plate gaps with thin/thick slit-plates to study effects of asymmetry and slit-plate thickness. As illustrated in the Fig. 2, a range of angles can be transmitted at each voltage setting due to the finite slit width. We define:

$x'_{\rm ref}$: the angle at which a particle enters and exits the chamber at the same x-position,

$x'_{\rm max\,/\,min}$: maximum/minimum transmittable angle,

$\Delta x' = x'_{\rm max} - x'_{\rm min}$: angular resolution,

ISBN: 978-3-95450-192-2 doi:10.18429/JACoW-IBIC2017-MOPCC14

where $x' \equiv dx/dz$ and $x = 0$ corresponds to the device center-line. Note that the points at which extreme trajectories touch the slits are shifted when the slits have finite thickness.

Particle transmission efficiency can be understood as follows. For any $x' \in [x'_{\min}, x'_{\max}]$, one can find a trajectory with initial angle x' that allows the particle to pass through both slits. Imagine shifting that trajectory along the x-axis, which is equivalent to changing the initial x-position. Among all shifted particles that enter the entrance slit with angle x', some are transmitted while others are scraped. This gives rise to a transmitted fraction (T) that depends on the initial angle value of x' which sets the shape of the trajectory. Assuming a uniform distribution of particle x-coordinates across the slit, we define $p(x')$ = (no. transmitted)/(no. entering), where $p(x'_{\text{ref}})$ is closest to unity and $p(x'_{\max}) = p(x'_{\min}) = 0$. Assuming uniform distribution in x' for $x' \in [x'_{\min}, x'_{\max}]$, $T(x'_{\text{ref}}) = \int_{x'_{\min}}^{x'_{\max}} p(x')dx' \Big/ \int_{x'_{\min}}^{x'_{\max}} dx'$ is the overall fraction of particles within the angular range that is transmitted.

We analytically calculate particle trajectories in the models by treating the biased plates as perfect hard-edge dipoles that extend over the axial length of the plates. Angular ranges $x'_{\max,\min}$ are determined by solving for the limiting particles that touch the entrance and exit slits at the coordinates illustrated in Fig. 2. Results are summarized in Table 1. $\mathcal{E}$ denotes the particle kinetic energy.

NUMERICAL MODEL

A Python code is employed to numerically integrate particle equations of motion in a realistic 2D field map of the device geometry that is generated from the electrostatic field code POISSON [7]. E_x and E_z electric field data is exported from POISSON onto a high-resolution x–z mesh with $dx = dz = 0.2$ mm, and imported into the Python code. Fields at the particle position are calculated using linear area interpolation from the gridded field data [8]. Image charges, beam space charge, and scattering effects are neglected. Non-relativistic equations of motion are exactly transformed from time t to axial coordinate z obtaining:

$$\frac{d}{dz}\begin{bmatrix} x \\ t \\ x' \\ t' \end{bmatrix} = \begin{bmatrix} x' \\ t' \\ \left(\frac{qE_x}{m} - \frac{qE_z}{m}x'\right)t'^2 \\ -\frac{qE_z}{m}t'^3 \end{bmatrix}$$

The state vector describing the particle trajectory is advanced using the ode package within Scientific Python (SciPy) [9] for specified initial particle coordinate x, angle x', and dipole voltage V_0 (field data scaled). The code takes into account scraping on all boundaries. To solve for $x'_{\max,\min}$, we note that the corresponding trajectory must touch the slits at two points (see Fig. 2). We employ a numerical root-finding procedure to solve for the initial x' that connects the upstream point to the downstream point. x'_{ref} is solved analogously with the condition $x = 0$ at both ends.

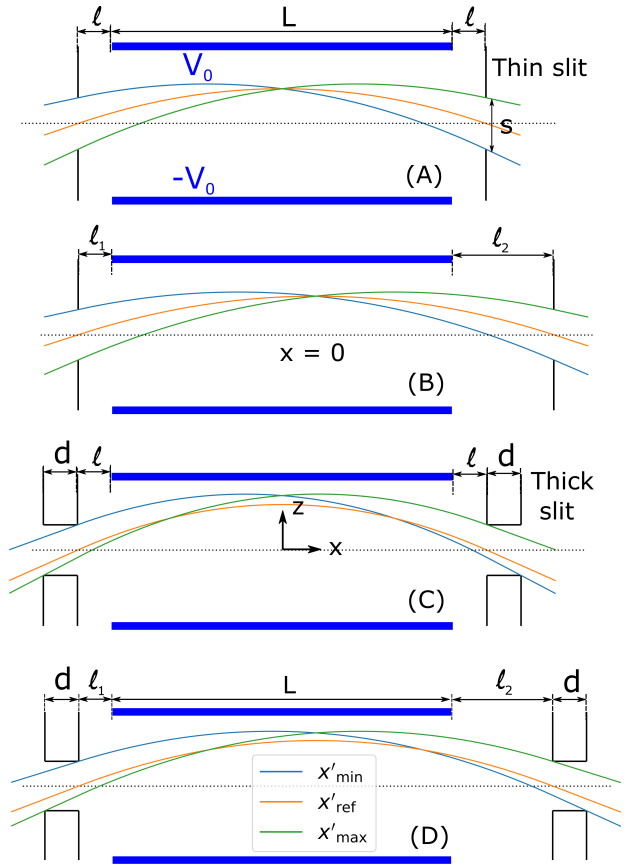

Figure 2: Four geometric models. Model A: zero end distances, thin plate; Model B: non-zero end distances, thin plate; Model C: zero end distances, thick plate; Model D: non-zero end distances, thick plate.

DATA ANALYSIS: TWO CORRECTIONS

The results from analytic and simulation studies reveal two significant corrections on measurement data from Allison scanners relative to ideal symmetric, thin-plate results [1,2]. The ideal results are summarized in column A of Table 1. Note that the ideal results allow symmetric slit-plate to dipole-plate gaps upstream and downstream. One correction alters the dipole voltage (V_0) to selected angle (x'_{ref}) relation of the device due to asymmetric gaps. The other correction characterizes how finite slit-plate thickness alters the transmitted current as a function of x'_{ref}. We illustrate these effects for the FRIB Allison scanner geometry shown in Fig. 1 for an Ar^{9+} ion with kinetic energy $\mathcal{E} = 12$ keV/u.

Voltage-to-Angle Relation

As shown in Table 1, when end distances are asymmetric, the reference angle x'_{ref} has an additional factor $(L+2l_2)/(L+l_1+l_2)$ relative to the ideal model results (column A) which deviates from unity. For the FRIB Allison scanner, $l_1 = 2.01$ mm and $l_2 = (2.06 + 3.18 - 0.254)$ mm $= 4.99$ mm. So the relief cuts generate significant effective asymmetry. In Fig. 3, x'_{ref} versus V_0 is plotted for numerical (realistic), ideal analytic (Table 1, column A), and improved analytic (Table 1,

ISBN: 978-3-95450-192-2 doi:10.18429/JACoW-IBIC2017-MOPCC14

Table 1: Analytic Results Corresponding to the Geometric Models in Fig. 2

Model	A	B	C	D
End-gap distances Plate	Symmetric Thin	Asymmetric Thin	Symmetric Thick	Asymmetric Thick
x'_{ref}	$\frac{1}{2}\frac{qV_0L}{g\mathcal{E}}$	$\frac{1}{2}\frac{qV_0L}{g\mathcal{E}}\left(\frac{L+2l_2}{L+l_1+l_2}\right)$	$\frac{1}{2}\frac{qV_0L}{g\mathcal{E}}$	$\frac{1}{2}\frac{qV_0L}{g\mathcal{E}}\left(\frac{L+2l_2}{L+l_1+l_2}\right)$
$x'_{\mathrm{max}} - x'_{\mathrm{ref}}$	$\frac{s}{L+2l}$	$\frac{s}{L+l_1+l_2}$	$\frac{s-x'_{\mathrm{ref}}d}{L+2l+d}$	$\frac{s-x'_{\mathrm{ref}}d}{L+l_1+l_2+d}$
$x'_{\mathrm{ref}} - x'_{\mathrm{min}}$	$\frac{s}{L+2l}$	$\frac{s}{L+l_1+l_2}$	$\frac{s-x'_{\mathrm{ref}}d}{L+2l+d}$	$\frac{1}{L+l_1+l_2+d}\left(s-\frac{L+2l_1}{L+2l_2}x'_{\mathrm{ref}}d\right)$
$\Delta x'$	$\frac{2s}{L+2l}$	$\frac{2s}{L+l_1+l_2}$	$\frac{2s}{L+2l+d}\left(1-\frac{x'_{\mathrm{ref}}d}{s}\right)$	$\frac{2s}{L+l_1+l_2+d}\left(1-\frac{L+l_1+l_2}{L+2l_2}\frac{x'_{\mathrm{ref}}d}{s}\right)$
$p(x')$ for $x' \geq x'_{\mathrm{ref}}$	$\frac{x'-x'_{\mathrm{ref}}}{x'_{\mathrm{max}}-x'_{\mathrm{ref}}}$		$\frac{x'-x'_{\mathrm{ref}}}{x'_{\mathrm{max}}-x'_{\mathrm{ref}}}\left(1-\frac{x'_{\mathrm{ref}}d}{s}\right)$	
$p(x')$ for $x' < x'_{\mathrm{ref}}$	$\frac{x'_{\mathrm{ref}}-x'}{x'_{\mathrm{ref}}-x'_{\mathrm{min}}}$		$\frac{x'_{\mathrm{ref}}-x'}{x'_{\mathrm{ref}}-x'_{\mathrm{min}}}\left(1-\frac{x'_{\mathrm{ref}}d}{s}\right)$	
$T(x'_{\mathrm{ref}})$	$\frac{1}{2}$	$\frac{1}{2}$	$\frac{1}{2}\left(1-\frac{x'_{\mathrm{ref}}d}{s}\right)$	$\frac{1}{2}\left(1-\frac{x'_{\mathrm{ref}}d}{s}\right)$

column B or D) models. The improved and numerical model results are almost identical, giving slopes of 88.5 mrad/kV and 88.4 mrad/kV, respectively. The minimal difference suggests that fringe field effects of the dipole electric fields near the slits have little impact on the transmitted particle trajectories. The ideal expression commonly used shows a 4% deviation relative to numerical model results with a slope of 85.3 mrad/kV, thereby showing significant impact of the effective asymmetry.

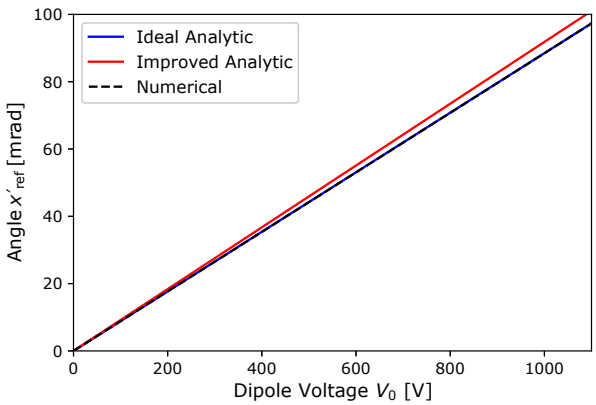

Figure 3: Voltage-to-angle relation for the selected beam.

Voltage-Dependent Weight Compensation

As evident from results in Table 1, for thick slit-plates, the angular resolution $\Delta x'$ and transmission ratio T both decreases linearly as a function of x'_{ref}. This has important implications.

Phase-space scans are typically performed by measuring the current at regular discrete steps in slit position (x-origin shift) and voltage (V_0). The data is represented by a grid in phase-space where each grid is a rectangle of size (position step) × (voltage step). In general, grid dimensions will not coincide with the spatial and angular acceptance of the device. Assuming a uniform distribution of particles within each grid, to calculate the actual beam current that falls within each phase-space grid, the current of data points should be multiplied by:

$$\frac{\text{Angular step}}{T \times \Delta x'} \times \frac{\text{Spatial step}}{\text{slit size}}.$$

Note that the multiplication of T and $\Delta x'$ renders the correction factor *quadratic* in $x'_{\mathrm{ref}}d/s$. When the plate-thickness to slit-width ratio d/s is small, this factor is small, and all data points are scaled almost uniformly as in the case of the ideal analysis. However, when slit-widths are small, $x'_{\mathrm{ref}}d/s$ is large, causing sampled data points to be rescaled differently depending on the angle ($x_{\mathrm{ref}'}$) of the data point. In Fig. 4, the angular resolution $\Delta x'$, transmission factor T, and the angular correction factor $\propto 1/(T\Delta x')$ are plotted as a function of dipole voltage V_0 for the FRIB Allsion scanner. Curves for numerical (accurate), ideal analytic (Table 1, Column A), and improved (Table 1, Column D) analytic model results are shown. The correction introduced by the effect of finite slit-plate thickness can be substantial. For example, in the FRIB device, when $x'_{\mathrm{ref}} = 70$ mrad,

$$\left(1-\frac{L+l_1+l_2}{L+2l_2}\frac{x'_{\mathrm{ref}}d}{s}\right)\left(1-\frac{x'_{\mathrm{ref}}d}{s}\right) \approx 0.5.$$

Therefore, if we apply the ideal model where all data points have equal weights, 0-mrad data points would wrongly weigh twice as much as ±70-mrad data points. Failure to rectify the weights would distort the measurement with increasing amplitude as characteristic beam angles increase.

FRIB APPLICATION

The front-end of the Facility for Rare Isotope Beams (FRIB) [10] commenced early commissioning activities in

ISBN: 978-3-95450-192-2 doi:10.18429/JACoW-IBIC2017-MOPCC14

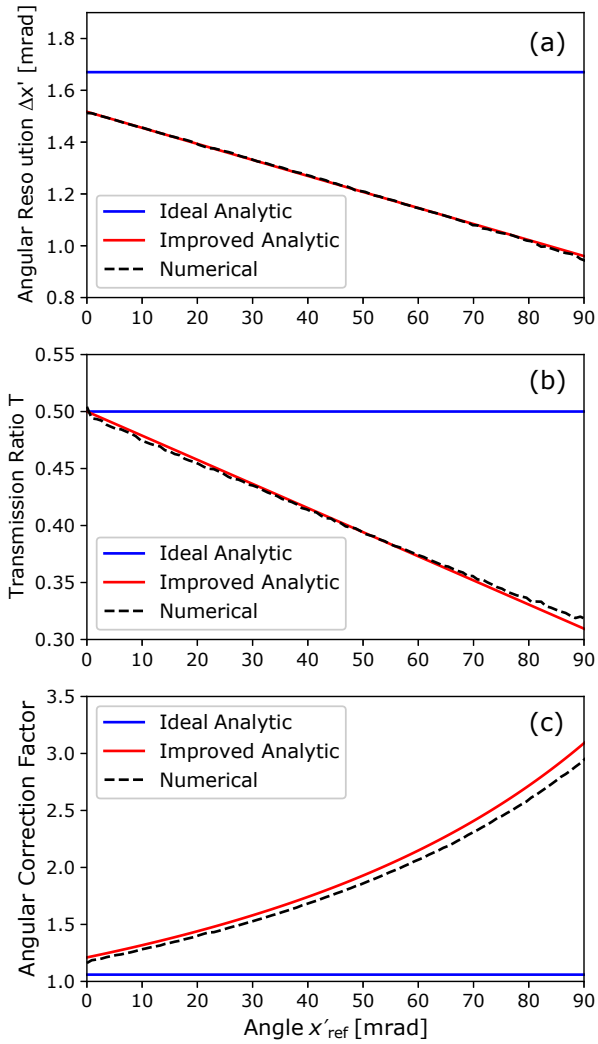

Figure 4: Plots of a) angular resolution $\Delta x'$, b) transmission ratio T, and c) angular correction factor as a function of x'_{ref}.

June 2017. Here we apply analytic model (Table 1, Column D) results to analyze changes in measurements of beam phase-space properties for a y-plane Allison scanner after species separation. Preliminary measurements for a Ar^{9+} ion beam with 20 µA (Faraday cup measure) are used to illustrate corrections. The ions are produced in an ECR source [11] with a 15 kV extraction voltage. The beam then traverses a short section with solenoid focusing and an electrostatic gap biased to accelerate the target ion species to 12 keV/u. Species are separated in a 90° magnetic dipole, downstream of which is an electrostatic quadrupole triplet before measurement by the Allison scanner. A y–y' phase-space projection (with corrections) is shown in Fig. 5. The scan is performed with spatial steps of $\Delta y = 1$ mm and voltage steps of $\Delta V_0 = 20$ V. We average data in a region with no beam to establish the background noise level, which is then subtracted from data points of interest. Corresponding first- and second-order beam moments including the normalized rms emittance are listed in Table 2. Moments

Table 2: Measured FRIB Beam Moments Corresponding to Fig. 5, Calculated with and without Corrections. $(\cdots\%)$ indicate percent deviations of corrected relative to uncorrected results.

Correction	None	x'_{ref}	x'_{ref} + Weight
$\langle y \rangle$ [mm]	-14.7	-14.7	-14.6 (0.4%)
$\langle y' \rangle$ [mrad]	6.95	7.21	7.55 (8.6%)
$\langle y^2 \rangle$ [mm^2]	6.49	6.49	6.97 (7.4%)
$\langle yy' \rangle$ [mm-mrad]	20.2	21.0	22.9 (13.4%)
$\langle y'^2 \rangle$ [mrad^2]	90.3	97.3	105.1 (16.4%)
$\varepsilon_{\text{n-rms}}$ [mm-mrad]	0.0675	0.0700	0.0729 (8.1%)

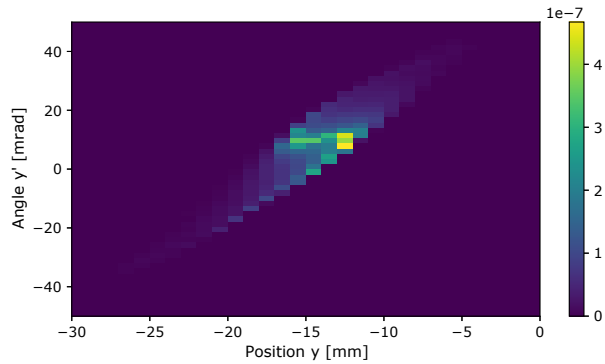

Figure 5: Measured FRIB y–y' phase-space projection (range truncated to better illustrate).

are computed both with (Table 1, Column D) and without (ideal model; Table 1, Column A) corrections to illustrate the deviation. The large centroid offset appears to be related to scanner reference coordinate offset (under investigation). All second-order moments have centroids subtracted, i.e., $\langle y^2 \rangle = \langle (y - \langle y \rangle)^2 \rangle$. We observe a $\gtrsim$10% difference in beam moments, thus confirming the importance of corrections for accurate measurements.

Lastly, we note that although the analysis was made for an Ar^{9+} ion, all results hold identically for other ions with 12 keV/u energy if the dipole voltage V_0 is rescaled by the dimensionless charge-to-mass ratio (A/Q) to keep the acceleration constant:

$$V_0 \rightarrow V_0 \frac{9}{39.95} \left(\frac{A}{Q} \right).$$

CONCLUSION

We identified two important effects for high-resolution Allison scanners that arise from geometric features. Asymmetric dipole-plate to slit-plate gaps at the two ends alter the voltage-to-angle relation for the selected beam, whereas slit-plate thickness $\gtrsim$ slit width requires a data point weight correction that is quadratic in voltage. These effects can significantly change results of phase-space measurements relative to idealized analysis commonly employed. We modeled these effects with analytic formulas that have been verified by

ISBN: 978-3-95450-192-2 doi:10.18429/JACoW-IBIC2017-MOPCC14

a more exact numerical model. Applying derived correction factors to preliminary Allison scanner measurement data in FRIB led to significant ($\gtrsim$10%) changes in beam moments. Since the effects grow with particle angle, corrections can be larger or smaller depending on the effective angular extents of the distribution measured.

REFERENCES

[1] P. W. Allison, J. D. Sherman, and D. B. Holtkamp, "An Emittance Scanner for Intense Low-Energy Ion Beams", *IEEE Transactions on Nuclear Science*, vol. 30, no. 4, pp. 2204-2206, 1983

[2] M.P. Stockli, R.F. Welton, R. Keller, and M. Leitner, "Emittance studies with an Allison scanner", *Rev. Sci. Instrum.*, 77(3), p.03B706, 2006

[3] M.P. Stockli *et al.*, "Low-energy emittance studies with the new SNS Allison emittance scanner", in *Proc. 23rd Particle Accelerator Conf. (PAC'09)*, Vancouver, Canada, May 2009.

[4] R. D'Arcy, M. Alvarez, J. Gaynier, L. Prost, V. Scarpine, and A. Shemyakin, "Characterisation of the PXIE Allison-Type Emittance Scanne", *Nucl. Instr. Meth.* A, vol. 815, pp. 7-17, 2014

[5] C. Ullmann *et al.*, "Status and computer simulations for the front end of the proton injector for FAIR", in *Proc. IPAC'14*, Dresden, Germany (2014)

[6] A. Laxdal *et al.*, "Allison Scanner Emittance Diagnostic Development at TRIUMF", in *Proc. LINAC2014*, paper THIOC02, Geneva, Switzerland (2014)

[7] Poisson/Superfish web site, `http://laacg.lanl.gov/laacg/services/download_sf.phtml`

[8] C. K. Birdsall and A. B. Langdon, *Plasma physics via computer simulations*, McGraw-Hill Book Company, New York (1985).

[9] E, Jones *et al.*, "SciPy: Open source scientific tools for Python", `http://www.scipy.org/`.

[10] J. Wei, "The FRIB Superconducting Linac - Status and Plans", in *Proc. LINAC2016*, paper M01A01, East Lansing, MI, USA, September 2016.

[11] G. Machicoane, D. Cole, J. Ottarson, J. Stetson, and P. A. Zavodszky, "ARTEMIS-B: A room-temperature test electron cyclotron resonance ion source for the National Superconducting Cyclotron Laboratory at Michigan State University", *Rev. Sci. Instrum.* 77, 03A322 (2006)

ISBN: 978-3-95450-192-2 doi:10.18429/JACoW-IBIC2017-MOPCF01

BEAM DIAGNOSTICS FOR LOW ENERGY ANTIPROTON BEAMS*

C. P. Welsch†, University of Liverpool/Cockcroft Institute, UK

Abstract

Beams of low energy antiprotons in the keV energy range are very difficult to characterize due to their low intensity of only 10^7 particles per shot, annihiliation, and low repetition rate. The project AVA [1] (Accelerators Validating Antimatter physics) is an Innovative Training Net-work within the H2020 Marie Skłodowska-Curie actions. It enables an interdisciplinary and cross-sector program on antimatter research across 3 scientific work packages. These cover facility design and optimization, advanced beam diagnostics and novel low energy antimatter exper-iments. This paper presents the AVA R&D into beam profile, position and intensity measurements, as well as detector tests which will provide an order of magnitude improvement in the resolution and sensitivity in closely related areas. It also summarizes the interdisciplinary training program that AVA will provide to its 15 Fellows, as well as to the wider antimatter and accelerator commu-nities.

INTRODUCTION

In July 1983, the very first ions were stored in the Low Energy Antiproton Ring (LEAR) at CERN in Geneva, Switzerland [2]. It was the first storage ring that was explicitly designed to address physics with low-energy antiprotons and opened the door to a field were several very fundamental questions in physics can be directly addressed. When this machine was prematurely shut down in 1996 to free resources for the Large Hadron Collider (LHC) project, an international user community pushed for the continuation of this unique research program. This led to the construction of the Antiproton Decelerator (AD) facility that became operational in 2000 [3]. This storage ring is presently the only facility in the world to allow the realization of experiments with low energy antiproton beams. It has led to the successful production of cold antihydrogen, which has been widely acknowledged in the scientific community, as well as in the public media. The successful storage of antihydrogen over an extended period [4] was selected as top physics highlight in 2010 by physics world. Other recent breakthroughs include successful two-photon laser spectroscopy of antiprotonic helium and the measurement of the antiproton-to-electron mass ratio [5], measurement of resonant quantum transitions in trapped antihydrogen atoms [6], one-particle measurement of the antiproton magnetic moment [7], the production of antihydrogen for in-flight hyperfine spectroscopy [8], direct measurements into the antihydrogen charge anomaly [9] and the comparison of antiproton-to-proton charge-to-mass ratio [10] in 2015. Due to the low intensity of only ~10^5 antiprotons/s and the availability of only pulsed extraction – one pulse every 85 seconds - the physics program is presently limited to the spectroscopy of antiprotonic atoms and antihydrogen formed in charged particle traps or by stopping antiprotons in low-density gas targets. Since the output energy of the AD (5 MeV kinetic energy) is far too high to be of direct experimental use, the standard deceleration cycle of the antiprotons consists of the following steps:

- Deceleration in the AD from 3.5 GeV/c down to 0.1 GeV/c;
- Degrading by a foil from 5 MeV kinetic energy down to a few keV;
- Electron and positron cooling of the particles trapped to meV energies.

The drawback of this procedure is the rather large increase of the beam divergence and momentum spread and the high loss rate of antiprotons in the degrader foil. These effects limit the capture efficiency to about 10^{-4} or even less. An improvement was achieved by the installation of a decelerating rf quadrupole structure (RFQ-D) used by the ASACUSA collaboration [11] that today provides beams at 100 keV energy. However, the rather large emittance ε=100 mm mrad and energy spread $\Delta E/E$ = 10% of the output antiproton beam require a large stopping volume and a high-power pulsed laser to induce transition for high precision spectroscopy. A cooled antiproton beam at such energy would greatly improve this situation and even CW laser spectroscopy may become feasible. The scientific demand for low-energy antiprotons at the AD continues to grow. By now there are six experiments at the AD, the most recent ones being AEgIS and BASE, and a seventh (GBAR) has recently been approved. These experiments, however, require significant improvements in the underpinning accelerator technology, beam cooling and handling techniques, novel instrumentation, as well as significant upgrades to the experiments themselves. The AD was not able to provide the required number of cooled antiprotons at lowest energies. CERN is currently finalizing the construction of a new Extra Low ENergy Antiproton ring (ELENA) [12] which promises a significant improvement over this situation. Commissioning of this machine started in 2016.

The *AVA* project focuses on R&D benefiting low energy antimatter facilities. The project will offer its Fellows the unique opportunity to make contributions to the ELENA machine development and physics R&D programs. Beyond the opportunities that ELENA will immediately provide it would be desirable to make experiments using the antiproton as a hadronic probe to study the nuclear structure [13] and to have RF bunching tools to switch between ns and long beam pulses for studies into the collision dynamics of matter and antimatter [14]. This range of experiments could be realized after appropriate

*This project has received funding from the European Union's Horizon 2020 research and innovation programme under the Marie Skłodowska-Curie grant agreement No 721559.
†c.p.welsch@liverpool.ac.uk

ISBN: 978-3-95450-192-2 doi:10.18429/JACoW-IBIC2017-MOPCF01

future upgrades to ELENA or at the proposed Facility of Low energy Antiproton and Ion Research (FLAIR) that shall become part of the future international Facility for Antiproton and Ion Research (FAIR) in Germany. Following external evaluation of the FLAIR proposal, this facility has been part of the core FAIR project since 2007. Recent progress at FAIR, in particular the approval of the modularized start version (MSV) by the FAIR council in September 2015, the early installation of the CRYRING@ESR and commissioning of the HITRAP facility [15] now provide a possible route to the FLAIR physics program. Whilst *AVA* targets primarily ELENA and upgrade scenarios, it also lays the basis for an excellent long-tern perspective through work related to FLAIR.

RESEARCH

To fully exploit the potential of ELENA and FLAIR, the *AVA* partners will carry out a closely connected R&D program in the following three work packages:

Facility Design and Optimization, addressing beam life time and stability in lowest energy storage rings, as well as beam cooling, deceleration and extraction through simulation and experimental studies, as well as innovative control systems;

Design, development and testing of novel **Beam Diagnostics** and establishment of a dedicated test stand, to fully determine the characteristics of an antiproton beam;

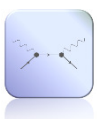

Design of novel low energy **Antimatter Experiments** through R&D into beyond state-of-the-art beam handling, storing and analysis techniques.

This paper gives an overview of the R&D which will be carried out in the beam diagnostics work package.

Transverse Profile Monitoring

A specific challenge of transverse beam profile monitoring is the detection of particles in the beam halo as these are particles that are likely to be lost and/or produce unwanted background noise in the experiment. This can be achieved with destructive devices such as wire scanners or scrapers [16] or secondary emission monitors which monitor particles produced when the beam interacts with residual or purposely injected gas [17]. A new high dynamic range, adaptive masking method to image the beam halo has recently been developed which uses a digital micro mirror-array device [18]. Ms Milena Vujanovic will be based at the University of Liverpool/Cockcroft Institute and adapt this method for advanced measurements that cannot presently be achieved with any other technique, namely *online, non-destructive high dynamic range beam profile measurements* using light generated by the primary beam. In a second step, measurements will be extended towards emittance and general 6D phase space diagnostics. This will be important for experiment optimization and in particular also for transferring the method to other applications, such as Free Electron Laser (FEL) facilities or the AWAKE experiment at CERN.

Instrumentation Test Stand

For the optimization of any detection technique towards low energy antiproton beams it is essential that detailed tests into the monitor characteristics can be carried out. Recent availability of keV antiprotons at AEgIS [19] has been used to carry out dedicated detector tests which have given important new results [20]. As the experiments mature, however, such opportunities of detector test disappear, while the need for a very low energy antiproton instrumentation test facility remains high. Mr Mattia Fani at CERN will design, build and establish a dedicated *diagnostics and detector test stand* at the AD and carry out investigations at different beam energies and intensities. A key aspect is that the setup needs to also contain the strong solenoidal magnets which are characteristic of all antiproton trapping devices. Consequently, multiple scattering in the degrading elements will result in very large beam divergence. In combination of simulations and technical design considerations the optimum geometry will be evaluated and whether e.g. a low momentum (weak field) magnetic filter would be beneficial. Space limitations, vacuum requirements, and tuneability of the degrader thickness will also be studied, to yield a polyvalent facility with great benefit in evaluating the performance of beam instrumentation for any low-energy antiproton facility.

Diamond Detector R&D

Diamond has been used for many applications in beam instrumentation [21]. Miha Cerv will be based at Austrian company CIVIDEC and study the use of *µm ultra-thin diamond layers as beam position and profile monitors* in low energy antiproton beam lines. He will develop a new type of beam monitor which is based on thin diamond membranes on the one hand and pixelized diamond electrode structures on the other. Initial simulations have indicated a position resolution in the sub-micrometer range and at extremely fast counting rates in the range of Gigahertz, fully exploiting the advances of diamond as radiation sensor material. The project will detail these simulations and prototype detectors will be established and thoroughly tested.

Beam Current Monitor

Beam current is one of the basic quantities in any accelerator and serves as an input for the optimization of machine performance as well as for experiments with the beam. The intensity of low energy antiproton beams is typically rather low, requiring sensitive devices with a detection threshold below 1 nA. Such threshold can be reached by a SQUID-based measurement of the beam's magnetic field [22]. However, this monitor still requires a second instrument to provide a meaningful dynamic range. Such *sensitive DC-transformer* is not commercial-

ISBN: 978-3-95450-192-2 doi:10.18429/JACoW-IBIC2017-MOPCF01

ly available and will be developed at GSI. David Haider will first study appropriate materials and modern high-performance electronics as a basis for beam current measurements with extremely wide dynamic range. He will then model sensitive current measurement methods and hardware realizations for different configurations using the CST Particle Studio simulation suite. In a next step, experimental tests with prototypes that will be built in-house will be done at GSI. These will form the basis for the final technical design. Sensitivity and dynamic range of the devices will then be experimentally tested at CRYRING@ESR

Liquid Target Detectors for Particle Tracking

For beam monitoring purposes, parallel plate avalanche counters (PPAC) and segmented Si-detectors are currently used at the AD, however, this will no longer be possible at energies of 100 keV or below as required for ELENA and FLAIR. Dominika Alfs will be hosted by Forschungszentrum Juelich (FZJ) in Germany and study the use of small *liquid hydrogen and deuterium targets* which will trigger annihilation events and allow monitoring of the beam track via straw tubes or scintillators. Using the expertise at FZJ in target development she will first carry out Monte Carlo simulation studies on expected signal levels. She will then design and build a prototype and carry out experimental studies at the AD. Based on results from measurements a final design for optimum integration into experiments at a low energy antiproton facility will then be made. For the target development, several approaches will be followed, including gaseous target cells with very thin walls and solid targets prepared by condensation at a cold backing. In order to transport the cooling power nearly masslessly, heat pipe techniques will be considered. Finally, careful balance between track resolution and straggling induced by the detector materials will be sought through studies of Si-μ-strips, straw-tubes, scintillation fibers and GEM-foil detectors.

Cryogenic Particle Detectors

Finally, trap experiments used e.g. for precision determination of the antiproton magnetic moment [23] require amplifier technologies with superior sensitivity and ruggedness. Ilia Blinov based at German company Stahl Electronics will advance the technology of current *single particle detectors*, integrated *in a cryogenic environment*. He will link the expertise available at the company with the one at GSI and carry out measurements for detector characterization. He will also investigate optimum trap design in close collaboration with the Max Planck Institute for Nuclear Physics. Ultimately, the goal will be to establish a novel detection system which will be easier to operate, rugged under adverse conditions and feature much higher detection sensitivity, down to single particles, by using latest generation electronic detectors from Stahl Electronics. Moreover, resonators connected to the system shall be abandoned, yielding true broad-band detection technology.

TRAINING EVENTS

Training within *AVA* consists of research-led training at the respective host, in combination with local lectures, as well as participation in a network-wide training program that is also open to external participants. This training concept is based on the successful ideas developed within the DITANET, oPAC and LA^{3}NET projects [24-26].

All Fellows will be given the opportunity to enroll into a PhD program. They will thus be embedded into a structured course program at their host university or, if their work contract is with an industry partner or a research center, with a collaborating university. Courses at the PhD awarding institution will include lectures on fundamental symmetries, precision experiments, electronics, detector design, as well as courses on the local language. It is widely recognized that best practice in researcher training involves cohorts of trainees rather than individuals. The ITN structure is ideal for this and to achieve the aspirations of the EU Principles for Innovative Doctoral Training AVA will take best advantage of industry participation and by providing regular network training to bring the Fellows together. Most network-wide events will also include external participation and will be open to the wider scientific community. The four AVA Fellows who had already started earlier in 2017 were invited to a researcher skills training at the University of Liverpool in April 2017 where they joined 15 Fellows from the OMA network [27]. This week-long School included sessions on project management, presentation skills, communication of research outcomes to diverse audiences, as well as IP rights and knowledge transfer. Two 1 week-long international Schools, open to all *AVA* Fellows and up to 50 external participants on Antimatter research, as well as on Fundamental Symmetries and Interactions will be organized. All Schools will be announced via the project home page [1]. To further promote knowledge exchange and ensure that all Fellows are exposed at highest possible level to the techniques and methodologies developed in the other WPs, three 2-day Topical Workshops covering two scientific WPs at a time will be organized. These will cover facility optimization via diagnostics, diagnostics in accelerators and axperiments and questions related to the machine-experiment interface. In the last year of the project a 3-day international conference will be organized, with a focus on the novel techniques and technologies developed within *AVA*.

SUMMARY

An overview of the beam diagnostics R&D and oeverall training program within the recently *AVA* project was given. With 4M€ of funding the network is one of the largest Marie Curie ITNs and will train 15 early stage researchers over the next four years. Schools, Topical Workshops, an international conference and various outreach events will all be open also for participants from outside of the consortium.

ISBN: 978-3-95450-192-2 doi:10.18429/JACoW-IBIC2017-MOPCF01

REFERENCES

[1] *AVA*, http://www.ava-project.eu
[2] The LEAR Team, "Performance of LEAR", *IEEE Transactions on Nuclear Science*, Vol. 3. No. 5 (1985).
[3] S. Baird et al., "The Antiproton Decelerator: AD", *Proc. Part. Acc. Conf.* (1997).
[4] G. B. Andersen, et al., *Nature Physics*, 7, 558 (2011).
[5] M. Hori, et al., "Two-photon laser spectroscopy of antiprotonic helium and the antiproton-to-electron mass ratio", *Nature* 475 (2011).
[6] C. Amole, et al., Resonant quantum transitions in trapped antihydrogen atoms, *Nature* 483, 439 (2012).
[7] J. DiSciacca, *Phys. Rev. Lett.* 110, 130801 (2013).
[8] N. Kuroda et al., *Nature Communications* 5, 3089 (2014).
[9] C. Amole, et al., *Nature Communications* 5, 3955 (2014).
[10] S. Ulmer, et al., *Nature* 524, 196-199 (2015).
[11] W. Pirkl, et al., *Proc. Part. Acc. Conf.*, Chicago, USA (2001).
[12] V. Chohan, et al., *ELENA TDR*, CERN (2014).
[13] A. Trzcinska, et al., *Nucl. Phys. A* 692 (2001) 176c.
[14] T.N. Rescigno, et al., *Science* 286 (1999) 2474. M. Baertschy, et al. and A.S. Kadyrov, et al., *Phys. Rev. Lett.* 91 (2003) 253202-1.
[15] F. Herfurth, et al., The Low Energy Storage Ring CRYRING@ESR, *Proc. COOL*, Murren, Switzerland (2013).
[16] J.D. Gilpatrick, *AIP Conf. Proc.* 693, 122 (2003).
[17] P. Cameron, et al., *Proc Part. Acc. Conf.*, New York, USA (1999).
[18] H. Zhang, C.P. Welsch, et al., "Beam halo imaging with a digital optical mask", *Phys. Rev. STAB* 15, 072803 (2012).
[19] A. Kellerbauer et al., *Nucl. Instr. Meth. B* 266 (2008) 351.
[20] N. Pacificoa, et al., *Nucl Instr Meth. A* (2014), A. Sosa, et al., Hyp. Inter. (2014) and S. Aghiona, et al., *JINST* 8 P08013 (2013).
[21] C. Weiss, et al., *Nucl. Instr. Meth. A* 732 (2013) 190–194 and C. Guerrero, et al., *Eur. Phys. J. A* (2013) 49:27 (2013).
[22] M. Fernandes, et al., 'Non-perturbative measurement of low-intensity charged particle beams', *Superconductor Science and Technology* 30, Number 1.
[23] Mooser et al., *Phys. Rev. Lett.* 110, 140405 (2013) and S. Ulmer et al., *Phys. Rev. Lett.* 106, 253001 (2011).
[24] *DITANET*, http://www.liv.ac.uk/ditanet
[25] *oPAC*, http://www.opac-project.eu
[26] *LA^{3}NET*, http://www.la3net.eu
[27] *OMA*, http://www.oma-project.eu

ISBN: 978-3-95450-192-2 doi:10.18429/JACoW-IBIC2017-MOPCF03

PRELIMINARY DESIGN OF BEAM DIAGNOSTIC SYSTEM IN THE HUST-PTF BEAMLINE*

X. Liu†, QS. Chen†, B. Qin, K. Tang, State Key Laboratory of Advanced Electromagnetic Engineering and Technology, School of Electrical and Electronic Engineering
W. Chen, Huazhong University of Science and Technology, Wuhan 430074, China

Abstract

Proton therapy is now recognized as one of the most effective radiation therapy methods for cancers. A proton therapy facility with multiple gantry treatment rooms is under development in HUST (Huazhong University of Science and Technology), which is based on isochronous superconducting cyclotron scheme. The 250MeV/500nA proton beam will be extracted from a superconducting cyclotron and injected into the beam-line. Many beam diagnostic instruments are distributed throughout the beam line to measure the beam profile, position, current, loss, energy and energy spread. Some of them will send the beam information to the treatment control system (TCS) and serve as the safety interlock. This paper presents the considerations for the distribution of beam diagnostic instruments and shows the layout of beam diagnostics monitors in the beamline.

INTRODUCTION

A proton therapy facility based on an isochronous superconducting cyclotron is under development in HUST, by a collaborative team from HUST, CIAE (China Institute of Atomic Energy), Tongji Hospital and Union Hospital affiliated to HUST. For HUST proton therapy facility (HUST-PTF), a 250 MeV proton beam with 500 nA will be extracted from a superconducting cyclotron. After passing through the energy selection system (ESS) in which the energy will be modulated in the range of 70~240 MeV, it will be switched and delivered to three treatment rooms: two gantry rooms and one room with fixed beam line. The main specifications [1] are listed in Table 1.

Many beam diagnostic instruments are distributed throughout the beam line to measure the beam profile, position, current, loss, energy and energy spread. In this paper, the primary design considerations of beam diagnostics system within one gantry beamline are described and the layout of beam diagnostics monitors in the beamline is presented.

* Work supported by The National Key Research and Development Program of China, with grant No. 2016YFC0105305, and by National Natural Science Foundation of China (11375068).
† Email address: lxhustliu@hust.edu.cn, chenqushan@hust.edu.cn

Table 1: Main Specifications of HUST-PTF

Parameter	Specification
Max. Beam Energy	250 MeV
Max. Beam Current	500 nA
Energy Range for ESS	70-240 MeV
Energy Modulation Time	≤150 ms per step
Gantry Type	360 degree, normal conducting
Treatment scheme	Pencil beam scanning (PBS)
Max. Dose Rate	3 Gy/L/min
Field Size	30 cm × 30 cm

OPERATION MODE

For a proton therapy facility, beam diagnostics system shall perform functions covering functions beam parameters measurement, and guarantee of the treatment safety. Several beam parameters shall be measured in real – time.to ensure the safety of treatment. Thus in the HUST-PTF system, the beam diagnostic instruments will operate in two modes: debugging mode and treatment mode. These two modes can arbitrary switch. The overview of this two modes is shown in Fig. 1.

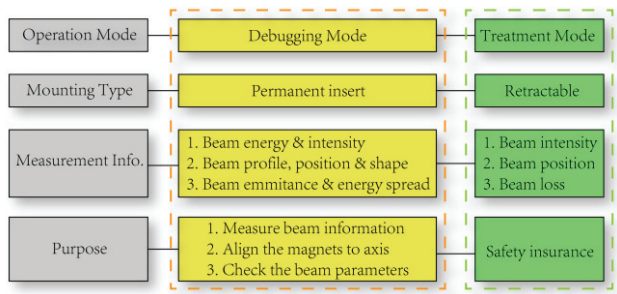

Figure 1: Overview of two operation modes.

Debugging Mode

In the debugging mode, all monitors are retractable and locate at the axis to measure the beam information. Based on the reading data, all dipole and quadrupole magnets can be aligned in the beam line. In addition, the beam envelop is rebuilt to check the beam optics.

ISBN: 978-3-95450-192-2 doi:10.18429/JACoW-IBIC2017-MOPCF03

Treatment Mode

For the destructive or semi-destructive instrument, it will create a bit of beam loss and increase the beam divergence angle due to the scattering with the monitor material. To avoid creating much beam loss in the monitors and ensure the safety of treatment, most monitors are retracted from the beam pipe and only a few monitors are reserved to detect beam current and beam loss in real time, and their signals shall be transferred to Treatment Control System (TCS) as a safety interlock.

MONITORS LAYOUT

The beam optics was designed and 1 sigma beam envelope of the beamline was calculated [1], as shown in Fig. 1, by using Transport code [2]. The beam energy and beam current in some key points which corresponds to the points in Fig.2 are listed in Table 2.

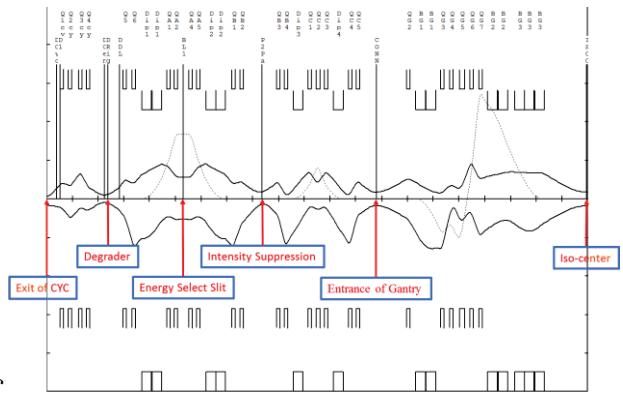

Figure 2: 1 sigma beam envelope for the main beamline including ESS and one gantry beamline (below: horizontal direction, above: vertical direction).

Table 2: Beam Energy and Current in some Key Points

Location	Beam Energy	Beam Current
Exit of CYC	250 MeV	500 nA
Degrader	70-240 MeV	2.65-105 nA
Energy Select Slit	70-240 MeV	0.4-89 nA
Intensity Suppression	70-240 MeV	0.4-4 nA
Entrance of Gantry	70-240 MeV	0.4-4 nA
Iso-center	70-240 MeV	0.4-4 nA

Figure 3 shows the layout of beam diagnostics monitors in the HUST-PTF beamline. The considerations of this layout will be subsequent described in detail. Some considerations have referred to monitors layout in the PSI PROSCAN project [3].

Exit of Cyclotron

At the exit of cyclotron, the designed beam parameters should be checked and acted as the input data of beamline. Beam energy, current, position, emittance and energy spread should be measured. The design specifications of extracted proton beam are listed in Table 3.

Table 3: Design Specifications of Extracted Proton Beam

Parameter	Specification
Beam Energy	250 MeV
Beam Current	500 nA
Emittance	< 5 π-mm-mrad
Energy Spread	< 0.5%

In front of the degrader, a scintillation screen is located to measure the beam position and emittance combined with a set of quadrupoles.

To switch the beam on/off mode in the spot scanning method, a kicker magnet is installed before the degrader. In front of degrader, a faraday cup (FC) locates above the axis 20mm in the treatment mode to collect the dump beam. This also can simultaneously realize the real-time beam current measurement.

In the ESS, the energy spread can be limited and changed for the need of treatment. This value will be fixed during the treatment and offline measured by the Multi-Leaf Faraday Cup (MLFC) after the switch magnet in the debugging mode.

ESS and Intensity Suppression Point

From the Table 2, the proton beam energy and current can be modulated with the help of ESS. In this part, we only measure the beam current and beam position and the beam energy will not be measured for two reasons: 1) The relationship between the thickness of degrader and the modulated beam energy will be tested and measured in advance. 2) The beam energy will be verified by the water tank at the iso-center.

In this region, a set of scintillation screens locate on the two sides of dipole magnet to detect the beam position in the debugging mode. A retractable faraday cup is set before the switch magnet and plays two roles: beam current measurement and beam stopper in the emergence condition which can stop the proton beam within 1s.

Gantry Section

In the gantry section, all instruments will rotate around the axis from −180° to 180°. In our design, the camera is integrated in the mechanical structure of scintillation screen, and the signal will be transferred by the network cable. It may be easily dropped out due to the rotation of gantry and thus it is not suitable to use scintillation screen in this section. Instead, four ionization chambers (IC) from PTC [4] are chosen to detect the beam information: profile, position and current. These ICs are all retractable.

ISBN: 978-3-95450-192-2 doi:10.18429/JACoW-IBIC2017-MOPCF03

The main specifications [5] of ionization chamber are listed in Table 4.

Table 4: Main Parameters of Pyramid Ionization Chamber

Parameter	Specification
Energy range	30 – 500MeV/n
Beam Current Density	10 pA/cm^2-20 nA/cm^2
Sensitive Area	38mm × 38mm
Readout strip geometry	16 strips, equal width 2.38 mm on 2.534 mm pitch.
Vacuum regime	1E-8 mbar
Travel	50 mm, Pneumatic

For safety concerns, a collimator is installed at the entrance of the gantry to guarantee the beam size and remove uncertainties from beam misalignment. It's important to monitor the beam position and intensity at the gantry beamline. With the help of four ICs and two sets of X/Y steering magnets, the beam can be aligned. In addition, a FC is installed in the end of fixed beam line. This plays the same role with FC before the switch magnet. The measurement of beam position and intensity in real time can be realized by three ionization chambers in the treatment head [6], which can detect the beam current, position and dose simultaneously.

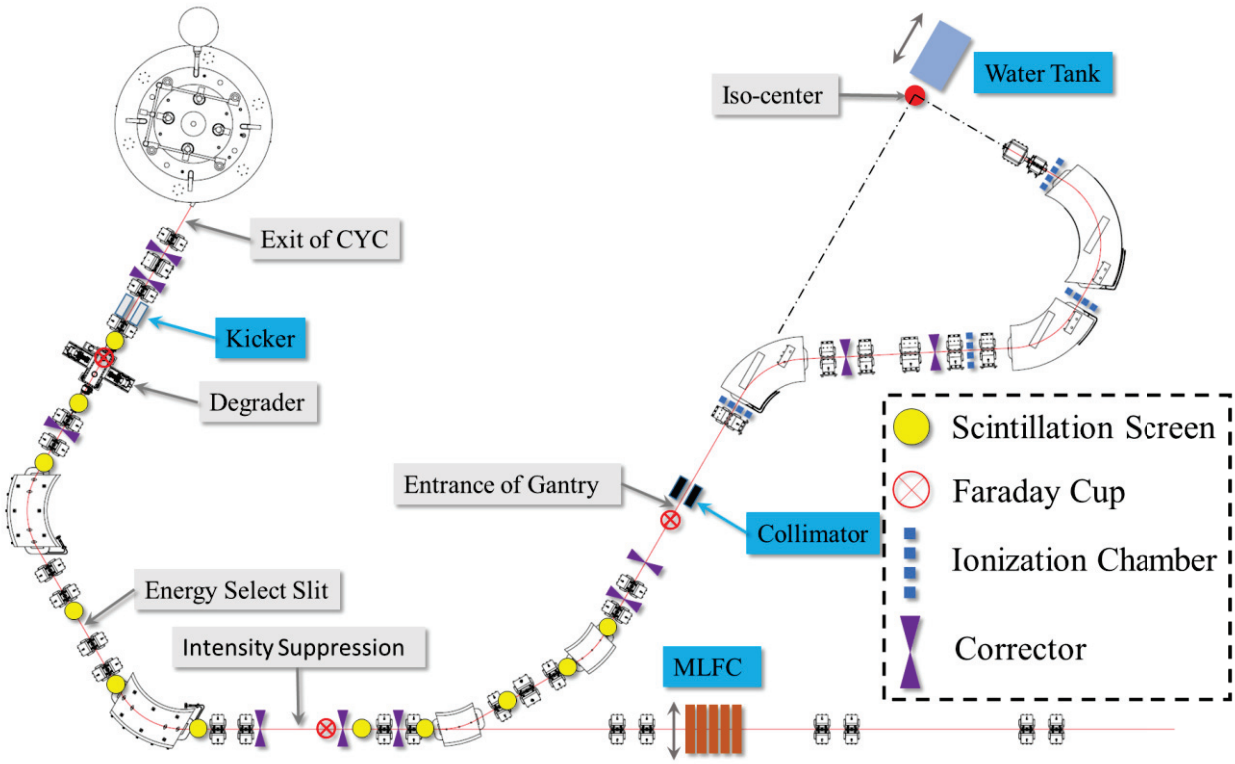

Figure 3: Layout of beam diagnostics monitors in the HUST-PTF beamline.

CONCLUSION AND OUTLOOK

HUST-PTF is a new proton therapy facility, and it's under development now. This paper introduces the primary design of beam diagnostics system in the beamline and presents the layout of monitors in the main beamline including ESS and one gantry. Two operation modes are switched in the commission and running stages. In the debugging mode, beam position, current are mainly detected and the beam parameters at the exit of cyclotron are also measured as the input data of beamline. In the treatment mode, we only detect the beam intensity in the beamline and set three faraday cups as the beam stopper in the emergency condition to ensure the safety of treatment. During the primary design, we only purchase two ICs and one faraday cup for testing, other monitors are still investigated and under design.

In the next stage, the position of monitors and correctors will be modulated and determined according to the calculation of misalignment and correct. The design and selection of monitors will be also completed.

ISBN: 978-3-95450-192-2 doi:10.18429/JACoW-IBIC2017-MOPCF03

REFERENCES

[1] B. Qin *et al*, "Progress of the beamline and energy selection system for HUST proton therapy facility", in *Proc. IPAC'17*, Copenhagen, Denmark, May 2017, paper THPVA112, pp. 4719-4721.

[2] U. Rohrer, "PSI Graphic Transport Framework," based on a CERN-SLAC-FERMILAB version by K. L. Brown *et al.*, 2007, http://aea.web.psi.ch/Urs_Rohrer/MyWeb/trans.htm

[3] R Dölling, "Diagnostics of the PROSCAN proton-therapy beam lines", in *Proc. DIPAC'03*, Mainz, Germany.

[4] Pyramid Technical Consultants Inc., http://www.ptcusa.com

[5] BPM16-38 Datasheet, Pyramid, http://www.ptcusa.com/files/datasheet/BPM16-38_DS_130520.pdf

[6] Huidong Guo *et al.*, "The optimization design and output characteristic analysis of ionization chamber dose monitor in HUST-PTF", presented at IBIC'17, Grand Rapids, MI, USA, Aug 2017, paper WEPCF09, this conference

ISBN: 978-3-95450-192-2 doi:10.18429/JACoW-IBIC2017-MOPCF05

BEAM INSTRUMENTATIONS AND COMMISSIONING OF LINAC IN CSNS

W. L. Huang†, T. G. Xu, P. Li, F. Li, J. L. Sun, J. M. Tian, M. Meng, L. Zeng, R. Y. Qiu, Z. H. Xu, T. Yang, J. Peng, S. Wang, S.N Fu
Dongguan Campus, Institute of High Energy Physics, Dongguan, China

Abstract

China Spallation Neutron Source (CSNS), the biggest platform for neutron scattering research in China, will be finished built and run in the end of 2017. It mainly consists of an 80MeV H- linac and an 80MeV to 1.6GeV Rapid Cycling Synchrotron, two beam transport lines, one target station and relative ancillary facilities. The linac beam commissioning with beam loss monitors, current transformers, BPMs, beam profile monitors and beam emission measurement has been the main task since last year. Beam instrumentations, commissioning of the temporary 60 MeV linac will be discussed in this paper.

INTRODUCTION

Beam instrumentations distributed on the CSNS linac are presented in Fig. 1. After the 50keV H- source, there are 2 beam current monitors and an emission monitor installed on the low energy beam transport line (LEBT). At the middle energy beam transport line (MEBT) there are 2 self-made FCTs to monitor the beam current, 7 strip-line beam position monitors and 4 wire scanners to monitor the beam profile for measuring the Twiss parameters of the RFQ output beam. The 4-tank 324MHz drift tube linac (DTL) is designed to accelerate the H- beam from 3MeV to 80MeV. At the exit of the 4th tank of an 80MeV drift tube linac (DTL), 5 Bergoz FCTs are used to monitor the beam phase for energy measurement by means of TOF. At present commissioning period, only 3 of the 4 klystrons are available to feed 3MW power into the corresponding DTL tank, therefore tank 1 to 3 have been commissioned and the beam was successfully accelerated to 61MeV. After that, the beam was transported through the last DTL tank and the linac to RCS Beam Transport line (LRBT), and finally directly to the LRDMP1. Until May 2017, four runs of linac beam commissioning have been performed [1].

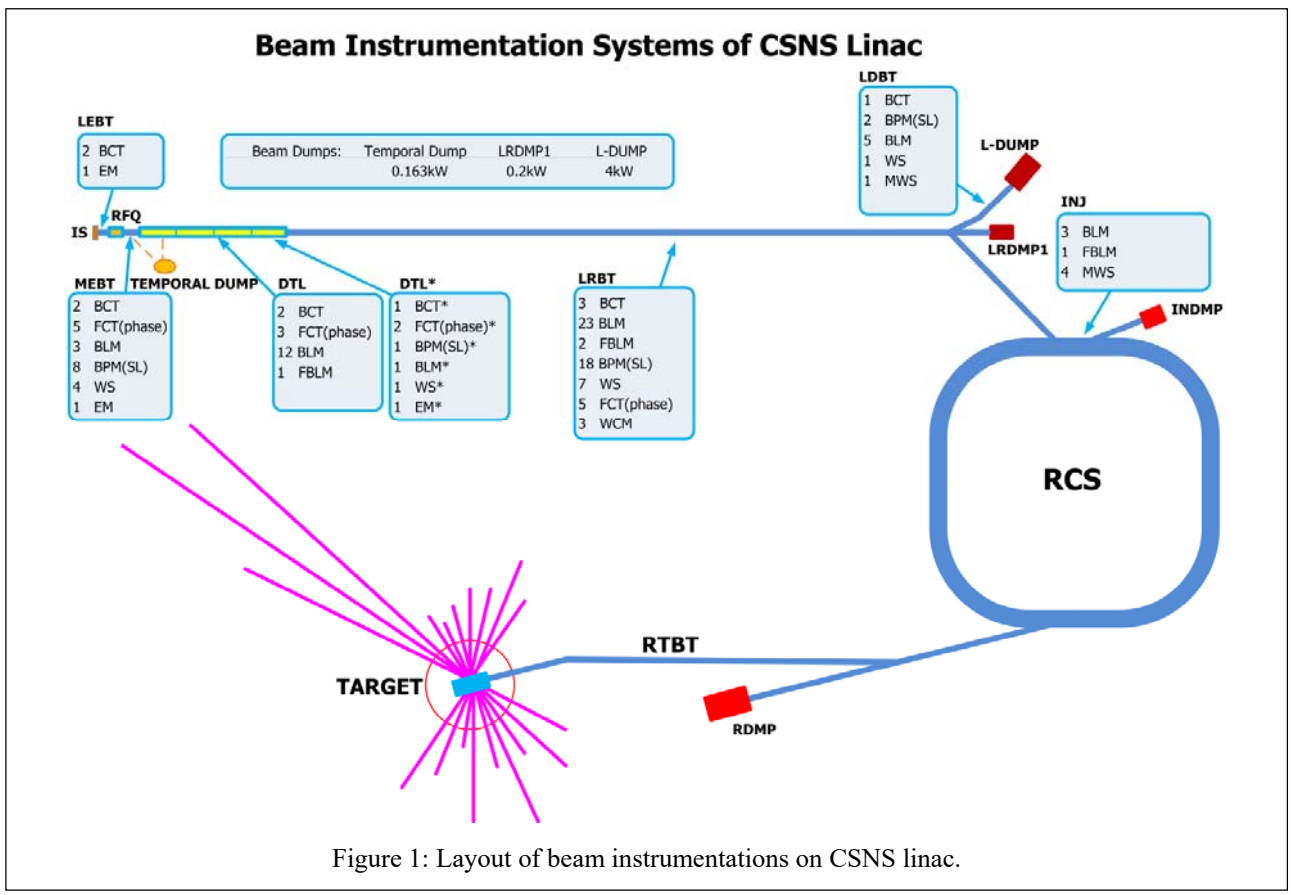

Figure 1: Layout of beam instrumentations on CSNS linac.

† huangwei@ihep.ac.cn

ISBN: 978-3-95450-192-2 doi:10.18429/JACoW-IBIC2017-MOPCF05

BEAM TRANSMISSION IMPROVEMENT

The beam current transformers (BCT) were made by the BI group of CSNS, which consist of amorphous magnetic cores with high permeability and were winded up by 150 turns of varnished wires. During the 500μs pulse width, the BCT output droop is less than 1%. A Bergoz FCT located at the exit of DTL tank 1 can also work as a BCT for phase detection, by using an RF switch to connect it to different electronics. When working as a BCT, the electronics and the read out system hold and recover the waveform to the beam envelope, just like other BCTs which are showed in Fig. 2. The beam current flat was averaged to provide the EPICS broadcast PV value for calculating the beam transmission efficiency at concerned sections of linac.

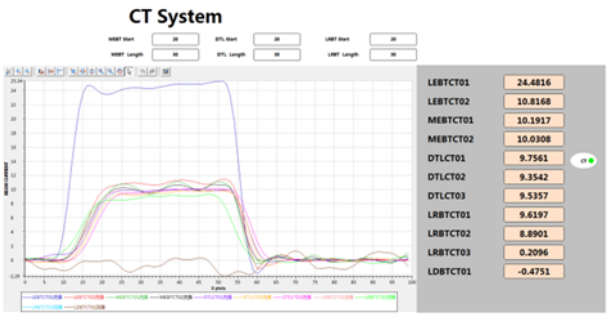

Figure 2: Beam current measurement results from the transformers along the LEBT, MEBT, DTL and LRBT

The plastic scintillators photomultiplier detector combination with a gain factor of 5×10^5 were adopted to monitor the beam loss on the MEBT, which are post-processed by Libera electronics. Two of the three sets were installed beside the bunchers and the third one at the end of MEBT. While ion chambers manufactured domestically with different gas filled were used to help improving the beam transmission. At the beginning of 20MeV beam (DTL1) commissioning, the sensitivity of original ion chambers (schematic drawing showed in Fig. 3) filled with 70%Ar+30%N_2 were not good enough to detect the beam loss, thus an instead plan B of filling with 90%Xe +10%CO_2, BF_3 or 90% Xe+10%Ar was tried and successful on detecting the gamma ray emission during the 20MeV beam commissioning (at the exit of DTL tank #1). When the beam current showed a decrease, the output of the ion chambers increased correspondingly. Commissioning by this method the beam transmission efficiency in DLT1 improved 2%. Readouts of the BLM electronics (designed by BI group) were shown as Fig. 4 on the screen in the accelerator control center. Finally, the beam transmission efficiency of the RFQ reached 80% and that of the DTL is about 97%.

Figure 3: Schematic of ion chambers in CSNS.

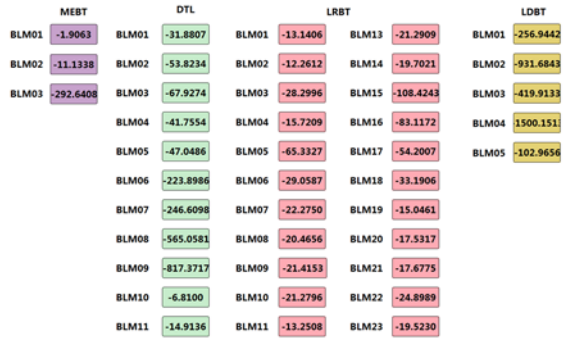

Figure 4: Readout value of BLMs in linac commissioning.

BEAM ENERGY MEASUREMENT

The H- beam energy was measured by means of Time of Flight (TOF) as illustrated in Eq. (1) and (2) . The beam phase is provided by Bergoz Fast Current Transforms (FCTs) which are located at the downstream of the measured cavity. Before the electronics of the phase detectors were manufactured and accepted by local test, wide bandwidth oscilloscopes such as Tektronix TDS7254B (2.5GHz, 10GSa/s, 250fs/pt) were used to measure the phases of FCT pairs. The sample rate of TDS7254B is suitable for a 324MHz RF signal and the phase measurement accuracy of TDS7254B achieved $\pm$ 1°.

When the electronics of FCT were available, with a phase resolution of 0.1° for a standard signal generator and a stability of 1° for the real beam, the beam energy were measured more accurately for DTL 1# to 3#. The details of the debuncher RF tuning using phase scan technique were presented in [1, 2]. A comparison of the designed energy and measurement is showed in Tab. 1. The deviation of measured beam energy from the designed value is less than 1%.

$$v = \frac{l}{nT + \frac{\Delta\emptyset}{360}T}, \quad where\ T = \frac{1}{324\text{MHz}} \qquad (1)$$

$$E_k = m_0c^2\left(\frac{1}{\sqrt{1-v^2/c^2}} - 1\right), \qquad (2)$$

ISBN: 978-3-95450-192-2 doi:10.18429/JACoW-IBIC2017-MOPCF05

Table 1: Comparison Design and Measurement Results of CSNS Linac Beam Energy [1]

	Design [MeV]	Phase scan [MeV]	TOF [MeV]
DTL1	21.669	21.802	21.685±0.01
DTL2	41.415	41.52	41.566±0.14
DTL3	61.072	60.917	61.09±0.34

BEAM POSITION MONITORS

Due to the high space resolution of strip-line (SL) beam position monitors, there are 7 BPMs (SL) installed on the MEBT and 21 ones on the DTL and LRBT of CSNS. The electronics for linac BPMs were commercial products of Bergoz (MX-BPM-324MHz) and Libera separately.

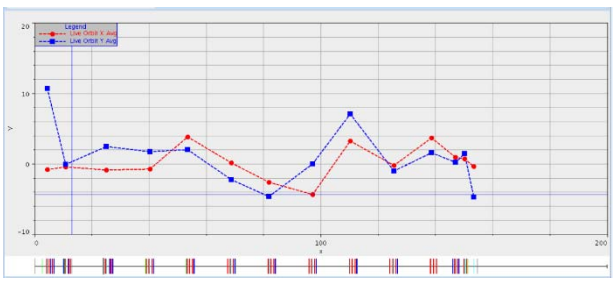

Figure 4: Beam orbit measured by LRBT BPMs.

An automatic BPM calibration system is showed in Fig. 5. The RF signal was generated by SRS382. The stepping motor was controlled by an NI PXI-7340 card and data acquisition by a PXI-6356card. The control program and data acquisition software were developed both for linac and RCS BPMs. A calibration accuracy of 0.1mm was achieved by trying different motor steps and moving ranges.

Figure 5: Automatic BPM Calibration System.

LINAC COMMISSIONING

In the commissioning of CSNS linac, the transverse matching includes RFQ to DTL (MEBT) and DTL to LRBT triplet section. There are four wire scanners (WS) on MEBT to measure the accurate beam size and emittance for Twiss parameters calculation [3]. Figure 6 gives a beam profile scanning results of MEBTWS03.

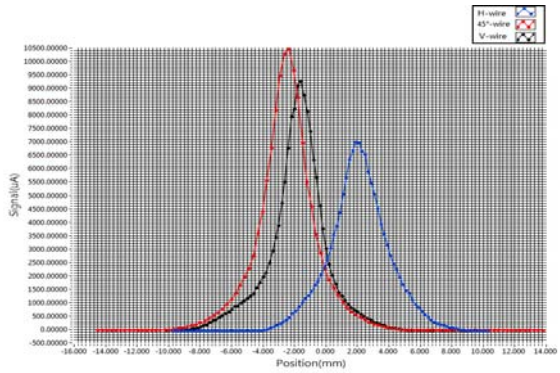

Figure 6: Beam profile measured by MEBTWS03.

Two bunchers were installed at the MEBT for longitudinal matching. The phase scan method is used for finding the RF set points of two bunchers [1]. Figure 7 gives the measured phase differences between two FCTs as functions of the buncher 01 cavity phase.

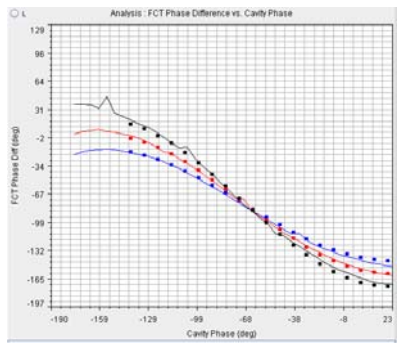

Figure 7: Measured phase differences (degrees) between two FCTs as functions of the buncher01 cavity phase.

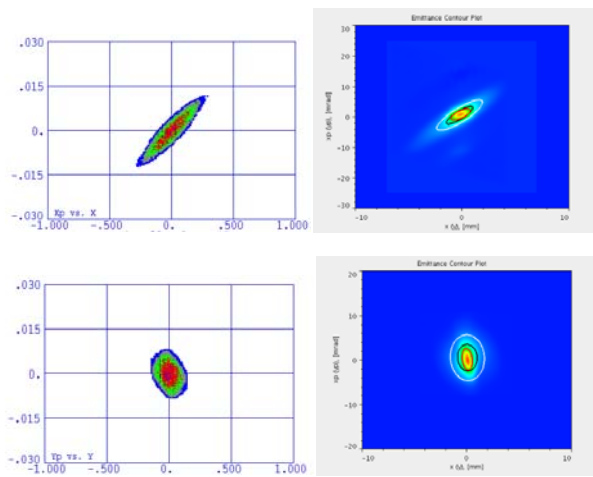

Figure 8: Comparison of the simulation and EM measurement of the beam distribution at the MEBT EM location.

ISBN: 978-3-95450-192-2 doi:10.18429/JACoW-IBIC2017-MOPCF05

CONCLUSION

The beam instrumentations of CSNS linac were tested fully in the commissioning on RFQ, MEBT, DTL and LRBT. The beam peak current, and energy have been achieved to the design value. The beam transmission efficiency of DTL tank 1# to 3# reached nearly 100%. The last DTL tank will be commissioned in autumn this year.

ACKNOWLEDGEMENT

The beam commissioning of CSNS linac has been endeavored by all the members of CSNS accelerator division. We would also like to acknowledge the help from the conventional facility division and the corresponding technicians of domestic factories.

REFERENCES

[1] J. Peng et al. in *Proc. IPAC'17*, paper TUOBA1

[2] T.L Owens et al., "Phase Scan Signature Matching for Linac Tuning", *Part. Accel.* Vol98, p.169-179, 1994.

[3] M. C. Ross et al. in *Proc. PAC1991*, pp. 1201-1203

ISBN: 978-3-95450-192-2 doi:10.18429/JACoW-IBIC2017-MOPCF09

BEAM DIAGNOSTICS SYSTEMS FOR SIRIUS LIGHT SOURCE

S. R. Marques*, LNLS, Campinas, Brazil
on behalf of the LNLS Accelerator and Engineering Divisions

Abstract

This paper gives an overview of Sirius diagnostics systems under commissioning or in planning phase. It includes beam position monitors for electron and photon beams, visible and X-ray synchrotron light monitors, transverse profile monitors, streak camera, beam loss monitors, current monitors, charge monitors, tune and filling pattern measurements. The paper focuses on the specification of the beam diagnostics systems and their motivation, parts selection, accompanying data acquisition systems, control software capabilities and development status.

INTRODUCTION

The Sirius light source facility is based on a 518 m circumference 5BA 3 GeV electron storage ring (SR), designed to achieve a bare lattice emittance of 0.25 nm·rad [1]. The machine is under construction at LNLS, in Campinas, Brazil. Machine installation is expected to start at the end of 2017 and beam commissioning in the middle of 2018.

The injector is composed of a 497 m circumference full energy booster synchrotron (BO) installed in the same tunnel as the SR, with a 3.5 nm·rad emittance at 3 GeV, a 150 MeV LINAC supplied by SINAP, LINAC-to-booster (LTB) and booster-to-storage ring (BTS) transfer lines.

The LINAC operates in single and multi-bunch modes, with 1 ns / 1 nC and 150 ns / 3 nC pulse length / charge, respectively. Maximum repetition rate is 10 Hz, but booster cycling will occur at 2 Hz.

The SR and BO rings operate at 500 MHz and have harmonic numbers 864 and 828, respectively. The LINAC operates at the 6th RF frequency harmonic (3 GHz). All of the instrumentation has been designed to allow injection in multi, single or hybrid bunch modes.

For brevity, LINAC diagnostics are not covered herein.

SIRIUS DIAGNOSTICS

In order to monitor the quality of the electron and photon beams, several diagnostics equipment will be installed along the accelerators and transfer lines. Parameters like bunch charge, transverse and longitudinal profiles, beam orbit, tunes, beam emittance and beam loss, the injection efficiency and beam stability will be constantly monitored. Table 1 briefly shows the main beam diagnostics devices of the accelerator complex.

Flags

In total 19 fluorescent screens (or beam flags) will be used in the commissioning phase and for general troubleshooting. In the transfer lines the fluorescent screens will be installed together with 6 cm stripline BPMs in order to provide beam profile measurements and non-destructive beam position measurements in the same location.

Table 1: Summary of Beam Diagnostics Components

	Linac	LTB	BO	BTS	SR
DCCT			1		2
FCT		1		1	
ICT	2	2		2	
Beam Flag	5	6	3	6	
Horizontal Slit		1			
Vertical Slit		1			
Button BPM			50		160
Stripline BPM	3	6		5	
Front-End Photon BPM					80
Filling Pattern Monitor					1
Horizontal scraper					1 pair
Vertical scraper					1 pair
Tune shaker			1		2
Tune pick-up			1		1
Bunch-by-Bunch kicker					2
Bunch-by-Bunch BPM					1
X-ray port					2
Visible light port					1
Streak camera					1
Beam Loss Monitor		tbd	tbd	tbd	
Gas Bremsstrahlung Monitor					tbd

The booster fluorescent screens are installed right after the injection point, a few meters apart from each other, in order to monitor the position and angle of the injected beam.

Cerium-doped Yttrium Aluminium Garnet (YAG:Ce) 0.1 mm thick screens, produced by Crytur, were selected for the flags. The screen is placed inside a bellows, which can be moved to intercept the beam.

The bellows is attached to a Huber 5101.20 X1 linear translation stage moved by a Vexta PK-266-02B stepper motor. The linear stage also contains a rotary encoder provided by Huber. This allows the usage of more than one screen, as the motor can move the bellows with micrometer precision, enough to place one of the available screens in the correct position to intercept the beam. The current approach is to use a YAG:Ce screen to intercept the beam and an additional screen with markers to calibrate the optics.

The stepper motor is driven by a single-axis Galil DMC-30017 controller. An IOC [2], communicating with the controller through Ethernet, is used to integrate the motion controller to the accelerator control system via EPICS [3].

* sergio@lnls.br

ISBN: 978-3-95450-192-2 doi:10.18429/JACoW-IBIC2017-MOPCF09

The screen plane is tilted 45 ° relative to the beam axis, so that the produced beam image can be seen through a vacuum chamber side window. The camera used is a Basler acA1300-75gm featuring a CMOS sensor and Gigabit Ethernet interface. A 45 ° mirror allows the camera to see into the side window. The camera is powered by Power-over-Ethernet (PoE) so that it can be remotely restarted through a PoE switch. The aravisGigE EPICS IOC [4] is used to attach the camera to the control system.

The transfer lines' fluorescent screens assembly is illustrated in Fig.1.

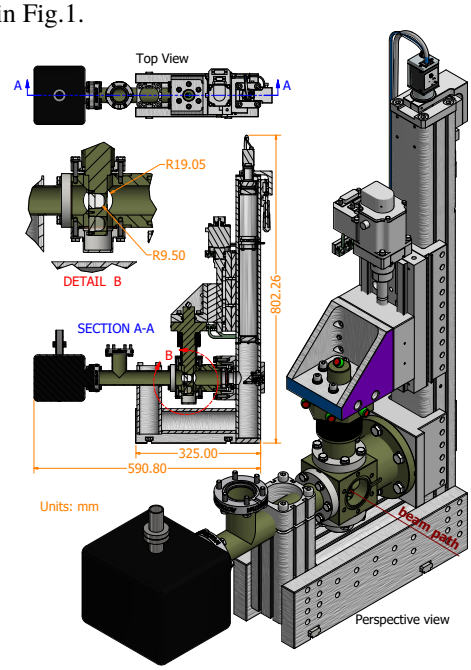

Figure 1: Mechanical project of the beam flags.

Injection Efficiency

After the commissioning phase Sirius will operate in top-up mode, which requires a stable operation of the whole injection system. In order to quantify the transmission of electrons from one accelerator to another, charge and current sensors are employed.

Integrating Current Transformers (ICT) [5] are installed at the exit of the electron gun, at the end of the LINAC and at the beginning and end of both transfer lines. The signals from the ICT transducer are processed by Bergoz BCM analog electronics [6] and further digitized by Keithley DMM7510 7½-digit multimeter [7]. The multimeter also allows for fast sampling at 1 MS/s, which is useful for troubleshooting.

Parametric current transformers, commonly known as DCCTs [8], are employed in the BO and SR to measure the circulating beam currents. The Bergoz New Parametric Current Transformer (NPCT) and its accompanying electronics was chosen. The analog DC signals generated by the NPCT electronics are digitized by the Keithley DMM7510 multimeter, the same instrument used on ICTs.

A common IOC has been developed to integrate the ICTs and DCCTs to the accelerator control system via EPICS [9]. Different modes of operation and parameters are set according to the instrument in use. Hence both the pulsed signals generated by the ICT electronics and slow varying voltages output by DCCTs are digitized by the same instrument controlled by a common software. It reduces the control software development and maintenance effort.

All devices, BCMs, NPCTs and digitizers are connected to the Sirius timing system [10], which provides acquisition triggers synchronized with the beam and adjustable delays.

Beam Slits and Scrapers

Tantalum horizontal and vertical beam slits will be installed in the LTB transfer line to delimit the portion of the beam that goes to the booster. In the storage ring, a pair of horizontal and vertical beam scrapers will serve various purposes, such as protection for insertion devices, beam loss control and diagnostics/physics machine studies.

Differently from the linear motion of the flags and the slits, the scrapers' plungers were designed under a concept of rotary motion – but still using linear actuators – hence providing smooth transitions throughout the beam image current path [11]. Figure 2 presents the mechanics of the prototypes of the beam slits and the scrapers, which are very similar to the mechanics of the beam flags, improving design reuse and reducing the diversity of the ordered parts. The scrapers use a Vexta PK-223PB stepper motor, a Huber 5101.07 X1 linear translation stage and the same rotary encoder as the beam flags. The slits use the same stepper motor as the scrapers, a Huber 5101.10 X1 linear translation stage with an absolute position Renishaw encoder.

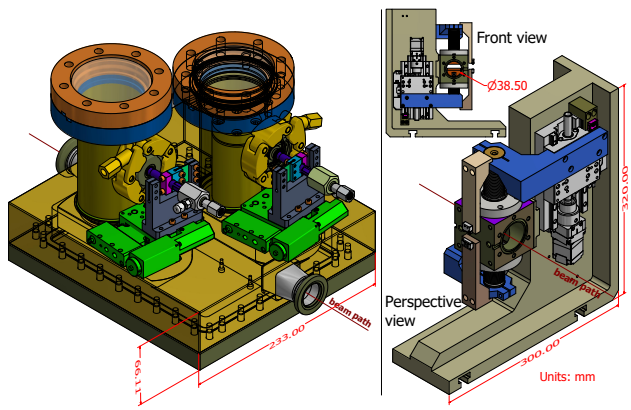

Figure 2: Horizontal scraper (left) – where some parts were set transparent – and vertical beam slits (right) mechanical assemblies. Vertical scraper and horizontal slits will follow the same concepts and structures shown.

Button BPM Sensors

After having prototyped several design ideas, the mechanical aspects of the SR button BPMs among the ones raised in [12] were defined. Regarding the choice of materials, a non-magnetic solution was selected: Ti_4Al_6V alloy body and housing, Mo button and Al_2O_3 ceramics, allowing satisfactory vacuum insulation through housing/body welding and housing/ceramics/button brazing. Geometry design

ISBN: 978-3-95450-192-2 doi:10.18429/JACoW-IBIC2017-MOPCF09

changes were mainly carried out in the body in order to keep the electrical center steady for even button heat load due to wake losses. Uneven loads, as studied in [13], are expected to be prevented by sorting the buttons.

SR BPM model is currently under production. Its parts are being machined by Brazilian companies and the assembly (brazing and welding) performed in-house. BO design has followed the same materials configuration from the SR model, although it had several geometry aspects simplified and is still at prototyping stage. Figure 3 depicts the referred mechanical projects.

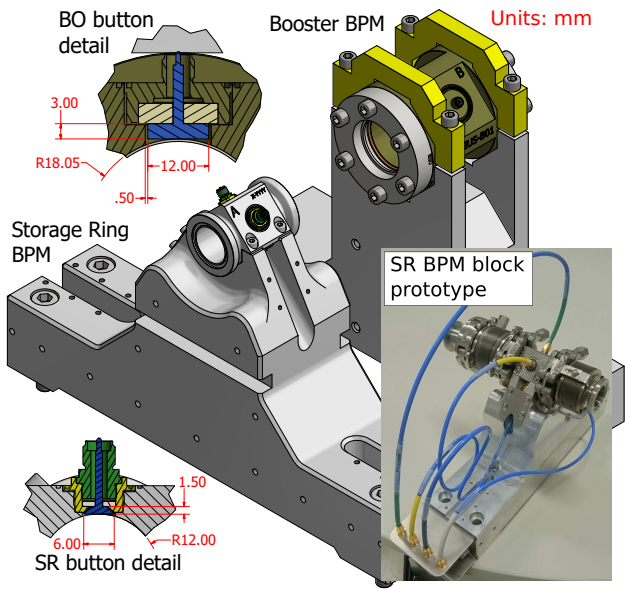

Figure 3: SR and BO BPM mechanical projects.

BPM Electronics

The in-house developed open source BPM electronics [14–16] is under final testing at LNLS. A fully populated rack comprising 13 RF BPM and 4 photon BPM electronics is assembled for performing short- and long-term beam position measurement stability tests as well as for debugging software and gateware components.

The procurement of the data acquisition subsystem (MicroTCA.4 crate, FPGA boards, ADC mezzanine cards) and RF front-end electronics has been made. The procurement of commercial components such as cables, racks, Ethernet switches is in the final stage of preparation. A local contractor has been hired to fully test and assemble the 20 BPM racks for the Sirius storage ring and booster. An additional rack with transfer line BPMs will be assembled by LNLS personnel. The complete system installation is foreseen for the first semester of 2018.

Striplines

Sirius stripline designs took into account the following aspects: pick-up (PU) or actuator (kicker/shaker) behavior, operation frequency and bandwidth, crosstalk between strips, line impedance matching and, only for the SR, beam impedance mitigation [11, 13]. Striplines for generic purposes were also designed and all models are currently in prototyping stage. Figure 4 shows BO stripline models and Fig. 5 SR ones. Their characteristics are detailed in Table 2.

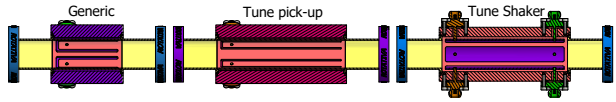

Figure 4: Side section view of the booster striplines mechanical design.

Table 2: Geometry Parameters of BO and SR Striplines: Strip Angular Aperture, Number of Strips per Assembly, Short-circuited (SC) Upstream End and Electrical Length

Stripline type	Strip aperture	# of strips	SC?	Elec. length
BO Tune PU	30 °	4	yes	$\lambda/4$
BO Tune Shaker	90 °	4	no	$\lambda/4$
BO Generic	45 °	4	yes	$\lambda/8$
SR Tune PU	30 °	4	yes	$\lambda/4$
SR Tune Shaker	90 °	2	no	$\lambda/4$
SR BbB Kicker	90 °	2	no	$\lambda/2.3$
SR Generic 1	40 °	4	yes	$\lambda/8$
SR Generic 2	40 °	4	yes	$\lambda/4$

The BbB stripline kicker had its electrical length reduced from the ideal $\lambda/2$ value due to physical space limitations. Another aspect worth noting is that every stripline actuator will be respectively aligned with the vertical and horizontal planes. The pick-ups follow the traditional 45 °-rotated orientation in order to avoid damage and/or false readings from synchrotron radiation incidence, with the exception of the transfer lines – not present in Table 2 – where the UVX storage ring stripline BPMs spare units [17] will be used, with axis aligned orientation.

Bunch-by-Bunch Feedback System

The BbB system chain consists of a button BPM as pick-up, a front-back-end (FBE) unit and three iGp12 processors from Dimtel [18]. For the transverse plane, the feedback signals are directly amplified by AR amplifiers 75A400 to drive the stripline kicker. The longitudinal feedback signal is upconverted in the FBE unit and then amplified by Mini-Circuits ZT-102 amplifiers before reaching the overloaded cavity kicker. The amplifiers are the present units for the

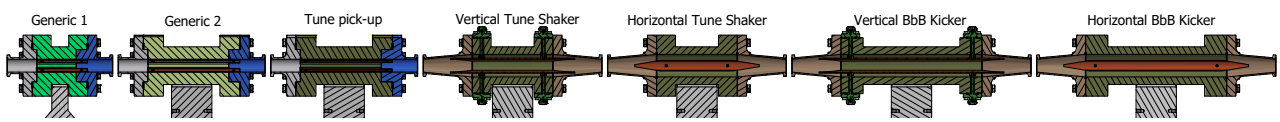

Figure 5: Side section view of the storage ring striplines mechanical design.

ISBN: 978-3-95450-192-2 doi:10.18429/JACoW-IBIC2017-MOPCF09

UVX storage ring and their use in Sirius will need to be reviewed due to power limitations.

Longitudinal feedback system was not initially planned for the initial Sirius user operation phases [19, 20], but the plan changed since its use was found to possibly be needed during Sirius commissioning and first users' phase, where Petra-III 7-cell cavities will be used in the storage ring.

Tune System

The BO and SR tune measurement systems will employ stripline kickers for beam excitation and stripline BPMs followed by broadband horizontal and vertical beam position measurements using hybrid couplers. Three different excitation/measurement techniques will be employed:

- Noise excitation + real-time spectrum analyzer: a band-limited white noise signal generated by an Agilent 33521A arbitrary waveform generator passively mixed with a carrier signal from a R&S SMB100A signal generator. The beam position signals are acquired by a Tektronix RSA603A real-time spectrum analyzer. The instruments and peak search algorithm are integrated to the accelerator control system via EPICS IOCs [21, 22].
- Spectrum analyzer: the tracking generator feature of the R&S FSL3 spectrum analyzer is used. The instrument and peak search are integrated to EPICS [23].
- Tune tracking: the PLL-based iGp12 tune tracking feature [24] of the BbB system. EPICS integration is readily available.

The combination of different instruments and techniques to measure the betatron tunes is part of a strategy to balance ease of use during commissioning, speed of measurement and mitigation of disturbances when operating for users. For instance, the use of a noise excitation aimed at fast measurements (< 10 ms sample rate) during booster ramps with tune resolution of 10^{-2}. Contrarily, the use of a standard spectrum analyzer in sweep mode with long averaging was chosen for achieving a high precision measurement ($< 10^{-4}$) during commissioning and first months of operation of the SR, besides providing an intuitive interface to operators and machine physicists. The long-term solution planned is to use the PLL-based iGp12 tune tracking feature for exciting and tracking only one bunch of the beam. This minimizes emittance disturbance caused by betatron tunes excitation.

For the first two systems, the excitation power will be provided by AR 50W1000D amplifiers, thus allowing operation in the 50 MHz to 1 GHz frequency range with up to 48 dBm excitation power. The EPICS IOC responsible for controlling the amplifiers is currently under development [25]. A MOXA CN2650I-16 Ethernet to RS-232 converter is used to interface the amplifier with the accelerator's control system.

X-ray and Visible Light Diagnostics

Two X-ray beamlines will provide emittance and energy spread measurements in the storage ring. An optical beamline will extract visible light for longitudinal beam profile and other measurements. A cost-effective solution was chosen for the streak camera: the Hamamatsu instrument model C5680, currently operating in the UVX storage ring at 199 MHz (476 MHz / 4) with 2 ps RMS resolution, will be modified by the vendor to operate at 125 MHz.

Beam Loss and Gas Bremsstrahlung Monitors

Gas Bremsstrahlung monitors based on the BPW34 pin diode and accompanying analog electronics are under development at LNLS and aim at providing data about the vacuum pressure by detecting the gamma-ray emission cone along the SR. Commercial BLMs with differential outputs [26] will also be employed at the Sirius transfer lines, BO and in some parts of the SR where there is room for installation. The analog signal conditioning circuitry as well as the data acquisition instrumentation, currently in development by the LNLS Instrumentation and Controls groups, will interface with the EPICS control system directly. This approach will provide a modular system allowing quick changes in the placement of sensor heads of both sensors.

CONCLUSION

The Sirius beam diagnostics solution has been summarized. Most of the detailed designs are finished and the systems with a high level of complexity or with a high number of components are in advanced production stages, but a few of them are still under development, notedly SR beam scrapers, transfer line slits and the flag to be installed downstream of the SR injection septum. A large part of the production is carried out by local companies, including the BPM sensors, a critical part of the SR. Currently, the biggest concern is the limited time available for testing the systems prior to the installation.

ACKNOWLEDGEMENT

The author is indebted to Carlos R. Scorzato from LNLS Instrumentation group and J. Guilherme R. S. Franco, Rafael C. Ito, Robert W. Polli, Patricia H. Nallin and Eduardo P. Coelho from LNLS Controls groups for providing the analog electronics and the digital compact data acquisition platform for counting BLM and Gamma-ray monitors' pulses; Flavio Rodrigues, Makoto Okuma, Adriano de Barros, Regis T. Neuenschwander and A. Ricardo D. Rodrigues for the mechanical design projects and fruitful discussions; Osmar R. Bagnato, Fernanda R. Francisco and Rafael Defavari from the LNLS Materials Engineering group for the BPM sensors and support stands development; and the LNLS Beam Diagnostics group for electronics and EPICS IOC development activities as well as electromagnetic design optimization of the in-vacuum components.

REFERENCES

[1] L. Liu, F. H. de Sá, and X. R. Resende, "A New Optics for Sirius," in *Proc. 7th Int. Particle Accelerator Conf. (IPAC'16)*, Busan, Korea, May 2016, pp. 3413–3416.

[2] *motorapp/Galil-3-0: ASYN based EPICS driver for Galil Products*, https://github.com/motorapp/Galil-3-0

ISBN: 978-3-95450-192-2 doi:10.18429/JACoW-IBIC2017-MOPCF09

[3] *EPICS - Experimental Physics and Industrial Control System*, http://www.aps.anl.gov/epics/

[4] *areaDetector/aravisGigE: An EPICS areaDetector driver using the glib aravis library for video acquisition with Genicam cameras*, https://github.com/areaDetector/aravisGigE

[5] *Integrating Current Transformer User's Manual*, Bergoz Instrumentation, http://www.bergoz.com/sites/www.bergoz.com/files/ictmanual3

[6] *Beam Charge Monitor (Modular Electronics) Integrate-Hold-Reset User's Manual*, Bergoz Instrumentation, Mar. 2008, http://www.bergoz.com/sites/www.bergoz.com/files/bcm-ihrmanual2.2

[7] *DMM7510 Graphical Sampling Multimeter*, http://www.tek.com/tektronix-and-keithleydigital-multimeter/dmm7510

[8] *New Parametric Current Transformer User's Manual*, Bergoz Instrumentation, July 2007, http://www.bergoz.com/sites/www.bergoz.com/files/npctmanuel1-11

[9] *lnls-dig/dmm7519-epics-ioc: EPICS IOC to operate the DMM7510 by Tektronix.*, https://github.com/lnlsdig/dmm7510-epics-ioc

[10] J. L. Brito Neto *et al.*, "Status and Development of Sirius Timing System," in *Proc. 15th Int. Conf. on Accelerator and Large Experimental Physics Control Systems (ICALEPCS'15)*, Melbourne, Australia, Oct. 2015, pp. 1007–1010.

[11] H. O. C. Duarte, L. Liu, and S. R. Marques, "Evaluation and attenuation of Sirius components impedance," in *Proc. 8th Int. Particle Accelerator Conf. (IPAC'17)*, Copenhagen, Denmark, May 2017, pp. 3048–3051.

[12] H. O. C. Duarte, L. Sanfelici, and S. R. Marques, "Design and Impedance Optimization of the SIRIUS BPM button," in *Proc. 2nd Int. Beam Instrumentation Conf. (IBIC'13)*, Oxford, UK, Sept. 2013, pp. 365–368.

[13] H. O. C. Duarte *et al.*, "Analysis and countermeasures of wakefield heat losses for Sirius," in *Proc. 8th Int. Particle Accelerator Conf. (IPAC'17)*, Copenhagen, Denmark, May 2017, pp. 3052–3055.

[14] *BPM wiki page at the Open Hardware Repository*, http://www.ohwr.org/projects/bpm/wiki

[15] S. R. Marques *et al.*, "Status of the Sirius RF BPM Electronics," in *Proc. 3rd Int. Beam Instrumentation Conf. (IBIC'14)*, Monterey, USA, Sept. 2014, pp. 505–509.

[16] D. O. Tavares *et al.*, "Development of an Open-Source Hardware Platform for Sirius BPM and Orbit Feedback," in *Proc. 14th Int. Conf. on Accelerator and Large Experimental Physics Control Systems (ICALEPCS'13)*, San Francisco, USA, Oct. 2013, pp. 1036–1039.

[17] F. S. Rafael and E. K. C. S. Hayashi, "Beam position monitor for the LNLS UVX synchrotron light source," in *Proc. 16th Particle Accelerator Conf. (PAC'95)*, Vol. 4, Dallas, USA, May 1995, pp. 2527–2529.

[18] Dimtel Products. http://www.dimtel.com/products/index

[19] F. H. de Sá, H. O. C. Duarte, and L. Liu, "Study of collective beam instabilities for Sirius," in *Proc. 5th Int. Particle Accelerator Conf. (IPAC'14)*, Dresden, Germany, May 2014, pp. 1653–1655.

[20] F. H. de Sá, H. O. C. Duarte, and L. Liu, "Update of the Collective Effects Studies for Sirius," in *Proc. 8th Int. Particle Accelerator Conf. (IPAC'17)*, Copenhagen, Denmark, May 2017, pp. 3680–3683.

[21] *lnls-dig/agilent33521a-epics-ioc: EPICS IOC for the Agilent 33521A Function/Arbitrary Waveform Generator* https://github.com/lnls-dig/agilent33521aepics-ioc

[22] *lnls-dig/rsa600-epics-ioc: EPICS IOC to operate the real-time spectrum analyzer RSA603a and RSA507A by Tektronix*, https://github.com/lnls-dig/rsa600-epics-ioc

[23] *lnls-dig/rsfsv-epics-ioc: Repository containing the EPICS IOC support for the R&S FSV signal analyzer*, https://github.com/lnls-dig/rsfsv-epics-ioc

[24] *iGp12 tune tracker feature*, http://www.dimtel.com/news/20140625

[25] *lnls-dig/ar-amp-epics-ioc: EPICS IOC to control the RF Amplifiers by AR*, https://github.com/lnls-dig/ar-amp-epics-ioc

[26] *Beam Loss Monitor User's Manual*, Bergoz Instrumentation, June 2017, http://www.bergoz.com/sites/www.bergoz.com/files/blmmanual2.0

ISBN: 978-3-95450-192-2 doi:10.18429/JACoW-IBIC2017-MOPCF10

ESTIMATION OF HEAVY ION BEAM PARAMETERS DURING SINGLE EVENT EFFECTS TESTING

V.S. Anashin, P.A. Chubunov, G.A. Protopopov, United Rocket and Space Corporaton, Institute of Space Device Engineering, Moscow, Russia
S.V. Mitrofanov, V.A. Skuratov, Y.G. Teterev, Joint Institute for Nuclear Research, Dubna, Russia

Abstract

During flight mission onboard electronic equipment of spacecraft exposed to outer space radiation. Impact of charged particles leads to errors and failures in electronic components (EC). The most critical problem for spacecraft engineers is heavy ions influence which cause single event effects (SEE) in EC [1,2]. To be assure that spacecraft electronics will work properly during the mission ground SEE testing is needed. For these purposes heavy ions accelerators are used. In this paper, we present facility for SEE testing including requirements to heavy ions beams, techniques and equipment used for control heavy ion beam parameters during SEE testing.

BASIC PRINCIPLES OF SEE TESTING

SEE are such effects, the cause of which is the interaction of the single charged particle with active area of semiconductor device. Such effects have a probabilistic nature and are not related to radTatTon "history" of the device. SEE can be classified into Destructive, Residual and Transient effects, by types of failures. Destructive SEE are Single event latch up (SEL) - inclusion of the parasitic four- layer p-n-p-n structure leading to harsh increase circuit current; Single event burnout (SEB) - secondary induced breakdown of p-n junction leading to its destruction; Single event gate rapture (SEGR) - breakdown of gate insulator along nuclear track of particle; Single event snapback (SESB) - secondary induced breakdown, determined the performance spurious bipolar structure in MOS transistor. Residual SEE are Single event upset (SEU) - inversion of logical state of memory unit or trigger circuit; Multiply byte upset (MBU) - inversion of logical state of several neighboring memory unit or trigger circuit; Single event functional interruption (SEFI) - inversion of logical state of memory unit or trigger circuit operation leading to violation of program progress (for example, program hangup). Transient SEE are analogue and digital Single event transient (ASET, DSET) - Short- time pulse in output element of linear or digital semiconductor devices.

General SEE testing foundation is The principle of equivalence thresholds LET for space heavy charged particles and monoenergetic ions, in which the electronic components having SEE :equality thresholds LET under the influence of space heavy charged particles, containing ions of different chemical elements with different spectral and energetic characteristics and any monoenergetic ion having a given value of LET, under the influence of which in electronic components appears SEE. Main SEE hardness characteristics are following: Threshold LET; Effect cross-section (saturation); Dependence of effect cross-section from ions LET, usually Weibull curve (see example on Fig. 1).

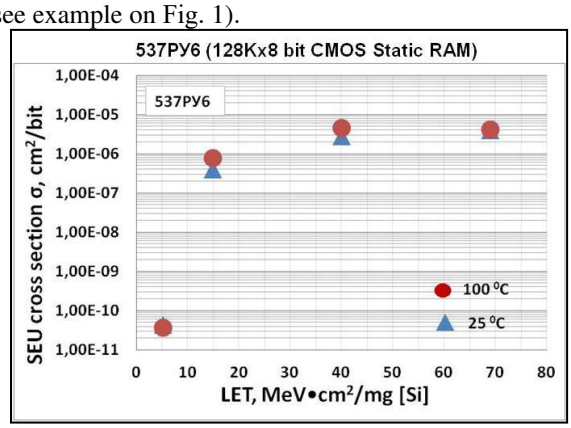

Figure 1: Dependence of SEU cross-section from ions LET for Russian-made SRAM at different temperatures.

TEST FACILITIES

A number of heavy ion test facilities are created under TCe BrancC of JSC "UnTted Rocket and Space Corporation" – "Institute of Space Device Engineerng" authorizing on the base of cyclotrons U400 and U400M (Flerov Laboratory of Nuclear Reactions (FLNR), Joint Institute for Nuclear Research (JINR), Dubna city, Moscow region) which have differential in the composition of output ions and their energy, the radiation area, range of temper-atures, by changeover time from one ion to another, vacu-um pumping time (see Table 1 for details). Currently our test facilities provide test operations of all EC functional classes on hardness to all types of SEE. Since 2010, by the effort of the five testing laboratories have been tested more than 3000 EC part types All test facilities are avail-able to carrying out tests (on request); there are no re-strictions for foreign organizations. Some pictures of test facilities are shown on Figs. 2-4.

Figure 2: Low energy test facility (IS OE PP).

ISBN: 978-3-95450-192-2 doi:10.18429/JACoW-IBIC2017-MOPCF10

Figure 3: High energy test facility (IS OE VE).

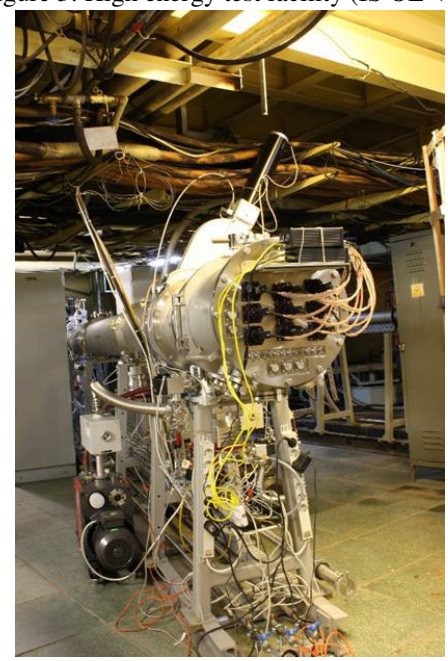

Figure 4: Low energy test facility (IS OI 400-N).

Device under test (DUT) mounted in test chamber is shown at Fig· 5.

Figure 5: Example of DUT in test chamber.

Table 1: The Technical Characteristics of the Test Facilities

Technical features	Low energy facilities	High energy facilities
Ion source	Cyclotrons U-400/U-400M	Cyclotron U-400M
Initial energy, MeV/nucleon	3 .. 4 (up to 6 on request)	15 .. 40 (>60 for light ions) Tunable with using degraders
Flux density, particle/(cm^2×s)	10 .. 10^5	10 .. 10^5 (10^4 for Bi)
Nonuniformity, %	± 10	± 15
Suit of ions	C, O, Ne, Ar, Fe, Kr, Xe, Bi	Ne, Ar, Kr, Xe (O, Fe, Bi)
LET (material), MeV × cm2/mg	0.5…99 (Depends on material of electronic component, type of ion and energy)	
Range in material, μm	≥30 (Depends on material of electronic component, type of ion and energy)	
Irradiation area, mm	150 x 200/ 200 x 200	Ø 60 (Ø 40 for Bi)
Operational pressure	Vacuum	For vacuum/ atmosphere
Charge overtime for gaseous ion, hour	6	6
Charge overtime for metal ion, hour	18	18
Vacuum pumping time, min	6 / 8	5
Temperature range, °C	-40 .. +125	-40 .. +125
Tilt, °	0 .. 90	0 .. 90

TEST PROCEDURE

The task of test is obtaining experimental cross section dependence of SEE from linear energy transfer (LET) of heavy ions energy in the wide range of LET. For this purpose it is needed to register not less than four points with effects during test campaign. With the facilities of low initial energy we have to use four different types of ions with specific LET for obtaining four experimental points. The most common combination of ions is Xe; Kr; Ar; Ne with LET approximately 69; 40; 15; 6 MeV cm^2/mg. The exact values of LET for each ion are determined on the basis of initial energy which is measured after the output of each ion.

The peculiarity of testing with low energy ion beams is necessity to vacuum ion guide tube and test chamber. This is a prerequisite for the delivery of ions from source to device under test with no loss of energy. Thus, by measuring initial energy in vacuum tube (channel) we obtain the data to following LET calculation. Another feature of systems with low energy is low range of ions in materials of electronic components (30-40 mkm). There-

ISBN: 978-3-95450-192-2 doi:10.18429/JACoW-IBIC2017-MOPCF10

fore, decapsulation of electronic devices is needed for SEE testing in order to ensure impact of heavy ions to open die (with no package). For most of modern electronic components such range of ions is sufficient to achieve sensitive volume of chip, since the thicknesses of the passive layers (passivation, metallization, etc) no more than 15 mkm. The information about type of ion and it initial energy is used for LET calculation. For LET estimation SRIM software is applied. A significant disadvantage of low energy facilities is long changeover time from one ion to another (from 6 hours for gaseous to 24 for metals), which increases the cost of tests.

The test bench with high initial energy is differs from low-energy facilities in that more powerful ion injector. With increasing of initial energy, the increasing of ion range while reducing of LET is observed. However, reducing the initial ion energy we can achieve similar values of LET in comparison with low energy facilities and a significant increase in particle range (from 200 to 2000 mkm for different LET). This allows us to test devices with a deep depth of sensitive volume or samples which cannot be fully decapsulated. Moreover, for obtaining several values of LET we do not need to change type of ion, so, for getting four experimental points we need only two ions. Since the change of initial energy in accelerator in short time is impossible, special thin foils (or stack of foils) are used. In this case, the information about type and initial energy (in channel) and also about material and thickness of energy absorber is used for LET calculations with SRIM software.

The EC irradiation is carrying out until the registration level is reached more than 100 SEE or until the destructive failure is occurred or until the fluence is 1E+7 cm^{-2}.

TECHNIQUES & EQUIPMENT FOR CONTROL BEAM PARAMETERS

Beam fluence and flux control system is based on joint application of scintillators based detectors and track membrane technique. Ion fluence is controlled by using polycarbonate or polyethylene terephthalate track detectors placed in close vicinity of any testing device in all irradiation runs. The result usually available in one hour after irradiation. Scintillators based detectors allow us control stability of the beam in online mode and used as reference point to metrologically certified track detectors. Interface of online fluence control system is shown on figure 6. Based on this data test engineer decides on the end of irradiation session for given DUT. At the backside of test chamber you can see scintillation detectors (Fig. 7). Photomultipliers for scintillators based detectors is located outside vacuum chamber (Fig. 8). An example of SEM micrograph of polymer track detector is shown on Fig. 9. Value of fluence is determined by counting holes in a certain area.

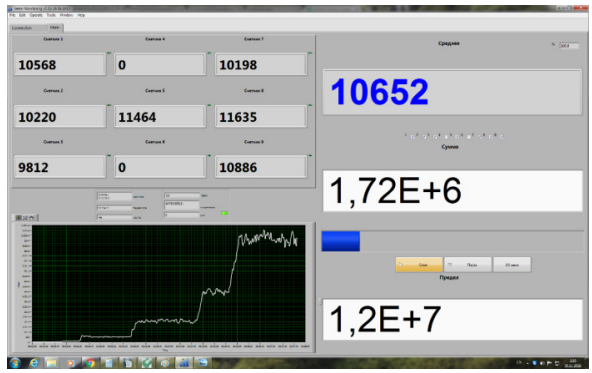

Figure 6: Online fluence control.

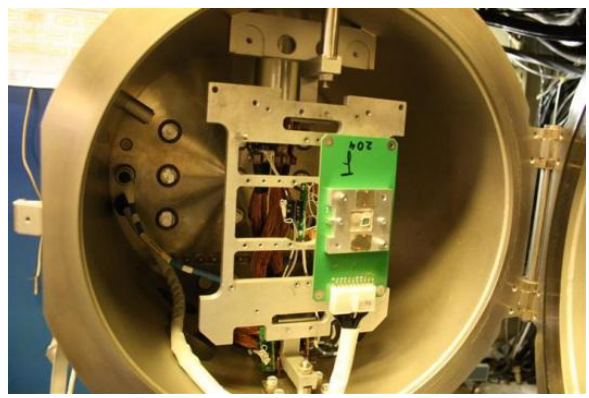

Figure 7: Scintillators on the back of chamber.

Figure 8: Photomultipliers for scintillators based detectors.

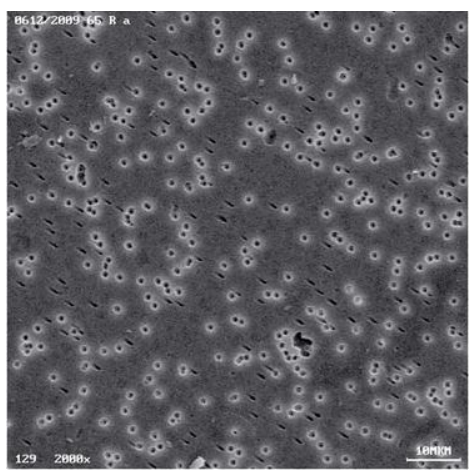

Figure 9: Picture of track detector after irradiation.

ISBN: 978-3-95450-192-2 doi:10.18429/JACoW-IBIC2017-MOPCF10

The main energetic parameters of the ion beam during SEE testing:

- Energy of ion in vacuum tract
- Energy of ion in test chamber
- LET in material of EC
- Range of ion in material of EC

Table 2: Applied Techniques for Estimation of the Main Ion Beam Parameters During SEE Testing

Characteristic	Low energy facility	High energy facility
Initial energy of ion	Measurements (TOF technique)	Measurements (TOF technique)
Energy of ion on DUT		Calculation (SRIM)
LET	Calculation (SRIM)	Calculation (SRIM)
Range of ion	Calculation (SRIM)	Calculation (SRIM)

Typical LETs and ranges in Si (as most common semiconductor) are shown in table below.

Table 3: LET and Ranges in Si at Test Facilities

Low energy facility (vacuum, energy of ion on DUT 3.5 MeV/nucleon						
Ion	C	O	Ne	Ar	Fe	Kr
LET (Si), MeV × cm2/mg	2.7	4.4	6.5	15.7	27.1	40.3
Range in Si, μ	50	43	39	37	34	38
High energy facility (forvacuum/atmosphere, energy depends of ion)						
Ion	O	Ne	Ar	Fe	Kr	Xe
LET (Si), MeV × cm^2/mg	0.5/ 0.5	0.9/ 1.0	4.5/ 4.8	9.7/ 11.2	18.0/ 21.9	42.2/ 57.9
Range in Si, μ	4720/ 4550	2800/ 2680	788/ 657	445/ 316	368/ 238	232/ 100
Energy of ion in vacuum tract, MeV/ nucleon	64	54	34	29	28.5	24.5

CONCLUSION

Facilities for SEE testing based on ion accelerators are presented. All of these test facilities are included in the Compendium on the international irradiation test facilities [3]. Described SEE Test Facilities were rewarded in the 2014, 2016, 2017 at International Exhibitions "Inventions Geneva", "Archimedes" and "IPITEX".

The standard practice of SEE testing implies using of heavy ions accelerators. Discussed test procedure is wide-ly used to determine the EC parameters of sensitivity to SEE.

The main directions of development these facilities are following: online control of beam parameters with accuracy increasing; creation of microbeam line; improvement and verification of energetic parameters calculations for ions after degraders and energy measurements on DUT.

REFERENCES

[1] "A travel in radiation activities through a Space Program", RADECS Conference 2011 Short Course, 2011.

[2] "Radiation Effects: Understanding the Evolving Risk for New Technologies and New Environments", RADECS Conference 2013 Short Course Notebook, 2013.

[3] Koziukov A., Tuzhikova I., Pellish J., Chubunov P., Paillet P., Ecoffet R., Anashin V. "Compendium of international irradiation test facilities", 2nd Edition// RADECS 2015, 2015

ISBN: 978-3-95450-192-2 doi:10.18429/JACoW-IBIC2017-MOPWC01

BUILDING THE THIRD SRF GUN AT HZDR

H. Vennekate[1]*, A. Arnold, P. Lu, P. Murcek, J. Teichert, R. Xiang
Helmholtz-Zentrum Dresden-Rossendorf, Germany
[1]also at Technical University Dresden, Germany

Abstract

The multipurpose accelerator ELBE at HZDR which is delivering a large set of secondary beams, is driven by a thermionic DC injector. In order to enhance the beam quality of the machine, the development of superconducting RF injector has been pursued since the early 2000's. The corresponding ELBE SRF Gun I of 2007 and Gun II of 2014 already delivered beam for the operation of several user beamlines, such as the FEL, positron generation, and THz facility. Currently, the next version – Gun III – and its cryomodule are being assembled, characterized, and prepared for the final commissioning throughout late 2017/early 2018. The new module benefits from the experiences gained with regard to emittance compensation and monitoring of operation variables made with the two predecessors.

MOTIVATION

The unique feature of the ELBE accelerator is its ability to run all its modules in continuous wave (CW) mode while delivering electron bunches at a frequency of up to 13 MHz. Hence, a flexible CW source is required for its operation. A superconducting radio frequency (SRF) electron gun represents the ideal solution for this task. Itcombines the advantages of RF injectors and DC guns, which are high field gradients causing enhanced beam parameters and large beam currents due to increased repetition rates, respectively. The ELBE SRF Gun project is an R&D effort to provide such an injector. The two implemented prototypes — Gun I and Gun II — successfully provided beam for several of the beamlines during machine tests as well as for user operation [1]. Due to a degradation of available maximum gradient of the cavity of the currently installed Gun II, the construction of the third version of the photoinjector was initiated. For this purpose, the niobium resonator of Gun I is being refurbished at DESY, Hamburg. In combination with a newly built cryomodule, this cavity is designated to be put in operation as the ELBE SRF Gun III within 2018.

EMITTANCE COMPENSATION

An important aspect of the beam dynamics of an SRF injector is the optimization of the emittance of the electron bunches, which presents more challenges than for a normal conducting gun. In the case of the ELBE SRF gun this is solved by a combination of RF focusing at the photocathode and a superconducting solenoid being integrated into the injector's cryomodule, as shown in the scheme in Figure 1. The use of these two mechanisms has shown a significant

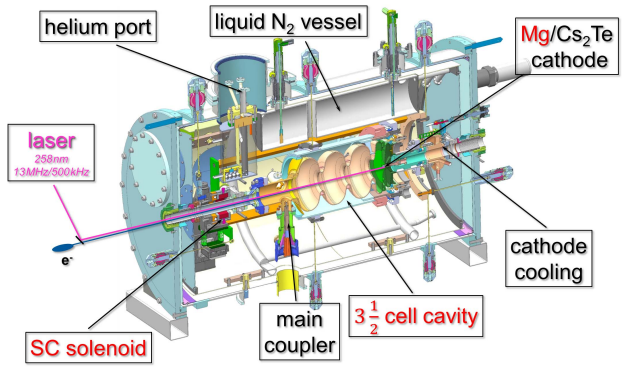

Figure 1: The current ELBE SRF Gun design featuring a 3.5 cell gun cavity and a superconducting solenoid at about 70 cm from the cathode.

reduction of the particle beam's transverse emittance and extent in both, simulation (see Figure 2) as well as in experiment (see Figure 3) [2]. This is of substantial importance for the successful integration into an accelerator's beam dynamics framework.

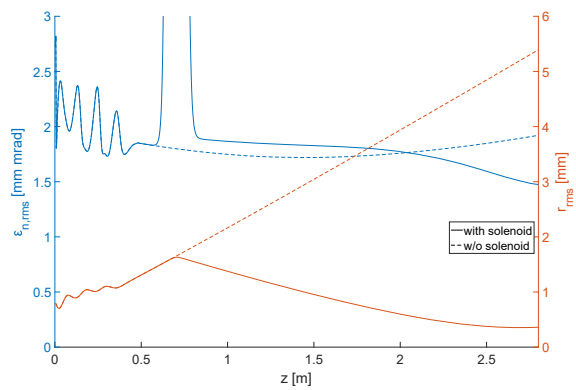

Figure 2: Simulation results of the evolution of a 250 pC bunch in emittance and radius along the first 3 m of beamline [2].

In addition to the characterization of the intentional displacement of the photocathode inside the superconducting cavity to control RF focusing [3], the superconducting magnet requires separate thorough examination and testing prior to its installation inside the module. The corresponding measurements conducted so far are described in the following.

* h.vennekate@hzdr.de

ISBN: 978-3-95450-192-2 doi:10.18429/JACoW-IBIC2017-MOPWC01

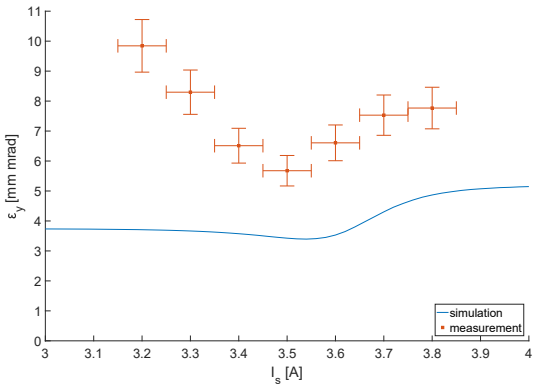

Figure 3: Emittance vs. solenoid current measured with Gun II for a 160 pC electron bunch at about 3 m, [2].

SOLENOID COMMISSIONING

Magnetic Field

In order to determine the field distribution of the magnet[1], a mapping setup, attached to the gun cryostat as shown in Figure 4, was installed. Using currents in the order of few tens of mA, the field in a cuboid shaped volume was recorded in front, inside, and behind the solenoid by a hall probe. The geometrical resolution of this room temperature measurement was 1 mm.

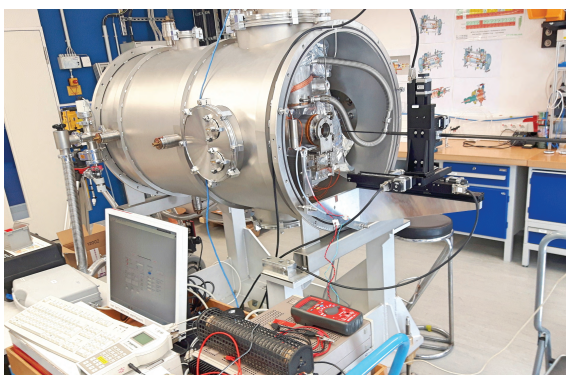

Figure 4: Measurement setup for the room temperature mapping of the solenoid.

For each transverse slice of the measured field the center of the distribution was computed using a two dimensional Gaussian fit. Due to the fact that only the longitudinal field component could be recorded with the available probe[2], the character of this center varies from a maximum in the domain of the fringe fields to a minimum inside the coil. The latter situation being the one depicted in Figure 5.

Using the results for each longitudinal position, a weighted fit for the total beam axis was generated. Here, a deviation from an ideal axis of $1.9 \pm 0.7°$ in one plane

[1] The installed solenoid magnet was manufactured by Niowave Inc. and is on loan from the Helmholtz-Zentrum Berlin.

[2] Recently, a three dimensional hall probe was acquired and is foreseen to be used for future measurements at HZDR.

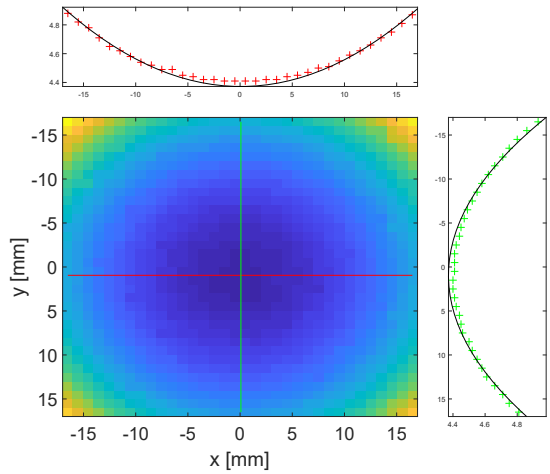

Figure 5: A slice of the longitudinal field inside the magnet's coil.

and $1.3 \pm 0.7°$ in the other was found [4] (see Fig. 6). Such misalignments typically induce steering and other alteration effects on the electron bunch during beam operation. Therefore, two cryogenic steppers are included in the final setup to enable small correction movements of the solenoid in the transverse plane. An error-free alignment of both, the cavity's electrical and the solenoid's magnetic axes is rather difficult prior to cooldown. However, experiences made with Gun II showed that those minor movements of the solenoid are sufficient to compensate for alterations.

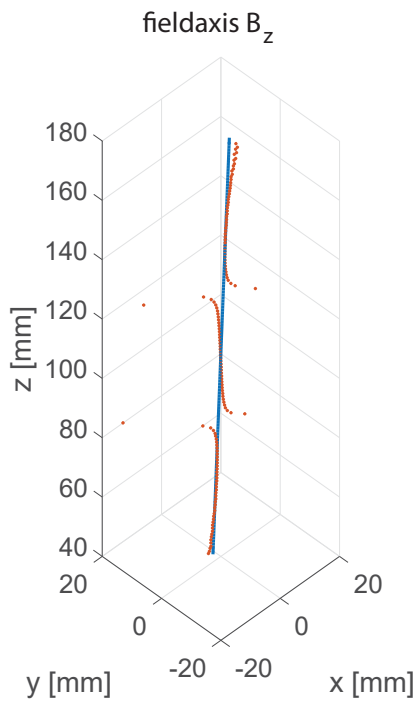

Figure 6: The result of a mapping measurement: the magnetic field axis is reconstructed with respect to the beam axis in 3d [4].

ISBN: 978-3-95450-192-2 doi:10.18429/JACoW-IBIC2017-MOPWC01

Thermal Testing

The entire module of the ELBE SRF Gun features many temperature sensors at relevant locations to monitor the thermal behavior during operation. Depending on the expected temperature range that has to be covered, the type of sensor varies. Taking into account the experiences with Gun II, all RhFe sensores are replaced with Cernox sensors in Gun III. Furthermore, additional copper heat sink bobbins — as shown in Figure 7 — are introduced close to the sensors to absorb the heat introduced by the read-out leads. In first cooling tests with liquid nitrogen and helium this modified setup already showed a significant improvement of the sensor sensitivity [4].

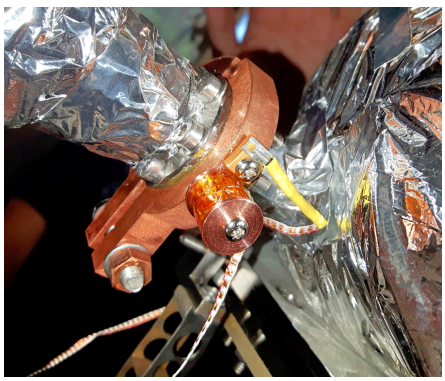

Figure 7: One of the newly installed Cernox temperature sensors at the helium supply line of the solenoid, featuring a heat sink bobbin where the sensor leads are wrapped around the copper body to connect it to the liquid helium system.

CRYOSTAT COMMISSIONING

The new cryomodule of Gun III itself is also undergoing early functional checks at HZDR. These include the obligatory vacuum/leak checks of all components as well as first temperature tests with cryogenic liquids. At its current state, the model does not include its liquid nitrogen or magnetic shield yet. However, the liquid helium reservoir, the superconducting solenoid, and a cavity model were already mounted. Cooling this limited helium system first test measurements could be performed in recent weeks, see Figure 8. These experiments were aimed at a first operation of the solenoid with larger currents, so in its superconducting state, followed by corresponding field measurements, compare [5] for results with Gun II. As the magnet's coil did not cool down sufficiently below its critical temperature, such a test was not possible so far. Nevertheless, the experiment enabled the recording of other valuable data such as the improved temperature signals mentioned above.

OUTLOOK

In the near future, further elements of the new module will be added to the setup and accordingly commissioned. This includes the liquid nitrogen shield, which will be followed by another cooldown of the solenoid. Furthermore, a room temperature magnetic shield has to be installed and will be checked for the magnitude of the remaining stray field at the future position of the niobium resonator. In parallel, the treatment of the gun cavity at DESY is proceeding with a currently pending vertical performance test.

Figure 8: The cryomodule of Gun III during cooling with liquid helium.

ACKNOWLEDGMENTS

We acknowledge the support of the European Community-Research Infrastructure Activity under the FP7 program (EuCARD-2, contract number 312453), as well as the support of the German Federal Ministry of Education and Research grant 05K12CR1 and the help of all the people of the ELBE shift personnel. In addition, we would like to thank the people of HZB for the loan of their magnet.

REFERENCES

[1] J. Teichert *et al.*, "Free-electron laser operation with a superconducting radio-frequency photoinjector at ELBE", *Nuclear Instruments and Methods in Physics Research* A, 114-120, 2014.

[2] H. Vennekate, "Emittance Compensation for SRF Photoinjectors", *Wissenschaftlich-Technische Berichte, HZDR*, 081, 2017.

[3] H. Vennekate *et al.*, "ELBE SRF Gun II – Emittance Compensation Schemes", in *Proc. SRF2015*, Vancouver, BC, Canada, paper THPB057, 2015.

[4] J. Kiefer, *Untersuchung des Magnetfeldes eines Solenoid-Magneten im normal- und im supraleitenden Zustand*, Diploma thesis, HTW, 2017.

[5] H. Vennekate *et al.*, "Emittance Compensation for an SRF Photo Injector", in *Proc. SRF2013*, Paris, France, paper MOP026, 2013.

ISBN: 978-3-95450-192-2 doi:10.18429/JACoW-IBIC2017-MOPWC02

MICROTCA.4-BASED LLRF FOR CW OPERATION AT ELBE – STATUS AND OUTLOOK

M. Kuntzsch†, R. Steinbrück, R. Schurig, Helmholtz-Zentrum Dresden-Rossendorf, Dresden, Germany
M. Hierholzer, M. Killenberg, C. Schmidt, M. Hoffmann, DESY, Hamburg, Germany
C. Iatrou, J. Rahm, Technische Universität Dresden – Chair of Distributed Control Engineering, Dresden, Germany
I. Rutkowski, M. Grzegrzółka, Warsaw University of Technology - Institute of Electronic Systems, Warsaw, Poland

Abstract

The superconducting linear accelerator ELBE at Helmholtz-Zentrum Dresden-Rossendorf is operated in continuous wave (CW) operation [1]. The analogue LLRF (low level radio frequency) system, used since 2001, is going to be replaced by a digital solution based on MicroTCA.4. The new system enables a higher flexibility, better performance and more advanced diagnostics. The contribution shows the performance of the system at ELBE, the hardware and the software structure. Further it will summarize the last steps to bring it into full user operation and give an outlook to the envisioned beam-based feedback system that will take advantage of the capabilities of the digital LLRF system.

SYSTEM STRUCTURE

Hardware

The ELBE injector uses a thermionic gun followed by two normal conducting (NRF) buncher cavities operating at 260 MHz and 1.3 GHz. The main accelerator consists of two cryo-modules, each is equipped with two TESLA-type superconducting cavities (SRF) that are operated routinely in CW mode.

For high bunch charge and high current beams with good beam properties a superconducting photo gun is currently being developed. It contains a 3.5-cell structure operating at 1.3 GHz [2].

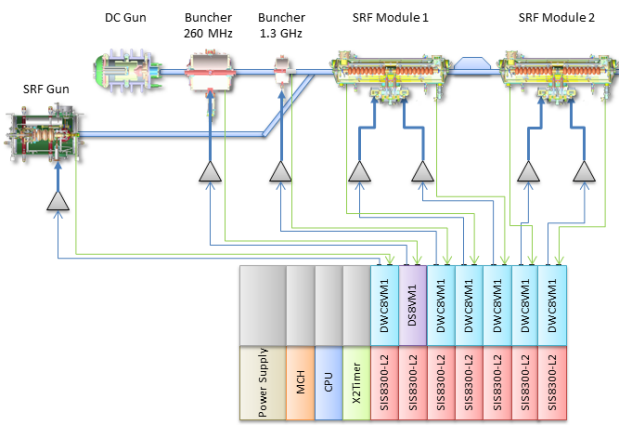

Figure 1: Digital LLRF schematic.

† m.kuntzsch@hzdr.de

In Figure 1 the main components and the associated hardware are shown. The digital LLRF system at ELBE is based on a modular system using MicroTCA.4 compatible hardware [3]. The standard separates the analogue circuits from the digital data processing. This allows an adaption of the analogue frontend to the desired application, while the digital part remains the same. For all cavities a SIS8300-L2 digitizer board is used which contains fast analogue-to-digital converters (ADCs) and a powerful Virtex 6 field programmable gate array (FPGA).

For the 260 MHz buncher cavity a direct sampling scheme is applied using the DS8VM1 analogue board [4]. For all 1.3 GHz cavities a mixer configuration with DWC8VM1 has been realized [5]. The cavity pickup signals are mixed with a local oscillator (LO) to an intermediate frequency (IF) which is sampled by the ADC sitting on the SIS8300-L2 [6]. The data processing and control loop is done inside the FPGA which allows parallel execution of processes with high data rate.

Software

All digitizer boards are connected to a CPU-board through a PCIe link. Status information and data traces are provided to a server application while this sets all the controller parameters and offers high level features.

For the first test phase a stand-alone DOOCS server application was used to control the system. It could only be accessed by remote login on to the MicroTCA.4-CPU and had no interface to the ELBE control system which is a network of programmable logic controllers (PLCs) and the graphical user interface (GUI) provided by a WinCC server-client system.

In order to overcome these limitations a new server application has been developed using the ChimeraTK framework [7]. This universal toolkit allows development of applications for different control systems like DOOCS and EPICS or the OPC-UA protocol. ChimeraTK enables collaboration and joint software development of institution that are using different control system architectures.

OPC-UA is a powerful protocol for industrial automation and is supported by many commercial suppliers [8]. The features integrated in the ChimeraTK framework are based on the open source implementation open62541 [9] that has been designed to run on different operating systems and hardware platforms.

ISBN: 978-3-95450-192-2 doi:10.18429/JACoW-IBIC2017-MOPWC02

The interface between WinCC and the digital LLRF server application is based on the OPC-UA protocol.

An expert panel for diagnostics and advanced features is envisioned which will be implemented in LabView. The basic communication scheme is shown in Figure 2.

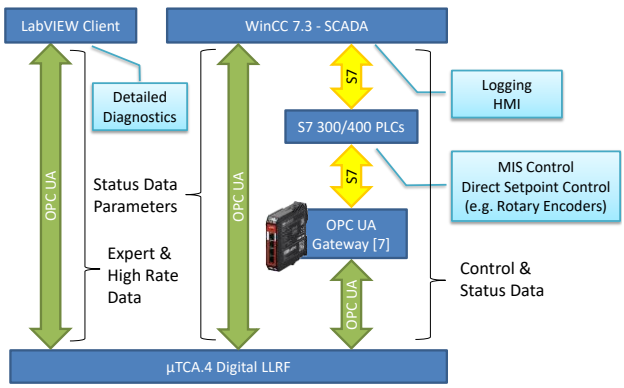

Figure 2: Digital LLRF communication scheme at ELBE

The machine interlock system is tightly connected to the PLCs and receives all relevant data from the LLRF system. It inhibits the drive signal of the vector modulator in the case not all conditions for RF operation are fulfilled.

SYSTEM PERFORMANCE

The phase stability has been measured with a signal source analyzer (SSA) and been compared to the legacy system. Since the controller firmware is still work in progress the results shown here have to be regarded as preliminary.

For the first superconducting cavity a gain sweep has been performed and a jitter of 24 fs rms has been measured (Figure 3). By increasing the gain, the low frequency noise could be reduced while the noise floor above 3 kHz increased.

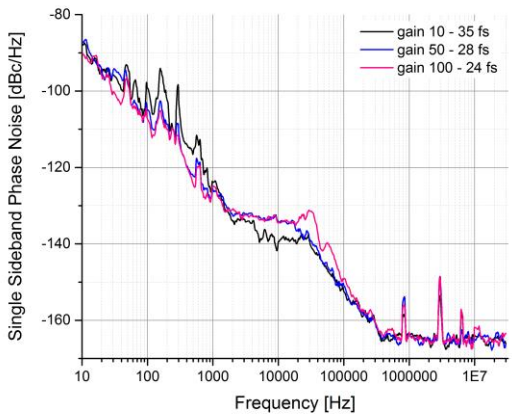

Figure 3: Single-Sideband phase noise from cavity 1 for different gain settings.

The amplitude stability of the system has been evaluated in-loop by measuring the residual amplitude noise and compared to the analogue system. With the digital control a stability level of 0.015 % could be achieved while the analogue control reached 0.053 %.

The digital control benefits from eight downconverter channels for every single cavity that allows to measure forward and reflected power of the cavity with high accuracy and to characterize the high power amplifier chain online.

OUTLOOK

Commissioning

Within the last years the hardware, software and firmware has been developed and tested in dedicated machine development shifts. The upcoming months will be used to bring the digital LLRF into routine operation.

A major step was the rewriting of the LLRF server application with the ChimeraTK framework which allowed the direct communication between the ELBE control system and the digital LLRF for the first time. The first test runs with the new software revealed no major problems but only little long term experience could be gained.

In a first step the NRF buncher cavities will be brought into routine operation since their control is much easier due to the higher bandwidth and lower sensitivity to microphonics.

Beam-Based Feedback

In order to take full advantage of a digital controller, an adaptive beam-based feedback algorithm will be implemented after the basic features and the long-term stability have been validated. The system will acquire measurement data from bunch arrival-time monitors (BAM), compression monitors (BCM) and beam energy sensors (Figure 4). This information will be used to stabilize the electron bunches at the target position or at the secondary source (e.g. free electron laser).

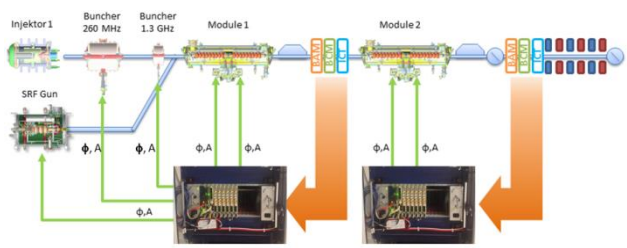

Figure 4: Feedback scheme for ELBE.

The feedback algorithm benefits from the high duty cycle of the CW beam at nominal repetition rate of 13 MHz. Since there is no macro pulse applied the controller can operate in a continuous regime.

CONCLUSION

The ELBE accelerator is in operation since 2001 and provides a CW electron beam for various secondary radiation sources to the users. Future experiments and secondary sources require a higher level of stability. One crucial

ISBN: 978-3-95450-192-2 doi:10.18429/JACoW-IBIC2017-MOPWC02

point is the control of the accelerating RF fields. In order to address this new demand a digital LLRF control has been implemented during the last years.

A crucial point was the data interface between the LLRF server application and the ELBE control system. In collaboration with the experts from DESY and Technische Universität Dresden, a robust solution based on the ChimeraTK framework and the OPC-UA protocol could be developed.

REFERENCES

[1] F. Gabriel, P. Gippner, E. Grosse *et al.*, Nucl. Instrum. Methods Phys. Res., Sect. B 161 – 163, 1143

[2] A.Arnold, H. Büttig, D. Janssen *et al.*, Nucl. Instrum. Methods Phys. Res., Sect. A 57-62, 593

[3] PICMG, https://www.picmg.org/openstandards/microtca/Referenz

[4] M. Grzegrzołka, K. Czuba, I. Rutkowski et al., "MTCA.4 RTM Module for direct sampling based applications", 21st International Conference on Microwave, Radar and Wireless Communications, 2016. 10.1109/MIKON.2016.7492120

[5] MicroTCA.4 for Industry and Research , http://mtca.desy.de/sites/site_mtca/content/e172206/e205636/e212582/e265135/DRTM-DWC8VM1_ Datasheet1_eng.pdf

[6] Struck Innovative Systeme, http://www.struck.de/sis8300-l2.html

[7] ChimeraTK, https://github.com/ChimeraTK

[8] OPC Foundation, https://opcfoundation.org/about/opc-technologies/opc-ua/

[9] open62541, https://open62541.org/

ISBN: 978-3-95450-192-2 doi:10.18429/JACoW-IBIC2017-MOPWC03

COMMISSIONING RESULTS AND FIRST OPERATIONAL EXPERIENCE WITH SwissFEL DIAGNOSTICS

V. Schlott†, V. Arsov, M. Baldinger, R. Baldinger, G. Bonderer, S. Borelli, R. Ditter, D. Engeler, F. Frei, N. Hiller, R. Ischebeck, B. Keil, W. Koprek, R. Kramert, D. Llorente Sancho, A. Malatesta, F. Marcellini, G. Marinkovic, G.L. Orlandi, C. Ozkan-Loch, P. Pollet, M. Roggli, M. Rohrer, M. Stadler, D. Treyer, Paul Scherrer Institut, Villigen, Switzerland

Abstract

SwissFEL is a free electron laser user facility at the Paul Scherrer Institute in Villigen, Switzerland designed to provide FEL radiation at photon energies ranging from 0.2 to 12 keV. Beam commissioning of the hard x-ray line ARAMIS has started in October 2016 and first lasing at 300 eV was achieved in May 2017. First pilot user experiments at photon energies ≥ 2 keV are foreseen for the end of 2017. This contribution comprehends commissioning results and first operational experience of various SwissFEL diagnostics systems, such as beam position monitors, charge and loss monitors as well as transverse profile measurements with screens and wire scanners. It also provides first results from the BC-1 compression monitor and summarizes the status of the electron and laser bunch arrival time monitors.

STATUS OF THE SWISSFEL PROJECT

The compact free electron laser user facility SwissFEL is presently under commissioning at the Paul Scherrer Institut (PSI) in Villigen, Switzerland. In its first project stage, the installation of the hard X-ray branch ARAMIS, which is designed to provide linearly polarized SASE radiation at photon energies between 2 and 12 keV to three user end stations, has been completed and the accelerator has been equipped with all required beam diagnostics systems. The soft X-ray branch ATHOS, which will deliver variably polarized radiation at photon energies between 0.2 and 2 keV, will be realized during a second construction phase during 2018 and 2020. All diagnostics systems for the ATHOS bypass line have been designed and successfully tested and most of the components are already ordered.

Since the delivery schedule for the solid-state modulators of the C-band LINACs drives the SwissFEL commissioning schedule, a staged commissioning approach has been chosen.

- In August 2016 first electrons at beam energies of 7.9 MeV have been generated by the 2 ½ cell S-band photo-injector RF gun and transported to the injector beam dump, including the first successful acceleration through one of the LINAC-1 C-band accelerator modules.
- In November 2016 first beam has been transported through the ARAMIS undulators with achievement of first lasing at 24 nm with moderate beam energies of 345 MeV, just in time for the SwissFEL inauguration ceremony on December 5th 2016.
- After a two months winter shut down, where some final installation and consolidation work was done, first SASE lasing in the nominal SwissFEL wavelength range (0.1 – 5 nm) could be achieved at 4.1 nm mid of May 2017. The electron beam energy was set to 910 MeV at bunch charges of 145 pC and bunch length of 400 fs (rms).

The accelerator set-up for lasing included careful optimization of the RF gun and photo-cathode laser operating points, transverse beam optics measurements and matching in the injector, tuning of the first bunch compressor (BC-1) with the S-band deflecting cavity, implementation of the computed beam optics in the LINACs and undulators and steering of the beam according to the BPM centres. Figure 1 shows the FEL gain curve at 4.1 nm, which was measured with a Neon gas photon intensity monitor.

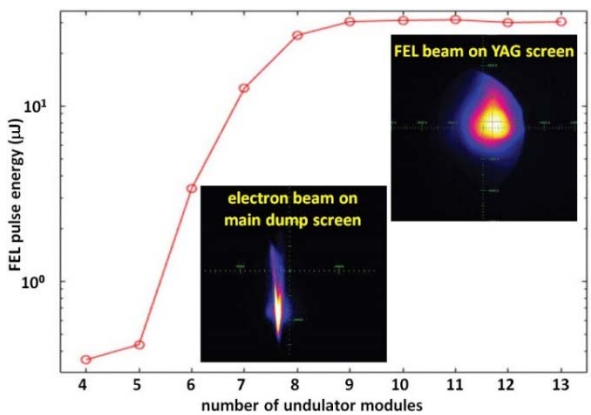

Figure 1: Gain curve for first lasing at SwissFEL at 4.1 nm. The inlets show the FEL beam on an ARAMIS front end YAG screen and the electron beam on the main dump screen monitor (LYSO screen).

After the first lasing attempts, which demonstrated the operability of most of the SwissFEL sub-systems, the commissioning is ongoing, presently focusing on the set-up of the bunch compression stages, beam optics matching and further characterization and calibration of diagnostics systems with beam. With further increase in beam energy by consecutively adding more C-band accelerator stations, a first pilot ("friendly user") experiment at photon energies ≥ 2 keV is envisaged for the end of 2017.

DIAGNOSTICS COMMISSIONING

Although the performance of the diagnostics monitors could be successfully demonstrated at the SwissFEL Injector Test Facility [1] and the front end, data acquisition and

† volker.schlott@psi.ch

ISBN: 978-3-95450-192-2 doi:10.18429/JACoW-IBIC2017-MOPWC03

data processing parts of the measurement systems has been implemented on generic electronics platforms [2, 3], the control system interfaces (e.g. motion control and bunch synchronous data reading) had to be adapted to the newly developed SwissFEL control system standards [4].

Table 1: Beam Diagnostics Devices for ARAMIS

Diagnostics Device	Type	Number
beam position	cavity BPMs	119
transverse profile monitors	scintillator screens	21
	wire scanners	22
	SR-monitors	3
charge monitors	Turbo ICT	4
loss monitors	scintillating (local)	38
	Cerenkov (dist.)	8
dose rate monitors	Rad-FET	32
beam arrival time	electro-optical	4
compression	THz / FIR-vis	1 / 2
laser arrival time	electro-optical	1
transverse deflector	S-band / C-band	1 / 1

Prior to their timely installation in the SwissFEL technical gallery, the final hardware and firmware configurations of the diagnostics systems were calibrated in the laboratory, so that the beam commissioning activities could be supported from the beginning. A list of the ARAMIS beam diagnostics devices is given in table 1.

Beam Position Monitors

A total of 119 cavity beam position monitors (CBPM) with apertures of 38 mm (7), 16 mm (88) and 8 mm (24) have been installed in the SwissFEL ARAMIS branch. All LINAC and transfer line pick-ups, which have to measure two (or more) bunches with 28 ns bunch spacing, are made of stainless steel with a low quality factor ($Q_L \sim 40$) at a working mode frequency of 3.3 GHz, while the undulator pick-ups, which will only be operated in single bunch mode, have been designed with a massive copper core brazed into an outer frame of stainless steel, resulting in a high quality factor ($Q_L \sim 1000$) at a frequency of 4.9 GHz. The BPM electronics uses the same modular digital back end for all BPMs in combination with customized RF front ends, applying IQ down-conversion to baseband for the low-Q CBPM-38 and CBPM-16 and mixing to an IF frequency of 133 MHz for the high-Q CBPM-8. Both, pick-up and electronics designs have been described in more detail in [5, 6, 7, 8, 9, 10].

The laboratory pre-calibration of the BPMs was sufficiently good to provide beam position and charge readings for threading the beam through the accelerator and the ARAMIS undulator into the main beam dump including orbit corrections to a 10 µm level. Beam-based calibration and further optimization by elimination of systematic effects is presently ongoing. The position resolution has been determined to 8 µm * pC for the 3.3 GHz low-Q BPMs and 5 µm * pC for the high-Q 4.9 GHz BPMs, which results to sub-µm resolution at 10 pC bunch charge and a few 100 nm at higher charges. The noise for the charge readings is at 0.07% for the low-Q BPMs and at 0.04% for the high-Q BPMs, which corresponds to 5 fC and 2 fC respectively.

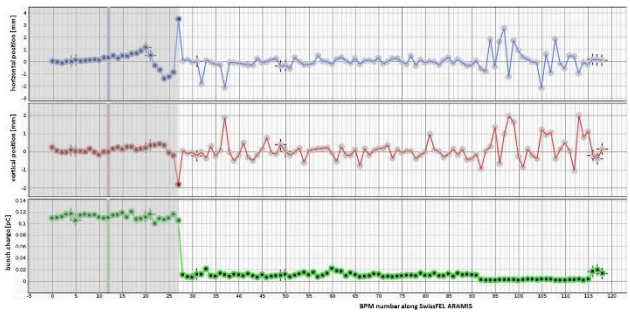

Figure 2: Display of BPM readings along SwissFEL ARAMIS. The beam is transported in the injector beam dump (grey area). Note that the bunch charge is 120 fC. The downstream BPM charge readings (white area) indicate the offset and noise levels of the low-Q CBPM-16 (no. 28 to 91 / 116 to 118) and the high-Q CBPM-8 (no. 92 to 115).

More detailed and elaborated status reports on the SwissFEL BPM commissioning are given in [11, 12]. Figure 2 shows a screen shot of the control room display of the beam position and charge readings for beam transport to the injector beam dump for very low bunch charges of 120 fC.

Charge and Loss Monitors

The charge and loss measurements provided crucial information on beam transmission during the early SwissFEL commissioning phase, where the different accelerator sections were progressively set-up. For the ARAMIS accelerator lines, a total of four Turbo-ICTs with BCM-RF electronics [13] are installed behind locations, where beam loss can occur. The Turbo-ICTs have been absolutely calibrated at the company to a 4 % level [14] and thus used for cross-calibration of the BPM charge readings, which are providing an accurate transmission mapping through the SwissFEL accelerator (lower part of Fig. 2). The Turbo-ICTs single-shot and integrated charge readings (e.g. over one hour) are also used for controlling pre-defined accelerator commissioning modes, where pre-set charge threshold values in the ICT firmware generate interlock signals for the SwissFEL machine protection system (MPS).

The longitudinal beam loss monitors (LBLM), which are based on glass fibres pulled along the accelerator and photo-multiplier read out [15], are also fully integrated in the SwissFEL MPS, providing interlocks and alarms (to the control room), when the beam loss exceeds the pre-defined threshold values. The MPS is then adjusting the bunch repetition rate such that the overall beam loss is kept below an acceptable level.

Screen Monitors

The SwissFEL screen monitors (SCR) have been designed to provide high spatial resolution (≤ 10 µm) for low bunch charges (≤ 10 pC) without being affected by coherent optical transition radiation [16], which is emitted by micro-bunched structures in highly brilliant electron beams. All 21 SCRs in the SwissFEL ARAMIS branch

ISBN: 978-3-95450-192-2 doi:10.18429/JACoW-IBIC2017-MOPWC03

have been equipped with YAG:Ce (Cer-doped Yttrium-Aluminium-Granat) and LYSO (Lutetium-Yttrium –Oxyorthosilicate) scintillators. They have been calibrated and successfully commissioned with the "*CamTool*" application, which provides SCM control and beam synchronous display of beam images. Although, linearity and saturation studies are still ongoing, the SCMs have been integrated in automated emittance measurements, which allow beam optics matching and optimization of different SwissFEL operation modes.

Wire Scanners

The SwissFEL wire scanners (WSC) are equipped with two pairs of wires of different thickness and material: 5 µm tungsten (W) wires for high resolution measurements and 12.5 µm Al(99):Si(1) wires for routine monitoring [17]. During WSC measurements, the wire-fork is continuously moved through the beam by means of a motorized UHV linear-stage, while the wire position is beam synchronously read out with an incremental optical encoder (0.1 µm resolution). Correlation of the encoder read out (wire position by presence of beam) with the signal from a nearby beam loss monitor (BLM) allows the reconstruction of the beam profile. In addition, the position and charge readings of two adjacent BPMs, located upstream and downstream of the WSCs, permits correction of the beam profile measurement by possible error due to charge and position jitter.

Beam commissioning of the overall 22 SwissFEL ARAMIS wire scanners is presently ongoing. Apart from a basic functionality check of all sub-systems, it includes the selection of the most suitable BLM and its PMT gain settings for the different SwissFEL operation modes with 10 pC up to 200 pC bunch charges [18].

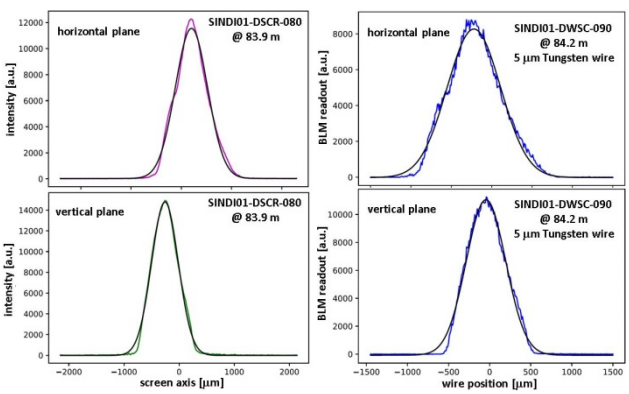

Figure 3: Comparison of transverse beam profile measurements with a LYSO screen monitor (left side) and an adjacent wire scanner (right side) in the SwissFEL injector at a bunch charge of 20 pC.

Comparative beam profile measurements with a wire scanner (5 µm tungsten) and a near-by screen monitor (LYSO scintillator) at bunch charges of 20 pC are shown in Fig. 3. After considering the differences in the β-functions at the locations of the screen and the wire scanners and correcting for the transverse beam jitter of ~ 4 µm (rms) during the WSC measurements by including the adjacent BPM readings in the profile analysis (charge variations were negligible), a horizontal rms beam size of 327 µm ± 3 µm and a vertical rms beam size of 238 µm ± 2 µm could be obtained with the wire scanner, which is in good agreement with the rms profiles measured with near-by SCM of σ_h = 319 µm ± 3 µm and σ_v = 240 µm ± 2 µm.

BC-1 Compression Monitor

The proper set-up of the first SwissFEL bunch compression stage (BC-1), which has been designed to provide nominal rms bunch lengths of a few hundred femto-seconds (223 fs at 10 pC bunch charge and 290 fs for 200 pC), is observed by a compression monitor (BCM), which uses coherent edge radiation (CER) from the 4th BC-1 bending magnet. The THz intensity is split into two signal paths, which are equipped with two different high-pass filters at 0.3 and 0.6 THz and broadband Schottky diodes, covering the whole spectral range of interest (0.3 - 2 THz). Relative CER intensity variations, which correspond to bunch length or bunch profile changes, are related to the amplitude and phase settings of the off-crest operated S-band (SINSB-03, SINSB-04) RF stations and the X-band (SINXB-01) linearizer at the end of the SwissFEL injector (upstream of BC-1).

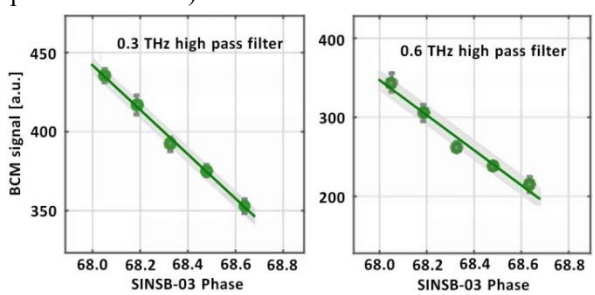

Figure 4: BCM output signals with respect to the phase settings of the off-crest operated S-band structure SINSB-03. Left side: CER signal path equipped with a 0.3 THz high-pass filter, right side: 0.6 THz high-pass filter.

In preparation of the first systematic bunching studies, the BCM signals were optimized by aligning the CER optical paths to the selected BC-1 compression angle and by eliminating initial ringing of the Schottky diode signals with THz absorption material in the BCM chamber. For determination of the BCM sensitivity on electron bunch length changes, the BC-1 compression factors were scanned between 4 and 4.4 (the nominal BC-1 compression factor for SwissFEL user operation will be set to 10) by using an automated "compression scan tool" [19]. It varies the off-crest phases of the last two S-band structures in the injector (SINSB-03 and SINSB04) simultaneously, while keeping the beam energy constant through readjustment of the SINSB03 and SINSB04 RF amplitudes. For this BCM commissioning run, the X-band linearizer phase was kept constant. During the compression factor scans the electron bunch length was measured with the S-band deflecting cavity, which is located directly behind BC-1. It varied between 560 and 610 fs (rms). In parallel, the BCM outputs

ISBN: 978-3-95450-192-2 doi:10.18429/JACoW-IBIC2017-MOPWC03

from both CER signal paths were recorded for different phase settings of the off-crest operated S-band structures around 68° (90° corresponds to on-crest acceleration). The BCM signals with respect to the SINSB-03 phase settings are shown in Fig. 4.

From the first commissioning shifts, it can be concluded, that the BCM sensitivity with respect to the SINSB-03 phase settings is already close to the resolution, which will be required to monitor and stabilize the off-crest S-band phases in case of the nominal operation of the first SwissFEL compression stage. The grey areas around the measurement points of the SINSB-03 phase scan in Figure 2 indicate a BCM phase sensitivity of 0.03° for the CER optical path with the 0.3 THz high-pass filter and 0.05° for the optical path equipped with the 0.6 THz high-pass filter. Further BCM studies are foreseen after the SwissFEL summer shut-down to optimize the THz filters to the nominal compression factors of BC-1 such that bunch length changes caused by S-band phase fluctuations as well as bunch shape variations caused by phase jitter of the X-band linearizer can be detected.

Electron Bunch Arrival Time Monitor

Key components of the bunch arrival time monitor (BAM), which was already successfully tested at the SwissFEL Injector Test Facility [20, 21], were subject to improvements, aiming for sub-10 fs resolution at low (10 pC) bunch charges. In addition, adaptations of the original design, accounting for space limitations and newly developed controls hardware for SwissFEL were made and the BAM user interface and data readout, including automated stabilization and control applications was improved for more user-friendly operation form the control room. Details on the latest SwissFEL BAM design are reported in [22]. For the first phase of the ARAMIS commissioning, two BAM stations have been installed so far. Beam commissioning is foreseen for September 2017 in view of the first "pilot user experiments", where the electron beam arrival time information will be taken into account for improving the overall time resolution.

Gun Laser Arrival Time Monitor

A balanced optical cross correlator (BOXC) based on two LBO crystals in type II phase matching and in collinear arrangement (single colour of 1040 nm, orthogonal polarization) is employed to measure the arrival time of laser pulses at the gun laser amplifier output against the oscillator pulses, which act as a local time reference. The resulting error signal gives the single shot variation in arrival time and in closed loop operation feeds back to a continuously variable optical delay stage to compensate for drift in the amplifier and in free space path caused by changes of environmental parameters like e.g. temperature and humidity (controlled to 24°C ± 0.1°C and 42.5% ± 2.5%) as well as air pressure (unregulated). With laser arrival time feedback on, the amplifier output is stabilized to below 10 fs rms (or < 50 fs peak-peak) over 1000 shots as shown in Fig 5. Without the arrival time feedback running, drifts in excess of 12 ps over 24h have been observed.

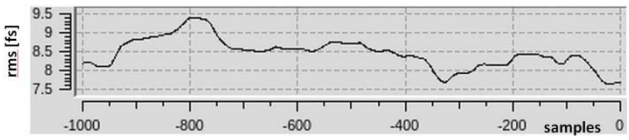

Figure 5: Display of SwissFEL gun laser stability behind its amplifier (1000 shots) with running IR/IR LAM feedback based on a BOXC.

This laser arrival time feedback loop includes the regenerative optical amplifier with an integrated optical path length of 1.3 km that is significantly longer than the combined remaining optical path for the UV generation and transfer line from the laser output to the photo-injector gun in the accelerator tunnel. Thus, the most significant sources of drift are already compensated with this BOXC-based IR/IR LAM feedback.

As in the current configuration the IR to UV conversion stage, the pulse-stacking scheme and the transfer line to the gun cathode are still out of loop, a UV/IR laser arrival time monitor (LAM) located next to the gun photocathode will be set-up in a next step to measure the UV pulses (260 nm) from the gun laser directly against the optical reference (1560 nm), which is delivered to the LAM location via a stabilized optical link. This LAM upgrade will include the entire gun laser chain (oscillator locked against the optical master oscillator, amplifier, UV conversion, pulse stacking and optical transfer line to gun photo cathode). The feedback will then provide the required SwissFEL gun laser stability of 40 fs (rms) for stable user operation.

SUMMARY AND OUTLOOK

Timely installation, pre-beam commissioning and precise laboratory calibration have made the SwissFEL ARAMIS diagnostics monitors valuable systems for beam property measurements since the first day of operation and supported beam optics commissioning as well as the first successful lasing attempts at SwissFEL. So far, all diagnostics systems fulfil or exceed the SwissFEL requirements, although improvements of absolute charge readings in case of the Turbo-ICTs and saturation studies of screen monitors are still pending but foreseen for the near future. More elaborate studies of systematic effects and limitations of the diagnostics monitors will be carried out side by side with the ongoing beam commissioning of all SwissFEL operation modes, so that the implementation of beam-based feedbacks should be possible in time for the start of the nominal user operation.

ACKNOWLEDGEMENTS

The timely provision and successful commissioning of the SwissFEL diagnostics systems has of course been a collaborative effort of the Diagnostics Section together with many other groups at PSI. Without explicitly naming individual people, we would like to thank many of our colleagues in the divisions of mechanical engineering, vacuum, electrical infrastructure, planning and installation, controls, beam dynamics and operations.

ISBN: 978-3-95450-192-2 doi:10.18429/JACoW-IBIC2017-MOPWC03

REFERENCES

[1] R. Ischebeck *et al.*, "Instrumentation Activities at the SwissFEL Injector Test Facility", *Proc. IBIC 2013*, Oxford, UK, 12 (2013).

[2] C. Ozkan Loch *et al.*, "System Integration of SwissFEL Beam Loss Monitors", *Proc. IBIC 2015*, Melbourne, Australia, 170 (2015).

[3] W. Koprek *et al.*, "Overview of Applications and Synergies of a Generic FPGA-based Beam Diagnostics Electronics Platform at SwissFEL, *Proc. IBIC 2015*, Melbourne, Australia, 165 (2015).

[4] M. Janousch *et al.*, "Overview and Status of the SwissFEL Project", *Proc. ICALEPS 2015*, Melbourne, Australia, 1169 (2015).

[5] B. Keil *et al.*, "Status of the SwissFEL BPM System", *Proc. IBIC 2015*, Melbourne, Australia, 497 (2015).

[6] B. Keil *et al.*, "Design of the SwissFEL BPM System", *Proc. IBIC 2013*, Oxford, UK, 427 (2013).

[7] F. Marcellini *et al.*, "Design of Cavity BPM Pickups for SwissFEL", *Proc. IBIC 2012*, Tsukuba, Japan 390 (2012).

[8] M Stadler *et al.*, "Development of the SwissFEL Undulator BPM System", *Proc. IBIC 2014*, Monterey, USA, 675 (2014).

[9] B. Keil *et al.*, "Beam-Based Calibration and Performance Optimization of Cavity BPMs for SwissFEL, E-XFEL and FLASH2", *Proc. IBIC 2014*, Monterey, USA, 665 (2014).

[10] M. Stadler *et al.*, "Low-Q Cavity BPM Electronics for EXFEL, FLASH-II and SwissFEL", *Proc. IBIC 2014*, Mon terey, USA 670 (2014).

[11] B. Keil *et al.*, "First Beam Commissioning Experience with the SwissFEL Cavity BPM System", *Proc. IBIC 2017*, Grand Rapids, USA, TUPCF17.

[12] M. Stadler *et al.*, "The SwissFEL High-Q Undulator BPM System", *Proc. IBIC 2017*, Grand Rapids, USA, TUPCF18.

[13] S. Artinian *et al.*, "Goubau Line and Beam Characterization of Turbo-ICT for SwissFEL", *Proc. IPAC 2013*, Shanghai, China, 476 (2013).

[14] F. Stulle and J. Bergoz, "Turbo-ICT Pico-Coulomb Calibration to Percent Level Accuracy", *Proc. FEL 2015*, Daejeon, Korea, 118 (2015).

[15] C. Ozkan Loch *et al.*, "System Integration of SwissFELBeam Loss Monitors", *Proc. IBIC 2015*, Melbourne, Australia, 170 (2015).

[16] R. Ischebeck *et al.*, "Transverse Profile Monitors for SwissFEL", *Proc. IBIC 2014*, Monterey, USA, 259 (2014).

[17] G.L. Orlandi *et al.*, "Design and Experimental Tests of Free Electron Laser Wire Scanners", *Phys. Rev. Special Topics Accelerators and Beams*, 19, 092802 (2016).

[18] G.L. Orlandi *et al.*, "First Experimental Results of the SwissFEL Wire-Scanners", *Proc. IBIC 2017*, Grand Rapids, USA, WEPCC16 (2017).

[19] I. Zagorodnov and M. Dohlus, "Semianalytical modelling of multistage bunch compression with collective effects", *Phys. Rev. Special Topics - Accelerators and Beams*, 14, 014403 (2011).

[20] V. Arsov *et al.*, "First Results from the Bunch Arrival Time Monitor at the SwissFEL Test Injector", *Proc. IBIC 2013,* Oxford, UK, 8 (2013).

[21] V. Arsov *et al.*, "Commissioning and Results from the Bunch Arrival-Time Monitor Downstream of the Bunch Compressor at the SwissFEL Injector Test Facility", *Proc FEL 2014*, Basel, Switzerland, 933 (2014).

[22] V. Arsov *et al.*, "Design and Commissioning of the Bunch Arrival-Time Monitor for SwissFEL", *Proc. IBIC 2017*, Grand Rapids, USA, TUPCC15 (2017).

ISBN: 978-3-95450-192-2 doi:10.18429/JACoW-IBIC2017-MOPWC05

ATF FACILITIES UPGRADES AND DEFLECTOR CAVITY COMMISSIONING*

C. Swinson†, M. Fedurin, M. A. Palmer, I. Pogorelsky, Brookhaven National Lab, NY, USA

Abstract

The Accelerator Test Facility (ATF) at Brookhaven National Lab is an Office of Science user facility focusing on advanced acceleration techniques. It houses several electron beamlines synchronized to high power lasers, including a TW-class carbon dioxide (10 μm) laser. Here we outline ongoing upgrades to both the accelerator and laser systems, give a brief overview of the experimental landscape, and report on the recent commissioning of a newly installed X-band deflector cavity [1]. The deflector cavity is implemented as a longitudinal electron beam diagnostic, which will allow us to measure the structure of ultra-short bunches.

INTRODUCTION

The mission of the ATF is to provide the advanced accelerator community with state-of-the-art facilities and scientific support. We also host beam instrumentation and transport R&D, laser research, and materials/condensed matter physics programs. Figure 1 highlights the major components of the ATF complex.

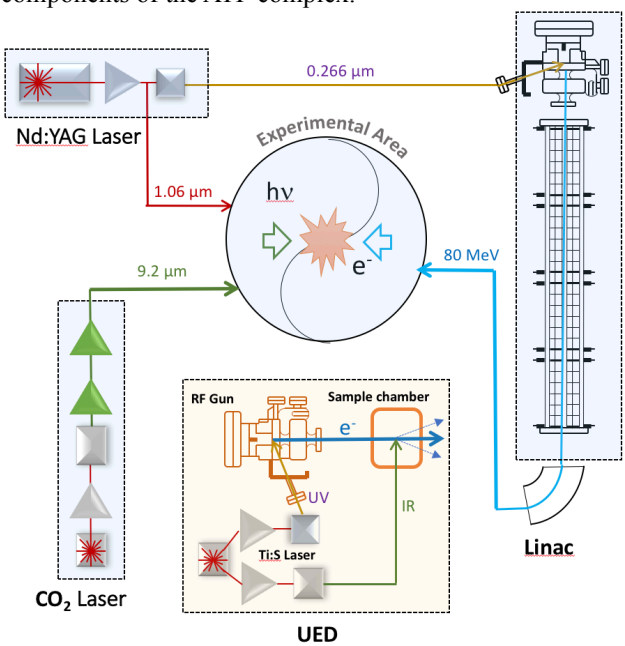

Figure 1: Schematic of the ATF, featuring the four ma-jor components. We plan to add a strong field laser to the ATF portfolio, in the near future.

* The ATF is a U.S. Department of Energy, (DOE) Office of Science User Facility operated for the DOE, Office of Science by Brookhaven National Laboratory under Contract No. DE-AC02-98CH10886

†cswinson@bnl.gov

PRESENT STATUS

The ATF is presently hosting a full user program. Table 1 shows the presently available electron beam parameters at the ATF. A maintenance program, currently underway and continuing over the next few months, will allow us to routinely reach the highest achievable beam parameters. This paper outlines upcoming R&D, designed to expand the CO_2 laser parameter space, shown in Table 2.

Table 1: Presently Electron Beam Parameters at ATF

Beam Property	Nominal	Best Achievable
Energy (MeV)	57	80
Rep. Rate (Hz)	1.5	3
IP Beam Size (μm)	50	5
Bunch Charge (nC)	0.01-1.5	3

Table 2: Present CO_2 Laser Parameters

Laser Property	Value
Energy (J)	7
Pulse length (ps)	3.5
Power (TW)	1.5
Power delivered IP (TW)	0.5
Rep. Rate (Hz)	1/20

Accelerator Improvements

The ATF is presently undergoing a program of accelerator improvements aimed at improving RF stability and beam reproducibility. Alongside such improvements, we report the recent commissioning of an X-band deflector cavity as a longitudinal bunch diagnostic, and a focus on providing <100 fs long electron bunches through magnetic bunch compression.

X-band Deflector Commissioning

An X-band (11.4 GHz), Traveling Wave, Deflection Mode Cavity [2] for Ultra-Fast Beam Manipulation and Diagnostics (fig. 2), developed and manufactured by Radiabeam Technologies, was recently installed in one of the ATF experimental beam lines. The system has been commissioned and has already been utilized by two user groups.

An initial estimate of time resolution showed better than 10 fs. This was done by using a microbunched beam of known spacing, produced using a mask technique [3]. The microbunched beam was used to calibrate a yag crystal screen downstream of the deflecting cavitiy. The measurement was limited by the resolution of the beam profile monitor camera.

ISBN: 978-3-95450-192-2 doi:10.18429/JACoW-IBIC2017-MOPWC05

The X-band system was recently used in measuring the length of a compressed electron bunch to be used as a drive bunch for beam-driven plasma wakefield research. The aim, to observe the effect of the plasma on the energy spread of the bunch. During the user experiment, data was taken to calibrate the deflection. The streak was calculated to be 1.04 μm/fs yielding a resolution measurement of 105 fs, for this optic [4].

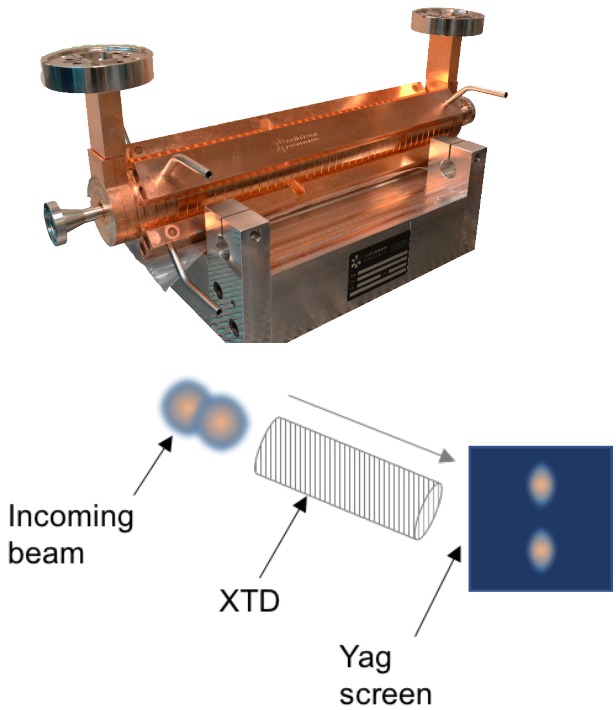

Figure 2: X-band deflector cavity (XTD), before installation in the ATF beamline (top). Layout of initial measurement using micro-bunched beam (bottom).

The next step for this plasma experiment is to optimize the beam optic for small transverse beam size at the downstream profile screen, to improve the time resolution, as in equation (1) [5]. This, while preserving the beam size at the plasma interaction point.

$$\Delta t = \sigma_y \frac{2mc^2\gamma}{L\omega eV_t} \qquad (1)$$

where Δt is the time resolution, σ is the transverse beam size, ω is the cavity resonant frequency, and V_t is the transverse voltage.

Figure 3 shows a plot of measured deflection for various deflector phase settings, as recorded for the plasma exper-iment.

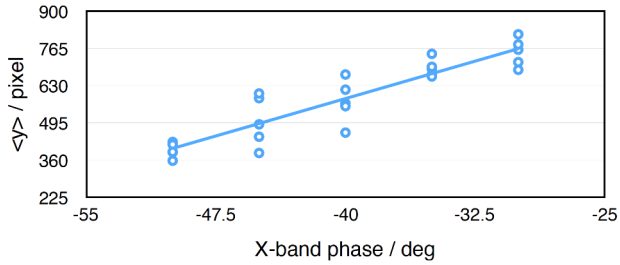

Figure 3: Plot of transverse beam size vs X-band RF phase.

Near-Term CO_2 Laser Upgrade

A staged upgrade in laser power is ongoing and in-place at the current ATF location, with a view to move to the new complex in the next few years. Figure 4 shows the layout of the near-term upgrade plan for the CO_2 laser system.

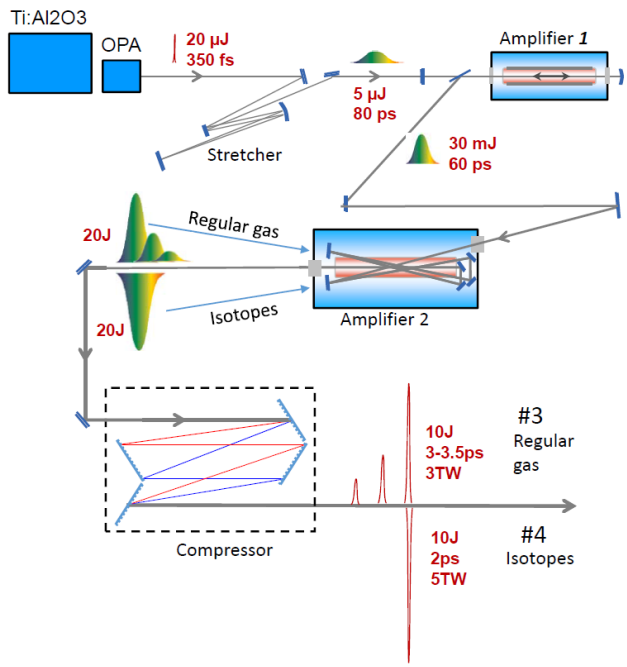

Figure 4: Layout of the near-term upgrade for the CO_2 laser system. The goal is to provide 3-5 TW peak power over the next few years.

The laser system currently has a full program of research in Compton scattering, inverse free electron lasers (IFEL), laser-plasma interactions (such as ion acceleration by shock wave and laser-wakefield acceleration), investi-gation of lasers in air, interaction with materials, etc.

Addition of UED to the ATF Complex

As a part of the ATF-II complex, an Ultrafast Electron Diffraction (UED) facility has been assembled and commissioned [6]. This resource will serve materials science and condensed matter physics users, and as a test bed for UED machine R&D.

ISBN: 978-3-95450-192-2 doi:10.18429/JACoW-IBIC2017-MOPWC05

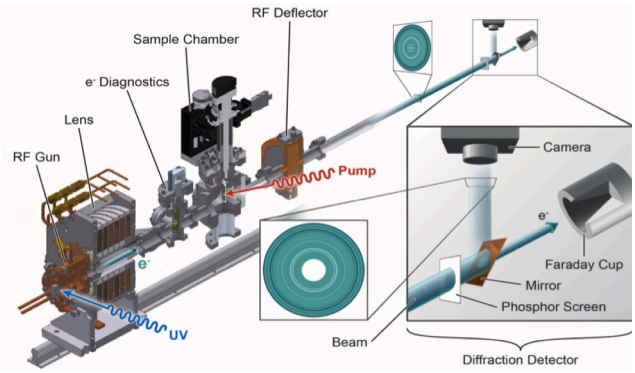

Figure 5: UED beamline layout. Allows observation of ultrafast processes, for example, as a material goes from an excited state (pumped by an IR laser) to the ground state.

Figure 5 shows the facility layout where there is presently one active R&D experiment, three active materials exper-iments and two more upcoming experiments. For this new facility, all users are presently internal BNL groups and we will begin considering outside proposals in 2018.

FUTURE UPGRADES

An upgrade to ATF-II is planned, including relocation of the facility to provide more experimental space and further upgrade of the CO_2 laser to > 5 TW [7]. The new ATF complex will also include a strong field laser (SFL) and an Ultrafast Electron Diffraction (UED) facility. The UED is already commissioned and serving, materials science and accelerator R&D, users at the ATF-II location. We plan to begin work on the strong field laser in the next year.

Longer-Term CO_2 Laser Upgrade

In the longer-term, laser operations will be transferred to the new site where further upgrades will take place. The first part of the plan is to increase peak power, be-yond 5 TW, by introducing additional amplification via the gas medium. Figure 6 shows the new amplifier discharge vessels along-side the present ATF setup.

Figure 6: Gas amplifier vessel, working at the ATF (top) and newly acquired vessels ready for construction of the new amplification system, to be implemented at the ATF-II.

SUMMARY

A large upgrade program is underway at the ATF, with multiple thrusts and the goal of providing users with high-quality, high-brightness electron beams and high-quality, high-power lasers. We hope to open up the landscape for electron-laser interaction research, focussing on utilizing the unique 10 μm laser system.

ACKNOWLEDGMENT

Thanks, should go to the design and commissioning teams for the X-band deflecting cavity and to our users for their support. Also, special thanks to Richard D'Arcy (DESY) and Gerard Andonian (Radiabeam) for taking the time to process preliminary data.

REFERENCES

[1] L. Faillace *et al.*, in *Proc. IPAC2'010*, pp. 1206-1208.
[2] R. Agustsson *et al.*, in *Proc. IPAC'2012*, pp. 3389-3391.
[3] P. Muggli *et al.*, Phys Rev Lett, 101(5), pp. 054801 (2008).
[4] R. D'Arcy *et al.*, Internal note.
[5] G. Burt, CERN-2011-007, pp. 395-405.
[6] M. Fedurin *et al.*, in *Proc. IPAC'2017*, pp. 554-556.
[7] I. V. Pogorelsky *et al.*, NIM A 829, 432–437, 2016.

ISBN: 978-3-95450-192-2 doi:10.18429/JACoW-IBIC2017-MOPWC06

BEAM DIAGNOSTICS FOR NEW BEAM TRANSPORT LINE OF PF-AR

R. Takai*, T. Honda, T. Obina, M. Tadano, H. Sagehashi,
KEK Accelerator Laboratory and SOKENDAI, 1-1 Oho, Tsukuba, Ibaraki, Japan

Abstract

The beam transport line (BT) for the Photon Factory Advanced Ring (PF-AR), which is a 6.5-GeV light source of KEK, has been recently renewed. The new BT dedicated to PF-AR allows not only simultaneous operation with the SuperKEKB storage ring, which has a much shorter Touschek lifetime, but also the top-up operation via 6.5-GeV full-energy injection. The construction, including tunnel excavation, was completed by the end of 2016, and the commissioning was performed for one month from February 2017. Standard beam monitors, such as stripline beam position monitors, screen monitors, beam loss monitors, and fast current transformers are installed in the new BT and contribute greatly to accomplishing the commissioning in a short period of time. This paper discusses details of these monitors and some commissioning results obtained by using them.

INTRODUCTION

The Photon Factory Advanced Ring (PF-AR), which is a 6.5-GeV electron storage ring of KEK, is a dedicated light source for generating pulsed hard X-rays. The beam transport line (BT) for injecting electron beams to PF-AR has been renewed recently [1]. Before the renewal, the continuous injection for KEKB, which is an electron-positron collider of KEK, had to be interrupted for about 15 min at each injection for PF-AR, because a part of the BT was shared with it. Following the upgrade of KEKB to SuperKEKB, the Touschek lifetime is shortened to ~10 min [2]; therefore, such interruptions should be avoided. This is the main reason why the dedicated BT for PF-AR was constructed. The principal parameters of PF-AR are listed in Table 1.

Table 1: Principal Parameters of PF-AR

Beam Energy	6.5 GeV
Max. Stored Current	60 mA
RF Frequency	508.57 MHz
Circumference	377.26 m
Harmonic Number	640
Number of Bunches	1
Revolution Frequency	795 kHz
Tunes (x/y/s)	10.17/10.23/0.05
Damping Time (x/y/s)	2.5/2.5/1.2 ms
Natural Emittance	294 nm rad
Natural Bunch Length	18.6 mm (62 ps)
Max. Injection Frequency	12.5 Hz
Operation Mode	Decay
Number of Stations	8

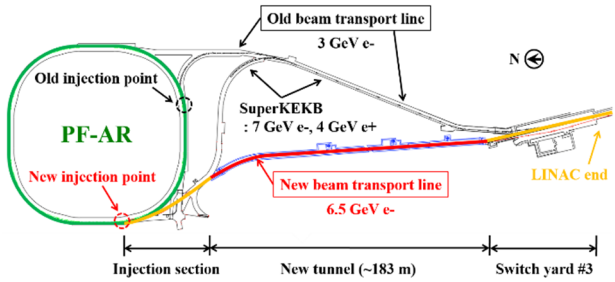

Figure 1: Schematic view of the old and new BTs for PF-AR. The total length of the new BT, from the LINAC end to the new injection point, is about 320 m.

The construction was started in FY2013, followed by the excavation of the new BT tunnel, the development of infrastructure in the tunnel, and the design and production of the required BT components sequentially. The final construction works, such as the deconstruction of the old BT, the relocation of magnets to be reused, the installation of the new BT components, and the reconstruction of the new injection point of PF-AR were proceeded in parallel for seven months from July 2016 to January 2017, and completed on schedule. Following these, the commissioning of the new BT was started and the necessary preparation to resume the user operation could be made in about one month. The new BT is designed for 6.5-GeV full-energy injection and enables not only the simultaneous operation with SuperKEKB but also top-up operations in near future. Besides, it resolves the difficult problems with stacking and accelerating of the 3-GeV short-bunch beam, such as the beam loss due to severe beam instabilities and the heat generation of beam ducts.

In this paper, we describe the beam monitors installed in the new BT for PF-AR in detail and some commissioning results obtained by them.

BEAM MONITORS FOR THE NEW BEAM TRANSPORT LINE OF PF-AR

Figure 1 shows a schematic of the old and new BTs for PF-AR. The new BT is about 320 m long and can be classified into three main sections: Switch Yard #3 for distributing beams to the lower rings at the end of LINAC (SY3), the new BT tunnel dedicated for PF-AR, and the beam injection section connected to the new injection point at the southwestern part of the ring after crossing the existing BT for SuperKEKB. The beam monitors installed in the new BT are listed in Table 2. As the three sections are separated from each other, the control systems of these monitors are arranged sporadically in several local control rooms (LCRs), and the output signals from each monitor are collected through the control network after being digitized at

* ryota.takai@kek.jp

ISBN: 978-3-95450-192-2 doi:10.18429/JACoW-IBIC2017-MOPWC06

the closest LCR (except for GigE cameras for screen monitors that are directly connected to the network). The details of each monitor, listed in Table 2 are as follows.

Table 2: List of PF-AR Beam Monitors

Monitor	Function	Quantity
BPM (Stripline)	Position, Charge	21
SCM (Al_2O_3:Cr)	Position, Profile	17
BLM (CsI:Tl + PMT)	Loss	7
CT	Charge, Timing	2

BPM (Beam Position Monitor)

Twenty-one stripline BPMs are installed in the new BT. Four electrodes are arranged so as to be inscribed in the beam duct of an inner diameter of 52 mm at an angle of 45° around the beam axis. The electrode length is 175 mm except for one BPM, where the electrode length is 125 mm, installed in the upper injection section due to limited installation space. As a result, the frequency, which gives the maximum sensitivity of electrodes becomes approximately an odd multiple of 430 MHz. The electrode thickness is 2 mm, and the width is fixed such that the opening angle relative to the beam axis is 45°. The characteristic impedance of each electrode is designed to be 50 Ω in order to suppress the reflection of beam signals. The electrode end at the lower side is grounded through a common spacer ring. Beam signals induced on the electrode are extracted to the outside through an SMA feedthrough (Kyocera, SMA-R), welded at the upper end of the electrode. The coefficient of the difference-over-sum ratio (an inverse of the position sensitivity coefficient) is 21.0 mm, based on the calculation using CST Particle Studio [3]. The difference-over-sum ratio obtained is approximately proportional to the beam position in the range of –8 to 8 mm from the beam axis. Figure 2 shows a schematic of the BPM head and its photograph after the installation.

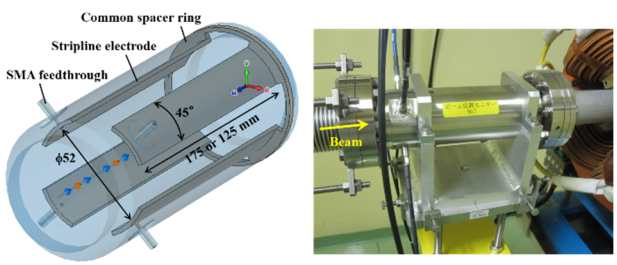

Figure 2: Schematic and photograph of the stripline BPM.

To detect beam signals, we use a log detection circuit originally developed for the compact energy recovery linac (ERL) [4]. The circuit has a band pass filter with a center frequency of 1.3 GHz, a bandwidth of 20 MHz, and a log-linear response to the input power in the range of –90 to –30 dBm, when the front-end attenuator is set to 0 dB. The detected beam signals are digitized by a 12-bit data acquisition unit (Yokogawa, SL1000) and then, the average amplitudes are used in the position calculation. This calculation is performed on the software IOC of the EPICS control system [5]. The transverse positions and charges (the sum of four output signals) of the injected beams measured by all BPMs are displayed on an orbit monitoring panel and updated synchronously with the beam trigger signals. Figure 3 shows a photograph of the inside of the log detection circuit.

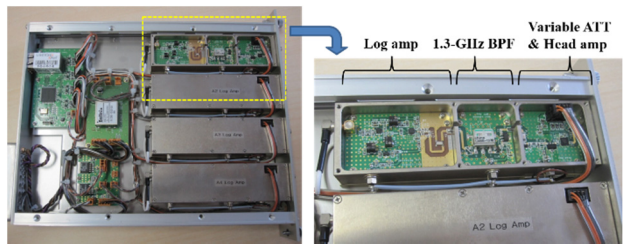

Figure 3: Photograph of the inside of the log detection circuit. The four circuits constitute one NIM module.

SCM (Screen Monitor)

Seventeen SCMs with a scintillating screen are used in the new BT. The internal structure is different between 14 SCMs above the DC septum magnet at the new injection point and the other three SCMs. In the former 14 SCMs, the screen is inserted downward at an angle of 45° to the beam axis and directly observed by a GigE camera (Allied Vision Technologies, Prosilica GC650), which is installed in a cylindrical dark box serving also as a support frame for the SCM duct. In the latter three SCMs, the screen is inserted sideways at an angle of 45° and observed by a camera via a mirror, which are installed in a dark box independent of the support frame. The screen material is a 1-mm-thick alumina scintillator (Desmarquest, AF995R). Four holes of 1-mm-diameter, each located at the peripheral parts of the screen are used for the focus adjustment and the magnification calibration of the imaging optics. A low-distortion CCTV lens with a diaphragm is used with the camera and the magnification is set such that the whole screen area of 30 mm × 30 mm fits within the CCD area. The gain and exposure time of the camera are adjusted carefully to prevent the saturation of the 12-bit CCD pixels. Each camera located around the new injection point, where an especially large amount of beam loss is predicted, is surrounded by a 2-mm-thick lead sheet to protect them from radiation-induced damage. In addition, all of the cameras can be rebooted remotely in case they are frozen due to

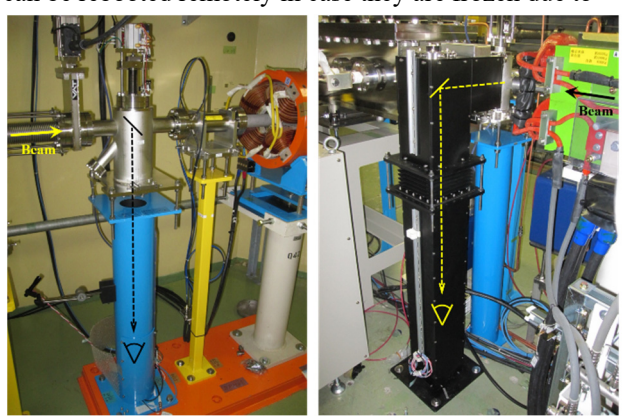

Figure 4: Photographs of the two types of SCMs.

ISBN: 978-3-95450-192-2 doi:10.18429/JACoW-IBIC2017-MOPWC06

noise caused by the pulse magnets for beam injection. Figure 4 shows the photographs of the two types of SCMs mentioned above.

The screen image is transferred to IOC for image processing through an Ethernet cable and displayed on each monitoring panel with the results from Gaussian fitting. Synchronizing the screen insertion timing with the start timing of data acquisition can restrict network bandwidth. An automatic measurement program to store the screen image while inserting the screen from the upper side one-by-one, is also provided and used to compare the injected beam profiles with the previous ones. Figure 5 shows a sample of the profile list captured by the automatic program.

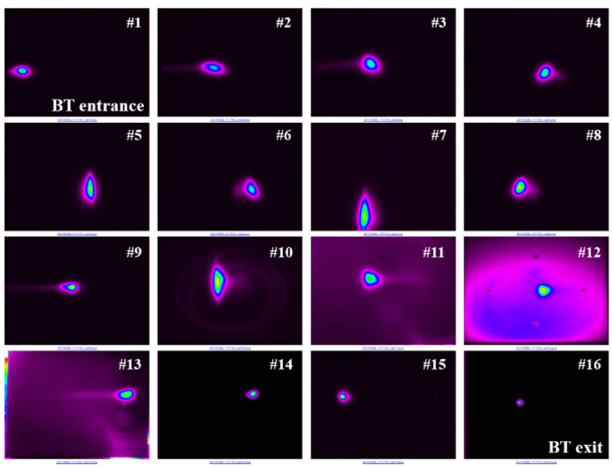

Figure 5: Injected beam profiles along the new BT measured by the SCMs. Data of the last SCM#17 are missing due to an insufficient adjustment of the camera optics.

BLM (Beam Loss Monitor)

Seven BLMs are used to detect radiations caused by the injected beam loss. They are installed at almost equal spacing along the new BT, and used to reduce the local beam loss during injections. At present, they are not included in an interlock system for radiation safety. The detection unit consists of a thallium-doped CsI scintillator and a small photosensor module with a built-in photomultiplier tube and a high voltage power supply (Hamamatsu, H10721). Although the time response of this scintillator is longer than that of a pure CsI scintillator, the sensitivity for the beam loss is higher because of the larger photon yield. Furthermore, since this unit is compact and inexpensive, it can be easily installed and extended. Output signals of the BLM are digitized by a general-purpose data acquisition unit similarly to that of the BPM. A power supply and gain of the photosensor module can be remotely controlled through the network. Figure 6 shows photographs of the detection unit.

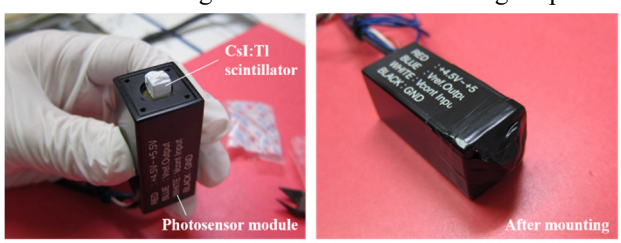

Figure 6: Photographs of the BLM detection unit. The CsI:Tl scintillator is mounted in front of a photoelectric surface of the photosensor module and light-shielded by a black polyester tape.

CT (Current Transformer)

Two CTs are provided at both ends of the new BT, one at each end. The transport efficiency of injected beams can be measured by comparing the area of their output signals. The entrance CT is included in an interlock system to limit the charge of the injected beams, and the exit CT is also used to adjust the timing of the pulse magnets for beam injection. A commercial CT is used, including a ceramic gap to prevent the wall-current flow and a wall-current bypass serving as the RF shield (Bergoz, In-flange ICT). Output signals are processed by a fast oscilloscope or a dedicated circuit attached to the sensor head. Figure 7 shows a photograph of the exit CT.

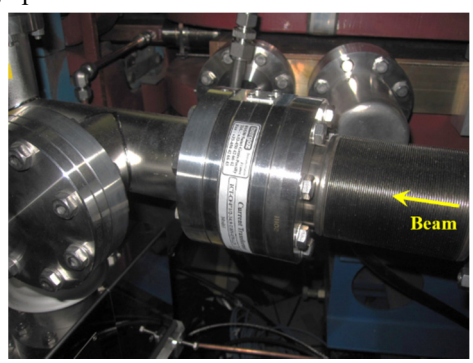

Figure 7: Photograph of the in-flange ICT installed near the exit of the new BT.

COMMISSIONING RESULTS

The beam monitors described in the previous section contributed greatly to accomplish the new BT commissioning in a short period of time. Two experimental results obtained with them during the commissioning are presented here.

The first data is the capture efficiencies of the respective injected beams measured by using the CT. Under the injection frequency of 1 Hz, the change in the capture efficiency during beam injection was investigated by comparing each beam charge with the corresponding increment of the stored current of PF-AR. Although the beam charge was initially supposed to be measured by the entrance CT, the sum of four output signals of a BPM located at the LINAC end, which was calibrated by another CT, was used instead because the entrance CT output was unreliable due to noise from nearby pulse magnets. The transport efficiency of injected beams was almost 100%, confirmed by using the calibrated BPM and the exit CT. The increment of the stored current was measured from the broadband output of a DC current transformer (DCCT) installed in the ring. The result is shown in Fig. 8. The horizontal axis indicates the

ISBN: 978-3-95450-192-2 doi:10.18429/JACoW-IBIC2017-MOPWC06

identification number of the successively performed measurements, and corresponds to the time of a second unit because of the 1-Hz injection. The left and right vertical axes indicate the capture efficiency of the injected beams and the stored current of the ring, respectively. During this measurement, beam charges injected from LINAC were stable at around 0.24 nC/pulse. The average of the measured capture efficiencies was approximately 85%, whereas it decreased slightly as the stored current increased. In the case of the 5-Hz injection, the averages of the injected beam charges and the capture efficiencies decreased to 0.23 nC/pulse and 83%, respectively. This measurement of the capture efficiency could also be utilized effectively for adjustments of the injection phase and the timing of the pulse magnets for beam injection.

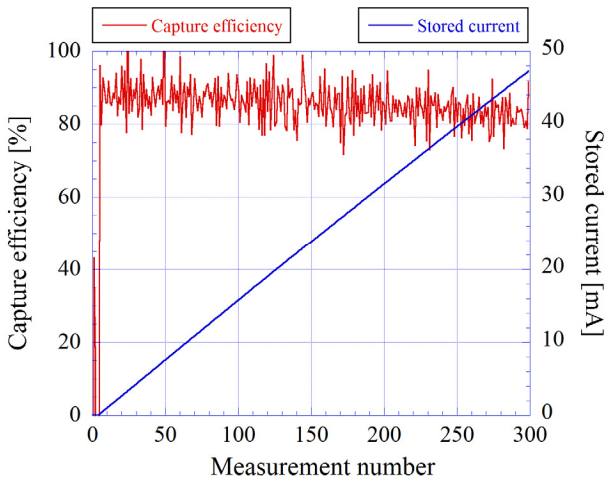

Figure 8: PF-AR capture efficiency measured by using the calibrated BPM and a DCCT for the ring.

The second data is the injected beam loss for every turn measured by using the BLM. As the camera of SCM#15 located between the DC septum magnet and the pulse septum magnet #1 (S1) deteriorated in a shorter period than the other ones, the beam loss was measured by the BLM unit installed under the S1 support frame. The results measured by an oscilloscope are shown in Fig. 9. The horizontal and vertical scales were respectively fixed at 1 μs/div and 20 mV/div, and it was confirmed in advance that a noise floor due to the stored beam loss was negligibly small. The upper figure is a result with no inserted screens. It can be seen that a portion of the injected beam was lost even under this condition, although only slightly. The lower figure is a result when the screen of SCM#16 located immediately below S1 was inserted, that is, the beam was injected through the screen. The amount of beam loss was increased to about 3 times that in the above condition, and the loss after six turns was also increased. This is because the oscillation of the injected beam grew due to the energy loss at the screen, and it is consistent with the fractional part of the horizontal tune of 0.17. The same BLM unit is planned to be installed around a movable mask located above the RF cavity by the next machine study, and use them to determine the mask length that can prevent the inside of the cavity from being irradiated by synchrotron radiations without the injected beam loss.

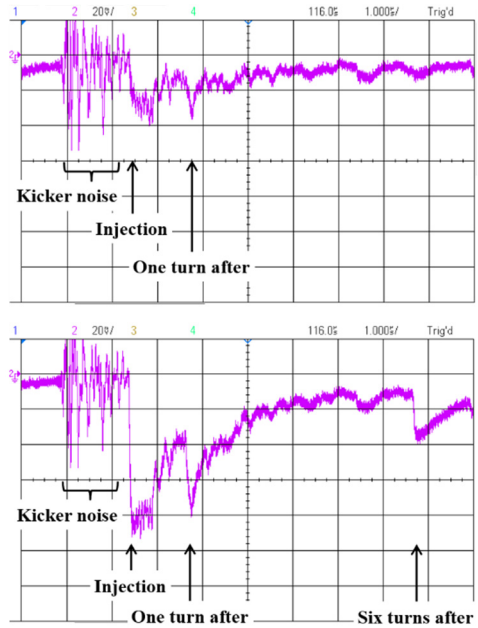

Figure 9: Turn-by-turn measurement of the injected beam loss using the BLM. Without (upper) and with (lower) inserted screens.

Although results are not shown here because they are not beam monitors for the new BT, a turn-by-turn beam position measurement using "Libera Brilliance+ [6]", which is adopted as a BPM circuit for PF-AR, is very useful in the first turn measurement and for the fine adjustment of the kicker timing.

SUMMARY AND FUTURE PLANS

The BT for PF-AR has been recently renewed, such that a full-energy injection can be performed. Standard beam monitors such as BPMs, SCMs, BLMs, and CTs were installed in the new BT, and owing to these the commissioning was completed in one month only. Since April 2017 the user operation without beam acceleration and deceleration has been resumed under full-energy injection. As the next step, we will continue efforts to realize top-up operation. Regarding the beam monitors for the new BT, we are planning the replacement of parts of the BPM circuits with ones with higher resolution, the introduction of high-precision multi-channel ADC boards, and the additional installation of scintillator or optical fiber BLMs.

ACKNOWLEDGEMENTS

The authors would like to thank all the staff of accelerator division VII for their cooperation during the construction and commissioning. We would also like to thank T. Michikawa and Y. Kameta for their support in the development of the control software.

ISBN: 978-3-95450-192-2 doi:10.18429/JACoW-IBIC2017-MOPWC06

REFERENCES

[1] N. Higashi *et al.*, "Construction and Commissioning of Direct Beam Transport Line for PF-AR", in *Proc. IPAC'17*, Copenhagen, Denmark, May 2017, paper WEPAB044, pp. 2678-2680.

[2] Y. Ohnishi *et al.*, "Dynamic Aperture Optimization in SuperKEKB", in *Proc. HF2014*, Beijing, China, Oct. 2014, paper FRT1B2, pp. 73-78.

[3] https://www.cst.com/products/cstps

[4] R. Takai *et al.*, "Design and Initial Commissioning of Beam Diagnostics for the KEK Compact ERL", in *Proc. IBIC'14*, Monterey, CA, USA, Sep. 2014, paper MOCYB2, pp. 7-11.

[5] http://www.aps.anl.gov/epics/.

[6] http://www.i-tech.si/accelerators-instrumentation/libera-brilliance-plus/.

ISBN: 978-3-95450-192-2 doi:10.18429/JACoW-IBIC2017-MOPWC07

COMMISSIONING OF THE BEAM INSTRUMENTATION FOR THE HALF SECTOR TEST IN LINAC4 WITH 160 MeV H- BEAM

G. Guidoboni†, J.C. Allica Santamaria, C. Bracco, S. Burger, G.J. Focker, B. Mikulec, A. Navarro Fernandez, F. Roncarolo, L. Soby, C. Zamantzas, CERN, Geneva, Switzerland

Abstract

In the framework of the LHC Injector Upgrade (LIU) project, the Proton Synchrotron Booster (PSB) will be extensively modified during the Long Shutdown 2 (LS2, 2019-2020) at CERN [1]. This includes a new injector, Linac4, which will provide a 160 MeV H- beam and a complete new injection section for the PSB composed essentially of a chicane and a stripping foil system. The equivalent of half of this new injection chicane, so-called Half-Sector Test (HST), was temporarily installed in the Linac4 transfer line to evaluate the performance of the novel beam instrumentation, such as, stripping foils, monitoring screens, beam current transformers, H^0/H^- monitor and dump, beam loss monitors, and beam position monitors. The results of the instrumentation commissioning of the HST are presented in this paper.

INTRODUCTION

The Half Sector Test project (HST) [2] aimed to test the new injection scheme of the PSB that will be installed during LS2. The beam instrumentation needed to commission the HST was temporarily installed in the Linac4 transfer line as shown in Fig. 1. In particular, the HST was composed by:

- The stripping foil system (TKSTR) and a beam imaging system based on a scintillating screen with radiation-hard camera (BTV1).
- Half of the injection chicane (BSW3 and BSW4 magnets).
- The monitor measuring the partially stripped and unstripped particles (H^0/H^- monitor) and the H^0/H^- dump integrated with BSW4.
- Beam Loss Monitors (BLMs) in the vicinity of the H^0/H^- dump, one ionisation chamber and one diamond detector for fast time-resolved measurements.
- One Beam Current Transformer upstream (BCT1) and one downstream (BCT2) of the HST for transfer efficiency measurements.
- A second beam imaging system (BTV2) for beam profile measurements and steering to the final (temporarily installed) dump.
- Beam Position Monitors (BPMs) installed along the Linac4 and the transfer line up to the HST.
- Vacuum equipment and services.

In the next section, the instrumentation will be described in more detail and their performance illustrated.

HST INSTRUMENTATION

Stripping oil and Optical Beam Systems

The stripping foil system is composed by:

- A stripping foil loader holding up to six foils that can be remotely interchanged and fine-adjusted to reduce the time for machine intervention (e.g. foil substitution) and thus less dose absorbed by the personnel [3].
- A retractable optical beam observation system (BTV), consisting of a 1 mm thick Chromox (Al_2O_3 doped with Cr_2) scintillating screen that can be placed at a distance of 6 mm in front of the foil.

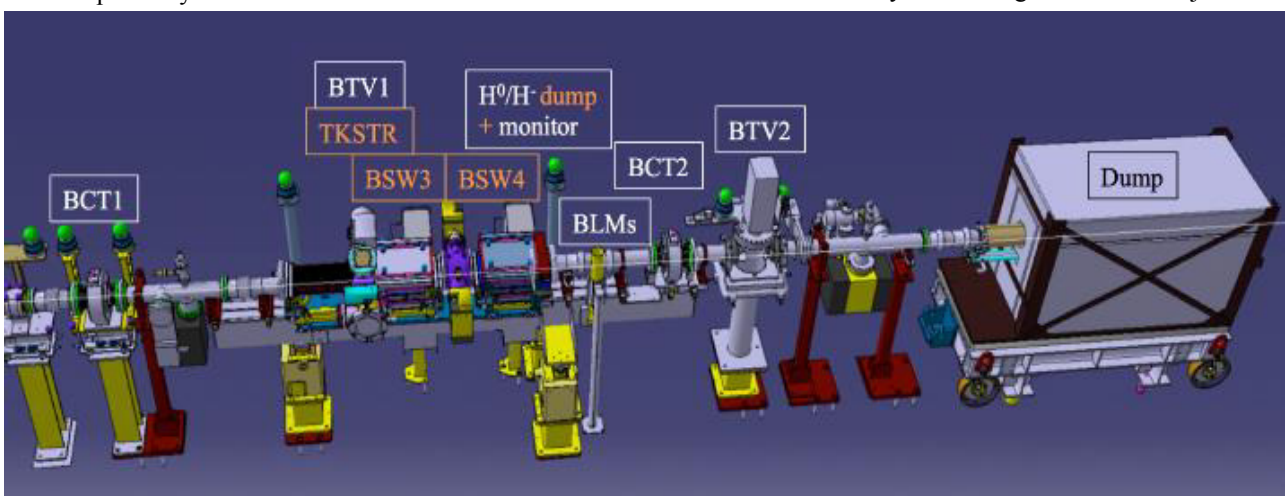

Figure 1: 3D drawing of the HST installation in the Linac4 transfer line (beam from left to right).

† greta.guidoboni@cern.ch

ISBN: 978-3-95450-192-2 doi:10.18429/JACoW-IBIC2017-MOPWC07

- A radiation-hard camera, allowing either to check the beam position on the screen or the integrity of the foil. Indeed, the camera yielded the possibility to detect partial foil ruptures that did not affect the current measured at the foil nor the intensity transmission.

A schematic view of the stripping foil system is shown in Fig. 2. More details on the stripping foil efficiency measurements can be found in [4].

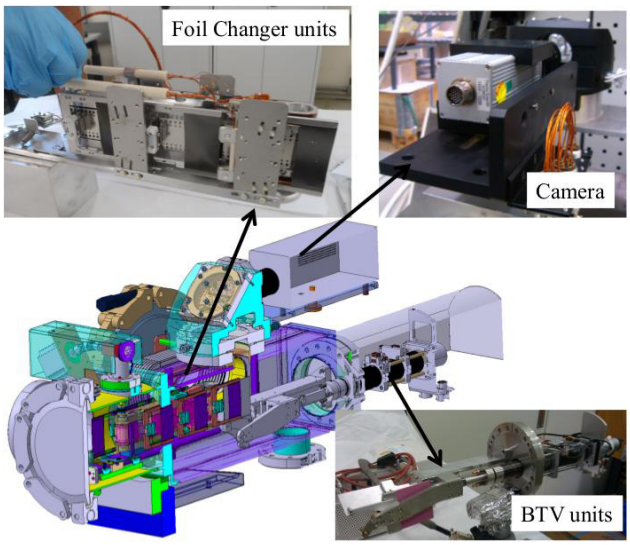

Figure 2: 3D drawing of the stripping foil system with a detailed view of the foil loader (top-left), the radiation-hard camera (top-right) and the retractable screen (bottom-right).

Beam Current Transformer (BCT)

The BCT consists of a magnetic core with a secondary winding (the beam replacing the primary winding) and a calibration winding. They are designed for the rather long Linac4 pulses of 400 – 600 µm with a droop that does not exceed 1%. In order to minimize the transformer sensitivity to external magnetic fields, 3 layers of mu-metal and 1 layer of ARMCO® magnetic shielding are employed. The signal is read out by a dedicated VME module (TRIC: TRansformer Integration Card).

The signal from the secondary winding is amplified by pre-amplifiers with two different gains and digitized in parallel into two 200 MHz ADC channels of the TRIC card. The samples are then averaged with a user-defined time resolution of between 10 ns (successfully used to measure the rise and fall times of the fast chopper) and several µs. The BCTs installed are regularly used to monitor the beam transmission along the different Linac4 sections up to the transfer line and trigger the interlock system ('watchdog') in case of poor transmission.

In particular, the two BCTs installed upstream and downstream the HST were cross-calibrated to provide precision measurements of the stripping foil efficiency at the percent level of accuracy. During the HST commissioning, a transmission higher than 100% between two subsequent BCTs was observed at the Linac4 dump and at the HST. This effect was finally attributed to the pre-amplifier saturation due to a strong 352 MHz RF component, which was well outside the presumed passband of the transformer. Once identified, this was successfully corrected by the addition of appropriate low pass filters.

H^0/H^- Monitor and ump

The H^0/H^- monitor consists of four Titanium plates located a few centimeters upstream of the in-vacuum Titanium beam dump, as shown in Fig. 3. It covers an area of 8 cm x 5.6 cm with 0.1 cm of thickness, enough to strip all the electrons and leave the resulting protons to reach the dump.

This system will serve two main functions:

- Monitor the efficiency of the stripping foil by detecting the amount of partially stripped (H^0) and unstripped (H^-) particles.
- Protect the dump from a high intensity beam impact by providing an interlock signal in case of stripping foil failure (integrated sum signal from the H^0/H^- plates).

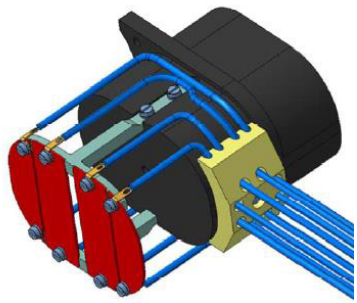

Figure 3: 3D design of the H^0/H^- monitor plates (in red) fixed in fort of the dump.

During the HST phase, a series of measurements was carried out in order to commission this new device. The four plates were first calibrated sending a low intensity H^- beam directly onto the monitor (i.e. no stripping foil inserted). The horizontal beam size was reduced as much as possible so that the entire beam spot could fit onto a single plate. An example of the transverse beam profile on the BTV1 (in front of the stripping foil) is presented in Fig. 4, for a pulse of 1.8 mA and 31 µs length. The beam

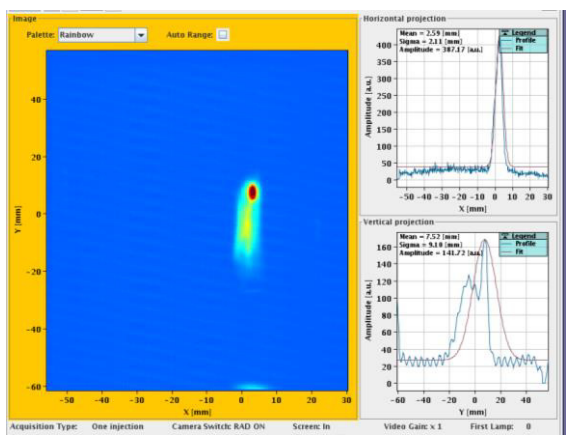

Figure 4: Beam spot on the BTV in front of the stripping foil, generated by a pulse of 1.8 mA and 31 µs.

ISBN: 978-3-95450-192-2 doi:10.18429/JACoW-IBIC2017-MOPWC07

spot is clearly visible in the centre of the BTV and on the right side of the application window the horizontal and vertical fits to the projected profiles can be seen. With this setup, each plate response to the impinging beam was measured for different beam intensities and fixed pulse length of 5 μs, allowing the extraction of the calibration factors to calculate the stripping foil efficiency [5].

Using the same beam setup, it was possible to observe the structure of the H^0/H^- monitor. The beam was moved from left (H^0L plate) to right (H^-R) by changing the current of the first chicane magnet (BSW3) while keeping the BSW4 constant (to guarantee the same magnetic field at the monitor/dump for the emitted secondary charged particles). An example is reported in Fig. 5, which shows the case of 1.8 mA beam current with 31 μs pulse length. On the y-axis there is the sum signal of the 4 plates normalized with the beam current measured at the BCT1. The zero on the x-axis corresponds to the centre of the H^0L plate. The first "hole" at about 8 cm, corresponds to the gap between the H^0 plates. The second one is deeper (this gap is twice as large as the first one) and corresponds to the space between H^0R and H^-L plates. The measurement in Fig.5 shows a distance between the gap centres of ~2 cm, in good agreement with the 2.3 cm of the mechanical drawing, taking into account the errors introduced by a beam entering the plates with an angle.

It was not possible to reach the H^-R plate without increasing the BSW4 current and using a steering magnet upstream the HST; for this reason the H^-R plate is not visible in Fig. 5.

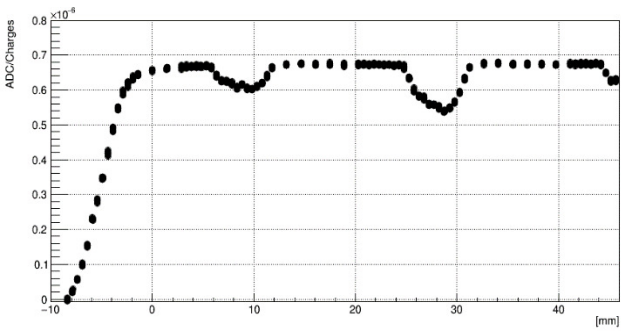

Figure 5: Sum of the four plate signals normalized over the beam current of BCT1 as a function of the beam position on the H^0/H^- monitor. The zero corresponds to the centre of the H^0L plate. The two "holes" correspond to the gaps between the plates.

After the calibration phase, the H^0/H^- monitor was used to measure the stripping foil efficiency in comparison with the beam transmission at the HST. For the stripping foils 1, 2, 3 (position on the foil loader), there was no signal on the H^0/H^- monitor, in agreement with the expected 100% stripping efficiency for that type of foil (XCF-200, arc evaporated amorphous Carbon, collodion coated), but 1% beam transmission inefficiency was detected at the HST BCTs. More interesting is the case of the stripping foils 5 and 6 (the number 4 was broken) where a stripping inefficiency was detected at the H^0/H^- monitor of ~0.25% and ~0.35% respectively, while a beam transmission inefficiency of ~1.25% and 1.35% was detected at the BCTs, as shown in Fig. 6.

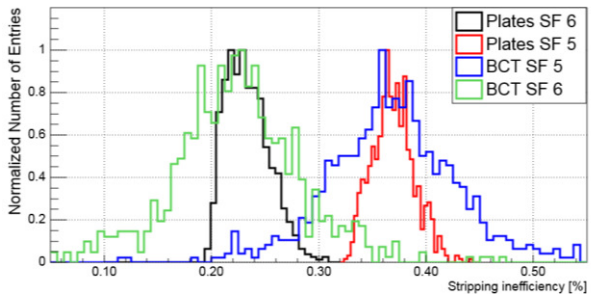

Figure 6: The comparison of the inefficiencies of the stripping foils 5 and 6 (green and blue curves) with the signals measured at the H^0/H^- monitor (black and red lines) shows an excellent agreement.

There are two important observations about this result: There is a systematic 1% of transmission inefficiency measured at the HST BCTs for all the stripping foils, which might come from either a measurement error of the BCTs, or not detected beam losses before the BCT2, or a combination of both. But subtracting the systematic 1%, the measured stripping inefficiencies at the H^0/H^- monitor for the stripping foils 4 and 5 agree perfectly with the transmission inefficiencies at the HST BCTs, validating the correct functionality of this device.

The H^0/H^- monitor electronics also provides the integrated sum of all particles on the four plates. This will be used in the PSB as an interlock in case of stripping foil degradation. For this acquisition chain, the limited HST beam time allowed only commissioning the system linearity, validated over a large intensity range from 20 to $140 \cdot 10^{10}$ charges per pulse.

Beam Loss Monitor (BLM)

The BLMs are essential machine protection elements that were installed in Linac4 to assure keeping operational losses below 1 W/m.

At the HST there were two types of BLMs installed:

- Ionization Chamber (IC), which is the same used for the LHC [6], but with a readout system adapted to the Linac4 requirements.
- Diamond BLM for a fast time-resolved readout (turn-by-turn losses in the PSB).

The IC BLM system has a very high dynamic range, being able to detect currents ranging from 10 pA to 200 mA. Processing is carried out with several integration windows ranging from 2 μs to 1.2 s. This type of BLM is installed along the Linac4 and its transfer line. For the moment they have been used only to qualitatively monitor local beam losses. The study of their calibration at different beam energies and the definitions of the thresholds that will interlock the beam permit will be a milestone of the Linac4 reliability run during this year.

On the other hand, the measurements with the diamond BLM were dominated by noise, which requires an im-

ISBN: 978-3-95450-192-2 doi:10.18429/JACoW-IBIC2017-MOPWC07

provement of the signal transmission for the final system deployment.

Beam Position Monitor (BPM)

The BPM sensor consists of shorted strip-line pick-ups that offer the versatility to fit into the limited space available, while ensuring good linearity and sensitivity. They were designed to monitor the beam position with 100 µm resolution and to provide the relative beam intensity between two monitors with 200 µA resolution.

As well as being extensively used to monitor and optimize the beam trajectory, they have also provided a useful cross-check of the beam transmission to identify the BCT pre-amplifier problem mentioned before. In addition, they have been essential to set up and tune the RF structures (from 12 to 160MeV) of Linac4 by using the Time of Flight (ToF) measurements to infer the beam energy at the exit of each cavity.

CONCLUSIONS

Beam diagnostics were essential for the successful commissioning of the HST with a 160 MeV H^- beam. During this period it was possible to verify the functionality of all instruments, debug software and, where necessary, to identify and correct issues, such as the saturation of the BCT pre-amplifiers.

More time would have been needed to fully establish the absolute accuracy of the H^0/H^- monitor, to study in details the interlock functionality and test the final version of the acquisition electronics. Ways to complete these studies during the Linac4 reliability run are now being investigated, together with threshold definition for different beam currents of the BLM system.

REFERENCES

[1] K. Hanke *et al*., "Status and Plans for the Upgrade of the CERN PS Booster", in *Proc. IPAC'15*, Richmond, VA, USA, May 2015, paper THPF090, pp. 3905-3907.

[2] B. Mikulec *et al*., "Commissioning and Results of the Half Sector Test Installation with 160 MeV H^- beam from Linac4", in *Proc. IPAC'17*, Copenhagen, Denmark, May 2017, paper MOPIK047, pp.619-622.

[3] W. Weterings *et al*., "First Experience with Carbon Stripping Foils for the 160 MeV H^- Injection into the CERN PB", in *Proc. INTDS16*, Cape Town, South Africa, November 2016, unpublished.

[4] C. Bracco *et al*., "Commissioning of the Stripping Foil Units for the Upgrade of the PSB H^- Injection System", in *Proc. IPAC'17*, Copenhagen, Denmark, May 2017, paper MOPIK041, pp.595-598.

[5] F. Roncarolo *et al*., "Beam instrumentation for the CERN Linac4 and PSB Half Sector Test", *in Proc. IPAC'17*, Copenhagen, Denmark, May 2017, paper MOPAB120, pp. 408-411.

[6] B. Dehning, "Beam Loss Monitors at LHC", CERN, Geneva, Switzerland, Rep. CERN-2016-002, Aug. 2016, pp.303-318, [arXiv:1608.03079 [physics.acc.ph]].

ISBN: 978-3-95450-192-2 doi:10.18429/JACoW-IBIC2017-TU1AB2

HIGH REPETITION-RATE ELECTRO-OPTIC SAMPLING: RECENT STUDIES USING PHOTONIC TIME-STRETCH

C. Evain, C. Szwaj, E. Roussel, M. Le Parquier, S. Bielawski*
PhLAM, Université Lille 1, France
Eléonore Roussel, J.-B. Brubach, L. Manceron, M.-A. Tordeux, M. Labat, P. Roy,
Synchrotron SOLEIL, Gif-Sur-Yvette, France
Nicole Hiller, Paul Scherrer Institute, PSI (Switzerland)
Edmund Blomley, Stefan Funkner, Erik Bründermann, Michael Johannes Nasse,
Gudrun Niehues, Patrik Schönfeldt, Marcel Schuh, Johannes Leonard Steinmann, Sophie Walter,
and Anke-Susanne Müller
Karlsruhe Institute of Technology (Germany)

Abstract

Single-shot electro-optic sampling (EOS) is a powerful characterization tool for monitoring the shape of electron bunches, and coherent synchrotron radiation pulses. For reaching high acquisition rates, an efficient possibility consists in associating classic EOS systems with the so-called *photonic time-stretch* technique. We present several setups that may be used for adding the time-stretch functionality to existing EOS systems, and focus on experimental tests made in two situations. At SOLEIL, we present a setup which is optimized for high SNR recording of THz CSR pulses. At KARA (Karlsruhe Research Accelerator), the storage ring of the test facility and synchrotron radiation source ANKA at KIT, we show how the time-stretch strategy can be tested using almost no modification of an existing spectrally-encoded EOS system. Finally we present recent results on CSR and the microbunching instability that have become accessible using photonic time stretch.

INTRODUCTION: HIGH REPETITION RATE EOS

Single-shot Electro-Optic Sampling [1] (EOS) is an efficient technique for monitoring electron bunch shapes [2–4] by recording the electric field in the near-field of the bunch, and is also capable of recording the Coherent Synchrotron Radiation emitted by the electrons [5]. The principle (Fig. 1a) consists of modulating a stretched laser pulse with the electric pulse to be characterized. As a result, the information is imprinted in the spectrum of the laser pulse, and the information can be retrieved by recording the spectrum shape. In classical spectral encoding EOS, the spectrum is typically recorded using a diffraction grating and a camera.

Although this technique is particularly efficient, operation of EOS at high repetition rates (1 MHz or more) remined up to recently a largely open challenge. The main bottleneck in high-speed EOS was the readout part, as commercial linear cameras are typically limited to the 100 KHz range. Two approaches to this problem have been undertaken recently: (i) one direction has been to develop specific cameras that can operate at several Megahertz, the KALYPSO project at Karlsruhe Institute of Technology [6, 7], (ii) a second research direction has been devoted to an alternate type of readout: photonic time-stretch [8–10].

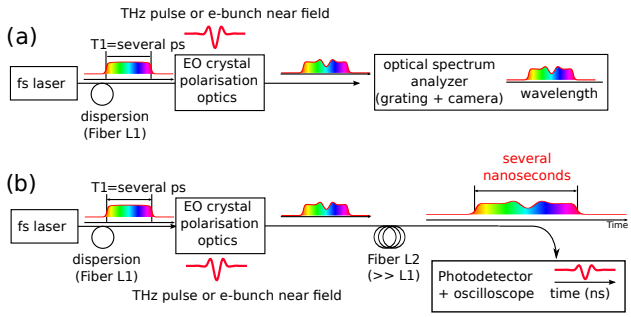

Figure 1: Principles of (a) usual spectrally-encoded EOS (b) photonic time-stretch EOS. In both cases a chirped laser pulse is modulated by the electric pulse under investigation, and the main difference concerns the readout. In classical spectral encoding, the output spectrum is recorded using a single-shot optical spectrum analyzer (usually composed of a grating and a camera). In photonic time-stretch, a long fiber (typically few kilometers-long) stretched the output signal, so that it can be recorded by a single pixel photodetector and an oscilloscope (typically with few GHz bandwidth).

In photonic time-stretch EOS [8–10], the output pulse (Fig. 1b) is dispersed in a long fiber (typically with few kilometers length). As a result, the EOS signal appears as slowed-down replica of the THz electric field, and can be recorded using a single pixel commercial photodetector and an oscilloscope (or acquisition board) with few GHz bandwidth. The acquisition rate can thus be pushed to the hundreds of MHz range, using commercial devices.

Historically, the photonic time-stretch technique has been introduced by the B. Jalali team in 1999 [11, 12] for increasing the bandwidth of A/D digitizers in general. Variants of the technique have also been widely used for recording optical spectra at hundreds of MHz rates [13] (a technique known as Dispersive Fourier Transform, or DFT), as well as high repetition-rate imaging [14–16].

* serge.bielawski@univ-lille1.fr

ISBN: 978-3-95450-192-2 doi:10.18429/JACoW-IBIC2017-TU1AB2

We present here result using the photonic time-stretch approach in the context of single-shot EOS. We present results at SOLEIL on free-propagating THz CSR pulses, and at KARA on near-field EOS of electron bunches.

RESULTS AT SOLEIL: ANALYSIS OF THZ CSR BURSTS

We first performed a test at SOLEIL in 2013 [8], where we could record THz Coherent Synchrotron Radiation (CSR) pulses in single bunch mode, at 850 KHz repetition rate. This first experiment has been performed in conditions of high electron bunch charge, in order to reduce as much as possible the SNR requirement.

Then we started to study the microbunching instability, by monitoring the CSR pulses in more challenging situations. First we considered nominal-alpha regimes at less intense current. Then we aimed at recording the CSR pulses on low-alpha mode, i.e., the prefered mode for users of CSR.

This led us to upgrade our time-stretch setup, with the aim to increase the sensitivity.

Detectivity Enhancement using "Near Extinction" Scheme with Balanced Detection

We first upgraded our laser system by adding a home-made Ytterbium amplifier. This allowed us to test the EOS configuration know as *near extinction*. Data analysis revealed that the strategy was indeed efficient for increasing the EOS signal. We also noticed that the SNR was essentially limited by the noise of the optical source.

In order to go further, and attempt approching shot-noise limited detection, a main challenge was to manage the optical noise of the laser source, and we thus searched a way for performing EOS while canceling out the laser source noise.

In a slightly different context, in Ref. [17], Ahmed Savolainen and Hamm presented a trick that allows a *near-extinction EOS setup* to provide two complementary outputs. Balanced detection can thus be perfomed ar the same time as near-extinction EOS, opening the way to a drastic noise reduction.

In practice, this upgrade could be performed by adding a set of Brewster plate just after the EO crystal, and using the two ports of the output polarizer. This setup is represented in Fig. 2, and a detailed characterization of the EO setup can be found in Ref. [9].

Results: Long Bunch and Short Bunch Modes

In Fig. 3, we displayed a typical series of THz pulses during a CSR burst in nominal-alpha (i.e., long bunch) mode. 5 bunches are simultaneously recorded in this experiment. These CSR pulses are produced by the microbunching instability, and are observed above a threshold for the bunch charge. As expected from theory, below threshold, the average shape of the electron bunch is unable to radiate coherently, as the emission is shielded by the vacuum chamber.

The situation is different with short electron bunches. If their size is sufficiently small, they can radiate CSR

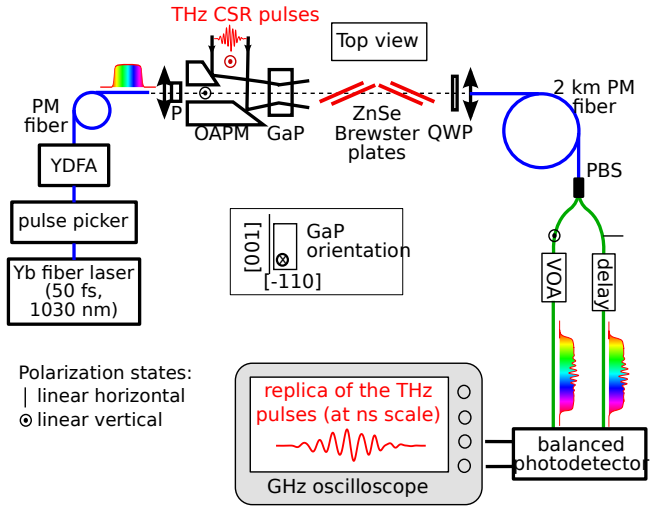

Figure 2: Photonic time-stretch setup designed for high sensitivity EOS. The EO modulation is performed in the Gallium Phosphide crystal. Then the time-stretch is provided by the 2 Km-long fiber. As a result, we obtain a "replica" of the THz pulses, on the oscilloscope, that are "slowed down" in time, with a factor of the order of 150-200. See Ref. [9] for details.

even below the threshold of the microbunching instability. Hence two regimes are expected in this case. Below the microbunching instability threshold, we expect a CSR radiation due to the "shortness" of the electron bunch. Above threshold, we expect also an emission due to the appearance of microstructures in the bunch. This scenario is displayed in Fig. 4, and studied in detail in Ref. [10].

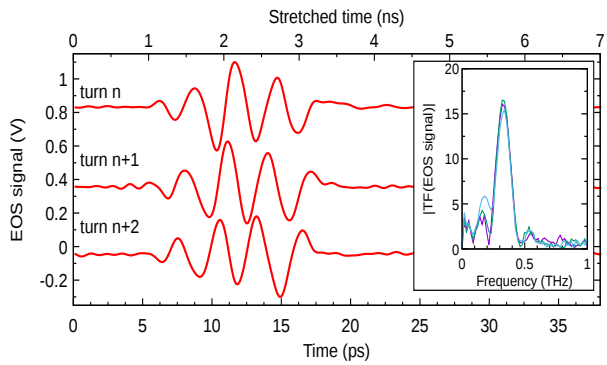

Figure 3: Series of CSR pulses obtained with long electron bunches (15 ps RMS), above the microbunching instability threshold.

PRELIMINARY RESULTS AT KARA: ELECTRON BUNCH NEAR-FIELD

In parallel, we started a joined PhLAM-ANKA/KARA collaboration aiming at testing the possibility to perform photonic time-stretch on a near-field electron-bunch EOS system. For this preliminary test, we did not specifically adapt the ex-

ISBN: 978-3-95450-192-2 doi:10.18429/JACoW-IBIC2017-TU1AB2

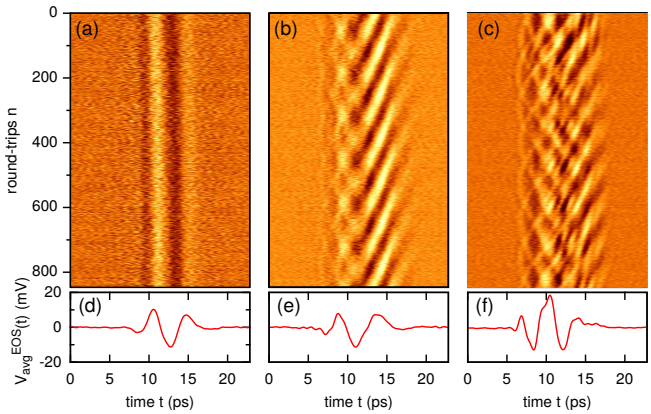

Figure 4: Series of CSR pulses obtained with short electron bunches in the so-called *low alpha* mode. (a): below, and (b), (c) above the microbunching instability threshold. (d), (e), (f): averages of the EOS signals. See Ref. [10] for details.

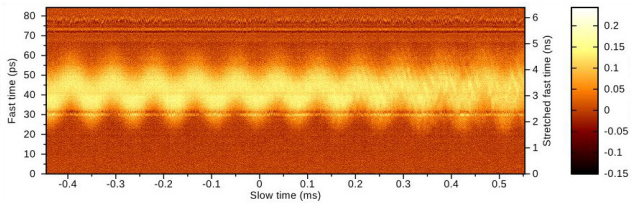

Figure 5: Preliminary result: Time-stretch EOS recording of the electron-bunch near-field at KARA, at each turn (i.e., at 2.7 MHz acquisition rate). Left vertical scale (Fast time) corresponds to the input time, Right vertical time (Stretched time) corresponds to the time at oscilloscope input. Horizontal time scale corresponds to the number of round-trips.

isting EOS setup. We mainly replaced the single-shot optical spectrum analyzer by a 2 km HI1060 fiber, followed by an amplified InGaAs photodetector (Discovery Semiconductor DSC-R412).

We optimized the dynamic range of the detection, by added an Ytterbium-doped fiber preamlifier before the stretching fiber. In order to subtract the reference laser pulses (without EOS signal) we proceeded in an analog way. We fed the two balanced detector inputs with successive laser pulses (with and without EOS signal). The stretch factor was M=80, and we low-pass filtered the data at 5 GHz at the processing stage.

A typical series of EOS signals (at each turn in the ring) is represented in Fig. 5. Although we did not work specifically on the SNR optimization, we can already see dynamical features as a global oscillation at the synchrotron frequency, and even the appearance of microstructures (at the right), which may be attributed to the microbunching instability.

Data analysis showed guidelines for further SNR improvement. The SNR is still limited by the available laser power. We thus expect improvements in the next experimental shifts, by optimizing the losses in the EOS setup. A second foreseen possibility is a modification of the EOS setup for cancelling out the laser common noise, using balanced detection technique of Ref. [9].

CONCLUSION, FUTURE DIRECTIONS

Photonic time-stretch appears as a viable candidate for high-repetition-rate acquisition of single-shot EOS signals. The acquisition rate can in be extended in principle up to the hundreds of MHz range (i.e., the typical repetition rate of laser oscillators). Tests can be made on existing EOS systems, with minimal modifications of the EOS part. When needed, SNR can be significantly improved by a slight modification of the EOS design for performing balanced detection [9].

Future works concern the improvements of time-stretch EOS performances for specific applications. Detection of free-propagating THz pulses requires high-sensitivity. Detection of electron bunch near-fields can required high dynamic range, when small structures (i.e., due to the microbunching instability) are the object of interest. Another important direction consists of performing time-stretch EOS at the 1550 nm wavelength, in order to take advantage of the widely developed high-quality (and low-cost) components of the telecommunication market.

Finally, another important question concerns the comparison of the performances of camera-based spectrally-encoded EOS, with photonic time-stretch, in order to evaluate their respective best domains of application.

ACKNOWLEDGEMENTS

The work has been supported by the BQR of Lille University (2015). The work has also been supported by the Ministry of Higher Education and Research, Nord-Pas de Calais Regional Council and European Regional Development Fund (ERDF) through the Contrat de Projets État-Région (CPER photonics for society), and the LABEX CEMPI project (ANR-11- LABX-0007). Preparation of the experiment used HPC resources from GENCI TGCC/IDRIS (i2015057057, i2016057057).The work performed at KARA, KIT has been supported by the German Federal Ministry of Education and Research (Grant Nos. 05K10VKC and 05K13VKA).

REFERENCES

[1] Jiang, Z. & Zhang, X.-C. Electro-optic measurement of THz field pulses with a chirped optical beam. *Appl. Phys. Letters* **72**, 1945 (1998).

[2] Wilke, I. *et al.* Single-shot electron-beam bunch length measurements. *Phys. Rev. Lett.* **88**, 124801 (2002).

[3] Steffen, B. *et al.* Electro-optic time profile monitors for femtosecond electron bunches at the soft x-ray free-electron laser flash. *Physical Review Special Topics-Accelerators and Beams* **12**, 032802 (2009).

[4] N. Hiller, A. Borysenko, E. Hertle, V. Judin, B. Kehrer, A.-S. Müller, M.J. Nasse, P. Schönfeldt, M. Schuh, N.J. Smale, J.L. Steinmann, B. Steffen, P. Peier, V. Schlott, "Single-shot

ISBN: 978-3-95450-192-2 doi:10.18429/JACoW-IBIC2017-TU1AB2

Electro-optical Diagnostics at the ANKA Storage Ring" in Proceedings of IBIC2014, Monterey, CA, USA, MOPD17, pp. 182-186 (2014).

[5] Müller, F. *et al.* Electro-optical measurement of sub-ps structures in low charge electron bunches. *Phys. Rev. ST Accel. Beams* **15**, 070701 (2012).

[6] L. Rota, M. Balzer, M. Caselle, M. Weber, N. Hiller, A. Mozzanica, C. Gerth, B. Steffen, D. R. Makowski, A. Mielczarek, "KALYPSO: A Mfps Linear Array Detector For Visible to NIR Radiation" in Proceedings of IBIC2016, Barcelona, Spain, WEPG46, pp. 740-743 (2016).

[7] P. Schönfeldt, E. Blomley, E. Bründermann, M. Caselle, S. Funkner, N. Hiller, B. Kehrer, M. J. Nasse, G. Niehues, L. Rota, M. Schedler, M. Schuh, M. Weber, A.-S. Müller, "Towards Near-Field Electro-optical Bunch Profile Monitoring in a Multi-bunch Environment" in Proceedings of IPAC2017, Copenhagen, Denmark, MOPAB055, pp. 227-230 (2017).

[8] Roussel *et al.* Observing microscopic structures of a relativistic object using a time-stretch strategy. *Scientific Reports* **5**, 10330 (2015).

[9] Szwaj, C. *et al.* High sensitivity photonic time-stretch electro-optic sampling of terahertz pulses. *Review of Scientific Instruments* **87**, 103111 (2016).

[10] Evain, C. *et al.* Direct observation of spatiotemporal dynamics of short electron bunches in storage rings. *Physical Review Letters* **118**, 054801 (2017).

[11] Coppinger, F., Bhushan, A. & Jalali, B. Photonic time stretch and its application to analog-to-digital conversion. *IEEE Trans. on Microwave Theory and Techniques* **47**, 1309 (1999).

[12] Mahjoubfar, A. *et al.* Time stretch and its applications. *Nature Photonics* **11**, 341–351 (2017).

[13] Goda, K. & Jalali, B. Dispersive fourier transformation for fast continuous single-shot measurements. *Nature Photonics* **7**, 102 (2013).

[14] Chen, C. L., Mahjoubfar, A. & Jalali, B. Optical data compression in time stretch imaging. *PloS one* **10**, e0125106 (2015).

[15] Chen, C. L. *et al.* Deep learning in label-free cell classification. *Scientific reports* **6** (2016).

[16] Mahjoubfar, A., Chen, C. L. & Jalali, B. Design of warped stretch transform. *Scientific reports* **5** (2015).

[17] Ahmed, S., Savolainen, J. & Hamm, P. Detectivity enhancement in thz electrooptical sampling. *Review of Scientific Instruments* **85**, 013114 (2014).

ISBN: 978-3-95450-192-2 doi:10.18429/JACoW-IBIC2017-TU1AB3

THE OPTICAL DISSECTOR BUNCH LENGTH MEASUREMENTS AT THE METROLOGY LIGHT SOURCE

D. Malyutin†, A. Matveenko, M. Ries, Helmholtz-Zentrum Berlin, Berlin, Germany
O. Anchugov, V. Dorokhov, S. Krutikhin, O. Meshkov, Budker Institute of Nuclear Physics, Novosibirsk, Russia

Abstract

The bunch longitudinal profile measurements using an optical dissector are introduced in the paper. The principles of the dissector operation are briefly discussed. The first measurements using the optical dissector at the Metrology Light Source are presented. Results are analyzed and compared with the bunch profiles from the streak camera measurements. Measurement errors and limitations of the both methods are estimated. Possible applications for the presented technique are discussed.

INTRODUCTION

Practically all present synchrotron radiation sources and electron-positron colliders use streak cameras as an important diagnostic tool, which may provide high spatial resolution (up to tens of micrometers) as well as ultimate temporal resolution up to hundreds of femtoseconds [1, 2]. In the seventies of the last century, the LI-602 dissector [3, 4] was developed at BINP to measure the longitudinal beam profile at circular accelerators. This electron-optical device is based on a stroboscopic approach and is designed for measurement of periodic light pulses of sub-nanosecond and picosecond duration. This dissector is used now for permanent control of the bunch length at the VEPP-2000, VEPP-4M electron-positron colliders and SIBERIA-2 synchrotron light source [5, 6]. However, the LI-602 dissector provides a limited temporal resolution of 20 ps, which is at least one order of magnitude higher than required for modern accelerator diagnostics. Later a new generation of picosecond dissectors was developed based on the PIF-01/S1 picosecond streak-image tube [7, 8] designed and manufactured at the GPI Photoelectronics Department [9, 10]. The experimentally determined temporal resolution of such dissector approaches 3.5 ps [11]. This value was obtained illuminating the tube-input photocathode with femtosecond laser pulses at 800 nm wavelength [12]. In this paper, we describe the test of this new dissector under real experimental conditions at the Metrology Light Source (MLS) [13]. A comparison between the dissector and a Hamamatsu streak camera C10910 [14] was undertaken.

DISSECTOR

The dissector is a device similar to the streak camera. The main difference is in the detector part. The basic schematic layout of the dissector is shown in Fig. 1 and a photo of the dissector vacuum tube is shown in Fig. 2.

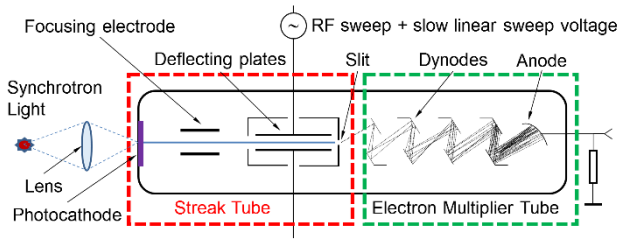

Figure 1: Dissector basic layout.

Figure 2: Dissector vacuum tube.

The synchrotron light pulse is focused on the photocathode and produces photoelectrons. These electrons are accelerated, focused and deflected transversely in a linear dependence of their longitudinal position. As a result, the vertical profile of the electron image at the slit plane will give directly the initial synchrotron light temporal profile, like in a streak camera. In the dissector a narrow slit cuts a small fraction of the electron image and this fraction of electrons is amplified in the electron multiplier tube. The amplified signal is measured by an oscilloscope or an ADC module.

Introducing a slow linear sweep voltage to the deflecting plates allows to scan the full electron image through the slit. The vertical profile is then measured as a function of time on the oscilloscope trace.

With a permanent light source like a flashlight the dissector can be calibrated: a typical signal from the dissector output will have the following appearance, Fig. 3.

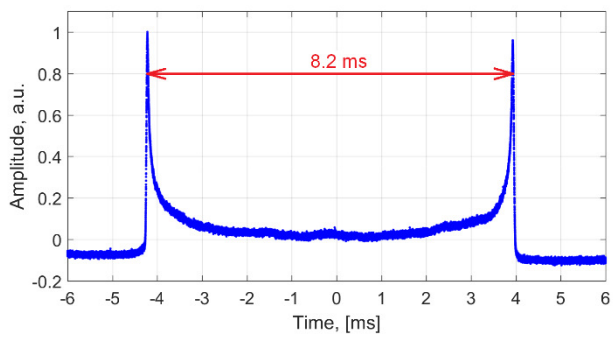

Figure 3: Dissector calibration. Signal from the dissector output for the permanent light source as an input.

† dmitriy.malyutin@helmholtz-berlin.de

ISBN: 978-3-95450-192-2 doi:10.18429/JACoW-IBIC2017-TU1AB3

The two peaks corresponds to the time points when the photo electrons have maximum deflection due to the RF sweep – so the distance between two the peaks is the half period of the dissector RF frequency. For the MLS case, the dissector is operated at the 93.8 MHz – the fifteenth harmonic of the MLS revolution frequency, which is about 6.25 MHz (MLS RF frequency is 500 MHz). The measured distance between the peaks (Fig. 3) is 8.2 ms (mostly defined by the speed of the slow linear sweep voltage and RF sweep amplitude) and corresponds to the time distance for the photo electrons of about 5.3 ns (a half of a period of the dissector RF sweep).

Switching off the RF sweep and running only the linear sweep voltage, the point spread function of the dissector can be measured, Fig. 4 (dissector response to the light pulse with "zero" duration).

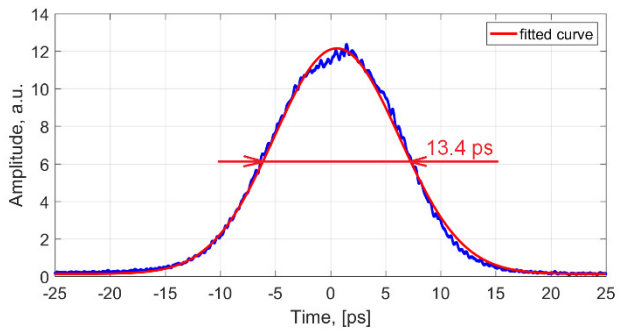

Figure 4: Point spread function of the dissector: dissector signal (the blue dots) and Gaussian fit (the red curve). The time axis is already scaled according to the calibration.

The FWHM from the Gaussian fit gives 13.4 ps. In other words, a bunch with "zero" bunch length will be measured by the dissector with a length of 5.2 ps. This number mainly depends on how well the alignment of the light path is performed and how small the light spot is at the dissector input. It also depends on how small the slit in front of the electron multiplier tube is and how well the electron optics is done, Fig. 1. For the used dissector vacuum tube, the slit width was about 50 µm.

MEASUREMENT RESULTS

Examples of the bunch profiles measured by dissector and streak camera are shown in Fig. 5 and Fig. 6 for 1.3 and 0.13 mA bunch current respectively. For the long bunch, about 24 ps FWHM, the bunch length measured by the both devices are similar, but the shape is different. Dissector cannot reproduce the fast change in the bunch current in comparison with the streak camera – point spread function of the dissector is bigger: 13.4 ps versus 2.6 ps for the streak camera. Also one can see not Gaussian profile of the bunch for the high charge.

For the short bunch, about 13 ps FWHM, dissector gives longer profile, which is about 18 ps. Subtracting the point spread function of the dissector one can get the bunch length close to the one obtained by the streak camera.

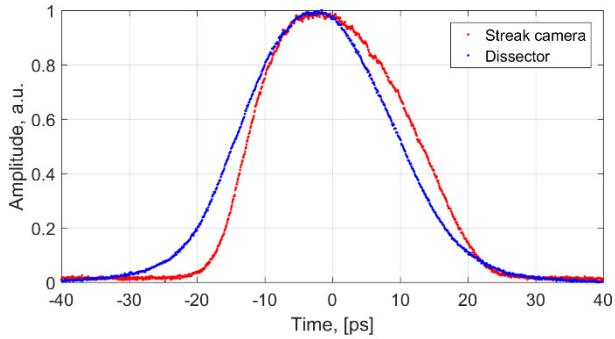

Figure 5: The bunch current profiles from the dissector and streak camera for 1.3 mA bunch current. Low alpha optics at MLS.

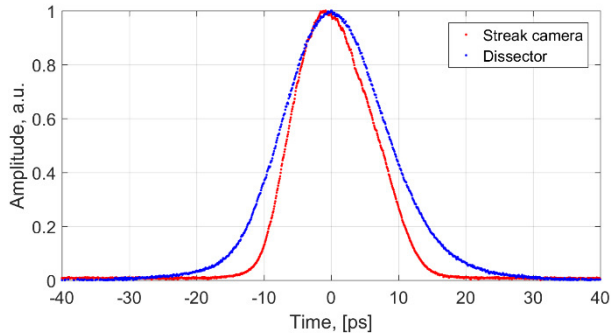

Figure 6: The bunch current profiles from the dissector and streak camera for 0.13 mA bunch current. Low alpha optics at MLS.

The result of the bunch length measurements as a function of the bunch current using dissector is shown in Fig. 7.

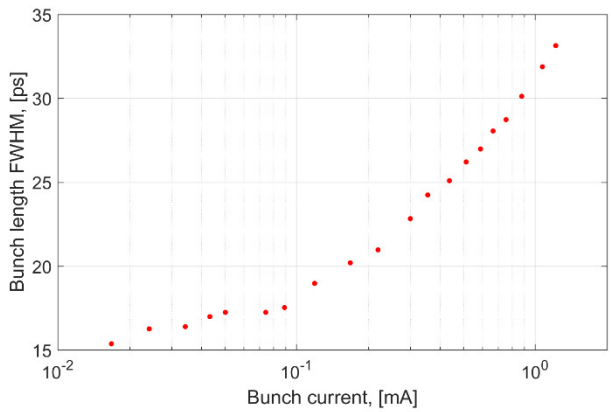

Figure 7: Measured bunch lengths as a function of single bunch current. Low alpha optics at MLS.

The measurements of the bunch length as a function of the RF cavity voltage are shown in Fig. 8 and Fig. 9 for standard user and low alpha optics settings of the MLS respectively. Measurements were performed by the dissector and the streak camera simultaneously: the synchrotron light was shared between the both devices by the edge of a mirror. The bunch length from the dissector was obtained as the FWHM of the scope signal, and the bunch length from the streak camera was obtained as the FWHM of the

ISBN: 978-3-95450-192-2 doi:10.18429/JACoW-IBIC2017-TU1AB3

fitted Gaussian to the image profile. Point spread function of both devices is subtracted.

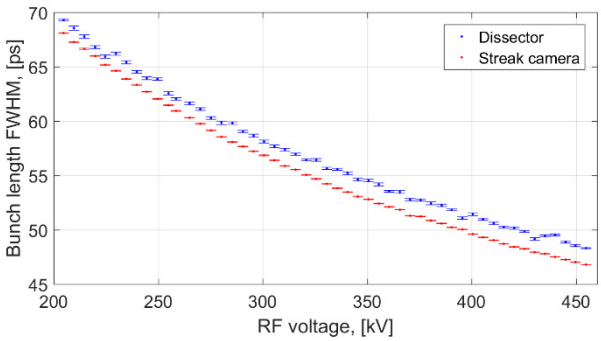

Figure 8: Bunch length at FWHM as a function of the RF cavity voltage measured with the dissector (the blue dots with error bars) and with the streak camera (the red dots with error bars) for the standard user optics at MLS and 0.9 mA bunch current.

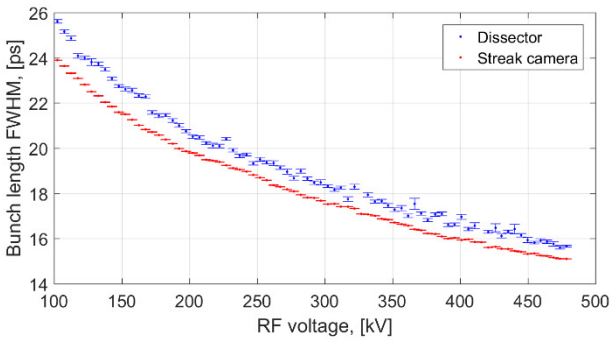

Figure 9: Bunch length at FWHM as a function of the RF cavity voltage measured with the dissector (the blue dots with error bars) and with the streak camera (the red dots with error bars) for the low alpha optics at MLS and 0.3 mA bunch current.

Error bars in figures represent the statistical errors: each voltage point corresponds to about forty measurements of the bunch length.

The dissector gives slightly larger values of the bunch lengths in comparison with the streak camera. Main reason is the error in the FWHM calculation: due to the noise of the dissector signal the scope calculates higher value of the FWHM than one can get from the Gaussian fit.

Another error comes from the calibration and can be estimated to be around 2%, Fig. 4. An additional error source is coming from the point spread functions of the devices. For the streak camera it was measured to be around 2.6 ps FWHM and for the dissector in the current set of measure-ments it was around 12.5 ps. Both values can be improved by a more careful alignment and fine tuning of the both systems. The best achieved value for the dissector was about 5 ps.

CONCLUSION

The bunch length diagnostic based on the optical dissector was successfully commissioned at the Metrology Light Source. The measured bunch profiles and the bunch lengths obtained by the dissector and the streak camera are in good agreement for the range from 70 ps down to 15 ps. Slight overestimation in the dissector data can be explained by the error of FWHM determination of the used scope: noise in the dissector signal yields a bigger value of the calculated FWHM than if one will get it from the smooth curve fit.

Next steps will be to perform a comparison of the devices for even shorter bunches down to 1 ps.

One of the possible application of the dissector can be bunch length measurement in the BESSY II booster where other diagnostics are not available up to now [15]. The dissector is simple and radiation hard device in contrast to the streak camera. In result is can be used for the permanent bunch length monitoring at the running facility.

ACKNOWLEDGEMENT

Experimental samples of dissectors with picosecond resolution were designed and manufactured at the Department of Photoelectronics of A.M. Prokhorov General Physics Institute, Russian Academy of Sciences. The authors wish to thank all the Department members and especially the members of its technological division, namely, G.P. Levina, V.A. Makushina, S.R. Ivanova, Yu.M. Mikhal'kov. The authors are grateful to P. A. Molyavin for technical assistance. We are very grateful to Physikalisch-Tech-nische Bundesanstalt (PTB) and Dr. Jörg Feikes for the possibility to perform the dissector commissioning at the MLS. We are very grateful to Dr. Roland Müller and Dr. Ji Li for masterful management of the MLS for our experi-ments. Also we would like to express our thanks to the all people who provide us the necessary equipment for the preparations, installations and the measurements: Arne Hoehl, Terry Atkinson, Ingo Müller, Hannes Stein, Bern-hard Schriefer and Andreas Heugel.

REFERENCES

[1] L. N. Vyacheslavov, M. V. Ivantzivskiy, O. I. Meshkov *et al., Phys. At. Nucl.,* 43, 451 (2012).
[2] M. Ya. Schelev, *Physics-Uspekhi,* 55, 607 (2012).
[3] E. I. Zinin *et al., At. Energ.,* 20, 320 (1966).
[4] E. I. Zinin *et al., Nucl. Instrum. Methods,* 208, 439 (1983).
[5] O. I. Meshkov, V.F. Gurko, A. N. Zhuravlev *et al.,* "The Upgraded Optical Diagnostic of the VEPP-4M collider", in *Proc. (EPAC'04)*, Lucerne, Switzerland, 2004, pp. 2739 – 2741.
[6] O. Meshkov, A. Stirin, G. Kovachev *et al.,* "A new station for optical observation of electron beam parameters at electron storage ring SIBERIA-2". *Journal of Instrumentation* 12/2016; 11(12):P12015-P12015
[7] V. P. Degtyareva, Yu. V. Kulikov, M. A. Monastyrsky, *et al.,* in *Proc. SPIE*, 491, 239 (1984).
[8] A. M. Prokhorov, N. S. Vorob'ev, V. I. Lozovoi, *et al., Quantum Electron.,* 32, 283 (2002).
[9] S. G. Garanin, S. A. Bel'kov, G. S. Rogozhnikov, *et al., Quantum Electron.,* 44, 798 (2014).
[10] E.I. Zinin and O.I. Meshkov, "Optical dissector for longitudinal beam profile measurement", *JINST,* 2015 1748-0221 10 P10024 doi:10.1088/1748-0221/10/10/P10024.

ISBN: 978-3-95450-192-2 doi:10.18429/JACoW-IBIC2017-TU1AB3

[11] E.I. Zinin, O.V. Anchugov, V.L. Dorokhov *et al.,* "Direct temporal-resolution calibration of new-generation dissector", *JINST,* 2016 1748-0221 11 T03001 doi:10.1088/1748-0221/11/03/T03001.
[12] O. I. Meshkov *et al.,* "Development, Calibration and application of new –generation dissector with picosecond temporal resolution", in *Proc. 5th Int. Beam Instrumentation Conf. (IBIC'16)*, Barcelona, Spain MOPG60, pp. 205-208.
[13] J. Feikes *et al.,* in *Proc. 11th European Particle Accelerator Conf.* (EPAC'08), Genoa, Italy, pp. 2010.
[14] https://www.hamamatsu.com
[15] D. Malyutin *et al.,* "Injection and Bunch Length Studies at the BESSY II Storage Ring", presented at the 6th Int. Beam Instrumentation Conf. (IBIC'17), Grand Rapids, Michigan, USA, August 2017, paper TUPCC06, this conference.

ISBN: 978-3-95450-192-2 doi:10.18429/JACoW-IBIC2017-TU2AB1

INTEGRATED PHOTONICS TO THE RESCUE OF FEMTOSECOND BEAM DIAGNOSTICS

Franz X. Kärtner
Center for Free-Electron Laser Science, Deutsches Elektronen-Synchrotron and
Universität Hamburg, Germany
also at Research Laboratory of Electronics, Massachusetts Institute of Technology, Cambridge, USA

Abstract

Beam instrumentation has always been using results from neighbouring communities. Over the last 10 years, a number of beam instruments and systems have successfully adopted optical solutions, pushing performances from ps to fs, exploiting optical set-ups or photonic components. A major advance for beam diagnostics and instrumentation was the introduction of an optical pulsed timing distribution system using low jitter mode-locked lasers. An outlook on future advances using integrated optical components will be given. The ultra low jitter optical pulse trains already present in today's facilities may also lend themselves to advanced photonic analogto-digtial convertors. Progress towards such devices especially in a practical integrated format and first demonstrations are discussed.

INTRODUCTION

Modern photon science facilities, such as X-ray Free-Electron Lasers (XFEL) are becoming more and more combined accelerator and laser facilities. Lasers play an essential role starting from the photo injector laser creating the electron bunch in the gun, over a potential seed laser down to the experimental station, which usually houses a pump and/or probe lasers to excite the sample under investigation or probe it at optical frequencies. Over the last decade great progress has been made in synchronizing all lasers as well as critical microwave sources in such facilities within 10 fs rms using optical techniques. This is at least one order of magnitude better than possible with microwave techniques. In this tutorial, we first review the principles behind the optical synchronization techniques and show their further development to the sub-femtosecond level. Then we give an outlook how the low jitter properties of mode-locked lasers can be further harnessed to advance beam diagnostics at the example of photonic analog-to-digital conversion (ADC), which becomes only useful in an integrated optical package. This is made possible by exploiting the low jitter properties of mode-locked lasers. More precisely photonically assisted ADC, where optics is only used to eliminate aperture jitter and enable demultiplexing to lower rate channels, which then can be electronically digitized with the required number of bits may potentially enable a thousand fold enhancement in the resolution-sampling rate product when compared to current electronic ADCs.

JITTER OF MODE-LOCKED LASERS

The noise properties of mode-locked lasers were theoretically studied in the framework of soliton perturbation theory by Haus and Mecozzi in their seminal paper published in 1993 [1]. It successfully predicted the noise behavior of many mode-locked solid-state and fiber lasers [2–5]. Recently, it was discussed that the scaling of phase diffusion found in the Haus/Mecozzi model is generally applicable, independent from soliton effects [6]. Here, we present a simple intuitive picture of the timing jitter scaling when transitioning from the traditional case of a microwave oscillator generating a microwave signal at let's say 10 GHz to the case of a mode-locked laser generating an optical pulse train with 100-fs pulses [7].

Figure 1 shows the time-domain picture of microwave signals and optical pulse trains when emitted from an ensemble of microwave oscillators and mode-locked lasers, respectively. The zero crossings of the microwave signal and the pulse positions of the optical pulse train undergo a random walk due to the fundamental noise sources in the signal generation processes such as output coupling and compensation of cavity losses by gain. For the microwave oscillator, this fundamental noise is additive noise due to the losses of the passive cavity (internal as well as output coupling losses) and the reservoirs in the amplifying medium. Clearly, the noise contributions of gain and loss are uncorrelated. The noise energy added to the cavity field within a cavity decay time due to the losses is determined by the fluctuation-dissipation theorem, and it must be equal to kT in thermal equilibrium.

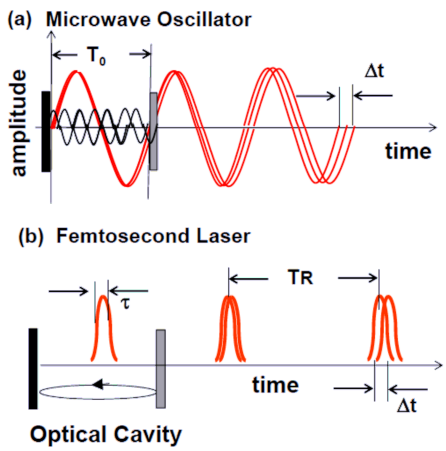

Figure 1: Random walk of (a) the phase in a microwave oscillator and (b) the pulse position in a mode-locked laser due to noise sources in the generation process [7]

ISBN: 978-3-95450-192-2 doi:10.18429/JACoW-IBIC2017-TU2AB1

For the case of a lossy optical resonator, the equivalent noise energy added during a cavity decay time is $\hbar\omega_c$ instead of kT to be conform with quantum mechanics. Therefore, one can show that the diffusion rates for timing of a microwave oscillator and mode-locked laser follows Eq. (1) and (2).

$$\frac{d}{dt} < \Delta t_{\mathrm{RF}}^2 > \sim T_0^2 \cdot \frac{1}{W_{\mathrm{mode}}} \cdot \frac{kT}{\tau_{cav}}, \quad (1)$$

$$\frac{d}{dt} < \Delta t_{\mathrm{ML}}^2 > \sim \tau^2 \cdot \frac{1}{W_{\mathrm{pulse}}} \cdot \frac{\hbar\omega_c}{\tau_{cav}}. \quad (2)$$

The corresponding diffusion rates are inversely proportional to the energy stored in the resonator and scale proportional to the characteristic timescale of the pulse or signal, which is the period in the case of the microwave oscillator and the pulse width in the case of a short pulse laser. This is obvious by inspection, if a small random signal is added to one of the waveforms shown in Fig. 1. The uncertainty in the zero-crossing of the signals is less with increasing slope of the signal, which is directly proportional to its bandwidth. It is the short pulse duration of femtosecond lasers, typically 100 fs, that makes the scaling of timing jitter for femtosecond lasers so much better than timing jitter in microwave oscillators of typically 10 GHz frequency with 100 ps period. The factor of 1000 does not materialize completely due to the higher noise of optical amplifiers versus microwave amplifiers, versus kT, of roughly 40, at room temperature. Still this makes short pulse lasers superb optical clocks, and their pulse trains can be easily and robustly distributed over large distances with very low loss via optical fibers.

HIGH RESOLUTION TIMING JITTER CHARACTERIZATION

A challenge arising in the pursuit of low timing jitter sources is the actual characterization of the timing jitter once approaching the 10 fs level, which is about the level that is supported by commerical signal source analyzers. For phase noise characterization of microwave oscillators, two techniques, the phase detector method and the phase delay method are usually used [8].

The phase detector method is limited by the noise of the reference oscillator used in the measurement process, which is on the 10 fs range for offset frequencies greater than 10 kHz for current microwave synthesizers implemented in signal source analyzers. The phase delay method is limited to the high frequency range because of the limited microwave delays that can be implemented with reasonable loss. The timing jitter of mode-locked lasers can be determined by photodetecton of the pulse train, followed by subsequent filtering of one of the harmonics of the resulting microwave signal and using the microwave techniques discussed. However, the limitations discussed above apply, and in addition, amplitude-to-phase noise conversion [9] in the photodetection process may further degrade the quality of the measurement. Since we have optical sources that are superior to their microwave counterparts in terms of timing jitter, it is therefore necessary to develop techniques that make use of optics to characterize the timing jitter with higher resolution than is possible in the microwave domain. This is possible by using balanced optical cross correlation (BOC) [10, 11]. An implemenation, that is especially advantageous in the 1.55 µm band, is shown in Fig. 2(a).

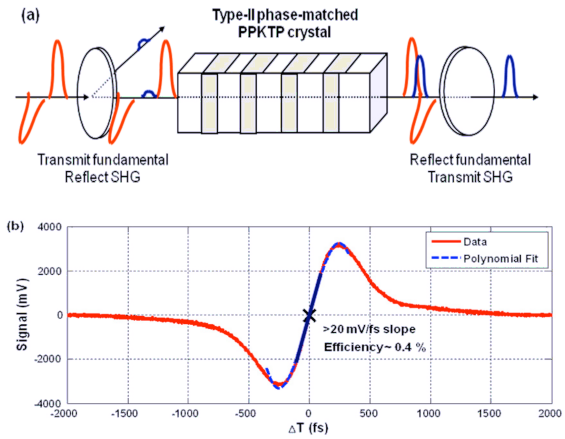

Figure 2: (a) Balanced optical cross correlator (BOC) based on PPKTP [11] and (b) measured cross correlation signal as a function of delay between input pulses [7].

A type-II phase-matched periodically poled KTP-crystal (PPKTP) [12] is used to generate a balanced cross correlation signal of two pulses with orthogonal polarization entering from the left. Due to the birefringence of the crystal (typically a few mm long) 100 fs pulses walk through each other by about 500 fs. Depending on their relative position at the entrance point into the crystal, a certain amount of second harmonic light (SHG) is generated in the forward direction and coupled out via a dichroic mirror. The remaining infrared pulses are reflected back into the crystal and continue to walk through each other generating another amount of SHG, which is then separated with a dichroic beamsplitter from the infrared light leaving the crystal. Each SHG component generated during the forward and backward propagation is then directed to the input of a balanced detector, which generates the cross correlation signal depicted in Fig. 2(b). Even for moderate pulse energies of a few tenths of pJ, a signal with a slope of 20 mV per femtosecond of delay between the two input pulses is derived. In comparison, typical microwave mixers generate timing error signals on the order of mVs per femtosecond delay for 10 GHz microwave signals. Therefore, such a balanced cross correlator can resolve on the order of 10 attoseconds of timing jitter. This device can essentially replace the microwave mixer in the established phase detector and phase delay method and translate them into a timing detector and timing delay method [8], see Fig. 3(a) for timing detector method used in the following. Figure 3(b) shows the timing jitter spectral density of the low jitter laser Origami from the company OneFive measured with the timing detector method above 1 kHz. The integrated timing jitter of the laser for offset frequencies above 1 kHz is less than 0.25 fs [13]. Such low jitter lasers,

ISBN: 978-3-95450-192-2 doi:10.18429/JACoW-IBIC2017-TU2AB1

when disciplined in repetiton rate to a microwave reference for long term stability, can be used as an optical master oscillator (OMO) in femtosecond to attosecond precision timing distribution systems.

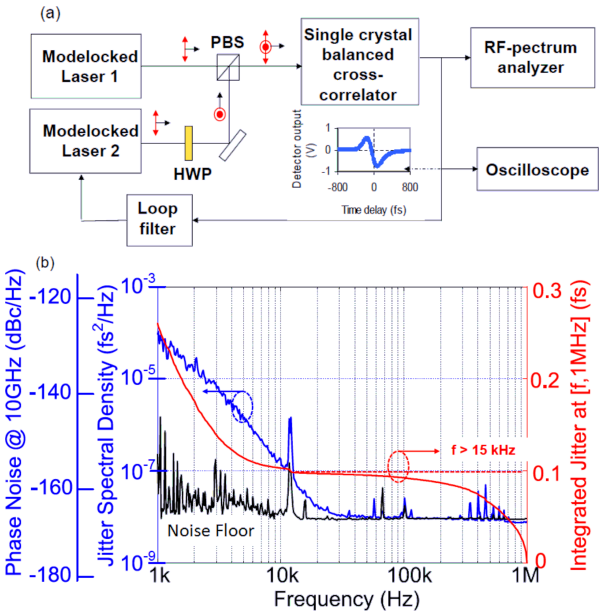

Figure 3: (a) Timing jitter measurement of a mode-locked laser using two identical lasers and an optical cross correlator based on PPKTP using the timing detector method [6] and (b) Timing jitter spectral density measurement of a low jitter laser (OneFive - Origami) using the timing detector method above 1 kHz.

OPTICAL PULSED TIMING DISTRIBUTION SYSTEM

A conceptual layout for a timing distribution system (TDS) for a large scale facility such as an X-ray FreeElectron Laser (XFEL) using the low jitter properties of mode-locked lasers is sketched in Fig. 4.

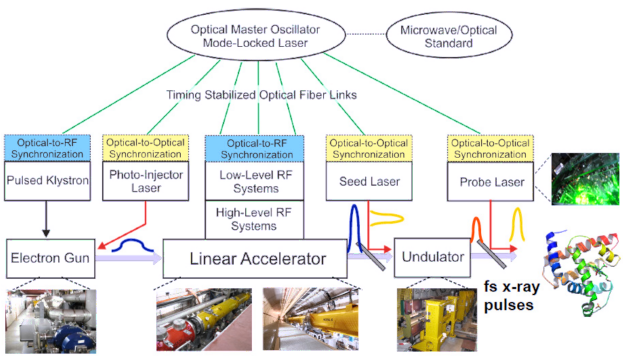

Figure 4: Schematic layout of an optical pulsed timing distribution system for a seeded XFEL facility.

The low jitter pulse train from a repetition rate stabilized OMO is distributed over timing stabilized fiber links to all timing critical positions within the facility. At the fiber link ends additional BOCs can synchronize lasers at the same wavelength (1.5 mm) as the OMO to the output pulse stream with sub-femtosecond precision or two-color balanced cross correlators can be implemented (TC-BOC) to tightly lock any other low jitter lasers to the precision fiber network [14].

Timing Stabilized Fiber Link

At the core of a TDS are timing stabilized fiber links, that use a BOC for precision measurement of the time of flight of femtosecond laser pulses through the fiber link (Fig. 5). Assuming that forward and backward propagation times are identical, the slow and fast expansion of the fiber can be sensed with attosecond precision and a PZT-based fiber stretcher, and, if necessary additional mechanical delays, can compensate for it to keep the time of flight within a round-trip fixed. A necessity is to use a dispersion compentated fiber link, by combining for example standard single-mode fiber (SMF) with standard dispersion shifted fiber (DCF). Limitations may be due to polarization mode dispersion (PMD) that may break the symmetry between the forward and backward propagating path and makes the link also sensitive to perturbations.

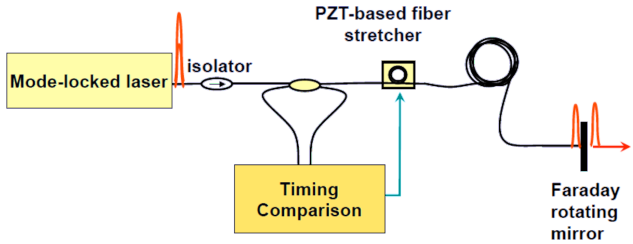

Figure 5: Schematic layout of a timing stabilized fiber link.

For that reason PM-fiber links have been developed recently [15]. For example, Fig. 6 shows the out-of-loop measured drifts between two fiber links in a commercal 16-link TDS over 60 hours, where some links are exposed to plus/minus 1°C temperature fluctuations using PMdispersion compensated links. Clearly, the rms drifts between links stays well below 1 fs.

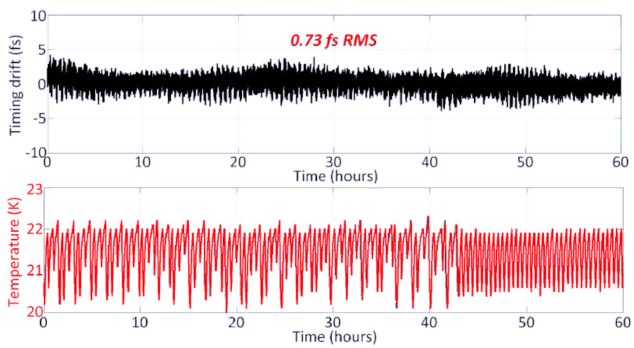

Figure 6: Out-of-loop measurment of timing drift between two fiber links in a commercal 16-link TDS over 60 hours, where some links are exposed to plus/minus 1° C temperature fluctuations [16].

ISBN: 978-3-95450-192-2 doi:10.18429/JACoW-IBIC2017-TU2AB1

Balanced Optical Microwave Phase Detector

Synchronization of microwave signals with optical pulse trains can be implemented using photo-detection filtering and implementation of a classic phase locked loop (PLL). However, nonideal behavior of the photo- de detection process such as AM-to-PM conversion and temperature pendent phase shifts in detectors and mixers typically limits timing drifts in such PLLs to about 100 fs. Careful selection of photo-receivers and temperature stabilization may help to get to the 10-fs range. To overcome these problems, a differentially-biased Sagnac fiber-loop and synchronous detection is used to implement a balanced optical-microwave phase detector (BOM-PD) [17]. Figure 7 shows the schematic a BOMPD. An optical pulse train with a repetition rate of fR is sent to the Sagnac fiber-loop. A reference signal with a frequency (n+1/2)fR is generated from the input pulse train for biasing of the Sagnac loop in a differential way and for synchronous detection. Both the microwave signal from the VCO and the reference signal are applied to the modulator. For high-frequency VCO signals (NfR), the traveling-wave nature of the phase modulator ensures a differential phase shift between the counter propagating pulses. The resulting output pulse train from the Sagnac loop is intensity-modulated at half the repetition rate, fR/2, as shown in Fig. 7. The modulation depth is, to first order, proportional to the phase error between the pulse train and the microwave signal from the VCO. A detailed quantitative derivation of this relationship can be found in [18]. The amplitude modulation is down converted into a baseband signal to drive the VCO.

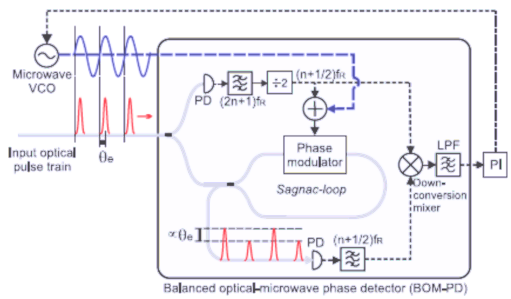

Figure 7: Schematic of the microwave signal to optical pulse train synchronization using a BOM-PD. The phase error is converted to an intensity modulation at the output of the differentially biased Sagnac loop. By synchronous detection using the downconversion mixer, a baseband error signal is generated from the BOM-PD [18].

When the PLL is locked, the pulse train is aligned with the zero crossings of the microwave signal. To demonstrate the quality of optical-to-microwave synchronization using the BOM-PD, we used two BOM-PDs: one for synchronizing the microwave signal with the optical pulse train, and the other for monitoring the out-of-loop timing jitter over 10 hours (more detailed information on the experiment and measurement setup can be found in [19]).

Figure 8 summarizes the measurement results. The top figure shows the out-of-loop SSB phase noise density at 10.225 GHz and the corresponding integrated timing jitter between the microwave signal and the optical pulse train. The bottom figure shows the out-of-loop drift, which is also slightly below 1 fs measured over 10 hours.

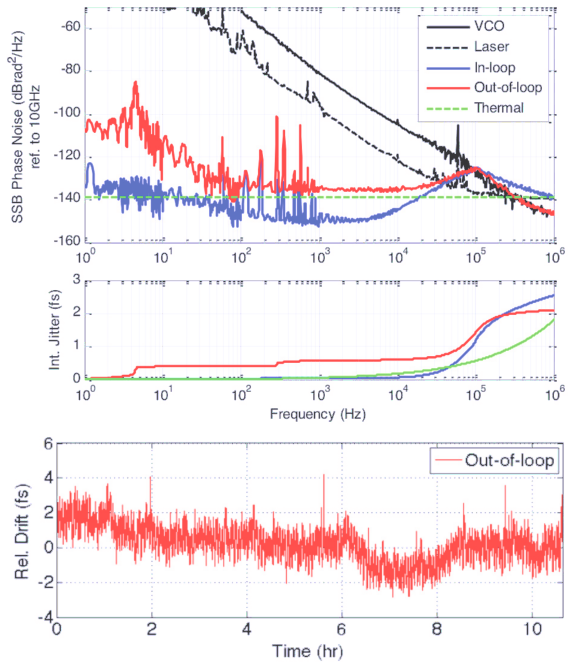

Figure 8: Out-of-loop measurement of timing jitter and drift of an optical-PLL between a 200 MHz laser (Menlo Systems M-Comb) and at 10.225 GHz VCO using a BOM-PD as the phase detector; (top) Short-term timing jitter measurements: single sideband residual phase error spectra; (bottom) integrated RMS timing jitter from 1 Hz; 1 fs conservative estimate for BOMPD residual noise floor up to 100-kHz; (bottom) The rms drift is also below 1 fs and peak-to-peak drift is less than 7 fs over 10 hours [19].

Attosecond Laser-Microwave Networks

Numerous improvements have been made over the years to push the precision of both BOCs and BOMPDs well below the 1-fs level and to minimize the interplay of nonlinear pulse propagation and laser noise in the fiber link. This results in km-scale networks of lasers and microwave sources synchronized to the sub-femtosecond level, see Fig. 9 [20].

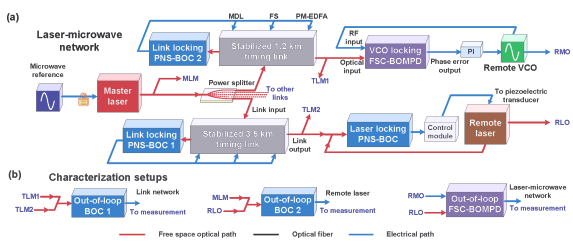

Figure 9: (a) Laser-microwave network (VCO, voltage-controlled oscillator); (b) Out-of-loop setups [20].

Figure 10 shows the integrated jitter and drift of the sub-circuits as well as the overall laser-microwave network not exceeding in total the 1 fs barrier over 10 hours.

ISBN: 978-3-95450-192-2 doi:10.18429/JACoW-IBIC2017-TU2AB1

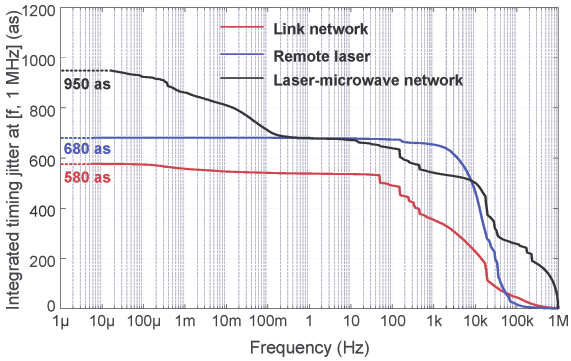

Figure 10: Integrated timing jitter of three characterization setups in the laser-microwave network [20].

Integrated Balanced Optical Cross Correlators

Further advances in pulsed optical timing distribution can be expected for implementation, robustness, size, cost as well as precision by introducing integrated optical components. At this point a waveguide BOC was fabricated using ion-exchanged waveguides in potassium titanyl phosphate (KTP), which was chosen because of its nonlinear optical properties, high-power handling, and wide acceptance bandwidth [21]. The sensitivity of the BOC device was measured using a 1560 nm mode-locked femtosecond laser with a pulse duration of 200 fs and 10 mW of total input power. The laser pulse was split into two paths with the polarization of one path rotated by 90 degrees. By varying the arrival time of the pulses, the balanced cross correlation trace of the device is generated (Fig. 11). The measured sensitivity is 79 mV/fs, a factor of 8 improvement over a previous free-space coupled bulk device.

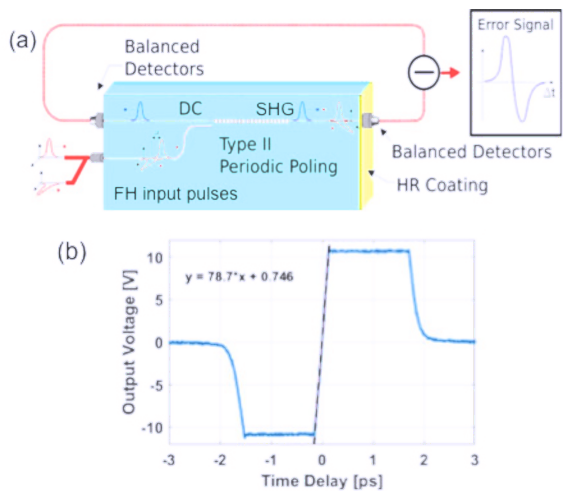

Figure 11: (a) Integrated waveguide BOC; (b) Measured balanced cross correlation of the integrated BOC device. The slope of the line is the sensitivity (79 mV/fs) [22].

PHOTONIC ADC

The field of electronic data conversion has witnessed significant progress over the last decade. With the unity gain frequency of CMOS technology reaching hundreds of gigahertz and matured SiGe technology, data converters based on the silicon platform operating at sampling rates of tens of GSa/s now exist. For instance, Fujitsu Inc. recently introduced a 65 GSa/s ADC in CMOS [23]. Prior to that, Nortel Inc. had demonstrated a 40 GSa/s CMOS ADC [24], and Rensselaer Polytechnic Institute had introduced its 40 GSa/s SiGe ADC [25]. While radio frequency (RF) electronic data converters are now running at unprecedented sampling rates, their performance, as defined by effective number of bits (ENOB), has not improved commensurately. A major factor limiting the progress towards higher rates and resolutions is aperture jitter, i.e. inability of ADCs to sample at precisely defined times. Figure 12 shows ENOB as a function of input frequency for high-performance electronic ADCs, as reviewed by Walden [26], including some ADCs that have appeared afterwards. Dashed lines represent ENOB limits due to jitter.

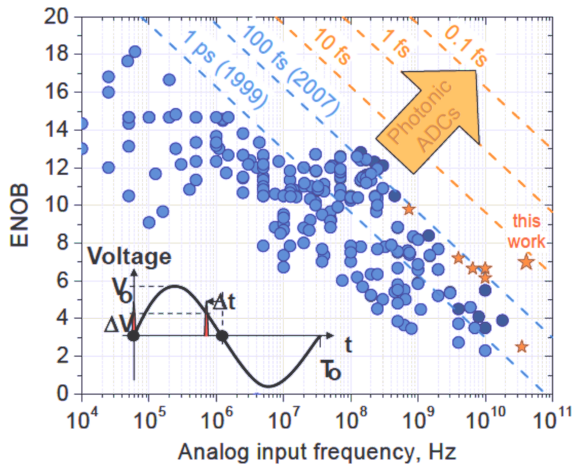

Figure 12: "Walden plot" showing ENOB of existing ADCs as a function of analog input frequency. Each point represents an ADC: blue circles correspond to the ADCs from Walden's survey of ADCs as of late 2007 [26], and dark blue circles correspond to some high-performance ADCs that have been demonstrated since 2007. The dashed lines are locii of constant values of aperture jitter, as indicated next to the lines together with the year when this jitter value was achieved. Photonic ADCs, operating with very low timing jitter, are envisaged to bring ADC performance to new levels, as indicated by the arrow labeled "Photonic ADCs". Some high-performance wideband photonic ADC results are shown with orange stars, with the large star corresponding to the result we discuss here in some detail. Details on data points used in this plot can be found in [26]. The figure is taken from [27].

The best electronic ADCs deliver jitter levels of 60-80 fs in the 100-400 MHz frequency range; reducing the jitter further becomes increasingly difficult, especially beyond gigahertz frequencies, and if the past is a good prediction for the future, it will take nearly a decade to improve the jitter performance by an order of magnitude [26]. As discussed

ISBN: 978-3-95450-192-2 doi:10.18429/JACoW-IBIC2017-TU2AB1

above, ultra-stable mode-locked laser sources with jitter levels many orders of magnitude lower exist today; if used for sampling, they could improve ADC performance by orders of magnitude.

The potential of the photonic approach is demonstrated by sampling a 41 GHz signal with record 7.0 ENOB with a discrete-component photonic ADC [28]. This performance is equivalent to 15 fs jitter, a significant improvement over today's state-of-the-art. A practical photonic ADC must be integrated on a chip, which can be realized using rapidly developing silicon photonics technology There are two standard architectures for photonic ADC systems. The first, known as photonic time stretch, utilizes dispersion of a chirped optical pulse to temporally magnify a segment of a wideband signal to be sampled [29]. After magnification, the signal can be electronically sampled and quantized at a lower sample rate. Photonic time stretch systems suffer due to dispersion-induced attenuation of high-frequency components in the analog waveform. A second photonic ADC architecture is known as time-interleaved optical sampling. With this approach, a stream of pulses or a single chirped pulse is used to sample the analog signal at a high sample rate. After sampling, the pulses are separated into several lower-rate streams using time-division multiplexing (TDM) [30] or wavelength-division multiplexing (WDM) [31] techniques. The TDM approach simplifies the requirements on the optical sampling source. However, the TDM demultiplexer can be difficult to implement and may limit the maximum sample rate. With the WDM approach the multiwavelength stream of optical pulses is de-interleaved using passive WDM demultiplexers, see Fig. 13.

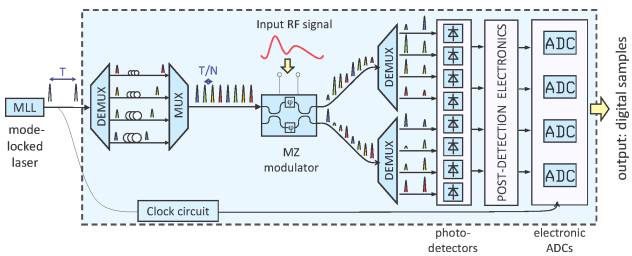

Figure 13: Layout of the photonic ADC studied in this work. The components of the ADC inside the dashed box can ultimately be integrated on a single electronic-photonic chip using a silicon photonics approach [27].

A low-jitter femtosecond laser, as described above, with repetition rates of a few hundred MHz or a few GHz emits a stream of pulses that is dispersed. Dispersion is chosen such that the chirped pulses cover the time interval between the pulses. The RF-waveform to be sampled is imprinted on the chirped pulse stream via an electro-optic modulator. The optical output is channelized via a WDMfilter bank with precisely-tuned center frequencies that map to certain sampling times. The signal from each channel, which corresponds to time interleaved sample sequence, can be separately digitized in low-rate highresolution ADCs, which are fed by an on-chip Si/Ge photodetector array converting each channel at a much lower rate into electrical signals. The total sampling rate is then the optical clock rate, i.e., the repetiton rate of the modelocked laser, times the number of WDM channels.

Figure 14 (a) shows only one of the integrated optical components necessary towards such an integrated ADC, the two matched 20-channel filter banks fabricated on a silicon chip. Each bank is intended to demultiplex one of the two complementary outputs of the MZ modulator. The filters are second-order microring-resonator filters. Microheaters fabricated on top of each ring are used to thermally tune resonant frequencies in order to compensate for fabrication errors and put the resonances on a desired grid. Figure 14(b) shows the measured transmission characteristics of the 20 channels; the overlapping red and the blue lines correspond to the two matched banks.

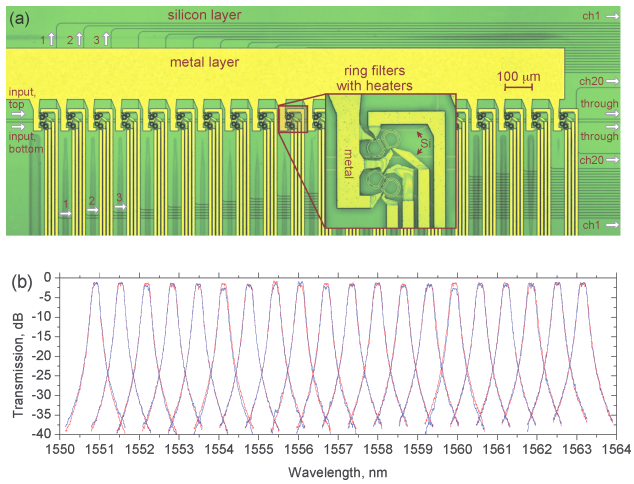

Figure 14: (a) Photograph of two matched 20-channel filter banks fabricated on a silicon chip. (b) Measured transmission of the 20 channels; the overlapping red and the blue lines correspond to the two matched banks [27].

CONCLUSION

The low jitter of femtosecond lasers, reaching attosecond levels in the high frequency range, enables much progress in beam diagnostic, controls and synchronization in accelerator and light source facilities. This development has by far not reached its ends. Advances in integrated optics, in combination with femtosecond lasers, either on or off chip or using the output from fiber distribution systems, enables photonic ADCs with much increased bandwidth-resolution products. Several orders of magnitude in improvement are possible.

ACKNOWLEDGEMENT

The author is indebted to students, postdocs and collaborators at both MIT and DESY, who worked over the last 15 years on the topics presented in this paper. Support through AFOSR, DOE, DARPA and the Helmholtz Association that supported various aspects of this work is gratefully acknowledged.

ISBN: 978-3-95450-192-2 doi:10.18429/JACoW-IBIC2017-TU2AB1

REFERENCES

[1] H. A. Haus and A. Mecozzi, "Noise of mode-locked lasers," *IEEE J. Quantum Electron.*, vol. 29, pp. 983, March 1993.

[2] M. E. Grein, L. A. Jiang, H. A. Haus, E. P. Ippen, C. McNeilage, J. H. Searls, and R. S. Windeler, "Observation of quantum-limited timing jitter in an active, harmonically mode-locked fiber laser," *Opt. Lett,* vol. 27, pp. 957, 2002.

[3] A. Schlatter, B. Rudin, S. C. Zeller, R. Paschotta, G. J. Spühler, L. Krainer, N. Haverkamp, H. R. Telle, and U. Keller, "Nearly quantum-noise-limited timing jitter from miniature Er:Yb:glass lasers," *Opt. Lett.*, vol. 30, pp. 1536-1538, 2005.

[4] S. Namiki and H. A. Haus, "Noise of the stretched pulse fiber laser. I. Theory," *IEEE J. Quantum Electron.*, vol 33, pp 649-659, May 1997.

[5] C. X. Yu, S. Namiki, and H. A. Haus, "Noise of the stretched pulse fiber laser. II. Experiments," *IEEE J. Quantum Eletron.*, vol 33, pp. 660-668, May 1997.

[6] R. Paschotta, "Noise of mode-locked lasers (Part II): timing jitter and other fluctuations," *Appl. Phys.* B, vol. 79, pp. 163-173, July 2004.

[7] F. X. Kärtner, J. Kim, J. Chen, and A. Khilo, "Photonic Analogto-Digital Conversion with Femtosecond Lasers," *Frequenz* 62, pp. 171 - 174, August 2008.

[8] Agilent Technologies, "Phase Noise Characterization of Microwave Oscillator," Product Note 11729C-2.

[9] E. N. Ivanov, S. A. Diddams, and L. Hollberg, "Study of the excess noise associated with demodulation of ultra-short infrared pulses," *IEEE Trans. Ultrason. Ferroelectr. Freq. Control*, vol. 52, no. 7, pp. 1068-1074, July 2005.

[10] T. R. Schibli *et al.*, "Attosecond active synchronization of passively mode-locked lasers by balanced cross correlation," *Opt. Lett.*, vol. 28, no. 11, pp. 947-949, June 2003.

[11] J. Kim, J. Chen, Z. Zhang, F. N. C. Wong, F. X. Kärtner, F. Loehl, and H. Schlarb, "Long-term femtosecond timing link stabilization using a single-crystal balanced cross correlator," *Opt. Lett.*, vol. 32, no. 9, pp. 1044-1046, May 2007.

[12] F. König and F. N. C. Wong, "Extended phase matching of second-harmonic generation in periodically poled KTiOPO4 with zero group-velocity mismatch," *Appl. Phys. Lett.*, vol. 84, pp. 1644 1646, March 2004.

[13] K. Safak, M. Xin, P. T. Callahan, M. Peng, and F. X. Kärtner, "All fiber-coupled, long-term stable timing distribution for free-electron lasers with few-femtosecond jitter," *Structural Dynamics*, vol. 2, issue 4, pp. 041715, June 2015.

[14] H. Li, L.-J. Chen, H. P. H. Cheng, J. E. May, S. Smith, K. Muehlig, A. Uttamadoss, J. C. Frisch, A. R. Fry, F. X. Kärtner, and P. H. Bucksbaum, "Remote two-color opticalto-optical synchronization between two passively modelocked lasers," *Opt. Lett.*, vol. 39, issue 18, pp. 5325-5328, September 2014.

[15] M. Y. Peng, P. T. Callahan, S. Valente, M. Xin, L. Grüner-Nielsen, E. Monberg, M. Yan, J. M. Fini, and F. X. Kärtner, "Long-term stable, sub-femtosecond timing distribution via a 1.2-km polarization-maintaining fiber link: approaching 10-21 link stability," *Opt. Exp.*, vol. 21, issue 17, pp. 19982-19989, August 2013.

[16] Private Communication, Cycle GmbH.

[17] J. Kim, F. X. Kärtner, and F. Ludwig, "Balanced optical-microwave phase detectors for optoelectronic phase-locked loops," *Opt. Lett.*, vol. 31, pp. 3659-3661, December 2006.

[18] J. Kim, F. Ludwig, M. Felber, and F. X. Kärtner, "Longterm stable microwave signal extraction from mode-locked lasers," *Opt. Exp.*, vol. 15, issue 14, pp. 8951-8959, July 2007.

[19] M. Y. Peng, A. Kalaydzhyan, and F. X. Kärtner, "Balanced optical-microwave phase detector for sub-femtosecond optical-RF synchronization," *Opt. Exp.*, vol. 22, issue 22, pp. 27102-27111, October 2014.

[20] M. Xin, K. Shafak, M. Y. Peng, A. Kalaydzhyan, W. Wang, O. D. Mücke, and F. X. Kärtner, "Attosecond precision multikm laser-microwave network," *Light: Science and Applications*, vol. 6, pp e16187; January 2017.

[21] P. T. Callahan, K. Safak, P. Battle, T. D. Roberts, and F. X. Kärtner, "Fiber-coupled balanced optical crosscorrelator using PPKTP waveguides," *Opt. Exp.*, vol. 22, pp. 9749-9758, April 2014.

[22] B. Jones, T. Hawthorne, P. Battle, K. Shtyrkova, M. Xin, P. T. Callahan, F. X. Kärtner, and T. Roberts, "Development of a waveguide-based optical cross-correlator for attosecond timing synchronization," *Ultrafast Optics UFO XI*, Jackson Hole, Wyoming USA, October 2017.

[23] Fujitsu Europe Press Release, "Fujitsu launches second generation ultra-fast 65 GSa/s 8-Bit ADC technology for 100G optical transport," `http://www.fujitsu.com/emea/news/pr/fseu-en_20100913-978.html` Sept. 13, 2010.

[24] Y. M. Greshishchev, J. Aguirre, M. Besson, R. Gibbins, C. Falt, P. Flemke, N. Ben-Hamida, D. Pollex, P. Schvan, and S.-C. Wang, "A 40 GS/s 6b ADC in 65 nm CMOS," *International Solid State Circuits Conference (ISSCC)*, paper 21.7, February 2010.

[25] M. Chu, P. Jacob, J.-W. Kim, M. R. LeRoy, R. P. Kraft, and J. F. McDonald, "A 40 GS/s time interleaved ADC using SiGe BiCMOS technology," *IEEE Journal of. Solid State Circuits*, vol. 45, no. 2, pp. 380-390, January 2010.

[26] R.H. Walden, "Analog-to-digital conversion in the early twenty-first century," *Wiley Encyclopedia of Computer Science and Engineering*, 1-14, September 2008.

[27] A. Khilo *et al.*, "Photonic ADC: overcoming the bottleneck of electronic jitter," *Opt. Exp.*, vol. 20, issue 4, February 2012.

[28] J. Kim, M. J. Park, M. H. Perrott, and F. X. Kärtner, "Photonic subsampling analog-to-digital conversion of microwave signals at 40-GHz with higher than 7-ENOB resolution," *Opt. Exp.*, vol. 16, issue 21, pp. 16509-16515, October 2008.

[29] Y. Han and B. Jalali, "Photonic time-stretched analog-todigital converter: Fundamental concepts and practical considerations," *J. Lightwave Tech.*, vol. 21, no. 12, pp. 3085-3103, December 2003.

[30] P. W. Juodawlkis, J. C. Twichell, G. E. Betts, J. J. Hargreaves, R. D. Younger, J. L. Wasserman, F. J. O'Donnell, K. G. Ray, and R. C. Williamson, "Optically sampled analog-to-digital converters," *IEEE Transactions on Microwave Theory and Techniques*, vol. 49, issue 10, pp. 1840-1853, October 2001.

[31] T. R. Clark, J. U. Kang, and R. D. Esman, "Performance of a time- and wavelength-interleaved photonic sampler for analog-digital conversion," *IEEE Photon. Technol. Lett.*, vol. 11, no. 9, pp. 1168-1170, September 1999.

ISBN: 978-3-95450-192-2 doi:10.18429/JACoW-IBIC2017-TU2AB3

SINGLE-SHOT LONGITUDINAL BEAM PROFILE AND TERAHERTZ DIAGNOSTICS AT MHz- TOWARDS GHz-RATES WITH HIGH-THROUGHPUT ELECTRONICS

M. Caselle*, L. Rota†, M. Balzer, M. Brosi, S. Funkner, B. Kehrer, M. J. Nasse, G. Niehues, M. Patil, P. Schönfeldt, M. Schuh, J. L. Steinmann, M. Yan, E. Bründermann, M. Weber, A.-S. Müller, Karlsruhe Institute of Technology (KIT), Karlsruhe, Germany
G. Borghi, M. Boscardin, S. Ronchin, Fondazione Bruno Kessler (FBK), Trento, Italy

Abstract

Accelerators with high bunch-repetition rates require high-throughput detector electronics to diagnose each individual bunch. KALYPSO with a 256-pixel detector line-array integrated in an fs laser-based electro-optical set-up allows longitudinal bunch profiling with sub-ps resolution as demonstrated at the storage ring KARA for single-bunch mode operation at 2.7 MHz and also at the European XFEL with a 4.5-MHz micro-bunch train. Improvements will enhance fs-time accuracy, reduce noise, and increase frame-rate. A custom front-end with an application-specific integrated circuit (ASIC) has been developed to operate with 10-MHz frame-rates at low noise. Several linear arrays with up to 1024 pixel and smaller pixel pitch were submitted for production. The development of a low-gain avalanche diode (LGAD) sensor will further improve the time resolution. Detector data is transmitted in the DAQ framework to external GPU-based clusters and processed in real-time at 7 GBytes/s with a few µs latency. For beam dynamics studies we also develop KAPTURE capable to analyze terahertz detector pulses at GHz-repetition rates. These developments open new possibilities in beam diagnostics of modern accelerators.

INTRODUCTION

The investigation of bunch-to-bunch interactions and beam dynamics during micro-bunching poses several challenges to both accelerator physicists and detector developers [1, 2]. The short bunch lengths and the dimension of substructures on the bunch profile impose tight requirements in the temporal resolution of detectors and front-end electronics technologies. Furthermore, if beam diagnostics setups require single-shot measurements on a turn-by-turn basis for long observation times, the front-end electronics and the Data Acquisition (DAQ) system must be able to sustain data rates of several GBytes/s.

At the Karlsruhe Institute of Technology (KIT), we are developing new experimental techniques and detector systems to meet the requirements of modern accelerators and enable ultra-fast beam diagnostics at high repetition rates. The development of new technological components is carried out in close cooperation with the accelerator facilities of KARA (Karlsruhe Research Accelerator) [3] and soon FLUTE (Fern-infrarot Linac- und Test-Experiment) [4], where the novel detectors systems are fully characterized and tested in a real accelerator environment, before their commissioning at other research centers.

In this paper we report about recent developments on two detector systems which have been developed for time-resolved beam diagnostics. The first system is KALYPSO, an ultra-fast camera developed for turn-by-turn longitudinal and transverse beam profile measurements. The second one is KAPTURE, a detector system which has been widely employed in the investigation of the fluctuations of terahertz (THz) Coherent Synchrotron Radiation (CSR) by micro-bunching instability (bursting). Both detectors have been integrated in a custom DAQ framework for real-time data processing based on Field Programmable Gate Arrays (FPGAs) and Graphic Processing Units (GPUs), in order to achieve high data throughput with low latency.

KALYPSO

KALYPSO (Karlsruhe Linear Array Detector for MHz repetition rate spectroscopy) is an ultra-fast 1D camera with a continuous frame rate of 2.7 Mfps [5]. KALYPSO has been originally developed for the upgrade of the Electro-Optical Spectral Decoding experimental setups at KARA and at the European XFEL. The front-end electronic components are mounted on the detector mezzanine card shown in Figure 1. Two types of semiconductor linear arrays can be employed, depending on the specific application. The first one is a Si microstrip sensor, originally developed at the Paul Scherrer Institute (PSI) for charge integrating X-ray

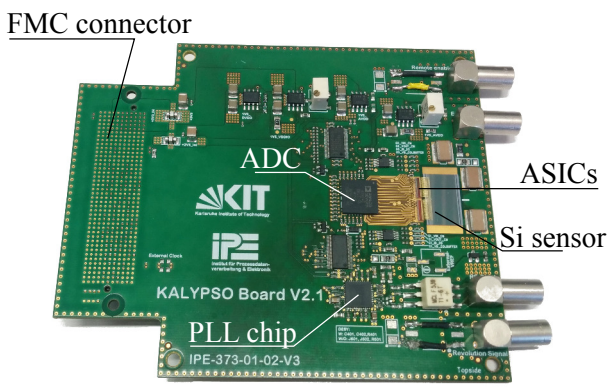

Figure 1: Photograph of the KALYPSO mezzanine board.

* Contact: michele.caselle@kit.edu
† Contact: lorenzo.rota@kit.edu

ISBN: 978-3-95450-192-2 doi:10.18429/JACoW-IBIC2017-TU2AB3

detectors. The second one is an InGaAs linear array from Xenics. The former is used in applications where visible light must be detected, while the latter is employed with near-infrared radiation. The current version of the detector, named KALYPSO II, is based on a modified version of the GOTTHARD front-end ASIC [6] and achieves a maximum frame-rate of 2.7 MHz. In the current version, two GOTTHARD chips are connected to a linear array sensor with 256 pixels and 50 µm pixel pitch. A commercial analog-to-digital converter (ADC) converts the analog samples with a sampling rate of 65 MS/s and 14-bit resolution. When connected to the DAQ system described below, KALYPSO sustains continuous data taking at the maximum repetition rate.

New Si Microstrip Sensors

As described above, the Si sensor employed in the current version of KALYPSO is not optimized for the detection of visible light and near-IR radiation. To improve the quantum efficiency at different wavelengths, we have designed a new Si sensor optimized for imaging applications. The new sensor features an optimized geometry, with a pixel pitch of 25 µm and a variable number of pixels (from 512 to 2048). A smaller pitch improves the spatial resolution while, at the same time, decreases the capacitance of each photodiode, resulting in a higher readout speed and lower noise. Moreover, different Anti-Reflective Coatings (ARC) will be applied to the sensor during the production phase. In particular, three different ARCs will be applied, optimized respectively for visible light, near-ultraviolet (300 nm to 400 nm) and near-infrared (up to 1.1 µm). With respect to a monolithic approach based on CMOS processes, a hybrid solution allows us to cover a wide range of experimental applications with a unique detector system. The final layout of the sensors has been completed and is shown in Figure 2. The sensors will be produced by FBK in the third quarter of 2017.

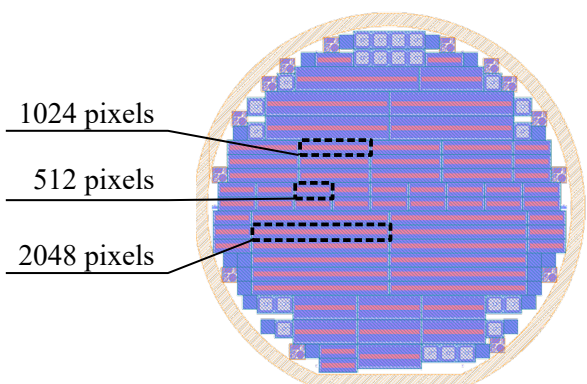

Figure 2: Layout of the wafer containing the new Si sensors for KALYPSO. The different versions of the sensor are shown.

KALYPSO III: Towards 10 MHz Repetition Rates

To further increase the frame rate of KALYPSO, we are currently developing a new front-end Application Specific Integrated Circuit (ASIC) in collaboration with PSI. Moreover, by optimizing the front-electronics with respect to the electrical proprieties of the new Si sensors described above, the noise performance can be improved despite the higher frame rate. A higher frame rate is nececssary to meet the requirements of different facilities (*e.g.,* the European XFEL with a repetition rate of 4.5 MHz) and further improve the temporal resolution of beam diagnostic applications. A prototype chip, designed in a commercial 110 nm CMOS technology and consisting of 48 channels, has been submitted in late 2016. The prototype is fully functional and achieves a frame rate of 12 MHz. After the submission of the final version of the chip, the production of KALYPSO III will start in early 2018.

High-speed Imaging with Ultra-fast Detectors

An important limitation in high-speed imaging applications is the response time of the semiconductor detector. With traditional Si sensors, the time required to collect the charges generated by the incoming radiation is typically around a few tens of ns, therefore limiting the maximum frame rate. When exposed to an incoming radiation with an higher repetition rate, the sensor would quickly saturate. While it is possible to install a gating-intensifier stage in front of the detector, such as the ones used in intensified CCD (ICCD) cameras, these can degrade the resolution and the uniformity of the detector.

In high-speed imaging detectors, Avalanche PhotoDiodes (APDs) are widely employed. Typically they are operated in linear mode, meaning that the intensity of the generated signal is proportional to the intensity of the incoming radiation. A device based on APDs for beam diagnostics applications is described in [7], where 16 pixels are operated with a maximum frame-rate of 50 MHz. However, several technological challenges hinder the possibility to realize APD linear arrays with a large number of channels. Therefore, this makes them unsuitable for many beam diagnostics applications demanding high spatial resolution, such as Electro-Optical Spectral Decoding.

In order to overcome the rate limitation of conventional Si detectors while maintaining high spatial resolution, we are currently evaluating the integration of KALYPSO with Low-Gain Avalanche Detectors (LGAD). LGADs have been recently proposed in the literature for 4D tracking applications in high energy physics detectors [8]. With respect to conventional APDs, LGADs feature a moderate internal gain, thus enabling the fabrication of finely-segmented microstrip and pixel detectors, while achieving charge collections times as low as 3 ns [9]. This would ensure that the sensor is not saturated by the incoming radiation, even if exposed to pulses with repetition rates of a few hundreds of MHz. The production of a prototype LGAD microstrip array for the

ISBN: 978-3-95450-192-2 doi:10.18429/JACoW-IBIC2017-TU2AB3

KALYPSO detector with a pixel pitch of 50 µm is currently planned for the end of 2017.

KAPTURE

KAPTURE (KArlsruhe Pulse Taking Ultra-fast Readout Electronics) [10] is a wide-band front-end electronics system for sampling ultra-short pulse signals generated by ultra-fast detectors. The wide-dynamic range at the input enables an high-compatibility with many fast detectors, *e.g.,* YBCO THz detectors [11], HEB [12], room-temperature Schottky diodes, Beam Position Monitors (BPMs) and diamond detectors. KAPTURE is able to digitize pulse shapes with a sampling time down to 3 ps and pulse repetition rates up to 500 MHz. The combination with ultra-fast THz detectors, also designed and produced at KIT [13], offers a complete detector and readout system for the measurement of CSR intensity in the THz region to the scientific community.

A second version of the KAPTURE board [14] has been designed and produced to overcome these limitations. The KAPTURE-2 mezzanine card is shown in Figure 3. KAPTURE-2 makes use of the latest advantages of the best components on the market. In particular, of a new generation of ultra high-speed ADCs and an ultra low-noise clock jitter cleaner with dual-loop PLL. The new fast ADC offers several advantages: a sampling rate up to 2 GS/s and voltage reference, offset and analog gain adjustable channel-by-channel by 15 bits. This last option is useful to compensate the gain mismatch between different sampling channels. The dual-loop PLL architecture is capable of 111 fs rms jitter which is 4 times less compared with the first KAPTURE version. The PLL provides an excellent clock distribution through two fully configurable delay logic, one coarse delay from 2.25 ns up to 261 ns with a time step of 500 ps and an analog fine delay from 0 to 475 ps with time resolution steps of 25 ps. The flexible and accurate time distribution allows an easy synchronization between the detector pulse and the sampling time system. The selected PLL synchronizes the distributed signal clocks, with a fixed and known phase relationship, between two or more PLL devices located on different KAPTURE boards. This special feature allows us to synchronize the sampling times of two or more KAPTURE boards, extending the sampling points beyond four samples. The comparison between the pulse sampling strategies of the first version of KAPTURE and the new version are shown in Figure 4.

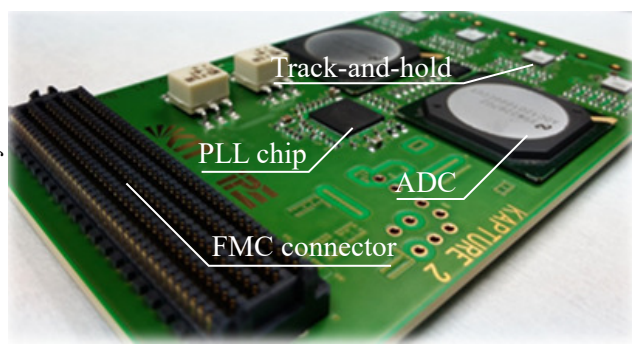

Figure 3: Photograph of the KAPTURE mezzanine board.

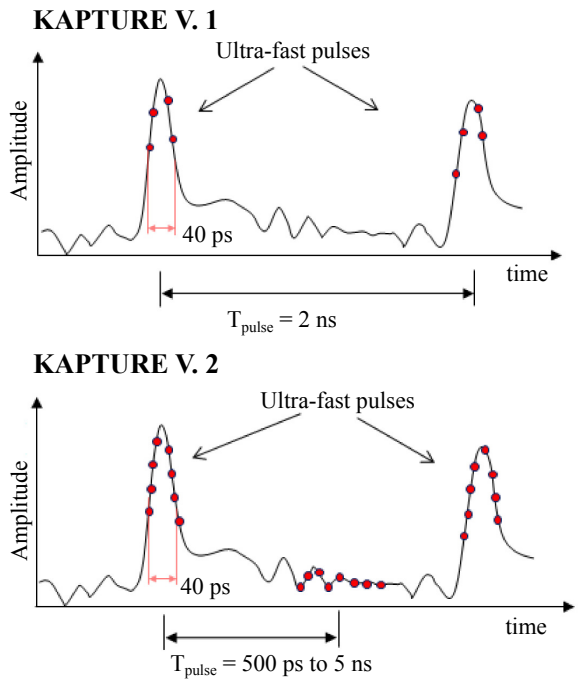

Figure 4: Comparison of the sampling strategies between the first (top) and second (bottom) KAPTURE versions. The sampling points are indicated by the red circles.

With the new version, two KAPTUREs can be connected together for direct sampling of detector pulses with up to eight sampling points with a pulse repetition rates of up to 2 GHz. Optionally, the system can be programmed to sample both the detector pulse and the baseline between two pulses with a constant pulse rate of up to 1 GHz. The FPGA will receive both the pulse amplitude and the baseline so that only the corrected amplitude will be sent to the GPU for data processing. The expand and flexible pulse repetition rate from 0.2 to 2 GHz makes the new design compatible with many synchrotron accelerator machines. The flexibility includes also the option of parallel detectors for acquisition. The system can digitize up to eight detectors in parallel with one sample point located at the peak amplitude of each detector pulse.

HIGH-THROUGHPUT DAQ SYSTEM

The front-end electronics of both systems have been developed as mezzanine cards based on the VITA FMC standard. In this way, the mezzanine cards are compatible with a large number of FPGA readout cards, thus allowing external users to integrate them within an existing DAQ system.

At KIT, the detectors have been integrated in a custom high-performance and heterogeneous DAQ system consisting of FPGAs and GPUs directly connected via PCI-Express. The different cards hosting the front-end electronics are connected to a custom FPGA board, named "High-Flex" [15].

ISBN: 978-3-95450-192-2 doi:10.18429/JACoW-IBIC2017-TU2AB3

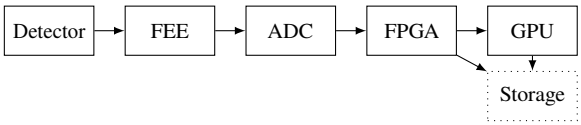

Figure 5: Data flow of the heterogeneous DAQ system based on FPGAs and GPUs.

The data flow in the DAQ system is shown in Figure 5. Data produced by the front-end electronics (FEE) on the mezzanine cards are acquired by the FPGA board, where they are pre-processed and temporarily stored in a local DDR3 memory. Data are then transmitted to external storage or computing nodes. A custom GPU-based processing framework enables user-friendly and on-line monitoring of the data produced by the detector systems [16]. As demonstrated in [17], our architecture allows scientists to develop high-performance processing algorithms without requiring specific knowledge of the underlying hardware architecture. Moreover, the low-latency performance of the DAQ system meets the requirements of fast feedback systems. With specific optimization of the data processing software components, a latency as low as a few microseconds has been achieved [18].

EXPERIMENTAL RESULTS AT KARA

Turn-by-turn Bunch Profile Measurements

The KALYPSO detector system has been installed at the near-field EOSD setup at KARA. A detailed description of the experimental setup can be found in [19]. Preliminary measurements have been performed at the maximum repetition rate of 2.7 MHz. Single-shot and turn-by-turn measurements of the longitudinal bunch profile have been achieved for long observation times, as reported in previous publications [20]. Due to improvements in both the detector system and the experimental setup, in particular with the commissioning of a new EO arm, a much higher sensitivity when observing sub-structures on the bunch profiles is expected [21]. KALYPSO is also installed as diagnostic tool at the EO setup of the European XFEL. The detector is connected to a custom FPGA readout card, developed at DESY, to ease the integration of the detector with the µTCA (Micro Telecommunications Computing Architecture) infrastructure of the European XFEL.

At KARA, a dedicated Visible Light Diagnostics (VLD) beamline hosts a fast gated intensified camera (FGC) to study the horizontal bunch profile and thus the energy spread [22, 23]. However, with the current setup the bunch profile can be measured only once every 6 turns, and only a limited number of profiles can be acquired in one measurement. To lift this limitation, a KALYPSO detector equipped with a Si sensor has been recently installed at the VLD port. Preliminary measurements have shown that the low-noise performance of the detector allows us to measure the horizontal bunch profile, even without employing an intensifier stage. Similar to the EOSD setup, turn-by-turn monitoring has been achieved for long observation times. However, the optimization of both the detector system and the optical setup at the VLD port are currently ongoing.

Far-field THz Diagnostics

KAPTURE has been integrated as a permanent diagnostic tool at KARA. Several studies have already been conducted with KAPTURE, such as the investigation of the emission of THz radiation in the bursting regime [1, 24] and the evolution of micro-bunching instabilities in multi-bunch environments [2]. With the quasi-simultaneous acquisition of bunches covering the full bunch current range, a spectrogram can be created from just one dataset. KAPTURE thus offers a way to quickly scan the beam behavior over several machine parameters and gain new insights into the behavior of different thresholds and the change of the spectrograms as recently shown in [25]. Moreover, the four sampling channels can be connected to different THz detectors, each one tuned to a specific frequency band, thus revealing the spectral proprieties of CSR [26].

Synchronized Measurements

KAPTURE and KALYPSO can be installed at different experimental stations and synchronized via the accelerator timing system. The synchronization procedure and the first experimental results obtained with both systems have been described in [22, 27]. After the upgrade and the optimization of the EOSD and VLD setups, further measurement campaigns will be carried out in the next months.

SUMMARY AND OUTLOOK

Two detector systems, KALYPSO and KAPTURE, have been developed for beam diagnostics requiring high temporal resolution and repetition rates in the MHz range. The current status and the major improvements planned for both systems have been described. Both systems are currently installed at different experimental setups at the KARA storage ring, such as the near-field EOSD monitor, the VLD port and the THz beamlines. Moreover, the commissioning of KALYPSO at the European XFEL is ongoing. With respect to other solutions, KAPTURE and KALYPSO achieve high repetition rates for long observation times, allowing scientists to study the beam behaviour over a wide range of time-scales.

ACKNOWLEDGMENTS

The authors would like to thank A. Mozzanica and B. Schmidt for providing us with the GOTTHARD chip, Fabio Colombo, Pia Steck and Simon Kudella for their help with the production of KALYPSO, and Alexander Dierlamm, Marta Baselga and Daniel Schell for their assistance during the design of the Si sensors. This project is partially funded by the BMBF contract number 05K16VKA.

ISBN: 978-3-95450-192-2 doi:10.18429/JACoW-IBIC2017-TU2AB3

REFERENCES

[1] A.-S. Müller *et al.*, "Studies of bunch-bunch interactions in the ANKA storage ring with coherent synchrotron radiation using an ultra-fast terahertz detection system," in *Proc. 4th Int. Particle Accelerator Conf. (IPAC'13)*, 2013, p. MOPEA019.

[2] M. Brosi *et al.*, "Studies of the micro-bunching instability in multi-bunch operation at the ANKA storage ring," in *Proc. 8th Int. Particle Accelerator Conf. (IPAC'17)*, 2017, p. THOBA1.

[3] [Online]. Available: http://www.ibpt.kit.edu/kara

[4] M. J. Nasse *et al.*, "Flute: A versatile linac-based thz source," *Review of Scientific Instruments*, vol. 84, no. 2, p. 022705, 2013.

[5] L. Rota *et al.*, "An ultra-fast linear array detector for MHz line repetition rate spectroscopy," in *IEEE-NPSS Real Time Conference (RT'2016)*, 2016.

[6] A. Mozzanica *et al.*, "The GOTTHARD charge integrating readout detector: design and characterization," *Journal of Instrumentation*, vol. 7, no. 01, p. C01019, 2012.

[7] V. Dorokhov and A. Khilchenko, "The new optical device for turn to turn beam profile measurement," in *Proc. International Beam Instrumentation Conference (IBIC'16)*, 2016, p. WEBL04.

[8] G. Pellegrini *et al.*, "Recent technological developments on lgad and ilgad detectors for tracking and timing applications," *Nuclear Instruments and Methods in Physics Research Section A: Accelerators, Spectrometers, Detectors and Associated Equipment*, vol. 831, pp. 24–28, 2016.

[9] G.-F. Dalla Betta *et al.*, "Design and tcad simulation of double-sided pixelated low gain avalanche detectors," *Nuclear Instruments and Methods in Physics Research Section A: Accelerators, Spectrometers, Detectors and Associated Equipment*, vol. 796, pp. 154 – 157, 2015.

[10] M. Caselle *et al.*, "An ultra-fast data acquisition system for coherent synchrotron radiation with terahertz detectors," *Journal of Instrumentation*, vol. 9, no. 01, p. C01024, 2014.

[11] P. Thoma *et al.*, "High-speed y–ba–cu–o direct detection system for monitoring picosecond thz pulses," *IEEE Transactions on terahertz science and technology*, vol. 3, no. 1, pp. 81–86, 2013.

[12] D. Rall *et al.*, "Energy relaxation time in nbn and ybco thin films under optical irradiation," *Journal of Physics: Conference Series*, vol. 234, no. 4, p. 042029, 2010.

[13] J. Raasch *et al.*, "Single-Shot THz Spectroscopy for the Characterization of Single-Bunch Bursting CSR," in *Proc. of International Beam Instrumentation Conference (IBIC'16)*, 2017, paper WEPG56.

[14] M. Caselle *et al.*, "Kapture-2. a picosecond sampling system for individual thz pulses with high repetition rate," *Journal of Instrumentation*, vol. 12, no. 01, p. C01040, 2017.

[15] M. Caselle *et al.*, "A high-speed DAQ framework for future high-level trigger and event building clusters," *Journal of Instrumentation*, vol. 12, no. 03, p. C03015, 2017.

[16] M. Vogelgesang *et al.*, "Ufo: A scalable gpu-based image processing framework for on-line monitoring," in *High Performance Computing and Communication & 2012 IEEE 9th International Conference on Embedded Software and Systems (HPCC-ICESS), 2012 IEEE 14th International Conference on*, 2012, pp. 824–829.

[17] M. Vogelgesang, L. Rota *et al.*, "A heterogeneous FPGA/GPU architecture for real-time data analysis and fast feedback systems," in *Proc. International Beam Instrumentation Conference (IBIC'16)*, 2016, p. WEPG07.

[18] H. Mohr *et al.*, "Evaluation of GPUs as a level-1 track trigger for the high-luminosity LHC," *Journal of Instrumentation*, vol. 12, no. 04, p. C04019, 2017.

[19] N. Hiller *et al.*, "Electro-optical bunch length measurements at the ANKA storage ring," in *Proc. International Beam Instrumentation Conference (IBIC'14)*, 2014, p. MOPME014.

[20] L. Rota *et al.*, "Kalypso: a Mfps linear array detector for visible to NIR radiation," in *Proc. International Beam Instrumentation Conference (IBIC'16)*, 2016, p. WEPG46.

[21] P. Schönfeldt *et al.*, "Towards near-field electro-optical bunch profile monitoring in a multi-bunch environment," in *Proc. 8th Int. Particle Accelerator Conf. (IPAC'17)*, 2017, p. MOPAB055.

[22] B. Kehrer *et al.*, "Time-Resolved Energy Spread Studies at the ANKA Storage Ring," in *Proc. 8th Int. Particle Accelerator Conf. (IPAC'17)*, p. MOOCB1.

[23] P. Schütze *et al.*, "A fast gated intensified camera setup for transversal beam diagnostics at the ANKA storage ring," in *Proc. 6th Int. Particle Accelerator Conf. (IPAC'15)*, 2015, p. MOPHA039.

[24] M. Brosi *et al.*, "Online studies of thz-radiation in the bursting regime at anka," in *Proc. 6th Int. Particle Accelerator Conf. (IPAC'15)*, 2015, p. MOPHA042.

[25] M. Brosi *et al.*, "Fast mapping of terahertz bursting thresholds and characteristics at synchrotron light sources," *Physical Review Accelerators and Beams*, vol. 19, no. 11, p. 110701, 2016.

[26] J. Steinmann *et al.*, "4-channel single shot and turn-by-turn spectral measurements of bursting CSR," in *Proc. 8th Int. Particle Accelerator Conf. (IPAC'17), 2017*, 2017, pp. 231–234.

[27] B. Kehrer *et al.*, "Simultaneous detection of longitudinal and transverse bunch signals at ANKA," in *Proc. 7th Int. Particle Accelerator Conf. (IPAC'16)*, 2016.

ISBN: 978-3-95450-192-2 doi:10.18429/JACoW-IBIC2017-TU3AB1

OPTICS MEASUREMENTS AT SuperKEKB USING BEAM BASED CALIBRATION FOR BPM AND BEAM BASED EXPERIMENT

Hiroshi Sugimoto, Yukiyoshi Ohnishi, Haruyo Koiso, Akio Morita, Masaki Tejima
KEK, Tsukuba, Japan

Abstract

SuperKEKB is an electron-position collider realizes a new luminosity frontier. The target luminosity is $8\times10^{35}\mathrm{cm}^{-2}\mathrm{s}^{-1}$. The initial beam commissioning started in February 2016 and operated until June 2016. Low Emittance Tuning (LET) is an important issue in the beam commissioning. The Beam-Based Calibration (BBC) scheme for Beam-Position-Monitor (BPM) has been applied in order to establish reliable beam measurement system. In the BBC, a response model among beam position, charge and output signals of the BPM electrodes are introduced to calibrate the relative gain of each electrodes. The gains are adjusted by least squares fitting so that the model reproduces the measured BPM signals. The Beam-Based Alignment (BBA) is also performed to determine the magnetic center of each quadrupole magnet. Using the BBC, the performance of the BPM system and optics correction has been successfully improved. After the series of the optics tuning and the BPM calibration, the vertical emittance of about 10 pm is achieved in the positron ring. This paper presents what we experienced during the beam commissioning focusing on the beam optics measurement and the BBC scheme for the BPM system.

INTRODUCTION

SuperKEKB [1] is an upgrade project of KEKB [2], which has been successfully finished at 2010 after about 10 years of operation with the world luminosity record of $2.1\times10^{34}\ \mathrm{cm}^{-2}\mathrm{s}^{-1}$. SuperKEKB consists of electron (HER) and positron (LER) storage rings with an injector linac and a newly constructed positron damping ring. The target peak luminosity is $8\times10^{35}\mathrm{cm}^{-2}\mathrm{s}^{-1}$.

The design concept is based on the nano-beam scheme [3], in which colliding beams are squeezed to nano-scale sizes in the vertical direction at the interaction point (IP). The key changes of machine parameters from KEKB are 2 times higher beam current, 1/20 times smaller vertical betatron function at the IP with a larger crossing angle. Low emittance beams are essential for the nano-beam scheme as well as squeezing the betatron function.

The SuperKEKB commissioning has stared after over 5 years of the upgrade work. The initial beam commissioning started on February 1st 2016 and finished on June 28th 2016. The final focus system to collide two beams is not installed in this commissioning period. The commissioning is devoted to the vacuum scrubbing and the setup of both hardware and software. The LET is the one of the most important issue. The nominal machine parameters in this commissioning period are listed in Table 1.

Table 1: Machine Parameters as of June 2016

Parameter	HER	LER	Unit
E	7	4	GeV
I	0.87	1.01	A
N_{bunch}	1576	1576	
ε_x	4.6	1.8	nm
α_p	4.44×10^{-4}	2.45×10^{-4}	
σ_E	6.30×10^{-4}	7.52×10^{-4}	
V_c	12.61	7.65	MV
U_0	2.43	1.76	MeV
τ_s	29	23	msec
σ_z	5.3	4.6	mm
ν_s	-0.0253	-0.0192	
ν_x	45.530	44.430	
ν_y	43.570	46.570	

Calibration of the BPM system is a key issue for better control of beam orbit and optics. We employ the BBC technique to the BPM system as at KEKB [4] . In BBC, both the relative gain of the BPM electrodes and the relative offset between the BPM electrical center and the magnetic center of a quadrupole are determined using measured BPM signals. In this paper we show the idea and results of BBC together with experience on the LET in the initial beam commissioning.

BPM SYSTEM

The SuperKEKB accelerator has about 900 quadrupole magnets, and BPM is attached to each quadrupole magnets for precise orbit control. Most of the BPMs installed in the HER are based on 1 GHz narrow-band system [5] reused KEKB since most of the vacuum chambers are same as those of KEKB. On the other hand, the vacuum chambers of LER are replaced with new ones with ante-chamber structure, and the cutoff frequency is lower than 1 GHz in SuperKEKB. Therefore a newly developed narrow-band system is installed in the LER.

TheBPM system is successfully used in the beam tuning with an averaging mode of 0.25 Hz. In addition to closed-orbit measurement, more than 100 BPMs can be used as gated turn-by-turn BPMs. The gated turn-by-turn BPM system was very helpful in the first injection tuning at the very early stage of the beam commissioning. Although optics measurement with turn-by-turn beam position data was performed in the initial commissioning and some results are already obtained, we concentrate on the BBC and beam measurement based on closed orbit analysis in this paper.

ISBN: 978-3-95450-192-2 doi:10.18429/JACoW-IBIC2017-TU3AB1

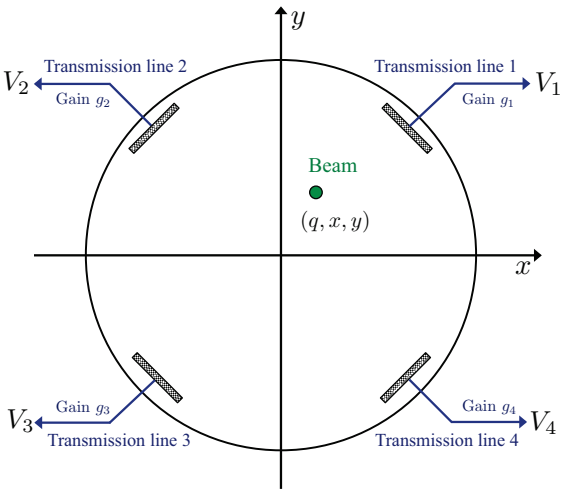

Figure 1: Schematic view of the BPM model used in BGC.

BEAM-BASED CALIBRATION

Two calibration factors are discussed here. One is calibration of relative gains of the BPM electrodes (BPM Gain Calibration, BGC) and the other is the determination of the BPM offset relative to the neighbour quadrupole magnet. In this section, we show a strategy of these calibration work and its result.

Gain Calibration

In the presented BPM system, a BPM has four button-type pickups and outputs four voltages $V_{1,2,3,4}$ induced by the beam as shown in Fig. 1. In order to eliminate dependency on beam intensity, normalized horizontal and vertical voltages (u, v) are used in the calculation of the beam position as,

$$u \equiv (V_1 - V_2 - V_3 + V_4)/\Sigma, \quad (1)$$

$$v \equiv (V_1 + V_2 - V_3 - V_4)/\Sigma, \quad (2)$$

where Σ is the sum of all four voltages. These normalized variables are transformed to horizontal and vertical beam positions (x, y) by using mapping functions as $x = F_x(u, v)$ and $y = F_y(u, v)$. The functions $F_{x,y}(u, v)$ are approximated by third order polynomial functions. The polynomial coefficients are obtained by a finite boundary element method with a two-dimensional electrostatics BPM model.

Assuming the ideal BPM with a perfectly conducting beam pipe and considering the transverse electric and magnetic field, the output voltage of i-th electrode is expressed by a single response function $F_i(x, y)$ as $V_i = qF_i(x, y)$. The voltage of each electrode is measured through a detector system after traveling through a different transmission path. Therefore the response of each electrode depends on the electrical characteristic of the transmission path and may be different from that of the ideal system.

We introduce a single calibration factor g_i to i-th electrode, called its gain, in order to describe the imbalance among the electrical characteristics of the four electrodes. The measured voltage is now re-written as $V_i = g_i q F_i(x, y)$, and all gains are equal to 1 for the ideal condition. Because only the relative value is essential in the calculation of beam positions as shown in Eqs. (1) and (2), we choose $g_1 = 1$ in the following.

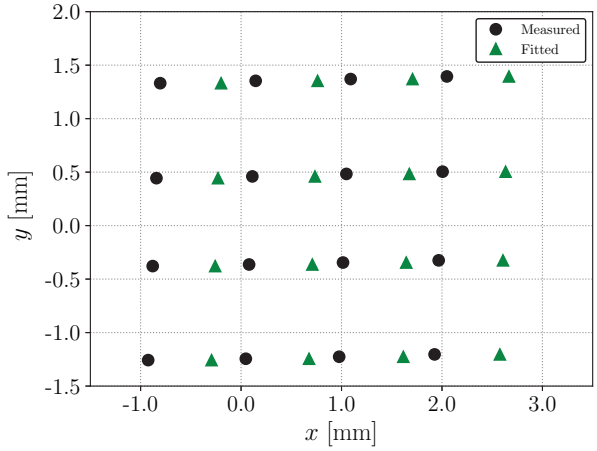

Figure 2: Example of the gain calibration. The dots represent measured beam position before the fitting, while the triangles represent beam positions obtained by the chi-square minimization.

The gain factor can be determined by a beam measurement so that the BPM model reproduces the measured BPM signals [6]. For this purpose we minimize a chi-square function,

$$\chi^2 \equiv \sum_i^4 \sum_j^m \frac{\left[V_{ij} - g_i q_j F(x_i, y_i)\right]^2}{\sigma_{ij}^2}, \quad (3)$$

where m is the number of measurements. The symbol σ represents the measurement error and is 10^{-3} in the presented system. The fitting parameters are three gain factors $g_{2,3,4}$, m sets of beam charges and positions (q_j, x_j, y_j). Therefore $3 + 3m$ parameters are determined by $4m$ measured voltages. It is expected that the unique solution can be obtained when $m > 4$ because the number of fitting variables becomes larger than that of measurement data. A sufficiently wide area of beam position data should be used to avoid degeneracy of the measurement data and failure in the chi-square minimization.

The response function $F_i(x, y)$ is approximated by a fourth order polynomial fit to numerical data obtained with the BPM model. The Levenberg-Marquardt algorithm [7, 8] is employed to minimizing χ^2. The BPM reading and gain factors at that point is used as an initial guess for the optimization algorithm.

Figure 2 illustrates experimental result obtained in the LER, where beam positions before the BGC and those obtained by the chi-square minimization are plotted. The electrode voltages are measured while changing strength of horizontal and vertical steering magnets. The chi-square χ^2 defined in Eq. (3) is converged from 4.8×10^8 to 1.3 after 17

ISBN: 978-3-95450-192-2 doi:10.18429/JACoW-IBIC2017-TU3AB1

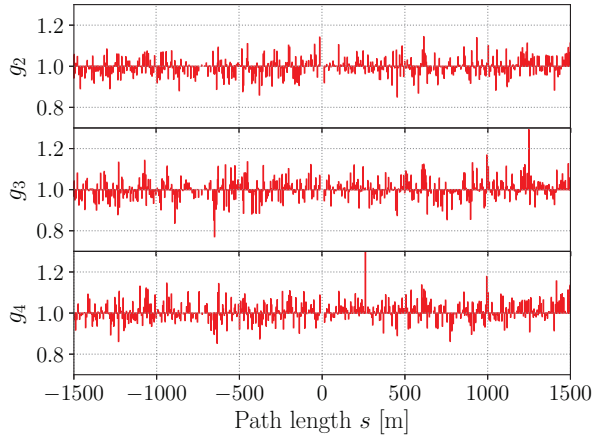

Figure 3: Gain parameters for the LER BPMs.

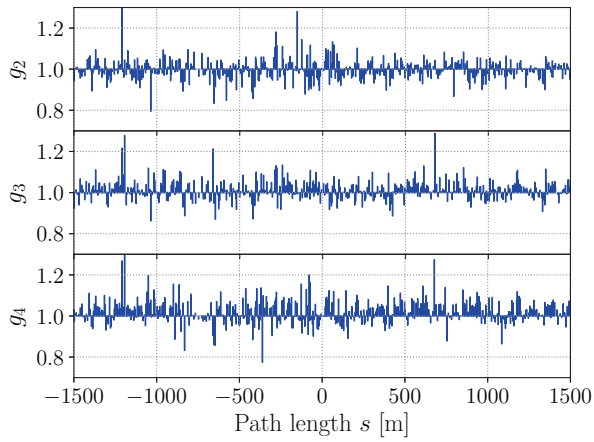

Figure 4: Gain parameters for the HER BPMs.

iterations of the minimization algorithm, and the resultant gains are $(g_2, g_3, g_4) = (0.994, 1.031, 0.987)$.

The BGC is performed for all BPMs in the both LER and HER. Two sets of horizontal and vertical steering magnets are used in the measurement considering betatron phase advance between them. The obtained gain factors are plotted along the ring in Figs. 3 and 4. The deviation from the ideal gain $\Delta g_{2,3,4} \equiv g_{2,3,4} - 1$ is about 5 % in the root-mean-square for both rings.

Beam Based Alignment

Another calibration parameter discussed in this paper is the BPM offset, that is, a misalignment between the magnetic center of a neighbour quadrupole magnet and the BPM electrical center. The BPM offset respect to the magnet causes unexpected orbit and optics distortion and may lead emittance degradation.

The offset respect to an adjoined quadrupole magnet is determined by Beam-Based-Alignment (BBA) technique [9]. We find a BPM reading which is insensitive to the field strength of the quadrupole magnet. The measurement is performed by using a semi-automated software implemented

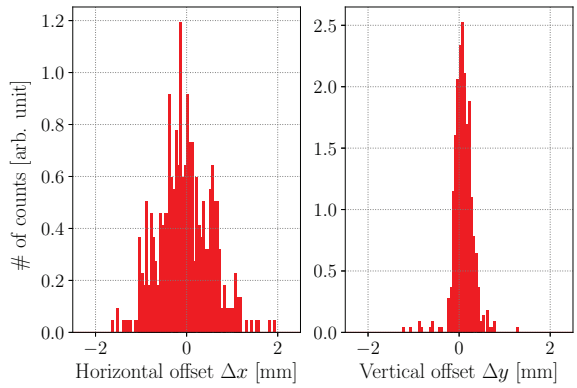

Figure 5: Offset distribution for the LER BPMs.

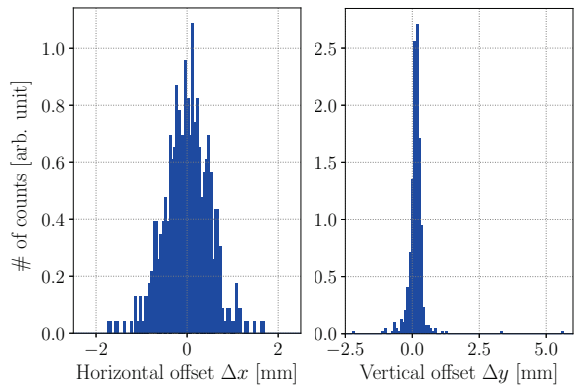

Figure 6: Offset distribution for the HER BPMs.

Table 2: Statistics of the Offset Distribution Shown in Figs. 5 and 6

Parameter [mm]	LER	HER
$\Delta x^{\min}$ / $\Delta y^{\min}$	-1.60 / -1.22	-1.73 / -2.24
$\Delta x^{\max}$ / $\Delta y^{\max}$	1.95 / 1.26	1.67 / 5.62
Δx^{rms} / Δy^{rms}	0.57 / 0.24	0.50 / 0.42

by the accelerator code SAD [10]. The offset information is incorporated into the BPM system.

The offset distributions are shown in Figs. 5 and 6, and their statistical information is summarized in Table 2. A few BPMs show relatively large vertical offset in the HER. In order to understand this unexpected vertical offset in the HER, some details on treatment of the offset parameters in the BPM system are described as follows.

The BBA technique finds out the BPM reading at which beam passes through the magnetic center, while the BGC redefines the electrical center of the four electrodes and changes the BPM reading. Therefore we should adjust the BPM offset parameter after BGC by considering the change of the BPM reading due to gain factor update, otherwise the BPM reading used in the orbit correction changes and unexpected orbit correction may be performed. To avoid this,

ISBN: 978-3-95450-192-2 doi:10.18429/JACoW-IBIC2017-TU3AB1

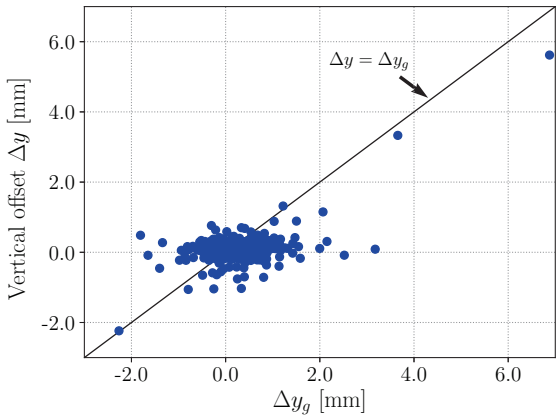

Figure 7: The vertical offset parameter Δy of the HER BPM system as shown in Fig. 6 against the offset Δy_g originated in the gain imbalance.

the offset parameter is adjusted after the BGC so that the BPM reading after the BGC is same as that before the BGC. This indicates the offset parameters shown in Figs. 5 and 6 are results from both the BGC and the BBA.

The change of horizontal and vertical BPM readings $(\Delta x_g, \Delta y_g)$ caused by a gain imbalance $\Delta g_{2,3,4}$ are given by, $\Delta x_g = A(\Delta g_2 + \Delta g_3 - \Delta g_4)$, $\Delta y_g = B(\Delta g_2 - \Delta g_3 - \Delta g_4)$ in the first order of $\Delta g_{2,3,4}$, respectively. The coefficients A and B can be evaluated by the mapping functions $F_{x,y}(u, v)$. The vertical offset parameter of the HER BPM system shown in Fig. 6 is plotted against Δy_g in Fig. 7. The extremely large offsets clearly have correlation with Δy_g, namely, the gain imbalance. The correlation indicates that the observed large offset does not mean misalignment of the mechanical center of the BPM and the magnetics center of the magnet, but a large gain imbalance among the electrodes.

OPTICS MEASUREMENT AND CORRECTION

Optics measurement and correction toward low emittance beams are iteratively carried out in parallel to the BBC during the commissioning period. The beam optics is measured by analyzing closed orbit distortions induced by horizontal dipole kicks to the beam or frequency change of rf cavities.

The important optics parameters in the LET are the vertical dispersion function and the coupling between horizontal and vertical betatron motions (xy-coupling parameter). The xy-coupling parameter is a correlation between horizontal and vertical betatron motions, thus a vertical leakage orbit induced by a horizontal dipole kick reflects xy-coupling parameters. Six kinds of vertical leakage orbits are measured by using six different steering magnets considering the betatron phase advance among them. The correction of xy-coupling is performed against these leakage orbits. Additional skew quadrupole coils are newly installed to sextupole magnets in SuperKEKB for the optics correction. The adjustment of the skew quadrupole filed is calculated with

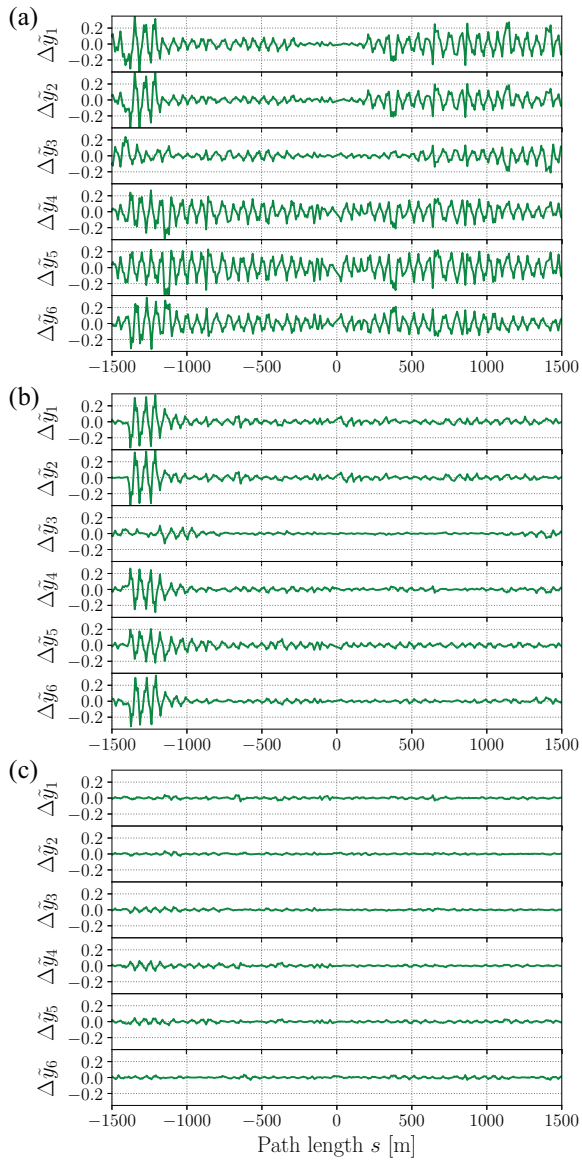

Figure 8: Measured vertical leakage orbits induced by horizontal dipole kicks in the LER ring (a) before correction, (b) after correction, (c) after two countermeasures for the leakage field of the Lambertson septum magnet. The vertical axis is normalized by root-mean-square amplitudes of the horizontal orbit.

the measured vertical leakage orbits and the model response matrix computed by SAD.

The vertical leakage orbits in the LER measured before and after the xy-coupling correction are shown in Figs. 8(a) and 8(b), respectively. After adjusting the skew quadrupole correctors, the vertical leakages are significantly suppressed. However, an uncorrectable leakage orbit was observed around $s = -1300$ m.

We find after a series of investigations that the uncorrectable xy-coupling is due to the leakage field from a Lambertson septum magnet which delivers aborted beams to

ISBN: 978-3-95450-192-2 doi:10.18429/JACoW-IBIC2017-TU3AB1

Table 3: Summary of the Optics Correction

Optics parameter	LER	HER
$\Delta y^{\rm rms}/\Delta x^{\rm rms}$ [10^{-3}]	9	6
$\Delta\eta_x^{\rm rms}$ [mm]	8	11
$\Delta\eta_y^{\rm rms}$ [mm]	2	2
$(\Delta\beta_x/\beta_x)^{\rm rms}$ [%]	3	3
$(\Delta\beta_y/\beta_y)^{\rm rms}$ [%]	3	3

a beam dump. Two cures are applied during the commissioning period. One is activation of skew quadrupole coils installed in the nearby sextupole magnets by using spare power supplies. Another cure is installation of permanent magnets. The specification of the permanent magnets is determined by considering the measured vertical leakage orbits shown in Fig. 8(b). We attached ferrite magnets with field strength of 0.07 T to the beam chamber near the septum magnet [11]. The xy-coupling due to the leakage field is successfully reduced by these cures as shown in Fig. 8(c). The same problem is observed in the HER, and we applied same cures to the HER. The residual of optics parameters respect to the model lattice is summarized in Table 3.

The history of vertical emittance of the LER beam during the commissioning period is plotted in Fig. 9. The vertical emittance is evaluated by vertical beam size measured by an x-ray beam size monitor [12]. The achieved lowest vertical emittance is about 10 pm. This value is consistent with that estimated by measured beam optics. On the other hand the vertical emittance of the HER beam is about 40 pm according to the beam size measurement. It is considerably larger than 10 pm expected from measured beam optics. The discrepancy in the HER is still under investigation.

One difference between the LER and the HER in beam size measurement is the vertical betatron function at the x-ray source point. The betatron function at the source point is 67 m in the LER, whereas 8 m in the HER. Therefore, required resolution in the beam size measurement is higher in the HER when the emittance is comparable in the both rings. We plan to enlarge the vertical betatron function from 8 to 28 m by installing pole changers to some quadrupole magnets, and investigate this issue more systematically in the next commissioning period.

SUMMARY

The BBC technique for the BPM system in the SuperKEKB first commissioning and the results of the LET are presented. Assuming the BPM model, the relative gains of the BPM electrodes are calibrated so that the model reproduces the measured output voltages. The BPM offset respect to the magnetic center of the neighbour quadrupole magnet is determined by finding the BPM reading which is insensitive to the quadrupole field strength.

The optics correction using the reliable BPM system is successfully worked. Though an unexpected problem due to the leakage field from the Lambertson septum magnet is revealed, it was resolved within the commissioning period.

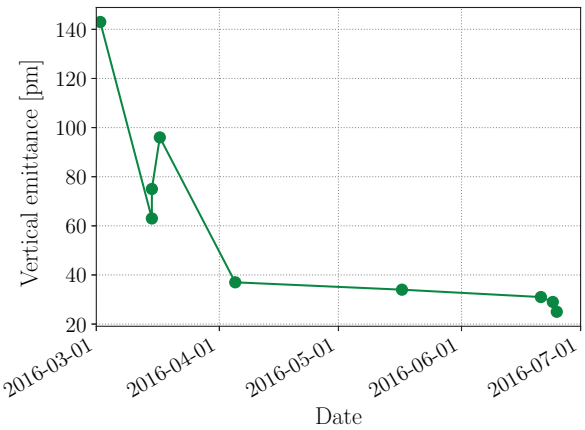

Figure 9: History of vertical emittance in LER.

The achieved vertical emittance in the LER ring is about 10 pm. The vertical emittance of the HER beam is about 40 pm according to the beam size measurement. It is considerably larger than that expected from measured beam optics. The vertical emittance in the HER is still under investigation. More detailed study is planned in the next commissioning period to fix this issue.

ACKNOWLEDGEMENT

The authors would like to thank the entire SuperKEKB accelerator group for developing the hardware system and supporting the beam measurement presented in this paper.

REFERENCES

[1] Y. Ohnishi *et al.*, *Prog. Theor. Exp. Phys.* 2013 03A011 (2013).

[2] T. Abe *et al.*, *Prog. Theor. Exp. Phys.* 2013 03A001 (2013).

[3] C. P. Raimondi, *2nd SuperB Workshop*, Frascati, Italy, Mar. 16-18, 2006.

[4] M. Tejima, in *Proc. of IBIC2015*, Melbourne, Australia, 2015 pp. 267-272.

[5] M.Arinaga *et al.*, *Prog. Theor. Exp. Phys.* 2013 03A007 (2013).

[6] K. Satoh and M. Tejima, in *Proc. of PAC1997*, Vancouver, Canada, 1997, pp. 2087-2089.

[7] D. Marquardt, *J. Soc. Indus. Appl. Math.*, Vol. 11, no 2, pp. 431-441, June 1963.

[8] H.B. Nielsen, *Technical Report*, IMM-REP-1999-05, Technical University of Denmark, 1999.

[9] M. Masuzawa *et al.*, in *Proc. of EPAC2000*, Vienna, Austria, 2000, pp. 1780-1782.

[10] K. Oide, Nucl. Inst. Meth. A 276, 427 (1989). `http://acc-physics.kek.jp/SAD/`

[11] N. Iida *et al.*, in *Proc. of IPAC2017*, Copenhagen, Denmark, 2017, pp. 2918–2921.

[12] E. Mulyani *et al.*, in *Proc. of IBIC2016*, Barcelona, Spain, 2016, pp. 524–527.

ISBN: 978-3-95450-192-2 doi:10.18429/JACoW-IBIC2017-TU3AB3

DIGITAL SIGNAL PROCESSING TECHNIQUES TO MONITOR BUNCH-BY-BUNCH BEAM POSITIONS IN THE LHC FOR MACHINE PROTECTION PURPOSES

J. Pospisil*, O. Bjorkqvist, A. Boccardi, M. Wendt, CERN, Geneva, Switzerland

Abstract

This paper presents the development of an upgrade to the beam position interlock system for the Large Hadron Collider (LHC) at the European Organization for Nuclear Research (CERN). The beam orbit at the beam dump kicker is continuously monitored by 16 beam position monitors that are part of the machine protection system. In case of unacceptable orbit movement the system has to trigger the beam abort immediately to prevent damage to the machine. An upgrade of the present system is underway with the aim of handling a larger dynamic range of bunch intensities, and coping with different bunch time structures (both the standard bunch spacing of 25 ns and special doublet bunches spaced by 5 ns).

The proposed architecture combines the analogue signals from opposite pickup electrodes on a single read-out channel, and stretches it with a delay-line based comb-filter. The resulting signal, covering a dynamic range of 60 dB, is digitized at 3.2 GSa/s and processed inside a Field-programmable Gate Array (FPGA) to extract a position value. Different signal processing techniques are compared on simulated ideal beam signals, and preliminary results of a prototype installation is presented.

INTRODUCTION

The interlock Beam Position Monitor (BPM) system is used to protect the aperture of the two LHC beam dump channels (one for each beam) by ensuring that the position of the circulating beam never exceeds what is considered to be a safe value whenever a beam dump is requested. It continually monitors the beam position of all bunches and will itself trigger a beam dump if the beam position lies outside a ±3.5 mm window for a predefined number of bunches over a predefined number of turns (linked to expected damage thresholds with respect to beam intensity and energy). It comprises 16 stripline BPMs, and at present is read-out using the standard *Wide-Band Time Normalizer* (WBTN) LHC position system electronics combined with dedicated FPGA firmware [1, 2]. This system performs bunch-by-bunch position measurements with a nominal resolution ranging from 150 µm to 50 µm, while covering a respective range of bunch intensities from 2×10^9 to 1.5×10^{11} charges per bunch (cpb). This is achieved using two sensitivity settings, one from 2×10^9 to 5×10^{10} cpb and the other from 2×10^{10} to 1.5×10^{11} cpb. The current system has several downsides:

- The need to switch sensitivity means that the system cannot effectively operate with bunches of very different intensity in the machine at the same time.
- The system suffers from performance degradation due to temperature drifts.
- The limited flexibility in terms of beam filling patterns, requiring a minimum bunch-to-bunch spacing of 25 ns.

This latter point is a major limitation for beam scrubbing runs, when the LHC is filled with 5 ns so-called "doublet bunches", i.e. a pair of bunches spaced by 5 ns, themselves spaced by a 25 ns from the next pair [3]. This operational mode and the other limitations mentioned call for a new read-out system for the LHC interlock BPMs.

SINGLE CHANNEL DIGITIZATION

In the proposed architecture shown in Fig. 1, the signals from both electrodes are time multiplexed onto a single read-out channel using a 12.5 ns delay transmission-line, Delay Multiplex Single Path Technology (DMSPT), where some minimum signal conditioning is applied before the conversion to the digital domain. This analog RF signal conditioning is limited to a delay-line based band-pass comb filter, an anti-aliasing low-pass filter and gain/attenuator stages. Most of the processing then takes place in a subsequent FPGA.

The two main advantages of this architecture are the direct digitization, which allows doublet bunches to be processed, and the single channel read-out scheme, which reduces beam position offset effects caused by asymmetries in the signal processing electronics [4–6].

Analog Signal Processing

The single bunch response from a stripline electrode is a bipolar pulse, which in the case of the LHC is, to first approximation, a single 500 MHz sinusoidal oscillation of ~2 ns duration. A band-pass comb filter, operating at the same central frequency combines four time-shifted replicas of the input signal from opposite electrodes to generate two ~8 ns sine-wave like bursts of four oscillation periods at 500 MHz. This can be seen in Fig. 2a with results of a beam measurement performed in the Super Proton Synchrotron (SPS) on a single bunch. In this case the ADC was running at 3.2 GSa/s giving up to 30 usable samples per electrode to reconstruct the signal amplitudes.

In the case of doublet bunches only some parts of each 8 ns bursts are unaffected by the doublet structure leaving only ~ 10 samples for signal reconstruction, see Fig. 2b.

* j.pospisil@cern.ch

ISBN: 978-3-95450-192-2 doi:10.18429/JACoW-IBIC2017-TU3AB3

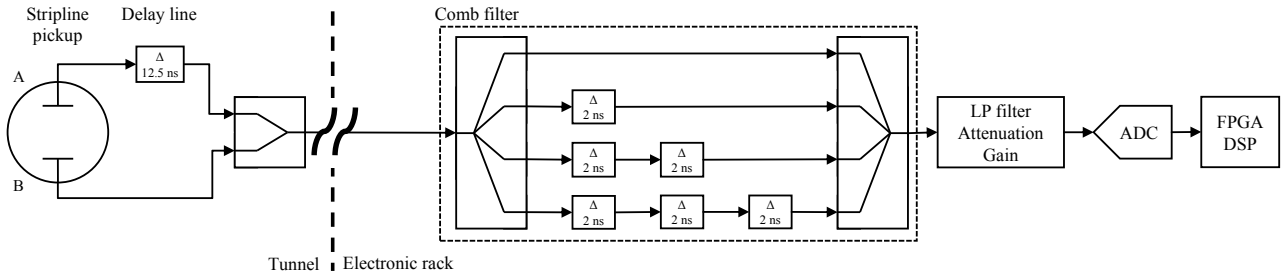

Figure 1: Overall scheme.

Digital Signal Processing

A circuit simulation of the analog front-end defined a 1.2 GHz high cut-off for the analogue processing bandwidth of the ADC to limit effects from signal ringing. This results in a minimum sampling rate of 2.5 GSa/s, assuming no undersampling. Decimation, normalization and calculation of the beam position is performed in real-time, bunch-by-bunch, using an FPGA.

The digital part of the system will be clocked asynchronously to the machine clock, to be able to operate fully independently from any external clock signals (a requirement of the machine protection system).

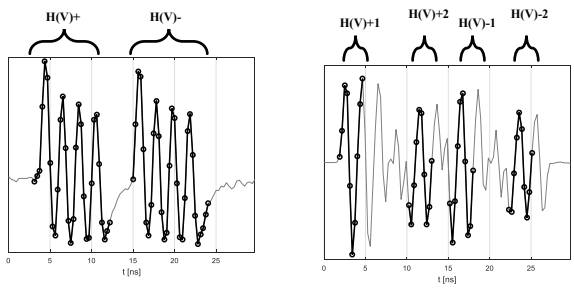

(a) Single bunch (measured). (b) Doublet bunch (simulated).

Figure 2: Band-pass filtered signal, as seen by the ADC.

PERFORMANCE ESTIMATION

A MATLAB framework was developed to simulate the BPM signal processing, and to evaluate the overall performance of the system. In this framework a signal generator module simulates the ADC output signal, based on an electromagnetic analysis of the stripline BPM combined with a circuit analysis of the analog front-end. Several parameters, like beam intensity and position, sampling time-shift, and ADC characteristics (noise, sampling frequency and number of bits per sample) can be varied and optimized. The second part of the simulation framework evaluates different signal processing algorithms to extract the bunch-by-bunch beam position, while in the final part the simulated results are compared for a variety of initial beam parameters.

Amplitude Extraction Algorithms

The beam position of each bunch is computed by comparing the intensity normalized amplitudes of opposite pickup electrodes:

$$\text{BeamPosition} = k\frac{A_+ - A_-}{A_+ + A_-}$$

where A_+, A_- are the amplitudes of the sampled waveforms of the processed electrode signals and k is a non-linear calibration function defined by the pickup geometry. In our case k can be considered a constant equal to 0.79 dB/mm, equivalent to a ∼1 % signal modulation for a beam displacement of 100 µm. Different algorithms have been tested and compared using the simulation framework to obtain A_+ and A_- from the raw ADC samples, including integration, analysis in the frequency domain, time and frequency convolution, and fitting algorithm. A simple, Root Mean Square (RMS) analysis turned out to be the best compromise between complexity and performance, where the signal amplitude is computed as:

$$A = M \cdot \sqrt{\frac{1}{n}\sum_{i=1}^{n} s_i^2}$$

where M is a calibration factor, n is number of samples and s_i is the i^{th} waveform sample.

Simulation Results

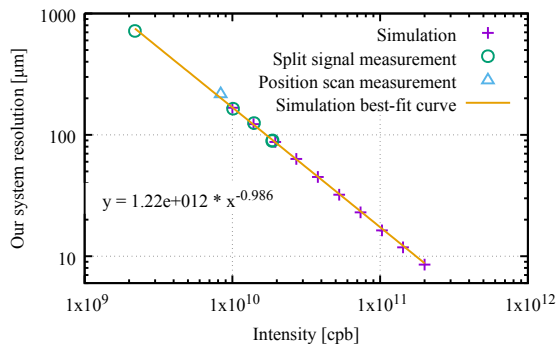

Figure 3: Position resolution from simulations and measurement campaigns obtained using the RMS algorithm.

The parameters of the initial MATLAB simulations are based on the characteristics of the ADC used for prototyping this BPM system: the ∼ 9 Effective Number of Bits (ENOB) 4 GSa/s *Texas Instruments* ADC12J4000 [7]. Figure 3 shows preliminary estimations of achievable resolution vs. bunch

ISBN: 978-3-95450-192-2 doi:10.18429/JACoW-IBIC2017-TU3AB3

intensity from both simulations and beam measurements performed in the SPS for the single bunch case. Simulation studies showed no measurable dependency of the position resolution on the sampling phase (time) with respect to the signal, and only a minor degradation for beams with large displacements (±7.5 mm). For a signal varying in amplitude by a factor of 20, covering almost the full-scale input range of the ADC, the single bunch position resolution ranges between 9 µm and 167 µm. Further simulation studies showed that the noise floor of the ADC remains the dominant limitation, with each additional ENOB improving the resolution by a factor 2. The same result could also be achieved by increasing the sampling frequency by a factor of 4.

PROTOTYPE PERFORMANCE

A prototype setup of the BPM signal processing chain similar to the layout shown in Fig. 1 was assembled for testing on a button-type BPM pickup in the SPS. The delay-line components used for the band-pass comb filter were made from connectorized RF power combiners/splitters and semi-rigid coaxial cables. For the ADC a commercial FMC mezzanine board *Vadatech* FMC225 [8] was hooked to an in-house developed VME carrier board [9] holding an *Altera* Arria V GX FPGA for the digital signal processing. The 4 GSa/s sampling rate of the ADC board had to be reduced to 3.2 GSa/s, a limit set by the data links to the FPGA.

Beam Measurements

Two measurement campaigns were performed, both looking only at the vertical plane and using single bunches. Even though the BPM pickup and bunch parameters differ slightly from those of the LHC interlock BPM, the signals generated are nevertheless very similar.

In the first measurement campaign, only one electrode was used with the signal split to simulate two independent electrode signals. In this way the beam displacement could be simulated independently from the actual beam orbit in the machine by inserting various RF attenuators. The dispersion of the long coaxial cables between beam pickup and electronics, and some residual ringing of the comb filter, resulted in some coupling between successive 8 ns burst waveforms and between consecutive bunches (see Fig. 4). This causes a position shift for the subsequent bunches which is in the order of the resolution of the system. The position resolution obtained from this measurement, applying the RMS algorithm, is inserted into Fig. 3 and agrees very well with the simulations.

In the second set of measurements, both electrodes were connected and a real beam position scan was performed. The beam orbit was altered in several steps over a range of ~6 mm, while monitoring the beam position with both the prototype BPM system and with operational SPS BPM system [10, 11]. Figure 5 shows a comparison of the acquired position scans. A very good agreement is observed with little change in resolution over this range of positions.

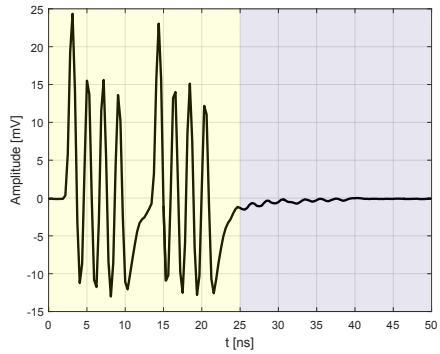

Figure 4: Inter-electrode and inter-bunch coupling shown for a single bunch (25 ns bunch boundaries highlighted).

The resolution of the prototype should not be directly compared to the one of the operational SPS system as the marked uncertainty for the prototype system refers to a bunch-by-bunch, single pass measurement, while for the operational system it is the residual noise after an average of 1 ms for all bunches in the machine. Moreover, the prototype was missing a gain stage, resulting in an equivalent intensity below the target measurement range.

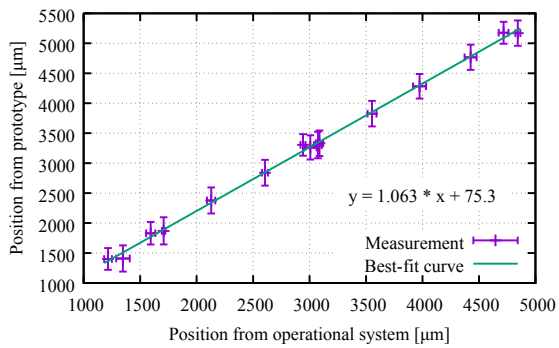

Figure 5: Position scan in the SPS comparing the prototype system to the operational BPM system.

CONCLUSION

A new bunch-by-bunch beam position monitoring system for the beam dump interlock of the LHC, based on a single-channel read-out scheme followed by direct digitization, has been presented. The estimation of BPM performance based on simulations showed the single-bunch, single-pass resolution to be in the range 9 µm to 167 µm for a position displacement up to ±7.5 mm, and an intensity from 1×10^{10} to 2×10^{11} cpb in a nominal filling scheme with 25 ns spaced bunches. This is in agreement with the initial results from beam measurements using a prototype installation in the SPS.

Additional studies need to be performed to characterize the proposed system for doublet bunch operation. The resolution is expected to be lower compared to that for nominal bunch spacing, but is still expected to be fully compatible with the interlock system requirements.

ISBN: 978-3-95450-192-2 doi:10.18429/JACoW-IBIC2017-TU3AB3

ACKNOWLEDGMENT

We would like to thank Thibaut Lefevre for supporting this project, Tom Levens and Michal Krupa for their valuable help with setup and beam measurements, and also the SPS operations crew, which allowed us to use a time-slot within the machine development period to acquire the position scan measurements.

REFERENCES

[1] D. Cocq and G. Vismara, "From narrow to wide band normalization for orbit and trajectory measurements," in *Proceedings of the 8th Beam Instrumentation Workshop*, (Stanford, California, USA, May 1998), Nov. 1998. DOI: 10.1063/1.56993. https://cds.cern.ch/record/370462

[2] D. Cocq, H. Schmickler, and G. Vismara, "A new wide band time normaliser circuit for bunch position measurements with high bandwidth and wide dynamic range," no. CERN-SL-98-064-BI, Nov. 1998. https://cds.cern.ch/record/370464

[3] Y. Papaphilippou, H. Bartosik, G. Rumolo, and D. Manglunki, "Operational beams for the LHC," 2015. https://cds.cern.ch/record/2031187

[4] T. Traber and R. Neumann, "Simulation of BPM electronics at DESY," in *Proceedings of the 4th CARE-HHH-ABI Workshop on Simulation of BPM Front-End Electronics and Special Mechanical Designs*, (Lüneburg, Germany, Nov. 2006), Mar. 2007. http://adweb.desy.de/mdi/CARE/Lueneburg/care_traber.pdf

[5] F. Schmidt-Föhre, A. Brenger, G. Kube, R. Neumann, and K. Wittenburg, "BPM system upgrades in the PETRA III pre-accelerator chain during the 2008 shutdown," in *Proceedings of the 9th European Workshop on Beam Diagnostics and Instrumentation for Particle Accelerators*, (Basel, Switzerland), May 2009. http://accelconf.web.cern.ch/AccelConf/d09/papers/mopd20.pdf

[6] B. Lorbeer, N. Baboi, H. T. Duhme, F. Schmidt-Föhre, and K. Wittenburg, "Development status and performance studies of the new MicroTCA based button and strip-line BPM electronics at FLASH 2," in *Proceedings of the 4th Int. Beam Instrumentation Conf.*, (Melbourne, Australia), Sep. 2015. http://accelconf.web.cern.ch/AccelConf/IBIC2015/papers/tupb014.pdf

[7] Texas Instruments Incorporated. (Aug. 2017). ADC12J4000: 12-Bit, 4.0-GSPS, RF sampling analog-to-digital converter, http://www.ti.com/product/ADC12J4000

[8] VadaTech. (Aug. 2017). 5.7 GSPS DAC, 4 GSPS ADC, digitizer, converter, A/D, D/A, FMC, module, http://www.vadatech.com/product.php?product=379

[9] A. Boccardi, M. Barros Marin, T. Levens, B. Szuk, W. Viganò, and C. Zamantzas, "A modular approach to acquisition systems for future CERN beam instrumentation developments," in *Proceedings of the 15th Int. Conf. on Accelerator and Large Experimental Physics Control Systems (ICALEPCS 2015)*, (Melbourne, Australia), Oct. 2015. DOI: 10.18429/JACoW-ICALEPCS2015-THHB2002. http://jacow.org/icalepcs2015/papers/thhb2o02.pdf

[10] J. C. De Vries *et al.*, "Real-time and control software for the new orbit measurement system of the CERN SPS," in *Proceedings of the Int. Conf. on Accelerator and Large Experimental Physics Control Systems (ICALEPCS 1999)*, (Trieste, Italy, Oct. 1999), 1999. https://cds.cern.ch/record/532671

[11] C. Boccard *et al.*, "Performance of the new SPS beam position orbit system (MOPOS)," in *Proceedings of the 4th European Workshop on Beam Diagnostics and Instrumentation for Particle Accelerators*, (Chester, UK, May 1999), Sep. 1999. https://cds.cern.ch/record/398772

ISBN: 978-3-95450-192-2 doi:10.18429/JACoW-IBIC2017-TUPCC01

CURRENT STATUS OF CVD DIAMOND BASED BEAM DETECTOR DEVELOPMENTS AT THE S-DALINAC*

A. Rost[1†], T. Galatyuk[12], J. Pietraszko[2]
[1]Institut für Kernphysik, TU Darmstadt, Darmstadt, Germany
[2]GSI Helmholtzzentrum für Schwerionenforschung GmbH, Darmstadt, Germany

Abstract

In this contribution a field-programmable gate array (FPGA) based read-out concept for diamond based beam monitoring detectors will be introduced. Furthermore for research and development of diamond based detectors a test setup will be installed at the Superconducting Darmstadt Electron Linear Accelerator (S-DALINAC) of TU Darmstadt. The preparatory work, with particular focus on beam transport simulations will be shown.

INTRODUCTION

For future experiments with the HADES [1] and CBM [2] detectors at the FAIR facility in Darmstadt, a radiation hard and fast beam detector is required. On the one hand the detector should handle high current beams, especially the CBM experiment plans to operate at up to 10^9 ions/s. On the other hand the detector has to perform precise T0 measurements ($\sigma_{T0} < 50$ ps) and should offer beam monitoring capabilities. These tasks can be fulfilled by utilizing single-crystal Chemical Vapor Deposition (scCVD) diamond based detectors. This material is well known for its radiation hardness and high drift velocity of both electrons and holes, making it ideal not only as Time-of-Flight (ToF) detectors placed in the beam but also as luminosity monitors. Challenging is the detection of minimum-ionizing particles (MIPS) traversing the diamond detector. The very small induced charges and expected high rates require special emphasis on the read-out electronics. The developed technology of producing mono-crystalline diamond material, which is almost free of structural defects and chemical impurities and thus provides very high charge collection efficiency, allows for building detectors for MIP based on single-crystalline diamond material. With the help of stripped read-out electrodes or by arranging several diamond detectors in a mosaic, a position information can be obtained for beam monitoring purposes. An example of such a diamond based mosaic detector is shown in Fig. 1.

TRB3 BASED BEAM MONITORING SYSTEM

A read-out concept for diamond based beam monitoring and diagnostic detectors is currently under development. It will be based on the already well established TRB3 (Trigger and readout board - version 3) platform [3, 4], developed at GSI Helmholtzzentrum für Schwerionenforschung in Darmstadt. The board provides 260 high precision (RMS < 12 ps) multi-hit FPGA-TDCs and serves as a flexible data acquisition system (DAQ). The available comprehensive software package allows on-line monitoring capabilities including basic analysis. A large variety of front-end electronics is available in order to extend its functionality. One of those front-end boards is the PADIWA discriminator board. It is designed to discriminate 16 detector signals. Due to its flexible analog input stage, it is possible to adjust it to a wide range of detector signals i.e. different Photomultiplier (PMT) types. A photography of the PADIWA board and the simplified read-out scheme is shown in Fig. 2. The input signals are amplified and afterward discriminated by the low-voltage differential signaling (LVDS) input buffers of an FPGA. Thresholds can be set via pulse width modulation in combination with a low pass filter. The arrival time and the time-over-threshold (ToT) is encoded in the leading edge and the width of a digital pulse. The digital pulse is afterwards sent via differential lines to the TRB3 for time measurements.

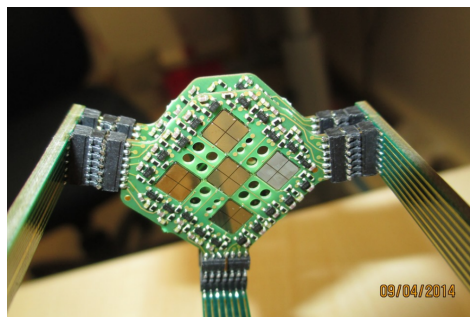

Figure 1: Diamond based mosaic detector which was located in front of the HADES target in a pion production beam time. An total area of 14 mm × 14 mm was covered. The first transistor based pre-amplification stage is located very close to the diamond material.

The read-out concept was already successfully employed to read out the Hodoscope detector in the HADES experiment, which is located at GSI Helmholtzzentrum für Schwerionenforschung (Darmstadt). The Hodoscope was placed behind the HADES spectrometer and was mainly used for beam-monitoring purposes during the beam-tuning. It consists of 16 stacked plastic scintillator rods with sizes of 10 mm × 5 mm × 100 mm. The scintillation light produced in the rods is read out from both sides by Hamamamtsu R3478 PMTs. The PADIWA-AMPS [5] front-end board (which is similar to the PADIWA board, with additional

* Work supported by the DFG through GRK 2128 and VH-NG-823
† a.rost@gsi.de

ISBN: 978-3-95450-192-2 doi:10.18429/JACoW-IBIC2017-TUPCC01

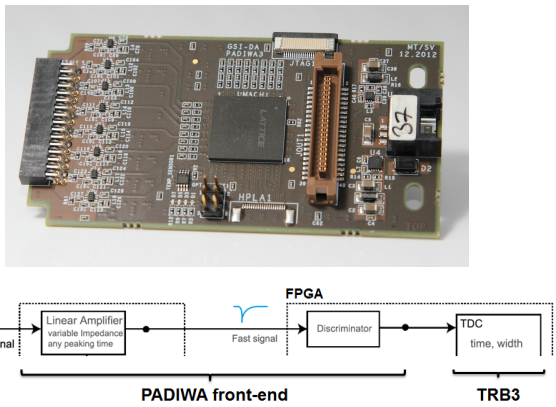

Figure 2: Upper panel: The PADIWA discriminator front-end board for the TRB3 platform. Lower panel: Simplified read-out scheme.

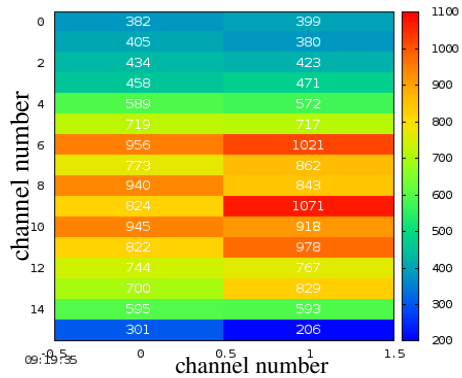

(a) Heat-map showing the hit-rate per second of all Hodoscope PMTs.

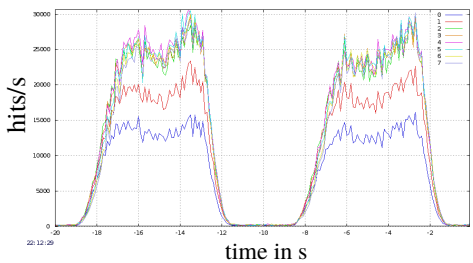

(b) Hit-rate of all Hodoscope PMTs over time.

Figure 3: During the beam-time the figures are displayed live in a web-browser. In the lower panel the spill structure of the pion beam is visualized.

charge measurement capability), in combination with a TRB3 was adapted to the PMT signals. In Fig. 3 the online monitoring screen of the hit rate and the spill structure during the beam-time as seen by the Hodoscope is shown. Currently the concept is being optimized to the signals of diamond based detectors. In this process the analog stage has to be redesigned in order to adapt it to the specifications of the pre-amplifier of the diamond detector.

DIAMOND DETECTOR TEST SETUP AT THE S-DALINAC

The Superconducting Darmstadt Electron Linear Accelerator (S-DALINAC) [6] of TU Darmstadt was currently upgraded with a third recirculation [7] which will allow an acceleration of electrons up to 130 MeV and the possibility to operate it in an energy recovery linac (ERL) mode. It has been demonstrated that the accelerator can provide excellent beam conditions for research and development of diamond based detectors, especially for minimum ionizing particles (MIPS). The main activity is now focused on the development of new diamond based beam detectors and the investigation of its time and energy resolution. Radiation damage studies in diamond material are of crucial importance for the long lifetime of the detectors. Moreover it is foreseen to build up a permanent multi-purpose test setup at the S-DALINAC which is suitable for other tracking detectors i.e. drift-chambers or even radiation tests of read-out electronics. The test setup will be located in the E5 beam line in front of the NEPTUN experiment. For that an additional dipole magnet will be installed into the beam line. An additional pair of quadrupoles will be used to focus the electron beam on the detectors under test. Desirable beam parameters for detector tests are currents in the order of several nA and energies up to 130 MeV. The floor-plan is shown in Fig. 4.

Beam Transport Simulations

Beam transport simulations have been performed using the XBEAM [8] software which was developed at TU Darmstadt. The software uses a matrix based code which calculates beam dynamics up to first (linear) order. The lattice from the extraction of the S-DALINAC to the NEPTUN experiment and the diamond detector test setup was simulated. The simulations must fulfill certain conditions. On the one hand the beam envelope should fit the beam tube at every point, but on the other hand the beam envelope should be minimized at the position of the NEPTUN target and the diamond detector test setup. In Fig. 5 the simulated beam envelope from the S-DALINAC extraction to the diamond detector setup is shown.

SUMMARY AND OUTLOOK

In this contribution a FPGA based beam monitoring system was introduced. The system was already successfully utilized for read out of PMT signals of the HADES Hodoscope. Currently the front-end electronic is optimized for the readout of diamond detector signals. Furthermore the current status of the preparatory work of a diamond detector test setup at S-DALINAC of TU Darmstadt has been shown. The beam transport simulations, which fix the position of the dipole and quadrupole magnets, are almost finished. The beam-line and the diamond detector test set-up are expected to be installed in near future. A first commissioning of the beam-line is planned for the end of 2017.

ISBN: 978-3-95450-192-2 doi:10.18429/JACoW-IBIC2017-TUPCC01

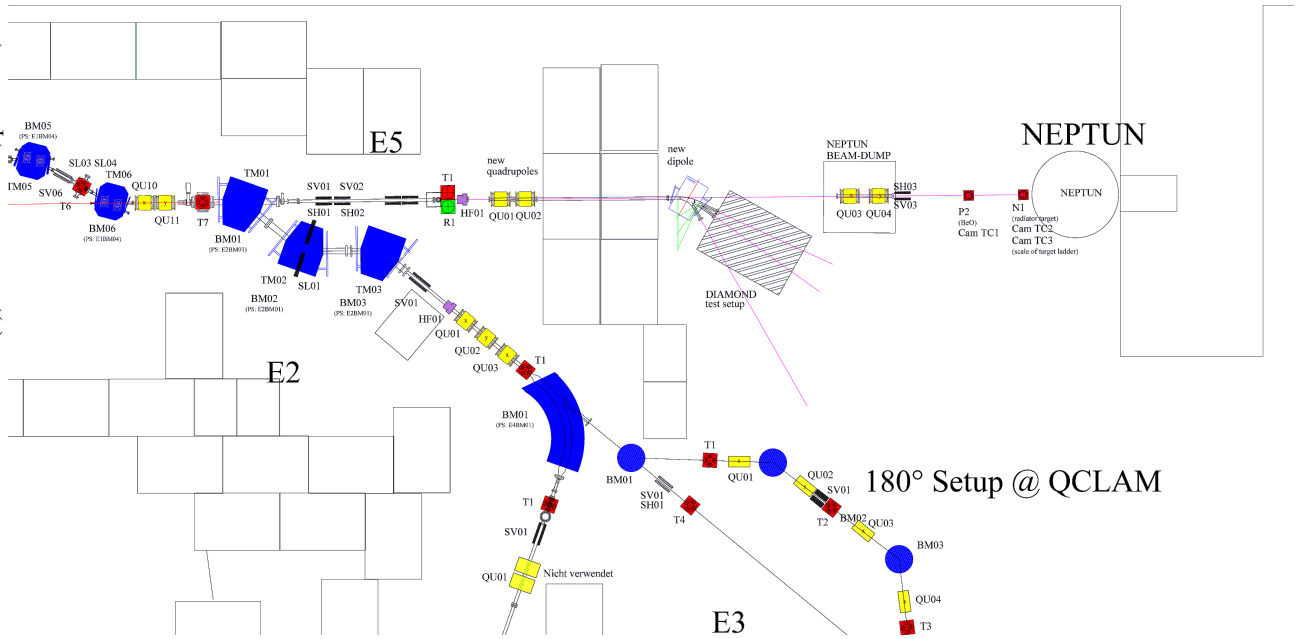

Figure 4: Floor-plan of the E5 beam line of the S-DALINAC. A dipole magnet will be installed and a pair of quadrupoles in order to focus the beam on the diamond detector setup.

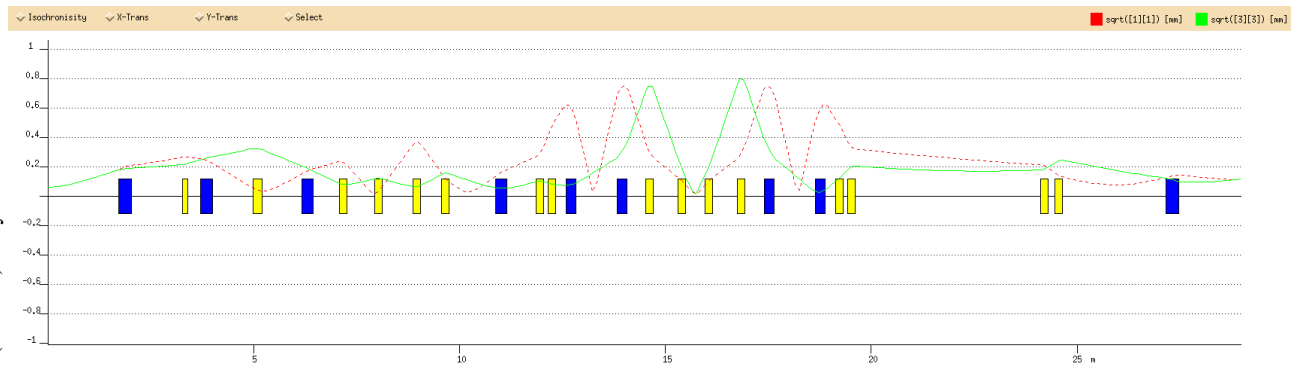

Figure 5: XBEAM simulation of the lattice from S-DALINAC extraction to the diamond detector test set-up. Dipoles are blue and quadrupoles are yellow. The envelope in x- (red) and in y-direction (green) is shown.

REFERENCES

[1] HADES collaboration, G. Agakishiev *et al.*, "The High-Acceptance Dielectron Spectrometer HADES", in *Eur. Phys. J. A 41 (2009) 243 [arXiv:0902.3478].*

[2] CBM collaboration, official website, `http://fair-center.eu/for-users/experiments/cbm.html`

[3] TRB collaboration, A. Neiser *et al.*, "TRB3: a 264 channel high precision TDC platform and its applications", in *2013 JINST 8 C12043.*

[4] TRB3, official website, `http://trb.gsi.de`

[5] TRB collaboration, A. Rost *et al.*, "A flexible FPGA based QDC and TDC for the HADES and CBM calorimeters", in *2017 JINST 12 C02047.*

[6] A. Richter, "Operational experience at the S-DALINAC", in *Proc. EPAC'96*, Sitges, Spain, June 1996, pp. 110–114.

[7] M. Arnold, "Construction and Status of the Thrice Recirculating S-DALINAC", in *Proc. IPAC'17*, Copenhagen, Denmark, May. 2017, paper TUPAB030.

[8] Software: XBEAM 2.1 by IKP TU Darmstadt.

ISBN: 978-3-95450-192-2 doi:10.18429/JACoW-IBIC2017-TUPCC03

ONLINE LONGITUDINAL BUNCH PROFILE AND SLICE EMITTANCE DIAGNOSTICS AT THE EUROPEAN XFEL

Ch. Gerth*, B. Beutner, O. Hensler, F. Obier, M. Scholz, M. Yan†
Deutsches Elektronen-Synchrotron DESY, Hamburg, Germany

Abstract

The longitudinal current profile and slice emittance are important bunch parameters for the operation of an X-ray free-electron laser. At the European XFEL, dedicated diagnostic sections equipped with transverse deflecting RF structures (TDS) have been installed for the control and optimisation of these parameters. Travelling-wave TDS in combination with fast kicker magnets and off-axis screens allow for the study of individual bunches without affecting the other bunches in the super-conducting linear accelerator which can generate bunch trains of up to 2700 bunches at 4.5 MHz within 600 microsecond RF pulses at a repetition rate of 10 Hz. The measurement of the slice emittance is realised in a static F0D0 lattice equipped with four individual screen stations.

Variations of the longitudinal bunch profile or slice emittance along the bunch train may lead to degraded FEL performance for parts of the train which reduces the effective available number of bunches for FEL operation. By gradually adjusting the timing, individual bunches along the bunch train can be measured in order to optimise the overall beam parameters for all bunches in the train. In this paper, we describe in detail the diagnostic concept and present first measurement results of the projected and slice emittance along the bunch train.

INTRODUCTION

The European XFEL, which is currently under commissioning, will deliver ultra-short X-rays in the photon energy range 0.25 keV to 25 keV [1]. The superconducting linear accelerator that will drive 3 FEL undulator beamlines will generate beam energies of up to 17.5 GeV. As is illustrated in Fig. 1, the RF accelerating field is pulsed at a frequency of 10 Hz with a flat-top duration of up to 600 µs, in which a train of electron bunches is accelerated. The bunch repetition rate can be up to 4.5 MHz (equal to a bunch spacing of 220 ns), which corresponds to a maximum of 2700 bunches per bunch train. In future, it is envisioned to operate the accelerator with constant bunch filling patterns that are advantageous in terms of operation stability. The photon pulse pattern can be chosen by sending unwanted electron bunches with fast kicker magnets into a local dump upstream of the FEL undulator beamlines.

Variations during the RF flat-top duration of either the laser pulse properties of the photo-cathode laser or the RF parameters of the accelerator modules in the injector may result in variations of beam matching or emittance of the bunches in the bunch train. This in turn may lead to substantial variations along the bunch train of the photon pulse energies of the X-rays that are delivered to the user experiments. Hence, there is a strong demand for diagnostic techniques with which electron bunch parameters such as the longitudinal current profile or slice emittance can be measured along the bunch train. This has been realised by utilising a transverse deflecting RF structure (TDS) in combination with kicker magnets and off-axis screens.

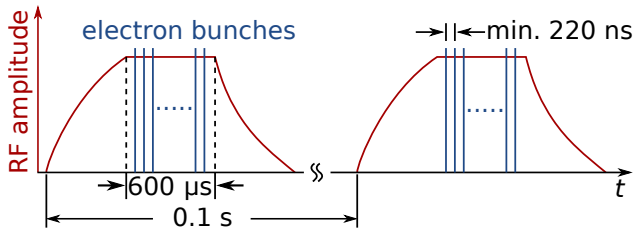

Figure 1: RF timing structure and electron bunch pattern of the European XFEL.

The RF field of the TDS induces a time-dependent transverse deflection of the electrons of one bunch in the bunch train by which the longitudinal bunch shape is transformed to the transverse plane. A fast kicker magnet downstream of the TDS is then used to deflect this bunch onto an off-axis screen without affecting the remaining bunches in the bunch train. The diagnosed bunch is taken out of the bunch train before the FEL undulators while the remaining bunches continue for the generation of FEL radiation. By utilising four kicker magnets with four off-axis screens in a static F0D0 lattice, the longitudinal bunch profile and slice emittance can be measured. Finally, these bunch parameters can be measured along the bunch train by properly adjusting the timing of the TDS, kicker magnets and camera systems of the screen stations. In this paper, we present the results of projected and slice emittance measurements obtained in the injector section of the European XFEL.

DIAGNOSTIC SECTION

Three dedicated beamline sections equipped with TDS have been designed for the measurement of the longitudinal profile and slice emittance as well as the longitudinal phase space [2]. A schematic layout of the TDS diagnostics sections, which are located downstream of the laser heater system in the injector section and downstream of the second and third bunch compressor chicane, is depicted in Fig. 2. Each section comprises a TDS, four kicker magnets, four screen stations with off-axis and on-axis screens, one dipole

* christopher.gerth@desy.de
† Current address: Karlsruher Institut für Technologie, 76131 Karlsruhe, Germany, minjie.yan@kit.edu

ISBN: 978-3-95450-192-2 doi:10.18429/JACoW-IBIC2017-TUPCC03

magnet and one screen station in the dispersive section behind the dipole magnet [3]. The four screen stations are located in the subsequent drift sections of a F0D0 cell structure, which allows for projected emittance measurements [4]. When the TDS is switched on, slice emittance and longitudinal profile measurements can be performed. Longitudinal phase space measurements can be carried out in the dispersive section only when the dipole magnet is switched on and, as a consequence, the whole bunch train is deflected to the local dump and FEL operation is interrupted.

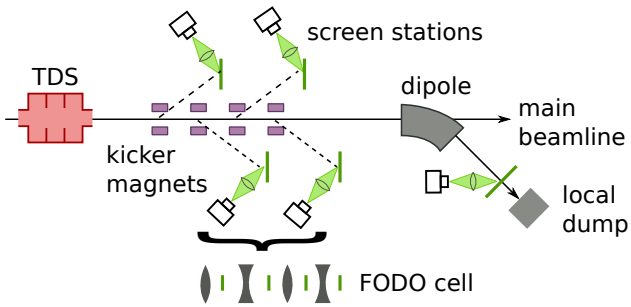

Figure 2: Schematic layout of the 3 TDS diagnostic sections at the European XFEL.

The TDS are disk-loaded *S*-band RF waveguide structures designed and manufactured by the Institute for Nuclear Research of the Russian Academy of Sciences (Moscow, Russia). They are operated in travelling wave $2\pi/3$ mode at a frequency of 2.997 GHz[1]. The TDS in the injector section comprises 16-cells and has a filling time below 110 ns, i.e. the RF pulse is short enough to act only on one bunch within the bunch train without affecting the other bunches.

The screen stations [5] are equipped with both full on-axis and half off-axis scintillator screens (LYSO:Ce) which are mounted perpendicular to the beam axis and imaged at an angle of 45° to the beam axis with CCD cameras in a Scheimpflug configuration. As a result, the screen stations provide a constant spatial (rms) resolution of 10 µm for the configuration with a magnification of 1 : 1 over the entire screen. The distance from the edge of the off-axis screen to the beam axis amounts to 6 mm.

As is illustrated in Fig. 3, the kicker magnets consist of a ceramic vacuum chamber, which has been sputtered at the inside with a layer of 1 µm thick stainless steel, and two flat copper bars outside the vacuum beam pipe at opposite sides with a length of 350 mm. One high-voltage pulser (up to 20 kV) is directly attached to each kicker magnet. The pulsers generate half cycles of a sine wave with a pulse duration of t_p = 380 ns at 10 Hz which enables deflection of single bunches onto the corresponding off-axis screens for diagnostics while the remaining bunches in the bunch train are not affected and proceed to the undulator beamlines for the generation of FEL radiation.

[1] The frequency of the TDS f = 332/144 · 1.3 GHz= 2.997 GHz is generated from the master oscillator frequency of 1.3 GHz and is an integer multiple of the bunch repetition rate of 4.5 MHz.

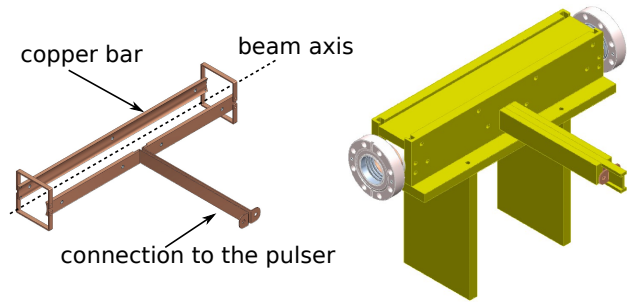

Figure 3: Schematics of a kicker magnet. The high-voltage pulser is not shown.

This is demonstrated in Fig. 4 for the operation of 2 bunches, of which the second bunch is kicked. On the left hand side the image of the two bunches on an on-axis screen is shown while on the corresponding image of the off-axis screen on the right only the kicked bunch is visible (and reflections on the edge of the scintillator).

A bunch with a certain bunch number within the bunch train can be chosen for diagnostics via the timing system by adjusting appropriately the trigger delays of the TDS, kicker magnets and camera systems. The diagnosed bunch experiences a betatron oscillation due to the kicker magnet and may get lost along the accelerator. This bunch is marked by the timing system and taken out of the bunch train by the fast kicker magnets upstream of the FEL undulator sections or, in case of beam loss, ignored by the fast machine protection system, which would inhibit the generation of further electron bunches. For an emittance measurement, the kicker magnets are toggled subsequently and typically 20 beam images are recoded per screen. One emittance measurement takes less than 20 secods as the screens do not have to be moved. By scanning the bunch number, the projected or slice emittance as well as the longitudinal bunch profile can be measured along the bunch train. The diagnostic sections also serve as matching sections, in which the beam is routinely matched to the design accelerator optics for transport into the subsequent beamline sections equipped with accelerating modules.

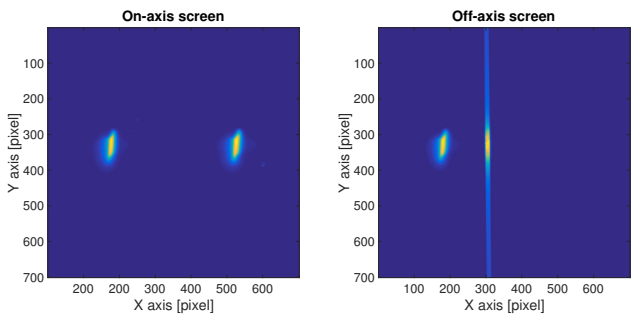

Figure 4: Beam operation with two bunches: the second bunch is kicked by a kicker magnet. Left: Image of on-axis screen with both bunches visible. Right: Image of off-axis screen with only the kicked bunch visible.

ISBN: 978-3-95450-192-2 doi:10.18429/JACoW-IBIC2017-TUPCC03

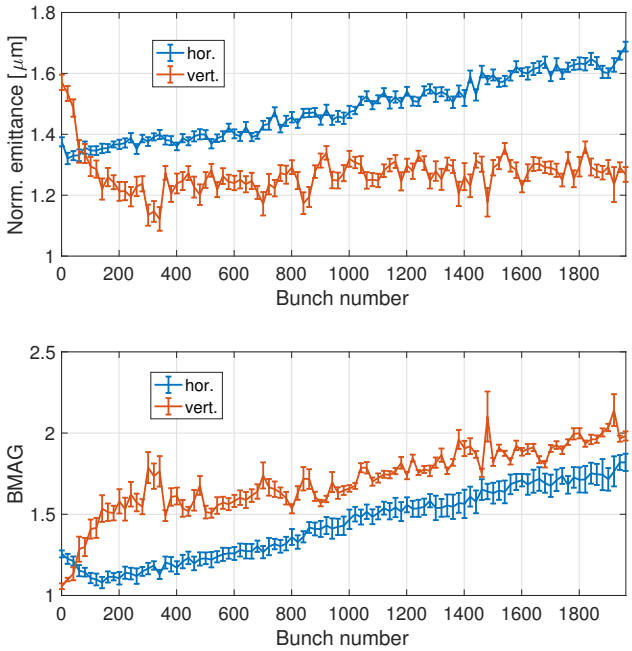

Figure 5: Intra-train emittance measurement for individual bunches along the train. Top: Projected normalized emittances. Bottom: Optics mismatch amplitude (BMAG) with respect to design optics.

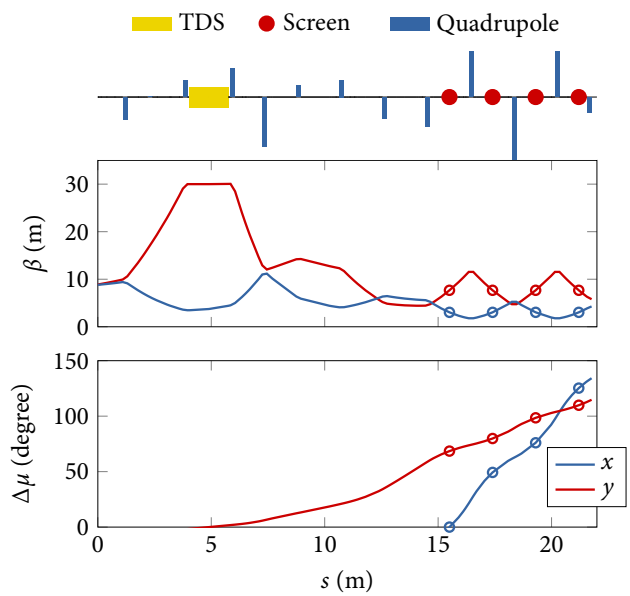

Figure 6: Accelerator optics for slice emittance measurements. Top: Schematic beamline layout; the quadrupole strengths are indicated by the height of the bars. Middle: Beta-functions. Bottom: Phase advances.

EMITTANCE MEASUREMENTS

The layout of the diagnostic sections and time structure of the electron bunches allow for novel phase space measurements of individual bunches along the train. In Fig. 5 an example of such a train emittance scan is shown. Each data point represents a transverse phase space measurement with the four screen stations in the F0D0 lattice. For each measurement a bunch is selected by the kicker magnet timing and sequentially kicked onto the four off-axis screens, and 20 beam images are recorded per screen station. A symmetric F0D0 optics with a phase advance of 76° per cell was chosen to give best results for the reconstruction of the projected emittances in both the x and y plane [6]. Phase space properties such as the beam Twiss parameters or transverse emittance are determined by a least square method using known beam transport functions [7]. The beam moments are varied at a reference point upstream of the F0D0 screen stations to best reproduce the measured beam spot sizes on the screens. A single emittance measurement for a certain bunch number takes less than 20 s.

For a train emittance scan, this procedure is repeated for bunches with different bunch numbers in the train. For the results shown in Fig. 5, every 20th bunch of the about 450 µs long train has been selected for a measurement. The measurements have been carried out in the injector section at on-crest operation with a beam energy of 130 MeV, bunch charge of 0.5 nC and bunch repetition rate of 4.5 MHz. In this particular example, the projected emittance and optics mismatch is not constant along the bunch train. The vertical emittance and optics mismatch exhibit a strong slope up to about bunch number 200. The horizontal emittance and optics mismatch increase slowly along the bunch train. This behaviour could be attributed to thermal effects in a part of the photo-cathode laser system, which could easily be corrected after being identified. This illustrates the utility of such a diagnostics setup which allows for optimising the phase space properties of each bunch in order to establish uniform FEL performance for all bunches in the train. The measurement time for this train emittance scan (measurement for every 20th bunch number) amounted to about 15 minutes.

Dispersion may be generated in the emittance measurement plane at the screen locations, when the kicker magnets are utilized for online emittance measurements. For relative energy spreads below $\sigma_\delta \sim 10^{-3}$, as is the case for on-crest operation, the relative error contribution in the calculated emittance is below 1%. A detailed error analysis of statistical and systematic errors that may contribute in the emittance measurement has been carried out in Ref. [6].

SLICE EMITTANCE MEASUREMENTS

By utilizing a TDS, the longitudinal bunch profile is transformed to one transverse plane while in the perpendicular plane the spot sizes can be measured for the longitudinal slices and slice emittances can be evaluated with the least square fit technique described in the latter section.

Figure 6 depicts an example of an accelerator optics optimised for a slice emittance measurement in the TDS diagnostic section with the beta-functions (middle) and phase advances (bottom) for both the emittance measurement plane x and TDS streak plane y. For a good longitudinal resolution

ISBN: 978-3-95450-192-2 doi:10.18429/JACoW-IBIC2017-TUPCC03

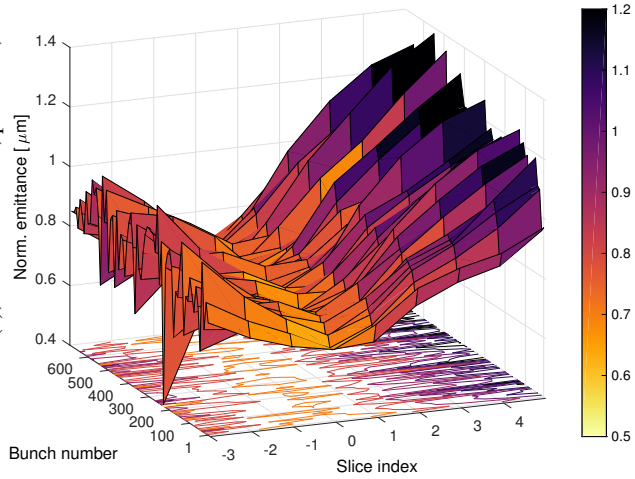

Figure 7: Nomalised horizontal slice emittance measured along the bunch train (in steps of 10 bunch numbers). Slice index 0 corresponds to the central slice with maximum bunch current.

in the streak plane, the accelerator optics has been optimised for a large beta-function $\beta_y = 30\,\mathrm{m}$ at the TDS, a phase advance of $\Delta\mu_y = 90°$ from the TDS to the centre of the F0D0 lattice (i.e. the centre of the second and third screen) and a small phase advance of $\Delta\mu_y = 30°$ per cell in the F0D0 lattice. For the reconstruction of the slice emittance, a phase advance of $\Delta\mu_x = 76°$ per cell has been chosen in the emittance plane as in the case of the projected emittance measurements.

Figure 7 shows the results of online slice emittance measurements scanned along the bunch train. The slice emittance measurements have been carried out for bunch numbers 1 to 671 in the train in steps of 10 bunch numbers, i.e. a total of 67 measurements. For each emittance measurement, 16 beam images have been recorded for each of the four screen stations. Each emittance measurement took about 20 s and the total measurement time for the scan amounted to about 25 min. The data has been taken in the injector section at on-crest operation with a beam energy of 130 MeV, bunch charge of 0.5 nC and bunch repetition rate of 1.125 MHz.

The slice index 0 corresponds to the central slice of the bunch with maximum bunch current. The results for the slices in the head and tail of the bunch have been omitted from the plot for better illustration as they exhibit large error bars due to a large beam optics mismatch and low image intensities. All individual measurements display a similar distribution of the normalised slice emittance along the bunch train for the slice indices plotted. The individual normalised slice emittances vary between 0.6 µm and 1.3 µm with the minimum value at the central index 0 and increasing values towards bunch head and tail. Before the scan, the beam optics was matched to the central slice of the bunch with bunch number 1.

CONCLUSION

The combined utilization of a TDS with fast kicker magnets and off-axis screens is a versatile diagnostics implementation to analyse individual bunches in a bunch train without affecting the remaining bunches. In this paper we presented the results of measurements of the projected and slice emittance along the bunch train. This is especially helpful when it is required to achieve uniform FEL performance along the bunch train as it is the case for the European XFEL which operates in a 10 Hz pulsed mode. Compared to the maximum number of bunches in a bunch train (2700 at a repetition rate of 4.5 MHz), the bunches sacrificed for diagnostics purpose are negligible, and the method can be regarded as semi-parasitic on-line diagnostics.

ACKNOWLEDGEMENT

The European XFEL is a joint achievement of many contributing institutes (for details see http://www.xfel.eu). The authors wish to thank all people working in different parts of the project for their contributions.

REFERENCES

[1] W. Decking and H. Weise, "Commissioning of the European XFEL Accelerator", in *Proc. IPAC'17*, Copenhagen, Denmark, May 2017, paper MOXAA1, pp. 1–6.

[2] M. Röhrs and Ch. Gerth, "Electron beam diagnostics with transverse deflecting structures at the European X-ray free electron laser", in *Proc. FEL'08*, Gyeongju, Korea, Aug. 2008, paper MOPPH049, pp. 90–93.

[3] J. Wychowaniak, Ch. Gerth, and M. Yan, "Design of Multi-setup TDS-based Electron Beam Diagnostics for the European XFEL", in *Proc. FEL'14*, Basel, Switzerland, Aug. 2014, paper THP075, pp. 909–912.

[4] M. Yan *et al.*, "Comparison of Quadrupole Scan and Multi-Screen Methode for the Measurement of Projected and Slice Emittance at the SwissFEL Injector Test Facility", in *Proc. FEL'14*, Basel, Switzerland, Aug. 2014, paper THP088, pp. 941–944.

[5] Ch. Wiebers *et al.*, "Scintillating Screen Monitors for the Transverse Electron Beam Profile Diagnostics at the European XFEL", in *Proc. IBIC'13*, Oxford, UK, Sept. 2013, paper WEPF03, pp. 807–810.

[6] M. Yan, "Online diagnostics of time-resolved electron beam properties with femtosecond resolution for X-ray FELs", DESY, Hamburg, Germany, DESY-THESIS-2016-017, July 2016.

[7] M.G. Minty and F. Zimmermann, "Transverse Beam Emittance Measurement and Control", in *Measurement and Control of Charged Particle Beams*, Springer-Verlag Berlin Heidelberg, 2003, pp. 99–130.

ISBN: 978-3-95450-192-2 doi:10.18429/JACoW-IBIC2017-TUPCC05

CONCEPT FOR THE MINIMIZATION OF THE ELECTRON BUNCH ARRIVAL-TIME JITTER BETWEEN FEMTOSECOND LASER PULSES AND ELECTRON BUNCHES FOR LASER-DRIVEN PLASMA WAKEFIELD ACCELERATORS*

S. Mattiello†, Andreas Penirschke, Technische Hochschule Mittelhessen, Friedberg, Germany
Holger Schlarb, DESY, Hamburg, Germany

Abstract

Using laser driven plasma wakefield accelerators, the synchronization between electron bunch and the ultrashort laser is crucial to obtain an stable acceleration. In order to minimize the electron bunch arrival-time jitter, the development of a new shot to shot feedback system with a time resolution of less than 1 fs is planned. As a first step, stable Terahertz (THz) pulses should be performed by optical rectification of high energy femtosecond laser pulses in a nonlinear crystal. It is planed that the generated THz pulses will energy modulate the electron bunches shot to shot before the plasma to achieve the time resolution of 1fs. The selection of the nonlinear material is a critical aspect for the development of laser driven THz sources. In this contribution we investigate systematically the influence of the optical properties, and in particular adsorption coeffient, of lithium niobate crystal on the conversion efficiency of the generation of THz pulses.

INTRODUCTION

The investigation of new concepts for accelerator technology is a challenging task for science as well as society. Particle accelerators allow to achieve crucial new discoveries, e.g. the Higgs boson or the strong interacting Quark Gluon Plasma. On the other side, they have several applications in material science, biology, medicine and industry. The size of conventional accelerators is extremely large and costly. Therefore, new concepts as well as the realization of compact and less expensive accelerators are needed. Plasma-based particle accelerators driven by either lasers or particle beams allow to overcome these problems because of the extremely large accelerating electric fields. This method is known as plasma wakefield acceleration (PWA). The period of these fields is in the range of 10 fs to 100 fs. In the case of laser driven plasma wakefield accelerators a stable synchronization of the electron bunch and of the plasma wakefield in the range of few femtoseconds is needed in order to optimize the acceleration.

Consequently, the central aim is the minimizing the electron bunch arrival-time jitter. In order to achieve this goal we are developing a new shot to shot feedback system with a time resolution of less than 1 fs. As a first step, stable Terahertz (THz) pulses should be performed by optical rectification of high energy laser pulses in a nonlinear crystal. With the generated THz-pulses an energy modulation of the electron bunch can be performed, in order to achieve the required resolution. In this contribution we focus on the first step of the feedback system, i.e. the generation of THz pulses.

Intense ultrashort terahertz pulses are an important tool, not only for our planed feedback system, but also for many new applications, in state solid physics, spectroscopy, chemistry and biology, for security purposes and point-to point communications [1]. Therefore, the development of robust and efficient strong THz pulses is strongly needed. Consequently, the main focus is to maximize the conversion efficiency of the THz generation defined by [2],

$$\eta = \frac{F_\mathrm{T}}{F_\mathrm{p}}, \tag{1}$$

where F_p and F_T indicate the pump and the THz fluence respectively. From this point of view the optical rectification (OR) is one of the best method for this purpose and the selection of the nonlinear material is a critical aspect. Because of its high nonlinear optic coefficient, is lithium niobate ($LiNbO_3$, LN) a suitable material for THz generation, by using tilted-pulse-fronts (TPF) as well as a periodically poled crystal (PPLN) [4]. In general, three main factors lead to increase the efficiency of the THz generation: *(i)* longer pump pulses, *(ii)* large pump size and energy, and *(iii)* cooling of the crystal [3].

Evidently, the first two factors are fixed by the laser properties. Therefore, although it has been shown that longer (1.3 ps) pulses lead to a sizeable enhancement about 2.5% of the efficiency, these factors cannot be modified in our setup [3]. Indeed, for our feedback system only the third point can play a significant role. In fact the cooling of the crystal reduce the value of the intensity adsorption coefficient of the THz radiation $\alpha_\mathrm{T}(\Omega)$, which leads to the suppression of η. The optical properties of the material and in particular of $\alpha_\mathrm{T}(\Omega)$ are important not only for the optimization of the efficiency, but also for its stability. Therefore, in this contribution we give a first estimation of the influence of refractive index $n(\Omega)$ and adsorption coefficient, on the efficiency. Firstly, we present the models for the description of the THz generation as well as for the calculation of the optical properties of the material. Therefore we investigate in this framework the influence of the optical properties of lithium niobate crystal on the conversion efficiency of the generation of THz pulses. The Conclusions finalize this work.

* The work of S. Mattiello is supported by the German Federal Ministry of Education and Research (BMBF) under contract no. 05K16ROA.
† stefano.mattiello@iem.thm.de

ISBN: 978-3-95450-192-2 doi:10.18429/JACoW-IBIC2017-TUPCC05

MODELING THE THz GENERATION

Starting from the Maxwell equations coupled wave equations for the optical and THz waves can be derived. Using the slowly-varying envelope approximation the equations system for the envelope at angular frequency ω of the electric field of the optical pump pulse $A_\mathrm{p}(\omega, z)$ and the envelope at angular frequency Ω of the THz field $A_\mathrm{T}\Omega, z)$ reads [4]

$$\frac{\partial}{\partial z}A_\mathrm{p}(\omega, z) = -\frac{\alpha_\mathrm{p}(\omega)}{2}A_\mathrm{p}(\omega, z) - I_\mathrm{p}, \quad (2)$$

$$\frac{\partial}{\partial z}A_\mathrm{T}(\Omega, z) = -\frac{\alpha_\mathrm{T}(\Omega)}{2}A_\mathrm{T}(\Omega, z) + I_\mathrm{T}, \quad (3)$$

where we define

$$I_\mathrm{T} = -i\frac{\Omega^2\chi^{(2)}_\mathrm{eff}(z)}{2k(\Omega)c^2}\int_0^\infty \mathrm{d}\omega A_\mathrm{p}(\omega+\Omega, z)A^*_\mathrm{p}(\omega, z)\mathrm{e}^{-i\Delta k(\omega)}. \quad (4)$$

Hereby k and Δk are the wave number and the wave-vector mismatch respectively, α_p indicates the adsorption coefficient of the optical wave, c is the velocity of the light in vacuum and I_p denotes an integral term analogous to the integral contribution for the THz component [4]. The parameter $\chi^{(2)}_\mathrm{eff}(z)$ is the effective second order nonlinear susceptibility which can be a function of the spatial coordinate z.

Because we consider in the following the undepleted approximation only, i.e. we neglect the equation of the optical wave, we omit to give a specific expression for this term[1]. The efficiency defined in Eq. (1) is a function of the amplitude of the THz wave and can be written as

$$\eta = \frac{\pi\epsilon_0 c\int_0^\infty \mathrm{d}\Omega\, n(\Omega)|A(\Omega, z)|^2}{F_\mathrm{p}}, \quad (5)$$

where ε_0 indicates the dielectric constant of the vacuum.

By a linear approximation of the mismatch vector Δk, i.e. by neglecting of the material dispersion (GVD-MD), which has to be relaxed in future works, the absolute value of the field squared reads

$$|A(\Omega, z)|^2 = \frac{\Omega^2 P^2_\mathrm{NL}(\Omega, z)}{4c^2n^2(\Omega)\varepsilon_0^2}\frac{1}{(\Delta k)^2 + a^2_\mathrm{T}(\Omega)/4} \times \left(\left(1-\mathrm{e}^{-\frac{\alpha_\mathrm{T}(\Omega)z}{2}}\right)^2 + 4\,\mathrm{e}^{-\frac{\alpha_\mathrm{T}(\Omega)z}{2}}\sin^2\left(\frac{\Delta k z}{2}\right)\right), \quad (6)$$

where the nonlinear polarization P_NL is given by

$$P_\mathrm{NL}(\Omega, z) = \varepsilon_0\chi^{(2)}_\mathrm{eff}(z)\int_0^\infty \mathrm{d}\omega\; A_\mathrm{p}(\omega+\Omega, z)A^*_\mathrm{p}(\omega, z). \quad (7)$$

MODELING THE MATERIAL PROPERTIES

Eq. (6) shows the importance of the purpose of this work, i.e. investigation of the influence of the optical properties on the conversion efficiency. In particular the adsorption coefficient should play a key role because of the exponential suppression factor. In order to determine the optical properties, we have to calculate the complex dielectric function $\varepsilon(\Omega)$ of the material. The relation between $\varepsilon(\Omega)$ and the refractive index and the adsorption coefficient is given in general by

$$n(\Omega) = \Re\sqrt{\varepsilon(\Omega)} \quad \text{and} \quad \alpha(\Omega) = \frac{2\Omega}{c}\Im\sqrt{\varepsilon(\Omega)}. \quad (8)$$

A physical motivated description for the dielectric function is based on an oscillator model, i.e.

$$\varepsilon(\Omega) = \varepsilon_\infty + \sum_j \frac{S_j\Omega_j^2}{\Omega_j^2 - \Omega^2 - i\Omega\Gamma_j}, \quad (9)$$

where the summation over the lattice oscillators with the strength S_j, angular resonance frequency Ω_j and resonance width Γ_j is performed and the bound electron contribution to the dielectric function is denoted as ε_∞ [5]. These parameters are to be evaluated by the comparison with the experimental data in the relevant frequency range. Another possibility is to fit the experimental data with polynomial function. For LN, a polynomial to the fourth or fifth degree is used for the refractive index [6, 7]. For α an explicit functional dependence has not been given, but only the experimental data are listed [6].

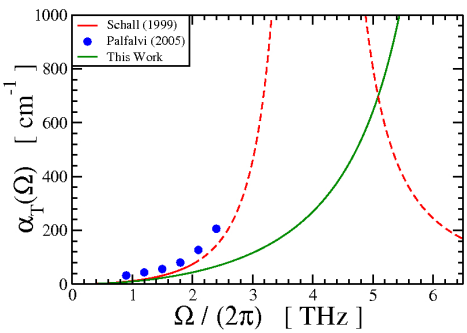

Figure 1: The adsorption coefficient as function of the frequency using the single oscillator model from Schall [5] (red line), the experimental data from Pálfalvi [6] (blue circles) and repararameterization of the fit by Kuznetsov [7] using a single oscillator model (green line).

The comparison of these models and results shows different values for their validity range as well as in general a large scattering of the results, in particular for the adsorption coefficient, even in the case of the same typology of crystal. As example we compare in Fig. 1 the adsorption coefficient for a congruent undoped LN at room temperature as function of the frequency using the single oscillator model from Schall [5] (red line), the experimental data from Pálfalvi [6] (blue circles) and repararameterization of the fit by Kuznetsov [7] using a single oscillator model (green line). We use as parameters of the one single oscillator model are $\varepsilon_\infty = 0.1$, $S_0 = 25.03$, $\Omega_0 = 45.46\,\mathrm{THz}$ and $\Gamma_0 = 3.04\,\mathrm{THz}$. In order to show the validity range, we plot

[1] Additionally we note, that in the integral term I_p different effects can be considered [4].

ISBN: 978-3-95450-192-2 doi:10.18429/JACoW-IBIC2017-TUPCC05

the red line as solid and dashed line for the value of the frequency within and outside of the validity range respectively. The differences between the models are sizeable and lead to no negligible modifications in the evaluation of η.

Another source of modifications by the determination of the conversion efficiency is given by the evaluation of the contribution to the optical properties by the free carries generated by the pump adsorption [8]. In order to describe this contribution a Drude model can be used, so that the whole dielectric function, in one single oscillator model, is given by

$$\varepsilon_{\mathrm{tot}}(\Omega) = \varepsilon_{\mathrm{osc}}(\Omega) + \varepsilon_{\mathrm{FC}}(\Omega), \tag{10}$$

where $\varepsilon_{\mathrm{FC}}$ can be written as

$$\varepsilon_{\mathrm{FC}}(\Omega) = \varepsilon_{\infty}^{\mathrm{FC}}\left(1 - \frac{\omega_{\mathrm{pl}}^2}{\Omega^2 + i\Omega/\tau_{\mathrm{sc}}}\right). \tag{11}$$

Hereby τ_{sc} denotes the electron scattering time and the plasma frequency ω_{pl}^2 is related to the density of free charge carries ρ_{FC} by

$$\rho_{\mathrm{FC}=}\frac{\varepsilon_0\varepsilon_{\infty}^{\mathrm{FC}} m_{\mathrm{eff}}}{e^2}\omega_{\mathrm{pl}}^2, \tag{12}$$

where $\varepsilon_{\infty}^{\mathrm{FC}}$ denotes the bound electron contribution to the dielectric function and e and m_{eff} are the electron charge and effective masse respectively [8]. In this work we use $\varepsilon_{\infty}^{\mathrm{FC}} = 5.3$, $\tau_{\mathrm{sc}} = 200\,\mathrm{fs}$ [8] and $m_{\mathrm{eff}} = 0.25 m_{\mathrm{e}}$, where m_{e} indicates the electron mass. Although in a consistent derivation the whole adsorption coefficient has to be extracted from the imaginary part of the total dielectric function given in Eq. (10), several calculations use a simple sum $\alpha_{\mathrm{T}}(\Omega) = \alpha_{\varepsilon}(\Omega) + \alpha_{\mathrm{FC}}(\Omega)$, where the two terms are calculated separately starting from a dielectric function without free carries and the dielectric function of the Drude model $\varepsilon_{\mathrm{FC}}$ respectively [8]. The Fig. 2 shows that this simplification leads to sizeable differences using the single oscillator model from Schall and the Drude model for a density $\rho_{\mathrm{FC}} = 4 \times 10^{20}\,\mathrm{m}^{-3}$, which can lead to a strong suppression of the conversion efficiency.

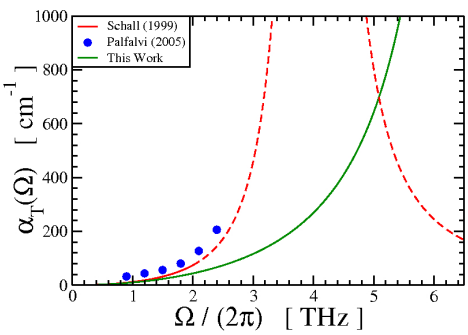

Figure 2: Comparison of the exact calculation (red line) and the approximated estimation (green line) of the whole adsorption coefficient as function of the frequency using the single oscillator model from Schall [5] and the Drude model for the free carries for a density $\rho_{\mathrm{FC}} = 4 \times 10^{20}\,\mathrm{m}^{-3}$.

FIRST RESULTS

In order to investigate the influence of the optical properties we consider a PPL congruent LN crystal with $\chi_{\mathrm{eff}}^{(2)} = 336\,\mathrm{pm\,V}^{-1}$ at room temperature with a Gaussian laser beam pulse centered at $\omega_0 = 800\,\mathrm{nm}$ and a pulse duration at full width of half-maximum $\tau_{\mathrm{FWHM}} = 25\,\mathrm{fs}$ [2, 4, 8]. In this case the amplitude and the fluence of the pump read

$$A_{\mathrm{p}}(\omega) = \frac{E_0\tau}{2\sqrt{\pi}}\exp\left(-\frac{\tau^2(\omega-\omega_0)^2}{4}\right), \tag{13}$$

$$F_{\mathrm{p}} = \sqrt{\frac{\pi}{2}}\frac{c\varepsilon_0 n_0}{2}E_0^2\tau, \tag{14}$$

where E_0 is the peak value of the electric field, τ is given by $\tau = (2\sqrt{2})^{-1/2}\tau_{\mathrm{FWHM}}$ and $n_0 = n(\omega_0) = 2.16$. With this optical beam the nonlinear polarization can be calculated analytically and one obtains

$$P_{\mathrm{NL}}(\Omega, z) = \varepsilon_0\chi_{\mathrm{eff}}^{(2)}\frac{E_0^2\tau}{2\sqrt{2\pi}}\exp\left(-\frac{-\tau^2\Omega^2}{8}\right). \tag{15}$$

For the PPL, the mismatching is given by

$$\Delta k = \frac{\Omega}{c}(n(\Omega) - n_{\mathrm{opt}}^{\mathrm{gr}}) - \frac{2\pi}{\Lambda}, \tag{16}$$

where $n_{\mathrm{opt}}^{\mathrm{gr}} = 2.25$ is the optical group velocity refractive index and $\Lambda = 237.74\,\mu\mathrm{m}$ is the quasi-phase-matching orientation-reversal period [4]. By neglecting the adsorption and under the assumptions that the refractive index is constant, $n(\Omega) \equiv n_1$, and that the length of the crystal is very larger than the coherence length $l_{\mathrm{c}} = \pi c/\Omega(n(\Omega) - n_{\mathrm{opt}}^{\mathrm{gr}})$, an analytic expression for the efficiency can be derived [2]. In this case the integral over the frequency in Eq. (5) is proportional to a delta-function $\delta(\Omega - \Omega_0)$, with $\Omega_0 = 2\pi c/\Lambda\Omega(n(\Omega) - n_{\mathrm{opt}}^{\mathrm{gr}})$. Finally one obtains

$$\eta_0 = \frac{\Omega_0^2\chi_{\mathrm{eff}}^{(2)} L F_{\mathrm{p}}}{2\varepsilon_0 c^2 n(\Omega) n_0^2(n_1 - n_{\mathrm{opt}}^{\mathrm{gr}})}\exp\left(-\frac{-\tau^2\Omega_0^2}{4}\right). \tag{17}$$

With these parameters we can investigate the efficiency as function of the crystal length L for different scenarios for a fixed pump fluence $F_{\mathrm{p}} = 5\,\mathrm{mJ\,cm}^{-2}$.

As first, we consider the limiting case $\alpha_{\mathrm{T}} \equiv 0$. In Fig. 3 we show η_0 (green line) using $n_1 = 4.96$, η using the same constant value for n_1 but performing the integration until to the convergence of the integral (red line) and η using different models to calculate the refractive index and stopping the integration at the upper limit of the validity of the models (see the legend of the figure). As expected, the behavior of the efficiency as function of the crystal length is linear, but the angular coefficient is model dependent. In particular, we see that the cut-off at slow frequency change the results dramatically.

In the case of no vanishing adsorption, the differences between the models become larger. The results are plotted in Fig. 4 for a fixed pump fluence $F_{\mathrm{p}} = 5\,\mathrm{mJ\,cm}^{-2}$. Although a similar qualitative behavior can be observed, i.e.

ISBN: 978-3-95450-192-2 doi:10.18429/JACoW-IBIC2017-TUPCC05

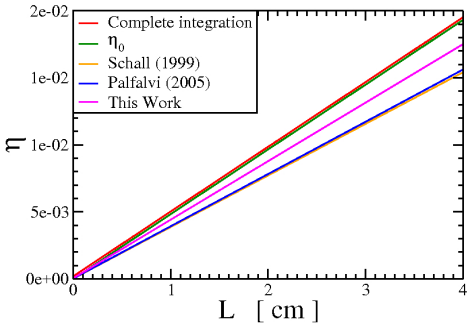

Figure 3: Conversion efficiency η for a fixed pump fluence $F_p = 5\,\mathrm{mJ\,cm^{-2}}$ as function of the crystal length L with constant refractive index $n_1 = 4.96$ with the complete integration (red line) and with different models for stopping the integration at the upper limit of the validity of the models as indicated in Fig. To comparison we show the analytic estimation η_0 (green line).

a saturation of η for large crystal lengths, the values of the plateau indicate the strong dependence of the conversion efficiency on the model and/or data. Similar sizeable modifications can be observed, if the contribution of the free carries is implemented. In Fig.5 we show $\eta(L)$ for a fixed pump fluence $F_p = 5\,\mathrm{mJ\,cm^{-2}}$ calculated using the Schall model without the free carries (orange line), using consistent approach presented in this work (red line) and using the approximation used in the literature [8] (green line) for a density $\rho_{FC} = 4 \times 10^{20}\,\mathrm{m^{-3}}$. The huge deviation from the exact calculation indicates clearly the necessity to perform consistent calculations of the optical properties.

CONCLUSION

The influence of the optical properties of the lithium niobate crystal on the conversion efficiency of the generation of THz pulses has been investigated. The comparison of different models for the estimation of the adsorption coefficient shows the necessity of a better description of the optical properties, not only in the THz range, but also at higher frequencies. The approximations that we used in this preliminary work should be relaxed in order to evaluate systematically the influence of the other factors on η.

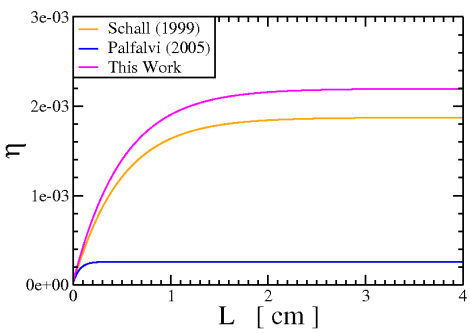

Figure 4: Conversion efficiency η for a fixed pump fluence $F_p = 5\,\mathrm{mJ\,cm^{-2}}$ as function of the crystal length L using the refractive index and the adsorption coefficient from different models as indicated in the legend.

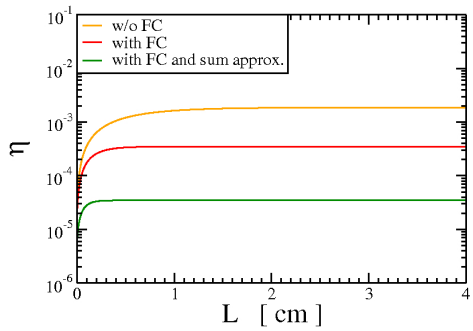

Figure 5: Conversion efficiency for a fixed pump fluence $F_p = 5\,\mathrm{mJ\,cm^{-2}}$ as function of the length using the Schall model [5] without the free carries (orange line), within the consistent calculation presented in this work and the approximation used in the literature [8] (red and green solid line respectively) for a FC density $\rho_{FC} = 4 \times 10^{20}\,\mathrm{m^{-3}}$.

ACKNOWLEDGEMENT

The work of S. Mattiello is supported by the German Federal Ministry of Education and Research (BMBF) under contract no. 05K16ROA.

REFERENCES

[1] A. G. Stepanov, S. Henin, Y. Petit, L. Bonacina, J. Kasparian, and J.-P. Wolf, "Mobile source of high-energy single-cycle terahertz pulses", *Appl. Phys. B*, vol. 101, no. 1, pp. 11–14, 2010.

[2] K. Vodopyanov, "Optical generation of narrow-band terahertz packets in periodically-inverted electro-optic crystals: conversion efficiency and optimal laser pulse format", *Optics Express*, vol. 14, no. 6, pp. 2263–2276, 2006.

[3] J .A. Fülöp *et al.*, "Generation of sub-mJ terahertz pulses by optical rectification", *Optics Letters*, vol. 37, no. 4, pp. 557–559, 2012.

[4] K. Ravi, D. Schimpf, and F. Kärtner, "Pulse sequences for efficient multi-cycle terahertz generation in periodically poled lithium niobate", *Optics Express*, vol. 24, no. 22, pp. 25582–25607, 2016.

[5] M. Schall, H. Helm, and S. R. Keiding, "Far Infrared Properties of Electro-Optic Crystals Measured by THz Time-Domain Spectroscopy", *International Journal of Infrared and Millimeter Waves*, vol. 20, no. 4, pp. 595–604, 1999.

[6] L. Pálfalvi, J. Hebling, J. Kuhl, Á. Péter, and K. Polgár, "Temperature dependence of the absorption and refraction of Mg-doped congruent and stoichiometric LiN", *Journal of Applied Physics*, vol. 97, no. 12, p. 123505, 2005.

[7] K. A. Kuznetsov *et al.*, "Dispersion of the dielectric function real part for Mg:LiNbO3 crystals at terahertz frequencies", *Appl. Phys. B*, vol. 101, no. 3, pp. 881–815, 2010.

[8] S. Zhong *et al.*, "Optimization of terahertz generation from LiNbO3 under intense laser excitation with the effect of three-photon absorption", *Optics Express*, vol. 23, no. 24, pp. 31313–31323, 2015.

ISBN: 978-3-95450-192-2 doi:10.18429/JACoW-IBIC2017-TUPCC06

INJECTION AND BUNCH LENGTH STUDIES AT THE BESSY II STORAGE RING

D. Malyutin†, T. Atkinson, P. Goslawski, A. Jankowiak, A. Matveenko, M. Ries,
Helmholtz-Zentrum Berlin, Berlin, Germany

Abstract

To improve the injection process into the BESSY II storage ring and allow for high injection efficiencies in all operational modes, one needs to know the development of the bunch length during acceleration in the booster synchrotron up to the extraction point. It will become even more important for the future BESSY VSR upgrade, when high efficiency injection into much shorter RF buckets needs to be guaranteed.

Measurements of bunch phase and energy during injection in the storage ring are presented. Studies of the bunch length evolution during the energy ramp of the booster synchrotron are described. Results are compared with numerical simulations and discussed.

INTRODUCTION

To provide new possibilities for time resolved experiments at the synchrotron light source BESSY II an innovative upgrade scheme to store both long and short bunches simultaneously in the storage ring is under realisation: the Variable pulse length Storage Ring BESSY VSR [1].

The most prominent aspect with respect to the injector is the evidence, that the bunch length on injection into the storage ring needs to be reduced from its present value, by at least a factor two in order to keep the by radiation protection required high injection efficiencies of above 90 % on an 4 h average. The problem arises from the large difference in the bunch lengths on injection and the reduced longitudinal bucket length (phase acceptance) due to the proposed VSR [2] technique as depicted in Figure 1.

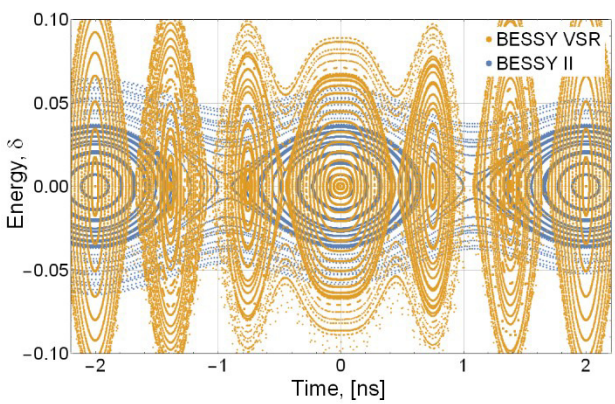

Figure 1: Longitudinal phase space comparison between BESSY II (blue) and the alternating bucket length scheme of BESSY VSR (yellow).

Presently the bunch length of the injected beam on injection into the storage ring is approximately 60 ps FWHM. Such bunch lengths will unfortunately not allow the required high efficient injection into the short BESSY VSR buckets. An upgrade of the injection systems to produce shorter bunches is foreseen.

Today there is no diagnostics at the BESSY II booster synchrotron to directly measure the bunch length during the energy ramp. One possible solution is to extract the beam during the ramp of the booster and to measure the bunch length just after injection into the storage ring. This can be achieved by reducing the energy of the storage ring, as well as the transfer line, and extracting the bunch earlier or later from the booster (with respect to a nominal energy). Then, a synchrotron light from a storage ring dipole magnet is used to get a bunch length with a dual-sweep synchroscan streak camera.

BUNCH LENGTH EVOLUTION

Figure 2 shows the evolution of the bunch length, the bunch energy and cavity voltage from elegant [3] simulations during the acceleration stage of the 10 Hz booster cycle.

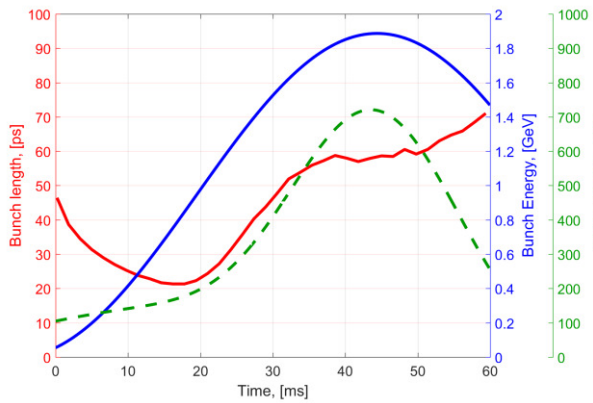

Figure 2: Simulation of the bunch length as a function of time over the 10 Hz booster cycle, the red curve, and the bunch energy, the blue curve and the cavity voltage the green dashed curve.

The beam energy is increased from 50 MeV on injection to 1.7 GeV at 35 ms on extraction. The simulation starts with parameters of the injected beam as measured during the site acceptance tests of the injector LINAC. The peak voltage in the cavity is set to 720 kV, the nominal values for booster operation. The voltage pedestal is none zero, so that the phase and with it the synchrotron frequency are also time dependent to match recent measurements in the booster.

The variation of the bunch length over the booster ramp is due to its inherent energy dependent parameters. The dy-

† dmitriy.malyutin@helmholtz-berlin.de

ISBN: 978-3-95450-192-2 doi:10.18429/JACoW-IBIC2017-TUPCC06

namic nature of the energy spread is an equilibrium between longitudinal damping and quantum excitation which dominate at low and high energies respectively [4].

For VSR the two most common ways to produce a shorter bunch are under investigation. Like the proposal for the storage ring, an upgrade of the RF gradient in the cavity or new optic to reduce the momentum compaction could be also implemented in the booster. The present optic in the booster is based on a simple FODO lattice with a 16-fold symmetry. The momentum compaction and hence optic to produce shorter bunch lengths is heavily restricted. Installing independent quadrupole power supplies and breaking the symmetry allows more tunable optic towards low alpha [5]. Similar simulations, as shown in Fig. 2, which include low-alpha optic, have shown good promise and will be a valid option for BESSY VSR [1].

MEASUREMENT PROCEDURE

All the measurements were conducted by using a dual-sweep synchroscan streak camera which uses the synchrotron light from a BESSY II storage ring dipole magnet. The streak camera was synchronised in such a way that acquisition starts a bit earlier than the bunch injection in the main ring and the data are recorded for about 500 µs, (~625 bunch turns in the storage ring).

The typical image from the streak camera is shown in Fig. 3 (a). The vertical axis is the fast sweep of the streak camera (the shown vertical range is about 400 ps) and the horizontal one is the slow sweep (the shown horizontal range is about 400 µs). To further analyse the data, the image was cut into horizontal slices and for each slice the mean vertical position and the vertical RMS size were calculated. Fig. 3 (b) and (c) show the calculated bunch mean position and the bunch length as a function of the turn number. The blue curves show the calculated values and the red curves are the sinusoidal fit (for the bunch length data the squared bunch length was fitted by a sinus).

Ramping the Energy of the Storage Ring

To measure bunch properties of the BESSY II booster at different energies, the bunch needs to be injected into the main storage ring. For such measurements all the magnetic elements of the ring and the transfer line must be ramped down proportionally. This includes the following steps:

- turn off all nonlinear magnetic elements,
- ramp down linearly the current of the linear magnetic elements proportionally to the desired energy (dipoles, quadrupoles, sextupoles, steerers, extraction and injection kickers),
- fine adjustment based on the tune measurements (not needed for the bunch characterization but for possible BESSY II operation at lower energy).

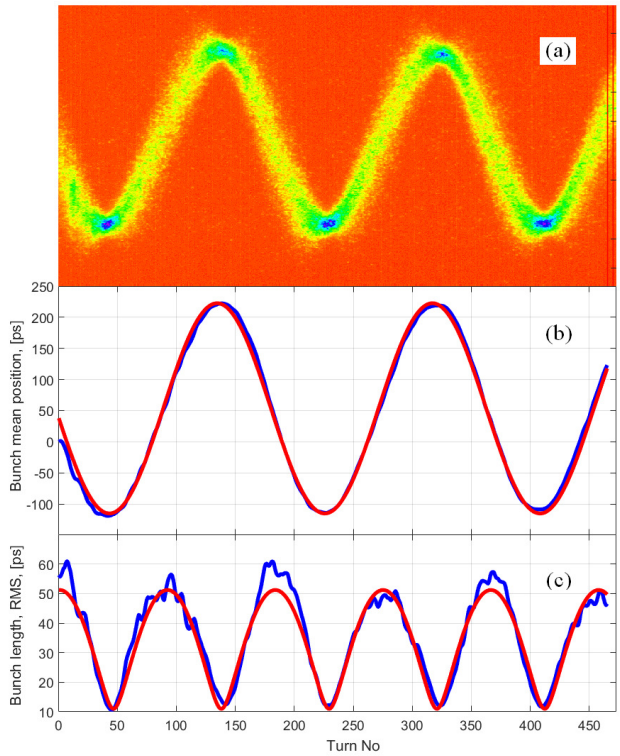

Figure 3: Result of 1700 MeV measurement: (a) is the streak camera image, (b) is the bunch mean position and (c) is the bunch RMS length. The blue curves are calculated values and the red curves are sinusoidal fits to the data.

MEASUREMENT RESULTS

The measurement results for the 1700 MeV beam energy are shown in Fig. 3. Extracting the phase and amplitude information from the fitted curve to the Fig. 3(b) the energy offset can be estimated using the equation of small synchrotron oscillation amplitudes [6]:

$$\delta = \frac{\Delta E}{E} = \frac{2\pi f_s}{\alpha} \cdot \Delta t, \qquad (1)$$

where E is the reference particle energy, f_s is the synchrotron frequency, α is the momentum compaction factor and t is the time amplitude of oscillation. For the measured time amplitude of 170 ps, Fig. 3(b), for E = 1700 MeV, for f_s = 6.8 kHz and for $\alpha = 7.3 \cdot 10^{-4}$ the amplitude of the energy oscillation will be ΔE = 17 MeV.

Increasing the energy of the injected bunch to 1717 MeV will compensate the energy offset and decrease the synchrotron oscillation amplitude, which can be seen in the measurement results in Fig. 4. The time amplitude of oscillations is only 16 ps, Fig. 4 (b), which corresponds to an energy oscillation of 1.6 MeV, Eq. (1). This oscillations can be further decreased by adjusting the injection phase delay (delay between the booster and the storage ring) by 16 ps.

ISBN: 978-3-95450-192-2 doi:10.18429/JACoW-IBIC2017-TUPCC06

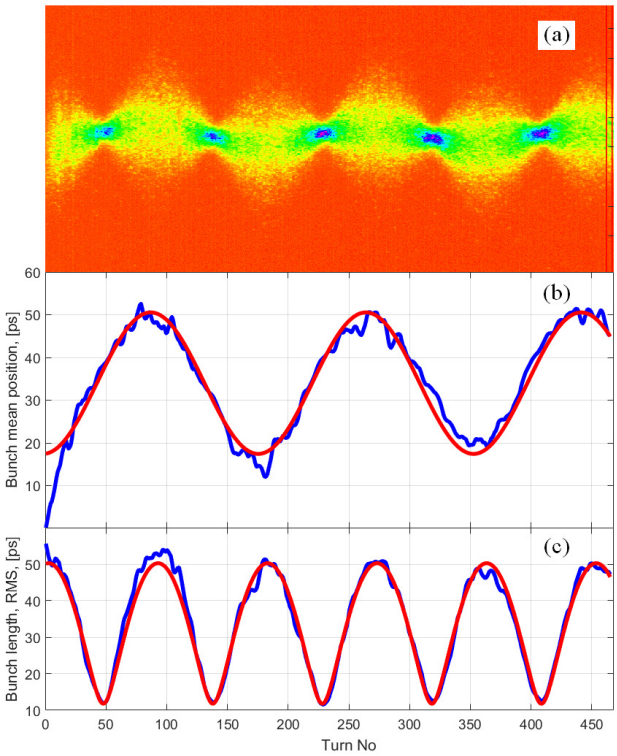

Figure 4: Result of 1717 MeV measurement: (a) is the streak camera image, (b) is the bunch mean position and (c) is the bunch RMS length. The blue curves are calculated values and the red curves are sinusoidal fits to the data.

The energy spread of the bunch injected in the main ring can be calculated as well using Eq.1 and the minimum measured bunch length during the synchrotron oscillations, Fig. 3 (c) or Fig. 4 (c). For 10 ps bunch length one can estimate the energy spread of the bunch as 1 MeV ($\delta = 6 \cdot 10^{-4}$).

The results of bunch length measurements as a function of the bunch energy in the booster are shown in Fig. 5 with blue dots. The expected bunch length from the numerical simulation with elegant is shown with red curve.

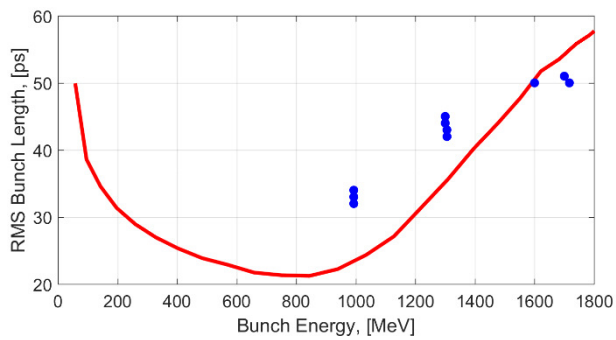

Figure 5: Bunch length as a function of the extracted bunch energy. The red curve is the simulation and the blue dots are measurements.

For the bunch energy of 1700, 1300 and 1000 MeV there were several measurements of the bunch length with a small deviation of energy or phase to find an optimum. The observed discrepancy with the numerical simulation need to be further studied and, moreover, more data points at different energies are needed to be measured.

CONCLUSION

Bunch properties at the BESSY II booster synchrotron can be measured by the storage ring diagnostics during the first turns. Ramping down the energy of the storage ring as well as the transfer line allows the bunch properties characterization during the energy ramp of the booster.

Presented technique can be used for the bunch length measurement at the BESSY II booster, until other diagnostics become available there. Measuring the synchrotron oscillation just after injection, the injection phase and energy can be reconstructed and optimized to decrease the oscillation amplitude and possible decrease particle loses during injection.

As an alternative for the bunch length measurement at the booster the optical dissector, as described in [7], can be used. This is a diagnostic device similar but simpler than a streak camera and can be routinely used in the accelerator tunnel. It provides sufficient temporal resolution for the expected bunch lengths in the booster.

REFERENCES

[1] A. Jankowiak *et al.,* "The BESSY VSR project for short X-ray pulse production", *in Proc. 7th Int. Particle Accelerator Conf. (IPAC'16)*, Busan, Korea, May 2016, paper WEPOW009, pp. 2833-2836.

[2] A. Jankowiak, J. Knobloch et al., "Technical Design Study BESSY VSR ", Helmholtz-Zentrum Berlin, 2015, http://dx.doi.org/10.5442/R0001

[3] M. Borland, "elegant: A Flexible SDDS-Compliant Code for Acceleration Simulation," Advanced Photon Source LS-287, September 2000.

[4] F. Kramer, "Study and optimization of the transverse beam parameters before injection into the storage ring BESSY II", Master thesis, HU Berlin, 2016.

[5] T. Atkinson *et al.,* "Status and prospects of the BESSY II injector systems", *in Proc. 7th Int. Particle Accelerator Conf. (IPAC'16)*, Busan, Korea, May 2016, paper WEPOW007, pp. 2826-2828.

[6] H. Wiedemann, *Particle Accelerator Physics*, 3rd ed. (Springer, New York, 2007), pp. 199-202.

[7] D. Malyutin *et al.,* "The optical dissector bunch length measurements at the metrology light source", presented at the 6th Int. Beam Instrumentation Conf. (IBIC'17), Grand Rapids, Michigan, USA, August 2017, paper TU1AB3, this conference.

ISBN: 978-3-95450-192-2 doi:10.18429/JACoW-IBIC2017-TUPCC08

IMPROVING THE SENSITIVITY OF EXISTING ELECTRO-OPTIC SAMPLING SETUPS BY ADDING BREWSTER PLATES: TESTS OF THE STRATEGY AT SOLEIL

C. Szwaj, C. Evain, M. Le Parquier, S. Bielawski*
PhLAM, Université Lille 1, France
J.-B. Brubach, L. Manceron, M.-A. Tordeux, M. Labat, P. Roy,
Synchrotron SOLEIL, Gif-Sur-Yvette, France

Abstract

For improving the sensitivity of electro-optic sampling (EOS), several techniques are used. Operation of the set of polarizing elements "close to extinction" is a technique used routinely for obtaining high responsivity (i.e., a large output signal for a given input electric field). This technique is widely used for monitoring electron bunches in linear accelerators and FELs. We show that a simple modification of these EOS systems enables to increase further the SNR, by cancelling out the laser noise. The idea is to introduce a set of Brewster plates, following the idea Ahmed, Savolainen and Hamm [1] in the EOS path, and performing balanced detection. We present detailed tests of this type of upgrade on the PhLAM-SOLEIL EOS system, destined to studies of THz CSR pulse dynamics [2, 3].

INTRODUCTION: CLASSICAL SNR IMPROVEMENT METHODS AND THEIR LIMITATIONS

For recording ultrafast electric field transient in single-shot, a particularly efficient method consists in using the spectrally encoded Electro-Optic Sampling (EOS) [4,5,5–8]. The electric field transient is imprinted onto a chirped laser pulse, by electro-optic modulation. Then the output pulse is analyzed using a single-shot spectrum analyzer.

High Responsivity Using Near-Extinction EOS Setups

In order to reach high SNR, a popular way consists in operating the setup in a configuration known as *near extinction* EOS [9,10] (Fig. 1a). In these conditions, an important limit to the SNR comes from the shot-to-shot fluctuations of the laser, which can be well above the shot-noise limit. This is particularly the case for laser systems with a fiber amplifier, which is known to add Amplified Spontaneous Emission noise.

Noise Cancellation Using Balanced Detection

Laser noise cancellation is possible using balanced detection [11–14] (Fig. 1b). However the combination with near-extinction (for reaching high responsitivety) is not trivial to realize.

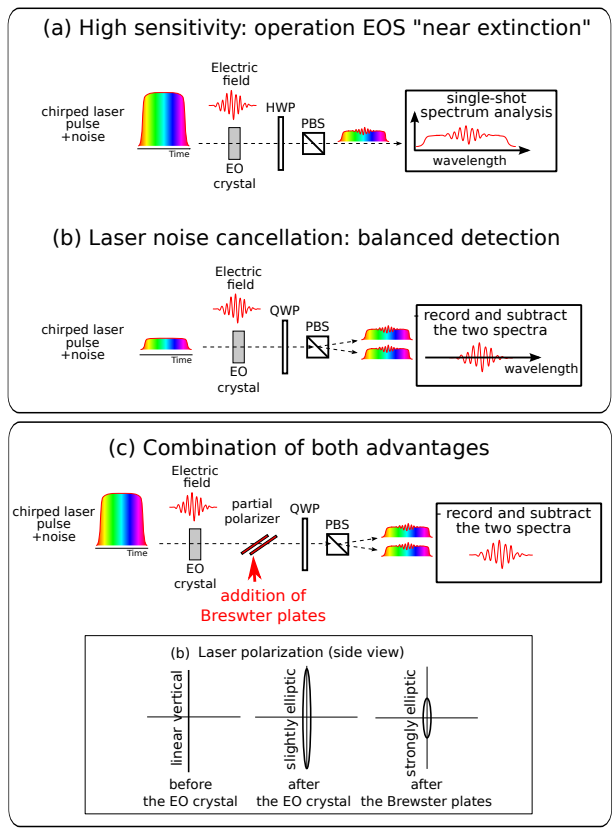

Figure 1: (a) and (b): classical EOS setups. In (a) operation near extinction can provide high responsivity (defined as the detected signal per unit electric field in the EO crystal). The balanced detection scheme (b) provides laser noise cancellation capability, but has a moderate responsivity. The EO setup (c) provides both advantages, i.e., high responsivity and laser noise cancellation. Lower inset represents the polarization states of the light in the setup.

PRINCIPLE OF THE METHOD

In a different context (scanned EOS), Ahmed Savolainen and Hamm demonstrated that the advantages of (i) near-extinction and (ii) balanced detection can be associated in a very simple way. The principle consists of introducing a partial polarizer (e.g., a set of Brewster plates) in a classical balanced detection EOS system, between the EO crystal and the polarizer [1, 1]. We tried to test this strategy in the case of single-shot spectrally-encoded detection. The basic principle is represented in Figure 1c.

* serge.bielawski@univ-lille1.fr

ISBN: 978-3-95450-192-2 doi:10.18429/JACoW-IBIC2017-TUPCC08

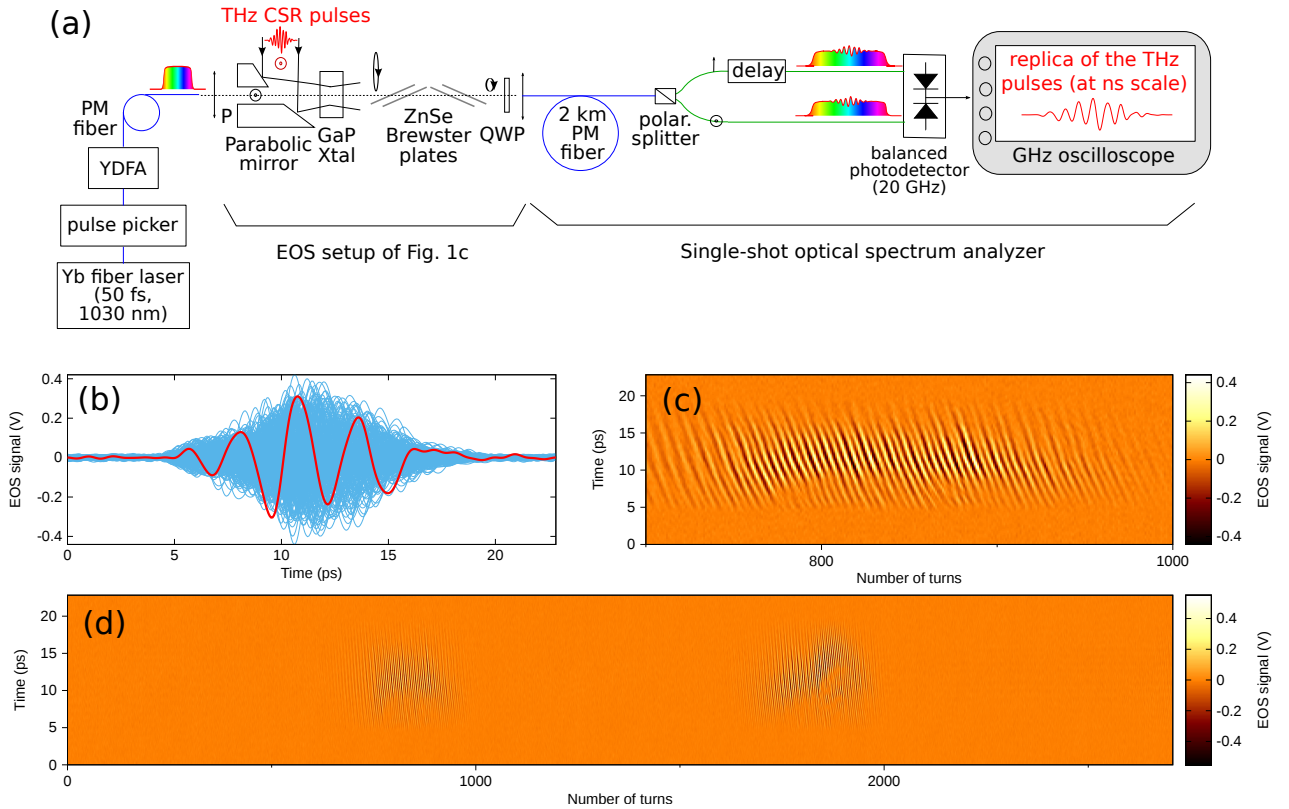

Figure 2: Results using the Brewster plate enhancement scheme. (a), Experimental setup. (b), Series of 250 EOS traces (blue) and example of a single pulse (red). (c) Same series of pulses represented as a colorscale diagram. (d), complete set of data displaying two bursts.

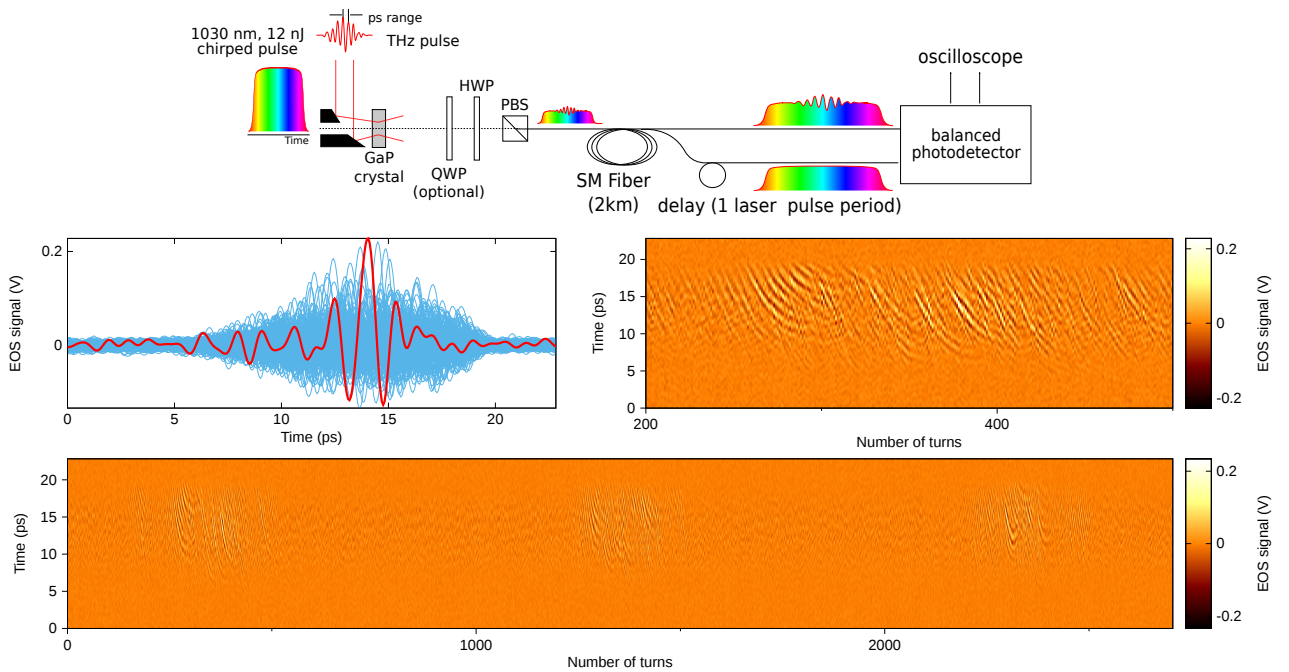

Figure 3: For reference, series of THz CSR pulses recorded using the classical *near extinction* setup (the scheme of Fig. 1a). (a) detailed setup. (b) series of 350 pulses, during a THz burst (blue curves), and example of single pulse (red). (c) The same series of pulses represented as a colorscale diagram, (c) complete set of data displayig 3 bursts. Note that the SNR is mainly limited by the laser source noise, which is visible between the bursts. Also, note the asymmetry in the shape of EOS signals in (b), which is due to second order distorsion (and not present in Fig. 2).

ISBN: 978-3-95450-192-2 doi:10.18429/JACoW-IBIC2017-TUPCC08

For a given optical power on the spectrum analyzer, the EO signal is proportional to $1/\sqrt{T}$, with T the power transmission of Brewster plates. This is formally similar to the "enhancement effect" of the near-extinction technique. However the setup of Fig. 1c provides two complementary outputs. Hence if we perform the difference between the two spectra, we expect to obtain also a noise cancellation effect.

TESTS AT SOLEIL

Details of the EOS Setup

We tested the strategy on the EO system destined to THz Coherent Synchrotron Radiation studies at SOLEIL. We basically realized the Fig. 1c system, but introduced an long (2 km) polarization-maintaining fiber between the quarter wave plate and the polarizer. With this setup (Figure 2), the spectra are obtained using the so-called Dispersive Fourier Transform technique (or time-stretch) [15–17]. After propagation in the fiber, the spectra are converted into a temporal signal which is recorded with a single-pixel photodetector. Apart from this specificity for the spectrum analysis, the system is equivalement to the setup of Figure 1c.

Results

A typical recordings obtained in normal alpha mode (user mode) at SOLEIL is represented in Figure 2b-d. Detailed measurements showed that the senstivity, i.e., the noise-equivalent input electric is of the order of 2.3 μV/cm/$\sqrt{\text{Hz}}$ in the 0-300 GHz band. The signal to noise ratio is increased by a factor 6.75 with respect to the balanced detection scheme, see Reference [2] for detailed measurements. We have also displayed typical results obtained with our previous near-extinction setup in Fig. 3.

The detectivity enhancement (with respect to the classic balanced detection scheme) can theoretically reach a =18.9 with our setup, if the power incident on the photodetector can be kept at its optimal value. In this test, the available power (12 nJ per pulse) was too low (by a factor 4) to reach this a = 18.9 value. Further improvements can be thus made by increasing the laser power.

Another advantage of the Brewster plate method (with respect to the near extinction scheme) concerns the non-linearity. The transmission of the Brewster plates scheme does not present quadratic distorsion. This is different from the near-extinction scheme, whiich exhibits quadratic distorsion. We have not quantified this effect. However this difference is visible in Figures 2b an 3b. The superposition of EOS traces (blue curves) presents an asymmetry in the the near-extinction case, that is not present with the Brewster scheme.

CONCLUSION

The introduction of a set of Brewster plates in an EO system appears as a promizing alternative to the *near-extinction* scheme, as it enables a cancellation of the laser noise. It is also important to note that this strategy is not restricted to EO setups with time-stretch readouts, but should also be feasible with classical spectral encoding EO systems.

ACKNOWLEDGEMENTS

The work has been supported by the BQR of Lille University (2015). The work has also been supported by the Ministry of Higher Education and Research, Nord-Pas de Calais Regional Council and European Regional Development Fund (ERDF) through the Contrat de Projets État-Région (CPER photonics for society), and the LABEX CEMPI project (ANR-11- LABX-0007). Preparation of the experiment used HPC resources from GENCI TGCC/IDRIS (i2015057057, i2016057057).

REFERENCES

[1] Ahmed, S., Savolainen, J. & Hamm, P. "Detectivity enhancement in thz electrooptical sampling", *Review of Scientific Instruments* **85**, 013114 (2014).

[2] Szwaj, C. *et al.*, "High sensitivity photonic time-stretch electro-optic sampling of terahertz pulses", *Review of Scientific Instruments* **87**, 103111 (2016).

[3] Evain, C. *et al.*, "Direct observation of spatiotemporal dynamics of short electron bunches in storage rings", *Physical Review Letters* **118**, 054801 (2017).

[4] Jiang, Z. & Zhang, X.-C., "Electro-optic measurement of THz field pulses with a chirped optical beam", *Appl. Phys. Letters* **72**, 1945 (1998).

[5] Wilke, I. *et al.*, "Single-shot electron-beam bunch length measurements", *Phys. Rev. Lett.* **88**, 124801 (2002).

[6] Steffen, B. *et al.*, "Electro-optic time profile monitors for femtosecond electron bunches at the soft x-ray free-electron laser flash", *Physical Review Special Topics-Accelerators and Beams* **12**, 032802 (2009).

[7] Judin, V. *et al.*, "Spectral and temporal observations of CSR at ANKA", in *Proc. IPAC'12*, New Orleans, Louisiana, USA, May 2012, TUPPP010.

[8] N. Hiller, A. Borysenko, E. Hertle, V. Judin, B. Kehrer, A.-S. Müller, M.J. Nasse, P. Schönfeldt, M. Schuh, N.J. Smale, J.L. Steinmann, B. Steffen, P. Peier, V. Schlott, "Single-shot Electro-optical Diagnostics at the ANKA Storage Ring", in *Proc. of IBIC'14*, Monterey, CA, USA, September 2014, MOPD17, pp. 182-186 (2014).

[9] Jiang, Z., Sun, F., Chen, Q. & Zhang, X.-C., "Electro-optic sampling near zero optical transmission point", *Applied Physics Letters* **74**, 1191 (1999).

[10] Shi-Xiang, X. & Hua, C., "A theoretical and experimental research on terahertz electro-optic sampling at near-zero optical transmission point", *Chinese Physics Letters* **25**, 152 (2008).

[11] Nahata, A., Weling, A. S. & Heinz, T. F., "A wideband coherent terahertz spectroscopy system using optical rectification and electro-optic sampling", *Applied Physics Letters* **69**, 2321–2323 (1996).

[12] Schmidhammer, U., De Waele, V., Marques, J.-R., Bourgeois, N. & Mostafavi, M., "Single shot linear detection of 0.01–10 thz electromagnetic fields", *Applied Physics B* **94**, 95–101 (2009).

ISBN: 978-3-95450-192-2 doi:10.18429/JACoW-IBIC2017-TUPCC08

[13] Wong, J. *et al.*, "Photonic time-stretched analog-to-digital converter amenable to continuous-time operation based on polarization modulation with balanced detection scheme", *J. Lightwave Tech.* **29**, 3099 (2011).

[14] Buckley, B. W., Fard, A. & Jalali, B., "Time-stretch analog-to-digital conversion using phase modulation and broadband balanced coherent detection for improving resolution", In *Optical Fiber Communication Conference*, OThW4 (Optical Society of America, 2011).

[15] Mahjoubfar, A. *et al.*, "Time stretch and its applications", *Nature Photonics* **11**, 341–351 (2017).

[16] Coppinger, F., Bhushan, A. & Jalali, B., "Photonic time stretch and its application to analog-to-digital conversion", *IEEE Trans. on Microwave Theory and Techniques* **47**, 1309 (1999).

[17] Goda, K. & Jalali, B., "Dispersive fourier transformation for fast continuous single-shot measurements", *Nature Photonics* **7**, 102 (2013).

ISBN: 978-3-95450-192-2 doi:10.18429/JACoW-IBIC2017-TUPCC09

ELECTRON BUNCH PATTERN MONITORING VIA SINGLE PHOTON COUNTING AT SPEAR3*

B. Xu, E. Carranza, A. Chen, S. Condamoor, A.S. Fisher and J.Corbett †
SLAC National Accelerator Laboratory, Menlo Park, CA, 94025, USA

Abstract

In recent years the synchrotron radiation program at SPEAR3 has moved toward laser/x-ray pump-probe experiments which utilize a single timing 'probe' bunch isolated by a ± 60 ns dark space on either side. In order to quantify bunch purity in the region near the timing bunch, time-correlated single photon counting is used. In this paper we investigate methods to optimize the fill pattern and resolve satellite bunches in the region near the timing bunch. Integration of the Matlab measurement and data processing software into EPICS is reported.

INTRODUCTION

SPEAR3 is a 234 m circumference electron storage ring with a 476MHz RF frequency. The electron beam can be injected into any of 372 RF buckets separated by 2.1 ns. As shown in Fig. 1, the 500 mA electron beam is configured in four electron bunch 'trains' each containing 70 bunches. The 30 ns gap between bunch trains allows for ion clearing to optimize beam lifetime. By design, the bunches in the four bunch trains contain equal charge. The single isolated timing bunch seen to the right is separated by ±60 ns dark space for time-resolved pump/probe experiments. With a 9 hr beam lifetime, the 1% beam loss is replenished every 5 min by a 10 Hz injector delivering single-bunches with ~50 pC charge/pulse.

For the injection process, a linear accelerator (linac) with a thermionic cathode gun transfers 120 MeV electrons to a booster ring which by design accelerates a single bunch of charge to 3 GeV prior to injection into SPEAR3. To avoid charge spill, the timing of each charge transfer process must be accurate to the sub-nanosecond level.

A visible-light diagnostic beam line on SPEAR3 is used to measure beam cross section, bunch length and injected beam dynamics. Time-Correlated Single Photon Counting (TCSPC) was added to monitor electron charge stored in each bunch [1-7]. With TCSPC, the bunch charge can be resolved with high dynamic range. The TCSPC data is used to monitor satellite bunches adjacent to the pump-probe timing bunch and to monitor evenness of charge in the bunch trains. The TCSPC system reported here uses a combination of Matlab for data acquisition and processing and EPICS for control. In this paper we report on recent developments with the data processing algorithm and the software environment.

* Work sponsored by U.S. Department of Energy, Office of Science, under Contract DE-AC02-76SF00515 and the DOE SULI.

† corbett@slac.stanford.edu

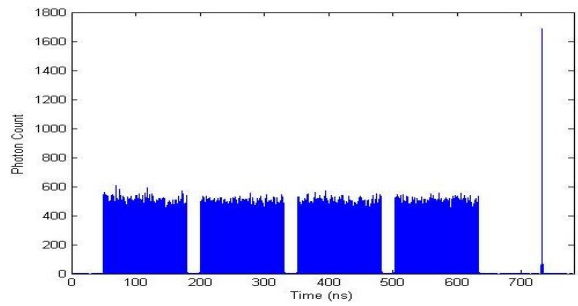

Figure 1: SPEAR3 timing bunch pattern with 4 bunch trains and 1 timing bunch (tall spike at right).

SPEAR3 TCSPC SYSTEM

Time Correlated Single Photon Counting is a slow yet accurate measurement process that can provide the dynamic range needed to detect low-charge bunches. The measurement depends on the fact that the rate of SR photon emission is proportional to the total charge in each bunch, and produces much higher resolution compared to conventional techniques such as oscilloscope sampling of a beam position monitor.

The SPEAR3 TCSPC detection system uses a PMA Hybrid single-photon detector with a PicoHarp300 pulse detector, both manufactured by PicoQuant [8]. The PicoHarp300 operates by detecting the arrival time of single photon emission events relative to a trigger, in this case the periodic beam revolution clock. For SPEAR3, the beam revolution time is 781 ns and the corresponding revolution rate is f=c/L=1.28 MHz. At each trigger event, the first photon arrival event is recorded in one of 65535 discrete 16 ps time bins which is sufficient to resolve the 2.1 ps bunch separations. The accumulation of counts in each time bin integrated over the total measurement interval generates a histogram of the electron beam bunch pattern in time.

Since the PicoHarp300 only records the first photon arrival event each trigger cycle, it is important to reduce the single photon arrival rate to avoid measurement pileup [5, 9]. An average photon arrival rate of one count per every 10 beam revolution triggers provides high accuracy.

SATELLITE ELECTRON BUNCHES

In practice, small inaccuracies in the charge acceleration process can cause electrons to be captured in RF buckets adjacent to the target bunch, a process referred to charge spill. These 'satellite' bunches can grow over time with repeated topup cycles.

The plot in Fig. 2 shows TCSPC data expanded around the timing bunch after approximately 10 days of periodic

ISBN: 978-3-95450-192-2 doi:10.18429/JACoW-IBIC2017-TUPCC09

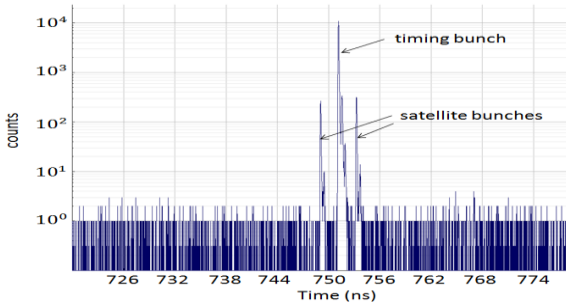

Figure 2: Zoom image of TCSPC data illustrating satellite bunches adjacent to the timing bunch.

top-up injection. In this case charge has accumulated in the upstream and downstream satellite bunches at the few percent level.

At SPEAR3 it is difficult to inject a 'pure' isolated timing bunch into the main storage ring because of imperfections in the charge transfer process between the 2856 MHz s-band linac and the 358 MHz booster synchrotron. As illustrated in Fig. 3, at each 10 Hz injection cycle a thermionic RF gun generates a 2 μs s-band bunch train with bunches separated by 350ps. A synchronized 'chopper' module is designed to select approximately 7 s-band bunches from the 2 μs bunch train, or ~2.5 ns of charge. Ideally, this charge is captured a single 2.8 ns booster RF bucket.

In practice, however, more than 7 s-band bunches pass through the chopper which can lead to charge spill into adjacent booster buckets (Fig. 4). As illustrated in Fig. 5, when the booster charge is transferred to SPEAR3, satellite bunches are generated.

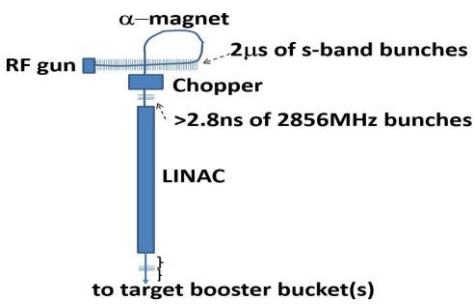

Figure 3: SPEAR3 pre-injector showing charge transfer from the electron gun to linac and booster.

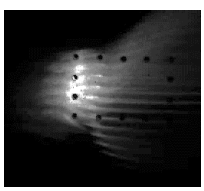

Figure 4: Camera image of the linac output beam prior to injection into the booster. s-band bunches are dispersed vertically due to action of the chopper and horizontally by dipole dispersion.

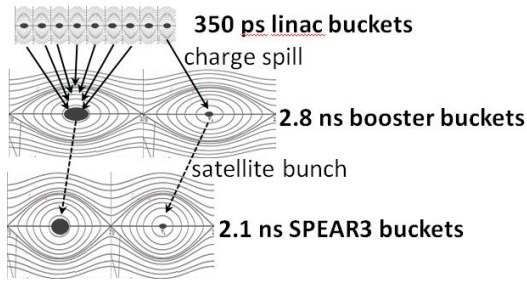

Figure 5: Charge spill from the linac bunch train generates satellite electron bunches in SPEAR3.

By adjusting the time between the linac and the booster, it is possible to minimize but not eliminate satellite bunches. Figure 6 shows measurements of the charge in the early and late satellite bunches in SPEAR3 as the SPEAR-to-Booster RF timing was adjusted. Jitter in the timing system and charge diffusion in longitudinal phase space can also lead to satellite bunches. When the bunch-by-bunch feedback system becomes operational in 2018 it will be possible to study charge diffusion directly [10].

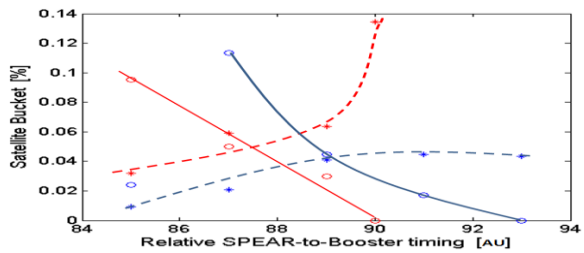

Figure 6: Early ('o') and late ('*') satellite bunch charge by percentage as a function of SPEAR-to-booster timing as for two linac timing settings (blue, red).

TOP-UP CONTROL

The current software algorithm used for charge topup targets numerically consecutive RF buckets in SPEAR3 during injection Fig. 7 (a). Although the total beam current is restored each top-up cycle, injection irregularities can create high and low charge bunches. To reduce or eliminate this effect, the bunch current pattern measured with TCSPC can be used to re-specify the injection filling sequence to achieve the desired result.

The simplest algorithm is to sequentially inject into bunches sorted from lowest to highest charge Fig. 7 (b). A more robust algorithm is to pre-calculate the impact of multiple injection shots into charge-deficient buckets Fig. 7 (c).

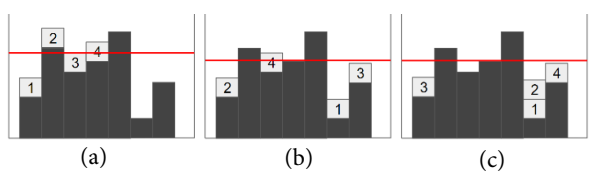

Figure 7: Results of using the consecutive refill pattern (a), the sorted refill pattern (b), and multi-shot refill pattern (c). Red lines indicate median bunch current after four refill shots.

ISBN: 978-3-95450-192-2 doi:10.18429/JACoW-IBIC2017-TUPCC09

Since TCSPC measures the bunch pattern in the terms of photon arrival events, the average number of counts per injector pulse can be calculated from

$$\frac{Count}{Shot} = \frac{Count}{Charge} * Q_{shot} = \frac{Count}{Charge} * (I_{shot} * t_{rev})$$

where

$$\frac{Count}{Charge} = \left(\sum_{buckets} x_i \right) (I_B * t_{acq})^{-1}$$

with I_{shot} the injected electron current per shot, t_{rev} the SPEAR3 revolution time, χ_i the TCSPC counts per bucket, I_B the total current and t_{acq} the acquisition time.

To evaluate efficiency of a topup algorithm, the standard deviation in charge across all bunches can be used as a metric. A Monte Carlo algorithm was used to compare the standard deviation in randomized bunch patterns for different top-up scenarios: the simulator artificially generated different bunch patterns and the injection algorithm attempted to reduce the rms spread of bunch charge [5]. As expected, the multi-shot algorithm is able to out-perform the single-shot sorting algorithm.

SOFTWARE ARCHITECTURE

In order to automate data acquisition and processing, the PicoHarp300 has been integrated into a Matlab/EPICS software architecture. The Matlab portion contains an outside 'wrapper' that provides a heartbeat to the EPICS control system (Fig. 8). At each heartbeat cycle, the wrapper software also calls a 'core' Matlab program that acquires and processes the data. In practice, the heartbeat operates at 1 Hz and the data is acquired every 5 sec. An additional, time-integrated histogram is accumulated every nth iteration of the 5 sec measurements where the accumulation variable 'n' is user-selectable.

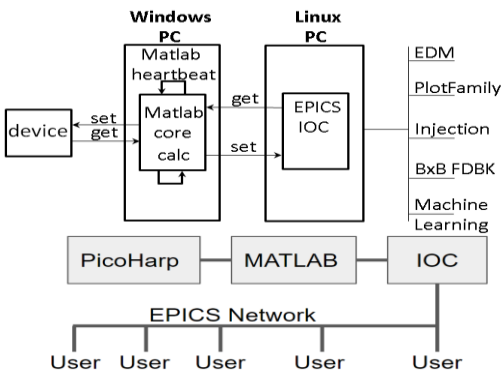

Figure 8: Schematic of the software architecture.

At each heartbeat cycle the PicoHarp300 data acquisition parameters are downloaded from EPICS, and at each 5 sec cycle both the full histogram waveform and the bunch current in all 372 buckets are uploaded to EPICs. The Matlab code can be compiled to increase operational stability.

On the EPICS side, a stand-alone input-output controller (IOC) was constructed to act as a server with a custom EPICS database. Figure 9 shows the EPICS EDM panel used to control the measurement parameters and

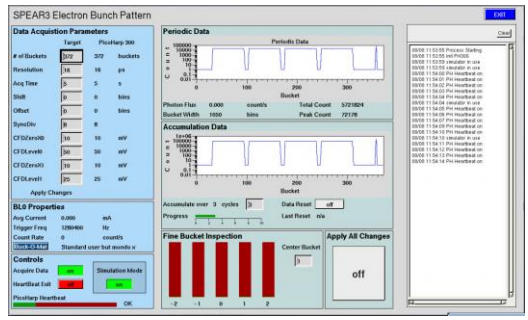

Figure 9: EPICS EDM panel to control and monitor Matlab software.

display the raw data. External users can also acquire the raw or processed data using Channel Access (C/A) to query the IOC. Control of the PicoHarp300 data acquisition system is possible through either Matlab or EPICS using C/A. For instance, a separate TCSPC analysis application can instruct the bunch-by-bunch feedback system to remove charge from unwanted satellite bunches or the bunch pattern can be plotted in the MML Plotfamily interface. At each 5 sec heartbeat cycle, key parameters are stored in the EPICS history buffer database.

Overall, the Matlab/EPICS software connection is one instance of several systems at SPEAR3 utilizing similar machine-independent software for the Matlab heartbeat and EPICS EDM panel for software uniformity. A Unix Watchdog system monitors the heartbeat communication of all applications running on the Unix servers including the Matlab/EPICS processes described here [7]. When an abnormal event occurs, audio and visual alarms are raised and the event is recorded in an error log.

SUMMARY

By recording single photon arrival events synchronized to the storage ring revolution clock, the TCSPC histogram measurement can reveal the bunch pattern with high dynamic range. The bunch pattern data can be used to specify when to remove unwanted satellite bunches or specify the next top-up injection sequence.

To facilitate operations, the data acquisition system is controlled by a Matlab program to acquire and process the raw data and maintain a monitored heartbeat for the EPICS control system. By choosing Matlab for the data processing, complex algorithms are easy to test and deploy in either native m-file or compiled format.

REFERENCES

[1] H. Wang,' Bunch pattern measurements via single photon counting at SPEAR3', SULI Report (2011).

[2] L. Zavala, 'Time-correlated single photon counting for analysis of the electron bunch profile at SPEAR3', SLAC SULI Report (2014).

[3] P. Leong, 'Electron cluster analysis using time-correlated photon counting', SULI Report (2014).

[4] J. Corbett, P. Leong and L. Zavala, 'Bunch Pattern Measurement via Single Photon Counting at SPEAR3', in *Proc. IBIC'14*, Monterey, CA (2014).

ISBN: 978-3-95450-192-2 doi:10.18429/JACoW-IBIC2017-TUPCC09

[5] B. Xu, et al, 'Electron bunch pattern monitoring via single photon counting at SPEAR3', summer student project, to be published as a SLAC-PUB (2017).

[6] A. Chen, 'TCSPC monitoring of SPEAR3 electron beam via EPICS', SLAC SULI Report (2017).

[7] E. Carranza, 'Development of Watchdog Applications for SPEAR3', SLAC SULI Report (2017).

[8] http://www.picoquant.com/

[9] A. Jeff, 'A longitudinal density monitor for the LHC', University of Liverpool, PhD Thesis (2012).

[10] K. Tian et al , 'Bunch-by-bunch feedback kickers for SPEAR3', in *Proc. IPAC'17*, Copenhagen, Denmark (2017).

ISBN: 978-3-95450-192-2 doi:10.18429/JACoW-IBIC2017-TUPCC10

TIME-RESOLVED ELECTRON-BUNCH DIAGNOSTICS USING TRANSVERSE WAKEFIELDS*

J. Wang†, D. Mihalcea[1], P. Piot[1]
Department of Physics, Northern Illinois University, DeKalb, IL 60115, USA
[1]also at Fermi National Accelerator Laboratory, Batavia, IL 60510, USA

Abstract

The development of future free electron lasers (FELs) requires reliable time-resolved measurement of variable ultrashort electron-bunchs characteristics. A possible technique is to streak the bunch in the transverse direction by means of time-dependent external fields. In this paper we explore the possible use of self-generated electromagnetic fields. A passive deflector, consisting of a dielectric-lined waveguide, is used to produce wakefields that impart a time-dependent transverse kick to the relativistic electron bunch passing off-axis. We investigate the technique and its performances and explore its possible application at the Fermilab Accelerator Science and Technology (FAST) facility.

INTRODUCTION

Modern physics accelerators sever a variety of science from high-energy physics and nuclear physics to radiation sources and electron microscopes. Conventional methods used in the preparation of beams for accelerator application often cannot keep pace with the new demands, thus, new approaches continue to emerge. Techniques to tailor the electron beam phase space distribution by means of external and internal fields have come to play an increasingly important role in linear accelerators over the last decade. Precise control of beam phase space distribution is foreseen for beam-driven advanced acceleration techniques and for novel radiation sources including free-electron lasers and THz radiators. A wide of techniques has been developed to utilize the fields to influence the beam distribution. One of the manipulations operates within one degree of freedom, e.g., those based on the use of external and internal fields to control the distribution in one of three 2D phase-spce planes: $(x - p_x)$, $(y - p_y)$, $(z - p_z)$.

In this paper, the self-generated wakfields, as the internal fields, is used as a tool to provide the transverse kick on the beam so as to introduce a correlation between time and the transverse beam distribution. The first part of this paper is to review the transverse equations of motion in the presence of wakefield and explore the use of a passive deflector to provide time-dependent deflecting kick to a relativistic electron bunch. Such a capability could enable the development of new passive (and cheap) beam diagnostics [1]. The passive deflector does not need to be powered and it is easier to be manufactured compared to a rf transverse deflecting structure, thus, resulting in a considerable cost saving. The passive deflector is self-synchronized with the beam by design, being the wakefield excited by the bunch itself when it travels through a dielectric tube. Thus, we could use it to perform time-resolved measurements of a relativistic electron bunch based on the self-transverse wakefield interaction of the beam itself passing off-axis through a dielectric-lined tube and reconstruct the beam profile from the resulting image of the streaked beam on the downstream profile monitor. The second part of this paper is to explore some possible ways to reconstruct the profile of the beam as a way of beam diagnostics.

* Work supported by the DOE award DE-SC0011831 to NIU. Fermilab is operated by the Fermi Research Alliance, LLC for the DOE under contract DE-AC02-07CH11359.
† Email:wangjinlong97888@gmail.com

BASIC EQUATIONS

We first introduce the coordinate system under consideration and take an electron propagating along an accelerator beam line with applied external fields. The transverse coordinates are x and y while the longitudinal laboratory coordinate along the straight beamline is z. In order to quantify the bunch dynamics, it is often convenient to introduced $\zeta(t) \equiv z(t) - c\int_0^t \beta(t')dt'$ where ζ represents the axial position of an electron with respect to the bunch centre ($\zeta = 0$) at the time t. Since the beam dynamics also involves the momenta we introduce p_i the conjugate momenta associated to the spatial coordinates $i = x, y, \zeta$ and note that for a bunch $p_\zeta \gg (p_x, p_y)$. For convenience we also introduce the angular divergence as $x' \equiv \frac{p_x}{p_z}$ and $y' \equiv \frac{p_y}{p_z}$. Finally we introduce the relative momentum spread as $\delta \equiv \frac{p}{\langle p \rangle}$ where $p^2 = p_x^2 + p_y^2 + p_z^2$.

In order to describe the dynamics of a bunch in presence of transverse wakefield it is often useful to describe the bunch as an ensemble of axial slices. The transverse position of these slices at a given position z along the beamline is a function of ζ and parameterized as $\boldsymbol{x}(\zeta, z)$ where the vector $\boldsymbol{x} \equiv (x, y)$. Considering the case of a transverse wakefield giving rise to the transverse Green's function $w_\perp(\zeta)$ along, e.g., the x direction we can write the corresponding transverse horizontal force as

$$F_x(\zeta, z) = e^2 \int_\zeta^\infty d\zeta' \rho(\zeta') w_\perp(\zeta - \zeta') x(\zeta', z) d\zeta' \qquad (1)$$

where e is the electronic charge. Consequently the transverse equation of motion can be written as [2, 3]

$$\frac{d}{dz}\left[\gamma(z)\frac{d}{dz}x(\zeta, z)\right] + K^2\gamma(z)x(\zeta, z) = r_0 \int_\zeta^\infty d\zeta' \rho(\zeta') w_\perp(\zeta - \zeta') x(\zeta', z) d\zeta' \qquad (2)$$

ISBN: 978-3-95450-192-2 doi:10.18429/JACoW-IBIC2017-TUPCC10

where $r_0 \equiv \frac{e}{mc^2}$ is the classical radius of the electron, $\gamma \equiv \frac{\mathcal{E}}{mc^2}$ is the relativistic Lorentz factor (here $\mathcal{E}^2 \equiv p^2c^2 + m^2c^4$ is the total energy), and K describes external focusing fields.

In a drift space ($K = 0$) and assuming the beam energy remains unchanged $\gamma(s) = \gamma$ and $\frac{d\gamma}{dz} = 0$, the latter equation simplifies to

$$\frac{d^2x(\zeta,z)}{dz^2} = \frac{r_0}{\gamma}\int_{\zeta}^{\infty} d\zeta' \rho(\zeta') w_{\perp}(\zeta - \zeta') x(\zeta', z) d\zeta'. \quad (3)$$

Taking the wakefield to be constantly applied over a length L the previous equation can be integrated to yield

$$\begin{aligned} x'(\zeta,z) &= \frac{dx(\zeta,z)}{dz} \\ &= \frac{Lr_0}{\gamma}\int_{\zeta}^{\infty} d\zeta' \rho(\zeta') w_{\perp}(\zeta - \zeta') x(\zeta', z) d\zeta'. \end{aligned} \quad (4)$$

The most-left equality is valid under the ultra-relativistic approximation $\gamma \gg 1$. Assuming that the slice position does not change during the interaction but only its divergence is affected (this is the so-called "impulse approximation") we can further simplify the previous equation into

$$\begin{aligned} x'(\zeta,z) &= \frac{dx(\zeta,z)}{dz} \\ &= x(\zeta,z)\frac{Lr_0}{\gamma}\int_{\zeta}^{\infty} d\zeta' \rho(\zeta') w_{\perp}(\zeta - \zeta') d\zeta'. \end{aligned} \quad (5)$$

This equation is the basis of transverse-wakefield calculation: knowing the longitudinal charge distribution $\rho(\zeta)$ and the transverse Green's function describing the electromagnetic wake, one can infer the transverse displacement of longitudinal slices.

BEAM DIAGNOSTICS

We now consider the possible use of transverse wake to streak the beam aka to what is commonly done with a transverse-deflecting cavity. This possibility was explored in Ref. [1] where it was pointed out that one could in principle reconstruct the longitudinal distribution and some preliminary results were presented. In this Section we first remind the principle of operation of an active transverse-deflecting cavity and then derive the equation for a passive deflector. We finally explore various ways of retrieving the longitudinal charge distribution.

Analysis of the Active Transverse Deflector

A common time-domain diagnostic method to infer the duration of sub-picosecond employs a transverse-deflecting resonant radiofrequency (RF) cavity [4]. The cavity usually operates on the TM_{110} mode and therefore sustains a transverse time-dependent magnetic field B. As the bunch travels through the cavity [5]. Resulting in a transverse kick (e.g. in the x direction) of the form

$$x'(\zeta,z) \simeq \frac{Lr_0E_0}{\gamma}\sin(k\zeta + \varphi), \quad (6)$$

where L is now the length of the cavity, E_0 the peak electric field provided by the cavity and φ an arbitrary phase shift we henceforth take to be $\varphi = 0$, and $k = \frac{2\pi}{\lambda_{rf}}$ is the wavevector associated to the wave supported by the RF cavity. In practice the bunch length σ_ζ is such that $\sigma_\zeta \ll \lambda_{rf}$ so that the sin() function can be approximated by its first-order Taylor expansion. In such a case we have

$$x'(\zeta,z) = \frac{Lr_0E_0}{\gamma}k\zeta \equiv \kappa\zeta, \quad (7)$$

and the kick is linearly dependent on the bunch longitudinal coordinate. In the previous equation κ is referred to as the normalized kicking strength. A typical experimental setup for measuring the longitudinal bunch distribution consists in recoding the transverse distribution $f_x(x)$ downstream the deflecting cavity. To analyze such a measurement we recall that the transverse phase-space coordinate $\boldsymbol{x} \equiv (x, x')$ downstream of a beamline with transfer matrix R is given by $\boldsymbol{x} = R\boldsymbol{x}_0$ where x_0 is the initial coordinate upstream of the beamline. Taking R to be the transfer matrix from the cavity exit to the observation point we can write for the position of one electron

$$x = R_{11}x_0 + R_{12}x'_0, \quad (8)$$

where $x'_0 = \kappa\zeta + x'_{0,-}$ with $x'_{0,-}$ understood as the electron's initial angle prior to receiving the deflecting kick. Under such an assumption the horizontal position of an electron at the observation point reduces to

$$\begin{aligned} x &= R_{11}x_0 + R_{12}(\kappa\zeta + x'_{0,-}). \\ &= R_{11}x_0 + R_{12}x'_{0,-} + R_{12}\kappa\zeta \equiv x_\beta + R_{12}\kappa\zeta, \end{aligned} \quad (9)$$

where x_β is position due to the betatronic motion. The latter equation can be rewritten as

$$x = x_\beta + x_\zeta, \quad (10)$$

which simplifies to $x = x_\zeta$ when the deflector is turned off. Introduction the probability distribution for x_β and x_ζ to be respectively $f_\beta(x_\beta)$ and $f_\zeta(x_\zeta)$ and further considering the variables to be independent, the probability distribution associated to x is given by the convolution

$$f(x) = \int_{-\infty}^{+\infty} f_\beta(x_\beta) f_\zeta(x - x_\beta) dx_\beta. \quad (11)$$

The longitudinal distribution is related to $f_\zeta(x)$ via the charge conservation relation $f_\zeta(x)dx = \rho(\zeta)d\zeta$ that is $\rho(\zeta) = |R_{12}\,\kappa|\, f_\zeta(R_{12}\,\kappa\zeta)$. Therefore we need to extract the function $f_\zeta(x)$ from Eq. (11). We note that $f(x)$ and f_β can be directly measured by recording the distribution at the observation point respectively with and without powering the deflecting cavity. One can then performed a deconvolution [6] to retrieve $f(x)$. Another possibility is to ensure the beta function at the observation point is very small so that $f_\beta(x_\beta) \simeq \delta(x_\beta)$ [where $\delta()$ is the Dirac's function] consequently simplifying Eq. (11) to $f(x) \simeq f_\zeta(x)$.

ISBN: 978-3-95450-192-2 doi:10.18429/JACoW-IBIC2017-TUPCC10

Equations for a Passive Deflector

Given the description of the active deflection scheme, we can now modify the previous equations to apply them to the passive-deflection technique. Equation (9) is especially modified as

$$x = x_\beta + R_{12} x_0'(\zeta), \tag{12}$$

where $x_0'(\zeta) \equiv x'(\zeta, z = 0)$ with $z = 0$ corresponding to the position where the kick is applied (i.e. the center of the deflecting structure in the impulse approximation); see Eq. (5). We point out that $x_\zeta \equiv R_{12}\, x_0{}'(\zeta)$ is now a nonlinear function of ζ.

Also, using the charge conservation relation $f_\zeta(x)dx = \rho(\zeta)d\zeta$, that is

$$\rho(\zeta) = |R_{12}\frac{dx_0'(\zeta)}{d\zeta}| f_\zeta(x) \tag{13}$$

Here we can get the derivative $\frac{dx_0'(\zeta)}{d\zeta}$ from Eq. (5). The wake function then can be obtained from Eq. [7], here the transverse wake function is the numerical result along ζ when the beam travels through the waveguide with offside $r_0 = b$. Here, the inner radius of the wave guide is $b = 4.50 \times 10^{-4}$ m and outer radius $a = 5.50 \times 10^{-4}$ m and the dielectric constant of the medium is $\epsilon = 4.41$. The result is shown in Fig. 1.

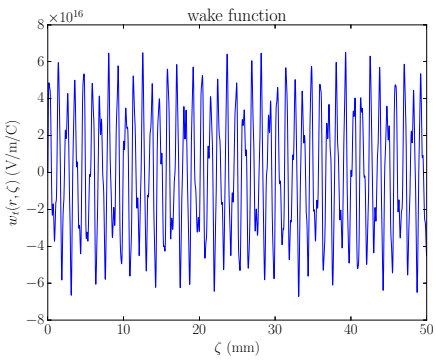

Figure 1: Transverse wake function along ζ.

Thus, through substituting the already known wake function in Eq. (5), we can obtain the derivative $\frac{dx'(\zeta)}{d\zeta}$. After we extract $f_\zeta(x)$ from Eq. (11), the the rest of the problem is to solve the self-consistent equation for the probability distribution $\rho(\zeta)$ along ζ. Since we can measure the probability distribution on the monitor, we can directly obtain the values of $f(x)$ and the probability distribution $f_\beta(x)$ when the deflecting is turned off in Eq. (11). Then we can use the deconvolution method to extract the longitudinal distribution $f_\zeta(x)$. Finally, we can get the longitudinal distribution $\rho(\zeta)$ through Eq. (13).

The algorithm implemented to to retrieved the longitudinal bunch distribution $\rho(\zeta)$ given the observed distribution $f_\zeta(x)$ consists of an iterative method summarized in the pseudo code 1. The algorithm we selected is a simple adaptive loop commonly used in feedback control systems. Specifically, we first make a guess of the longitudinal charge density $\rho(\zeta)$ and compute the corresponding projected function $f_\zeta(x)$ from which the incoming charge density is recovered. The adaptive loop consists in readjusting the initial longitudinal charge density given as detailed in the pseudo code 1.

Algorithm 1 Longitudinal charge distribution retrieval

define $\mathcal{G}$ ▷ gain for the adaptive loop
read $f_\zeta^m(x)$ ▷ measured beam profile after deconvolution
initialize $\rho_0(\zeta)$ ▷ initial (guessed) charge distribution
for $i \in [0, N]$ **do**
  $x(\zeta)$=TransWake[Green, $\rho_i(\zeta)$] ▷ compute deflecting kick for a given Green's function
  $f_\zeta(x)$=Streak[$\rho_i(\zeta)$, $x(\zeta)$] ▷ evaluate streaked profile
  $\rho_i^e(\zeta) = f_\zeta(x) \times |\frac{dx}{d\zeta}|$ ▷ estimated charge distribution from streaked profile
  $\rho_{i+1}(\zeta) = \rho_i + \mathcal{G} \times (\rho_i^e(\zeta) - \rho_i)$ ▷ successive approximation
  $\epsilon_i = \sum_x [|(|\, f_\zeta(x) - f_\zeta^m(x))|]$
end for
plot $\rho_N(\zeta)$

The algorithm is proved to be practical by using a generated super gaussian longitudinal distribution as in Fig. 2. The red line is the generated initial distribution and the blue dot line is the reconstructed distribution after enough times of iterations. We can see they fit very well.

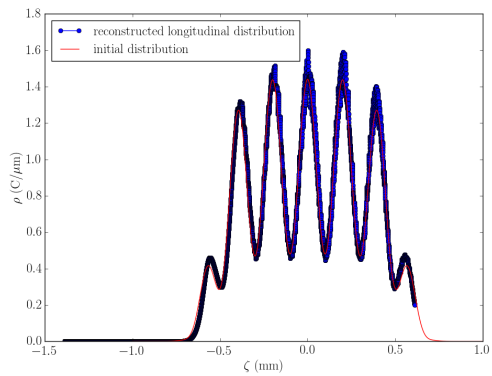

Figure 2: Comparison between the initial longitudinal distribution and the reconstructed distribution

To verify the validation of the method mentioned above, we firstly produce a beam bunch by the ELEGANT [8]. To better verify the this, the beam bunch is designed with some periodic peaks in the direction of x and y. The total charge of

ISBN: 978-3-95450-192-2 doi:10.18429/JACoW-IBIC2017-TUPCC10

the beam is $1\times10^{-7}C$ with total particle number of 100, 000. The undeflected beam is shown as in Fig. 3:

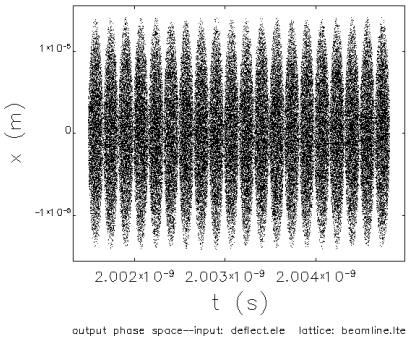

Figure 3: Undeflected beam along t in the longitudinal direction.

After the beam passes through the waveguide with an offside, the beam is deflected by the self-generated wake field, and the shape changes as in Fig. 4 and Fig. 5:

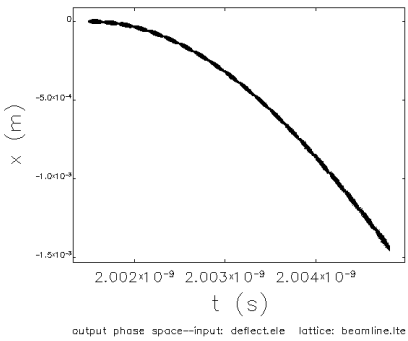

Figure 4: Deflected beam along t in the longitudinal direction.

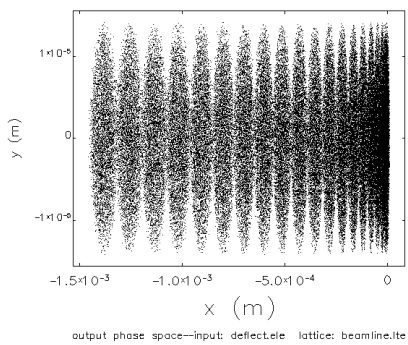

Figure 5: Deflected beam projected on the monitor $x - y$ direction.

We then test the proposed method to reconstruct the longitudinal profile of the beam bunch, using the density distribution of the deflected beam and undeflected beam along x on the $x - y$ monitor. We can see that the result basically fits well with Fig. 3.

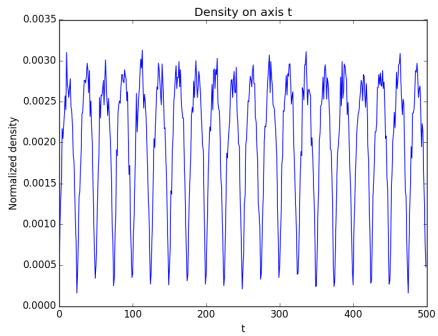

Figure 6: Normalized density along binned t .

CONCLUSION

Thus, in this paper, we proved the deconvolution and iteration method to extract the longitudinal profile of a ultrashort beam in simulation. The result basically agrees with the measurement of the simulation. Thus, the result of the time-resolved measurement based on the passive deflector of a relativistic beam is valid. Also, other methods need to be explored and tested, and further experiment should be verified.

REFERENCES

[1] S. Bettoni, P. Craievich, A. A. Lutman, and M. Pedrozzi, "Temporal profile measurements of relativistic electron bunch based on wakefield generation", *Phys. Rev. Accel. Beams* **19**, 021304 (2016).

[2] A. W. Chao, B. Richter, C.Y. Yao, "Beam emittance growth caused by transverse deflecting fields in a linear accelerator", *Nuclear Instruments and Methods*, **178** (1), 1 (1980).

[3] C. L. Bohn and J. R. Delayen, "Cumulative beam breakup in linear accelerators with periodic beam current", *Phys. Rev.* A **45**, 5964 (1992).

[4] C. Behrens *et al*., "Few-femtosecond time-resolved measurements of X-ray free-electron lasers", *Nature Communications* **5**, Article number: 3762 (2014).

[5] M. Cornacchia and P. Emma, "Transverse to longitudinal emittance exchange", *Phys. Rev. ST Accel. Beams* **5**, 084001 (2002).

[6] D. X. Wang, G. A. Krafft, and C. K. Sinclair, "Measurement of femtosecond electron bunches using a rf zero-phasing method", *Phys. Rev.* E 57, 2283 (1998).

[7] Ng, King-Yuen, "Wake fields in a dielectric-lined waveguide", *Physical Review* D 42.5 (1990): 1819.

[8] M. Borland, "elegant: A Flexible SDDS-Compliant Code for Accelerator Simulation", *Advanced Photon Source* LS-287, September 2000.

ISBN: 978-3-95450-192-2 doi:10.18429/JACoW-IBIC2017-TUPCC12

BUNCH SHAPE MONITORS FOR MODERN ION LINACS

S. Gavrilov†, A. Feschenko
Institute for Nuclear Research of Russian Academy of Sciences, Troitsk, Moscow, Russia

Abstract

In recent years several Bunch Shape Monitors were designed for new modern ion linacs, such as Linac4 CERN, Proton and CW-linac FAIR GSI, FRIB MSU, ESS ERIC. Each of these accelerators has its own requirements for a phase resolution, mechanical design and operating conditions of the monitor. An overview of the most interesting features of different monitors is presented. Some results of laboratory tests and on-site beam measurements are discussed.

INTRODUCTION

The technique of a coherent transformation of a temporal bunch structure into a spatial charge distribution of low energy secondary electrons through RF-modulation was initially implemented by R. Witkover [1] for BNL linac. An energy (longitudinal) RF-modulation of secondary electrons was used. In the Bunch Shape Monitor (BSM) [2], developed in INR RAS, a transverse RF-scanning is used. The general principle of BSM operation has been described many times previously and is clear from Fig. 1.

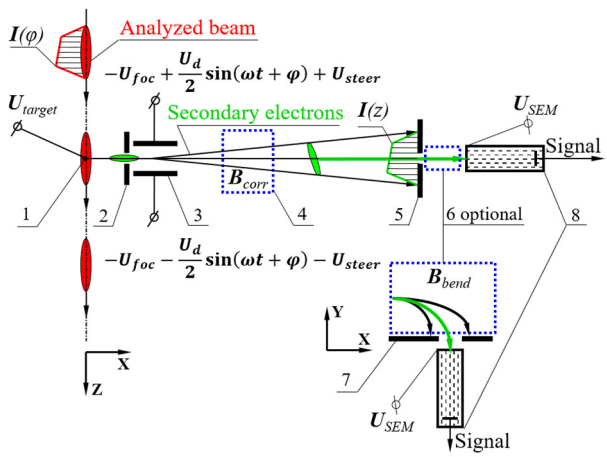

Figure 1: BSM scheme: 1 – tungsten wire target, 2 – inlet collimator, 3 – RF-deflector, 4 – correcting magnet, 5 – outlet collimator, 6 – optional bending magnet, 7 – registration collimator, 8 – secondary electron multiplier.

The series of the analysed beam bunches crosses the wire target 1 which is at a high negative potential. Interaction of the beam with the target results in emission of low energy secondary electrons. The electrons are accelerated by electrostatic field and move almost radially away from the target. A fraction of the electrons passes through inlet collimator 2 and enters RF-deflector 3. The field in the deflector is a superposition of electrostatic focusing and steering field and RF-deflecting field Ud with a frequency equal (or multiple) to the bunch sequence frequency.

† s.gavrilov@gmail.com

CURTAIN RANGE EXTENDER

Two groups of electrons passing the deflector with the phase shift of 180° get through the outlet collimator and their intensity is detected (Fig. 2).

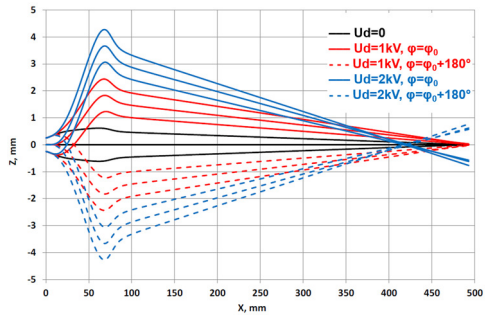

Figure 2: Trajectories of electrons in BSM.

If the bunch length is bigger than 180°, then the signals corresponding to two longitudinal points shifted by 180° are superimposed and the results of the measurements are distorted. Hence the standard phase range of measurements of BSM is equal to half a period of the deflecting field. The range of the measurements can be increased to a full period if one of the two groups of electrons is blocked. To do it the flag-type rotatable curtain can be used at the exit of the RF-deflector. The idea of the curtain was initially proposed by A. Tron and one of the paper's authors, however it was realized in practice for the first time in BSM for FAIR GSI linacs (Fig. 3).

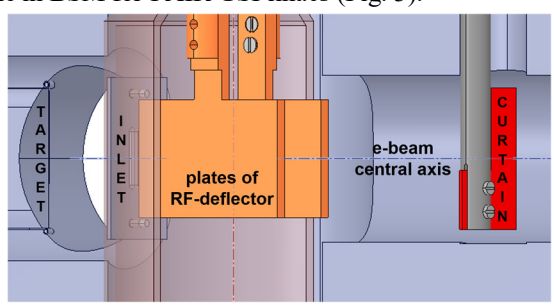

Figure 3: Internal layout of BSM for GSI with curtain.

Rotating the curtain, one can absorb the electrons (Fig. 4) corresponding to one of the two half-periods of the deflecting field thus avoiding superimposing of the signals corresponding to the particles shifted by half a period.

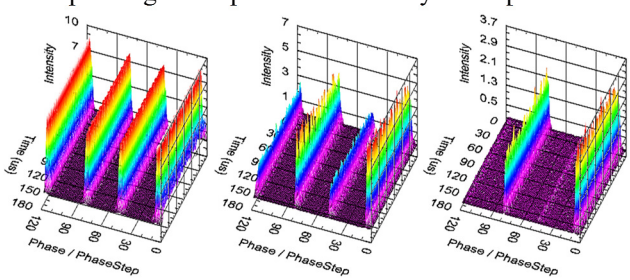

Figure 4: Experimental results for curtain rotation.

ISBN: 978-3-95450-192-2 doi:10.18429/JACoW-IBIC2017-TUPCC12

λ-TYPE RF-DEFLECTOR

The opposite problem arises at linacs with rather short bunches, like ESS ERIC, which is foreseen to operate with RMS bunch lengths of about 1.5°÷2.5° at medium energies and even shorter at high energies, so at least 0.5° phase resolution is required, that corresponds to about 4 ps time resolution for 352.2 MHz operating RF.

To achieve such resolution the uniformity of both deflecting and focusing fields in a RF-deflector must be improved. Typically, BSM deflectors are asymmetric RF-cavities, based on parallel wire lines with capacitive plates. An electrical length of the deflectors is usually λ/4 or λ/2. To improve the phase resolution, a new λ-type symmetric cavity has been developed for ESS (Fig. 5).

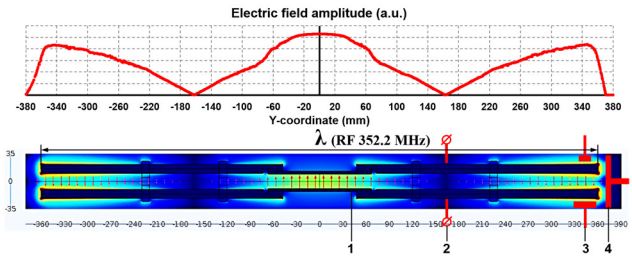

Figure 5: E_Y-field distribution in a λ-type RF-deflector.

The electrodes with deflecting plates 1 are supported by ceramic insulators. Focusing potentials are applied to the electrodes through spring contacts 2 at zero field points. Capacitive adjustable couplers 3 are used to drive the cavity and to pick up the RF-signal. The fine tuning of the resonant frequency is provided with capacitive tuner 4 via the manual actuator from outside the vacuum.

Figure 6 shows the distribution of the RF-field E_Z-component in YZ-plane (X = 0) in non-symmetric (λ/2) and symmetric (λ) RF-deflectors. The non-uniformity of the field in a zone of the electron beam passage is an order of magnitude less for the symmetric type.

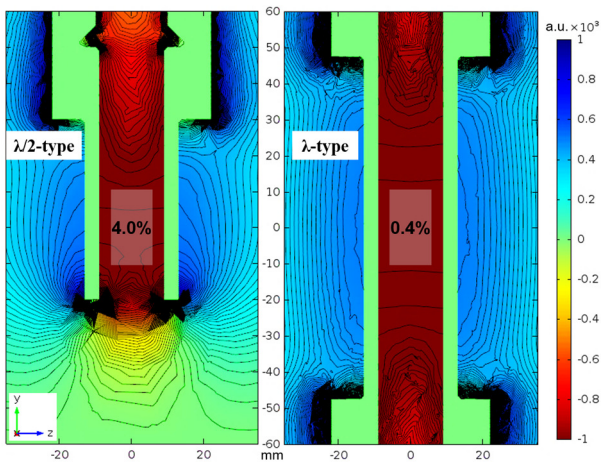

Figure 6: RF-field E_Z-component distribution in YZ-plane (X = 0) of λ/2- and λ-type BSM deflectors.

The λ-type deflector is a crucial feature for BSM resolution improvement up to the fundamental level, determined by a time dispersion of secondary electron emission with the measured upper limit equal (4±2) ps [3].

VIBRATION DAMPERS

At low operating frequencies RF-deflector becomes longer and consequently more sensitive to external vibrations originated from mechanical vacuum pumps, installed at beam pipes, especially in case of λ/4 or λ/2-type design with electrodes extended in cantilever. Vibrations result in oscillations of the electrodes at their mechanical eigenmodes (Fig. 7a), that change the total capacitance of the deflector and as a result spread the resonance frequency and the phase response function of the deflector.

This effect was observed in the deflector 108.408 MHz of BSM for FAIR GSI with the length 610 mm and the main mechanical eigenfrequency about 61 Hz. In fact, the electrodes cannot be identical so their eigenfrequencies must be a bit different, that results in a low frequency modulation. During measurements the range of phase $\Delta\Phi$ and the time Δt required to adjust the phase within this range are related as: $\Delta\Phi=\delta\varphi \cdot F_b \cdot \Delta t$, where $\delta\varphi$ is a phase adjustment step, F_b - beam pulse repetition rate.

Fig. 7b shows the experimental measurements done with the 0.1° phase step at F_b=3.6 Hz. The period of modulated oscillation equals about 3.2 s. The spread of the phase modulation can be estimated about 4°, that means the modulation amplitude of 2° per 0.8 s. The deflecting field phase is adjusted by about 0.3° at the same time, so there are oscillations superimposed on the smooth bunch shape. The modulation can still be distinguished for 0.5° (Fig. 7c) and absolutely disappears for 2° phase step (Fig. 7d).

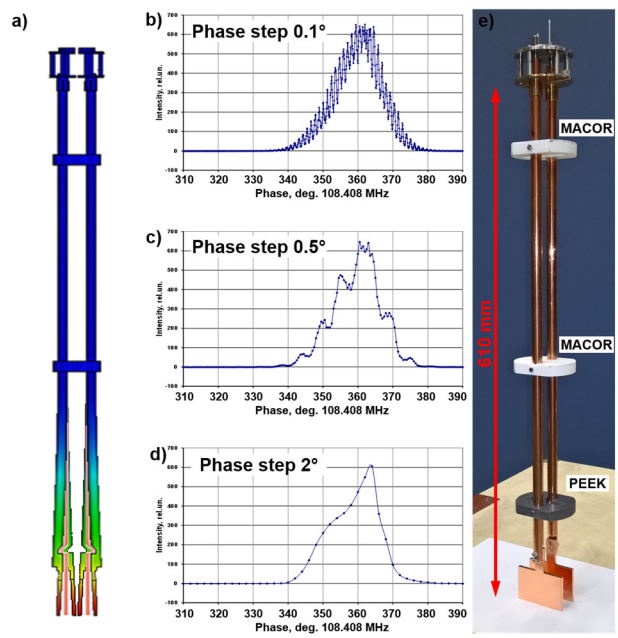

Figure 7: a) Simulated main eigenmode of the electrodes oscillations in a λ/4-type deflector. b-d) Experimental bunch shape measurements in the presence of vibrations. e) Photo of the RF-deflector with extra PEEK holder.

To damp parasitic oscillations the third electrode holder made of PEEK™ was added close to the plates (Fig. 7e). PEEK™ has twice smaller permittivity and loss tangent, than MACOR™ used for prime holders, it is meaningful because of abrupt increase of E-field in this region.

ISBN: 978-3-95450-192-2 doi:10.18429/JACoW-IBIC2017-TUPCC12

MAGNETIC SHIELD AND CORRECTOR

Often BSMs are installed in a close vicinity of magnetic focusing elements with strong fringe fields both static and alternating. In this case a magnetic shield must be used to provide a non-distorted e-beam transport inside BSM.

Typical BSM shield represents a sectional jacket made of 2 mm low-carbon steel. Additionally, the interior surfaces are covered with a 160 μm foil made of an amorphous cobalt-iron alloy with high μ_r. Fig. 8 shows the effect of the BSM shield on the fringe field of a quad located close to the BSM ESS. Even better results can be obtained if additional 2 mm low-carbon steel plate screens are added upstream and downstream of BSM – the remnant fields decrease to the level less, than the Earth's magnetic field, and their influence will be negligible.

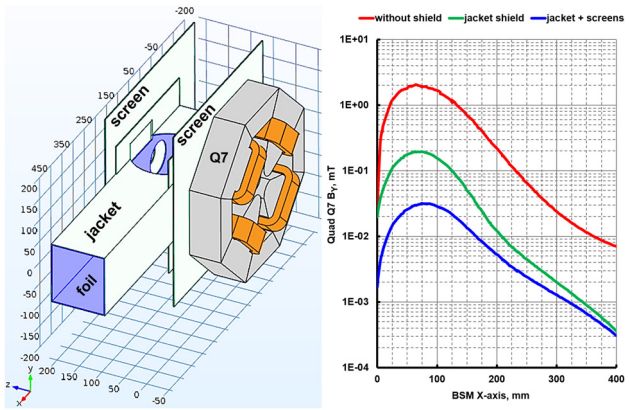

Figure 8: BSM shield design and the quad B_Y distribution.

An influence of remnant moderate static magnetic fields inside the standard shield as well as unavoidable misalignments can be compensated by adjusting the steering voltage U_{steer} in Z-direction and by a special magnetic corrector in other directions. The correcting magnet with the combination of dipole and quadrupole fields (Fig. 9a) was foreseen firstly in BSM for FRIB MSU. The dipole field moves the electron beam along Y-axis. The quadrupole field enables to adjust the tilt of the e-beam in YZ-plane (Fig. 9b).

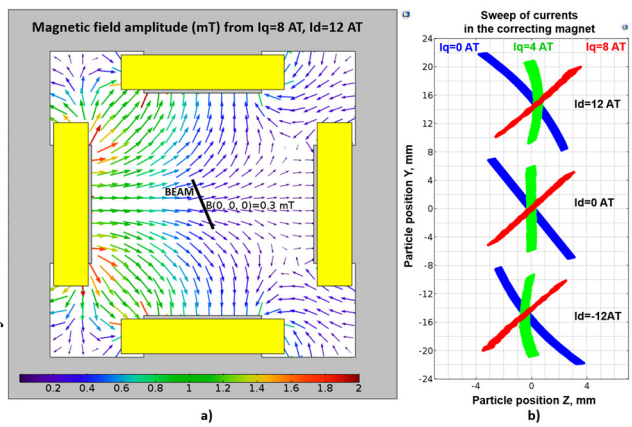

Figure 9: (a) Magnetic corrector with fields superposition. (b) E-beam in the plane of the outlet collimator for different quadrupole Iq and dipole Id coil currents (Ampere·Turns).

CONCLUSION

Bunch Shape Monitor is a reliable tool for longitudinal diagnostics during optimization of beam dynamics in ion linacs. It plays a unique role for the commissioning stage, because allows to observe an evolution of charge longitudinal distribution in bunches within a beam pulse.

Fig. 10 shows the experimental results from the commissioning of LINAC4 CERN. The behaviour of the bunch shape (Fig. 10a) in time reveals a strong instability of longitudinal distribution at the beginning of the beam pulse (Fig. 10b), that can be explained by data about the beam loading in DTLs of the linac (Fig. 10c).

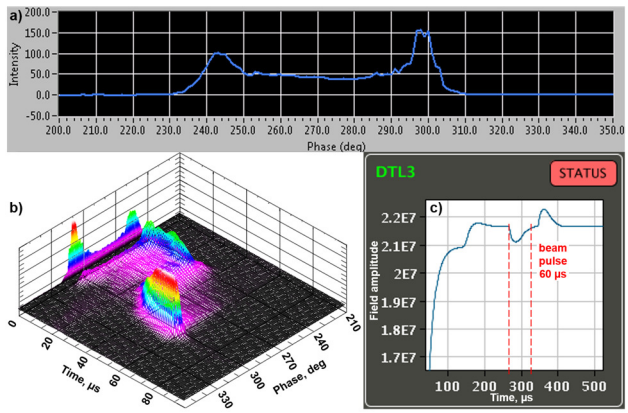

Figure 10: Experimental data from LINAC4 CERN. a) A bunch shape with 1° resolution. b) Evolution of a bunch shape during a beam pulse. c) Behaviour of the field amplitude in DTL3 in the presence of the beam.

A beam microstructure, measured by BSM, allows to tune parameters of bunchers and accelerating cavities (Fig. 11) and also to define some other beam parameters, for example, a longitudinal emittance.

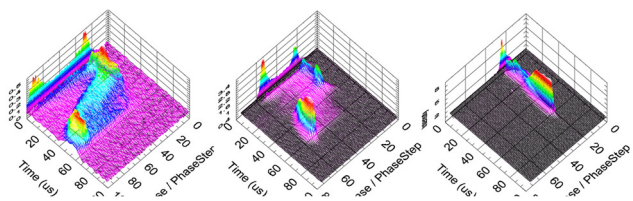

Figure 11: A bunch shape constriction by tuning the phase of the field in PIMS 11-12 LINAC4.

Developed improvements enable to achieve about 4 ps time resolution, that corresponds to 0.5° for hundreds of MHz, and to use the monitor for all typical ion beams of existing and forthcoming linacs.

REFERENCES

[1] R. Witkover, "A non-destructive bunch length monitor for a proton linear accelerator", *Nucl. Instr. Meth.*, vol. 137, no. 2, pp. 203-211, 1976.

[2] A. Feschenko, "Technique and instrumentation for bunch shape measurements", in *Proc. RUPAC2012*, Saint-Petersburg, Russia, Oct. 2012, pp. 181-185.

[3] E. Ernst, H. Von Foerster, "Time dispersion of secondary electron emission", *J. of Appl. Phys.*, vol. 26, no. 6, pp. 781-782, 1955.

ISBN: 978-3-95450-192-2 doi:10.18429/JACoW-IBIC2017-TUPCC13

DESIGN AND DEVELOPMENT OF BUNCH SHAPE MONITOR FOR FRIB MSU

S. Gavrilov†, A. Feschenko, Institute for Nuclear Research of Russian Academy of Sciences, Troitsk, Moscow, Russia

Abstract

Bunch Shape Monitor was developed and tested in INR RAS for the Facility for rare isotope beams to fulfil the requirements of a half a degree phase resolution for 80.5 MHz FRIB operating frequency. The configuration of the λ/4-type RF-deflector based on the parallel wire lines with the shorting jumper and capacitive plates was selected. Special separation of secondary electrons by energy is foreseen to decrease a possible influence of the electrons detached from the ions in the wire target. Peculiarities of the design and development process are described. Results of laboratory tests are presented.

INTRODUCTION

The operation principle of the Bunch Shape Monitor (BSM), developed in INR RAS, is based on the technique of a coherent transformation of a temporal bunch structure into a spatial charge distribution of low energy secondary electrons through a transverse RF-scanning [1, 2] and is clear from Fig. 1.

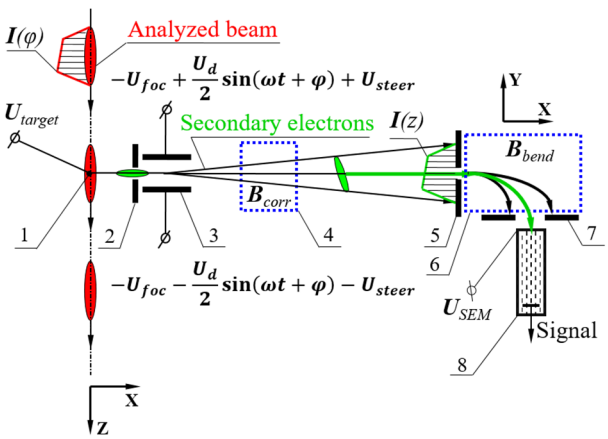

Figure 1: BSM scheme: 1 – tungsten wire target, 2 – inlet collimator, 3 – RF-deflector combined with electrostatic lens, 4 – correcting magnet, 5 – outlet collimator, 6 – bending magnet, 7 – registration collimator, 8 – secondary electron multiplier.

The series of the analysed beam bunches crosses the wire target 1 which is at a high negative potential about -10 kV. Interaction of the beam with the target results in emission of low energy secondary electrons, which characteristics of importance for bunch shape measurements are practically independent of beam energy and charge states of ions, so the monitor can be used for any location along the accelerator without design modification (Fig. 2).

† s.gavrilov@gmail.com

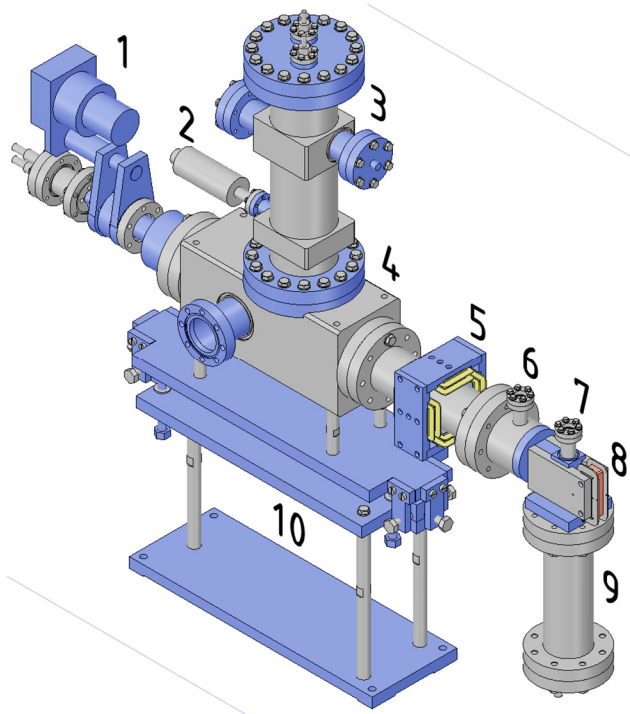

Figure 2: BSM design: 1 – target actuator, 2 – tuner, 3 – RF-deflector, 4 – BSM box, 5 – quadrupole + dipole correcting magnet, 6, 7 – viewports for optical control of e-beam, 8 – bending magnet, 9 – SEM-detector, 10 – support with 3D-adjustment.

The electrons are accelerated by electrostatic field and move almost radially away from the target. A fraction of the electrons passes through inlet collimator 2 and enters RF-deflector 3, where electric field is a superposition of electrostatic focusing and steering fields and RF-deflecting field with a frequency equal to the second harmonic of RF-field frequency in the linac: 161 MHz.

Passed electrons are scanned by the RF-field and an intensity of electrons passed through outlet collimator 5 represents a fixed point of the longitudinal phase distribution of the primary beam. Another points can be obtained by changing the phase of the deflecting field with respect to the RF-reference. If the phase of the deflecting field is adjusted in a wide range, then the bunch can be observed twice per the period of the deflecting field.

By adjusting the steering voltage one can change the measured phase position of the observed bunches and obtain the periodicity of bunches to be exactly equal to π. If the bunch duration is larger than π, the intensities corresponding the phase points differed by π are superimposes and the results of bunch shape measurements become wrong.

ISBN: 978-3-95450-192-2 doi:10.18429/JACoW-IBIC2017-TUPCC13

RF-DEFLECTOR

BSM deflector is a RF-cavity with electrical length λ/4, based on parallel wire lines with capacitive plates (Fig. 3).

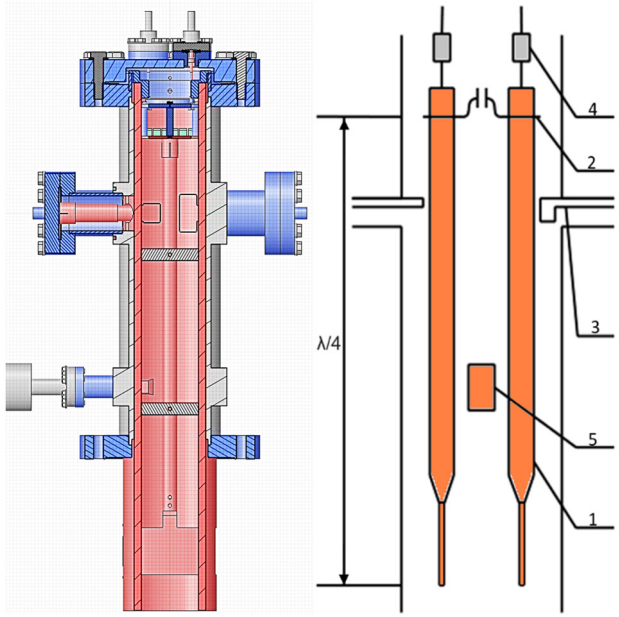

Figure 3: Cut plane and schematic diagram of λ/4-type RF-deflector of FRIB BSM.

Two electrodes 1 with deflecting plates are supported by ceramic insulators. The resonant frequency is adjusted by moving a short 2. The short consists of two collets connected by ceramic capacitors. Coupling loops 3 are used to drive the cavity and to detect the RF-signal. Focusing potentials are supplied through ceramic 1 MΩ resistors 4 which are used to diminish the influence of the external connections. Tuner 5 is intended for a fine manual tuning of the cavity from outside a vacuum in the range of about ±80 kHz.

MAGNETIC CORRECTOR AND SPECTROMETER

Despite of focusing and steering electric fields, shaping the electron beam at the exit of the RF-deflector, there are extra distortions of electron trajectories up to outlet collimator due to the presence of external fringe magnetic fields. The correcting magnet with the combination of dipole and quadrupole fields (Fig. 4a) is implemented. The dipole field produced with two coils moves the electron beam along Y-axis. The quadrupole field produced with another four coils enables to adjust the tilt of the beam image in YZ-plane (Fig. 4b). The set of electric and magnetic corrections provide an exhaustive fit of the electron beam and the outlet collimator, thus compensating misalignments and an influence of external moderate static magnetic fields.

In case of strong fields from adjoining focusing elements (quads and correctors) or alternating magnetic fields, which cannot be corrected with the technique described above, sectional magnetic shield is foreseen.

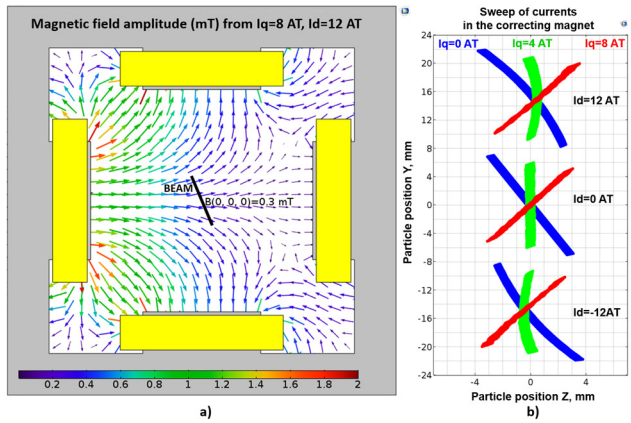

Figure 4: (a) Superposition of dipole and quadrupole fields of the correcting magnet. (b) Cross-sections of the e-beam in the plane of the outlet collimator for different quadrupole Iq and dipole Id coil currents (Ampere·Turns).

The results of measurements can be also influenced by electrons produced due to dissociation of the multicharged ion beam in the target. The signals due to detached electrons are superimposed on the useful signals and distort the measured function. The energy of the detached electrons differs from that of low energy ones, and to decrease an influence of the detached electrons a separation by energy with the help of bending magnet installed downstream of outlet collimator is used. Energy resolution of the 90° magnetic spectrometer is defined mainly by the size of registration collimator. A relatively low value of resolution about 10% is selected to avoid losses of the useful low energy secondary electrons.

TARGET HEATING LIMITS

The target is a tungsten wire with 0.1 mm diameter, and its maximum heating is limited by rising of an electronic thermionic emission at the temperature about 1700÷1800 K. Experimentally the thermionic emission is manifested as an increase of the background from the beginning to the end of a beam pulse, including the phases outside the bunch. Simulated peak steady temperatures of the target-wire for typical beam parameters are shown in Fig. 5. The mode of 1 Hz is suitable for all beams with pulse duration up to 200 μs.

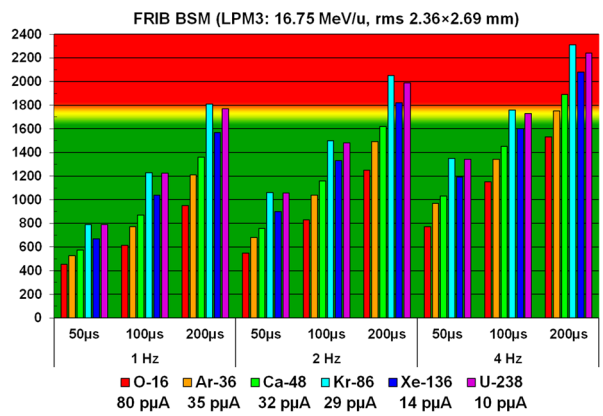

Figure 5: Peak steady temperatures of the target wire for different typical parameters of FRIB ion beams.

ISBN: 978-3-95450-192-2 doi:10.18429/JACoW-IBIC2017-TUPCC13

PHASE RESOLUTION AND ACCURACY

We consider two types of errors: a phase reading error and a phase resolution correspondingly. Due to a phase reading error (accuracy) a measured phase coordinate along the bunch does not correspond to a real one. Due to a finite phase resolution (precision) the measured distributions are smoothed and a fine structure can be lost.

Phase reading errors appear only due to a space charge of the analysed beam, but this effect becomes significant at a pulse electrical current >10 mA.

BSM resolution can be defined as a full width at a half maximum of a spread function for infinitely short bunches. For a real secondary electron beam with a finite width of focusing a phase resolution may be defined as a minimum phase range of secondary electrons, passed through the outlet collimator, thus it can be simulated, considering factors of e-beam optics and dispersion of secondary emission delay, which results in extra defocusing in case of RF-deflecting field turned on. The value of time dispersion is not known exactly, however the experimental estimations give the upper limit of this value (4±2) ps [3].

Figure 6 shows simulated transverse cross-sections of a e-beam in the plane of the outlet collimator.

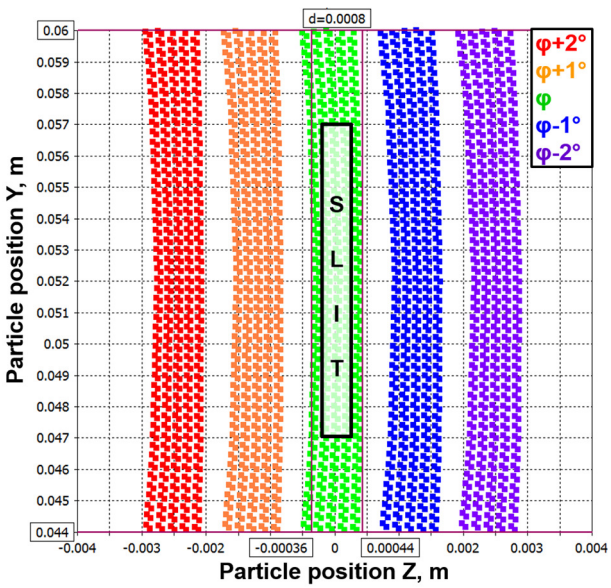

Figure 6: Transverse cross-sections of e-beam in the plane of the outlet collimator at different phases (φ-2°÷ φ+2°) of the deflecting voltage.

The simulations show, that for the inlet collimator 0.5 mm, U_d = 1000 V the distance between the centers of e-beams frequency sweep in the plane of the outlet collimator $\Delta Z_0 \approx 1.3$ mm for phases φ and $\varphi + 1°$. At the plane of the outlet collimator the beam can be focused down to the size of the inlet collimator slit at U_{foc} = 4250 V, but full width of the beam waist increases up to 0.8 mm due to the RF-defocusing. Thus, a phase resolution $\Delta\varphi$:

$$\Delta\varphi = \frac{Width_{outlet\ collimator} + Width_{e-beam}}{2 \cdot \left(Z_0(\varphi) - Z_0(\varphi + 1°)\right)} = 0.5°,$$

at 161 MHz or 0.25° for 80.5 MHz in case of proper e-beam optics for 0.5 mm inlet/outlet collimators.

LABORATORY TESTS

After complete design, development and fabrication process BSM was assembled (Fig. 7), pumped, tuned and tested for proper operation of all systems: vacuum, RF, high voltage, electronics and control system. Electron beam optics was also tested with the help of thermal electrons: heating the wire target, it is possible to observe through the viewport the thermal electron beam on the phosphor covering the front surface of the outlet collimator plates (Fig. 7 a, b). The e-beam coincides with 0.5 mm slit at U_{foc} = 4050 V and currents in the correcting magnet coils about Iq = 2.0 AT, Id = 12.5 AT.

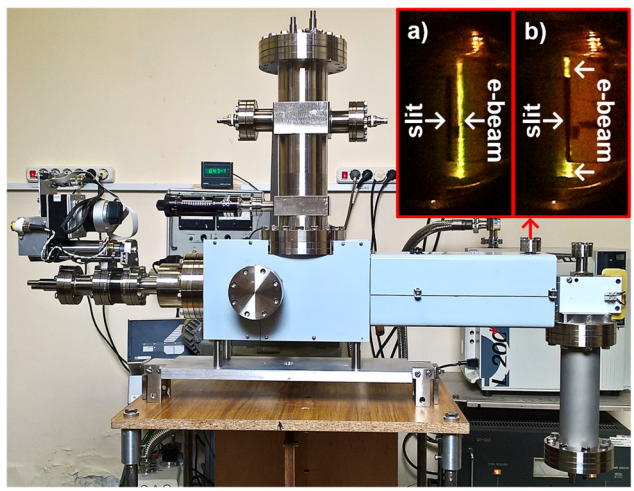

Figure 7: Photo of assembled BSM with magnetic shield. Photos through the viewport: a) Thermal electron beam parallel to the slit of the outlet collimator for comparison. b) Thermal electron beam passing through the 0.5 mm slit of the outlet collimator.

CONCLUSION

Bunch Shape Monitor was developed for FRIB linac. Special magnetic shield for protection against external fringe magnetic fields and correcting magnet with the combination of dipole and quadrupole fields for compensation of remnant magnetostatic fields and misalignments of BSM elements were implemented. Magnet separation of secondary electrons by energy was foreseen to decrease a possible influence of the electrons detached from the multicharged ions in the wire target. The monitor enables to achieve a quarter of a degree phase resolution for 80.5 MHz RF, that corresponds to about 9 ps, and can be used at any location along the accelerator.

REFERENCES

[1] R. Witkover, "A non-destructive bunch length monitor for a proton linear accelerator", *Nucl. Instr. Meth.*, vol. 137, no. 2, pp. 203-211, 1976.

[2] A. Feschenko, "Technique and instrumentation for bunch shape measurements", in *Proc. RUPAC2012*, Saint-Petersburg, Russia, Oct. 2012, pp. 181-185.

[3] E. Ernst, H. Von Foerster, "Time dispersion of secondary electron emission", *J. of Appl. Phys.*, vol. 26, no. 6, pp. 781-782, 1955.

ISBN: 978-3-95450-192-2 doi:10.18429/JACoW-IBIC2017-TUPCC15

DESIGN AND COMMISSIONING OF THE BUNCH ARRIVAL-TIME MONITOR FOR SwissFEL

V. Arsov†, F. Buechi, P. Chevtsov, M. Dach, M. Heiniger, S. Hunziker, M. Kaiser, R. Kramert, A. Romann, V. Schlott, Paul-Scherrer-Institute (PSI), Villigen, Switzerland

Abstract

The Bunch Arrival-Time Monitor for SwissFEL (BAM) is based on the concept which was successfully tested at the SwissFEL Test Facility (SITF). During the gap between the SITF decommissioning and the start of SwissFEL, all key components underwent design improvement. In this paper, we report on some of these new developments and on the commissioning progress.

INTRODUCTION

SwissFEL is an X-ray free-electron laser user facility with two beamlines. The first one, Aramis, designed for electron energies between 2.1 and 5.8 GeV and for hard X-rays in the range 1.8 to 12 keV, has been inaugurated in December 2016 [1] and is presently under commissioning to reach its final design parameters. The second beamline, Athos, designed for energies between 2.65 and 3.4 GeV and for soft X-rays between 0.2 and 2 keV, is scheduled for commissioning in 2018-20.

According to the initial concept, totally five BAMs had been foreseen for the Aramis and two more BAMs for the Athos beam lines. These BAMs are capable for two bunch operation with 28 ns bunch separation at 100 Hz with <10 fs resolution in the charge range of 10 to 200 pC (simultaneous, single-shot non-destructive measurement).

Presently all pick-ups, most of the electronics and cabling, including the optical fibres, have been installed. Two stations, BAM1 at the laser heater and BAM3 after LINAC1 between the two bunch compressors, are fully equipped and presently under commissioning.

DESIGN OVERVIEW AND IMPROVEMENTS

The BAM concept was successfully demonstrated with two stations in SITF [2,3]. In view of the different girder and space limitations, for SwissFEL the BAM-box underwent a redesign. In SwissFEL the boxes are located under the granite girder, which serves as a radiation shield. Lead and boron-doped polyethylene sheaths are used for additional shielding. For servicing the box can be lifted up on wheels and pulled from below the girder. The last few meters of the cable tree and the optical fibres are laid in a flexible cable chain and are retracted together with the box. The housing lids provide additional isolation against acoustical noise and radiation. They are easily removable to allow servicing.

Pick-up and RF-Front End

The BAM pick-ups are cone-shaped buttons with 2.39 mm base (DESY design [4]), but modified for the SwissFEL beam pipe, 8 mm behind the undullator lines (BAM5 and 7) and 16 mm for the rest of the BAMs. The vacuum chamber mounts have five micrometer screws for vertical and lateral fine centring of the chamber axis to the beam.

The button pairs in each of the two orthogonal axis are combined together to minimize the orbit dependence. The 20 mm long PhaseMaster160 cables (Teledyne) and the couplers, type PS2-55-450/17S, Pulsar Microwave, are fixed in dedicated mounts close to the pick-up chamber. The output of the coupler is connected to the EOMs with armoured PM160 cables, 0.7 m for the EOM1 (high resolution branch) and 1.2 m for the EOM2.

To prevent orbit dependence and spoiling of the pick-up RF-transient quality, the relative group delay of the two branches from the pickup to the combiner has to be minimized. Initially the combiners were measured separately and then matched to a cable pair, which best compensated the relative group delay of the two combiner ports. An example from BAM4, located after LINAC3, is shown on Fig. 1. Up to 40 GHz the pk-pk relative phase between the combiner inputs is 5.5 deg (380 fs mean group delay difference), red curve. A cable pair from many samples has been selected to have 5.4 deg relative phase difference (384 fs mean group delay), blue curve. The entire package has 3.0 deg pk-pk relative phase difference (103 fs mean group delay), green curve. This best possible match is not perfect. The reason is the amplitude and phase relations at higher frequencies for the high bandwidth PS2-55-450 combiners (1 - 40 GHz).

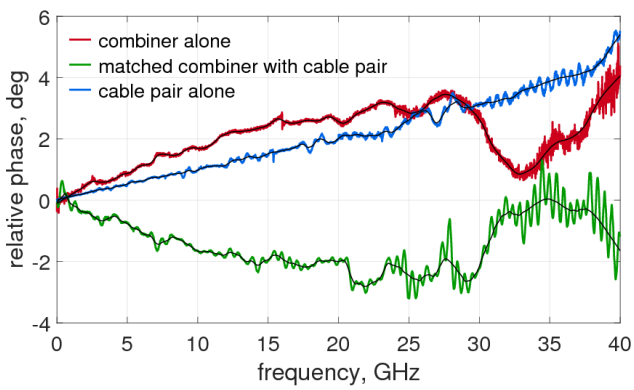

Figure 1: Phase match of the RF combiner and cables (BAM4).

Optomechanical Front End (BAM-Box)

The BAM-box is temperature stabilized with 8 large surface Peltiers. The mechanical design was improved to reduce the shear stress between the regulated base plate and the heat sinks by using flexible fixtures. Typical temperature stability for the components in contact with

† vladimir.arsov@psi.ch

ISBN: 978-3-95450-192-2 doi:10.18429/JACoW-IBIC2017-TUPCC15

the regulated base is <5 mK over 1 h and <10 mK over 12 h. The typical box volume stability is 20 mK.

The EDFAs are commercial components from Photop, customized for PSI. They are bidirectional, high gain (>10 dB), operated either in constant current or constant power mode. The fibre length from the input to the output is 2 m (excluding the gain fibre, 0.8 m Liekki ER-80/125). The controller board is mounted directly on the housing and is interfaced to EPICS via RS232. Four diodes monitor the optical power in the forward and the backward directions. EDFA1 is set for optimum power in the link, EDFA2 optimizes the power for the readout electronics. Its output power is actively used in the user applications, described below.

The polarization scanner (PSC-15-2-1, Fig. 2) is a commercial component from Phoenix Photonics. The polarization is controlled with EPICS. The DC voltages for the three quarter waveplates are delivered from a DAC in the technical gallery. The signals are low pass filtered. PSC-15 is modified such that to be constantly enabled by the supply voltage. PSC precedes the Faraday rotating mirror (reflection/transmission = 10/90, PN: 500-25290-12-1, Lightel) and is thus part of the fibre optical link.

Two EOMs are used for BAM detection. The one for high BAM resolution, Power Bit SD40, II-VI company, has 40 Gb/s bandwidth and 4.5 V half-wave voltage. The one for the large dynamic range, MXAN-LN10, Photline, has 10 GHz bandwidth and 6.5 V half-wave voltage. To reduce the distance to the pickups, the EOMs are mounted on a 165 mm high holder. The so increased distance to the temperature stabilized base plate is a trade off for the reduced drift and attenuation in the RF cables from the pick-up. When the box reaches thermal equilibrium, the EOM temperature equals the one of the regulated base plate, namely few mK over 12 h.

To reduce the length of the out-of-loop fibres in the BAM-box, no bias controllers are implemented. The EOM bias working point setting and the bias stabilization are made with EPICS by using the available rack electronics in the technical gallery.

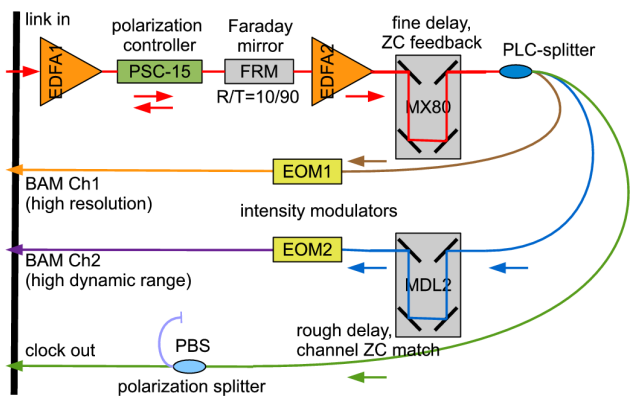

Figure 2: Layout of the BAM-box components.

The core of the BAM front end is a high-end precision linear servo motor positioner, 3 phase, 8 poles, 100 mm travel range, Type MX80, Parker, with a built-in digital incremental encoder and resolution of 10 nm (Renishaw RGH24O). This stage is used for zero crossing feedback of the arrival time signal and for calibration of the BAM slopes. Because the feedback requires frequent movement within few mm, no piezo-driven or spindle positioners can hold. The MX80 stage was used already in the SITF BAM prototypes with no failure due to radiation or a mechanical wear off.

The controller, ACJ-055-18, Coupley Controls, is also mounted in the BAM-box. There are fully implemented digital current, velocity and position loops, which are pre-programmed on the controller. The control is made with ASCII commands from a RS232 server in the technical gallery, providing the travel trajectory, homing, velocity, acceleration, position, etc. The maximum velocity is 30 mm/s and the accelerations are 60 mm/s^2.

The controller actively uses the readouts of the digital incremental encoder and in addition also outputs the raw quadrature signals, thus allowing independent (deterministic) position readout and bunch ID stamping.

After SITF decommissioning, a VME encoder counter counter card, type ECM514, was successfully tested for bunch ID stamping and is presently installed for all BAM stations in SwissFEL. The standard firmware was changed such, that a dedicated index register holding the motor encoder positions is triggered by the event system and the value is latched until the next cycle, during which EPICS assigns the bunch number and the event valid flag.

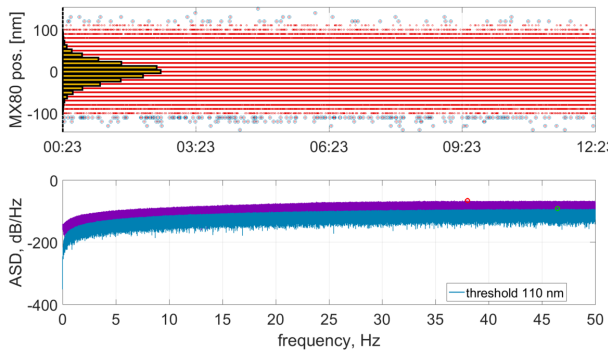

Figure 3: BAM3 delay stage position jitter.

Without a holding current the MX80 stage is loose, but when operational, the three loops keep it rigidly in place. Depending on the loop settings, when not moved, the motor performs small oscillations around the set values. The amplitude is < 1 fs, which is well below the required BAM sensitivity. Potentially the stage is susceptible to vibrations, but long term observations with the two BAM stations installed in SwissFEL show no significant disturbances even during heavy instillation work on the site. Presently there is an EPICS application and a Matlab tool with which large deviations of the motor positions are captured and the expert is informed via Email or SMS. Also there is a dedicated buffer, which captures the motor positions at 100 Hz and from which the acceleration spectral density (ASD) is calculated. Thus potential disturbances up to 50 Hz can be identified. So far on very rare occasions specific peaks were detected. An example from BAM3 for a typical undisturbed operation is shown

ISBN: 978-3-95450-192-2 doi:10.18429/JACoW-IBIC2017-TUPCC15

on Fig. 3. The rms jitter is 24 nm (80 as) and the pk-pk value is 290 nm (1 fs). Only few positions (blue circles on Fig. 3) exceed the alarm threshold set at 110 nm (366 as).

The free space defined by the MX80 stage marks the border between the single mode and the polarization maintaining fibres in the BOX (Fig. 2). The sender and the receiver collimators, Type CLB-155-28 (SMF28) and CLB-155-15 (Panda PM), Princetel, have a focal length of 11 mm, divergence of 0.5 mrad and beam size of 2 mm.

A typical coupling efficiency profile over the travel range is shown on Fig. 4. for measurements on different days at circumstances explained in the legend. The example is from BAM1. The coupling efficiency is normalized to the peak power. It varies between 0.2 dB and 0.27 dB, but the profile shapes remain similar. The largest deviation was measured when the BAM-box was transported from the lab to the SwissFEL tunnel before re-alignment. After that the stability of the coupling efficiency remained constant over months without the necessity for realignment.

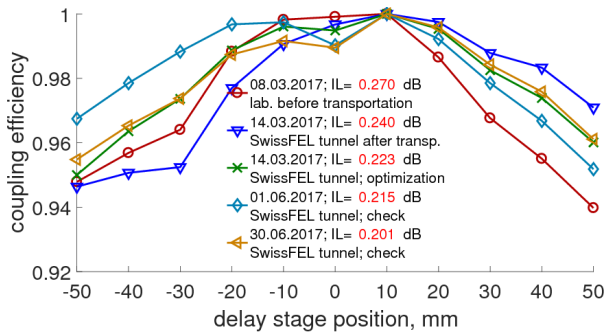

Figure 4: BAM1 delay stage collimator alignment.

EXPERT USER APPLICATIONS

During the SITF phase multiple expert applications ran with Matlab on PC consoles in the control network. After the decommissioning at the end of 2014 one station was kept as a development platform for a variety of new advanced techniques, including a method for embedding MATLAB programs into the EPICS IOCs.

EOM Bias Scan Tool

The tool allows determining of the EOM transmission curves, and setting of the working point. There are two user selectable modes - setting for the maximum and for quadrature. The first one is used for system tuning, the second one is the standard BAM acquisition mode. The tool outputs parameters, which are used by other routines, such as the bias slope, the insertion loss at the working point, the half-wave voltage, etc. The actuator for the bias scan is a "slow" DAC (20 kHz, 16 bit Hytec 8402), the detectors are "slow" ADCs (100 kHz 16 bit Hytec 8401), which measure the DC photocurrents from the EOM1 and EOM2 channels of the BAM photoreceiver (PRX). All the electronics is located in the BAM racks in the technical gallery.

With proper range setting, the embedded script which runs with EPICS, finishes the scan in approximately 15 s, 5 times faster than the previous Matlab script deployed on a remote console.

Polarization Stabilization Tool

The BAM fibre links are standard single mode fibres. The EOM transmission is polarization dependent, therefore for stable BAM detection the polarization has to be stabilized.

The polarization variation is slow, therefore the network speed is not a limiting factor. The stabilization tool is made with onboard HW components and by using EPICS. The actuators are the three quartar-waveplates of the polarization scanner, controlled by DACs in the technical gallery (Fig. 2). The fibre polarization beam combiner is the analyser. The polarization dependent insertion loss (IL) is defined by the EDFA2 output power, provided to EPICS by the EDFA controller via RS232, and the DC photocurrent of the PRX clock channel, measured with an ADC.

The routine follows a standard optimization logic, which applies also for manual polarization adjustment. First, waveplate one (WP1) is toggled in small steps until the insertion loss in the PRX clock channel is minimized. Then, after a certain delay, the second and finally the third waveplates (WP2 and 3) are changed. The scanning steps and the delays are selectable from the expert panel. Also, if desired, any waveplate can be excluded from the cycle. A safety feature disables the script if the EDFA2 output is low.

From the GUI there is a possibility to visualize the polarization stability for 1 h and for 12 h (buffers on softioc). The tool opens five strip charts, which display the buffers for the insertion loss (IL), the absolute power of the PRX clock channel and the variation of the three waveplates. The sampling rate is 1 s. In addition the statistics on all curves is calculated - minimum, maximum, peak-peak, average and standard deviation values. For all these there are dedicated EPICS channels which can be extracted for processing and archiving, e.g. with Matlab. An example from the BAM3 station, placed after LINAC1 between the two bunch compressors, is shown on Fig. 5.

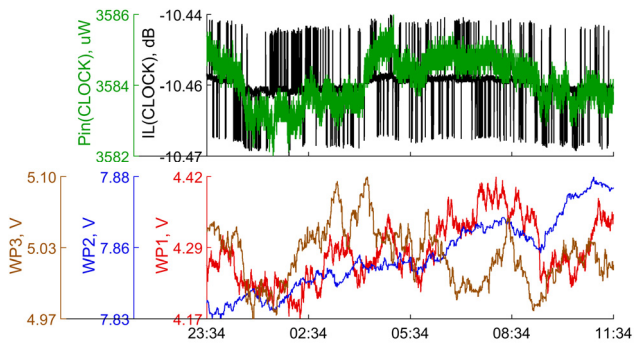

Figure 5: BAM3 polarization stability over 12 hours.

The peak-peak stability of the insertion loss over 12 h is 0.02 dB. The absolute pk-pk power variation is 4 μW. At stable conditions the variation of the waveplates is small, in the order of few hundreds of mV.

ISBN: 978-3-95450-192-2 doi:10.18429/JACoW-IBIC2017-TUPCC15

EOM Bias Stabilization Tool

The experience from SITF showed that after a bias scan, when the working point for BAM measurement was set, the EOM transmission would drift. The smaller the EOM half-wave voltage, the bigger the drift. After few iterations for readjusting of the bias manually, the drift became small. One explanation for the effect is the building up of space charge in the EOM crystal with the changing laser power (short pulses).

There are commercial EOM bias controllers on the market, some of them with a small footprint, e.g. MBC-DF-UC-U from Pharad. We have tested such controllers and considered their integration in the new BAM-box design, including the special fibre management.

The combination of an EOM and a bias controller requires a closed fibre loop between them. For the splicing, a minimum fibre length is necessary, which makes the handling difficult and in addition increases the length of the out-of-loop fibres in the Box. The new Box design solves the problem with the fibre handling, but in order to reduce the fibre drift, we decided initially not use the controllers. Instead the bias stabilization is done with EPICS in a similar way as the polarization control tool.

There are two versions of the script which differ in complexity, but deliver similar results. Both use the EOM insertion loss, defined by the EDFA2 output power and the DC photocurrent of the PRX EOM1 (or EOM2) channel, measured with an ADC

The first bias stabilization script compares the instantaneous EOM insertion loss with the set value and if the difference is larger than a certain preset value, a correcting bias is applied. The loop set point, the set point tolerance and the gain are selectable from an expert GUI. The values for the loop set point and the bias slope are automatically overtaken from the EOM bias scan script, but the expert can change them also by hand.

The script uses different step sizes depending on how far is the instantaneous insertion loss from the set value. Thus the required bias is achieved within seconds and then is slowly controlled over hours. It is possible to go to the working point form any initial value, e.g. starting from maximum. This is especially convenient, because the 3 dB offset between the maximum and quadrature can be easily set in the GUI.

From the GUI it is possible to display the bias stability for each of the two EOMs for 1 h and for 12 h (buffers running on softiocs). The tool opens three strip charts with the buffer values for the EOM insertion loss (IL), the absolute power of the PRX EOM channel and the EOM bias voltage. The sampling rate is 1 s. In addition the statistics on all curves is calculated. The script is automatically disabled, if the input optical power is low.

An example from the BAM3 station for the EOM bias stabilization with the "simple" script is shown on Fig. 6. The peak-peak stability of the EOM insertion loss over 12 h is 0.03 dB. The absolute pk-pk power variation is 7 µW. The lowest plot shows the correcting DC bias, which peak-peak value is 40 mV.

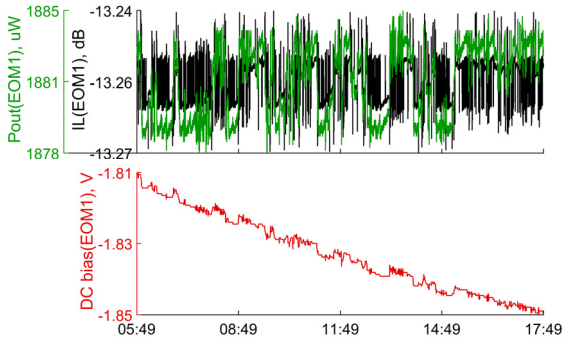

Figure 6: EOM1 bias stability over 12 hours for BAM3.

The second EOM bias stabilization script uses PID approach. In the expert GUI the user can select the insertion loss set point, the loop time constant, the P, I and D gains. The instantaneous insertion loss is measured in EPICS in a similar way as in the "simple" script, but the error signal is calculated according to the PID gains and the EOM bias slope, determined beforehand with the bias scan tool. The proper choice of the gain parameters requires expertise. Good results are obtained with the Ziegler-Nichols method [5] when initially the I and D gains are set to zero and the P gain is increased until the loop starts to oscillate. The period of oscillation is then used to set I and D. As with the other tools, the script was written initially in Matlab and then embedded into the IOCs. An example from the BAM test station after SITF decommissioning is shown on Fig. 7.

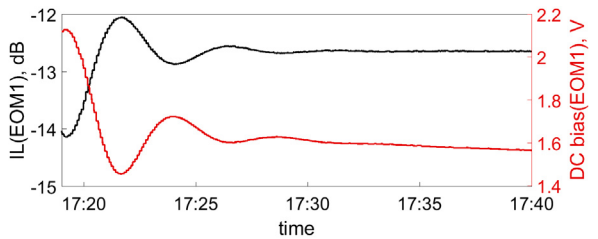

Figure 7: Settling of the EOM bias with the PID stabilization script.

CONCLUSION

The first two SwissFEL BAM stations have been taken into operation. Commissioning with beam is ongoing.

REFERENCES

[1] C. Milne *et al.,* "SwissFEL: The Swiss X-ray free electron laser," *Appl. Sci.,* vol. 7, p. 720, 2017.

[2] V. Arsov *et al.*, in *Proc. IBIC13*, Oxford, UK, Sept. 2013, paper MOAL4, pp. 8-11.

[3] V. Arsov *et al.*, in *Proc. FEL14*, Basel CH, August 2014, paper THP085, pp. 933-936.

[4] A. Angelovski, *et al.*, "High bandwidth pickup design for bunch arrival-time monitors for free-electron laser," *Phys. Rev. ST. Accel. Beams*, vol. 15, p. 112803, 2012.

[5] J. G. Ziegler and N. B. Nichols, "Optimum settings for automatic controllers," *Transactions of the ASME,* vol. 64, pp. 759–768, 1942.

ISBN: 978-3-95450-192-2 doi:10.18429/JACoW-IBIC2017-TUPCC16

STATUS OF THE THZ STREAKING EXPERIMENT WITH SPLIT RING RESONATORS AT FLUTE

V. Schlott†, M. Dehler, R. Ischebeck, M. Moser, Paul Scherrer Institute, Villigen, Switzerland
T. Feurer, M. Hayati, Z. Ollmann, R. Tarkeshian, University of Berne, Berne, Switzerland
E. Bründermann, S. Funkner, A.-S. Müller, M.J. Nasse, G. Niehues, R. Ruprecht, T. Schmelzer, M. Schuh, M. Schwarz, M. Yan, Karlsruhe Institute of Technology, Karlsruhe, Germany

Abstract

THz streaking with split ring resonators (SRR) promise ultra-high (sub-femtosecond) temporal resolution even for relativistic electron bunches. A proof-of-principle experiment in collaboration between the University of Bern, the Paul Scherrer Institute (PSI) and the Karlsruhe Institute of Technology (KIT) is currently prepared at the FLUTE facility (Ferninfrarot Linac und Test Experiment) at KIT. Most of the critical components have been designed, tested and set-up in the 7 MeV diagnostics part of FLUTE. In this contribution we will present an update on the experimental set-up and report on SRR configurations which have been optimized for highest THz deflection, while simultaneously accounting for the restrictions of the manufacturing process. Test measurements characterizing the SRR samples and the THz source, which has been matched to the FLUTE gun laser, will also be presented.

INTRODUCTION

Low charge operation of electron accelerators opens up the possibility of generating highly brilliant beams with micrometre transverse sizes and femto-second bunch length. Beam instrumentation for single-shot measurement of such ultra-short electron bunches is either limited in time resolution to some tens of femto-seconds for electro-optical methods [1, 2] or requires quite complex and expensive infrastructure as in case of RF deflectors, which are capable of providing the desired time resolution even for highly relativistic beams [3].

The test accelerator for far-infrared experiments (FLUTE) at the Karlsruhe Institute of Technology [4] is presently being set-up and commissioned to generate ultra-short and intense THz pulses and to provide a test infrastructure for femto-second electron beam studies aiming for the development of advanced diagnostics. Based on the proposal of using high frequency THz fields, which are enhanced in a split ring resonator (SRR), to streak an electron beam for its temporal characterization [5], a proof-of-principle experiment is presently prepared at FLUTE, intending to make use of the 7 MeV beam from the RF photo-injector gun in order to demonstrate the applicability of this method in a real accelerator facility [6, 7]. The tasks in this research collaboration between the University of Berne, KIT and PSI are distributed in the following way:

- KIT provides the FLUTE accelerator, the photo-injector laser system to generate the electron beam and the THz radiation as well as beam optics simulations for ultra-low charge operation.
- The University of Berne provides the SRR and the THz pulse generation.
- PSI participates in the design optimizations of the SRR and provides the beam diagnostics for the FLUTE experiment.

STATUS OF THE SRR EXPERIMENTAL SET-UP AT FLUTE

The UHV-chamber for the SRR experiment has been installed at about 1.7 m behind the photo-cathode, where ASTRA simulations indicate, that transverse rms beam sizes of ≤ 10 µm can be achieved at low ($\leq$ 100 fC) bunch charges [7]. In the experimental chamber, a set of SRRs can be accurately positioned to the electron beam path by means of UHV-compatible translation stages. A scintillator screen in combination with a high resolution optical telescope allows matching of the beam through the SRRs. Presently all components are interfaced to the FLUTE control system. The Ti:Sa FLUTE laser system, which provides the ps long UV (266 nm) pulses for the RF photo-injector gun and which is used to generate the short and intense THz pulses for exciting the SRRs, is in operation and the laser transfer line from the optics hutch to the FLUTE accelerator bunker is presently under commissioning. The THz pulse generation is set-up on an optical breadboard outside of the experimental chamber, from which the THz radiation is imaged through a CF-40 z-cut crystalline quartz UHV-window onto the SRRs by using an off-axis parabolic mirror. Overlap of the electron bunches with the sub-ps rise times of the THz streaking field is achieved with a motorized delay stage, while the synchronization is inherently provided through the use of the same laser for the electron beam and THz pulse generation. RF conditioning of the FLUTE gun is ongoing so that first acceleration of electrons is expected by October 2017.

THZ PULSE GENERATION

The intense single-cycle THz pulses for exciting the SRRs are generated by optical rectification [8-10] of the ultrashort FLUTE gun laser pulses (Coherent Astrella provides pulse energies of 6 mJ at a wavelength of 800 nm and a FWHM pulse length of < 35 fs with 1 kHz repetition rate) in a $LiNbO_3$ crystal.

Tilted Pulse Front Generation

Optical rectification, as any other nonlinear frequency conversion process, requires excellent phase matching in order to be efficient. Proper phase matching in $LiNbO_3$

† volker.schlott@psi.ch

ISBN: 978-3-95450-192-2 doi:10.18429/JACoW-IBIC2017-TUPCC16

needs special geometries because the refractive index mismatch between the optical pump and the generated THz pulse is comparatively large. A viable and widely used geometry is the tilted pulse front pumping technique. The implementation, which has been chosen for the THz source of the SRR experiment at FLUTE, is depicted in Figure 1, where the pulse front tilt of the pump laser beam is created by the combination of a diffraction grating and an imaging system.

Optimal THz imaging was provided by a 4f imaging system consisting of a 200 mm focal length (SL1) and a 50 mm (SL2) focal length UHMWPE lens (see inset of Figure 3). The measured THz spot is shown in Figure 3. It was measured with a pyroelectric beam profiling THz camera (Spiricon Pyrocam IV). The FWHM THz spot dimensions are 0.92 mm in horizontal direction and 1.15 mm in vertical direction. From these measurements we deduce maximum electric field strengths of 14 MV/m for the FLUTE THz pulse set-up.

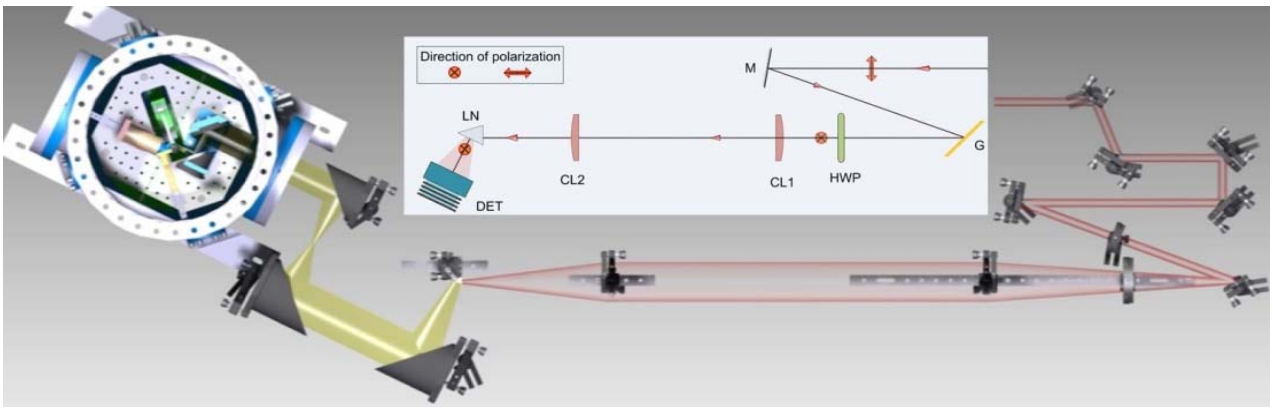

Figure 1: Layout of the THz source at FLUTE (shown in red and schematically in the inlet). M: dielectric mirror; G: reflection grating; HWP: λ/2 retardation plate; CL1: plane convex cylindrical lens (f = 421 mm); CL2: plane convex cylindrical lens (f = 250 mm); LN: MgO doped stoichiometric $LiNbO_3$ prism. The THz-transport to the SRR in the vacuum chamber is also shown (yellow beam path).

Experimental Results

The main challenge was the optimization of the source geometry to the FLUTE gun laser, which provides pulse durations of only 35 fs (FWHM) and a maximum pump pulse energy of 3.35 mJ that is allocated for the THz pulse generation. A calibrated SLT THz 20 type pyroelectric THz energy meter (DET) was used to measure the energy of the THz pulses and the results are shown in Figure 2 (black dots) as function of the pump laser energy. We find a monotonic increase of THz energy with pump energy up to the highest pump energies used. The maximum THz pulse energy was 0.8 μJ resulting in a laser-to-THz conversion efficiency of up to 0.024 % as also shown in Figure 2 (blue stars).

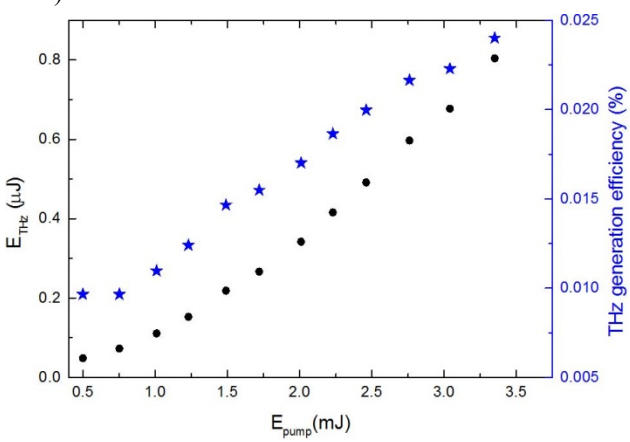

Figure 2: THz pulse energy (black dots) and conversion efficiency (blue stars) as a function of pump energy.

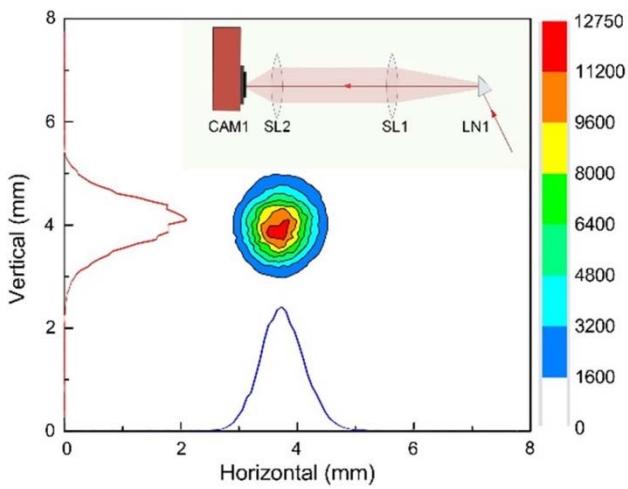

Figure 3: Camera image of the THz beam at the image plane of a 4f THz imaging system. A schematic of the 4f imaging system is seen in the inset.

SPLIT RING RESONATOR DESIGN OPTIMIZATION

The original design concept of a THz-driven streak camera was based on a classical split ring resonator as shown in picture (a) of Figure 4, which poses quite a few challenges for use in an accelerator environment. Mounting the resonator without perturbing the field pattern of the resonance would require a dielectric holder attached to the SRR. This would cause two problems, one is the charging up of the SRR by halo electrons with subsequent breakdowns and the second a strong heat up of the resonator by

ISBN: 978-3-95450-192-2 doi:10.18429/JACoW-IBIC2017-TUPCC16

halo electron bombardment (or by an accidental hit with the main beam). An alternative design has thus been followed, where the resonator is milled and drilled out of a solid 80 µm thick plate, which simultaneously serves as a mount for the SRR to be fixed on a motorized stage for precise (µm-level) and reproducible positioning. The new SRR configuration is shown in part (b) of Fig. 4, while parts (c) and (d) show images of the prototype, which was manufactured from glass and was gold coated subsequently.

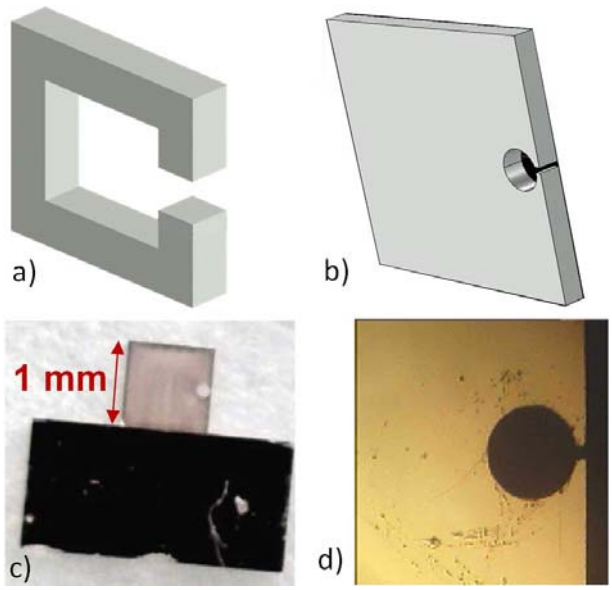

Figure 4: a) "Classical" SRR [5] with gap dimensions of 20 µm (height) x 20 µm (width) x 20 µm (length), b) manufacturing design with increased gap length / plate thickness of 20 µm x 20 µm x 80 µm, c) and d) images of the prototype SRR made from glass with gold coating.

In addition to the improved mechanical stability, the larger gap length of 80 µm for the new SRR design (b) increases the interaction region between the electron beam and the THz field, resulting in larger kick strength. With the measured THz field strength of 14 MV/m, a kick strength of 12 keV/c can be applied by the SRR to the 7 MeV beam at FLUTE. This provides a sufficiently large streaking (chirp) of the beam, clearly detectable on the downstream screen monitor in the gun spectrometer.

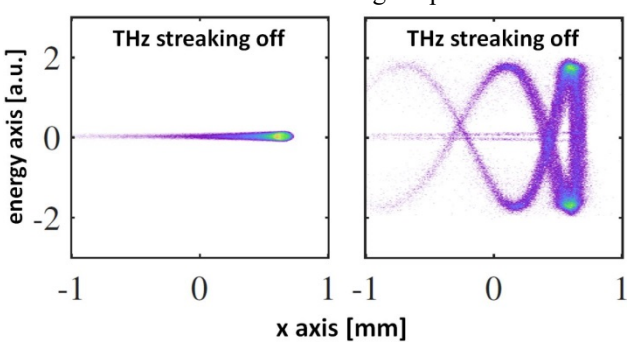

Figure 5: Simulated screen images on the FLUTE spectrometer showing the effect of 5 keV/c kick strength [7].

Figure 5 shows simulated screen images in the FLUTE low energy spectrometer calculated with the ASTRA code for conservatively assumed kick strengths of 5 keV/c where e.g. losses in the THz transport are taken into consideration. The resulting streaking structure of the ps long FLUTE beam is clearly visible.

SUMMARY AND OUTLOOK

The SRR chamber has been installed in the FLUTE beam line at 1.7 m behind the photo cathode. The THz pulses for exciting the SRR are generated by optical rectification in a $LiNbO_3$ crystal using the ultrashort FLUTE gun laser pulses. The experimental set-up has been tested and maximum field strengths of 14 MV/m have been achieved with the available pump pulse energy of 3.35 mJ. With the optimized SRR design, kick strengths of 12 keV/c are expected, which should result in a time resolution of $\leq$ 20 fs for the THz streaking experiment at FLUTE.

After RF conditioning of the photo-injector gun and control system integration of all sub-systems, first electrons are expected in the FLUTE facility by fall of this year, so that that it should be possible to execute the SRR experiment by the end of 2017.

REFERENCES

[1] B. Steffen, "Electro-Optic Methods for Longitudinal Bunch Diagnostics at FLASH", Dissertation, University of Hamburg (2007)

[2] S. Jamison, et al., "Limitations of Electro-Optic Measurements of Electron Bunch Longitudinal Profile", Proc. EPAC 2008, Genoa, Italy, 1149 (2008)

[3] C. Behrens et al., "Few-femtosecond time-resolved measurements of X-ray free-electron lasers", Nature Communications, 5, 3762 (2014)

[4] M.J. Nasse et al., „FLUTE: A Versatile LINAC-based THz Source", Rev. of Sci. Instrum. 84, 022705 (2013)

[5] J. Fabianska et al., "Split Ring Resonator based THz-driven electron streak camera featuring femtosecond resolution", Scientific Reports 4, 5645 (2014)

[6] M. Dehler et al., "Design Concept for a THz Driven Streak Camera with Ultra High Resolution", Proc. IBIC 2015, 156 (2015)

[7] M. Yan et al., " Design of a Time-Resolved Electron Diagnostics Using THz Fields Excited in a Split Ring Resonator at FLUTE, Proc. IBIC 2016, Barcelona, Spain, 475 (2016)

[8] J. Hebling, et al., "Velocity matching by pulse front tilting for large area THz-pulse generation", Opt. Express, 10, 1161-1166 (2002)

[9] J. Hebling, et al., "Tunable THz pulse generation by optical rectification of ultrashort laser pulses with tilted pulse fronts", Applied Physics B, 78, 593-599 (2004)

[10] J.A. Fülöp, et al., "Efficient generation of THz pulses with 0.4 mJ energy", Opt. Express, 22, 20155-20163 (2014)

ISBN: 978-3-95450-192-2 doi:10.18429/JACoW-IBIC2017-TUPCC17

ULTRA-STABLE FIBER-OPTIC REFERENCE DISTRIBUTION FOR SwissFEL C-BAND LINACS BASED ON S-BAND RADIO-OVER-FIBER LINKS AND FREQUENCY DOUBLER / POWER AMPLIFIERS

S. Hunziker†, V. Arsov, F. Buechi, M. Dach, M. Heiniger, M. Kaiser, R. Kramert, A. Romann, V. Schlott, Paul Scherrer Institut, CH-5232 Villigen, Switzerland

Abstract

The reference distribution for the SwissFEL accelerator is based on ultra-stable Libera Sync 3 fiber-optic links operating at 3 GHz with <2.4 fs added timing jitter. While s-band injector RF stations are directly supplied with these actively stabilized reference signals at 2.9988 GHz, the same 3 GHz optical links are used to transmit reference signals at 2.856 GHz (half c-band frequency) to the c-band LINACs, combined with a frequency doubler-amplifier at the link end. A novel zero AM/PM-conversion frequency doubler and an amplitude-/phase-controlled power amplifier have been implemented in a compact 1HU 19inch unit. Key design concepts and measurement results will be presented. It will be shown that this inexpensive doubler-amplifier system adds only insignificant jitter and drift to the transmitted reference signals. As the same actively stabilized 3 GHz links can be used for s- and c- band RF stations, development of a more expensive 6 GHz fiber-optic link could be avoided. A higher quantity of the same link type can thus be manufactured and the number of spares is reduced as only one link type is utilized for the SwissFEL injector and LINAC RF reference signals.

SwissFEL C-BAND REFERENCE DISTRIBUTION

The concept of the reference distribution for the SwissFEL accelerator RF stations and first performance measurements of the group delay stabilized Instrumentation Technologies Libera Sync 3 (3 GHz) prototype fiber-optic links have been presented in [1]. It is based on using 3 GHz radio-over-fiber links for distributing s-band (2.9988 GHz) as well as c-band (5.712 GHz) reference signals. For the c-band links the basic idea is not to transmit the c-band frequency itself but half of it (2.856 GHz) by means of a 3 GHz Libera Sync 3 link and then double and ampli-fy the transmitted signal frequency at the end of the link (Fig. 1). So we can use the same links for both s-band and c-band stations, which saves development and production costs for the fiber-optic links and simplifies testing and inventory.

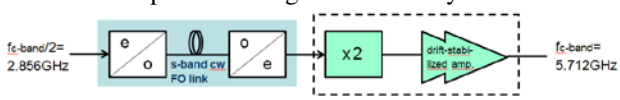

Figure 1: Concept of the radio-over-fiber based c-band link for the SwissFEL RF reference distribution. Dashed: frequency doubler / power amplifier. The timing jitter and gain / timing drift performance of the actual Libera Sync 3 link used in SwissFEL is shown in Figs. 2 and 3.

† stephan.hunziker@psi.ch

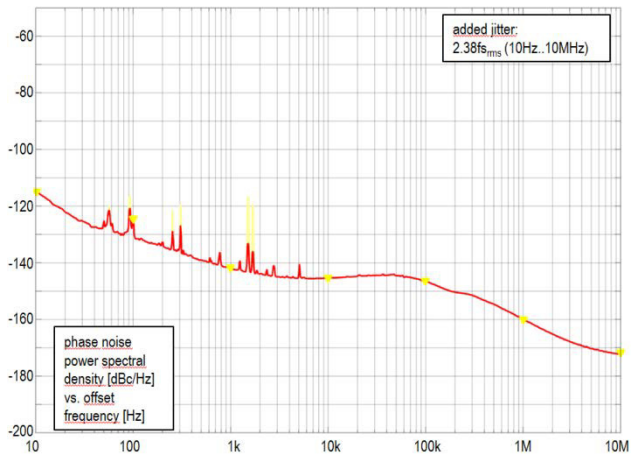

Figure 2: Libera Sync 3 fiber-optic link Added jitter at 2.9988 GHz for 500 m link span (standard SM fiber).

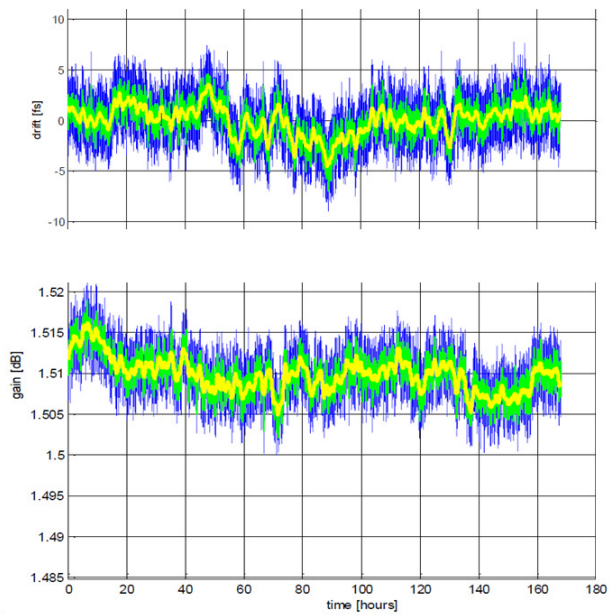

Figure 3: Libera Sync 3 drift measurement at 2.9988 GHz. Lower: Timing drift over 7 days: 11.9 fs_{p-p} (2.2 min avg.), 8.2 fs_{p-p} (1 h avg.), 2.6 fs_{rms}. Upper: Gain variation over 7 days, 0.017 dB_{p-p} (2.2 min avg.), 0.011 dB_{p-p} (1 h avg.).

As no frequency doubler / power amplifiers with the desired performance (particularly low phase drift and at the same time low jitter at high output power) are available on the market, such a device has been developed at PSI.

ISBN: 978-3-95450-192-2 doi:10.18429/JACoW-IBIC2017-TUPCC17

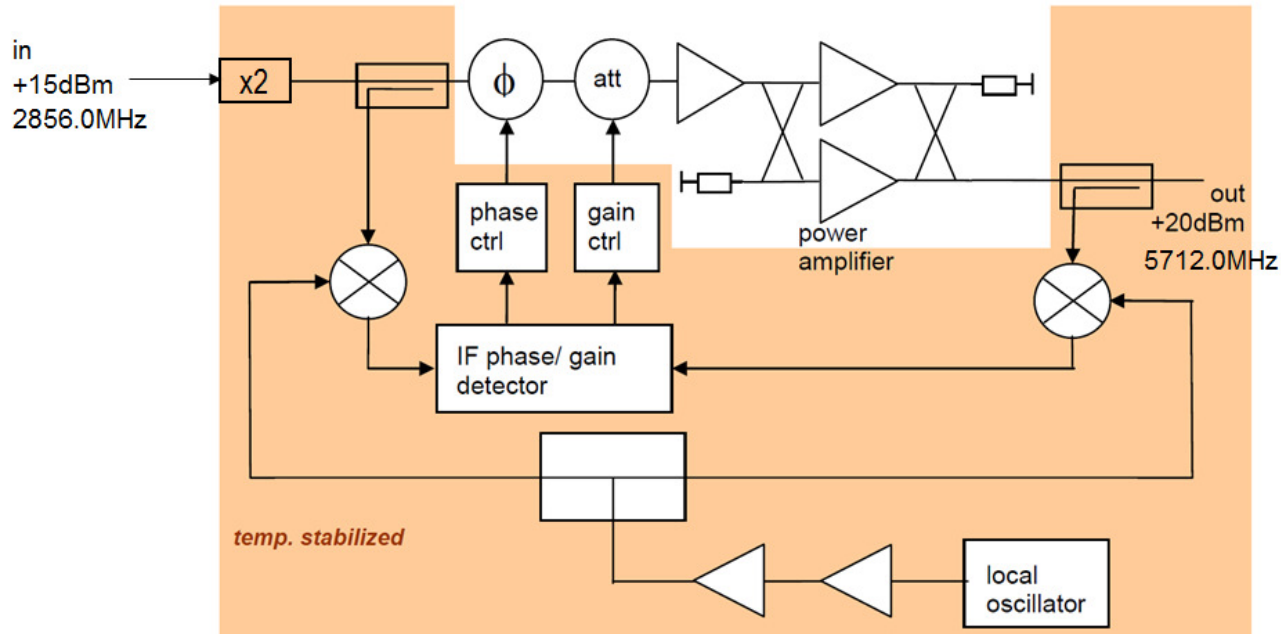

Figure 4: Block diagram of the frequency doubler / power amplifier.

3 GHz TO 6 GHz FREQUENCY DOUBLER / POWER AMPLIFIER DESIGN

The frequency doubler / power amplifier basically consists of two parts: a low jitter and low drift frequency doubler as well as a low drift and low jitter power amplifier (Fig. 4). The goal is to add virtually no jitter and a maximum drift of approximately 20 fs_{pp}.

Frequency Doubler

Commercially available frequency doublers are based on full wave bridge switching rectifier topologies. This is a relatively ideal topology regarding AM/PM conversion, which is considered the primary source of timing drift, furthermore Schottky diodes used in such devices yield low parasitic delay variations and added noise [2,3].

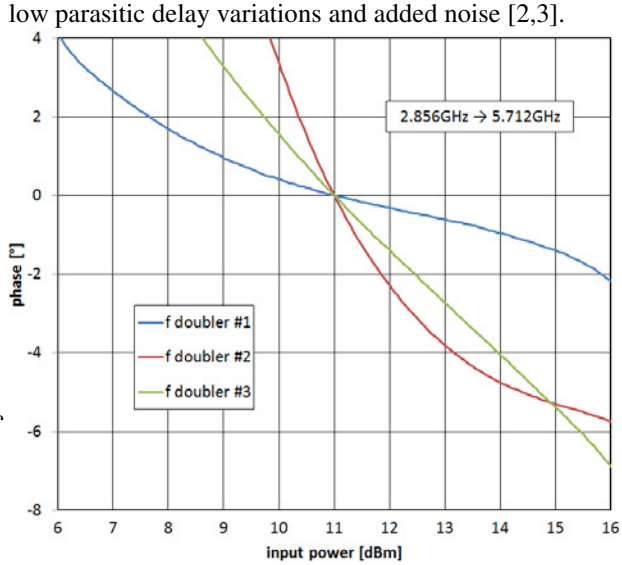

Figure 5: AM/PM conversion of commercial high performance frequency doublers.

Figure 5 shows the measured AMs ensitivity of three commercial high performance frequency doublers. The conversion loss of these doublers is approximately 10..12 dB. The AM/PM conversion coefficient varies between -50 m°/ 0.1 dB and -150 m°/ 0.1 dB (≈ -25.. -75 fs/ 0.1 dB) for realistic input power values. The frequency doubler with the lowest AM/PM conversion would al-ready eat-up the drift budget and leave no margin for the power amplifier, cables. To avoid this, a new doubler with optimized drift performance has been designed. The core of this new circuit is a double balanced mixer, which is a Schottky diode switching multiplier very similar to a full wave bridge rectifier but with two diodes reversed and two inputs instead of one. We split the input power and distribute it approximately equally to the two input ports of this doubler (mixer RF and IF ports), whereas the 2nd harmonic appears at the LO port (Fig. 6). The key idea is to vary the phase between the two input signals to active-ly compensate parasitic and unbalancing effects until the AM/PM conversion of the 2nd harmonic at the output vanishes. Figure 7 shows such an optimization. The conversion loss of the optimized doubler is approximately 16 dB. The optimum has been chosen such that it occurs at the maximum available input power. This yields maxi-mum output power of the doubler. The frequency doubler / amplifier unit has a switchable calibration output which allows adjustment of the doubler input port phase differ-ence by means of an electronically variable integrated phase shifter.

ISBN: 978-3-95450-192-2 doi:10.18429/JACoW-IBIC2017-TUPCC17

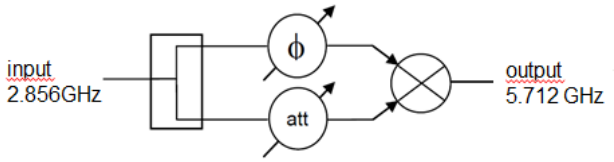

Figure 6: Core of the new frequency doubler.

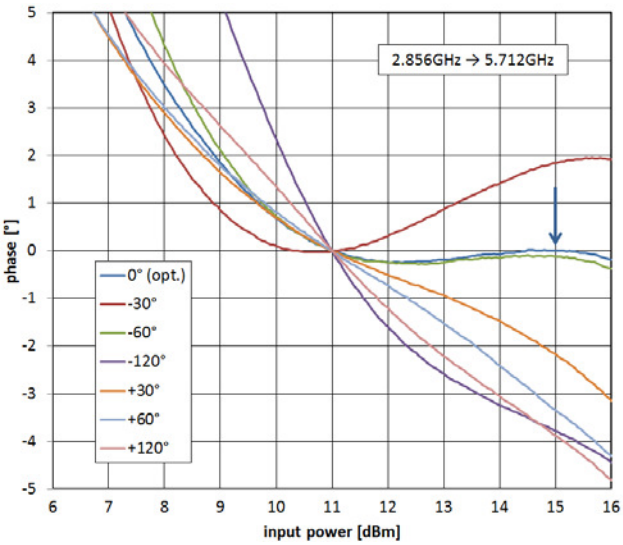

Figure 7: Optimized frequency doubler with virtually no AM/PM conversion (Marki M1-0310LEZ1 mixer based). Arrow: operating point.

The curves in Figs. 5 and 7 have been measured with a Keysight N5224A vector network analyzer (calibrated converter measurements with embedded LO).

Power Amplifier

The power amplifier's transfer function (gain and phase) is stabilized for the operating frequency of 5.712 GHz to minimize drift, using a two-loop controller (see Fig. 4). The key component of this controller is the well-known Analog Devices AD8302 gain / phase detector. The whole amplifier PCB is temperature stabilized to a few mK. Actually the detector part only is critical regard-ing temperature, as depicted in Fig. 4. InGaP HBT based active devices have been used for low phase noise. The output stage is a balanced configuration, which has some advantages over single ended as e.g. increased output power, better output match and reliability.

Gain / Phase Detector for Power Amplifier Stabilization

The following setup has been used for the AM sensitivity characterization of the AD8302 phase detector and find an appropriate operating frequency: A signal generator is modulating the injection current of a laser diode with a sinusoid (Mitsubishi 1550nm coaxial pigtailed DFB LD), whose output power is equally split to two channels of a remote controlled multichannel MEMS-based variable optical attenuator. The outputs of these attenuator channels are detected by two optical receivers (Discovery DSC50S lab buddies, operated with optical power that yields nearly zero AM/PM conversion), the phase difference of which is measured by the DUT (AD8302 gain/phase detector). The amplitude of one channel (one of the phase detector inputs) has been varied using one of the variable optical attenuator channels. Fig. 8 shows the measured sensitivity curves. These measurements reveal that the phase measurement should be done at a frequency of around 300..500 MHz for minimum AM sensitivity. It has been shown in [1] that this detector has a pp stability of a few fs over a day if it is stabilized within a few mK, even at the less convenient frequency of 3 GHz. If the 3 GHz input signal is downconverted to a few 100s of MHz and the same time the AM at the phase detector inputs can be minimized, which further reduces the effect of the remaining low AM sensitivity, a temperature stabilized AD8302 can well measure sub-10 fs_{pp} drifts over a day or longer in a carefully built setup (shielded against air flow, stabilized supply voltages, symmetric low drift cabling). The stability of the Libera Sync 3 link's input signal is better than 0.1 dB and its gain is extremely stable (see Fig. 2), which means that the frequency doubler (roughly constant conversion loss) hardly exhibits output power variations above 0.1 dB. The output signal of the power amplifier is stabilized by means of an in-loop variable microwave attenuator. Therefore the phase detector input amplitude variations will always stay below 0.1dB (stable LO power).

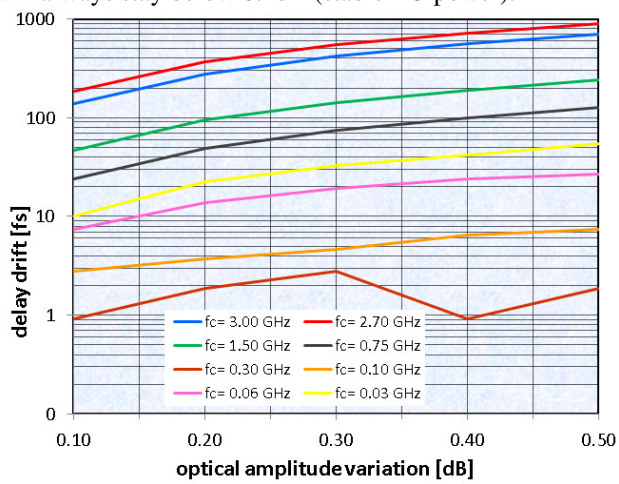

Figure 8: Frequency dependence of the AD8302 gain / phase detector AM/PM conversion, measured with a virtually AM/PM-conversion-free optical attenuator-based setup. Note that $\Delta P_{RF} = 2\Delta P_{opt}$. Resolution: a few fs.

PROTOTYPE MEASUREMENTS

A prototype frequency doubler / power amplifier has been developed and some first characterization has been done. More detailed measurements will follow later. The internally shielded and temperature stabilized 19' unit is quite compact (Fig. 9) and can be controlled via LAN interface. Later a small terminal on the front panel will be added for local control. Figs. 10 and 11 show jitter and drift measurements of the prototype unit. The latter has been done in the SwissFEL test injector laser hutch (temperature and humidity variations during this measurement were 0.3 °C and 3 %RH, respectively).

ISBN: 978-3-95450-192-2 doi:10.18429/JACoW-IBIC2017-TUPCC17

Figure 9: Fabricated frequency doubler / power amplifier prototype (19", 1HU).

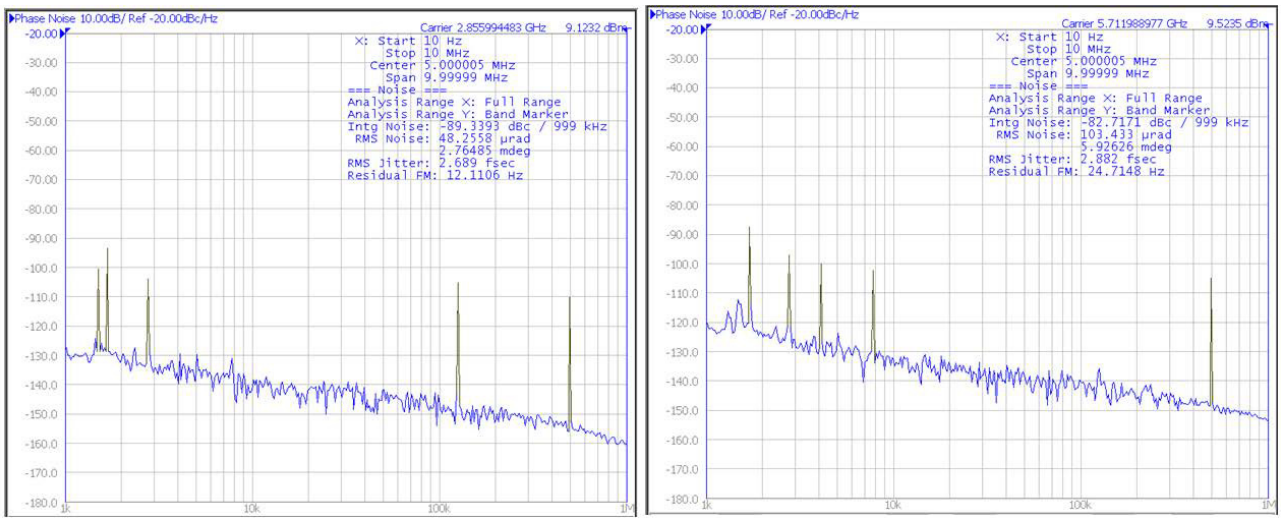

Figure 10: Phase noise / jitter measurement of the fabricated frequency doubler / power amplifier using an Agilent 5052B SSA. Left: Input phase noise spectrum / timing jitter. Right: Output phase noise spectrum / timing jitter. The phase noise is approximately 6dB higher than at the input (ideal frequency doubler). The added jitter of the frequency doubler / amplifier unit is approximately 1 fs in the critical range (1 kHz..1 MHz). The source was a Laurin reference generator.

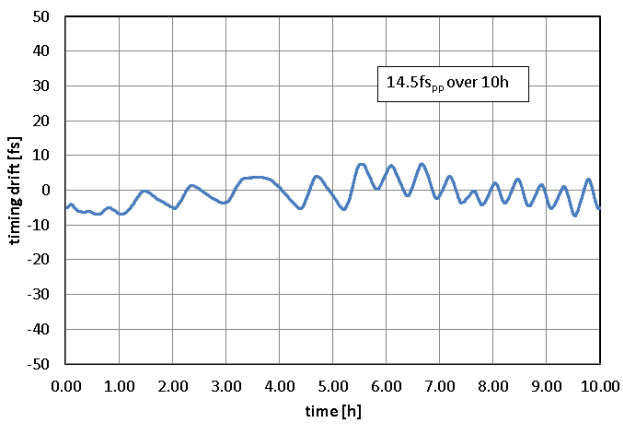

Figure 11: Timing drift measurement (avg. over 15min.) of the first frequency doubler / power amplifier prototype over 10h with not yet optimized temperature controller.

There was no time for extensive long term measurements yet but a first drift measurement shows the potential of the doubler / power amplifier' long term stability (Fig. 11). During this first drift measurement the lab air condition produced pronounced ringing in the relative humidity of ΔRH ≈ 3 % (SwissFEL sync room ΔRH specification is <2 %), which is exactly reproduced in the drift curve. Nevertheless the pp drift over 10 h was below 15 fs with potential for <10 fs after further optimization.

CONCLUSION

A frequency doubler / power amplifier unit for converting a 3 GHz radio-over-fiber link to a c-band link has been developed. Details on its design and first prototype measurements were presented. In combination with Instrumentation Technologies Libera Sync 3 3 GHz fiber-optic link the unit will be used to distribute c-band reference signals (5.712 GHz) in the SwissFEL facility. It adds only minor jitter and drift (potential for sub-10 f_{pp} drift) to the reference signals.

ACKNOWLEDGMENT

We acknowledge the support from the SwissFEL project. Uwe Kolb helped assembling the prototype units.

REFERENCES

[1] S. Hunziker, V. Arsov, F. Buechi, M. Kaiser, A. Romann, V. Schlott, P. Orel, and S. Zorzut, "Reference distribution and synchronization system for SwissFEL: Concept and first results," *Proc IBIC '14*, pp. 29-33, MOCZB2, Monterey, CA (USA), 2014.

[2] R. A. Baugh, "Low noise frequency multiplication," *Proc. 26th Ann. Frequency Control Symp., pp. 50-54, Atlantic City, NJ (USA), 1972.*

[3] C. L. Wenzel, R. Koehler, and R. Irion, "A sub-picosecond phase stability frequency multiplier." http://www.wenzel.com

ISBN: 978-3-95450-192-2 doi:10.18429/JACoW-IBIC2017-TUPCC18

BEAM ARRIVAL TIME MEASUREMENT AT SXFEL*

S. S. Cao†, Y. B. Leng‡, R. X. Yuan, J. Chen
SSRF, SINAP, Shanghai, China

Abstract

Shanghai Soft X-ray Free Electron Laser (SXFEL) is a fourth-generation light source which could provide coherent X-rays for various scientific researches. One of the key issues of its operation is the measurement of bunch arrival time because it is important for the synchronization of a bunch and seeded laser. The measurement utilized a newly designed beam arrival time monitor (BAM). The BAM contains two different frequencies of cavities. Thus a new scheme, dual-cavities mixing method, can be applied in this experiment to evaluate the beam arrival time resolution. In this paper, we presented the scheme, calculated the measured resolution with this method and evaluated the stability of the new monitor.

INTRODUCTION

SXFEL is a XFEL facility and it is under construction [1]. For this facility, it is of importance to measure the beam arrival time within 100 fs to keep the synchronization of a bunch and a seeded laser. One method to conduct the measurement is to compare the phase difference between reference signal and measured signal. To reduce the noise introduced by the reference signal during transmission, a dual-cavity BAM was applied in this experiment. Since the high energy electron beam almost reaches the speed of light and the cavities distance is very short, the phase difference measured at the two cavities is constant. Thus the system errors from cavities cables and RF front-end electronics can be evaluated. In the preliminary work, we are committed to minimize these system errors as much as possible.

To carry out this experiment, a dual-cavities BAM was designed and the pickups were based on C-band monopole cavities [2]. Figure 1 shows the photograph of the prototype BAM.

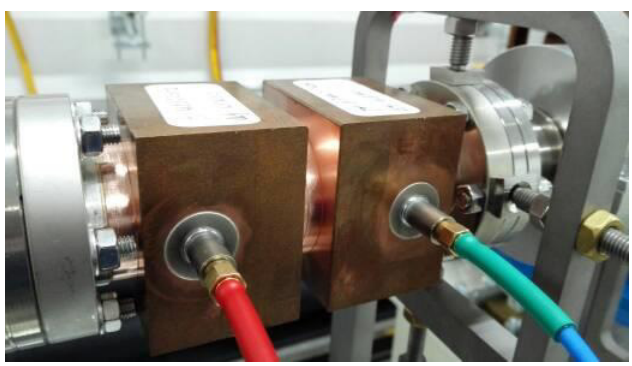

Figure 1: Photograph of the prototype BAM.

* Work supported by National Natural Science Foundation of China (No.11575282)
† caoshanshan1992@sinap.ac.cn ‡ lengyongbin@sinap.ac.cn

The prototype BAM has been developed and installed at SXFEL. The two pickups work at 4.685GHz and 4.72GHz, respectively. The frequency difference of the two cavities is about 35 MHz. The distance between the two cavities is more than 60 mm to avoid the cavity crosstalk. Table 1 shows the parameters of the BAM pickups. The parameters were calculated by Computer Simulation Technology (CST) Microwave Studio.

Table 1: BAM Pickup Parameters

Parameter	Value (#1)	Value (#2)	Unit
Frequency	4.685	4.72	GHz
Unloaded quality factor (Q_0)	4796	4835	-
External quality factor (Q_e)	1.8e5	1.9e5	-
Loaded quality factor (Q_L)	4671	4716.4	-
R over Q	107.2	107.9	Ohm
Bandwidth (BW)	1.002	1.025	MHz
Decay time constant (τ)	317.7	318	ns

In this study, the beam induced signal from downstream pickup served as a local oscillator signal input to the mixer. And the RF signal form upstream pickup was used as input signal for the mixer. Thus an intermediate frequency (IF) signal of about 35 MHz were obtained.

MEASUREMENT

There are four BAMs on the SXFEL facility. Two of them are installed at the drift section after the injection; the other two are placed in the modulator section. The experiment was conducted near the modulator because the noise in the experiment hall compared to the injection is smaller. Figure 2 presented the schematic diagram of the beam arrival time resolution evaluation [3]. An RF signal is generated when an electron beam passes through the BAM cavities. The RF signal was extracted with four antennas in the BAM wall and delivered to the RF front end in the experiment hall with long cables. The signals were processed with four channels of the RF front end system. In this system, two set of frequency mixer were applied for down conversion. The signals from port 1 and port 2 were used as local oscillator (LO) signal of mixer; signals from port 3 and port 4 were served as RF input signal. Then the low pass filters were used to filter out the high frequency signal, thus the IF signal was retained. A 12 bit Analog-to-Digital Converter (ADC) with a sampling rate of 500 MHz was then adopted to sample the IF signal.

ISBN: 978-3-95450-192-2 doi:10.18429/JACoW-IBIC2017-TUPCC18

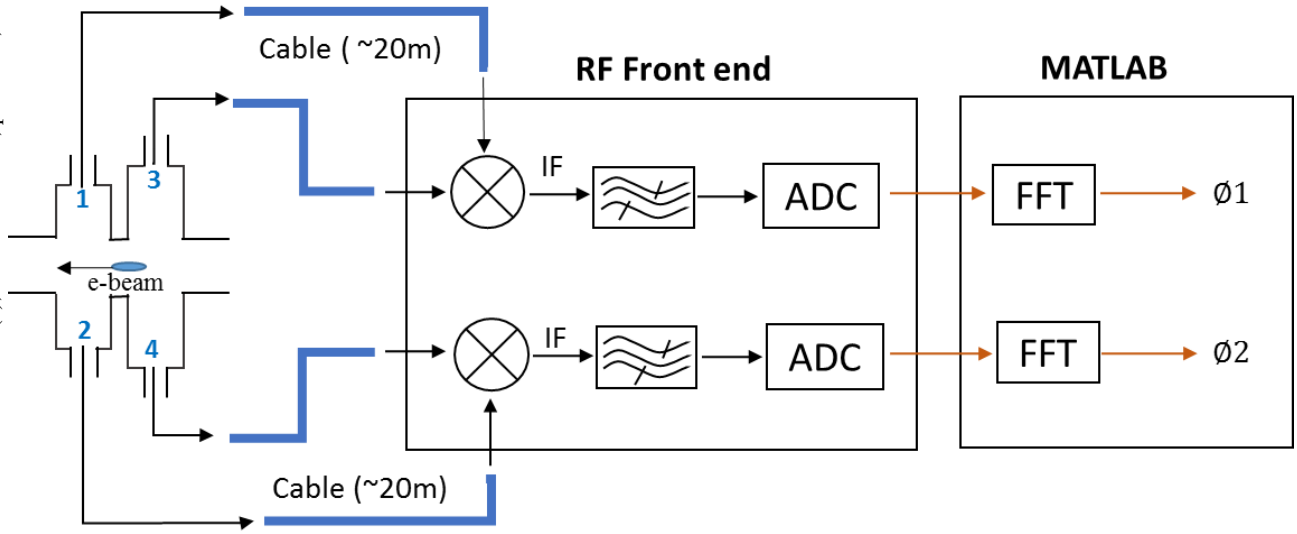

Figure 2: Schematic diagram for beam arrival time measurement.

The phases of the two IF signal can be written as:

$$\emptyset_{IF1} = \emptyset_1 + \emptyset_{noise1}$$

$$\emptyset_{IF2} = \emptyset_2 + \emptyset_{noise2}$$

Since $\emptyset_2 - \emptyset_1$ is constant, the measured resolution limitation thus mainly is system noise.

SIGNAL PROCESS

MATLAB was used for digital IF signal processing. Figure 3 reveals the raw signal of two pickups. The two figures showed a time delay and amplitudes variation.The former is what to be measured. The later has to be considered in the down conversion section. And the delayed RF signal should be used as LO signal. Figure 4 presented the raw IF signal. Theoretically, the two IF signal should be exactly the same, however, the two port signal from the same cavities are different mainly because of manufacturing error.

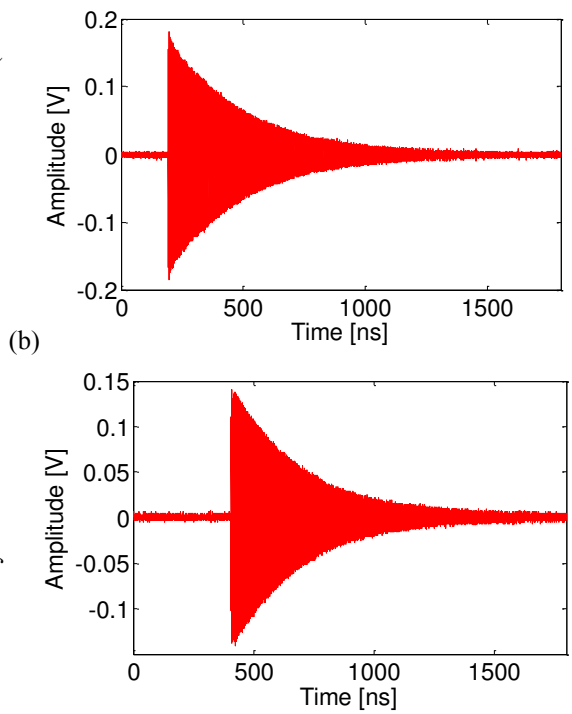

Figure 3: The raw RF signal for 200 pC bunch charge; a) port 3, b) port 1.

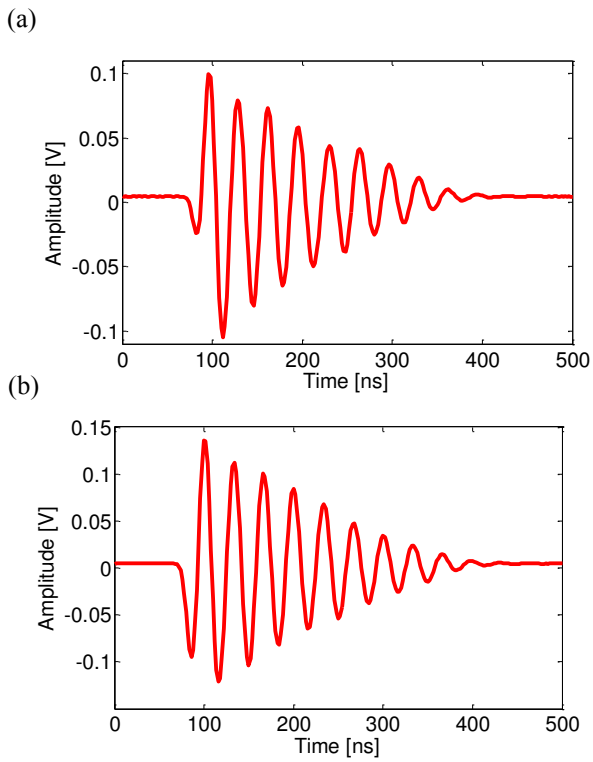

Figure 4: The raw IF signal for 200 pC bunch charge; a) port 1 and 3, b) port 2 and 4.

Although the phase of the above two IF signals are slightly different and the phase difference is about 0.004,

ISBN: 978-3-95450-192-2 doi:10.18429/JACoW-IBIC2017-TUPCC18

the frequencies are exactly the same, which is 29.7 MHz, as shown in Fig.5.

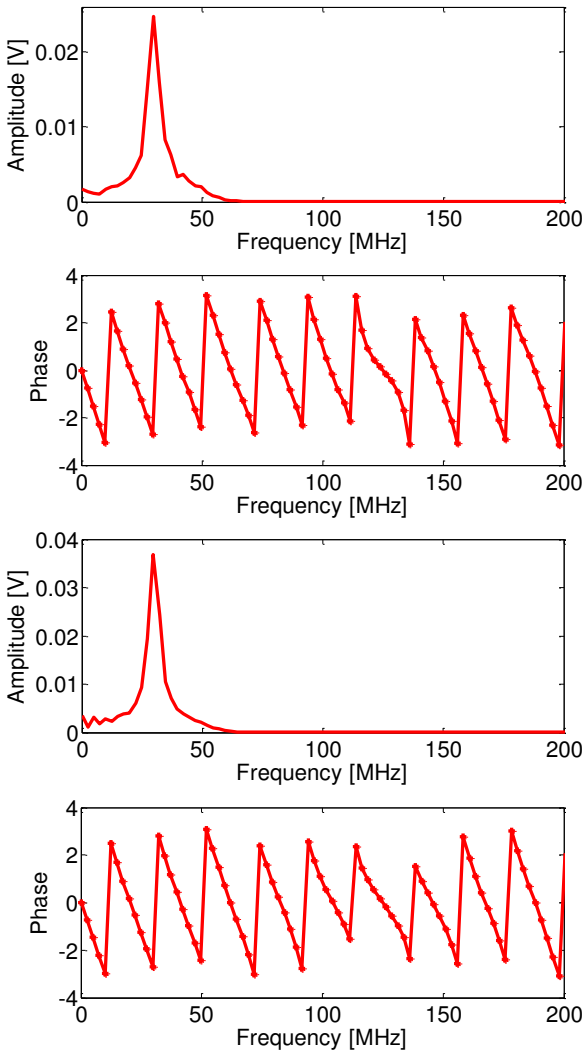

Figure 5: Magnitude spectrum and phase spectrum of two IF signal.

After 200 times measurements, the correlation plot of the two phases can be seen in Fig. 6. And it has exhibited a well linear relation. Moreover, in Fig. 7, a short-term measurement resolution of 67.7 fs can be calculated by comparing the two phase.

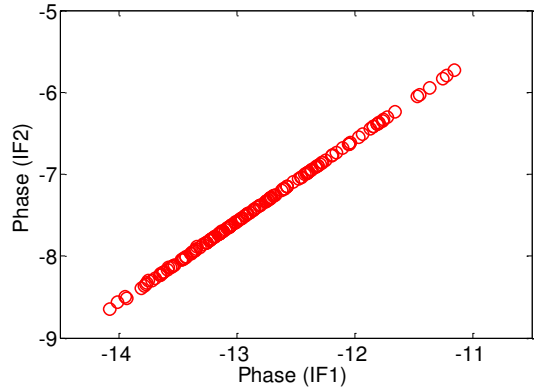

Figure 6: A correlation plot of the IF signals phase.

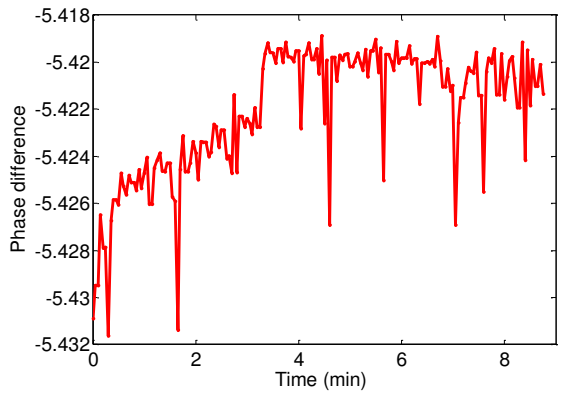

Figure 7: Short-term measurement resolution at the bunch charge of 200 pC.

SUMMARY

In the first BAM measurement the calculated temporal resolution was 67.7 fs with dual-cavity BAM prototype. This is larger than most published results. The main limitations probably comes from the BAM electronics. The cavity manufacturing error also has an impact on the BAM resolution. Currently, the studies on the BAM electronics are ongoing. Moreover, phase-stable cables will be applied in the future experiment. Besides, there are several ideas to improve the resolution. We hope all these improvement can help the next experiment obtain better results.

REFERENCES

[1] S.Y. Chen, *et al.*, SXFEL Design Report, 2007.

[2] S. S. Cao, *et al*, "Dual-cavity beam arrival time monitor for SXFEL," unpublished.

[3] Hong, J., *et al.* "Bunch arrival time monitor for PAL-XFEL," in *Proc. IBIC'14*, Monterey, CA, USA, September 2014, MOPD19, pp.191.

ISBN: 978-3-95450-192-2 doi:10.18429/JACoW-IBIC2017-TUPCF02

MODELING THE FAST ORBIT FEEDBACK CONTROL SYSTEM FOR APS UPGRADE*

P. Kallakuri†, D. Paskvan, J. Carwardine, N. Sereno, and N. Arnold,
Argonne National Lab, Lemont, USA.

Abstract

The expected beam sizes for APS Upgrade (APS-U) are in the order of 4 microns for both planes. Orbit stabilization to 10% of the beam size with such small cross-sections requires pushing the state of the art in Fast Orbit Feedback (FOFB) control, both in the spatial domain and in dynamical performance; the latter being the subject of this paper. In this paper, we begin to study possible performance benefits of moving beyond the classic PID regulator to more sophisticated methods in control theory that take advantage of a-priori knowledge of orbit motion spectra and system non-linearities. A reliable model is required for this process. Before developing a predictive model for the APS Upgrade, the system identification methodology is tested and validated against the present APS storage ring. This paper presents the system identification process, measurement results, and discusses model validation.

INTRODUCTION

The current APS real-time orbit feedback system has been in routine operation for more than 20 years and was the first digital truly global orbit feedback system to be implemented at a light-source. A distributed array of DSPs compute orbit corrections at 1.6 kHz using a matrix of 160 bpms x 38 correctors per plane. Unity-gain bandwidth is 60-80 Hz [1]. The regulator uses just the integral term of a classical PID, and is tuned for minimum residual broad-band rms orbit motion. A higher K_i than optimal gives better attenuation at lower frequencies but comes at the expense of amplifying residual motion at higher frequencies. The optimum value of K_i therefore depends on the spectral content of the orbit motion. A new orbit feedback system is under development for the APS Upgrade, where the smaller beam size drives orbit stability requirements that are considerably more stringent than the present APS. The new orbit feedback system will use a distributed array of DSPs to compute orbit corrections at 22.6 kHz (12x faster than the present system) and using a matrix of 560 bpms and 160 correctors. The target unity-gain bandwidth is 1 kHz. We need to study the possible performance benefits of moving beyond classic PID regulator and investigate different controller design methods in advanced control theory that are applicable to electron beam stabilization. A reliable model is required for this process since most of the advanced control algorithms are model based. We start this investigation by first modeling the FOFB system. Prototype feedback controllers, and fast corrector power supplies developed under R&D for APS-U have been integrated in prototype feedback system in APS Sector 27/28 for beam stability studies [2]. This system uses present storage ring corrector magnets. The modeling results are tested and validated against this prototype before developing the predictive model for APS-U.

Main tasks involved in the system modeling are: to develop a open loop system model, to create a simulation model of the DSP controller, and use them to implement a real time simulation setup that represents FOFB control system for APS-U. The layout of the FOFB system in closed loop is shown in Fig. 1. The open loop dynamics are represented by the process transfer function from corrector power supply set point to BPM read backs. Let $H[z]$ be the transfer function of open loop system with present corrector magnet. We assume,

$$H[z] = H_1[z] \cdot H_M[z] \tag{1}$$

where $H_M[z]$ is the transfer function of the present corrector magnet, and rest of the dynamics are represented by the transfer function $H_1[z]$. Then, the predicted open loop dynamics of the FOFB system for APS-U can be represented by,

$$H_U[z] = H_1[z] \cdot H_{UM}[z] \tag{2}$$

where, $H_{UM}[z]$ is the transfer function of the prototype fast corrector magnet. Developing the simulink model of the DSP controller is the next step in the process. BPM readbacks are the input to this model and the outputs are the corrector set points to power supply.

In this work, Matlab System Idendification Toolbox is used for model estimation. Data pre-processing, model validation are done in Matlab and Simulink environment.

SYSTEM IDENTIFICATION PROCEDURE

In this modeling we assume the FOFB system in open loop is linear time-invariant. The model application in our case is to use it for control design, so having accurate model around the crossover frequency is important.

Data Collection

The modelling process starts with collecting the data required for matlab system identification tool. Experiments are conducted to measure open loop time and frequency response data. For open loop measurements, input is the corrector setpoint to power system and output measured is BPM readbacks. Time response is measured with an unit step signal input at corrector drive. The measured step response data is preprocessed by smoothing and removing the zero offset. For open loop frequency response measurements, sine sweep signal with step changes in frequency

* Work supported by the U.S. Department of Energy, Office of Science, under Contract No. DE-ACO2-O6CH11357.
† pkallakuri@anl.gov

ISBN: 978-3-95450-192-2 doi:10.18429/JACoW-IBIC2017-TUPCF02

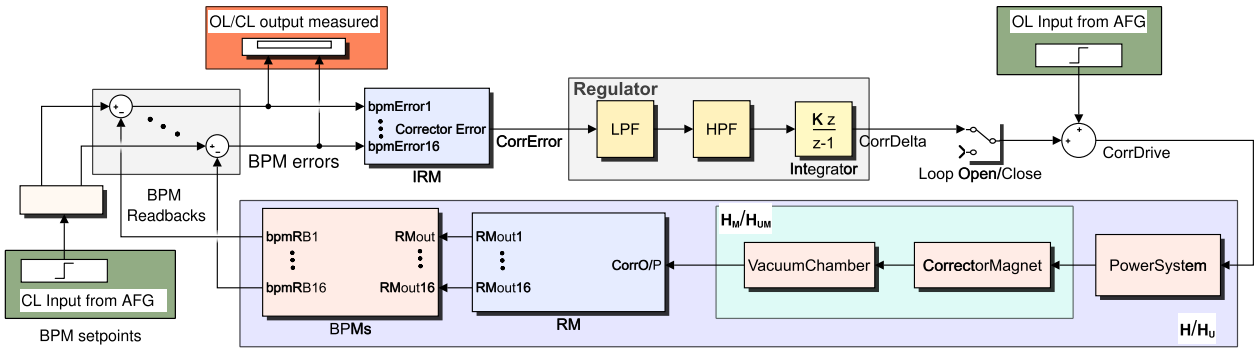

Figure 1: Fast Orbit FeedBack System layout for a single Fast Corrector.

ranging from 15 Hz - 6 kHz is used as input. The measured sine sweep response is detrended to zero to remove the offset and smoothed. This data is then used to calculate the magnitude and phase at each discrete frequency. In this paper we present the modeling results of the Single Input Single Output (SISO) transfer function from S27AH3 fast corrector to S27AP0 BPM. The measured step response data is shown in Fig. 2, and the frequency response data is shown in Fig. 3.

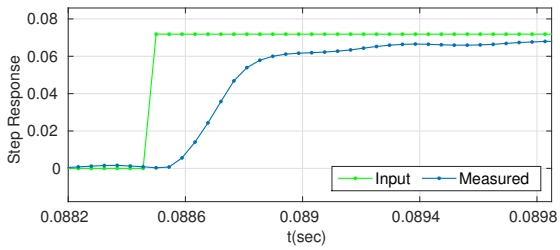

Figure 2: Measured step response.

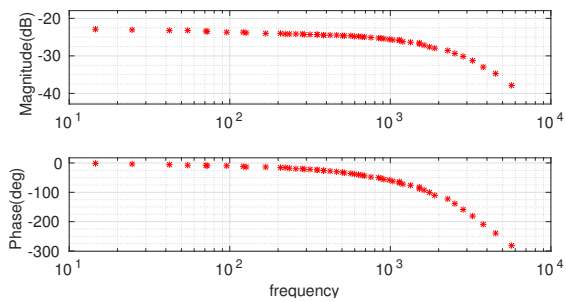

Figure 3: Measured frequency response.

From the step response data we have the information about the stationary gain and time delay of the system. In our case the delay is approximately 1-tick of the sample time. From the calculated frequency response data we can find possible relative degree (difference between number of poles and zeros) of the system transfer function. It can be calculated from the high frequency slope of frequency response magnitude. For this data the possible relative degree is either one or two.

Model Estimation

The next step in the system identification process is model estimation. Measured step/frequency response data and time delay are used as the input to the transfer function estimation. The combination of line search algorithms available in Matlab System Identification Tool are used to fit measured data in to the selected transfer function structure. Open-loop beam-based measurements give the observed change in the orbit to an applied change in the corrector power supply drive, and hence they include the dynamics of the power supply, magnet, vacuum chamber and bpms. The estimated model should therefore reflect the convolution of the transfer functions of the individual components. Based on a-priori knowledge of the physical components, the following assumptions were made in order to make an initial estimate of the order of the transfer function:

- From bench measurements, the transfer function of the corrector power supply is assumed to be second-order with complex poles located around 10 kHz.
- The corrector magnets surround an Inconel bellows, and eddy-current effects are assumed to be fast compared with the magnet response. Although eddy-current effects are not fully-representable in an LTI model, we assume an approximation of a small delay plus a high-frequency roll-off of at least one pole.
- The magnet response is assumed to start rolling off in the range of a few 100's of Hz, and can be approximated by two or more poles (at least one pole to account for magnet core losses).

Transfer function structures with different orders (4 and above), and relative degree one or two are considered for estimation. Two ways to incorporate the delay are explored. One, measured data with delay is fit in to a single transfer function. Other, delay is considered as a separate component. Transfer function models are estimated using different choices discussed above. Six pole, four zero transfer function model $H[z]$ shown in Eq. (3) looks to be a good fit with measured data. In this model, delay is not separated from the transfer function.

$$H[z] = C_1[z] \cdot C_2[z] \cdot C_3[z] \tag{3}$$

where,

$$C_1[z] = 0.939 \frac{1 - 1.536z^{-1} + 0.861z^{-2}}{1 - 1.583z^{-1} + 0.889z^{-2}}$$

ISBN: 978-3-95450-192-2 doi:10.18429/JACoW-IBIC2017-TUPCF02

$$C_2[z] = \frac{-0.120(1-2.880z^{-1})}{(1+0.489z^{-1})(1-0.522z^{-1})(1-0.681z^{-1})}$$

$$C_3[z] = 0.855\frac{1-0.974z^{-1}}{1-0.978z^{-1}}$$

By inspecting pole-zero locations, $H[z]$ is futher seperated into three transfer functions in series. Both $C_1[z]$ and $C_3[z]$ has gains close to unity, their step responses are shown in Fig. 4. $C_1[z]$ shows expected dynamics of the power supply i.e., it has 2 poles, and has fast rise time with considerable settling time. $C_3[z]$ has critically damped step response, is close to expected dynamics of the vacuum chamber. We then consider $C_2[z]$ represents dynamics of fast corrector magnet. Simulated step responses of the magnet, magnet with vacuum chamber, and complete open loop dynamics are shown in Fig. 5.

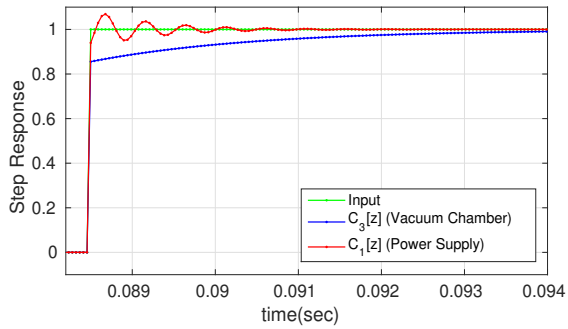

Figure 4: Step Responses of C_1 and C_3

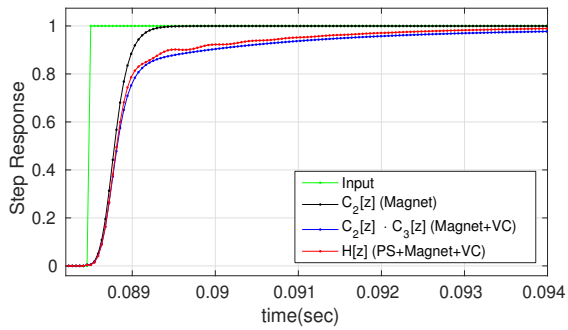

Figure 5: Step Responses of C_2, $C_2 \cdot C_3$, and H

MODEL VALIDATION

Open loop system model

The estimated model is validated by checking the consistency of the simulated model response with the measured data in open loop and in closed loop (with a known stabilizing controller). Figure 6 shows the comparison of the simulated and measured open loop step responses.

Simulink model of closed loop system is implemented using the estimated model and a single integrator. Step input is given at BPM set point. Measured and simulated corrector drive signal responses are compared. Figure 7 shows the comparison of the simulated and measured closed loop step responses for $K_i = 0.2$. The model reasonably represents open loop and closed loop behavior of the present system. We plan on refining it as per the requirements in future.

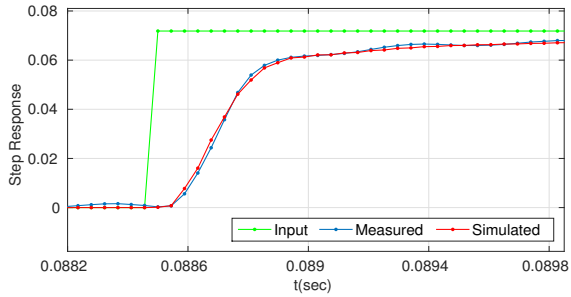

Figure 6: Measured vs Model open loop step response.

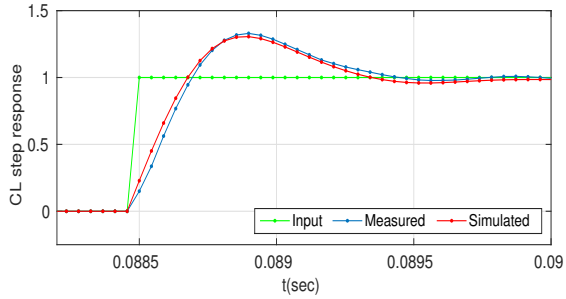

Figure 7: Measured vs Model closed loop step response, $K_i = 0.2$.

Simulink model for DSP controller

The controller schematic is modeled in Matlab Simulink and is implemented on DSP eval board using the same algorithms for each element. Significant elements of the controller model are IRM, and the regulator with LPF, HPF and PID controller. The output of the controller for different operation testcases are compared to validate that the Simulink model and the DSP implementation are equivalent.

CONCLUSIONS

System modeling plan to develop a FOFB system predictive model for APS-U is summarized. SISO transfer function model representing the single fast corrector to single BPM dynamics, is estimated using Matlab System Identification Tools. Estimated model response is validated against the measured open loop and closed loop step response data. At present we are assuming all the correctors will have the same dynamics. The next step is to model the relative differences in dynamics of different correctors.

REFERENCES

[1] J. Carwardine and F. R. Lenkszus, "Real-Time Orbit Feedback at the APS", in *Proc. 1998 Beam Instrumentation Workshop. (BIW'98)*, Stanford, CA, May 1998.

[2] N. S. Sereno *et al.*, "Beam Stability R&D for the APS MBA Upgrade", in *Proc. 6th Int. Particle Accelerator Conf. (IPAC'15)*, Richmond, VA, USA, May 2015, paper M0PWI011, pp. 1167–1169.

ISBN: 978-3-95450-192-2 doi:10.18429/JACoW-IBIC2017-TUPCF03

THE RF BPM PICKUP ELECTRODES DESIGN FOR THE APS-MBA UPGRADE*

X. Sun†, R. Lill, B. Stillwell, ANL, Argonne, IL 60439, U.S.A.

Abstract

The Advanced Photon Source (APS) is currently in the preliminary design phase for a multi-bend achromat (MBA) lattice upgrade. Beam stability is critical for the MBA and will require roughly 570 rf beam position monitors (BPMs) to provide the primary measurement of the electron beam trajectory through the insertion device (ID) straight sections and in the storage ring arcs. The BPM assembly features 8 mm diameter pickup electrodes that are welded to a stainless steel chamber and integrated shielded bellows both upstream and downstream of the chamber to decouple the BPM electrodes from mechanical motion of adjacent chambers. The design, simulations, and prototype test results will be presented.

INTRODUCTION

The APS Upgrade project (APS-U) requires rf BPMs at roughly 570 locations in the APS storage ring to achieve the beam stability requirements outlined in Table 1 [1]. For the preliminary design, the horizontal AC rms beam stability requirement is based on 10% the rms beam size at the ID source points from 0.01 to 1000 Hz, while the vertical requirement in microns will remain at the conceptual design values, with 10% of beam size being an operational goal. In addition, long-term drift over a 7 day period may be no more than 1 μm.

Table 1: MBA Beam Stability Requirements

Plane	AC rms Motion (0.01 – 1000 Hz)	Long-term Drift (100 s – 7 days)
Horizontal	1.3 μm 0.25 μrad	1.0 μm 0.6 μrad
Vertical	0.4 μm 0.17 μrad	1.0 μm 0.5 μrad

THE RF BPM PICKUP ELECTRODES R&D OVERVIEW

The four pickup electrodes used in each BPM are evenly distributed circumferentially around the circular MBA beam pipe and provide the primary measurement of the electron beam trajectory in the storage ring. Their sensitivities, charge induced voltages and wake impedance are all critical for the beam stability.

"As-built" 10.8 mm diameter APS button pickup electrodes and the elliptical APS standard chamber were modelled as shown in Fig. 1. The simulation was made using CST Microwave Studio (MWS) [2] for 24-siglet fill pattern 102 mA (15 nC per bunch, rms bunch length 10 mm). Measurements on as-built BPM electrodes installed in the existing APS storage ring were also made to validate the simulation model. Simulation results agreed well with the measured data, as shown in Fig. 2.

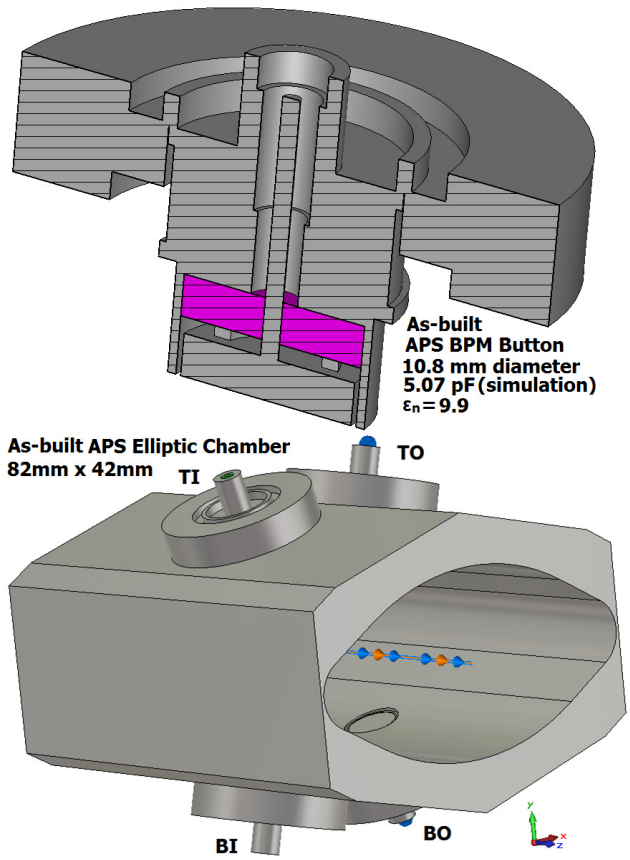

Figure 1: As-built APS BPM button and elliptic chamber.

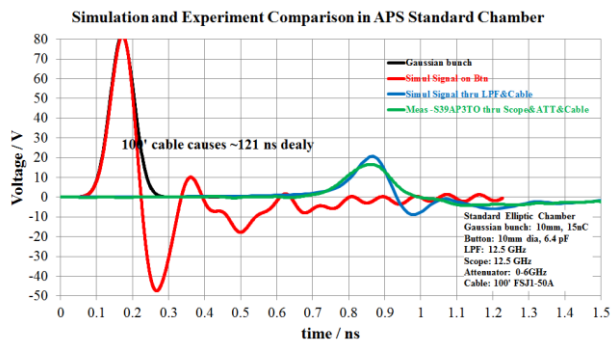

Figure 2: Simulation and experiment in APS elliptic chamber with BPM.

An MBA pickup electrode design has been developed which is essentially a scaled version of that for existing APS BPMs to match the planned MBA beam pipe aperture.

To help validate the new design, two sets of four prototype button pickup electrodes were purchased from two independent suppliers (vendors A and B) and then bench

* Work supported by the U. S. Department of Energy, Office of Science, Office of Basic Energy Sciences, under Contract No. DE-AC02-06CH11357.
† xiang@aps.anl.gov

ISBN: 978-3-95450-192-2 doi:10.18429/JACoW-IBIC2017-TUPCF03

tested. One of the sets, from vendor B, was delivered fully assembled into a vacuum chamber assembly with two rf-shielded bellows, as planned for APS-U, shown in Fig. 3.

Figure 3: MBA integrated BPM / rf-lined bellows from vendor B.

Experience with the prototype pickup electrode assembly and integrated shielded bellows informed design improvements to both. The outer shell of the pickup electrode was thinned to reduce the heat required to weld the part to the chamber and reduce the amount of heat conducted to brazed joints. A decision was also made to use an alternative bellows rf liner scheme, which uses leaf springs to maintain contact between the flexible and rigid portions of the bellows liner.

MBA PICKUP ELECTRODE DESIGN

Design goals for button pickup electrodes are exceptional sensitivity, high charge induced voltage on the button to maximize signal-to-noise ratio, and low wakefield impedance. The pickup electrode design parameters are shown in Table 2.

Table 2: MBA BPM Pickup Electrode Design Parameters

Fill Pattern	Mode	Current (mA)	Single Bunch Current (mA)	Bunch Charge (nC)	Bunch Length (ps/mm)
48	User	200	4.2	15.34	75.8/22.7
324	User	200	0.6	2.27	56.1/16.8
Single	Studies	1	1	3.68	57/17.1

The baseline model was designed, simulated, and optimized based on a trade-off analysis of critical parameters. The cross section of the final design is shown in Fig. 4.

INTEGRATED BPM / RF-LINED BELLOWS DESIGN

The MBA button pickup electrodes are welded to a stainless steel chamber, which is integrated within a pair of rf-lined welded bellows to minimize mechanical motion due to thermal growth and vibration on adjacent vacuum chambers [3, 4]. The "outside fingers" design, shown in Fig. 4, will reduce or eliminate error in the electrode signal due to displacement of the rf fingers as is expected with heating of the BPM assembly and neighboring chambers by synchrotron radiation and induced surface currents.

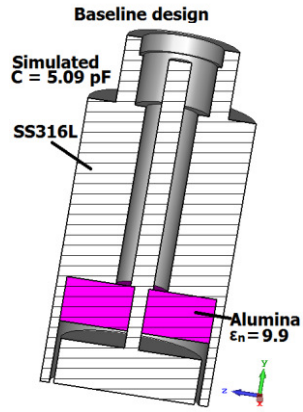

Figure 4: 8 mm diameter MBA button pickup electrode baseline design.

The beam power loss and the power dissipation on the metals and loads for full BPM assembly indicated by simulations using CST MWS and assuming a 48-siglet fill pattern at 200 mA (15 nC per bunch, rms bunch length 21 mm) is shown in Fig. 5 and summarized in Table 3.

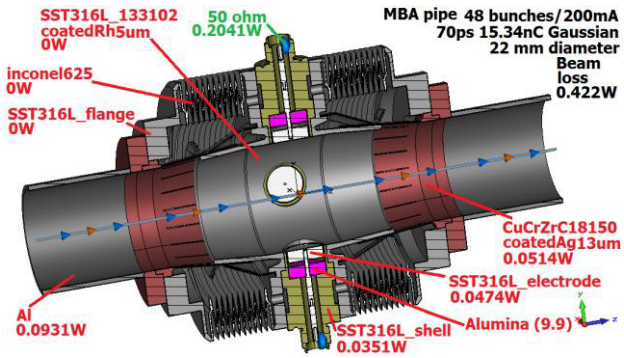

Figure 5: The simulated beam power loss and the power dissipation in MBA integrated BPM / rf-lined bellows with "outside fingers' and chamber.

Table 3: Simulated Beam Power Loss and Power Dissipation in MBA Integrated BPM/rf-lined Bellows with "Outside Fingers" and Chamber

200 mA/48 Fill Pattern, Bunch Length 21 mm	Metals	Four Loads (50 Ω)	Beam Power Loss
Subtotal (W)	0.227	0.204	
Total (W)		0.43	0.42

The charge induced voltages on the pickup electrodes for different beam offsets were also found using simulations, (Fig. 6). The computed sensitivity is found to be 0.117 mm^{-1} which compares favorable with existing APS button sensitivities of 0.058 mm^{-1} (horizontal) and 0.055 mm^{-1} (vertical plane).

ISBN: 978-3-95450-192-2 doi:10.18429/JACoW-IBIC2017-TUPCF03

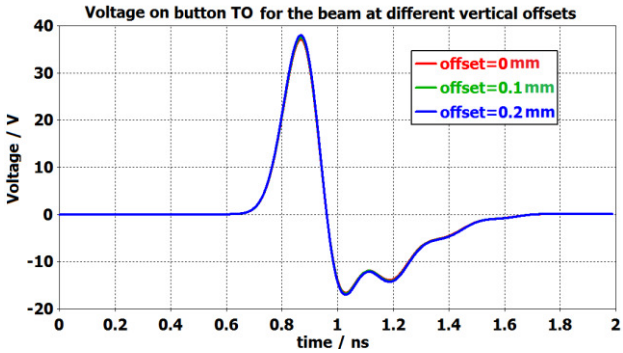

Figure 6: Simulated charge induced voltages on the MBA pickup electrodes for the beam at different vertical offsets.

THE PICKUP ELECTRODE PROTOTYPES TESTING

Each of the vendors that supplied the prototype button electrodes suggested modifications to the design to better accommodate their fabrication processes. None of these modifications were found to have a significant impact on performance.

Dimensional checks of the prototypes received from both vendors were generally good. Vacuum leaks and distortion of the center conductor were found in the electrodes provided by vendor B, however it is believed that these occurred as a consequence of overheating during welding of these to the chamber.

Electromagnetic measurements were made and compared with simulation results. The set of four button pickup electrode prototypes from Vendor A was measured by time-domain reflectometry (TDR). The results of TDR test and TDR simulation are shown in Fig. 7 and they agreed well.

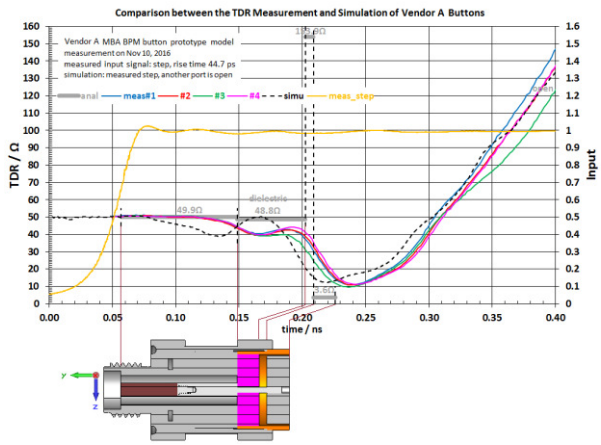

Figure 7: Vendor A BPM button TDR measurement, analysis and simulation.

The capacitances of the buttons provided by Vendor A were measured and calculated using different methods. The results are summarized in Table 4.

Table 4: Vendor A Button Pickup Electrode Capacitance

Analytic	Simulated		Lab Measured	
formula	Static	Smith Chart at 352 MHz#	Capacitance Meter	Network Smith Chart at 352 MHz#
4.12	4.70	5.02	4.1	3.85
			4.2	4.00
			4.4	4.19
			4.2	3.95

simulated or measured from the SMA end.

A transmission (S_{21}) measurement on a pair of pickup electrodes was made using the setup shown as Fig. 8. A G10 (a high-pressure fiberglass laminate) tube supports the two electrodes with buttons facing each other. The support also allows the gap between the two buttons to be adjusted.

The transmission between two prototype buttons from Vendor A was measured back-to-back with 5 mm gap and the results are shown in Fig. 9. The measurements of different buttons were consistent and agreed well with the simulation.

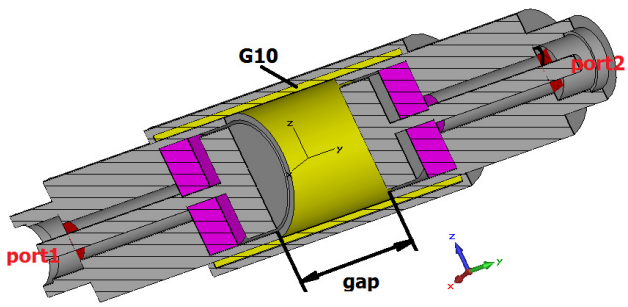

Figure 8: Transmission (S_{21}) of buttons back-to-back measurement setup.

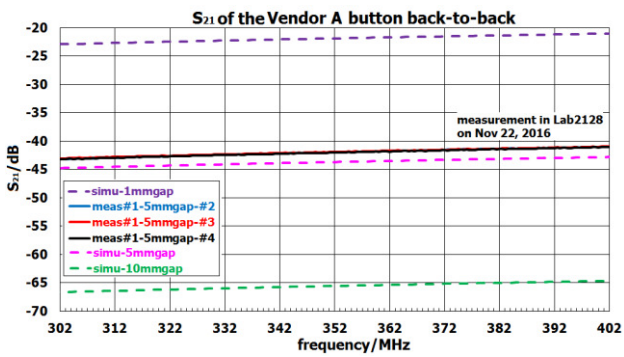

Figure 9: S_{21} comparison of the measurement and simulation between two buttons from Vendor A in back-to-back setup with 5 mm gap.

CONCLUSION

The APS "as-built" 10.8 mm diameter button pickup electrode and elliptic standard chamber were modelled and simulated. The model and simulation was validated by beam measurements.

ISBN: 978-3-95450-192-2 doi:10.18429/JACoW-IBIC2017-TUPCF03

The MBA button pickup electrode baseline model has been analysed and designed. Prototypes have been manufactured and measured. The results of analysis, simulation and measurement were consistent. The dimensional and electric checks of the button pickup electrode prototypes from Vendor A were good.

The MBA BPM assembly integrated inside pair of rf-lined welded bellows has been designed and optimized. Its electromagnetic performance was simulated. It will be bench tested in the lab and beam tested in APS storage ring.

ACKNOWLEDGMENT

The authors would like to thank Jingsong Wang for his support and help with CST MWS simulations.

REFERENCES

[1] R. Lill, private communications, 2017.

[2] CST, https://www.cst.com

[3] B. Stillwell et al., "Conceptual Design and Analysis of a Storage Ring Beam Position Monitor for the APS Upgrade", Proc. of IPAC15, p. 1170 (2015).

[4] B. Stillwell, private communications, 2017.

ISBN: 978-3-95450-192-2 doi:10.18429/JACoW-IBIC2017-TUPCF04

FEEDBACK CONTROLLER DEVELOPMENT FOR THE APS-MBA UPGRADE*

H. Bui†, D. Paskvan, A. Brill, S. Veseli, A. Pietryla, T. Fors, S. Shoaf, S. Xu, N. Sereno, R. Lill, N. Arnold, J. Carwardine, G. Decker

Advanced Photon Source, Argonne National Laboratory, Argonne, IL 60439, USA

Abstract

The Advanced Photon Source (APS) is currently in the preliminary design phase for the multi-bend achromat (MBA) lattice upgrade. Broadband Root Mean Square (rms) orbit motion should stay within 10% of a beam cross-section of the order 4 µm x 4 µm rms at the insertion device source-points. In order to meet these stringent AC beam stability requirements, a new orbit feedback system is under development and is being tested on the existing APS storage ring. The controller prototype uses Commercial Off-The-Shelf (COTS) hardware that has both high-performance Xilinx Field-Programmable Gate Array (FPGA) and two high-performance Texas-Instruments Digital Signal Processors (DSP) onboard. In this paper, we will discuss the rationale for a combined DSP/FPGA architecture and how functions are allocated. We then present the FPGA architecture and the results of using Infinite Impulse Response (IIR) filtering to mitigate Beam Position Monitor (BPM) switching noise and aliasing.

INTRODUCTION

The Feedback Controller (FBC) receives turn-by-turn (TbT or 271 kHz) BPM data from commercial Instrumentation Technologies Libera Brilliance+ BPM electronics [1], decodes and performs data integrity check, notifies the DSPs to generate corrector setpoints, and forwards corrector setpoints to the fast corrector power-supply interface.

Currently, the prototype Feedback Controller uses a CommAgility AMC-V7-2C6678 [2] module as a base development platform. The AMC-V7-2C6678 is a single width, mid-size Advanced Mezzanine Card (AMC), is comprised of two Texas Instrument (TI) TMS320C6678 DSPs, each with 8 cores running at 1.25 Giga Hertz (GHz), and a Xilinx Virtex-7 VX415T [3] FPGA. The combined architecture of a FPGA and a DSP shortens the development cycle time by taking full advantage of a vast library of highly-optimized DSP code and algorithms developed over the past 20 years for the present APS real-time feedback system (RTFB), which is running on a previous-generation of TI DSP. Investigations may be performed in the future to determine if any functionalities handled by the external DSPs can be implemented using resources inside the FPGA to improve system performance.

Figure 1 shows the simplified block diagram of the prototype FBC system. Light-blue blocks represent functionalities that are implemented inside the Virtex-7 FPGA, while orange blocks represent the two external TI DSP devices.

Xilinx FPGA's Gigabit transceivers and Peripheral Component Interconnect Express (PCIe) 2.0 are used to transfer data between the FPGA and DSP subsystem.

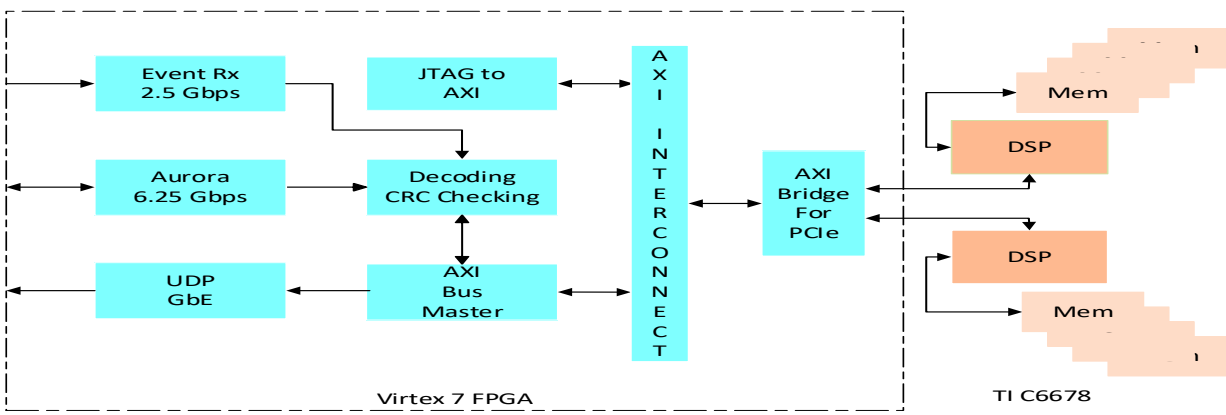

Figure 1: Simplified Block Diagram for the prototype FBC.

* Work supported by the U.S Department of Energy, Office of Science, under Contract No. DE-AC02-06CH11357
† hbui@aps.anl.gov

ISBN: 978-3-95450-192-2 doi:10.18429/JACoW-IBIC2017-TUPCF04

FPGA IMPLEMENTATION

The FBC Functional blocks implemented inside the FPGA are:

- Embedded Event Receiver
- Aurora 64b/66b
- UDP for GbE
- Data decoding and CRC checking
- AXI Bus Master
- AXI Interconnect
- AXI bridge for PCIe
- JTAG to AXI

Embedded Event Receiver

An Embedded Event Receiver, developed by Lawrence Berkeley National Laboratory (LBNL) re-targeted in a Xilinx Virtex-7 FPGA, receives the system timing serial events from a Micro Research Finland (MRF) timing system event generator over a 2.5 Gb/s fiber link. It decodes the events, provides timestamps, and generates trigger signals, which are synchronized with the machine clock. One of these trigger signals is called the 12th turn event, which is used to down sample TbT BPM data.

Aurora 64b/66b

An Aurora 64b/66b module uses standard 64b/66b encoding. It is a lightweight high-speed serial communication protocol for use with Xilinx gigabit transceivers. The prototype FBC uses four Libera Brilliance+ units (16 BPMs) across two sectors of the APS storage ring. Each Libera Brilliance+ can be configured to have up to four BPM modules and one Gigabit Data Exchange (GDX) module for streaming TbT data from the BPM modules. The FBC utilizes a Xilinx 6.25 Gb/s Aurora fiber link to receive 16 TbT BPM data packages from four daisy-chained Libera Brilliance+ GDX modules. The structure of a BPM package conforms to 16 by 32-bit data words; it consists of a programmable package identification (ID), BPM button amplitudes, calculated BPM horizontal and vertical positions, timestamps, status, and Cyclic Redundancy Check (CRC).

UDP for GbE

User Datagram Protocol (UDP) for Gigabit Ethernet (GbE) is implemented in the FPGA logic. LBNL provided modifications to their existing UDP implementation to assist the APS during development. In order to keep the transmission latency at a minimum, the UDP communication link is on a dedicated network using a cut-through switch. The FBC uses UDP to broadcast the 22.6 kHz corrector set points to the corrector power-supply controllers.

Data Decoding and CRC Checking

The Data decoding and CRC checking blocks perform data integrity and validity checks for every BPM data package received from the Aurora link. Incoming BPM data is decoded and sorted based on the pre-assigned package ID. The CRC for every package is re-computed then compared against the transmitted CRC value, and a CRC error is generated when there is a mismatch between the two CRC values. If the CRC is good, BPM data of the current package is selected and sent downstream for further processing, otherwise the previous saved valid data set will be sent instead.

AXI Interconnect

An Advanced eXtensible Interface (AXI) Interconnect is a Xilinx general-purpose core that provides connections for transferring data for any combination of AXI master and slave devices connected to an AXI Interconnect. It performs all the necessary conversions for any connected master and slave that have different data widths, clock domains, or AXI protocol.

AXI Bridge for PCIe

An AXI Bridge for PCIe is a Xilinx core that serves as an interface between the FPGA and DSPs using a Xilinx integrated block for PCIe. The PCIe interface is a two lane PCIe running at 5Gbaud/lane. The AXI Bridge for PCIe performs the address translations between the AXI memory space and PCIe memory space. The AXI Bridge allows the FPGA; configured as a PCIe endpoint; to perform Direct Memory Access (DMA) transactions between internal AXI connected peripherals and an external host device over the PCIe links.

AXI Bus Master

An AXI Bus Master module is implemented using the AXI4 protocol. It is an AXI memory mapped bus master capable of transferring a data burst up to 256 data beats, which can vary in size ranging from eight bits to 1024 bits, with a single start address. The AXI Bus Master waits for the 12th turn event from the Embedded Event Receiver and initiates an AXI burst write of BPM data with timestamps to the PCIe memory space. It then notifies the DSP to compute the corrector set points, waits for the DSP to indicate that new corrector set points are available, performs an AXI burst read from the PCIe memory space, and sends the corrector set points to the power supply controllers via UDP. Burst data transfers between the FPGA and the DSP are going across the AXI Bridge for PCIe.

JTAG to AXI

The Joint Test Action Group (JTAG) to AXI is a Xilinx core that acts as an AXI bus master. The JTAG to AXI generates AXI transactions by driving all the required AXI control signals to communicate to all the downstream slaves. The FBC uses the JTAG to AXI as a debugging tool. It provides a command line interface to hardware through which internal system memory can be easily accessed via a console.

ISBN: 978-3-95450-192-2 doi:10.18429/JACoW-IBIC2017-TUPCF04

DSP IMPLEMENTATION

The prototype FBC is currently using three out of the 16 available cores on the DSPs. Core 0's main function is to execute the real-time feedback algorithm. It consists of calculating corrector errors that is done by a matrix multiplication of the Inverse Response Matrix and the BPM errors. The corrector errors are then fed into the regulator, which consists of a high pass filter, low pass filter and Proportional Integral Derivative (PID) controller.

Core 0 of the DSP receives interrupts from the FPGA at the rate of 22.6 kHz. The FPGA writes BPM data into the DSP memory over PCIe bus and interrupts the DSP to generate new corrector set points. When the new corrector set points are available, the DSP generates an interrupt to the FPGA to read corrector set points from DSP memory over PCIe bus. The DSP takes approximately 11uS to execute the algorithm. In order to minimize execution time, other tasks are off loaded to core 1 and core 2. Core 1 performs the control and supervisory tasks. This core is responsible for receiving all control parameters and writing out collected data. Core 2 is the management core that handles all the communication between core 0 and core 1.

FILTER IMPLEMENTATION

The GDX module of the Libera Brilliance+ is equipped with a configurable Infinite Impulse Response (IIR) filters that can be applied to the TbT data stream for each BPM. The IIR implementation is a Direct Form II biquad, with a cascaded series of four biquads forming an eighth order IIR filter. Filter coefficients and gains are defined using Matlab's fdatool plugin. By choosing the desired characteristics of the filter, the fdatool generates the required filter coefficients to apply to the IIR for each BPM.

To improve long-term stability the Libera Brilliance+ uses ADC switching, which results in spikes at harmonics of 3.4 kHz. The FBC down samples TbT data to 22.6 kHz, which causes aliasing of signal above the Nyquist frequency of 11.3 kHz.

To mitigate the two noise sources, the filter we designed consists of second order notch filters for the first two switching harmonics, and a fourth order low pass filter with a cut-off frequency of 10 kHz for antialiasing. This was chosen as a compromise between antialiasing performance and group delay.

Figure 2 shows the antialiasing filter performance. It clearly shows that those spikes caused by aliasing higher switching harmonics are suppressed when the IIR filter is enabled.

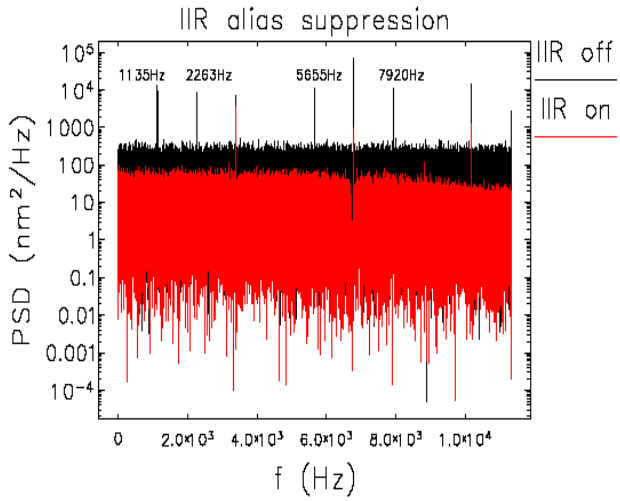

Figure 2: Antialiasing Filter Performance.

As the low pass cut off frequency is reduced, the group delay increases, reducing the orbit correction bandwidth of the FBC. Our fourth order low pass Butterworth filter has a group delay of 14 samples. A second order low pass Butterworth filter with a cut off frequency of 10 kHz reduces the group delay to six samples. Studies with beam revealed that the orbit correction bandwidth of the FBC is more sensitive to latency than to aliased noise. The system latency added by enabling the IIR filter reduces the orbit correction bandwidth of the FBC. More studies will be conducted to further investigate and improve filter performance.

CONCLUSION

The current architecture and technology used to develop the prototype Feedback Controller increases the feedback rate from 1.5 kHz to 22.6 kHz. First beam test results [4] and on-going integrated testing indicate that the prototype Feedback Controller is capable of achieving the stringent beam stability goals required for the APS upgrade.

ACKNOWLEDGMENT

The authors would like to thank Eric Norum and the LBNL team for their contributions to the development of the prototype Feedback Controller. We also would to thank all of the members of the APSU team.

REFERENCES

[1] Instrument Technologies, http://www.i-tech.si/accelerators-instrumentation/libera-brilliance-plus/benefits_1

[2] CommAgility Limited, https://www.commagility.com/products/hardware/435-amc-v7-2c6678

[3] Xilinx Inc., https://www.xilinx.com/products/silicon-devices/fpga/virtex-7.html

[4] N. S. Sereno *et al.*, "First Beam Tests of the APS MBA Upgrade Orbit Feedback Controller," in *Proc IBIC2016*, Barcelona, Spain, Sept. 2016, pp. 39 – 42.

ISBN: 978-3-95450-192-2 doi:10.18429/JACoW-IBIC2017-TUPCF05

THE ORBIT MEASUREMENT SYSTEM FOR THE CERN EXTRA LOW ENERGY ANTIPROTON RING

O. Marqversen†, R. Ruffieux, L. Søby, J. Molendijk, M.E. Angoletta, J. Quesada, M. Jaussi, CERN, Geneva, Switzerland
R. Marco-Hernandez††, IFIC, Valencia, Spain

Abstract

The CERN Extra Low ENergy Antiproton ring (ELENA), intended to further decelerate anti-protons coming from the CERN Antiproton Decelerator (AD) from a momentum of 100 MeV/c to 13.7 MeV/c, has been equipped with an orbit measurement system consisting of 10 horizontal and 10 vertical electrostatic pick-ups. Using charge amplifiers the signals are converted into sum and difference signals that, once digitized, are down converted to baseband and used to calculate intensity independent beam positions. The system is implemented on seven VME switched serial based (VXS) FPGA / DSP boards carrying direct digital synthesisers and analogue to digital converters on standard FPGA mezzanine cards. The switched serial high-speed bus allows intercommunication between DSPs and thus averaging of the signals from all pick-ups in real-time to be used either in the RF radial feedback system or for longitudinal Schottky diagnostics. The system implementation and initial orbit measurements with the H^- beam used for ELENA commissioning will be presented, as well as future upgrades for trajectory and longitudinal Schottky measurements.

INTRODUCTION

An overview of the ELENA Orbit system is given in [1]. The system is being implemented in steps; the closed orbit measurement, the trajectory measurement and the longitudinal Schottky measurement. The analogue and digitization electronics are common to all measurements, the difference coming from the subsequent treatment of this data in the Field Programmable Gate Array (FPGA) and Digital Signal Processing (DSP) code. The orbit measurement is already operational and is being used for the ELENA commissioning, with first measurements presented here. Trajectory and longitudinal Schottky measurements will follow in the future.

The ELENA orbit system is built with the same VXS-DSP-FMC-carriers and FMC boards as the CERN AD orbit system [2] and the Firmware, DSP code and real-time software share a common base.

ELENA is CERNs Extra Low ENergy Antiproton ring intended to decelerate antiprotons injected at an energy of 5.3 MeV from the CERN AD to 100 keV. To minimize impact on the CERN AD physics program the ELENA ring is initially being commissioned using H^- ions injected at the intended antiproton extraction energy. Due to problems with the H^- source the achieved energy has only reached 85 keV, challenging the low energy end of the RF system, and forcing the system to run at the second RF harmonic (2·132 kHz). The orbit measurement system, measuring the beam position from a signal down mixed to baseband, has been designed to follow this.

The system

The orbit system consists of electrostatic pick-ups equipped with charge amplifiers, preamplifiers and VXS-DSP-FMC-Carriers [3]. The charge amplifiers send sum and difference signals from the pick-ups, via preamplifiers to ADCs placed on FMC boards. The ELENA RF system sends the actual revolution frequency as an integer value via an optical gigabit link, from which the orbit system will generate its own local oscillator frequency on the wanted harmonic used for digital down mixing of the sum and difference signals. Position calculations are performed in DSP modules and the results are sent to the real-time software that makes the data available to the control room. The orbit system also computes a real-time mean radial horizontal position for the RF radial feedback. The system is only capable of producing beam position data during the times when the beam is bunched.

INITIAL MEASUREMENTS

All pick-up signals after the charge and pre-amplifier are also made available to the CERN Oasis system (an online oscilloscope) allowing operators to plot the beam sum or difference signal from any pick-up. During commissioning of ELENA the H^- beam is injected using a 700 ns kicker pulse, which for a revolution frequency of 132 kHz (energy 85 keV) results in a bunch like structure even before RF is applied (Figure 1). The number of charges, N_q Eq (1) has been estimated, knowing the charge amplifier feedback capacitance and following amplifier gains. The voltage integrated over the bunch length is divided by the time where a single charge is contributing to the voltage i.e. the effective length of the pick-up divided by the particle speed. The effective length of the pick-up is obtained from the shape of the image charge for a given relativistic β, assuming a centred beam [4].

$$N_q = \frac{C_{feedback} \int V(t)dt}{e \cdot Gain \cdot \frac{l_{PU\_eff}}{v}} \qquad (1)$$

Where $C_{feedback}$ is the feedback capacitance in the charge amplifier, $\int V(t)dt$ the voltage integrated over the bunch length at the output of the amplifier (Figure 1, trace 2), e the electric charge, l_{PU_eff} the effective length of the pick-up, and v the speed of the particle. The effective length of the pick-up is given by

† Ole.marqversen@cern.ch
†† Ricardo.Marco@ific.uv.es

ISBN: 978-3-95450-192-2 doi:10.18429/JACoW-IBIC2017-TUPCF05

$$l_{PU\_eff} = l_{PU\_real} + \frac{r_{PU}}{\gamma \cdot \sqrt{2}} \qquad (2)$$

Where l_{PU_real} is the physical pick-up length, r_{PU} is the pick-up radius and γ the Lorentz factor.

Using these formulae, the measured intensity at injection was estimated to be 1x10^7 H$^-$ particles. ELENA is designed to work with $1 \cdot 10^7$ - $4 \cdot 10^7$ antiprotons. No other measurement of intensity is yet available in ELENA.

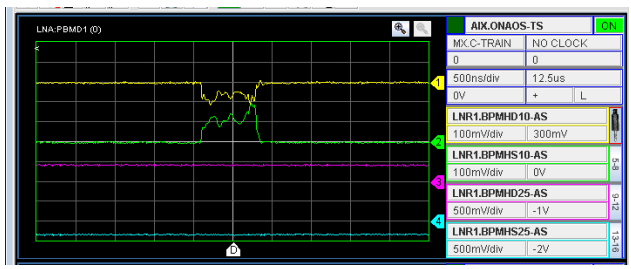

Figure 1: Difference (1) and Sum (2) signals from a pick-up as it enters the ADC after the charge amplifier and pre-amplifier.

Beam Position

To obtain the beam position, both sum and difference signals are sampled and down-converted to baseband in the FPGA, before being further processed in the DSP to produce the final position (difference/sum). The DSP performs a position calculation every 10 µs (100 kHz) using the most recent data from the down converter. The read out of position data is made via four 2k buffers, with individual start time and sampling rates (lower then 100 kHz), allowing the user to both cover long cycles and look at details. Figure 2 shows the read out at 1 ks/s rate starting a few milliseconds before injection, showing the position from all available horizontal pick-ups versus time. When decimating (here 100 kHz to 1 kHz) average values are used.

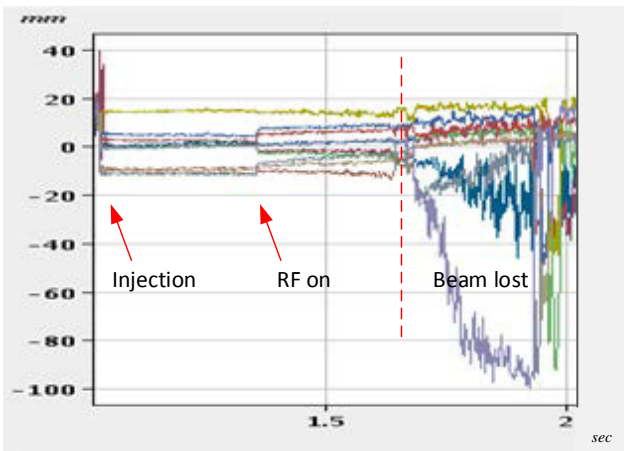

Figure 2: Beam position measurement from 10 horizontal PUs in ELENA. Data rate of 1 kHz. Only the first 1k values of 2k buffer values are shown.

The first part (after injection) is with no RF, with RF applied at approximate 1.35 s (the time is relative to the start of the magnetic cycle, not injection). The beam is captured and remains in the machine for around 0.35 s (corresponding to 1.7 s in Figure 2). The system "as is" (summer 2017) will present data making no decision on whether to discard data due to too low intensity. This means that if the sum signal (i.e. the denominator in the Difference/Sum calculation) becomes too small the DSP will output a non-physical position of -100 mm for the relevant samples. These values are (for now) filtered together with valid data, resulting in the "towards -100 mm" behaviour observed for some pick-ups in Figure 2, as the beam is being lost.

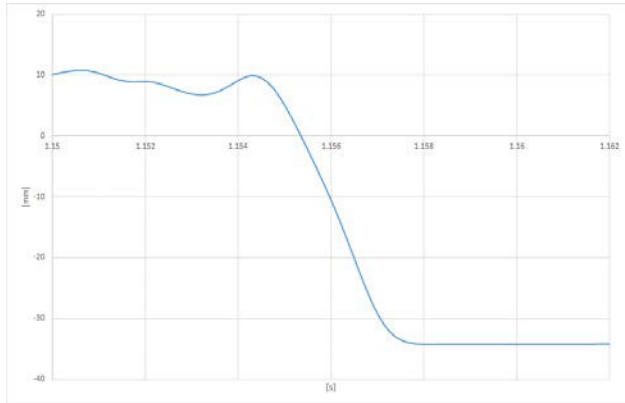

Figure 3: Step response from one ELENA pick-up after application of a calibration signal at 1.145 s. Data rate of 10 kHz.

The measured step response of the system is shown in Figure 3 where the output position signal of a single pick-up is shown; at 1.15 s to 1.154 s no signal nor beam is present, the calibration signal is then switched on and shows the step response of the system, which is critically damped with a time constant of approximate 2 ms. The step time is given by intern filtering and can therefore be changed. The calibration signal is a sinusoidal signal generated (DDS on FMC) at the actual revolution frequency injected on the "negative" PU plate, resulting in a position matching the maximum negative -35 mm displacement.

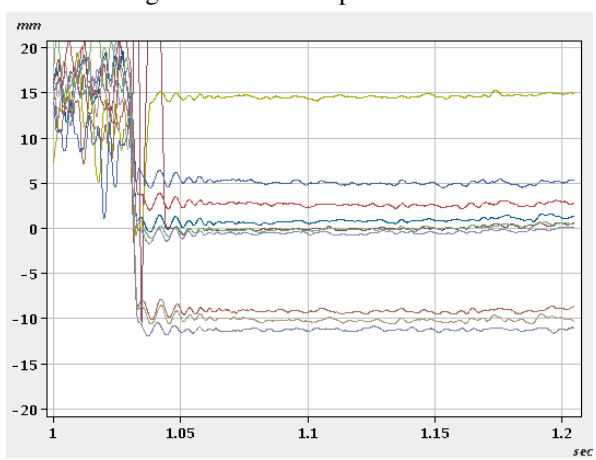

Figure 4: Beam position measurement in ELENA with H$^-$ injected at 1.03 sec. Data rate of 10 kHz.

Shown in Figure 4 is the beam position at injection with a 10 kHz sampling rate. Once the beam position is stable, an upper limit on the resolution of the system can be estimated as the standard deviation from measurement to

ISBN: 978-3-95450-192-2 doi:10.18429/JACoW-IBIC2017-TUPCF05

measurement, calculated to be 0.1 mm, matching the requirement.

The closed orbit can be plotted for any time in the acceleration cycle (where position data is available i.e. when the beam is bunched). The orbit can then be entered into the standard CERN orbit correction application. Figure 5 shows one of the very first times this was successful performed in ELENA; in pink the initial orbit, and in green the corrected orbit. Only horizontal correction was performed, with the vertical measurement showing good reproducibility of both the machine and the measurement.

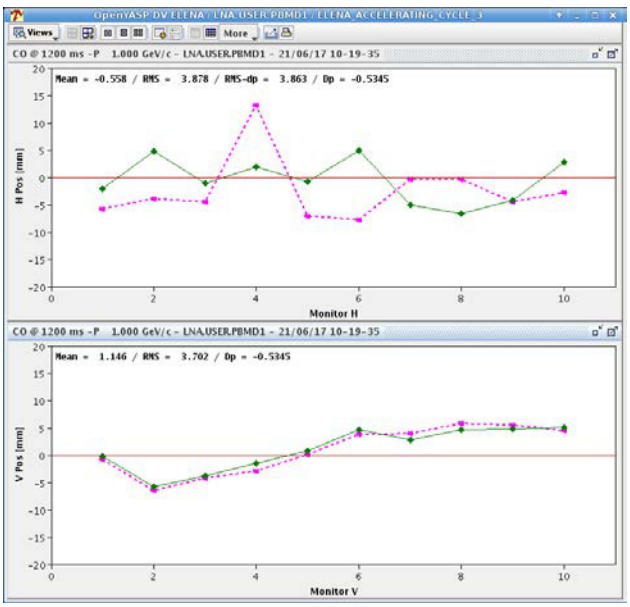

Figure 5: Orbit measurement (x-axis is the 10 pick-ups in each plane for which the position is given in mm) before (pink) and after (green) a horizontal orbit correction in ELENA.

Mean Radial Position

The system has two VXS switch cards allowing high speed serial communication between the VXS-DSP-FMC carriers; this is implemented in a "sushi train style" where blocks of data (32x32 bytes) are passed from all cards both right and left in a circular manner allowing all boards to communicate. Passing one block of data between two neighbouring boards takes approximately 340 ns. In the ELENA setup seven VXS-DSP-FMC-carriers are in use i.e. 1 µs is needed to pass one block of data to all cards (maximum of 3 transfers required). This carrier intercommunication is used to pass the calculated beam position from each DSP to one central DSP that is used to calculate the mean radial position (from selected pick-ups). The calculated value is updated every 10 µs and made available via a giga-bit link on optical fiber to the low level RF system for radial feedback.

TRAJECTORY

To enable measurements of the turn by turn trajectory at injection, knowledge of the RF frequency and phase is required. The ELENA low level RF system, in its fixed sample frequency scheme, can provide this via the already existing gigabit link. Also including the stable phase function giving the relation between RF phase and beam. The FMC-MDDS generating the FMC-ADC sample frequency, can then be omitted in the orbit system. The turn by turn position will be calculated from the difference and sum signal averaged over one bunch length i.e. no inter bunch position.

LONGITUDINAL SCHOTTKY

The longitudinal Schottky signals will be measured using all 20 sum signals (vertical and horizontal), phase compensated and then averaged together to gain signal to noise ratio (a theoretical 13 dB SNR gain is possible). The phase compensation will take into account the physical position of each pick-up as well as cable delays etc. The analogue bandwidth of the system is limited to 40 MHz by the anti-aliasing filters mounted on the FMC-ADCs. With the total power equal in all Schottky harmonics, spectral density will be lower at higher harmonics, as the spectra are wider. However, a wider spectrum makes it faster to get a given relative frequency resolution (FFT frequency resolution is given by the total sampling time) Fast measurement are preferred, i.e. highest possible harmonic will be chosen. Initial calculation [5] indicates SNR will be sufficient for Schottky measurement up to the 110th harmonic. The 40MHz bandwidth will limit this at injection. The FPGA sampling of data can be paused allowing the DSPs to perform the necessary FFTs uninterrupted.

CONCLUSION

The status of the orbit system developed for, and used during, commissioning of the CERN ELENA ring has been presented with measurements showing its capability to measure the closed orbit with a time resolution of 10 µs, a step response time of approximately 2 ms and a position resolution of 0.1 mm for $1 \cdot 10^7$ H^- particles. No measurements are presented with antiprotons as they have not yet been circulating in ELENA. The orbit measurements have been integrated into the CERN control system allowing for automatic orbit correction. The system also makes available the mean radial position to the radial feedback of the RF system. The next step will be to implement the necessary modifications for the addition of trajectory and longitudinal Schottky measurements to the system.

REFERENCES

[1] L. Søby *et al.*, "ELENA Orbit and Schottky measurement system," in *Proceedings IPAC 2015*, Richmond, VA, USA.

[2] R. Marco-Hernandez *et al* A New orbit system for the CERN antiproton decelerator," in *Proceedings IBIC,15* Melbourne, Australia.

[3] M. E. Angoletta *et al.*, "A Leading Edge Hardware Family for Diagnostics Applications and Low Level RF in CERN's ELENA Ring," in *Proceedings IBIC'13*, Oxford, UK.

[4] Maurice Cohen-Solal, "Design, test and calibration of an electrostatic beam position monitor," *Physical Review.*

[5] F. Pedersen, "Ideas and choices for low noise longitudinal pick-ups and diagnostics for ELENA", CERN, Switzerland.

ISBN: 978-3-95450-192-2 doi:10.18429/JACoW-IBIC2017-TUPCF06

PERFORMANCE OF THE AWAKE PROTON BEAM LINE BEAM POSITION MEASUREMENT SYSTEM AT CERN

M. Barros Marin*, A. Boccardi, T. Bogey, J. L. Gonzalez, L. K. Jensen,
T. Lefevre, D. Medina Godoy, M. Wendt, CERN, Geneva, Switzerland
J. Boix Gargallo, UAB-IFAE, Barcelona, Spain

Abstract

The Advanced Proton Driven Plasma Wakefield Acceleration Experiment (AWAKE), based at CERN, explores the use of a proton driven plasma wake-field to accelerate electrons at high energies over short distances. This paper introduces the Beam Position Measurement (BPM) system of the proton beamline and its performance. This BPM system is composed of 21 dual plane button pickups distributed along the 700 m long transfer line from the CERN Super Proton Synchrotron (SPS) extraction point to beyond the plasma cell. The electrical pulses from the pickups are converted into analogue signals proportional to the displacement of the beam using logarithmic amplifiers, giving the system a high dynamic range (>50 dB). These signals are digitized and processed by an FPGA-based front-end card featuring an ADC sampling at 40 MSps. Each time a bunch is detected, the intensity and position data is sent over 1km of copper cable to surface electronics through a serial link at 10 Mbps. There, the data is further processed and stored. The dynamic range, resolution, noise and linearity of the system as evaluated from the laboratory and 2016 beam commissioning data will be discussed in detail.

INTRODUCTION

The Advanced Proton Driven Plasma Wakefield Acceleration Experiment (AWAKE) [1] is a proof-of-principle experiment installed in the former CERN Neutrinos to Gran Sasso (CNGS) facility and is the first proton driven plasma wake-field acceleration experiment world-wide. The AWAKE experiment aims to accelerate electrons from low energy (~15 MeV) up to the multi-GeV energy range over short distances (~10m). This is achieved using the wake-field of a plasma to accelerate electrons. The wake-field is induced in the plasma by a high-energy (~400GeV) proton bunch extracted from the CERN Super Proton Synchrotron (SPS) via a 700 m long transfer line.

THE PROTON BPM SYSTEM

The Beam Position Monitor (BPM) system of the AWAKE proton beam line, is composed of 21 dual plane button pickups, distributed along a 700 m beam transfer line. The read-out electronics is divided into two parts: the front-end electronics located close to the pick-ups in the tunnel and the back-end electronics sitting in a service gallery. The back-end communicates with all the different front-ends and concentrates the BPM control and data acquisition to a single point. The communication between the front-end and back-end is performed using a custom protocol running at 10 Mbps over 1 km of copper cable. This system has been optimized for the low repetition rate (~30 s) and high dynamic range (~40 dB) of the AWAKE proton beam. Its target resolution is better than 100 µm for nominal bunches ($3.5e^{11}$ protons).

Front-End Electronics

For each BPM, the front-end electronics is composed of two analogue, logarithmic amplifier boards (LogAmp), a Digital Front-End board (DFE) and a power supply unit. The LogAmp board receives the electrical pulses from the pick-up and shapes them using 30 MHz band-pass filters, before processing them with logarithmic amplifiers and sending the resulting analogue signals to the DFE board for digitization. The LogAmp board also features an on-board calibrator emulating pickup signals of known displacement. The DFE is an FPGA-based digital board featuring a multi-channel ADC sampling at 40 MSps. Due to the low radiation levels expected in the AWAKE beam line, radiation-tolerant components are not required. An image of the pick-up and front-end electronics under test in the laboratory is shown in Figure 1.

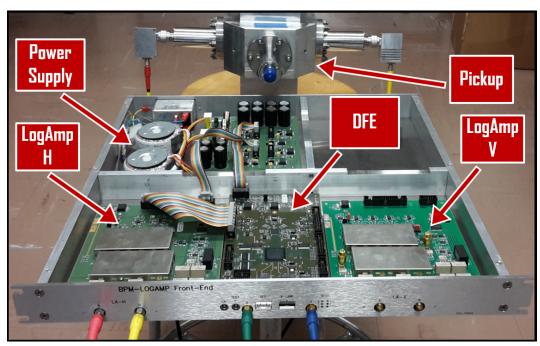

Figure 1: Pickup and front-end electronics.

The front-end electronics provides both a difference signal (Dif) and a summation signal (Sum) per plane. As for all BPM systems based on logarithmic amplifiers, the Dif signal is obtained from the difference in the logarithm of opposite electrodes, Log[electrode1] – Log[electrode2] = Log[electrode1/electrode2] and is directly proportional to the normalized beam position. The Sum signal is obtained by summing the logarithmic signal of both electrodes and is a function of the beam intensity. The Sum signal is used for auto-triggering the acquisition system. All signals are

* manoel.barros.marin@cern.ch

ISBN: 978-3-95450-192-2 doi:10.18429/JACoW-IBIC2017-TUPCF06

processed by the FPGA on the DFE board that continuously compares the digitized Sum with a pre-set threshold value. A beam presence flag is generated when the threshold is surpassed. This flag initiates the data transmission to the back-end acquisition electronics through the electrical serial link. A block diagram of the front-end electronics as well as a plot of the Sum and Dif data for a single bunch after digitization at 40 MHz are depicted in Figures 2 and 3 respectively.

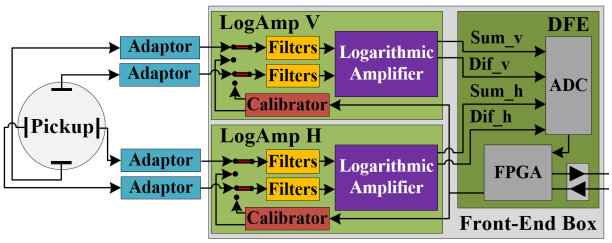

Figure 2: Diagram of the pickup and front-end electronics.

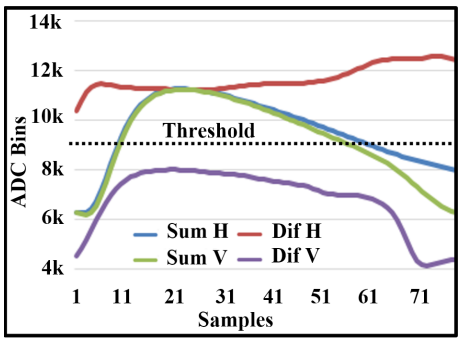

Figure 3: Sum and Dif signals after digitization at 40 MSps and showing the auto-trigger threshold.

Back-End Electronics

The back-end electronic comprises two VME boards (VFC-HD) [2], and their respective auxiliary electronics boards (AWAKE Patch Panel and AWAKE Patch FMC). The VFC-HD is the standard back-end FPGA-based (Altera Arria V GX), FMC-HD carrier board used by the CERN Beam Instrumentation Group. This board receives and stores the raw Sum and Dif data from different front-ends (up to 16 front-ends per VFC-HD) for further processing. After each proton beam extraction from the SPS, this data is made available to the operational software. The role of the AWAKE Patch Panel and Patch FMC is to interface the VFC-HD to all the serial communication link cables coming from the BPM front-ends. An image of the back-end electronics as installed is shown in Figure 4.

System Timing and Calibration

As the system is using logarithmic processing, the Dif data is not meaningful unless the Sum data exceeds a certain minimum value. To find the optimal integration window during which processing can take place, the following procedure was followed. The first step was the storage of hundreds

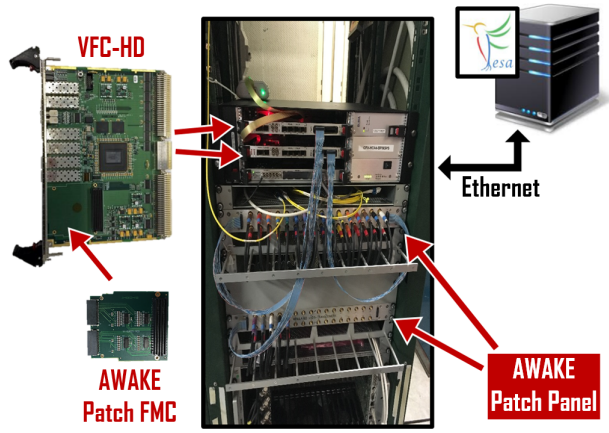

Figure 4: Back-end electronics.

of acquisitions in the laboratory using a beam emulator. A software algorithm was then used to search for the Least Noise Sample (LNS) in the Dif data by evaluating the standard deviation at each point using a sliding window after the point corresponding to the maximum of the Sum data. Once the LNS has been identified, the algorithm averages the LNS with its two adjacent samples. If the standard deviation of the resulting average is less than the noise of the LNS, the process is repeated, adding two new samples until the standard deviation of the new window is higher than that of the previous window. The window with the lowest standard deviation is considered the Optimal Window (OW). An example of LNS and OW is depicted in Figure 5. The defined OW found in the laboratory using this method is used with beam to give the optimal window where all ADC samples are summed to give a value (Δ_{avg}) for calculating the beam position. The standard deviation of each sample, used to calculate the LNS, as well as that for the window length, used to calculate the OW, are illustrated in Figure 6. For converting Δ_{avg} to distance units (x), it is necessary to apply the scaling factor derived from the on-board calibrator (Δ_{Offset} (0 dB), Δ_{Max} (+6 dB) and Δ_{Min}(-6 dB)), linear corrections related to the pickup geometry as well as any physical offset of the pick-up ($Offset_{Phy}$):

$$Scale_{Cal} = \frac{\Delta_{Max} - \Delta_{Min}}{2} \quad (1)$$

$$x = \left[\left(\frac{5.0672}{Scale_{Cal}}\right)\left(\Delta_{avg} - \Delta_{Offset}\right)\right] - Offset_{Phy} \quad (2)$$

Operation

The first proton beam for AWAKE was extracted from the SPS in June 2016 whilst the beam line was further commissioned in September 2016. Since then, the system has successfully accumulated hundreds of hours of operation. During operation, the proton beam position is monitored and stored on a shot-by-shot basis for beam steering or further analysis (see example in Figure 7).

ISBN: 978-3-95450-192-2 doi:10.18429/JACoW-IBIC2017-TUPCF06

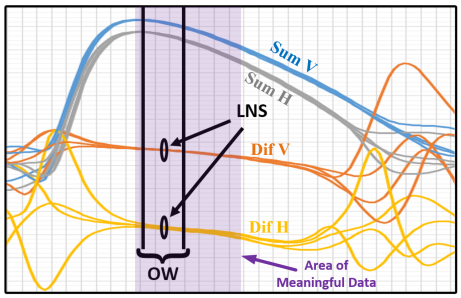

Figure 5: Example of LNS and OW.

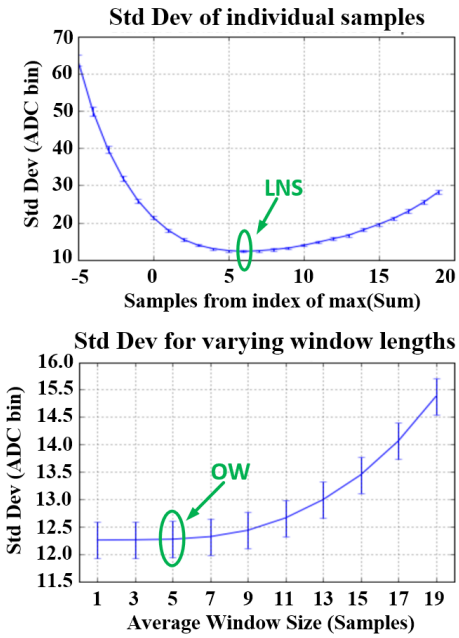

Figure 6: Standard deviation of the individual samples showing the LNS (top) and standard deviation for varying window lengths showing the OW (bottom).

PERFORMANCE

In order to evaluate the performance of the system, qualification studies in terms of resolution, linearity and dynamic range have been carried out. The details of these studies are presented in the following sections.

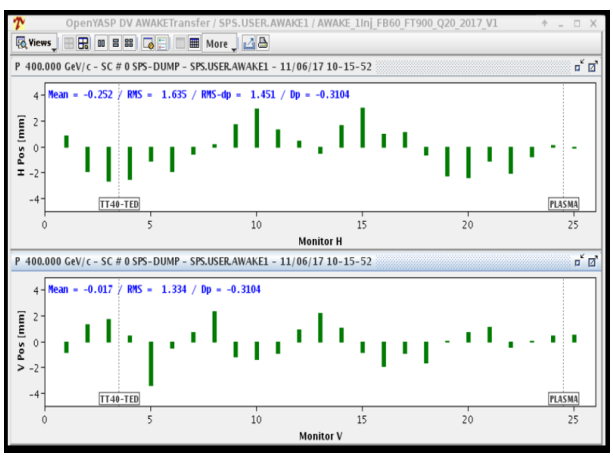

Figure 7: Trajectory measurements as shown by the AWAKE BPM software. Each individual bar represents the position from one BPM.

Resolution (Noise)

For qualifying the resolution of the system, more than 2000 acquisitions of the reference bunch trajectory were analysed. The standard deviation of these trajectories include both the shot-to-shot jitter of the extracted beam and the electronic noise of the system. The acquired trajectories, as well as the standard deviation for each plane of each BPM, are plotted in Figures 8 and 9. It is clearly seen that there is a large difference between the values for the horizontal and vertical plane clearly pointing to beam reproducibility issues as electronics is the same for both planes.

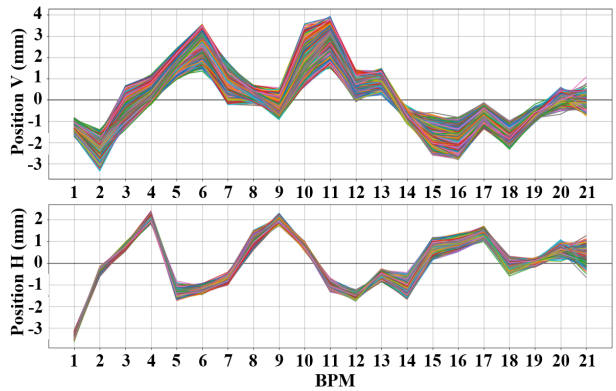

Figure 8: Proton beam trajectories.

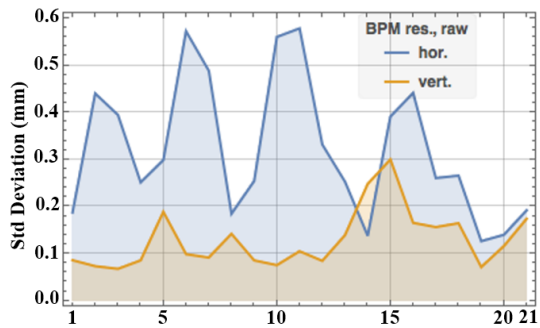

Figure 9: Standard deviation in horizontal and vertical planes.

As a consequence, to estimate the electronic resolution, it was necessary to remove the correlated beam motion effects from the measurement. This was performed using Singular Value Decomposition (SVD). Typically this correlated beam motion in a linac/transport-line can be decomposed into four dominant "modes", those related to: beam position (x), beam angle (x'), beam energy and beam phase. In this case, 2058 synchronous beam measurements (p) of 21 BPM (m) were arranged in a matrix B(p × m). This matrix was then de-composed by applying the SVD technique. The correlated beam motion can be subtracted from the measurement by setting the 4 highest eigenvalues (modes) in the decomposed matrix to zero and recalculating B. This cor-

ISBN: 978-3-95450-192-2 doi:10.18429/JACoW-IBIC2017-TUPCF06

relation is illustrated in Figure 10, while the measurements with this correlated beam motion subtracted are presented in Figure 11. The actual resolution of the electronic acquisition system can then be estimated to be between 50–80 µm for most BPMs.

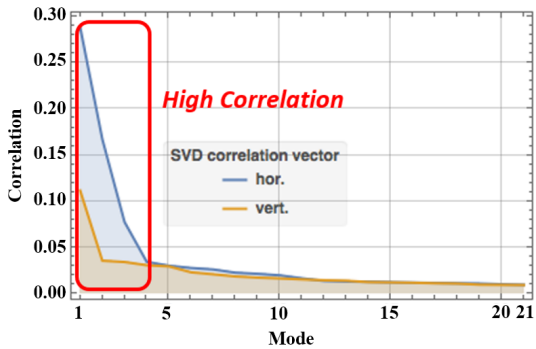

Figure 10: SVD modes correlation.

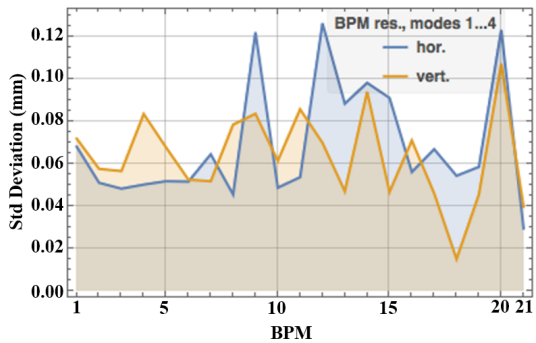

Figure 11: Standard deviation in horizontal and vertical planes after SVD.

Linearity

The linearity of the system has been qualified by measuring orthogonal displacements from -4mm to 4mm with a granularity of 1mm using a single BPM with no non-linear elements between it and the corrector used to produce the displacement. An average of 50 acquisitions per orthogonal displacement was used. To minimize the impact from beam jitter all the measurement were acquired in the vertical plane. The linearity error was measured to be lower than 15 µm over the range of the measurement, well within specification (see Figure 12).

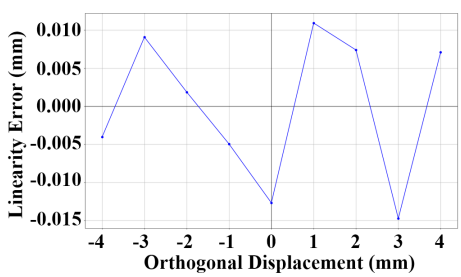

Figure 12: Linearity error.

Dynamic Range

As previously mentioned, the AWAKE proton bunch has a nominal intensity of $3.5e^{11}$ protons, but can also have an intensity as low as $5e^{9}$ protons (pilot bunches), typically for set-up purposes. The minimum dynamic range of the BPM system must therefore be ~40 dB. A comparison of the trajectories of nominal and pilot bunches (see Fig. 13) demonstrated that the dynamic range of the system is adequate, with measurements at both intensities giving similar reproducibility, indicating that shot-to-shot trajectory variation remains the dominant source of this non-reproducibility. The resolution of the BPM system for pilot bunches is therefore much better than the reproducibility of the extracted trajectory.

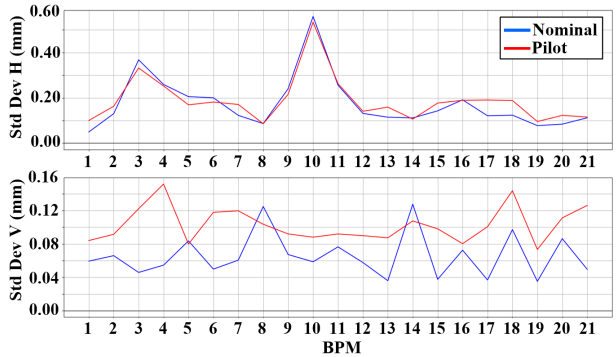

Figure 13: Comparison of the reproducibility of the BPM readings for nominal and pilot bunch trajectories.

CONCLUSION

The Advanced Proton Driven Plasma Wakefield Acceleration Experiment (AWAKE), based at CERN, explores the use of a proton driven plasma wake-field to accelerate electrons up to multi-GeV energy range over short distances (~10 m). A BPM system for the AWAKE proton beam line has been designed, implemented and successfully commissioned. The performance of this proton BPM system, based on logarithmic amplifiers, has been successfully qualified with beam and shown to have a single bunch, single pass resolution better than 80 µm, a linearity better than 0.4% in the area of interest and a dynamic range of 40 dB.

ACKNOWLEDGMENT

The authors would like to thank S. Mazzoni, V. Kain, S. J. Gessner, C. Bracco and the other members of the AWAKE team for their help with the performance studies of the AWAKE proton BPM system.

REFERENCES

[1] A. Caldwell *et al.*, "Path to AWAKE: Evolution of the concept", *Nucl. Instr. Meth.* A, vol. 829, pp. 3-16, 2016.

[2] A. Boccardi *et al.*, "A Modular Approach to Acquisition Systems for Future CERN Beam Instrumentation Developments", in *Proc of ICALEPCS'15*, Melbourne, Australia (2015).

ISBN: 978-3-95450-192-2 doi:10.18429/JACoW-IBIC2017-TUPCF07

THE DESIGN IMPROVEMENT OF TRANSVERSE STRIPLINE KICKERS IN TPS STORAGE RING

P.J. Chou†, C.K. Chan, C.C. Chang, K.T. Hsu, K.H. Hu, C.K. Kuan and I.C. Sheng
National Synchrotron Radiation Research Center, Hsinchu 30076, Taiwan

Abstract

An improved design of horizontal stripline kicker for transverse feedback system has been replaced in January 2017. A rapid surge of vacuum pressure near the old horizontal kicker was observed when we tested the high current operation in TPS storage ring in April 2016. A burned vacuum feedthrough of the horizontal kicker was discovered during a maintenance shutdown. The improved design has reduced the reflection of the driving power from horizontal feedback system and the beam induced RF heating. Based on the experience learned from this improved design of horizontal stripline kicker, we also work out the improved design for the vertical kickers as well. The major modifications of the improved designs for both the horizontal and the vertical stripline kickers are described. The results of RF simulation performed with the electromagnetic code GdfidL are also reported.

INTRODUCTION

The designs of both the horizontal and the vertical stripline kickers for bunched beam feedback in Taiwan Photon Source (TPS) were adapted from the SLS/ALBA design [1, 2]. The type-N vacuum feedthroughs of horizontal kicker were found damaged due to over heating during high current operation in 2016. The original horizontal kicker was replaced by an improved design in January 2017. Details of the design improvement of horizontal stripline kicker have been reported [3]. Since the same type of vacuum feedthroughs are used in the vertical kickers, there is a concern whether we will encounter similar problems as the original horizontal kicker did or not. To ensure a reliable operation at the designed beam current 500 mA in the future, we embark on the design improvement for the vertical stripline kicker.

From the beam experiments conducted with the improved horizontal kicker, we discover that the beam induced signal is the dominant source which could damage the drive amplifier connected at the downstream ports. The priority is given to the matching of even mode impedance when we improve the design of vertical kicker. The same design concept that is effective in greatly reducing the loss factor of horizontal kicker [3] is also applied to the vertical kicker. A 3-D electromagnetic code GdfidL [4] is used for the simulation studies of this improved vertical kicker.

† pjchou@nsrrc.org.tw

DESIGN IMPROVEMENT

Since there is limited space available for the installation of transverse kickers in TPS storage ring, there is no taper section in the design of stripline kickers. The transverse profile of kicker electrodes should be flushed to the inner surface of racetrack beam pipe in order to reduce the broadband impedance. A section view of the existing vertical stripline kicker is shown in Fig. 1. The width of electrodes is 42.7 mm, the length is 280 mm and the cross section of racetrack beam pipe is 68 mm x 20 mm.

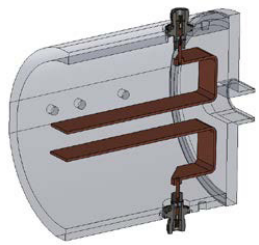

Figure 1: The section view of the existing vertical stripline kickers in TPS storage ring. The longitudinal gap between the electrodes and the end plate is 10 mm.

Impedance Matching

To prevent the beam induced signal propagating towards the downstream ports, the even mode impedance Z_{even} should be matched to the terminating line impedance (typically 50Ω). For maximum transmission of signal coming from the drive amplifier at the downstream ports, the necessary condition given by the theory of coupled transmission lines should be satisfied [5, 6]:

$$Z_{even}Z_{odd} = Z_0^2 \quad (1)$$

where Z_0 is the terminating line impedance.

For beam pipes of small cross section, it is difficult to satisfy both conditions for a good impedance matching of stripline electrodes. We choose to match the even mode impedance in order to minimize the beam induced signal at the downstream ports where the drive amplifier of feedback system is connected to.

The geometry of proposed improvement of vertical stripline kicker is shown in Fig. 2. The stripline electrodes are flushed to the inner surface of racetrack beam pipe for the reduction of broadband impedance. The summary of mode impedance for the existing vertical stripline kicker and the proposed improvement is listed in Table 1. The distribution of electrical fields of the odd mode of the improved design is shown in Fig. 3. The comparison of simulated results of the time domain reflectometry (TDR) for the existing and the improved vertical kicker is shown in Fig. 4.

ISBN: 978-3-95450-192-2 doi:10.18429/JACoW-IBIC2017-TUPCF07

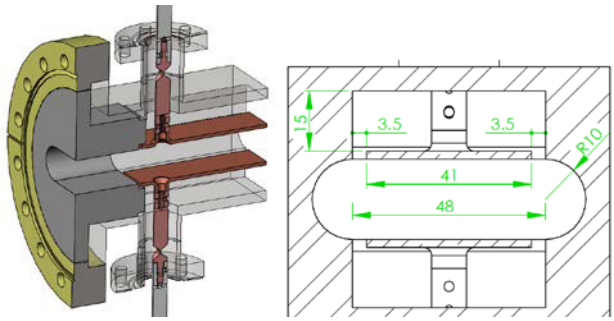

Figure 2: A 3-D section view (left) and 2-D cross section drawing of the improved vertical stripline kicker (right). The dimensions are in units of [mm].

Table 1: The Summary of Mode Impedance for the Existing Vertical Kicker and the Proposed Improvement

	Existing kicker	Improved design
Z_{even} [Ω]	150.55	50.08
Z_{odd} [Ω]	49.92	34.27
Z_{even}* Z_{odd}	7515	1716

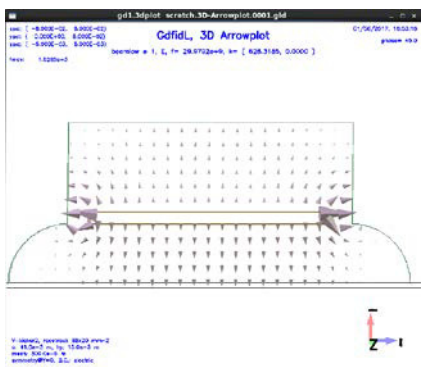

Figure 3: The simulated pattern of electrical fields of the odd mode in the improved design. Only half the structure is depicted.

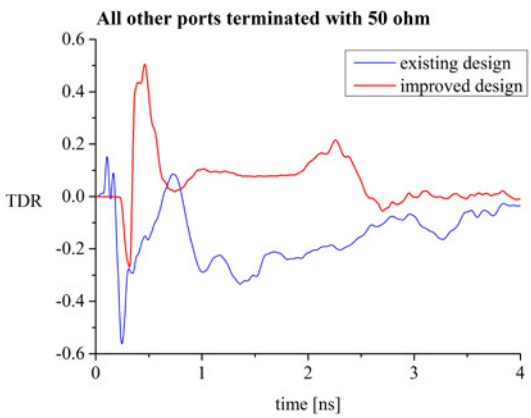

Figure 4: The simulated results of TDR for the existing (blue) and the improved vertical kicker (red). All other three ports are terminated with 50 Ω in the simulations.

The simulated spectra of S_{11} parameter for the existing vertical kicker and the improved design are shown in Fig. 5. As shown in Fig. 4 and Fig. 5, the reflection of driving signal from the power amplifier at the downstream port is much reduced in the improved design. The improved design of vertical kicker has a better impedance matching than the existing one in present user operation.

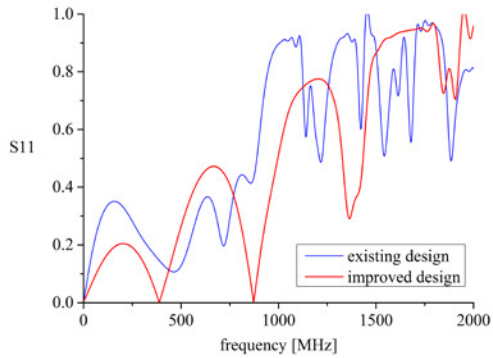

Figure 5: The simulated spectra of S_{11} parameter for the existing vertical kicker (blue) and the improved design (red).

Reduction of Loss Factor of the Kicker Module

One of the design objectives is to achieve a significant reduction of loss factor of the entire kicker module. A rectangular indentation of depth 4 mm is machined on the end plate to shield the edge of stripline electrode as depicted in Fig. 6. The length of stripline electrode is 276 mm. The 7/8 EIA vacuum feedthroughs made by Kyocera are adopted for this improved design.

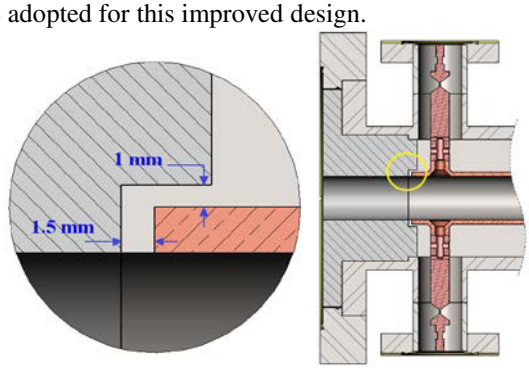

Figure 6: The design of end plate used to reduce the loss factor of kicker module (right). The edge of stripline electrode is shielded by a rectangular indentation of depth 4 mm on the end plate (left).

The calculated loss factors for the existing design and the improved design are listed in Table 2. There are 864 RF buckets in TPS storage ring. In routine operation the storage ring is typically filled with 600 bunches. The average power dissipated by particle beams at 500 mA total current is estimated approximately by the following expression:

$$\langle P \rangle \approx \frac{\Delta E}{T_b} \qquad (2)$$

ISBN: 978-3-95450-192-2 doi:10.18429/JACoW-IBIC2017-TUPCF07

where ΔE is the parasitic energy loss per bunch, and T_b is the RF period. The loss factor of the improved design is a factor of 4.5 smaller than the existing vertical kicker.

Table 2: The Calculated Loss Factor and Average Power Dissipated by Particle Beams at 500 mA Total Current (rms bunch length= 4.5 mm)

	Loss factor [V/pC]	Dissipated Power [W]
Old design	1.070	1108.6
Improved design	0.238	246.6

The trapped longitudinal higher-order-mode (HOM) is analyzed by GdfidL using both the time-domain solver and the eigenmode solver with absorbing boundary conditions. The longitudinal impedance of the entire kicker module of the improved design is shown in Fig. 7. The RF parameters of dominant resonant modes calculated by GdfidL are list in Table 3. The longitudinal coupled bunch instabilities driven by these resonant modes are considered for total beam current 500 mA. The calculated growth time using formulas of the theory of bunched beam instabilities [7] for total beam current 500 mA is listed in Table 3. The longitudinal radiation damping time of TPS storage ring is 6.08 ms. The improved design of vertical kicker will not cause longitudinal coupled bunch instabilities at 500 mA.

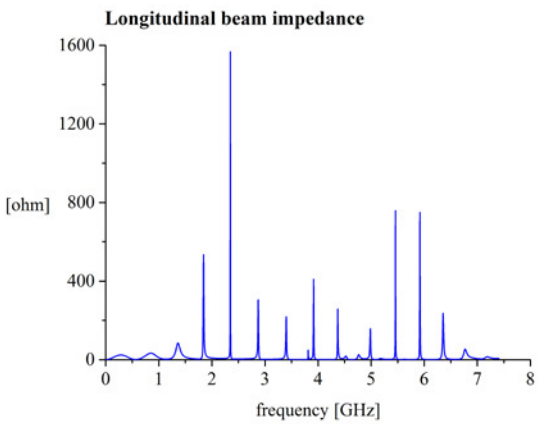

Figure 7: The longitudinal impedance simulated by GdfidL for the entire kicker module of improved design. The spectral resolution is 0.4 MHz.

Table 3: RF Parameters of Dominant Resonant Modes Calculated by GdfidL and the Estimated Instability Growth Time

f [GHz]	R/Q [Ω]	Q_{total}	Growth time [ms] at 500 mA total current
2.348	1.879	834	78.1
5.918	0.507	1480	83.7

Calculation of Transverse Shunt Impedance

We use the results of analytical theory [8] and simulations of GdfidL to estimate the transverse shunt impedance of vertical kicker. The relation between the longitudinal beam impedance $Z_{\parallel}$ and the longitudinal shunt impedance $R_{\parallel}$ of a rectangular stripline kicker with a matched load is [8]

$$Z_{\parallel} = \frac{R_{\parallel}}{4} \tag{3}$$

For devices like a cylindrical resistive wall pick/kicker, the following relations hold [8]

$$R_{\perp} = R_{\parallel}(1/kb)^2 \tag{4}$$

$$Z_{\perp} = \frac{Z_{\parallel}}{kb^2} \tag{5}$$

where k is the wave number, $R_{\perp}$ the transverse shunt impedance, $Z_{\perp}$ the transverse beam impedance, and b is the radius of beam pipe. If we approximate the vertical gap of a racetrack beam pipe as the diameter of a cylindrical pipe, we can get an approximate relation between the transverse shunt impedace and the transverse beam impedance as [9]

$$R_{\perp} = \frac{4\,\mathrm{Re}(Z_{\perp})}{k} \tag{6}$$

One can simulate the transverse beam impedance of the entire kicker module with GdfidL and deduce the transverse shunt impedance by using Eq. (6). This is the method-1 we used to calculate the transverse shunt impedance.

Another approach to obtain the transverse shunt impedance is to calculate the transverse beam voltage $V_{\perp}$ or kick voltage exerted on the particle beam by the feedback system for a given input power P_{in}. Then, the shunt impedance is given by the definition $R_{\perp} = V_{\perp}^2 / 2P_{in}$. The transverse beam voltage is defined as [8]

$$V_{\perp} = \frac{\beta c \Delta p_{\perp}}{e} \tag{7}$$

For an ultra-relativistic particle beam interacting with the electromagnetic fields, the transverse beam voltage becomes

$$V_{\perp} = \int \{\vec{E}_{\perp}(\vec{r},t) + [\vec{c} \times \vec{B}(\vec{r},t)]_{\perp}\} ds \tag{8}$$

In the simulation code GdfidL, the transverse wakepotential is calculated from the simulated longitudinal wakepotential by using the Panofsky-Wenzel theorem [4],

$$W_{\perp}(x,y,z) = \int_{-\infty}^{z} \nabla_{\perp} W_{\parallel}(x,y,\tau) d\tau \tag{9}$$

The transverse wakepotential defined in GdfidL has the units of [V]. For ultra-relativistic particle beam interacting with the electromagnetic fields, the expression of transverse wakepotential as defined in GdfidL becomes the one given by Eq. (8). One can excite the downstream ports of stripline kicker and calculate the transverse wakepotential with a very small drive charge in GdfidL

ISBN: 978-3-95450-192-2 doi:10.18429/JACoW-IBIC2017-TUPCF07

simulations. As long as the drive charge used in GdfidL simulations is small enough, the calculated transverse wakepotential is only contributed by the electromagnetic fields excited by the input power in downstream ports. This is the method-2 we used to calculate the transverse shunt impedance. We excite each downstream port of vertical kicker by 0.5 W (total input power of 1 W) and calculate the transverse wakepotential with a small drive charge 10^{-22} C. The amplitude of transverse wakepotential is the amplitude of transverse beam voltage. The transverse shunt impedance is calculated from the expression $V_\perp^2/2$ [4]. A comparison of transverse shunt impedances calculated by the analytical theory, method-1, and method-2 for the improved design is shown in Fig. 8.

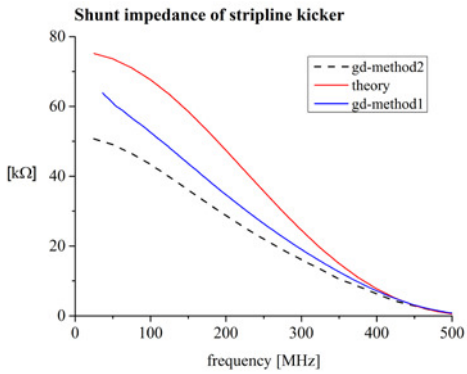

Figure 8: The transverse shunt impedance of the improved design calculated by the analytical theory and GdfidL simulations.

The effects of electromagnetic fields excited in a transverse kicker is to cause an angular kick to the beam trajectory,

$$\Delta y' = \int F_\perp ds \Big/ (e\upsilon B_0\rho) = V_\perp/(cB_0\rho) \qquad (10)$$

where $B_0\rho$ is the magnetic rigidity of particle beam. Using the definition of transverse shunt impedance, the kick strength per turn of the feedback system is rewritten as

$$\Delta y' = \frac{\sqrt{2P_{in}R_\perp}}{cB_0\rho} \qquad (11)$$

When the damping limit of the transverse feedback is reached, the beam induced voltage/turn equals to the maximum transverse beam voltage (kick voltage)/turn [10]. The maximum input power required for a transverse kicker at its damping limit is given by [10]

$$P_{\max} = |V_b|^2/2R_\perp \qquad (12)$$

where $V_b = I_0 \Delta y Z_{y,eff}$.

The following parameters are used: chromaticity= 2, I_0= 500 mA, Δy= 3 mm, fractional vertical tune q_y= 0.24, and all phase-I insertion devices (IDs) in TPS storage ring. The effective vertical impedance due to resistive wall at the strongest unstable mode (1-q_y) is $Z_{y,eff}$ = 3.95 MΩ/m. If we drive the improved vertical kicker with a maximum input power 500 W, the kick voltage/turn, the kick strength/turn, and the maximum input power required at the damping limit of kicker are listed in Table 4.

Table 4: The Calculated Vertical Kick Voltage/Turn and the Kick Strength/Turn for an Input Power of 500 W

	Theory	Method-1	Method-2
$R_\perp$ [kΩ]	75	65	51
$P_{\max}$ [W]	234	270	344
$V_\perp$ [V]/turn	8660	8062	7141
$\Delta y'$ [μrad]/turn	2.88	2.68	2.37

SUMMARY

We have improved the design of horizontal and vertical stripline kickers. The loss factor is reduced by a factor of 3.37 for the horizontal kicker and 4.50 for the vertical one. The simulation reveals that trapped longitudinal resonant modes in both the horizontal and vertical stripline kickers will not cause the longitudinal coupled bunch instabilities at the designed beam current 500 mA. The emphasis of impedance matching for the improved vertical kicker is placed on the matching of even mode impedance to the impedance of terminating lines (50 Ω). The transverse shunt impedance is calculated from GdfidL simulations using two different methods. The estimated kick strength per turn of the improved vertical kicker indicates the kick strength is sufficient to damp the resistive wall instabilities with all phase-I IDs at 500 mA.

ACKNOWLEDGEMENT

The authors would like to thank W. Bruns for his help on GdfidL simulations. We also thank A. Blednykh for helpful discussions.

REFERENCES

[1] M. Dehler *et al.*, in *Proc. EPAC2000*, pp. 1894-1896.

[2] U. Iriso, T.F. Günzel, and F. Pérez, in *Proc. DIPAC2009*, pp. 86-88.

[3] P.J. Chou *et al.*, in *Proc. IPAC2017*, pp. 1961-1963.

[4] W. Bruns, *The GdfidL Electromagnetic Field Simulator*, http://www.gdfidl.de

[5] R.G. Brown, R.A. Sharpe, W.L. Hughes, and R.E. Post, "Matrix representation of transmission-line circuits", in *Lines, Waves, and Antennas*, 2nd ed. New York, NY, USA: Wiley, 1973, pp. 136-146.

[6] D.M. Pozar, "Power dividers and directional couplers", in *Microwave Engineering*, 4th ed. New York, NY, USA: Wiley, 2012, pp. 317-379.

[7] T. Suzuki, "Effective impedance", in *Handbook of Accelerator Physics and Engineering*, 2nd ed., A.W. Chao, K.H. Mess, M. Tigner, and F. Zimmermann, Eds., Singapore: World Scientific, 2013, pp. 262-263.

[8] D.A. Goldberg and G.R. Lambertson, "Dynamic devices: a primer on pickups and kickers", in *AIP Conf. Proc. No.249*, M. Month & M. Dienes, Eds. New York, NY, USA: AIP, 1992, pp. 537-600.

[9] A. Blednykh, W. Cheng, and S. Krinsky in *Proc. PAC2013*, pp. 895-897.

[10] J.M. Byrd and J.N. Corlett, in *Proc. PAC1993*, pp. 3318-3320.

ISBN: 978-3-95450-192-2 doi:10.18429/JACoW-IBIC2017-TUPCF08

BEAM STABILITY DIAGNOSTICS WITH X-RAY BEAM POSITION MONITOR IN THE TAIWAN PHOTON SOURCE

C. H. Huang†, P. C. Chiu, C. Y. Wu, Y. Z Lin, Y. M. Hsiao, J. Y. Chuang, Y. S. Cheng, C. Y. Liao, C. K. Kuan, K. H. Hu, K. T. Hsu
NSRRC, Hsinchu 30076, Taiwan

Abstract

To monitor the stability of photon beams, X-ray beam position monitors (BPMs) with quadrant PIN photodiodes or blades are installed in the beam lines and front ends. Although there are about 200 electron BPMs installed in the storage ring, the beam-line managers or users prefer X-ray BPMs to monitor beam stability. Among the beam lines, different electronics are used to acquire data at various sampling rates. A method to calculate the beam intensity fluctuation within different frequency ranges is described in this report. The results of calculations are shown in the control system and saved in the archive system thus helping to monitor and analyse beam quality on- and off-line. Initial experiences with this system will be discussed in this report.

INTRODUCTION

An X-ray beam position monitor (BPM) is a device used to measure the centroid of the synchrotron radiation. Many devices have been used to detect the beam position such as: fluorescent screens, split plate ionization chamber, blade-type BPM, quadrant PIN photodiodes BPMs (QBPMs) and so on. For continuous use, non-destructive blade-type BPMs and QBPMs are installed in the front ends and beam lines of the Taiwan Photon Source (TPS) to monitor the beam position and density fluctuation.

The first blade-type BPM is used in the front end of an insertion device (ID) reported by Mortazavi et al. in 1986. Shu et al. at the Advanced Photon Source used chemical vapour deposition (CVD) diamond as the blade material with metal (Au, Pt and Ti) coating for good photoemission [1]. This blade-type BPM provides submicron resolution at high power density absorption capability. The heat load in a beam line becomes greatly reduced downstream of the double crystal monochromator making the QBPM a good candidate to monitor the beam position due to its reduced sensitivity to beam profile [2].

In the TPS, two blade-type BPMs are installed in each front end with one being located at the entrance to the front end and the other downstream of the fast closing valve as shown in Fig. 1. Numbers and types of X-ray BPMs are different for most beam lines, due to different consideration.

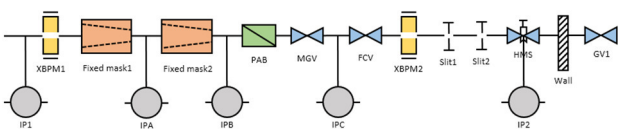

Figure 1: Layout out of front-end instrumentation.

† huang.james@nsrrc.org.tw

In this paper, the data acquisition electronics for X-ray BPMs is introduced first, followed by a discussion of beam position observations with X-ray BPMs. In order to define a reference to quantify beam stability, we discuss this issue in the third part.

SYSTEM SETUP

For the X-ray BPMs (XBPM) in the front end, we use two kinds of electronics to acquire and evaluate the beam position with the old and new version of the Libera Photon system. These devices provide several acquisition types for different sampling rates. An input/output controller (IOC), based on the experimental physics and industrial control system (EPICS), is embedded in these devices and the acquisition data are transferred to the control network through process variables (PVs). For example, the slow acquisition (SA) data is 10/25 Hz and the fast acquisition data is 160 Hz/5 kHz for the old/new version electronics. The layout of the XBPM in the front end is shown in the Fig. 2. For the XBPMs in the beam line, there are three types of electronics in use now. One uses the FMB Oxford F-460 to convert the current to voltage and read the voltage with a NI-9220. For this type of electronics, the data can only be read by the local computer and the sampling rate is 2 kHz now. Another type of electronics is a home-made device with 0.5 Hz update rate and its data are published in the control system while fast data can only be acquired by local instruments now. A third type is used with a new Libera Photon system. The display of the position with various sampling rates is done by the extensible display manager (EDM) and Matlab, shown in Fig. 3. The spectrum of the beam motion can also be shown in the control console as shown in Fig. 4.

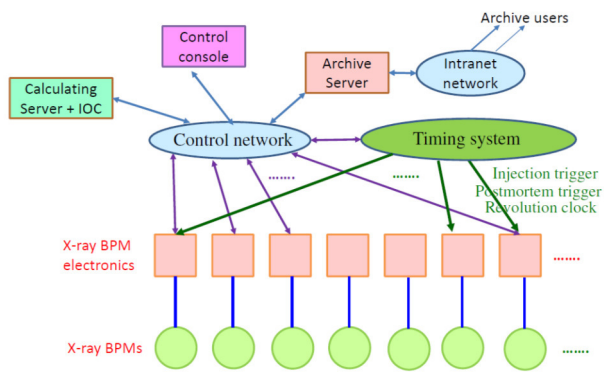

Figure 2: Layout of the XBPM electronics setup in the front end.

ISBN: 978-3-95450-192-2 doi:10.18429/JACoW-IBIC2017-TUPCF08

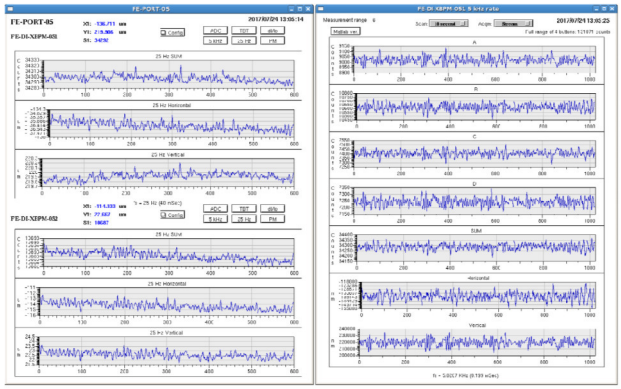

Figure 3: Graphical user interface for beam position monitoring produced by the extensible display manager (EDM).

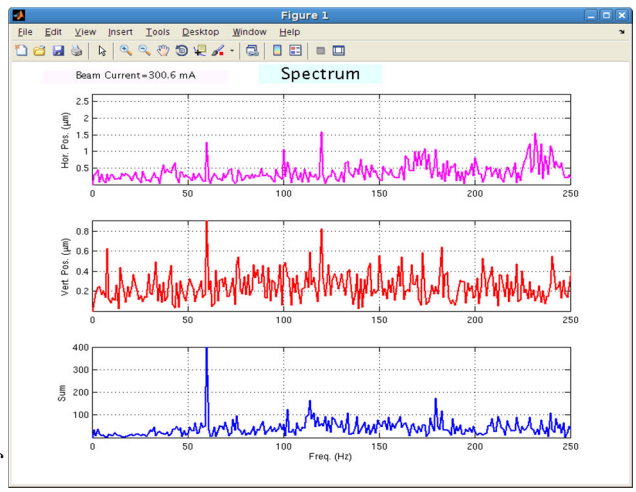

Figure 4: Beam position spectrum as observed at the TPS-05A QBPM2.

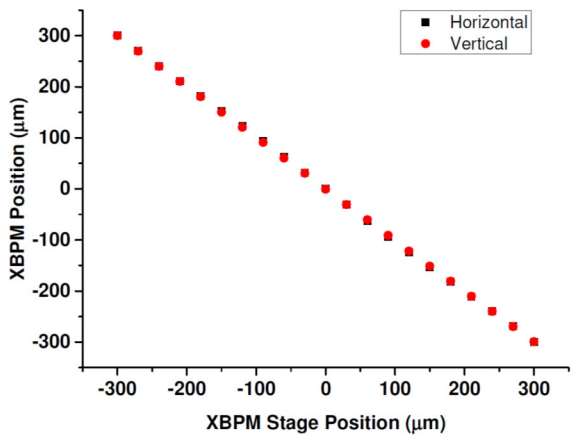

Figure 5: Photon beam position vs. stage position in the first XBPM of front end 25 for k_x = 6.48 and k_y = 2.61 mm.

BEAM POSITION OBSERVATION

Before application of the XBPM to get the beam position, the calibration factors k_x/k_y must be determined. At first, the XBPM stage is moved to adjust the reading counts for all four blades to be almost equal. Then the stage is moved alone in the horizontal and vertical direction for +/- 0.3 mm to determine the calibration factor [3]. This range is compatible with the in-vacuum undulator (IU) gap of gap of 7 mm. Figure 5 shows the beam position readings vs. stage position in the first XBPM of the front end 25 (XBPM25-1) when k_x = 6.48 and k_y = 2.61 mm. The calibration factor varies with gap as shown in Fig. 6. For the second XBPM in the front end, both XBPM position readings indicate a horizontal and vertical movement by similar magnitudes while the stage is moved in the horizontal direction only. As the stage is moved along the vertical direction, the position coupling is much smaller (~ 10 %). More studies are required to correct this unexpected behaviour in the second XBPM.

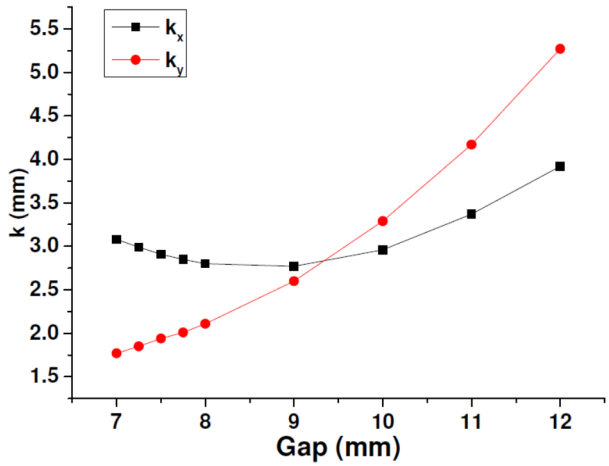

Figure 6: Calibration factor versus gap in the first XBPM of the front end 23.

In order to correlate the photon beam motion relative to the electron beam motion, the spectrum of the electron beam motion upstream of the front end 05 is recorded. The photon beam motion detected by the first XBPM in the front end 05 (XBPM05-1) and by the QBPM in the beam line 05A is also shown in Fig. 7 showing that the spectrum of the electron beam motion is similar to the photon beam motion at XBPM05-1 but the photon motion at XBPM05-1 is higher than the electron motion. For the QBPM2 at BL05A, several peaks at the mains frequency and its harmonics can be observed which do not appear in the electron BPM and XBPM05-1. These peaks are generated by electronics noise which may be due to contamination on the beam line side and need to be clarified and corrected.

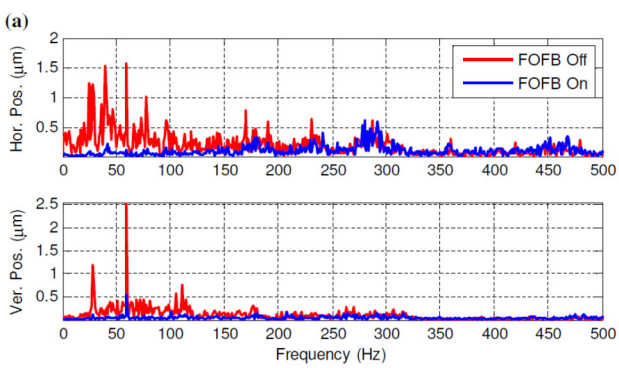

Figure 7a

ISBN: 978-3-95450-192-2 doi:10.18429/JACoW-IBIC2017-TUPCF08

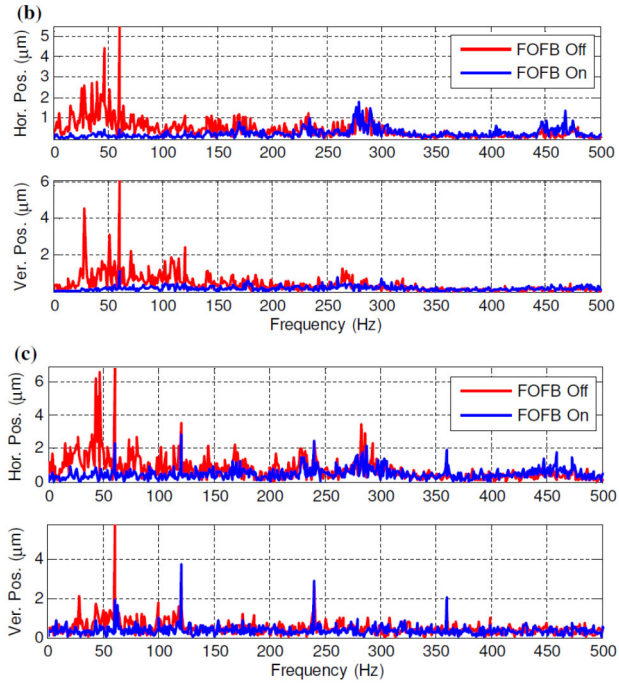

Figure 7: The spectrum of electron/photon beam motion (a) in the e-BPM027 installed upstream of front-end 05; (b) in the first XBPM of the front end 05; (c) in the QBPM2 of the beam line 05A.

PHOTON FLUX STABILITY MONITOR

For statistical data acquisition of beam stability during routine operation, the relative beam intensity fluctuation ($\Delta I_0/I_0$) is calculated by a dedicated sever using the sum signs from the four blades/diodes. As mentioned before, the beam position information obtained by the three types of beam position electronics can be obtained in the control network at various sampling rates. Three programs are used to calculate the $\Delta I_0/I_0$ with Matlab and to publish the results with the soft PVs of the pre-established IOC in the server. Some of the calculated results are saved in the archive server and the saved data can be acquired through the Intranet as shown in Fig. 1.

Because one program is used to deal with data acquisition from several devices, a program must be executed to check which devices are on-line. For the home-made XBPM electronics, the update rate is only 0.5 Hz. Therefore, the I_0 and ΔI_0 is defined as

$$I_0 = \sum_{i=1}^{N} s_i/N \quad (1)$$

$$\Delta I_0 = \sum_{i=1}^{N} \sqrt{(s_i - I_0)^2/N}, \quad (2)$$

where s_i is the ith sum signal. When we take N=10, the update rate of $\Delta I_0/I_0$ would be 20 seconds as shown in Fig. 8. For the other XBPM electronics, the sampling rates are much higher (160 Hz/5 kHz), the data can be acquired during one or several seconds and the power spectral density would be

$$PSD(f) = 2D(f)D^*(f)/T. \quad (3)$$

Here, $S(f)$ is the Fourier transform of the signal and T is the duration of the signal. The integrated root-mean-square intensity variation (ΔI_0) from frequency f_1 to f_2 would be

$$\Delta I_0 = \sqrt{\int_{f_1}^{f_2} PSD(f)df}. \quad (4)$$

The $\Delta I_0/I_0$ is calculated from 0-10 Hz, 0-50 Hz and 0-100 Hz for comparison and shown in Fig. 9. Note that the date does not update during injection.

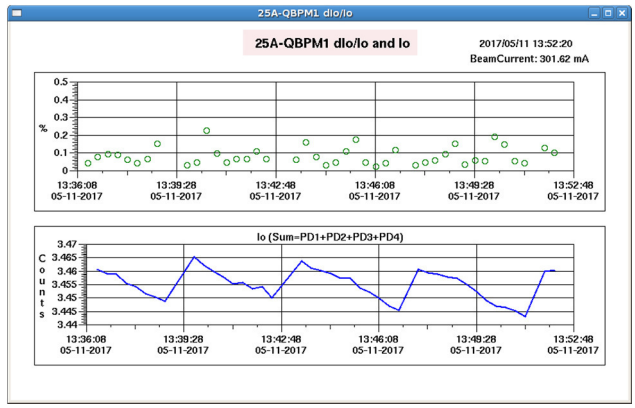

Figure 8: $\Delta I_0/I_0$ and I_0 calculated from the data of the home-made reader with 20 seconds updated rate.

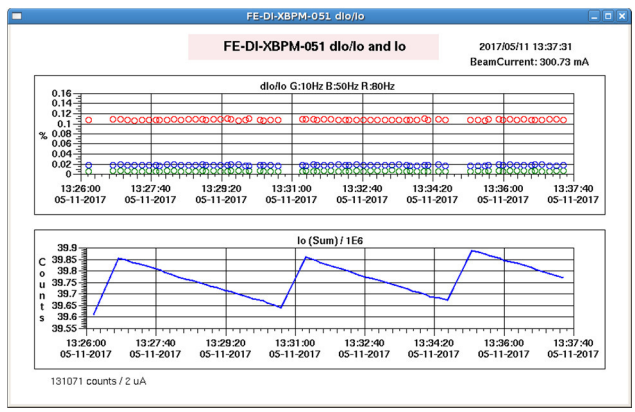

Figure 9: Graphical user interface of $\Delta I_0/I_0$ in the first XBPM in front end 05.

SUMMARY

There are two blade-type XBPMs installed in each front end to monitor the beam position and flux variation. Several types of XBPMs are installed in the beam line for different design considerations. Four types of electronics are used to acquire data. Most can be integrated into the control system to display the information in the control room. In order to monitor beam stability, dedicated programs are used to determine relative intensity fluctuation in several frequency rages to provide a reference for beam stability monitoring in each beam line. This integration provides on-line information on the photon stability to determine beam quality in each beam line.

REFERENCES

[1] D. Shu, *et al.*, "Development of an x-ray beam position monitor for TPS EPU beam line front ends", *J. Phys.: Conf.*, vol. 425, pp. 042003, 2013.

ISBN: 978-3-95450-192-2 doi:10.18429/JACoW-IBIC2017-TUPCF08

[2] R. W. Alkire, *et al.*, "Design of a vacuum-compatible high-precision monochromatic beam-position monitor for use with synchrotron radiation from 5 to 25 Kev", J. Synchrotron Rad. Vol. 7, pp.61-68, 2000.
[3] B. X. Yang, *et al.*, "Design and development for the next generation X-ray beam position monitor system at the APS", in *Proc. IPAC'15*, Richmond, Virginia, USA, paper MOPWI014, pp. 1175–1177.

ISBN: 978-3-95450-192-2 doi:10.18429/JACoW-IBIC2017-TUPCF09

TURN-BY-TURN TIMING SYSTEMS FOR SuperKEKB DAMPING RINGPOSITION MONITORS

Makoto Tobiyama* and Hitomi Ikeda,
KEK Accelerator Laboratory, 1-1 Oho, Tsukuba 305-0801, Japan
Graduate University for Advanced Studies (SOKENDAI), 1-1, Oho, Tsukuba 305-0801, Japan

Abstract

Turn-by-turn timing systems for SuperKEKB beam position monitors using Xilinx Zynq FPGA have been developed. The RF frequency divider with external synchronization circuit creates a fiducial signal synchronized to the accurate injection timing from the injector event system. As the Log-Ratio turn-by-turn monitors (Digitex 18k11) need clock timing deviation to the beam signal within 8 ns, the cable length from the BPM heads to the detectors have been adjusted with the maximum deviation less than 1 ns using TDR. The time delay to adjust each cable lengths and the BPM placements have been created by using 32-ch RF timing delay with the step of 2 ns. The start trigger to the 18k11 has been made by using the digital delay (SRS DG645) from the injection trigger. The measured performance of the frequency divider, the 32-ch RF timing delay and start trigger system will be shown.

INTRODUCTION

The KEKB collider has been upgraded to the SuperKEKB collider with a final target of 40 times higher luminosity than that of KEKB. It consists of a 7 GeV high energy ring (HER, electrons) and a 4 GeV low energy ring (LER, positrons). About 2500 bunches per ring will be stored at total beam currents of 2.6 A (HER) and 3.6 A (LER) in the final design goal.

Due to strong focus at the interaction point, the dynamic apertures of both rings will be spoiled with the squeezing of the beam. To cure the LER injection efficiency and to reduce the beam noise coming from injected beam, the positron damping ring (DR) has been constructed in the linac with energy of 1.1 GeV after the production target, to damp the emittance of the positron beam. Table 1 shows the main parameters of the SuperKEKB damping ring.

Since the beam circulating time in the normal operation is short, from 40 ms to 200 ms depending on the injection repetition, and since the bucket filling pattern and injected bucket changes due to the bucket selection system to fill the beam as uniform as possible at LER, we have decided to use turn-by-turn beam position detector with Log-Ratio detection scheme using Digitex 18K11 [1]. As it is the time-domain detection system, we need to prepare following timing signals:

- Position data acquisition start trigger with good time relationship from the injected beam.
- Master clock timing for the ADC of 18K11 (Fiducial, 2.21 MHz) synchronized to the measuring bunch.
- Delayed timing to compensate the BPM placements in the ring and cable delays for each BPM.

To generate such timing signals, we have developed following timing generation circuits:

- RF frequency divider with external synchronization circuit using Zynq FPGA.
- Multi-channel (32-channels) digital delay working with the RF timing using Zynq FPGA.
- Start trigger generator with fine digital delay starting from the external signal (injection timing) under the software control (enable /disable start).

The measured performance of the systems such as the jitter of the timing will be shown in this paper.

Table 1: Major Parameters of SuperKEKB Rings

	DR
Energy (GeV)	1.1
Circumference(m)	135.5
Max. Beam current (mA)	70.8
Max. Number of bunches	4
Bunch separation (ns)	>96.3
Natural bunch length (mm)	6.5
RF frequency (MHz)	508.887
Harmonic number (h)	230
T. rad. damping time (ms)	11
x-y coupling (%)	5
Beam emittance at Inj (nm)	1700
Equilibrium emittance (nm)	41.4/2.07
Max. injection rate (Hz)	50
Number of BPMs	83
Number of BPM stations	4

BEAM POSITION MONITORS

Since the storage time of a beam in DR is normally short, less than 200 ms, we have constructed the turn-by-turn based beam position monitor systems with Log-Ratio detector (Digitex 18K11). From the measured narrow pulse response of 18K11 detector shown in Fig. 1, we have adjusted the timing deviations between the four signal-

*makoto.tobiyama@kek.jp

ISBN: 978-3-95450-192-2 doi:10.18429/JACoW-IBIC2017-TUPCF09

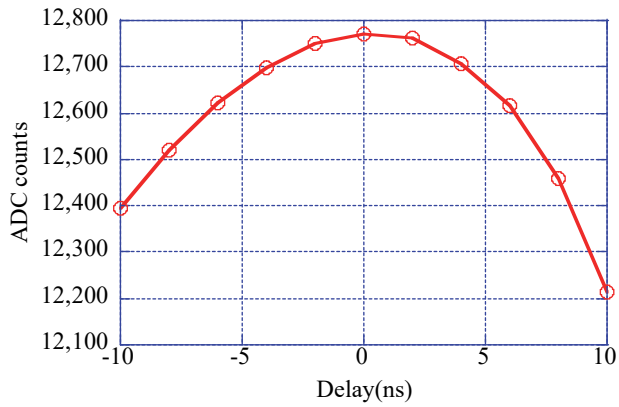

Figure 1: Pulse response of 18K11 L/R detector.

cables from the BPM feedthrough to 18K11s less than few mm by the cable length adjustment using TDR function of Agilent E5071C Network Analyzer. While the timing deviation before the adjustment distributed from 1 to 5 cm on the typical cable length of around 30 m, the final deviation was 30 ps in standard deviation. It is also clear that it is needed to control the ADC timing within 4 ns for each 18K11 to guarantee good response.

Though the data transfer speed from 18K11s to VME IOC (MVME5500) has been increased by using 64bit DMA transfer [2], it still needs more than 3 seconds to process 10 or 11 18K11 cards (transfer 32k turns of data to CPU, calculate the beam position using 3rd order polynomial fit using data from the mapping data) due to low CPU power. The start trigger is needed to be disabled during the data transfer and calculation to avoid re-triggering the modules that have finished the data processing.

DR BPM TIMING SYSTEM

Figure 2 shows the block diagram of the timing system for DR. It consists of mainly three parts; start trigger generation system, frequency divider with external synchronizer, and 32-channel clock delay per each station.

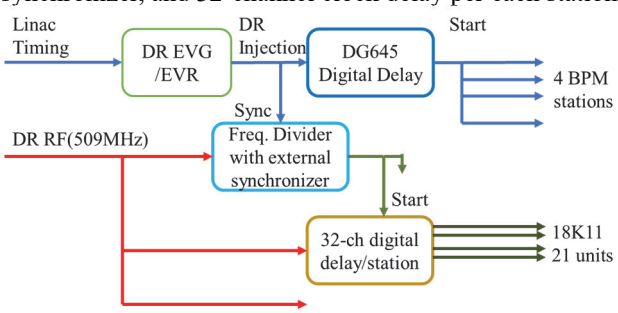

Figure 2: Block diagram of DR BPM timing system.

Start Trigger Timing Generation

In the normal operation, we want to get the position data in the similar timing slot, starting with the same delay after the injection. The start-trigger is also needed to be disabled during the processing time of the beam position monitor system. On the other hand, manual or continuously repeating trigger will be needed during the long storage timing mainly on the machine development time.

To realize the requirements, we have constructed a start trigger generation system using digital delay with external trigger (SRS DG645) [3] controlled by EPICS software sequencer. We have prepared three operation modes as:

- Normal operation mode. If the status of the end node of 18K11 is ready, the sequencer enables the single shot external trigger input. Start trigger (Single Shot pulse) is initiated by the injection timing signal with pre-set delay. EPICS sequencer waits for the ready status of 18K11 and automatically re-initiate the trigger.
- Storage mode. It is similar to the normal mode but start trigger is periodically initiated by the software timing without injection timing.
- Manual mode. Start trigger is controlled by the software. The mode will be used mainly on the special optics measurements such as dispersion measurement or chromaticity measurement where optics tool will govern all the measurement timing.

We have tested the start trigger system with the storage mode more than 6 months and had no difficulties up to now. Typical cycling time of the measurement is about 4 s where we have inserted extra 1 second of sleeping time of data acquisition to enable enough communication timing for EPICS channel access.

Frequency Divider with External Synchronization Timing

As the injection timing signal supplied by the linac / DR event system has enough precision with the typical timing jitter less than 10 ps, we generate the DR revolution timing synchronized to a injected bucket by re-synchronizing the frequency divider (1/230) with the injection timing. We have developed a 32-bit universal frequency divider with 32-bit clock delay and re-synchronized function (SKI-16115). Figure 3 shows the block diagram of SKI-16115.

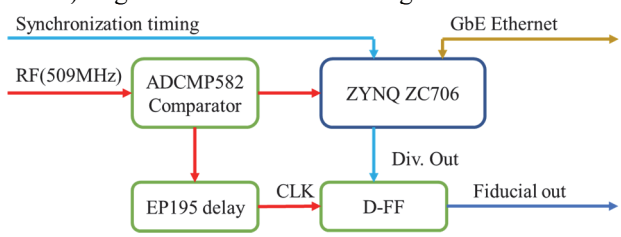

Figure 3: Block diagram of SKI-16115 universal frequency divider.

It consists of a Xilinx ZC706 evaluation board and a daughter card connected with FMC connector and installed in an EIA-1U case. All the functions of the board such as the set/read the frequency divide ratio, digital delay setting, enable/disable external synchronization, EP195 delay are accessible from a EPICS Soft-IOC through socket communication controlled by the Peta-Linux on the ZYNC FPGA.

The timing deviation and the timing jitter with the delay (RF and EPE195) change at the frequency division ratio of

ISBN: 978-3-95450-192-2 doi:10.18429/JACoW-IBIC2017-TUPCF09

230 has been measured using histogram function of Tektronix DSA8200 with 80E07 (30 GHz BW) module. Figure 4 shows the photo of the setup of the jitter measurement. The measured results are shown in Fig. 5, where the peak to peak deviation was about 4 ps with the flat timing jitter of less than 2.6 ps in all delay setting. By the comparison with the RTD temperature sensor near SKI-16115 and DSA8200, the change of the mean position

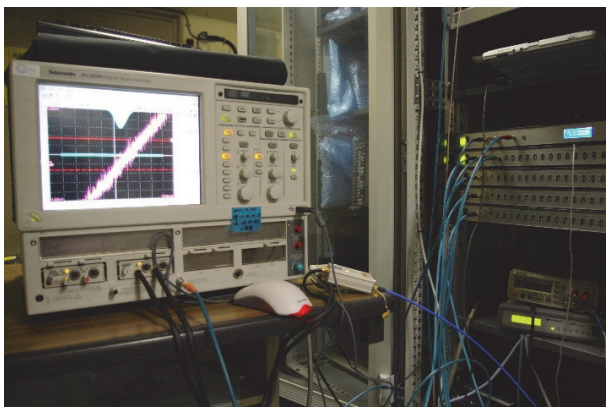

Figure 4: Photo of the jitter measurement setup.

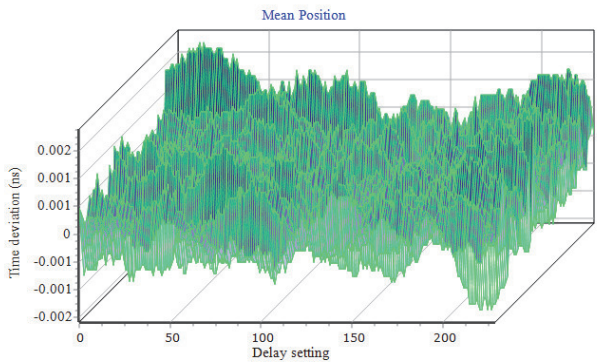

Figure 5: Measured timing jitter of frequency divider. Traces on depth axis correspond to delay for EP195 from 0 to 2 ns with 100 ps step.

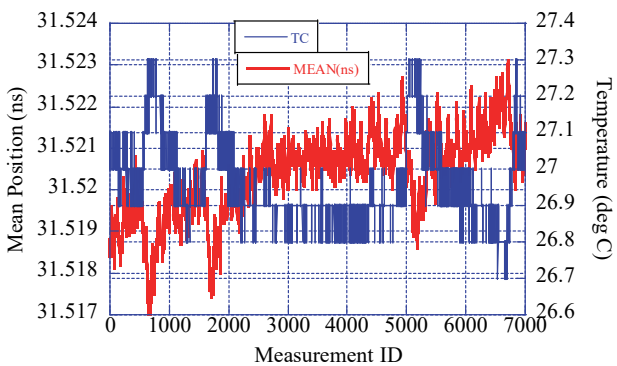

Figure 6: Temperature dependence of the output.

shows clear correlation, roughly 2ps / 0.4 deg. C as shown in Fig. 6.

As the design and the resources needed for the frequency divider has been established with this system, we are fabricating the new board with the same functions by employing smaller ZYNC FPGA (702) with the final form factor of NIM 1W.

32-Channel Digital Delay

From the measured cable length and the BPM location in the ring, the fiducial timing delays for each 18K11 module have been calculated relative to the latest signal in a BPM station. Though the ring size is not large, the largest delay for two stations amounts to more than 180 ns. As it is not suitable to prepare such long delay with the change of cable length, we have decided to develop a 32-channel 32-bit digital delays (SKI-17029) also with the form factor of EIA-1U based on the code for SKI-16115 which counts RF clock (509 MHz) starting with the external timing (coming from SKI-16115) and distributes the fiducial timing for each 18K11 with the arbitrary delay with step of 2 ns. It consists of a Xilinx ZC702 evaluation board with a daughter card which has a RF comparator, 32 D-FFs and the level shifters from LVDS to PECL and PECL to NIM as shown in Fig. 7.

Figure 7: Photo of the 32-channel digital delay (SKI-17029).

Figure 8 shows the measured timing deviations and its standard deviation of jitter using the similar setup as that for frequency divider with the external fiducial input from SKI-16115 (div=230).

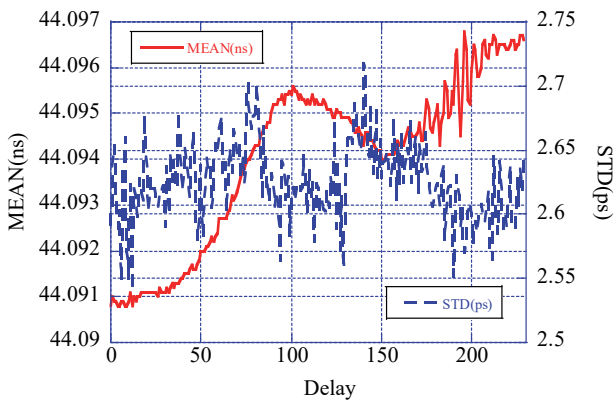

Figure 8. Measured timing jitter (mean position: red solid line, standard deviation: blue dashed line) of 32-channel delay (SKI-17029).

The change of the mean position also has clear correlation with the change of the environment temperature

ISBN: 978-3-95450-192-2 doi:10.18429/JACoW-IBIC2017-TUPCF09

and has no correlation with the temperature of the SKI-17029 (around 40 deg. C on the top of the box). It is therefore the temperature dependence of the DSA8200 system is supposed to be the main source of the mean position change. Of course, unexpected very high temperature of SKI-17029 needs to be decreased for safer operation. Presumably due to so tight space in the box with so many PECL ICs and so large resources in the FPGA, the temperature of SKI-17029 reaches more than 50 deg. C in the box. Though the 32-channel. delay is working without trouble more than a week with this temperature, we are planning to add cooling fans with improved air conductance to reduce the temperature. If the leakage of the RF signal from this module is small enough not to affect the 18K11 modules in the same rack, we might open the top panel for better cooling. The EPICS (asyn) device support based on the socket communication protocol has been developed and tested and confirmed to be working.

SUMMARY

We have constructed the timing systems for the SuperKEKB DR beam position monitor systems. The start trigger system generates the data acquisition start signal synchronized to the beam injection timing with output veto not to disturb the data transfer and data processing.

The 32-bit universal frequency divider with 32-bit delay (SKI-16115) generates the master fiducial timing also synchronized to the fine injection timing. The time deviation and jitter due to the change of delay has been measured to be small enough.

To provide the individual ADC timing to 18K11 detectors in the BPM station, 32-channel, 32-bit digital delay (SKI-17029) has been developed using the resource of SKI-16115. The time deviation and jitter due to the change of the delay has also measured and confirmed to be small enough. The unexpected higher temperature of SKI-17029 needs to be solved soon.

Both SKI-16115 and SKI-17029 use the ZYNC FPGA with ARM core inside. Up to now, we have installed embedded Linux system on the FPGA (Peta-Linux) and controlled the function through GbE Ethernet. After the initial setting just after the first beam storage, it might be fairly rare to change the parameters such as individual delay. Therefore, we do not have strong motivation to optimize the communication, such as the tuning in the communication buffer, to increase the data transfer or to reduce communication error with very crowded condition. Nevertheless, we are trying to install EPICS system on the FPGA which should have enough computing resources. Working without external server should be preferable especially for the new universal frequency divider with NIM form factor.

The authors would like to thank our colleague of SuperKEKB beam instrumentation group for numerous supports on the development and construction. Discussion with the control / timing group of Linac and ring are so fruitful.

This work is partly supported by the US-Japan collaboration in High Energy Physics (R&D for SuperKEKB and the next generation high luminosity colliders).

REFERENCE

[1] H. Ikeda *et al.,* "Beam Diagnostics of SuperKEKB Daming Ring" presented at the 2nd Int. Beam Instrumentation Conf. (IBIC'2013), Oxford, U.K. paper MOPC05, this conference.

[2] M. Tobiyama et al., "Improvement of Data Transfer Speed of Large Memory Monitors" presented at the 3rd Int. Beam Instrumentation Conf. (IBIC'2014), Monterey, CA, USA, paper WEPD05, this conference.

[3] Stanford Research Systems, http://www.thinksrs.com/

ISBN: 978-3-95450-192-2 doi:10.18429/JACoW-IBIC2017-TUPCF10

MEASUREMENT OF THE LONGITUDINAL COUPLED BUNCH INSTABILITIES IN THE J-PARC MAIN RING

Y. Sugiyama*, M. Yoshii, KEK/J-PARC, Tokai, Ibaraki, Japan
F. Tamura, JAEA/J-PARC, Tokai, Ibaraki, Japan

Abstract

The J-PARC Main Ring (MR) is a high intensity proton synchrotron, which accelerates protons from 3 GeV to 30 GeV. Its beam power for the fast extraction reached 470 kW, which corresponds to 2.4×10^{14} protons per pulse, in February 2017, and the studies to reach higher beam intensities are in progress. We observed the longitudinal dipole coupled bunch instabilities in the MR for the beam power beyond 470 kW. To investigate the source of the instabilities and to mitigate them, we analyzed the beam signals throughout the acceleration cycle to obtain the oscillation modes and their growth by using two methods. One focuses the motion of the bunch centers and the other used the frequency spectrum of the beam signal. We describe the methods and the measurement results of the longitudinal coupled bunch instabilities in the J-PARC MR.

INTRODUCTION

The Japan Proton Accelerator Research Complex (J-PARC) is a high intensity proton accelerator facility, which consists of the 400 MeV linac, the 3 GeV Rapid Cycling Synchrotron (RCS), and the 30 GeV Main Ring (MR). The MR delivers the proton beams to the neutrino experiment by the fast extraction (FX), and to the hadron experiments by the slow extraction (SX). The operation parameters of the J-PARC MR and the RF system for the fast extraction are shown in Table 1.

Table 1: Operation Parameters of the J-PARC MR and the RF System for the Fast Extraction

energy	3–30 GeV
repetition period	2.48 s
accelerating period	1.4 s
accelerating frequency f_{RF}	1.67–1.72 MHz
revolution frequency f_{rev}	185–191 kHz
harmonic number h_{RF}	9
number of bunches N_b	8
maximum rf voltage	300 kV
fundamental harmonic cavities	7
second harmonic cavities	2
Q-value of rf cavity	22

The MR delivers 2.4×10^{14} protons per pulse, which corresponds to the beam power of 470 kW, to the neutrino experiment as of February 2017, and studies toward higher beam intensity are in progress. During studies, the longitudinal bunch oscillation appeared to be an issue to achieve higher beam intensities than 500 kW.

* yasuyuki.sugiyama@kek.jp

LONGITUDINAL BUNCH OSCILLATION IN THE J-PARC MR

The beam signal from an Wall Current Monitor (WCM) [1] is recorded by an oscilloscope, LeCroy WP715Zi, with the sampling frequency of 500 MHz.

Figure 1 shows the typical mountain plot of the beam signal at the beam power of 480 kW for the fast extraction during the studies. The bunches start the dipole oscillations from the middle of the acceleration and their amplitudes keep increasing until the extraction. One can notice that the amplitudes and the phases of the oscillations of the bunches are different.

This kind of the oscillations is called the coupled bunch (CB) oscillation, and the instability caused by the CB oscillation is called the CB instability (CBI). The identification of the CB oscillation mode is necessary to find the source of the CBI.

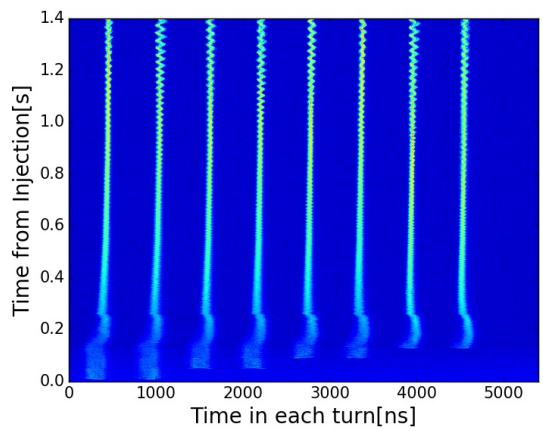

Figure 1: The mountain plot for the fast extraction in the J-PARC MR with the beam power of 480 kW during the studies.

COUPLED BUNCH OSCILLATION

For M bunches, there are M modes of the CB oscillation with the mode number $n = 0...M-1$. The phase difference of the synchrotron oscillation between adjacent bunches is $2\pi n/M$. For each mode, all bunches oscillate with the same frequency and the amplitude but with different phases.

The CB modes can also be seen in the spectrum of the beam signal as sidebands of the harmonic components [2].

ISBN: 978-3-95450-192-2 doi:10.18429/JACoW-IBIC2017-TUPCF10

The frequency of the CB mode n can be expressed as follows:

$$f_{p,m,n} = |(pM + n)f_{\mathrm{rev}} + mf_s|, (-\infty < p < \infty), \quad (1)$$

where f_{rev} is the revolution frequency, f_s the synchrotron frequency, and m the type of the synchrotron motion. The case with $m = 1$ corresponds to the dipole oscillation. The CB modes appear as the Upper Side Bands (USBs) and the Lower Side Bands (LSBs) in the cases of $p \geq 0$ and $p < 0$, respectively. Below the accelerating frequency, the USB and the LSB with the CB mode n can be expressed as follows:

$$f_n^{\mathrm{USB}} = nf_{\mathrm{rev}} + mf_s \quad (2)$$
$$f_n^{\mathrm{LSB}} = (M - n)f_{\mathrm{rev}} - mf_s. \quad (3)$$

There are 9 CB modes for the J-PARC MR since the harmonic number of the J-PARC MR is 9. The spectra of the CB modes in the MR up to the harmonic $h = 11$ are illustrated in Figure 2.

There are two sidebands with different CB modes in each harmonic component.

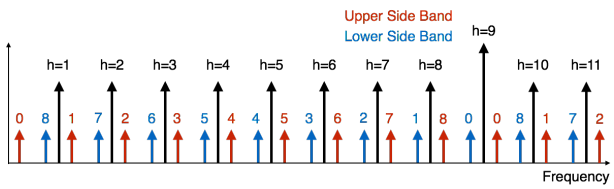

Figure 2: The coupled bunch oscillation mode for the J-PARC MR.

COUPLED-BUNCH OSCILLATION ANALYSIS

We use two different methods to analyze the CB oscillation. We apply these method to the measured beam signal and compare the results.

Bunch Center Motion Analysis

The CB modes can be identified by analyzing the phase difference of the synchrotron oscillation between bunches [3].

The phases of the synchrotron oscillations for the bunchs are obtained by analyzing the motion of bunch centers. The bunch centers are calculated from the the center of mass of the WCM signal for each bunch. Figure 3 shows the track of the bunch centers obtained from the WCM signal shown in Figure 1. The differences of the amplitude and the phase between bunches can be clearly seen in Figure 3 .

The phase and the amplitude of the synchrotron motion are obtained by fitting the track of the bunch center for each bunch with a sinusoidal function as:

$$y_i = a_i \sin(2\pi f_s t + \theta_i) + C_i, \quad (4)$$

where y_i is the track of the center of mass of $i-$th bunch, a_i and θ_i are the amplitude and the phase of the synchrotron oscillation for $i-$th bunch, respectively. The fit range is

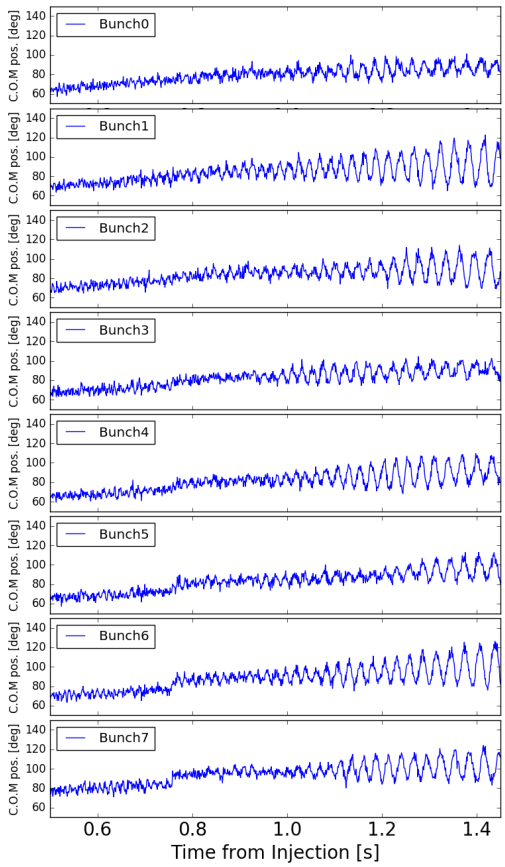

Figure 3: The tracks of the bunch centers.

determined to cover two cycles of the synchrotron oscillation estimated by the operation parameters.

The amplitudes and the phases of the CB modes are obtained by applying the DFT according to

$$A_n e^{-i\Theta_n} = \frac{1}{M} \sum_k a_k e^{-i\theta_k} e^{2\pi ikn/M}, \quad (5)$$

where A_n and Θ_n are the amplitude and the phase of the CB mode n. Figure 4 shows the time variation of the amplitudes of the CB modes during the acceleration for the WCM signal shown in Figure 1. The CB mode $n = 8$ has the largest amplitude for the most of time during the acceleration. In addition to the CB mode $n = 8$, the amplitude of the CB modes with $n = 4, 6, 7$ are increasing until the extraction.

Frequency Spectrum Analysis

To identify the CB modes from the beam spectrum, the LSBs and USBs of the harmonic components must be extracted from the beam signal. We apply the single side band filtering [4] to obtain the LSBs and USBs.

Figure 5 shows the procedure of the single side band filtering. In the offline analysis, the single side band filtering is applied to the recorded waveform of the beam signal from WCM.

The harmonic components of the beam signal are detected by the quadrature detection [5]. If we assume the beam

ISBN: 978-3-95450-192-2 doi:10.18429/JACoW-IBIC2017-TUPCF10

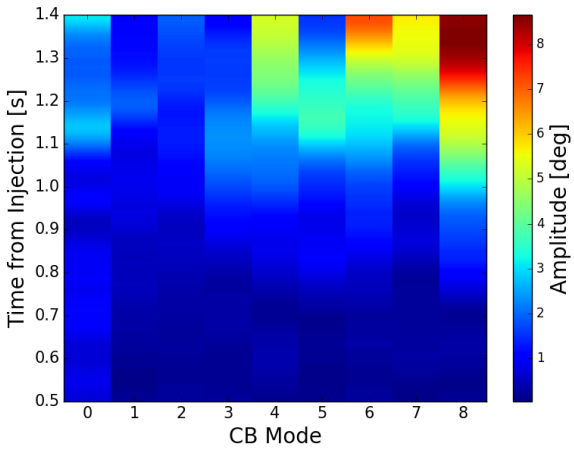

Figure 4: The amplitudes of the CB oscillation modes.

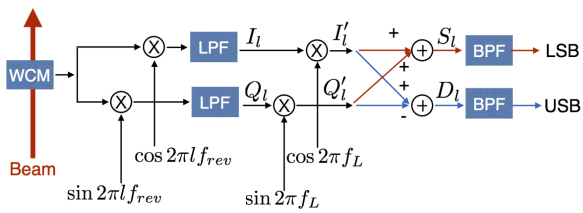

Figure 5: Procedure of the single side band filtering.

spectrum as

$$y = \sum_l A_l(t)\sin(2\pi l f_{\rm rev} + \phi_l(t)), \tag{6}$$

the IQ signal for the harmonic component ($h = l$) after the quadrature detection are expressed as

$$I_l = \frac{A_l(t)}{2}\sin\phi_l(t) \tag{7}$$

$$Q_l = \frac{A_l(t)}{2}\cos\phi_l(t) \tag{8}$$

Figure 6 and 7 show the spectrograms for I_8 and Q_8, respectively. There is a strong sideband with decreasing frequency in both figures. The frequency of the sideband is consistent with the estimated synchrotron frequency shown as red dotted line the figure.

Since the frequency of the sidebands in IQ components agree with the estimation, the sidebands can be extracted by the single sideband filtering using the estimated frequency. The I and Q signals are multiplied by the unity signals, $\cos 2\pi f_L t$, $\sin 2\pi f_L t$, respectively, to obtain the $I_l^{'}$, $Q_l^{'}$, where f_L is the frequency satisfying $f_L = f_s + f_c$, and f_c is the carrier frequency which can be chosen freely.

$$\begin{aligned} I_l^{'} &= I_l \cos 2\pi f_L t \\ &= \frac{A_l(t)}{4}(\sin(\phi_l(t) + 2\pi f_L t) \\ &\quad + \sin(\phi_l(t) - 2\pi f_L t)) \end{aligned} \tag{9}$$

$$Q_l^{'} = Q_l \sin 2\pi f_L t$$

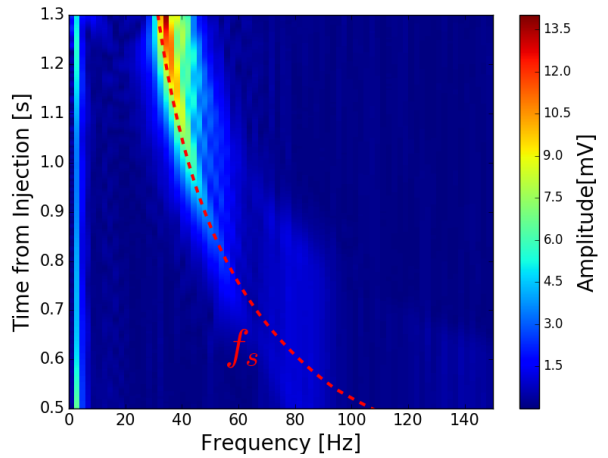

Figure 6: Spectrogram for the I component h=8 (I_8). Red dotted line represents the estimated synchrotron frequency.

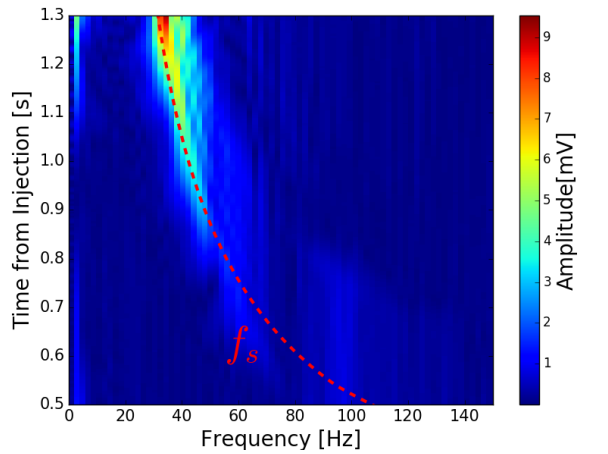

Figure 7: Spectrogram for the Q component h=8 (Q_8). Red dotted line represents the estimated synchrotron frequency.

$$\begin{aligned} &= \frac{A_l(t)}{4}(\sin(\phi_l(t) + 2\pi f_L t) \\ &\quad - \sin(\phi_l(t) - 2\pi f_L t)) \end{aligned} \tag{10}$$

The sum and the difference of $I_l^{'}$, $Q_l^{'}$ are calculated to obtain S_l, D_l, respectively.

$$S_l = \frac{A_l(t)}{2}\sin(\phi_l(t) + 2\pi f_L t) \tag{11}$$

$$D_l = \frac{A_l(t)}{2}\sin(\phi_l(t) - 2\pi f_L t) \tag{12}$$

The D_l oscillates with the carrier frequency f_c in the case of the USB ($\phi_l(t) = 2\pi f_s t$), and the S_l oscillates with f_c in the case of the LSB ($\phi_l(t) = -2\pi f_s t$). The LSB and the USB of the harmonic component with $h = l$ are obtained by applying the BPF with the pass band around f_c to S_l and D_l.

Figure 8 and Figure 9 show the time variation of the amplitudes of the LSB and the USB of the harmonic components for the WCM signal shown in Figure 1. The sidebands with the largest amplitude are the USB of the harmonic component $h = 8$ and the LSB of the harmonic component $h = 10$.

ISBN: 978-3-95450-192-2 doi:10.18429/JACoW-IBIC2017-TUPCF10

Both sidebands correspond to the CB mode $n = 8$. In addition to the sidebands for the CB mode $n = 8$, the amplitudes of the sidebands corresponding to the CB mode $n = 2, 4, 6, 7$ are increasing until the extraction.

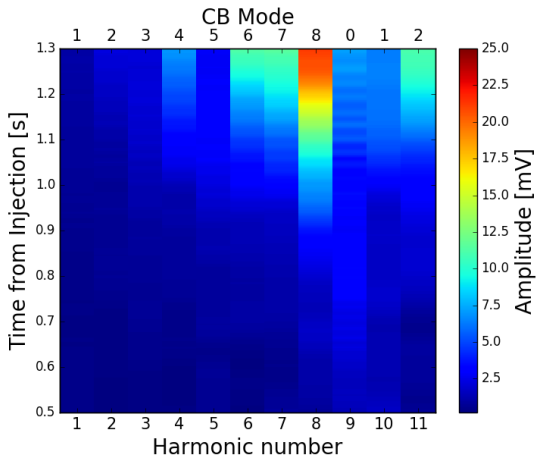

Figure 8: The time variation of the amplitudes of the USBs of the harmonic components.

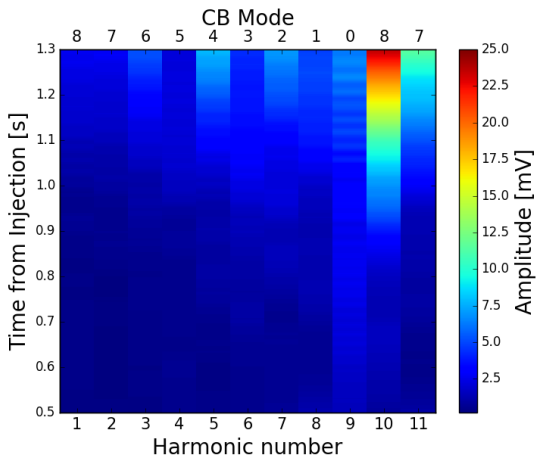

Figure 9: The time variation of the amplitudes of the LSBs of the harmonic components.

DISCUSSION

The results from both methods show that the CB mode $n = 8$ has the largest amplitude. Figure 10 shows the comparison of the time variation of the amplitudes of the CB mode $n = 8$ between the results of the bunch center motion analysis and the beam spectrum analysis. Both results show similar trend of growth. Thus, it is convincing that both methods are observing the same CB mode. The relation between the observables of two methods is left for the future study.

The strongest CB mode is found in the sidebands of the neighbor harmonics of the acceleration harmonic $h = 9$. The RF cavities have relatively large impedances in the neighbor

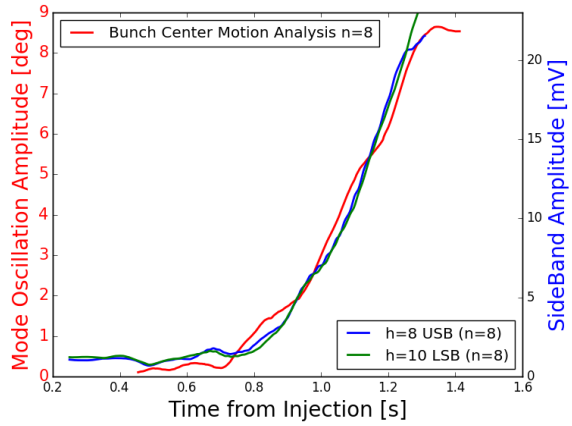

Figure 10: Comparison between the bunch center motion analysis (Red) and the frequency spectrum analysis (Blue for the USB of $h = 8$, Green for the LSB of $h = 10$).

harmonics and these impedance are compensated by the RF feedforward system [5]. The remaining impedances in the neighbor harmonics due to imperfection of the compensation is considered to be the possible source of the CBI in the MR.

Many CB modes with noticeable amplitudes other than $n = 8$ are observed in the results of both methods. The uneven bunch filling pattern of the J-PARC MR, in which 8 out of 9 buckets are filled by the bunches, is a possible source of of the excitation in the multiple CB modes.

SUMMARY

The coupled bunch instability is an issue to achieve the beam intensities beyond 500 kW in the J-PARC MR. To mitigate the CBI, we apply two methods to identify the CB modes. One method uses the motion of bunch centers, and the other uses the frequency spectrum. Both methods show a consistent result that the CB mode $n = 8$ had the largest amplitude. Both methods show similar trend of growth for the CB mode $n = 8$. Thus, we consider that the CBI of the same CB mode is observed by two methods with different aspects. Since the strongest CB mode is found in the sidebands of the neighbor harmonics of the acceleration harmonic $h = 9$, the remaining impedances of the RF cavities in the neighbor harmonics due to imperfection of the compensation is considered to be the possible source of the CBI in the MR.

REFERENCES

[1] T. Toyama *et al.*, Proc. PAC05, 2005, pp. 958-960.

[2] F. Pederson *et al.*, IEEE-TNS, NS-24, 1396, 1977.

[3] H. Damerau *et al.*, Proc. PAC07, 2007, pp. 4180-4182.

[4] B. Kriegbaum *et al.*, IEEE-TNS, NS-24, 1695, 1977.

[5] F. Tamura *et al.*, PRST-AB, 16, 051002, 2013.

ISBN: 978-3-95450-192-2 doi:10.18429/JACoW-IBIC2017-TUPCF11

UPGRADE OF THE BEAM POSITION MONITORING SYSTEM AT THE J-PARC MAIN RING FOR HIGH INTENSITY OPERATION *

Aine Kobayashi†, Takeshi Toyama, Kenichiro Satou, Hironori Kuboki,
High Energy Accelerator Research Organization (KEK),
J-PARC Center, Tokai-mura, Naka, Ibaraki, Japan

Abstract

For the T2K neutrino oscillation experiment an upgrade programs of J-PARC are on-going for higher beam intensity. The goal of 10-year upgrade plan is to achieve a beam power of 1.3 MW in the main ring [1], a significant increase compared to the presently achieved power of 470 kW. Beam loss causes the limitation on the proton bunch intensity. A precise orbit correction is necessary in order to reduce the beam loss. Beam position monitor (BPM) is a vital element providing accurate measurements of the beam positions for the control of closed orbit distortion (COD). The current position resolution is a few 10 μm in the COD mode, a few 100 μm in the turn-by-turn mode [2], and the goal is make one tenth of it. Currently an apparent dependence of RMS of COD on the beam intensity is observed (about 100 ~ 200 μm). In order to understand the nature of the phenomenon, investigations are being made on the BPM response and its intensity dependence as well as on the effects of wake field, local orbit bumps to COD and septum. Status of the studies will be discussed.

PROCESSING CIRCUIT FOR THE MR BPMS

The BPM of the MR is a diagonal cut which is nondestructive to the beam, readout from both horizontal and vertical electrodes as shown in Fig. 1. The number of BPM is 186, placed around the MR. After signal processing with Fourier transformation, the position of the beam is defined. The calibration such as beam based alignment (BBA) and beam based gain calibration (BBGC) are implemented [3].

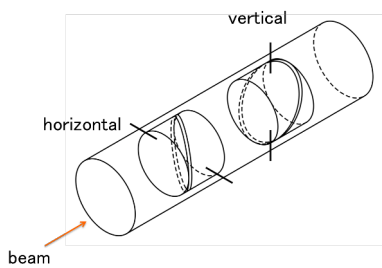

Figure 1: The schematic view of the MR BPM.

COD WITH INTENSITY DEPENDENCE

There are 9 RF buckets in the MR and up to 8 bunches can be filled. The kickers [4] inject bunches every 40 ms at K1, K2, K3 and K4 timing. After 10 ms of the K4 timing, acceleration is started. Usually, the RMS of COD is not dependent on the number of bunches. But an apparent dependence on the beam intensity is observed [5]. When the beam intensity exceeds about 10^{14} ppp, the RMS of COD is observed to grow by 100 ~ 200 μm as shown in Fig. 2.

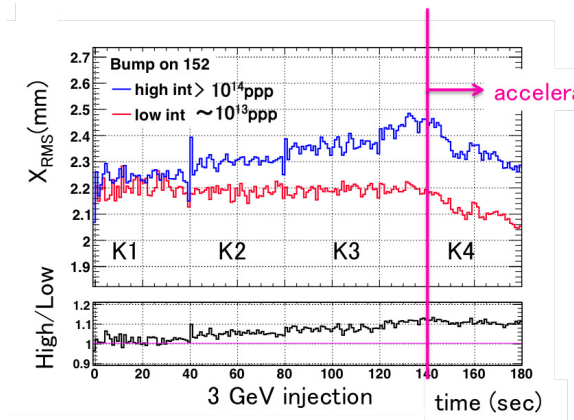

Figure 2: COD excursion of high intensity (> 10^{14} ppp) compared to low intensity (~ 10^{13} ppp) with bump on QFR152.

MEASUREMENTS

Referring to the study which investigated the COD made by a transverse impedance of a local bump in VEPP-4M accelerator, Russia [6], a measurement menu was contained with changing the local bump as well as changing a beam intensity. The fast extraction (FX) kicker and the septum are chosen as the position of the local bump. The size of bumps were arranged with the aperture and not to exceed beam loss about 10^{12} ppp. The taken sets with high beam intensity ($> 2.4 \times 10^{14}$ ppp) are: without bump, with a bump on QFR152 with 10 mm for the FX kicker, with a bump on QFR152 with 4 mm for the septum, and with bumps on both QFR152 (10 mm) and QFR82 (4 mm). Also, the data of low beam intensity (~ 6.0×10^{13} ppp) with a bump on QFR152 wih 10 mm. About 10 to 20 shots were taken for each sets. The MR power was 470 kW at most, with 3 GeV extraction. The number of bunches was up to 8.

BPM RESPONSE

It is necessary to examine BPM signals that are processed to the COD. The typical signals of high intensity beam are shown in Fig. 3, the number of counts from horizontal (upper) and vertical (bottom) electrodes. This measurement

* Work supported by JSPS-JP16H06288
† aine.kobayashi@kek.jp

ISBN: 978-3-95450-192-2 doi:10.18429/JACoW-IBIC2017-TUPCF11

was done with 2 bunches, and the counts (up to 3000) are lower than the maximum $2^{13} \sim 8000$, where the BPM has linearity. Figure 4 shows the peak-to-peak of signals as a function of all the BPM, around the MR. The details of the monitor systems are described in references such as [7]. The above statement that the intensity dependent COD increment does not come from some particular BPMs malfunction, was also confirmed with the result of Fourier transform of the COD (increment), in which the peak is at 21st harmonic of one MR revolution, closest integer to the horizontal tune.

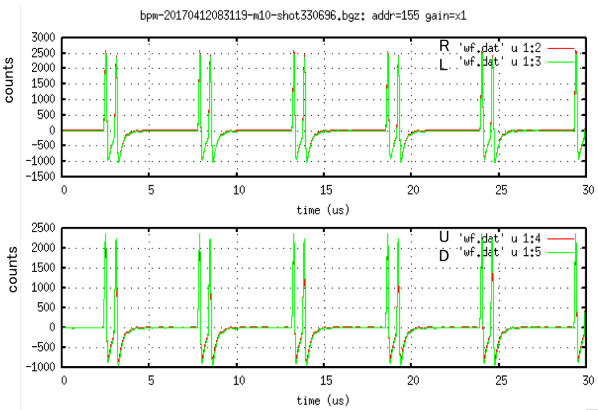

Figure 3: A typical BPM response at high intensity.

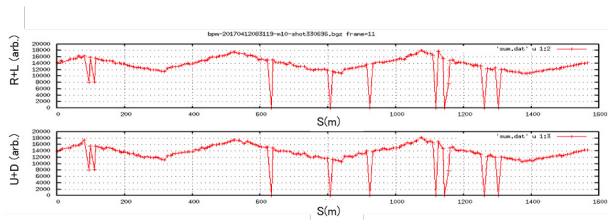

Figure 4: All the BPM counts. The discontinuity of the counts, corresponding to BPM # 13 and 15 has a special amp for some test, and the other with count zero are masked BPM. The detail of the monitor system is described in the reference [7].

COD DATA ANALYSIS

COD Data Correction

The measured COD contains the contribution from ripple noise ($\Delta B/B$) and momentum dispersion ($\eta_s \Delta p/p$), which have to be removed before the analysis [8]. The MR bending magnets are divided into 6 families for connecting power supplies. The dispersion function can be defined by fitting with each of 6 families. The measured COD ($x_{\mathrm{measured}}(s)$) is given as Eq. (1).

$$x_{\mathrm{measured}}(s) = x_{\mathrm{COD}}(s) + \sum_{k=1}^{6} \lambda_k \eta_k(s) \qquad (1)$$

Here, η_k is a dispersion function of a k^{th} family, and an unknown quantity λ_k is defined by fitting to the data. Using the twiss parameters given by the optics calculation, fitting function can be made as shown in Fig. 5. The results by fitting and then subtracted are shown in Fig. 6 and 7.

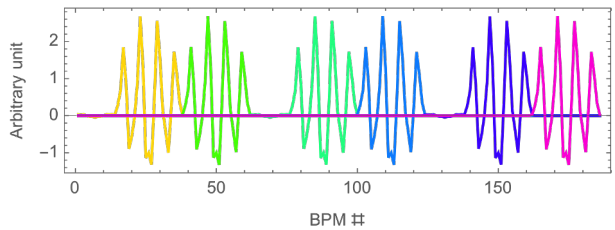

Figure 5: Momentum dispersion function from optical calculation.

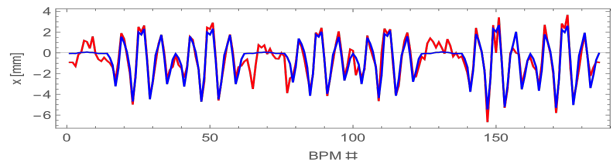

Figure 6: Fit with dispersion function. The red line is the measured value and the blue line is fitting result.

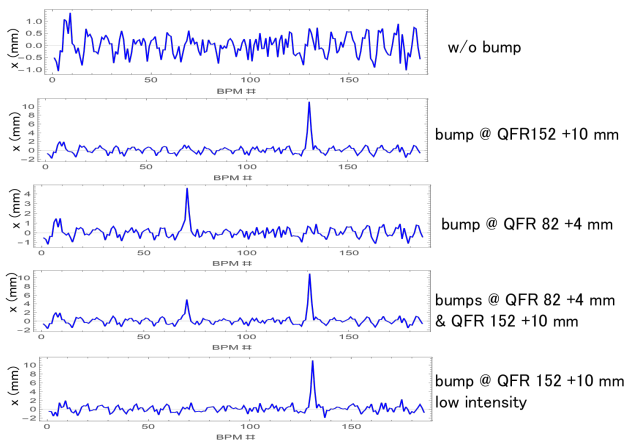

Figure 7: Dispersion effects subtracted from COD of each data-sets. QFR82 and QFR152 corresponding to BPM#71 and 131.

Error Source Search

The error source, which causes the COD excursion was searched by optics calculation tool, SAD [9]. The way of optics correction with small number of magnets by chi-square is described in a paper such as [10]. The COD $x(s_j)$ is measured as Eq. (2) with transport matrix and error source $\theta(s_i)$.

$$x(s_j) = \sum_{i=1} \frac{\sqrt{\beta(s_j)\beta(s_i)}}{2\sin(\pi\nu)} \cos(\pi\nu - |\psi(s_i) - \psi(s_j)|)\theta(s_i) \qquad (2)$$

The COD correction algorithm derives the $\theta(s_i)$ of each given source. In this study, Micado which is implemented

ISBN: 978-3-95450-192-2 doi:10.18429/JACoW-IBIC2017-TUPCF11

in SAD a kind of chi-square cod correction was applied. The candidates of the error source were given 93 steering magnets ZSH, 13 kicker magnets KM, 14 magnetic septa MS, and 2 slow magnet septa SMS.

In order to compare the difference in intensity, the same local bump but different intensity sets were used. The Fig. 8 (top) shows the averaged COD at K4 timing <K4> in high intensity which is large COD and that of K1 intensity <K1> at K1 timing which is small COD. As expected, the position having a local bump was indicated as an error sources when using the COD subtracted <K1> from <K4> as shown in Fig. 8 (bottom). Searching the error sources, Fig. 9 was obtained. Applying Micado to find the largest ten error sources in the given candidates, Fig. 10 (top) was obtained. Then simulated COD with single kicks corresponding the ten error sources is shown in Fig. 10 (bottom).

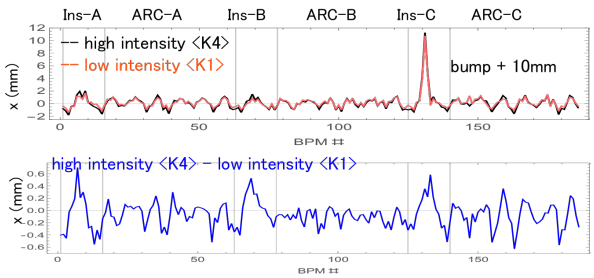

Figure 8: The COD with bump on QFR152 (BPM131) with high and low intensity (top), their difference is the bottom.

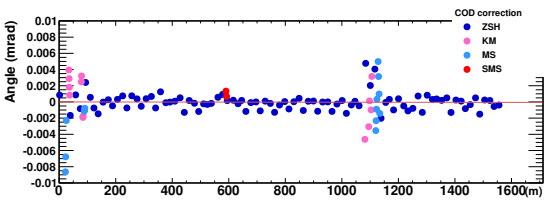

Figure 9: Correction from each sources for COD subtracted <K1> of low intensity from <K4> of high intensity.

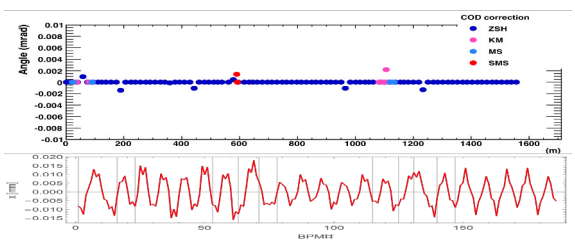

Figure 10: The largest ten error sources in the given candidates (top) and that of simulated COD (bottom).

In the same way, as shown in Fig. 11, the error source search using the COD with or without a local bump were performed. These results also indicates the position of the local bump. Note that the aperture of the septum at QFR82 is small, no more than 4 mm local bump could be made.

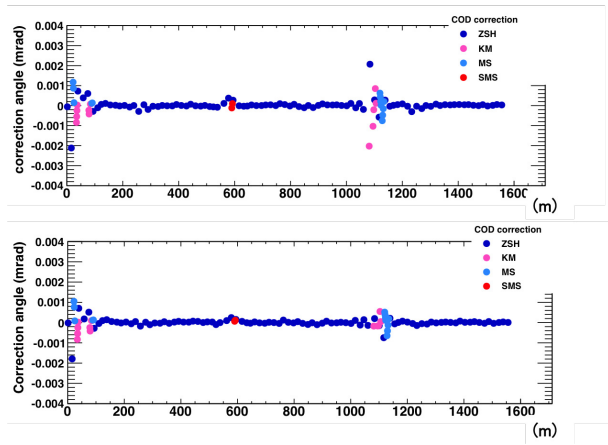

Figure 11: The error source of COD, subtracted the COD of <K4-K1> without bump from the COD <K4-K1> with bump on QFR152 (top) and QFR82 (bottom).

WAKE FIELD ESTIMATION

The most suspected near QFR152 is the FX kicker. Therefore, a wake field caused by a beam when passing through the FX kicker with a local bump was calculated using CST PARTICLE STUDIO [11]. The kicker was modeled as Figs. 12 and 13 referring to [12, 13]. The beam was set to away from center by 10 mm, and the integral path for wake field calculation was set to go along the center. A wake potential and a wake impedance were given as shown in Fig. 14, 15 and 16. The result is close to the previous stretched-wire measurement [14]. The kick factor can be given as Eq. (3) [15].

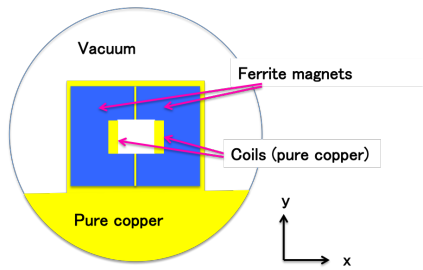

Figure 12: The schematic view of the simplified FX kicker cross-section. The kicker is made of ferrite magnets, pure copper coils and plates, and resistive elements, putting into a vacuum duct.

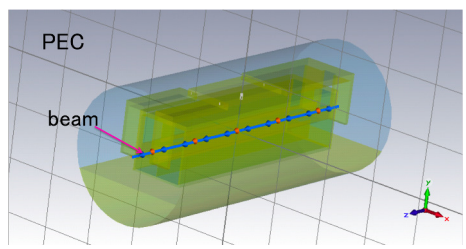

Figure 13: The simplified FX kicker model for a wake field estimation. The appropriate boundary conditions and a simplified resistive circuit [12, 13] were applied.

ISBN: 978-3-95450-192-2 doi:10.18429/JACoW-IBIC2017-TUPCF11

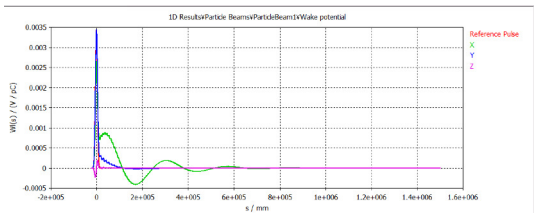

Figure 14: Wake potential.

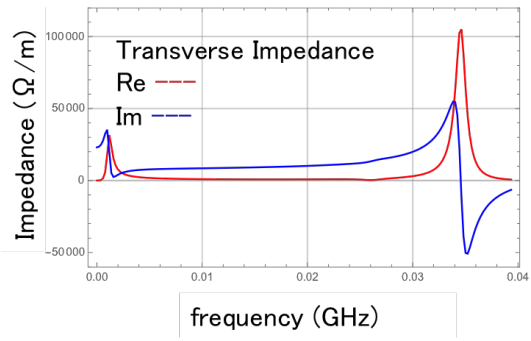

Figure 15: Transverse wake coupling impedance of real part (red) and imaginary part (blue), applied FFT with a roll-off factor 0.2.

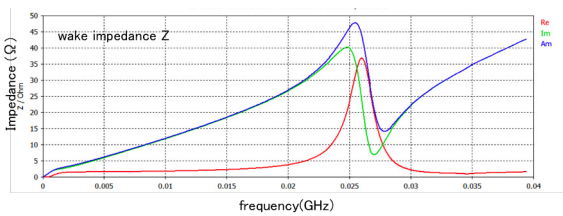

Figure 16: Wake coupling impedance of Z. The results is consists of the previous measurement [14].

$$\kappa_\perp = \frac{1}{\pi}\int_0^\infty d\omega Im\left(Z_\perp(\omega)\right)h(\omega), \tag{3}$$

where $Z_\perp$ is the transverse impedance, ω is the frequency and h is the bunch power spectrum. Then, the kick angle with 10 mm local bump on the kicker per one bunch can be estimated as 0.001 mrad from Eq. (4).

$$\Delta\theta = \frac{q}{(B\rho)c}\kappa_\perp \Delta x, \tag{4}$$

where q is the bunch charge, and $B\rho$ is the magnetic rigidity, c is the speed of light and Δx is the transverse offset of the bunch. The result is in the same order with SAD calculation as shown in a previous section. Nevertheless precise agreement remains for further investigation.

CONCLUSION

For upgrade of MR beam intensity, it is necessary to make clear to what causes the COD excursion. Using the optics simulation and the electromagnetic simulator, the effects from wake field at a local bump were studied. The obtained kick angle was almost consist with a previous measurement.

The correlation between COD and betatron tune shift need to be carefully examined. A tune shift measurement was performed with single bunch in 2×10^{13} ppp beam intensity on 2015 [16]. The measurement with 8 bunch in high intensity is planned in the near future.

A study for both development and improvement of the BPM are also planning for high intensity beam operation.

ACKNOWLEDGEMENT

This study was supported by MR staff members. Special thanks to S. Igarashi, Y. Sato and N. Yamamoto for instruction of SAD and useful suggestions, and J. Takano for operating bumping orbit. This work was supported by JSPS Grant-in-Aid for Specially Promoted Research Grant Number JP16H06288.

REFERENCES

[1] Y. Sato, “MR upgrade”, presented at ATAC2017, J-PARC, 2017.

[2] T. Toyama *et al.*,“Repair and improvement of the J-PARC MR BPM”, in *Proc. PASJ'10*, paper SUP075, 2010.

[3] M. Tejima *et al.*,“Beam based calibration for beam position monitors”, in *Proc. IBIC'2015*, paper TUBLA01, 2015.

[4] T. Sugimoto *et al.*,“Performance of Injection Kicker Magnet for the J-PARC Main Ring”, in *Proc. PASJ'9*, paper THLR08, 2009.

[5] S. Igarashi, 2017 March, private communication, J-PARC.

[6] V. Kiselev and V. Smaluk, “Measurement of local impedance by an orbit bump method”, NIM A 525(2004) 433-438.

[7] S. Hatakeyama *et al.*,“A system for monitoring of the transverse injection error and betatron tune in J-PARC MR”, in *Proc. PASJ'7*, paper WEPS098, 2007.

[8] T. Toyama *et al.*, “Beam-based Alignment of the BPMs at J-PARC MR”, in *Proc. PASJ'11*, paper SAP088, 2011.

[9] SAD homepage. `http://acc-physics.kek.jp/SAD/index.html`

[10] B. Autin and Y. Marti, “Closed orbit correction of A.G. machines using a small number of magnets”, CERN ISR-MA/73-17 (1973).

[11] CST - Computer Simulation Technology homepage. `https://www.cst.com/products/cstps`

[12] Specifications of the FX-kicker magnet and circuit, from K. Ishii.

[13] K. Koseki *et al.*, “Status of the Fast Extraction Kicker of the J-PARC-MR”, presented at ATAC2010, J-PARC, 2010.

[14] T. Toyama *et al.*, “Instability: Observation and Study Results of MR”, presented at ATAC2011, J-PARC, 2011.

[15] B. W. Zotter and S. A. Kheifets, “Ipmpedances and Wakes in High-Energy Particle Accelerators”, ISBN: 9789810226268.

[16] T. Toyama *et al.*, “Impedance and Instabilities”, presented at ATAC2016, J-PARC, 2016.

ISBN: 978-3-95450-192-2 doi:10.18429/JACoW-IBIC2017-TUPCF12

MEASUREMENT OF EACH 324 MHz MICRO PULSE STRIPPING EFFICIENCY FOR H⁻ LASER STRIPPING EXPERIMENT IN J-PARC RCS

P.K. Saha*, K. Okabe, A. Miura, N. Hayashi, H. Harada and M. Yoshimoto
J-PARC Center, KEK & JAEA, Japan

Abstract

In 3-GeV RCS (Rapid Cycling Synchrotron) of J-PARC (Japan Proton Accelerator Research Complex), a proof-of-principle experiment for 400 MeV H⁻ stripping to protons by using only lasers is under preparation. The experiment requires precise measurements of all three charge fractions of only a single H⁻ micro pulse of 324 MHz at the downstream of laser and H⁻ interaction point (IP). It is very essential to establish a new measurement method for that purpose, which has not yet been studied anywhere in that direction. We consider measuring BPM (beam position monitor) pickup signal by using a fast oscilloscope with more than 4 GHz bandwidth. To test the system, we have done some experimental studies, where charge-exchange type beam halo scrapper, placed at the L-3BT (linac to 3-GeV beam transport) was used for H⁻ stripping. The un-stripped H⁻ and stripped proton (p) separated by bending magnets at the downstream of IP were simultaneously measured by two BPMs. The stripping efficiency of each 324 MHz micro pulse is precisely and separately obtained from the measured H⁻ and p pulses depending on the scrapper position settings. A detail of the present study results are presented.

INTRODUCTION

In 3-GeV RCS (Rapid Cycling Synchrotron) of J-PARC (Japan Proton Accelerator Research Complex), carbon stripper foil is used for multi-turn H⁻ stripping injection [1]. The injected beam energy is 0.4 GeV, while it is accelerated up to 3-GeV and simultaneously delivered to the muon and neutron production targets at the Material and Life Science Facility as well as injected into the Main Ring Synchrotron. At present RCS beam power for operation is much lower than its designed 1 MW, and no serious issues yet with foil lifetime. However, real lifetime and rapid foil failure due to overheating of the foil, especially at high intensity are always serious concerns [2]. The real lifetime means, how long a foil can be put in service until when foil degradation is tolerable. Foil degradation such as, change of foil thickness, pinhole formation as well as deformation of the foil deteriorate the stripping efficiency rapidly, resulting a significant increase of the waste beam at the injection beam dump. It is then determine the foil lifetime even if a foil failure does not occur [3]. On the other hand, residual activation near the stripper foil due to foil scattering beam losses during injection is also another uncontrollable factor and a serious issue for facility maintenance [4].

In order to overcome realistic issues and limitations involved in the conventional H⁻ stripping injection by using stripper foil, a POP (proof-of-principle) experiment for 400 MeV H⁻ stripping to proton (p) by using only lasers is under preparation at J-PARC [5]. Figure 1 shows a schematic view of present method [6]. Similar to the laser-assisted H⁻ stripping method [7], it also has 3 steps, but high field magnetic stripping in the 1st (H⁻ to H⁰) and 3rd (H⁰* to p) steps are replaced by lasers. Widely available high power Nd:YAG lasers can be used for those purposes in order to utilized large photo-detachment and photo-ionization cross sections [8], in the former and later steps, respectively. The 2nd step is an excitation of ground state (n=1) H⁰ atoms to two level higher (n=3) states, where we considered ArF Excimer laser of 193 nm for that purpose. The strategy of

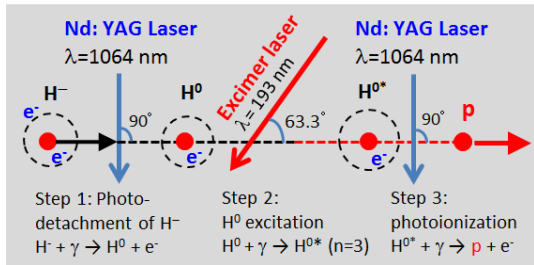

Figure 1: Schematic view of principle for H⁻ stripping to proton by using only lasers. Noted parameters are typical ones estimated for 400 MeV H⁻ beam energy.

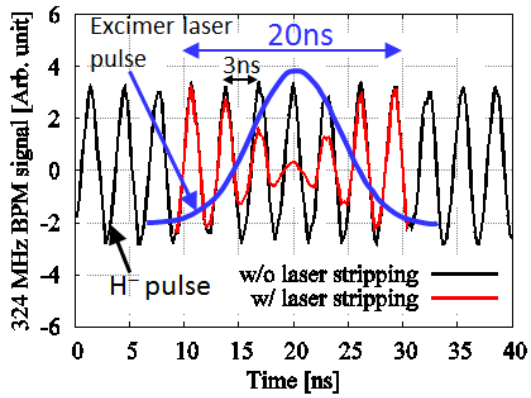

Figure 2: The H⁻ (black) micro pulse signal measured by BPM pickup. The blue curve is a typical laser pulse. The red curve is an expected H⁻ signal out of the laser pulses.

POP experiment is to strip only a single H⁻ micro pulse of 324 MHz. This is because, the whole micro pulses (~ 10^5) can be covered by using laser storage ring [9], which is under development for this purpose. The POP experiment requires precise measurements of not only the stripped protons but also (if any) neutral H⁰ and H⁻ of only a single micro pulse at the downstream of laser and H⁻ interaction

* E-mail address: saha.pranab@j-parc.jp

ISBN: 978-3-95450-192-2 doi:10.18429/JACoW-IBIC2017-TUPCF12

point (IP). For that purpose, we considered using stripline BPM (beam position monitor) pickup signal taken by a fast oscilloscope. Figure 2 shows such a typical measured H^- signal of a BPM pickup (black). If we assume a Gaussian laser pulse like the blue curve, we expect the original H^- will be changed like the red curve, due to its stripping protons at the overlapping region with laser pulses. Here we assume 90% stripping efficiency, estimated based on the laser peak power at the center of the laser pulse, especially for the Excimer laser.

We performed some experimental studies, where at present charge-exchange type beam halo scrapper (carbon foil), placed at L-3BT (linac to 3-GeV beam transport), and near to the IP is used for H^- stripping. The un-stripped H^- and the stripped protons (p) separated by bending magnets at the downstream of IP are simultaneously measured by two BPMs. The stripping efficiency of each 324 MHz micro pulse is precisely and separately obtained from the measured H^- and p pulses depending on the scrapper position settings.

BRIEF CONFIGURATION OF THE STRIPLINE BPM

Figure 3 shows a schematic view for the configuration of 1 stripline pickup out of 4 implemented in each BPM installed at the L-3BT of J-PARC Linac [1]. The shape of the striplines of BPMS at the L-3BT are circular, where striplines are placed just outside of the beam pipe aperture, typically 0.185 m transmission line for the largest BPM types. Transverse beam positions in the horizontal and vertical directions are determined from the difference of the signal of pair pickups in respective directions.

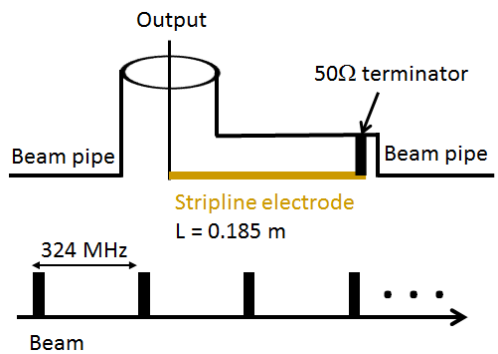

Figure 3: Schematic view of configuration of 1 stripline pickup of the BPM installed in the L-3BT of J-PARC Linac. Four such pickups are implemented in each BPM.

As was shown in Fig. 2, signal of pickup with exactly 324 MHz can be well detected, but due to mainly extremely longer pulse length of more than 200 ps (rms) and also wider momentum spread ($\Delta p/p$), the characteristic features of the pulse shape is not clear. For example, the separation between pulses created at the upstream of the pickup and its reflection with opposite sign as well as separation among 324 MHz pulses. The length of the striplines were also

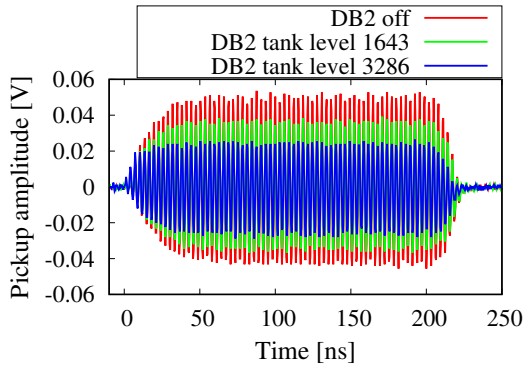

Figure 4: Pickup signal with respect to variation of debuncher amplitude. In this study, data was taken by one 324 MHz BPM placed at the 1st arc section of the RCS.

not particularly optimized for sophisticated purposes, like the present study. However, by using upstream accelerating cavities, the bunch length can be manipulated in order to obtain better time resolution as well as relative change of the bunch length, which is important for the POP experiment. As the magnitude of the output pulse of the pickup depends on the image current times the characteristic impedance of the stripline, amplitude of the output pulse can be used for relative optimization of the longitudinal beam parameters. Experimental studies on that direction are also in progress.

Figure 4 shows preliminary data taken by varying amplitude of the 2nd debuncher (DB2) in order to manipulate $\Delta p/p$ of the H^- beam. The DB2 is placed several 10 meters upstream of the IP, which is mainly used for manipulating $\Delta p/p$ of the H^- beam as required for the RCS. The present data was taken by using a similar BPM, but it is placed in RCS 1st arc section. The signal amplitude increases as DB2 tank level is decreased, and it is thus maximum when DB2 is kept off. Although absolute values of $\Delta p/p$ can not be determined from this data, but one can obtained information of relative change of the longitudinal bunch length.

MEASUREMENT PRINCIPLE OF MICRO PULSE STRIPPING EFFICIENCY

Figure 5 shows a schematic view of the end of L-3BT of J-PARC Linac, where POP experimental devices for H^- stripping by using lasers will be installed at the red rectangular box. Downstream of the IP (laser and H^- interaction point), all three charge fractions can be simultaneously measured. The stripped p and un-stripped H^- separated by bending magnets at the downstream of IP go to 100-degree beam dump and RCS injection BT, respectively. The neutral charge H^0 (if any) goes to the 90-degree beam dump, and those can be measured by further stripping them to p by installing a stripper foil at the upstream of 90-degree in future.

At present, instead of laser, we used one scrapper for stripping H^- to protons, placed near the IP [10]. The scrapers are charge-exchange type and used for cleanup halo or unexpected long tail in the H^- beam. The scrapped H^- are

ISBN: 978-3-95450-192-2 doi:10.18429/JACoW-IBIC2017-TUPCF12

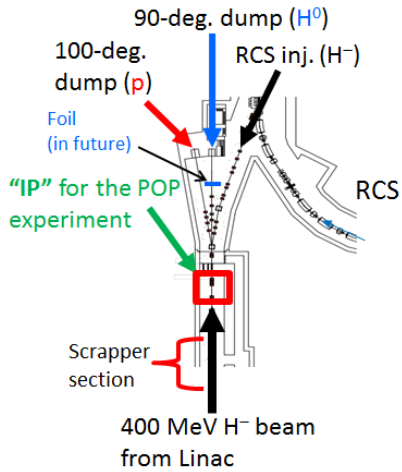

Figure 5: Schematic view of the end section of L-3BT. The H^- laser stripping experimental devices will be installed at the red rectangular box. All three charge fractions can be simultaneously measured at the downstream of IP.

Scrapper & Beam	To 100-deg. Dump (p)	To 90-deg. Dump (H^0)	To RCS (H^-)
Scrapper OUT	- - -	- - -	H^- 100%
Half IN	p 49.999%	1×10^{-3} %	H^- 50%
Fully IN	p 99.998%	2×10^{-3} %	$< 10^{-10}$ %

Figure 6: Schematic view of expected charge fractions at the downstream of IP as a function of scrapper insertion.

stripped to p, and dumped to the 100-degree beam dump (see Fig. 5). The scrapper foil is thick enough (600 µg/cm^2) to strip more than 99.998% of H^- to protons, if intercepted by the scrapper [11]. In order to check the measurement principle, we used one horizontal scrapper as a charge-exchange foil. Figure 6 shows a schematic view of the scrapper insertion for H^- scrapping and the corresponding charge fractions in downstream beam lines. Similar situation can be expected when inserting a vertical scrapper.

MEASUREMENT RESULT

In this experiment, a horizontal scrapper was gradually inserted to the beam line and BPM pick signals of stripped p un-stripped H^- were simultaneously measured by two independent BPMs at 100-degree beam dump and RCS injection BT, respectively. Figure 7 shows raw signals of p (left) and H^- (right) measured by BPM pickups for different position of the scrapper. The horizontal axis is time, where vertical axis is the pickup signal. The data is taken for one typical intermediate pulse of the H^- beam, where a more than 600 of such pulses are injected into the RCS. The non-flatness

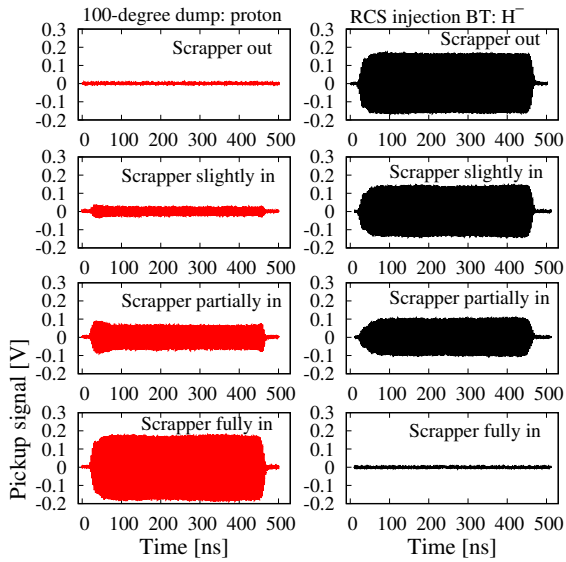

Figure 7: Simultaneously measured p and H^- raw signals for different positioning of the scrapper. The stripping/scrapping efficiency was independently obtained by using FFT analysis of the whole bunch as well as by integration of each pulse.

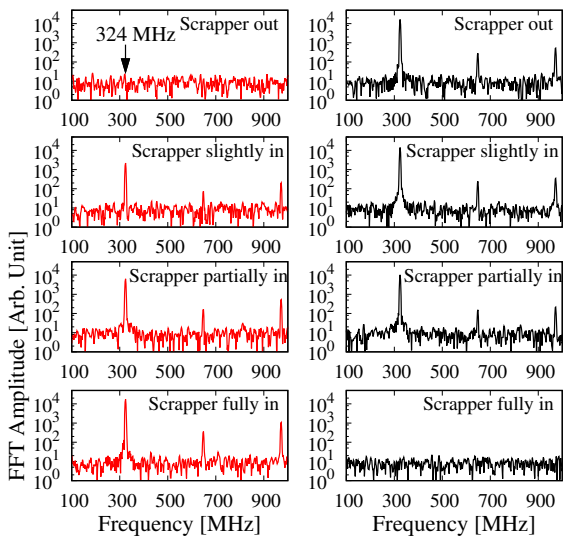

Figure 8: FFT spectra of proton and H^- raw signals shown in Fig. 7. The FFT amplitude corresponds to the micro pulse frequency of 324 MHz was used for the analysis.

at the beginning and at the end of the pulse might be due to character behavior of the chopper system and/or due insufficient beam loading compensation. The response of the signal with respect to the scrapper position can easily be seen. A similar situation is thus expected for H^- stripping by using lasers.

Figure 8 FFT (Fast Fourier Transformation) analysis of the raw signals, used for obtaining independent charge fractions from the FFT amplitude at 324 MHz. Figure 9 shows p and H^- fractions as a function of scrapper position as obtained from the FFT spectra. The stripped p and remaining un-

ISBN: 978-3-95450-192-2 doi:10.18429/JACoW-IBIC2017-TUPCF12

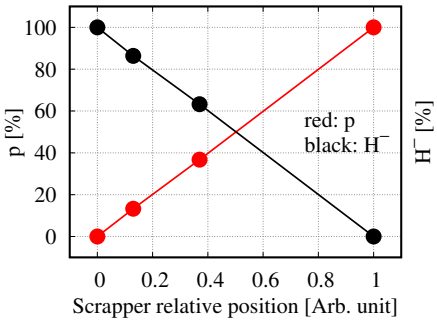

Figure 9: Stripping/scrapping efficiencies as a function of scrapper position as obtained from the FFT spectra. The fraction of scraped p were found to be consistent with expected un-stripped H^- fractions for any scrapper positions.

stripped H^- were precisely measured independently. The sum of p and H^- was obtained be to almost expected 100%, as neutral H^0 fraction was estimated be negligibly small.

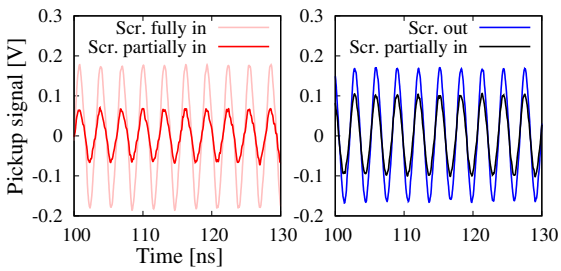

Figure 10: Expanded view of raw signals for some micro pulses, used to calculate individual charge fractions.

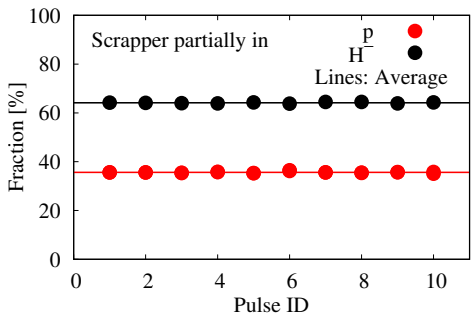

Figure 11: The p and H^- charge fractions of each individual micro pulse were was as obtained from the ratio of integrated yields with different scrapper position as shown in Fig. 10.

Next, we extracted stripping efficiency of each 324 MHz micro pulse, which is essential for the POP experiment as shown in Fig. 2. Figure 10 shows, expanded views of raw signals with and without scrapper, together with partially inserting the scrapper. The p charge fraction for each pulse was obtained from the ratio of integrated yields with scrapper partially in (red) to that with scrapper fully in (pink). The H^- fraction for were also individually obtained in the same day (ratio of data with black and blue). Figure 11 shows p and H^- charge fractions for some typical pulses, when the scrapper was partially inserted. The solid lines are averages values for these 10 pulses and were obtained to be 35.67±0.26%, and 64.15±0.25%, for p and H^-, respectively.

The present measurement technique can be thus demonstrated to obtain precise information of each 324 MHz micro pulse. The present method can be successfully utilized for the POP experiment of H^- stripping by using lasers, in order to precisely measure stripping efficiency of a single micro pulse. On the other hand, measurement of each individual micro pulse is also useful for optimization and adjustment of both H^- beam and laser pulses in the POP experiment. Such an individual measured information each micro pulses can be also used for multi-dimensional purposes, such as beam dynamics studies, optimization of micro level H^- beam, any any other purposes.

SUMMARY

The POP (proof-of-principle) experiment for H^- stripping by using only lasers, which is under preparation at J-PARC, requires precise measurements of all three charge fractions of only a single H^- micro pulse of 324 MHz at the downstream of IP. In order to obtain stripping efficiency of each individual micro pulse, we established a method measuring BPM pickup signal by using a fast oscilloscope. Instead of laser, we used charge-exchange type beam halo scrapper, and simultaneously measured the stripped p and un-stripped H^-. The p and H^- charge fractions as a whole with respect to scrapper positions were precisely obtained by using FFT analysis, where those for each individual micro pulses were also accurately obtained based on integration yields of each micro pulse. In order to obtain better time resolution, further better oscilloscope can be used, but the present measurement method can already be successfully utilized for the POP experiment.

ACKNOWLEDGMENT

The authors acknowledge all members of J-PARC for continuous support and cooperation in the present study.

REFERENCES

[1] High-intensity Proton Accelerator Project Team, "Accelerator Technical Design Report for J-PARC", *JAERI-Tech* 2003-044 and *KEK Report* 2002-13.

[2] M. Plum *et al.*, *Phys. Rev. ST Accel. Beams* 14, 030101 (2011).

[3] P.K. Saha *et al.*, *J. Radioanal. Nucl. Chem.* 305, 851 (2015).

[4] M. Yoshimoto *et al.*, in *Proc. IPAC'17*, p. 2300 (2017).

[5] P.K. Saha *et al.*, in *Proc. of HB'16*, Malmo, Sweden, paper TUPM7X01, p. 310 (2016).

[6] I. Yamane *et al.*, *Journal of PASJ*, Vol. 13, No. 2, 80 (2016).

[7] S. Cousineau *et al.*, *Phys. Rev. Lett.* 118, 074801 (2017).

[8] L. M. Branscomb, "Physics of the One-And-Two-Electron Atoms", edited by F. Bopp and H. Kleinpoppen, North-Holland, (1968).

[9] I. Yamane *et al.*, *Journal of PASJ*, Vol. 10, No. 1, 20 (2013).

[10] K. Okabe *et al.*, *Nucl. Ins. and Meth.* A 811, 11 (2016).

[11] P.K. Saha *et al.*, *Nucl. Ins. and Meth.* A 776, 87 (2015).

ISBN: 978-3-95450-192-2 doi:10.18429/JACoW-IBIC2017-TUPCF13

NEW DESIGN OF A TAPERED-COUPLER BPM TOWARD SIMPLER GEOMETRY AND FLATTER FREQUENCY RESPONSE*

T. Toyama†, T. Koseki, H. Kuboki, M. Okada, KEK, Ibaraki, Japan
W. Uno, A. Ichikawa, K. Nakamura, T. Nakaya, Kyoto University, Kyoto, Japan

Abstract

The tapered-coupler stripline beam position monitor has been used for the intra-bunch feedback system in the J-PARC MR. It should be realized with a special shaped stripline whose width is tailored exponentially and whose gap distance between the inner surface of the beam pipe should be also decreasing as a exponential function in order to keep the characteristic impedance at 50 ohm. This 3D varying geometry makes it difficult to achieve the good balance between the electrode responses to the beam. We propose a new design method with a groove, which may give simpler geometry and flatter frequency response.

INTRODUCTION

In J-PARC (Japan Proton Accelerator Research Complex) a 10-year upgrade plan is running in which a proton beam power is to be upgraded from 470 kW to 1.3 MW in the Main Ring [1]. In this process an intra-bunch transverse feedback system plays an important role [2,3]. As operating beam intensity gets higher, growth rate of collective instabilities becomes larger. In addition a wider operating condition search in which betatron tune and/or chromaticity are optimized for a stable incoherent motion sometimes conflicts with the stability of collective motions. It is, therefore, crucial to get the stronger damping of the collective instabilities. We observe the larger Δ-signal in the vertical plane as shown in Fig.1. We are using the tapered-coupler BPM as a position sensor (Fig.2) [3]. Investigation of the bench test data with TDR indicates that one vertical electrode is deformed. Due to the wideband characteristic of this monitor and its high pass filter response, the unbalance seems to become large in high frequencies. It is still unclear because the FIR filter in the signal processing system should reduce the revolution signal, yet we have larger output in the vertical system and cannot raise the loop gain. A good balanced electrode pair needs better machining and assembling of the three dimensionally shaped electrodes, which seems not straightforward. This motivates the new design of a tapered-coupler BPM toward simpler geometry. This design can also achieve flatter frequency response that was difficult in the previous design.

PROPERTIES OF STRIPLINE PICKUPS

The stripline pickup with straight electrode is schematically shown in Fig. 3. The signal is terminated with resistors at both ends. The coupling constant of the pickup which is defined as the induced voltage on the pickup per unit beam current, is constant, k_0, in this case [4]. With the relativistic beam ($v \approx c$) and the electrode length ℓ, we obtain the frequency response as

$$F(\omega) = jk_0 e^{-j\omega\ell/c} sin(\omega\ell/c).$$

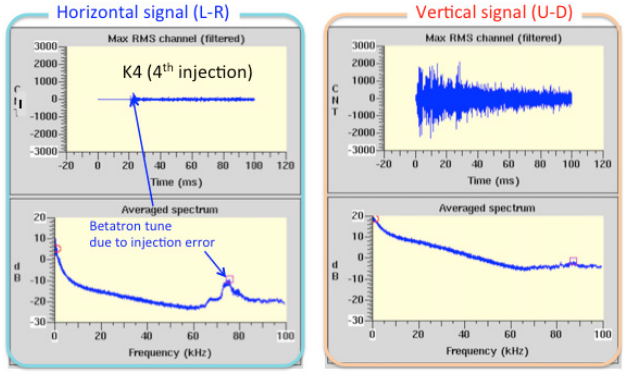

Figure 1: Signals from the left-right pair (left plots) and up-down pair (right plots). Upper plots are time domain signals and lower plots are frequency domain signals.

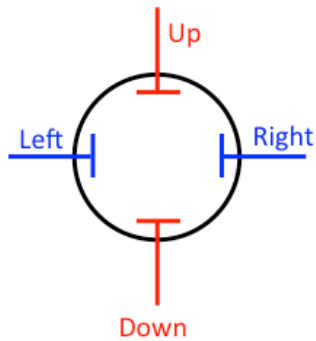

Figure 2: Layout of the BPM electrodes.

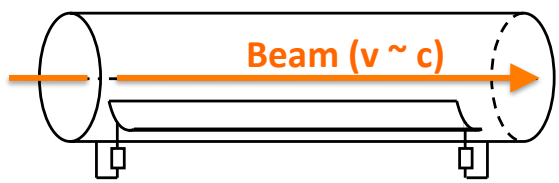

Figure 3: Stripline pickup with a constant electrode width.

In the case of an exponentially tapered stripline as Fig. 4, the coupling constant is $k(z) = k_0\, e^{-\alpha z/\ell}$ and the frequency response is

* Work partially supported by MEXT KAKENHI Grant Number 25105002
† takeshi.toyama@kek.jp

ISBN: 978-3-95450-192-2 doi:10.18429/JACoW-IBIC2017-TUPCF13

$$F(\omega) = k_0 \frac{j\omega\ell(1 - e^{-\alpha - j\frac{2\omega\ell}{c}})}{c(\alpha + \frac{2j\omega\ell}{c})}$$

where z is the longitudinal coordinate and α is a constant which decides the exponential decay of the electrode [4,5]. The electrode starts at $z = 0$ and ends at $z = \ell$. In the setup as Fig. 4 the width of the electrode and the gap between the electrode and the inner surface of the beam pipe should go to as small as possible at the downstream end in order to obtain the flatter frequency response. In the case that the coupling constant ends at a certain finite value as shown in Fig. 5 (a), the amplitude and phase responses have ripples in the frequency domain. In Fig. 5 (b) the amplitude response is plotted. When the coupling constant ends at a sufficiently small value, which means the electrode becomes very thin at the end, the response can be close to the simple high pass filter response [5]. Figure 6 suggests this tendency.

In a practical realization of these kinds of shape, 3D varying shape in Fig. 7 is already not easy to machine and assemble. Moreover, achieving the thin end of the electrode adds another difficulty [6].

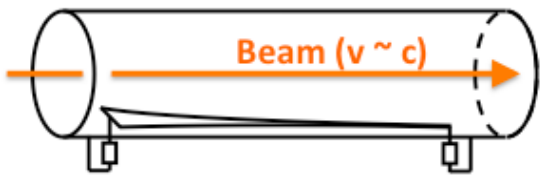

Figure 4: Stripline pickup with an exponential electrode.

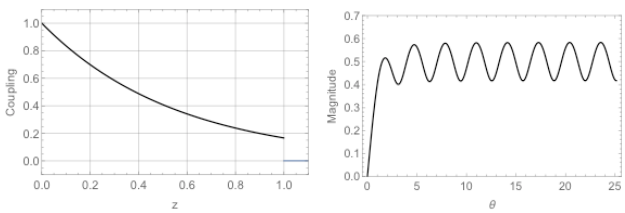

(a) (b)

Figure 5: Coupling constant and frequency response with a larger end width.

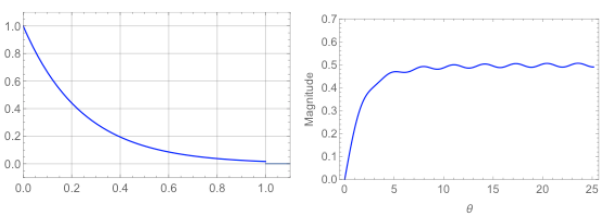

(a) (b)

Figure 6: Coupling constant and frequency response with a smaller end width.

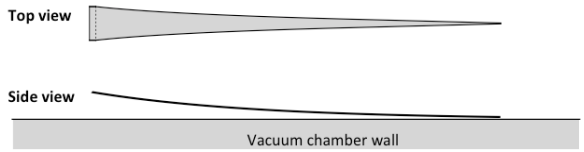

Figure 7: Top and side views of the conventional tapered coupler.

NEW DESIGN

The key of the response is the coupling constant k(z). It should have smooth reduction as an exponential function or other functions of z and approach to zero at the end [6]. It can be realized by other simple geometries with a groove, a slot and a simpler shaped electrode. Two designs are proposed here.

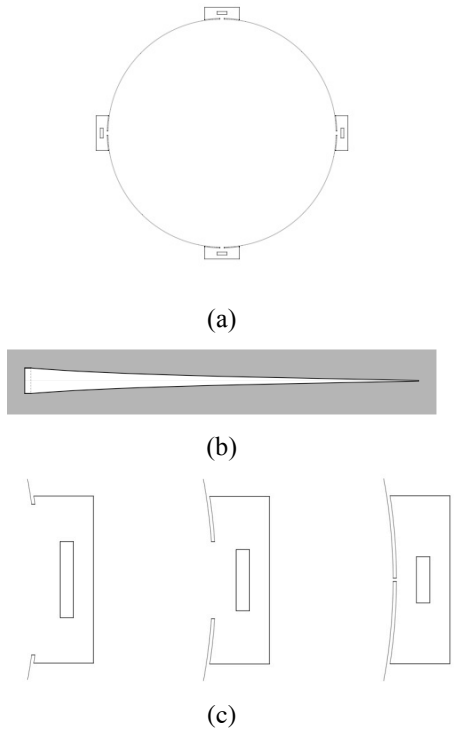

(a)

(b)

(c)

Figure 8: Geometry of the groove, slot and electrode. (a) the detector cross section, (b) the slot and (c) the enlarged cross section of the electrode part, the upstream end to the downstream end from the left to right.

Electrode in a groove covered by a tapered slot

The first design candidate is to set the electrode in the groove and covered by the tapered slot as shown in Fig. 8. The control of the coupling constant is performed with varying the slot width. To keep the characteristic impedance at 50 Ω the electrode width is varied. The example below was optimized with a 2.5D calculation that is a combination of 2D boundary element method and 1D transmission line analysis [7]. Figure 9 (a) shows the amplitude of the frequency response and Fig. 9 (b) is the phase response. Although there still remains a ripple, the flatness is improved comparing with Fig. 5 (b). Better

ISBN: 978-3-95450-192-2 doi:10.18429/JACoW-IBIC2017-TUPCF13

response might be possible with further geometry optimization.

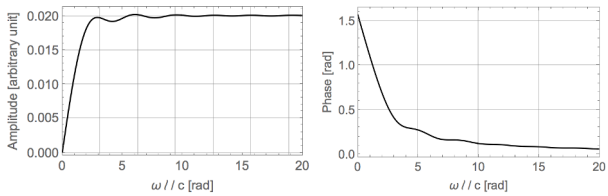

(a) (b)

Figure 9: Frequency response of the electrode in a groove covered by a tapered slot. (a) and (b) are amplitude and phase response in frequency domain, respectively.

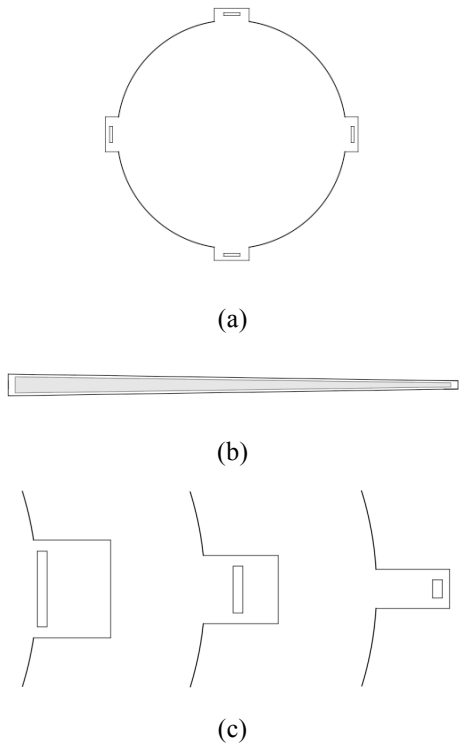

(a)

(b)

(c)

Figure 10: Geometry of the groove, slot and electrode. (a) the detector cross section, (b) the slot and (c) the enlarged cross section of the electrode part, the upstream end to the downstream end from the left to right.

Inclined tapered electrode in a tapered groove

The second design candidate is to set the inclined tapered electrode in the tapered groove as shown in Fig. 10. There are several parameter choices. One is to vary the groove depth and the electrode width and gap [8] and another is to vary the groove width and the electrode width and gap. The example below was optimized with a latter method and 2.5D calculation as in the previous section.

Figure 11 (a) shows the amplitude of the frequency response and Fig.11 (b) is the phase response.

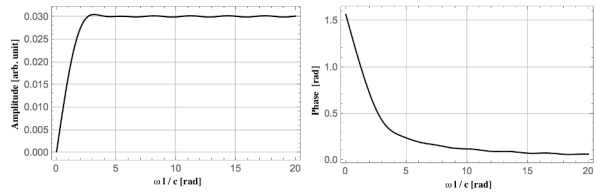

(a) (b)

Figure 11: Frequency response of the inclined tapered electrode in a tapered groove. (a) and (b) are amplitude and phase response in frequency domain, respectively.

CONCLUSION

New designs with simpler electrode geometries are proposed. First one is to set the electrode in the groove and covered by the tapered slot. Another is to set the inclined tapered electrode in the tapered groove. Machining and assembling difficulty seems to be reduced. These structures are estimated to have flatter (small ripple) frequency responses than the previous design with a practical parameter, using 2.5D numerical calculations.

The 3D simulation and manufacturing test setups are on going.

ACKNOWLEDGEMENT

This work was partially supported by MEXT KAKENHI Grant Number 25105002.

REFERENCES

[1] Y. Sato, ATAC2017, J-PARC, Feb. 2017.

[2] T. Toyama, "Status of the Intra-bunch Feedback at J-PARC Main Ring" presented at IBIC'15, TUBLA03, unpublished.

[3] K. Nakamura *et al.*, "Performance Evaluation of the Intra-bunch Feedback System at J-PARC Main Ring", in *Proc. IBIC'14*, THCXB2, pp.727-730.

[4] B. M. Oliver, "Directional Electromagnetic Couplers", Proc. I.R.E., Vol.42, No.11, pp.1686-1692, 1954.

[5] T. Linnecar, "The High Frequency Longitudinal and Transverse Pick-ups used in the SPS", CERN-SPS/ARF/78-17.

[6] Y. Shobuda *et al.*, "Triangle and concave pentagon electrodes for an improved broadband frequency response of stripline beam position monitors", *Phys. Rev. Accel. Beams*, vol.19, p.021003, Feb. 2016.

[7] T. Toyama, "A Multi-conductor Transmission Line Model for the BPMs", in *Proc. IPAC'14*, THPME131, pp.3550-3552.

[8] W. Uno *et al.*, "Improved Tapered Coupler", presented at US-Japan collaboration, Nov. 2016. https://indico.fnal.gov/conferenceOtherViews.py?view=stan dard&confId=13080

ISBN: 978-3-95450-192-2 doi:10.18429/JACoW-IBIC2017-TUPCF14

BENCHTOP BPM CALIBRATION USING HELICAL PULSE LINES FOR NON-RELATIVISTIC BEAMS*

C. Richard#, National Superconducting Cyclotron Laboratory, East Lansing, USA
S. Lidia, Facility for Rare Isotope Beams, East Lansing, USA

Abstract

Calibration of capacitively-coupled beam position monitors (BPMs) for use in non-relativistic beam lines has proven to be challenging. This is due to the fields generated by the beam being non-transverse causing the measured signals to depend on the measured frequency and the beam velocity [1]. In order to correct for these effects, calibration of BPMs may be done with an apparatus that is capable of simulating the fields generated by non-relativistic beams for several beam velocities. One possible method of simulating these beams is to use a helical pulse line. This paper studies the ability of helical lines to simulate the fields generated by slow beams for BPM calibration.

INTRODUCTION

Capacitative beam position monitors (BPMs) are commonly used to measure the orbit of relativistic beams in particle accelerators. They can also be used in non-relativistic beamlines, however, the measured positions from the BPMs become dependent on the beam velocity and measurement frequency [1, 2]. These effects are due to the electromagnetic fields generated by the beam no longer being pancaked by relativistic effects. For an off axis beam, this results in a difference in the extents of the fields along the pipe which cause the BPM pickups on opposite sides to measure a different frequency spectrum. This effect needs to be carefully calibrated in order to achieve accurate measurements.

Typical calibration of BPMs is performed using a straight wire strung through the BPM. Signals are sent down the wire that create electromagnetic fields that mimic the fields generated from a beam. The wire is moved along a grid of positions in the pipe and at each location the position of the wire is calculated from the BPM signals using a difference-over-sum formula. By comparing the calculated wire positions to the actual positions, non-linear effects and abnormalities in the measured positions can be determined.

However, signals on a straight wire propagate at the speed of light, therefore straight wires cannot be used to calibrate BPMs that will be used to measure non-relativistic beams. Currently, BPMs for non-relativistic beamlines are calibrated primarily with simulations to determine non-linear effects as well as frequency and velocity dependence of the measurements. Benchtop, straight wire calibrations are also performed to determine the effects of any physical abnormalities of each BPM [3].

* Work supported by Michigan State University and the National Science Foundation: NSF Award Number PHY-1102511
#richard@nscl.msu.edu

To ensure proper calibration of BPMs for use in non-relativistic beamlines, the signals sent through the BPM should travel at the expected beam velocity to properly simulate the fields on the pick-ups.

Helical Wire Phase Velocity

One method to propagate signals at low velocities is to send pulses down a helical wire. Helical lines in free space have been shown to propagate signals at any phase velocity less than the speed of light by choosing the correct parameters for the helix [4].

A singal propagating down a helical line can be modelled using the sheath helix approximation. A sheath helix is constructed by winding a thin wire in a helix. A second thin wire is then wound directly above the first and this process

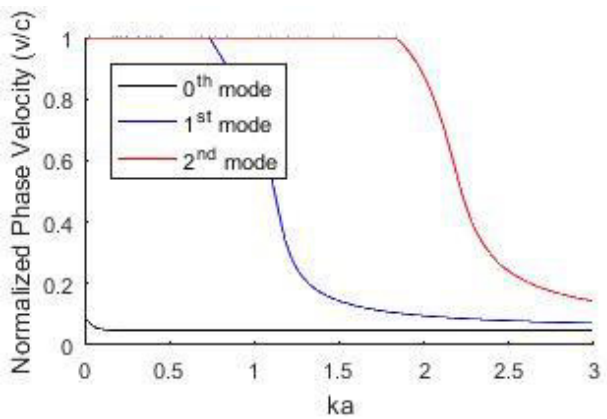

Figure 1: Normalized phase velocity of the first three modes of a sheath helix, pitch angle is 0.048 rad and R/a=4. K is the free space propagation constant and a is the helix radius.

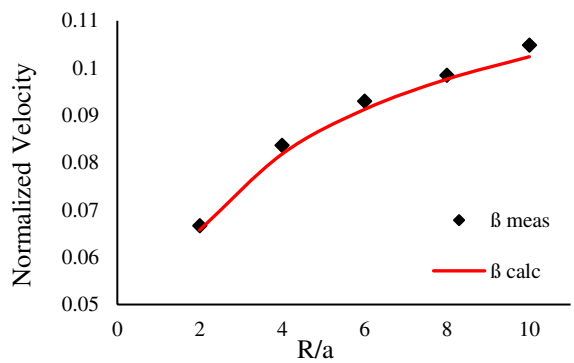

Figure 2: Velocity comparison for different ratios of pipe radii, R, to helix radius, a. Sheath helix phase velocity of 0th mode in red and results of simulations in black.

ISBN: 978-3-95450-192-2 doi:10.18429/JACoW-IBIC2017-TUPCF14

is repeated until the entire gap in the helix is filled. Taking the limit of the wire radii going to zero, the result is a cylinder or sheath where the surface current travels along a helical path. This model is used to simplify the boundary conditions at the helix by removing azimuthal and longitudinal variations.

Using the sheath helix model the phase velocity can calculated for a helix with pitch angle, φ, and radius, a, inside a pipe of radius, R (figure 1). The high frequency limit of the phase velocity for all modes is v/c=sin(φ). The low frequency limit of the phase velocity for all modes except for the lowest order mode is the speed of the light. For the lowest order mode, the pipe causes the low frequency phase velocity to level off below the speed of light. For small enough pitch angles the phase velocity plateaus at approximately v/c=sin(φ)ln(R/a). If pipe is removed from the calculation then the low frequency limit of the phase velocity of the lowest mode goes to the speed of light, the same as the other modes, and the high frequency limit does not change. The behaviour of the higher modes remains the same in this case. Without the pipe it would be necessary to go propagate signals above ka=1, which can correspond to tens gigahertz. The reduction of the phase velocity of the lowest mode at low frequencies caused by the pipe allows for helices to be used to reproduce beam signals.

HELIX SIGNALS

In order for helical lines to be used for BPM calibration they must be able to propagate signals of a desired shape at a specific velocity to be consistent with a bunch. The properties of the signals propagated on a helical line in a pipe were simulated using CST Suite® [5] and compared to the sheath helix model where applicable. The apparatus consisted of a 400 mm long helix in a 410 mm long pipe with inner diameter of 40 mm. The extra 5 mm of pipe on each side was used to transition the helix to a straight wire before the end caps. The ends of the pipe are blocked by plates that touched the pipe with a 50 Ω line for inputting and outputting signals. The end plates are not attached to the pipe to allow for the pipe to be moved to simulate different beam positions (Figure 3). The electromagnetic fields were measured using field probes at the inside surface of the pipe allowing for the fields that would be detected by a BPM to be measured. Currently, there is not a BPM in the simulation to simplify the model and reduce simulation time.

Pulse Velocity

The velocity of 1ns Gaussian pulses on the helical line was measured from the simulations and compared to the sheath helix approximation for several different pitch angles and pipe radii (figure 2). For all parameters used, the velocity of the primary pulse differed less than 2.5% from the low velocity limit of the lowest order pulse.

Pulse Shape

When a Gaussian pulse was propagated through the helical line, the signal separated into several lobes (Figure 4). Each consecutive lobe travels at a slightly slower velocity causing the lobes to spread apart as the signal propagates. The farther the signal propagates the amplitude of each lobe grows.

This effect may be explained by the pulse exciting multiple modes of the helix, however, the sheath helix model predicts that the n^{th} mode can only be excited by frequencies above approximately ka=n or f=nc/a where a is the helix radius and c is the speed of light. For the simulated 5mm radius helix, the first excited mode requires a frequency above 60 GHz. This is a much higher frequency than any of the simulated input signals contained. Another issue is the higher modes are capable of propagating with velocity from c·sin(φ) to c. Because of this large range of velocities, a faster propagating lobe would be expected to exist. The absence of this behaviour makes higher mode excitation seem unlikely.

Another explanation is the formation of the lobes is caused by the input signal exciting the lowest order mode at a range of frequencies. This interpretation narrows the necessary frequency range to a range expected given the input signal. However, this explanation fails to explain the formation of discrete lobes because the Gaussian input pulse has no local peaks in the frequency spectrum to correlate with the phase velocity of the individual lobes.

Both these explanations fail to adequately explain the formation of the lobes, however, they agree that the lobes form due to higher signal content. This was found to be true. When Gaussian pulses of different widths were input into the same helix, the shorter pulses caused the lobes to form faster than the longer pulses. In fact, almost no deformation of the signal is seen if the initial pulse is broad enough (see Fig. 4).

Signal deformation is also impacted by the pitch angle of the helix. A helix with a smaller pitch angle will cause the amplitude of lobes to grow faster which results in more

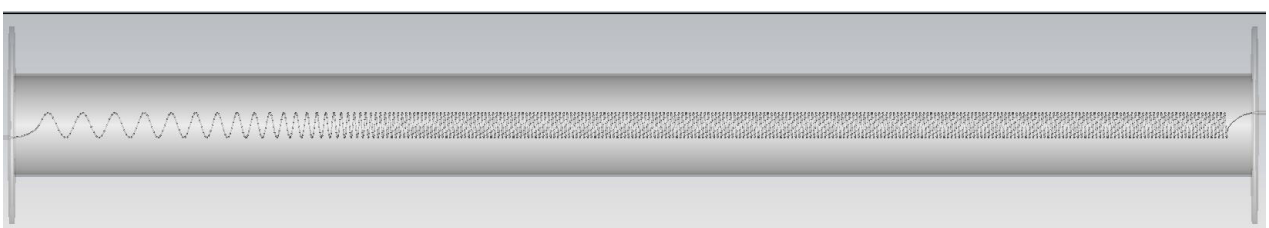

Figure 3: Model of helix in a pipe. The left side of the helix has a decreasing pitch angle for impedance matching and to improve signal shape.

ISBN: 978-3-95450-192-2 doi:10.18429/JACoW-IBIC2017-TUPCF14

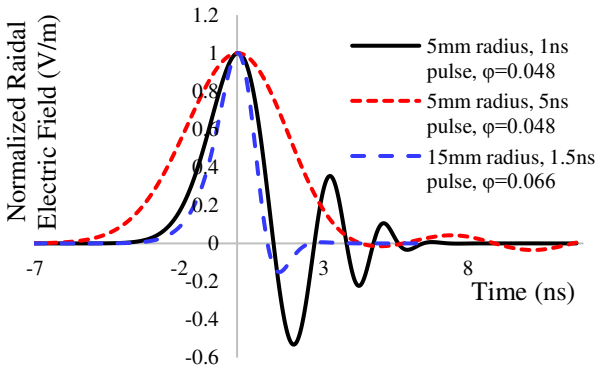

Figure 4: Example of lobe formation in a helix after Gaussian signal propagating 150mm. Increasing the pulse length decreases the signal deformation as well as increasing the helix radius and the pitch angle, φ.

lobes forming than a looser helix for the same input pulse. Therefore, the signal deformation can be reduced by increasing the pitch angle of the helix. However, this also causes the phase velocity to increase, but that can be compensated by increasing the radius of the helix to lower the R/a ratio.

The lobe formation can also be reduced by creating a section of helix with decreasing pitch angle. In these sections the input signal is compressed in length by the decreasing distance between the turns of the wire. If the signal is being compressed faster than the lobes are spreading apart due to differing phase velocities then the lobes cannot split from the original pulse. However, as soon as the pitch becomes constant the lobes diverge from the primary pulse. Therefore, if the BPM being calibrated is placed just passed the reducing pitch angle section of the helix it is possible to measure a pulse with minimal deformation that is traveling at the appropriate velocity. Another possibility is to decrease the pitch angle across the entire helix then the BPM can be moved to the region with the desired phase velocity.

These methods of reducing the formation of lobes have been found empirical and while they reduce the signal deformation they cannot completely remove it, nor do they address the root cause of the deformation. Because the signal deformation appears to be caused by the geometry of the helix, it is likely that the deformation cannot be completely removed. Therefore, it is recommended that the BPM is placed as close to the start of the line or end of the pitch reduction section to minimize the formation of the lobes.

IMPEDANCE MATCHING

To properly calibrate BPMs for non-relativistic beamlines, several frequencies should be tested because of the frequency dependence of the measurements. Therefore, to use the helical line for benchtop BPM calibration, the impedance of the input and output must be matched to the helical line across a range of frequencies.

Direct calculation of the impedance from the sheath helix model has proven to be insufficient, most likely due to the difference in the fields near the helix. Calculating the impedance at the input and output ports is further confounded because the wire must deform from the helix near the end cap in order to exit at the 50Ω line.

While a direct calculation of the impedance would be useful for exactly matching the impedance at a specific frequency it is less useful for broadband matching because the impedance may change greatly over a range of frequency. Instead geometric means can be used to help impedance matching. The decreasing pitch angle section described above not only compresses the signal it also slowly changes the impedance of the line. Therefore, by slowing decreasing the pitch angle from π/2, a straight wire, at the helix to the desired angle, the impedance is changed from that of a coax line to the impedance of the desired helix line. Matching the input to the helix then becomes a matter of matching two coax lines, a much simpler problem. Simulations show this can increase in the amplitude of the propagated signal by a factor of eight, without attempting to optimize the decrease in the pitch angle. Similarly, the output matching can be improved by increasing the pitch angle from the desired helix to π/2.

However, reducing reflections in this matter is best down by slowly decreasing the pitch of the helix. But, in order to maintain pulse shape, the pitch angle must be quickly decreased to stop the lobes from spreading apart. Therefore, when using this method a trade-off must be made between signal shape and impedance matching.

CONCLUSION

While helical lines show promise for use in benchtop BPM calibration. They are capable of propagating pulses are any desired velocity less than the speed of light by changing the parameters of the helix. Therefore the same device can be used for calibrating for different beam velocities simply by changing the helix. Also, signal deformation can be almost completely removed by increasing the pitch angle and propagating a longer pulse.

However, there are still some issues to be worked out. Most importantly, the impedance matching needs to be improved and the signal deformations need to be reduced for tighter helices and shorter pulses. However, varying the pitch of the helix is a major step in alleviating both these problems.

REFERENCES

[1] R. Shafer, "Beam Position Monitor Sensitivity for Low-ß Beams", in *Proc. LINAC'94*, Tsukuba, Japan, Aug. 1994, pp.905-907.

[2] P. Kowina *et al.*, "FEM Simulations – A Powerful Tool for BPM Design", in *Proc DIPAC'09*, Basel, Switzerland, May 2009, Paper MOOC03, pp.35-37.

[3] Oren Yair *et al.*, "FRIB Beam Position Monitor Pick-up Design", in *Proc. IBIC'14*, Montery, Ca, USA, Sep. 2014, paper TUPF16, pp.355-360.

[4] S. Sensiper, "Electromagnetic Wave Propagation on Helical Conductors", Ph.D. thesis, MIT, 1954.

[5] CST Studio Suite, https://www.cst.com.

ISBN: 978-3-95450-192-2 doi:10.18429/JACoW-IBIC2017-TUPCF15

S-BAND CAVITY BPM READOUT ELECTRONICS FOR THE ELI-NP GAMMA BEAM SOURCE

M. Cargnelutti, B. Baričevič, Instrumentation Technologies, Solkan, Slovenia
G. Franzini, D. Pellegrini, A. Stella, A. Variola, INFN-LNF, Frascati, Italy
A. Mostacci, Sapienza Università di Roma, Rome, Italy

Abstract

The Extreme Light Infrastructure – Nuclear Physics Gamma Beam Source (ELI-NP GBS) facility will provide an high intensity laser and a very intense gamma beam for various experiments. The gamma beam is generated through incoherent Compton back-scattering of a laser light off a high brightness electron beam provided by a 720MeV warm LINAC. The electrons are organized in compact trains with up to 32 bunches, each separated by 16ns. To optimize the laser-electron interaction and therefore the generation of the gamma rays, one big challenge is to precisely monitor the trajectory of each electron bunch.

To match this requirement, at the interaction point two S-band cavity beam position monitors will be used, and the related readout system should perform bunch-by-bunch position measurements with sub-µm resolution. Using 500MS/s ADC converters and dedicated data processing, the readout system proposes an alternative measurement concept. In this paper the architecture of the system, the implemented signal processing and the results of the first laboratory tests will be presented.

INTRODUCTION

The ELI-NP accelerator facility employs a warm C-band electron LINAC [1]. At every injection, up to 32 electron bunches are accelerated and delivered to two interaction points (IP) with energies of 280MeV and 720MeV. The beam structure at the interaction point is represented in Figure 1.

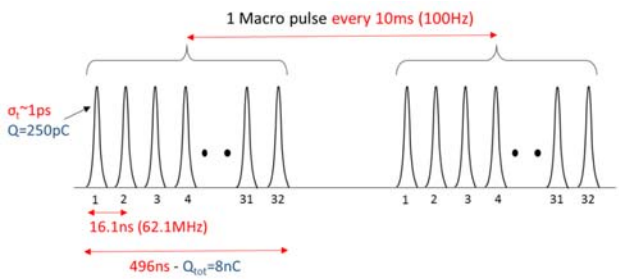

Figure 1: Electron beam structure at the interaction point.

In order to align the beam with the laser at the IP, the position of each bunch should be measured with µm resolution, in the range of ±1mm. For this purpose four low-Q cavity beam position monitors (BPMs) will be installed immediately before and after the IPs [2].

The cavity BPM pick-up is the same BPM16 used at PSI [3]. It consists of one reference cavity and one position cavity, with low quality factor (Q=40) and a resonant frequency of 3.284GHz. This makes sure that the signal excited by each bunch will decay fast enough to not interfere with the signal coming from the next bunch: this is necessary condition to perform individual bunch measurements.

THE READOUT ELECTRONICS

The concept and a first prototype of readout electronics was presented in [4] and further developed into a commercial readout electronics called Libera CavityBPM, shown in Figure 2.

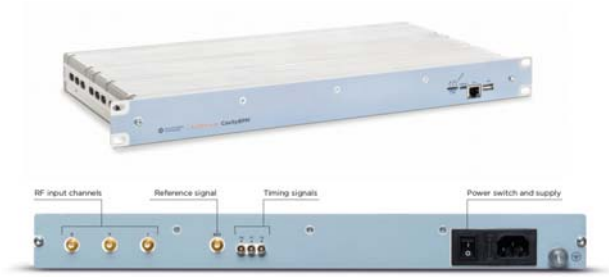

Figure 2: Cavity BPM readout electronics.

The cavity signals are processed by an RF front-end, which filters out the unwanted frequency components. A variable attenuation stage is used to adjust the position full-scale and to optimize the signal level depending on the beam conditions (e.g. charge, position). Finally the signals are down-converted to an intermediate frequency (IF) in the 2nd Nyquist zone, and filtered again to remove the signal components which are outside of the bandwidth of interest. A block-scheme of the RF front-end is shown in Figure 3.

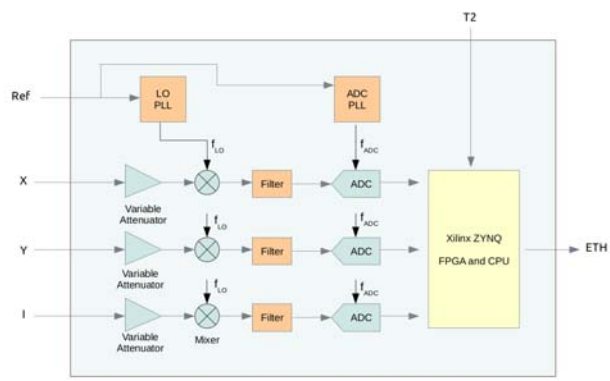

Figure 3: RF front-end of the readout electronics.

ISBN: 978-3-95450-192-2 doi:10.18429/JACoW-IBIC2017-TUPCF15

The local oscillator (LO) frequency component and the A/D converters sampling rate (ADC) are generated by two PLLs which are locked to the accelerator reference frequency of 62.087MHz.

500MS/s Digitizer and Bunch Decoupling

The signals are later digitized by 14bit dual A/D converters, sampling at 500MSps. The high sampling rate is required to collect enough information from each bunch: with a separation of 16.1ns, only 8 samples per bunch are available. The ADC data is continuously transferred through serial interfaces to a Xilinx ZYNQ 7035 System-on-Chip which provides all the necessary computing resources: FPGA, CPU and internal shared memory. Every time a new injection happens, the trigger signal enables the storage of up to 4k ADC samples in the memory of the device, ready to be further processed.

Once the signals are digitized, the samples belonging to different bunches need to be separated. In the proposed solution, a 100-bin FIR filter is used to extract the individual bunch signals from their superposition, and to compress them to occupy exactly 8 samples. The filter is called "*Deconvolution filter*" and its coefficients are calculated starting from the single-bunch response of the cavity. An example of how the filter works with a single bunch input signal is presented in Figure 4.

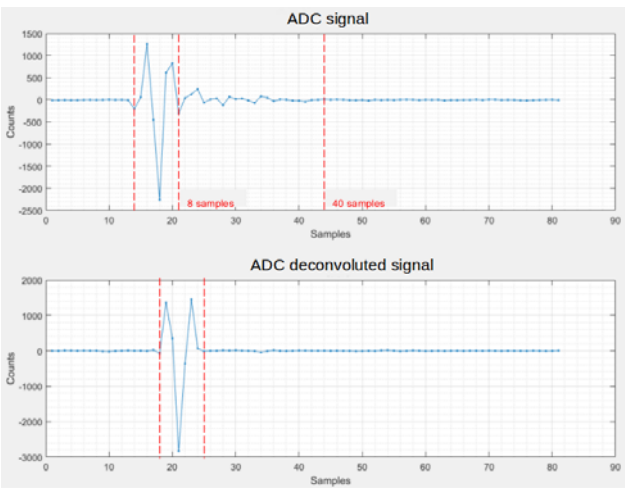

Figure 4: Bunch separation through deconvolution filter.

Position Calculation and Calibration

Once the data of each bunch is separated, it is possible to calculate the amplitude (V_x, V_y, V_r) associated to each cavity signal through a sum-of-squares formula and to calculate the absolute position value with the equations:

$$X = K_x \frac{V_x}{V_r} \qquad Y = K_y \frac{V_y}{V_r}$$

where K_x, K_y are calibration constants which depend on the sensitivity of the cavities and on the relative value of the variable attenuators. As the position is calculated through the ratio between two channels, each error on one of the channels is reflected directly in the instrument accuracy. For this reason a calibration procedure is required to characterize the attenuation and phase shift introduced by the variable attenuators and the installation setup (cables, connectors, etc...), and to correct his effect when calculating the amplitudes.

Finally, to determine the sign of the position, the phase relation between the position and the reference cavity, and this is done in parallel through I/Q demodulation.

LABORATORY SETUP AND MEASURES

A delicate aspect in the validation of the Cavity BPM readout electronics is how to reproduce in the laboratory an input signal which is a good approximation of the signal produced by the beam. The test setup is prepared by INFN-LNF and is presented in Figure 5.

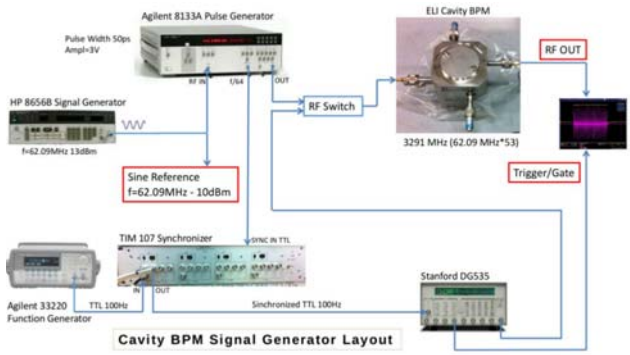

Figure 5: Laboratory test-setup.

The best way to to generate a signal which has the same resonant frequency and decay time as the real one, is to use directly the same BPM16 cavity which will be used in the machine. A pulse generator feeds pulses to one port of one position cavity and from the other port the resonant output signal is split in two and connected to the position and reference cavity inputs of the electronics. The pulse generation is continuous and a gate is used to select only a certain number of pulses, from 1 to 32 to reproduce the real beam structure.

Although the setup produces a very good approximation of the beam signal, there are some limits compared to the real measurement conditions:

- the high insertion loss of the cavity limits the signal level at the instrument input;
- the pulse generator is not ideal interims of cleanliness amplitude fluctuations;
- splitting the output of the cavity results in two input signals with correlated noise;

Single-Bunch Measurements

In the single-bunch measurements, the signal shown in the upper part of Figure 4 is provided to the system. The deconvolution filter is not used, therefore 40 ADC samples are considered in the calculation of the signal

ISBN: 978-3-95450-192-2 doi:10.18429/JACoW-IBIC2017-TUPCF15

amplitudes. The internal attenuators are set at the same level and the input signal is equally split among the position and reference cavity. In this way the measured position is always at the full scale, in this case equal to 1mm. For the analysis, the ratio between the standard deviation of the position and its mean value is considered.

Figure 6 presents how this ratio depends on the phase difference between the two input channels considered. For each point, 100 independent measurements were taken in order to calculate the statistics.

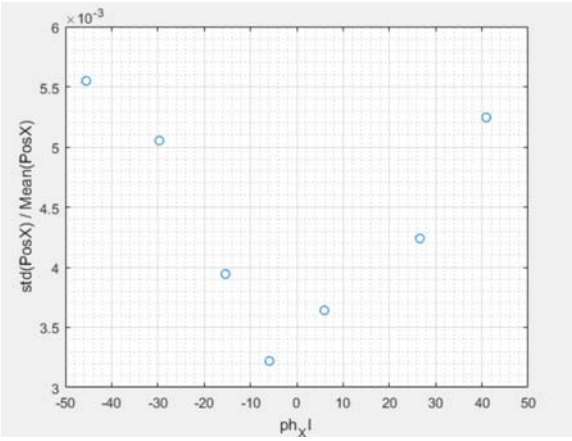

Figure 6: Performance in single-bunch mode.

As it is possible to see, the best performance is achieved when the two signals are perfectly in phase: this point is equivalent to a 3.2µm RMS over a full scale of one mm. When the phase changes the ration goes up to 5.5%. This effect has still to be fully understood, however one possible reason is the fact that with no phase shift, the correlated noise gets cancelled by the position calculation ratio. This is not true any more when the phase is changed. This aspect will require further analysis on a real machine.

Bunch Train Measurements

A train of 32 bunches was generated with the setup, and the input signal for the cavity is shown in Figure 7.

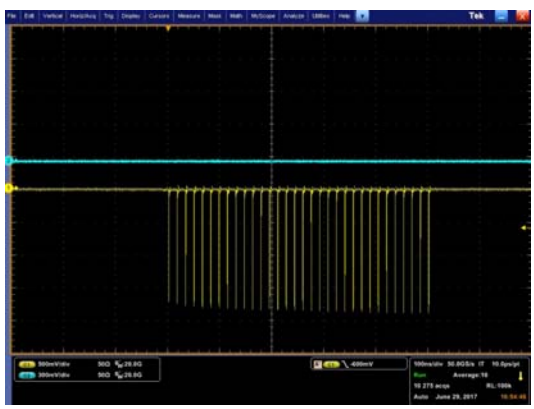

Figure 7: Multi-bunch input signal for the cavity.

In order to process this signal and calculate individual bunch positions, the deconvolution filter was used. Each bunch position along the train was individually analyzed and the results are presented in Figure 8.

It is possible to see that the behaviour is more stable in the inner part of the train, while it slightly deviates in its head and tail. The standard deviation of the position for each bunch is comparable with the results achieved in single-bunch.

Changing the phase relation between the two input signals results in the same behavior observed in single bunch, with the performance getting slightly worse.

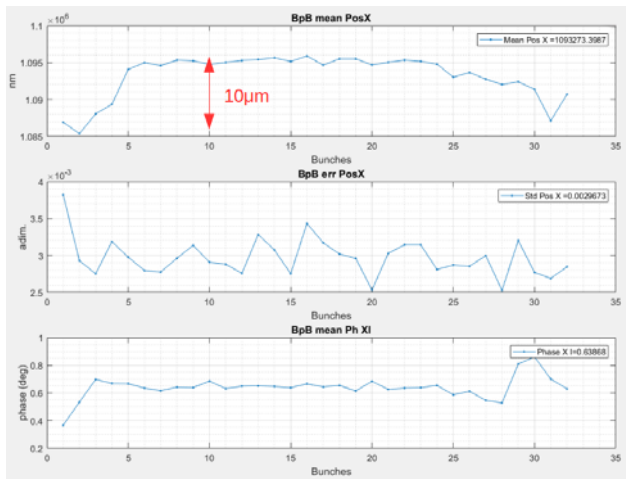

Figure 8: Performance in bunch train mode.

Linearity and Long-Term Stability

The measurements in this section were done to characterize the HW in terms of linearity and long-term stability. To judge the linearity of the system, one of the two input signals was progressively attenuated using an external attenuator, and the position was monitored through the instrument. Figure 9 presents the results of the measurements which show a good linearity.

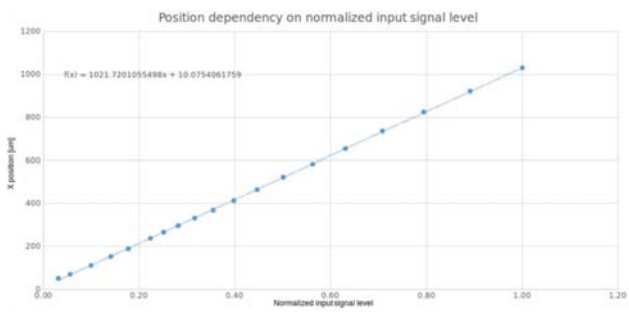

Figure 9: Linearity of the position calculation.

To evaluate the long-term stability, the setup was left running for 48 hours. The input signal was a train of bunches and the analisys focused on the measurements on the 10th bunch inside of the train. As it is possible to see from Figure 10, both input signals measure the changes in the signal levels due the environment condition deviations between day and night. As the position comes from the ration between the two amplitudes, this influences cancel

ISBN: 978-3-95450-192-2 doi:10.18429/JACoW-IBIC2017-TUPCF15

out in the position, which remains within ±1μm, as it is visible in Figure 11.

The excellent long-term stability is also due to the method chosen to cool the instrument: the big heatsink, together with heat pipes provides uniform temperature conditions for the RF chains, which are therefore not exposed to gradients which would be visible in the position.

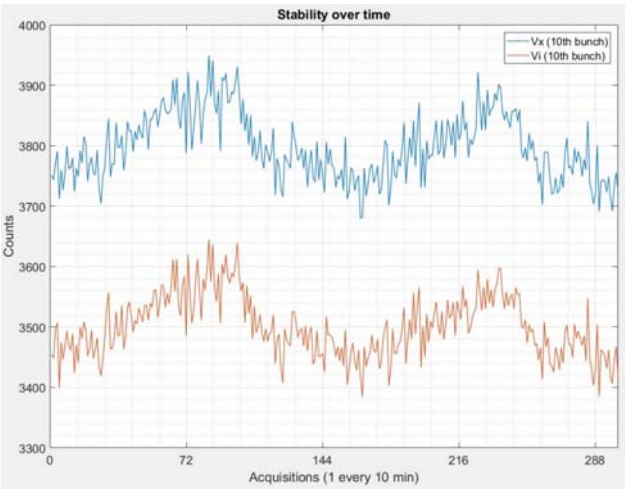

Figure 10: Long-term evaluation of signal amplitudes.

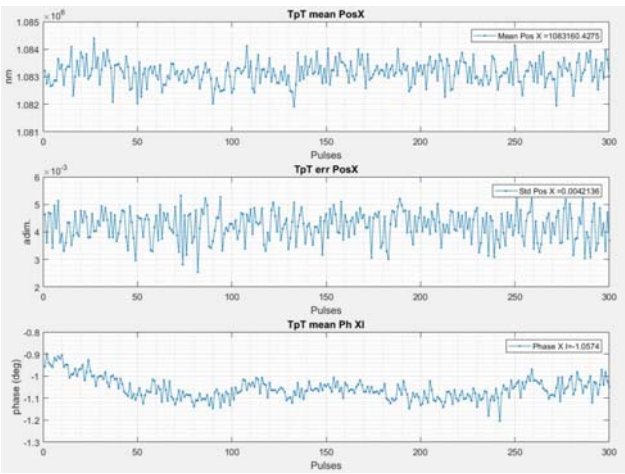

Figure 11: Long-term evaluation of position.

CONCLUSIONS

Based on simulations and extensive prototyping, the cavity BPM readout electronics for the ELI-NP GBS were developed into a commercial system. In order to fulfill the requirements of the project, the electronics employ 500MSps A/D converters and a novel approach for separating the bunches using deconvolution filters.

In order to evaluate the performance of the system in the laboratory, the people from INFN-LNF organized a test-setup able to generate test-signals which are a good approximation of the signals expected from the machine. The setup uses a pulse generator and the BPM16 cavity which will be installed in the accelerator.

The results from the measurements are in line with the expectations: despite of the non-ideal input signals the achieved RMS position resolution is within 5μm for a position range of ±1mm. The deconvolution filter concept has been validated with individual and multiple-bunch sequences. The long term stability and linearity are excellent.

Still there are some aspects to be understood, in particular the influence of the phase difference between the input channels on the position resolution. Measurements on the real machine will help to clarify this aspect.

ACKNOWLEDGEMENT

The authors would like to thank M. Serio for the helpful discussions and feedback during the project. We also thank the technical staff of the SELCED laboratory of INFN-LNF for the accurate technical support during the measurements presented in this article.

REFERENCES

[1] L. Serafini et al., “Technical design report EuroGammaS proposal for the ELI-NP Gamma Beam System”, July 2014.

[2] G. Franzini et al., “Beam diagnostics for charge and position measurements in ELI-NP GBS”, in *Proc. IBIC'16*, Barcelona, Spain, Sept. 13-18, 2016.

[3] F. Marcellini et al., "Design of cavity BPM pickups for SwissFEL", in *Proc. IBIC'12, Tsukuba, Japan, 2012.*

[4] M. Cargnelutti et al., “Design and simulations of the cavity BPM readout electronics for the ELI-NP Gamma Beam System”, in *Proc. IPAC'16*, Busan, Korea, May 2016.

ISBN: 978-3-95450-192-2 doi:10.18429/JACoW-IBIC2017-TUPCF16

STRIPLINE BEAM POSITION MONITOR MODELLING AND SIMULATIONS FOR CHARGE MEASUREMENTS

G. Castorina*, A. Mostacci, M. Maroungiu, University of Rome "La Sapienza", Rome, Italy
G. Franzini, B. Spataro, INFN-LNF, Frascati (Rome), Italy
A. A. Nosych, ALBA-CELLS, Barcelona, Spain

Abstract

Strip line Beam Positions Monitors (BPMs) are the main devices used for non-intercepting position measurement for the electron LINAC of ELI-NP (Extreme Light Infrastructure - Nuclear Physics). All the 29 BPMs have the same design, with the exception of the one installed in one of the dump line, which has a much larger acceptance than the others. BPMs will also be used to measure the charge of the beam, by measuring the sum of the pickups signals and calibrating it with beam charge monitors installed along the LINAC. An analytical model has been developed for the proposed BPMs. This model has been checked by means of electromagnetic simulations, in order to obtain the pickups signals at the passage of the beam and to study the effects of BPMs non-linearities, particularly on charge measurements. Details of the analytical model, results of the numerical simulations and the correction algorithm proposed for charge measurements are described in this paper.

INTRODUCTION

An S-Band photo-injector and a C-band LINAC will be used at the Compton Gamma Source in construction at the ELI (Extreme Light Infrastructure) Nuclear Physics facility in Romania. They will operate with a repetition rate of 100 Hz with macro pulses of 32 electron bunches, separated by 16 ns and with 25–250 pC nominal charge range and a temporal duration of 0.91 ps [1].

Stripline BPMs will be installed along the beam path in order to measure the position of bunches. Each BPM has an approximate length of 235 mm and is composed by four steel electrodes with an angular width of 26 deg. The distance from the beam pipe is 2 mm and they have a width of 7.7 mm, see Fig. 1. The impedance of the transmission line created by the the electrode and the pipe chamber is roughly 50 Ω. The acceptance of the BPM is 34 mm. A further BPM with an acceptance diameter of 100 mm will be installed on the dump line after the low energy interaction point. [2]. The BPMs on the beam line have been calibrated on a test bench. On the contrary the dump line BPM cannot be calibrated with the test bench used for the other BPM because of its larger dimension.

These BPMs can be also employed to measure the macro pulse charge. By this way it is possible to have a non destructive estimation of the macro pulse charge along the beam line. Four Integrating Current Transfmorers (ICT) will be installed in the critical points of the machine: after the RF gun of the photo-injector, after the first six accelerating structures and before the interaction chambers. The measurement of the bunch charge is proportional to the sum of the four voltage signals from the output ports of the BPM. However, due to the non linear behaviour of the pick-up devices, a calibration curve should be applied to the readings. A full characterization of the voltage signals picked from the output port of the BPMs has been done by means of an analytical model and with full 3D simulations. Aim of this work is the development of a numerical calibration method for the charge measurement. The curve obtained with the simulation results has been compared with the experimental data and an estimation error is provided. This numerical method will be used for the calibration of the BPM for the dump line.

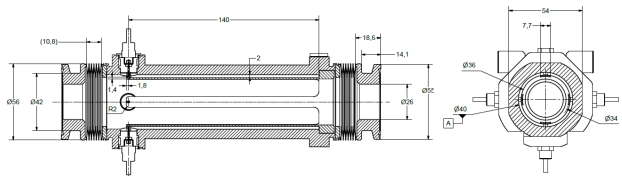

Figure 1: Main BPM CAD model for ELI-GBS. Units in mm.

CHARACTERIZATION OF A STRIP LINE BPM AS A CHARGE MONITOR

The BPMs described in the previous paragraph have been characterized with an approximate analytical method and with the aid of 3D electromagnetic simulations. The results are summarized and compared with the measurements in Fig. 2. The curves in the three analysis cases (analytical model, simulations and measurements) have been evaluated over a grid of 841 points with 29 points for both horizontal and vertical axis. The points are in the span length of ±7 mm around the centre with a fixed step of 0.5 mm. The traces have been normalized to the central value of the grid.

The excitation signal used in the measurement setup is a 500 MHz sinewave. Therefore it is not a reproduction of the ELI_NP macro pulse charge and only a comparison of the normalized curves is possible. The normalization is based on the measurements in the central position, i.e. $y = x = 0$.

The agreement between the analytical model, the simulation results and the measurements is quite good. The measurements have been carried out at ALBA with the wire stretching method [3]. The details of the analytical model and of the simulation analysis are described in the next sections.

* giovanni.castorina@uniroma1.it

ISBN: 978-3-95450-192-2 doi:10.18429/JACoW-IBIC2017-TUPCF16

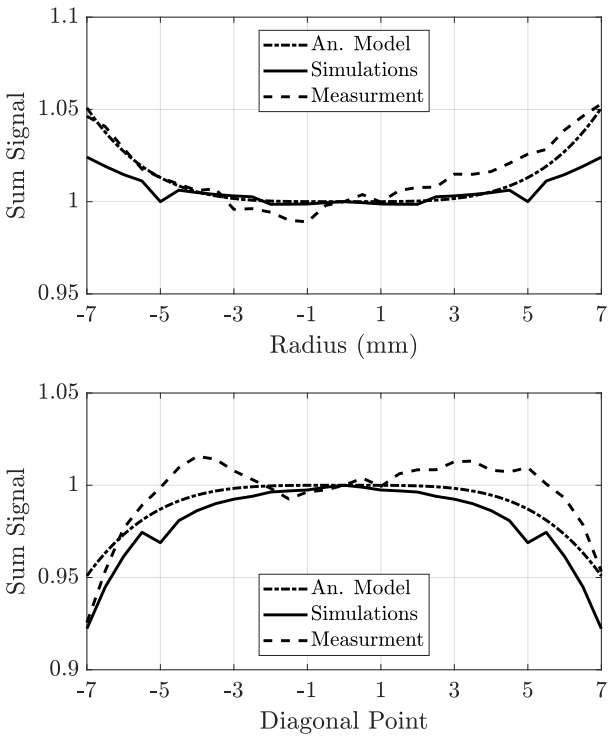

Figure 2: Sum of the voltage signals from the four ports versus the x axis (top plot) and the diagonal line, $y = x$ (bottom plot).

Analytical Model

The model is based on the assumption that an image current is induced on the stripline when the bunch (which is considered dimensionless in the transverse plane) pass though the BPM. The 2D profile of the BPM has been outlined like in Fig. 3. The external circle is the vacuum pipe. Four striplines with an azimuthal coverage of α are considered and the beam distance from the axis is given in polar coordinate, r for radius and θ for angle. The ϕ angle is the azimuthal coordinate.

The wall density current induced in the stripline is equal to [4]:

$$j_{im}(\phi) = \frac{I_{beam}}{2\pi a} \cdot \frac{a^2 - r^2}{a^2 + r^2 - 2ar\cos(\phi - \theta)} \qquad (1)$$

where I_{beam} is the current of the beam and a is the distance of the stripline from the centre of beam line. The current delivered to the coaxial cable can be found with an integration over the coverage angle of the stripline:

$$I_{im} = \int_{-\alpha\backslash 2}^{\alpha\backslash 2} a \cdot j_{im}(\phi) d\phi \qquad (2)$$

The voltage signal at the output port is proportional to the current therefore the calculation of the impedance of the coaxial cable is not necessary for the comparison of the normalized curves.

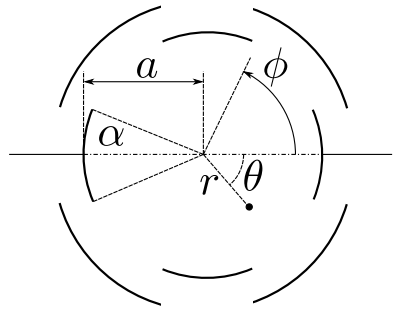

Figure 3: 2D electrostatic model for the analytical calculation of the voltage signal.

Simulations

The voltage signals at the output ports have been simulated by means of numerical simulation. The CST® particle studio code has been used, in particularly the wakefield module [5]. The beam has been simulated as a pencil beam without transverse dimension and only one packet of the macro-pulse has been considered. A perfect electric conductor (PEC) has been adopted for the striplines and the vacuum chamber. The striplines, as in the realized BPM, are terminated on a short circuit in one of the two sides and with a coaxial cable in the other one, see Fig. 4.

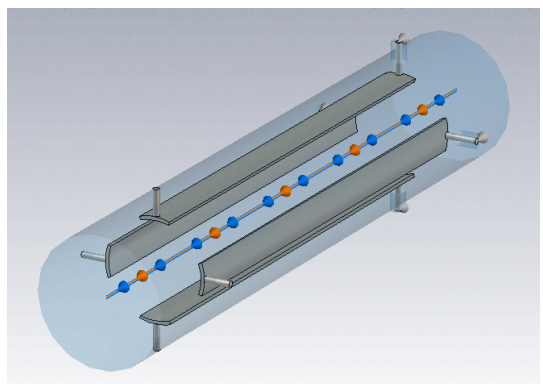

Figure 4: CAD draw for the 3D simulations.

The voltage signals are recorded during the simulation time: the maximum of the signals have been taken into account for the determination of the calibration curve. However other options, for example the integral of the curve, are possible. In order to save computational resources the simulation time is limited to 0.9 ns.

The simulation was performed with the beam in different position over an area of 7 mm × 7 mm with 0.5 mm step, for a total of 841 points. Thanks to the geometrical symmetry[1] of the device only an eight of these points should be simulated, i.e the points inside the region bounded by the curves $y = 0$, $y = x$ and $x = 7$ mm. The remaining points can be found with a simple post processing operation.

[1] In general, symmetry planes cannot be used in the simulations but for the points over the $y = 0$ line.

ISBN: 978-3-95450-192-2 doi:10.18429/JACoW-IBIC2017-TUPCF16

POLYNOMIAL FITTING

In order to use the full BPM acceptance of ±7 mm area a correction algorithm based on a polynomial fit of the curve is here developed. The correction algorithm for the charge reading will be implemented as a high-level application within the control system. This algorithm has been enforced only for the simulation results (validated by the analytical model) and measurement readings.

A polynomial function of the x and y position of the fourth grade is adopted:

$$\begin{aligned} f(x,y) = {} & a_{00} + a_{10}x + a_{01}y + a_{20}x^2 + a_{11}xy + a_{02}xy^2 \\ & + a_{30}x^3 + a_{21}x^2y + a_{12}xy^2 + a_{03}y^3 + a_{40}x^4 \\ & + a_{31}x^3y + a_{22}x^2y^2 + a_{13}xy^3 + a_{04}y^4 \end{aligned} \quad (3)$$

therefore a total number of 15 coefficients, for both simulation and experimental case, are necessary in order to full characterize the fit equations. The obtained coefficients are listed in Table 1.

Table 1: Polynomial Fit Coefficients

Index	Coeff.	Sim.	Meas.
1	a_{00}	+1.00709	+9.88728e-01
2	a_{10}	+1.85821e-17	+1.52370e-03
3	a_{01}	+3.34763e-19	+1.29374e-03
4	a_{20}	-2.34095e-04	+5.84219e-04
5	a_{11}	-4.13974e-18	-5.49711e-04
6	a_{02}	-2.34095e-04	+7.27711e-04
7	a_{30}	-9.08888e-19	-3.05091e-05
8	a_{21}	-4.04803e-20	-1.23042e-05
9	a_{12}	+6.13145e-20	+5.54398e-05
10	a_{03}	-1.57277e-19	+1.20780e-05
11	a_{40}	+1.43842e-05	+1.03114e-05
12	a_{31}	+5.56406e-20	+2.17884e-06
13	a_{22}	-5.04218e-05	-7.80406e-05
14	a_{13}	+7.96769e-20	+4.19682e-06
15	a_{04}	+1.43842e-05	+1.18798e-05

Because of the parabolic behaviour of the non-linearities the most import coefficients are a_{20} and a_{02} which are in great agreement between simulations and experimental results. The linear terms, a_{10} and a_{01}, are not zero in the measurement fit because of the geometrical imperfection of the realized BPM and/or for the different gain level of the four channel of the electronic read-out. This dependency from the linear terms is not captured by the simulation already done. The mixed terms (a_{ij} for $i, j \neq 0$), with the exception of a_{22} coefficient, are nearly zero in the simulation results. Nevertheless, in the measurement fit, they are one or two order of magnitude lower of the a_{20} and a_{02} terms due to the linear dependence from x and y.

The polynomial surface and the points for the fit are shown in Fig. 5. The R-squared coefficient for the simulation fit is 96.95% and for the experimental data is 98.10 %.

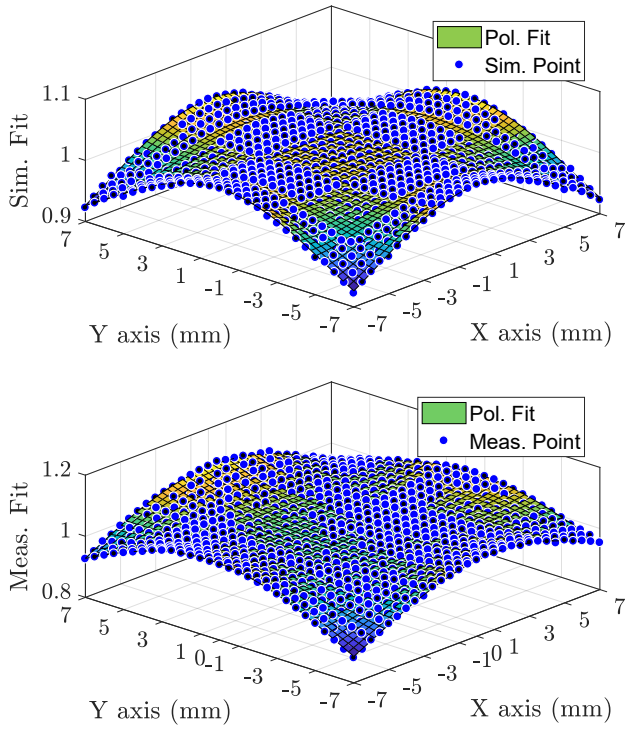

Figure 5: Polynomial fitting for the simulation results (top plot) and measurement data points (bottom plot).

The difference between the two fitted surface equations is shown in the Fig. 6. A very good agreement between the two fit equations is found. In the full acceptance area of 196 mm^2 the maximum error is equal to 5.4%.

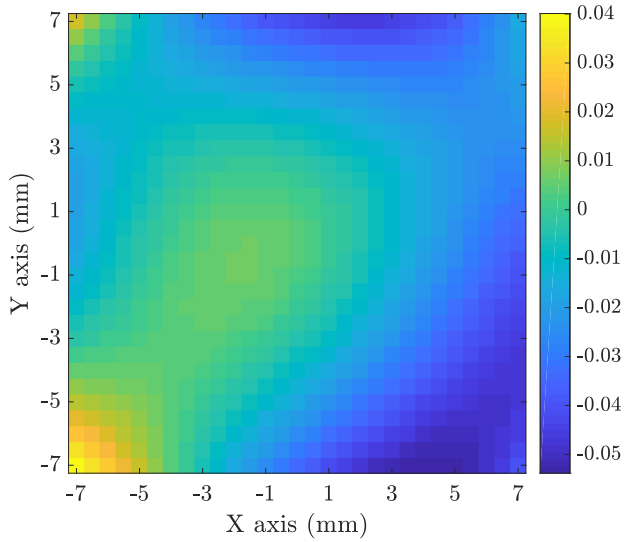

Figure 6: Difference between the two fitted surface equations.

ISBN: 978-3-95450-192-2 doi:10.18429/JACoW-IBIC2017-TUPCF16

CONCLUSION

A correction algorithm for compensation of the non linearities in charge measurement by means of a stripline BPM has been developed. In addition to ICT measurements, it will be possible to have charge measurements along the beam line. The algorithm has been evaluated thanks to an analytical model and numerical simulations. The correction algorithm proposed here is based on a polynomial fit of the simulation results. The order of the polynomial equation is four for both the x and y coordinate. Therefore a total of 15 coefficients are necessary for the correction of the non linearities. In the full acceptance area of 196 mm^2 the maximum error between the correction algorithm based on the simulation results and the one based on the experimental data is equal to the 5.4%. This error is mainly due to the imperfect realization of the BPM and/or to the different gain level of the electronics channels. However the numerical correction method here discussed can be used for the BPM of the dump line with a reasonable error respect to the measurement characterization.

REFERENCES

[1] L. Serafini *et al.*, "Technical report eurogammas proposal for the ELI-NP Gamma Beam System", arXiv:1407.3669, 2014.

[2] Giovanni Franzini *et al.*, "Analysis and Correction of Geometrical Non-Linearities of ELI-NP BPMs on Position and Current Measurements", in *Proc. 8th Int. Particle Accelerator Conf. (IPAC'17)*, Copenhagen, Denmark, 14-19 May, 2017. JACOW, Geneva, Switzerland, 2017.

[3] A.A. Nosych *et al.*, "Measurements and Calibration of the Stripline BPM for the ELI-NP facility with the Stretched Wire Method", in *Proc. IBIC'15*, Melbourne, Australia, paper TUPB048.

[4] B.G. Pine, CARE-ABI Workshop Luneburg 2006, https://mdi.desy.de/sites2009/site_mdi/content/e37820/e37935/e38711/e38712/infoboxContent38753/LueneburgCARE-proc.pdf (2006).

[5] https://www.cst.com/products/cstps

ISBN: 978-3-95450-192-2 doi:10.18429/JACoW-IBIC2017-TUPCF17

FIRST BEAM COMMISSIONING EXPERIENCE WITH THE SwissFEL CAVITY BPM SYSTEM

Boris Keil, Raphael Baldinger, Robin Ditter, Daniel Engeler, Waldemar Koprek, Reinhold Kramert, Fabio Marcellini, Goran Marinkovic, Markus Roggli, Martin Rohrer, Markus Stadler, Daniel Marco Treyer, Paul Scherrer Institute, Villigen, Switzerland

Abstract

SwissFEL is a free electron laser facility designed to produce FEL radiation at wavelengths from 0.1 to 7 nm. The beam commissioning of its hard X-ray undulator line ("Aramis") started 10/2016, and first lasing was observed in 12/2016. Presently, a 2nd undulator line ("Athos") for soft X-rays is being constructed, with 1st beam scheduled for mid-2019. In the injector, linac and Aramis beam transfer lines, 95 low-Q cavity BPMs operating at 3.3 GHz are used that were designed to support the future two-bunch operation mode with 28 ns bunch spacing and 100 Hz repetition rate. The Aramis (and future Athos) undulator lines will only be operated with single bunches by means of a fast beam distribution kicker system, and are thus equipped with high-Q cavity BPMs operating at 4.9 GHz. The BPMs are not only used for beam trajectory optimization, but also for beam energy measurements (using standard cavity BPMs in the bunch compressors and beam dumps), beam charge and transmission measurements, or improvement of the performance of other monitors like wire scanners for profile measurement. This paper will report about the first operation experience with the BPM system, including a performance comparison of low-Q and high-Q BPMs.

INTRODUCTION

BPM Pickups

Table 1 gives an overview of the number and type of BPMs (119 overall) that are presently operational in SwissFEL. CBPM38 low-Q pickups are only used at a few locations where their large aperture is needed (1st bunch compressor, beam distribution area, beam dumps). Undulator intersections are equipped with high-Q CBPM8 pickups, while low-Q CBPM16 pickups are used everywhere else.

Table 1: SwissFEL BPM Types and Quantities

	CBPM38	CBPM16	CBPM8
Quantity	7	96	24
Usage	Linac, Transfer Lines		Undulators
Aperture	38 mm	16 mm	8 mm
Length	255 mm	100 mm	
#Bunches/ Train	1-3		1
Bunch Spacing	28 ns		10 ms
Frequency	3.2844 GHz		4.9266 GHz
Q_L	40		1000

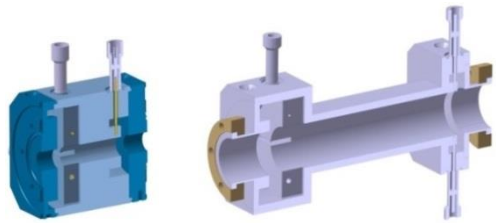

Figure 1: SwissFEL CBPM16 pickup (left) and CBPM38 pickup (right).

CBPM38 and CBPM16 pickups (shown in Figure 1 and Figure 2) differ in aperture and length, but were designed to deliver (nearly) the same sensitivity and RF parameters [1], thus providing similar performances.

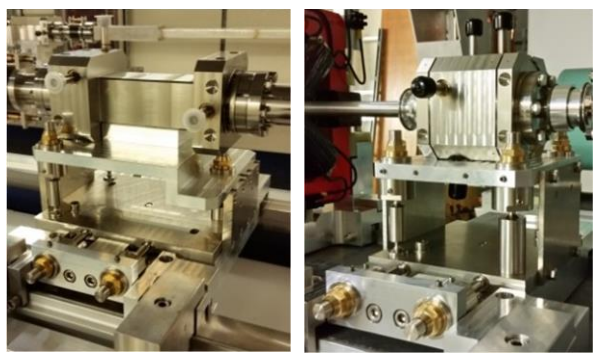

Figure 2: CBPM38 (left) and CBPM16 pickup (right) with manually adjustable supports.

Like the SwissFEL C-band accelerating structures, the BPM pickups (incl. CBPM8) have no tuners but were precision-machined to the nominal frequency and other RF parameters. The achieved very small deviations [1] have negligible impact on the performance.

The position resonators of the pickups have two ports both for the horizontal (X) and vertical (Y) position signals. The two signals in each plane are added using an external RF combiner near the pickup that is connected with short flexible low-loss cables, thus improving the position resolution at low charge.

The relevant RF parameters of all pickups and long-range ½'' Sucofeed RF cables from pickups to the electronics racks (located outside the SwissFEL accelerator tunnel) were measured before 1st beam. The results were used to verify the quality of the system and do determine scaling factors for the conversion of raw signal amplitudes to charge and position in physical units already before 1st beam, followed by a more accurate beam-based calibration that is still in progress.

ISBN: 978-3-95450-192-2 doi:10.18429/JACoW-IBIC2017-TUPCF17

BPM Electronics

Low-Q and high-Q BPMs have the same electronics, except for the RF front-ends (RFFEs), where the low-Q RFFEs perform IQ downconversion to baseband, (see Figure 3) while the high-Q RFFEs mix to an IF of ~134 MHz that is sampled by 16-bit ADCs at 161 MSPS and then digitally mixed to baseband (see Figure 4 and ref. [2]).

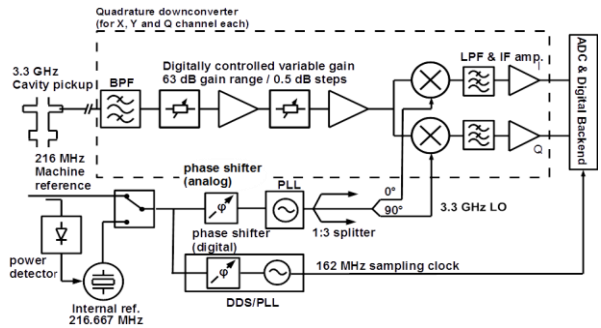

Figure 3: Simplified schematic of CBPM16/CBPM38 CBPM RFFE electronics, showing only one of its three input channels (one reference and two position signal channels).

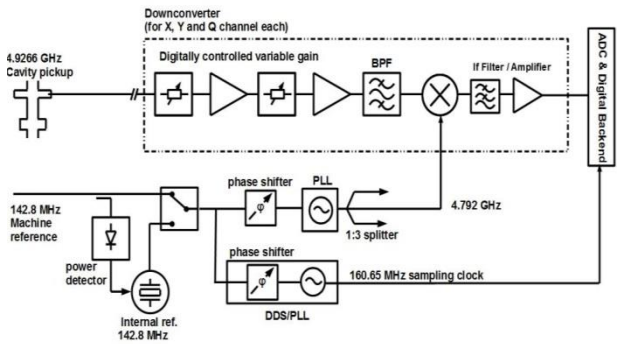

Figure 4: Simplified schematics of CBPM8 RFFE electronics, showing only one of its three input channels.

The BPM electronics consists of a customized crate called Modular BPM Unit (MBU, see Figure 5) [1][3] that contains two BPM-specific RFFEs, as well as a number of generic boards and modules, e.g. a modular power supply, or an FPGA carrier board (GPAC = Generic PSI ADC carrier) with two 6-channel 16-bit ADC mezzanine boards.

Figure 5: Modular BPM unit, with two cavity BPM RFFEs (top) and FPGA carrier board with two ADC mezzanines (bottom).

FPGA Board

The FPGA board version (called GPAC3) used in the SwissFEL MBUs is backward-compatible to the previous version (GPAC2) used in E-XFEL [3] regarding external interfaces and ADC mezzanine connectors. However, the GPAC3 uses newer FPGAs: Three Xilinx Artix7 200T and one Kintex7 160T, instead of three Virtex-5 FX70T and three Spartan-3A on the GPAC2. This reduced the production costs of the board by a factor 2 while providing a longer FPGA availability (last buy 2030 vs. 2022). Moreover, the GPAC3 is supported by the latest Xilinx FPGA design tools (Xilinx Vivado), while the development of the previous tool Xilinx ISE/EDK (used by GPAC2) was frozen by Xilinx in 2013.

The FPGA board PCB layout was changed from a 2+12+2 layer microvia stackup for GPAC2 (that is more sensitive to thermal stress during soldering) to a 16-layer through-hole design for GPAC3, which improved the production yield of soldered boards from typ. 87% to >98%. The GPAC3 uses Megtron-6 as PCB material, thus minimizing losses for the multi-gigabit links between the FPGAs and to the outside world (via SFP+ fiber optic transceivers) that can run at up to 10.3 Gbps for the soldered speed grades of the Kintex-7 (enabling e.g. 10G Ethernet) and 6.6 Gbps for the Artix-7 on the GPAC3, compared to 6.5 Gbps for the GPAC2.

Timing and Control System Integration

The SwissFEL BPM system uses fiber optic multi-gigabit links with optical multimode SFP+ transceivers as external high-speed interfaces. One transceiver is used as direct connection to the SwissFEL timing/event system that was developed by the company MicroResarch (like the older SLS system). The GPAC3 directly decodes the event data stream in one of its FPGAs using an event receiver implemented by PSI, thus saving the costs for a dedicated event receiver card (that is needed for most other SwissFEL systems).

The SwissFEL control system is based on EPICS and VME64x, while the SwissFEL BPM electronics is control system agnostic and can be interfaced to various control system hardware standards (e.g. uTCA used at E-XFEL). For SwissFEL, the data of all MBUs is collected by only seven VME64x CPU boards running EPICS, using additional boards with two quad SFP+ mezzanines in the VME64x crates to collect the data from the MBUs.

In contrast to the GPAC2 that only has two mezzanine connectors (e.g. for ADCs), the GPAC3 has a third (smaller) mezzanine connector for an optional microprocessor mezzanine (that could be equipped e.g. with a Xilinx Zynq SoC), which would allow to run EPICS directly on this mezzanine in the MBU (rather than using external CPU boards) if needed. Having the processor on a mezzanine rather than on the mainboard itself allows to add the processor only if needed and to choose different processors for different applications, thus saving costs and extending the board availability (where many processors tend to get obsolete earlier than FPGAs).

ISBN: 978-3-95450-192-2 doi:10.18429/JACoW-IBIC2017-TUPCF17

BEAM MEASUREMENTS

Scaling Factor Calibration

All SwissFEL BPM RFFEs have digital step attenuators (DSAs) with 63dB overall range in their position and charge channels that allow to achieve excellent resolution over a very wide bunch charge range. The DSAs as well as other RFFE parameters (e.g. IQ imbalance of the low-Q BPMs) are calibrated in the lab using test signal generators, where the FPGA then uses the calibration data (stored in an EEPROM on the RFFE) to calculate charge and beam positions. Combined with the previously mentioned pre-beam measurement of pickup and RF cable parameters, the SwissFEL BPM system was able to provide position and charge readings in physical units already at 1st beam with typ. 10-20% scaling factor error.

After steering the beam through the accelerator with negligible beam loss (verified e.g. via dedicated loss monitors), the charge readings of the BPMs were then calibrated using dedicated charge monitors (Bergoz ICTs).

Nearly all CBPM8 are mounted on motorized movers together with a quadrupole (in the undulator intersections), which allowed easy calibration of the position scaling factors via the very accurate mover encoders. In contrast, only two CBPM38 (in bunch compressor BC1) and two CBPM16 (in BC2) are mounted on motorized movers (that move the complete bunch compressor with BPMs, 2rd and 3rd bending magnet, and beam pipe). Thus, we used these movers to determine the systematic error of the pre-beam calibration of these BPMs, and then corrected this error for all other BPMs (having manually adjustable movers) as 1st step of the beam based calibration. The 2nd step – a beam based calibration using an optics model that itself is calibrated against screen monitors, wire scanners and CBPM8 etc. – is still to be performed, while the present uncertainty of the position scaling factors is expected to be <10% and thus sufficient for the ongoing commissioning of the SwissFEL accelerator and experiments.

Nonlinearity

Figure 6 and Figure 7 show the nonlinearity of a CBPM16 and CBPM38, measured by mechanically moving the BPM pickups in BC1 / BC2 and recording the BPM position readings (for a larger number of shots, to suppress noise/jitter) as function of the mechanical position encoder readings of the bunch compressors. The vertical axis shows the deviation from a linear fit (i.e. from perfect linearity). The measurement was performed first with automatic range control (ARC) active, where the FPGA changes the attenuators in 1dB steps to keep ADC readings at 50-70% full scale, and then with ARC inactive (DSA attenuation constant during pickup position scan). With ARC off, the nonlinearity is determined by the active components of the RFFE input signal chain, with ARC on the nonlinearity is determined mainly by the accuracy of the DSA calibration performed in the lab, where the DSA have a different attenuation (and different calibration constant) for each point in the plot.

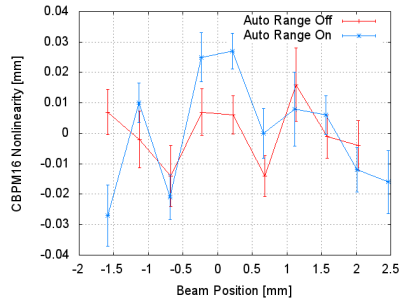

Figure 6: CBPM16 nonlinearity

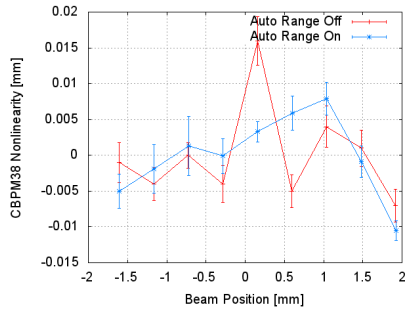

Figure 7: CBPM38 nonlinearity

Charge Resolution

Figure 8 and Figure 9 show the relative and absolute charge resolution of CBPM16 and CBPM8 BPMs, determined by correlating the readings of adjacent BPMs and assuming that there is negligible beam loss between the BPMs. Table 2 summarizes the result.

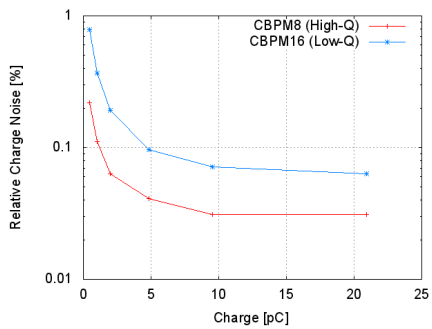

Figure 8: Relative single-bunch charge resolution, as a function of the bunch charge.

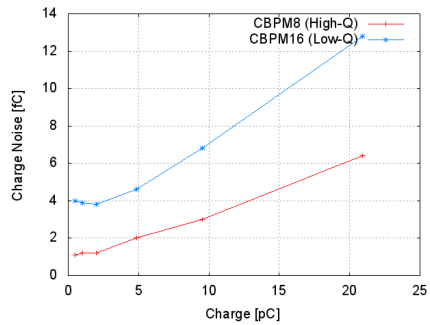

Figure 9: Absolute single-bunch charge resolution, as a function of the bunch charge.

ISBN: 978-3-95450-192-2 doi:10.18429/JACoW-IBIC2017-TUPCF17

It should be noted that the BPM charge resolution is much better than the resolution of the dedicated charge monitors (ICTs and Faraday cups) of SwissFEL. Therefore the dedicated monitors are primarily used to calibrate the BPMs as well as for safety purposes (e.g. machine protection system), while the BPMs provide excellent resolution for the measurement of relative charge variations. It should be noted that the resolution was measured with constant DSA settings. The calibration error of the DSAs is presently not as good as the charge resolution, but could be improved to or beyond the charge resolution using beam-based inter-BPM correlation rather than a lab signal source for calibration.

Table 2: Measured SwissFEL BPM Charge Noise

	CBPM38 CBPM16	**CBPM8**
Relative Charge Resolution	< 0.07%	< 0.04%
Absolute Charge Resolution	< 5 fC	< 1.5 fC
Charge Range	0-400pC	

It should also be noted that all RFFEs have fixed additional attenuators in their charge channel (that are not needed in the position channel), to avoid that the RFFE is destroyed at very high bunch charge, where the SwissFEL RFFEs are guaranteed to survive continuous operation at 800pC beam (4x the nominal upper charge limit). If this upper "destruction" charge limit was reduced (e.g. by using an electron gun that cannot generate such high bunch charges), the charge resolution at very low bunch charge could still be improved significantly by removing the above mentioned fixed attenuators.

Position Resolution

Figure 10 shows the position resolution at smaller beam offsets as a function of the bunch charge, Figure 11 the product of resolution and charge that converges to a constant value towards very low bunch charges. Table 3 summarizes the results.

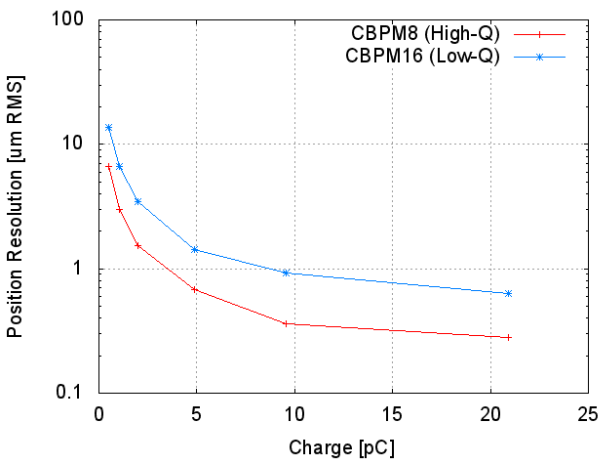

Figure 10: Absolute single-bunch position resolution as a function of the bunch charge.

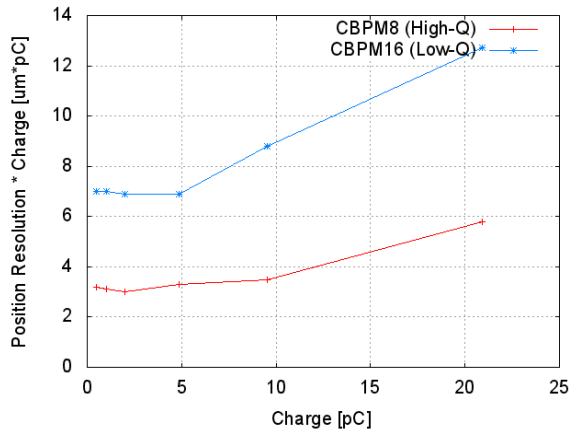

Figure 11: Product of single-bunch position resolution and charge, as a function of the bunch charge.

The resolution was determined by correlating the readings of three adjacent CBPMs of same type with similar beam offsets, where automatic range control was disabled. The method could not be applied to CBPM38 since there are no three adjacent pickups of this type in SwissFEL. However, CBPM38 and CBPM16 RF parameters are very similar, thus their resolution should be comparable (but is still to be measured with alternative methods).

Table 3: Measured Position RMS Noise

	CBPM16	**CBPM8**
Position Noise @ 10-200pC	< 1 µm	< 0.5 µm
Position Noise @ 1pC	< 8 µm	< 5 µm

SUMMARY AND CONCLUSION

The SwissFEL cavity BPM has been successfully put into operation. The measured position and charge resolution over the nominal charge range of 10-200pC exceeds the requirements (i.e. <0.1% for charge, <1µm for CBPM8, < 3µm for CBPM16, < 10 µm for CBPM38) and enables the future operation of SwissFEL at lower bunch charge. Already now, SwissFEL was operated at bunch charges down to 120fC during accelerator R&D shifts e.g. to generate ultra small beams, where the BPMs were still operational and provided usable orbit readings. While the basic commissioning of the BPM system is finished, work on beam-based calibration and improvement of the system is still in progress.

REFERENCES

[1] B. Keil *et al.*, "Status of the SwissFEL BPM System", *Proc. IBIC'15*, Melbourne, Australia, 2015.

[2] M. Stadler *et al.*, "The SwissFEL High-Q BPM System", presented at IBIC'17, Grand Rapids, MI, USA, 2017, these proceedings.

[3] B. Keil *et al.*, "The European XFEL Beam Position Monitor System", *Proc. IPAC'10*, Kyoto, Japan, 2010.

ISBN: 978-3-95450-192-2 doi:10.18429/JACoW-IBIC2017-TUPCF18

THE SwissFEL HIGH-Q UNDULATOR BPM SYSTEM

M. Stadler*, B. Keil, F. Marcellini, G. Marinkovic, Paul Scherrer Institute, Villigen, Switzerland

Abstract

In 10/2016, PSI started the beam commissioning of Aramis, the hard X-ray undulator line of the SwissFEL free electron laser. The injector, linac and transfer line BPMs have 3.3 GHz low-Q cavity BPMs to support 2-bunch operation with 28ns bunch spacing. In contrast, Aramis as well as the future 2nd soft X-ray undulator line called "Athos" are equipped with 4.9 GHz high-Q cavity BPMs, since the undulator will only be operated with single bunches by means of a fast beam distribution kicker system. The undulator BPM system uses 4.9GHz double-resonator pickups having a nominal loaded-Q of 1000. The associated front-end electronics applies single-stage analog down conversion to a 135 MHz IF frequency, subsampling ADC and digital quadrature down conversion. A detailed description of the BPM pickup and front-end design and signal processing will be given. Laboratory test and calibration methods and results of pickups and electronics will be compared with first beam measurements.

INTRODUCTION

The SwissFEL Aramis beam-line BPM system uses three types of pickups: Low-Q (Q=40) at 3.3GHz having 16mm or 38mm aperture in the linac and transfer line sections, and high-Q (Q=1000) 4.9GHz with 8mm aperture in the undulator section. A detailed description of the pickup design is given in [1].

Bunch spacing is 28ns in linac and transfer sections. Hence, low-Q cavity BPMs (CBPMs) are used in order to minimize signal leakage from the first into the second bunch. In contrast, the undulator section operates only with single bunches at a maximum repetition rate of 100 Hz. A high-Q cavity pickup is adequate here and provides higher resolution.

FRONT-END ARCHITECTURE

The high-Q CBPM front-end uses a combined analog/digital two-stage frequency conversion scheme. Figure 1 shows the front-end block diagram. The BPM signal enters an RF chain consisting of a first variable attenuator, a first RF amplifier, a second variable attenuator, a second RF amplifier and a band-pass filter. The variable attenuators establish a gain range of 60dB. The band-pass filter is centered at the nominal pick-up signal frequency, which is 4926.6 MHz.

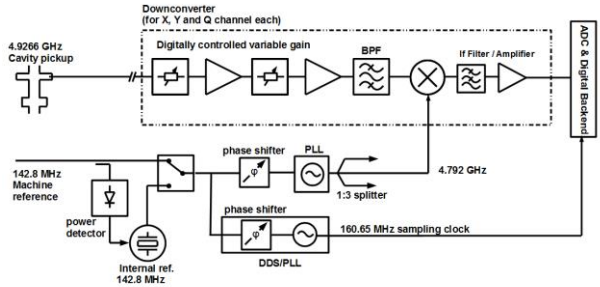

Figure 1: RFFE Block Diagram.

The band-pass filter rejects signal components and noise especially at the image frequencies, thereby improving resolution and reducing reading errors due to RF phase shifts. A local-oscillator signal at 4792 MHz is derived from a reference at 142.8 MHz. In the first (analog) down conversion stage the BPM signal is shifted to an IF frequency of 134 MHz. The IF section consist of an IF band-pass filter and an output amplifier. Both RF and IF stages are identical for position channels (x and y) and charge channel. A phase-adjustable 165.65 MHz clock used by the (separate) digitizer board is also generated on the RF front-end module. In nominal operation the reference frequency of 142.8 MHz is provided to the RFFE by the SwissFEL timing system. This signal is strictly bunch-synchronous. In case of reference failure an internal free-running reference oscillator switches in automatically. All frequencies generated are multiples of a common super-period frequency, which is 142.8MHz/72.

The second and final frequency conversion is done digitally on the separate FPGA board and will be described in the signal processing section.

Primary Design Guidelines

Development was guided by following major requirements:

- Nominal charge range: 10pC-200pC
- Useful readings below 1pC.
- No damage to the RFFE for charges up to 1nC, independent of gain setting.
- Single-shot resolution <1µm within nominal charge range
- Robust position and charge readings at varying RF phase and/or reference signal phase.

Front-End Module Construction

The front-end electronics is assembled on a 6-layer printed-circuit board. The size fits into a double width standard VME64x slot (Figure 2) of the modular BPM unit (MBU) crate. SMA connectors are provided at the

* markus.stadler@psi.ch

ISBN: 978-3-95450-192-2 doi:10.18429/JACoW-IBIC2017-TUPCF18

front-panel for the machine reference signal, the ADC sampling clock, the RF inputs from the pick-up and differential IF output signals to the ADC. Electrical shielding and isolation between the front-end channels is provided by milled shields of aluminium on top and bottom side. The PCB is sandwiched between the screwed shields (Figure 3).

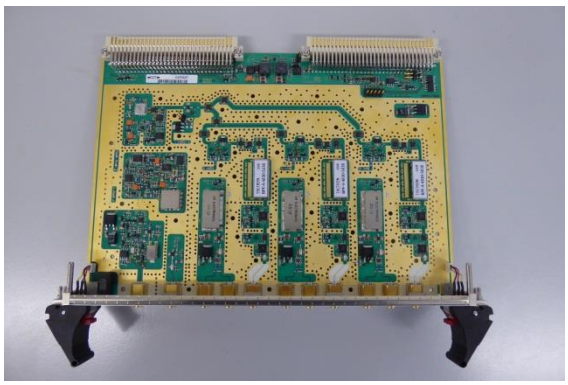

Figure 2: RFFE Electronics.

Figure 3: Front-End Module.

PICK-UP CONSTRUCTION

The BPM pickup uses a double resonator structure (Figure 4) and has been described in [1].

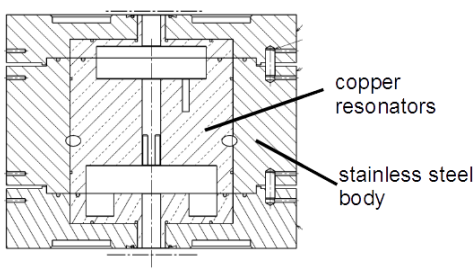

Figure 4: Cross-section of Undulator BPM Pickup.

The characteristic numbers of the pickup are given in Table 1.

Table 1: Cavity Parameters

Parameter	Value
Nominal Signal Center Frequency	4926.6 MHz
Reference Signal Sensitivity	58 V/nC
Position Signal Sensitivity	4.3 V/(nC·mm)
Loaded-Q	1000
Aperture	8 mm

The measured sensitivities of installed pickups vary less than +/-5% from their nominal values (Figure 5). These are 4.3 V/mm/nC for the position channels and 58 V/nC for the charge channel.

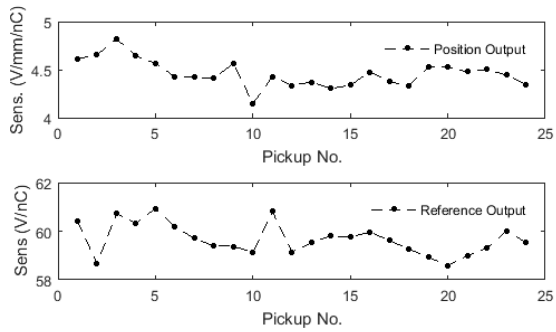

Figure 5: Sensitivity Parameter Variation.

The measured signal frequencies also have very little variation and are within ±4 MHz of the design value.

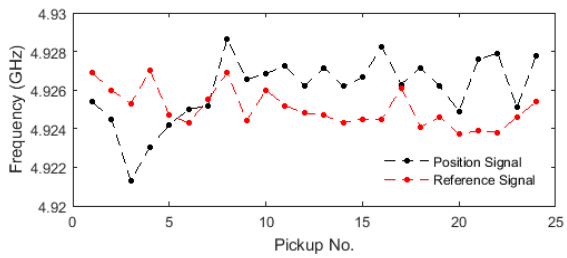

Figure 6: Signal Frequency Variation.

BPM INSTALLATION LAYOUT

Two 180°-hybrid signal combiners are attached to the pickup support (Figure 7). They combine the ports Y+/Y- and X+/X-, respectively, in order to gain signal amplitude. Several meters of ½'' corrugated RF cables take the pickup signals to the electronics rack located outside the tunnel in the technical gallery. The hybrid is connected to the pickup ports by short flexible RF cables.

ISBN: 978-3-95450-192-2 doi:10.18429/JACoW-IBIC2017-TUPCF18

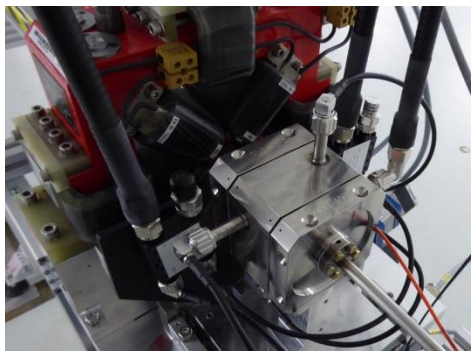

Figure 7: 8mm Undulator BPM Pickup at SwissFEL.

The reference resonator signal path contains a fixed attenuator mounted at the patch panel in the electronics rack. It reduces the potentially high reference pickup signal peak voltage to a safe level (Figure 8).

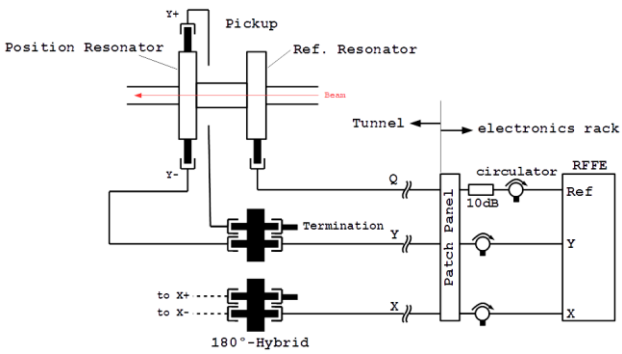

Figure 8: BPM Layout.

All RF signals run through isolators before entering the BPM electronics. The isolators reduce the impact of the gain-dependent input reflection factor on the BPM reading.

SIGNAL PROCESSING

The ADC signal samples are multiplied on the FPGA board of the BPM system by NCO sine and cosine waveforms (digital I-Q-downconversion, see Figure 9). This stage does the second frequency translation from IF to baseband. The sum signals are subsequently removed by a FIR low-pass filter.

The FIR output samples represent the in-phase and quadrature signal. Its amplitude and phase relationship are processed further into charge and position information.

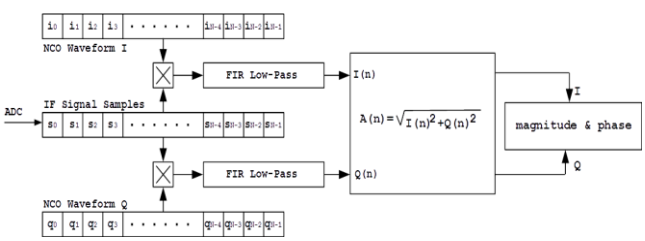

Figure 9: Sample Processing Scheme (One Channel).

Measured waveforms are shown in Figure 10.

The digital IF-signal (upper waveforms) is the analog IF (at 134 MHz) sampled at a rate of 161 Msps. These waveforms are multiplied by NCO generated in-phase and quadrature signals at 27 MHz. Figure 10 (bottom) shows the baseband signal of reference channel after FIR 10 MHz low-pass filtering.

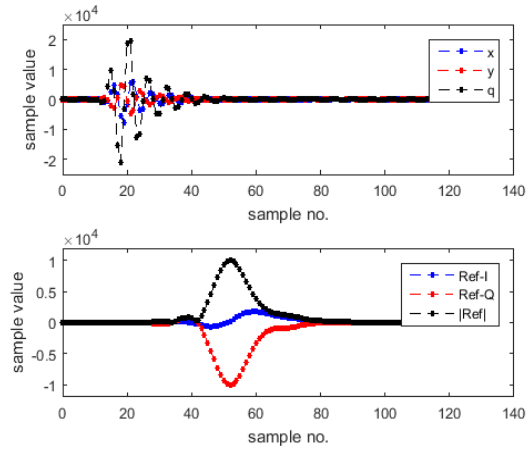

Figure 10: Digital IF Waveforms (top) and Reference Channel FIR Output (below).

Sampling phase adjustment is applied to keep one sample at the top of the magnitude waveform. This top-sample defines the sample number at which magnitude and signal phase is derived.
The pulse magnitude (that is then used to obtain beam positions and charge) is calculated from a quadratic interpolation taking into account the top sample and the two samples adjacent on both sides [2].

CALIBRATION

Due to component tolerances and other effects each BPM electronics unit is normally put through a calibration process in the laboratory prior to installation. The goal is to have charge and position reading independent from the setting of the RFFE gain. In addition charge and position readings are supposed to be sufficiently accurate for beam commissioning.

Procedure

The calibration is performed in two steps:

1. Calibration of the digital step attenuator stages due to non-ideal components characteristics.
2. Calibration of overall scale factors.

The laboratory calibration setup uses a signal generator with a 3x output splitter (Figure 11). In order to calibrate the digital step attenuator (DSA) of the RFFE, the signal generator provides a CW output signal at the nominal BPM cavity signal frequency. This results in a 27 MHZ CW waveform at the ADC output. The BPM system then records amplitude and phase of the generator output signal while scanning through all DSA settings automatically. Processing this information, a calibration table is generated and stored in local EEPROM on the RFFE board.

ISBN: 978-3-95450-192-2 doi:10.18429/JACoW-IBIC2017-TUPCF18

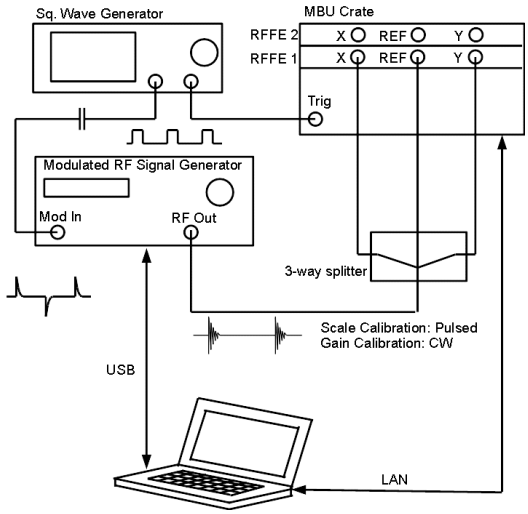

Figure 11: Calibration Set-Up.

This table corrects the measured signal amplitude based on the commanded gain and is further used in the calculation of position and charge.

Attenuator calibration using CW signals is sufficient. The use of artificial (decaying) pickup signals is not necessary due to the high Q of the pickups.

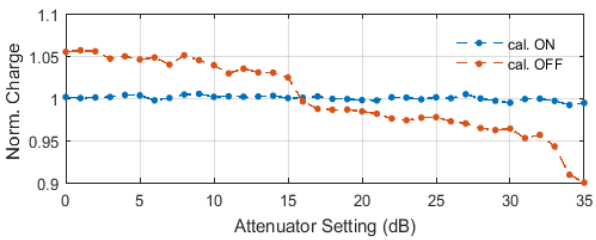

Figure 12: Charge Reading: Calibration on/off.

Figure 12 shows the charge reading while stepping channel attenuation from 0 dB to 35 dB at constant input signal amplitude. An uncalibrated attenuator leads to a reading error that may exceed 10%. Laboratory calibration reduces the error to below 1%. Further reduction requires beam-based procedures, because parameters of the installation (cable length, signal reflections in cable and feed-through, etc.) also affect the BPM calibration.

Scale factors essentially translate the results of the calculated digital baseband pulse amplitudes into the physical units of charge and position. Each BPM channel uses an internal scale factor (set by calibration routines in the lab and then left unchanged) and an external scale factor.

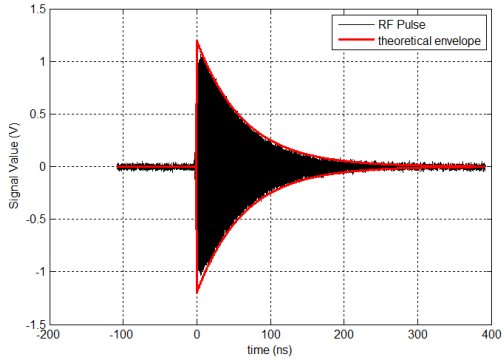

Figure 13: Calibration RF Pulse.

The internal scale factor calibration uses a modulated RF signal of defined amplitude and whose decay closely matches that of an actual cavity signal pulse having a loaded-Q of 1000. The external scale factor must be adapted individually at BPM commissioning by taking into account actual signal loss and pickup sensitivity for each BPM channel separately.

CONCLUSION AND OUTLOOK

The high-Q undulator BPM system installed at SwissFEL (Aramis beamline) has been described. Cavity pickup and measured parameters have been shown. The front-end electronics and its calibration have been described. Calibration procedure and verification measurements have been included. The high-Q BPM system has been successfully commissioned with beam, showing submicron resolution over the nominal bunch charge range [3]. User operation at SwissFEL will start in 2018, with pilot experiments already scheduled for late 2017.

ACKNOWLEDGEMENTS

The authors would like to thank Martin Rohrer and the PSI mechanics workshop for their contributions to the construction and production of the BPM pickups, as well as the PSI diagnostics section and controls group for their support with the installation, commissioning and control system integration of the BPM system.

REFERENCES

[1] M. Stadler *et al.*, “Development of the SwissFEL Undulator BPM System”, in *Proc. IBIC’14*, Monterey, USA, 2014.

[2] M. Stadler *et al.*, “Low-Q BPM Electronics for E-XFEL, FLASH-II and Swiss-FEL”, in *Proc. IBIC’14*, Monterey, USA, 2014.

[3] B. Keil *et al.*, “First Beam Commissioning Experience with the SwissFEL Cavity BPM System”, presented at IBIC’17, Grand Rapids, MI, USA, TUPCF17.

ISBN: 978-3-95450-192-2 doi:10.18429/JACoW-IBIC2017-TUPCF19

PRODUCTION TESTS, CALIBRATIONS, AND COMMISSIONING OF BUTTON BPMS FOR THE EUROPEAN XFEL*

D.M. Treyer, B. Keil, W. Koprek, PSI, Villigen, Switzerland
D. Lipka, DESY, Hamburg, Germany

Abstract

Commissioning of the entire European XFEL started early 2017. More than 300 button-electrode type beam position monitors (BPMs) are used in its cold Linac and warm beam transfer lines. Signal processing in the BPM RF front-end (RFFE) electronics employs signal stretching by chirp filtering, switchable gain stages, digital step attenuators, and peak detection. In this paper we present details on RF front-end production tests, calibration, and BPM beam commissioning results. Furthermore, a calibration pulser circuit that is built into each BPM electronics is presented. The setup and algorithms for production calibration of all RFFEs are described. Finally, resolution measurements obtained by correlation among all XFEL BPMs (including cavity and re-entrant types) are presented, confirming that the system can be used for orbit correction and transmission measurement down to bunch charges of a few pico-Coulombs.

INTRODUCTION

The European XFEL (E-XFEL) is a free electron laser with a 17.5 GeV superconducting linac and currently five experimental end stations with three undulators for producing trains of (sub-)fs-duration X-ray pulses with a wavelength range down to 0.1 nm. The accelerator works in train-pulsed mode at 10 Hz repetition rate. Up to 2700 bunches with a bunch spacing down to 222 ns can be produced in a single train. The accelerator is built in underground tunnels of >5 km total length. It is equipped with ~460 BPM pickups of five types: warm and cold buttons [1], cold re-entrant cavities, and warm dual-resonator cavities with two aperture sizes. More than 304 BPMs use cold and warm button pickups. The E-XFEL is an international project where Switzerland provides electronics for all electron BPMs [2] except 24 re-entrant BPM RFFEs, as well as the transverse intra-train beam based feedback system (IBFB) [3] as in-kind contributions. Production and commissioning of this comparatively large amount of BPM electronics motivated an automated production test system. The tasks of this test system include quality checks of the produced electronic boards, calibration and performance verification of complete BPM electronics, and documentation of test results as a part of the deliverables.

BUTTON BPM ELETRONICS OVERVIEW

Electronics for up to four button BPMs (four channels each) are housed in a modular BPM unit (MBU), a customized crate that can be used for different types of BPMs [4]. On the rear side it has slots for modular power supply and interface boards. On the front side it has slots for a digital carrier board (GPAC) with two analog-to-digital converter (ADC) mezzanine boards, and up to four button BPM RF front ends (RFFEs). Mixed configurations consisting of button, cavity, and/or re-entrant type BPMs are also possible.

The task of the RFFEs is to condition the signals from the beam pickups for digitization by the ADCs. Figure 1 shows the block diagram of the button BPM type RFFE [5]. One out of four identical channels is shown. In summary, the RFFE electronics first stretches the very short incoming pickup signal pulse by a dispersive chirp filter, then amplifies/or attenuates the stretched signal, and finally detects its amplitude by diode based peak detectors. An onboard pulser can generate pickup-like signals for beam emulation, self-testing, and calibration purposes. Switches at the RF inputs allow selection of the beam pickup or the on-board pulser signal.

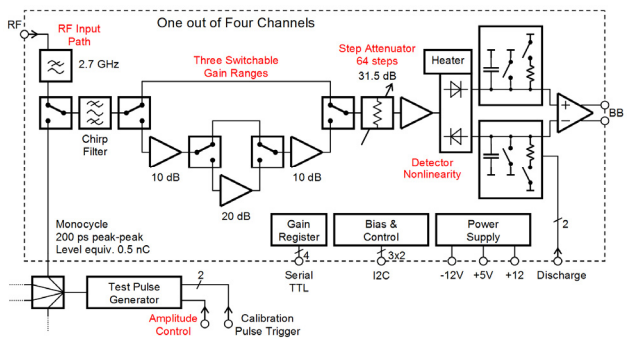

Figure 1: Block diagram of a single RFFE channel. Red labeled items need calibration.

CALIBRATION PULSER

The purpose of the onboard calibration pulser is to enable RFFE built-in test and calibration without the need for an external test signal source. The pulser should therefore ideally provide a signal having waveform, spectrum, and repetition rate matching the typical E-XFEL button pickup. An earlier design based on an avalanche transistor was later superseded by a design based on a step-recovery diode (SRD). This resulted in higher repetition rate (5 MHz), excellent pulse amplitude stability (1‰ rms), much better spectral matching to the pickup signal (peak at 2 GHz), and the ability to adjust the pulse amplitude (≈8 Vpp max.) over a wide range (26 dB).

Figure 2 shows the pulser block diagram. After the trigger rising edge, the SRD is forward biased during roughly 50 ns. Then the current is reversed and boosted

*Work supported by Swiss State Secretariat for Education, Research and Innovation.

ISBN: 978-3-95450-192-2 doi:10.18429/JACoW-IBIC2017-TUPCF19

by roughly a factor of five over a transition time of <2 ns. After a few nanoseconds, the SRD snaps, thereby producing a very abrupt current edge with a transition time of <150 ps. This edge is converted to a monocycle pulse by the pulse shaping networks. Keeping the ratio of the adjustable SRD forward to reverse currents constant reduces the parasitic dependence of trigger latency on amplitude. See Fig. 3 for the resulting output waveform and amplitude control characteristics.

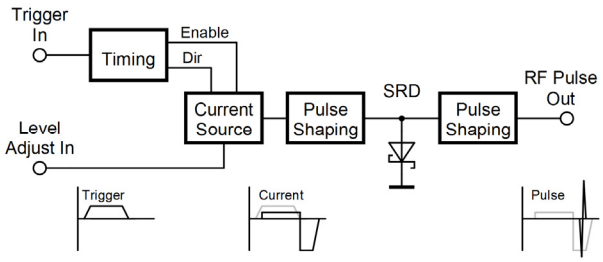

Figure 2: Block diagram of the pulser circuit.

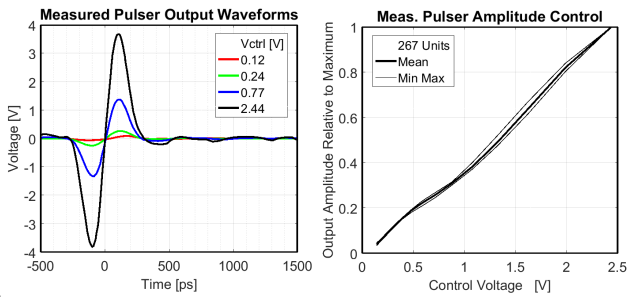

Figure 3: Exemplary measured pulser output waveform (left), and amplitude control characteristic (right).

PRODUCTION TESTS

PSI delivered fully tested and calibrated BPM electronics to E-XFEL, thus allowing to reliably measure beam position and transmission at first beam. This required not only functional tests of RF/analog and digital electronics, but also calibration of the RF/analog signal paths. To achieve this, the following test and calibration sequence was applied:

1. MBU crate and GPAC digital carrier board test
2. ADC tests
3. Pre-calibration RFFE functional test
4. RFFE calibration with onboard pulser
5. RFFE calibration and test with external pulser
6. Burn-in test of complete BPM electronics

The test setup used two 19" racks where a total of 16 MBUs could be tested. This allowed running automated calibrations on MBUs in one rack, while setting up MBUs and performing pre-calibration tests in the other rack.

The calibration with the onboard pulser takes half an hour per RFFE, and was done in parallel on several RFFEs. In contrast, the RFFE calibration with external pulser requires the test operator to connect RF cables and thus is time consuming. Two external pulsers developed at PSI were used, allowing to perform this calibration simultaneously on two MBUs.

All tests and calibrations were automated by Matlab scripts. Comprehensive test reports were generated for individual components (MBU, GPAC, ADC, and RFFE), as well as for each complete BPM electronics unit.

PRODUCTION CALIBRATION OF EACH RF FRONT-END ELECTRONICS

This section describes the theory and algorithms used for the previously mentioned RFFE calibration with onboard pulser and RFFE calibration with external pulser.

Detector Linearization

Since the amplitude detectors are based on diodes, they exhibit a nonlinear transfer characteristic. To achieve minimal charge-dependence of measured beam position, the nonlinearity must be accounted for. During operation, this is achieved by applying an inverse nonlinear function to the measured pulse heights in the FPGA-based digital post-processing. During production time, the nonlinearity was measured and fitted to a suitable model.

Exemplary transfer functions are shown in Fig. 4 (black). They were measured by using the RFFE onboard pulser and varying the digital step attenuator (in the lowest of the three gain ranges) to generate an amplitude sweep of the detector input signal, while the detector output voltage (pulse height) was measured by the ADC.

Note that due to unavoidable production tolerances of the electronic components and slight differences in the component layout of the four channels, each channel of each RFFE has to be calibrated individually. This is the case not just for the detector linearization but for all applied calibration procedures.

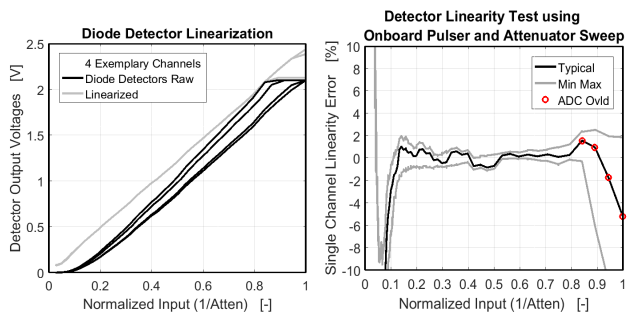

Figure 4: Detector linearization (left), and linearization residual error (right) of ≈300 units.

A suitable approximation for the detector nonlinear transfer function is:

$$y = \sqrt[c]{a^c + (bx)^c} - a \qquad (1)$$

Here y is the detector output voltage measured by the ADC (pulse height), and x is the detector RF input voltage amplitude. Parameter a is an offset in x, parameter b is a gain (detector sensitivity and RF chain), and parameter c is the curvature at the threshold of the detector. The threshold itself is at $x = a/b$, and becomes more pro-

ISBN: 978-3-95450-192-2 doi:10.18429/JACoW-IBIC2017-TUPCF19

nounced (edged) as c is increased. This approximation describes the asymptotic behaviour of the detector correctly, and does have an inverse.

The linearized detector characteristics are also shown in Fig. 4 (grey). Good linearity is achieved for normalized input signals ranging from 0.15 to 0.85, where the lower limit is determined by the diode detector threshold, and the upper limit by the ADC saturation level. This is illustrated by the graph on the right, which shows the relative deviation from an exactly linear transfer function.

The linearity of the RFFE is calibrated before the calibration of the step attenuators. However, by using many attenuator steps, and due to the limited degrees of freedom of the detector transfer function approximation, the effects of step attenuator errors are averaged out. This method provides absolute levels for detector output voltage y, where the precision is mainly determined by the ADC and its voltage reference.

Gain Range and Step Attenuator Calibration

When the gain range or digital step attenuator settings are changed while the beam orbit remains constant, the measured beam position should remain unchanged. This requires precise knowledge of gain and attenuation values of the three gain ranges and the digital step attenuator for each channel. Because of electronics component tolerances and the effects of internal signal reflections, the gain ranges and digital step attenuators need to be calibrated to achieve the desired performance.

The applied calibration procedure utilizes the onboard pulser and the (already calibrated) detectors to measure the effects of different gain range and step attenuator settings. The dependence of detected signal level D on pulser amplitude P, gain range G and step attenuator A is given by the following equation:

$$P_p + G_g^i - A_a^i = D_{p,g,a}^i \qquad (2)$$

Here P_p is the p-th pulser amplitude in [dBm], G_g is the gain value in [dB] of the g-th gain range, A_a is the attenuation value in [dB] of the a-th attenuator step, and $D_{p,g,a}$ is the resulting detected signal level in [dBm]. Index i is the channel number. Equation (2) can be written as a linear system of equations and solved for P_p, G_g, and A_a, given that measurements are available at sufficient combinations of p, g, and a. Since P, G, and A are not independent, two constraints are added: The *measured* mean attenuator value is forced to equal the *nominal* mean attenuator value for every channel; and the mean measured gain at lowest gain is forced to zero:

$$\sum_a A_a^i - A_{a,nom}^i = 0 \quad \text{and} \quad \sum_i G_1^i = 0 \qquad (3)$$

Calibration results are shown in Fig. 5 in the form of deviations of attenuation and gain values from their nominal values. The measured $G_g{}^i$ and $A_a{}^i$ are saved to the RFFE's EEPROM, and later used by the FPGA board for position and charge calculations.

The deviation of measured gain from its nominal value increases for higher gain ranges, because more amplifier stages are involved. This calibration also yields the measured pulser amplitude P_p vs. pulser control voltage characteristics, as shown in Fig. 3.

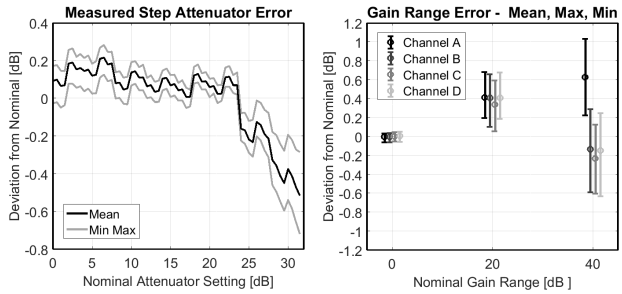

Figure 5: Calibration results from step attenuators (left) and gain ranges (right) for ≈300 units.

RFFE Calibration with External Pulser

The signal paths from the RF inputs to the RF switches (see block diagram) cannot be tested (for defects) and calibrated by means of the onboard pulser. Also, the onboard pulser is not an absolute amplitude reference. A known signal must therefore be applied to obtain gain correction factors for the four RF inputs and for absolute charge calibration. For this purpose, two button pickup signal generators (BPSGs) with four output channels each have been built, carefully characterized, and utilized.

The BPSGs are also used to verify the gain range and step attenuator calibration previously performed with the onboard pulser. Residual beam position and charge measurement errors caused by the limitations of the calibration are shown in Fig. 6. For the typical units shown, the multiple marks seen at every attenuator setting correspond to measurements taken at different signal levels. The spread is caused by residual detector linearity errors and pulser signal level errors (the latter affecting charge only).

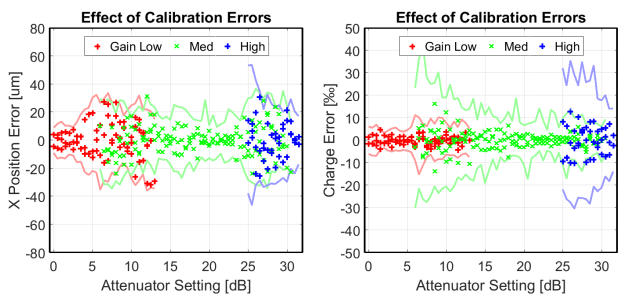

Figure 6: Effect of calibration errors on measured beam position and charge for a typical RFFE (crosses) and ≈50 RFFEs (solid lines).

BURN-IN TEST

The very last step of the production process was the burn-in test, typically running over several days, to verify reliable operation of the fully assembled, ready-to-ship BPM systems. During burn-in, the onboard pulser was emulating the BPM pickup signal of an electron beam running at 10 Hz repetition rate.

ISBN: 978-3-95450-192-2 doi:10.18429/JACoW-IBIC2017-TUPCF19

The FPGAs processing the BPM data have an on-chip microprocessor that reads the measured charge and position values from the FPGAs, and performs continuous real-time calculations of statistical quantities such as average values, standard deviations, and peak-peak variations. These quantities were collected and observed by external test software (Matlab script) through each MBU's Ethernet interface, and used as acceptance criteria for the burn-in test, by detecting MBUs where the peak-peak values were outside the acceptance range.

Since each RFFE has its own onboard pulser and each pair of BPMs shares one embedded processor, burn-in tests of all BPMs could be performed in parallel for a large number of MBUs before shipment. During the burn-in tests, units were also switched off and on several times, to introduce thermal stress, and to verify that they were fully functional after each power cycle.

RESOLUTION MEASUREMENTS AT EUROPEAN XFEL

First position and charge resolution measurements of button, re-entrant, and cavity type BPMs in the E-XFEL injector have already been presented earlier [6] for a fixed bunch charge of 400 pC. Figure 7 shows mean values of measured single-bunch position and charge resolutions of BPMs in the E-XFEL linac as a function of bunch charge.

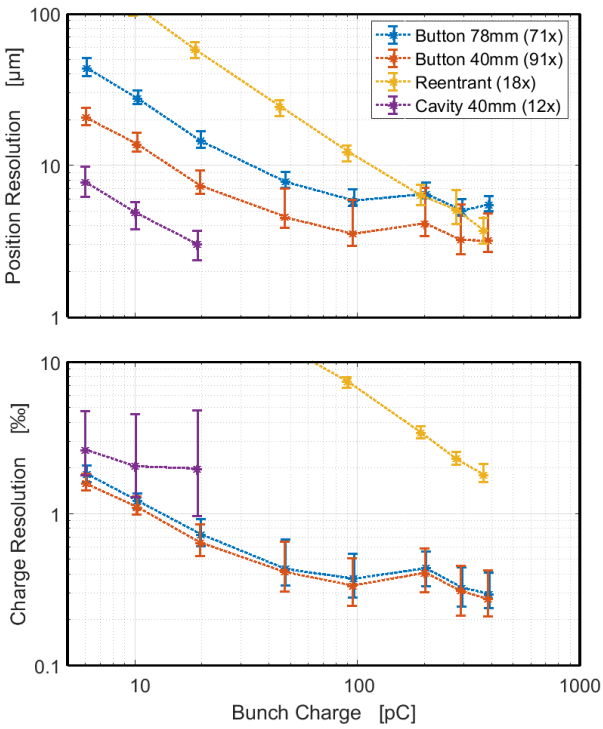

Figure 7: Measured BPM single-bunch resolutions.

The numbers of BPMs used for the statistics (mean values and ±1σ bars) are indicated in the legend (bracket values). Measured single-bunch position and charge resolution values are also shown in Table 1 for 20 pC and 100 pC bunch charges.

It should be noted that the measured resolutions (rms random noise) may have been degraded by systematic measurement errors resulting from changes of RFFE attenuator and gain range settings by the action of the automatic gain control algorithms in the FPGAs. The presented resolution measurements are based on correlation analysis among all BPMs along the machine [7].

Table 1: Measured BPM Single-bunch Resolutions

BPM Type	Position Resolution [µm]		Relative Charge Resolution [‰]	
	20 pC	100 pC	20 pC	100 pC
Cold Buttons	15	6	0.75	0.4
Warm Buttons	8	4	0.65	0.4

CONCLUSIONS

Electronics for more than 300 button-electrode type BPM systems were produced, calibrated and delivered to the European XFEL. So far about 240 systems were installed in the E-XFEL tunnel and have been delivering charge and position measurements since first beam in beginning of 2017. Only one RFFE board had to be replaced shortly after installation due to hardware failure, which proves the effectiveness of the quality checks. The electronics work very reliably, and the resolutions measured with beam show that the requirement (e.g. <50 µm for single-bunch position at 100 to 1000 pC) are not only achieved, but significantly exceeded by a factor of almost ten. This allows to operate the E-XFEL at very low bunch charges, and to characterize the accelerator more accurately at higher bunch charges. The reported resolutions were achieved with electronics calibrated in the laboratory only. Remaining systematic errors could be further reduced by beam-based calibration methods in the future.

REFERENCES

[1] D. Lipka *et al.*, "Button BPM development for the European XFEL", in *Proc. DIPAC'11*, Hamburg, Germany, 2011, pp. 83-85.

[2] B. Keil *et al.*, "The European XFEL beam position monitor system", in *Proc. IPAC'10*, Kyoto, Japan, 2010, pp. 1125-1127.

[3] W. Koprek *et al.*, "Status of the transverse intra-bunch train feedback of the European XFEL", presented at IBIC'17, Grand Rapids, MI, USA, paper TU3AB2, this conference.

[4] B. Keil *et al.*, "A generic BPM electronics platform for European XFEL, SwissFEL and SLS", in *Proc. IBIC'12*, Tsukuba, Japan, 2012, pp 133-137.

[5] D.M. Treyer *et al.*, "Design and beam test results of button BPMs for the European XFEL", in *Proc. IBIC'13*, Oxford, UK, 2013, pp. 723-726.

[6] D. Lipka *et al.*, "First experience with the standard diagnostics at the European XFEL injector", in *Proc. IBIC'16*, Barcelona, Spain, 2016, pp.14-19.

[7] N. Baboi *et al.*, "Resolution studies at beam position monitors at the FLASH facility at DESY", in *Proc. BIW'06*, Fermilab, Batavia, Illinois, USA, 2006, in *Proc. AIP Conf. vol. 868*, Ed. T.S. Meyer, R.C. Webber, pp. 227-237.

ISBN: 978-3-95450-192-2 doi:10.18429/JACoW-IBIC2017-TUPCF20

COSY ORBIT CONTROL UPGRADE

C. Böhme, I. Bekman, V. Kamerdzhiev, B. Lorentz, S. Merzliakov, M. Simon, C. Weidemann
Forschungszentrum Jülich, Germany

Abstract

The Cooler Synchrotron COSY can store and deliver proton and deuteron beam in the momentum range from 0.3 GeV/c to 3.65 GeV/c for internal and external experiments. New requirements of the Jülich Electric Dipole Moment Investigation (JEDI) experiment requires a RMS beam orbit distortion smaller than 100 μm. This requirement lead so far to the replacement of the BPM readout electronics, an introduction of a slow beam orbit correction and feedback system and the re-alignment of the magnets. All three projects are close to completion, therefore first results are presented.

INTRODUCTION

The COoler SYnchrotron (COSY) of the Forschungszentrum Jülich is a 184 m long racetrack-shaped synchrotron and storage ring for protons and deuterons from 0.3 GeV/c (protons) or 0.6 GeV/c (deuterons) up to 3.65 GeV/c. Built in are devices for stochastic as well as electron cooling. The stored ions can be polarized or unpolarized. Commissioned in 1993, the machine was mainly used for target experiments. Therefore no special focus was laid on the beam orbit, as long as the target overlap was maximized.

With the JEDI (Jülich Electric Dipole moment Investigations) experiment new requirements concerning the overall RMS beam orbit deviation were introduced [1]. Therefore an automatized beam orbit control system was developed. Furthermore other components were identified being in need to be upgraded or to be added. One example is the analog BPM readout electronics, which offsets prevents an accurate position determination especially around the 0 position. Another example is the positioning of the magnets, which drifted out of their position over the years [2].

BPM SYSTEM

COSY is equipped with a total of 33 BPMs whereas 29 are shoebox-style BPMs utilizing a standard readout electronics. During commissioning of COSY 27 BPMs of two types were installed, a cylindrical type with 150 mm diameter and a rectangular type with 150 mm · 60 mm inner size [3]. The selection was made to fit into the beam pipe, which is round in the straight sections and rectangular in the arcs in order to fit into the dipole magnets. Recently 4 BPMs were added with special geometries. Two of them are designed to fit within the 2 MeV electron cooler [4]. Another 2 are based on Rogowski coils in order to have a minimal longitudinal length for the Wien Filter of the JEDI experiment [5]. These four use their own, non-standard electronics for readout.

Analog BPM Signal Processing

At the commissioning of COSY, a BPM readout system was build based on a mainly analog processing [6]. Pre-amplifiers are directly connected to the N-type vacuum feedthrough of the pick-ups. This pre-amplifier has a fixed gain of 13.5 dB with an input impedance of 500 kΩ and a bandwidth of 100 MHz (-3 dB). The gains and offsets of two pre-amplifiers have been exactly matched for one plane of one BPM in order to avoid incorrect measurements. The pre-amplified signals are fed into an analog processing module, where sum and delta signals are generated using a hybrid. These signals are then treated separately and can be further amplified in 6 dB steps from 0 dB to 66 dB. Both the sum and the delta branches have two signal paths. A narrowband path features 3 possible filter settings with bandwidths of 10 kHz, 100 kHz, or 300 kHz and an additional amplifier that can be set from 0 dB to 18 dB in 6 dB steps. A broadband path with 10 MHz bandwidth can be used for direct sampling of the signals. The analog outputs are unipolar, the sign of the narrowband delta signal is detected separately and the information is transmitted by a separate TTL signal line. After the analog signal processing the signals are digitized in a separate module. This is done using 20 MHz 8 bit ADCs. For the narrowband signal the sampling frequency is lowered to 1 MHz or 100 kHz, depending on the selected analog bandwidth. For the sum signal only 7 of the 8 bits of the ADC are used, the 8th bit is used to indicate the polarity of the delta signal. The digital module generally has the capability to buffer 4096 data points, while few modules can store up to 64k data points. The CPU in the VXI crate calculates out of the narrowband signal the beam position. It is also possible to transfer the raw broadband data to the control system in order to display and export it, for e.g. computation of the turn-by-turn position.

Despite the outdated digital hardware and the increasing failing rate, the main issue lays within the split signal path of the differential signal and the sign of the position. An offset of the differential signal is measured on all modules, even directly after calibration. Because of this the measured beam position never reaches the zero position [7]. Using the introduced orbit correction system this leads to incorrect correction settings.

Digital BPM Signal Processing

Because of these problems with the analog BPM signal processing system, a new system was introduced with digital signal processing. The decision was made to utilize the commercially available Libera hadron system [8]. The system was recently put into operation and commissioning is ongoing. First results are presented later in this article.

ISBN: 978-3-95450-192-2 doi:10.18429/JACoW-IBIC2017-TUPCF20

The system samples the input signal with a 250 MHz 16 bit ADC without further analog signal processing. From the digitized signals the Libera Hadron derives several data sets:

- The ADC raw data can be stored in a 2GB dedicated memory, which allows the readout of about 1 second of data.
- The bunch by bunch information is stored in another dedicated 2 GB memory, which allows at COSY the storage of about 1 minute of turn by turn data, depending on the beam's revolution frequency.
- Based on the bunch by bunch data a FFT analysis is performed, allowing tune measurements.
- An integrated 10 Hz continuous bunch position information is streamed out of the system.

Amplifiers

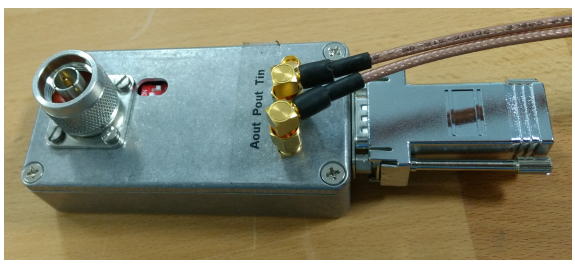

Figure 1: Newly developed amplifier for connection directly to the pick-ups. The amplifier features a signal output after a fixed gain pre-amplifier of 13.5 dB or 20 dB (selectable via switch), a second output after two additional adjustable gain amplifier stages and a calibration signal input. On the right side in the picture a connector for the supply voltages and the gain control signals is located.

The input of the Libera system has a fixed input range. Therefor the necessity of adjustable gain amplifiers was seen, in order to cover the beam intensity range of COSY while achieving the best possible beam position resolution. The former BPM system used a fixed-gain pre-amplifier directly attached to the pick-ups and switchable amplifiers within the BPM electronics. This system showed the disadvantage if only a pre-amplified signal is conveyed over the connecting cables, which resulted in increasing noise levels with cable length. To overcome this disadvantage, the former BPM electronics was re-located close to the pick-ups into the accelerator tunnel. With this in mind in the new system a tradeoff was made: The main amplification was located in the amplifiers directly connected to the pick-ups, allowing longer cables with a better signal to noise ratio, but with the disadvantage of more complex electronics being located in the tunnel compared to a fixed-gain amplifier. The Amplifiers consist of three stages:

- 1st stage: a fixed gain amplification with 13.5 dB or 20 dB, defined by dip-switches.
- 2nd stage: a continuously adjustable amplifier with 0 dB to 50 dB amplification
- 3rd stage: a continuously adjustable amplifier with -20 dB to 10 dB amplification

The amplifier has 2 output paths, as shown in Fig. 1. The first output is after the first fixed-gain stage, in order to connect to the analog BPM electronics to keep the usual functionality during the commissioning process. A second output after all three stages is connected to the digital BPM electronics. A third connector features a calibration signal input, which is fed into the 1st stage with a 50 dB signal attenuation.

The amplification of the 2nd and 3rd stage are controlled with an analog voltage. The control is realized utilizing a Beckhoff Ethercat system. A 0 V to 10 V DAC controls the second stage of all 4 amplifiers of one BPM together. The third stage is controlled individually for each amplifier using a 0 mA to 20 mA DAC, which is transformed in the amplifier to a voltage control signal. The connection to the control system is done with DLS-ethercat from Diamond Light Source [9]. Tests of the amplifier showed an input noise of 1.4 nV/$\sqrt{Hz}$ at 10 MHz. The gain control scheme is designed to allow gain control resolution of 0.001 dB (which translates to the μm level in terms of beam position).

ORBIT CONTROL

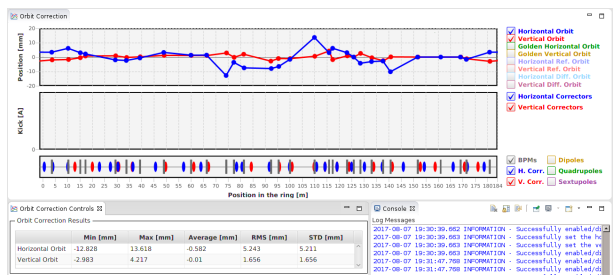

Figure 2: GUI of the orbit control system developed in cooperation with Cosylab d.d. The GUI can be used for orbit position visualization (mode shown) and for orbit correction towards a configurable orbit. In the most upper part the actual orbit measurement is shown, beyond the actual settings of the correction magnets is displayed when in orbit correction mode. For reference the position of the BPMs and magnets can be visualized in the part below. The GUI also automatically calculates the RMS orbit deviation and displays it. Control buttons for e.g. activation of the orbit correction are not shown in the picture.

In cooperation with Cosylab d.d., an orbit control system was introduced [10]. The GUI of this system is shown in Fig. 2. This system is operational since late last year and initially interfaced with the analog BPM system and the function generators, controlling the corrector magnets power converters. Using the analog BPM system as base for the orbit correction, the speed of the system is limited to the reaction time of the system, which allows about one measurement

ISBN: 978-3-95450-192-2 doi:10.18429/JACoW-IBIC2017-TUPCF20

every 4 seconds. The system uses an iterative process to correct towards the desired orbit, with the correction strength adjustable. A result of the orbit control mechanism is shown in Fig. 3. In this example the systems tries to put the orbit to zero at all BPMs, resulting in an overall RMS value of about 1.6 mm.

The system was build in the perspective, that the BPM readout system will be replaced. Therefore the communication to the BPM electronics and the correction magnets controllers was done utilizing the EPICS protocol and a program module doing the actual interfacing between the EPICS protocol and the self developed command interface of the analog BPM system and the correction magnet controllers. By adapting the EPICS variables to the digital BPM readout system, the orbit correction system can utilize the data of the digital system without changing the core functionality. This was successfully implemented. The modification was made utilizing the 10 Hz continuous position data stream.

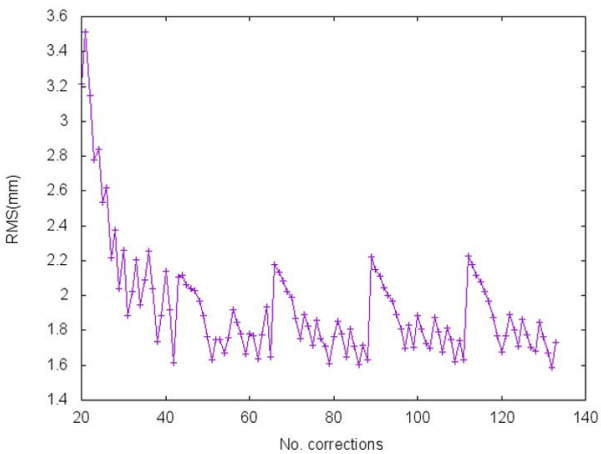

Figure 3: Example of the RMS orbit with activated orbit control towards a zero orbit using the analog BPM system, which, because of offsets, gives false values around the zero position. The RMS is reduced to about 1.6 mm. The spikes every 25 correction cycles are the result of a new beam injection.

CURRENT STATUS

- All 29 standard BPMs have been connected to the digital BPM signal processing system. This includes the new amplifiers.
- 8 Libera Hadrons have been successfully put into operation. The necessary signals like trigger signals or RF reference are connected from a single point with equally long cables.
- First measurements with the digital BPM readout system were performed and ADC raw data, bunch by bunch data and slow position data were successfully measured.
- The connection between the Ethercat master and the EPICS control utilizing the DLS-ethercat package was at the point the presented data was recorded not fully functional, so temporary the control was realized using a HTML page. It is successfully implemented in the meantime.
- The orbit control software was adapted to work with the digital BPM readout system, which was successfully tested.

FIRST MEASUREMENTS

First measurements were performed using different beam settings. The beam intensity was varied to test different settings of the amplifiers. Local orbit bumps were introduced to check the performance of the readout system and an Orbit Response Matrix was measured to check for wrongly cabled BPMs. Fig. 4 shows an example of an ADC measurement for one BPM with about 10^{10} particles stored and a low gain of the amplifiers. This results in a rather high signal level with relatively low noise.

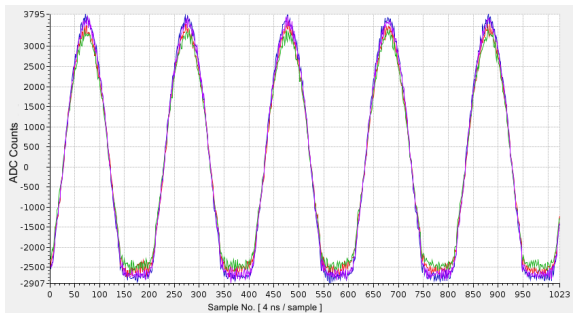

Figure 4: Example of the ADC measurements for all four pick-ups of one BPM.

To compare performance, the amount of stored particles was reduced to $5{\cdot}10^{8}$ particles. The BPM with the most noise is shown in Fig. 5 as an example. This was measured with a total amplification of 55 dB, with a maximum of 80 dB possible. The other BPMs had a much lower noise level, so that it can be expected that the position measurements will also work with an even lower amount of stored particles. The noise level was significantly reduced later on by resolving a grounding issue within the amplifier enclosure.

CONCLUSIONS

To match the requirements of the EDM precursor experiment, an automated orbit control system was introduced, in order to minimize the overall beam orbit RMS deviation down to 100 μm. In this context the performance of the analog BPM signal processing was found to be causing issues, as described above. Therefore an upgrade to the BPM signal processing system was done using the Libera Hadron. Because of the fixed input parameters of the Libera Hadron new amplifiers were developed in-house. The gain control of this amplifiers was done using an Ethercat system which is controllable through the EPICS control system protocol.

The whole system was put into operation end of July this year and first measurements were performed successfully.

ISBN: 978-3-95450-192-2 doi:10.18429/JACoW-IBIC2017-TUPCF20

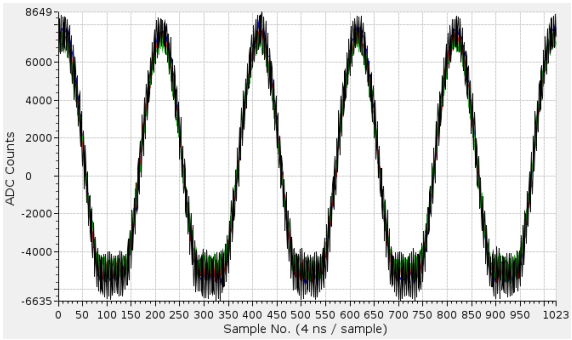

Figure 5: ADC measurement with a rather low amount of stored particles, about $5{\cdot}10^8$. All 4 pick-up signals of the most noisy BPM are shown. The noise level was significantly reduced later on by resolving a grounding issue within the amplifier enclosure. This gives room for position measurements with an even lower amount of stored particles.

OUTLOOK

Although the new BPM readout system was put into operation, the signal generators providing the calibration signals were not yet installed. The hardware as well as the corresponding software will be commissioned within a few months. An automatic gain calibration on a daily basis is envisaged for the system.

One power supply is used to power up to 8 amplifiers. Short circuit protection based on a specialized integrated circuit was implemented for individual channels. High failure rate of the protection circuitry was observed during the commissioning phase. A new design is on the way.

As described before, mainly the 10 Hz output of the Libera Hadron system is used for operation. The EPICS transfer of this information stops several times a day, therefore a more stable mode of operation has to be found.

In addition, the EPICS position information could be quickly implemented into the earlier designed orbit control system. But for a full integration the control of the Libera Hadron will be implemented in the system.

REFERENCES

[1] M. Rosenthal *et al.*, "Spin Tracking Simulations Towards Electric Dipole Moment Measurements at COSY", in *Proc. IPAC'15*, Richmond, VA, USA, May 2015, THPF032.

[2] V. Schmidt *et al.*, "Analysis of Closed-Orbit Deviations for a First Direct Deuteron Electric Dipole Moment Measurement at the Cooler Synchrotron COSY", in *Proc. IPAC'17*, Copenhagen, Denmark, May 2017, TUPVA083.

[3] R. Maier *et al.*, "Non-Beam Disturbing Diagnostics at COSY-Jülich", in *Proc. EPAC'90*, Nice, France, June 1990, p. 800.

[4] V. B. Reva *et al.*, "COSY 2 MeV Cooler: Design, Diagnostic and Commissioning", in *Proc. IPAC'14*, Dresden, Germany, June 2014, MOPRI075.

[5] J. Slim *et al.*, "Design of the electrical circuit of the new RF Wien Filter at COSY-Jülich", 22nd International Spin Symposium, Champaign, IL, USA, September 2016.

[6] J. Biri *et al.*, "Beam Position Monitor Electronics at the Cooler Synchrotron COSY Jülich", Eighth Conference on Real-Time Computer Applications in Nuclear Physics, Vancouver, June 1993.

[7] F. Hinder *et al.*, "Beam Position Monitors @ COSY", JEDI Collaboartion Internal Note, 13/2015, June 16, 2015.

[8] C. Böhme *et al.*, "Cosy BPM Electronics Upgrade", in *Proc. IBIC'16*, Barcelona, Spain, September 2016, TUPG26.

[9] R. Mercado *et al.*, "Integrating Ethercat Based IO into EPICS at DIAMOND", in *Proc. ICALEPCS'11*, Grenoble, France, October 2011, WEMAU004.

[10] M. Simon*et al.*, "COSY Slow Orbit Feedback System", in *Proc. IPAC'17*, Copenhagen, Denmark, May 2017, TUPIK050.

ISBN: 978-3-95450-192-2 doi:10.18429/JACoW-IBIC2017-TUPCF21

TRANSVERSE DAMPER USING DIODES FOR SLIP STACKING IN THE FERMILAB RECYCLER*

N. Eddy#, B. Fellenz, P. Prieto, S. Zorzetti, Fermilab, Batavia, IL 60510, USA.

Abstract

During slip stacking in the Recycler, up to six batches of 84 bunches each are slipped by each other to and then captured to double the intensity of the extracted beam. For nominal chromaticity settings, a bunch by bunch transverse damper system is needed to maintain beam stability but this system is blind to the bunches as they are slipping. The initial solution was to drastically raise the chromaticity to keep the beam stable. A new frequency based damper using diode detectors was developed to provide damping during slip stacking and allow the chromaticity to be reduced to nominal settings.

INTRODUCTION

Slip stacking refers to the process in which batches (84 bunches) of beam are injected and captured with slightly different RF systems so that they have slightly different energies and travel on separate orbits allowing them to slip by one another. The process was first implemented in the Main Injector to increase proton beam power for the MINOS neutrino experiment at Fermilab [1]. As part of the NOvA neutrino upgrade the Recycler anti-proton storage ring which shares the same tunnel with the Main Injector was re-purposed as a proton stacker [2]. In this configuration, slip stacking is done in the Recycler while the Main Injector is ramping which allows the overall cycle time to be reduced, further increasing the beam power.

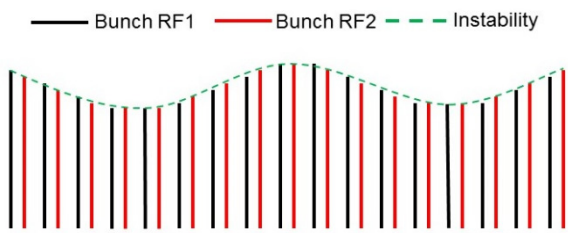

Figure 1: Cartoon showing slip stacking bunches with coupled bunch instability superimposed.

Initially the Recycler had a bunch by bunch digital damper very similar to the one used in the Main Injector [3]. These bunch by bunch systems were blind during the slipping process and needed to be disabled. This drastically increased chromaticity and subsequently tunes to provide beam stability while the dampers were off. As the Recycler struggled to reach design intensity, the high losses during the slipping forced the development of a system capable of damping the beam during the slip stacking.

* This work was supported by the DOE contract No.DEAC02-07CH11359 to the Fermi Research Alliance LLC.
# eddy@fnal.gov

As shown in Figure 1, the damper is required to suppress the coupled bunch instabilities which are dominant at low frequencies. The first mode is at about 50KHz and the expected bandwidth is a few MHz. Because the two beams are effectively coupled, we just need to detect the envelope of the instability frequency.

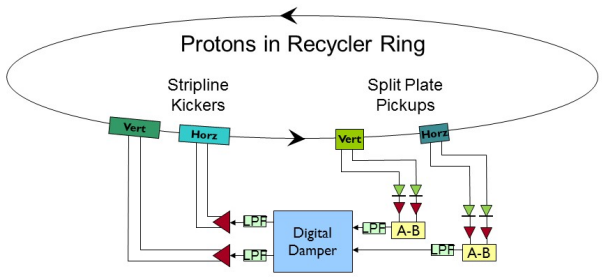

Figure 2: Overview of the current Diode Damper system in the Recycler.

SYSTEM OVERVIEW

The slip stack damper was implemented using existing components from the original Recycler anti-proton damper [4]. An overview of the system is shown in Figure 2. The system consists of a BPM pickup, input filters, digital signal processing, output amplifiers, and stripline kickers. To damp the slip stacked beam, a technique to detect the relatively low frequency coupled bunch beam instability was developed.

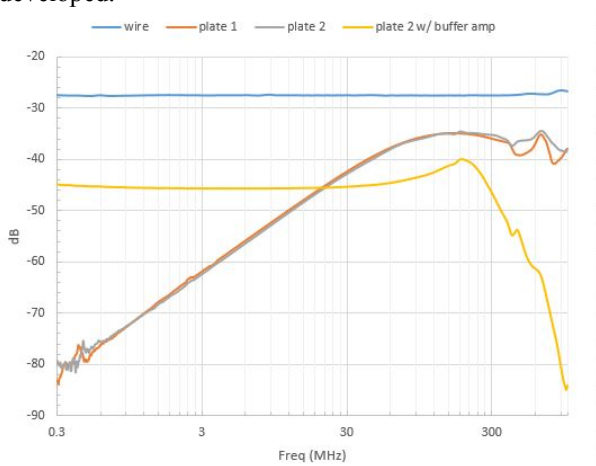

Figure 3: Measured frequency response for the split tube beam position monitor using a frequency matched wire.

The Pickup Response

The damper system uses the same split plate pickups installed in the Recycler . To measure anti-proton beam, high impedance pre-amps were installed in the tunnel to extend the frequency response of the pickup down to about 100KHz. The frequency response of the pickups is shown

ISBN: 978-3-95450-192-2 doi:10.18429/JACoW-IBIC2017-TUPCF21

in Figure 3 and with the addition pre-amps is shown in Figure 4. For high intensity operation with short 53MHz bunches it is not feasible to use this technique. Another method is needed to extend the pickup response down to 50KHz which is needed to damp the lowest coupled bunch instability.

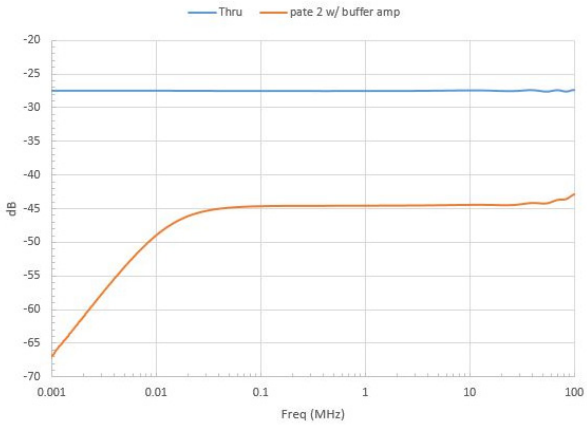

Figure 4: The frequency response of the pickup plus a high impedance buffer amplifier.

Diode Detection Technique

Several techniques were considered, but the simplest implementation was to use diodes in a configuration very similar to that used in the direct diode detection technique [5]. Fast schottky diodes were chosen which were able to detect the low frequency amplitude modulation from the beam instability riding on top of the slipping 53MHz bunches. Note, there is some secondary modulation effects due to the amplitude of the bunches increasing as they walk past one another but to first order, this is cancelled with a difference amplifier.

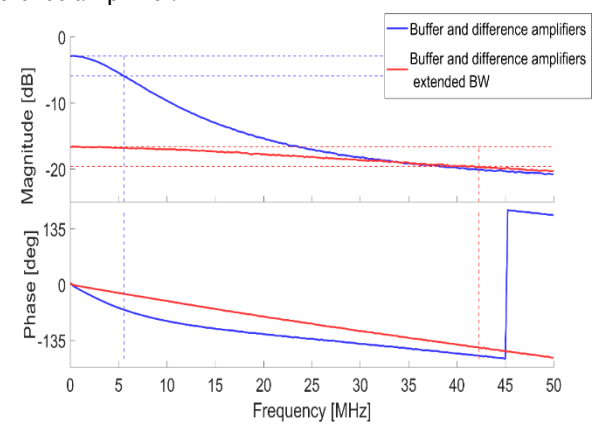

Figure 5: The frequency response of the schottky diode, buffer amplifier, and difference amplifier for the initial configuration and modified configuration.

Results of bench tests for the input circuit are shown in Figure 5. The initial configuration shown in blue had about 5 MHz of bandwidth which was thought to be sufficient. As noted in the figure, it also had non-linear phase shift over this range which could not be completely compensated for by our digital delay. The buffer amplifier was modified to extend the bandwidth and improve the system performance as the linear phase response allowed for better timing and hence damping at lower frequencies (red trace in Figure 5). The gain was reduced, but we had over 20dB of attenuation in the system which was removed to compensate for this attenuation.

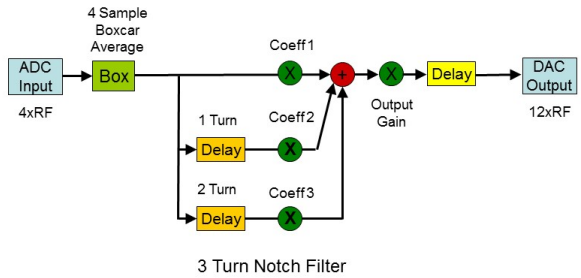

Figure 6: Block diagram for the damper firmware which consists of settable coefficients, gain, and delay.

Digital Signal Processing

The current system differs from the original anti-proton damper in that we now have one pickup instead of two. This required modifying the design to incorporate a three turn filter to notch the revolution harmonics and adjust the pickup to the kicker phase advance. A simplified block diagram of the digital filter is shown in Figure 6. For this system four bit coefficients are used which allow roughly 8° steps for the pickup to kicker phase. All relevant parameters can be controlled by the user.

COMMISSIONING

The first step in commissioning is to verify the timing and gain settings. This requires dedicated study time with low intensity beam so that open loop response measurements can be made. The results for the vertical and horizontal systems are shown in Figure 7 and Figure 8 respectively. As the tunes are near half integer, the plots are shown centered on 0.5 tune. The upper sideband is on the left and the lower sideband is on the right. The phase is inverted so that ideal damping occurs when the phase is zero at the peak.

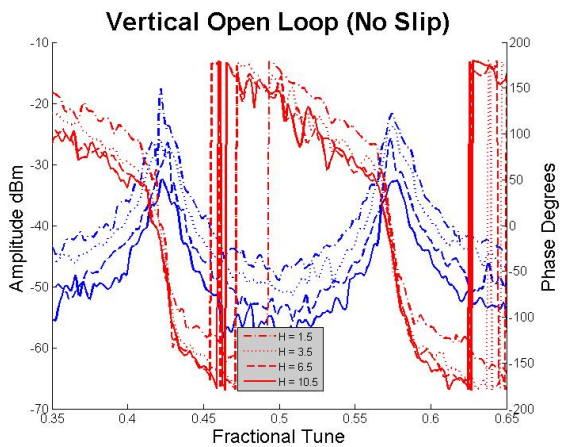

Figure 7: Vertical open loop system response. Upper sideband for n+q on the right and the lower sideband for n+1-q is on the left.

ISBN: 978-3-95450-192-2 doi:10.18429/JACoW-IBIC2017-TUPCF21

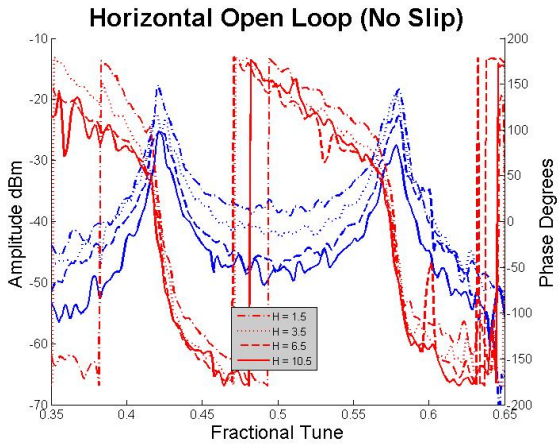

Figure 8: Horizontal open loop system response. Upper sideband for n+q on the right and the lower sideband for n+1-q is on the left.

Once the system is timed-in, the loop can be closed. Note, since one observes two tune peaks for the split tunes all open loop measurements are done with non-slipped beam. This is done to make certain the system is actually working. The sign can be flipped to anti-damp for a short time. Figure 9 shows the vertical position (blue), horizontal position (purple) traces, beam intensity (green), and the damping gate (yellow) at the end of the cycle on fully slipped beam. In this case, there is significant damping due to chromaticity, but the damper is able to overcome this and cause slow growth.

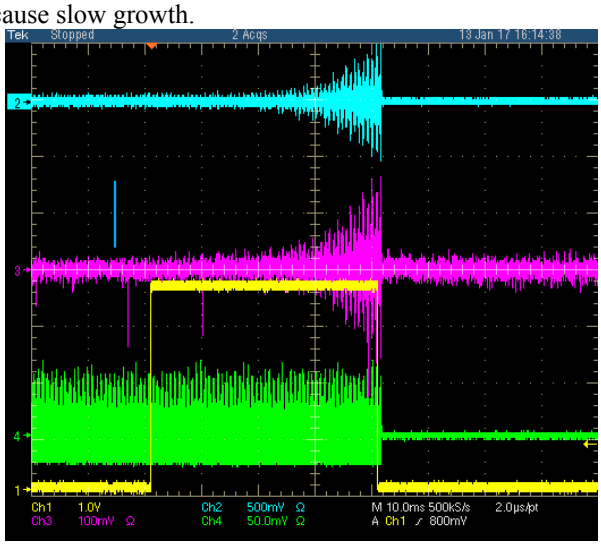

Figure 9: Ant-damped slipped beam. Blue – vertical, Purple – horizontal, Green – beam from WCM, Yellow – damping gate.

Once the damper was made operational, the Recycler experts began tuning the machine to lower the chromaticity and tune on other machine parameters. Within a matter of days of the system becoming operational, the Recycler began achieving record intensities and soon after the complex was regularly operating at or above the design 700kW beam intensity. It is also possible to use the damper system to make closed loop measurements even at full intensity as shown in Figure 10. It is possible to see the split tunes during slip stacking caused by the two different momentum beams.

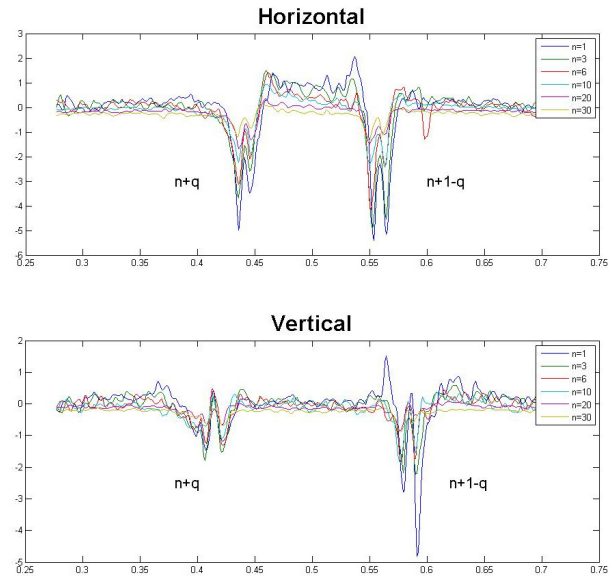

Figure 10: Closed loop response at full intensity during slip stacking.

SUMMARY

A diode detector envelope front-end was developed to allow detection of the low frequency coupled bunch instability on slip stacking beam in the Recycler. Once implemented the system allowed much easier tuning of the machine, lower losses, and achievement of design intensity operation.

ACKNOWLEDGMENT

This manuscript has been authored by Fermi Research Alliance, LLC under Contract No. DE-AC02-07CH11359 with the U.S. Department of Energy, Office of Science, Office of High Energy Physics. The U.S. Government retains and the publisher, by accepting the article for publication, acknowledges that the U.S. Government retains a non-exclusive, paid-up, irrevocable, world-wide license to publish or reproduce the published form of this manuscript, or allow others to do so, for U.S. Government purposes.

REFERENCES

[1] K. Seiya *et al.*, "Mult-Batch Slip Stacking in the Main Injector at Fermilab", in *Proceedings of PAC2007*.

[2] P. Adamson, "700kW Main Injector operations for NOvA at FNAL", in *Proceedings of IPAC2015*.

[3] P. Adamson *et al.*, "Operational performance of a bunch by bunch digital damper in the Fermilab Main Injector", in *Proceedings of PAC2005*.

[4] N. Eddy and J. Crisp, "Transverse digitial damper system for the Fermilab anti-proton Recycler", in *Proceedings of BIW 2006*.

[5] M. Gasior and R. Jones, "High sensitivity tune measurement by direct diode detection", in *Proceedings of DIPAC 2005*.

ISBN: 978-3-95450-192-2 doi:10.18429/JACoW-IBIC2017-TUPCF23

FIRST BEAM TESTS AT THE CERN SPS OF AN ELECTRO-OPTIC BEAM POSITION MONITOR FOR THE HL-LHC

A. Arteche*, S. E. Bashforth, G. Boorman, A. Bosco, S. M. Gibson,
Royal Holloway, University of London, Egham, UK
N. Chritin, M. Krupa, T. Lefèvre, T. Levens, CERN, Geneva, Switzerland

Abstract

An Electro-Optic Beam Position Monitor is being developed for the High Luminosity Large Hadron Collider (HL-LHC), aimed at the detection of high order proton bunch instabilities and as a diagnostic for crabbed bunch rotation. A prototype EO-BPM was installed in the CERN SPS during 2016 and recent first beam tests of the EO pick-up are presented. The tested system comprises two opposing pick-ups, each equipped with 5 mm cubic $LiNbO_3$ crystals in vacuum, illuminated by polarized light from a fibre-coupled CW 780 nm laser. The 1 ns proton bunch induces a temporal modulation in the polarization state of light emerging from each birefringent crystal, by the Pockels effect. The modulation is analyzed, then recorded by a fibre-coupled fast photodetector in the counting room. The very first experimental signals obtained by the EO pick-ups of a passing proton bunch are reported as a proof of concept of the idea. Moreover, the expected response of the beam signal is measured with respect to remotely controlled changes in the polarizer and analyser orientations. The data are compared with analytical and electromagnetic simulations. Following the first detection, we report the latest status of the prototype design and future prospects.

MOTIVATION

The crab cavities are one of the main upgrades in the High-Luminosity LHC scenario designed to induce a bunch rotation before and after the interaction point, in order to make the bunches collide head-on and thus maximizing the luminosity [1]. The control of the bunch rotation induced by the crab cavities requires precise diagnostic techniques capable of monitoring intra-bunch transverse position for a 1 ns proton bunch. Whereas the performance of conventional head-tail (HT) monitors is typically limited with a bandwidth of 6 GHz [2], the electro-optic (EO) BPM stands out as a promising innovative candidate aiming to perform with an improved time resolution (<50 ps) due to the faster optical response, expanding the bandwidth up to 10-12 GHz, sufficient for optimizing the crab cavities performance as well as the detection of high order HT instabilities.

Currently the technology is under development and a prototype has been successfully installed at the CERN SPS, where two variants were tested during the 2016 and 2017 SPS runs, respectively [3, 4].

* alberto.arteche.2014@live.rhul.ac.uk

ELECTRO-OPTIC PICK-UP PROTOTYPE

The EO pick-up prototype includes button-like devices that comprise a compact optical system formed of a $LiNbO_3$ (LNB) crystal sample and two prisms in combination with an optical beam (OB) [5]. Figure 1 depicts the design with the optical path superimposed for both prototype variants, zero and one: the 10 mm side right-angle prisms align the laser beam propagating in free-space through the crystal and back-reflect it out of the pick-up. The button body is shielded by a flange and a viewport that permits the transmission of the OB in and out of the optical system embedded in the vacuum.

The key piece of the EO pick-up is the LNB sample assembled in the core of the opto-mechanical body. The fundamental principle of detection exploits the Pockels effect exhibited by the LNB crystals, since its birefringence is modified by the action of the Coulomb field propagating from a passing particle bunch. The system imitates an EO amplitude modulator where the initial linear polarization at 45° is rapidly modified at the emerging beam by the action of the field on the crystal [6]. The extent of the optical modulation depends on the field strength and the crystal length. The output beam is incident upon an analyser which measures this modulation. Therefore, the transverse displacement can be obtained in the same fashion as the traditional BPM layouts, taking the difference in optical response between pick-ups on the opposite sides of the beam pipe.

The prototype pick-up variants differ when comparing the dimensions of the crystal and the use of electrodes. For pick-up zero, the propagating Coulomb field decays sharply at the crystal interface due to the LNB dielectric constant $\epsilon_{33} = \epsilon_z = 30$ in the propagating direction z [4, 7]. The field strength limitation caused by the dielectric constant can be partially overcome by placing electrodes to direct more field lines towards the crystal, following the mechanism shown in Figure 1. According to the CST simulations [8] carried out for each case using SPS nominal bunch of length 4σ=1 ns and intensity of 1.15×10^{11} protons, the estimated electric field in the crystal for pick-up zero is 0.65 kV/m whereas the field strength for pick-up one will be enhanced up to 2.8 kV/m. Furthermore, given the same field the optical modulation is enlarged by a factor 1.8 for pick-up one as it holds a 9 mm long crystal while pick-up zero employs a cubic 5 mm sample. Consequently, the overall effect of the crystal elongation in combination with the field increase predicts an EO signal ~8 times higher for pick-up one with respect the first proposal pick-up zero for the same nominal bunch conditions [6].

ISBN: 978-3-95450-192-2 doi:10.18429/JACoW-IBIC2017-TUPCF23

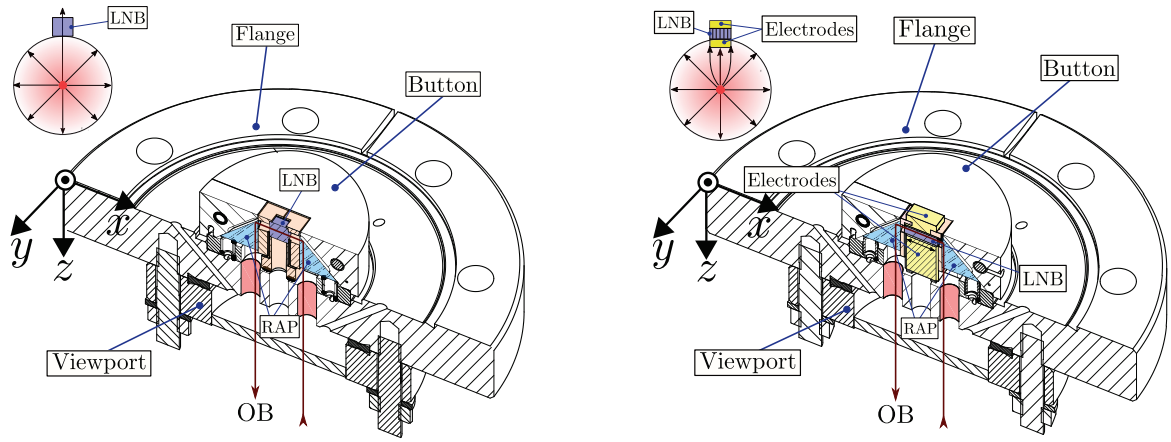

Figure 1: Prototype pick-up variants: zero (a) with only a crystal; and one (b) with an additional electrode.

EXPERIMENTAL SETUP

Optical Setup

The light source is a 780 nm laser that provides a < 200 kHz linewidth OB that is vertically polarized. The fibre-coupled output is split and connected to two PM fibres that carry the OB from the instrumentation room to the location where both prototypes are installed on the SPS ring, as in Figure 2.

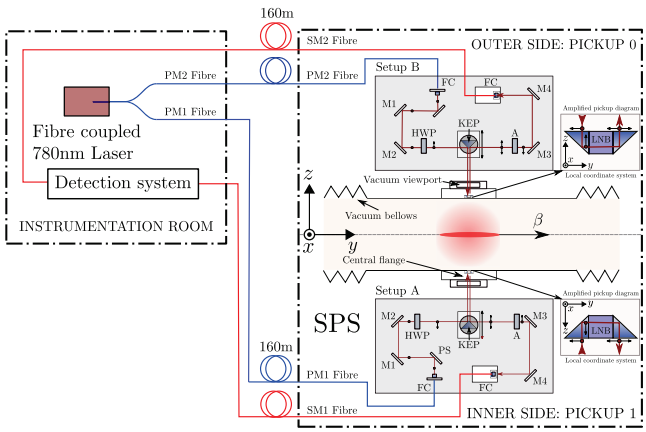

Figure 2: Diagram of the optical setup.

At the other extreme of each PM fibre, the OB is delivered vertically polarized by a 6.24 mm focus distance fibre collimator (FC). Furthermore, the vertical polarization is filtered by a polarizing plate splitter (PS). Two mirrors M1 and M2 are used to align the optical path correctly towards a knife-edge prism (KEP), which reflects the beam trajectory by 90° into the EO pick-up. The OB returned via the EO pick-up is steered towards a remote controlled 3-D stage with the assistance of mirrors M3 and M4. The beam is coupled back into a single mode (SM) return fibre held by a 3-D stage that transports the light 160 m back to the detection system, housed in the same instrumentation room as the laser. Since the setup must emulate an optical modulator configuration, a half-wave plate (HWP) and an analyser are placed before and after the KEP respectively. Furthermore, both HWP and analyser are held by rotation stages connected to a PC in the instrumentation room to permit remote control of the initial input polarization, as well as the analyser orientation.

There are two optically symmetric setups adjacent to each EO pick-up in the horizontal plane. The two pick-ups mounted on the outer and inner sides of the SPS ring are variants zero and one, respectively.

Preliminary Detection System

Since LNB is a naturally birefringent crystal, the initial polarization is modified in the absence of any passing bunch. Therefore, a certain amount of light power is transmitted through the analyser and carried by the return fibre that is coupled to a fast detector in the instrumentation room. A preliminary detection scheme was set up with a relatively low bandwidth amplifier that was available for the initial tests described here. The DC bias monitor output V_{DC} of the detector monitors the average input light power, whereas the RF output provides the EO signal from the return fibre which is induced when a proton bunch is passing. The signal at the RF output V_{RF} is magnified by an effective gain G_e due to a 210 MHz amplifier. Finally, both DC bias monitor and RF signal readouts are recorded by a 12-bit oscilloscope. Figure 3 depicts the entire chain of signal detection that separates the baseline and transforms an optical power signal into a voltage signal.

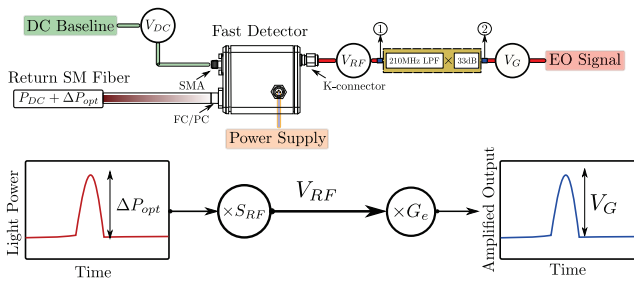

Figure 3: Preliminary detection chain scheme.

ISBN: 978-3-95450-192-2 doi:10.18429/JACoW-IBIC2017-TUPCF23

PICK-UP 0: FIRST ELECTRO-OPTIC SIGNAL

Prototype pick-up zero on the outer side of the CERN SPS ring was used to carry out the first tests that culminated in the very first electro-optic detection of a proton beam in December, 2016. The measurements were taken parasitically during the AWAKE experiment run in the SPS, which provided an average bunch length of 4σ=1.8 ns and a bunch charge of between 1.5×10^{11} and 3.5×10^{11} protons.

In these very first studies, the aim was to observe a signal corresponding to the Coulomb field of the passing bunch interacting in the electro-optic crystal, as a modulation of the light intensity through the system. For clarity, single shot measurements were not performed, rather, an average optical signal was recorded during multiple revolutions of an AWAKE bunch within a CERN SPS cycle.

According to the numeric simulations for these parameters, the Coulomb field penetrating the crystal E_{LNB} is much lower than E_π for the 5 mm LNB sample integrated in pick-up zero, e.g. $E_{LNB} \simeq 1$ kV/m $\ll E_\pi = 711$ kV/m, for a bunch formed of 3.0×10^{11} protons bunch. In these conditions the signal sensitivity is strongly dependent on the crystal output polarization, which is determined by the natural birefringence. The sensitivity is maximum for circular polarization and it will have no sensitivity for linear polarization [6]. The fit curve of the detector DC bias monitor output taken as a function of the analyser position is shown in Figure 4a, which represents an anticlockwise scan of the polarization state projection depicted on the bottom right. The measured elliptical polarization value leads to a sensitivity of 90% of the maximum during signal acquisition.

A fast electro-optically induced signal peak, corresponding to the proton bunch was observed using pick-up 0. The electro-optic signal is presented in Figure 4b for different positions of the transmission direction (TD) of the analyser, from vertical at 90° to 210° keeping a constant input linear polarization at 45° into the crystal. Due to the preliminary configuration of the pick-up and detection scheme, the Signal-to-Noise Ratio (SNR) was low, so it was necessary to average over the entire AWAKE cycle (digitizing ~600 turns) to achieve detection. Therefore, the simulated optical power modulation ΔP_{opt} was scaled accordingly with the average bunch length and charge of each cycle, as well as considering the crystal experimental output polarization. The dashed blue line represents the estimated peak voltage signal V_G obtained from applying the detection chain to the expected power signal assuming a PD response S_{RF} of -148 V/W scaled to the working wavelength 780 nm, and also an effective gain of 27 dB in the amplifier that corresponds to the typical AWAKE bunch length mentioned previously.

In a crossed polarizers scenario when the analyser is at 135°, the EO signal is expected to be maximum; on the contrary, when the analyser position is placed either vertical (90°) or horizontal (180°), the optical modulation will be undetectable. In the intermediate cases the signal decays or enhances accordingly. Since the detector has negative response, a positive signal indicates that the polarization projection is decreasing when the beam is passing, and equivalently, the sign is swapping from positive to negative when the analyser is reading the projection reduced due to the passing bunch. For the set of measurements presented in this paper, the projection along the analyser position parallel to 135° is squeezed while the perpendicular direction at 225° (45°) is elongated.

In conclusion, the first electro-optic signal of a proton beam has been observed and the signal peak is found to change sign in accordance with the electro-optic theory. Additionally, the signal level estimations agree with the numeric-analytic simulations well within an order of magnitude, even before any optimization of the preliminary pick-up design and detection scheme.

PICK-UP 1: POSITION SENSITIVITY

Even after significant amplification and considerable averaging, the Signal-to-Noise Ratio (SNR) of both prototypes was too poor to directly observe the pick-up's sensitivity to the transverse beam position. Recent measurements prove that the unfavourable SNR is a consequence of the photodetector's noise floor. Future direct measurements of the pick-up's beam position sensitivity will require a significant improvement of the photodetection network.

Nevertheless, the beam position correlation of the EO pick-up's signal was indirectly observed by measuring the narrow-band frequency spectrum around one of the higher harmonics of the SPS revolution frequency. The measurements were carried out with a single bunch of about 2×10^{10} protons stored in the SPS ring at the energy of 270 GeV for several hours during a so-called "coasting beam" operation.

The coasting beam conditions were very favourable for measurements of the EO pick-up. As the beam is stored at a constant energy, the pick-up's output signal can be averaged over a long time which reduces the noise. Moreover, due to constant revolution frequency, synchronous detection techniques can be applied which leads to further SNR improvement. In total, the coasting beam measurements were conducted with a noise floor of -100 dBm which translates to some 2 μV_{RMS} across a 50 Ω load.

Figure 5 shows the frequency spectrum of the EO pick-up's output acquired around the 39.992 MHz component which was the 922nd harmonic of the 43.375 kHz revolution frequency. The peak at the central frequency is surrounded on either side by two sharps peaks: at ±6 and ±8 kHz. These frequencies correspond to, respectively, 0.138 and 0.184 fractions of the revolution frequency:

$$\frac{6}{43.375} = 0.138 \qquad \frac{8}{43.375} = 0.184$$

The nominal horizontal and vertical betatron tunes in the SPS are $Q_h = 0.13$ and $Q_v = 0.18$. For position dependent sensors, these tunes constitute themselves as sidebands around the n-th revolution frequency harmonic [9]:

$$f_{Qn} = n \times f_{\text{rev}} \pm Q \times f_{\text{rev}}$$

ISBN: 978-3-95450-192-2 doi:10.18429/JACoW-IBIC2017-TUPCF23

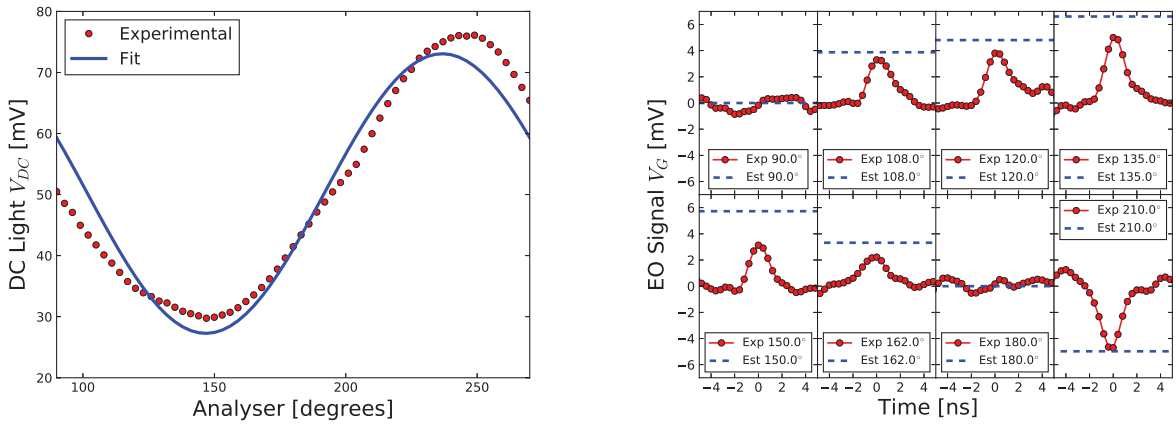

(a) (b)

Figure 4: Analyser polarization scan of pick-up zero (a) and EO Signal for different analyser positions (b).

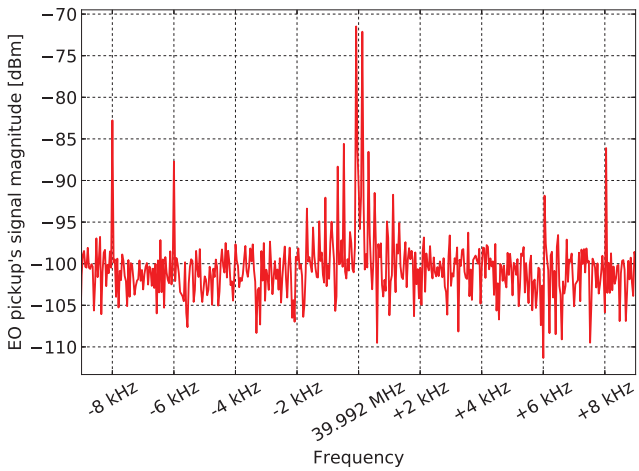

Figure 5: Frequency spectrum of the EO pick-up's signal around the 922nd harmonic of the SPS revolution frequency.

As the tunes in the SPS drift from their nominal values during the coasting beam operation, it is fair to conclude that the sideband peaks around the 922nd revolution frequency harmonic shown in Fig. 5 correspond to the vertical and horizontal SPS tunes during the measurements. This, in turn, proves that the EO pick-up is sensitive to the transverse beam position.

SUMMARY AND FUTURE WORK

The tests for the first two electro-optic pick-ups on the SPS have been presented in this paper. The signal observed from pick-up zero demonstrates a proof of concept that the electro-optic modulation induced by a passing proton bunch responds as expected from electromagnetic and analysic simulations. A modified pick-up design, including a beam facing electrode to shape the field, was found to enhance the signal by a factor ~8.

Even though the SNR with the preliminary system was low, indirect measurements of the vertical and horizontal betatron tunes were taken with a spectrum analyser, which demonstrate that the device is sensitive to transverse position. To further improve the signal it is necessary to refine the pickup design, such that the induced field strength E_{LNB} is increased to a magnitude similar to the E_{π} of the crystal. Two areas for future improvement include: modifying the electrode geometry to increase the field density; and lengthening the crystal. Simulations have shown that the synergy of both effects result in a significant signal enhancement.

ACKNOWLEDGEMENTS

We thank the CERN vacuum group, the CERN mechanical and materials engineering group, and the SPS operation team for their support. Work funded by UK STFC grant ST/N001583/1, JAI at Royal Holloway University of London and CERN.

REFERENCES

[1] Y. Miyahara, *NIM. Phys. Res.* A 588 (2008) 323–329.

[2] R. Steinhagen et al., "A Multiband-Instability-Monitor for High-Frequency intra-bunch Beam Diagnostics', TUBL3, Proc. of IBIC 2013, Oxford, UK.

[3] S. M. Gibson et al., "High frequency electro-optic beam position monitors for intra-bunch diagnostics at the LHC", WEDLA02, Proc. of IBIC 2015, Melbourne, Australia.

[4] A. Arteche et al., "Development of a prototype electro-optic beam position monitor at the CERN SPS", WEPG09, Proc. of IBIC 2016, Barcelona, Spain.

[5] P. Y. Darmedru, *"Conception mécanique d´un instrument de mesure de position d´un faisceau de particules"*, CERN EN report, Groupe 2A04, 2015.

[6] A. Yariv P. Yeh, *"Optical waves in crystals"*, pp. 241-243, pp. 282-283.

[7] R. S. Weis and T. K. Gaylord, *Appl. Phys.* A37 191-203 (1985).

[8] Computer Simulation Technology, *http://www.cst.com*

[9] M. Gasior and R. Jones, "The principle and first results of betatron tune measurement by direct diode detection", LHC Project Report 853, 2005, CERN, Geneva, Switzerland

ISBN: 978-3-95450-192-2 doi:10.18429/JACoW-IBIC2017-TUPCF26

STRIPLINE BEAM POSITION MONITOR FOR THE PAL-XFEL

C. Kim*, S. Lee, J. Hong, D. Shin, H. S. Kang, I. S. Ko
Pohang Accelerator Laboratory, POSTECH, Pohang 790-834, Korea

Abstract

The X-ray Free Electron Laser of the Pohang Accelerator Laboratory (PAL-XFEL) produces 0.1 nm wavelength X-ray with a femtoseconds pulse width by using the self-amplification of spontaneous emission (SASE). For the successful commissioning and the stable operation of the PAL-XFEL, Beam Position Monitors (BPMs) are most the impor-tant instrument among the various kinds of electron diagnos-tic tools. In this work, the BPM system for the PAL-XFEL is introduced. From the pickup to the electronics, details of the BPMs are presented.

INTRODUCTION

After upgrade of the Pohang Light Source (PLS-II), the Pohang Accelerator Laboratory (PAL) had rushed into the construction of the X-ray Free Electron Laser (PAL-XFEL) [1]. The project period was from 2011 to 2015 and the project budget was 400-million-dollar. In the PAL-XFEL, an electron beam with 200 pC charges can be generated from a photocathode RF gun with 60 Hz repetition rate and can be accelerated to 10 GeV energy by using a 780 m-long linear accelerator (linac). After the acceleration, electron beams pass through a 250 m-long undulator section to produce 0.1 nm-wavelength hard x-ray with the self-amplification of spontaneous emission (SASE) [2-4].

To send an electron beam from the gun to the linac end, transverse beam-position measurements along the linac are the most important issue in the beam diagnostics. The electron beam should pass through the center of the quadrupole magnet to keep the beam size and shape symmetrically and to make the orbit as close as possible to the ideal one. In this reason, a good performance of the Beam Position Monitor (BPM) is a critical element for the stable operation of the PAL-XFEL.

The electron beam of the PAL-XFEL has a small charge (20 pC ~ 200 pC) and a short bunch length (50 fs ~ 5 ps). In addition, In the PAL-XFEL, different BPM resolutions were required for the linac and the undulator section. 10 μm resolution is enough for the linac operation. On the other hand, 1 μm resolution is needed for the beam based alignment of the undulator section. Under these requirements, a stripline and a cavity BPMs were selected for the linac and undulator BPMs. In this paper, we introduce the stripline BPM of the PAL-XFEL. It includes the details of the pickup design, and measurement results of the resolution by using the electron beam. The hardware and the software of the BPM electronics are presented, as well.

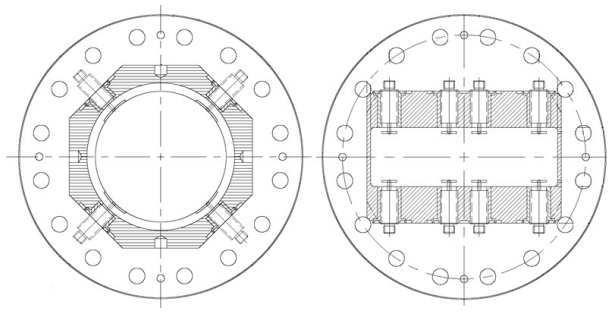

Figure 1: Transverse cross-sections of the circular (left) and the rectangular (right) chamber BPMs with CF 6 inch flanges.

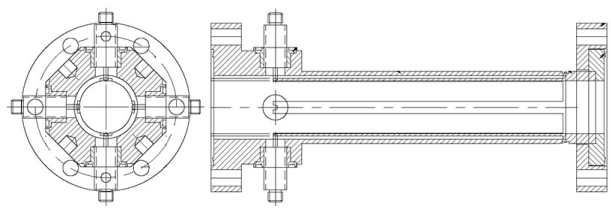

Figure 2: The transverse (left) and the longitudinal (right) cross-sections of the stripline BPM with CF 2.75 inch flanges.

PAL-XFEL STRIPLINE BPM

The stripline BPM in the linac can be separated into two groups. One is the circular chamber BPM and the other is the rectangular one for the bunch compressor. Most of the linac components have circular chambers as the aperture of the accelerating column. In the bunch compressor, however, the beam size can be increased to the horizontal direction because of the dispersion, and rectangular vacuum chambers were introduced. Even in the case of the rectangular vacuum chamber, CF flanges were used for the connection with other linac components. CF 2.75 inch, 4.5 inch, and 6 inch flanges were selected for the circular chamber, and CF 6 inch and 8 inch flanges were used for the rectangular one in the bunch compressor. Figure 1 shows transverse cross-sections of the circular and the rectangular chamber BPMs with CF 6 inch flanges.

BPMs with CF 2.75 inch flanges are widly distributed in the linac and its number is much bigger than that of BPMs with other types of flanges. A large number means that there are many requirements as well, and BPMs with CF 2.75 inch flanges have various lengths because of the limited space in the linac. Especially in the injector, lots of components were packed in a short space to minimize the emittance grow-up. Thus, the length of the BPM was reduced to a minimum

* chbkim@postech.ac.kr

ISBN: 978-3-95450-192-2 doi:10.18429/JACoW-IBIC2017-TUPCF26

Table 1: Summary of PAL-XFEL BPMs

Position	Flange (in)	Chamber	I.D. (mm)	Length (mm)	Angle (°)	Hard X	Soft X	Total
Linac	2.75	Circular	26.4	90	0	4	-	4
Linac	2.75	Circular	26.4	165	0	38	32	70
Linac	2.75	Circular	26.4	230	0	5	-	5
Linac	2.75	Circular	26.4	295	0	45	-	45
Linac	2.75	Circular	26.4	320	0	7	-	7
Linac	2.75	Circular	26.4	350	0	1	1	2
Linac	4.5	Circular	44	180	45	15	5	20
Dump	6	Circular	79	180	45	2	1	3
B.C.	6	Rectangular	100×31.6	180	-	2	1	3
B.C.	8	Rectangular	150×31.6	180	-	1	-	1
Total	-	-	-	-	-	120	40	160

value (90 mm). Where the space problem was released in the linac, 165 mm length BPMs with CF 2.75 inch flanges were installed.

In the linac, a quadrupole magnet can be found between two accelerating columns to make the FODO lattice, and the BPM was installed in the quadrupole magnet to save the space. This requirement imposed strong boundary conditions for the BPM geometry to the longitudinal and the transverse direction, simultaneously. To the longitudinal direction, the BPM should be long enough for the quadrupole magnet installation. At the same time, however, the total length of the BPM should be reduced down as much as possible for other components in the linac. BPM lengths with CF 2.75 inch flanges were decided to 230 mm, 295 mm, 320 mm, and 350 mm depend on quadrupole magnet lengths.

To the transverse direction, the outer diameter of the stripline BPM chamber was limited to less than 30 mm, owing to the quadrupole magnet pole. On the other hand, the inner diameter of the stripline was decided to 22 mm, considering of the 19 mm aperture of the S-band accelerating column. Thus, the stripline and the vacuum chamber should be placed in the space between 22 mm and 30 mm to the radial direction. For the decision of the width and the thickness of the stripline, the impedance matching was considered carefully, because the attenuation and the reflection of the beam signal can be increased when the impedance matching is poor. Figure 2 shows the transverse and the longitudinal cross-sections of the BPM with CF 2.75 inch flanges.

Circular chamber BPMs with CF 4.5 inch and 6 inch flanges and rectangular chamber BPMs with CF 6 inch and 8 inch flanges have the same length of 180 mm. These BPMs were installed in the energy spectrometer, the beam transport line (BTL), or the beam dump, and no space limitation was in there. Even though BPMs have various lengths to the longitudinal direction, the stripline length in them was all the same as 120 mm, except that of the 90 mm length BPM. Parameters of PAL-XFEL BPMs are summarized in Table 1.

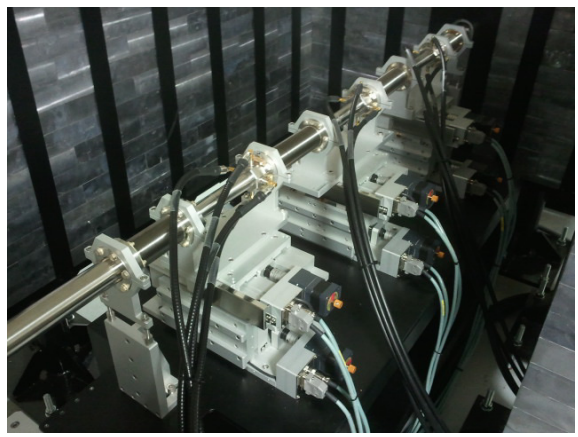

Figure 3: The BPM test stand in the injector test facility. Three BPMs have the same separation along the beam direction and each BPM is installed on a two-dimensional translation stage.

BPM PICKUP RESOLUTION

After fabrication of prototype BPMs, the resolution of the pickup was measured by using the electron beam. In 2012, the Injector Test Facility (ITF) was installed in the PAL to check the performance of the PAL-XFEL injector [5]. It consists of a photocathode RF gun, two accelerating columns, and diagnostic systems including BPMs, screen monitors for the beam size measurement, and a transverse deflection cavity for the bunch length measurement. In addition, at the end of the ITF, a BPM test stand was installed to check the performance of the BPM system as shown in Fig. 3.

In the BPM test stand, three BPMs were installed on two-dimensional stages so that BPMs can be moved to the horizontal and the vertical directions, independently. The distance between the first and the second BPMs are equal to the distance between the second and the third ones, and the BPM resolution was obtained by the three BPMs method. Figure 4 shows the measurement result of the BPM resolution. The horizontal and the vertical axis show the second BPM reading and the calculation result from the first and the third

ISBN: 978-3-95450-192-2 doi:10.18429/JACoW-IBIC2017-TUPCF26

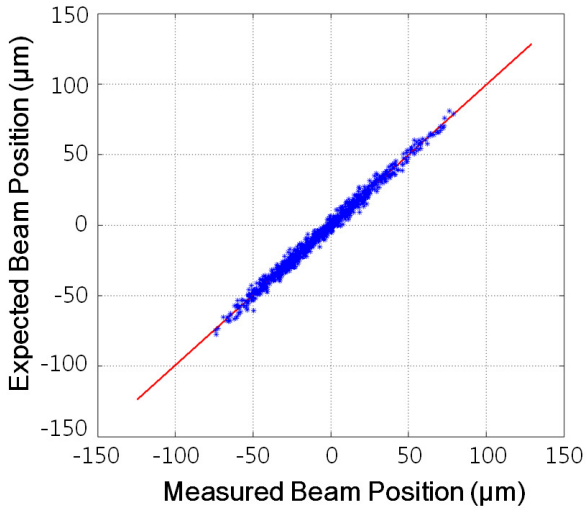

Figure 4: Measured beam positions of the second BPM versus expected beam positions from the first and the third BPM readings in the BPM test stand. The width of the blue dot distribution is the resolution of the BPM system and the measured resolution was less than 3 μm with 200 pC charge.

BPMs, respectively. The red line is an ideal case when second BPM reading is equal to the calculation result from the first and the third BPMs. In reality, however, measurement results (blue dots) are not equal to calculation results, and the width of the blue dot distribution gives us the resolution of the BPM system. Note that the electron beam trajectory may have fluctuations during the measurement, but they are measured in all BPMs, so that they can be canceled out. The measured resolution of the CF 2.75 inch flange BPM was less than 3 μm in both planes with the electron beam charge of 200 pC. The same method was applied to CF 4.5 inch and 6 inch flange cases, and the measured resolutions were 5 μm and 7 μm, respectively. These measurement results meet the requirement of the PAL-XFEL BPM resolution of less than 10 μm.

BPM ELECTRONICS

The BPM electronics calculates the beam position by using pickup signals and its performance is critical for the good resolution of the beam position measurement. Recently, the Stanford Linear Accelerator Center (SLAC) introduced a high-performance BPM electronics based on the μTCA technology [6]. The μTCA had been widely mentioned as a next-generation control platform, and the PAL decided to use it for the PAL-XFEL BPM system. Figure 5 shows a μTCA based BPM electronics from the SLAC. The μTCA BPM electronics consists of a crate (Elma), a central processing unit (CPU, Concurrent), a channel manager (NAT), a power module (Wiener), seven Analogue Digital Converter (ADC) (Struck, SIS8300) with a rear transition module (SLAC), and one PMC carrier card (Vadatech). In addition to that, the SLAC designed EVR fan-out module is used. The input frequency and the bandwidths are 300 MHz and 30 MHz,

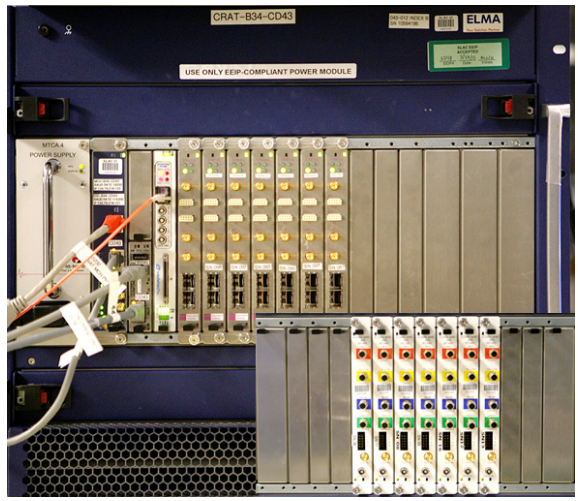

Figure 5: A picture of the μTCA BPM electronics (front and rear).

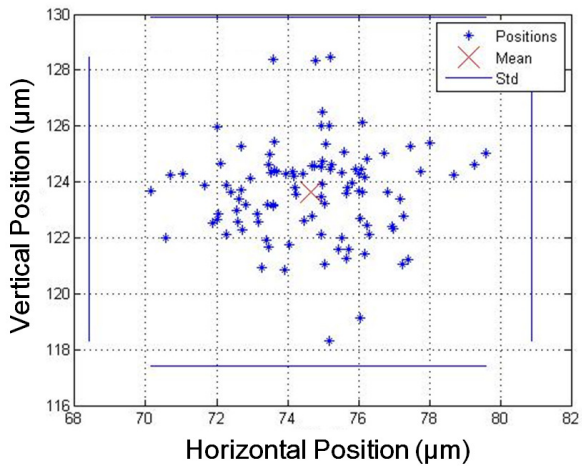

Figure 6: One hundreds points of the BPM reading when input signals had the same amplitude ratio. The width of distribution showed 1.9 μm and 1.7 μm resolution to the horizontal and the vertical directions, respectively.

respectively. The ADC has 250 MHz sampling speed and 16-bit resolution.

Figure 6 shows the resolution measurement result of the μTCA BPM electronics. A 300 MHz signal was generated from a signal generator and it passed through the 4-way divider. Divided signals were sent to the BPM electronics to calculate the beam position. In an ideal case, beam positions should be same in all measurements, because the amplitude ratio of 4 signals is same in every time. However, they have fluctuation in real measurements and the width of the Gaussian fitting curve gives us the electronics resolution. The measured resolution was 1.9 μm and 1.7 μm for the horizontal and the vertical directions, respectively.

The BPM electronics calculates the beam position after reading of four stripline signals. In this process, different equations are used for the calculation depend on BPM geometries. A different BPM geometry, however, is nothing

ISBN: 978-3-95450-192-2 doi:10.18429/JACoW-IBIC2017-TUPCF26

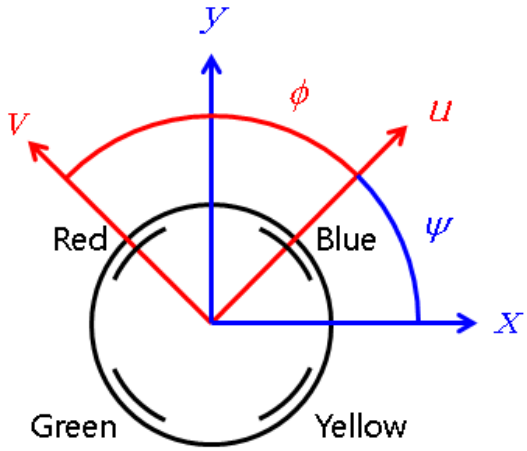

Figure 7: Coordinate systems for the beam position measurement.

but a coordinate transformation, and the μTCA electronics uses u and v coordinates for the beam position calculation as shown in Fig. 7. Note that u and v coordinates are exactly matched with the stripline positions inside a BPM. From u, v coordinates, one can get the beam position in x, y coordinates by first scaling of u, v which are given by

$$u = u \times u_{scale} + u_{offset} \tag{1}$$

$$v = v \times v_{scale} + v_{offset}. \tag{2}$$

Next, a rotation is applied by using

$$x_{raw} = a_{11} \times u + a_{12} \times v \tag{3}$$

$$y_{raw} = a_{21} \times u + a_{22} \times v \tag{4}$$

where $a_{11} = \sin(\psi - \phi)/\sin\psi$, $a_{12} = \sin\phi/\sin\psi$, $a_{21} = -\cos(\psi - \phi)/\sin\psi$, and $a_{22} = \cos\phi/\sin\psi$. Here, ψ is the rotation of u, v axes against x, y axes. ϕ is the angle between the stripline axes when conformally mapped into a circular domain. In the case of normal BPMs, ϕ is 90° but it may differ from that for rectangular BPMs which is used in the bunch compressors. Then scale and offset in the x and y domain are applied by

$$x = x_{raw} \times x_{scale} + x_{offset} \tag{5}$$

$$y = y_{raw} \times y_{scale} + y_{offset}. \tag{6}$$

Input parameters of the coordinate transformation can be changed in the control panel of the BPM electronics as shown in Fig. 8. In the control tab, x and y offset settings, x and y scale settings, the rotation and the axes angle settings can be applied. Scale setting of u, v, and u/v can be done in the calibration tab.

SUMMARY

For the PAL-XFEL linac, a stripline type BPM is selected for the BPM pickup considering the small charge and the short bunch length of the electron beam. The circular and the rectangular chamber were used for BPM bodies and the rectangular chamber was introduced in the bunch compressor. CF 2.75 inch, 4.5 inch, 6 inch and 8 inch flanges were selected for connections with other components and BPMs with CF 2.75 inch flanges were mainly used in the linac. In many cases, BPMs with CF 2.75 inch flanges were installed in the quadrupole magnet and the BPM geometry was strongly affected by it. A BPM electronics, which is based on μTCA, was installed under the collaboration with SLAC. The μTCA electronics showed a good performance, in addition to the advanced method for the beam position calculation.

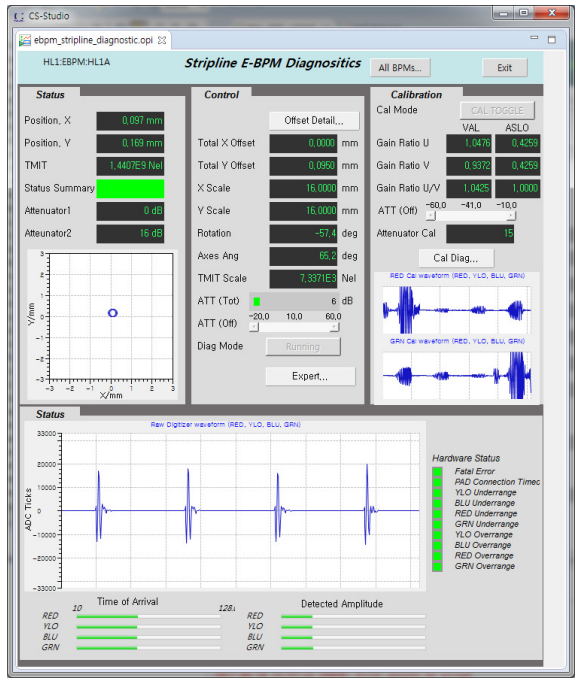

Figure 8: The control panel of a stripline BPM electronics.

ACKNOWLEDGMENT

Authors would like to give thanks to the collaborators at SLAC for the stripline BPM development.

REFERENCES

[1] H. S. Kang, K.-W Kim, I. S. Ko, in *Proc. IPAC'15*, p. 2439.

[2] A. M. Kondratenko and E. L. Saldin, *Part. Acc.*, vol. 10, p. 207, 1980.

[3] R. Bonifacio, C. Pellegrini, and L. Narducci, *Opt. Commun.*, vol. 50, p. 373, 1984.

[4] J. B. Murphy and C. Pellegrini, *Nucl. Instr. Meth. A*, vol. 237, p. 159, 1985.

[5] J. H. Han *et al.*, in *Proc. FEL'14*, p. 615.

[6] C. Xu *et al.*, in *Proc. IBIC'13*, p. 731.

ISBN: 978-3-95450-192-2 doi:10.18429/JACoW-IBIC2017-TUPWC01

THE APPLICATION OF DIRECT RF SAMPLING SYSTEM ON CAVITY BPM SIGNAL PROCESSING*

L. W. Lai, Y. B. Leng†, J. Chen, S. S. Cao, T. Shen, L. Y. Yu, R. X. Yuan, T. Wu, F. Z. Chen, J. Chen
SSRF, SINAP, Shanghai, China

Abstract

Cavity BPM signal processing system normally consists of two modules, first one is RF conditioning module(RF front end) to down convert the BPM signal to IF, second one is IF signal digitizer and digital signal processing module (DAQ) to calculate beam position and communicate with control system. The RF front end complicates the system and introduces noise. A direct RF sampling system has been constructed to process the cavity BPM signal, which structure is more concise and performance is better compared to the conventional system. The evaluation tests and an on-line RF DAQ system will be introduced in this paper.

INTRODUCTION

As the fourth-generation light source, FEL (free electron laser) is widely developed due to its outstanding performance. And in China, several FEL facilities have been built, such as DCLS (Dalian Coherent Light Source) and SXFEL (Shanghai Soft X-ray Free Electron Laser).

SXFEL is a high gain FEL. It is constructed at the bottom of 2016, now is under commissioning. The main parameters are listed in Table 1.

Table 1: SXFEL Parameters

Parameters	Value
Status	Commissioning
Wavelength	3-9 nm
Length	~300 m
FEL principle	HGHG, EEHG
Beam energy	0.84 GeV
Peak current	500 A
Normalized emittance	1 mm.mrad
Bunch length(FWHM)	1 ps
Harmonic number	30th

The improvement of FEL performance leads to higher requirement on beam-diagnose technology. Cavity beam position monitor (CBPM) is one of the important diagnostic component on FEL for its high resolution to dozens of nanometers. The output signal from CBPM is narrowband signal centralized at up to several GHz. For example, the central frequency of TM110 and TM010 signal of CBPM on SXFEL is 4.7 GHz [1], while LCLS is 11.424 GHz. This high frequency signal is hard to be sampled and processed directly limited by electronic technology. A traditional method is to down convert the RF signal to IF signal (MHz) firstly, so that the following ADC and signal processing module (data acquisition system, DAQ) can deal with the signal.

Figure 1 is the block diagram of CBPM signal processing system on SXFEL. The front end consists of preamplifier in tunnel, local oscillator (LO), mixer, filters, et al. CBPM output signal is down converted to about 500 MHz after the front end. DAQ system is an in-house designed digital beam position processor (DBPM), which central frequency is 500 MHz, four channels 16 bits ADC sampling at 119 MHz [2, 3].

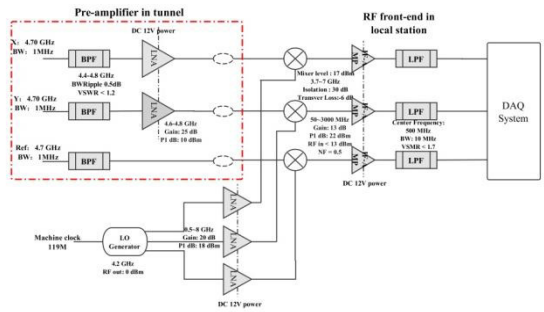

Figure 1: CBPM signal processing system on SXFEL.

This structure not only increase the costs, large numbers of RF components also make the system complex and fragile, and the components introduced extra noise will degrade the system performance. Considering this, the ideal BPM read-out electronics should contain no RF front-end [4, 5]. But this vision is infeasible in most cases, because the CBPM output signal frequency always out of the bandwidth range of most ADC. Fortunately, current electronics already enables this "ideal electronics" (6 GHz bandwidth oscilloscope) on the C band Cavity BPM system on SXFEL (4.7 GHz).

BEAM TESTS ON SXFEL

Two bunch arrival time measurement (BAM) cavities have been installed at the injection section and accelerator section to evaluate the BAM performance on SXFEL. The BAM monitor consists of two reference cavities. The central frequency of the two cavities respectively is designed to 4720 MHz and 4680 MHz. The output signal of the reference cavities can also be used to measure the bunch charge [6]. Then the BAM system can be used to evaluate the system performance by measuring the bunch charge.

RF DAQ Test

Figure 2 is the system diagram of RF direct sampling test. It consists of two BAMs in tunnel (IN-BAM01 at

*Supported by The National Science Foundation of China (Grant No.11375255, 11575282); The National Key Research and Development Program of China (Grant No. 2016YFA0401990, 2016YFA0401903).
† lengyongbin@sinap.ac.cn

ISBN: 978-3-95450-192-2 doi:10.18429/JACoW-IBIC2017-TUPWC01

injection section and LA-BAM01 at LINAC section), band-pass filters (BPF) to reject RF interference signal, a 6 GHz bandwidth oscilloscope Tektronix DPO70604. Figure 3 shows the picture of the installed BAM and the ICT that used for calibration.

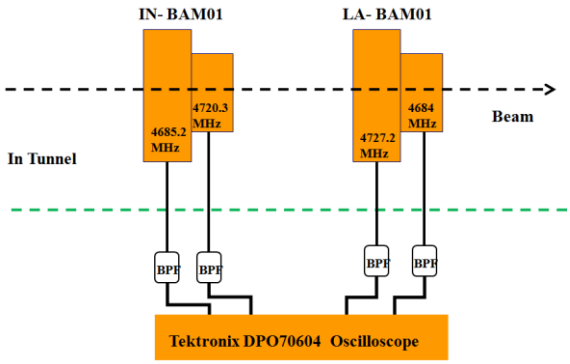

Figure 2: System diagram of RF direct sampling test.

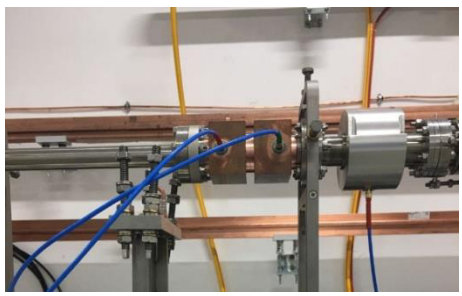

Figure 3: The installed BAM.

The DAQ is a high performance oscilloscope Tektronix DPO70604, which is 4 channels 6 GHz bandwidth and sampling rate up to 25 GHz. A band pass filter (BPF) is used to eliminate the affection of RF signal. The bunch charge is get from the peak value of calculated FFT amplitude, and calibrated with ICT.

The relative charge resolution of IN-BAM01 and LA-BAM01 were shown in Fig. 4 and Fig. 5. The results show that the relative resolutions of the two monitors are better than 0.3%.

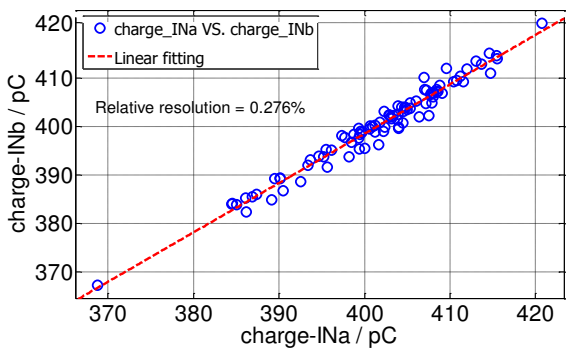

Figure 4: Resolution of direct sampling IN-BAM01.

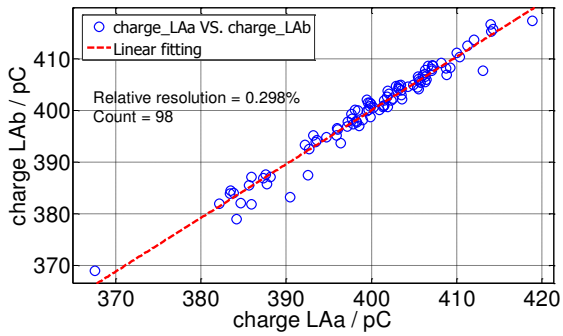

Figure 5: Resolution of direct sampling LA-BAM01.

Traditional DAQ test

At the same time, a traditional down-converting DAQ system has been constructed for comparison. Except for BPF and oscilloscope, the system contains LO generator which can generate a sinusoidal signal with a frequency of 4706 MHz and an amplitude of 17 dBm, a mixer to down-convert the RF signal by LO signal, a LPF removes the high frequency signal and out of band noise. The system diagram can be seen in Fig. 6, and Fig. 7 is the field picture of the system.

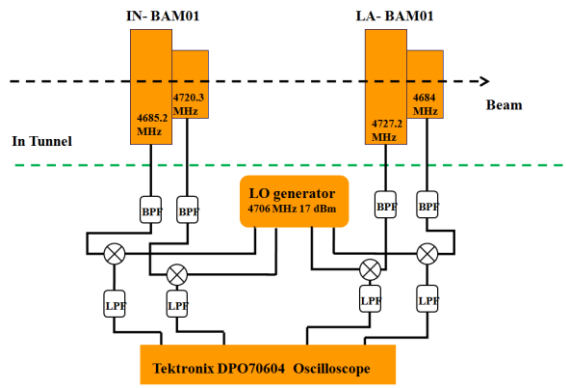

Figure 6: System diagram of traditional down-converting DAQ system.

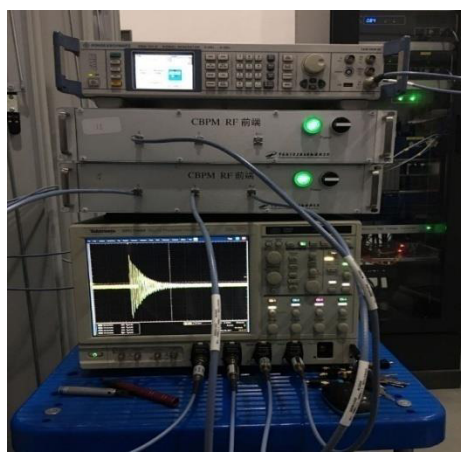

Figure 7: The field picture of experiment platform.

ISBN: 978-3-95450-192-2 doi:10.18429/JACoW-IBIC2017-TUPWC01

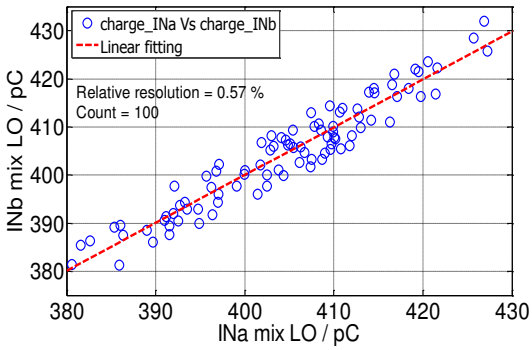

Figure 8: Resolution of down-convert sampling IN-BAM01.

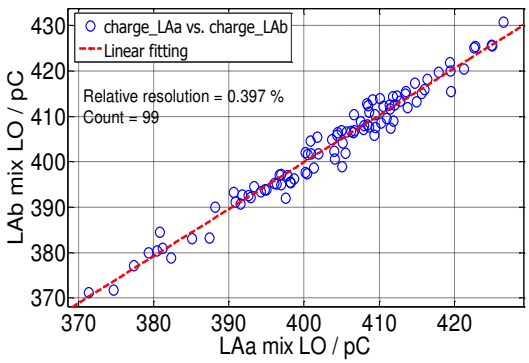

Figure 9: Resolution of down-convert sampling LA-BAM01.

The test results in Fig. 8 and Fig. 9 show that relative resolution of the two monitors is about 0.6% and 0.4% respectively. Obviously the performance is worse than direction sampling DAQ system. The reason is the down-converting components introduced noise. The relative resolution is about 0.3% while the ADC of DPO70604 is 8 bits, we can expect it should be better than 0.1% after applying 12 bits ADC.

NEXT STEP: ON-LINE RF DAQ SYSTEM

With the rapid development of analog-to-digital conversion technology, an on-line RF direct sampling equipment with high bits and high bandwidth is not out of reach. Figure 10 is a demo board EV12AD500A from company E2V. It contains a dual channel 12 bits ADC, which input bandwidth is ultra-high to 5.2 GHz and the sampling rate up to 1.5 GSps. Figure 11 is the corresponding connectivity board VC709 from XILINX. It contains a Virtex-7 FPGA XC7VX690T, dual DDR3 small outline dual-inline memory module (SODIMM) memories, an 8-lane PCI Express interface, etc. Combing with the two boards, an on-line direct RF sampling DAQ system can be built to process CBPM signal. The system is not ready yet, the progress will be introduced in the future.

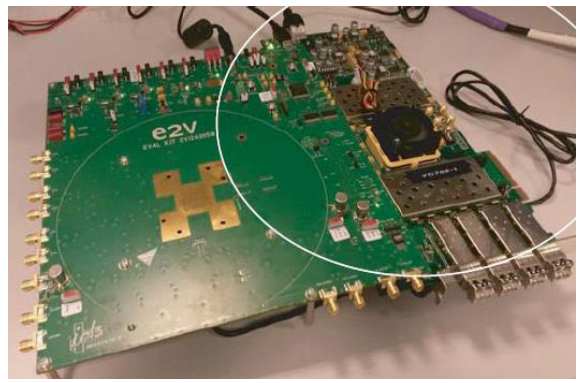

Figure 10: ADC demo board EV12AD500A.

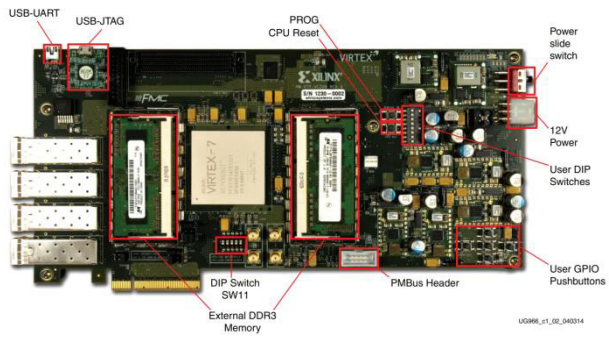

Figure 11: XILINX VC709 FPGA board.

CONCLUSION

The tests shown that the relative resolution of direct RF sampling DAQ is obviously better than traditional down-converting structure. In the next stage, an on-line RF DAQ system will be constructed with commercial boards.

REFERENCES

[1] J. Chen *et al.*, "Beam Test Results of High Q CBPM prototype for SXFEL", *Nuclear Science and Techniques.*, vol. 28, pp.51(1-8), 2017.

[2] L.W. Lai *et al.*, "Batch application of digital BPM processors from the SINAP". in *Proc. IBIC'16*, Barcelona, Spain, Sep. 2016, paper WEPG17, pp. 658-660.

[3] L.W. Lai *et al.*, "Design and performance of digital BPM processor for DCLS and SXFEL". in *Proc. Ipac'17*, Copenhagen, Denmark, May. 2017, paper WEPG17, pp. 658-660.

[4] M. Wendt *et al.*, "Direct (Under) sample vs. analog down conversion for BPM electronics". in *Proc. IBIC'14*, Monterey, CA, USA, Sep. 2014, paper MOPAB092, pp. 338-340.

[5] M. Stadler *et al.*, "Low-Q cavity BPM electronics for E-XFEL, FLASH-II and Swiss-FEL". in *Proc. IBIC'14*, Monterey, CA, USA, Sep. 2014, paper WEPD12, pp. 670-674.

[6] J. Chen *et al.*, "Beam charge measurement using the method of double-cavity mixing". presented at IBIC'17, Michigan, USA, Aug. 2017, paper WEPCF01, this conference.

ISBN: 978-3-95450-192-2 doi:10.18429/JACoW-IBIC2017-TUPWC02

THREE-DIMENSIONAL BUNCH-BY-BUNCH POSITION MEASUREMENT AT SSRF*

Y. M. Zhou†, L.W. Duan, Y. B. Leng[1], N. Zhang[1]
Shanghai Institute of Applied Physics, Chinese Academy of Sciences, Shanghai, China
[1]also at Shanghai Synchrotron Radiation Facility, Chinese Academy of Sciences, Shanghai, China

Abstract

Measurement of the bunch-by-bunch particle beam position related to dynamic instability is a useful input to accelerator optimization. And the bunch-by-bunch information has been contained in the BPM signals, including bunch charge, transverse position and longitudinal phase information. This paper reports a 3D beam position monitor system based on a high speed digital oscilloscope, which has been used to capture three-dimensional position information during the injection transient at the Shanghai Synchrotron Radiation Facility. With this information the traces of stored bunch and refilled bunch, and the mismatch of energy, transverse position and longitudinal phase between them can be precisely retrieved. The progress of this work and several particular experimental results will be discussed in this paper. The details of data processing method so-called software re-sampling technique will be discussed as well.

INTRODUCTION

In the operation of the third generation light source, the beam instability will be caused by rail noise. The beam instability, such as beam position shift, beam tune drift and beam wake field effect, will affect the effective operation of the accelerator. In the SSRF (Shanghai synchrotron radiation facility), turn-by-turn beam position measurement has been realized and the resolution has reached 2 μm [1]. In order to improve the resolution, it is important to measure the beam position bunch by bunch. At the same time, higher resolution is essential for the study of beam position shift and the mismatch of energy during the injection transient process. In this paper, the traces of the stored bunch and refilled bunch can be achieved. And the three-dimensional beam motion can be constructed according to the three-dimensional position information. The beam position can be obtained from the amplitude difference among four signals extracted by the button electrode. The difference-over-sum method is usually used in the beam transverse position measurement. However, in the longitudinal phase measurement, the bunch phase is detected from the difference between a beam pulse and a reference frequency signal. In this paper, the longitudinal phase is calculated by using the zero-crossing fitting method. Since the original signal of the storage ring button electrode already contains the transverse position and longitudinal phase information, the original signal can be extracted directly by a high sampling rate oscilloscope. The three-dimensional bunch-by-bunch position information was calculated by the off-line data processing. Shanghai light source as the third generation synchrotron radiation source, the storage ring energy reached 3.5 GeV with 432 m in circumference. There are totally 140 BPMs (Beam Position Monitor) around the storage ring. For SSRF, a practical filling pattern is a 500 −bunch train filled in the storage ring, leaves a 220 bucket empty gap. The harmonic number is 720 and the RF frequency is 499.654 MHz.

PRINCIPLE

Typical BPMs used in the storage ring are button-type electrode and strip-type electrode. When the beam passes through the button electrode, the electric quantity obtained by each electrode is closely related to the distance from the surface of the button electrode to the beam due to the electrostatic induction. The three-dimensional position information of the beam can be calculated from the original signal outputted from the electrode. Figure 1 shows the cross section of the button electrode used in the Shanghai light source storage ring. For the non-center bunch response, the amount of induced charge on the electrode is different when the bunch whose current is $I_b(t)$ passes through the non-center position of the button electrode. As shown in Fig. 1, the bunch is in the (δ, θ) position, the radius of the vacuum chamber is b, and the distance from the electrode to the vacuum chamber is a.

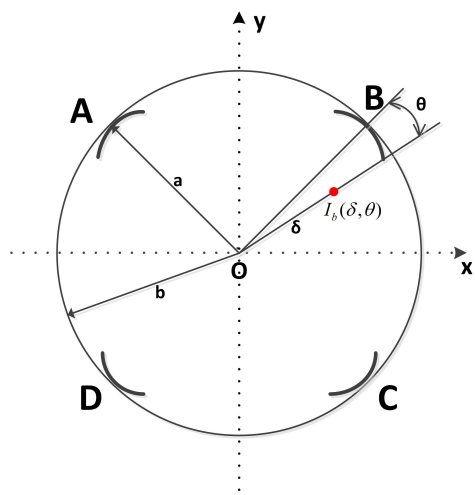

Figure 1: Cross section of button-type position monitor.

In the following analysis [2], a Gaussian distribution of the beam is used. Considering N particles of charge e in a bunch of the half width σ, the induced voltage generated by

* Work supported by National Science Foundation of China (No. 11575282, No. 11375255, No. 11305253)
† zhouyimei@sinap.ac.cn

ISBN: 978-3-95450-192-2 doi:10.18429/JACoW-IBIC2017-TUPWC02

the bunch on the electrode is:

$$V_b(t) = \frac{\pi a^2 Z}{b\beta c} I_n 2 f_0 A sin(\omega_s t + \phi) \times \times \exp^{in\omega_0(t+Acos(\omega_s t+\phi))} F(\delta,\theta), \quad (1)$$

with

$$I_n = I_0 \exp^{-\frac{n^2\omega_0^2\sigma^2}{2}}, \quad (2)$$

$$I_0(t) = \frac{eN}{\sqrt{2\pi}\sigma} \exp(-\frac{t^2}{2\sigma}). \quad (3)$$

And the position information is:

$$F(\delta,\theta) = \frac{a^2-\delta^2}{a^2+\delta^2-2a\delta cos\theta}, \quad (4)$$

$$\delta = \sqrt{x^2+y^2}, \quad (5)$$

$$\theta_{A,B,C,D} = \frac{m\pi}{4} - tan^{-1}(\frac{y}{x})(m = 3, 1, 7, 5). \quad (6)$$

When the geometrical shape of the probe is determined, the electrode induced voltage is related to the two parts of information. One is the beam intensity I_0 and the bunch length σ, and the other part is the transverse position F(δ,θ) and longitudinal phase ϕ of the bunch through the button electrode. The original signal of the button electrode can be extracted by using the bunch-by-bunch 3D beam position monitor system based on a broadband oscilloscope, which contains information such as the bunch charge, transverse position and longitudinal phase. Bunch charge can be derived by measuring peak voltage of sum signal, which has been measured in the Shanghai light source [3]. The equivalent beam position is obtained from the amplitude difference among four signals by difference-over-sum processing (Δ/Σ). In the transverse position measurement, the result of the measurement is that the stored bunch mixed with the refilled bunch. It is necessary to separate the refilled bunch from the stored bunch by off-line data processing. It is known that the measured sum signal is:

$$X_m = k_x \frac{\Delta m}{\Sigma m} = k_x(\frac{\Delta s + \Delta r}{\Sigma s + \Sigma r}), \quad (7)$$

where k_x is the compensation coefficient. Δs, Σs are the difference signal and sum signal of the stored bunch, and Δr, Σr are the difference signal and sum signal of the refilled bunch. Then the refilled signal from the measured signal can be got by:

$$X_r = \frac{\Sigma s}{\Sigma r}(X_m(1+\frac{\Sigma r}{\Sigma s}) - X_s). \quad (8)$$

As the beam signal is related to the amount of charge, the type can be simplified as:

$$X_r = \frac{Q_s}{Q_r}(X_m(1+\frac{Q_r}{Q_s}) - X_s). \quad (9)$$

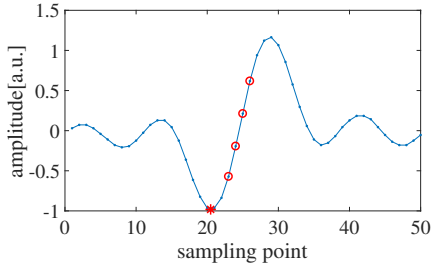

Figure 2: Sampling points in the position measurement.

In order to improve the accuracy of beam position measurement, this paper measured the negative peak of the button electrode signal to obtain the beam transverse position. The sampling points is shown in Fig. 2 (red star).

Since the RF frequency is 499.654 MHz and the sampling rate of the oscilloscope is 25 GHz, it cannot obtain the peak voltage directly from the measurement signal. A so-called software re-sampling technique based on cubic spline interpolation algorithm has been performed in the SSRF [4]. It is necessary to obtain the exact time interval $T_r f$ between two bunches. A FFT algorithm was used to obtain the RF frequency. To improve the measurement precision, zero-padding method was used to extended the data length to the integer powers of two. Because the length of the signal cable from four electrodes to the oscilloscope is not exactly equal and the sampling clock of each channel is not synchronous, the first peak point was chosen as the starting point for each channel. Then the bunch-by-bunch BPM signal could be obtained from the raw waveform data with the sampling interval $T_r f$. At the same time, this method can be also used in the longitudinal phase measurement. To improve the accuracy of phase measurement, four sampling points at the zero-crossing point is chosen for phase calculation. By linear fitting, the bunch phase can be obtained by the intercept with the timeline, as shown in Fig. 2 (red circle).

EXPERIMENT

The experiment is performed during the injection process. Particles will generate an obvious oscillation in the injection transient process. It is important for the optimization of our accelerator and the study on the injection process if the three-dimensional position displacements can be observed. In the experiment, three-dimensional displacement results have been obtained. Figure 3(upper) shows the horizontal displacement, it can be seen that a small oscillation in the stored bunch and the refilled bunch oscillate around the stored bunch. Figure 3(lower) shows the vertical displacement, compared with the horizontal displacement, the vertical oscillation amplitude is much smaller and the oscillation of the stored bunch is almost zero.

At the same time, the longitudinal phase shift also can be detected by the 3D position monitor system. From Fig. 4, a regular oscillation can be achieved. The longitudinal position displacement is 200 ps in the storage ring. And it is not symmetrical relative to the stored bunch. If we magnify

ISBN: 978-3-95450-192-2 doi:10.18429/JACoW-IBIC2017-TUPWC02

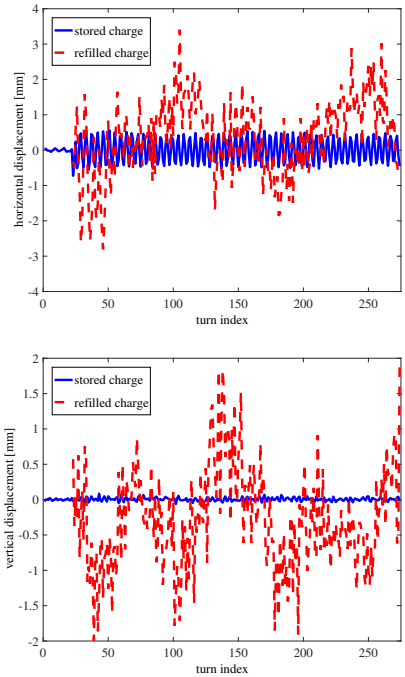

Figure 3: Transverse displacement of the injected bunch. Upper is the horizontal displacement and lower is the vertical displacement.

the picture, as shown in Fig. 5, the details in longitudinal displacement of the stored bunch can be observed. The stored bunch still make a small range oscillation and the peak displacement is just several picoseconds.

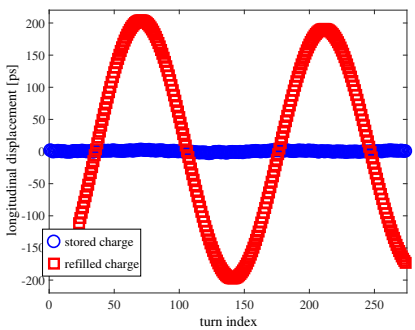

Figure 4: Longitudinal oscillation displacement of the injected bunch.

On the other hand, the beam tune can be also measured by the frequency spectrum of the injected bunch. From Fig. 6, it shows that the transverse tune is (0.22 , 0.30) and the longitudinal tune is 0.007

CONCLUSIONS

A bunch-by-bunch 3D position monitor system has been developed in the SSRF. Three-dimensional position information can be measured directly from the button electrodes.The refilled bunches have been separated from the stored bunches.

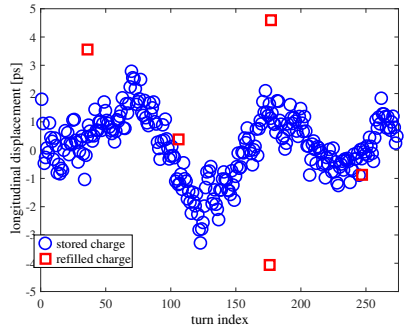

Figure 5: Details in longitudinal displacement of the stored bunch.

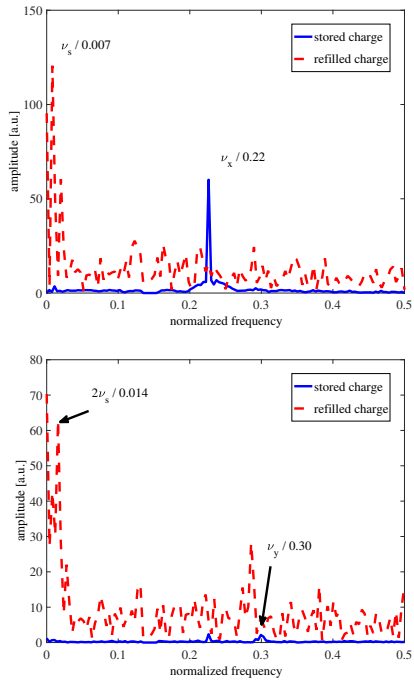

Figure 6: Frequency spectrum of the injected bunch.

During the transient injection process, the refilled bunches oscillated around the stored bunches. The transverse displacement of the refilled bunches is about 2 mm and the longitudinal displacement is 200 ps.

REFERENCES

[1] Y. B. Leng *et al.*, "The development of a new digital bpm processor", *Nuclear Techniques*, 34(5):326–330, 2011.

[2] R. E. Shafer, "Beam position monitoring", *AIP conference proceedings*, 249(1):601–636, 1992.

[3] Y. B. Leng, Y. B. Yan, L. Y. Yu, and W. M. Zhou; "Data Acquisition for SSRF Ring Bunch Charge Monitor", in *Proc. IPAC'10*, pages 1047–1049, Kyoto, Japan, 2010.

[4] Y. Yang, Y. B. Leng, Y. B. Yan, and N. Zhang, "Bunch-by-bunch Beam Position and Charge Monitor Based on Broadband Scope in SSRF", in *Proc. IPAC'13*, pages 595–597, Shanghai, China, 2013.

ISBN: 978-3-95450-192-2 doi:10.18429/JACoW-IBIC2017-TUPWC03

DESIGN OF A NEW TYPE OF BEAM CHARGE MONITOR BASED BUNCH BY BUNCH DAQ SYSTEM *

F. Z. Chen , L. W. Lai†, Y. B. Yan, Y. B. Leng
SSRF, SINAP, Shanghai, China

Abstract

Beam current is one of the fundamental parameters to be measured in storage ring. The Shanghai Synchrotron Radiation Facility (SSRF), a third generation light source with the RF frequency of 499.68 MHz, used adopt commercial product to monitor beam charge. However, the maintain and upgrade is not always straightforward. Thus, a new type of beam charge monitor (BCM) based on beam positon monitor (BPM) sum signals has been developed for the online beam current measurement on SSRF storage ring. This system has been convincingly validated by mathematical analysis, and has been demonstrated with beam experiments during machine study time.

INTRODUCTION

We used to employ the commercially BCM manufactured by Acqiris, however, the maintain and upgrade is not always straightforward. In the electron accelerator, the beam position detector can be used to measure beam charge. Since BPM sum signals provide a new type of solution of beam charge monitor in SSRF, and there're 140 BPMs in the storage ring, we choose the one meet the criteria for this particular usage under particular measurement [1]. For data acquisition system, obviously, the higher the sampling rate, the more precise the original signal reconstruction. However, consider of the sampling rate measurement accuracy and equipment cost, we choose sample rate at RF frequency.

The DBPM processor system played a vital role in beam diagnostics system. The BI group of SSRF developed a new type of DBPM processor to handle the BPM data acquisitions and the position calculations. The BPM processor carry FPGA and ARM, available for further application development. The processor also could use external trigger and external clock. Under the circumstances, we design a new type of BCM based on BPM sum signals using the DBPM processor, namely, a DBPM-BCM. .We design a new type of BCM based on BPM sum signals using a new type of BCM

The DBPM-BCM consist of three parts: pick up, front-end electronics and the data acquisition. In order to monitor beam charge bunch by bunch, consider of DBPM external clock sampling rate, we divide the storage ring bunches into four parts. Using delay line to generate RF frequency interval, make the sum signal reach 4 channels at different interval, in our system which is a 2 ns interval one after one. This design of signal transmission guarantee each channel acquire a different quarter of bunch cluster in storage ring. Adjusting the sampling clock phase to acquire signals peak value is the core requirement of the system, and has a profound effect on the measurement accuracy and reliability. Therefore, the sampling phase must be cautious adjust. Another one of the key challenges of the system is to find a suitable sample frequency, and delay the signals to ensure every single bunch in the storage ring should be captured. The transmission phase also needs to be cautiously adjusted.

The main reason why the bunch-by-bunch separation sample method chosen is that independent test can extract the irrelevant four bunch clusters in storage ring. This feature assures every single bunch in the storage ring has been monitored. The total design is neat and obvious. That makes the method easy to be implemented and work online.

DESIGN AND REALIZATION OF THE SYSTEM

System Requirements Analysis

Take full use of the existing beam diagnostic equipment in the storage ring, establish a set of bunch-by-bunch BCM data acquisition system (DAQ) system, given the current intensity information of each bunch, the measurement accuracy should meet the top-up actual operational indicators.

DBPM has a 16-bit resolution, DC-700 MHz bandwidth baseband data acquisition card, which meets our present needs. The electron accelerator could provide accuracy RF frequency demultiplication, and in our system it should be a quarter of RF frequency used for external sample clock.

The Principle of BCM

According to model building and formula proving, the relationship between the average beam current and four electrode sum signals can be expressed by Eq. (1):

$$I_{avg} = \frac{k(x,y)*V_{sum}}{Z} \quad (1)$$

Where the Z is the equivalent impedance constitute detection electrode and the signal transmission network, k(x,y) is the current intensity correction factor dependent on beam position, V_{sum} is detect electrode output sum signal voltage [2]. Using the button electrode BPM and the sum signal pulse measure pulse current intensity. The equation also suit for beam charge monitor.

When the ADC sample rate could reach RF frequency, we can realize bunch-by-bunch beam charge monitor. The criteria are the following: use four channels of DBPM processor to acquire sum signals, each channel has a 2 ns

*Work supported by National Natural Science Foundation of China (No.11575282No.11305253)
†lailongwei@sinap.ac.cn

ISBN: 978-3-95450-192-2 doi:10.18429/JACoW-IBIC2017-TUPWC03

delay compare to ahead channel, and we set the external sample clock a quarter of RF frequency.

A central element of the system is capturing the peak phase signal. In order to realize the high precision measurement of bunch-by-bunch beam charge monitor, we design the system based on accuracy phase positon regulate.

The architecture of the system is described below. A high-level overview is provided of the hardware, embedded software and control system (Fig. 1).

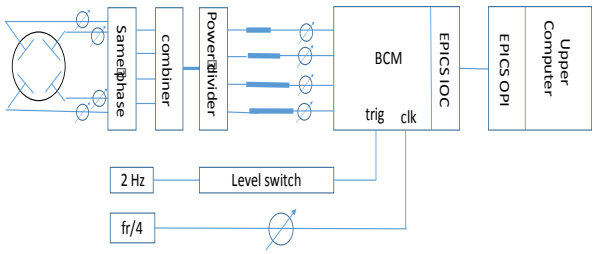

Figure 1: The overview architecture of BCW test system.

The beam charge monitor in the SSRF storage ring represent this new design and satisfy the high precision measurement of the top-up current injection mode.

Hardware Design

Four channels of RF signal extract from the button BPM electrode, signals transmit to synthesizer through the coaxial cable, using adjustable phase shifter to keep four channel signals in-phase, the combiner take signals four in one. Then, using power divider divide the sum signal into four channels. The delay line and phase shifter control the signals reach time difference.

The phase control system consists of three main components: signal extract port need phase shifters to make sure four channels in-phase; sum signal divide to four channel to provide four bunch clusters, and the phase shifter works on external clock to help sample at signals peak value.

The design takes fully use of the hardware facility of SSRF and turns out to be a cost-effective solution.

ADC sampling clock from the storage ring high frequency clock, to ensure that ADC sample are synchronization with bunch-by-bunch data to avoid phase slide.

Software Design

The architecture of the entire system software is based on the EPICS and Linux environments. Upper software control data acquisition card. The DBPM-BCM embedded EPICS IOCs, running Linux operation system. The soft IOC has good real-time performance, portability and extensibility. DBPM-BCM IOC collects data from four channels. The EDM panel consists of two main parts: one is display windows showing readouts acquired through EPICS IOCs, and the other is parameter setting. We set the sample external clock and external trigger using the EDM panel.

MATLAB gets PVs from DBPM-BCW processor via labCA, which is an EPICS channel access interface for MATLAB developed by SLAC. We designed a dedicated algorithm to realize four channels split joint.

LABORATORY TEST

Test Platform

The test system has already set up in the laboratory as the photo shown below. The platform followed the principal of compact. Both of the sum signals and timing signals come from accelarator provide by a equipment cabinet.

Figure 2: Photo of platform in laboratory.

Test Results

The test system get four channels raw ADC data simultaneously from the DBPM processor, each channel get a train of storage bunch cluster. Figure 3 below is the independence test, which could prove four channels acquire a different bunch cluster. Considering the limitation of bandwidth and crosstalk, the independence test showing the different channels are not completely irrelevant variables.

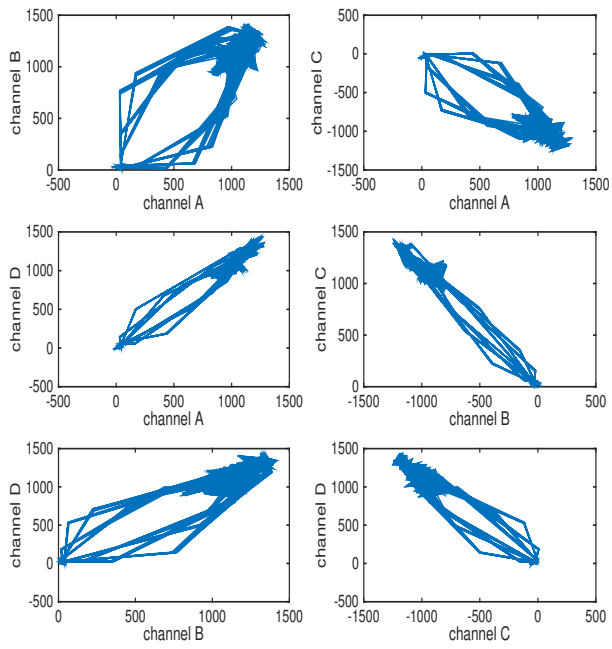

Figure 3: Independence test of each channel.

We could optimize the system in the future. Therefore, the four channels could split joint the complete storage beam charge, which is also shown below in Fig. 4.

ISBN: 978-3-95450-192-2 doi:10.18429/JACoW-IBIC2017-TUPWC03

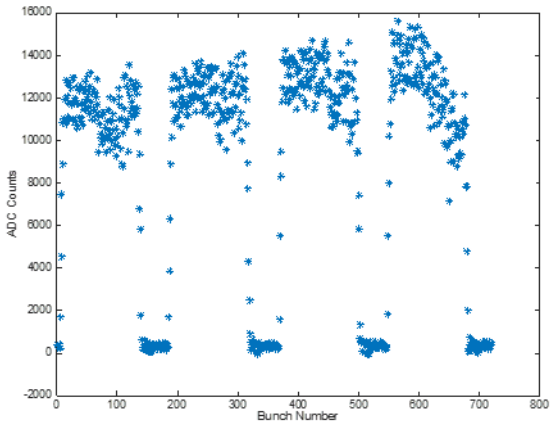

Figure 4: BCM of the storage ring.

Calibration Algorithm for Bunch-by-Bunch Current Intensity

The sampled value obtained by ADC sampling is not real bunch-by-bunch current intensity, but there is a certain proportional relationship between the value and the real current intensity. In addition, the current intensity of the bunch could be obtained by calibration. The calibration factor K can be calculated using the following formula:

$$K = \frac{I_{DCCT}}{(f_{rf}/720)} / sum(Q) \quad (2)$$

I_{DCCT} is the mean current of the circulating beam, measured by parametric DC current transformer (DCCT), which measures average beam current, but not capable of measuring the charge of an individual bunch. The frequency of RF is also read by EPICS PVs in real time. So the numerator is the total current intensity in the storage ring. The denominator is the sum of the signals sampled by the ADC, where the Q is the ADC readouts. In the process, each time the calculation requires the reading of the DCCT to calculate the new calibration factor. Current intensity calibration coefficient is difficult to accurately calculate or calibrate off-line, must through the beam experiment and other current intensity detector (such as DCCT) for on-line calibration.

CONCLUSION AND OUTLOOK

The BPM sum signal has been used as an alternative to beam charge monitor in SSRF storage ring. The paper has shown the DBPM-BCW bunch-by-bunch DAQ test system in terms of hardware, firmware and software. Its complete integration into the EPICS based control system allows other extension applications, which could be further development.

The current can be simply the useful quantity in itself, but often it is an intermediary for measuring beam lifetime or for machine safety systems in storage ring. Because of the flexibility of this system, we can develop other applications based on FPGA, such as the beam lifetime analysis in the electron storage ring, providing more details of beam charge measurements during operation. We plan one of the upgrades is beam lifetime calculation application.

Finally, this system still exist many problems, such as the phase slide, which could be arisen by signal transmission and other kinds of random error. In terms of resolution and stability, there is a demand to improve the performance and optimize the algorithm. We can use FPGA algorithm to realize waveform reconstruction, in that way, the system could be more stabilization.

ACKNOWLEDGEMENT

The authors would like to thank everyone who contributed to the test system through discussions and suggestions.

REFERENCES

[1] Z. C. Chen *et al.*, "BPM selection for beam current monitoring in SSRF", in *Proc. IBIC'12*, Tsukuba, Japan, May 2012, pp. 341-343.

[2] Y. B. Leng, Y. B. Yan, and W. M. Zhou *et al.*, "Precise Beam Current Measurement for Storage Ring Using Beam Position Monitor", *High Power Laser and Particle Beams*, vol. 22, pg. 2973–2978, 2010.

ISBN: 978-3-95450-192-2 doi:10.18429/JACoW-IBIC2017-TUPWC04

EXPERIMENTAL DAMPING SYSTEM WITH A FERRITE LOADED KICKER FOR THE ISIS PROTON SYNCHROTRON

A. Pertica*, D. W. Posthuma de Boer, ISIS, STFC, Rutherford Appleton Laboratory, Oxfordshire, OX11 0QX, UK

Abstract

The ISIS neutron and muon source, located in the UK, consists of a H^- linear accelerator, a rapid cycling proton synchrotron and extraction lines towards two target stations. Transverse beam instabilities are one of the major factors limiting the intensity of the proton beam. In order to mitigate these instabilities an experimental damping system is being developed for the ISIS synchrotron. This system uses a split electrode beam position monitor (BPM) as a pickup and a ferrite loaded kicker as a damper. This kicker is ordinarily used to excite the beam with a fast rise time pulse for tune measurements. This paper describes the utilization of this device within a fast feedback system, using the continuous waveform provided by a split electrode BPM, which is processed by an FPGA board.

INTRODUCTION

The ISIS Synchrotron

The ISIS synchrotron accelerates two proton bunches, with a total of 3×10^{13} protons, from 70 MeV to 800 MeV at a repetition rate of 50 Hz, delivering a mean beam power of 0.2 MW to two tungsten targets. Protons are accelerated over 10 ms by first and second harmonic RF cavities, with a fundamental frequency sweep of 1.3 MHz to 3.1 MHz.

Instabilities at ISIS

A coherent instability has been observed at ISIS, causing vertical emittance growth around 2 ms into the 10 ms acceleration cycle. BPM measurements taken over a number of turns have previously identified vertical oscillations along each bunch [1]; see Fig. 1. The sum signal in this figure shows the longitudinal profile of the bunch, while the difference signal provides an indication of the vertical position along the bunch. The oscillations shown in the difference signal are characteristic of a transverse $m = 1$ head-tail instability [2].

Operationally the head-tail instability is suppressed by ramping the vertical tune over the appropriate time interval. While this technique is effective, it is limited by losses as the vertical tune approaches the half-integer resonance [3].

The Feedback System

A broadband, fast feedback system based on a stripline pickup & kicker has been designed to actively damp the effects of transverse instabilities and is currently being manufactured. Progress has been made on the feedback system itself by making use of the existing equipment in the ISIS synchrotron, specifically a split-plate BPM and a ferrite loaded kicker, the betatron exciter. The general set-up of the existing system is shown in Fig. 2.

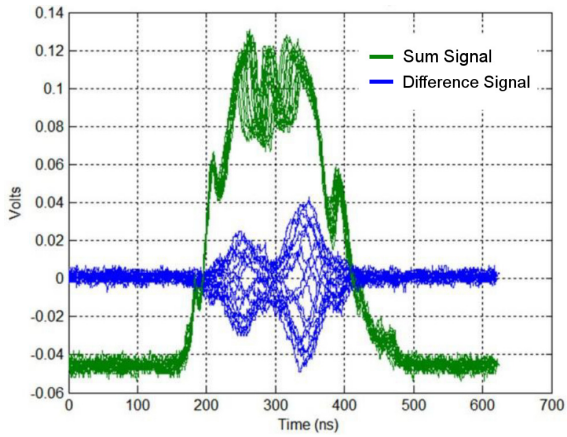

Figure 1: Sum and difference signals from a vertical BPM showing oscillations along a bunch [3].

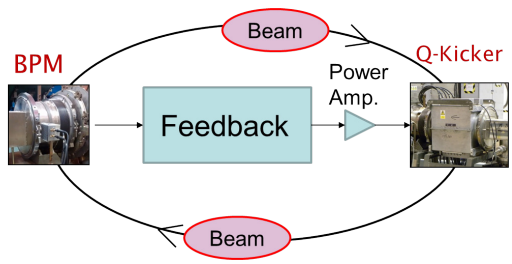

Figure 2: Set-up of the existing ISIS feedback system.

The Betatron Exciters

The ISIS betatron exciters; or "Q-Kickers", are window frame ferrite loaded kickers in the synchrotron which are ordinarily used for measurements of beam tune; there is one such kicker for each transverse plane. They are formed of two high-voltage plates opposite to one another and surrounded by ferrite yokes. The plates are both terminated with a high-power 10 Ω load resistor. The layout of the Q-kicker is shown schematically in Fig. 3.

The Q-kickers are normally excited with 4 kV pulses of opposite polarity sent to each plate. The resulting electric and magnetic fields kick the beam for only a single turn. This kick produces betatron oscillations which are observed on BPMs around the ring.

* alex.pertica@stfc.ac.uk

ISBN: 978-3-95450-192-2 doi:10.18429/JACoW-IBIC2017-TUPWC04

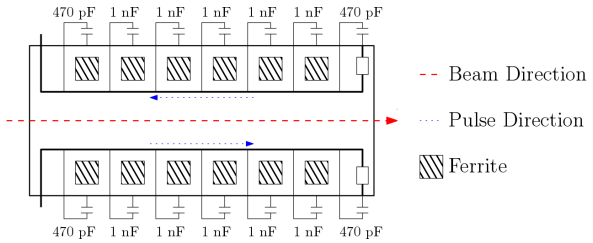

Figure 3: Internal layout of a Q-kicker, the direction of the two applied pulses is indicated as well as the beam direction.

The Betatron Exciter as a Damper

As the Q-Kicker is typically used for tune measurements, it is often available during normal machine operation. For this reason it was decided to use it within a feedback system as a kicker to damp existing beam instabilities on the vertical plane. This has been achieved by driving the device with a linear power amplifier system at the end of a feedback chain, instead of a high voltage pulse generator.

THE FAST FEEDBACK SYSTEM

Kicker

In order to match the characteristic impedance of the Q-kicker, each of the two excitation plates are fed by a set of five 50 Ω URM67 coaxial cables from the electronics racks located 150 m away. As the Q-kickers are still needed as a betatron exciter no modifications have been made to the kicker itself. This allows the Q-kicker to be a damper or a betatron exciter by switching the inputs.

Pick-up

A split-electrode BPM is used as a pick-up for the vertical plane. These monitors have a bandwidth that ranges from a few tens of kHz up to more than 50 MHz. The BPM located at the position with optimal betatron phase advance [4] (for a mean vertical tune of 3.8 around 2 ms) is used by another system. The next available BPM with the smallest phase advance error is located at 266° beta phase-advance upstream of the Q-kicker. Both electrode signals are amplified and sent through coaxial cables into the feedback electronics.

Power Amplifiers

Each set of five coaxial cables is powered by a custom made *Eltac Ltd RA994 amplifier* providing five 50 Ω outputs. Both amplifiers are driven in anti-phase by the low level radio frequency (LLRF) stage. The amplifiers specifications are given in Table 1.

Table 1: Power Amplifier Specifications

Property	Value
Frequency range	50 kHz - 20 MHz
Phase linearity	10° max variation
Gain	51.5 dB nominal (±1 dB)
Rated Output Power	20 W per output

Feedback Electronics

Figure 4 shows the block diagram for the feedback electronics. The LLRF stage receives the two electrode signals from the vertical BPM. One of these signals is feed through a programmable step attenuator, so the closed orbit offset can be subtracted from the differential signal at the 180° combiner. The resulting signal is then fed into the FPGA stage ADC. After being processed, it is fed back from the FPGA stage DAC into a programmable gain amplifier, a gating amplifier and a 180° splitter that provides the anti-phase signals for both power amplifiers.

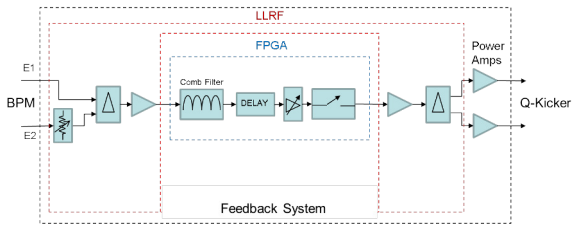

Figure 4: Block diagram of the feedback electronics.

The FPGA stage consists of a National Instruments NI-5781, 100 MS/s transceiver Flex-Rio front end module [5], backed by a PXIe-7962R Flex-Rio FPGA card. The first one samples the BPM differential signal to be processed by the FPGA and provides an analogue output for the LLRF stages. Both, the clock for the ADC/DAQ module and the FPGA processing stage are driven by a frequency synthesiser that multiplies the RF fundamental frequency by 30, tracking the bunch revolution frequency in order to simplify the filter implementation and delays adjustments. This block contains a comb filter to remove the revolution frequency and subsequent harmonics as well as the DC component.

Another stage produces a fixed delay for a calculated number of turns to apply the optimal kick (including the electronics and cable delays) and a dynamic delay that decreases as the revolution frequency ramps up. This stage also provides gating for the feedback signal – in order to apply the corrections only at a chosen time during the acceleration cycle. The gating and the look-up table managing block are driven by a 100 MHz clock in order to simplify the acceleration cycle synchronisation.

INITIAL RESULTS

The initial tests aimed to check the suitability of the damping system for the existing head-tail motion in the synchrotron, around 2 ms after injection. First, measurements were taken with the feedback system disabled to record the existing instability. The system was then switched on with a gating time of 1.5 ms to 3.5 ms and optimised to produce the maximum damping. Afterwards, the signal fed to the power amplifiers was reversed in order to drive the beam and compare the effects. All graphs correspond to data sampled at 2.8 ms after injection where the instability effects were more noticeable. Beam parameters at 2.8 ms are listed in Table 2.

ISBN: 978-3-95450-192-2 doi:10.18429/JACoW-IBIC2017-TUPWC04

Table 2: Beam Parameters 2.8 ms after Injection

Property	Value
Mean Vertical Tune	3.7
Revolution Frequency	948 kHz
Kinetic Energy	157 MeV

Figure 5 shows the frequency spectrum with the feedback system disabled. The beam instability sidebands are evident around the fundamental RF frequency (1.886 MHz as there are two bunches in the ring).

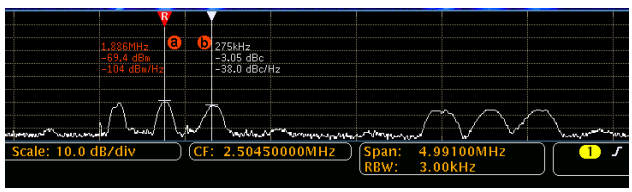

Figure 5: Frequency spectrum of the vertical BPM difference signal with the damping system disabled, showing the sidebands.

After switching the damping system on, the sidebands are attenuated by around 10 dB, as can be seen in Fig. 6

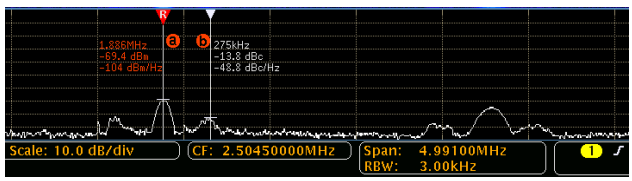

Figure 6: Frequency spectrum of the vertical BPM difference signal with the feedback system damping, showing the reduced sidebands.

By reversing the output signal polarity, in order to drive the beam, the initial sidebands were slightly increased, additional large sidebands were also observed; see Fig. 7.

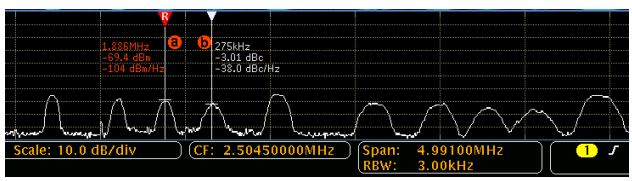

Figure 7: Frequency spectrum of the vertical BPM difference signal with the feedback system driving, showing additional sidebands.

The FFT waterfall graph in Fig. 8 shows the difference between the three scenarios. Each horizontal line in the waterfall graph corresponds to a set of FFT data acquired at a repetition rate of 1.6 Hz. The line at the bottom corresponds to the latest acquisition.

The top third corresponds to the damping system switched off, showing the sidebands clearly. The middle third corresponds to the damping system on, showing the sidebands

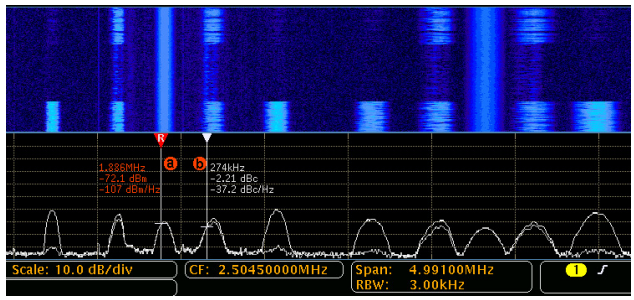

Figure 8: Waterfall plot demonstrating the effects of damping and driving with the feedback system.

reduced significantly. The bottom third shows the damping system driving the beam, with the sidebands slightly increased and the additional sidebands clearly visible.

Beam loss levels were compared between the three scenarios, integrating them during the time window between 1.5 ms and 2.5 ms. The reduction in beam loss with the damping system enabled was less than 5% and difficult to measure as the instability varied significantly between cycles. Further loss reduction may be achieved by tuning other beam parameters. The increase in loss was more evident while driving the beam.

SYSTEM MODELLING

Modelling of the Q-Kicker has been performed using CST Microwave Studio® (MWS) [6]. The general structure of the model is shown in Fig. 9. The main features of the model are: the outer conductive casing, the ceramic vacuum vessel (green), the six ferrite window frames (blue), the plates connected via the feedthroughs, the lumped capacitors (blue, top and bottom) and the lumped resistors. The ferrite material was modelled as *Ferroxcube 4M2* with an electrical resistivity of $1 \times 10^5\ \Omega\,\mathrm{m}$, a constant relative permittivity of $\varepsilon = 10$ and a frequency dependent, complex relative permeability as specified in the material data sheet [7]. The beam apertures were modelled with open boundary conditions and the main body was grounded with space added above the electrical connections. The simulations were performed in the frequency domain as this allowed the permeability of the ferrite yokes to be interpolated rather than fit as is required in MWS time domain simulations.

Plate Coupling

In order to test the validity of the model, initial simulations were performed which allowed comparison with experimental measurements. As the Q-kickers have been installed in the synchrotron only the 10 Ω plate input feedthroughs were available for measurement.

The coupling between the plates was measured with a Rohde & Schwarz ZVL vector network analyser (VNA). A resistive matching network was used to couple the VNA's 50 Ω ports to the 10 Ω feedthroughs, but was not included in the VNA calibration; the attenuation was added later. This setup was simulated by defining both of the 10 Ω feedthroughs

ISBN: 978-3-95450-192-2 doi:10.18429/JACoW-IBIC2017-TUPWC04

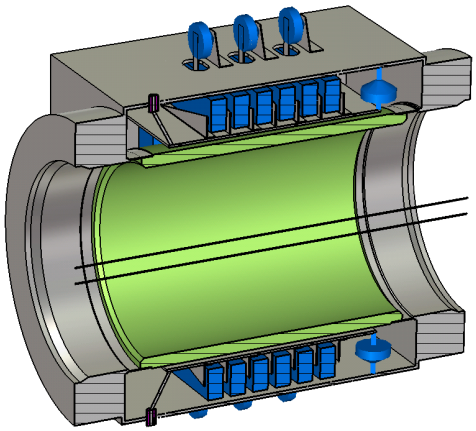

Figure 9: CST model of the Q-kicker with lumped elements and a two displaced wires.

as waveguide ports. The results of this simulation are shown in Fig. 10.

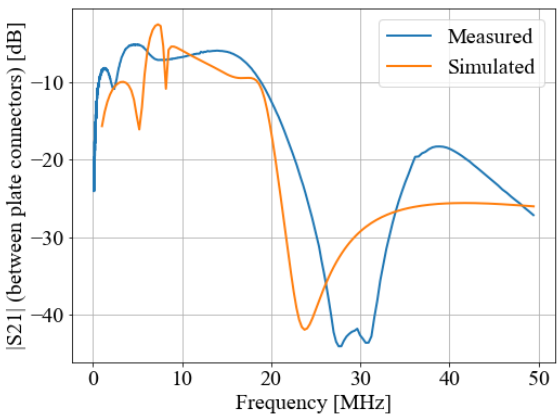

Figure 10: Simulated S-parameter magnitude of the coupling between opposing plates in the Q-kicker.

The measured results appear to match the simulated ones reasonably well between 6 MHz and 35 MHz. Some variation is expected due to mechanical and electrical imperfections. Below this frequency range however the simulated results consistently predict a smaller coupling between the plates than was measured; a difference of close to 7 dB at 1 MHz. Simulations with increased mesh density will be performed to investigate this observation.

Q-Kicker Frequency Response

The frequency response of the Q-kicker was simulated by exciting a two wires, vertically displaced from the central axis; see Fig. 9, with opposite polarity using the multi-pin port feature of MWS. The two 0.5 mm radius, perfectly electrically conducting wires were displaced by ±1 cm from the central axis. The coupling to one plate connector was then obtained; see Fig. 11. The simulated response drops off significantly for lower frequencies. At 20 MHz the coupling

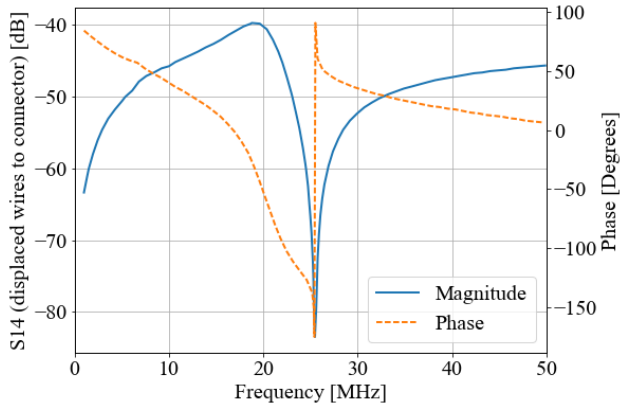

Figure 11: Simulated scattering parameters between two excited thin, displaced wires of opposite polarity and a 10 Ω feedthrough on one plate.

is predicted to be −40 dB, while at 1 MHz the coupling is less than −60 dB. Further simulation and beam-based measurements are required to verify whether this response is representative. Future simulations will excite the two plates simultaneously with opposite polarities, thus modelling real operation.

CONCLUSION

Initial tests have shown a reduction of the instabilities around 2 ms with the feedback system on and in damping configuration, but was not consistent between pulses. More work can be done to improve the system by:

- Optimizing the parameters setup
- FPGA code improvements
- Power amplifier optimization
- Use a BPM in a more suitable location by duplicating electrodes signals

A simulation of the coupling between opposing plates in the Q-kicker has been compared with experimental measurements. The simulated and measured results share common features, with some appearing to have been shifted in frequency. Further work will be done to improve the model; this will initially look at improving the feedthrough geometry.

The simulated frequency response of the Q-kicker to two displaced wires showed a reduced response at lower frequencies, which could be investigated with beam-based measurements. Further simulations will be performed to verify this result.

REFERENCES

[1] G. H. Rees, "Interpretation of the Higher Mode, Head-Tail Motion Observed on ISIS", *Part. Accel.*, vol 39, pp.159–167, 1992.

[2] F. J. Sacherer, "Transverse bunched-beam instabilities", CERN, Rep. CERN-PS-BR-76-21, Nov. 1976.

[3] R. Williamson, B. Jones and C. Warsop, "Development of Physics Models of the ISIS Head-Tail Instability", in *Proc. HB 16*, Malmö, Sweden, Jul. 2016.

ISBN: 978-3-95450-192-2 doi:10.18429/JACoW-IBIC2017-TUPWC04

[4] Z. Xie, "Transverse Beam Stability and Determination of Gain and Delay for Mixed-signal Transverse Feedback Dampers in Particle Accelerators", Ph.D thesis, University of Wisconsin-Madison, 2015.

[5] "NI-5781 Transceiver Adapter for FlexRIO", http://www.ni.com/en-gb/support/model.ni-5781.html,

[6] CST Microwave Studio®, www.cst.com, 2016.

[7] Ferroxcube, "4M2 Material Specification", http://www.ferroxcube.com/FerroxcubeCorporateReception/datasheet/4m2.pdf

ISBN: 978-3-95450-192-2 doi:10.18429/JACoW-IBIC2017-TUPWC05

NEW RF FEEDBACK SYSTEM AND SIMULATIONS FOR SUPPRESSION OF COUPLED-BUNCH INSTABILITIES AT SuperKEKB

Kouki Hirosawa*, Kazunori Akai[1], Eizi Ezura[1], Tetsuya Kobayashi[1],
Kota Nakanishi[1], Michiru Nishiwaki[1], Shin-ichi Yoshimoto[1],
SOKENDAI (the Graduate University for Advanced Studies), Tsukuba, Japan
[1]also at High Energy Accelerator Research Organization (KEK), Tsukuba, Japan

Abstract

SuperKEKB is an asymmetric electron-positron circular collider based on nano-beam scheme at interaction region and large beam current. Longitudinal coupled-bunch instabilities (CBI) near RF frequency modes become bigger as the beam current increase. We developed new CBI damper to suppress newly arisen CBI modes (μ = -1, -2, -3) in SuperKEKB. The new damper will install in Low Level RF control system. LLRF control system was digitalized; it is a FPGA- based system on the microTCA for the high beam current operation of SuperKEKB. New CBI damper is independent of main LLRF control components. In test-bench measurements, our new CBI damper performed very well and satisfied required specifications. For SuperKEKB Phase-2 commissioning from January 2018, we calculated simple feedback model to estimate feedback loop gain of the new CBI damper.

INTRODUCTION

SuperKEKB is a high-luminosity asymmetric electron-positron collider upgraded from KEKB. The SuperKEKB Phase-1 commissioning was operated from February to June in 2016, and the Phase-2 will be carried out from January in 2018. Table 1 provides the main parameters of SuperKEKB [1] for this study. The SuperKEKB storage ring consists of a 7 GeV high-energy ring (HER) for electrons and a 4 GeV low-energy ring (LER) for positrons. One of the major differences between SuperKEKB and KEKB is increase of the beam current. In SuperKEKB design, longitudinal coupled-bunch instabilities (CBI) from the interaction between the beam and the accelerating mode of cavity will be serious, and there is every possibility of higher modes ($\mu = -2$ and -3) destabilized. So we need new mode-feedback system to counteract these multi-bunch oscillations.

Table 1: SuperKEKB and Cavity Parameter

parameters for SuperKEKB	value LER	HER
Energy: E	4.0 GeV	7.0 GeV
Beam current: I_0	3.6 A	2.62 A
Mom. compact.: α_c	3.25×10^{-4}	4.55×10^{-4}
Synch. freq.: f_s	2.43 kHz	2.78 kHz
Harmonic number: h	5120	
RF frequency: f_{rf}	508.877 MHz	
$f_0 = f_{rf}/h$	99.39 kHz	
Number of cavity	22	ARES 8, SC 8
for Cavity	**ARES**	**SC**
$V_c/cavity$	0.5 MV	1.5 MV
R_s/Q_0	15 Ω	93 Ω
Q_0	1.1×10^5	2.0×10^9
coupling factor: β	5.0	4.0×10^4

In the KEKB operation, the lowest mode of CBI called μ = -1 mode had been excited, and we suppressed it by using the CBI damper, which corresponds to only μ = -1 mode [2]. While upgrading to SuperKEKB, we predict that μ = -1, -2 mode instabilities will be excited at design beam current (LER: 3.6 A, HER: 2.6 A). To reach SuperKEKB design current, $\mu = -2$ mode will occur and $\mu = -1$ mode will become more serious (Figure 1). So we developed a new CBI damper as an RF feedback (FB) component [3]. We expect that CBI $\mu = -1, -2, -3$ mode will be suppressed by using this new damper in SuperKEKB operation.

COUPLED-BUNCH INSTABILITIES CAUSED BY ACCELERATING MODE

We reuse the KEKB RF system [4], which has two cavity types. One is a normal conducting (NC), and the other is superconducting (SC). In HER, a NC and SC cavity are used, and in LER, only NC cavity. The NC cavity is a unique cavity of KEKB and SuperKEKB called "ARES" [5]. ARES has a three-cavity structure: an accelerating cavity is coupled with an energy storage cavity via a coupling cavity in order to reduce cavity-detuning by beam loading [5]. The reason why CBI caused by accelerating mode become serious is that cavity detuning amount become larger as the beam current increases (following equation). $\Delta f = -(I_0 \sin\phi_s/2V_c) \cdot (R_{sh}/Q_0) \cdot f_{rf}$, where I_0 is beam current, ϕ_s is synchronous phase, V_c is accelerating voltage, R_{sh} is shunt impedance, Q_0 is unloaded quality factor, and f_{rf} is accelerating frequency.

To evaluate power of CBI, we use growth rate which is well known in Equation (1).

$$\tau_\mu^{-1} = AI_0 \sum_{p=0}^{\infty} \{ f_p^{(\mu+)} \mathrm{Re}Z^{\parallel}(f_p^{(\mu+)}) - f_p^{(\mu-)} \mathrm{Re}Z^{\parallel}(f_p^{(\mu-)}) \} \tag{1}$$

$$f_p^{(\mu+)} = (pM + \mu) f_0 + f_s, \quad f_p^{(\mu-)} = \{(p+1)M - \mu\} f_0 - f_s$$
$$f_{rf} = h f_0 \quad ,$$

* hirosawa@post.kek.jp

ISBN: 978-3-95450-192-2 doi:10.18429/JACoW-IBIC2017-TUPWC05

where τ_μ^{-1} is growth rate, $Z^{||}$ is longitudinal impedance, f_s is synchrotron frequency, and h is harmonic number. Detuning impedance condition was applied to resonance frequency of $Z^{||}$. Figure 1 shows calculations of growth-rate for CBI modes caused by accelerating mode (Top : LER, Bottom : HER). As we calculated this Radiation Damping Rate, wiggler magnets are set to work maximum of SuperKEKB design.

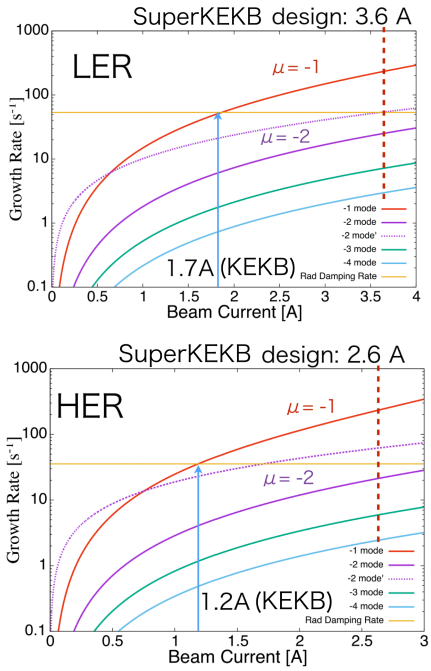

Figure 1: Growth rate by beam current. Dotted curve indicates μ = -2 mode in the case of a cavity parked with 150-kHz detuning.

RF FB SYSTEM FOR CBI DAMPER

Low level RF (LLRF) control system is newly developed in digital for large beam current in the SuperKEKB operation [6]. New system is performed by FPGA boards worked on microTCA platform. Main functions are Vc FB control, cavity tuner control, and RF level detectors for interlock as shown Figure 2. At SuperKEKB Phase-1 commissioning, this new LLRF control systems worked well without serious trouble.

Figure 3 shows a block diagram of a RF FB system for CBI damper (mode feedback). CBI damper signals are combined to Vc FB control signals. Figure 4 shows a block diagram of new CBI damper. The CBI damper consists of single-side band filter (SSBF) which is analog circuit and digital bandpass filter (BPF) which is made on FPGA board (KC705, Xilinx) [3]. The fundamental method of this system is based on the KEKB damper. First step of CBI damper, only lower sideband of transmit signals can be passed through SSBF. RF are input as reference signals for up/down conversion. This SSBF was improved, and it has very good characteristics [3]. Second step, only frequency of CBI modes are transmitted, which is attained by using digital BPF (Fig. 4 bottom). To suppress CBI $\mu = -1, -2, -3$ modes at the same path of a RF system, one SSBF and three digital BPFs are combined in parallel (Fig. 4 top). Since the BPF can be adjusted the phase independently for each CBI mode, feedback signals are optimized conforming with the phase frequency characteristics of several components in entire RF system. The control parameters of the digital BPF can be given remotely by EPICS records.

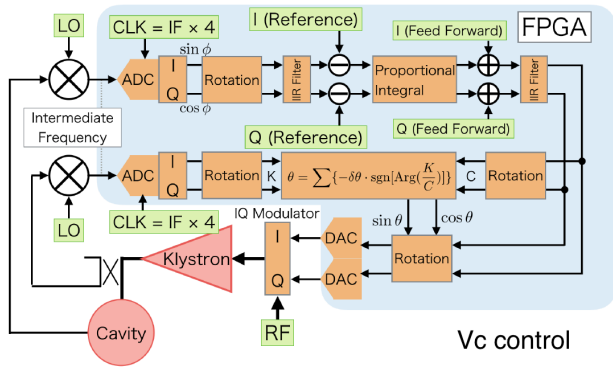

Figure 2: Block diagram of the digital Vc FB control system.

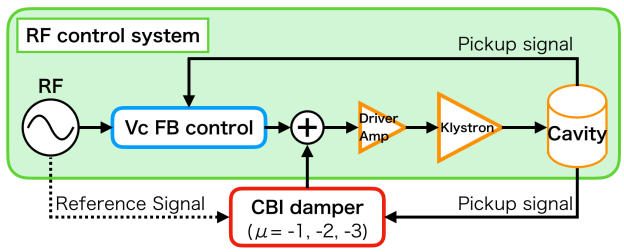

Figure 3: Block diagram of an RF FB system for CBI damper.

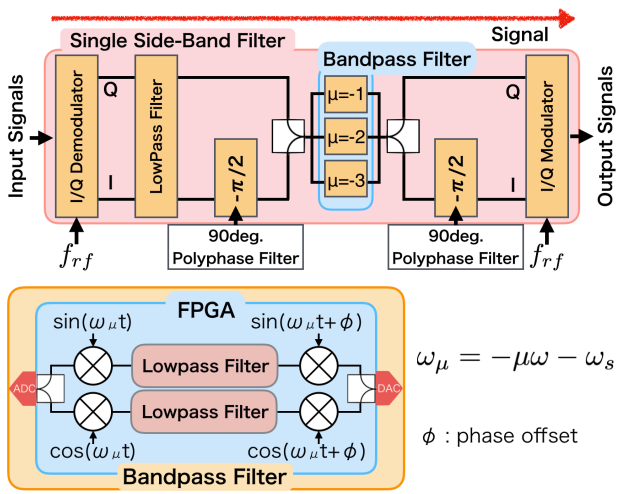

Figure 4: Block diagram of a new CBI damper.

Before practical use at beam commissioning, we have to make sure of CBI damper performance. The nucleus of

ISBN: 978-3-95450-192-2 doi:10.18429/JACoW-IBIC2017-TUPWC05

this damping instabilities method is attenuation of apparent impedance only at frequency that excites CBI. Figure 5 shows the test-bench measurement of impedance damping with a simulant cavity(Q = 9000). The impedance is reduced in accordance with the set loop gain and parameters of digital BPF (e.g. passband frequency of several filters). It found that CBI damper performs following our expectation. At SuperKEKB Phase-2 commissioning, we will try to suppress beam oscillations by using new CBI damper.

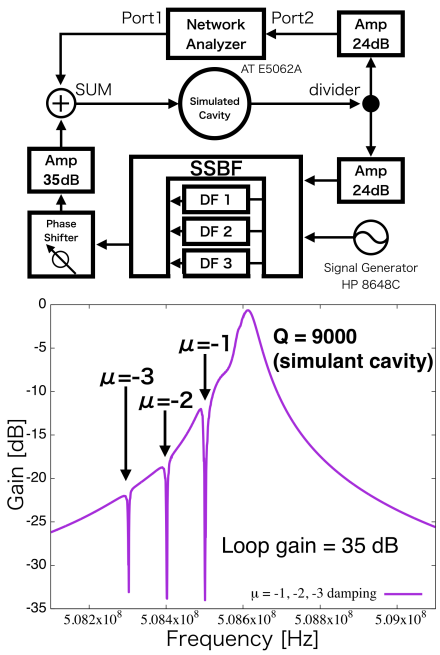

Figure 5: Block diagram for the FB loop evaluation (Top), and the damping characteristics for the FB loop (Bottom).

ESTIMATION OF THE DAMPING EFFECT

Looking ahead to SuperKEKB operation, we calculated RF FB to suppress multi-bunch oscillations. Because the number of CBI damper applied to cavities cannot be identified without evaluation of loop gain. The main idea of CBI damping simulation is that bunches are kicked by wake fields and FB RF fields at cavities. The CBI is an instability caused by the interaction between the impedance of the entire accelerator and the multi-bunch beam. If CBI dampers are applied to all RF stations of storage ring, it is enough to supply the damping effect over the entire circumference of the ring. However it is necessary to suppress CBI with the installation of CBI dampers as few units as possible (for example, it is hard to install in stations of SC cavity because SC is more sensitive than NC). This simulation is evaluation of the effect of difference of the number of RF stations which CBI damper is applied to. The relation between pickup signals and wake fields level in a cavity is estimated from SuperKEKB Phase-1 commissioning measurement. Figure 6 shows estimation of the effectiveness of CBI damping in beam-current change for the difference of the number of the CBI damper applied to each RF station for LER (CBI dampers and RF stations have a one-to-one relationship). In this figure, horizontal axis denotes beam current, and vertical axis is amplitude ratio of bunch oscillations to zero-current condition. Initial gain of pickup signal is fixed to +60dB (since intensity of pickup signals was so weak). The gain control system may be required, so we plan to consider a new system including it after Phase-2 commissioning. As an estimation result, it was found to need some CBI dampers for reach SuperKEKB design beam current.

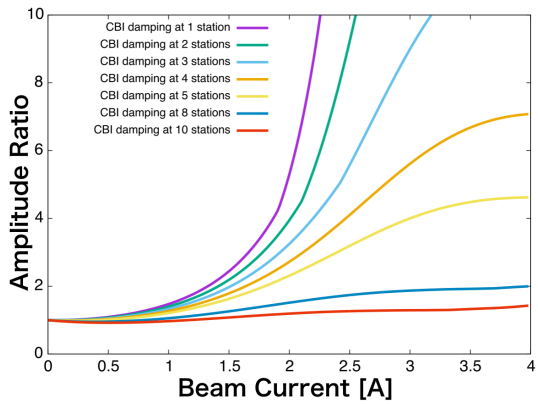

Figure 6: Estimation of the effectiveness of CBI damping for the different numbers of the CBI dampers applied to each RF station.

CONCLUSION

Developed new CBI damper performance satisfies our required specifications [3]. SSBF and digital BPF was improved and their characteristics is very well. In calculation of CBI growth-rate (especially $\mu = -1$ mode), amplitude of bunch oscillation with beam current increase depends strongly on the number of the dampers applied. It is found that we need CBI dampers more than one, but we still have not clarified the exact number of dampers required. In SuperKEKB Phase-2 commissioning, we expect that CBI can suppress by new CBI damper, and we will define how many dampers should be applied for the design beam current.

REFERENCES

[1] Y. Ohnishi *et al.*, *Prog. Theor. Exp. Phys.*, 03A011 (2013)

[2] S. Yoshimoto, KEK Internal 2013-2, pp. 1-6 (2013)

[3] K. Hirosawa *et al.*, in *Proc. of IPAC2017*, pp. 3989-3991 (2017)

[4] K. Akai *et al.*, *Nucl. Instr. Meth.* A. 499, pp. 45-65 (2003)

[5] T. Kageyama *et al.*, in *Proc. of PASJ2011*, pp. 1245-1249 (2011)

[6] T. Kobayashi *et al.*, in *Proc. of IPAC2015*, pp. 924-926 (2015)

ISBN: 978-3-95450-192-2 doi:10.18429/JACoW-IBIC2017-TUPWC06

DEVELOPMENT OF KICKER FOR TRANSVERSE FEEDBACK SYSTEM IN BEPCII

J. S. Zhou, J. X. Zhao, Y. F. Sui, J. H. Yue, J. S. Cao, IHEP, Beijing, P. R. China
also at the University of Chinese Academy of Science, Beijing, P. R. China

Abstract

This paper introduces the necessary design parameters of transverse feedback system. Meanwhile, it mainly contains the design of stripline as feedback system kicker. The transverse kicker has 4 striplines, so that it can work in vertical and horizontal area. In the experiment, the shunt impedance is 1500 Ω which is simulated by HFSS and the system only needs 120 W to suppress the coupled beam bunch instabilities. According to the results of parameter S (1, 1) and S (2, 1), power loss and reflection is convenient. Recently, the prototype is calibrated.

INTRODUCTION

In order to receive more specific beam position instances and suppress beam instability as much as possible, we need to develop the kicker for BEPCII transverse bunch-by-bunch feedback system in storage ring. Comparing with the current transverse kicker, the new one provides superior dipole oscillation damping and detects the electrical field signal more sensitively [1]. According to calculation and simulation results, the amplitude reflection rate parameter is lower than 1% and a shunt impedance of 1500 Ω at 250 MHz working bandwidth can be reached. It needs 120 W power to suppress all unstable coupled bunch modes and the transmission efficiency is more than 99%. Meanwhile, this design aims to increase the space utilization rate in the storage ring, so the four-stripline-type kicker is adopted. This kicker tube consists of 2 striplines in horizontal and another 2 striplines in vertical direction. The important dimensions include the stripline length of 300 mm and the total length of the transverse kicker which is less than 500 mm. The innovation of this development is improving the beam intensity and lifetime, and the analysis and diagnosis ability of the beam detection system.

PARAMETER SIMULATION

Relevant Parameters Deduction

BEPCII has collide mode and synchrotron mode. At the beginning of the design of the transverse kicker, physics analysis needs to refer to some details of BEPCII in two different mode [2]. Table 1 shows the main parameters which play an important role in this work.

Table 1: Main Parameters of BEPCII

Parameters	Collide mode	Synchrotron mode
Energy E_0 (GeV)	1~2.1	2.5
Circumference (m)	234.53	241.13
RF frequency (MHz)	499.8	499.8
Harmonic number	396	402
Revolution frequency (MHz)	1.264	1.243
Revolution period (ns)	792	804

Table 2 shows the main parameters of the new transverse kicker, which is based on the relevant parameters in Table 1. The other part of this paper concerns the details of the design. Because of synchronous mode in BEPCII, the bucket will be filled by beam bunch one by one. So the system bandwidth is a half of RF frequency. The maximum output voltage is calculated by the Eq. (1):

$$V_{FB\perp} = 2\frac{T_0}{\tau_{FB}} \cdot \frac{E}{e} \cdot \frac{\Delta x}{\sqrt{\beta_m \beta_k}} \quad (1)$$

According to shunt impedance and maximum output voltage, the maximum power needed by this system is 120 W, and Eq. (2) shows how to calculate it

$$P = \frac{1}{2}\frac{\Delta V_{FB}^2}{R_k} \quad (2)$$

Table 2: Main Parameters Transverse Kicker

Parameters	Transverse Kicker
System Bandwidth (MHz)	250
Shunt Impedance (Ω)	1500
Maximum Feedback Voltage (V)	600
Maximum Output Power (W)	120
Stripline Length (mm)	305
Tube Inner Radius (mm)	50
Stripline Flare Angle	60°

* This work was supported by Accelerator Division, IHEP
† zhoujs@ihep.ac.cn

ISBN: 978-3-95450-192-2 doi:10.18429/JACoW-IBIC2017-TUPWC06

The shunt impedance of the kicker's stripline is calculated by Eq. (3)

$$R_k = 2Z_c(g_\perp \frac{l}{a} \cdot \frac{sin\ kl}{kl})^2 \qquad (3)$$

In this equation, Z_c = 50 Ω, stripline radius is a = 38 mm, the number of wave k = ω/c, the length of stripline l = 300 mm. According to the chart, the approximate solution of shunt impedance is 1.5 kΩ while the frequency is 250 MHz. $g_\perp \approx 1$. Figure 1 shows the shunt impedance at different frequencies (calculated from 50 MHz to 500 MHz).

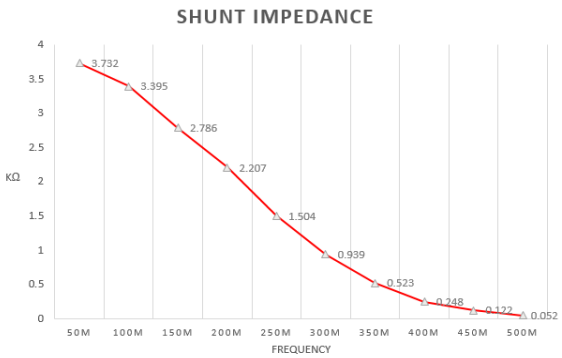

Figure 1: The shunt impedance at different frequencies.

S Parameter Results

Figure 2 is the coefficient of power input port at different frequencies. Parameter S (1, 1) is the ratio of reflected wave voltage in power feed point to incident wave voltage [2]. In order to transmit the maximum power to stripline (which is from amplifier) and reduce the reflected power, the stripline needs to be impedance matched with external port and transmission cable. The thickness of the cavity internal wall is adjusted so that the reflection of wave range is lower than 10% and reflected power is less than 1%.

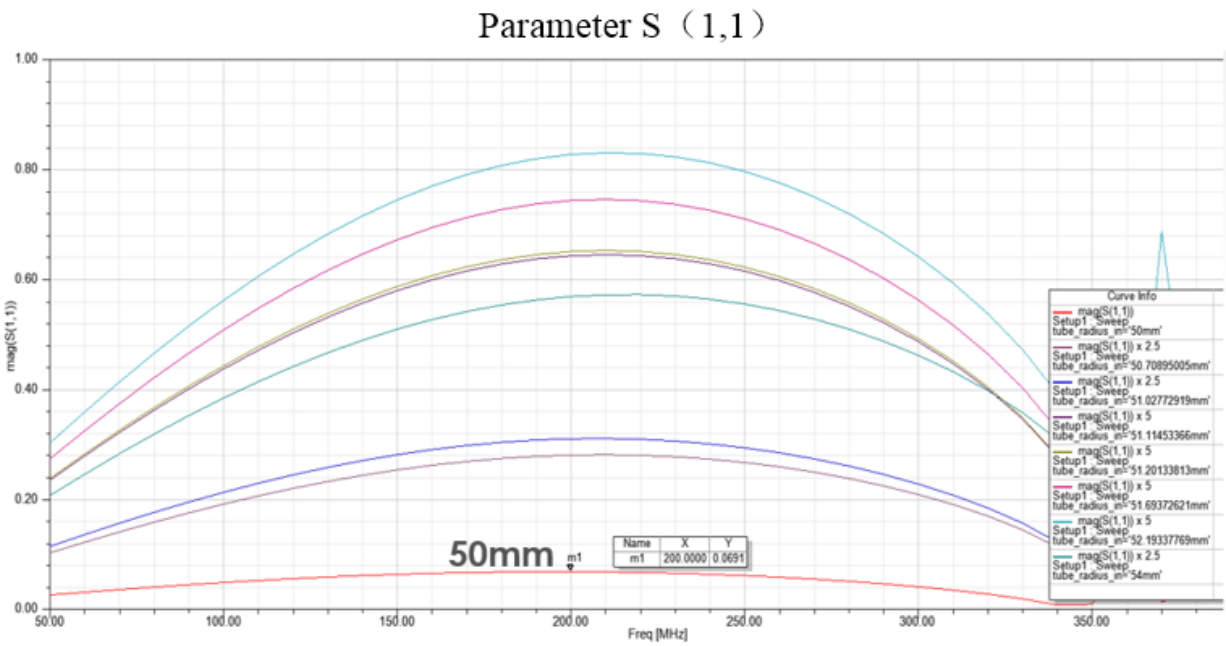

Figure 2: The results of S (1, 1) for different internal radii.

Figure 3 can be regarded as the efficiency of power transmission with power through the stripline at different frequencies. As we can see, when the cavity internal radius is 50 mm, transmission efficiency is 99.76% and the power reflecting factor is lower than 1%.

ISBN: 978-3-95450-192-2 doi:10.18429/JACoW-IBIC2017-TUPWC06

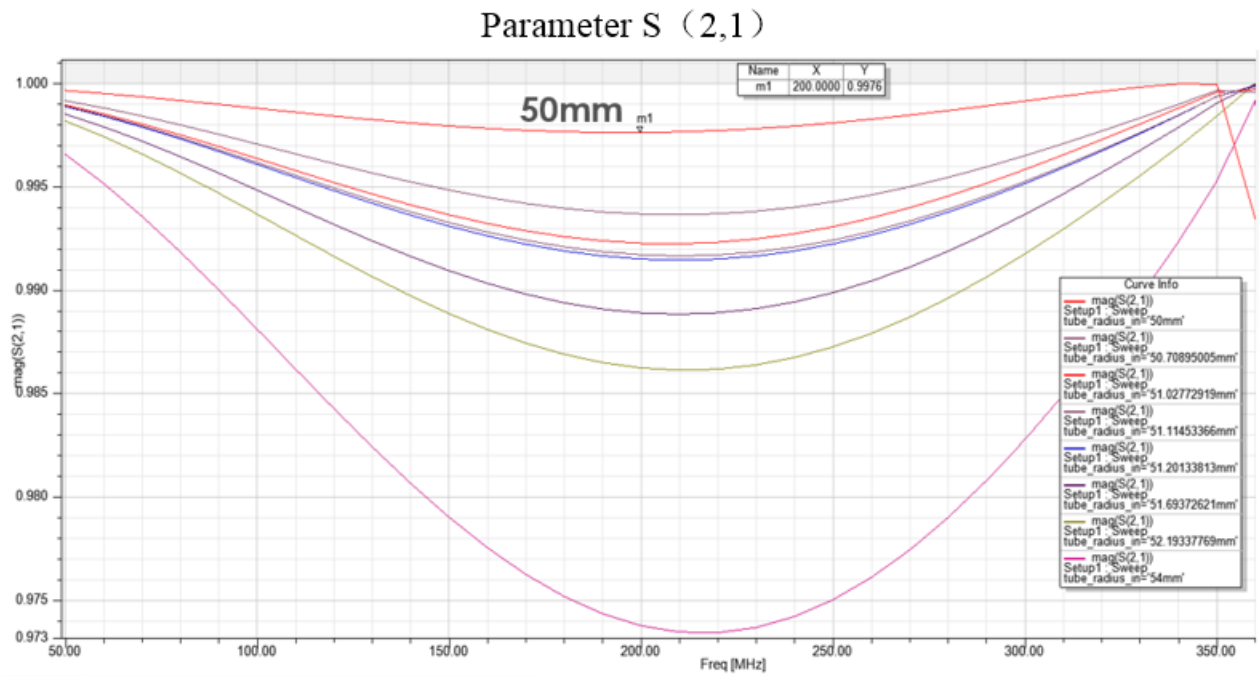

Figure 3: The results of power transmission parameter for different internal radii.

CONCLUSION

In this article we have illustrated the design of the development of transverse kicker for BEPCII and emphatically introduced important parameter, such as shunt impedance, power reflecting factor and power transmission efficiency. In simulating experiment, we designed the transverse kicker as a four striplines type so that it is able to operate in x and y direction at the same time. We finally calculated the shunt impedance is 1500 Ω by the use of HFSS while the length of stripline is 300 mm. Then we could easily calculate that the beam bunch instability can be suppressed if the power is 120 W. In transmission simulation, power reflecting factor was lower than 1% and power transmission efficiency was more than 99%.

REFERENCES

[1] E. Kikutani, T. Obina, T. Kasuga *et al.*, “Front-end electronics for the bunch feedback system for KEKB”, Preprint 94 -131[R]. Tsukuba: KEK, 1994.

[2] J. H. Yue, R. X. Yuan, L. Ma, J. S. Cao, “The design of the stripline kicker for the BEPCII transverse feedback system”, *Proc. APAC’04*, Gyeongju, Korea, March 2004.

ISBN: 978-3-95450-192-2 doi:10.18429/JACoW-IBIC2017-TUPWC08

THE COLD BEAM POSITION MONITORS FOR THE C-ADS INJECTOR I PROTON LINAC*

Y.F. Sui, J.S. Cao, H.Z.Ma, Q. Ye, L.D. Yu, J.H. Yue
Institute of High Energy Physics, Beijing, China
also at Key Laboratory of Particle Acceleration Physics and Technology, IHEP, Beijing, China

Abstract

The injector I of China Accelerator Driven Subcritical system (C-ADS), which is composed of an ECR ion source, a low energy beam transport line (LEBT), a radio frequency quadrupole accelerator (RFQ), a medium energy beam transport line (MEBT) and cryomodules with SRF cavities to boost the beam energy up to 10 MeV. The injector linac is equipped with beam diagnostics. Cold beam position monitor (BPM) is one of instrumentations of the injector. This paper describes the design and fabrication of the cold BPM pick-ups, and also the application of the BPM in commissioning of SRF cavities. Discussion of the promotion and other aspect will also be presented.

INTRODUCTION

The Chinese ADS project is aimed to solve the nuclear waste problem and the resource problem for nuclear power plants in China. With its long-term plan lasting until 2030th, the project will be carried out in 3 phases: Phase I of R&D facility, Phase II of experiment facility and Phase III of industry demonstration facility. The driver linac of the CADS consists of two injectors to ensure its high reliability. Each of the two injectors will be a hot-spare of the other. Although the two injectors that are installed in the final tunnel will be identical, two different design schemes, named injector I and II respectively are being pursued in parallel by the Institute of High Energy of Physics (IHEP) and the Institute of Modern Physics (IMP). [1] The Injector I ion source is based on ECR technology. The beam will be extracted with an energy of 35 keV. The ion source will be followed by a Low Energy Beam Transport line (LEBT), which consists of 2 solenoids, a fast chopper system and a set of beam diagnostics including CTs and faraday cup. A Radio Frequency Quadrupole (RFQ) will accelerate the beam up to 3.2 MeV and will be followed by the first Medium Energy Beam Transport line (MEBT1), fully instrumented and also equipped. The next section is two cryogenic modules named CM1 and CM2 with seven cold beam position monitors in each, which accelerate beam up to about 10 MeV. The last section is the second Medium Energy Beam Transport line (MEBT2). The drift tubes between magnets provide the gap for diagnostics.

Table 1: The Beam Characteristics of CADS Injector I

Parameters	Value
Beam energy	3.5Mev~10MeV
Bunch frequency	325MHz
Beam pulse length	30us-CW
Peak current	10mA

To monitor the parameters of injector I, Several beam diagnostic and monitoring instruments are used. BPM as an essential part of beam diagnostics was designed and manufactured to measure the displacement of the beam. The BPMs provide the basic diagnostics tool for commissioning and operation of accelerators. The BPMs will provide information about both the transverse position of the beam and the beam phase that can be used to detect energy on line using the time-of-flight (TOF) method [2]. 27 BPMs including 14 cold BPMs are installed on the injector I. There are 7 cold BPMs, 7 superconducting quadruple magnet (SCQ) and 7 superconducting RF (SRF) cavities in each cryostat. The cold BPM is installed between SCQ and SRF cavity. So the SRF or SCQ is adjusted one to one based on BPM. The cold BPM is shown in Fig.1.

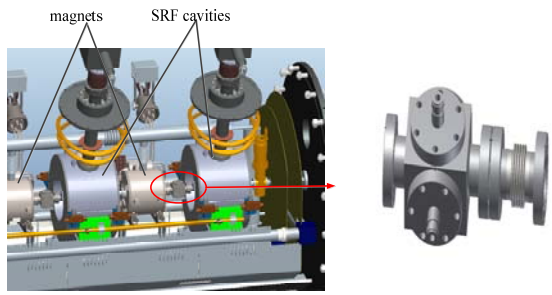

Figure 1: The position of the BPM in the cryostat and the structure of BPM.

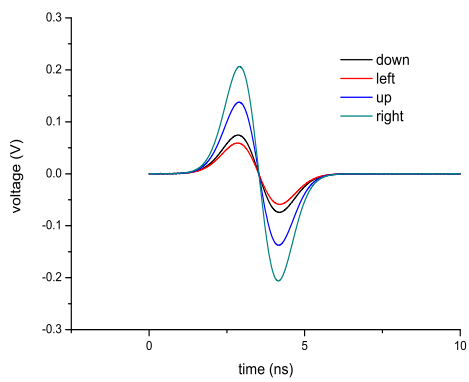

Figure 2: Voltages versus time during one period on four BPM electrodes from a passing transversely displaced (x = 2r/7; y =r/7) bunch.

*Work supported by China ADS Project (XDA03020000) and the National Natural Science Foundation of China (NO. 11205172, NO. 11475204)

ISBN: 978-3-95450-192-2 doi:10.18429/JACoW-IBIC2017-TUPWC08

THE COLD BPM DESIGN

As mentioned above, there are seven BPMs for each cryostat. The button pickups are selected for cryogenic BPMs. Removable feedthroughs are used in the cold BPMs for maintenance and replacement. The button diameter is 10mm and the beam pipe is 35 in diameter. The cryogenic BPM is modelled and simulated in CST PS. Though the beam energy varies from the entrance to the exit of the cryomodule, we adopted the unique beam energy 3.5 MeV to compute the model. The signal induced by the beam is shown in the Fig.2. [3]

Figure 3: The liquid nitrogen test of the BPM pick-ups.

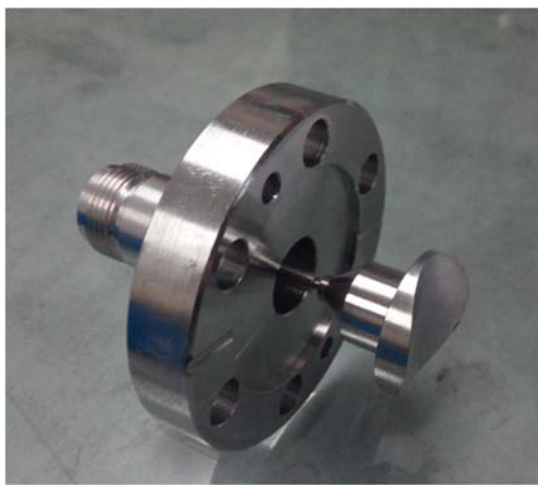

Figure 4: Removable feed through of cold BPM.

The stability of the cold BPM must be considered first. So the pick-ups and the cables in the cryostat are carefully design to satisfy the demands. The prototype of cold BPM pick-up is carefully designed and fabricated. Liquid nitrogen test is carried to verify the stability of the prototype. In the test, the pick-up is soaked in liquid nitrogen for long time， so that the temperature of pick up is as low as liquid nitrogen. Then the pick-up is transferred to a high temperature furnace and forced the temperature to rise quickly. This is one cycle of the test. After several cycles, the vacuum leakage of wielding part is checked carefully. Another vulnerable part is feed through for the ceramic seal suffered to drastic change in temperature. And also need to check for safety.

For the cold bpm pick-ups are all installed in cryostat, totally 28 cables used to feed the signal out of the cryostat for all pick-ups. The heat transferring by the cable should be considered to reduce heat load of cryogenic system. The conduction heat is calculated with different parameter cable. The main difference is inner conductor. The result is shown in Table 2.

Table 2: The Thermal Load of Two Type Cable at 2K

No.	Inner Conductor	Outer Conductor	Dielectric	Thermal Load @2K (W)
1	1. Silver Coating, 99.9% pure 2. Copper center conductor, 99.9% pure	OFHC Copper outer conductor	PTFE Dielectric	0.343
2	1. Silver Coating, 99.9% pure 2. Copper cladding, 99.9% pure 3. ASTM Class 40HS steel center conductor			0.486

Measurement of the particle beam position in injector I proton linac is an essential part of cold beam position monitor. Based on this, operator can steer the beam to reduce beam loss which is critical for high intensity proton accelerators. The beam positions in cryomodule section are listed as Fig. 5. Beam based phase scan is the most simple and effective method for measuring cavity phase and amplitude. For the first cavity phase measurement, the second cavity is detuned and the two following BPMs is used to measure energy after calibrating the offset between the BPMs. Because the significant velocity changes in superconducting cavity at low energy section, the effective voltage is changing with cavity phase, meanwhile the synchronous phase is non-linear with LLRF phase. [4] The phase and amplitude setting of superconducting cavity are very important at the operation of accelerator, so beam based measurement of cavity phase and amplitude is necessary. In ADS injector I, the method is used to determine the phase and amplitude of all SRF cavities. The Fig. 6 shows the beam phase scan result using cold BPMs. The line in different colour indicates different cavity amplitude. The cold bpm system plays important role in the commissioning of superconducting cavities. The last function of BPM system is interlock. The signal of pick-ups are used for machine protection, if one of them output is much bigger than some thresholds, the electronics will provide signal to the fast interlock protection system. In this way, the accelerator is prevented from serious damage.

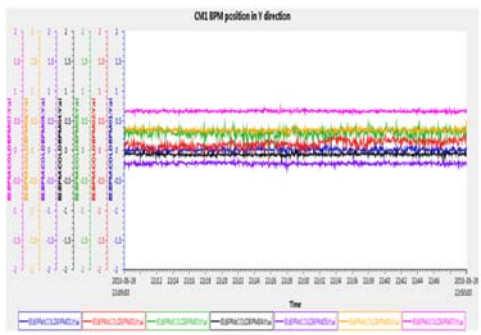

Figure 5: Beam position in cryostat by cold BPMs.

ISBN: 978-3-95450-192-2 doi:10.18429/JACoW-IBIC2017-TUPWC08

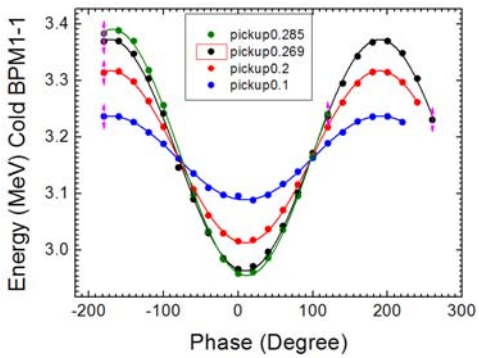

Figure 6: Phase scan with the cold BPM system

CONCLUSION & ACKNOWLEDGEMENT

The cold BPM system is carefully designed and fabricated. After that strict testing is carried out on the BPM pick-ups to ensure the system stability. The cold BPM system is set up and play important role in SRF cavities commissioning. After a long run, The system is still stable operation. We acknowledge Bian Lin for the help in thermal load calculation. The authors are grateful for the help and cooperation from the operators of the test beam line. Thanks are also given to the members of the beam instrumentation group for their useful discussions and suggestion.

REFERENCES

[1] Jingyu Tang and Zhihui Li (ed.), "Conceptual physics design of the C-ADS accelerators", *IHEP-CADS Report/2012-01Eg*.

[2] Peter Forck, "Lecture Notes on Beam Instrumentation and Diagnostics", Joint University Accelerator School, March 2011.

[3] Y.F. Sui *et al.*, "Design and Simulation of Beam Position Monitor for the CADS Injector I Proton Linac", *Proceedings of IBIC'13*, Oxford, UK, September 2013, WEPC17, P710-712.

[4] C. Meng, H. Geng, Z. Xue, F. Yan, L. Yu, Y.L. Zhao, "Superconducting Cavity Phase and Amplitude Measurement in Low Energy Accelerating Section", *Proceedings of IBIC'13,* Oxford, UK, September 2013, MOPOY031, P922-924.

ISBN: 978-3-95450-192-2 doi:10.18429/JACoW-IBIC2017-TUPWC09

REDUCING CURRENT DEPENDENCE IN POSITION MEASUREMENTS OF BPM SYSTEMS BY USING PILOT TONE: QUASI-CONSTANT POWER APPROACH

G. Brajnik*, S. Bassanese, G. Cautero,
R. De Monte, M. Ferianis, Elettra-Sincrotrone Trieste, Trieste, Italy
G. Rehm, Diamond Light Source, Oxfordshire, UK

Abstract

In BPM systems, the dependence of measured position on beam current is a well-known behaviour due to many factors. Measurements were carried out at Diamond Light Source with the pilot-tone compensated RF front end developed at Elettra and they evidenced a strong link between that issue and the integral non-linearity (INL) of the ADCs. A potential way to reduce this dependence is to change the gain of the preamplifiers following the beam current variation, trying to coerce the ADC into working as close as possible to a specific level. In this paper, along with the results of the tests performed at Diamond, which confirm once again the effectiveness of the front end and of the compensation strategy, an alternative technique is proposed to mitigate the current dependence by using the pilot tone itself. The idea is to maintain constant the total amplitude at the input of the ADCs, which is composed of the signal from the beam plus the pilot tone. Our data demonstrate how, by changing the latter in a convenient way during the current variations, we can achieve a reduction of the dependence by a factor of 10 considering an equivalent current ramp from 10 to 300 mA.

INTRODUCTION

The analog front end developed at Elettra for electron BPM applications has already been presented in previous papers [1, 2]. The proposed compensation strategy used has proven its effectiveness in several tests both on bench and on the storage ring during the normal operation of the machine.

In order to verify the excellent performances on different accelerators with different parameters, a new measurement session was carried out at Diamond Light Source. The results are reported in the first part of this manuscript, while the second part is focussed on some unexpected behaviours, mainly related to the integral non-linearity of the ADCs.

TESTS AT DIAMOND

A first test was realized in the laboratory of Diamond's Beam Diagnostics Group to ensure the correct operation of the system: a fixed beam was emulated by an RF generator and a 4-way splitter connected with semi-rigid coaxial cables to the front end. This last one was coupled with a Libera Spark as a fast 4-channel digitizer and the decimated IQ data were used for the analysis, calculating the FFT and working on carrier and pilot amplitudes.

* gabriele.brajnik@elettra.eu

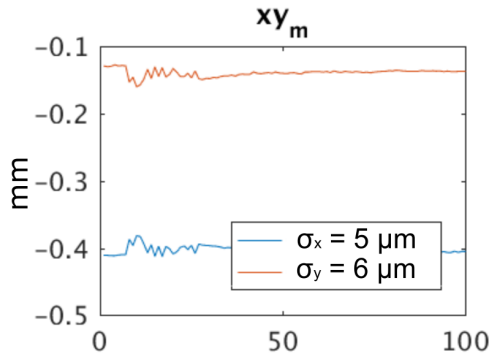

Figure 1: Calculated position while wobbling cables.

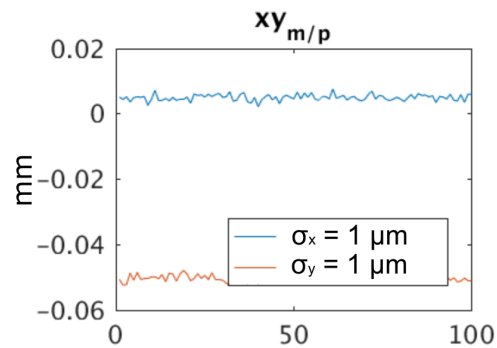

Figure 2: Compensated position while wobbling cables: note the different y scale.

During the acquisitions, the cables from the front end to the Libera Spark were twisted and wobbled: Figure 1 shows the calculated position with the movements due to the cables and Figure 2 illustrates the compensated position using the pilot tone. An improvement of a factor of 5 on the standard deviation has been obtained, and more than a factor of 10 considering the peak-to-peak value, virtually cancelling the shifts introduced by the cables. Note the different y scales of the two figures.

Results with Beam

The analog front end was subsequently placed in Diamond storage ring tunnel and connected to button BPMs (radius of 10.3 mm, scale factor $K_x = 10.3$ mm, $K_y = 10.4$ mm) by means of four 2-metres cables to detect the signal at 499.680 MHz. Power and communications were supplied by an Ethernet cable (PoE equipped). The output of the front

ISBN: 978-3-95450-192-2 doi:10.18429/JACoW-IBIC2017-TUPWC09

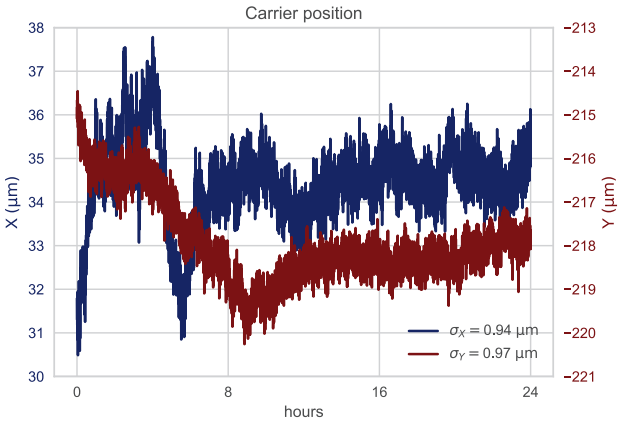

Figure 3: Beam position in a time window of 24 hours.

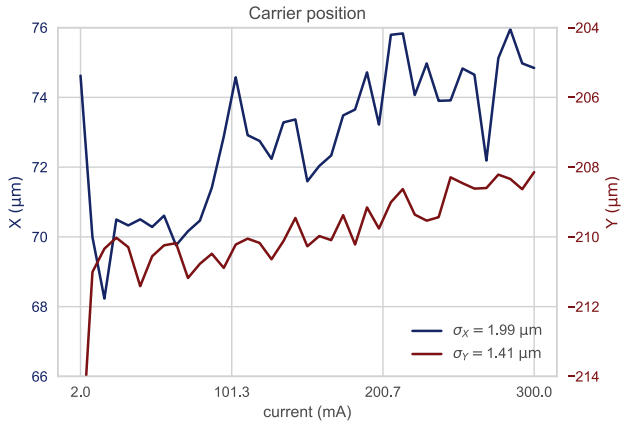

Figure 4: Beam position during a current ramp.

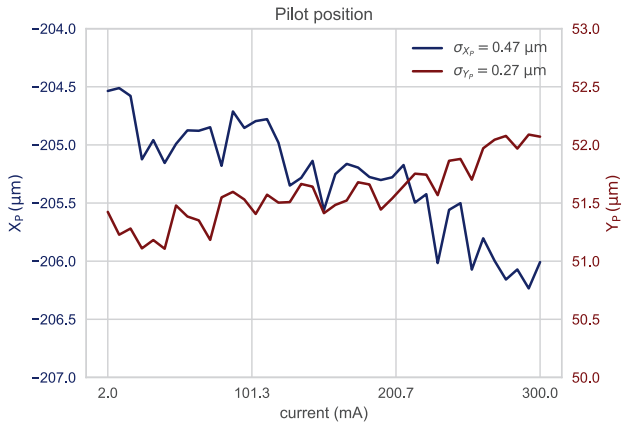

Figure 5: Pilot position during a current ramp.

end was connected to the 16-bit, 160 MS/s assembled digitizer [2] located in the CIA (Control and Instrumentation Area) with more than 20 metres of cables. A clock conditioner ensured the correct synchronization of the system clocks with the storage-ring clock (533.8 kHz), generating both a low-jitter sampling clock for the ADCs and a reference clock for the pilot-tone synthesizer. Every position sample was calculated through an FFT of 2.4 million samples.

A long-term acquisition has been captured in a time window of 24 hours, while the machine was running for the users in top-up mode (3 GeV and 300 mA): Figure 3 illustrates the compensated beam position with a standard deviation less than 1 µm for both horizontal and vertical coordinates.

Then, we used a machine-dedicated beamtime to test the system with various machine conditions, in particular to investigate the beam current dependence without changing the gain of the preamplifiers. Figures 4 and 5 show the positions of the carrier and of the pilot respectively during a current ramp from 2 to 300 mA in a short time (about six minutes).

While a different thermal load of the machine could explain the small drift in the carrier position (real different orbit) during the ramp, the position shift of the pilot should not be related to the current. The signal levels were far from saturation and intermodulation points, so our suspicion pointed to ADCs behaviours.

ADC NON-LINEARITY

A dedicated testbench for the ADCs was prepared to better understand the described specific behaviours. It was composed of two RF generators with the same reference oscillator (one for the pilot, one for the carrier), a passive combiner, a passive 4-way splitter, four rigid cables and four 6 dB attenuators at the ADCs input stages for wideband impedance matching purposes. The positions were calculated in the same way as the measurements at Diamond Light source, except for the radius of the pick-ups. The scale factor was fixed at 20 mm as the BPM buttons located in Elettra storage ring, so all the standard deviations and the detected movements have a factor of two respect to Diamond's ones.

First of all, an equivalent current ramp from 10 to 310 mA was generated with the carrier only: results in Figure 6 show a significant variation in position due to integral non-linearity within the range specified by the manufacturer of the ADCs [3].

Moreover, we tried to keep a constant total amplitude at the input of the ADCs, simultaneously changing the power of both RF generators during the current ramp. The strategy

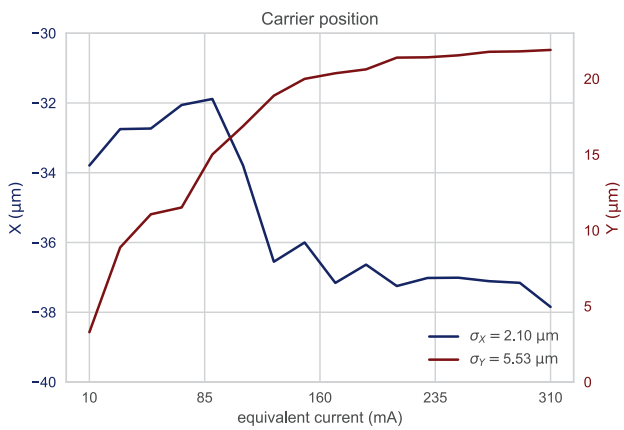

Figure 6: Carrier position during an equivalent current ramp of 10-310 mA.

ISBN: 978-3-95450-192-2 doi:10.18429/JACoW-IBIC2017-TUPWC09

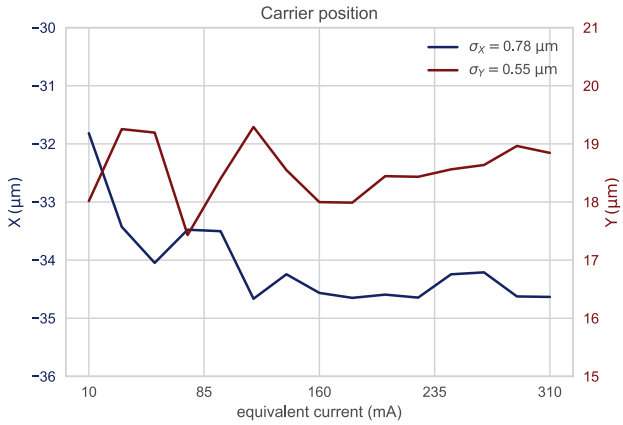

Figure 7: Constant amplitude at ADCs input: carrier position during an equivalent current ramp of 10-310 mA.

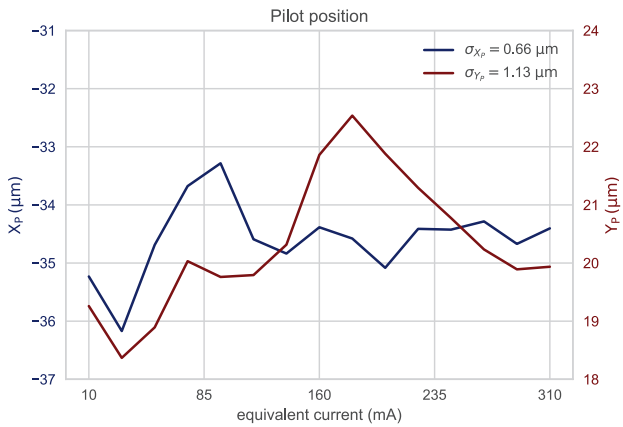

Figure 8: Constant amplitude at ADCs input: pilot position during an equivalent current ramp of 10-310 mA.

followed was to decrease the pilot amplitude while the carrier amplitude increased. An improvement in accuracy is clearly visible in Figures 7 and 8: in particular the standard deviation of the y coordinate has been reduced by a factor of 10, with values similar to the drifts with the real beam noted in Figure 5.

We measured the integral non-linearity of the ADCs using the same testbench. The results confirmed that the ADCs exhibit this behaviour, which, although better than the manufacturer's specifications, is large enough to affect the calculated position at micrometre scale.

CONCLUSION

In this paper we reported the correct functionality of the front end and also of the compensation on a machine different from Elettra. Sub-micron resolution and good long-term stability has been achieved on measurements performed at the Diamond storage ring. In addition, some issues related to the behaviour of the ADCs have been investigated, in particular the integral non-linearity. The latter is known to strongly influence beam position measurements, and its effects can be mitigated in several modes, such as controlling the amplitudes of the signals in order to coerce the ADC to work at an optimum level (automatic gain control, AGC).

However, the idea of maintaining constant amplitude at the ADC inputs by varying the pilot tone has been proven to be useful in reducing these unwanted effects. This technique can be considered as another tool that can help to achieve the desired linearity, particularly when a gain variation is not feasible (gain already at maximum).

Nevertheless, these analyses confirm once again that BPM systems are extremely sensitive to a wide range of parameters that cannot be overlooked. If a well-designed analog front end is mandatory to achieve the required performances, it needs to be coupled with an adequate digitizer in order not to lose most of the benefits gained from the former.

ACKNOWLEDGEMENT

We thank all the staff of Beam Diagnostics Group at Diamond for the support and the productive discussions during the measurements and the analysis of data.

REFERENCES

[1] G. Brajnik, S. Carrato, S. Bassanese, G. Cautero and R. De Monte, "Pilot tone as a key to improving the spatial resolution of eBPMs", *AIP Conference Proceedings*, vol. 1741, p. 020013 (2016).

[2] G. Brajnik, S. Bassanese, S. Carrato, G. Cautero, and R. De Monte, "A Novel Electron-BPM Front End With Sub-Micron Resolution Based on Pilot-Tone Compensation: Test Results With Beam", in *Proc. IBIC2016*, pp. 308–311, (2017).

[3] Linear Technology, LTC2209 Datasheet.

ISBN: 978-3-95450-192-2 doi:10.18429/JACoW-IBIC2017-TULAB1

DEVELOPMENT OF THE ELECTROMAGNETIC BOOM AND MOP SYSTEMS (EMOP)

A. Warner†[1], D. Cathey, G. Cullen, J. Nelson, Natural Science LLC., Big Rock IL, USA
P. Kasper, A. Lumpkin, Natural Science, LLC - Consultant
[1]also at Fermilab, Batavia IL, USA

Abstract

Several large-scale oil spills typically occur in the USA and other places around the world, and the Great Lakes are not immune from such threatening events. The clean-up process is inefficient and can have severe environmental impacts. An innovative, electromagnetic-based approach for oil spill remediation has been developed by Natural Science, LLC that uses micron-sized magnetite (Fe_3O_4) particles which are reusable, recoverable, and environmentally safe.

INTRODUCTION

In the past four decades, there has been an oil spill somewhere in the world each year, and in some years there are several. While many of these are small, larger spills are not uncommon. Though oil spills are inevitable, the techniques we use to combat them are choices based on available technologies, insight, and innovation.

Clean up of these spills is still largely inefficient, time-consuming, and expensive. One of the most widely used devices during an oil spill is the boom, which is supposed to provide a containment barrier for the spilled oil and to protect our shores. Although some effort has gone into the design of deployment mechanisms and designs aimed to improve the tow rates and buoyancies of these passive devices, no innovation has been made toward making these devices active. The ability to deploy a single device (system) that controls and efficiently removes spilled oil is a much-needed innovation to adequately protect and prepare for future oil spills worldwide.

In addition, standard oil booms and skimmer combinations generally target surface oil. However, a relatively recent complication is starting to emerge. The explosion in tar sands production in western Canada also means increasing amounts of heavy crude oil is making its way to the American Midwest via the Great Lakes. There is a growing concern regarding our ability to remediate spills for such heavy hydrocarbons that have the potential to sink. The magnetite particles used in our process have been demonstrated to target oil below the water surface. The particles will descend in pure water until they encounter and bond with oil. The electromagnetic field of our booms can extend some distance below the surface and will attract any magnetizable oil within its reach.

The likelihood for spills has increased over time, but environmentally safe methods of remediation, control and manipulation of oil have not been fully developed. The electromagnetic boom technology is a potentially game-changing advance [1]. The process works when micron-sized magnetite (Fe_3O_4) particles are dispersed in oil on water. The particles form a unique and preferential bond with the oil due to a combination of forces, dominated by the Van der Waals force. Magnetic fields can then be used to manipulate, trap and remove the oil with high efficiency. In the case of oil spills on water, the water becomes the primary transport medium for manipulating the oil. Both the particles and the oil are recaptured and separated for reuse. This process is being applied to electromagnetic systems that can replace and/or increase the efficiency of the passive boom and skimmer systems used today. In addition, the methods described can be used to remove oil from other surfaces and can target oil on the order of scale of the particles (micron scales).

THE FUNDAMENTAL CONCEPTS

The fundamental concepts involved in the seeding of oil with magnetite, the magnetic manipulation of the combination, the separation of the magnetite particles at the end of the process, and the magnetorheological effects are described in this section.

Seeding Process

This invention [2] provides a seeding process that preferentially targets oil on water by trapping the micron sized magnetite or iron oxide particles (the "particles") in the oil/water combination. The process is dominated by the Van der Waals force in the aqueous phase. The particles preferentially bond with the oil while passing through any water free of oil. As a result, this provides a method to determine where the oil is located at the micron scale (even when it is not visible to the naked eye). Figures 1 and 2 below illustrate the concept. The limiting scale is of the order of the size of the magnetite particles used. This method can therefore be used as a probe for targeting oil on water at the micron scale and above and thus

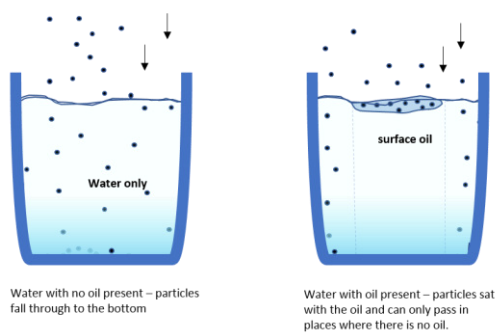

Figure1: Illustrating the fact that the particles preferentially stay with the oil.

† awarner@naturalscienceusa.com

ISBN: 978-3-95450-192-2 doi:10.18429/JACoW-IBIC2017-TULAB1

render it magnetic. The application of the appropriately designed magnetic fields can then be used to manipulate the oil and is described later.

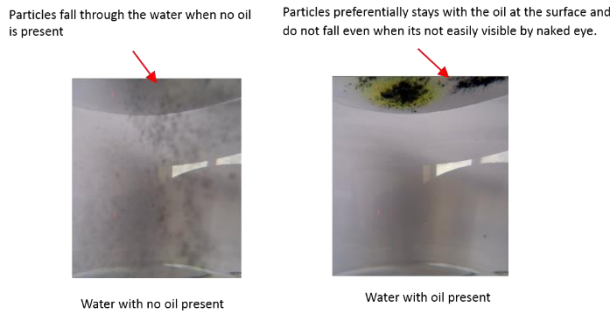

Figure 2: Magnetite particles preferentially bond with the oil when it's present in the water.

Magnetic Manipulation

Oil on water will typically diffuse outward as shown in Fig. 3 under its own viscous forces until it reaches an equilibrium. We demonstrate in Fig. 4 that this diffusion rate is reduced (or inhibited) as a consequence of the seeding process depending on the concentration of particles dispersed. In the absence of external forces, the parcel of oil is confined and can be controlled by magnetic forces.

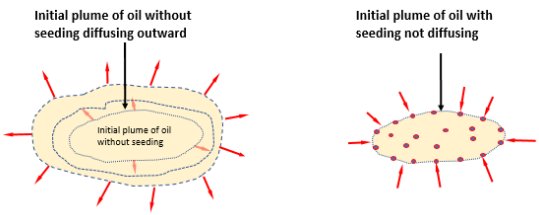

Figure 3: Illustration showing a parcel of oil diffusing outward without magnetite particles. The same parcel of oil does not diffuse outward if the particles are added.

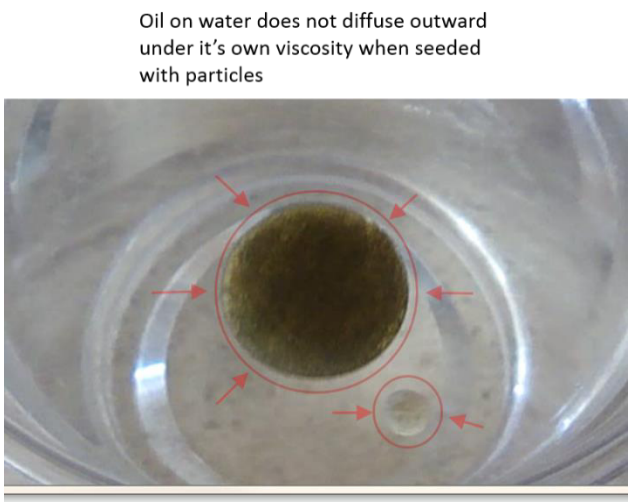

Figure 4: Oil seeded with magnetite is held from diffusing outward to cover the entire surface area as normally would when the particles are not present.

It is not necessary to uniformly distribute the particles to achieve confinement. The entire parcel of oil sits on water and moves when magnetic forces are applied as shown in Fig. 5. The water serves as the transport medium [3].

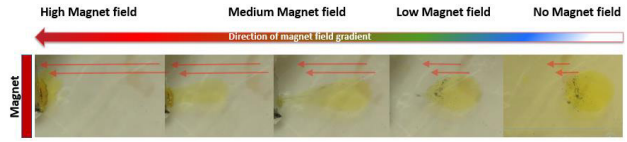

Figure 5: Snapshot of oil with a small amount of magnetite on water moving in the presence of a magnetic field. The arrows show the direction of the field gradient and the force direction.

Magnetic Separation

Due to the size of the particles and the nature of the bond with the oil, magnetic forces work well at moving the combination (oil + magnetite) on water. At the interface of the water with another surface (the container in this case) the friction and surface tension forces differ enough to extract the particles as they pileup at the boundary interface between the magnet and the water. The magnet can easily lift the particles from the water against this interface. See snapshot images below in Fig. 6.

Figure 6: Sequence of images illustrating the magnetic separation of the magnetite particles from the oil using a permanent magnet.

Magnetorheological Effect

When the particles are dispersed in oil on water or on any non-porous surface they are for the most part randomly distributed. In the presence of an applied magnetic field the particles will align themselves with the direction of the magnetic field.

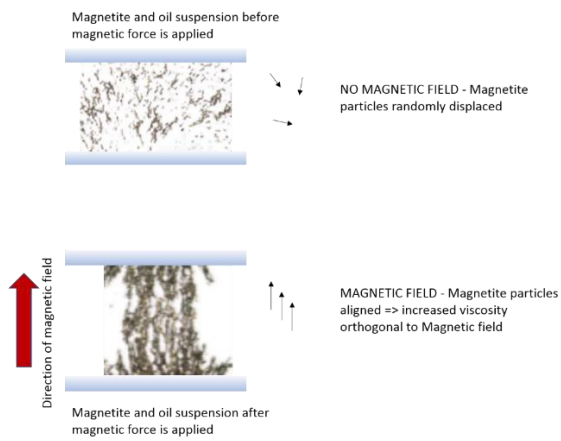

Figure 7: Oil and particles without the magnetic field and with a magnetic field present.

Each particle is essentially a very small dipole magnet in the presence of the external magnetic field. In addition to

ISBN: 978-3-95450-192-2 doi:10.18429/JACoW-IBIC2017-TULAB1

aligning with the field, they also attract each other. This directional alignment adds rigidity to the fluid combination (oil + magnetite) which enhances its viscosity effects orthogonal to the direction of the induced field. This induced viscosity effectively ("effective viscosity") produces the rigidity that allows the combination to be lifted either from water or from other surfaces. Figure 7 shows snapshot images of the combination before and after the magnetic field is applied.

DESIGN CONCEPT

We have demonstrated how oil moves on water when we add magnetite particles and apply a magnetic field. We are engineering a system that will automate the process by shaping the magnetic fields so that we can guide spill oil efficiently to a separation system where it is then collected, and the particles that were injected are removed for reuse. The system consists of modular boom structures made of solenoid magnets that are driven by a time dependent pulsed current. This current, which gradually grows stronger axially, is distributed along the boom creating a magnetic field gradient that attracts the magnetizable oil. The last solenoid in a module is coupled to a magnetic belt (conveyer ramp) system illustrated in Fig. 8. The boom, which has a Teflon-like exterior, traps and moves the oil along its axis. The rate at which this magnetized oil moves along the axis is directly proportional to the magnetic field gradient and viscosity of the spilled oil. The water acts as the medium for transporting the oil.

Once this magnetized oil moves along this electromagnetic boom it will eventually reach the belt that is magnetically coupled to the boom. Due to the angle of inclination of the belt system, the belt speed, and the magnetic force, any excess water drips off the belt system while it keeps the magnetized oil, delivering it to a separation container. This container (not shown) is designed with a yet stronger magnetic field at its base. The magnetite naturally goes to the strongest magnetic force and will stick to the bottom of the container while the oil and any remaining water separate. This allows for the magnetite to be reused and the oil to be removed. An animated demonstration is available here: http://www.naturalscienceusa.com/products.html.

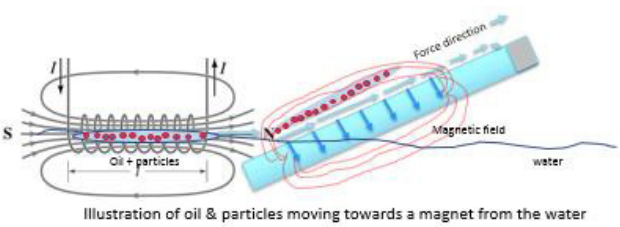

Figure 8: Simplified schematic of gradient solenoid and magnetic ramp system.

Pulsed Magnetic Field Concept

A traveling magnetic "pulsed-wave" gradient field system has been designed that produces the magnetic potential which attracts and moves oil on water. The system parameters are based on a stepped multiphase concept. The number of phases is chosen based on power consumption, flow efficiency, magnetic field strength, timing and the spacing of the magnets. This also includes the geometric factors associated with the magnets.

For the case of the solenoid magnets, chosen to produce a time varying magnetic gradient pulse that travels along its axis, the magnets are separated spatially by ~0.79 times the radius "R" of the coils. This spatial configuration provides gradient coupling between the coils because this spacing is less than the so called "Helmholtz spacing" for the coils. The dynamics of the system can be described in terms of the magnetic gradient of the configuration or analogously in terms of the magnetic potential of the configuration. The magnetic potential is proportional to the magnetic field squared. All of the parameters mentioned above are optimized to accommodate the magneto-fluid dynamics associate with oil flow on water in the presence of a magnetic force. This depends on the gradient of the magnetic force, the viscosity of the oil, drag force due to water and coupling among the particles in the oil.

The diagram in Fig. 9 shows a group of thin solenoid magnets that are pulsed in a 4-phase sequence. The resultant direction of flow is in the direction of the magnetic gradient which results from the pulse which moves to the right in the diagram. Figure 10 shows the magnetic potential, the flow direction, and the motion of the magnetic particle represented here by plus (+) signs.

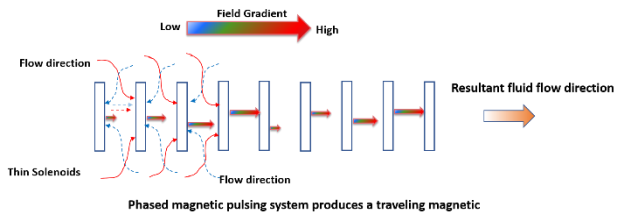

Figure 9: Illustration of a pulsed magnetic system of magnetics for moving oil along the axis from left to right.

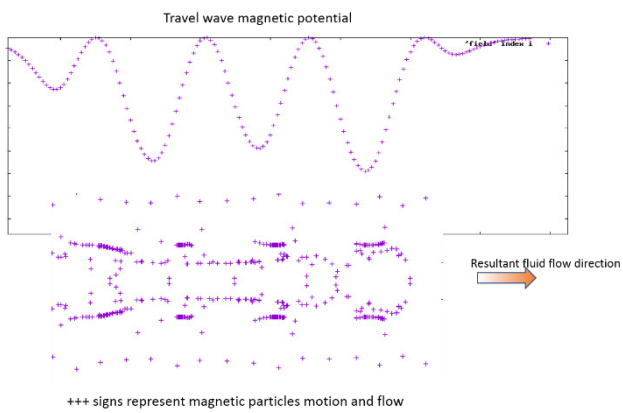

Figure 10: Magnetic potential and particle motion.

ISBN: 978-3-95450-192-2 doi:10.18429/JACoW-IBIC2017-TULAB1

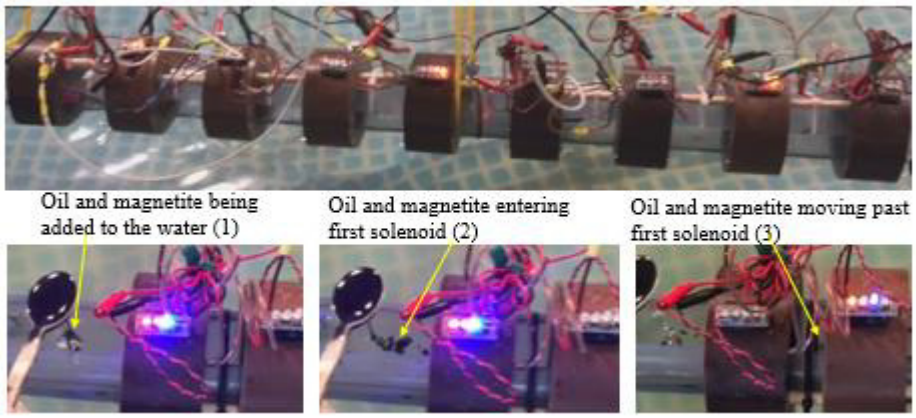

Figure 11: Sequence of images showing oil and magnetite moving.

Engineering Demonstration

An engineering test of the "pulsed wave" system was conducted with oil and magnetite at various concentrations in a test pool of water to optimize the dynamics and efficiency for fluid flow. Figure 11 shows a module consisting of 9 solenoids optimally spaced and powered to provide a traveling magnetic gradient. Three (3) snapshots of the flow are shown. The light emitting diodes (l.e.d.) on the magnets indicate the amplitude of the voltage across each solenoid and the timing of the pulse sequence for each magnet. In snapshot 1, the oil and magnetite particles which have already been mixed are poured into the water as the magnetic pulse is initiated at the first solenoid. Snapshot 2 shows the fluid flowing into the first coil, and snapshot 3 shows the time at which the first solenoid is turned off and the second one is turned on. The arrow points to the combination entering this second solenoid. This pattern of flow repeats as the combination travels along the axis of the system from magnet-to-magnet as the magnetic field gradient moves through the 9-magnet arrangement in a pulsed sequence.

Description of the Pulsed Wave Sequence

Each magnet in a module goes through an identical on/off cycle governed by four variables illustrated in Fig. 12.

- The ramp time, T_{ramp}, mentioned above is the time it takes for the magnet to turn on or off and is fixed at 0.1319 s in our example.
- The peak time, T_{peak}, is the time in which the solenoid is at its peak current of 25 amps for this case.
- The off time, T_{off} is the time between pulses
- The delay time, T_{delay}, is the time between the start of a magnet's power cycle and the start of the next magnet's power cycle.

We also define a magnet's on time, $T_{on} = T_{ramp} + T_{peak} + T_{ramp}$, as the total time in which the magnet receives power, and the power cycle period $T_{period} = T_{on} + T_{off}$. In order to produce a chain of magnetic dipole fields that move from one end of a string of magnets to the other, T_{delay} must divide evenly into T_{period}. The optimum separation between the dipole fields occurs when $T_{on} = T_{off}$. This was verified to be the cases where $T_{delay} = T_{on/2}$, $T_{on/3}$, and $T_{on/4}$.

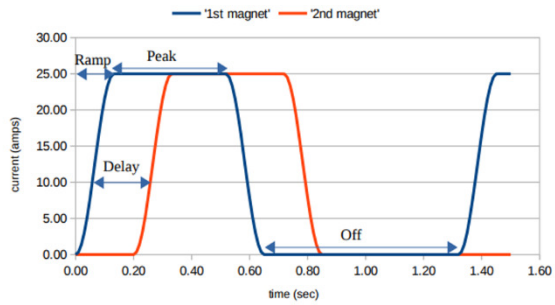

Figure 12: A schematic plot of current versus time indicating the different time variables.

THE EMOP SYSTEM

The system will be modular and scalable. The final size and scale of the boom modules will be determined by the power and gradient optimization calculations. However, preliminary calculations suggest a starting size of 18 inch (0.45 m) O.D. x 60 inch (1.52 m) long would be adequate to demonstrate the principle. The maximum magnetic field on axis and the maximum achievable gradient should be optimized with all the functional requirements considered.

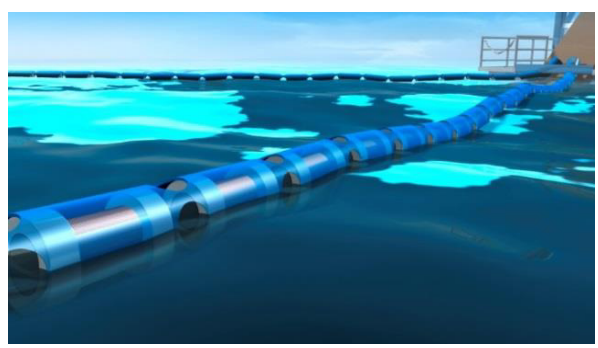

Figure 13: Modules combined to form electromagnetic boom.

ISBN: 978-3-95450-192-2 doi:10.18429/JACoW-IBIC2017-TULAB1

A visualization of the design concept for a configuration with several modules is shown in Fig. 13, and a cut-away of a standard module is shown in Fig.14.

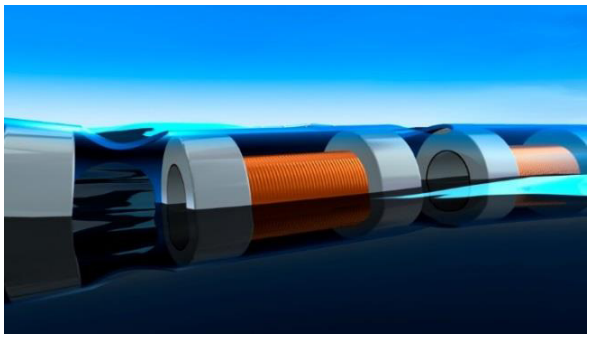

Figure 14: Cut-away view of a standard module.

The electromagnetic boom system with separator will involve a unique set of capabilities compared to passive boom technology. The main aspects are: (1) the fundamental effects of the gradient of the boom solenoid fields on magnetized oil flow rate, (2) the pulsing of the field strength through the boom for "pumping action", (3) dispersal of the magnetite, (4) the efficacy of the magnetized conveyor belt coupled to the boom (see Fig. 15), and (5) the separation efficiency in the collection area for oil and magnetite. However, the bottom line will still be quantifying oil removal efficiency by comparing the collected separated oil volume to the initial spill oil volume. Another critical aspect will be the rate of recovery where the dynamics may be affected by temperature, oil viscosity, field gradient, conveyor belt speed, and other factors. These results can be compared to passive skimmer technology results previously obtained.

Figure 15: Schematic of collector and separator component of the system.

SUMMARY

In summary, we have described the fundamental concepts including the process that renders the oil magnetizable and susceptible to manipulation and control by gradient magnetic fields. We have also shown the model and the engineering test for a system based on gradient solenoidal coils. These provide the bases for the scalability of an electromagnetic boom system capable of remediating an oil spill on water. The technique uses micron-sized magnetite or other iron oxide particles which are recoverable, reusable, and environmentally benign compared to chemical dispersants.

PATENTS

[1] A. Warner, Inventor, "Electromagnetic boom and environmental cleanup applications for use in conjunction with magnetizable oil", US patent 8,795,519, Aug. 5, 2014.

[2] A. Warner, Inventor, "Electromagnetic boom and environmental cleanup applications", US patent 9,249,549, Feb. 2, 2016.

[3] A. Warner, Inventor, "EMOP applications", US 14/947,201, May. 26, 2016.

ISBN: 978-3-95450-192-2 doi:10.18429/JACoW-IBIC2017-WE1AB1

THE SPS WIDEBAND FEEDBACK PROCESSOR: A FLEXIBLE FPGA-BASED DIGITAL SIGNAL PROCESSING DEMONSTRATION PLATFORM FOR INTRA-BUNCH BEAM STABILITY STUDIES

J. E. Dusatko#, J. D. Fox, C. H. Rivetta, O. Turgut (SLAC National Accelerator Laboratory, Menlo Park, California USA), E. Bjorsvik, W. Höfle (CERN, Geneva Switzerland)

Abstract

A flexible digital signal processing platform based on FPGA technology has been developed for vertical intra-bunch beam stability studies at the CERN SPS. This system is unique in that samples at a very high rate (4GSa/s) in order to measure and control motion within the 1.7ns proton beam bunch. The core of the system is an FPGA-based digital signal processor. Being programmable, it enables fast development of control algorithms. The processor, together with its supporting components forms a complete platform for demonstration studies of beam instability measurement and control. This system is capable of operation as either a stand-alone arbitrary waveform generator for driven mode instability studies, a closed-loop feedback control system for stability control and as a diagnostic instrument for measurement of beam motion. Recent measurements have shown the system is effective at damping single-bunch and bunch train intra-bunch instabilities with growth times of 200 turns. This paper summarizes the system design, provides some operational highlights, describes the upgrades performed to date and concludes with a description of the next generation processor now in development.

INTRODUCTION

The CERN Super Proton Synchrotron (SPS) accelerates protons for injection into the LHC. Control of performance-limiting transverse vertical bunch beam instabilities is normally handled a by dedicated transverse damper system [1]. For the planned High Luminosity LHC Upgrade (HL-LHC) [2], concerns have arisen that with the higher beam intensities, transverse intra-bunch motion driven by transverse mode coupling instability (TMCI) and the electron cloud instability (ECI), may become a limiting factor in the luminosity of the upgraded LHC [3,4]. Transverse beam instabilities within the SPS are being addressed in three ways: machine lattice configuration, vacuum chamber coating with amorphous carbon and active electronic feedback control, which is the role of the wideband feedback system (WBFB).

The hardware details of this system are described in another publication [5], presently we describe the design of the system with a focus on the signal processor.

SYSTEM DESCRIPTION

The comprehensive Wideband Transverse Feedback System (WBFB) consists of an ensemble of components. The system block diagram is shown in Figure 1.

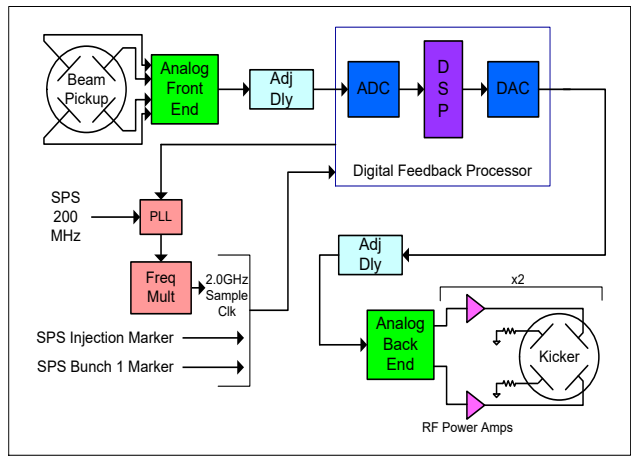

Figure 1: System Block Diagram.

DIGITAL FEEDBACK PROCESSOR

The Feedback Processor is designed as a general-purpose digital signal processing system with integrated data converters. A block diagram is shown in Figure 2. An FPGA implements all of the data formatting, system control and signal processing functions, as well as ancillary/support functions (e.g. control of the input trigger comparator threshold DACs). This is the most complex subsystem. Its functions and design will now be described.

Feedback Mode

In feedback mode, the processor can selectively compute corrections for [1…64] bunches or [1…32] scrubbing bunch doublets [6]. In non-doublet mode a 5ns sample window across the bunch takes 16 samples or slices (these parameters are 2x for doublets). The current control algorithm treats each slice as an independent signal and applies a non-recursive Finite Impulse Response (FIR) digital filtering function to that signal. Thus there are 16 FIR filters for each bunch, the filters have identical coefficients and are 16 taps long. The FIR filter is expressed as:

$$y(n) = \sum_{k=0}^{15} h(k)x(n-k)$$

*Work supported by the U.S. Department of Energy under contract DE-AC02-76SF00515, the US LHC Accelerator Research program (LARP), the CERN LHC Injector Upgrade Project (LIU) and the US-Japan Cooperative Program in High Energy Physics.
#jedu@slac.stanford.edu

ISBN: 978-3-95450-192-2 doi:10.18429/JACoW-IBIC2017-WE1AB1

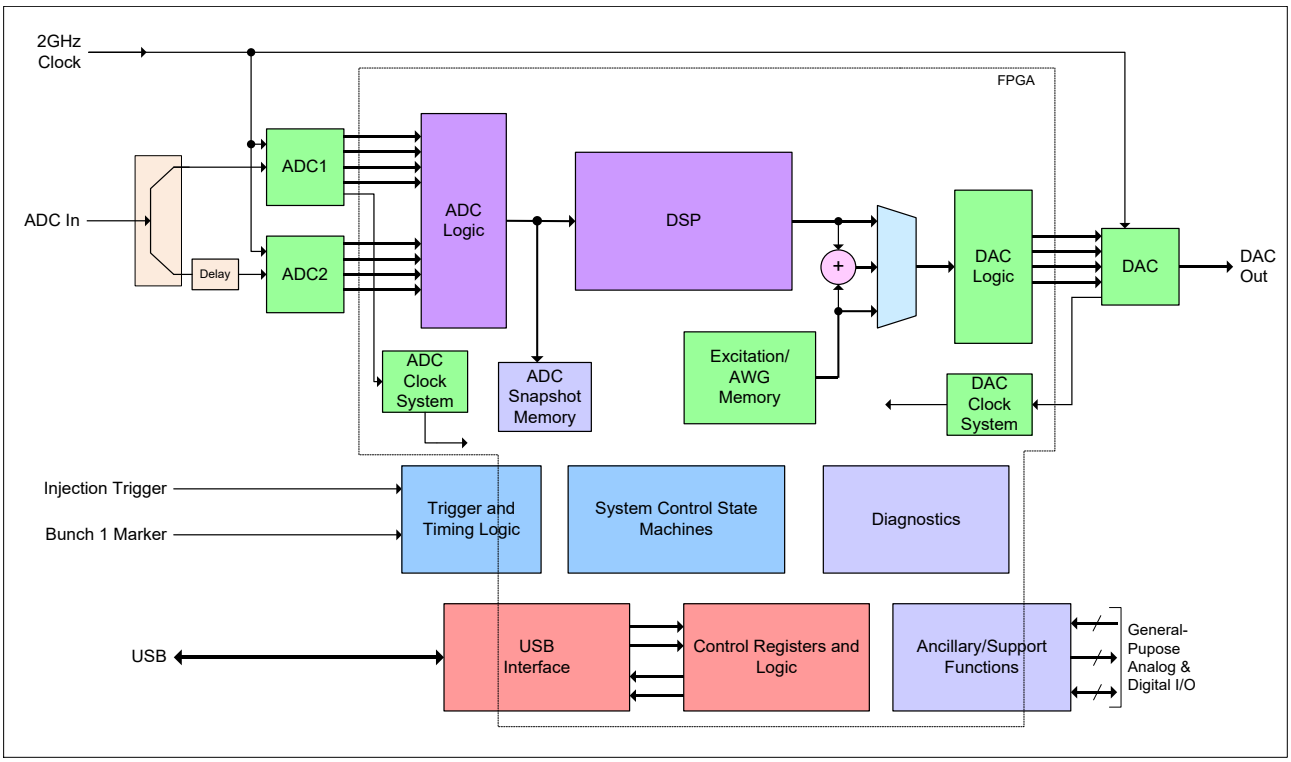

Figure 2: Feedback processor block diagram.

The coefficients are loadable from a configuration file. A useful feature is the ability to program the filter between two coefficient sets based on counting the number of ring fiducials. This allows us to "swap" the coefficients, selectively applying a different feedback mode (e.g. positive, then negative) for a programmable period of time

This is very useful for grow/damp studies where the beam can be dynamically driven into instability and then damped, simply by swapping coefficient sets.

Excitation Mode

For driven mode studies, the system can act as arbitrary waveform generator by loading its excitation memory with any desired sequence (e.g. chirps, spatial shaping, etc.) and playing it out based on programmed timing parameters. The waveform memory is loaded from an external file, and selectively drives a single bunch.

Special Modes

A variant of Feedback and Excitation mode, called Feedback Excitation Combined (FEC) is available that allows both modes to run in parallel for driven feedback studies. The feedback and excitation signals are numerically summed before being sent to the DAC. This eliminates the need for a separate excitation system.

Another special mode provides the ability to selectively control the gain of each individual slice over a range of [+1…-1] to allow unique gain (and sign) of feedback for each slice.

A selective mode has been added to compensate for the long tail present in the transient response of the RF power amplifiers, which can interfere with the next beam bunch. Compensation is accomplished by adding in a pre-amble, post-amble or split pre-/post-amble to the output DAC waveform. These added components act to upconvert the low frequency information onto a higher frequency carrier. The waveform is then sampled by the beam and mixed back down to the low frequency. This mode has been verified in operation.

Diagnostic Features

While driving and controlling the beam are the central functions for the feedback processor, it is also crucial to study the bunch motion directly as a diagnostic. The system includes a snapshot memory that can record all 16 samples from one selected bunch over many (up to 65536) turns. A future upgrade will use on-board DDR3 memory for recording of multiple bunches over many turns.

Hardware Design

The feedback processor is designed with combination of commercial and custom components. A commercial FPGA motherboard (Dini Group, Inc DNMEG_V6HXT, Figure 3.) was selected that offered high-density I/O connectors. The board contains a Xilinx XC6VHX565T FPGA device. Though optimized for high-speed serial I/O, it contains 566K logic cells, with a smaller complement (864) of DSP slices. The motherboard also contains provision for a DDR3 memory DIMM.

ISBN: 978-3-95450-192-2 doi:10.18429/JACoW-IBIC2017-WE1AB1

The DAC device used is a Maxim Semi MAX19693 4GSa/s 12-bit device (used in 8-bit mode) it accepts four parallel LVDS data streams. It is designed onto a custom daughterboard, which also contains a USB2.0 interface used to communicate with the host computer, trigger input conditioning circuitry, diagnostic strobe output circuity, clock circuitry as well as general-purpose low speed digital and analog I/O. It interfaces to the FPGA motherboard, via a high-density connector.

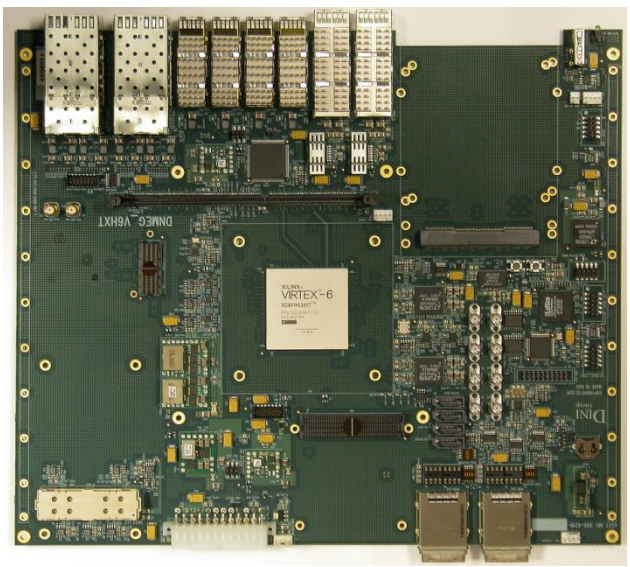

Figure 3: Commercial FPGA motherboard.

Analog to digital conversion at 4GSa/s was not common place when the feedback processor was originally designed. This was accomplished by time-interleaving two Maxim Semi MAX109 2GSa/s 8-bit ADCs, each with 2.2GHz of analog bandwidth. Time interleaving is accomplished by splitting and delaying the ADC analog signal on one leg by one half the sample clock period. Each ADC outputs four parallel LVDS streams. Time and budget constraints did not allow a custom board to be designed. Instead, two MAX-109EVB evaluation boards were used with a custom high speed coaxial parallel cable assembly developed in collaboration with the Samtec corporation.

Gateware Design

The FPGA implements a major portion of the system functionality. A convenient consequence of this is ease of reconfigurability. All development is done in VHDL. The design can be roughly broken down into three major sections: signal dataflow/processing, diagnostics and control & support.

The dataflow section is a pipeline structure that receives the ADC data, formats it, computes the correction and then reformats it for the DAC output. The pipeline, located inside the DSP block is buffered by two FIFO memories at the input and output with the processing algorithm in the middle. Clock domain crossing between the ADC and DAC is handled by the output FIFO. The design is structured so that the processing algorithm can be easily plugged/un-plugged in the system.

The current signal processing algorithm is a multichannel bank of 16, 64-channel, 16-tap FIR filters. All data is processed in 8-bit, two's complement format. Fitler coefficients are 8-bits as well, producing a 20-bit computational result. A shift gain/saturation block is used to programmably scale the filter result to the 8-bit DAC window and handle over- and under-flow properly by saturating full-scale in the appropriate direction.

The diagnostic section contains the snapshot and excitation memories as well as timing diagnostics (e.g. detect missing fiducial trigger). Both memories are implemented with on-chip SRAM. The FPGA motherboard has provision for up to 16GB of DDR3 memory, which we plan to use for deep snapshot recording of multiple bunches.

System control is handled by a hierarchy of three state machines. The master state machine receives the trigger markers, counts the fiducial pulses and directs and sequences the operation of the two other units which control the ADC/DSP and DAC, respectively. A set of memory mapped control and status registers are exposed through the USB2.0 interface. A limiting factor in the transfer of large datasets to and from system is the USB bottleneck, plans exist to implement an 1Gbps Ethernet interface to alleviate this.

Software Design

As in any modern electronic system, much functionality is implemented via software. The WBFB software design is broken into two categories: hardware interface & control and offline applications for configuration and analysis.

The interface to the system is implemented in Microsoft Visual Basic (VB), which connects to the hardware via USB driver calls. VB has proven to be a fast, simple way to implement complex functions in a GUI-based environment. System setup is simplified using a text-based configuration file loaded at system startup. The passing of setup information (filter coefficients, excitation data, etc.) and snapshot data is facilitated using text-based files. These files are auto-generated by the offline and VB applications, respectively.

The offline applications are developed using Matlab. Several applications exist to enable the design of excitation waveforms, digital filter functions, snapshot data viewing and in-depth signal analysis. These applications exist as both GUI-based and command line tools.

OPERATIONAL HIGHLIGHTS

The WBFB system has been used in multiple Machine Development (MD) studies at the SPS [7-9]. In these studies, beam dynamics were measured in different situations: driven-mode only with no feedback, driven-mode with feedback, positive and negative feedback and specical configurations of the SPS lattice where conditions were created to enhance bunch instabilities. Both single- and multi-bunch dynamics were studied. In driven-mode

ISBN: 978-3-95450-192-2 doi:10.18429/JACoW-IBIC2017-WE1AB1

studies, we have been able to demonstrate excitation of low mode intra-bunch instabilities by either driven excitation or positive feedback, followed by damping of those instabilities.

Using ADC snapshot data taken during a June 2016 MD at the SPS, Figure 4 shows a multibunch case zooming in on bunch 71 of batch 4 of a typical LHC fill. The top graph shows the no feedback case: the bunch becomes

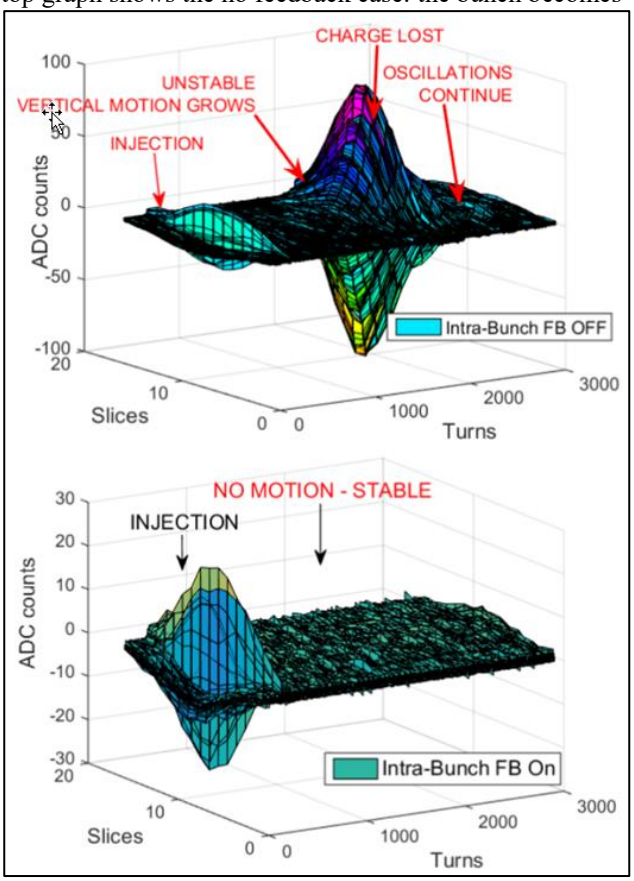

Figure 4: Feedback effect on bunch stability.

unstable after injection, oscillating in mode 0, growing in amplitude, eventually losing charge but still remaining unstable. The second graph shows the same scenario, but with feedback turned on: the bunch injection transient starts to oscillate just after injection, but is quickly damped after approximately 200 turns and the bunch remains stable. Additionally these measurements provide useful data for our simulation and modelling efforts [10].

UPGRADES AND NEXT GENERATION

With the successful demonstration of the WBFB, several upgrades are proposed to enhance performance and usefulness. In addition to the aforementioned DDR memory and Ethernet interface upgrades, we plan on adding an active bunch orbit offset rejection mechanism to extend the dynamic range of the ADC. We plan on upgrading the FPGA motherboard to allow control of the full SPS ring as well as explore different processing algorithms (IIR filter structures, observer based MIMO feedback controllers, etc.). The latter requires extensive matrix calculations which could be implemented using high-level signal processing design tools such as Xilinx System Generator which allows the designer to draw the algorithm in Simulink and compile that into an FPGA block.

Semiconductor technology has improved to the point where it is now possible to increase the system sampling rate to 8GSa/s. This opens up multiple possibilities such as more detailed diagnostics, dual sensor controller architectures, etc. To this end, a prototype 8GSa/s system has been designed similarly using a combination of commercial and custom components. The ADC uses two time-interleaved e2v Inc. EV10AQ190AD 12b, 5GSA/s devices and the DAC device used is a Euvis Inc. MD662H 8GSa/s 12b device. Each data converter device exists on evaluation boards which interface to a commercial Xilinx Virtex-7 FPGA (higher capacity) motherboard. The ADCs require a custom interface board, which has been designed. The PCB fabrication and FPGA development are

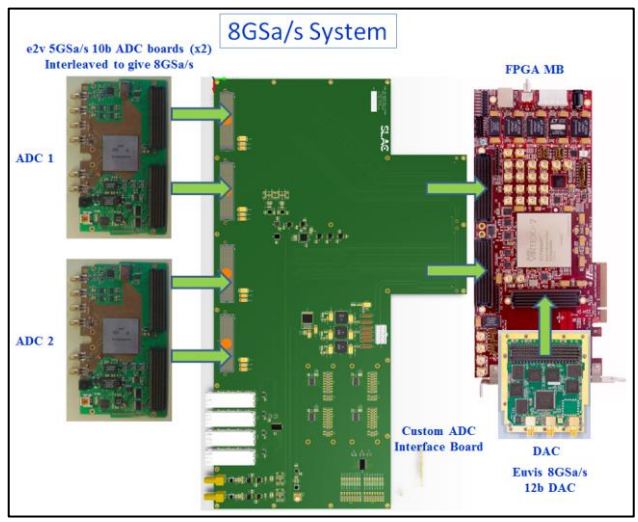

Figure 5: 8GSa/s Prototype System.

awaiting funding to proceed. Figure 5 shows a pictorial view of the 8GSa/s prototype system components.

ACKNOWLEGEMENTS

At CERN, we wish to thank Urs Wherle for his contributions and support in integrating the WBFS into SPS. We thank Hannes Bartosik, Gerd Kotzian, Tom Levens and Kevin Li for their assistance during the recent SPS MDs. At SLAC, we wish to thank Jeff Olsen for developing the VB GUI software and Chuck Yee for his diligence in PCB layout and WBFS chassis design.

REFERENCES

[1] G. Kotzian, "The SPS Transverse Damper" https://indico.cern.ch/event/510321/contributions/2281341/attachments/1339512/2016638/160920_SPS_Transverse_Damper_gkotzian.pdf

[2] J. Coupard *et.al.*, "LHC Injectors Upgrade Technical Design Report – Volume 1: Protons," CERN Document, 15-December-2014, CERN-ACC-2014-0337.

ISBN: 978-3-95450-192-2 doi:10.18429/JACoW-IBIC2017-WE1AB1

[3] G. Arduini *et.al.*, "Beam Observations With Electron Cloud In The CERN PS & SPS Complex" ECLOUD04 Proceedings, 2004.

[4] E. Shaposnikova, "Intensity Upgrade Plans for CERn-LHC Injectors", 42nd ICFA Advanced Deam Dynamics Workshop, Nashville, Tenn., USA, 2008, CERN-AB-2008-065

[5] J. Dusatko *et.al.*, "The Hardware Implementation of the CERN SPS Ultrafast Feedback Processor Demonstrator" IBIC2013, Oxford, UK, paper MOPC28, pp. 124-127.

[6] G. Iadarola *et.al.*, "Recent Electron Cloud Studies in the SPS" IPAC2013, Shanghai, China. paper WEPEA014, pp. 2525-2527.

[7] C. Rivetta *et.al.*, "Control of Intrabunch Dynamics at the CERN SPS Ring Using 3.2GSss Digital Feedback Channel" PAC2013, Pasadena, CA, USA. paper FROAA3, pp. 1430-1433.

[8] J. D. Fox *et.al.*, "Wideband Vertical Intra-Bunch Feedback at the SPS – 2015 Results and path Forward" IPAC2015, Richmond, VA, USA, paper TUAC2, pp. 1353-1355.

[9] J. D. Fox *et.al.*, "Control of Intra-Bunch Vertical Instabilities at the SPS – Measurements and Technology Demonstration" IPAC2017, Copenhagen, Denmark, paper TUPIK119, pp. 2005-2007.

[10] O. Turgut *et.al.*, "Identification of Intra-Bunch Transverse Dynamics for Model Based Feedback Control at the CERN Super Proton Synchrotron" IPAC2015, Richmond, VA, USA, paper MOPWI041, pp. 1249-1252.

ISBN: 978-3-95450-192-2 doi:10.18429/JACoW-IBIC2017-WE2AB3

A NANOFABRICATED WIRESCANNER: DESIGN, FABRICATION AND EXPERIMENTAL RESULTS

M. Veronese*, S. Grulja, G. Penco, M. Ferianis, Elettra-Sincrotrone Trieste, Trieste, Italy
S. Dal Zilio, S. Greco[1], M. Lazzarino, IOM-CNR Laboratorio TASC, Basovizza, Trieste, Italy
L. Fröhlich, Deutsches Elektronen-Synchrotron DESY, Hamburg, Germany
[1] also at Graduate School of Nanotechnology, University of Trieste, P.le Europa 1, Trieste, Italy

Abstract

Measuring the transverse size of electron beams is of crucial importance in modern accelerators, from large colliders to free electron lasers to storage rings. For this reason several kind of diagnostics have been developed such as: optical transition radiation screens, scintillating screens, laser scanners and wirescanners. The last ones although providing only a multishot profile in one plane have proven capable of very high resolution. Wirescanners employ thin wires with typical thickness of the order of tens of microns that are scanner across the beam, whilst ionizing radiation generated from the impact of the electrons with the wires is detected. In this paper we describe a new approach to wirescanners design based on nanofabrication technologies. This approach opens up new possibilities in term of wires shape, size, material and thickness with potential for even higher resolution and increase flexibility for instrumentation designers. We describe the device, the fabrication process and report measurement performed on the FERMI FEL electron beam.

INTRODUCTION

It is of importance for a wide variety of accelerators to have accurate control of machine optics to reach the desired high electron densities. This task is accomplished with the help of transverse profile instrumentation. Through the decades several concepts of transverse profile instrumentation has been explored depending on the specific parameters of the accelerator and the resolution requirements. Two of the most extensively deployed in electron accelerators are imaging screens and wirescanners (WSC). The imaging screens are capable of providing a two dimensional profile in a single shot but have resolution hardly better than 10 µm (scintillator screens) [1]. In the case of a metallic screen emitting transition radiation they may be plagued by coherent optical transition radiation (COTR) [2]. The wirescanners on the other side can provide only one dimensional multishot measurement of the profiles but can reach better resolution than screens. Typical WSC detection is based on measurement of the ionizing radiation dose produced by the electron beam hitting the wires. For high brightness electron beams where the beam sizes are below 100 µm, the wirescanner designer has the possibility to choose amongst wires of different materials, such as: tungsten, aluminum and carbon [3–5], and wire diameter to reach the needed compromise between signal, resolution and mechanical robustness. For a detection based on ionizing radiation the larger the atomic number and density of the material the larger the signal. The mechanical robustness of the wires equipped diagnostics is mostly related to the vibrations induced by the motorized actuator used for the scan while beam induced heating may be an issue mainly for high repetition rate machines. The resolution of a measurement performed with a wire of diameter d corresponds to the r.m.s. of the cylindrical distribution i.e. $d/4$ [5]. In practice the diameter of the wire is typically limited to about 5 µm. In this paper we describe a novel device manufactured using nanofabrication techniques providing several potential benefits in terms of instrumentation design including the potential for sub-micron resolution.

DEVICE DESIGN

The basic idea is to create thin bridges across a robust frame. By nanofabrication these structures can be made thinner and narrower than a traditional wire. For this purpose we use a silicon substrate (thickness 500 µm) coated by 2 µm low stress silicon nitride (SiN) film. After the patterning the SiN coating with suitable structures, the etching of the substrate allowed the release of suspended structures bridged on a 3x9 mm free window. The structures made in this way have a rectangular cross section and from now on we will refer to them as nanofabricated wires (NF wires). Their width w determines the resolution. It can be demonstrated that the r.m.s. of a rectangular distribution is $w/\sqrt{12}$. With nanofabrication the width can made as small as 0.5 µm and thus the resolution can potentially reach 0.15 µm. The energy loss per unit thickness of a high energy electron beam scales with the square of the atomic number Z of the target material and is linear in its density ρ [6]. While in general more signal is better, for potential applications such as intra undulator diagnostics having a lower ionizing dose is a beneficial property. SiN has a low density of $\rho(Si)$ =3 gcm^{-3}). Considering $Z(Si)$ = 14 and that $Z(N)$ = 7 an effective atomic number can be calculated for SiN according to [7] to be $Z(SiN)$ = 12.5. on the basis of this two quantities a first approximation of the relative yield between wires can be calculated. Considering for example a NF wire of width of 10 µm and a thickness of 2 µm the dose generated by a 2x10 µm SiN NF wires is calculated to be 929 times less the one generated by a 10 µm tungsten wire ($Z(W)$ = 74, $\rho(W)$ =19.35 gcm^{-3}).A comparison between cylindrical wires and NF wires can be found in Table 1. A benefit of the NF wires compared to a traditional

* marco.veronese@elettra.eu

ISBN: 978-3-95450-192-2 doi:10.18429/JACoW-IBIC2017-WE2AB3

wires is that the ionizing yield can be chosen independently from the desired resolution. In our device, for example, we made a coating of silver with thickness of 0.5 µm on both sides of the device. The Ag film increases the device dose emission of about an order of magnitude without changing the resolution.

Table 1: Relative Ionizing Radiation Dose of Wires

Type	Dimensions	Material	Rel. Yield
Wire	10 µm	W	929
Wire	5 µm	Al	1
Bridge	0.5/2/0.5x10 µm	Ag/SiN/Ag	26.7
Bridge	2x10 µm	SiN	0.84

IONIZING RADIATION SIMULATIONS

A simulation with the Monte Carlo particle tracking code Fluka [8, 9] has been performed to compare the radiation field created by the four wire types described in Table 1. The simulation contains exclusively electromagnetic interactions and tracks electrons and positrons down to a kinetic energy of 20 keV, photons down to 5 keV. The simulated electron beam has a Gaussian profile of σ =50 µm and no divergence. It hits the wire centrally at z=0. For the sake of simplicity, the rest of the simulation space is empty (vacuum). The first relevant finding is that the electron and not the photons are dominating the ionizing radiation dose. This means that the approximation used in Table 1 is not valid. A second aspect is related to the amplitude of the cross sections involved which is small. This means that also the divergence of the ionizing shower of primary electrons is small. to better understand all the relevant aspects of dose emission simulations have been carried out. The Figure 1 depicts the equivalent dose delivered in the plane orthogonal to the electron beam and set at 10 meters downstream the impact point. The simulation evaluates almost the same dose for 2 µm SiN NF wire vs the 5 µm Aluminum wire. It predicts 7.5 time higher dose for the Ag/Si/Ag NS wire and about 175 times higher dose for the 10 µm tungsten wire.

DEVICE FABRICATION AND CHARACTERIZATION

The device used in the experiment has been fabricated at IOM-CNR Laboratory in Trieste. The fabrication process has been completed starting from a double polished Silicon wafer substrate (500 um thickness) coated by LDCVD low stress SiN film (2000 nm) and DC Sputtered chromium (100 nm). Suitable pattern has been produced on coated optical resist (MEGAPOSIT SPR220 1.2) by classical UV lithography process, defining on one side the windowing structure and, on the other one, the bridged wires. Following wet etching protocol allowed to reproduced the pattern on the Cr thin film, exploited as a mask for high aspect ratio dry etching ICP-RIE process for the removal of exposed SiN layer. The sample have been transferred in KOH wet etchant

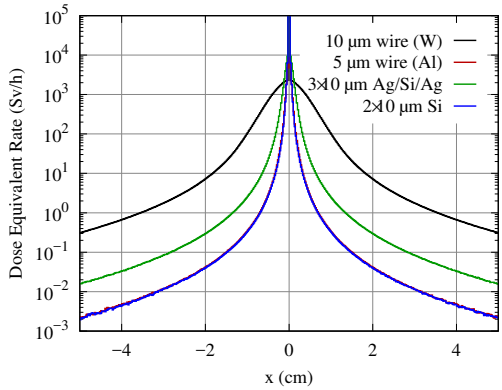

Figure 1: Cross sectional distribution of ionizing radiation dose for different wires at a distance of 10 meters from the impact point.

solution (33% in wt, 75°C) in order to selectively remove the Si substrate and complete the release of the suspended SiN wire. Well set protocol has been implemented in order to dry the samples avoiding the damage of obtained structures. The following metal coating step has been performed by thermal metal evaporation of selected material: in order to reduce the stress induced by metal film, the deposition has been done on both the device sides. The fabrication process just described was applied to obtain suitable for a proof of principle test. For this test only the horizontal projection of the bunch transverse profile was of interest. For this purpose the device was fabricated with five parallel bridges each at a distance of 1.5 mm from the other. The length of the bridges are 3 mm and their width is: 20.6 µm, 13.5 µm, 6.7 µm, 4.5 µm. The larger bridges were intended for initial setup of the measurement. While the thinner for performance assessment.

In Figure 2 a scanning electron microscope (SEM) image of a 10 µm bridge is reported to show the high quality of the fabrication process.

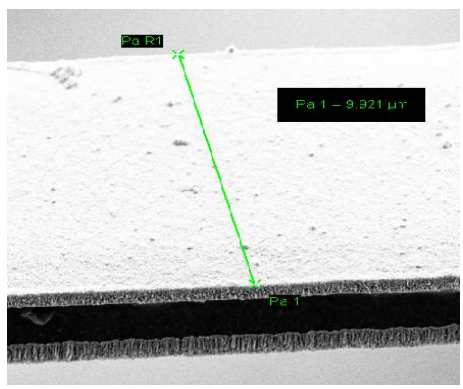

Figure 2: Scanning electron image of a 9.9 µm NF wire.

EXPERIMENTAL SETUP

The experiment was conducted at the FERMI FEL in Trieste (Italy) [10]. The device described in the previous section

ISBN: 978-3-95450-192-2 doi:10.18429/JACoW-IBIC2017-WE2AB3

was installed in the intra undulator imaging screen n.4 of the FEL1 undulator chain [11]. The main reason for this choice is the in situ capability of comparison with high resolution screen, the availability of a motorized actuator fitted with independent optical encoder for wire scanning and the availability of ionizing radiation detectors. Moreover both the high energy and the low beta optics in this machine position produce electron beam sizes of the order of 100 µm that are ideal for the measurements. Finally the chosen location was also suitable for an initial evaluation of compatibility of such a device with the operation of the accelerator for what concerns the damage to the undulators. During the experiment the FERMI beam charge was of 700 pC, and the energy of 1.285 GeV. Figure 3 shows a layout of the FERMI FEL1 area involved in the experiment. The ionizing radiation detectors installed in the FELs region are of two types: Cherenkov fibers and ionization chambers. They are part of the machine protection system (MPS) of FERMI [12] and were used as measurement devices. The Cherenkov fibers run along the entire undulator vacuum chamber. The light produced by high energy particles hitting the fiber is transferred out of the tunnel to an optical to electrical conversion unit based on MPPC detector. The electrical signal is then acquired by means of a VME ADC board with 12 bits resolution and 250 Msamples/s sample rate. The ionization chambers are installed in the vicinity of each imaging screen chamber. The ionization chambers are filled with air at atmospheric pressure and connected to the controller which supplies the high voltage (1 KV) and acquires the signal via an embedded picoammeters. The ionizing chamber (IC4, Ic5 and IC6) are depicted in figure as green rectangles. As an addition for the experiment we installed a spool of Cherenkov fibers at about 12 meters downstream the NF wires.

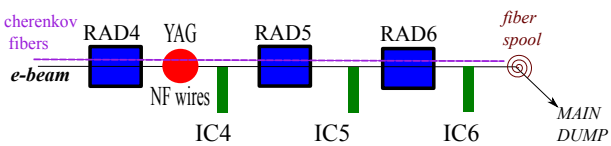

Figure 3: Experimental layout. The ionizing chamber are in green. The imaging screen diagnostics chamber containing the YAG and the NF device are depicted as red circle. The FEL radiators are in blue.

MEASUREMENT RESULTS

The signal detected from the ionizing shower induced by the NF wires is rather small. To obtain the best signal to noise ratio, we took care that both optics and trajectory in FEL1 were optimal, to avoid any beam scrapering which would cause a background in our measurements. Considering a vertical beam size of 100 µm this means that the vertical aperture of 3 mm is about 30 times the vertical size. So no core electrons are expected to contribute to the background. On the other side vertical halos due to wakefields may become relevant. The signal from the halos can potentially become of the same magnitude of a 10 µm wire if the halo size is so large to hit the frame. We took care during the measurements to verify that the contribution from the halos was suppressed. Figure 4 shows the beam losses signal measured by the Cherenkov fibers, while scanning the NF wires position with a step of about 25 µm. The scanning step was chosen in relationship with the expected beam spot size of few hundred microns. Each data point plotted in the figure corresponds to the average over five consecutive shots and the error bars are the standard deviation. Concerning

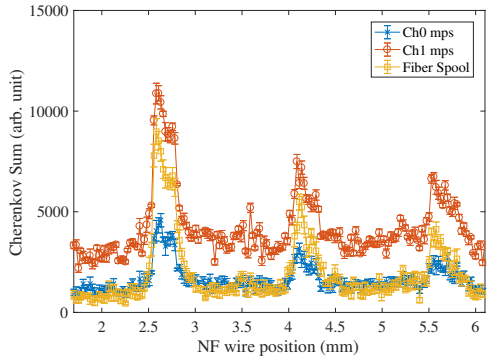

Figure 4: Beam losses signal from three wires acquired by the Cherenkov fibers diagnostics.

the Cherenkov fibers, we report the peak and the integrated signal for each wire position. Figure 5 shows the beam losses signal measured by the Ionization Chambers IC4, IC5 and IC6. The different signal amplitudes derived from each wire

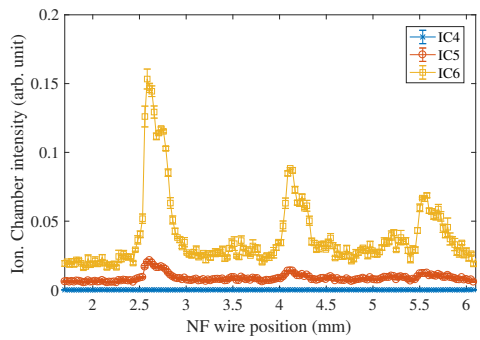

Figure 5: Beam losses signal from the ionization chambers during the wire scan.

depend only on the width of the wires. The IC6 and the fiber spool signals have a comparable SNR which is better than the other detector. The difference in the relative amplitude of the ionization chambers depends on the position of the chamber with respect to the NF wire which is located in the same position of IC4. IC5 which is located 3.7 meters downstream the wires shows a detectable signal but IC6 which is located at 7.4 meters shows maximum signal. The measured beam spot size measurement obtained analyzing the data in the above figures is in good agreement between detectors. For example considering the 20.6 µm NF wire the measured electron beam size is 129 µm ± 6 µm). Being a proof of principle experiment we wanted to compare a profile measured

ISBN: 978-3-95450-192-2 doi:10.18429/JACoW-IBIC2017-WE2AB3

from the nanofabricated device against our imaging high resolution scintillating screen. These imaging screens employ a COTR immune detection geometric and they are capable of measuring beam sizes down to 15 µm [11]. Figure 6 shows the horizontal profile of the electron beam obtained with the nanofabricated 13.5 µm wire averaging step by step over 20 consecutive shots. Figure 7 the electron beam transverse

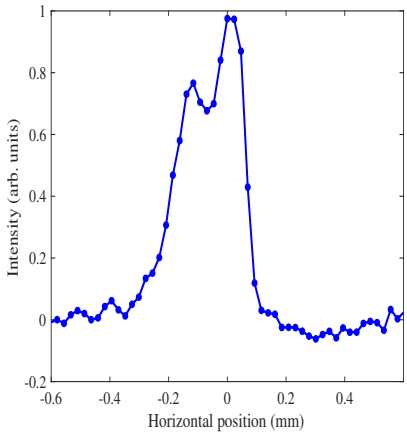

Figure 6: Horizontal profile obtained with the 13.5 µm NF wire.

image from the IUFEL imaging system is reported. The

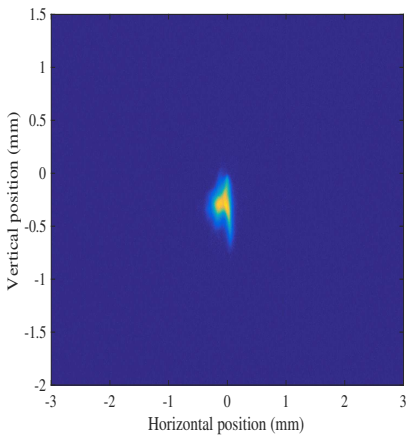

Figure 7: Comparison of nanofabricated wire profile with double gaussian function.

beam sizes obtained by the wire and the screen are in very very good agreement.

CONCLUSIONS AND PERSPECTIVES

We have reported the design, fabrication and proof of principle experiment of a wire scanner based on a nanofabricated device. The experimental data of the transverse been profile obtained with such device show good agreement with the high resolution scintillating imaging screen diagnostics. The technology underling this device offers potentially higher resolution, more flexibility and ease of installation compared to traditional wire scanners. The device is best suited for high brightness electron beams with beam size smaller than a few hundred microns. A technological limitation is the size of the aperture obtainable along the wire length to avoid breaking the bridges which cannot be higher than 3-4 mm. A single device with 2 wires at 90 deg with each other that is moved into the beam at 45 deg with the wires can be manufactured leading to a very compact wirescanner diagnostics. Application to photon sources from UV to soft X-ray is feasible by measuring the photo-ionization current. Application to FELs is also possible if the photon densities involved are below the damage threshold.

REFERENCES

[1] M. Yan *et al.*, in *Proc. DIPAC2011*, Hamburg, Germany. pp. 440–442 (2011).

[2] R. Akre, D. Dowell, P. Emma, J. Frisch, S. Gilevich, *et al.*, *Phys. Rev. ST Accel. Beams* 11 (2008), 030703.

[3] H.-D. Nuhn *et al.*, Report No. SlAC-PUB-19098, 2006.

[4] U.Hahn *et al.*, *Nucl. Instrum. Methods Phys. Res Sect.* A, 592, 189, (2008)

[5] G. Orlandi *et al.*, *Physical review Accelerator and Beams*, 19, 092802, (2016).

[6] R.C. Fernow, "Introduction to Experimental Particle Physics", Cambridge University Press, Cambridge, England, (1986).

[7] R. C. Murty, *Nature* 207, 398-399 (24 July 1965)

[8] T. T. Böhlen, F. Cerutti, M. P. W. Chin, A. Fassò, A. Ferrari, P.G. Ortega, A. Mairani, P. R. Sala, G. Smirnov, and V. Vlachoudis, "The FLUKA Code: Developments and Challenges for High Energy and Medical Applications", *Nuclear Data Sheets* 120, 211-214 (2014)

[9] A. Ferrari, P.R. Sala, A. Fassó, and J. Ranft, "FLUKA: a multi-particle transport code", CERN-2005-10 (2005), INFN/TC-05/11, SLAC-R-773

[10] C. Bocchetta *et al.*, FERMi@Elettra Conceptual Design Report, Tech Report No. ST/F-TN-07/12, 2007.

[11] M. Veronese *et al.*, in *Proc. IBIC2012*, pp. 519-523, Tsukuba, Japan, August 2012.

[12] L. Fröhlich *et al.*, in *Proc. FEL'10*, pp. 667-670, Malmö, Sweden, August 2010.

ISBN: 978-3-95450-192-2 doi:10.18429/JACoW-IBIC2017-WE2AB5

FIRST RESULTS FROM THE OPERATION OF A REST GAS IONISATION PROFILE MONITOR BASED ON A HYBRID PIXEL DETECTOR

J.W. Storey, D. Bodart, B. Dehning, G. Schneider, R. Veness, CERN, Geneva, Switzerland
W. Bertsche, H. Sandberg, University of Manchester, Manchester, UK
S. Gibson, S. Levasseur, Royal Holloway, University of London, London, UK
M. Sapinski, GSI, Darmstadt, Germany
K. Satou, Accelerator Laboratory, KEK, Ibaraki-ken, Japan

Abstract

A novel rest gas ionisation profile monitor which aims to provide continuous non-destructive bunch-by-bunch measurement of the transverse emittance is currently under development for the CERN Proton Synchrotron (CPS). The instrument consists of an electric drift field to transport ionisation electrons onto a measurement plane, a self-compensating magnet to maintain the transverse position of the ionisation electrons and an imaging detector to measure the transverse position of the ionisation electrons. Uniquely for this type of instrument the imaging detector consists of an array of pixelated silicon sensors which are read-out using Timepix3 readout chips. This so-called hybrid pixel detector is sensitive to single ionisation electrons and therefore removes the need for electron amplification with Multi-Channel Plates which typically suffer from aging phenomena and distorts the measured profile. The use of a pixel detector also offers the promise to significantly improve the time and spatial resolution of the position measurement compared to existing instruments. An ambitious program has been undertaken to develop a pixel based imaging detector that is compatible with operation directly inside the beam pipe vacuum together with the necessary radiation hard control and data acquisition electronics. A prototype version of the instrument was recently installed in the CPS and first results from the operation of this novel instrument will be presented.

INSTRUMENT DESIGN & REALISATION

An overview of the instrument design is shown in Fig. 1. Rest gas ionisation electrons are accelerated by an electric drift field towards an electron imaging detector located beneath a honeycomb structured radio-frequency shield. A magnetic field parallel to the electric field, formed by a self-compensating 0.2 T dipole magnet, helps to maintain the transverse position of the ionisation electrons during transport to the measurement plane. The electric drift field is formed by a single -11 kV cathode, without side-electrodes. The cathode includes an ion trap that prevents ion induced secondary electrons from re-entering the vacuum chamber and reaching the imaging detector [1]. The instrument is mounted on a rectangular vacuum flange with a ConFLat-type seal [2].

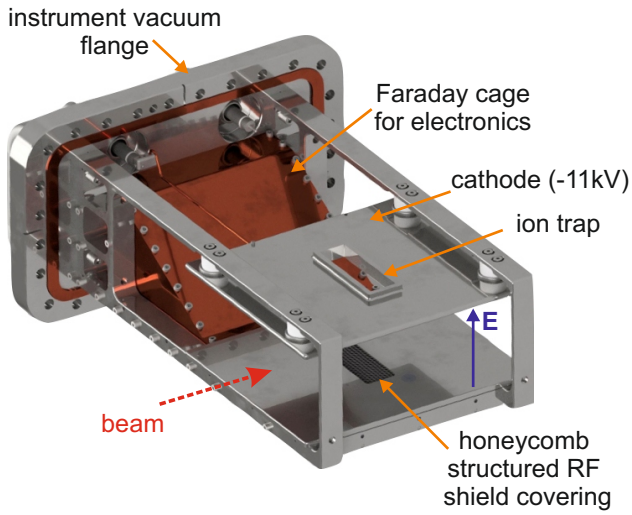

Figure 1: Rest gas ionisation profile monitor for the CERN PS.

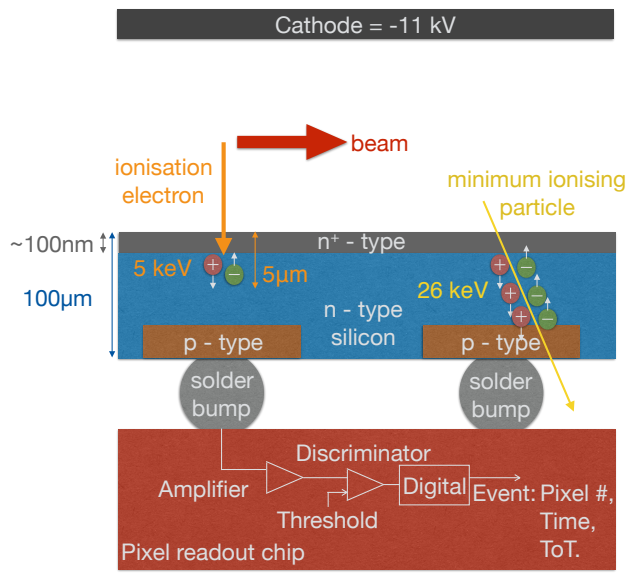

Figure 2: Detection of rest gas ionisation electrons with a hybrid pixel detector.

Detection of Rest Gas Ionisation Electrons With a Hybrid Pixel Detector

The ionisation electron imaging detector consists of four 14 × 14 mm hybrid pixel detectors mounted side-by-side creating a measurement plane 56 mm wide (transverse to the beam direction) and 14 mm long (in the direction of the

ISBN: 978-3-95450-192-2 doi:10.18429/JACoW-IBIC2017-WE2AB5

beam). Each hybrid pixel detector consists of a pixelated p-on-n silicon sensor bonded to a Timepix3 readout chip. Figure 2 illustrates the method by which ionisation electrons are detected in the hybrid pixel detector. Electrons produced by protons ionising the rest gas in the center of the beam vacuum chamber reach the surface of the detector with an energy of 5.5 keV due to the 11 kV voltage applied to the cathode. The aluminum metalization layer typically deposited on the front face of silicon sensors has been removed from the sensors used in the pixel detector to allow these low energy electrons to reach the silicon. The 5.5 keV electrons are completely stopped in the first 5μm of the sensor and the energy they deposit in the depletion layer of the silicon produces electron-hole pairs which can be collected by each pixel's electrodes. Charge from each of the 65,536 55 μm $\times$ 55 μm silicon sensor pixels is amplified and digitized by a Timepix3 readout chip directly bonded to the silicon sensor [3]. If the charge exceeds a pre-defined threshold an event is created consisting of: 1) the pixel location, 2) the time of the event relative to an external trigger and 3) the time that the signal remains above threshold. The time resolution for each event is 1.625 ns. Events are readout from each chip on 8 parallel links at a combined speed of up-to to 5.12 Gbps.

Since the pixel detector is located directly inside the ultra high vacuum environment of the beam pipe the total out gassing rate must be less than than 5.0×10^{-6} mbar.l.s^{-1} after 10 hours of pumping. The in-vacuum pixel detector electronics developed to meet this requirement are shown in Fig. 3 [4]. The four hybrid pixel detectors are mounted on a carrier board consisting of two metal layers and a 114.3 x 114.3 x 0.389 mm^3 ceramic substrate. The Timepix3 power and data signals are connected via wire bonds to pads on the top layer of the carrier board from which the signals are routed to two micro-connectors on the board. A flexible printed circuit board consisting of two metal layers and a 50μm thick Liquid Crystal Polymer (LCP) substrate is used to transmit the signals from the micro-connectors to the front-end read-out electronics via a 182-pin electrical vacuum feedthrough. The four Timepix3 chips generate 12 W of heat that needs to be actively removed to ensure continuous operation of the chips inside the vacuum. Active cooling is provided by a continuous flow of de-mineralized, room temperature water flowing through a stainless steel pipe that is brazed to a copper plate holding the ceramic carrier. A radio frequency shield, consisting of a stainless steel honeycomb structure with 0.125" cell size, is located immediately above the pixel detector to minimize interference between the Timepix3 chips and the electromagnetic field of the beam. The honeycomb is part of a Faraday cage that shields the Timepix3 chips and the electrical signals on the carrier board and flex cables.

Data Acquisition, Slow Control and Monitoring

The front-end electronics are located in a radiation environment close to the accelerator beam pipe, requiring a complete radiation tolerant data acquisition and control system for the pixel detector to be implemented. This is responsible for: sending commands to and reading data from the four Timepix3 chips, serializing data onto an optical link, and forwarding the acquisition triggers to the chips. The front-end is based on a multipurpose radiation hard FPGA board developed by the CERN Beam Instrumentation group that uses the GigaBit Transceiver (GBT) and Versatile Link components developed by CERN for upgrades to existing LHC experiments [5]. Single mode optical fibers connect the front-end electronics to the back-end electronics located 200 m away in a non-radiation environment. The back-end functionality includes: buffering data from the front-end, managing external timing and trigger signals, and providing a standard Ethernet interface to a computer. The first version of this back-end electronics is based on a commercial off-the-shelf Xilinx VC707 FPGA development board.

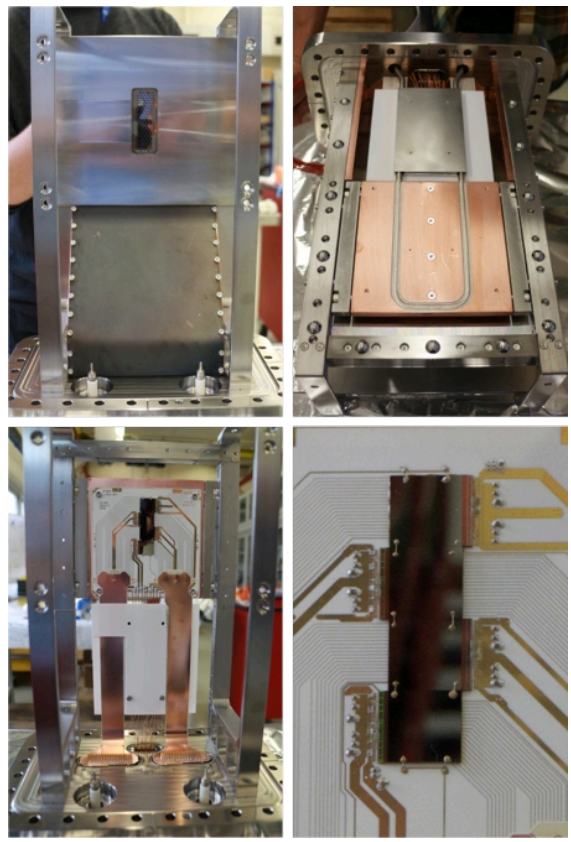

Figure 3: Ionisation profile monitor installed in the CPS. The beam passes horizontally from left to right. Top left: Cathode removed to reveal pixel detector beneath honeycomb RF-shield. Faraday cage cover is carbon coated to minimize the creation of secondary electrons. Top right: Copper cooling plate with stainless steel pipe for cooling water. Bottom left: Pixel detector mounted on ceramic carrier board, flexible cables connecting carrier to the electrical vacuum feedthrough. Bottom right: The four hybrid pixel detectors mounted on the ceramic carrier board.

A Programmable Logic Controller (PLC) based control system has been developed for the slow control and monitoring of: the cathode high voltage, pixel detector bias voltage,

ISBN: 978-3-95450-192-2 doi:10.18429/JACoW-IBIC2017-WE2AB5

front-end power supplies, detector cooling and temperature monitoring. The PLC will turn off the pixel detector power supplies if it detects the loss of the cooling circuit and prevents the power supplies exceeding pre-defined current and voltage limits.

Installation in the CERN PS

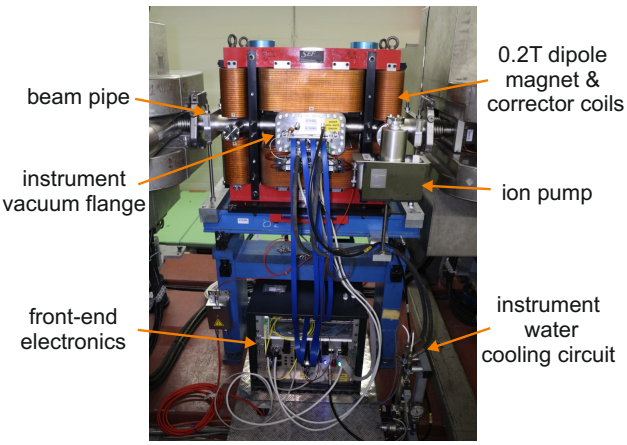

Figure 4: Pixel detector based rest gas ionisation profile monitor installed in the CERN PS.

Before installation in the CERN PS out-gassing tests were performed to qualify the instrument for operation in an ultra-high vacuum environment. RF measurements were also made to ensure that there was no significant contribution to longitudinal beam impedance [6]. The vacuum chamber, instrument, front-end electronics, cooling circuit and self-correcting dipole magnet were installed in PS straight section number 88 during the 2016/17 winter shutdown. The complete installation is shown in Fig. 4. After a 24 hour vacuum pump down down the pressure in the vicinity of the instrument reached 1×10^{-8} mbar and has reached a steady-state pressure of 2×10^{-10} mbar.

RESULTS

Operation During the Acceleration Cycle

Before attempting to detect rest gas ionisation electrons tests were made to verify the operation of the chips inside the beam pipe vacuum during an acceleration cycle. After configuring the pixel matrix registers, which included setting the threshold voltage for each pixel, images as shown in Fig. 5 of single inelastic hadronic interaction were acquired. This confirmed successful operation of the the detector under vacuum.

Detection of Rest Gas Ionisation Electrons

The pixel detector is sensitive to ionisation electrons and any other charged particle that deposits energy in the silicon sensor. The latter may come from beam loss in the vicinity of the pixel detectors and are typically high energy minimum ionising particles. The expected energy deposited in

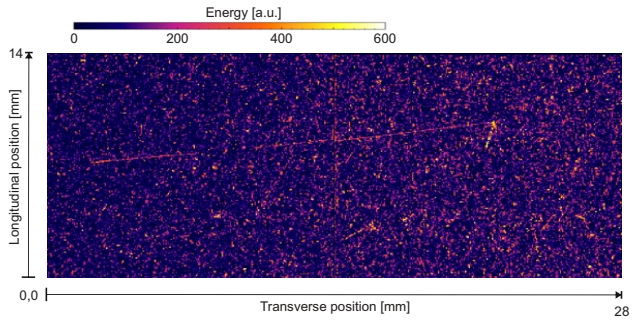

Figure 5: Inelastic hadronic interaction observed in the pixel detector during an acceleration cycle. Heavily ionising tracks - indicated by the higher deposited energy - originate from a common vertex, together with with a less heavily ionising track that crosses two hybrid pixel detectors.

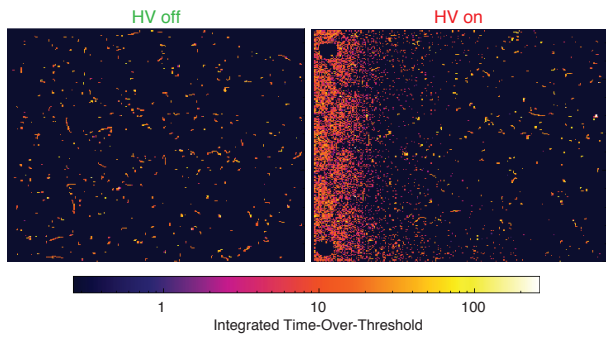

Figure 6: Integrated energy measured on one pixel detector with cathode high voltage OFF (left) and ON (right).

the pixel detector for 1) a 5.5 keV rest gas ionisation electron and 2) a minimum ionising particle is shown in Fig. 2. The ionisation electron will be stopped in less than 5μm, however, not all of the 5.5 keV kinetic energy will create charge carriers since some energy will be deposited in the quasi-conductive heavily doped n+ top layer the depth of which is not well known. A high energy minimum ionising particle (MIP) will travel completely through the 100μm deep silicon sensor and deposit 26 keV - almost five times more energy than the ionisation electron. Images observed on one of the four pixel detectors are shown in Fig. 6 for acquisitions taken without and with high voltage applied to the cathode. The images were recorded with the dipole magnet at 0.1 T, during a 100 ms period with an intensity of 6×10^{12} protons. Without high voltage applied to the cathode the image contains short tracks consistent with MIP activity, however, with high voltage applied to the cathode an image is observed on the left side of the detector consistent with the expected position of the proton beam. Ionisation electrons do not have sufficient energy to pass through the honeycomb RF shield nor the circular glue deposits used to attach the bias wire to the non-metalized sensor. These regions therefore show-up as shadows in the image with high voltage applied to the cathode. The single pixel energy distribution is shown in Fig. 7 for acquisitions with and without high voltage. Without high voltage the energy deposited in a single pixel is consistent with a Landau distribution with

ISBN: 978-3-95450-192-2 doi:10.18429/JACoW-IBIC2017-WE2AB5

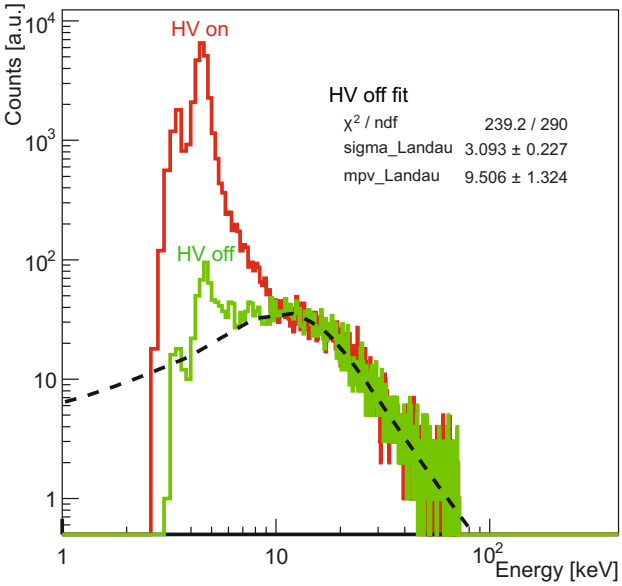

Figure 7: Distribution for energy deposited in a single pixel detector for acquisitions with and without high voltage applied to the cathode.

a most probable value of 9.5 keV, which is consistent with the expected 26 keV deposited by MIPs shared amongst a number of pixels depending upon the incidence angle of the particle track. With the high voltage applied to the cathode there is a significant peak at 4.5 keV consistent with a 5.5 keV ionisation electron. A smaller peak is also visible at 3.5 keV the origin of which is still to be determined but could be due to charge sharing between neighboring pixels.

Beam Profile Measurement

An image acquired by two of the four pixel detectors is shown in Fig. 8. This is consistent with the expected transverse position of the beam. The counts in each pixel column are integrated to produce the beam profile shown in Fig. 9. The pixel data is currently not corrected for the inhomogeneity of the honeycomb shadow, but nonetheless the measured transverse beam profile is consistent with a Gaussian beam profile of width 1.22 ± 0.01 mm. The expected beam size at the location of the ionisation profile monitor from wire scanner measurements is 1.20±0.01 mm, in very good agreement with the value measured by the ionisation profile monitor.

CONCLUSIONS AND OUTLOOK

An ionisation profile monitor that uses a pixel detector to measure ionisation electrons has been installed directly in the PS beam pipe vacuum and operated successfully during the acceleration cycle. Rest gas ionisation electrons have been detected with the pixel detector and a first beam profile has been measured, in good agreement with wire scanner measurements. Future efforts will be directed towards exploiting the unique characteristics of the pixel detector technology to improve the accuracy of the beam profile measurement and to minimize the number of turns needed to measure the profile of a single bunch.

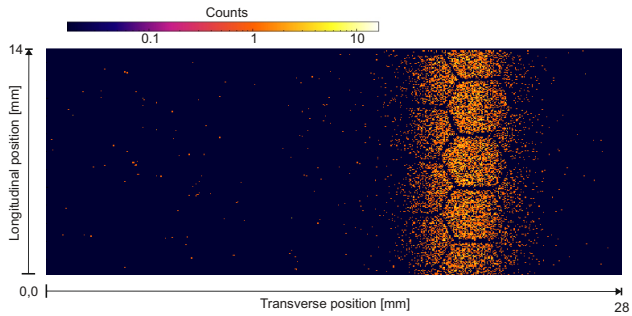

Figure 8: Pixel detector image of an LHC cycle in the CPS acquired during a 10 ms window at extraction energy. Dipole magnetic field at 0.2 T and cathode high voltage set at -13 kV.

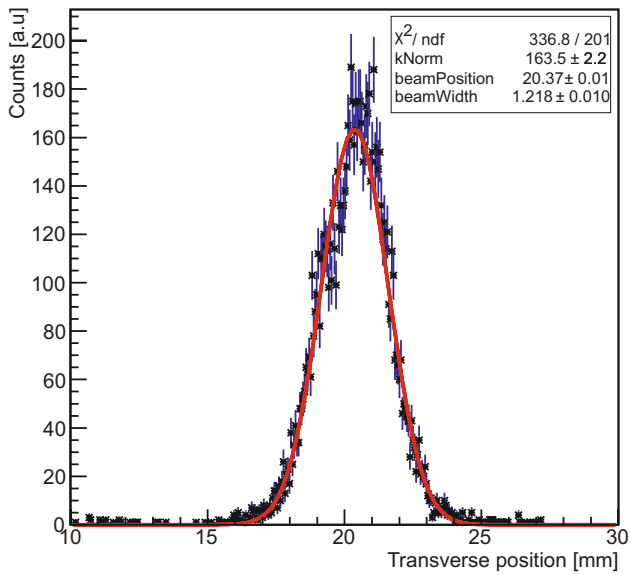

Figure 9: Horizontal beam profile obtained from the image shown in Fig. 8.

ACKNOWLEDGMENTS

The authors would like to thank Michael Campbell, Xavi Llopart Cudie and Jerome Alozy from the CERN Microelectronics group for expert help with the Timepix3 chip. We wish to dedicate these results to the memory of our former colleague Bernd Dehning, who initiated the project, who passed away on 14th January 2017.

REFERENCES

[1] D. Bodart *et al.*, "Development of an Ionization Profile Monitor based on a Pixel Detector for the CERN Proton Synchrotron", in *Proc. IBIC15*, Melbourne, Australia, paper TUPB059.

[2] A. Miarnau, G. Schneider, R. Veness, "Development and test of a rectangular CERN ConFlat-type flange", *Elsevier Vacuum* 121 (2015) 202-206.

[3] T. Poikela *et al.*, "Timepix3: a 65K channel hybrid pixel readout chip with simultaneous ToA/ToT and sparse readout", 2014 *JINST* 9 C05013.

[4] S. Levasseur *et al.*, "Development of a Rest Gas Ionisation Profile Monitor for the CERN Proton Synchrotron Based on a Timepix3 Pixel Detector", in *Proc. TWEPP2016*, Karlsruhe, Germany.

ISBN: 978-3-95450-192-2 doi:10.18429/JACoW-IBIC2017-WE2AB5

[5] M. Barros Marin, "The Giga Bit Transceiver based Expandable Front-End (GEFE) – a new radiation tolerant acquisition system for beam instrumentation", in *Proc. TWEPP2015*, Lisbon, Portugal.

[6] N. Nasr Esfahani *et al.*, "Evaluation of Longitudinal Beam Impedance in the Beam Gas Ionization Monitor of the CERN-PS Accelerator", in *Proc. IPAC2017*, Copenhagen, Denmark, doi.org/10.18429/JACoW-IPAC2017-WEPIK095

ISBN: 978-3-95450-192-2 doi:10.18429/JACoW-IBIC2017-WE3AB1

THE LHC BEAM GAS VERTEX DETECTOR - A NON-INVASIVE PROFILE MONITOR FOR HIGH ENERGY MACHINES*

S. Vlachos†, A. Alexopoulos, C. Barchel[1], E. Bravin, G. Bregliozzi, N. Chritin, B. Dehning‡, M. Ferro-Luzzi, M. Giovannozzi, R. Jacobsson, L. Jensen, R. Jones, V. Kain, R. Matev, M. Rihl, V. Salustino Guimaraes, R. Veness, B. Würkner, CERN, Geneva, Switzerland
A. Bay, F. Blanc, S. Giani, O. Girard, G. Haefeli, P. Hopchev, A. Kuonen, T. Nakada, O. Schneider, M. Tobin, Q. Veyrat, Z. Xu, EPFL, Lausanne, Switzerland
R. Greim, W. Karpinski, T. Kim, S. Schael, A. Schultz von Dratzig, G. Schwering, M. Wlochal, RWTH Aachen University, I. Physikalisches Institut, Aachen, Germany
[1]also at Cockcroft Institute and University of Liverpool, UK

Abstract

The Beam Gas Vertex (BGV) monitor is being developed as part of the High Luminosity LHC project with the aim of providing measurements with less than 5% error on the beam size with an integration time of 5 minutes. It will be an instrument capable of non-invasive beam size measurements throughout the LHC acceleration cycle with high intensity physics beams. A prototype BGV monitor has been installed in the LHC since 2016. Particles emerging from beam-gas interactions are recorded by two tracking stations made of scintillating fibres. Based on vertex reconstruction of the detected tracks, this monitor allows for a non-invasive measurement of the beam profile with bunch-by-bunch resolution. A dedicated computer farm performs track reconstruction and event analysis online so that real-time beam profile measurements can be provided. Data taken in 2016 and 2017 will be presented that demonstrate the potential of this method.

INTRODUCTION

The LHC Beam Gas Vertex (BGV) detector is a non-invasive beam profile monitor being developed for use as part of the high luminosity LHC upgrade (HL-LHC) [1]. The BGV system reconstructs the transverse beam profile by detecting particles from inelastic beam-gas collisions [2]. A gas tank is installed in the path of each circulating beam so that noble gas (initially Ne) is injected in the beam's trajectory. Particles emerging from the beam-gas collisions are detected by several planes of scintillating fibre detectors (SciFi) to enable a precise track reconstruction. These tracks are in turn used to reconstruct the vertex of each collision building-up a picture of the transverse beam profile. This method, originally developed for the LHCb experiment [3], allows profile measurements in real time. The pressure in the gas volume can be tuned to accommodate a large range of accelerator luminosity and/or inelastic beam-gas cross-section (i.e. beam energy). Using five minutes of beam time data, the BGV system is intended to provide an absolute measurement of the transverse beam profile with less than 10% error [4]. The transverse profile of individual bunches may also be reconstructed. Based on the beam width and given the β-function and dispersion of the magnetic lattice (measured independently), the emittance ϵ can be calculated. With enough statistics the detector can in addition measure beam tilt. Furthermore, relative bunch populations and ghost charges (beam intensity in nominally empty RF buckets) can be quickly estimated by using the BGV trigger system as for these measurements no precise tracking or vertex reconstruction is needed.

The addition of a precise timing detector (with a resolution of approximately 50 ps) would allow also the measurement of the longitudinal beam profile.

One BGV demonstrator is currently installed at Point 4 of the LHC on the beam 2 ring. A location where β_x and β_y are similar was selected, giving similar profiles in both planes and allowing the use of a reduced diameter beam pipe around the main detector so that it can sit as close as possible to the beam line. At the BGV location the 7 TeV beam to be monitored is expected to have a transverse profile with $\sigma_{x,y} \approx 0.22$ mm. The BGV system is composed of three independent parts: The gas target where beam-gas interactions occur, the trigger system that selects interactions originating from the volume of interest and the precise tracking system used to reconstruct tracks and vertices (Fig. 1).

THE GAS TARGET SYSTEM

The gas target vacuum system was designed to have a minimal impact both on the passing beam and on the particles emerging from the beam-gas interactions. It is made of aluminium (Al 2219) and is approximately 2 metres long. It consists of three parts: a 0.75 m long conical tube at the beam entry (to minimise beam impedance) followed by the gas target itself, a 1.25 m long cylinder with a diameter of 200 mm, and ending with a thin exit window towards the trigger and tracking detectors. The exit window has a thickness ranging from 3.25 mm at its edges to 1.15 mm close to the beam pipe, in order to minimise the multiple scattering of the emerging particles. The beam pipe around the end of the conical section has been reduced to a diameter of 58 mm (instead of the nominal 80 mm) and around the tracking detectors to a diameter of 52 mm. This serves two purposes. First of all it allows the BGV tracking detectors to be as

* Research supported by the HL-LHC project
† S.Vlachos@cern.ch
‡ Deceased January 14, 2017

ISBN: 978-3-95450-192-2 doi:10.18429/JACoW-IBIC2017-WE3AB1

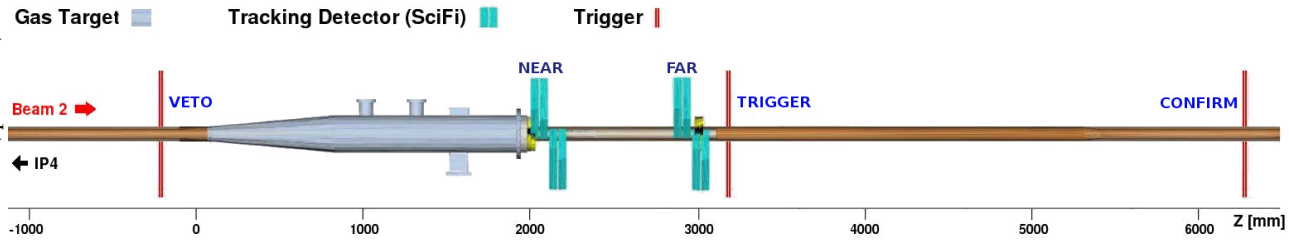

Figure 1: The BGV detector with its three main components: The gas target, the tracking detector and the trigger system.

close as possible to the beam pipe in order to increase the detector acceptance as most of the particles produced are in the very forward direction, and improve the track and vertex resolution by reducing the extrapolation distance. Secondly, the reduced beam pipe dimensions act as a gas flow restriction that allows the target gas pressure to reach $1 \cdot 10^{-7}$ mbar, while the pressure in the adjacent beam pipes can be kept at the nominal LHC vacuum pressure ($1 \cdot 10^{-11}$ mbar).

Neon is currently being used for the gas target in the BGV system. The expected beam-gas interaction rate R per bunch can be estimated by the following formula:

$$R = \int_{z_a}^{z_b} \rho(z) dz \, \sigma_{\mathrm{pA}}(E) N f_{\mathrm{rev}} \qquad (1)$$

where $\rho(z)$ is the gas density, $\sigma_{\mathrm{pA}}(E)$ the proton-nucleus cross-section for proton energy E, N is the number of protons per bunch and f_{rev} the bunch revolution frequency (11.245 kHz). The integral boundaries z_a, z_b, represent the approximate detectors acceptance limits. Assuming a uniform gas distribution within the target region, Eq. 1 reduces to:

$$R(\mathrm{Hz}) = 2.5 \cdot 10^{-11} p(\mathrm{mbar}) \Delta z(\mathrm{cm}) \sigma_{\mathrm{pA}}(\mathrm{mb}) N f_{\mathrm{rev}}(\mathrm{Hz}) \quad (2)$$

Using $p = 10^{-7}$ mbar, $\Delta z = 100$ cm, $\sigma_{\mathrm{pA}} = 295$ mb (for 7 TeV protons and Ne gas target) and $N = 10^{11}$p/bunch, one gets an expected rate of beam-gas inelastic events $R = 81$ Hz per bunch. It should be noted that as $\sigma_{\mathrm{pA}}(E) \approx \sigma_{\mathrm{pp}}(E) A^{2/3}$, a heavier gas would lead to an increased event rate.

THE TRIGGER SYSTEM

In order to identify beam-gas interactions the BGV detector is using a dedicated trigger system composed of three scintillator stations. The first (VETO) is upstream of the target region volume to reject particles not originating from the gas target. The second (TRIGGER) is just after the tracking detectors, while a third trigger station (CONFIRM) further downstream is used in coincidence with the TRIGGER station to identify particles passing through the whole BGV set-up. The trigger stations are placed outside the gas target to precision detector region so that no additional multiple scattering element is introduced into the system. Each trigger station is comprised of two 30×30 cm^2, 1 cm thick plastic scintillator plates placed above and below the beam line, connected to a photomultiplier and read out using a simple level discriminator. During normal LHC operation at a nominal bunch intensity of 10^{11}p/bunch and with nominal gas pressure at the BGV gas target volume this trigger system gives a rate of about 300 Hz per bunch.

By comparing the response time of the TRIGGER and the CONFIRM trigger stations for the same events, the time resolution of each station can be measured. Figure 2 shows the time difference distribution between these two scintillators. It has a width of 1.1 ns which implies a time resolution per station of 0.8 ns. This resolution is well in accordance with expectations given the time jitter generated by the scintillation process. In the near future the tails of the distribution will be further reduced by using constant fraction discriminators. This will also reduce the trigger rate as it will allow fine tuning of the trigger coincidence time windows. The

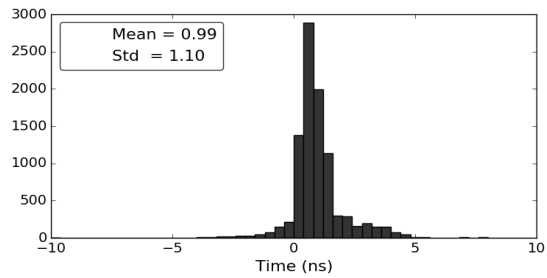

Figure 2: Time difference between signals at the TRIGGER and CONFIRM trigger stations.

excellent timing properties of the BGV trigger system allows it to be used independently for beam quality measurements as the exact beam bunch ID of each triggered event can be identified (LHC bunches are 25 ns apart). The relative bunch intensity and its time evolution can therefore be measured as well as the ghost charge fraction (the fraction of protons in RF buckets that are nominally empty). Figure 3 shows the full LHC bunch structure as measured by the BGV trigger system (and compared for reference with the measurements of the LHC Beam Current Transformer (BCT) system). From the data in Fig. 3 the ghost charge fraction for LHC fill 6053 is measured to be 2.9‰. By performing a similar measurement without injecting gas in the BGV gas target volume the systematic error of this measurement is estimated to be of the order of 0.3‰. The comparison of trigger rates with and without gas injected showed that the trigger background contamination is at the level of 10^{-4}.

ISBN: 978-3-95450-192-2 doi:10.18429/JACoW-IBIC2017-WE3AB1

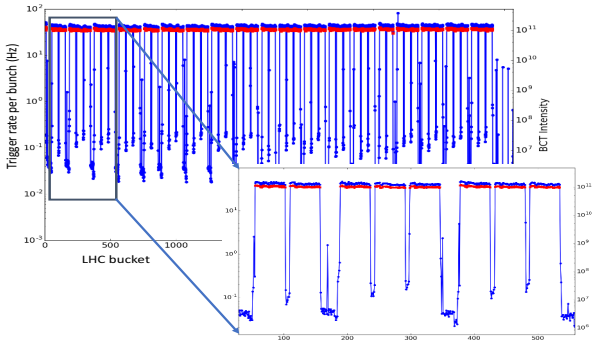

Figure 3: The LHC bunch structure as measured by the BGV trigger system (blue points). The insert is a zoom in an area of a few LHC bunches demonstrating the ability of the system to clearly identify individual bunches and their relative intensities. For comparison the intensity measurements from the Beam Current Transformer (BCT) are superimposed (red points). The BGV rate is not normalized to the absolute LHC beam intensity.

THE PRECISION TRACKING DETECTOR

The BGV precision tracking system consists of two tracking stations. One (the NEAR station) is situated just after the gas target exit window, and the other (the FAR station) one metre further downstream. For beam profile measurements the important parameter to be measured per track is its impact parameter (IP) (the distance of closest approach to the z-axis) and its error σ_{IP} (see the following section for more details). This error can be decomposed into two parts. One is due to the detector resolution and its impact on the track extrapolation to the point of closest approach. The other is due to multiple scattering introduced by material in the detected particle's path: $\sigma^2_{\mathrm{IP}} = \sigma^2_{\mathrm{Extrap}} + \sigma^2_{\mathrm{MultScat}}$. If tracks are measured by two consecutive detector planes placed at positions z_1 and z_2 from the interaction point and each position measurement has an error σ_{hit} then:

$$\sigma_{\mathrm{Extrap}} = \sqrt{\frac{z_1^2 + z_2^2}{(z_2 - z_1)^2}}\,\sigma_{\mathrm{hit}} \tag{3}$$

The multiple scattering error can, in a simplified approximation, be given by the following formula:

$$\sigma_{\mathrm{MultScat}} = z_1 \frac{13.6\,\mathrm{MeV}}{p}\sqrt{\frac{x}{X_0}} \tag{4}$$

where p is the detected particle's momentum and x/X_0 the thickness of the material transversed in units of radiation lengths. For the material thickness calculation both the gas volume exit window and the first, upstream, tracking module should be taken into account. Given an expected hit resolution of σ_{hit} ~70 µm, the distance between the two tracking stations was selected such that σ_{Extrap} remains smaller than $\sigma_{\mathrm{MultScat}}$, and the whole tracker was placed as close as possible to the BGV gas volume.

Each BGV tracking station has 4 scintillating fibre (SciFi) modules, one pair placed above the beam pipe and the other pair below. Within a pair, the modules have their fibres oriented perpendicular to each other to allow a 2-dimensional measurement. Each SciFi module contains two fibre mats with 4 (NEAR station) or 5 (FAR station) layers of scintillating fibres of 250 µm diameter [5]. The NEAR station has fewer layers in order to reduce multiple scattering effects. The two mats are rotated by 2° with respect to each other in order to facilitate pattern recognition. A one-dimensional position measurement resolution of 32 µm has been achieved with a test beam setup [6] for well separated tracks in a low background environment. The fibres are read out with silicon photomultipliers (SiPMs) which are cooled with liquid C_6F_{14}. Cooling is needed to improve the signal to noise ratio by reducing the SiPM dark count rate which increases with radiation dose. The radiation dose absorbed by the detector is monitored by a RadMon active detector [7], as well as 6 PIN diodes placed close to the SiPMs.

The read-out chain of the BGV system uses hardware from the LHCb experiment. Each SciFi module is read-out by 16 128-channel SiPM arrays operated in Geiger-Müller mode. Beetle front-end ASICs [8] then receive the analogue signals from the SiPMs. The Beetle ASIC has an analogue input memory of 160 steps maximum length with an analogue, serial output at the LHC bunch frequency of 40 MHz. This serialized analogue output data is time-multiplexed on 4 ports of 32 channels to form an analogue link (A-link) over which data is forwarded to the VELO repeater boards situated a few metres away from the BGV detector inside the LHC tunnel. They amplify the signal data and send it over 60 m of cables to the service cavern where radiation levels are considerably lower. There the analogue signals are digitised by TELL1 boards [9].

The timing control of the data acquisition system is supervised by the LHCb ODIN board [10]. For every trigger signal received from the BGV trigger system it initiates and controls the front-end (Beetle) data transmission. Dedicated timing studies with real data have been performed to ensure that the correct slot of the Beetle memory is retrieved [5].

THE DATA ANALYSIS METHOD

In order to measure the transverse beam profile with the BGV data, one has first to process the raw data and transform SciFi hits to clusters induced by passing particles. These clusters then need to be analysed for tracks through an adequate pattern recognition method. With these tracks fitted the final relevant event parameters are found. Raw data has first to be corrected for effects related to the SiPMs and the read-out electronics. The corrections are applied in the reverse order to how they are introduced in the read-out chain and include: pedestal subtraction, common mode noise suppression and channel correlation corrections. In the future, these steps will be implemented in the front-end FPGAs of the TELL1 boards and will be performed online. Fur-

ISBN: 978-3-95450-192-2 doi:10.18429/JACoW-IBIC2017-WE3AB1

ther studies and analysis of these corrections can be found in [11, 12].

Energy deposited by particles transversing a SciFi plane is dispersed over several SiPM detector channels. A cluster has therefore to be formed using the amplitude information of all channels hit by a single particle. The clustering is performed by groups of 64 channels and uses a three threshold algorithm to suppress noise. Initially, a search is made for a signal over a given threshold (ADC Seed Threshold). Clusters are then formed by including neighbouring channels that themselves contain a significant amount of signal (ADC Neighbour Threshold). Finally only clusters with a considerable total energy deposited are retained (sum of amplitudes in a cluster above ADC Sum Threshold). For each cluster its central position is calculated as the weighted average of the signal amplitudes within it [13]. The SiPM hit read-out and clustering algorithm are shown in Fig.4.

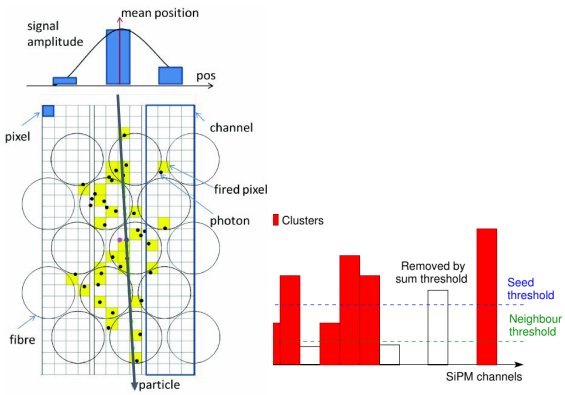

Figure 4: Left: Signal formation in a SciFi module. Scintillation photons are detected by several SciFi fibres. The sum of signals within a SiPM channel is read out. A weighted average is used to measure the exact coordinate of a hit. Right: Clustering algorithm and thresholds [11].

Using the clusters found per event a simple 3D pattern recognition method identifies clusters that belong to the same particle originated from the BGV gas volume. This starts from clusters at the furthest downstream SciFi plane and then searches the other planes using a search window that links the original clusters to the BGV gas target area. If clusters are found along this path (normally seven or eight are found) they are grouped together for a track fit. This is a simple straight line fit with the χ^2 method used to define the corresponding line parameters. A typical reconstructed BGV event is shown in Fig. 5.

Once tracks are found, and their parameters established, two methods allow the reconstruction of the beam profile. A vertex fit may be performed using all reconstructed tracks of each event. The vertex distribution on the (x, y) plane then provides a 2D image of the passing beam. Alternatively the beam width may be estimated using the beam impact parameter correlation (IPC) method.

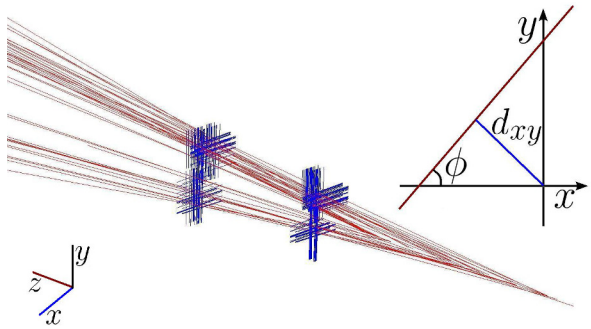

Figure 5: An event display at the BGV detector using the LHCb software *Panoramix*. Blue lines are the individual SciFi identified clusters. Red lines represent the tracks reconstructed for this event. The impact parameter d_{xy} and the azimuthal angle ϕ of the track are also defined in the insert.

For the IPC method two parameters are calculated per track: the impact parameter d_{xy} which refers to the distance of closest approach of the reconstructed track to the z-axis; the azimuthal angle of the track ϕ , which is defined as the angle between the x-y projection of the track and the x-axis (for a visualisation of these two variables see Fig. 5). These two parameters are related for a given position (x_0, y_0) of the primary vertex by:

$$d_{xy} = x_0 \sin(\phi) - y_0 \cos(\phi) \tag{5}$$

The event-by-event displacement due to the finite beam width affects all particles of a beam-gas interaction in the same way, thus a correlation is introduced. In the case of an untilted beam ellipse, and assuming the beam width at the BGV location to have $\sigma_x = \sigma_y = \sigma_{\text{beam}}$, this correlation can be described as [14, 15]:

$$\langle d_{xy}^{(1)} d_{xy}^{(2)} \rangle = \sigma_{\text{beam}}^2 \cos(\phi_1 - \phi_2) \tag{6}$$

For the present study the IPC method was used as it provides directly the beam width irrespective of the vertex position and resolution. In the future however both methods will be used and their results will be compared to determine the optimal BGV analysis method.

FIRST BEAM PROFILE MEASUREMENTS

After installation in 2014–2015 and commissioning in 2016, several data taking campaigns with the BGV systems have taken place. Data collected was primarily used to develop and fine-tune all necessary algorithms and data analysis procedures. The results presented in this section were obtained during LHC fill 6082 (August 2017). The pressure in the gas target volume was $5 \cdot 10^{-8}$ mbar. The SiPMs were cooled to −10 °C. All SiPM channels were read out (more than 99% of the channels were active) and the corrections and clustering were performed offline. The BGV trigger rate

ISBN: 978-3-95450-192-2 doi:10.18429/JACoW-IBIC2017-WE3AB1

was about 1 kHz. The data sample presented corresponds to ~5 minutes of real-time data taking. The following selection criteria have been applied to the dataset used:

Cluster requirements:

1. ADC Seed Threshold = 40 (corresponding to approximately 6 SiPM photoelectrons),
2. ADC Neighbour Threshold = 30,
3. ADC Sum Threshold = 70.

Track requirements:

1. Tracks with clusters in all 8 consecutive SciFi planes,
2. χ^2/ndf of track fit < 0.5,
3. 0 m < z at point of closest approach < 2 m
4. 0 mm < d_{xy} < 1 mm

Event requirements:

1. 2 < total number of tracks found < 50,
2. matching BCID between selected events and LHC beam 2 fill pattern.

Figure 6 shows the distribution of the impact parameter of the reconstructed tracks along the z-axis. It compares well with Monte-Carlo simulation. This distribution is also a clear indication that, as expected, there is no significant residual gas pressure outside the BGV gas target volume and that the gas pressure is almost uniform within the volume.

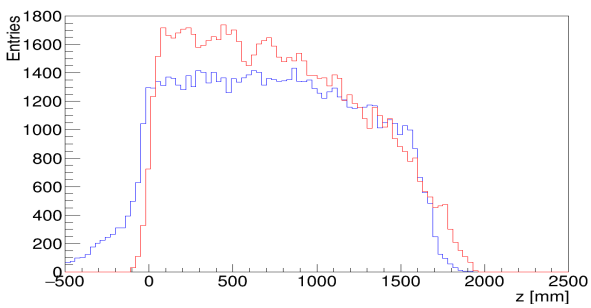

Figure 6: The distribution along the z-axis of the points of closest approach of the reconstructed tracks. Real data (blue) and Monte-Carlo simulation (red).

The distribution of the impact parameter d_0 as a function of the azimuthal angle ϕ is shown in Fig. 7. Fitting this data with the function of Eq. 5 the beam position is estimated to be $x = -0.60$ mm, $y = 0.26$ mm with respect to the (0,0) of the BGV detector's reference frame.

Once the beam offset with respect to the BGV reference frame is established all tracks are shifted accordingly so that they point around $(x, y) = (0, 0)$. In that way no systematic bias is introduced in the beam width analysis. Figure 8 shows the, corrected for the measured beam position, distribution of the correlation of the impact parameter of track pairs from the same event $\langle d^1_{xy} d^2_{xy} \rangle$ as a function of the cosine of their relative azimuthal angle ϕ ($\cos \Delta\phi$). A fit with the function in Eq. 6 yields the transverse beam width to be $\sigma_{\text{beam}} = 0.17 \pm 0.10(\text{stat.})$ mm. Further refinement of the tracking algorithm along with better event selection through improved triggering will lead to a considerable improvement of the statistical error and allow a full comparison with other LHC beam profile measurement devices.

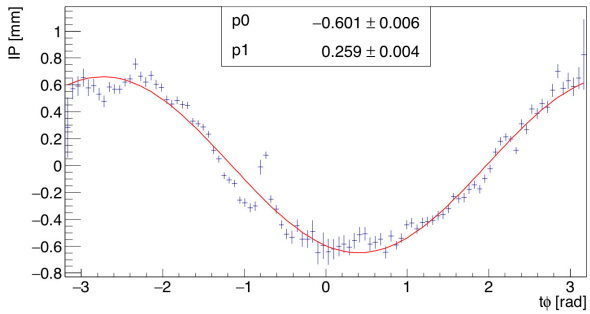

Figure 7: Beam position estimation using the the d_0 vs ϕ method. The impact parameter of reconstructed tracks is plotted as a function of their azimuthal angle ϕ. Fitting with the function of Eq. 5 (red curve) the beam position is estimated to be at $(x, y) = (-0.60\,\text{mm}, 0.26\,\text{mm})$ with respect to the detector's reference frame (0,0).

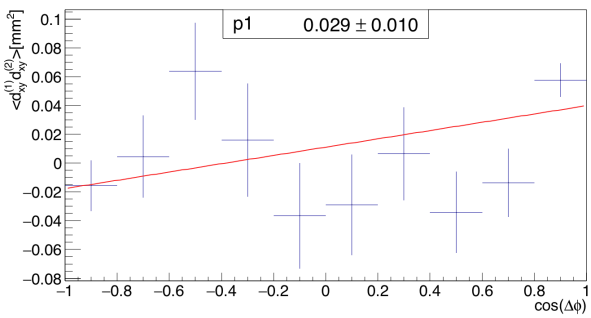

Figure 8: Beam width estimation using the IPC method. The impact parameter correlation is plotted as a function of the cosine of their relative azimuthal angle ϕ. Fitting with the function in Eq. 6 (red line) the transverse beam width is estimated to be $\sigma_{\text{beam}} = 0.17 \pm 0.10(\text{stat.})$ mm.

FUTURE UPGRADES FOR THE BGV SYSTEM

The current BGV system is beginning to demonstrate its ability to reconstruct beam profiles for the LHC. The final systems to be built for HL-LHC will implement a series of improvements as dictated by the current measurements.

Changing the target gas from Neon (20.2 atomic mass) to Argon (39.9 atomic mass) will increase the trigger rate by approximately 50%, with a similar increase expected in the number of tracks produced per beam-gas interaction. This simple upgrade would considerably shorten the integration time required to achieve similar resolution results.

Undoubtably, multiple scattering has a considerable impact on the track reconstruction accuracy and consequently on the beam width measurement resolution. The main source

ISBN: 978-3-95450-192-2 doi:10.18429/JACoW-IBIC2017-WE3AB1

of multiple scattering in the BGV system is its aluminium gas target exit window. A redesign to achieve a thickness of approximately 1 mm over its full radius would lead to a 30% to 50% reduction in multiple scattering effects. A further factor of 2 reduction of these effects can be achieved by using an exit window made entirely of beryllium, but this brings with it other safety related issues.

Two options are also under investigation for upgrading the BGV precision tracking detector. One option is based on silicon-strip detectors and the other on micro pattern gas detectors (MicroMegas) [16]. The former has the advantage of using commercially available sensors, while the latter can be made with very thin sensors (about 100 µm thick compared to 250 µm for Si). They can both operate efficiently in the radiation field around the HL-LHC and have a measurement resolution of approximately 70 µm for a strip pitch (200 µm to 300 µm) that would keep the total number of read-out channels at reasonable levels. Further development of both technologies may allow the usage of double-sided sensors, further reducing their multiple scattering impact.

The BGV system can be upgraded to measure the longitudinal beam profile as well. At the LHC (or HL-LHC) proton bunches have a length of 9 cm which translates to a time spread of 300 ps. Therefore, in order to reconstruct the bunch longitudinal profile with at least 5-6 points, the arrival time at a given detector plane of beam-gas events would have to be registered with a time resolution of 50 ps. Under study for the BGV application is a version of a Micromegas plane detector that is based on measuring the Cherenkov radiation of particles crossing a thin radiator [17]. In this detector design, the UV photons produced travel only a few hundred μm. This allows time measurements with a resolution of 20 ps to 30 ps.

SUMMARY - OUTLOOK

The BGV beam profile monitor was successfully commissioned in 2016 and first measurements with 2017 data are already very encouraging. The gas injection system is very reliable and can, without any interference with the LHC operation, increase the pressure in the BGV gas volume up to $1 \cdot 10^{-7}$ mbar. The trigger system efficiently selects beam gas interactions, while the SciFi tracking detector has excellent resolution, is very reliable and has more than 99% of its channels operational. This allows for a very good reconstruction of tracks emerging from beam gas interactions. Preliminary results show that the BGV system measures the transverse beam width with a resolution of 0.13 mm (5 minutes integration time, 1 kHz read-out rate), a result that is for the moment limited by statistics. The zero suppression implementation in the front-end electronics will allow the read-out rate to reach 100 kHz. Together with the use of a CPU farm for real-time track reconstruction and profile measurement [18], this should allow beam profiles to be available in the LHC control room before the end of 2017. A cross-calibration of the BGV measurements with other existing beam profile monitors during special runs with well defined operational conditions will allow the determination of any systematic corrections needed.

In the near future improvements in the BGV trigger system (better time resolution and more stringent coincidence in time of the scintillator signals) will improve the purity of the BGV event sample. In that way the processing time of recorded data will be significantly reduced so that beam profile measurements may be provided faster in real time.

If the BGV demonstrator manages to achieve its goal of providing non-invasive, accurate, real-time, bunch-by-bunch beam profile measurements, then it could become the main beam profile monitor for the HL-LHC era, and would surely be a good candidate for both transverse and longitudinal beam size diagnostics in any future high energy hadron machines.

In addition there is no limitation that would exclude its use at future higher luminosity or energy machines.

ACKNOWLEDGMENTS

We would like to thank the LHCb Collaboration, in particular Clara Gaspar, Niko Neufeld and Markus Frank, for the support in the development of the BGV online control system. We wish to express our sorrow over the recent death of Bernd Dehning, a leading collaborator of the BGV project, and dedicate these first results to his memory.

REFERENCES

[1] "HL-LHC Preliminary Design Report: Deliverable: D1.5", Nov 2014, CERN-ACC-2014-0300, https://cds.cern.ch/record/1972604.

[2] A. Alexopoulos et al., "First LHC transverse beam size measurements with the Beam Gas Vertex detector", in Proc. 8th Int. Particle Accelerator Conf. (IPAC17), Copenhageg, Denmark, May 2017, paper TUOAB1, pp. 1240–1243, doi:10.18429/JACoW-IPAC2017-TUOAB1, http://jacow.org/ipac2017/papers/tuoab1.pdf

[3] M. Ferro-Luzzi, "Proposal for an absolute luminosity determination in colliding beam experiments using vertex detection of beam-gas interactions", Nucl. Instrum. Meth. A **553** (2005) 388.

[4] P. Hopchev et al., "A Beam Gas Vertex Detector for Beam Size Measurement in the LHC", in Proc. 5th Int. Particle Accelerator Conf. (IPAC14), Dresden, Germany, June 2014, paper THPME175, pp. 3680-3683.

[5] M. Rihl et al., "Employing Beam-gas interaction vertices for transverse profile measurements", in Proc. 7th Int. Particle Accelerator Conf. (IPAC16), BEXCO, Busan Korea, May 2016, paper MOPMR027, pp. 296-298.

[6] O. Girard, L. An, A. Kuonen, G. Haefeli, "BGV fibre module: Test beam report", EPFL, Lausanne, 2016, http://lphe.epfl.ch/publications/2016/LPHE-2016-004.pdf.

[7] G. Spiezia et al., "The LHC Radiation Monitoring System - RadMon", 2011, CERN, Geneva, Switzerland, PoS RD **11** (2011) 024.

[8] S. Löchner and M. Schmelling, "The Beetle Reference Manual - chip version 1.3, 1.4 and 1.5", LHCb-2005-105, CERN-LHCb-2005-105.

ISBN: 978-3-95450-192-2 doi:10.18429/JACoW-IBIC2017-WE3AB1

[9] G. Haefeli et al., "The LHCb DAQ interface board TELL1", Nucl. Instrum. Meth. A **560** (2006) 494.

[10] R. Jacobsson, "The Final LHCb Readout Supervisor "ODIN", Sep 2002, LHCb-TALK-2002-044.

[11] O. Girard, L. An, A. Kuonen, H. Li, G. Haefeli, "BGV fibre module read-out, signal correction and clustering", EPFL, Lausanne, 2016, http://lphe.epfl.ch/publications/2016/LPHE-2016-002.pdf.

[12] R. Aaij et al., "Performance of the LHCb Vertex Locator", JINST **9** (2014) 09007 doi:10.1088/1748-0221/9/09/P09007 [arXiv:1405.7808 [physics.ins-det]].

[13] LHCb Collaboration, "LHCb Tracker Upgrade Technical Design Report", CERN-LHCC-2014-001.

[14] R. Mankel, "Measurement of the Transverse Beam Line Width Using Impact Parameter Correlations", CMS Analysis Note, CMS-AN-2010/196, 25 June, 2010, CERN, Geneva, Switzerland.

[15] S. Donati, L. Ristori, "Measuring beam width and SVX impact parameter resolution", CDF-Note-4189, 2003, Fermilab, Batavia, IL, U.S.

[16] S. Andriamonje et al., "Development and performance of Microbulk Micromegas detectors", JINST **5** (2010) P02001 doi:10.1088/1748-0221/5/02/P02001.

[17] T. Papaevangelou et al., "Fast Timing for High-Rate Environments with Micromegas", arXiv:1601.00123. [physics.ins-det].

[18] M. Frank, C. Gaspar, B. Jost and N. Neufeld, "The LHCb Data Acquisition and High Level Trigger Processing Architecture", J. Phys. Conf. Ser. **664** (2015) no.8, 082011.

ISBN: 978-3-95450-192-2 doi:10.18429/JACoW-IBIC2017-WE3AB3

COMMISSIONING AND FIRST RESULTS OF THE ELECTRON BEAM PROFILER IN THE MAIN INJECTOR AT FERMILAB*

R. Thurman-Keup†, M. Alvarez, J. Fitzgerald, C. Lundberg, P. Prieto, J. Zagel,
FNAL, Batavia, IL, 60510, USA
W. Blokland, ORNL, Oak Ridge, TN, 37831, USA

Abstract

The planned neutrino program at Fermilab requires large proton beam intensities in excess of 2 MW. Measuring the transverse profiles of these high intensity beams is challenging and often depends on non-invasive techniques. One such technique involves measuring the deflection of a probe beam of electrons with a trajectory perpendicular to the proton beam. A device such as this is already in use at the Spallation Neutron Source at ORNL and a similar device has been installed in the Main Injector at Fermilab. Commissioning of the device is in progress with the goal of having it operational by the end of the year. The status of the commissioning and initial results will be presented.

INTRODUCTION

Traditional techniques for measuring the transverse profile of proton beams typically involve the insertion of an object into the path of the proton beam. Flying wires for instance in the case of circulating beams, or secondary emission devices for single pass beamlines. With increasing intensities, these techniques become riskier both for the device and the radioactivation budget of the accelerator. Various alternatives exist including ionization profile monitors, gas fluorescence monitors, and the subject of this report, electron beam profile monitors.

The concept of a probe beam of charged particles to determine a charge distribution has been around since at least the early 1970's [1-3]. A number of conceptual and experimental devices have been associated with accelerators around the world [4-8]. An operational device is presently in the accumulator ring at SNS [9].

An Electron Beam Profiler (EBP) has been constructed at Fermilab and installed in the Main Injector (MI) [10]. The MI is a proton synchrotron that can accelerate protons from 8 GeV to 120 GeV. The protons are bunched at 53 MHz with a typical rms bunch length of 1-2 ns. In this paper, we discuss the design and installation of the EBP and present some initial measurements.

THEORY

The principle behind the EBP is electromagnetic deflection of the probe beam by the target beam under study (Fig. 1). If one assumes a target beam with $\gamma \gg 1$, no magnetic field, and $\rho \neq f(z)$, then the force on a probe particle is [11]

$$\vec{F}(\vec{r}) \propto \int d^2\vec{r}'\rho(\vec{r}')\frac{(\vec{r}-\vec{r}')}{|\vec{r}-\vec{r}'|^2}$$

and the change in momentum is

$$\Delta\vec{p} = \int_{-\infty}^{\infty} dt\ \vec{F}\left(\vec{r}(t)\right)$$

For small deflections, $\vec{r} \approx \{b, vt\}$, and the change in momentum is

$$\Delta\vec{p} \propto \int_{-\infty}^{\infty} dx' \int_{-\infty}^{\infty} dy'\ \rho(x',y') \cdot \int_{-\infty}^{\infty} dt\ \frac{\{b-x', vt-y'\}}{(b-x')^2+(vt-y')^2}$$

where {} indicates a vector. For small deflections, $\vec{p} \approx \{0, p\}$ and the deflection is $\theta \approx \frac{|\Delta\vec{p}|}{|\vec{p}|}$. The integral over time can be written as $\mathrm{sgn}(b - x')$ leading to an equation for the deflection

$$\theta(b) \propto \int_{-\infty}^{\infty} dx' \int_{-\infty}^{\infty} dy'\,\rho(x',y')\,\mathrm{sgn}(b-x')$$

where $\mathrm{sgn}(x) = -1$ for $x < 0$ and $+1$ for $x \geq 0$.

If one takes the derivative of $\theta(b)$ with respect to b, the sgn function becomes $\delta(b - x')$ leading to

$$\frac{d\theta(b)}{db} \propto \int_{-\infty}^{\infty} dy'\,\rho(b,y')$$

which is the profile of the charge distribution of the beam. Thus, for a gaussian beam, this would be a gaussian distribution and the original deflection angle would be the error function, $\mathrm{erf}(b)$.

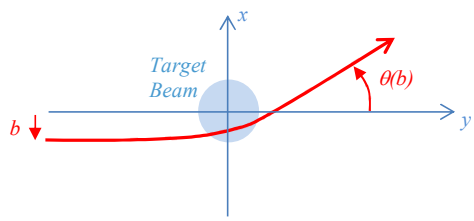

Figure 1: Probe beam deflection (red) for some impact parameter b.

EXPERIMENTAL TECHNIQUE

To obtain $\theta(b)$, one needs to measure the deflection for a range of impact parameters. This can be accomplished in a single shot by sweeping the electron beam through the proton beam provided the sweep time is much smaller than the r.m.s. bunch length of the proton beam to avoid coupling the longitudinal and transverse distributions. In the main injector, this would be challenging considering

* Operated by Fermi Research Alliance, LLC under Contract No. De-AC02-07CH11359 with the United States Department of Energy.
† keup@fnal.gov

ISBN: 978-3-95450-192-2 doi:10.18429/JACoW-IBIC2017-WE3AB3

its bunch length is 1-2 ns. The electron beam can also be stepped through the proton beam while recording the deflection at each step as demonstrated in Fig. 2 [12].

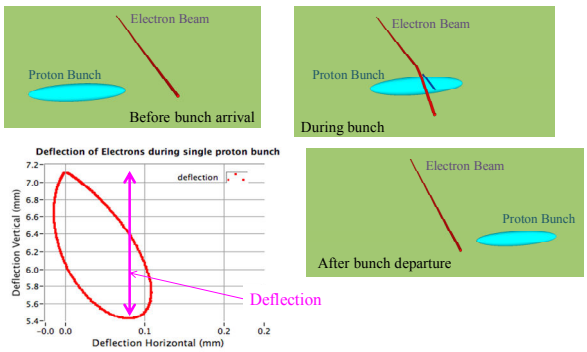

Figure 2: Trajectory followed by a stationary electron beam as the proton bunch passes by. There is some deflection along the proton beam direction due to the magnetic field of the proton beam, but it is much smaller than the deflection transverse to the proton beam.

The method chosen for the MI implementation is a variation of the slow stepping. Instead of a stationary electron beam at each step, the beam is swept along the direc-tion of the proton beam producing an approximate longitudinal distribution (Fig. 3). This technique has the potential to allow longitudinal slicing of the transverse profile assuming the longitudinal distribution either remains constant over the series of impact parameter measurements or can be corrected for synchrotron motion.

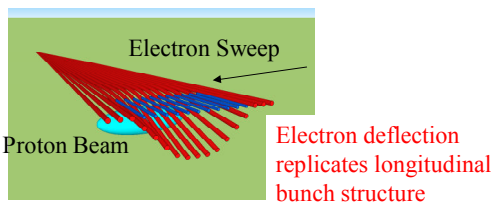

Figure 3: The electron beam is swept along the direction of the proton beam with a sweep time comparable to the proton bunch length. This records the deflection as a function of longitudinal position. A series of these sweeps is collected at different impact parameters to obtain $\theta(b)$.

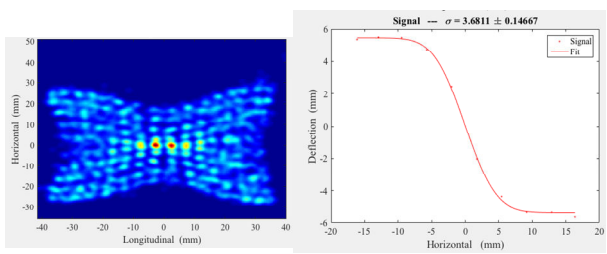

Figure 4: Simulated image of successive electron beam sweeps along the proton beam direction. The sweeps near the center are difficult to separate and may need to be split across multiple camera frames.

Simulations of the deflection are shown in Fig. 4. Here successive sweeps along the proton direction at different impact parameters are displayed in the same image. Each simulated electron produces a Gaussian spot with an rms of 1 mm. The simulation was done for injection parameters of 3 mm horizontal proton beam size, and 2 ns bunch length. One can see that the central deflections may overlap each other. Problems such as these must be overcome through, for example, timing shifts or interleaving across multiple camera frames.

APPARATUS

The device that was constructed for the MI consists of an EGH-6210 electron gun from Kimball Physics, followed by a cylindrical, parallel-plate electrostatic deflector, and finally a phosphor screen acting as the beam dump (Fig. 5).

The gun (Fig. 6) is a 60 keV, 6 mA, thermionic gun with a LaB_6 cathode, that can be gated from 2 μs to DC at a 1 kHz rate. The gun contains a focusing solenoid and four independent magnet poles for steering/focusing. The minimum working spot size is <100 μm. The electrostatic deflector (Fig. 6) contains 4 cylindrical plates that are 15 cm long and separated by ~2.5 cm. Following the electrostatic deflector is the intersection with the proton beamline. There is a pneumatic actuator at this point with a stainless-steel mirror for generating optical transition radiation (OTR) to be used in calibrating the electron beam.

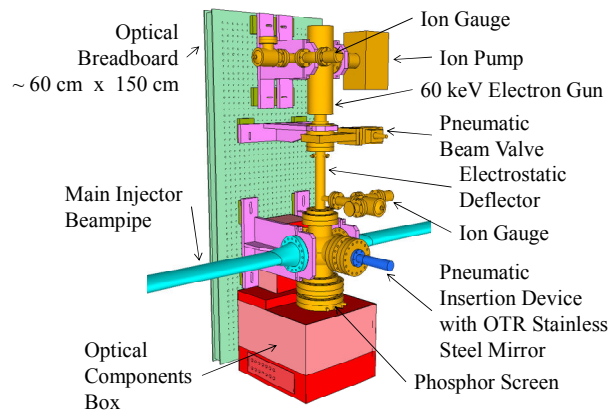

Figure 5: Model of the EBP showing the main components.

After the proton beam intersection, there is a phosphor screen from Beam Imaging Systems (Fig. 6). It is composed of P47 (Y_2SiO_5:Ce3+) with an emission wavelength of 400 nm, a decay time of ~60 ns and a quantum yield of 0.055 photons/eV/electron. The phosphor screen has a thin conductive coating with a drain wire attached. Both the OTR and the phosphor screen are imaged by a single intensified camera system (Fig. 7). The source is chosen by a mirror on a moving stage. Each source traverses a two-lens system plus optional neutral density filters or polarizers before entering the image intensifier (Hamamatsu V6887U-02). The output of the intensifier is imaged by a COHU CCD camera with C-mount lens. This setup will likely change in favour of a CID camera from Thermo-electron (now Thermo Scientific) fiber-

ISBN: 978-3-95450-192-2 doi:10.18429/JACoW-IBIC2017-WE3AB3

optically coupled to the intensifier through a fiber-optic taper to improve light collection.

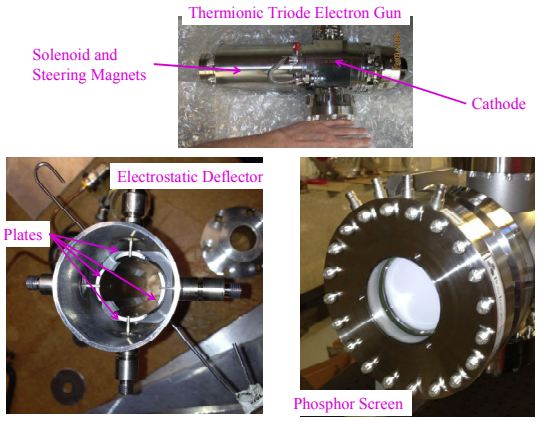

Figure 6: Top) Commercial electron gun. Left) Inside view of the electrostatic deflector showing the cylindrical parallel plates. Right) Phosphor screen mounted to an 8 in conflat flange with viewport. A drain wire is attached between the screen and one of the SHV connectors.

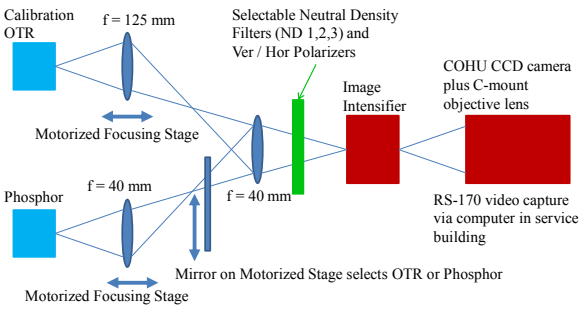

Figure 7: Conceptual layout of the optical paths followed by the OTR light and the phosphor screen light. Of the two lenses in each path, the second one is shared.

TEST STAND RESULTS

A test stand was setup to measure beam characteristics of the electron gun. It consisted of a pair of OTR screens used to measure the spot size and divergence to verify the manufacturer's specifications and for use in the simulation. The beam measurements were carried out using the solenoidal magnet in the gun to focus the beam at the first screen, allowing a measurement of the emittance of the electron beam (Fig. 8). Although these measurements were done at 50 keV, the intensity of the MI beam requires an electron energy of only 10-15 keV.

INSTALLATION

The EBP was installed in the MI during the 2014-2016 maintenance periods (Fig. 9). The location is near the end of a straight section just upstream of a horizontal focussing quadrupole. The expected horizontal rms beam size at this location is expected to be 1-3 mm. Because of the proximity to the MI magnet busses, the entire EBP beamline was wrapped in three layers of mumetal, mostly eliminating electron beam movement due to bus currents.

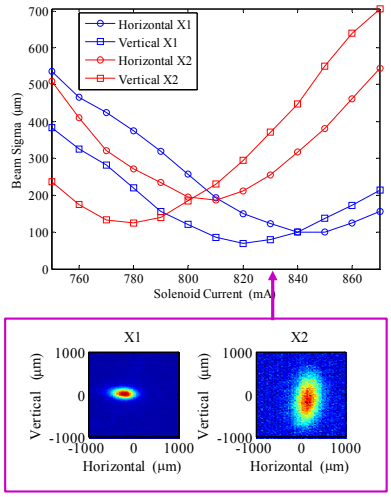

Figure 8: Horizontal and vertical rms beam sizes at the first (blue) and second (red) crosses in the test stand. The measurements are from OTR taken at ~50 keV and 1 mA beam current onto the stainless-steel mirrors.

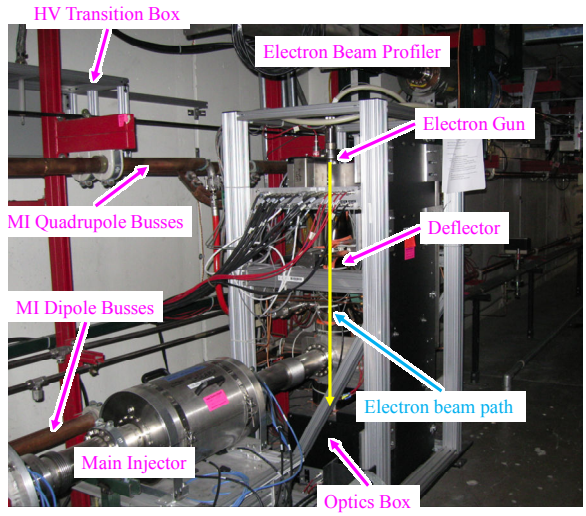

Figure 9: EBP installed in the end of a straight section in the MI. One can see the close proximity to the magnet busses.

RESULTS

Initial measurements of transverse profiles of the MI beam have been made with stationary electron beams. Figure 10 shows the deflection of the stationary electron beam as the proton bunches pass by the electron beam. The bright spot is the undeflected electron beam as seen in the bottom pictures where there is no proton beam. There is still a bright spot in the upper pictures due to the gaps between the proton bunches when the electron beam is not deflected. These images are taken just after injection into the MI at 8 GeV. The expected horizontal beam size is about 3 mm at this location at injection.

Using the amount of deflection in the images, a plot of deflection vs. impact parameter can be formed from which to extract the proton beam size (Fig. 11). The

ISBN: 978-3-95450-192-2 doi:10.18429/JACoW-IBIC2017-WE3AB3

measured rms horizontal beam size at injection is about 3.7 mm.

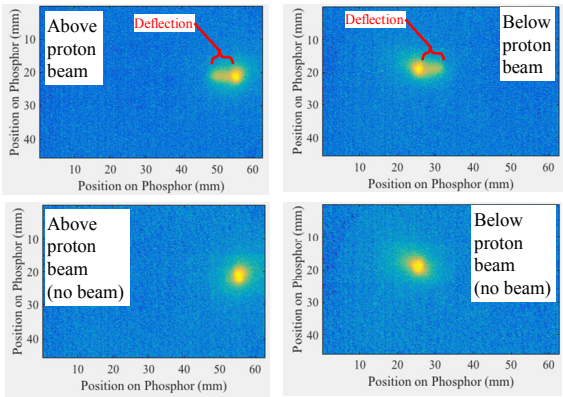

Figure 10: Deflection of the electron beam (top) for cases of the electron beam above and below the proton beam. The bottom images are without the proton beam.

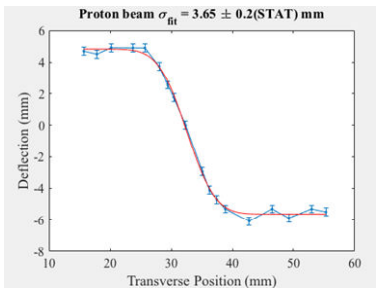

Figure 11: Electron beam deflection as a function of impact parameter with the proton beam. The uncertainties are just an estimate of how well one can determine the peak deflection from the images in Fig. 10.

Measurements were also taken at extraction from MI at 120 GeV and near transition crossing at about 19 GeV (Fig. 12). The expected rms beam size at extraction is about 1 mm. The other features to note in these images are the amount of deflection and the intensity of the deflected part of the electron beam. The bunch length of the protons is shorter at extraction than at injection and is particularly short near transition. There are two consequences of these facts: the charge density is higher at extraction and transition which produces larger deflections, and the shorter bunches result in a smaller proportion of deflected beam. This is consistent with what is seen in the images in Fig. 12.

To study the intended fast deflection along the proton beam line (Fig. 3), the deflector was tested using a FET-based HV pulser, without the proton beam present. An electron beam streak is shown in Fig. 13. This image contains both the primary sweep (~20 ns), and the return sweep which is about 5 times slower. Thus, the intensity of just the primary would be significantly less.

SUMMARY

An electron beam profiler has been built and installed in the MI at Fermilab and has been used to make some measurements of the horizontal proton beam size. The measurements are in fairly good agreement with the expected values. There are several repairs and improvements that need to be made. Some of these are in progress during the current maintenance period. The phosphor screen will be replaced and the camera system will be modified to be more radiation and noise tolerant.

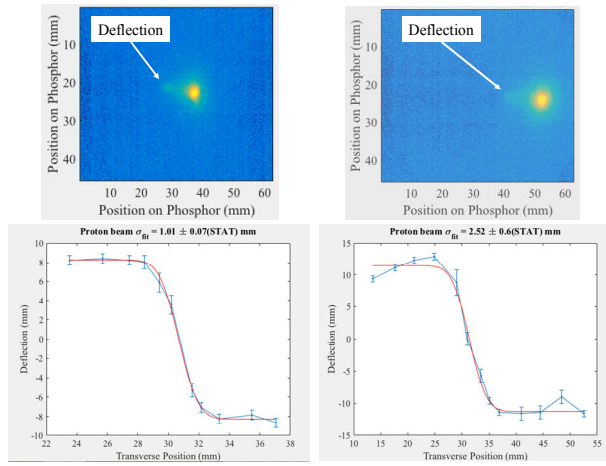

Figure 12: Deflection vs. impact parameter for extraction (left) and transition crossing (right). The bunch length at transition is shorter than extraction, so the deflection is larger due to increased charge density. The intensity is also slightly less, since the electron beam spends less time being deflected.

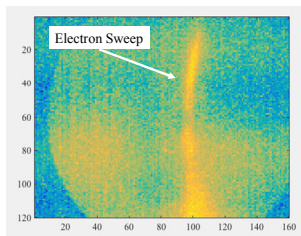

Figure 13: Electron beam streak using the deflecting plates. The image contains both the primary and return streaks. The curvature is due to the curved deflecting plates.

ACKNOWLEDGEMENTS

The authors would like to acknowledge the help of the MI, Mechanical, Electrical, and Instrumentation departments for all their assistance in the construction and installation of this device. This manuscript has been authored by Fermi Research Alliance, LLC under Contract No. DE-AC02-07CH11359 with the U.S. Department of Energy, Office of Science, Office of High Energy Physics. The United States Government retains and the publisher, by accepting the article for publication, acknowledges that the United States Government retains a non-exclusive, paid-up, irrevocable, world-wide license to publish or reproduce the published form of this manuscript, or allow others to do so, for United States Government purposes.

REFERENCES

[1] Paul D. Goldan, "Collisionless sheath – An experimental investigation", *Phys. Fluids,* vol. 13, p. 1055, 1970.

ISBN: 978-3-95450-192-2 doi:10.18429/JACoW-IBIC2017-WE3AB3

[2] C. H. Stallings, "Electron beam as a method of finding the potential distribution in a cylindrically symmetric plasma", *J. Appl. Phys*., vol. 42, p. 2831, 1971.
[3] C. W. Mendel Jr., "Apparatus for measuring rapidly varying electric fields in plasmas", *Rev. Sci. Instrum.*, vol. 46, p. 847, 1975.
[4] J. Shiloh *et al*., "Electron beam probe for charge neutralization studies of heavy ion beams", *Rev. Sci. Instrum.*, vol. 54, p. 46, 1983.
[5] V. Shestak *et al*., "Electron beam probe for ion beam diagnostics", TRIUMF, Rep. TRI-DN-87-36, 1987.
[6] P. Gross *et al*., "An electron beam probe for ion beam diagnosis", in *Proc. European Particle Accelerator Conference 1990*, Nice, France, June 1990, p. 806.
[7] J. Bosser *et al*., "Transverse profile monitor using ion probe beams", *Nucl. Instrum. Methods Phys. Res. A,* vol. 484, p. 1, 2002.
[8] P. V. Logatchov *et al*., "Non-destructive singlepass monitor of longitudinal charge distribution in an ultrarelativistic electron bunch", in *Proc. Particle Accelerator Conference 1999,* New York, NY, USA, March 1999.
[9] W. Blokland and S. Cousineau, "A non-destructive profile monitor for high intensity beams", in *Proc. Particle Accelerator Conference 2011,* New York, NY, USA, March 2011.
[10] R. Thurman-Keup *et al*., "Installation status of the electron beam profiler for the Fermilab Main Injector", in *Proc. International Beam Instrumentation Conference 2015*, Melbourne, Australia, September 2015.
[11] A. Aleksandrov *et al*., "Feasibility study of using an electron beam for profile measurements in the SNS accumulator ring", in *Proc. Particle Accelerator Conference 2005*, Knoxville, TN, USA, May 2005, pp. 2586 – 2588.
[12] W. Blokland, "Collaboration report on e-beam scanner for Project X beam instrumentation", unpublished, October 2011.

ISBN: 978-3-95450-192-2 doi:10.18429/JACoW-IBIC2017-WEPCC02

UniBEaM - BEAM PROFILER FOR BEAM CHARACTERIZATION AND POSITION FEEDBACK

D. E. Potkins, M. P. Dehnel, D-Pace Inc., Nelson, BC, V1L 4B6, Canada
N. Lobanov, The Australia National University, Canberra, ACT 2601, Australia
T. Kubley, O. Toader, Michigan Ion Beam Laboratory, Ann Arbor, MI 48109, USA

Abstract

A beam profiler called UniBEaM is based on passing 200 micron cerium-doped optical fibers through a charged particle beam and measuring the scintillation light. In order to characterize UniBEaM over its entire kinetic energy range: keV to GeV; current range: pA to mA; and particle type range: light ions to heavy ions, and electrons, an Early Adopter Programme (EAP) was established to test UniBEaM's performance. EAP's: Australia National University (ANU) and Michigan Ion Beam Laboratory (MIBL) report on their use of UniBEaM at their facilities.

INTRODUCTION

A beam profiler based on doped SiO_2 optical fibers was designed and tested at the Albert Einstein Center for Fundamental Physics (AEC), Laboratory for High Energy Physics (LHEP), University of Bern, Switzerland [1]. This beam profiler, called the Universal Beam Monitor (UniBEaM™) was licensed and commercialized by D-Pace Inc., Canada. This paper provides example measurements made by two early adopters of this device: the Department of Nuclear Physics of the Australian National University (ANU), and the Michigan Ion Beam Laboratory (MIBL).

SYSTEM DESCRIPTION

D-Pace's commercial version of UniBEaM was described in detail by Potkins *et al*. [2].

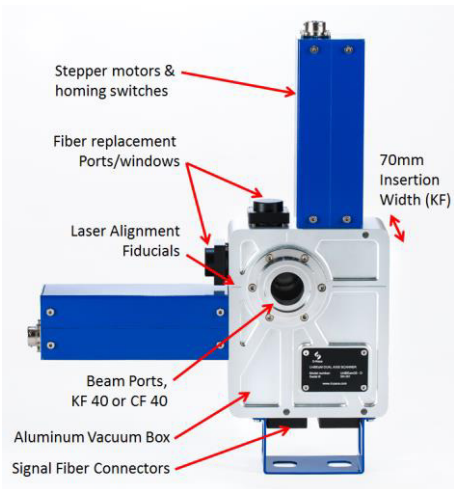

Figure 1: UniBEaM Probe.

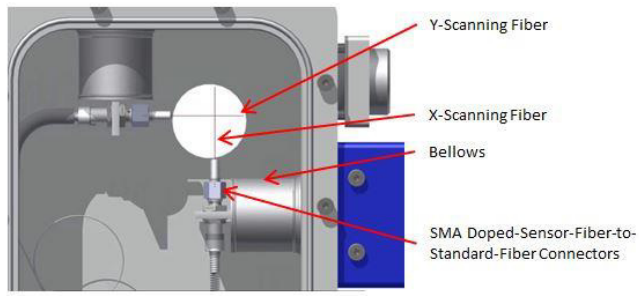

Figure 2: Internal view of UniBEaM showing the X & Y scintillating sensor fibers and fiber connector.

The UniBEaM probe (Figs. 1 & 2) has two sensing fibers; one for X-profiles and one for Y-profiles. The sensor fibers are moved through the beam by stepper motor actuators. The sensor fibers are made from SiO_2 doped with Ce^{+3} ions, and have a diameter of 200 µm. Silicon photo multipliers (SiPMs), located in the UniBEaM controller 10's of meters from the probe, measure the scintillation light, and subsequently amplify and digitize the signal. The UniBEaM software controls the scan resolution, and start and stop positions. X and Y beam profiles may be scanned separately or simultaneously. The software also calculates the beam centroid and the integral of the intensity profile.

The UniBEaM25 probe measures nominal 25 mm diameter beams, has a 35 mm aperture, and is provided with KF40 or CF40 flanges.

TESTING

Signal to Noise Assessment with 1MeV $16O^{+1}$

ANU installed UniBEaM on the beam line of a high energy ion implanter. The implanter utilizes an NEC 1.7 MV tandem accelerator able to reach energies up to 10 MeV. The BPM provides the feedback required for the operator to produce a well-focused and aligned beam on the target, and to measure the beam response to beam steering devices.

ANU utilized UniBEaM to measure beam profiles of a $16O^{+1}$, 1 MeV beam at low beam currents to investigate the noise floor of UniBEaM and compare the results with profiles acquired using an NEC BPM 80 helical wire scanner.

UniBEaM plots separate profiles for the orthogonal X and Y scans. The X and Y profiles may be scanned and displayed individually, or in the same plot. The horizontal axis of the UniBEaM plots are in mm. Figure 3 shows a scan of a $16O^{+1}$, 1 MeV, 80 pA beam to evaluate the noise floor of UniBEaM for this beam.

ISBN: 978-3-95450-192-2 doi:10.18429/JACoW-IBIC2017-WEPCC02

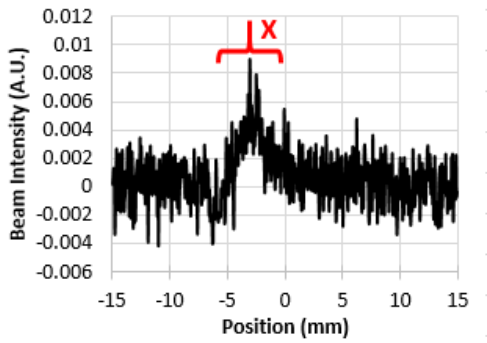

Figure 3: UniBEaM X profile, $16O^{+1}$ 1 MeV 80 pA.

The NEC helical wire scanner uses a rotating wire helix to collect secondary electrons from the grounded scanning wire. It has a nominal beam pipe diameter 10 cm with a 2.54 cm molybdenum beam entrance aperture. It produces a single plot representing pseudo-orthogonal X & Y profiles in a single oscilloscope trace, along with a second trace to allow the user to calibrate the horizontal axis time units displayed on the scope into approximate distance units (Fig. 4).

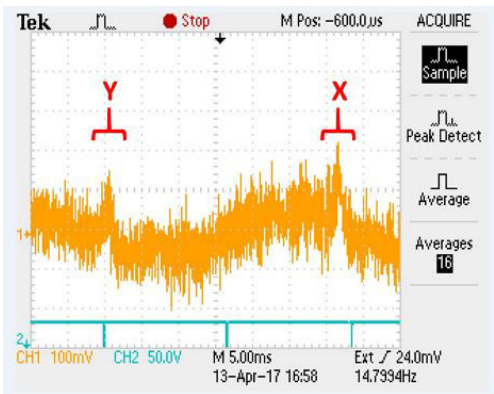

Figure 4: BPM 80 X & Y profiles, $16O^{+1}$ 1 MeV 80 pA.

Comparing the two scans shown in Fig. 3 and Fig. 4, the UniBEaM and helical wire scanners have similar signal-to-noise ratios for the $16O^{+1}$ beam. Figures 5 and 6 show profiles for the same $16O^{+1}$ 1MeV beam when the beam current was increased to 2.6nA.

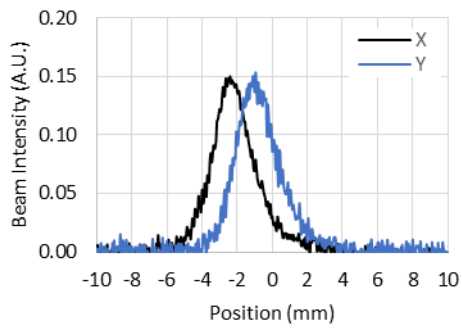

Figure 5: UniBEaM X & Y profiles. $16O^{+1}$ 1 MeV 2.

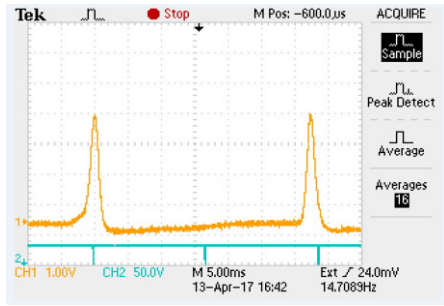

Figure 6: NEC BPM 80 X & Y profiles with 16x averaging. $16O^{+1}$ 1 MeV 2.6 nA beam.

Low Energy Beams

ANU also utilized UniBEaM on low energy beams after the inflection magnet, before injection into their 14UD electrostatic pelletron accelerator. Negative beams of H, Ni, O, Al_2O_3 and S were tested.

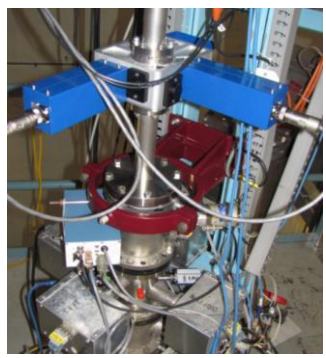

Figure 7: UniBEaM installed at the entrance to pelletron accelerator.

Since the UniBEaM system utilizes two separate signal paths for the X & Y channels, gain and offset adjustments are required to account for the different dark currents and gains of the light sensors for each channel, as well as the variability between X & Y channel optical connectors. These adjustments were made to the profiles shown in Figs. 5 and 8.

In the nA current range, the UniBEaM exhibited better signal-to-noise and spatial resolution than the NEC BPM 80 (Figs. 8 & 9).

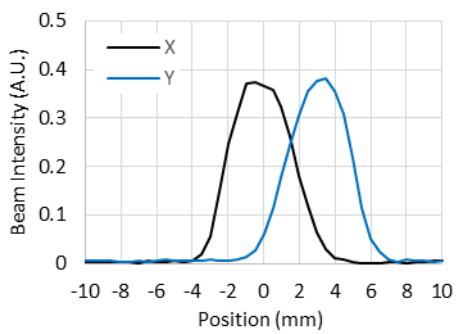

Figure 8: UniBEaM X & Y profiles. $32S^{-1}$ 150 keV 300 nA.

ISBN: 978-3-95450-192-2 doi:10.18429/JACoW-IBIC2017-WEPCC02

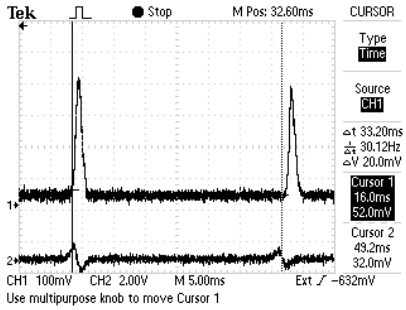

Figure 9: NEC BMP 80 profiles. 32S^{-1} 150keV 300nA beam.

Raster Scanning Feedback

The Michigan Ion Beam Laboratory (MIBL) used UniBEaM to profile ion implanter (Ar, Ag, Fe and Ni) beams. Figure 10 shows a UniBEaM scan where 107Ag and 109Ag are resolved in the beam profile.

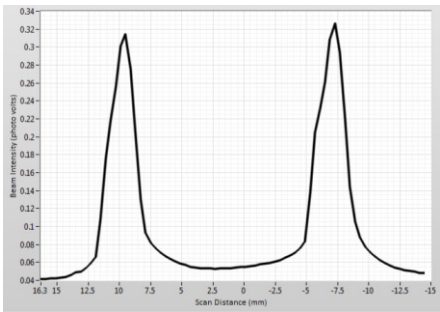

Figure 10: 107Ag and 109Ag, 370 keV 3 µA. Resolved peaks in Y profile scan of beam.

Figures 11, 12 and 13 show UniBEaM profiles taken for focussed, rastered, and defocussed Argon beams, where UniBEaM was used as a tool to assess beam uniformity for ion implanting.

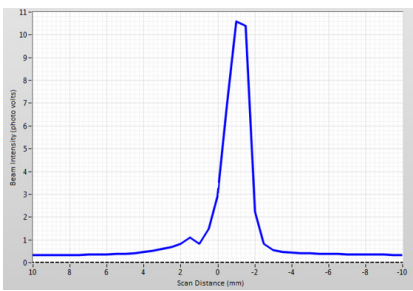

Figure 11: Ar 370keV 3µA, Y profile of focussed beam.

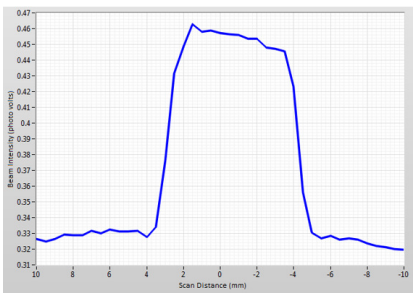

Figure 12: Ar 370keV 3µA, Y profile of rastered beam with 6mm x 6mm aperture.

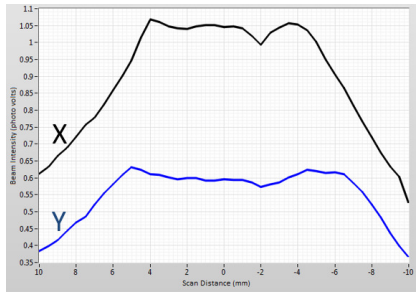

Figure 13: Ar 370 keV 3 µA, X & Y profiles of rastered beam with no aperture.

FURTHER DEVELOPMENTS

Further investigation will be required to determine if the properties of the sensor fibers change as a result of ion implantation into the sensor fibers themselves, thereby changing their optical or emission properties.

D-Pace will investigate the utility of an optional collimator to limit the exposure of the sensor fibers where beam characteristics allow particles to reach the optical fiber in its parked position.

D-Pace is developing a version of UniBEaM for pulsed beams, where sensor fiber movements and measurements are synchronized with the beam pulses, for pulse rates up to 1000 pulses per minute.

D-Pace is working on a high sensitivity version of UniBEaM where a photon counting approach is used to further improve signal-to-noise for low current beams. The University of Bern utilizes photon counting methods.

CONCLUSION

UniBEaM is an alternative to conventional wire scanners, and offers the particle accelerator industry a compact and cost effective means of measuring charged particle, electron and x-ray beam intensity profiles over a large range of currents and beam energies.

ACKNOWLEDGMENTS

On behalf of D-Pace, the author gratefully acknowledges the financial contributions of the following Canadian government programmes: SRED and NRC. In addition, the author wishes to express his appreciation to the AEC-LHEP, University of Bern for their ongoing support with the commercialization of UniBEaM, and to the Department of Materials Science, University of Milano-Bicocca for their expertise in scintillating optical fibers. D-Pace also thanks Buckley Systems (Auckland, NZ) for their financial support of this project.

REFERENCES

[1] M. Auger *et al.*, "A detector based on silica fibers for ion beam monitoring in a wide current range", *Journal of Instrumentation*, vol. 11, p. 03027, March 2016.

[2] D. Potkins *et al.*, "A Low-Cost Beam Profiler Based On Cerium-Doped Silica Fibers", in *Proc. CAARI 2016*, Fort Worth, Texas, USA, Oct. 2016, un-published.

ISBN: 978-3-95450-192-2 doi:10.18429/JACoW-IBIC2017-WEPCC03

PERFORMANCE ASSESSMENT OF PRE-SERIES FAST BEAM WIRE SCANNER PROTOTYPES FOR THE UPGRADE OF THE CERN LHC INJECTOR COMPLEX

J. L. Sirvent, L. Garcia, J. Tassan-Viol, G. Trad, J. Emery, P. Andersson, F. Roncarolo, W. Andreazza, D. Gudkov, R. Veness, B. Dehning, CERN, Geneva, Switzerland

Abstract

A new generation of beam wire scanner (BWS), for transversal beam profile monitoring, is under development on the framework of the LHC Injector Upgrade project at CERN. Two pre-series prototypes have been built and installed in the Super Proton Synchrotron and Proton Synchrotron Booster, to assess the performance of the upgraded BWS concept.

This contribution shows the outcome of the measurement campaigns carried out on the first BWS prototypes, both in the laboratory and with proton beams. An evaluation of a high dynamic range acquisition system for the measurement of the secondary showers produced by the beam-wire interaction is also presented.

INTRODUCTION

The High Luminosity upgrade of the Large Hadron Collider (HL-LHC) will feature higher intensity proton beams in the whole injector chain. In addition, this upgraded scenario requires that the normalized transverse emittance of these beams be measured with a precision better than 5%. For beam wire scanners, the reference transverse beam profile monitors at CERN, this translates into a required wire position measurement uncertainty of a few micrometers.

The performance of the current operational beam wire scanners at CERN is limited by electronic noise on the signal from their position sensitive potentiometers, by the reproducibility of their motion mechanics and by the dynamic range of the acquisition system measuring the resulting secondary showers. The current wire position measurement uncertainty is in the order of ±100µm for the fast rotating scanners in the Proton Synchrotron (PS) and its Booster (PSB) at a speed of $15ms^{-1}$ [1], ±30µm for the rotating scanners ($6ms^{-1}$) in the Super Proton Synchrotron (SPS) and ±18µm for the linear scanners ($1ms^{-1}$) installed in the SPS and LHC [2]. The linear scanners are limited for use with low intensity beams as at higher intensity the deposited energy can lead to sublimation of the carbon wires used. In addition, all of these systems use bellows for motion transfer to the in-vacuum mechanics, this represent reliability issues when performing thousands of scans per year. The current scanners cannot therefore fulfill the HL-LHC specifications in terms of reliability and precision.

The need for higher measurement reproducibility at higher speeds has motivated the design of an innovative high precision beam wire scanner for the LHC Injectors Upgrade (LIU) project [3]. The upgraded concept is based on a rotational architecture with a frameless motor, where all mobile parts are located in vacuum on a shared shaft, eliminating the need of bellows. The wire position is determined through a high accuracy optical encoder [4], see schematic of Fig. 1. The secondary showers produced through the beam-wire interaction will be acquired using a high dynamic range acquisition system to eliminate the tedious set-up of operational parameters when switching between different beam configurations [5].

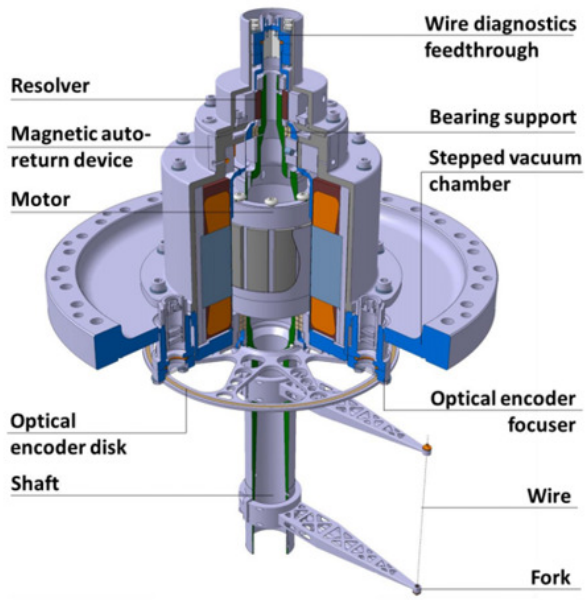

Figure 1: LIU beam wire scanner schematic.

SPS PROTOTYPE PERFORMANCE

The precision validation of the SPS BWS prototype [6] (BWS.51740.V) was carried out by measuring a single bunch with $2.3x10^{10}$ protons, during a period in which it was accelerated to 270 GeV and left circulating for several hours. Due to beam dynamic aspects, this beam suffers an emittance increase during this time and negligible beam intensity losses.

A standard linear scanner (BWS.51731.V) was operated in parallel with the prototype for performance comparison. The linear scanner performed scans at $1ms^{-1}$, while the nominal speed of the prototype was $20ms^{-1}$. With the circulating bunch interacting with the wire every 23µs (the SPS revolution period) and the prototype running 20 times faster than the linear scanner, the number of times the bunch intercepts the wire (points per sigma) is reduced for the prototype, thus providing less information for the Gaussian fitting routine used on the resulting profile.

ISBN: 978-3-95450-192-2 doi:10.18429/JACoW-IBIC2017-WEPCC03

Whereas the linear scanner was equipped with a CERN standard scintillator/photo-multiplier (PM) detector for measuring the secondary shower, the prototype was equipped with both a scintillator-PM system and an experimental pCVD diamond system.

The beam emittance uncertainty for each scanner was determined from the residuals around a linear fit applied to the emitance growth in time (Fig. 2). The normalized emittance was calculated from the sigma value of a Gaussian fit applied to each measured profile, the accelerator optics and the beam energy. The normalized emittance measured by both scanners is the same, however, the absolute sigma values differ for both scanners due to the accelerator optics (beta functions are different for each scanner location). The measurement results are summarized in Table 1.

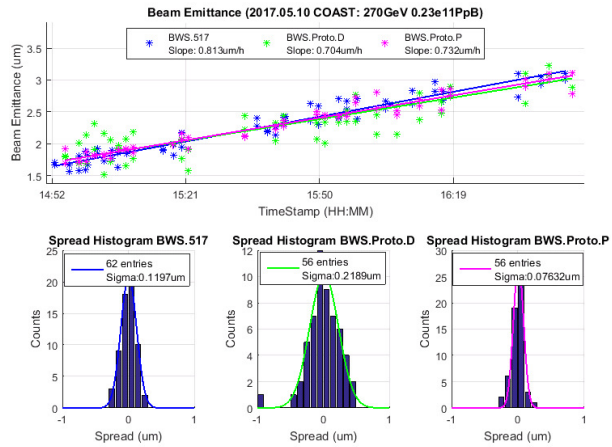

Figure 2: Beam emittance evolution and measurement spread for the linear scanner BWS.51731.V (blue traces) and the rotational prototype BWS.51740.V using a scintillator-PM (magenta traces) and a diamond detector (green traces).

Table 1: SPS BWS Performance Summary on Beam Test with a COAST (single bunch $2.3x10^{10}$ protons at 270GeV)

Scanner	BWS.51731.V	BWS.51740.V	
		PMT	Diam.
Speed	1	20	
Points per σ	39	1.7	
Sigma (µm)	900 ± 28	800 ± 18	800 ± 35
(σ %)	3.0 %	2.3 %	4.3 %
Emit. (µm)	2.5 ± 0.12	2.5 ± 0.07	2.5 ± 0.22
(σ %)	4.7%	3.0 %	8.7 %
Centroid (σ µm)	94	48	66

Despite the drastic decrease in the number of points per sigma of the prototype, due to its increased speed with respect to the linear scanner, it nevertheless showed a 1.5 times lower spread on the beam width determination and a factor 2 precision improvement on the beam centroid measurement. This is ultimately translated into a higher reproducibility on the emittance calculation.

When normalizing to the same number of points per sigma as the linear scanner, and with a factor of 2 lower wire position uncertainty, the beam width precision is improved by a factor 2.

Due to its limited detection area (10 by 10 mm^2) the diamond detector profiles were highly influenced by statistical noise that degraded its performance. The operational scanner also featured a systematic difference on the beam centroid measurement of 1mm between IN and OUT scans that was not observed on the prototype scanner.

PSB PROTOTYPE STUDIES

Instrument Laboratory Characterization

The wire position accuracy and precision of the BWS was determined by means of an optical bench. The system consists of a mobile laser that is displaced along the BWS scanning axis. For each laser position, the angular information given by the optical position sensor is determined at the moment of the wire/laser interception. Repeating this process for different laser positions the angular-to-projected transformation of the wire trajectory can be determined.

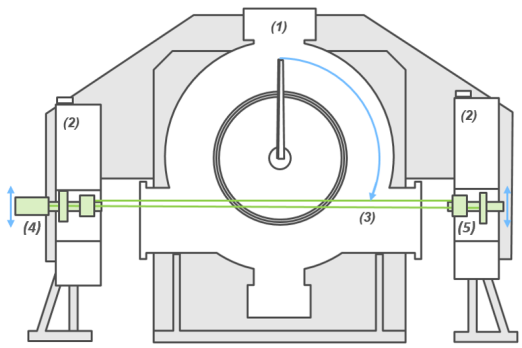

Figure 3: PSB calibration bench schematic showing scanner tank (1), mobile stages (2) and optical system (on green) with laser (4) and photo-diode (5). Wire trajectory (in blue) and interaction point (3) are also displayed.

The optical system consists of a Gaussian 532nm laser followed by a focusing lens and a beam displacer mounted on a mobile stage. These elements generate two parallel beams separated by a known and constant distance (2.94mm) that are focused on the laser/wire interaction region. On the other side of the scanner tank, a second mobile stage contains similar beam displacer which combines both beams for entry into a single photo-diode (see Fig. 3). As the carbon wire passes through each of the parallel laser beams, it generates a Gaussian dip in the photo-diode response. The angular interaction point is defined as the mid-point between the two dips observed.

The scanner was characterized along ±50mm from the central beam position at both $8ms^{-1}$ and $20ms^{-1}$. The measurements were then fitted with an analytical approximation based on the scanner geometry, with the wire position uncertainty expressed as the spread in the fit residuals.

The complete calibration analysis resulted in a position uncertainty of 6µm and 11.5µm for $8ms^{-1}$ and $20ms^{-1}$ respectively (see Fig. 4).

ISBN: 978-3-95450-192-2 doi:10.18429/JACoW-IBIC2017-WEPCC03

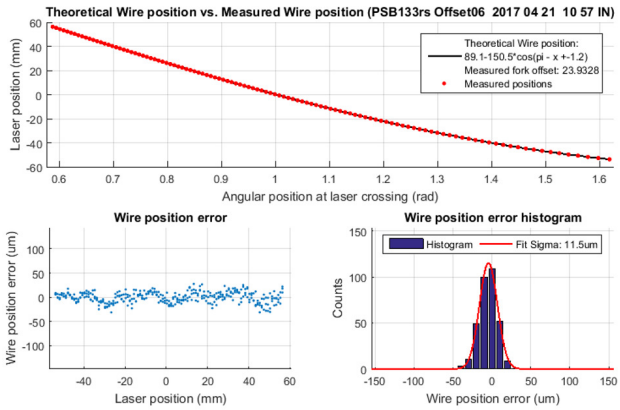

Figure 4: PSB calibration results at 20m/s.

The measured wire position exhibited an oscillatory behavior around the analytical approximation, reproducible over successive calibrations. These systematic oscillations were dependent on the scan speed, which suggests some kind of mechanical vibration or wire oscillation during the scan.

The accuracy and precision of the wire position measurement can be determined through a deeper analysis of the fit residuals. Systematic deviations from the analytical motion curve define the accuracy of the instrument and random errors its precision.

The Fig. 5 shows the systematic and random fit errors for several calibrations at different speeds. This shows a position dependent systematic error (accuracy) of ±10µm, resulting from these suspected oscillations, with a frequency dependent on the scan speed. The measurement spread at each position (precision), is strongly dependent on the scan speed with a standard deviation of 2.5µm and 6.2µm for $8ms^{-1}$ and $20ms^{-1}$ respectively

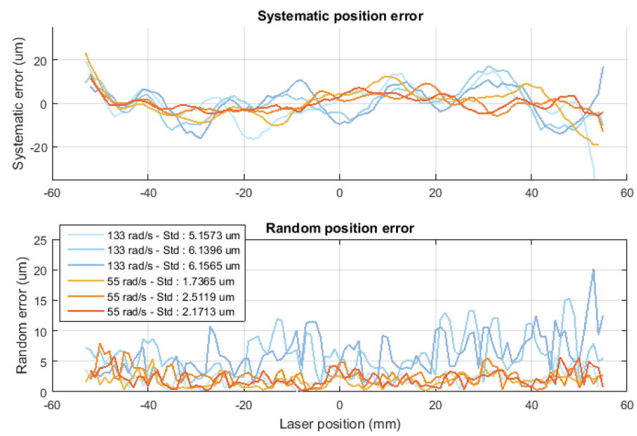

Figure 5: Analysis of fit residuals for several calibrations at 8 (orange) and 20 (blue) m/s.

A set of 100 scans performed at a fixed laser position gave a projected precision of about 3µm for $8ms^{-1}$ and 6µm for $20ms^{-1}$ confirming the previous analysis.

Studies carried out under vacuum and ambient air conditions provided similar results in terms of accuracy, however, the measurement precision for each laser position was a factor of 2 better with no vacuum at nominal speeds. The in-vacuum degradation could be linked to vibrations induced by the vacuum pump. The overall results are summarized in Table 2.

Table 2: PSB BWS Instrument Characterization

Speed (m/s)	8		20	
Conditions	Air	Vac.	Air	Vac.
Post-Calibration position error (um)	5.5	6	11.5	11.6
Accuracy (µm)	10			
Precision (µm)	2.5	2.7	6	11

Performance with LHC and ISOLDE Beams

The PSB prototype (BR3.BWS4L1.H) [7] was equipped with a standard scintillator-PM system and was tested with both, a nominal LHC beam ($1.8x10^{12}$ protons) and ISOLDE beams ($8.2x10^{12}$ protons). The operational scanner BR3.BWS.2L1.H was used for comparison.

The standard-PM signal of the prototype was digitally treated to emulate the operational scanner electronics, averaging the beam profile over multiple turns.

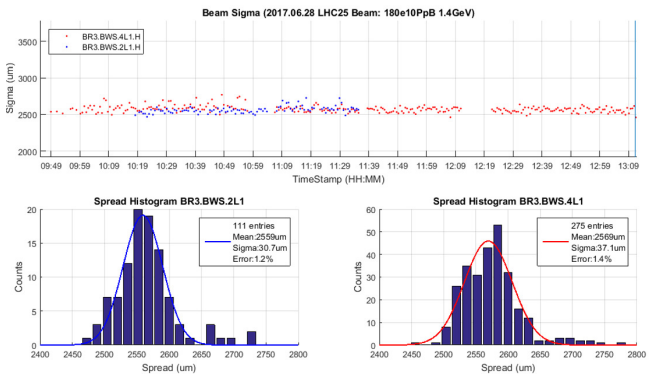

Figure 6: Beam sigma measured by PSB prototype (red) and reference (blue) scanners. LHC25ns at 1.4GeV.

As shown on Fig. 6, operational and prototype scanner measure similar beam widths, as expected since the accelerator optics are similar on both locations. The comparable measurement spread shown in both beams (always around 1% of the beam size) can be explained by the high number of points per sigma (200-700 in both scanners) and the averaging effect of the acquisition. While beam width variations over consecutive injections seem not to contribute on the beam width measurement spread, further studies are required for confirmation. The mean beam width and incertitude is shown in Table 3 for each measurement period.

Table 3: PSB Beam Width Measurements Summary for Operational and Prototype Scanner

Beam Type	**BR3.BWS.2L1**	**BR3.BWS.4L1**
LHC25 1.4GeV	2559 ± 31, 1.2%	2569 ± 37, 1.4%
ISO 588 MeV/c	8021 ± 125, 1.6%	8245 ± 52, 0.6%
ISO 886 MeV/c	6354 ± 88, 1.4%	6571 ± 46, 0.7%
ISO 1.39 GeV/c	5302 ± 44, 0.8%	5538 ± 38, 0.7%
ISO 1.92 GeV/c	4880 ± 53, 1.1%	5025 ± 34, 0.7%

ISBN: 978-3-95450-192-2 doi:10.18429/JACoW-IBIC2017-WEPCC03

Studies of a High Dynamic Range Acquisition System for the Measurement of the Secondary Showers

For the measurement of the secondary particle shower, resulting from the beam-wire interaction, operational BWS systems are equipped with big organic BC-408 scintillator blocks coupled to a wheel of selectable neutral density filters followed by a single PMT. In this configuration the operators need to find the correct working point (filter setting and PMT gain) to avoid PMT saturation while matching the PMT output to the dynamic range of the digitization electronics. Incorrect settings strongly influence the measurement quality, it often results in poor signal to noise ratio or PMT non-linearity when near saturation.

To avoid this setting dependency in the future systems, a quad-PMT (Q-PMT) detector system was tested. On this detector, each of the four PMT is intended to operate at different photon intensity levels. The Q-PMT signals were acquired using radiation tolerant front-end electronics located in the tunnel [5], these are based on a quad-channel 40MHz integrator ASIC (ICECAL). Data from all four channels were collected simultaneously with the best working point automatically selected in post processing by choosing the highest amplitude channel which presented no ADC clipping.

Standard scintillator-PM and Q-PMT systems were used simultaneously to acquire the profiles of the prototype scanner for ISOLDE and LHC beams throughout the PSB acceleration cycle. Under such conditions, due to the beam dynamics, the effective scintillator light intensity varied by 3 orders of magnitude. Fig. 7 shows the beam sigma, in time, measured with both standard and QPMT systems. Whereas the standard system required many filter changes for suitable operation (changes are high-lighted on the plot) and featured PM saturation for several measurements, the Q-PMT system allowed operation with no tunable parameters during the complete acceleration cycles of both beam types measured.

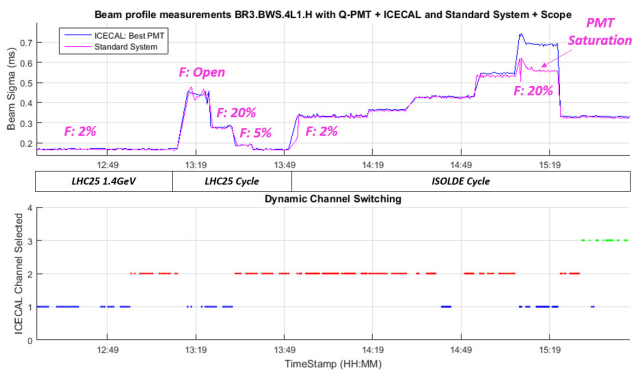

Figure 7: Top: Beam sigma measured by standard (magenta) and Q-PMT systems (blue). Bottom: Q-PMT channel selection in post-processing.

SUMMARY

The next generation of fast wire scanners at CERN are aimed to provide reliable operation with highly reproducible beam profile measurements at scanning speeds up to $20ms^{-1}$. Laboratory measurements have shown that a wire position precision of 6µm is obtainable at this maximum speed with an overall accuracy of ±10µm. The SPS beam tests have shown that the performance of the upgraded systems is comparable to that of the slow linear scanners despite 20 times less points per sigma. The beam width uncertainty in the SPS prototype was shown to be smaller than 2.5%, fulfilling the LIU requirements for emittance determination with < 5% uncertainty. Initial beam tests in the PSB have shown that the prototype scanners gives a slightly better precision than operational systems, well below the 2.5% specified by the LIU.

Test of a high dynamic range acquisition system based on a Q-PMT requiring no parameter tuning successfully demonstrated the applicability of such a system for secondary shower measurements covering several orders of magnitude.

REFERENCES

[1] J. Koopman, A.G. Ollacarizqueta and. Lokhovitskiy, "Fast wire scanner Calibration", in *Proc. DIPAC'09*, Basel, Switzer-land, May 2009, paper TUPB05, pp. 170-173.

[2] G. Baud, B.Dehning, J. Emery, J.J. Gras, A. Guerrero and E.Piselli., "Performance assessment of wire scanners at CERN", in *Proc. IBIC'13*, Oxford, UK., Sept. 2013, paper TUPF03, pp. 449-502., CERN, Geneva, Switzerland, Rep. CERN-ACC- 2014-0337, Dec. 2014

[3] "LHC Injectors Upgrade Technical Design Report: Volume 1 Protons", CERN, Geneva, Switzerland, Rep. CERN-ACC-2014-0337, Dec. 2014

[4] B. Dehning, J.Emery et al., "A fast and accurate wire scanner instrument for the CERN accelerators to cope with severe environmental constraints and increased demand for availability", in *Proc. IEEE CCA'14*, Juan Les Antibes, France, Oct. 2014, pp. 1139-1145

[5] J.L. Sirvent,"Beam Secondary Shower Acquisition Design for the CERN high Accuracy Wire Scanner", Ph.D. thesis, Universitat de Barcelona, Barcelona, Spain, unpublished.

[6] R. Veness et al., "Experience from the construction of a new fast wire scanner prototype for the CERN-SPS and its opti-misation for installation in the CERN-PS Booster", in *Proc. IBIC'15*, Melbourne, Australia, Sept. 2015, paper TUPB061, pp. 479-482.

[7] R. Veness et al., "Installation and test of pre-series wire scanners for the LHC injector upgrade project at CERN", in *Proc. IPAC'17*, Copenhagen, Denmark, May 2017, paper MOPAB121, pp. 412-414.

ISBN: 978-3-95450-192-2 doi:10.18429/JACoW-IBIC2017-WEPCC04

AN OPTICAL AND TERAHERTZ INSTRUMENTATION SYSTEM AT THE FAST LINAC AT FERMILAB*

R. Thurman-Keup†, A. H. Lumpkin, J. Thangaraj, FNAL, Batavia, IL, 60510, USA

Abstract

FAST is a facility at Fermilab that consists of a photoinjector, two superconducting capture cavities, one superconducting ILC-style cryomodule, and a small ring for studying non-linear, integrable beam optics called IOTA. This paper discusses the layout for the optical transport system that provides optical radiation to an externally located streak camera for bunch length measurements, and THz radiation to a Martin-Puplett interferometer, also for bunch length measurements. It accepts radiation from two synchrotron radiation ports in a chicane bunch compressor and a diffraction/transition radiation screen downstream of the compressor. It also has the potential to access signal from a transition radiation screen or YAG screen after the spectrometer magnet for measurements of energy-time correlations. Initial results from both the streak camera and Martin-Puplett will be presented.

INTRODUCTION

The Fermilab Accelerator Science and Technology (FAST) facility has been constructed for advanced accelerator research [1-3]. It will eventually consist of 3 entities: a photoinjector-based linac followed by an ILC-type cryomodule, an RFQ-based proton injector, and a small ring called IOTA (Integrable Optics Test Accelerator) for studying non-linear optics among other things. Presently, the facility has the linac, cryomodule, and beamline to a high-energy dump. The IOTA ring is under construction and should be completed next year. The proton source is also under construction and will be completed in the next couple of years. When the full beamline to IOTA has been completed, the electron linac will provide beam to IOTA to map out the optics of the ring in preparation for injecting protons once the source is completed. In addition to the experiments in the IOTA ring, there are various experiments in the linac; both before the cryomodule and after. In support of these experiments, there is an optical / THz instrumentation system containing a a Hamamatsu streak camera and a Martin-Puplett interferometer. This paper will describe the system and present some initial measurements from it.

FAST FACILITY

The FAST injector starts with a 1.3 GHz normal-conducting rf photocathode gun with a Cs_2Te coated cathode. The photoelectrons are generated by irradiation with a YLF laser at 263 nm that can provide several μJ per pulse [4]. Following the gun are two superconducting 1.3 GHz capture cavities that accelerate the beam to its design energy of around 50 MeV. After acceleration, there is a section for doing round-to-flat beam transforms, followed by a magnetic bunch compressor and a short section that can accommodate small beam experiments. At the end of the experimental section is a spectrometer dipole which can direct the beam to the low energy dump. If the beam is not sent to the dump, it enters the ILC-type cryomodule where it receives up to 250 MeV of additional energy and is sent to either a high-energy dump or the IOTA ring. Table 1 lists the typical beam parameters.

Table 1: Beam Parameters for FAST

Parameter	Value
Energy	20 – 300 MeV
Bunch Charge	< 10 fC – 3.2 nC
Bunch Frequency	0.5 – 9 MHz
Macropulse Duration	≤ 1 ms
Macropulse Frequency	1 – 5 Hz
Transverse Emittance	> 1 μm
Bunch Length	0.9 – 70 ps

OPTICAL AND TERAHERTZ INSTRUMENTATION SYSTEM

The optical / THz instrumentation system (OTIS) [5] is located near the low energy dump. The transport system is constructed of stainless steel pipes and flanges connected between boxes containing mirrors for steering the light (Fig. 1).

There are currently three source points for the radiation. One each from the third and fourth dipoles in the bunch compressor, D3 and D4, and one from a cross downstream of the bunch compressor, X121. There is also the possibility of implementing one from the cross (X124) in the low energy dump beamline that normally measures the energy spread.

The source points D3 and D4 in the bunch compressor provide coherent synchrotron edge radiation (CSR) from the entrance of the corresponding dipole magnets. The CSR is generally in the high GHz / low THz region [6].

The source point at X121 consists of an aluminized, silicon wafer on a translatable actuator (Fig. 2). The wafer can be inserted all the way into the beam to generate both coherent transition radiation (CTR) and optical transition radiation (OTR). The screen can also be extracted partly, with its edge a few mm above the beam, to generate coherent diffraction radiation (CDR).

*Operated by Fermi Research Alliance, LLC under Contract No. De-AC02-07CH11359 with the United States Department of Energy.
† keup@fnal.gov

ISBN: 978-3-95450-192-2 doi:10.18429/JACoW-IBIC2017-WEPCC04

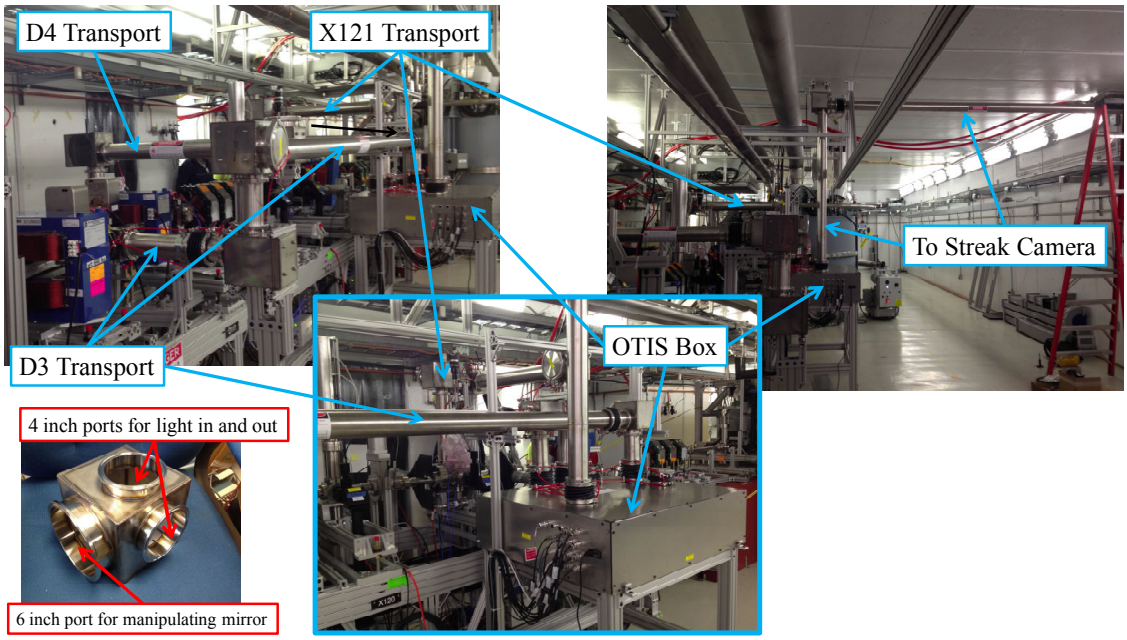

Figure 1: OTIS transport system. The transport pipes run between boxes (lower left) containing 4 inch flat mirrors.

All the sources converge to the OTIS box containing translatable mirrors to switch between the various inputs (Fig. 3). There are effectively three outputs from the box: a Hamamatsu streak camera, a Martin-Puplett interferometer, which is housed inside the OTIS box, and a 'user' location in the box which is currently unpopulated. Any input can be switched to any output. In addition, the mirror to switch light to the streak camera is a dielectric bandpass mirror with a reflection bandwidth of 400 – 700 nm. This transmits GHz/THz radiation to the Martin-Puplett interferometer.

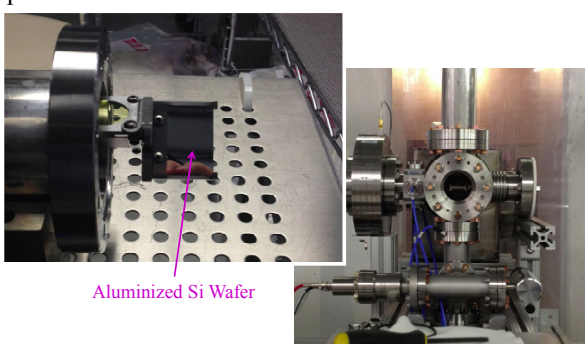

Figure 2: Left) X121 actuator retracted; OTR wafer is visible. Right) X121 cross with actuator installed.

The transport lines consist of stainless steel, 4 inch diameter pipes with quick disconnect flanges (Tri-clamp). In the bunch compressor, light is extracted through a single crystal quartz viewport. Since space is limited at these ports, a small box with one or two flat mirrors is attached to the port to redirect the radiation to a more readily accessible location. The radiation is then collimated by a pair of 3 inch diameter, 90° off-axis, parabolic, aluminium coated, UV-enhanced mirrors located in stainless steel boxes. A pair is needed since the focal length of the mirrors is much smaller than the closest distance to the dipole source point. The mirrors are mounted in an adjustable mirror mount which sits on a translatable stage to enable both direction and focusing adjustments. For X121, the light is also extracted through a single-crystal-quartz viewport. Here it is not necessary to have two focusing mirrors, since the mirror can be positioned at its focal point.

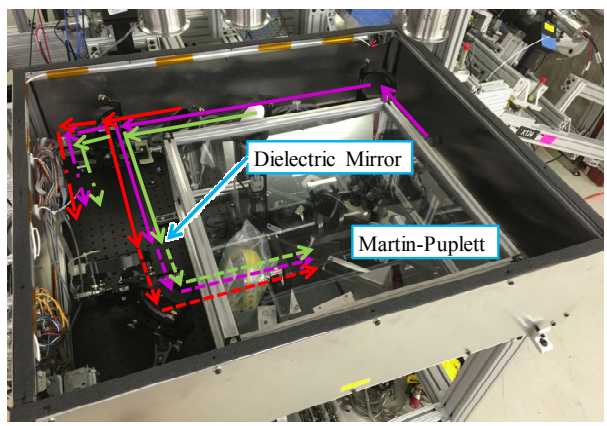

Figure 3: Light path inside the OTIS box. The colors indicate source, Purple – D3 in bunch compressor, Red – D4 in bunch compressor, Green – X121. Solid lines go to the streak camera. Dashed lines go to the interferometer, Dot-Dash lines go to the user area in the box.

Ninety-degree bends in the transport are handled by 4 inch diameter, flat, aluminium-coated, UV-enhanced mirrors mounted in an adjustable mount. To enable the system to be disassembled when access to the beamline is needed, the longer pipes are cut in two and have a rubber bellows between them.

The streak camera is located outside the accelerator enclosure. The pipe running to the streak camera goes through one of the penetrations to the outside where the streak camera is housed in a small enclosure.

ISBN: 978-3-95450-192-2 doi:10.18429/JACoW-IBIC2017-WEPCC04

ALIGNMENT

The OTIS setup has many mirrors which forces one to consider how to align everything such that light gets from one end to the other. For the D3 and D4 ports, a laser is directed down the beamline with its waist at the location of the radiation source point. The mirrors are adjusted first for directionality and then for focus with the process iterated as necessary. At X121, a permanent alignment laser upstream is used to set the OTR screen angle, while a local laser is used to set the transport alignment and focusing. Figure 4 shows the local alignment laser.

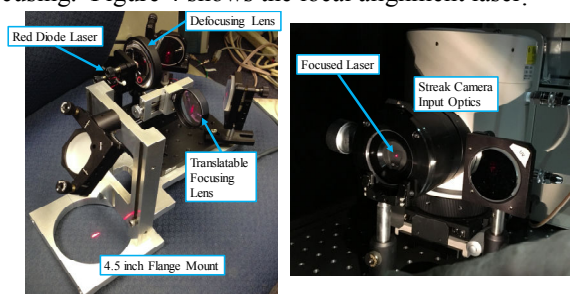

Figure 4: Left) Local alignment laser. It is designed to attach to a 4.5 inch Conflat flange. The focusing lens is on a linear stage to adjust the laser waist and provide a proper source point for focusing adjustments in the transport line. Right) Focused laser spot on the input slit of the streak camera after ~14 meters and 12 mirrors.

INSTRUMENTATION

The end points of the optical and THz radiation include a Hamamatsu streak camera and a Martin-Puplett interferometer, both of which are used for bunch length measurements.

Streak Camera

The streak camera [7] is a Hamamatsu C5680 mainframe with S20 PC streak tube that can accommodate a vertical sweep plugin unit and a horizontal sweep unit or blanking unit. The device is fitted with all-mirror input optics enabling the assessment of the UV OTR component as well as the visible light OTR. The mirror optics also mitigate the streak image blurring due to the inherent chromatic temporal dispersive effects of the lens-based input optics for broadband sources such as OTR. The unit is equipped with the M5675 synchroscan unit with its resonant circuit tuned at 81.25 MHz such that the streak image has jitter of less than 1 ps from the system itself.

Interferometer

The Martin-Puplett interferometer is a polarizing-type interferometer with wire grids as the polarizer and beam splitters (Fig. 5). The wire grids are 10 μm diameter Tungsten wires with a 45-μm wire spacing. The device uses pyroelectric detectors to measure GHz/THz frequencies needed to determine the bunch length. The pyroelectric detectors are mounted on remote-controlled 2-D linear stages to allow optimization of the detected signal.

TRANSPORT SIMULATION

The transport of GHz and THz frequencies over long distances is problematic due to the combined effect of diffraction and apertures. Simulations have been done for CTR/CDR at a frequency of 250 GHz. The simulation is written in MATLAB. It calculates the near-zone transition radiation from the X121 source using the prescription of [8]. The electric fields are evaluated at the first mirror location in the transport line and propagated from there using the vector diffraction formulation in [9]. The propagation presently takes into account the aperture of the mirrors, but not the change in direction. The intensity distributions at various points along the transport are shown in Fig. 6.

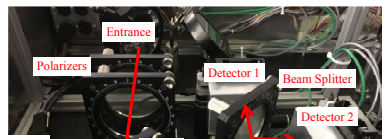

Figure 5: Interferometer light path. The GHz/THz is split and recombined from different path lengths. The interference determines the frequency content which in turn determines the bunch length.

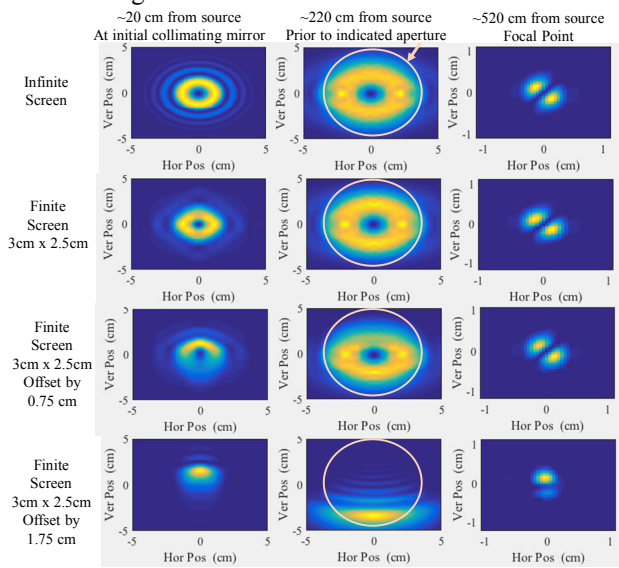

Figure 6: Simulated images along the transport line for several CTR screen scenarios. The bottom row is with the CTR screen withdrawn past the beam and functioning as a CDR screen. The asymmetric source point in this last scenario causes the light to propagate off-axis and impinge more severely on the aperture restrictions.

The apertures of the mirrors cause a loss of intensity down the transport line. The relative loss varies with CTR screen position. This effect can be understood qualitatively from the images where the peak intensities shift from the centered CTR screen version. This shift causes

ISBN: 978-3-95450-192-2 doi:10.18429/JACoW-IBIC2017-WEPCC04

more light to be lost to the apertures. Figure 7 quantifies the loss down the transport line for various CTR screen positions.

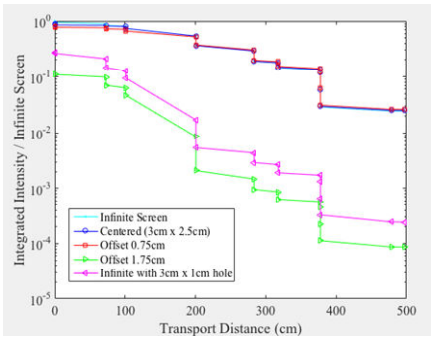

Figure 7: Integrated intensity along the transport line for a variety of CTR screen scenarios. The vertical steps in the intensity are due to either mirror apertures or polarizers. The offset of 1.75 cm corresponds to the screen acting as a CDR source.

INITIAL DATA

The system has been used to measure the bunch length as a function of rf chirp induced by the second accelerating cavity (CC2). Figure 8 shows the rms bunch length as measured by the streak camera as a function of degrees off crest (DOC) of the rf accelerating gradient in CC2. The minimum bunch length is a bit under 1 ps. Other streak camera measurements can be found in [10].

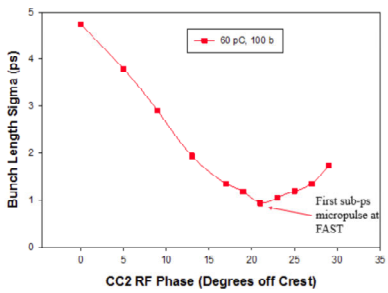

Figure 8: Streak camera measurements of rms bunch length using OTR from the X121 source point [11].

Initial setup of the Martin-Puplett involved scanning the pyroelectric detectors to find the peak signal. Figure 9 shows the measured and simulated signals. The interferometer has been used to make several autocorrelation measurements at varying bunch charges (Fig. 10). The bunch lengths were too long to distinguish subtle differences in length for different bunch charges, however the presence of an autocorrelation trace with a reasonable spectrum is promising for future measurements.

SUMMARY

A general purpose optical and terahertz instrumentation system has been installed and partially commissioned at the FAST facility at Fermilab. Measurements have been taken utilizing the streak camera, and some initial measurements have been done using the Martin-Puplett interferometer. Further commissioning and use is expected in experiments planned for the next several months.

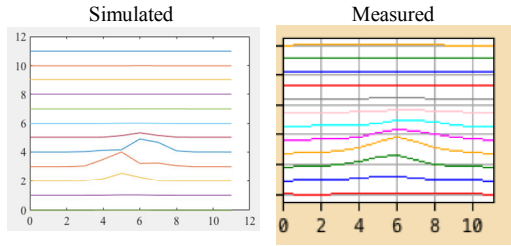

Figure 9: Simulated and measured scans of pyroelectric intensity. The pyroelectric detector is 2 mm x 2 mm. These scans are approximately 20 mm x 20 mm so each line is composed of ~10 4-mm^2 pixels. There is reasonably good agreement between measurement and simulation.

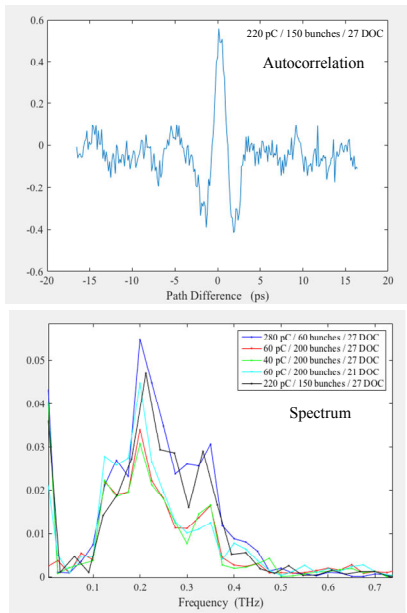

Figure 10: Top) Autocorrelation trace of CTR from electron beam near maximum compression. Bottom) Spectra reconstructed from autocorrelation data for myriad bunch charges and # of bunches. The spectra are approximately what one would expect for an rms bunch length near 1 ps.

ACKNOWLEDGEMENTS

The authors would like to thank the FAST department staff for their efforts in constructing and installing this system. This manuscript has been authored by Fermi Research Alliance, LLC under Contract No. DE-AC02-07CH11359 with the U.S. Department of Energy, Office of Science, Office of High Energy Physics. The United States Government retains and the publisher, by accepting the article for publication, acknowledges that the United States Government retains a non-exclusive, paid-up, irrevocable, world-wide license to publish or reproduce the published form of this manuscript, or allow others to do so, for United States Government purposes.

REFERENCES

[1] P. Garbincius *et al.*, "Proposal for an accelerator R&D user facility at Fermilab's Advanced Superconducting Test Ac-

ISBN: 978-3-95450-192-2 doi:10.18429/JACoW-IBIC2017-WEPCC04

celerator (ASTA)", FNAL, Batavia, IL, USA, Rep. Fermilab-TM-2568, October 2013.

[2] S. Antipov *et al*., "IOTA (Integrable Optics Test Accelerator): facility and experimental beam physics", *Journal of Instrumentation*, vol. 12, p. T03002, 2017.

[3] D. Edstrom, Jr. *et al*., "50-MeV run of the IOTA/FAST electron accelerator", in *Proc. NAPAC'16*, Chicago, IL, USA, October 2016, paper TUPOA19.

[4] J. Ruan *et al*., "Commission of the drive laser system for advanced superconducting test accelerator", in *Proc. IPAC'13*, Shanghai, China, May 2013, paper WEPME057.

[5] R. Thurman-Keup *et al*., "Terahertz and optical measurement apparatus for the Fermilab ASTA injector", in *Proc. IBIC'14*, Monterrey, CA, USA, September 2014, paper TUPD03.

[6] J. C. T. Thangaraj *et al*., "Experimental studies on coherent synchrotron radiation at an emittance exchange beam line", *Phys. Rev. ST Accel. Beams* vol. 15, p. 110702, 2012.

[7] A. H. Lumpkin *et al*., "Commissioning of a dual-sweep streak camera with applications to the ASTA photoinjector drive laser", in *Proc. FEL'14*, Basel, Switzerland, August 2014, paper MOP021.

[8] A. G. Shkvarunets and R. B. Fiorito, "Vector electromagnetic theory of transition and diffraction radiation with application to the measurement of longitudinal bunch size", *Phys. Rev. ST Accel. Beams* vol. 11, p. 012801, 2008.

[9] T. J. Maxwell *et al*., "Vector diffraction theory and coherent transition radiation interferometry in electron linacs", in *Proc. PAC'07*, Albuquerque, NM, USA, paper FRPMS035.

[10] A. H. Lumpkin *et al*, "Initial demonstration of 9 MHz framing camera rates on the FAST drive laser pulse trains", in *Proc. NAPAC'16*, Chicago, IL, USA, October 2016, paper TUPOA25.

[11] A. H. Lumpkin *et al*., "Initial observations of micropulse elongation of electron beams in a SCRF accelerator", in *Proc. NAPAC'16*, Chicago, IL, USA, October 2016, paper TUPOA26.

ISBN: 978-3-95450-192-2 doi:10.18429/JACoW-IBIC2017-WEPCC05

GAS JET PROFILE MONITOR FOR USE IN IOTA PROTON BEAM*

S. Szustkowski†[1], S. Chattopadhyay[1,2], D. Crawford[2], B. Freemire[1]
[1]Northern Illinois University, DeKalb, IL 60115, USA
[2]Fermi National Accelerator Laboratory, Batavia, IL 60510, USA

Abstract

The Integrable Optics Test Accelerator (IOTA) at the Fermilab Accelerator Science and Technology (FAST) Facility will attempt to demonstrate novel techniques for high current accelerators. An electron beam of 150 MeV/c momentum and a proton beam of 70 MeV/c momentum will be used for a number of experiments, including nonlinear focusing integrable optics, space charge compensation, and optical stochastic cooling. The low energy proton beam will provide a space charge dominated regime with which to investigate Hamiltonian diffusion and chaos. A non-invasive beam instrumentation device is needed to study emittance evolution and halo formation without destroying the beam. A supersonic gas jet curtain can be injected perpendicular to the proton beam, which will preserve the integrity of the beam and provide a two-dimensional turn-by-turn profile measurement. Currently, IOTA and the gas jet monitor are being built and commissioned at Fermilab.

INTRODUCTION

The Integrable Optics Test Accelerator (IOTA) is a storage ring designed to test novel high current accelerator techniques. A RFQ based proton source will provide a low energy beam for injection into IOTA. The ring will allow a sufficient number of turns to observe nonlinear effects in a space charge regime. Nonlinear decoherence in nonlinear integrable lattices will suppress halo formation of the beam. To preserve the lifetime of the beam, a non-invasive detector is required [1]. Simulation studies of the beam distribution, with various lattices, turn-by-turn are made using Synergia [2] code running on a server maintained by RadiaSoft [3]. The gas jet parameters, such as the gas density and the detector location, can be optimized for a higher resolution of the beam profile. A gas jet sheet is produced in the interaction chamber of the beam line. The beam ionizes the gas, producing an electron-ion pair. A transverse electric field will direct the electrons toward a micro-channel plate (MCP), which will provide a signal amplification of 10^6. Finally, a phosphor screen and CCD camera will image the signal.

IOTA PROTON BEAM PARAMETERS

The previously existing HINS (High Intensity Neutrino Source) RFQ will be used for injection of protons into the IOTA ring. The source will provide IOTA a beam energy of 2.5 MeV bunched at 325 MHz [4]. Bunches will spread out after a few turns due to the momentum spread and low energy. A dual purpose RF cavity will be used to bunch the beam at 2.18 MHz. The IOTA lattice (Fig. 1) has two integrable lattice sections (upper corners) where the transverse beta functions are matched and dispersion is zero (see Fig. 2). The lower left corner has a RF cavity and the lower right section will contain the electron lens/column. Table 1 provides a summary of HINS and IOTA main parameters.

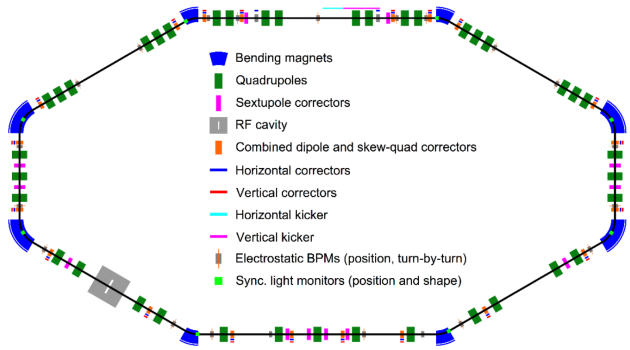

Figure 1: IOTA ring layout

Table 1: Summary of IOTA Proton Beam Parameters

PARAMETER	VALUE
Kinetic Energy	2.5 MeV
dp/p	0.1 %
Circumference, C_0	39.97 m
Revolution period, T_0	1.83 μs
RF bunching	2.18 MHz
Average beam current	8 mA
Vacuum	$6x10^{-10}$ Torr
Beam lifetime	300 s
Pulse rate	<1 Hz
Pulse width	1.77 μs

BEAM SIMULATIONS

The Synergia code has been used to simulate and propagate the beam including space charge effects. A lattice for IOTA with one nonlinear section was used. The nonlinear element in the lattice can be turned on and off. The initial KV beam is randomly distributed and propagated starting at the injection point (middle of the top section in Fig. 1). A virtual detector was placed s = 8.711 m from the right nonlinear section (middle of the lower right section in Fig. 1). The beam was propagated through the lattice for 200 turns with 10240 macro particles. A toolkit in Synergia, 2D

* Work supported by US Department of Energy, Office of High Energy Physics, General Accelerator Research and Development (GARD) Program.
† sszustkowski1@niu.edu

ISBN: 978-3-95450-192-2 doi:10.18429/JACoW-IBIC2017-WEPCC05

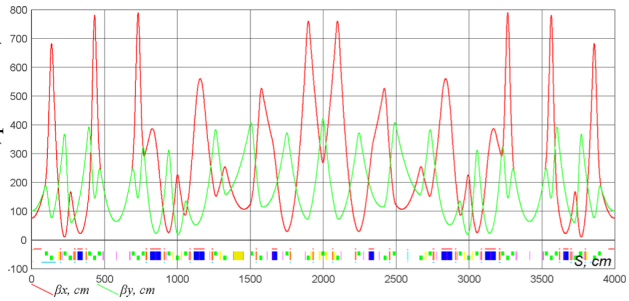

Figure 2: Lattice functions for IOTA with one nonlinear section. The nonlinear inserts are at approximately s = 6 m and 34 m [1].

open boundary condition Hockney space charge solver was used. For the purpose of this study, the dispersion function was set to zero.

Table 2: Beam Size with and without the Nonlinear (NL) Element

	no NL element	NL element	Units
$\epsilon_{x,y,I}$	5.00, 4.99	5.00, 5.00	mm-mrad
$\epsilon_{x,y,F}$	8.64, 9.94	6.46, 5.72	mm-mrad
$RMS_{x,y,I}$	2.37, 3.98	2.58, 3.27	mm
$RMS_{x,y,F}$	3.21, 5.68	2.87, 3.95	mm
X,Y^{I}_{max}	4.74, 8.01	5.21, 6.49	mm
X,Y^{F}_{max}	11.99, 21.30	9.82, 14.0	mm

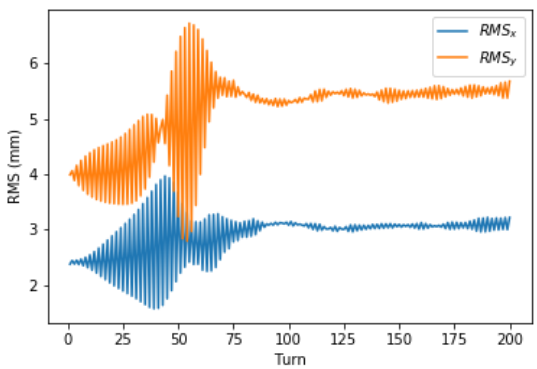

Figure 3: Beam Evolution without non-linear element.

Table 2 has the first and final turn beam emittance, x and y RMS, and max value in the transverse plane for with and without the nonlinear element. A measurement at each turn can determine the beam evolution and studies of the halo can be made.

Figure 3 shows the RMS beam size as it evolves through 200 turns without the nonlinear element. After approximately 100 turns the beam envelope stabilizes. The beam distribution is shown in Fig. 4 for both the nonlinear insert on and off. Without the nonlinear element, the transverse emittance significantly grew by 72% and 99% in x and y,

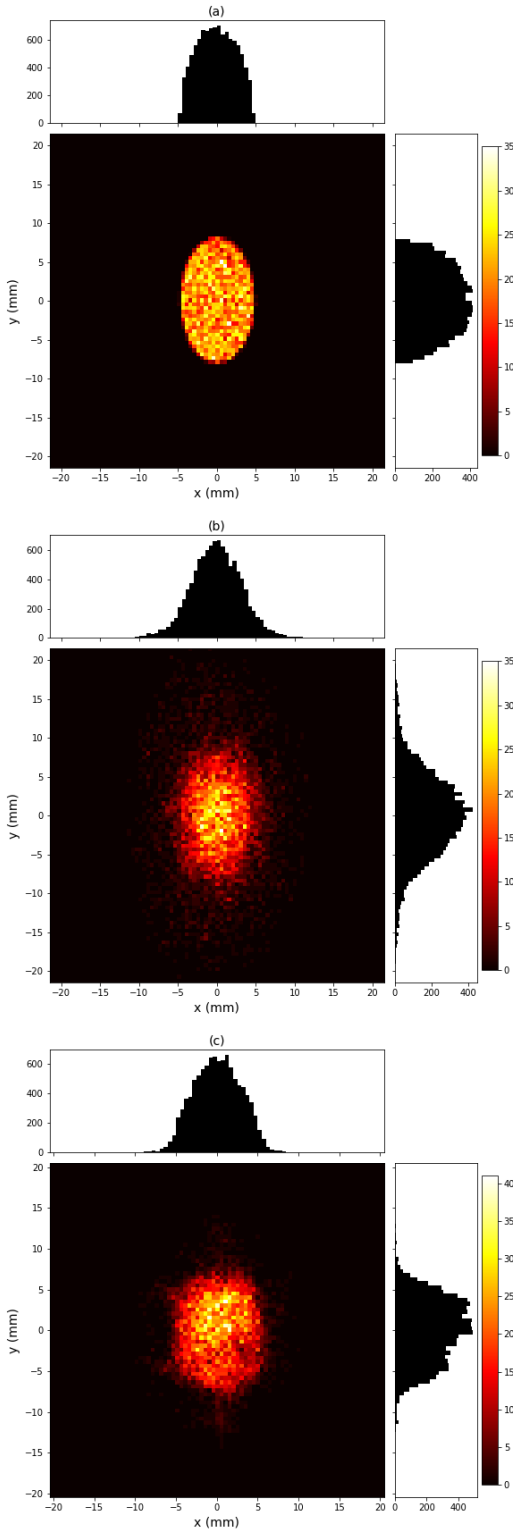

Figure 4: First turn particle distribution (a). Final particle distribution with non-linear element off (b) and non-linear element on (c).

respectively. The x and y RMS grew by 35% and 42%. With the nonlinear element the emittance grew marginally by 29% and 14% in x and y, while the RMS grew by 11% and 20%.

ISBN: 978-3-95450-192-2 doi:10.18429/JACoW-IBIC2017-WEPCC05

BEAM-GAS INTERACTIONS

The lifetime of the beam in the IOTA ring will be limited by interactions with residual gas. At energies above a few hundred keV, ionization is dominant over excitation for protons in nitrogen gas [5]. The cross section for ionization of nitrogen by 2.5 MeV protons is 7.19×10^{-17}cm^2 [6]. For the circumference of the IOTA ring given in Table 1 and assuming a gas sheet thickness of 0.2 cm, the path length through the residual gas is 2×10^4 greater than that through the gas sheet. To produce no more than a 1% effect on the lifetime of the beam, for the vacuum pressure given in Table 1, the pressure of the gas jet would have to be 1.2×10^{-7} torr.

At room temperature, the gas jet would have a density of 3.9×10^9 cm^{-3}. The number of electron-ion pairs produced per second by the beam can be found by:

$$\dot{N} = \sigma \frac{I_b}{q} n_g \, l \tag{1}$$

where σ is the ionization cross section, I_b is the beam current, q is the proton charge, n_g is the gas number density, and l is the gas sheet thickness. The total number of electron-ion pairs produced per turn (i.e. 8.85×10^{10} incident protons) is 5.03×10^3.

A more accurate estimation would take into account excitation, secondary ionization, etc., and is derived from measurements of the average energy required to ionize a gas molecule [7–9]. In this case, the number of electron-ion pairs produced per second is:

$$\dot{N} = \frac{dE}{dx} \frac{I_b}{q} \frac{\rho_g \, l}{W_i} \tag{2}$$

where dE/dx is the stopping power of protons in nitrogen, ρ_g is the mass density of the gas, and W_i is the average energy required to ionize a gas molecule. Using 118 MeV cm^2/g for dE/dx and 36 eV for W_i, the total number of electron-ion pairs produced per turn is 1.14×10^4.

HARDWARE

Groups at the Cockcroft Institute and KEK [10, 11] have previously developed gas jet monitors. The device to be used in IOTA will be based on these designs, with modifications to fit the experiment constraints. Various skimmers and capillary configurations will be tested for optimal gas jet thickness, orientation, and velocity. Vacuum requirements will be maintained to ensure minimal residual gas along the beam pipe. Other hardware such as the MCP and CCD array will be configured to the beam revolution period to have an integrated measurement at each turn.

OUTLOOK

Further simulation of the beam gas interaction to be done includes propagating the beam for a larger number of turns and implementing an electric extraction field where the gas jet is to be placed to determine if perturbation of the beam preserves integrability. Currently a gas-jet monitor test bench is being installed in FAST at Fermilab. It is planned to test various parameters of the gas jet for optimal performance. A proton beam in the IOTA lattice is expected in 2019.

REFERENCES

[1] S. Antipov, *et al.,* "IOTA (Integrable Optics Test Accelerator): facility and experimental beam physics program", *JINST*, vol. 12, no. 03, p. T03002, Mar. 2017

[2] J. Amundson, P. Spentzouris, J. Qiang, R. Ryne, "Synergia: An accelerator modeling tool with 3-D space charge", *Journal of Computational Physics*, **211**, 1, (2006).

[3] RadiaSoft, LLC `http://radiasoft.net`

[4] E. Prebys, S. A. Antipov, K. Carlson, H. Piekarz, and A. Valishev, "Proton Injection into the Fermilab Integrable Optics Test Accelerator (IOTA)", in *Proc. IPAC2016*, pp. 1638–1640,

[5] B.C. Edgar, W.T. Miles, and A.E.S. Green, "Energy Deposition of Protons in Molecular Nitrogen and Applications to Proton Auroral Phenomena", *J. Geophys. Res.* **78**, 28 (1973).

[6] M.E. Rudd, R.D. DuBois, L.H. Toburen, C.A. Ratcliffe, and T.V. Goffe, "Cross Sections for Ionization of Gases by 5-4000-keV Protons and for Electron Capture by 5-150-keV Protons", *Phys. Rev. A* **28**, 6 (1983).

[7] R.A. Lowry and G.H. Miller, "Ionization Yield of Protons in Nitrogen and Argon", *Phys. Rev.* **109**, 3 (1958).

[8] C.J. Bakker and E. Segrè, "Stopping Power and Energy Loss for Ion Pair Production for 340-Mev Protons", *Phys. Rev.* **81**, 4 (1951).

[9] H.V. Larson, "Energy Loss Per Ion Pair for Protons in Various Gases", *Phys. Rev.* **112**, 6 (1958).

[10] V.Tzoganis, A. Jeff, C.P. Welsch, "Gas dynamics considerations in a non-invasive profile monitor for charged particle beams", *Vacuum*, **109**, pp. 417-424, (2014).

[11] Y. Hashimoto *et al.*, "Development of a Beam Profile Monitor Using a Nitrogen-Molecular Jet for the J-PARC MR", in *Proc. IBIC2013*, pp. 848-851

ISBN: 978-3-95450-192-2 doi:10.18429/JACoW-IBIC2017-WEPCC06

SIMULATION SUPPORTED PROFILE RECONSTRUCTION WITH MACHINE LEARNING

R. Singh, M. Sapinski and D. Vilsmeier, GSI, Darmstadt, Germany

Abstract

Measured IPM profiles can be significantly distorted due to displacement of residual ions or electrons by interaction with beam fields for high brightness or high energy beams [1–6]. It is thus difficult to deduce the characteristics of the actual beam profile from the measurements. Artificial neural network with multilayer perceptron (ANN-MLP) architecture is applied to reconstruct the actual beam profile from the measurement data. The MLP is trained using Virtual-IPM simulation program [7] developed under the IPMSim collaboration [8]. The first results are presented in this contribution.

INTRODUCTION

Ionization Profile Monitors (IPM) are used for non-destructive transverse beam profile measurements at many accelerator facilities. The principle of operation is the following; the primary beam ionizes the residual gas and the ionized particles (ions or electrons) are extracted via electric fields and sometimes in conjunction with magnetic fields to confine the movement of ionized particles in the plane transverse to the electric field. The profile of the extracted particles reflects the transverse profile of the primary beam with the assumption that ionized particles are created at rest and the effect of induced fields by the primary beam on ionized particles can be neglected. The choice between ions or electrons for profile reconstruction is based on the requirement for the speed of device operation and potential influence of beam space charge.

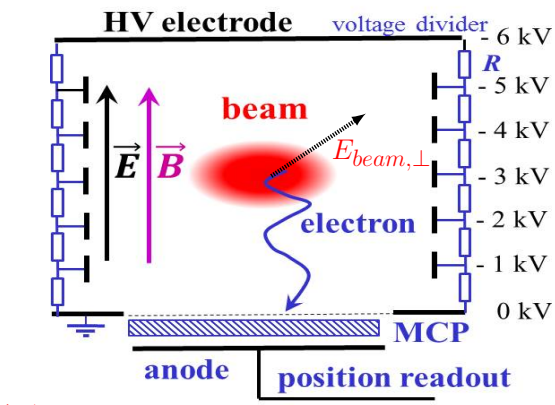

Figure 1: Operating principle of the IPM.

Figure 1 shows the typical components present in an IPM where both the electric and magnetic fields are utilized to confine the ionized particles [9]. The support electrodes/rods between the top and bottom electrodes are used to reduce the fringe fields and improve field homogeneity. The field homogeneity is important in order to avoid any distortion in the measured profile and therefore static EM simulations for the full geometry are usually performed. IPMs are often used for non-destructive measurements in low pressure conditions such as storage rings and hence they usually have to be equipped with a high amplification multi-channel plate (MCP) for obtaining sufficient signal to noise ratio. The output of MCPs are connected to data acquisition system directly or via phosphor screens and optical system. Figure 2 shows the image of the horizontal IPM formerly installed at LHC relevant to the discussions in this paper [4]. The dipole magnet has been moved in order to make the IPM chamber visible. In the next section, we will discuss the distortion in measured IPM profiles due to beam space charge and discuss previous efforts on correcting or reducing the distortion. Following that, the simulation tool and the beam and device parameters used to train the artificial ANN-MLP are discussed. Finally, the ANN-MLP parameters, training and validation are presented and the results are summarized.

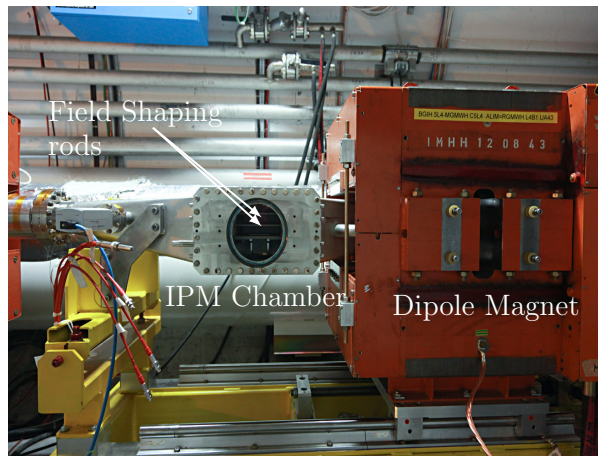

Figure 2: IPM installation at LHC. The dipole magnet (orange) has been shifted, revealing the IPM chamber.

SPACE CHARGE EFFECTS ON IPM PROFILE

IPM profile distortion due to beam fields depends on a variety of parameters such as device geometry, beam properties, extracted particle types (ions or electrons) and if IPM uses only electric field or also magnetic field. Initial IPM developments were focused around devices utilizing only electric fields. The distortion of IPM profiles has long been observed and the first attempt to make a simulation-based correction was by Thern [1] at AGS. Calculation of actual beam profile width from measured profile as a function of applied electric field and bunch population for coasting and bunched

ISBN: 978-3-95450-192-2 doi:10.18429/JACoW-IBIC2017-WEPCC06

beams was found. Further modifications were made to the Thern analytical model and were experimentally applied at FNAL [2]. Such analytical models made assumptions concerning the beam profile shape and predictions diverged for dense beams. A numerical approach was attempted at CEA Saclay during development of LIPAc IPMs, where very high space charge is expected [3]. In that correction procedure, first simulations were used to map the actual profile with the measured profile and the mapping was stored in matrices for a range of actual beam profiles modelled as generalized Gaussian distribution and for a range of beam currents. A fast iterative procedure was implemented to utilize these matrices for profile reconstruction experimentally. Practical limitations of this approach was that error in reconstructed profile was dependent on the size or coarseness of the simulation grid, and further reduction of grid size increased the number of reconstruction matrices significantly due to curse of dimensionality. Alternative approach for dealing with profile distortion is to use magnetic fields to confine the generated ionized particles around the point of generation. However, in addition to being expensive, required magnetic field strengths are prohibitory for extremely dense beams as discussed below for our target case. First major distortion for an IPM with magnetic fields was seen for LHC IPMs at high energies, where the beam profile was significantly broader compared to wire scanner measurements [4]. First solution envisaged to solve the issue was to raise the magnetic fields in the IPM to 1 T [5]. This field strength should be viewed in perspective of the strength of LHC main dipoles which is 8.5 T at top energies and is considered impractical. Following that, correction methods such as quartile and sieve method were contemplates to reconstruct the beam profile [6] but such attempts were either impractical or unsuccessful.

Recently reliable IPM simulation tools has been developed as joint effort between several labs [8]. Availability of reliable description of IPM system including the profile distorting effects such as space charge and initial velocity distribution of ionized particles transforms the problem of IPM profile correction into a "supervised learning" problem. In a supervised learning problem, the input and output of an unknown system are provided and the system is approximated with a variety of machine learning algorithms [10]. We have chosen the multi-layer perceptron architecture of artificial neural network (ANN-MLP) as a first approach to reconstruct actual beam profile from the measured distorted profile. We have also simplified the problem by assuming Gaussian primary beams for first tests presented here, however these are not limitations of the method itself and can be extended to arbitrary profiles.

VIRTUAL-IPM AND SIMULATION DATA DETAILS

The Virtual-IPM simulation program has been used in order to generate beam profiles for LHC parameters. Table 1 shows the parameters which have been used for the simulations. σ_x, σ_y, σ_l and the bunch population N_p have been varied to cover the relevant operational region. The simulation used a Gaussian bunch shape and an analytical solution for the electric field of a Gaussian bunch in two dimensions, neglecting the longitudinal field component. This is justified because the bunch is highly relativistic and is longitudinal size is significantly larger than transverse size. The initial velocities of electrons were sampled from the Voitkiv double differential cross section [11] for a Hydrogen target. Each case simulated 1×10^6 particles whose final positions were grouped into profiles with 100 µm bin size.

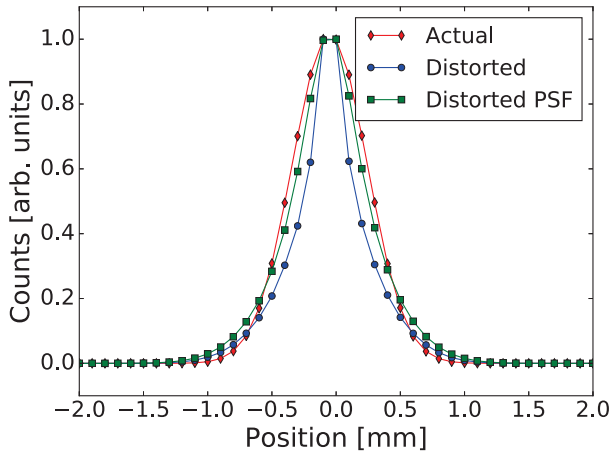

Figure 3: Simulation of profile distortion due to space charge using Virtual IPM.

Table 1: Parameters Used for the Simulation. σ_x, σ_y, σ_l and the Bunch Population Have Been Varied within the Specified Intervals.

Particle type	Protons
Energy/u	6.5 TeV
Bunch population N_p	1.1×10^{11} to 1.7×10^{11}
Bunch length σ_l (4σ)	0.9 ns to 1.2 ns
Bunch width σ_x (1σ)	0.29 mm to 0.37 mm
Bunch height σ_y (1σ)	0.4 mm to 0.6 mm
Electrode distance	85 mm
Applied voltage	4 kV
Magnetic field	0.2 T

One million particles were used in each simulation providing rather smooth profiles. The bin size is 0.1 mm and Gaussian point spread function with $\sigma = 0.125$ mm was used to represent the effect of optical acquisition system in the LHC IPM system. Figure 3 shows the actual primary beam profile, the distorted profile due to space charge and the profile read at the end of the acquisition system after application of point spread function of the optics. The input parameters to simulation were $N_p = 1.7 \times 10^{11}$, $\sigma_l = 0.9$ ns, $\sigma_x = 0.29$ mm, and $\sigma_y = 0.4$ mm . There is a 20 % increase in the second central moment of the measured profile (with PSF) with respect to actual (initial) profile.

ISBN: 978-3-95450-192-2 doi:10.18429/JACoW-IBIC2017-WEPCC06

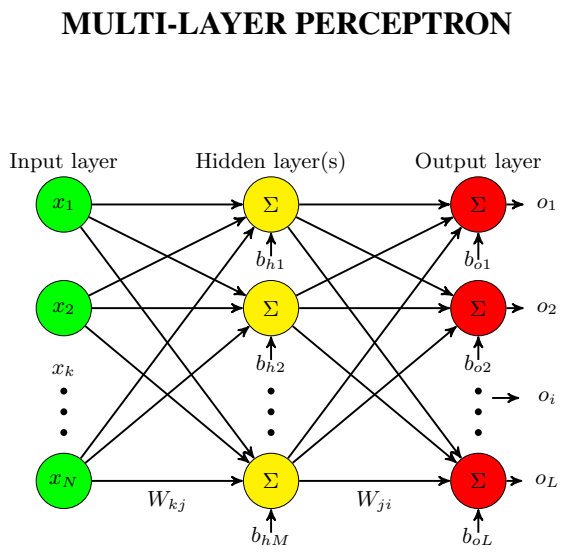

Figure 4: Schematic showing the architecture of the ANN-multilayer perceptron.

Figure 4 shows the single layer MLP, where each of the nodes in the hidden and output layer sums all the inputs and transforms them using a non-linear "activation function" g. The activation function can be any differentiable non-linear function. Typically used activation functions are "sigmoid" and "tanh". A multilayer perceptron with at least one hidden layer is known to be a universal approximator [12] and can be shown to represent any function with sufficient number of nodes. For the given training inputs x and outputs y, the hidden function is approximated by,

$$o_i = g\left(\sum_{j=1}^{M} W_{ji} \cdot g\left(\sum_{k=1}^{N} W_{kj} \cdot x_k + b_{hj}\right) + b_{oi}\right) \quad (1)$$

Weights are randomly initialized and iteratively updated in order to minimize the selected loss function,

$$E = \sum_{i=1}^{L} (y_i - o_i)^2 \quad (2)$$

A commonly used loss function is mean square error, and the gradient of the loss function with respect to network weights and biases are calculated using gradient descent method at each step and back propagated to the weights in previous layers. This full procedure is referred to as back-propagation. There are several variants for calculating the gradients during backpropagation [10].

Figure 5 shows the process of generating the training and validation data and its usage in the training of the ANN-MLP. The training data is used to optimize the weights and biases of each node in the ANN-MLP to approximate the function f' with Eq. 1 and validation data is used to check if the approximated/learned function generalizes to intermittent space within the training grid.

The training ANN-MLP is performed with three distinct parameters, measured profile (100 points in each profile),

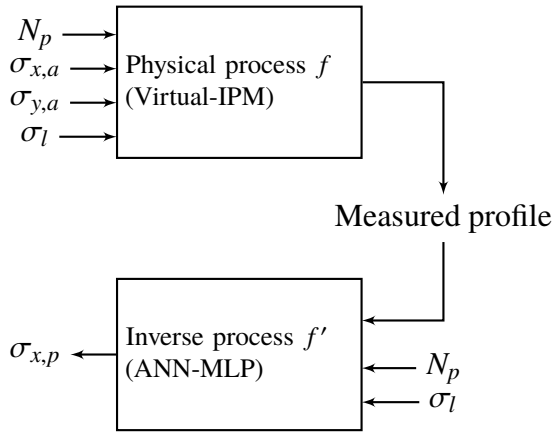

Figure 5: Physical process modelled by Virtual-IPM and the inverse process approximated by ANN-MLP.

particle number N_p (1 point) and bunch length σ_l (1 point) as inputs forming an array of 102 points for each training sample while the output is actual width denoted by $\sigma_{x,a}$ to differentiate from predicted width $\sigma_{x,p}$. $\sigma_{y,a}$ is not used for the training process since in any experimental usage, it will not be available as an input to the trained network for pre-diction of $\sigma_{x,p}$. 375 training samples were generated with a parameter scan in N_p, $\sigma_{x,a}$ and $\sigma_{y,a}$ (5 parameters each) and σ_l (3 parameters). Table 1 shows the parameter range over which training data was generated. Validation data was generated at a spacing 1 %, 25 % and 50 % off the training data sites in each parameter space forming 372 validation samples. In addition to that 0.5 % Gaussian white noise (rel-ative to the maximum value in each parameter space) was added to the profiles to depict ADC/camera noise on the measured profile as well as measurement uncertainty on N_p and σ_l. Tensorflow [13] library with Keras [14] interface was used to define and train the ANN-MLP. We have utilized two hidden layers of 60 and 30 nodes each and 1 output node in our MLP architecture. The activation function used is "tanh" and "adam" optimizer is selected for calculation of gradient of loss function with respect to MLP parameters. Training was performed in batch learning mode in batches of 4 and 200 epoches were performed. One complete training took less than a minute on a standard PC.

RESULTS AND DISCUSSION

Figure 6 shows the reconstructed beam width for the validation data by the trained ANN-MLP plotted against actual (initial) beam width. The training and validation grids are marked. Though the variation of parameters are performed in the four-dimensional parameter space, only the grid for parameter σ_x is indicated in the plot. Figure 7 shows the histogram of the percentage error of beam σ_x prediction, and a bias and variance of less than 1 % was obtained.

Robustness

The influence of measurement uncertainties on the artificial neural network training and prediction was also studied.

ISBN: 978-3-95450-192-2 doi:10.18429/JACoW-IBIC2017-WEPCC06

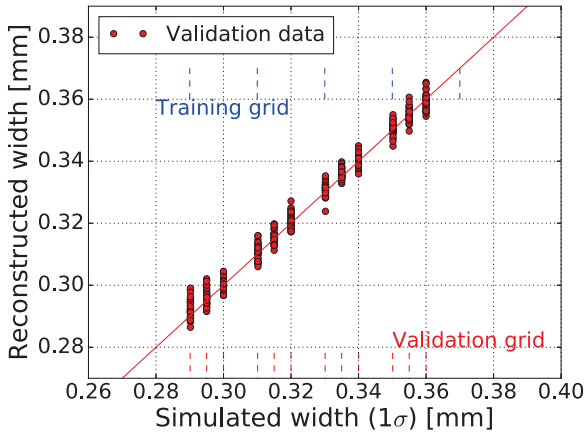

Figure 6: Prediction of actual profile width from distorted measured profile using an ANN-MLP.

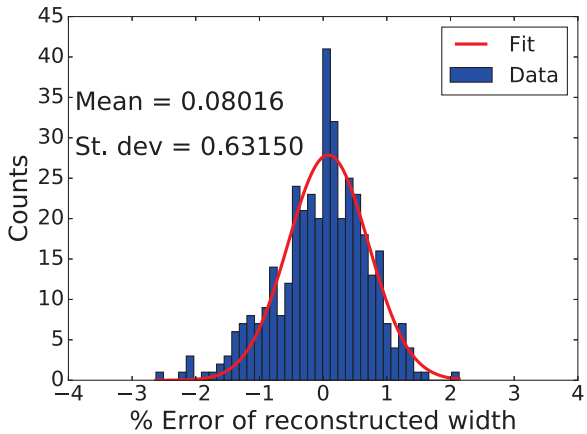

Figure 7: Histogram showing the percentage prediction error of the approximated function by the ANN-MLP.

Gaussian white noise was added to each channel on the ANN input for both training and validation data in the range of σ_{noise} = 0.5 % to 10 % relative to the maximum value to that parameter. For each set of noisy training data, the ANN training was performed 10 times and the bias and variance of prediction error was plotted against the added noise as shown in Fig. 8. A linear trend in seen in the increase of prediction error variance and bias hovers around zero. The error bar on each point denotes the variation and bias during these 10 independent runs of the training. Typical measurement uncertainties are expected to lie between 0.5-2 % in experimental scenarios.

SUMMARY

The reconstruction of distorted profiles for Gaussian beams were performed using artificial neural networks and reconstruction errors below 1 % were obtained even with the inclusion of measurement uncertainties. At this point, no good experimental data exists for the discussed case and tests with experimental data are foreseen in near future. Further, other machine learning algorithms for prediction like support vector machines will be explored and alternative instrument based training and online reconstruction of initial width from distorted profiles will be attempted.

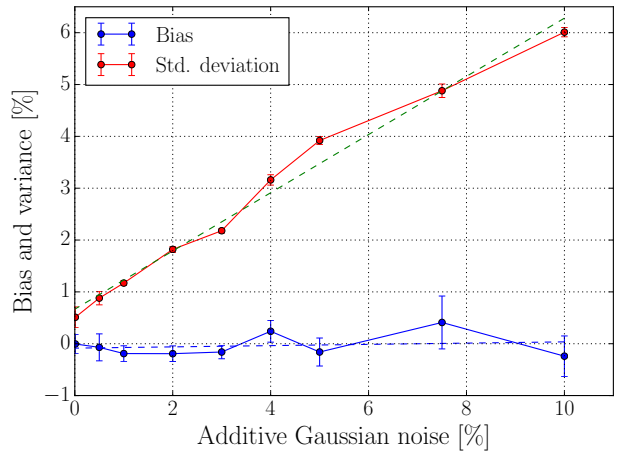

Figure 8: Evolution of bias and std. deviation of predictions with respect to noise in training and validation data.

REFERENCES

[1] R. E. Thern, "Space-charge distortion in the brookhaven ionization profile monitor", PAC 1987, Washington, D.C., USA, March 1987.

[2] Amundson *et al.*, "Calibration of the Fermilab Booster ionization profile monitor", *Phys. Rev. ST Accel. Beams*, vol.6, 102801 (2003).

[3] J. Egberts, "IFMIF-LIPAc Beam Diagnostics: Profiling and Loss Monitoring Systems", PhD thesis, University Paris Sud, (2012).

[4] M. Sapinski *et al.*, "The first experience with LHC beam gas ionization monitor", Proceedings of IBIC 2012, Tsukuba, Japan, October 2012.

[5] M. Patecki *et al.*, "Electron tracking simulations in the presence of the beam and external fields", Proceedings of IPAC 2013, Shanghai, China, June 2013.

[6] D. Vilsmeier *et al.*, "Investigation of the effect of beam space charge on electron trajectories in Ionization profile monitors", HB 2014, East Lansing, MI, USA, November 2014.

[7] D. Vilsmeier *et al.*, "A modular application for IPM simulations", IBIC 2017, Grand Rapids, MI, USA, August 2017, paper WEPCC07 , these proceedings.

[8] M. Sapinski *et al.*, "Ionization profile monitor simulations - status and future plans", Proceedings of IBIC 2016, Barcelona, Spain, September 2016.

[9] P. Forck, "Lecture notes in beam instrumentation", JUAS, 2017.

[10] K. P. Murphy, "Machine Learning: A Probabilistic Perspective", *The MIT Press*, 2012.

[11] A. Voitkiv *et al.*, "Hydrogen and helium ionization by relativistic projectiles in collisions with small momentum transfer", *J. Phys. B: At. Mol. Opt. Phys*, vol. 32, 1999.

ISBN: 978-3-95450-192-2 doi:10.18429/JACoW-IBIC2017-WEPCC06

[12] K. Hornik, "Approximation Capabilities of Multilayer Feed-forward Networks", *Neural Networks*, 4(2), 251-257, (1991).

[13] M. Abadi *et al.*, TensorFlow: Large-scale machine learning on heterogeneous systems, 2015. Software available from https://www.tensorflow.org/

[14] Chollet, François *et al.*, Keras, 2015. Software available at https://github.com/fchollet/keras

ISBN: 978-3-95450-192-2 doi:10.18429/JACoW-IBIC2017-WEPCC07

A MODULAR APPLICATION FOR IPM SIMULATIONS

D. Vilsmeier, P. Forck, M. Sapinski, GSI, Darmstadt, Germany

Abstract

Simulating the electron and ion tracking in Ionization Profile Monitors is an important tool for specifying and designing new monitors. It is also essential for understanding the effects related to the ionization process, guiding field non-uniformities and influence of the beam fields which may lead to a distortion of measured profiles. Existing simulation codes are often tuned to the specific needs of a laboratory, are not well documented and lack a practical user interface. This work presents a generic simulation tool which combines the features of existing codes in order to provide a common standard for IPM simulations. The modular structure of the application allows for exchanging the computational modules depending on the use case and makes it extensible to new use cases. By this means simulations of Beam Induced Fluorescence monitors based on supersonic gas jets have been realized. The application and all involved methods have been tested and benchmarked against existing results. The code is well documented and includes a graphical user interface. It is publicly available as a git repository and as a Python package.

INTRODUCTION

Ionization Profile Monitors (IPM) allow for measuring the transverse profile of particle beams. They take advantage of the ionization process which is induced by the interaction of the particle beam with the (rest) gas and measure the resulting ionization products. An electric field is used for guiding ionized electrons or ions towards an acquisition system.

Several simulation codes have been developed at different accelerator laboratories in order to study effects which influence the quality of measured profiles or to design new devices [1, 2]. Two workshops dedicated to IPM simulations [3, 4] have shown a broad interest in this topic and also revealed the benefits of combining efforts and existing developments into a single application. For that reason the idea of a common, generic simulation tool was born. This application shall include the features of existing codes as well as be extensible to new methods.

USE CASES

While the motivation for such an application emerged mainly from simulations of IPMs it can be easily extended to other beam instruments such as Beam Induced Fluorescence monitors (BIF) or Electron Wire Scanners. Because such simulations involve many similarities it is useful to include them into a single application (in order to reuse the relevant parts for the different scenarios). For IPM simulations the influence of beam space charge [5, 6] or guiding field non-uniformities [7] are interesting subjects to study. Also the effect of secondary electrons emerging from ion impact on detector elements can be important to estimate. Other scenarios include the usage of supersonic gas jets for IPMs and BIFs or simulations of Electron Wire Scanners. Simulations involving the influence of multiple beams, for instance in case of diagnostics for electron lenses, are also of great interest.

MODULES

In order to fulfill the above mentioned use cases, common aspects have been separated into different modules and were realized in form of the following models. A model is a specific implementation for a given module, applicable to one or more specific use cases. The structure of the simulation framework, including the different modules and models, is shown in Fig. 1.

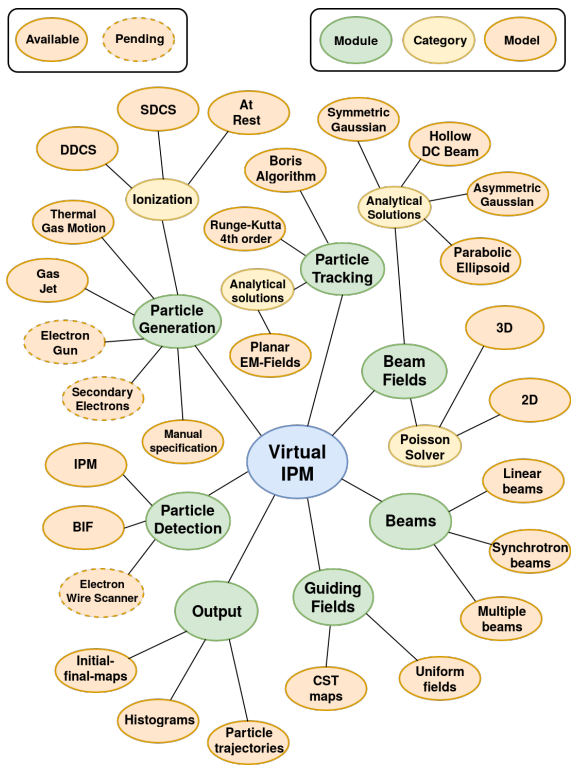

Figure 1: The different components (modules) of the simulation framework together with their corresponding models. Dashed ellipses indicate models in development.

Particle Generation

Particle generation models define the initial parameters for particles when they enter the simulation. Typically this involves the ionization or excitation process induced by the particle beam however other methods are possible (for example secondary electron generation). The following methods

ISBN: 978-3-95450-192-2 doi:10.18429/JACoW-IBIC2017-WEPCC07

for sampling the initial momenta of ionized particles are available:

- Double differential cross sections [8]
- Thermal rest gas motion
- Gas jets
- Generate at rest, i.e. with zero momentum

Particle Tracking

Particle tracking models are responsible for updating the particles' positions and momenta at each simulation step hence they propagate the particles during the simulation. Both accuracy and efficiency are desirable for such computationally heavy methods. They commonly involve a trade-off between the number of steps and the accuracy when tracking for a given time, in form of a time step size Δt for which a single update is performed. Running a few cases with varied Δt and observing the resulting trajectories to converge is usually a good indicator for a sufficiently small time step size. The following methods are available for particle propagation:

- Runge-Kutta method of 4th order
- Boris algorithm [9]
- An algorithm which is based on the analytical solution of the equations of motion for uniform planar electromagnetic fields [10]

Particle Detection

Particle detection models define when the tracking for a particle should stop because it was either detected or it reached an invalid state (e.g. because it hit a boundary of the chamber).

The current implementations include an IPM model which supports tracking until particles reach a specific position (the detector) and a BIF model which determines the decay of excited states based on a pseudo-random statistical process corresponding to spontaneous emission (a particle is considered *detected* when its excited state decays).

Guiding Fields

Guiding field models describe the external electric and magnetic fields which are used to guide and to confine the tracked particles. Different models for emulating uniform fields or for loading CST field maps are available.

Beam Fields

One main purpose of running such simulations is to study the influence of the electromagnetic fields of particle beams on the movement of ions and electrons. The electric field of a bunch is computed in the rest frame of that bunch and then transformed to the laboratory frame in order to obtain the electromagnetic field as seen by the non-relativistic ionization products. Various models for the electric field computation are available ranging from analytical solutions for specific charge distributions to numerical Poisson solvers which can handle arbitrary charge distributions. The available implementations include:

- Analytical solutions for two-dimensional Gaussian charge distributions (the longitudinal field component is neglected) [11]
- Analytical solution for a parabolical-ellipsoidal charge distribution [12]
- Analytical solution for a hollow DC beam
- Numerical Poisson solvers for two- and three-dimensional (arbitrary) charge distributions

COMPARISON WITH EXISTING CODES

Two benchmark cases have been established for the comparison amongst simulation codes. Table 1 contains the parameters for those two cases (LHC & PS case) which have been explored already by the following two well-established IPM simulation codes:

- **PyECLOUD-BGI** [13]: This code uses an analytical solution for the electric field of a two-dimensional elliptical Gaussian charge distribution. The beam magnetic field is neglected. The guiding fields are assumed to be uniform. The tracking algorithm is based on the analytical solution for a uniform planar electromagnetic field configuration. The initial electron momenta are sampled from a double differential ionization cross section.
- **JPARC-Code** [14]: This code uses a two-dimensional Poisson solver in order to compute the transverse electric field of the bunch's charge distribution. The beam magnetic field is neglected. Fields maps as generated by for example CST Studio or uniform fields are used for the guiding fields. The tracking algorithm uses the Runge-Kutta method of 4th order. The initial electron momenta are sampled from various ionization cross sections.

Table 1: Parameters for the Studied Benchmark Cases and the SIS-18 Measurements ("B." abbreviates "Bunch")

Case	LHC	PS	SIS-18
Particle type	Protons	Protons	$^{124}Xe^{43+}$
Energy/u [GeV]	6500	25	0.6
B. pop. $[1 \times 10^{11}]$	1.3	1.33	0.02
B. length ($4\sigma_z$) [ns]	1.25	3.0	44
B. width ($1\sigma_x$) [mm]	0.229	3.7	7.81
B. height ($1\sigma_y$) [mm]	0.257	1.4	2.03
Electrode dist. [mm]	85	70	180
Applied voltage [kV]	4	20	0.8
Magnetic field [T]	0.2	0 †	0

† The actual PS IPM uses a magnet generating 0.2 T field strength.

Figures 2 and 3 show the results of the comparison which are in good agreement. The computational methods which are used by the respective reference code were selected for the comparison.

Unfortunately, to our best knowledge, no good experimental IPM data for those two cases were available by the moment of this publication.

ISBN: 978-3-95450-192-2 doi:10.18429/JACoW-IBIC2017-WEPCC07

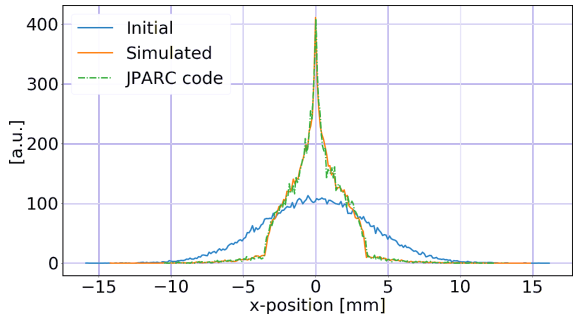

Figure 2: Comparison of simulated profiles with the JPARC code for the PS case (electron tracking).

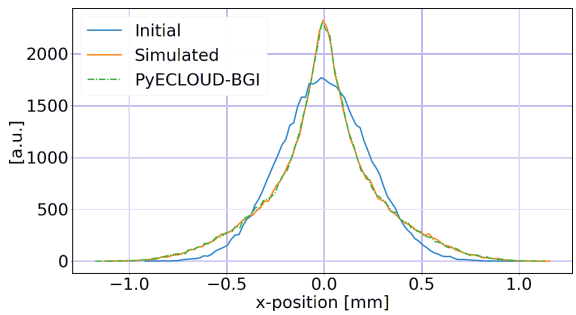

Figure 3: Comparison of simulated profiles with the PyECLOUD-BGI code for the LHC case (electron tracking).

COMPARISON WITH MEASUREMENTS

Measurements have been performed at the SIS-18 synchrotron in GSI with an electron detecting IPM equipped with an optical acquisition system at arbitrarily small extraction voltages in order to make a profile distortion visible. An ion detecting IPM with an electronic read-out system has been used in parallel in order to verify the actual beam profile. The measured ion profiles were fit with a Gaussian distribution (also because the actual profiles seemed to have tails) and were used as an input to the simulation. The parameters for the measurements are shown in Table 1 (SIS-18 case).

The result of the simulation compared to the measurements are shown in Fig. 4. The electron measurement shows a large broadening of the beam profile which is reproduced by the simulated profile. The deviation between measurement and simulation is ascribed to the effect of stray fields from neighboring magnets and to the inaccuracy of initial velocity generation under the assumption of a (atomic) Hydrogen target.

BIF SIMULATIONS

Simulations of Beam Induced Fluorescence monitors have been considered an important use case so in this section we show simulation results that were obtained for the more complex setup of foreseen HL-LHC electron lens diagnostics, based on BIF monitor and supersonic gas jet, with preliminary parameters [15].

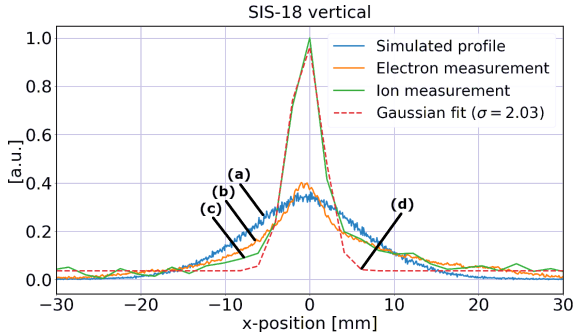

Figure 4: Profile measured at SIS-18 (vertical device) (b) compared to the result of the simulation (a). The profile of the ion-IPM (c) has been fit with a Gaussian distribution (d) in order to overcome the noise at the tails and to serve as a reference profile.

The parameters for the simulation are summarized in the following. The 7 TeV proton beam is represented by Gaussian bunches with 2.4 mm transverse FWHM (which corresponds to $\sigma_{x,y} = 1.02$ mm) and a length of $4\sigma_z = 1.25$ ns. Each bunch consists of 2.2×10^{11} protons and bunches arrive at a frequency of 40 MHz. The 10 keV electron beam is represented by a 5 A hollow DC beam with flat profile between inner radius of 1.2 mm and outer radius of 1.8 mm. The longitudinal electric field of the proton beam is neglected because of its highly relativistic energy. The magnetic fields of both beams are taken into account. An external solenoid field of $B_z = 4$ T (along the beam direction) is included. Excitation arises from the interaction of the beams with a transverse N_2 gas jet at 30 K temperature and with mean velocity $v_y = 800\,\mathrm{m\,s^{-1}}$. The relevant excited state $(N_2^+)^*_{391\,\mathrm{nm}}$ has a lifetime of 60 ns. For proton induced excitation the simulation was run for 420 ns in order to capture at least 99.9 % of all particles. Electron induced excitation was considered during the first 25 ns because after that period the situation repeats with respect to the electromagnetic fields.

The simulation performs discrete time steps of size Δt and the probability p_s that an excited state decays during a single step is constant during the simulation and can be determined as $p_s = 1 - \exp(-\lambda \Delta t)$ where λ is the decay rate of the excited state.

Figure 5 shows the one-dimensional projection (along y-direction) of the simulated profile of the proton beam. Most of the time the excited ions are subject to the electromagnetic field of the electron DC beam because of the short length of the proton beam ($4\sigma_z = 2.5$ ns). Together with the $B_z = 4$ T solenoid field the ions shift towards the center of the profile.

Figure 6 shows the simulated two-dimensional profile of the electron beam. The ions similarly move towards the center of the profile in the presence of the DC and the solenoid field. At $\sqrt{x^2 + y^2} = 1.2$ mm the attracting DC electric field drops to zero and below that boundary the ions are only subject to the opposite, repelling field from the proton beam. These counteracting effects lead to the ions accumulating in this region.

ISBN: 978-3-95450-192-2 doi:10.18429/JACoW-IBIC2017-WEPCC07

The above results suggest possible difficulties when estimating the profiles of the proton and electron beam with the simulated BIF monitor.

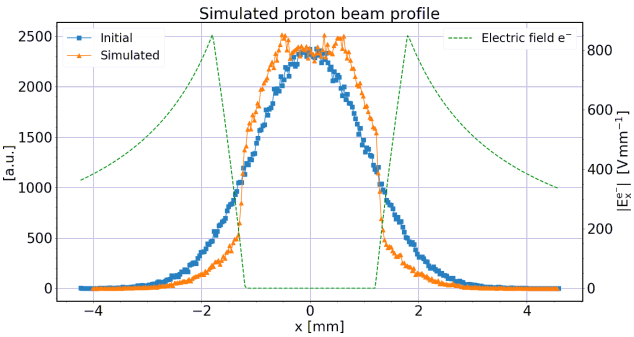

Figure 5: Simulated profile of the proton beam, integrated along y-direction. The bin size is 30 µm. The (radial) electric field of the DC electron beam is indicated (dashed line).

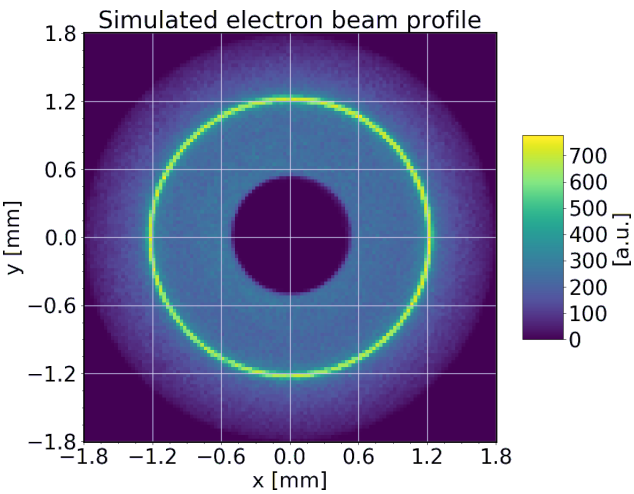

Figure 6: Simulated two-dimensional profile of the electron beam. The bin size is 30 µm. The original electron beam profile ranges from $\sqrt{x^2 + y^2} = 1.2$ mm to 1.8 mm.

SUMMARY

A new simulation tool – "Virtual-IPM" – has been established in order to combine various use cases, many of which have been realized already. It integrates numerous methods that are available in existing simulation codes and which have been benchmarked accordingly. The application includes a graphical user interface which facilitates the configuration of simulation cases. The code is publicly available as a git repository and is open for collaboration [16]. It includes a comprehensive documentation [17] and is available on the Python Package Index [18]. Future development of the application is already scheduled in order to include additional methods and use cases.

REFERENCES

[1] M. Sapinski *et al.*, "Ionization Profile Monitor Simulations – Status and Future Plans", in *Proceedings of IBIC2016*, September 2016, paper TUPG71, p. 520.

[2] K. Satou, "Simulation and Progress in Ionization Profile Monitors for High Intensity Proton Beam", presented at IBIC2017, Grand Rapids, MI, USA, paper WE3AB2, this conference.

[3] IPM Workshop 2016, CERN, Geneva, Switzerland, https://indico.cern.ch/event/491615/

[4] IPM Workshop 2017, GSI, Darmstadt, Germany, https://indico.gsi.de/event/IPM17/

[5] R. Singh *et al.*, "Simulation Supported Profile Reconstruction With Machine Learning", presented at IBIC2017, Grand Rapids, MI, USA, paper WEPCC06, this conference.

[6] D. Vilsmeier, "Profile distortion by beam space-charge in Ionization Profile Monitors", CERN-THESIS-2015-035, 2015

[7] C. C. Wilcox *et al.*, "An Investigation into the Behaviour of Residual Gas Ionisation Profile Monitors in the ISIS Extracted Beamline", in *Proceedings of IBIC2016*, paper WEPG68, 2016

[8] A. B. Voitkiv *et al.*, "Hydrogen and helium ionization by relativistic projectiles in collisions with small momentum transfer", *J.Phys.B: At.Mol.Opt.Phys*, vol. 32, 1999

[9] J. P. Boris, "Relativistic Plasma Simulation-Optimization of a Hybrid Code", in *Proceedings of the Fourth Conference on Numerical Simulation of Plasmas*, 1970, p. 3-67

[10] G. Iadarola, "Electron Cloud Studies For CERN Particle Accelerators and Simulation Code Development", CERN-THESIS-2014-047, 2014, p. 34-38

[11] M. Bassetti and G. A. Erskine, "Closed expression for the electrical field of a two-dimensional Gaussian charge", CERN-ISR-TH/80-06, 1980

[12] P. Strehl, "Chapter 8: The Electromagnetic Fields of Bunches", *Beam Instrumentation and Diagnostics*, Springer, 2016,

[13] M. Sapinski, "The modified pyECLOUD code and main results", IPM Workshop 2016, CERN, Geneva, https://indico.cern.ch/event/491615/contributions/1169448/attachments/1237092/1818180/pyECloud.pdf

[14] K. Satou, "Python based particle tracking code for monitor design", IPM Workshop 2016, CERN, Geneva, https://indico.cern.ch/event/491615/contributions/1169450/attachments/1237859/1818556/presentation_file_final.pdf

[15] S. Udrea *et al.*, "Preparatory Work For A Fluorescence Based Profile Monitor For An Electron Lens", in *Proceedings of IBIC2016*, September 2016, paper TUPG73, p. 528-531

[16] *Virtual-IPM Git repository*, https://gitlab.com/IPMsim/Virtual-IPM, version 1.2

[17] *Virtual-IPM Documentation*, https://ipmsim.gitlab.io/Virtual-IPM/, version 1.2

[18] *Virtual-IPM on PyPI*, https://pypi.org/project/virtual-ipm/, version 1.2

ISBN: 978-3-95450-192-2 doi:10.18429/JACoW-IBIC2017-WEPCC08

DEVELOPMENT OF A FLUORESCENCE BASED GAS SHEET PROFILE MONITOR FOR USE WITH ELECTRON LENSES: OPTICAL SYSTEM DESIGN AND PREPARATORY EXPERIMENTS

S. Udrea†, P. Forck, GSI Helmholtzzentrum für Schwerionenforschung, Darmstadt, Germany
E. Barrios Diaz, N. Chritin, O. R. Jones, P. Magagnin, G. Schneider, R. Veness,
CERN, Geneva, Switzerland
V. Tzoganis, C. Welsch, H. Zhang, Cockcroft Institute, Warrington, United Kingdom

Abstract

A hollow electron lens is presently under study as a possible addition to the collimation system for the high luminosity upgrade of the LHC, while an electron lens system is also proposed for space charge compensation in the SIS-18 synchrotron for the high intensities at the future FAIR facility. For effective operation, a precise alignment is necessary between the high energy hadron beam and the low energy electron beam. In order to achieve this a beam diagnostics set-up based on an intersecting gas sheet and the observation of beam-induced fluorescence is under development. In this contribution we give an account of the design and performance of the optical detection system and report on recent preparatory experiments performed using a laboratory gas curtain set-up.

BEAM-INDUCED FLUORESCENCE SET-UP OVERVIEW

The beam-induced fluorescence (BIF) set-up for transverse beam diagnostics for electron lenses has as main components a supersonic gas sheet generator and an intensified camera system with an appropriate lens. The supersonic gas sheet is supposed to cross the charged particle beams under consideration and emit fluorescence radiation as a consequence of the interaction between the charged particles and the gas atoms or molecules. Part of the emitted radiation is collected by the lens and an image of the interaction region and thus of the transversal beam profiles is formed at the detector of the camera system.

The electron lens under study for the future high luminosity upgrade of the LHC (HL-LHC) will generate a hollow, 5 A, 10 keV electron beam which will be stabilized around the axis of the high energy proton beam by a 4 T magnetic field produced by a superconducting solenoid. Presently two BIF stations are foreseen, one at each end of the solenoid. At these positions the electron beam will not be in full compression, so is expected to have an outer diameter of approximately 10.5 mm and an inner one of about 7 mm, while the proton beam will have a sigma of approximately 0.3 mm. Thus the gas sheet is planned to have a width of about 11 mm and a thickness of less than 1 mm to allow for a proper interaction region. As working gases both Nitrogen [1] and Neon are presently under consideration. A 3D model of the diagnostics test set-up using a low current electron beam is shown in Fig. 1. This prototype is planned for commissioning at the Cockcroft Institute, UK towards the end of 2017.

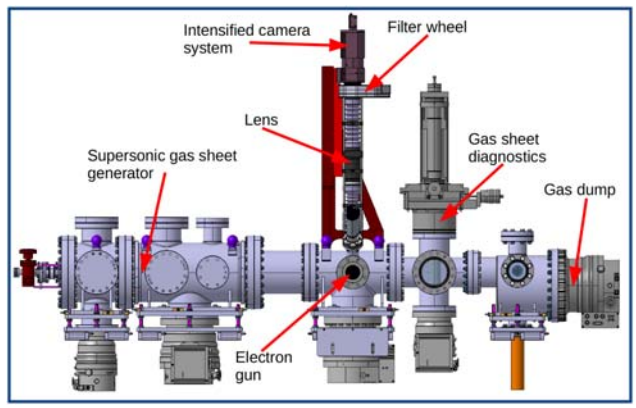

Figure 1: 3D model of the full prototype set-up to be commissioned end of 2017. An electron beam generated by a commercially available electron gun will be used for testing purposes.

THE INTESIFIED CAMERA SYSTEM

The cross-sections and integration times estimated for both Nitrogen [1] and Neon show that a camera system with the capability to detect single photons is required. Recent studies carried out at GSI [2] showed that an image intensifier based on MCP technology is currently still the best choice. Thus a ProxiKit PKS 2581 TZ-V image intensifier made by ProxiVision and using a Ø 1" double MCP in Chevron configuration has been acquired. Its main characteristics are:

- UV enhanced S20 photocathode, see Fig. 2 for sensitivity dependence upon wavelength
- P43 phosphor screen
- 28 lp/mm (line pairs per mm) maximum spatial resolution at the phosphor screen plane
- gated, TTL-triggered HV supply, minimum gate time 25 µs, no limit is imposed to the maximum, repetition rate up to 1 kHz
- Schneider Componon 12 35/2.8 lens system as optical relay to image the phosphor screen on a camera sensor
- C-mount adapters for objective and camera

† s.udrea@gsi.de

ISBN: 978-3-95450-192-2 doi:10.18429/JACoW-IBIC2017-WEPCC08

The use of a relay lens allows for maximum flexibility in the choice of the camera to be employed in conjunction with the intensifier and also makes several image ratios possible (values of 18:8, 18:11, 25:8, 25:11 are recommended by the manufacturer).

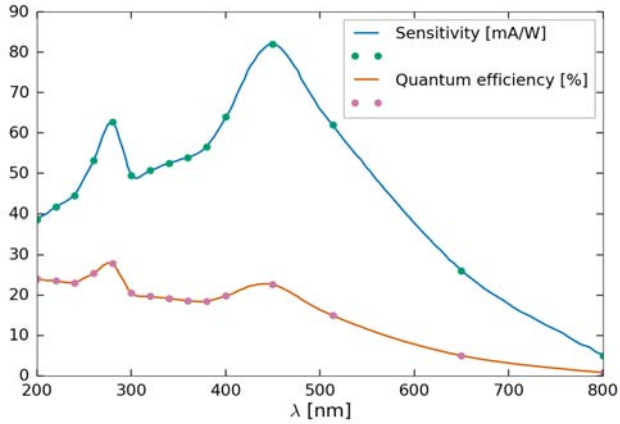

Figure 2: Wavelength dependency of sensitivity and quantum efficiency for the UV enhanced S20 photocathode according to the manufacturer.

For the prototype beam diagnostics set-up a BASLER acA1920-40gm CMOS camera has been chosen. It uses a Sony IMX249 chip with an 11.25 x 7.03 mm sensitive area and a resolution of 1920 x 1200 pixels. The minimum exposure time is 40 µs@12-bit and a maximum frame rate of 42 fps can be achieved. No upper limit is specified for the exposure time, which can be set by the duration of the trigger pulse.

THE LENS SYSTEM

The resolution of the intensified camera system is 28 lp/mm at the phosphor screen. Due to the small transversal size of the proton and electron beams to be measured one can still manage a proper resolution in object space if the magnification is large enough. The lens should also collect as much light as possible to keep integration times low. These conditions lead to a small depth of field (DOF) [1]. This is relevant if a typical geometry is chosen in which the gas curtain is at 45° to both the beam and optical axes. For the prototype set-up this is the envisaged geometry and thus one has to find an appropriate compromise, for which a 40 mm diameter apochromatic triplet optimised for a magnification of 1 has been acquired from Bernhard Halle Nachfl. GmbH. The focal length is 160 mm resulting in a working distance of about 320 mm at nominal magnification. To reduce geometrical errors and provide for a larger DOF an iris with a maximum opening of Ø 25 mm has been mounted in front of the lens. This leads to a maximum solid angle of $4\pi \cdot 3.8 \cdot 10^{-4}$ sr, corresponding to only 0.038 % of the total emission sphere, at nominal magnification.

To assess the expected resolution, simulations have been performed with ZEMAX. These show that, in the case of a source emitting broad spectrum radiation from 300 to 700 nm, the lens provides a resolution of up to about 40 lp/mm. Nevertheless, since measurements will be performed with filters limiting the spectral range to that of interest, a better resolution can be achieved. Thus the lens has a relatively small effect on the overall resolution of the detection and imaging set-up which is mainly determined by that of the image intensifier.

The complete optical arrangement is presented in Fig. 3. The 60 mm cage system manufactured by THORLABS allows for accommodating the 40 mm lens and for proper alignment of the optical elements including a filter wheel. Due to the single photon detection scheme the optical path and the filter wheel are shielded from stray light by bellows and a custom housing respectively.

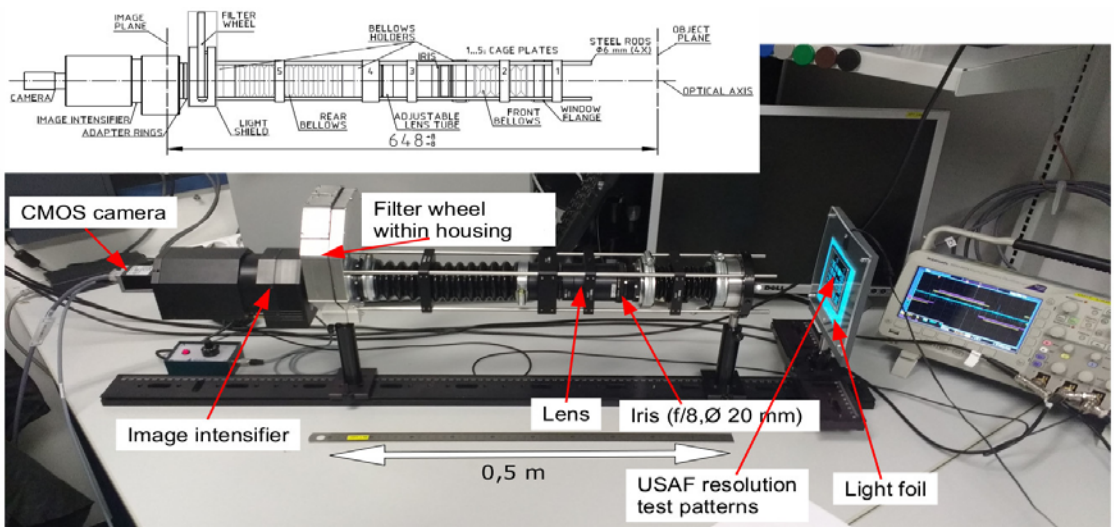

Figure 3: Complete detection and imaging set-up as used for tests at the GSI.

ISBN: 978-3-95450-192-2 doi:10.18429/JACoW-IBIC2017-WEPCC08

COMMISSIONING

First tests of the complete detection and imaging set-up (Fig. 3) were performed at the GSI. This included: resolution measurements with and without image intensifier, depth of field measurements, assessment of the background due to dark counts and stray light. For all measurements the iris had an opening of Ø 20 mm.

To determine the achievable resolution a USAF 1951 glass test chart has been employed, backlit by means of a light foil. This test chart consists of patterns arranged in numbered groups. Each group contains six numbered elements with each element including one horizontal and one vertical pattern of the same resolution R, which can be computed in lp/mm according to [3]:

$$R = 2^{G} \cdot 2^{\frac{E-1}{6}}$$

Here G and E are the group and element number respectively.

Without image intensifier the limiting resolution of the optical system has been assessed to be 57 lp/mm, which is larger than that predicted by simulation. This can be explained by the fact that the emission of the light foil has a relatively narrow spectrum and that the test set-up had a magnification of approximately 1.2. With the image intensifier used in imaging mode (lowest amplification) the best resolution one can expect is 20 lp/mm. A comparison of these two cases is shown in Fig. 4.

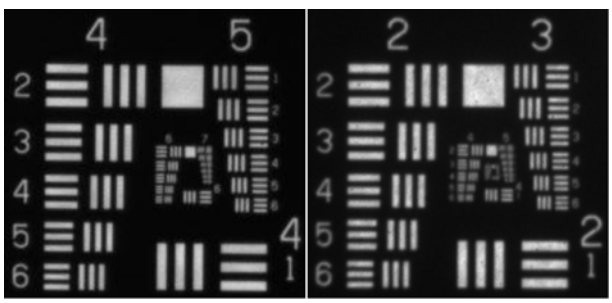

Figure 4: Images of the USAF 1951 test chart obtained without (left) and with (right) image intensifier. Resolution increases with group (top) and element number (side). Due to the difference in resolution, the two images show different groups of patterns.

For assessing the DOF the USAF 1951 test chart was displaced along the optical axis until the resolution dropped to about 10 lp/mm in the image obtained without the intensifier. This resulted in a value of 4.5 ± 0.5 mm. If this should prove insufficient one may consider a set-up with the optical axis perpendicular to the gas curtain or a so called Scheimpflug configuration [4].

The background level due to dark counts and stray light was also investigated. To obtain an estimation of the number of dark counts to be expected, the image intensifier was detached from the set-up and used in photon counting mode (maximum amplification) with the input closed by its protective cap. For a gate time of 40 ms 124 counts were identified. Taking into consideration the imaging ratio of the relay lens and the size of the CMOS detector this results in 886 ± 60 counts/cm^2/s. With the image intensifier attached to the set-up with its input covered, 520 counts were identified, corresponding to 3714 ± 120 counts/cm^2/s. Since in both cases the illumination of the laboratory was kept at usual levels, the difference between the two measurements arises from imperfections in the stray light shield of the set-up. This can be mitigated by improving the shielding or reducing the environmental light level.

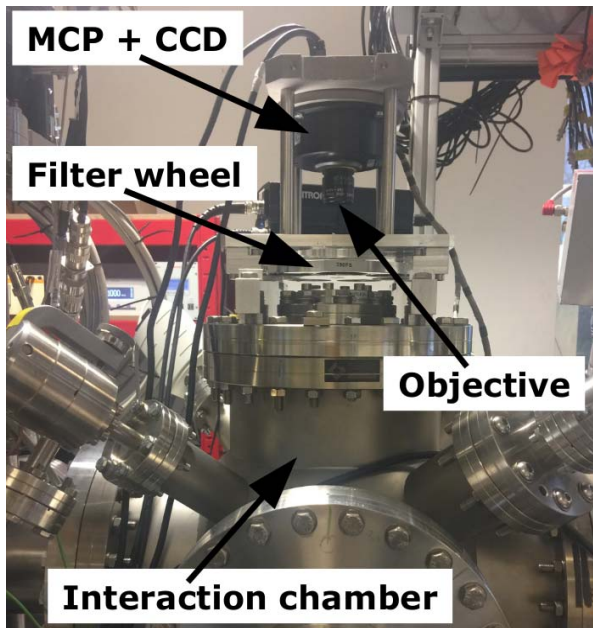

Figure 5: The set-up used for preparatory experiments during the development of the prototype for the future BIF detection and imaging installation.

PREPARATORY EXPERIMENTS

During the development phase of the prototype a series of measurements were performed using the existing gas jet curtain installation at the Cockcroft Institute [5] with equipment already available at the GSI [6]. The BIF detection and imaging set-up was composed of a ProxiVision image intensifier with a double MCP in

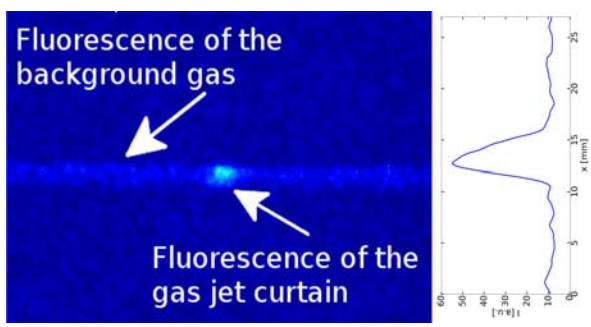

Figure 6: Profile of a 3.5 keV electron beam due to its interaction with a supersonic N_2 gas curtain. The profile appears enlarged due to the low spatial resolution of the optics used in the preparatory experiments.

ISBN: 978-3-95450-192-2 doi:10.18429/JACoW-IBIC2017-WEPCC08

Chevron configuration coupled through fiber optics to a Basler A311f CCD camera. This was combined with a Pentax B2528-UV objective with f=25 mm and F#=2.8-16, having a transmission band from 230 to 800 nm, and a filter wheel with four 10 nm bandwidth filters at 337, 390, 430 & 470 nm, see Fig. 5. The electron gun used at the time provided only 10 µA of beam current at a maximum energy of 5 keV. The transverse profile of this beam was estimated to have a width of about 1 mm. The density of the gas jet curtain was $\approx 2.5 \cdot 10^{-10}$ cm^{-3} [5]. Due to the low electron current and small aperture of the objective very long exposure times of up to 8000 s were needed for the successful generation of images, Fig. 6. To improve on this in future experiments, it is foreseen to increase the electron current up to 300 µA at 10 keV.

NEON AS WORKING GAS

Because of considerations related to the vacuum system at the HL-LHC, Neon might be a better choice than Nitrogen as working gas. We will briefly present here the estimations made for the fluoresce cross-section corresponding to the strongest emission line of neutral Ne, which is due to the $2s^2 2p^5(^2P°_{1/2})3p\ ^2[^1/_2]_0 \rightarrow 3s\ ^2[^1/_2]_1$ (Paschen notation: $2p_1 \rightarrow 1s_2$) transition at 585.4 nm [7]. The Ne atom is also of special interest, because its movement during the time spent in the upper excited state is not influenced by the electric and magnetic fields of the charged particle beams and the solenoid. Moreover this lifetime is ≈ 15 ns [8], four times shorter than that of the relevant N_2 state [9].

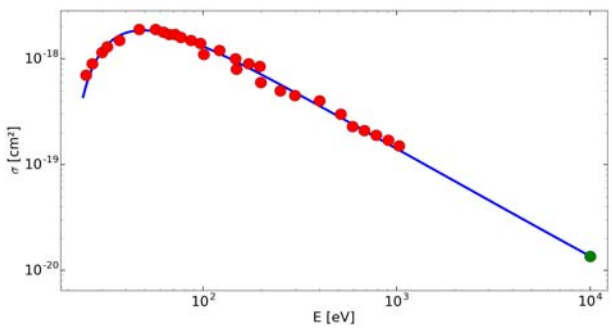

Figure 7: Fluorescence cross-section for electrons and Ne as working gas. Red dots: data from literature; fit and extrapolation: blue line and green dot.

Fluorescence cross-sections are available for Neon up to an energy of 1 keV for electrons and 1 MeV for protons [7,10]. For electrons the extrapolation to 10 keV is performed using a formula similar to the one proposed in [11]:

$$\sigma^e_{585} = \frac{8 \cdot \pi \cdot a_0^2 \cdot R}{m_e \cdot c^2} \cdot F \cdot \left[\frac{1 - \left(D \cdot \frac{1}{\beta^2} \right)^u}{1 - D^u} \right]^v \cdot \left[\frac{1}{\beta^2} \right]^w$$

F, u, v and *w* are fit parameters, a_0 the Bohr radius, *R* the Rydberg constant, m_e the electron rest mass, *c* the speed of light in vacuum, β the electron's speed divided by *c*, $D = 2 \cdot W/(m_e \cdot c^2)$, and *W* the excitation energy of the $2p_1$ level with respect to the ground state. Figure 7 shows the available experimental data together with the corresponding fit and extrapolation with $F \approx 2.5 \cdot 10^{-2}$, $u \approx 1.75$, $v \approx 2.49$ and $w \approx 1.03$. Thus the fluorescence cross-section σ^e_{585} has an estimated value of $1.4 \cdot 10^{-20}$ cm^2. Considering a gas curtain with a density of $2.5 \cdot 10^{-10}$ cm^{-3}, a thickness of 0.5 mm and using parameters as for the prototype set-up described above, the expected average photon detection time is $1.1 \cdot 10^{-3}$ s/photon for a 5 A electron beam, still more than sufficient to give a good image on second timescales. In comparison, Nitrogen fluorescence at 391.4 nm would result in an average photon detection time of about $4 \cdot 10^{-6}$ s/photon under otherwise identical conditions.

Presently, the only way to estimate the cross-section for 7 TeV protons is by the principle of equal velocities, i.e. from the cross-section for 3.8 GeV electrons. This results in $\sigma^p_{585} \approx 4.7 \cdot 10^{-22}$ cm^2 by the above formula. The detection time thus estimates to 0.15 s/photon for a proton beam with an average current of 1 A, compared to $\approx 5 \cdot 10^{-4}$ s/photon in the case of Nitrogen. Several minutes would therefore be necessary to acquire decent images of the proton beam with Ne as target gas.

CONCLUSION

A prototype BIF detection and imaging set-up for transverse beam diagnostics on electron lenses has been developed and successfully tested offline. First preparatory experiments with N_2 as working gas lead to promising results. Detection times for photons emitted by Ne at 585.4 nm have been estimated based on available cross-section data and extrapolation to higher energies and further experiments are now planned both with N_2 and Ne following the installation of an upgraded electron gun.

ACKNOWLEDGEMENT

S. Udrea and P.Forck acknowledge the support of C. Andre with the realisation of the test set-up at the GSI.

REFERENCES

[1] S. Udrea *et al.*, in *Proc. IBIC'16*, pp. 529-532.

[2] Y. Shutko *et al.*, in *GSI Sci. Rep. 2014*, p. 463.

[3] USAF 1951, https://en.wikipedia.org/wiki/1951_USAF_resolution_test_chart

[4] Ch. Wiebers *et al.*, in *Proc. IBIC'13*, pp. 807-810.

[5] V. Tzoganis and C. P. Welsch, *Appl. Phys. Lett.*, vol. 104, p. 204104, 2014.

[6] C. Andre *et al.*, in *Proc. DIPAC'11*, pp. 185-187.

[7] M. Eckhardt, D. Hasselkamp, and K.-H. Schartner, *Z. Physik A*, vol. 292, pp. 337-345, 1979.

[8] A. Kramida, Yu. Ralchenko, J. Reader, and NIST ASD Team (2015), NIST Atomic Spectra Database (ver. 5.3), http://physics.nist.gov/asd

ISBN: 978-3-95450-192-2 doi:10.18429/JACoW-IBIC2017-WEPCC08

[9] M. A. Plum, E. Bravin, J. Bosser, and R. Maccaferri, *Nucl. Instr. Meth. A*, vol. 492, pp. 74-90, 2002.

[10] J.E. Chilton, M.D. Stewart, Jr., and C.C. Lin, *Phys. Rev. A*, vol. 61, pp. (052708)1-12, 2000.

[11] V. Puech and S. Mizzi, *J. Phys. D: Appl. Phys.*, vol. 24, pp. 1974-1985, 1991.

ISBN: 978-3-95450-192-2 doi:10.18429/JACoW-IBIC2017-WEPCC09

HORIZONTAL OPENING OF THE SYNCHROTRON RADIATION AND EFFECT OF INCOHERENT DEPTH OF FIELD FOR HORIZONTAL BEAM SIZE MEASUREMENT

T. Mitsuhashi†, KEK, Ibaraki, Japan
J. Corbett, SLAC, Menlo Park, CA, USA
M. J. Boland, SLSA, Clayton, Australia

Abstract

The incoherent depth-of-field due to the instantaneous opening angle of dipole SR emission can influence horizontal beam size measurements. In particular, for double-slit spatial interferometry, the opening angle introduces an intensity imbalance across the two slits that reduces interference contrast and therefore increases the apparent beam size. To investigate this effect, the instantaneous horizontal opening of the SR light must be known. Schwinger's theory gives the vertical opening angle and the qualitative theory of K.J. Kim gives an estimation for horizontal opening angle. An extension of Schwinger's theory to the horizontal plane by one of the authors leads to the same Bessel function distribution as the vertical plane using integration by parts. Neglecting the cubic phase term in the exponent, the expression agrees with Kim's diffraction theory. Using this result to correct for incoherent depth-of-field effects in double-slit measurements at the Australian Synchrotron, ATF and SPEAR3, the measured horizontal beam size is in good agreement with design values.

INTRODUCTION

For the measurement of horizontal beam size, the incoherent depth of field due to horizontal instantaneous opening of the Synchrotron Radiation will modify the spatial coherence in the horizontal direction. In particular, for double-slit spatial interferometry, the opening angle introduces an intensity imbalance across the two slits that reduces interference contrast and therefore increases the apparent beam size. To investigate this effect, the information of instantaneous horizontal opening of the SR light must be known. It is well known that the theory for the Synchrotron radiation which emitted from Circular trajectory is investigated by J. Schwinger, and he gives the vertical opening angle for the spectral density [1]. The qualitative theory of K.J. Kim gives an estimation for both of vertical and horizontal opening angle by using diffraction concept [2]. In this paper, a simple introduction for K.J. Kim's paradigm and Schwinger's theory, then we discuss an extension of Schwinger's theory to the horizontal plane using integration by parts. Using this result to correct for incoherent depth-of-field effects in double-slit measurements at the SPEAR3, Australian Synchrotron and ATF, the measured horizontal beam size is in good agreement with design values.

†email address: toshiyuki.mitsuhashi@kek.jp

EFFECT OF INCOHERENT DEPTH OF FILED FOR HORIZONTAL INTERFEROMETRY

In the horizontal plane, the interferogram includes the additional effect of incoherent depth of field (IDOF) by the instantaneous opening of the SR in the horizontal plane [3][4]. The IDOF has two effects, the first is the apparent horizontal beam size becomes bigger and the second is the visibility of the horizontal interferogram reduces by intensity imbalance at two opening of double slit. Using the instantaneous intensity distribution of SR in horizontal plane by $I(\theta)$ as a function of horizontal observation angle θ, the apparent beam shape $\sigma_\alpha(x)$ including the intensity imbalance factor is given by,

$$\sigma_a(x)=\int \frac{2\sqrt{I\left(\theta+\frac{D}{2R}\right)I\left(\theta-\frac{D}{2R}\right)}}{I\left(\theta+\frac{D}{2R}\right)+I\left(\theta-\frac{D}{2R}\right)}\cdot I(\theta)\cdot\frac{\exp\left[\frac{-\left[x-\rho\{1-\cos(\theta)\}\right]^2}{2\sigma^2}\right]}{\sigma\cdot\sqrt{2\pi}}d\vartheta \tag{1}$$

where the original beam profile is assumed to be ~~a~~ Gaussian. The visibility of the interferogram $\gamma_h(D)$ is given by Fourier cosine transform of the apparent beam shape as follows,

$$\gamma_h(D)=\int \sigma_a(x)\cdot\cos\left(\frac{2\pi\cdot D\cdot x}{R\cdot\lambda}\right)dx \tag{2}$$

For the discussion of horizontal spatial coherence, we need knowledge of instantaneous intensity distribution of SR in horizontal plane.

HORIZONTAL INSTANTANEOUS SR OPENING BY K.J.KIM

A horizontal instantaneous opening of the SR is qualitatively discussed by K. J. Kim [2]. He considers an apparent shape of circular trajectory by using time scale change factor (Doppler factor) as indicated in Fig. 1. According to his paradigm, the kink shaped apparent trajectory due to strong temporal squeezing in observer

ISBN: 978-3-95450-192-2 doi:10.18429/JACoW-IBIC2017-WEPCC09

time radiate the Synchrotron Radiation. The radiation is propagating with the diffraction by kink size.

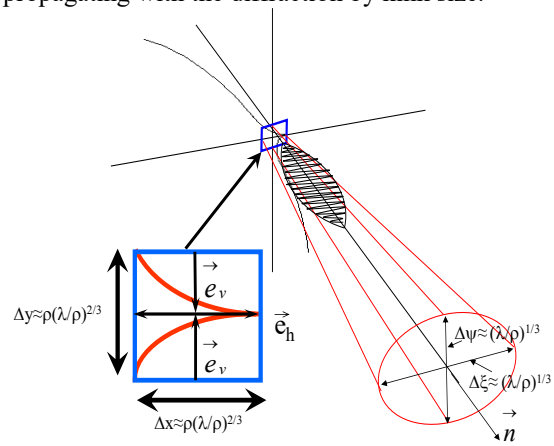

Figure 1: Apparent shape of circular trajectory by using time scale change factor (Doppler factor).

The horizontal and vertical sizes of the kink are given by

$$\Delta x \approx \rho\left(\frac{\lambda}{\rho}\right)^{2/3} \quad , \quad \Delta y \approx \rho\left(\frac{\lambda}{\rho}\right)^{2/3} \tag{3}$$

Then, the horizontal opening $\Delta\xi$ and vertical opening $\Delta\psi$ of radiation is given by diffraction of this source size,

$$\Delta\xi \approx (\lambda/\rho)^{1/3} \quad , \quad \Delta\psi \approx (\lambda/\rho)^{1/3} \tag{4}$$

These results indicate instantaneous horizontal opening of the SR is same as vertical opening.

In next chapter, let us discuss quantitative theory by extending the Schwinger's theory for SR.

EXTENSION OF SCHWINGER'S THEORY TO HORIZONTAL INSTANTANEOUS SR OPENING

The SR from circular trajectory is written by Schwinger in 1945 [1]. He only gave his theory for horizontal observation angle ξ=0. Before discuss the general case, ξ≠0, let us simply refer the Schwinger's theory for horizontal observation angle ξ=0.

Let us start the vector potentials for parallel and perpendicular components of the radiation as follows,

$$\mathbf{A}_{\parallel}(\omega) \cong \frac{c}{\rho}\int_{-\infty}^{\infty} t' exp\left\{ i\frac{\omega}{2}\left[\left(\frac{1}{\gamma^2}+\psi^2+\xi^2\right)t' + \frac{c^2}{3\rho^2}t'^3 + \frac{c}{\rho}\xi t'^2\right]\right\} dt' \tag{5}$$

$$\mathbf{A}_{\perp}(\omega) = \psi\int_{-\infty}^{\infty} exp\left\{ i\frac{\omega}{2}\left[\left(\frac{1}{\gamma^2}+\psi^2+\xi^2\right)t' + \frac{c^2}{3\rho^2}t'^3 + \frac{c}{\rho}\xi t'^2\right]\right\} dt' \tag{6}$$

Putting the horizontal observation angle ξ=0. The vector potentials becomes

$$\mathbf{A}_{\parallel}(\omega) \cong \frac{c}{\rho}\int_{-\infty}^{\infty} t' \exp\left\{ i\frac{\omega}{2}\left[\left(\frac{1}{\gamma^2}+\psi^2\right)t' + \frac{c^2}{3\rho^2}t'^3\right]\right\} dt' \tag{7}$$

$$\mathbf{A}_{\perp}(\omega) = \psi\int_{-\infty}^{\infty} \exp\left\{ i\frac{\omega}{2}\left[\left(\frac{1}{\gamma^2}+\psi^2\right)t' + \frac{c^2}{3\rho^2}t'^3\right]\right\} dt' \tag{8}$$

After some change of variables, and using Airy integrals, and alternatively as modified Bessel functions, consequently the intensity radiated per unit frequency interval per unit solid angle is given by

$$\frac{d^2 I}{d\omega d\Omega} = \frac{e^2}{3\pi^2 c}\left(\frac{\omega\rho}{c}\right)^2\left(\frac{1}{\gamma^2}+\psi^2\right)^2\left[K_{2/3}^2(\zeta) + \frac{\psi^2}{\frac{1}{\gamma^2}+\psi^2}K_{1/3}^2(\zeta)\right] \tag{9}$$

Where

$$\zeta = \frac{\omega\rho}{3c}\left(\frac{1}{\gamma^2}+\psi^2\right)^{\frac{3}{2}} \tag{10}$$

The intensity distribution as a function of vertical observation angle is indicated in Fig. 2 for SR at wavelength of 500nm. This calculation is using the condition of bending magnet at Australian Synchrotron.

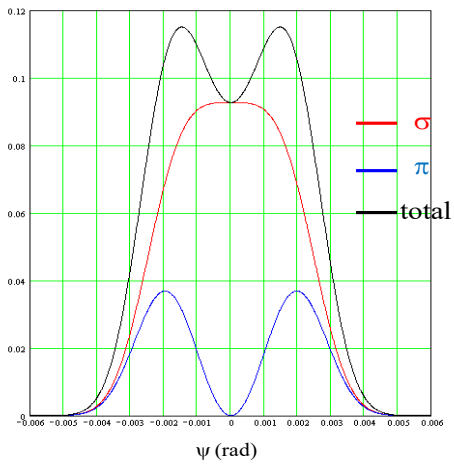

Figure 2: The intensity distribution as a function of vertical observation angle.

Let us move on to general case for horizontal observation angle ξ≠0. Return to vector potential of parallel component, Eq. (5), rewritten exponent into the product of linear + cubic term of t' and quadratic term of t' the vector potential becomes,

$$\mathbf{A}_{\parallel}(\omega) \cong \frac{c}{\rho}\int_{-\infty}^{\infty} t' exp\left\{ i\frac{\omega}{2}\left[\left(\frac{1}{\gamma^2}+\psi^2+\xi^2\right)t' + \frac{c^2}{3\rho^2}t'^3 + \frac{c}{\rho}\xi t'^2\right]\right\} dt'$$

$$= \frac{c}{\rho}\int_{-\infty}^{\infty} t' exp\left\{ i\frac{\omega}{2}\left[\left(\frac{1}{\gamma^2}+\psi^2+\xi^2\right)t' + \frac{c^2}{3\rho^2}t'^3\right]\right\} \cdot exp\left\{ i\frac{\omega}{2}\frac{c}{\rho}\xi t'^2\right\} dt' \tag{11}$$

Then, integrating the vector potential by parts gives,

ISBN: 978-3-95450-192-2 doi:10.18429/JACoW-IBIC2017-WEPCC09

$$\mathbf{A}_{\parallel}(\omega) \cong \frac{c}{\rho}\left[\int_{-\infty}^{\infty} \boldsymbol{t'} exp\left\{i\frac{\omega}{\mathbf{2}}\left[\left(\frac{\mathbf{1}}{\gamma^2}+\psi^2+\xi^2\right)t'+\frac{\boldsymbol{c^2}}{\mathbf{3}\rho^2}\,t'^3\right]\right\}dt'\cdot exp\left\{i\frac{\omega}{\mathbf{2}}\frac{c}{\rho}\xi\, t'^2\right\}\right.$$
$$\left.+\int_{-\infty}^{\infty} f(t')\cdot i\frac{\omega}{\mathbf{2}}\xi\frac{c}{\rho}\frac{\mathbf{1}}{\mathbf{2}}t'\cdot \boldsymbol{exp}\left\{i\frac{\omega}{\mathbf{2}}\xi\frac{c}{\rho}t'^2\right\}dt'\right] \quad (12)$$

Where $f(t')$ is,

$$f(t') = \int_{-\infty}^{\infty} t' \exp\left\{i\frac{\omega}{2}\left[\left(\frac{1}{\gamma^2}+\psi^2+\xi^2\right)t'+\frac{c^2}{3\rho^2}t'^3\right]\right\}dt' \quad (13)$$

The same way to derive Eq. (9) from Eq. (8), $f(t')$ can replaced by modified Bessel function $K_{2/3}$. The second term in right hand of Eq. (12) becomes,

$$i\frac{\omega}{2}\xi\frac{c}{\rho}\frac{1}{2}\mathrm{a}\cdot \mathrm{K}_{2/3}\int_{-\infty}^{\infty} t'\cdot exp\left\{i\frac{\omega}{2}\xi\frac{c}{\rho}t'^2\right\}dt' \quad (14)$$

This integral is Fresnel transform of odd function t', and it becomes zero. Then, the vector potential becomes,

$$\mathbf{A}_{\parallel}(\omega) \cong \frac{c}{\rho}\int_{-\infty}^{\infty} t' \exp\left\{i\frac{\omega}{2}\left[\left(\frac{1}{\gamma^2}+\psi^2+\xi^2\right)t'+\frac{c^2}{3\rho^2}t'^3\right]\right\}dt'\cdot \exp\left\{i\frac{\omega}{2}\frac{c}{\rho}\xi\, t'^2\right\} \quad (15)$$

The quadratic phase term in right hand of this equation,

$$\exp\left\{i\frac{\omega}{2}\frac{c}{\rho}\xi\, t'^2\right\} \quad (16)$$

Since phase term having unit amplitude becomes 1 after calculating intensity (absolute value), so we can neglect this constant phase term from the vector potential. We can write the vector potential for parallel component as follows,

$$\mathbf{A}_{\parallel}(\omega) \cong \frac{c}{\rho}\int_{-\infty}^{\infty} t' \exp\left\{i\frac{\omega}{2}\left[\left(\frac{1}{\gamma^2}+\psi^2+\xi^2\right)t'+\frac{c^2}{3\rho^2}t'^3\right]\right\}dt' \quad (17)$$

In the same way, the vector potential for perpendicular component is given by,

$$\mathbf{A}_{\perp}(\omega) \cong \psi\int_{-\infty}^{\infty} \exp\left\{i\frac{\omega}{2}\left[\left(\frac{1}{\gamma^2}+\psi^2+\xi^2\right)t'+\frac{c^2}{3\rho^2}t'^3\right]\right\}dt' \quad (18)$$

The intensity radiated per unit frequency interval per unit solid angle is given by

$$\frac{d^2I}{d\omega\, d\Omega} = \frac{e^2\omega^2}{4\pi^2 c}\left|\mathbf{A}_{\parallel}(\omega)+\mathbf{A}_{\perp}(\omega)\right|^2 \quad (19)$$

After some change of valiables, and using Airy integrals, and alternatively as modified Bessel functions, consequently the intensity radiated per unit frequency interval per unit solid angle is given by

$$\frac{d^2I}{d\omega d\Omega} = \frac{e^2}{3\pi^2 c}\left(\frac{\omega\rho}{c}\right)^2\left(\frac{1}{\gamma^2}+\psi^2+\xi^2\right)^2\left[K_{2/3}^2(\zeta)+\frac{\psi^2}{\frac{1}{\gamma^2}+\psi^2+\xi^2}K_{1/3}^2(\zeta)\right] \quad (20)$$

Where,

$$\zeta = \frac{\omega\rho}{3c}\left(\frac{1}{\gamma^2}+\psi^2+\xi^2\right)^{\frac{3}{2}} \quad (21)$$

The result given by Eq.(20) indicates both of vertical intensity distribution and horizontal instantaneous intensity distribution have same angular dependence. This result is same as in the result from qualitative discussion in K.J. Kim.

SOME CALCULATION FOR HORIZONTAL INTENSITY DISTRIBUTION

Some calculation for intensity distribution using Eq.(20) was performed at several vertical observation angle.

Results are shown in Fig. 3. In this calculation, the condition of bending magnet of SPEAR 3 in SLAC was used.

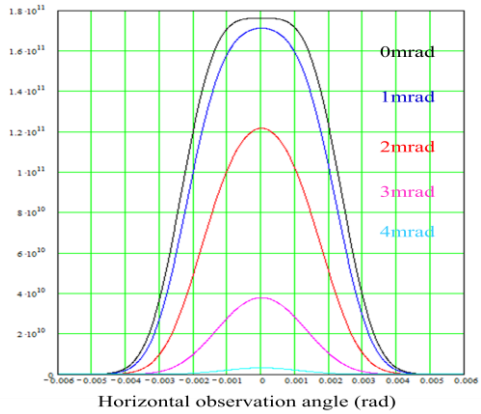

Figure 3: Horizontal intensity distribution of SR at several vertical observation angle.

To see the intensity destitution by modified Bessel function, the normalized intensity plots are shown in Fig. 4.

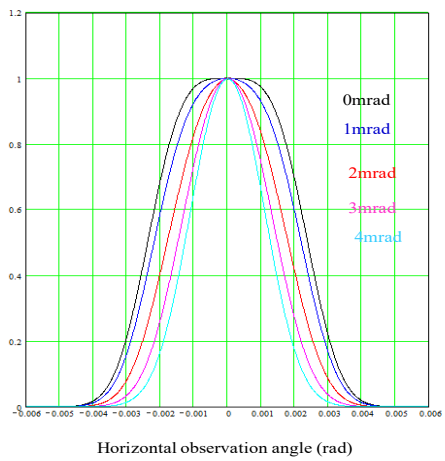

Figure 4: Normalized intensity distribution at several vertical observation angle.

ISBN: 978-3-95450-192-2 doi:10.18429/JACoW-IBIC2017-WEPCC09

To see Fig. 4, Intensity distributions for each vertical observation angle has different distribution, because of the distribution is given by modified Bessel function. To watch two dimensional distribution of radiation written by eq. (20), two dimensional plot is indicated in Fig. 5.

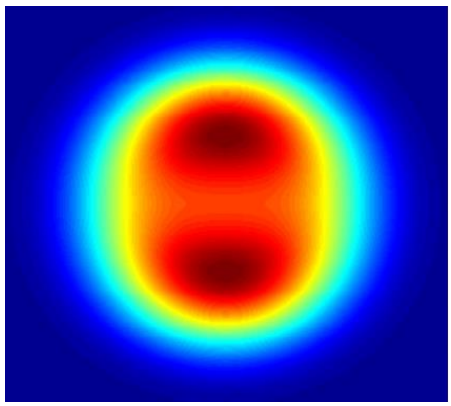

Figure 5: Two dimensional plot of Eq. (20).

HORIZONTAL BEAM SIZE MEASUREMENT USING HORIZAONTAL INTENSITY DISTRIBUTION

Horizontal beam size measurements are performed including the IDOF effect and horizontal intensity distribution at SPEAR3, ALS, and ATF [6].

Result the visibility at SPEAR3 as a function of the slit separation is shown in Fig. 6 [5][6]. Two analysis methods, one is including the IDOF and other is not including IDOF are shown in this figure. The result of horizontal beam size is 132.7μm. Due to a large horizontal beam size, the effect of IDOF is rather small.

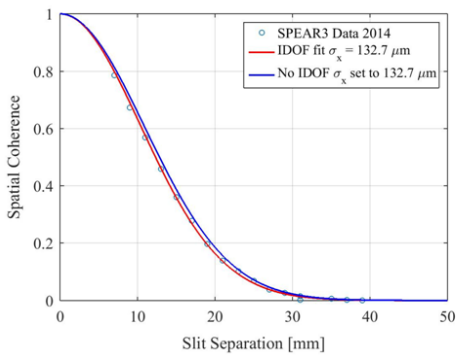

Figure 6: Horizontal visibility measured at SPEAR 3 as a function of slit separation.

The second is a measurement at the Australian Synchrotron ALS [6]. The measured horizontal visibility is shown in Fig. 7 and the horizontal beam size taking IDOF into account is 88μm. Due to a smaller horizontal beam size at the source point the effect of IDOF is larger than at SPEAR3.

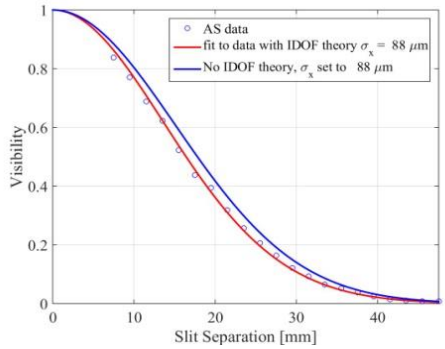

Figure 7: Horizontal visibility measured at ALS as a function of slit separation.

The third is a measurement at the ATF [7]. The measured horizontal visibility is shown in Fig. 8 and the horizontal beam size taking IDOF into account is 38.5μm. Due to smaller horizontal beam size, the effect of IDOF is the largest in these tree measurements.

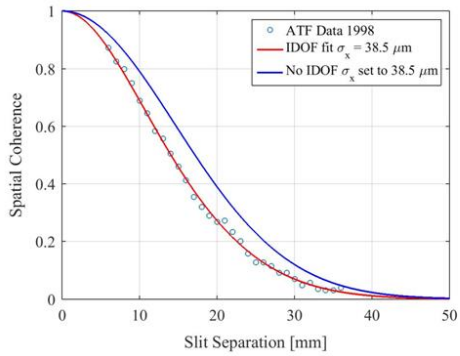

Figure 8: Horizontal visibility measured at ATF as a function of slit separation.

In each case, the results for horizontal beam sizes are in good agreement with designed values when the IDOF effect with horizontal intensity distribution is taken into account.

CONCLUSIONS

The horizontal intensity distribution of SR from circular trajectory is investigated by extending Schwinger's theory for SR. As a result, we derived the same Bessel function distribution as in the vertical plane for the horizontal intensity distribution. The IDOF effect for horizontal beam size measurement via interferometry including the horizontal intensity distribution is investigated by through the measured visibility at SPEAR3, ALS and ATF. For the three measurements, the results for horizontal beam size measurements are in good agreement with designed values when the IDOF effect with horizontal intensity distribution is included.

ACKNOWLEDGEMENT

Authors acknowledge to Prof. Oide of CERN for helpful discussion and his encourage for this work. Thanks also due to Dr. Georges Trad of CERN for his calculation of two dimensional distribution of SR intensity.

ISBN: 978-3-95450-192-2 doi:10.18429/JACoW-IBIC2017-WEPCC09

REFERENCES

[1] J. Schwinger, "On Radiation by Electron in a Betatron", published in A quantum Legacy : Seminal paper of J. Schwinger, World Scientific,p.307 (2000). Also see J. Schwinger, Phys.Rev.75p.1912 (1949)

[2] K.J. Kim, "Characteristics of Synchrotron Radiation", in AIP conference proceedings 184, p565 (1989).

[3] T. Mitsuhashi, "Beam Profile and Size Measurement by SR Interferometer" in Beam measurement, Ed. by S.Kurokawa *et al.*, 399-427,World Scientific(1999).

[4] T.Mitsuhashi, Proceedings of IPAC2015, p3663, (2015).

[5] Jeff Corbett, private communication.

[6] M. Boland, Jeff Corbett and T. Mitsuhashi, Proc. Of IPAC 2015, p1391, (2015).

[7] T. Naito and T. Mitsuhashi, Phys. Rev. ST Accel. Beams 9, 122802 (2006).

ISBN: 978-3-95450-192-2 doi:10.18429/JACoW-IBIC2017-WEPCC10

ANALYSIS OF MIE SCATTERING NOISE OF OBJECTIVE LENS IN CORONAGRAPH FOR HALO MEASUREMENT

T. Mitsuhashi†, KEK, Accelerator Laboratory, Tsukuba, Ibaraki, Japan

Abstract

In beam halo measurements by means of a coronagraph viewing visible SR light, the theoretical image contrast is dominated by leakage of the diffracted fringe pattern from the Lyot stop. On other hand, the noise background in an actual coronagraph also contains light scattered from imperfections in the first objective lens. Most of this light is due to Mie-scattering from dig imperfections on the surface of objective which can reduce the image contrast to the 10-3 range for a lens with 60/40 scratch and dig figures. By introducing a high-quality objective lens into the system the theoretical value of 10-5-10-6 image contrast can be recovered for the Lyot coronagraph. In this paper, Mie-scattering due to dig imperfections is analyzed theoretically and results from measurements of the Mie scattering are presented.

INTRODUCTION

For high energy or high power accelerators such too much beam in the halo can lead to damage of accelerator components, either due to instantaneous beam loss or through long term irradiation. Beam halo control is essential and is best achieved by tuning the machine to avoid populating the tails of the bunch distribution. The beam diagnostic challenges here lie in developing non-invasive techniques with a high enough dynamic range to resolve a beam halo a factor 10^{-5} lower in intensity than that in the beam core. Synchrotron light sources, FELs and high energy hadron accelerators, such as the LHC, can all use synchrotron light to provide a non-invasive, transverse image of the beam distribution. To be able to measure the beam halo, however, requires an imaging system that eliminates the diffraction fringes created by the intense light from the beam core as is passes through the aperture of the first optical element. These fringes can have an intensity as high as 10^{-2} of the peak intensity and would hide any halo at the 10^{-5} level. To reduce this effect a coronagraph, developed by Lyot [1] in 1936 for solar astronomy, can be used. Such a technique has already been demonstrated by one of authors at the KEK Photon Factory to achieve a $6x10^{-7}$ ratio for background to peak intensity [2]. In this way, the coronagraph can escape from background due to diffraction fringe, but in other hand, strong illumination for objective lens can produce another background. The Mie scattering from digs on the surface of the objective lens. With typical commercial-available lens has scratch and dig 60/40 optical polishing quality, the Mie scattering background can make a background as like as intensity of diffraction fringe. In this paper, it is described analysis of Mie scattering from dig on the lens surface, and discuss the contribution to background in the coronagraph.

CORONAGRAPH

The optical layout of the coronagraph is illustrated in Fig. 1 [2]. The objective lens makes a real image of the object (beam image) on to a blocking mask which makes artificial eclipse. Second lens (field lens) which is located just after the blocking mask makes a real image of the objective lens onto a mask so-called Lyot Stop. The diffraction fringes on focal plane of the objective lens is re-diffracted by field lens aperture and making a diffraction ring onto the focal plane of field lens. The Lyot's genius idea of the coronagraph is to remove this diffraction rings by a mask, so-called Lyot stop in today and relay the hidden image such as Sun corona by a third lens onto final observation plane. The background light on the final observation plane is now mainly come from the leakage of diffraction fringe inside of Lyot stop and the scattering of the input bright light by the objective lens. Theoretically, diffraction fringe leakage to next stage can reduce greatly, and we can reduce the background light less than 10^{-6} to the peak intensity of blocked main image at final stage. With this coronagraph, we can observe a hidden image of beam halo in accelerator surrounding from the bright beam core image.

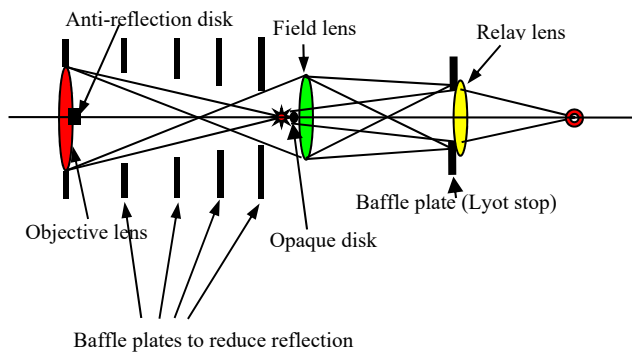

Figure 1: Layout of optical system of the coronagraph.

MIE SCATTERING SOURCE ON SURFACE OF OBJECIVE LENS

After blocking the central bright image and cutting the light from diffraction fringe, we have still scattered light (Mie scattering) from the defects in the objective lens such

†email address: toshiyuki.mitsuhashi@kek.jp

ISBN: 978-3-95450-192-2 doi:10.18429/JACoW-IBIC2017-WEPCC10

as scratches and digs on its surfaces. Figure 5 shows a surface of objective lens with the typical surface with optical polishing scratch & dig 60/40. The optical surface quality 60/40 guarantees no larger scratches than 6μm width, and no larger dig larger than 400μm. From this observation, we can find many digs (small spots in the photograph) with 10-100μm in diameter.

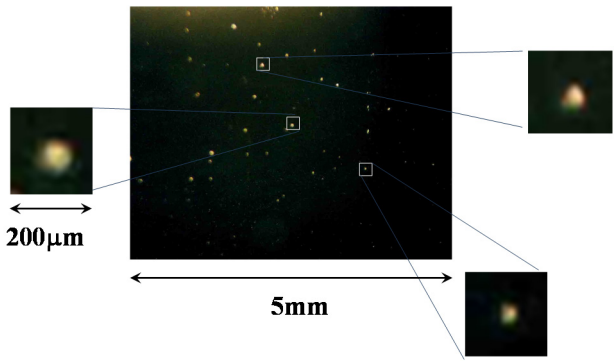

Figure 2: A microscope image of the digs on the surface of lens with normal optical polishing scratch & dig 60/40. This photo is taken by illuminating from the side.

MIE SCATTERING BY MEANS OF DIFFRACTION TREATMENT

Let us consider the Mie scattering by means of diffraction phenomena from dig on pupil.

Case 1, Consider the dig on the entrance pupil of the objective lens.

Let us introduce a generalized pupil function having the digs in the entrance aperture of the objective lens as shown in Fig. 3. In here, the dig is represented by a small opaque spot with a radius r_0 on the pupil.

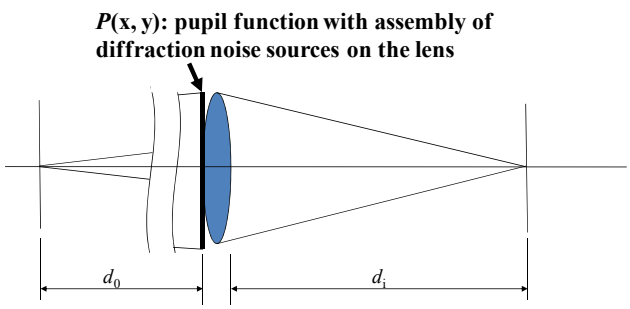

Figure 3: Case 1, the noise source in the entrance pupil of the objective lens

Using the Babinet's principle, we can replace such dig as opaque spot with a small hole having a same radius as shown in Fig. 4.

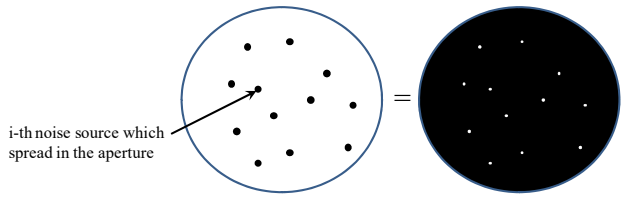

Figure 4: Babinet's principle for calculating diffraction from dig as the pupil having an opposite contrast.

Let us assume the shape of the dig is simple round shape, the pupil function of i-th hole is given by,

$$P_i(r_0, x, y) = circ(r_0, x_i, y_i) \quad (1)$$

When the separations between the holes are smaller than coherent length of the illuminated light, the pupil function is given by,

$$P(\bar{r}, x, y) = \sum_i P_i(r_0, x, y) \cdot exp(-ik(x_i + y_i)) \quad (2)$$

In other hand, the separations of the holes are enough lager than coherent length, the pupil function is give by incoherent summation.

$$P(\bar{r}, x, y) = \sum_i P_i(r_0, x, y) \quad (3)$$

Using these pupil functions, the impulsive response on the image plane is given by,

$$h(x_i, y_i; x_0, y_0) = \frac{1}{\lambda d_0 d_i} \iint P(\bar{r}, x, y) \cdot exp\left\{-i\frac{2\pi}{\lambda d_i}[(x_i + Mx_0)x + (y_i + My_0)y]\right\} dxdy \quad (4)$$

In here, $M = d_i / d_0$ denotes geometrical magnification.

In the case of separation between the holes are larger than coherent length of illuminating light, The diffraction intensity is given by incoherent summation of diffraction from holes.

Case 2, We consider Mie scattering source in front of Objective lens.

Let us consider the Mie Scattering source on the generalized pupil function at distance d_s in front of the objective lens as shown in Fig. 5. This case is corresponding to some optical component such as mirror in front of the objective lens.

ISBN: 978-3-95450-192-2 doi:10.18429/JACoW-IBIC2017-WEPCC10

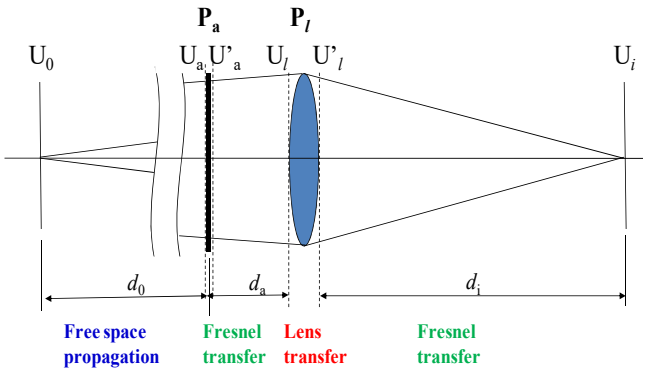

Figure 5: Case 2, Noise source in front of the lens.

In this case, impulsive response on the image plane is calculated by 3 stages, stage one; Fresnel transform of pupil function U'_a onto lens pupil U_l, stage 2; paraxial lens transform U_l to U'_l, stage 3, Fresnel transform of U'_l onto image plane U_i. The result of impulsive response on the image plane is given by,

$$U_i(x_i,y_i)=\iint\left[\iint P_a(x_a,y_a)\exp\left\{i\frac{k}{2}\left(\frac{1}{d_0-d_a}-\frac{1}{d_a}\right)\left(x_a^2+y_a^2\right)\right\}\cdot\exp\left\{-ik\left(\left(\frac{x_0}{d_0-d_a}+\frac{x_l}{d_a}\right)x_a+\left(\frac{y_0}{d_0-d_a}+\frac{y_l}{d_a}\right)y_a\right)\right\}dx_a dy_a\right]$$

$$\cdot P_l(x_l,y_l)\exp\left\{i\frac{k}{2}\left(\frac{1}{d_l}+\frac{1}{d_i}-\frac{1}{f}\right)\left(x_l^2+y_l^2\right)\right\}\cdot\exp\left\{-i\frac{k}{d_i}\left(x_i\,x_l+y_i\,y_l\right)\right\}dx_l dy_l \quad (5)$$

The first integral in this equation represents the Fresnel diffraction by Mie scattering source, and the second integral represents the Fresnel diffraction of the lens pupil.

This result indicates when d_a is shorter, out of focus image of noise source with Fresnel like diffraction, and when d_a is longer, quasi-focused image of noise source with Fraunhofer like diffraction.

SIMULATION OF MIE SCATTERING BACKGROUND FOR CASE 1

The Mie scattering background for case 1 using impulsive response equation 4 is simulated for several diameters of digs. In this simulation, the density of digs is estimated from Fig. 2.

Simulation results for dig diameter of 50,100,200 and 400μm are shown in Fig.6 with diffraction pattern of objective lens aperture. The vertical scale for each diffraction pattern is normalized by peak intensity of diffraction of the lens aperture.

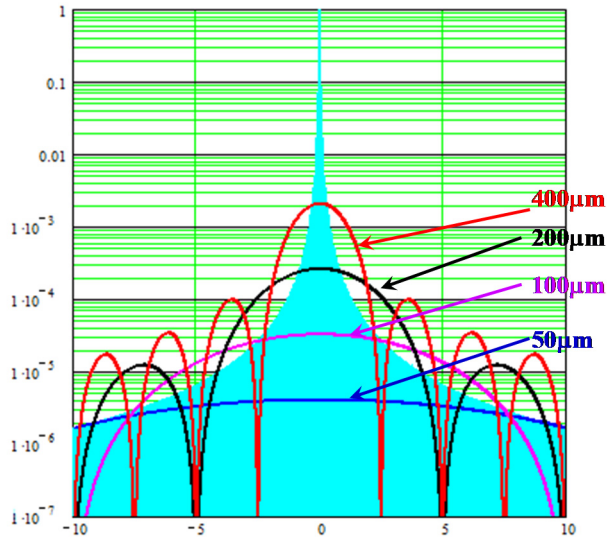

Figure 6: Simulation results for dig diameter of 50,100,200 and 400μm with diffraction pattern of lens aperture.

A close-up of Fig. 6 in horizontal axis is shown in Fig. 7. From these results, Mie scattering background from smaller dig such as 50μm is widely spread, and having contrast level of 10^{-5} to 10^{-6} of the peak intensity of the diffraction from lens aperture. More lager digs has lager noise. For example, dig larger than 100μm can make almost same noise intensity level as like as the intensity of diffraction fringes by lens aperture.

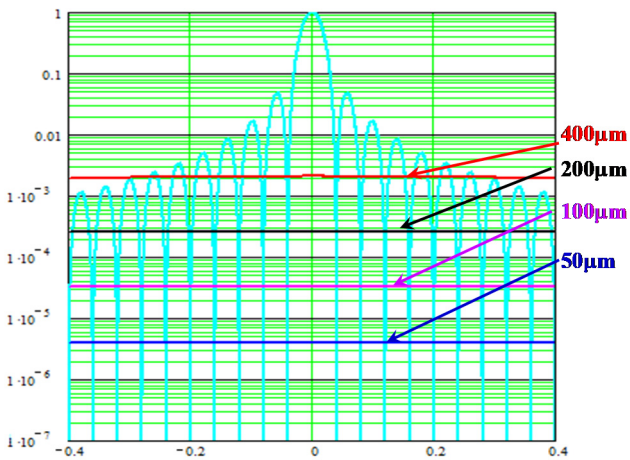

Figure 7: A close-up of Figure 6.

OBSERVATION OF MIE SCATTERING BACKGROUND FOR CASE 2

The Mie scattering background for case 2 is observed by spraying dust on the mirror which is located 2m in front of the objective lens. A result of this observation is shown in Fig.8. The white frame indicates aria on the mirror which is illuminated by input light.

ISBN: 978-3-95450-192-2 doi:10.18429/JACoW-IBIC2017-WEPCC10

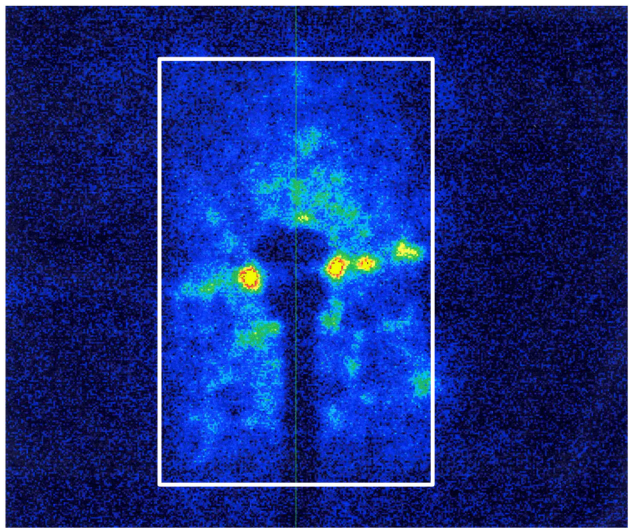

Figure 8: Result of observation for Mie scattering background from the dust on the mirror. The mirror is located 2m in front of the objective lens.

The dark circle in the centre is corresponding to opaque disc with supporting load for artificial eclipse. This observation is corresponding to shorter d_a . The out of focus image of noise source (dust) with Fresnel like diffraction is observed.

Without such Mie scattering background, we can observe beam halo with high contrast as shown in Fig. 9 [2].

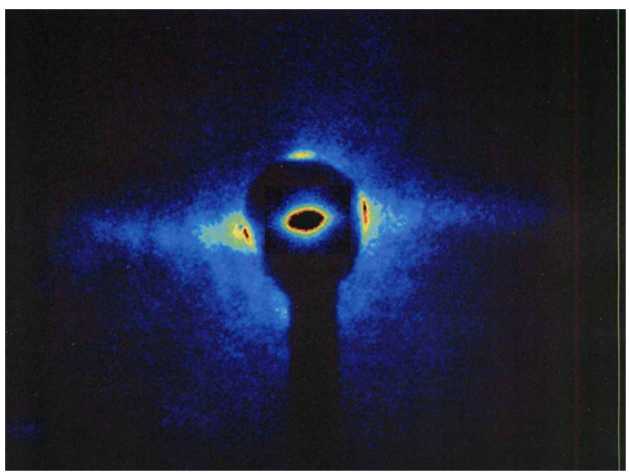

Figure 9: A result of beam halo observation with coronagraph at Photon Factory in the KEK. The profile of beam core image is super imposed in inside of opaque disk image.

CONCLUSIONS

The theoretical analysis for Mie scattering from dig by using a diffraction treatment is discussed for two cases. The case 1, dig is located on the lens surface, and Case 2 Mie scattering source is located in front of the objective lens. In the case 1, the Mie scattering background from smaller dig such as 50μm is widely spread, and having contrast level of 10^{-5} to 10^{-6} of the peak intensity of the diffraction from lens aperture. More lager digs has lager noise. For example, dig larger than 100μm can make almost same noise intensity level as like as the intensity of diffraction fringes by lens aperture. For the case 2, the result indicates when d_a is shorter, out of focus image of noise source with Fresnel like diffraction, and when d_a is longer, quasi-focused image of noise source with Fraunhofer like diffraction. From these results, we can conclude we need Mie-scattering background free objective lens for the First stage of the coronagraph and optical components such as mirrors in near front of objective lens.

REFERENCES

[1] B.F. Lyot Month. Notice Roy. Ast. Soc, p 580, 99 (1939).

[2] T. Mitsuhashi, "Beam halo observation by coronagraph", in *Proc. DIPAC'2005*, Lyon, France.

ISBN: 978-3-95450-192-2 doi:10.18429/JACoW-IBIC2017-WEPCC11

PROFILE MONITOR ON TARGET FOR SPALLATION NEUTRON SOURCE

Shin-ichiro Meigo*, Hiroki Matsuda and Hayanori Takei
J-PARC center, Japan Atomic Energy Agency (JAEA), 319-1195, Japan

Abstract

Materials and Life Science Experimental Facility (MLF) in J-PARC is aimed at promoting experiments using the world highest intensity pulsed neutron and muon beams which are produced at a thick mercury target and a thin carbon graphite target by 3-GeV proton beams, respectively. Since damage due to the short pulsed proton beam at the mercury target vessel is proportional to the 4th power of the peak current density of the beam, decrease of the peak density is crucial for the beam injection system. To decrease peak density, a beam transport based on the nonlinear optics was developed. For reliable beam operation with the high-intensity beam, a reliable online 2D profile monitor with a long lifetime is indispensable to observe the beam introduced to the target. Furthermore, in J-PARC future facilities, high current density on the target will be required so that research and development have started to accept high density.

INTRODUCTION

In the Japan Proton Accelerator Research Complex (J-PARC) [1], a MW-class pulsed neutron source, the Japan Spallation Neutron Source (JSNS) [2], and the Muon Science facility (MUSE) [3] will be installed in the Materials and Life Science Experimental Facility (MLF) shown in Fig. 1. Since 2008, this source has produced a high-power proton beam of 300 kW. In 2015, we successfully ramped up beam power to 500 kW and delivered the 1-MW beam to the targets. To produce a neutron source, a 3 GeV proton beam collides with a mercury target, and to produce a muon source, the 3 GeV proton beam collides with a 2-cm-thick carbon graphite target. To efficiently use the proton beam for particle production, both targets are aligned in a cascade scheme, with the graphite target placed 33 m upstream of the neutron target. For both sources, the 3 GeV proton beam is delivered from a rapid cycling synchrotron (RCS) to the targets by the 3NBT (3 GeV RCS to Neutron facility Beam Transport) [4–6]. Before injection into the RCS, the proton beam is accelerated up to 0.4 GeV by a LINAC. The beam is accumulated in two short bunches and accelerated up to 3 GeV in the RCS. The extracted 3 GeV proton beam, with a 150 ns bunch width and a spacing of 600 ns, is transferred to the muon production target and the spallation neutron source.

Beam profile monitoring plays an important role in comprehending the damage to the target. Therefore it is very important to watch continuously the status of the beam at the target at the JSNS especially for the peak current density. We have developed a reliable beam profile monitor for the target by using Multi-Wire Profile Monitor (MWPM). In order to watch the two-dimensional profile on the target, we have also developed the profile monitor based on the imaging of radiation of the target vessel after beam irradiation. For observation beam introduced to the target, MWPM was placed at the proton beam window. In J-PARC center, facilities for research and development for Accelerator Driven System (ADS) is planned. Furthermore, to satisfy the demand of neutron and muon beam, second target facility is also expected. In those facilities, the beam will be more collimated than the JSNS so that a profile monitor will be required, which will stand higher current density than the JSNS.

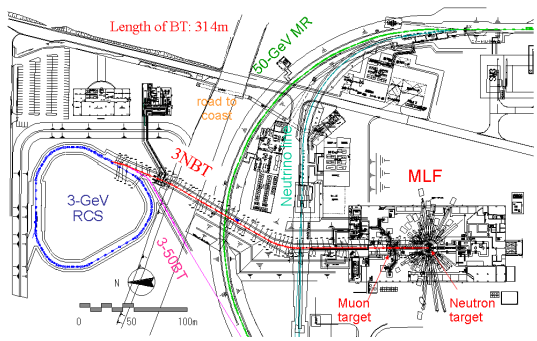

Figure 1: Plan of rapid cycling synchrotron (RCS) at the Materials and Life Science Experimental Facility (MLF) at J-PARC.

BEAM MONITOR SYSTEM AT THE BEAM TRANSPORT TO THE TARGET AT JSNS

Monitors Placed at Proton Beam Window

Continuously observing the characteristics of the proton beam introduced to the spallation target is very important. Due to the high activations caused by the neutron produced at the target, remote handling technique is necessary to exchange the beam monitor for the target. In order to decrease the radiation produced at the spallation neutron target, shielding above the monitor was required. To reduce the difficulties of the exchange work and decrease of the shielding, we combined the beam monitors with a Proton Beam Window (PBW) for separation between the vacuum region of the accelerator and the helium region around the neutron target. The PBW is better to be placed closer to the target where the distance between the target and the PBW is 1.8 m, which gives reliable profile at the target. In Fig. 2, the MWPM placed at the center of a vacuum chamber of the PBW is

* meigo.shinichiro@jaea.go.jp

ISBN: 978-3-95450-192-2 doi:10.18429/JACoW-IBIC2017-WEPCC11

shown. To avoid exceed heat at target vicinities, beam halo monitors are placed as well. The chamber of the PBW has inflatable vacuum seal called pillow seal. Due to the pillow seal, the monitors can be changed by the remote handling. To calibrate the sensitivity of each wire, the signal was observed by the scanning the position with narrow width beam. It was found that the difference of individual sensitivity was 6 % at most.

In an actual beam operation, the heat at the target vicinities such as shielding, which mainly does not have water cooling channel, is necessary for reducing the peak density. Beam halo monitors attached at the PBW to observe the heat deposition at the target vicinities such as reflector and shielding, which is not allowed to exceed 1 W/cm^3. A view of the beam halo monitor is shown in Fig. 3. We placed two types of beam halo monitors to obtain the thermal information by thermocouples and the emission of an electron by the electrode. Since the emission of electron indicates relative intensity of the beam halo, the beam halo relative strength, which can be normalized by the following thermal observation, can be obtained by several shots of the beam. To observe the absolute intensity of the halo, the thermocouple type was implemented, which consists of copper strips coupled with the thermocouple. With 5 minutes of 25 Hz beam operation, the absolute intensity of the beam halo can be determined by the differential of temperature by time. These procedures were normally performed in actual beam operation.

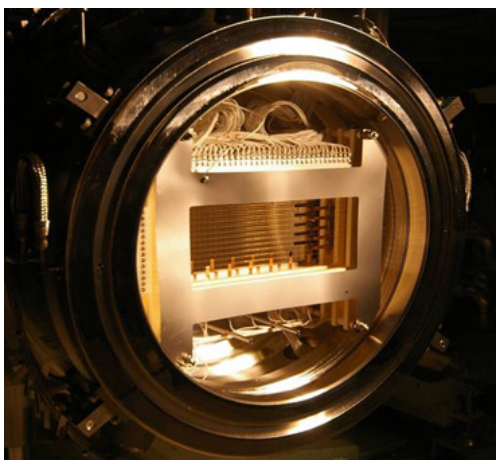

Figure 2: MWPM and beam halo monitors placed at the Proton Beam Window (PBW).

Since wires at the MWPM placed at the PBW are fixed type and continuously irradiated with the beam, long lifetime wire is required. The profile monitor at the PBW is important so that a redundant system using SiC and tungsten wires was applied. In summer of 2013, some spots were observed at the surface of helium side of the PBW, which were thought to be produced by the erosion of nitric acid produced by the radiolysis around the target. We decided to change the 1st PBW already received the integration beam power of 2000 MWh to the new one. After exchange 1st PBW, because of

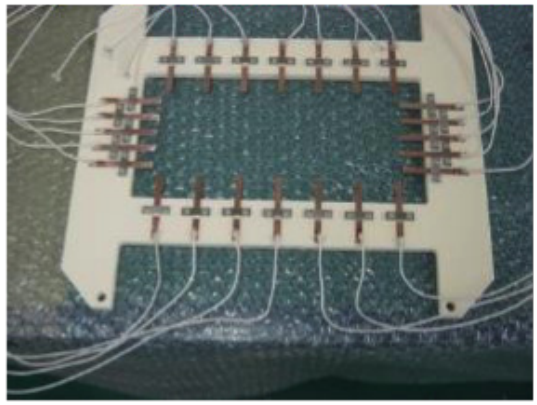

Figure 3: Thermocouple type of beam halo monitors placed at the Proton Beam Window (PBW).

stability of signal, only SiC wires were employed, which were deployed 2nd PBW. After 4 years operation, the 2nd PBW was changed in summer of 2017.

Lifetime of SiC Wires

As a material of sensitive wire, usually tungsten wire is selected due to the large emission amount of the electron and having a high-temperature melting point. In the present system, silicon carbide (SiC) was chosen due to the high resistance of the radiation [7], which is thought to survive up to 80 DPA. To obtain accurate displacement on the wire, we have a plan to measure the DPA cross section.

Due to the interaction, the beam loss is caused, which is one of the issues of the high-intensity proton accelerator and the optimization of the beam loss is important. The angular differential cross-section of Rutherford scattering is proportional to a square of an atomic number of the wire material. Therefore wire material with the low atomic number has an advantage for beam loss. Here, we compare property between tungsten and SiC. Since the average atomic number of SiC is 10, the differential cross-section of SiC becomes 1/55 times of the cross-section of tungsten.

Until 2000 MWh, the wires still gave normal signals and, it was not found severe damage by inspection after irradiation. However, slight elongation of the SiC wires was observed as shown in Fig. 4 after changing spent the PBW. In future, by changing fixing part of the wire, such elongation can be thought to be mitigated.

subsectionBeam Profile with Nonlinear Optics

To obtain the beam profile at the neutron source, SAD code is utilized, which provide beam information by fitting the result given by the MWPM placed at upstream of the octupole magnet. Also revised DECAY-TURTLE [8] by Paul Scherrer Institute (PSI) [9] is utilized to simulate multiple scattering at the muon target. Figure 5 shows results of beam profile for 800 kW beam with and without excitation of the octupole magnets. The beam profile is shown in Fig. 5, which was observed by the MWPM placed at the PBW. It can be found that considerable flat distribution can be obtained by the nonlinear optics. The calculation results

ISBN: 978-3-95450-192-2 doi:10.18429/JACoW-IBIC2017-WEPCC11

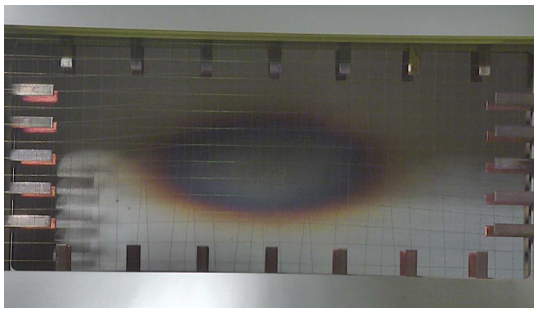

Figure 4: Inspection of SiC wire for MWPM placed at the PBW #1.

with and without excitation are also shown in Fig 5. The calculation results show good agreement with the experimental ones with and without octupole magnetic field. It is also confirmed that the calculated beam profile by using the muon target showed good agreement with the experiment for both cases with and without octupole magnetic field. By the calculation result, the peak density can be thought to be reduced by 30% compared with the linear optics.

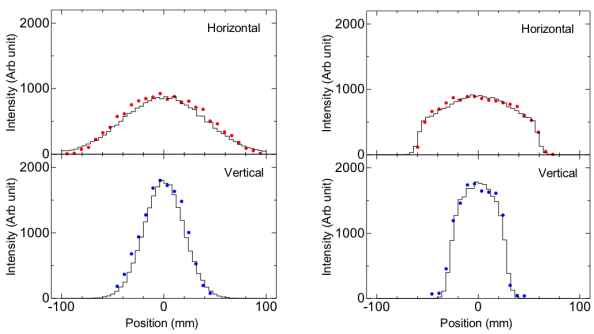

(a) OCT 0A (b) OCT 698A

Figure 5: Beam profile obtained with calculations (line) compared with result by the MWPM (dots) supplying current of (a) 0 A and (b) 698 A to octupole magnet . Upper and bottom figure represents for horizontal and vertical directions, respectively.

DEVELOPMENT OF NEW PROFILE MONITOR

Until now the monitor wire survived up to 2000 MWh, which was at attached the first and the second PBW, however, it is not clear that the MWPM will survive for the long duration of 1 MW beam. The lifetime of the PBW is expected as 2 years for 1 MW beam [10], which has proton fluence 2 $\times 10^{21}$ /cm^{-2} and the integral beam power of 10000 MWh. To observe 2D profile, an online type profile monitor is desired because the present 2D beam profile by IP can be obtained after the irradiation. Therefore a new beam profile monitor based on luminescence due to the beam was started to develop.

Beam Imaging Test Using Ar Beam

In order to obtain a 2D profile on the target, luminescence monitor is planned which is painted on the vessel of the mercury target. It was reported that degradation of luminescence was observed at the SNS in ORNL so that the intensity of light was observed by using $^{40}Ar^{+15}$ beam having the energy of 150 MeV with flat-shaped distribution by using nonlinear optics [11] at Takasaki Advanced Radiation Research Institute (TIARA) of Quantum Beam Science Research Directorate (QST). In the experiment, Desmarquest AF995R (Al_2O_3 99.5% and CrO_3 0.5%) with a thickness of 5 mm and DRZ-High (Gd_2O_2S:Tb) with a thickness of 5mm were irradiated with Ar beam. The luminescence of AF995R was observed with the spectrometer (Flame-NIR: Ocean Photonics).

For the development of profile monitor system, the image of the luminescence from the AF995R and DRZ-High (Gd_2O_2S:Tb) was observed with the ordinary CCD camera through imaging fiber (Fujikura FISR-20) having 20000 pixels and length of 5 m having high radiation hardening.

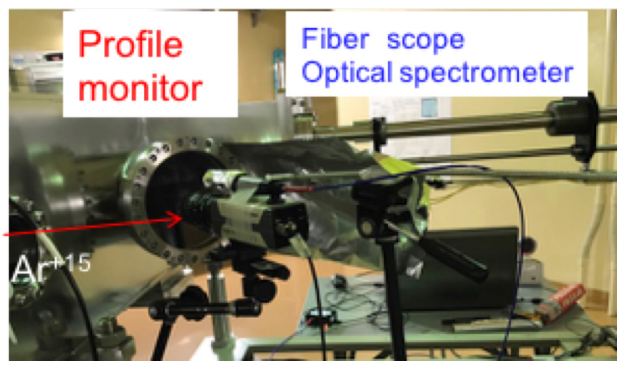

Figure 6: Experimental setup for imaging system.

Result of Beam Imaging

The 2D image of the beam obtained by the AF995R and DRZ-High is shown in Fig. 7, which is utilized square flat beam by nonlinear optics. Since the ordinary CCD camera is insensitive to the light with longwave length, the intensity of the red light emitted from the AF995R was very low intensity. In future, using 3 CCD camera, which has less dependence on wavelength, the image will be obtained. Since the DRZ-High emits short wavelength, the image has high intensity. It is confirmed that the image of the profile of the beam can be obtained with the present system.

Result of Luminescence Spectrum and Intensity

The spectrum is shown in solid line in Fig. 6 for the first shot of beam. The spectrum has a prominent peak at 694 nm with several unresolved shoulder peaks produced by the excitation state of Cr^{3+}. After the irradiation of Ar beam with 75 nA for 2.4 h to AF995R, it was found that the peak intensity decreased by 35% as shown in Fig. 8. In the first 0.2 h from the beginning, the intensity decreased rapidly. After the 0.2-h irradiation, the intensity decreased slowly and

ISBN: 978-3-95450-192-2 doi:10.18429/JACoW-IBIC2017-WEPCC11

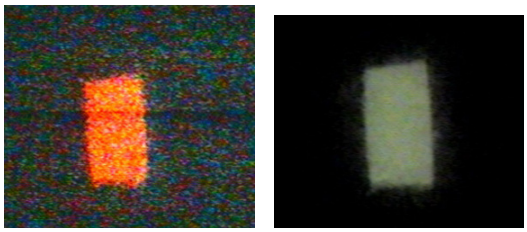

(a) AF995R (b) DRZ-High

Figure 7: Beam profile obtained with fiber imaging system for (a) AF995R and (b) DRZ-High.

steadily, which can be fit well by one-dimensional function as shown in solid line in Fig. 9. The spectrum after the 2.4-h irradiation is also shown in dot line in Fig. 8. The intensity of the unresolved peak with wavelength region shorter than 694 nm had less decreased than the intensity at the peak of 694 nm. By observing the light in shorter wavelength with optical filter cutting long wavelength, the influence of degradation may mitigate.

Spectrum for UV Light

In future, many materials will be tested by irradiation of Ar beam. To identify the luminescence of sample, it is better without Ar beam before irradiation. Therefore, we tried to determine the luminescence by using ultraviolet (UV) light so-called black light. In Fig. 10, the spectrum of luminescence was compared with Ar and UV. It is confirmed that the luminescence shows good agreement for both cases.

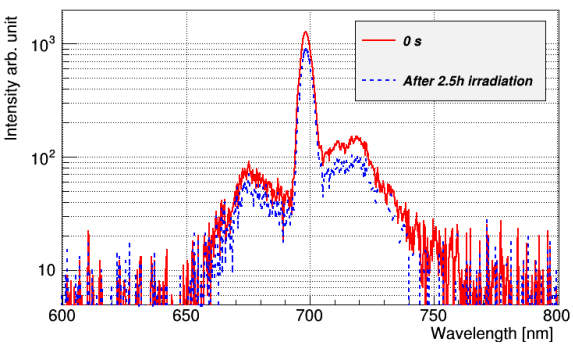

Figure 8: Spectrum of luminescence before and after irradiation Ar beam for 2.4 h.

CONCLUSION

For reliable beam operation at the JSNS in J-PARC, beam monitor system with the MWPM and the halo monitor was developed. By using the MWPM, beam parameter such as the emittance and Twiss parameter can be obtained by several shots of the beam. To mitigate pitting erosion at the mercury target, a beam transport system with nonlinear optics has been developed. By introducing nonlinear optics, peak current density can be reduced by 30%, which decreases the damage of pitting erosion about 80%.

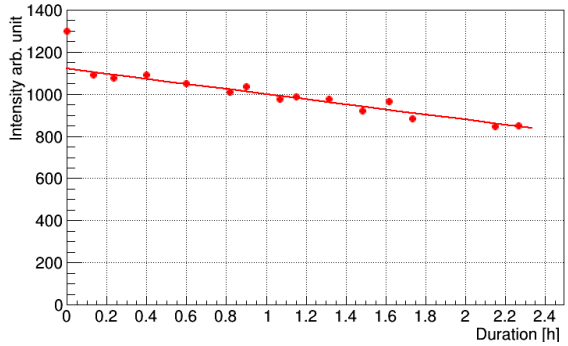

Figure 9: Trend of peak intensity for long duration irradiation of Ar beam with 75 nA. Line shows fitting result.

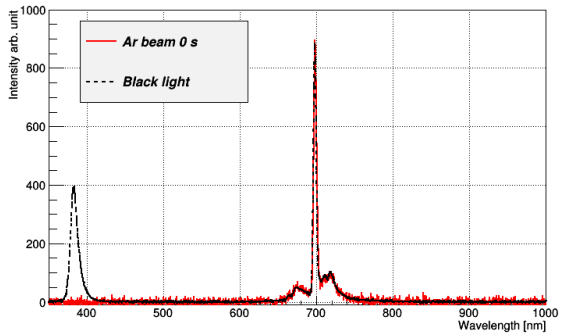

Figure 10: Comparison of spectrum of luminescence induced by black light (blue dot line) and Ar beam (red solid line).

Elongation of wires for profile monitors due to radiation damage was found after replacing the monitor. Some modifications will be applied to next profile monitors to observe correct beam profile. Just started development of luminescence profile monitor by using low energy Ar beam and degradation of luminescence was observed. In future, new material will be developed by the Ar beam experiment.

REFERENCES

[1] The Joint Project Team of JAERI and KEK, JAERI-Tech 99-56, 1999.

[2] Y. Ikeda, Nucl. Instrum. Meth. **A600**, (2009) 1.

[3] Y. Miyake, et al., Physica B **404** (2009) 957.

[4] S. Meigo, et al., Nucl. Instrum. Meth. **A562**, (2006) 569.

[5] S. Sakamoto, et al., Nucl. Instrum. Meth. **A562**, (2006) 638.

[6] S. Meigo, et al., Nucl. Instrum. Meth. **A600**, (2009) 41.

[7] G. E. Youngbllood, et al., J. Nucl. Matler. , **258 - 263**, 1551 (1998).

[8] K.L. Brown, Ch. Iselin and D.C. Carey: Decay Turtle, CERN 74-2 (1974).

[9] PSI Graphic Turtle Framework by U. Rohrer based on a CERN-SLAC-FERMILAB version.

[10] S. Meigo, et al., J. Nucl. Matler. , **450**, 141 (2014).

[11] Y. Yuri, et al., Phys Rev ST Accel. Beams **10**, 10401 (2007).

ISBN: 978-3-95450-192-2 doi:10.18429/JACoW-IBIC2017-WEPCC12

MODIFICATION OF THE SYNCHROTRON RADIATION INTERFEROMETER AT THE TPS

M.L. Chen, K.H. Hsu, T.C. Tseng, S.Y. Perng, W.Y. Lai, H.C. Ho, H.S. Wang, C.J. Lin, D.G.Huang, C.Y.Liao, C.K. Kuan, NSRRC, Hsinchu, Taiwan

Abstract

During TPS operation, the stability of beam size measurement with the synchrotron radiation interferometer (SRI) does not compare well with the older SRI at the TLS. Ground vibrations appear to transmit to the SRI optics. This paper describes how to reduce the effect of vibration and improve the system stability to improve the stability of the SRI beam size measurement dramatically. To enhance the SRI sensitivity, an intensity imbalance method is incorporated and its results are discussed.

INTRODUCTION

The Taiwan Photon Source (TPS) was commissioned in 2015 and operates now routinely at 300 mA and 3 GeV energy. To measure the transverse beam size, two monitors are installed in the 40th beam port of the TPS. One is a synchrotron radiation interferometer (SRI) and the other a X-ray pinhole camera [1,2].

The SRI monitors horizontal and vertical beam sizes and its measurement results agree well with the pinhole camera, but the stability of the beam size measurements are not acceptable. In this paper, we present the recent work to stabilize the SRI beam size response.

PRINCIPAL FEATURES OF THE SYNCHROTRON RADIATION INTERFEROMETER

The synchrotron radiation interferometer, presented by Dr. T. Mitsuhasi in KEK, is now widely used to monitor beam sizes in synchrotron light sources [2,3,4,5]. The basic principle of a SR interferometer is to measure the profile of a small beam through the spatial coherence of light, and is based on the Van Citter-Zernike theorem. The distribution of intensity of the object is given by the Fourier transform of the complex degree of first-order spatial coherence. The intensity of the interferogram pattern is defined in Eq.1 as a function of position y1, where λ is the wavelength, R the distance from the light source to a double slit, D the double slit separation and a the half-height of the slits.

$$I(y1) = I_0 \left[sinc(\frac{2\pi a}{\lambda R} y_1)\right]^2 \left[1 + |v| \cos\frac{2\pi D}{\lambda R}\, y_1 + \varphi\right] \quad (1)$$

The visibility v is related to the complex degree of coherence by a factor involving the intensity of each beam.

The quantity ρ is the power imbalance ratio of the double slit defined by the ratio of the power intensities I1 and I2 from the double slits

$$\rho = \frac{I_1}{I_2} \quad (2)$$

The beam size is observed by the visibility of the interferogram and the beam size is given by

$$\sigma_{beam} = \frac{\lambda R}{\pi D}\sqrt{\frac{1}{2}\ln(\frac{1}{\gamma})} \quad (3)$$

where

$$\gamma = v\frac{1+\rho}{2\sqrt{\rho}} \quad (4)$$

Using the power imbalance method, the visibility γ can be reduced by lowering the imbalance ratio ρ while bringing the interferogram fringes above the noise level and increase the dynamic range of the SRI [6].

MONITOR SYSTEM SETUP

An SRI beam-size monitor is installed at the 40th beam port of the TPS and the beam line structure is shown in Fig. 1. The radiation produced from a dipole magnet propagates 19.2 m to pass through the shielding wall.

After a beryllium mirror in the vacuum chamber, the light passes through the extraction window and an aluminium reflection mirror, and then through the shielding wall. Outside of the shielding wall, two folding aluminium mirrors are used to deflect the synchrotron light to the optical table in the hutch.

The light is collected in the SRI beam size monitoring system by a diffraction-limited high-quality lens with 2 m focal length followed by a polarizer and a band-pass filter to obtain quasi-monochromatic light. The centre wavelength of the bandpass filter is 500 nm with 10 nm bandwidth. An eyepiece is applied to magnify the interferogram on the CCD; Two CCDs are used to separately observe the horizontal and vertical interferograms.

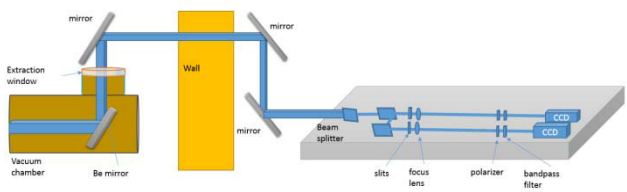

Figure 1: Optical set-up of the TPS SRI system at the 40th beam port.

VIBRATION MEASURMET

Since the stability of the TPS SRI does not match the stability achieved at the SRI in the TLS, laboratory ground vibrations are suspected and checked by an accelerometer (PCB393B31) and velocity sensor (MST-1031). As shown in Figs. 2 and 3, vibrations were observed not only on the ground but also on the optical table.

Observing the intensity variations of the interferograms on the CCD, we noted that the intensity variations are

ISBN: 978-3-95450-192-2 doi:10.18429/JACoW-IBIC2017-WEPCC12

caused by the slits, because the mechanical stability of the optical setup is not firm enough. To improve the systems rigidity, we performed some experiments as described in the following.

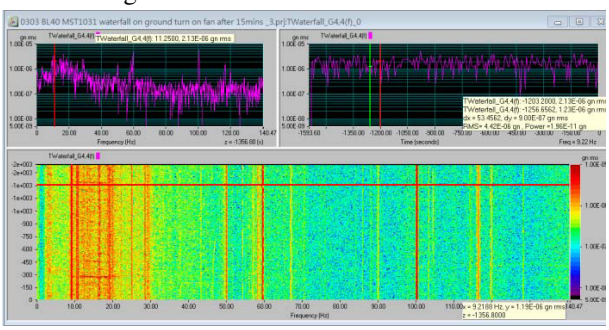

Figure 2: A time-frequency vibration graph of the hutch floor. The horizontal axis is frequency and the vertical axis is time. Many vibrations appear at low frequencies.

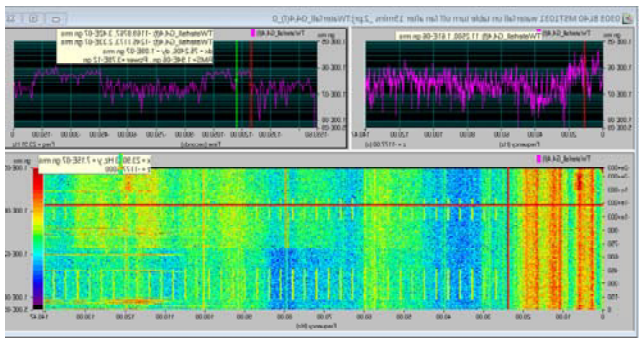

Figure 3: Time-frequency vibration graph of the experimental optics table. The horizontal axis is frequency and the vertical axis is time. There are many low frequency vibrations and periodically higher mode frequencies appearing on the optical table.

STABILITY IMPROVEMENT EXPERIMENT

Vibration Suppression

In an attempt to improve the problem of intensity variation, the distribution of synchrotron light from the front end is checked by a power meter, as shown in Fig. 4. While the centre area of the synchrotron light is more uniform, the slit position is adjusted in the lower intensity gradient area. Furthermore, the slit separation (D) is reduced to less than the centre area.

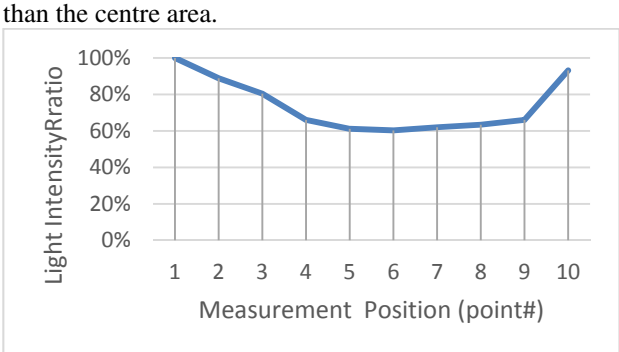

Figure 4: Intensity distribution of synchrotron light.

To absorb the vibration of the SRI opto-mechanism, vibration damping materials (Nitto D-300N) are added to the mechanisms. The damping films are attached to the slit and mirror holders.

This not only absorbs vibration, but also strengthens the mechanical stability. From observations, we know that the slit holder is the most sensitive part in the system. The holding design influences obviously the stability as shown in the following Table1.

Table 1: Horizontal Beam Size Measurement Results of Two Holding Methods. Clearly, the beam size stability is related to the strength of the holding jig.

	1	2	3
CCD exposure time	2ms	2ms	2ms
Wavelenth bandwidth	10nm	10nm	10nm
Slit Seperation (D)	30mm	30mm	30mm
SlitOpening (A)	a5	a5	a3
Holding Method	Method A	Method B	Method A
Beam size	54.20	58.49	53.30
rms	0.56	1.14	0.60

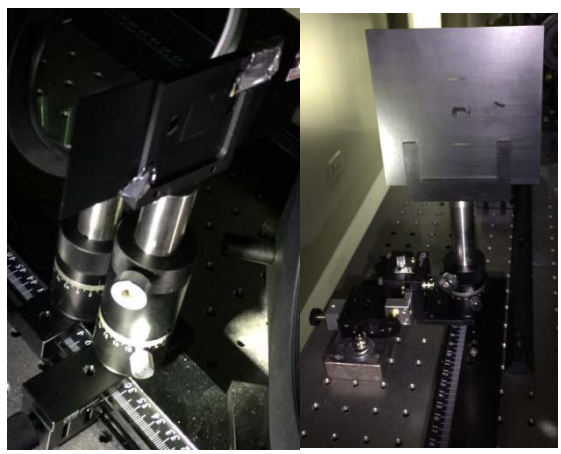

Figure 5: The double slit is supported by two types of mechanisms. (A) Method A: The slit holder is fastened on a single rod with a damping pad. (B) Method B: The slit holder is installed on a stage with two axis adjustments.

CCD Exposure Time Minimization

The CCDs are used to catch and integrate the interferogram. To prevent the signal vibration to integrate on the CCD, the exposure time is minimized to decrease vibration signal accumulation.

To minimize the CCD exposure time, the slit opening (a) is enlarged from 1mm to 5 mm and the exposure time is reduced to 2 ms. As Fig. 6 shows, the stability of the meas-ured beam size is proportional to the exposure time and the beam size can now be measured to better than 1 um.

ISBN: 978-3-95450-192-2 doi:10.18429/JACoW-IBIC2017-WEPCC12

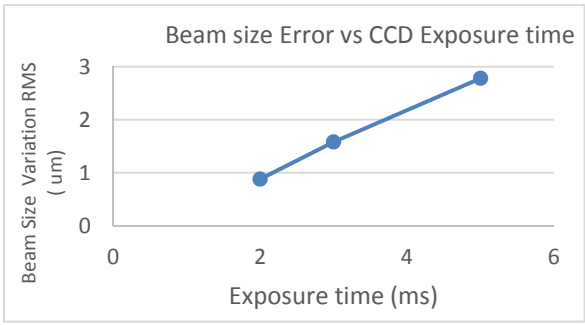

Figure 6: Relation between stability of the measured beam size and the CCD exposure time.

Air Disturbance Elimination

We also examined the air flow to prevent air turbulence and related vibrations. The synchrotron light exits the vacuum chamber through a window and passes through three aluminium reflection mirrors followed by a long path from the storage ring to the experimental area.

The air pressure in the storage ring and experimental area is different because the air flows continuously from the tunnel to the experimental laboratory area along the optical path through the shielding wall. Therefore, a flat optical window has been installed on the shielding wall to cut off this air flow (Figure 7).

Figure 7: Flat optical window installed on the shielding wall to block the air flow.

Table 2: Beam Size Measurements After Applying all Countermeasures as Described

	Beam SizeX	Beam SizeY
exposure time	2ms	2ms
bandwidth	10nm	10nm
average	10	10
Double slit	D30	D45
	a5	a5
average	54.20	35.21
rms	0.56	0.35

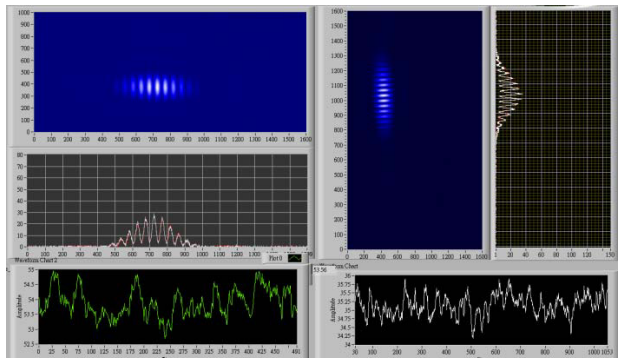

Figure 8: Interferograms of the horizontal and vertical channels.

After vibration suppression, minimization of the CCD exposure time and elimination of air turbulence, the RMS beam size variation is reduced to 0.3 um and the stability is equal to that of the TLS SRI.

POWER IMBALANCE METHOD

A method of power imbalance has been introduced to verify the visibility of the interferogram. Power meters measure the light intensity passing through the double slits and different transmission ND filters are used in the vertical BSM system to produce different power imbalance ratios. While reducing the power imbalance ratio, the visibility parameter γ is also reduced and the interferogram fringes exceed the noise level.

The experimental results are shown in Fig. 9 where the beam size variation is related to the imbalance ratio. A lower imbalance ratio improves the beam size variation as shown in Fig. 10. When the power imbalance factor is introduced in the vertical BSM system, the vertical beam sizes are corrected from 35.8um to 35.2um.

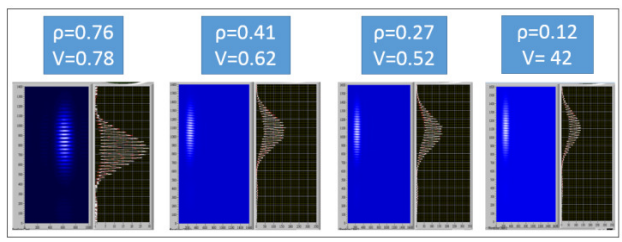

Figure 9: The power imbalance ratio is reduced by ND filters which also reduces the visibility parameter γ and the interferogram fringes become more prominent.

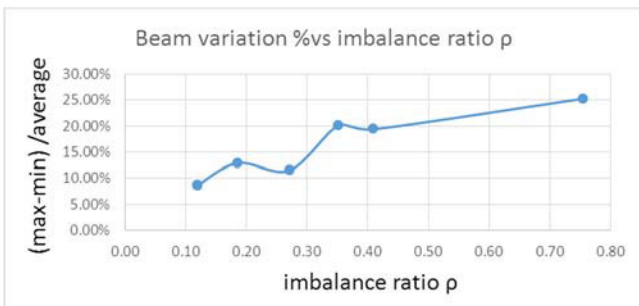

Figure 10: Beam size variation improves as the imbalance ratio ρ is lowered.

ISBN: 978-3-95450-192-2 doi:10.18429/JACoW-IBIC2017-WEPCC12

CONCLUSION

A SRI beam size monitor was installed in the NSRRC TPS. Ground vibrations translate to the SRI causing beam size variations. In order to improve the system stability, vibrations were suppressed, the CCD exposure time was reduced and air turbulence in the optical path were eliminated. This improved the beam size stability to 0.3 um which is equal to that achieved in the TLS SRI. Introducing also an intensity imbalance method to the vertical BSM system, the beam size variation could be improved and the beam size measurements are optimized by adjusting power imbalance ratios.

REFERENCES

[1] C.K. Kuan *et al.*, "Beam size monitor for TPS", in *Proc. IBIC'2012*, Tsukuba, Japan, paper MOPB88, pp.1-3.

[2] M.L. Chen *et al.*, "Measurement of Beam Size with a SR interferometer in TPS", in *Proc. IPAC2016*, Busan Korea, paper MOPMR032 , pp. 313-315.

[3] T. Mitsuhashi, "Recent trends in beam size measurements using the spatial coherence of visible synchrotron radiation", *in Proc. IPAC'2015*, Richmond, VA, USA, paper THYC2, pp. 3662-3667.

[4] T.Naito *et al.*, "Very small beam-size measurement by a reflective synchrotron radiation interferometer", *Physical Review Special Topics- Accelerator and Beams*, 9, 122802 (2006).

[5] T.Naito *et al.*, "Improvement of the operation of a SR interferometer at KEK-ATF damping ring", in *Proc. IPAC10*, Kyoto, Japan, paper MOPE009, pp.972-974.

[6] M.J.Boland et al,"Intensity Imbalance Optical Interferometer Beam Size Monitor", in *Proc. IBIC'2012*, Tsukuba, Japan, paper WECC03, pp.566-570.

ISBN: 978-3-95450-192-2 doi:10.18429/JACoW-IBIC2017-WEPCC13

PRELIMINARY STUDY ON IPM FOR CADS INJECTOR I*

J. He†, Z. Z. Wang, J. S. Zhou, Y. F. Sui, J. H. Yue, J. S. Cao
Key Laboratory of Particle Acceleration Physics & Technology,
Institute of High Energy Physics, Beijing 100049, China

Abstract

The Ionization Profile Monitor (IPM) based on the residual gas molecule is designed and fabricated for high power proton beam accelerator China Accelerator Driven Subcritical system injector I. The method of calculating the intensity of ionization signal is explored. The device uses the electric field generated by electrode to guide the ions, using Microchannel plates (MCP) to amplify ionization signals. A screen and a camera is used to detect the output electrons of the MCP, which present the distribution of the beam. The electric field distribution is optimized by CST ELECTROMAGNETIC STUDIO calculation. The IPM is installed on the ADS injector I and tested by beam. It measures the proton profile successfully during the CW commission. The experiment results agree well with the theoretical value which proves that the equipment can be used for CADS main linac in future.

INTRODUCTION

The Ionization Profile Monitor (IPM), also known as Residual Gas Monitor (RGM), is one of the most popular non-destructive profile detection device, mainly used for the machine which the beam size is in the range from mm to cm. High intensity and high power hadron accelerators usually implies the usage of non-destructive methods[1]. For the high power beam, the interception materials such as the phosphor screen [2], the wire target [3], the secondary electron grid may be damaged by the beam. Laser scanning [4], electron beam scanning [5] and residual gas detectors will not have this problem. There are a lot of IPM research experience in different lab, such as FNL [6, 7], KEK [8, 9], BNL [10], and CERN [11]. Several IPM systems have been installed and several workshops focus on this topic have been held in GSI [12, 13, and 14].

With the development of China high-power proton accelerator, there is a growing demand for non-destructive profile detection, such as Chinese Spallation Neutron Sources (CSNS) and Accelerator Driven Subcritical systems (ADS). There are several wires have been destroyed by beam both in CSNS and ADS. Two non-invasive beam profile measurement methods were developed including the electron scanner and IPM on ADS Injector I. The Fig.1 (a) shows the layout of the injector and the locations of both electron scanner and IPM. The Fig.1 (b) shows the RMS beam size from the exit of the ion source to the dump, the blue curve is the horizontal size and the red curve is vertical size. As shown in Fig. 1 (b), the theoretical beam size at the IPM location is 15 mm × 5mm.

The most important parameters that affects IPM systems is the ionization yield, which is how much electron-ion pairs are generated per second. It is determined by the beam parameters and the vacuum parameters, including the pressure and the composition of the residual gas. The Bethe-Bloch formula describes the energy loss caused by the collision between the beam and residual gas which is related to the energy of the beam. The total ionization number N can be expressed as: $N=\Delta E/I_0$, where the ΔE is the total energy loss in the gas volume, and I_0 is the average energy required to produce an electron-ion pair, also known as ionization energy, usually is about 20~30 eV. According $N_D = (-dE/dx)\cdot l \cdot I_{current} / I_0$, for the ADS beam, $I_{current}$=10 mA, assume that the residual gas is H_2 and the pressure is 1×10^{-5} Pa, the detector longitudinal length l = 3 cm, I_0 = 33 eV, the N_D is 3.86 x 10^7 pps for CW beam.

EXPERIMENT

The experiment set up is shown as Fig. 2. The device is working in ion collection mode. In order to produce a guild field of 1 kV / cm, ±4 kV is applied to the upper and lower oxygen-free copper electrodes, respectively.

Table 1: IPM Design Parameters for ADS Injector I

Parameters	Value
Electric field（V/m）	10^5
Distance of two plates（cm）	8
Size of MCP（mm）	Φ75
Size of EGA (mm)	Φ70
Detector	P43 +CCD
Work mode	Ions
Magnetic field	0

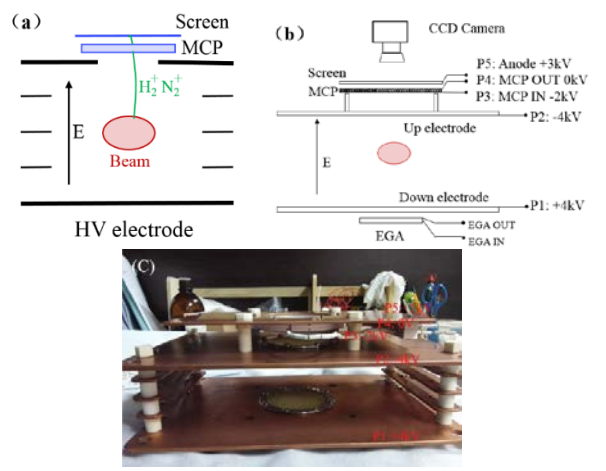

Figure 2: (a) Schematic of ion collection by E-field IPM (b) potential distribution MAP of IPM different components (c) picture of Oxygen-free copper electrodes and MCP.

* Work supported by the NSFC under grant No.11305186
† hejun@ihep.ac.cn

ISBN: 978-3-95450-192-2 doi:10.18429/JACoW-IBIC2017-WEPCC13

The distance of the two electrodes is 8 cm. The potential of other components is shown in Fig. 2 (b). The MCP is a two-stage V type with a nominal gain of 10^5, the potential difference between the output and input of the MCP is 2 kV as shown in Fig. 2 (b). The potential difference between the MCP out and the anode phosphor screen is 3 kV which to allow the MCP output electrons to be accelerated and hit the screen to produce photons, EGA from the PHOTONIS company has not been installed at this stage, it will adding to the device in future. The photo of the electrode and MCP are shown in Fig. 2 (c), there are two nets made by brass with a transmittance of 90% in the upper and lower electrodes. The design parameters are shown in Table 1.

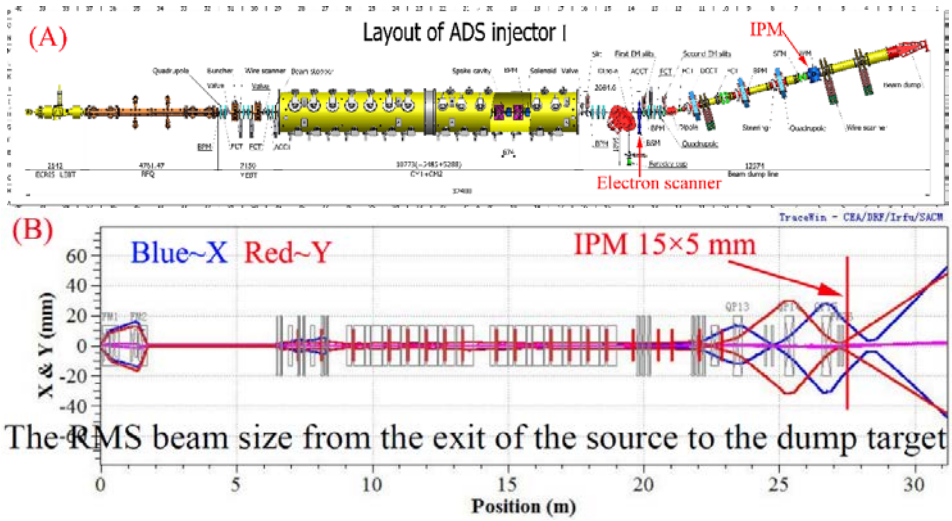

Figure 1: (a) the layout of ADS Injector I and the location of the non-invasive profile measurement (b) Beam size of the Injector I, 15×5mm at the IPM location.

In order to ensure that the generated ions (from initial ionization position to the detector) travel along the straight line, a higher and uniform Ey is better. (As shown in Fig. 3, assume horizontal direction is x, the vertical direction is y, longitudinal direction is z). The six small electrodes are helping to get a more uniform field. The two holes make the E-field worse in the centre of the electrode, it will be better after adding the brass nets and small electrodes as shown in Fig. 3 (a) and Fig. 3 (b). Fig. 3 (c) shows the Ey of the centre line (black curve) as shown in Fig. 3 (b). Small electrodes are connected with a 10 MΩ resistance. To increase the number of small electrodes, increase the size of the entire electrode x direction can improve the central area Ex, the electrode longitudinal size has little effect on the Ex, but can slightly improve the uniformity of Ey.

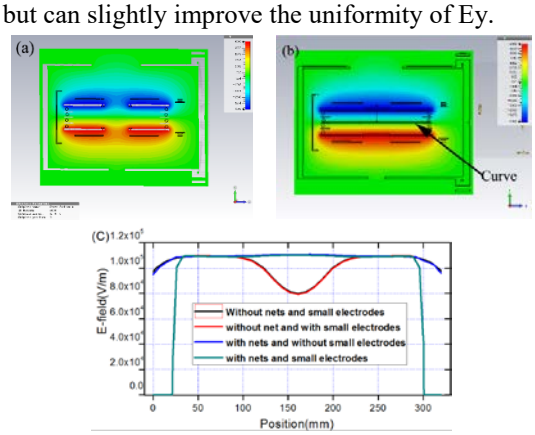

Figure 3: (a) The distribution of equal potential curve in my plane without the net (b) with the net (c) Ey in the Z direction (as shown in Fig. 3 (b).

Figure 4 shows the mechanical design and photos of the IPM system. Fig. 4 (a) is a mechanical design. The size of the large electrode is 320 mm × 220 mm × 3 mm, the size of the small electrode is 180 mm × 30 mm × 3 mm, the electrodes are supported and insulated with ceramics, and the longitudinal size of system is 450 mm. The image is recorded by an industrial camera with a resolution of 1360 × 1024, the pixel size of the sensor is 5.3 μm × 5.3 μm. With an external trigger function, it can simultaneous exposure with beam. The after time of P43 phosphor screen is 1ms from 90% to 10%, is 1.6 ms from 10% to 1%

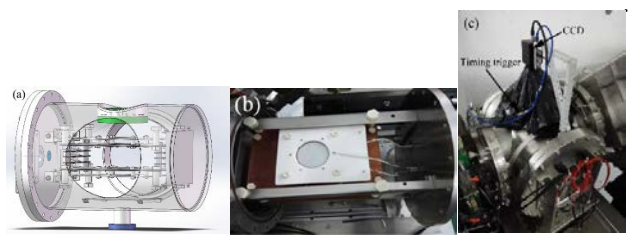

Figure 4: The Ionization profile monitor system, (a) mechanical design, (b) interior photos, (c) exterior photos.

Figure 5 is IPM system measurement results. Figure 5 (a) is the screen image before adding a cover, the shadow in the centre is produce by the CCD camera and bracket, it will remove after adding the black cloth shield as shown in Figure 4 (c). Figure 5 (b) is a pseudo-colour image of the screen with a duty factor of 10% proton beam after the stray light is masked. The time from camera receiving the trigger signal to stat to exposure is about 3 μs. The cable delay are in ns range and the afterglow time of the screen is 2~3 ms. the digital delay generator (DG645)

ISBN: 978-3-95450-192-2 doi:10.18429/JACoW-IBIC2017-WEPCC13

is used to control the exposure time synchronize with the beam. The Figure 5 (c) is the profile Gaussian fitting results. The dash line is the summation along the horizontal in the area in Figure 5 (b) indicate by the red lines. The RMS width is 13.72 mm ± 0.28 mm, which is close to the theoretical value of 15 mm. The result is worse in the lower duty ratio (<1%). The deviation from the Gaussian distribution is mainly due to the synchronization of the exposure time, the afterglow time and the beam are not exactly matched.

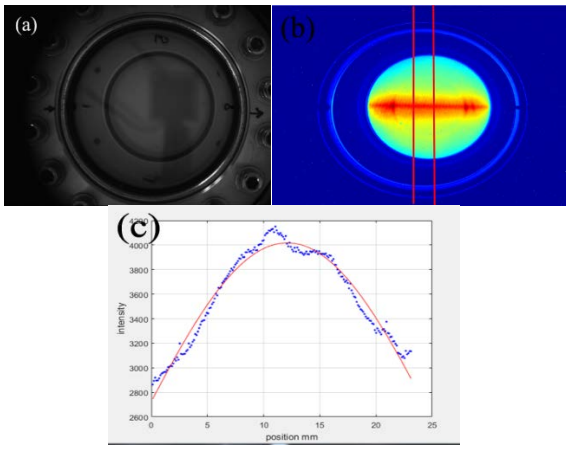

Figure 5: Results of IPM measurement. (a) Picture of screen without a beam, (b) picture of screen with a 10% duty factor beam, (c) horizontal profile by fitting the curve with Gaussian.

CONCLUSION

A In order to measure the profile of proton of CADS which will operated in a CW mode, two noninvasive beam profile measurement methods were developed. The paper mainly introduces the results of IPM system, including the mechanical design and fabrication. The CST calculation is used for optimize the guide E-field, the effect of adding small electrodes and metal net is shown. In addition, the method of assessing the intensity of ionization signals based on beam and vacuum parameters are also studied. The experiment details, such as the potential distribution, the 2-stage MCP, optical system, calibration system EGA are also introduced. Finally, the IPM system have been installed on the ADS injector I, the beam measurement shows the results agreement with the theoretical expectation very well. The possible reason of the no-Gaussian distribution in a low duty factor is the synchronization is not perfect and the noise ratio is not good enough. Further study is under the way of this problem. Experiment results show that IPM is an effective method to measure the transverse profile a high power proton beam, and it will play an important role in the following projects such as CSNS and CIADS.

ACKNOWLEDGEMENT

The author thanks the experts in KEK and GSI for valuable discussion.

REFERENCES

[1] P. Forck. Lecture Notes on Beam Instrumentation and Diagnostics. CERN Accelerator school beam diagnostics 2016 and P. Forck" in *Proc. IPAC'2010*, pp.1261.
[2] Bravin E. Transverse beam profile. CERN Accelerator school beam diagnostics 2009.
[3] Y.F. Sui, H. Z. Ma, J. S. Cao, et al. Chinese Physics C, 2008, 32(5):397-399.
[4] J. He, C. Zhang, Q. Y. Deng, et al. "High Power Laser and Particle Beams 2015", 27(6):065103
[5] W. Blokland, Cousineau S. in *Proc. IPAC'2011*, pp.1438
[6] Denton K M. Philip A, David C, et al. in *Proc. IPAC'2011*, pp. 519-521.
[7] J. Zagel, A. Jansson, T. Meyer, et al. in *Proc. IBIC'2010,* pp. 111-115.
[8] K. Satou, S. Lee, T. Toyama, et al. in *Proc. EPAC'2008*, pp. 1275-1277.
[9] K. Satou, S. Lee S, T. Toyama, et al. in *Proc. HB'2010*, pp. 506-508.
[10] R. Connolly, J. Fite, S. Jao, et al. in *Proc. IBIC'2010,* pp. 116-118.
[11] C. Bal, V. Prieto, R. Sautier, et al. in *Proc. DIPAC'2007*, pp. 120-122.
[12] T. Giacomini T, P. Forck, D. Liakin, et al. in *Proc. DIPAC'2011*, pp. 419-421.
[13] C. Bohme, J. Dietrich, P. Forck, et al. in *Proc. DIPAC'2009*, pp. 191-193.
[14] http://indico.gsi.de/event/5366/

ISBN: 978-3-95450-192-2 doi:10.18429/JACoW-IBIC2017-WEPCC14

A STUDY OF THE EFFECT OF IMPERFECTIONS IN THE OPTICAL PATH OF THE SNS* TARGET IMAGING SYSTEM USING A MOCK-UP

W. Blokland†, F. Garcia[1], Oak Ridge National Laboratory, Oak Ridge, TN, USA
[1] also at the University of Tennessee, Knoxville, TN, USA

Abstract

The Spallation Neutron Source sends a 1 GeV proton beam to a mercury filled target to generate neutrons. The Target Imaging System (TIS) provides an image of this proton beam on the target to help center the beam and determine the peak density. Most of the TIS optical path is installed together with the proton beam window, which is replaced every two to three years. Using the next-to-be-installed proton beam window and a mock-up of the target and the beam pipe to the target, we have studied imperfections in the optical path to estimate their effect on the TIS measurements. In this paper, we show the effect of geometric distortion and light reflections, as well as the difference in the performance of two optical fiber bundles with different resolutions and contrasts.

INTRODUCTION

To produce the neutrons used for materials research, 1 GeV protons hit the stainless-steel target vessel filled with mercury. The Target Imaging System (TIS) helps optimize the target's lifetime by steering the beam to the center of the target's nose cone. The nose cone is coated with aluminum oxide doped with chromia. This layer luminesces when the protons hit, thus producing an image of the beam on the target. The light is collected by an off-axis parabolic mirror at the Proton Beam Window (PBW) and guided by optics and a radiation resistant high purity fused silica fiber bundle to a camera outside the high radiation area, see Fig. 1 and [1-3].

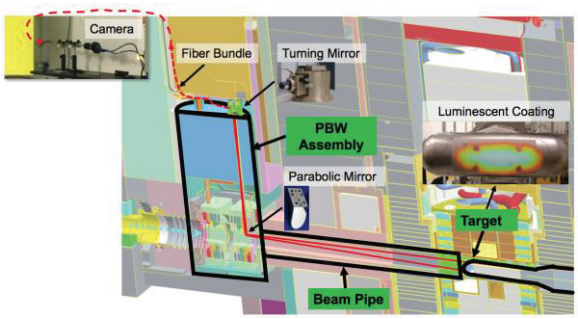

Figure 1: The layout of the TIS.

The TIS calculates the position of the beam to monitor that we are keeping the beam centered within ± 4 mm vertically and ± 6 mm horizontally. The beam can also be steered by equalizing the temperature read-backs from the thermocouples at the PBW. This method requires a symmetric beam halo and a flat orbit.

The TIS also provides estimates for the width of the beam, which is used to calculate the peak density. During operations, we must keep 90% of the beam within a 200 by 70 mm footprint and keep the peak density within certain limits, depending on beam power. A program called the RTBT Wizard (Ring to Target Beam Transferline) uses the beamline optics elements, 4 RTBT wire scanners, and the RTBT harp to predict the width of the beam on the target. The difference between the two width measurements has significantly varied, even more than 30%, with the Wizard usually providing a higher peak density. To be on the safe side, the higher number has been used for operations.

The difference in estimates can be due to the difference in analysis routines, imperfect knowledge of the magnetic fields of the quadrupole magnets, uncertainty in the calculation of the Proton Beam Window's beam scattering effect, widening of the TIS proton image by luminescence due to particles other than protons, a temperature gradient sensitivity in the luminescence across the coating, and imperfections in the TIS optical path. In this paper, we study the effects of imperfections of the optical path, specifically the reflections of light in the beam pipe and the geometric distortion by the optical elements. We will also show what effect the differences in the quality of the optical fiber bundles has on the TIS image.

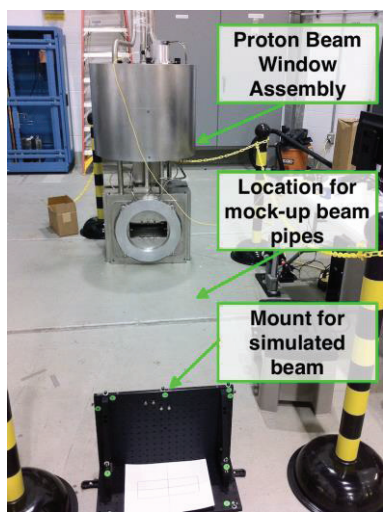

Figure 2: The proton beam window setup.

* This manuscript has been authored by UT-Battelle, LLC, under Contract No. DE-AC0500OR22725 with the U.S. Department of Energy.
† blokland@ornl.gov

ISBN: 978-3-95450-192-2 doi:10.18429/JACoW-IBIC2017-WEPCC14

MOCK-UP

An optical test bench was available to do testing during the development of the TIS. Now we can only do testing on a new Proton Beam Window (PBW) that is to be installed. The PBW assembly, see Fig. 2, is available before installation in the beam line to install the TIS optical components and, at that time, we can also do our testing. Notice that Fig. 1 accentuates with black borders the elements of the mock-up.

LIGHT REFLECTIONS

To study the reflections of the light, two beam pipe mock-ups where created, a reflective and a non-reflective version. The inside of reflective mock-up duplicates the geometry of the inside of the beam pipe from the PBW to the target. This mock-up was laser cut from a hard foam material according to the beam pipe drawings. The inside was layered with reflective tape to emulate the shine of the actual beam pipe. The non-reflective mock-up was made from optical blackboard to minimize the reflection and does not follow the internal beam pipe geometry, as the only goal was to shield outside light and minimize reflections. The mock-ups are shown in Fig. 3.

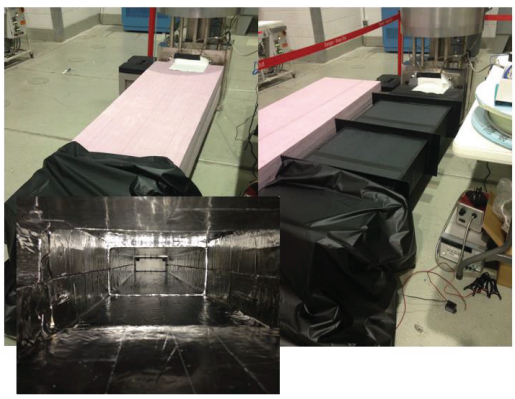

Figure 3: On the left, the laser-cut foam mock-up with the reflective inside, and on the right, the optical black hard-board, non-reflective mock-up.

Simulation of Proton Beam Image

To simulate the beam footprint, we used an electroluminescent sheet as a uniform area light source. In front of it we put a transparency printout of a two-dimensional super-Gaussian to attenuate the light and form a similar light footprint as the proton beam on the target nose, see Fig. 4.

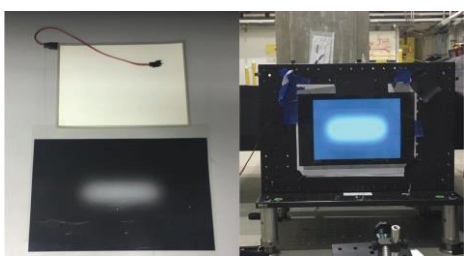

Figure 4: On the left, the electroluminescent sheet with the beam mask, and, on the right, the simulated beam.

Effects of Reflective Light

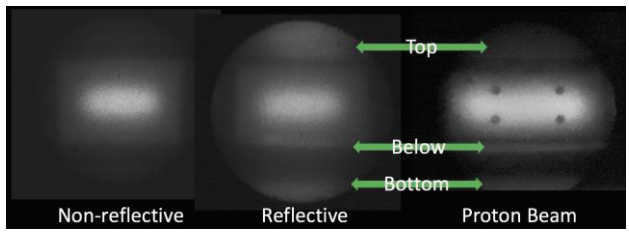

Figure 5: Images of the non-reflective (left) and reflective mock-ups (middle), as well as the actual beam (right).

Using the two mock-ups and the simulated beam image, we can now compare the simulated images with that of the actual proton beam, see Fig. 5. The images have been intensified so that the reflections are easier to see.

We clearly see reflections in the reflective mock-up that do not show up in the non-reflective mock-up. In both the reflective and proton beam images, we have reflections on top, just below the beam spot, and at the bottom. Not visible in these images are very small reflections that can occur on the far left and right.

We now apply the TIS analysis routines to the simulated images to see the effect on the profiles. This is shown in Fig. 6. The top left image shows the reflective mock-up and the bottom left image shows the non-reflective mock-up. Both images are in false colors. On the right, the obtained profiles show for horizontal and vertical, the darker blue and darker red are the reflective cases.

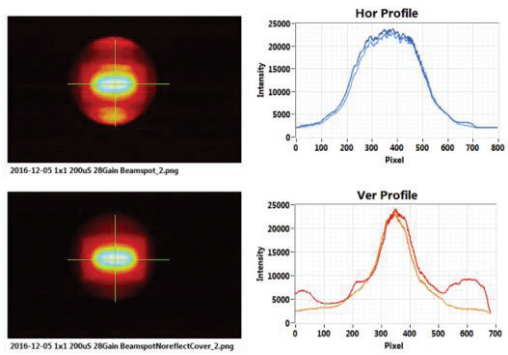

Figure 6: Images and calculated profiles of the non-reflective and reflective mock-up.

The profiles show that there is not much effect on the horizontal profile but a significant effect on the tails of the vertical profile. However, the main TIS analysis program does not extend its analysis to the tails, thus mostly avoiding the effect of this reflection.

We analyzed seven reflective and non-reflective mock-up images, using the standard TIS program, to get an estimate for the effect of the reflections on the real image. The results are shown in Table 1. This shows that the effect on horizontal position is < 0.1 mm and on the vertical position is < 0.5 mm, and that the effect on the peak density is < 3% lowered peak density due to the reflections. The effects of the reflections are more pronounced in the simulated image than in the actual image, see Fig. 7, so we assume that our results are an upper limit of the effect.

ISBN: 978-3-95450-192-2 doi:10.18429/JACoW-IBIC2017-WEPCC14

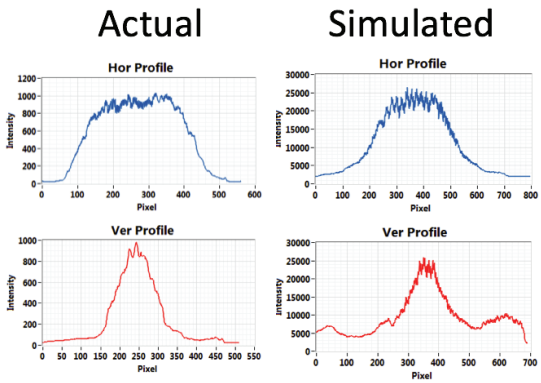

Figure 7: Comparison of actual proton beam profiles, left, versus reflective mock-up profiles, right.

Table 1: Analysis of the Simulated Beam with the Reflective and Non-reflective Mock-ups

Non-reflective	Position mean (mm)	Position STD (mm)	Width mean (mm)	Width STD (mm)
Horizontal	-1.63	0.016	28.7	0.02
Vertical	1.13	0.018	16.6	0.09
Reflective				
Horizontal	-1.69	0.02	28.91	0.02
Vertical	0.72	0.02	17.03	0.09
Difference	**Position (mm)**	**Width**		**Peak density**
Horizontal	+0.06	-0.20%		+3%
Vertical	+0.42	-0.47%		

EFFECT OF OPTICAL DISTORTION

Reference Image for Geometric Correction

To estimate the effect of the optical distortion, we placed a flat sheet of evenly spaced LEDs at the location of our mock-up target. The sheet is shown in Fig. 8. We used a flat surface to mount the sheet and not the curved surface of the target nose cone because the beam is projected onto the target and not wrapped around the target nose cone. We then took an image of the sheet through the TIS optics and used a geometric correction function from the LabVIEW vision toolkit to correct the distortion, see Fig. 9.

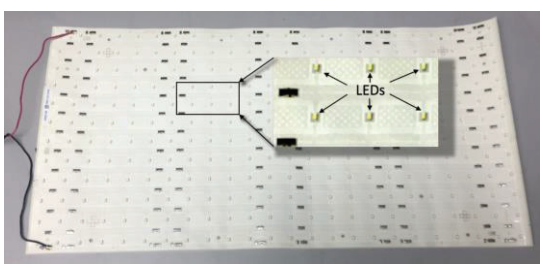

Figure 8: The sheet with evenly spaced LEDs.

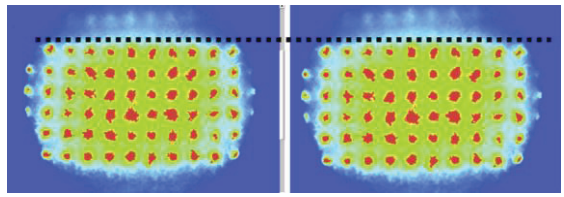

Figure 9: On the left is, in false colors, the original image as seen by the TIS camera, and on the right, the corrected image. The dotted line helps the eye see that a dip on top has been corrected.

Correction Results

When the correction is applied to a simulated image, we find a lowered peak density of about 8.3%. When applied to a production beam image, we find a 6.2% lower peak density. However, we should now recalibrate our image, as the distortion correction affected the scaling, pixels per mm, by about 4%. When this is applied, we see a difference of less than 1.5% in peak density both to a simulated image or a corrected production beam image, see Table 2. This makes the impact of the distortion a minor effect.

Table 2: Effect of the Distortion on the Peak Density

	Horizontal (mm)		Vertical (mm)		Peak Density
	center	width	center	width	(cnt/px)
Original	0.4	56.0	0.6	28.1	894.7
Corrected	0.2	55.4	0.3	28.0	907.5
Change	-0.2 mm	-1.1%	-0.3 mm	-0.4%	+1.4%

FIBER BUNDLE

The contrast of the fiber bundle is important to the quality of the image of the proton beam. Figure 10 shows images of a pie chart made with different fiber bundles.

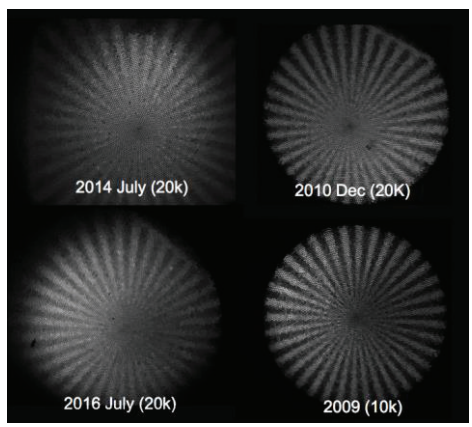

Figure 10: Pie chart images from different fiber bundles.

Three of the bundles have 20,000 fibers and one has 10,000 fibers. The 2010 20,000 fiber bundle was of higher quality, with a contrast of 0.6, but became too expensive due to manufacturing issues. The 2014 bundle was made with a new process, but had a contrast of only 0.4.

ISBN: 978-3-95450-192-2 doi:10.18429/JACoW-IBIC2017-WEPCC14

An improvement to this new process was delivered with the 2016 fiber bundle, with a contrast around 0.5. An older fiber bundle, made around 2009, but with only 10,000 fibers, shows a very good contrast, at about 0.7. It is easier to manufacture a bundle with less fibers and the less dense spacing allows for less light leakage among the fibers. The contrast was measured by calculating the modulation between dark and light spots along concentric circles crossing the pie chart segments, see Fig 11.

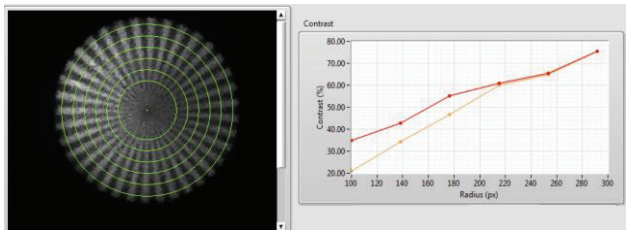

Figure 11: Analysis of the contrast based on a pie chart image through the optical system of the TIS.

We suspect that this difference in contrast is the main impact that lowered the image quality of later TIS installations. One consequence of the lowered contrast is that the image processing software can no longer reliably find the fiducials, and, therefore, the calibration can no longer be automatically done, see Fig. 12. The variation in the positions also increased, from about 1 mm peak-to-peak to about 2 mm. This is still within requirements, and averaging of the results brings the variation back to within 1 mm.

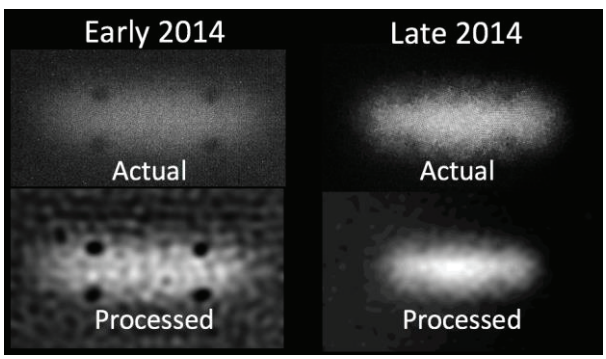

Figure 12: Beam images with the higher contrast bundle on the left and the lower contrast on the right.

MIRROR CORROSION

A water leak developed in the space between the PBW and the target. This water, combined with air and the radiation, caused the aluminum mirror to corrode, see Fig. 13. Note that this figure also shows the thermocouples sticking out from the sides. Unfortunately, the water leak was not fixed as hoped with the next PBW installation and the current mirror is now also corroded.

As it can take up to three years before the PBW will be replaced, we are now left without a functioning TIS and we will have to rely on the RTBT Wizard and the thermocouples for steering and beam width calculations.

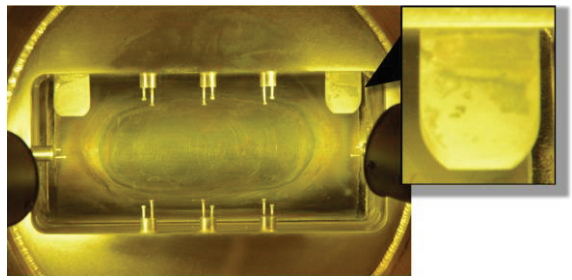

Figure 13: A view of the Proton Beam Window with the corroded mirror.

DISCUSSION

The effect of the reflections and distortions combined is that the TIS calculates at most a 4.4 % lower value for the peak density. More likely, this is less than 3%, given the more intense reflections in the mock-up. This increased intensity is most likely due to using aluminum tape for our reflective material while the inside of the beam pipe is less reflective than that. The combined effects on the position is limited to less than 0.5 mm as the effects go towards cancelling each other out. This means that the studied effects are minor compared to the observed disagreements, and that we must further pursue other possible effects on the TIS calculations.

We plan to compare the different analysis routines using existing data to see if we find a reason for the disagreement between RTBT Wizard and the TIS.

Already, ESS and ORNL have been looking at the luminescence of particles other than the protons on the coating, see [4,5], and experiments are planned.

Given the mirror corrosion problem, from now on we will assume that a water leak can always happen and plan to investigate coatings for the mirror. We plan to use the RaDIATE collaboration, see [6], to expose sample mirrors with different coatings to water and radiation to determine if any coatings are suitable for our environment.

ACKNOWLEDGMENT

The authors would like to acknowledge Syd Murray for his help with setting up the PBW assembly.

REFERENCES

[1] T. Shea *et al.*, "Installation and Initial Operation of an On-Line Target Imaging System for SNS", ICANS 2010.
[2] L. C. Maxey *et al.*, "A hybrid reflective/refractive/diffractive achromatic fiber-coupled radiation resistant imaging system for use in the Spallation Neutron Source (SNS)", Proc. SPIE 8142, Sept. 27, 2011; doi:10.1117/12.894125.
[3] W. Blokland, "Experience with the SNS* Target Imaging System", 5th High Power Targetry Workshop, Fermilab, Batavia, IL, May 20-23, 2014.
[4] A. Takibayev and T. Shea, "Monte Carlo simulation of target coating", ESS-0068316, Lund, Sweden, Dec. 2015
[5] W. Lu and T. McManamy, "Study of the Energy Deposition Effect of the Alumina Coating on the Beam Profile", SNS Internal Memo, Oak Ridge, USA, 2016.
[6] RaDIATE website: https://radiate.fnal.gov

ISBN: 978-3-95450-192-2 doi:10.18429/JACoW-IBIC2017-WEPCC16

FIRST EXPERIMENTAL RESULTS OF THE COMMISSIONING OF THE SwissFEL WIRE-SCANNERS

G.L. Orlandi*, A. Alarcon, S. Borrelli, A. Gobbo, P. Heimgartner, R. Ischebeck, D. Llorente, F. Loehl, C. Ozkan Loch, P. Pollet, B. Rippstein, V. Schlott,
Paul Scherrer Institut, 5232 Villigen PSI, Switzerland.
R. Vintar, Cosylab, Ljubljana, Slovenia.

Abstract

Several wire-scanners - 19 out of 22 - are presently installed in SwissFEL, the hard X-ray FEL facility under commissioning at Paul Scherrer Institut (www.psi.ch). Thanks to a wire-fork designed to be equipped with two different pairs of scanning wires (5 μm tungsten and 12.5 μm Al(99):Si(1)), high resolution measurements of the beam profile - and emittance - and, alternatively, a minimally-invasive beam monitoring during FEL operations can be performed. First experimental results of the SwissFEL wire-scanner commissioning will be presented as well as a summary of the prototyping design and characterization.

INTRODUCTION

SwissFEL is a Free Electron Laser (FEL) facility [1] presently under commissioning at Paul Scherrer Institut (www.psi.ch). Two undulator lines - so called ATHOS and ARAMIS - will provide X-rays pulses at a repetition rate of 100 Hz in the wavelength region $7 - 0.7$ nm and $0.7 - 0.1$ nm, respectively. The SwissFEL linear accelerator is a compact machine - the length of the entire facility including photon transfer lines and experimental hall is about 720 m - with a relatively moderate beam energy: 5.8 GeV being the maximum energy required to reach the saturation regime of coherent radiation emission in the given wavelength range. In order to meet such constraints of compactness and energy, the beam acceleration is mostly ensured by a C-band RF linac and the compression scheme is optimized to preserve the high brightness quality of the electron beam, which is characterized by a transverse normalized slice emittance of 0.4/0.2 mm.mrad for the two nominal charge operation modes 200/10 pC of the machine. The electron beam - emitted by a photo-cathode with an initial bunch length of 3/1 ps (rms) and with a two-bunch temporal macrostructure of 28 ns - is accelerated by a 2.5 cell S-band gun up to 7.1 MeV at a repetition rate of 100 Hz. The further acceleration of the electron beam is performed by a S-band RF linear booster - up to 330 MeV - and by a C-band linac up to $2.1 - 5.8$ GeV. During the transition from the S-band to the C-band RF sections, the S-Band induced energy chirp of the electron beam is linearized by a pair of X-band RF cavities and converted to a longitudinal compression of the electron beam - 300/200 fs (rms) - by a magnetic chicane. After a further compression stage in a second magnetic chicane - 20/3 fs (rms) - at a beam energy of about 2.1 GeV, an RF kicker and a magnetic switch-yard deviate the orbit of the second bunch of the two-bunch train from the ARAMIS arm to the ATHOS arm. After a further acceleration stage, the two bunches are separately injected at 100 Hz into the two undulator lines (ARAMIS and ATHOS).

In a FEL driver linac, wire-scanners (WSCs) [2, 3, 4, 5] complement view-screens to monitor the beam profile monitor. Compared to view-screens, WSCs are normally immune to non-linear effects of the signal response and can perform high resolution measurements which ultimately depends on the wire diameter and scanning speed. In SwissFEL, the WSCs are designed to absolve two main tasks [6, 7]: high resolution characterization of the beam profile for high precision measurement of the beam emittance and a routinely and minimally-invasive monitoring of the beam profile under FEL operations. Moreover, because of the afterglow characterizing the YAG:Ce crystals of the view-screens, in SwissFEL only WSCs can discriminate in time the two-bunch temporal macrostructure (28 ns) of the electron beam. The SwissFEL wire-fork is motorized by a stepper motor and equipped with two pairs of metallic wires, see Fig.1: 5 μm tungsten (W) and 12.5 μm Al(99):Si(1). As the wire scans the beam, a shower of primary scattered electrons and secondary emitted particles is produced in proportion to the fraction of the beam sampled by the wire. In SwissFEL, the forward - high energy and small scattering angle - component of the particle shower ("wire-signal") is out-vacuum detected by means of Beam-Loss-Monitors (BLMs) [8]. The beam-synchronous acquisition (BSREAD) [9] of both the encoder and the BLM readouts permits to reconstruct the one-dimensional transverse profile of the electron beam. The beam-loss sensitive material of the BLMs is a scintillator fiber (Saint Gobain BCF-20, decay time 2.7 ns) wrapped around the vacuum pipe. The scintillator fiber is matched by means of a Plastic Optical Fiber (POF) to a photomultiplier (PMT) having a remotely adjustable gain in the range $5 \times 10^3 - 4 \times 10^6$. The PMT signal is finally digitized and integrated in time by an ADC unit. In a WSC measurement, together with the signals from the encoder and the BLM, also the charge and position signals from Beam Position Monitors (BPMs) upstream and downstream the WSC are BSREAD acquired at every RF shot in order to correct the reconstructed beam

* gianluca.orlandi@psi.ch

ISBN: 978-3-95450-192-2 doi:10.18429/JACoW-IBIC2017-WEPCC16

profile by possible errors due to a charge and transverse jitter of the electron beam.

A total of 22 wire-scanners (WSCs) will be operated in SwissFEL: 19 of them belong to the ARAMIS section of the machine which is presently under commissioning. In the present proceeding, first results of the commissioning of the SwissFEL WSCs will be presented as well as details about the prototyping work.

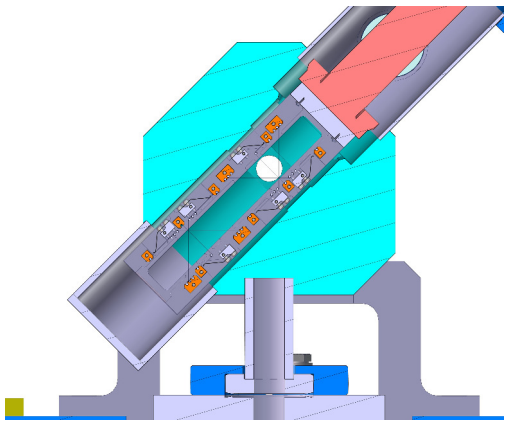

Figure 1: Section view of the SwissFEL WSC fork in the vacuum chamber.

MEASUREMENT SET-UP

The measurement set-up of the SwissFEL WSC composes of an in-vacuum beam-probe and an out-vacuum pick-up of the "wire signal".

About the wire-signal detection, this is out-vacuum performed by a BLM - see previous section - which is placed downstream the WSC at an optimum distance in the range from 3 to 6 m according to the indications drawn from the beam tests carried out at the 250 MeV SwissFEL Injector Test Facility (SITF, Paul Scherrer Institut, CH) and at FERMI (Elettra-Sincrotrone Trieste, Italy) [6]. For more details about BLMs, refer to [8].

The WSC in-vacuum system is composed of a planar wire fork motorized by a Ultra-High Vacuum (UHV) linear stage which is equipped with a 2-phase stepper motor (2-phase, 1.8deg/step, 200steps/turn) and an incremental optical encoder (0.1 μm resolution), see Fig.1. The wire-fork axis forms 45^o with respect to the vertical direction. The wire-fork can be equipped with two pairs of wires scanning the beam either along the horizontal direction (X) or the vertical one (Y), each wire being oriented + or - 45^o with respect to the fork axis. The wire holder in the fork is suitably designed for metallic wire. The metallic wire can be indeed fixed between two pins and submitted to a slight mechanical tension thanks to a metallic spring. Thanks to the applied tension, the frequency band of the oscillation eigenmode of the fixed wire can be maintained above the low frequency stepper-motor induced vibrations of the wire-fork. About the choice of the most suitable wire material, this was initially suggested by the consolidated experience of other FEL facilities where tungsten wires are normally used because of the excellent robustness to the thermal loading (melting point, about 3400 ^oC) and to the mechanical stress (tensile strength, about 1900 MPa). Tungsten wires with a diameter of 5 μm (geometrical resolution of about 1.3 μm) were finally selected for the wire pair supposed to be employed in high resolution measurements of the beam profile and emittance in SwissFEL. The choice of the second pair of wires - to be possibly used for minimally invasive monitoring of the beam profile under FEL operations - was not straightforward and conventional. The tricky question was to find a metallic material for the wire that could be able to ensure, on the one hand, a sufficiently high beam and mechanical robustness and, on the other hand, to have a sufficiently low density and Atomic number to minimize as much as possible the beam-losses. After a work of investigation and test of possible candidate materials, 12.5 μm Al(99):Si(1) wires were finally selected. Compared to pure aluminium, this alloy shows a similar melting point (about 600 ^oC) but a much higher tensile strength (about 300 MPa) which is beneficial to the mechanical strength and elasticity of the wire. Both wire solutions - 5 μm tungsten and 12.5 μm Al(99):Si(1) wires - were tested at high charge and energy at FERMI [6]. Experimental results of the beam tests confirmed the suitability of the proposed choice as well as a strong reduction of the beam losses when scanning the beam with a 12.5 μm Al(99):Si(1) wire instead of a 5 μm tungsten wire. Compared to a 5 μm tungsten wire, a drastic reduction of a factor 11 was observed in radiation dose-rates measured by the ionization chambers of the FEL1 undulator line at FERMI when scanning the beam (charge of 700 pC and energy of 1.325 GeV) with a 12.5 μm Al(99):Si(1) wire [6]. The ratio of the beam-losses measured at FERMI - when passing from a 5 μm tungsten wire to a 12.5 μm Al(99):Si(1) wire - was observed to scale down linearly with the material density ρ and quadratically with the Atomic number (Z) in agreement with the formula:

$$\frac{\Delta E}{\Delta x} = \frac{E}{L_R}, \quad (1)$$

where E and ΔE are the energy and the energy loss, respectively, and L_R is the radiation length of the material with $1/L_R$ depending quadratically on Z and linearly on ρ [10].

The mechanical stability of the entire in-vacuum set-up of the WSC was the object of a careful investigation as well [6]. Wire-vibration measurements showed that the wire stability stays largely below the geometrical resolution 1.3 μm (rms) of the wire in the motor speed range 0.1-6.0 mm/s with the exception of the motor speed range 0.5-0.6 mm/s where an anomalous wire vibration - 2.1-1.6 μm - slightly exceeding the tolerance limit was observed. Narrow resonances are a unavoidable feature in a stepper-motor driven linear-stage but, in the specific case, not-detrimental and also simply to be deselected from the range of the allowed motor-speeds in a scan.

ISBN: 978-3-95450-192-2 doi:10.18429/JACoW-IBIC2017-WEPCC16

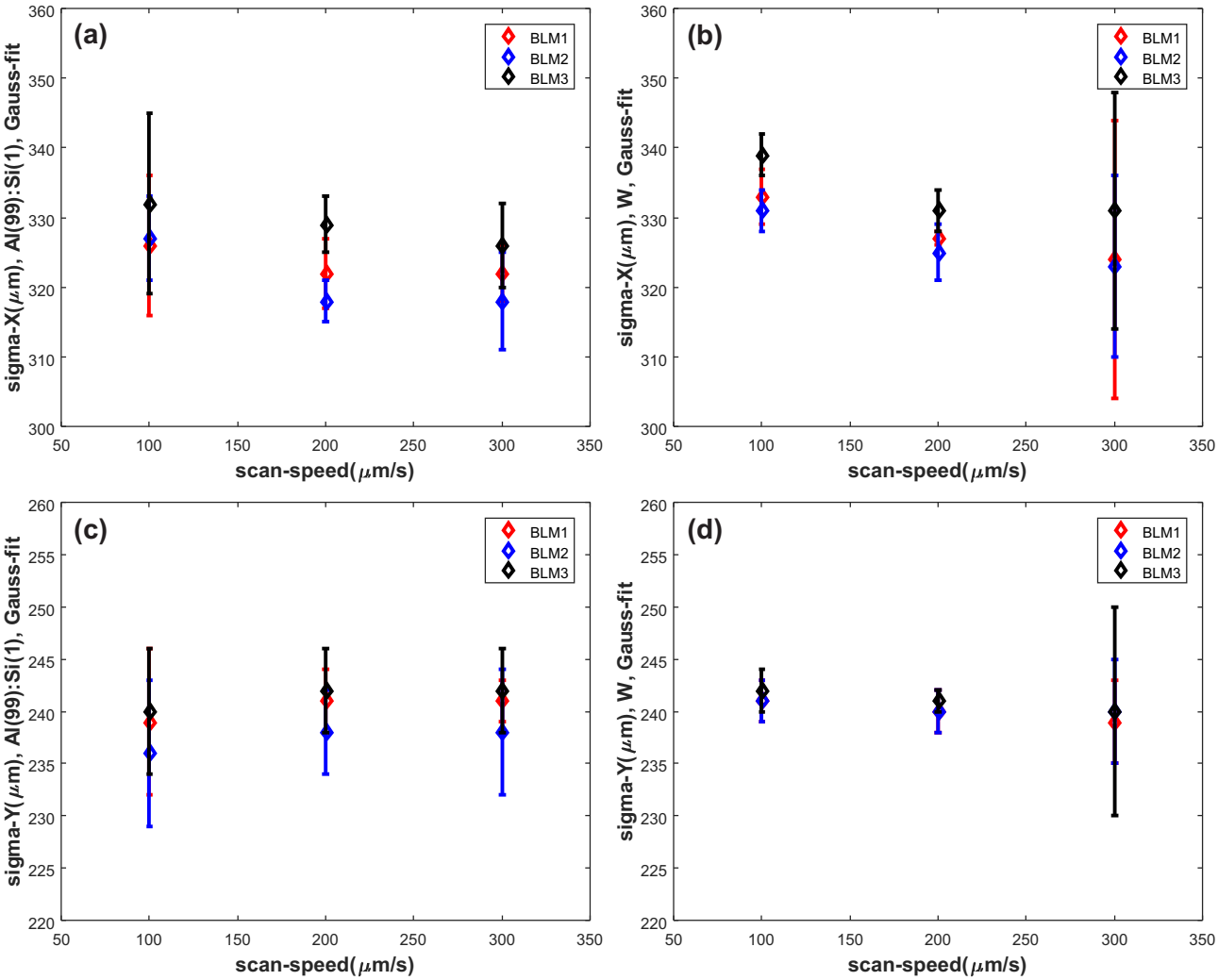

Figure 2: Gauss fit estimates of WSC measured beam size: (a,b) results of horizontal scan with Al(99):Si(1) and W wires, respectively; (c,d) results of vertical scan with Al(99):Si(1) and W wires, respectively. Beam energy 330 MeV, charge 20 pC, repetition rate 10 Hz.

The multi-shot feature of a WSC measurement requires acquiring all the signal of the concerned instruments in a beam synchronous mode at every RF shot (BSREAD) and assigning to each signal an identifying ID global number. The motor controller is provided with a timing card which permits to stream the BSREAD encoder readout to an EPICS channel with a time jitter of about 0.1 ms. Together with BLM signals, signal readouts of BPMs upstream and downstream the WSC are BSREAD acquired as well in order to correct the WSC measurement by possible effects of charge and position jitter. Finally, a high-level application, developed using the PShell workbench [11], provides the user interface and manages the measurement process: setting of the scan parameters (interval of scan, number of cycles, motor speed); acquiring and saving of the BSREAD stream of the instrument signals; preliminary profile analysis and real-time displaying of the scan on-progress.

FIRST COMMISSIONING RESULTS

The commissioning of the SwissFEL WSCs is on-going. First goals of the commissioning are: (1) functionality check of all the sub-systems involved in a WSC measurement (wire integrity, BSREAD of motion and detection signals, data processing and saving); (2) determination of the most suitable BLMs for the WSC under commissioning from the point of view of the signal-to-noise ratio and optimization of the PMT gain; (3) cross-check of the WSC measured size of the electron beam with view-screen measurement; (4) comparative study of the Al(99):Si(1) and 5 μm W wire performance from the point of view of the measurement accuracy and produced beam-losses; (5) evaluation of the effect of the charge and position jitter of the beam on a WSC measurement and implementation of a correction procedure if needed. First WSC to be commissioned in SwissFEL is placed between the first bunch compressor (BC1) and the injector energy spectrometer. In the

ISBN: 978-3-95450-192-2 doi:10.18429/JACoW-IBIC2017-WEPCC16

WSC measurement session hereby described, the machine was set at a charge of 20 pC, a repetition rate of 10 Hz and at a maximum beam energy of 330 MeV in the beam line between BC1 and the injector spectrometer. Three different BLMs - BLM1, BLM2, and BLM3 placed respectively at 2.2, 6.5 and 20.5 m from the WSC - were simultaneously acquired together with the readout of the beam charge and position of 2 BPMs placed, respectively, immediately upstream and dowstream the WSC. Several scans were performed with both Al(99):Si(1) and W wires along the X and Y directions (6 cycles per scan). The gain of the PMT was optimized separately for Al(99):Si(1) and W scans in order to have a signal response of each BLM covering the full scale of the 12 bit ADC. The results of the analysis of the measured beam profiles - well fitted by a Gauss function - are shown in Fig.2. The gain of the PMTs is normally higher for an Al(99):Si(1) scan than for a W scan. Moreover, for a given wire material, the PMT gain increases from the closer to the outer BLM. Consequently, the signal-to-noise ratio is different for the 3 BLMs. Nevertheless, the results of the beam profile analysis reported in Fig.2 indicate an excellent agreement - within the statistical errors - of the beam profiles which can be reconstructed by the signal of the 3 BLMs when scanning the beam with both Al(99):Si(1) and W wires. Moreover, the measurement accuracy of the beam size still maintains consistent in the considered range of scan-speeds, 100, 200 and 300 μm/s. According to the signals acquired by BLM2 - which showed the highest signal-to-noise ratio - for a scan speed of 100 μm/s, the beam profile measured at the WSC position is: $(327\pm1\mu\mathrm{m})$ in X and $(240\pm2\mu\mathrm{m})$ in Y with W wire; $(322\pm5\mu\mathrm{m})$ in X and $(241\pm3\mu\mathrm{m})$ in Y with Al(99):Si(1) wire. In order to crosscheck the results of the WSC measurement, the beam profile has been also measured with a view-screen placed 28 cm upstream the WSC. After a suitable re-scaling of the measured beam size at the view-screen according to the ratio of the Twiss beta function at the two positions, the estimate of the beam profile at the WSC is: $(328\pm3\mu\mathrm{m})$ in X and $(240\pm2\mu\mathrm{m})$ in Y. About charge and position jitters, the effects of them on a WSC measurement are negligible in the considered experimental session. Thanks to the BSREAD signals (charge and position) of the two BPMs immediately upstream and downstream the WSC and the knowledge of the magnetic optics in between, it was possible to correct the BLM signal by the shot-to-shot fluctuations of the bunch charge and to estimate the beam jitter at the WSC as a function of the the beam position readouts from the two BPM. The charge jitter correction resulted to be absolutely negligible. The position jitter at the WSC is also negligible with respect to the statistical error. The estimate of the beam jitter at the WSC is 4.0 μm in X and 3.4 μm in Y to be compared with the measured beam jitter at the adjacent view-screen: 3.0 μm and 3.4 μm, respectively. Finally, a preliminary comparative analysis of Al(99):Si(1) vs. W scans indicates that the beam-losses measured by BLM1 and BLM2 show a reduction by about a factor 12 and 6, respectively.

CONCLUSIONS

First results of the on-going commissioning of the SwissFEL wire-scanners (WSCs) are presented. They confirms the reliability of the system as already observed in prototype tests previously carried out in other FEL facilities [6]. In comparison with the 5 W μm wire, the innovative solution of 12.5 Al(99):Si(1) μm wire shows similar performances in terms of beam robustness and measurement accuracy as well as a significative reduction of the beam-losses. This confirms the measurement strategy of SwissFEL to use 5 W μm wire in high precision measurement of the beam profile and emittance under protection conditions of the undulator line and to use 12.5 Al(99):Si(1) μm wires to routinely monitor the beam under FEL operations. For the two different types of wires, the resolution limit still need to be measured as well as the mapping of the distribution of the beam-losses along the machine has to be completed. An extensive work of matching the 22 WSCs installed in SwissFEL with the BLMs which have the best signal-to-noise ratio has to be done as well as the determination of the optimal PMT gain interval for the two charge operation modes (10/200 pC) of SwissFEL. Finally, a procedure of emittance measurement with WSCs has to be tested and settled. The beam-synchronous acquisition of the signals from all the instruments involved in a WSC measurement (motor encoder, beam-loss-monitor, beam-position-monitor) is properly running. The WSC high-level application managing the setting of a measurement parameters, the instrument control, the preliminary processing, displaying and saving of the acquired data is fully operational. Further development step will be the integration of the WSC high-level application with the functionalities required by an emittance measurement.

REFERENCES

[1] SwissFEL Conceptual Design Report, PSI Bericht Nr. 10-04 April 2012.

[2] H.-D. Nuhn, P.J. Emma, G.L. Gassner, C.M. LeCocq, F. Peters, R.E. Ruland, *Electron Beam Alignment Strategy in the LCLS Undulators*, SLAC-PUB-12098 (2006).

[3] H. Loos, R. Akre, A. Brachmann, R. Coffee, F.-J. Decker, Y. Ding, D. Dowell, S. Edstrom, P. Emma, A. Fisher, J. Frisch, S. Gilevich, G. Hays, Ph. Hering, Z. Huang, R. Iverson, M. Messerschmidt, A. Miahnahri, S. Moeller, H.-D. Nuhn, D. Ratner, J. Rzepiela, T. Smith, P. Stefan, H. Tompkins, J. Turner, J. Welch, W. White, J. Wu, G. Yocky, *Operational Performance of LCLS Beam Instrumentation*, SLAC-PUB-14121.

[4] J. Wu, P. Emma, R.C. Field, *Electron Signal Detection for the Beam-Finder Wire of the Linac Coherent Light Source Undulator*, SLAC-PUB-12120 LCLS-TN-06-7, April 2006.

[5] U. Hahn, N.v. Bargen, P. Castro, O. Hensler, S. Karstensen, M. Sachwitz, H. Thom, Nuclear Instruments and Methods in Physics Research A 592 (2008) 189196.

[6] G.L. Orlandi, M. Ferianis, P. Heimgartner, R. Ischebeck, C. Ozkan Loch, G. Penco, S. Trovati, P. Valitutti, V. Schlott, Physical Review Accelerators and Beams **19**, 092802 (2016).

ISBN: 978-3-95450-192-2 doi:10.18429/JACoW-IBIC2017-WEPCC16

[7] G.L. Orlandi, M. Ferianis, R. Ischebeck, C. Ozkan Loch, G. Penco, V. Schlott, Proceedings of IBIC2016, Barcelona, Spain (2016) 225-228.

[8] C. Ozkan Loch, S. Borrelli, R. Ischebeck, D. Llorente, F. Loehl, G.L. Orlandi, P. Pollet, V. Schlott, WEPWC04 contribution, IBIC'17.

[9] S. Ebner, H. Brands, B. Kalantari, F. Maerki, L. Sala, Poster MOPGF059, ICALEPCS2015 Conference, Melbourne, Australia (2015).

[10] R.C. Fernow, *Introduction to Experimental Particle Physics*, Cambridge University Press (1986).

[11] A. Gobbo, S. Ebner, Poster MOPGF061, ICALEPCS2015 Conference, Melbourne, Australia (2015).

ISBN: 978-3-95450-192-2 doi:10.18429/JACoW-IBIC2017-WEPCC17

2D NON-DESTRUCTIVE TRANSVERSE DIAGNOSTICS BY BEAM CROSS-SECTION MONITOR

S. Gavrilov[1,2†], P. Reinhardt-Nickoulin[1], A. Titov[1,2]
[1] Institute for Nuclear Research of the Russian Academy of Sciences, Moscow, Russia
[2] Moscow Institute of Physics and Technology (State University), Moscow, Russia

Abstract

Beam Cross-Section Monitors implemented at INR RAS proton linac provide an efficient non-destructive registration of real 2D beam cross section, beam position and profiles, phase space ellipses reconstructed from profiles data as well as real-time evolution of these parameters in the entire range of beam energies and intensities. Features of the monitor's design and image processing system are described. Measurement accuracy and precision analysis are discussed. A variety of available experimental results are presented.

INTRODUCTION

The reconstruction technique of a two-dimensional beam density distribution *I(x, y)* through a residual gas ionization was initially proposed by V. Mihailov et al. [1] in Kurchatov institute. Beam Cross-Section Monitors (BCSMs) [2], based on ion components of a residual gas ionization, were implemented later and upgraded at INR RAS linac for in-flight non-destructive diagnostics. The general principle of BCSM has been described many times previously and is clear from Fig. 1.

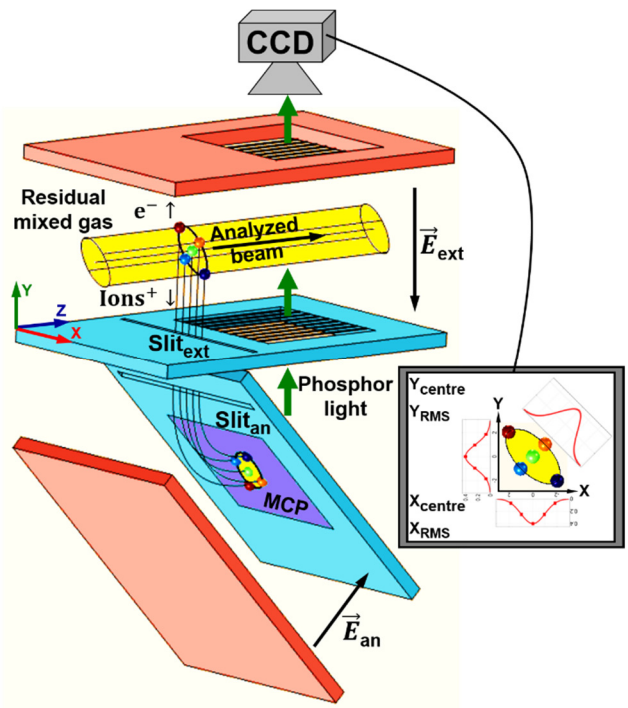

Figure 1: BCSM scheme.

The beam under study passes the area of a quasi-uniform electrostatic field and ionizes molecules of a residual gas. The energy of extracting ions in a double slit filter depends on their original Y-coordinates, so their energy distribution reproduces the transverse density distribution of the analyzed beam along Y-axis, while the distribution of the ions along X-axis keeps the same as that in the beam. Due to a potentiality of electric fields all types of ions, regardless of a specific charge: H_2^+, N_2^+, H_2O^+, etc. contribute to a 2D image formation of particle density distribution in analyzing beam cross-section (BCS).

DESIGN FEATURES

There are four main components of BCSM measurement errors. Two physical: thermal motion of ions and beam space charge and two technical: optical image processing system and internal mechanical design.

The design defines uniformity of extracting and analyzing fields as well as an Y-scale of the BCS image at electro-optical converter (MCP + phosphor). In case of uniform fields, the original distance Y_{ext} from the ion to extracting slit and converted distance L_{an} from the ion image to analyzing slit along the electrode are related as $L_{an} = 2 \cdot Y_{ext} \left({}^{E_{ext}}/_{E_{an}} \right)$. The image on the phosphor screen is detected by CCD-camera directed parallel to Y-axis. In case ${}^{E_{an}}/_{E_{ext}} = \sqrt{2}$ the detected image is identical to the analyzed BCS.

The fields in a simple, but effective, design (Fig. 2a) can be improved by several times with multiple extra correction electrodes (Fig. 2b), which decrease a non-uniformity of extracting and analyzing fields down to less than 1%. For Z-axis field symmetry extra cuts with special calculated forms can be implemented.

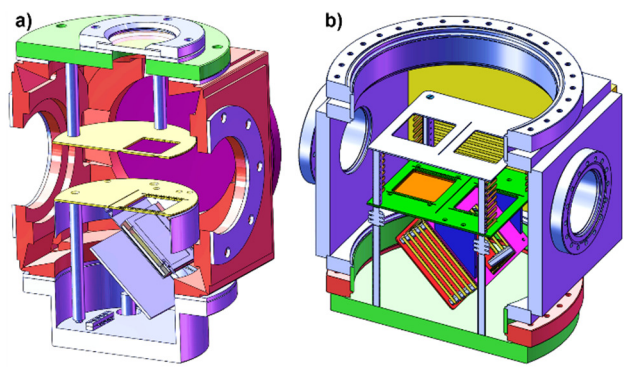

Figure 2: BCSM internal designs: a) used one (initial), b) improved one by extra correction electrodes and cuts.

† s.gavrilov@gmail.com

ISBN: 978-3-95450-192-2 doi:10.18429/JACoW-IBIC2017-WEPCC17

EXPERIMENTAL RESULTS

INR RAS linac provides beams for several research facilities: three neutron sources (time-of-flight radiation experiment, pulse neutron source, lead neutron slowing-down spectrometer), complex of proton therapy and proton irradiation facility. Therefore, a universal non-destructive diagnostics is preferable: both for high-intensity beams, which can destroy diagnostic device, and low-intensity beams, which can be destroyed totally during measurements. BCS (Fig. 3) is one of the most informative beam parameters, enabling simultaneous measurements of beam position and beam profiles at any angle.

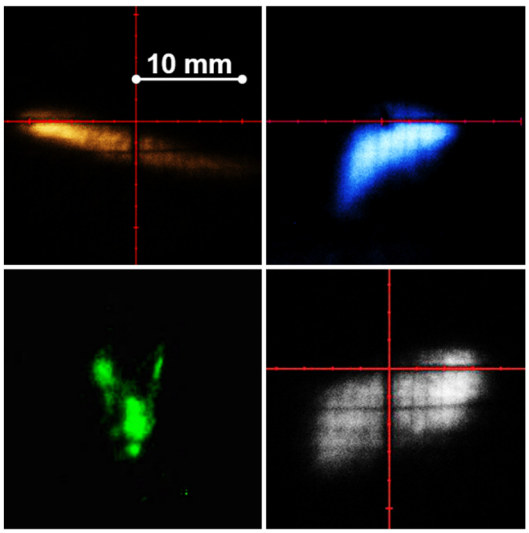

Figure 3: BCS images, registered during the linac tuning.

BCSM provides in-flight measurements in a wide range of beam parameters (Fig. 4) and reproduces as simple as complex beam cross-section images with a resolution about 300 μm. Experimentally tested range at INR linac: 5 μA, 7 μs ÷ 10 mA, 120 μs at energies 74÷247 MeV with the pressure of residual gas about 10^{-7} Torr.

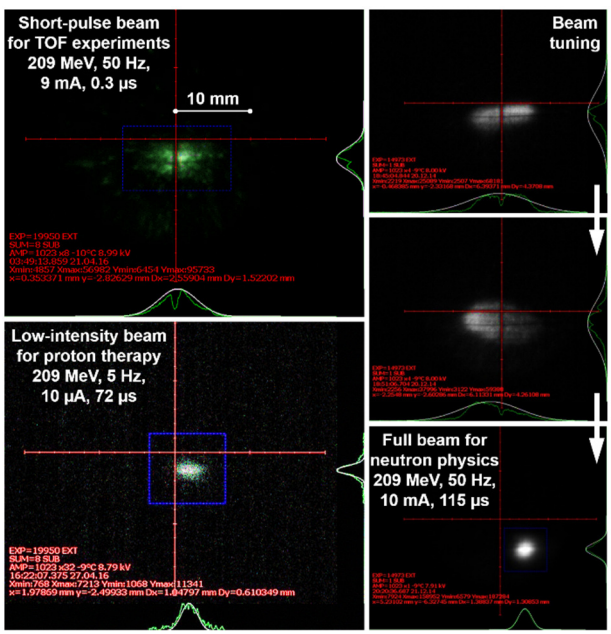

Figure 4: Routine beam measurements by BCSM.

Our experience shows, that during normal operation, the shape of the beam cross-section is close to the elliptical one and is unvaried in time. Typically, the invariance of the cross-section indicates the stability of the accelerator parameters. Besides, the monitor enables to observe beam tails (Fig. 5), which are of importance in high-intensity accelerators in terms of beam losses. That is why BCSM can be used as a convenient tool for in-flight transparent control of a general beam quality.

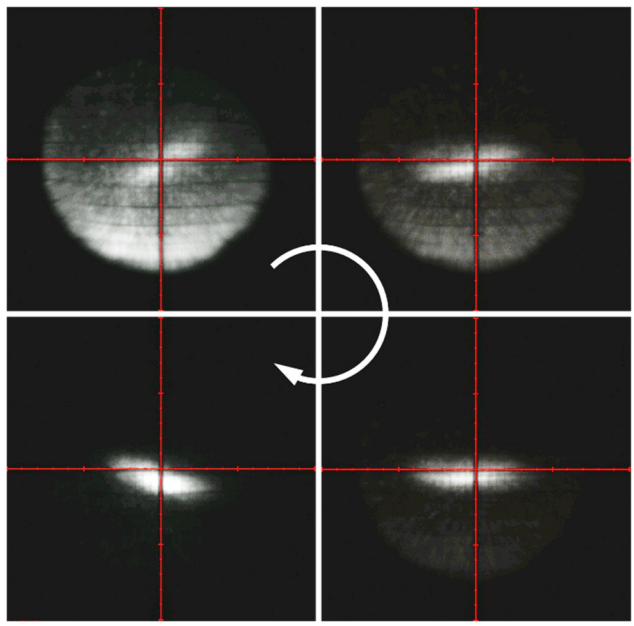

Figure 5: Successive decreasing of beam tails during the beam rotation by a group of quadrupole doublets.

Emittance equivalent phase ellipses, reconstructed from profiles data (Fig. 6) in combination with adjustable beam focusing elements for linear transformations in phase space, can be obtained also with subsequent calculation of the Twiss-parameters.

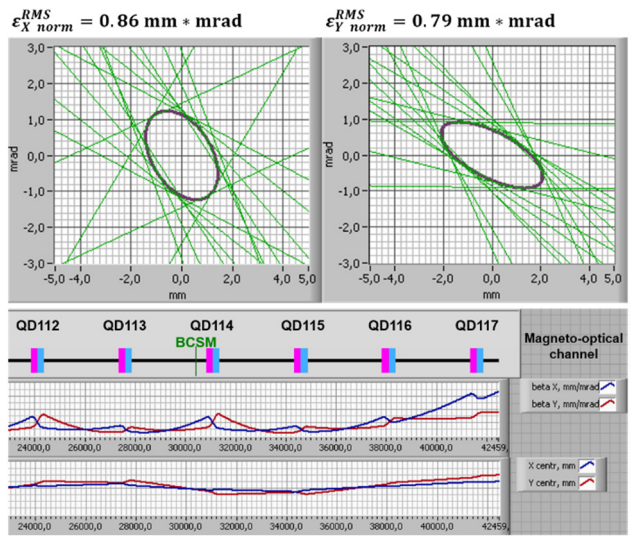

Figure 6: Equivalent phase ellipses of a 127 MeV proton beam, reconstructed from BCSM profile data, and the evolution of beta-function and beam position in the magneto-optical channel.

ISBN: 978-3-95450-192-2 doi:10.18429/JACoW-IBIC2017-WEPCC17

IMAGE PROCESSING SYSTEM

A CCD- or CMOS-camera, which are used for direct image detection, can provide simple high-resolution registration. However interactions between beam losses and a beam pipe produce both γ-quanta and neutron fluxes, causing damages and disruptions in a radiation sensitive camera matrix, that leads to decreasing of a signal to noise ratio (Fig. 7) and following irreversible damage of pixels.

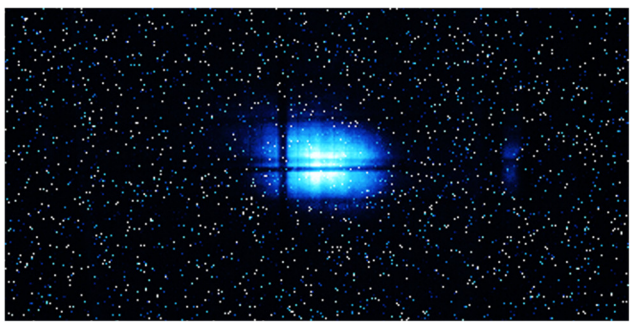

Figure 7: "Hot" pixels (white) and parasitic pixels (shades of blue) from beam losses at CCD-matrix during registration a BCS by the camera installed near beam pipe.

To avoid these problems, catadioptric periscope system is used (Fig. 8). Sizes and optical parameters of lenses and mirrors can be chosen so, that the system will collect and transmit optical radiation from phosphor screen of BCSM to the camera behind 70 cm of a concrete shield of the linac tunnel without significant loss of a light flux.

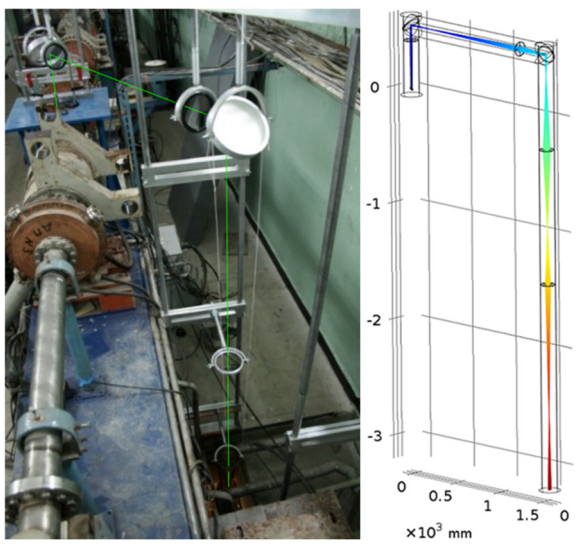

Figure 8: Installed catadioptric system and 3D-model with the light tracing through it.

Unfortunately, as well as every non-compensated optical system with one type of lenses, this one generates errors connected with distortions and spherical aberrations. The type and the absolute value of the resulting effect depend on the final magnification (Fig. 9), i. e. the focal length of a camera lens. Pincushion distortion is associated with long-focal telephoto lenses, while barrel distortion is normal for short focus. Besides, the spherical aberration appears and results in uncompensated defocusing.

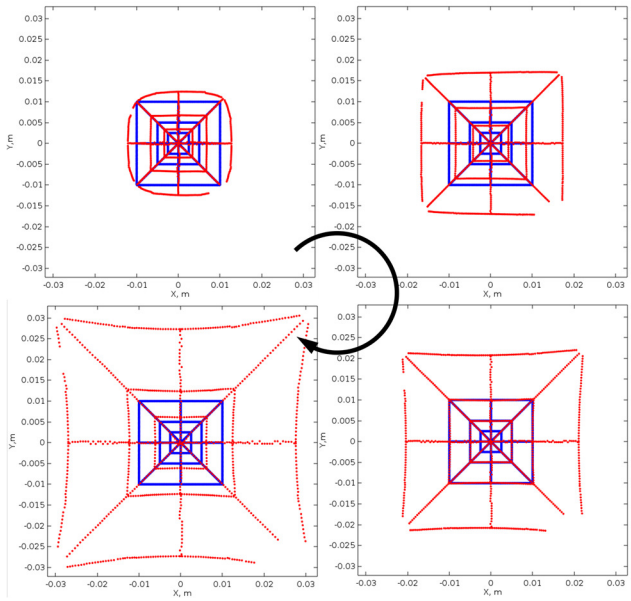

Figure 9. Transmitting of initial image (blue square with diagonals) through the periscope system with different magnifications by variation of a camera lens focal length.

One can note, there is a focal point, where distortions are minimized for working region. Nevertheless, such system demands extra software correction, for example, by using special calibrating mask at the phosphor screen (Fig. 10).

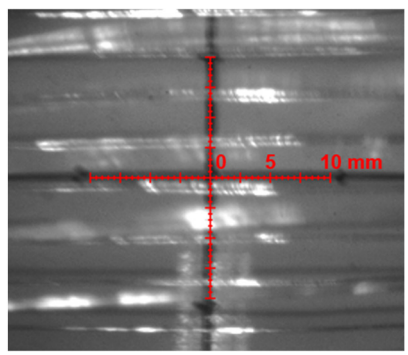

Figure 10. The phosphor screen with physical and software calibration crosses.

CONCLUSIONS

BCSMs, implemented at INR RAS proton linac, provide a unique non-destructive 2D observation and measurements of beam cross-section, position and profiles in a wide range of beam intensities. Used image processing system is an operating example of a simple extension of the camera life-time in an accelerator tunnel on condition of proper alignment and extra software correction, however it needs upgrade for design simplification and further elimination of the standard optical distortions.

REFERENCES

[1] V. Mihailov et al., General-purpose ionization detectors for accelerated particle beams, *Instr. and Exp. Tech.* 6 (1995) 39.

[2] S. Gavrilov et al., "Two-dimensional non-destructive diagnostics for accelerators by Beam Cross Section Monitor", 2014 *JINST* 9 P01011.

ISBN: 978-3-95450-192-2 doi:10.18429/JACoW-IBIC2017-WEPCC18

AN UPGRADED SCANNING WIRE BEAM PROFILE MONITORING SYSTEM FOR THE ISIS HIGH ENERGY DRIFT SPACE

D. M. Harryman*, C. C. Wilcox†, STFC Rutherford Appleton Laboratory, Didcot, UK

Abstract

The ISIS Neutron and Muon Source, based at the Rutherford Appleton Laboratory, begins with an injector line that accelerates an H^- ion beam to 70 MeV. The beam then travels through a High Energy Drift Space (HEDS) before passing through an electron stripping foil upon injection into the proton synchrotron, which provides acceleration up to 800 MeV.

During machine setup, beam profile measurements in the HEDS are taken using scanning wire monitors, which drive a single pair of measuring wires, one per plane, through the beam aperture using an analogue servo motor. Many of these monitors have been in operation since ISIS was commissioned in 1984 and as such are coming to the end of their operational lifetimes, meaning a new suite of monitors is required.

A prototype monitor has been developed along with new electronics and a control system to test the operation of a new drive mechanism based around a stepper motor and resolver, providing increased precision and reliability. This paper discusses the development of a new multi-wire monitor design, and the associated upgrade to the electronics and control system.

INTRODUCTION

The ISIS linac accelerates H^- ions to 70 MeV, producing a 50 Hz pulsed beam with a pulse length of 200 µs. This beam travels through a HEDS before injection into an 800 MeV proton synchrotron. After acceleration, protons are transferred into one of two Extracted Proton Beamlines (EPBs) and delivered to a tungsten target, driving the neutron spallation process.

Measurement of the beam's profile throughout the accelerator is vital during machine setup, whilst also providing valuable information during accelerator studies, and for understanding beam loss mechanisms. Three types of profile monitor are in use around ISIS: wire scanners and wire grid ('harp') monitors, which are both destructive to the beam [1]; and Ionisation Profile Monitors (IPMs), which provide non-destructive measurements. IPMs are used for profile measurements around the synchrotron ring, as any induced beam loss would quickly build to unsustainable levels over multiple orbits. Non-destructive profile monitoring at ISIS is described in further detail in [2] [3].

Destructive profile monitors are installed around the HEDS and EPBs and are crucial during machine setup, providing trusted and reliable measurements of the beam. Profiles are taken by moving conducting wires into the path of the beam and measuring the current generated by secondary electron emission, induced as beam particles pass through the wires. ISIS is operated at a slower rate of 1.6 Hz while these monitors are in use, reducing both the levels of induced beam loss and the risk of damage to the measuring wires.

Harp monitors are installed along both EPBs, consisting of retractable grids of wires which are inserted into the beam aperture using a pneumatic system. The grids contain 24 wires per plane with spacing set to either 6 mm or 10 mm, depending on the beam distribution in each location. Along the HEDS the beam is significantly smaller, with beam widths typically between 10-30 mm. As a result wire scanners are used here instead to allow higher resolution profiles to be measured, in addition to being cheaper to manufacture and causing less beam loss.

A single pair of measuring wires is scanned across the beam aperture by a motor driven linear stage, mounted at 45° to the beam (Fig. 1). As a result, wire displacement in both the horizontal and vertical planes is equal when the wire head is moved, with the distance travelled along each plane inversely proportional to the linear stage motion by a factor of √2. The wires are moved through the beam in horizontal and vertical steps, typically of 4 mm, and a reading is taken at each position to build up a 2D profile measurement over multiple beam pulses.

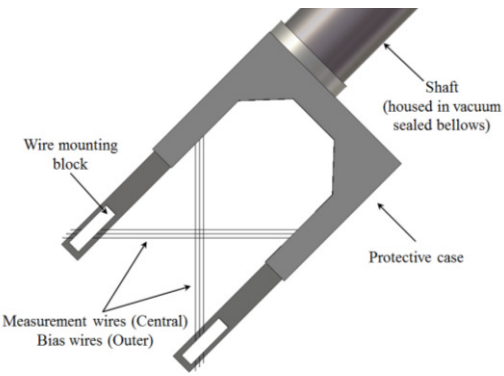

Figure 1: Orientation of a wire scanner head, with a signal wire and pair of bias wires mounted in each plane.

There are currently 15 wire scanners installed along the ISIS HEDS, many of which have been operational for over 30 years and have surpassed their design lifetimes. As a result a replacement programme is now underway, and a new monitor design has been developed alongside an upgraded control system and electronics.

MONITOR DESIGN

A prototype monitor of the new design has been built, tested and recently installed in the ISIS HEDS. The monitor offers improved measurement resolution and precision compared with existing monitors, in addition to enhanced reliability. As the motion undergone during measurement

* daniel.harryman@stfc.ac.uk
† christopher.wilcox@stfc.ac.uk

ISBN: 978-3-95450-192-2 doi:10.18429/JACoW-IBIC2017-WEPCC18

causes wear in several components, predicted lifetime usage was a key factor during the design phase. All components were selected to ensure a design lifetime of 20 years heavy use, corresponding to 8,000 scanning cycles.

Measuring and Bias Wires

Silicon Carbide (SiC) coated carbon wires with diameters of 142 µm are used for the measuring wires. This material is an ideal choice due to its rigidity and high emissivity, meaning it does not suffer from excess heating whilst intercepting the beam [4].

The wires are left unconstrained at their outermost extent to allow for thermal expansion to occur without causing damage. Instead the wires threaded through small guide holes cut into Macor® mounting blocks to ensure they remain aligned during operation.

Each measuring wire is flanked by a pair of bias wires (Fig. 1), these can be set to a positive bias voltage of up to 200 V to attract electrons emitted from the measuring wire, preventing recombination from affecting the beam-induced signal during measurement.

Motion System

A radiation hardened stepper motor, resolver and brake, manufactured by Empire Magnetics, is used to drive the linear stage and wire head through the beam (Fig. 2) [5]. Stepper motors rotate in small, discrete steps, ensuring highly accurate levels of rotation. Additionally a strong holding torque is generated while these motors are energised and at rest. An electromagnetic brake, released when supplied with current, is connected to prevent shaft movement when the system is not in use, and provides a safeguard in the event of power failure.

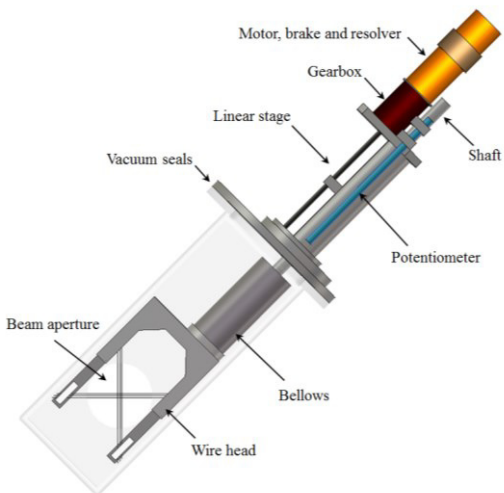

Figure 2: Simplified layout of the profile monitor.

A 5:1 gearbox is connected between the motor and the linear stage, providing extra protection from the compression force generated by the bellows when the wires are withdrawn from the beam aperture. The resolver provides a measurement of the wire positions, producing signals induced by the motor's rotations which are then passed through a resolver to encoder converter for processing in the motor drive unit. The overall system can theoretically measure the position of the wires to a resolution less than 0.1 µm, comfortably exceeding the precision required.

The scanning speed required is set by the reduced rate of 1.6 Hz at which ISIS is operated during measurement. Movement of the wires between each scan position is completed during the time between adjacent beam pulses, ensuring the profile is measured as quickly as possible.

Honeywell 9HM1 microswitches, suitable for use in radiation environments, are used as limit switches and positioned to set the linear stage stroke to 156 mm, 6 mm larger than the beam aperture [6]. When the monitor performs a profile scan, the wires are centred in the beam aperture relative to these switches, meaning precise switch activation positions are vital. During testing the switches demonstrated excellent precision, with the measured shaft positions at each limit undergoing variations of just 40 µm over 2,000 cycles of operation.

Direct Position Measurement

A linear potentiometer is attached to the monitor shaft, providing a secondary reading of the wire positions. This is useful for detecting slipping of the monitor's shaft position, which can occur over a number of years. It also provides a method of position measurement in the event of a power failure causing the motor control unit's encoder to reset. The potentiometer measures at a lower resolution of approximately 1 mm but is more robust and provides an independent safeguard to show if the wire head is positioned inside the beam aperture inadvertently. The voltages measured by the potentiometer range between 1- 4 V, chosen so that should anything happen to the 15 V supply fed to the potentiometer it would be instantly visible to the electronics.

Radiation Protection

The monitor's limit switches and motor systems were selected for their suitability for use in radiation environments, as previously mentioned. However these components are significantly more expensive as a result, and potentially unnecessary as in some monitor locations the expected dose is relatively low. To test these dose levels a TID (Total Ionisation Dosimeter) monitoring system, recently developed at ISIS, will be used to measure radiation levels along the HEDS, to test whether more cost effective components can be used on some of the new monitors [7].

ELECTRONICS

Setup

Two units are used to control the profile monitor: a custom motor control unit, used to control the monitors drive system and provide a live position of the monitor; and a National Instruments cRIO embedded controller, which interfaces with the ISIS accelerator control system and acquires data from the monitor [8].

ISBN: 978-3-95450-192-2 doi:10.18429/JACoW-IBIC2017-WEPCC18

Motor Control Unit

Figure 3 shows the main components inside the motor control unit, and how they interface with the embedded controller and profile monitor.

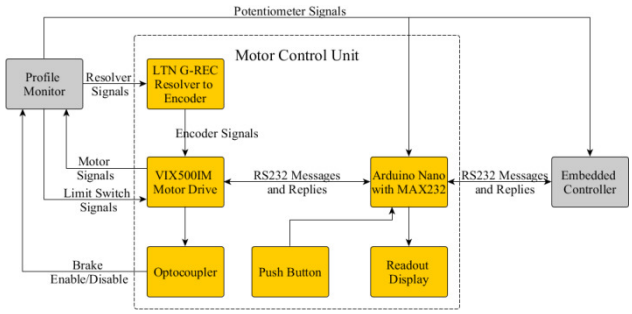

Figure 3: Block diagram of the motor control unit.

RS232 serial commands are sent to the motor control unit from the embedded controller, and are used to control the drive system. Inside the motor control unit is a VIX500IM stepper motor drive from Parker Hannifin. This unit converts the RS232 signals into the electrical signals that control the motor drive [9].

As the profile monitor produces a destructive measurement, it is possible that a failure in the embedded controller or the ISIS control system may result in the wires being inadvertently left in the beam aperture. As such, a requirement for the motor control unit is that the position of the linear stage can be seen on the unit, and that the drive can be used to directly move the measuring wires to a park position, outside the beam aperture, without the use of another system.

To allow for direct motor control, an Arduino Nano mounted on a PCB with a MAX232 IC and associated components are used [10]. The MAX232 is used to convert the messages sent and received from the Arduino and embedded controller from RS232 to UART and vice-versa. Under normal operation, messages sent through the Arduino between the embedded controller and the motor drive are simply passed through. When a push button, located on the motor control unit, is pressed to drive the monitor to the park position, the mode of the Arduino changes and it will ignore communications with the external RS232 port, replying to all messages with a "BUSY" response. The necessary serial commands are then sent to restart the motor drive, send the drive to the park position, engage the brake and turn off the motor.

Figure 4: Motor control unit readout display.

The Arduino is also used to display the position of the drive and other useful information. Figure 4 shows the display and the information shown on it. The displayed position is calculated from the voltage of the potentiometer, giving an absolute position measurement.

Also inside the motor control unit is an optocoupler and relay, used to step up a digital signal from the motor drive from 5 V to 24 V. This signal is used to enable and disable the monitor's electromagnetic brake (Fig. 2). As the VIX500IM expects an encoder signal, a resolver to encoder is also present in the motor control unit, specifically an LTN G-REC convertor [11]. All these components and their associated parts (such as power supplies) are mounted inside a custom 2U chassis. Connections to the embedded controller are made via the front panel and connections to the profile monitor via the back panel (Fig. 5).

Front

Back

Figure 5: Front and back panels of the motor control unit.

Embedded Controller

The embedded controller used for this application is an NI cRIO with a NI 9870 module for RS232 communication, and a NI 9205 module for analogue input measurements. The controller itself features a real-time processor and FPGA that are both programmed using LabVIEW. The analogue input and RS232 signals are routed from the modules into the FPGA; the FPGA then processes this data and sends it to the real time processor that will inter-face with the ISIS control system.

Currently this controller is used to interface between the ISIS control system and the motor control unit. Specifically it's used to control the profile monitors drive and acquire data about the drive from the VIX500IM and the potentiometer. It does not yet take profile measurements, as all fifteen wire scanners at ISIS are connected to a single data acquisition system. Eventually the profile measurements will be acquired by this system as more of the monitors are upgraded.

CONTROL SOFTWARE

Embedded Controller Software Architecture

The software used to program the embedded controller is written using object oriented LabVIEW code. Figure 6 shows how the different software classes interact and the threads that are run on the controller. Three of the threads;

ISBN: 978-3-95450-192-2 doi:10.18429/JACoW-IBIC2017-WEPCC18

Webservice, RS232 Serial, and Analogue Input Potentiometer, are run to interface with the different devices and systems used. API classes are then used to interface the Profile Monitor thread to these. The Profile Monitor class and thread is essentially a state machine that decides what action the motor drive should take given the data from the other threads and its current state.

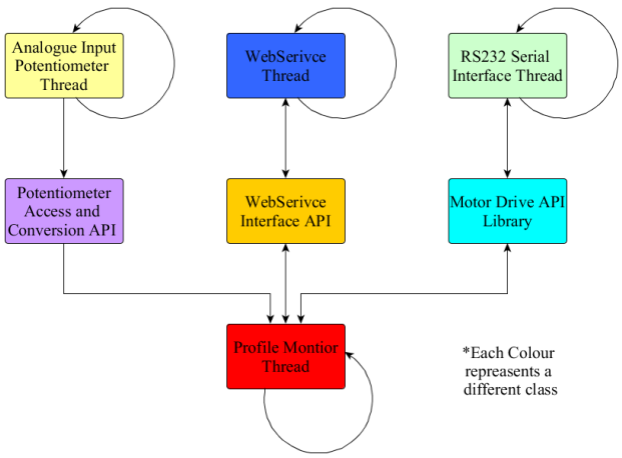

Figure 6: Software Architecture.

The RS232 interface thread manages the communication through the NI 9870 module to the motor control unit; a motor drive API library is then used so that the exact serial commands sent to the drive are abstracted away. The Analogue Input Potentiometer thread will constantly acquire data from the potentiometer, so when the Profile Monitor thread requests information about the potentiometer it will always be the latest value. The Webservice thread is there to host a number of networked variables on the embedded controller that can be interfaced with the ISIS control system. These variables and values are then used to decide the next state for the Profile Monitor state machine.

In its current configuration the software and hardware of the embedded controller can support up to four wire scanner monitors. In software all this would require is for more Profile Monitor threads to be initialised and spawned. More than four monitors are possible, however as the NI 9870 module only supports four serial ports this is its current maximum.

Control System Interface

The main control system used on the ISIS accelerator is Vsystem, from Vista Control System Inc [12]. Vsystem is a commercial SCADA solution that provides communication between many of the different devices and systems used at ISIS. Communication between different devices is made primarily over Ethernet. Databases and channels are stored and hosted by devices that communicate using Vsystem. For newer devices an XML file is hosted on the device that will specify the channels and their data types. HTTP GET and POST requests can then be made from the ISIS control system to update the database and channels hosted on the XML file.

The profile monitor hosts a number of channels to control its operation. At the start of each set of measurements a Boolean channel is set to True, starting a routine that will drive the motor into the reverse limit switch, edge off of it, and zero the encoder. This is done so that all measurements are taken relative to a known position. Other channels are used to enable movement of the drive, or set a desired position for it to move to. The encoder and potentiometer position as well as the limit switches are all read using these channels.

The data acquisition system for all of the wire scanners at ISIS hosts its own channels used to acquire the beam profiles. During operation, a Vsystem program is run, moving the monitors to the correct position and acquiring the beam profile, all via databases and channels.

FUTURE WORK

Following testing of the prototype monitor, the design has been revised to incorporate some additional improvements, and to address difficulties encountered during the process. This revised design will serve as the template for the rest of the monitor replacement programme.

The most substantial change is an increase to 18 measuring wires, nine per plane, to allow for significantly increased measurement speed over fewer beam pulses. By placing the wires 3 mm apart, the full beam profile can be measured with a single pulse, due to the small beam sizes in the HEDS. Finer resolution measurements will also be feasible, requiring far fewer beam pulses than the current system. To maximise the number of measuring wires available, the bias wires will not be included in the revised design. Testing has found these to have an insignificant effect on the existing monitors [13].

The monitor's layout has also been rearranged to take advantage of the larger bellows that are required for the additional wires. The result is that it will be possible to remove the wire head whilst leaving the vacuum vessel and remaining monitor components in place. This will allow easier access for inspection and/or replacement of the wire head in the event of damage to the measuring wires, something that has been recently observed in some of the currently installed monitors.

Due to the changes planned for the profile monitors design, the electronics and software will be updated accordingly. To take profile measurements with the new style of monitor the channel count will need to be higher due to the larger number of measurement wires.

REFERENCES

[1] P. Strehl, *Beam Instrumentation and Diagnostics*, Springer, 2006, p. 105.

[2] C. C. Wilcox, B. Jones, A. Pertica, R.E Williamson "An Investigation into the Behaviour of Residual Gas Ionisation Profile Monitors in the ISIS Extracted Beamline," in Proc. IBIC2016, Barcelona, 2016. pp. 807-810.

[3] P. G. Barnes, *et al,* "A Micro-Channel Plate Based Gas

ISBN: 978-3-95450-192-2 doi:10.18429/JACoW-IBIC2017-WEPCC18

Ionisation Profile Monitor with Shaping Field Electrodes for the ISIS H- Injector," in *Proc. IPAC2011*, San Sebastián, 2011. pp. 1371-1373.

[4] D. W. P. d. Boer, A. Pertica, "Thermal Simulations of Wire Profile Monitors in ISIS Extracted Proton Beamline 1," in *IBIC2016*, Barcelona, 2016. pp. 785-787.

[5] Empire Magnetics Inc. [Online]. Available: http://www.empiremagnetics.com/

[6] Honeywell, "9HM1" [Online]. Available: https://sensing.honeywell.com/9HM1-sealed-basic-switches. [Accessed 14 08 2017].

[7] D. M. Harryman, A. Pertica, "Online Total Ionisation Dosimeter (TID) Monitoring Using Semicondustor Based Radiation Sensors in the ISIS Proton Synchrotron," in *IBIC2016*, Barcelona, 2016. pp. 379-382.

[8] National Instruments, "The CampactRIO Platform," [Online]. Available: http://www.ni.com/compactrio/. [Accessed 09 08 2017].

[9] Parker Hannifin, "ViX250IM VIX500IM Stepper Drives User Guide," 2004.

[10] Texas Instruments, "MAX232x Dual EIA-232 Drivers/ Receivers," Feb. 1989. [Revised Nov 2014].

[11] LTN, "G-REC Resolver to Encoder Converter," Jun. 2016.

[12] B. Mannix, T. Gray "Vista Controls Vsystem at the ISIS pulsed neutron facility," presented at ICALEPCS 2007, Knoxville TN, Oct. 2007. unpublished.

[13] T. Kershaw, *Private Communication.* Aug. 2017.

ISBN: 978-3-95450-192-2 doi:10.18429/JACoW-IBIC2017-WEPCC19

A FAST WIRE SCANNER FOR THE TRIUMF ELECTRON LINAC

P. Dirksen, M. Lenckowski, W.R. Rawnsley, M. Rowe, V. Verzilov,
TRIUMF, Vancouver, Canada

Abstract

The superconducting CW LINAC presently being commissioned at TRIUMF will accelerate up to 10mA of electrons to the energy of 30 – 50 MeV. Thus, beam powers up to 0.5 MW are eventually expected. To support high beam power operation modes, a Fast Wire Scanner (FWS) capable of velocities up to 3 m/s over a 70 mm range was developed. A stepper motor driven helical cam allows for a long stroke enabling two orthogonal wires to scan both axes in one scan. The radiation produced when the wires pass through the beam is detected by a BGO scintillator coupled to a photomultiplier (PMT), while wire position is measured with a precision linear potentiometer. A Struck SIS3302 VME transient recorder, synchronized to the beam pulses, simultaneously captures both signals to produce the beam profiles in the EPICS control system. The design of the FWS and initial beam measurements will be presented.

INTRODUCTION

As a part of the effort to substantially expand the Rare Radioactive Isotope Beam (RIB) program, TRIUMF is currently in a construction phase of a 50 MeV 10 mA CW superconducting electron LINAC, to act as a driver for production of neutron-rich isotopes via photo-fission reactions [1]. The electron accelerator comprises a gridded 10 mA 300 keV thermionic gun operated at 650 MHz, a 50 MeV superconducting CW LINAC and a 70 m long beam transport line to deliver the electron beam to RIB production targets. The LINAC presently consists of two cryomodules housing three 1.3 GHz 9-cell cavities of TESLA type. Two additional cavities in a separate cryomodule will be added to the setup in the future. The first beam was accelerated to 22 MeV in 2014 and presently various accelerator systems are still undergoing commissioning to prepare the machine for high beam power operation.

Although the beam tuning is typically done with beam currents of a few microamperes using diagnostic devices such as view screens and Faraday cups [2], the actual RIB production will require monitoring of beam parameters at the full beam current. To support production modes several diagnostic devices have been developed including the FWS.

Calculations show that a carbon wire needs to travel at speeds of about 3 m/s to survive the 10 mA and 50 MeV electron beam with the size of about 0.5 mm FWHM [3]. Wire scanners operated at even higher speeds exist [4] but employ a rotary motion of the wire. For the sake of compatibility with the standard diagnostics vacuum chamber, the TRIUMF design is based on a linear motion. The linear motion allows both X- and Y-plane scans in a single pass using two orthogonally mounted wires on the same frame. To our knowledge this is the fastest linear wire scanner presently in operation.

MECHANICAL DESIGN

The FWS design was inspired by the wire scanner developed for FLASH at DESY [5], which utilizes a slot winding cylinder that engages a follower to produce a 48 mm stroke with 24 mm working range at speeds of 1 m/s. The short travel range of the DESY design requires a dedicated device for measuring each plane. For the TRIUMF FWS (Fig. 1) we required a longer working range of 70 mm to allow one FWS to scan both planes, and a speed up to 3 m/s which resulted in an overall stroke of 170 mm. To achieve the longer stroke in a compact device, a multi-turn helical cam was developed.

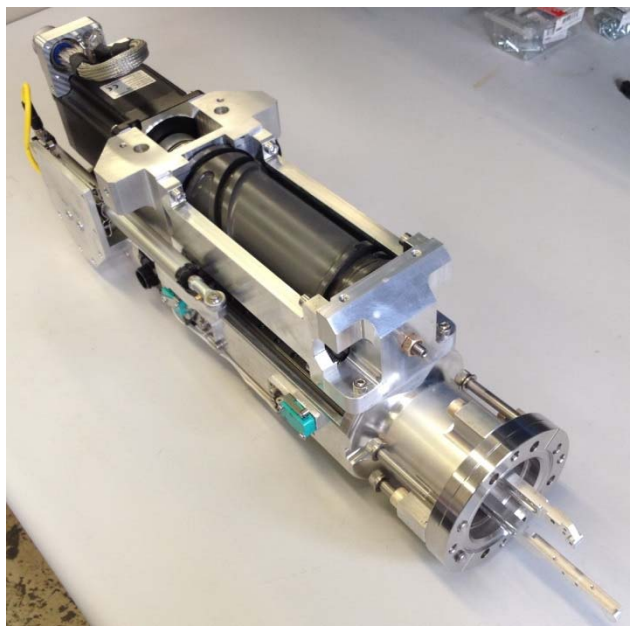

Figure 1: TRIUMF Fast Wire Scanner assembly.

The TRIUMF FWS mounts a wire fork assembly to a carriage which is supported on the main frame by linear bearings, and is driven in and out by the cam. To minimize the momentum generated at high accelerations, the mass of the moving parts is minimized where possible to a total of 816 grams.

Cam Design

The cam is a hollow 75 mm diameter cylinder constructed of aluminium and is hard anodized after machining. The 170 mm stroke includes two 70 mm ramps, and 30 mm of constant 168 mm/rev pitch in the middle. The motion of the FWS minimizes jerk by using a sinusoidal velocity ramp which is machined into the cam profile. The flat section at the end allows the cam to reach full speed before the carriage motion begins.

ISBN: 978-3-95450-192-2 doi:10.18429/JACoW-IBIC2017-WEPCC19

Cam Endless Slot

The cam follower is 8 mm in diameter, made of phosphor bronze, and supported by two ball bearings. During bench testing, it was found that a stepper motor stall causes the cam to freewheel until the follower collides with the end of the cam slot. To prevent this, a continuous slot with a decreasing depth was made at both ends. This allows a spring loaded follower pin to skip around when the cam is rotated in one direction, and drive the carriage when rotated in the opposite direction. Monitoring the height of the follower is also used to index the cam position.

Cam Equations

The cam slot is machined by a multi-axis CNC machine which uses 3D coordinates generated in MATLAB to ensure the slot conforms to the motion equation. Each section of the cam, illustrated by the colours in Fig. 2, uses a different set of equations which are stitched together to create the full curve.

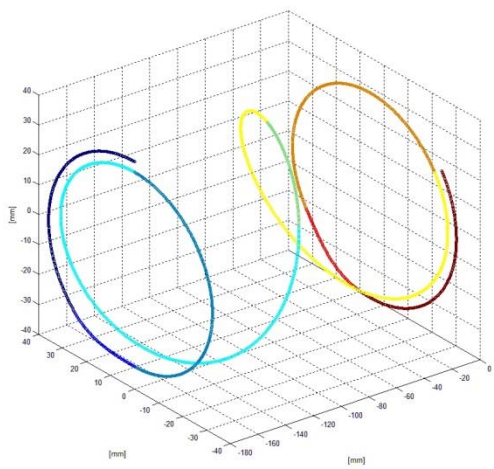

Figure 2: MATLAB 3D cam curve.

The equations used to generate the sinusoidal velocity ramp shown in yellow are as follows:

$$x = r\cos(\theta) \tag{1}$$

$$y = r\sin(\theta) \tag{2}$$

$$z = \frac{(\theta - 2\theta_i + \theta_f)p}{4\pi} - \left(\frac{l}{\pi}\right)\sin\left(\frac{(\theta - 2\theta_i + \theta_f)p}{4l}\right) - l + z_i \tag{3}$$

For:

$$\theta_i \le \theta \le \theta_f \tag{4}$$

Where:

$$\theta_f = \theta_i + \frac{4\pi l}{p} \tag{5}$$

Here x, y, z are the curve coordinates in mm, r is the radius in mm of the bottom of the cam slot, l is the length of the ramp in the z direction in mm, p is the maximum cam pitch in mm/rev, θ_i is the start angle of the ramp in radians, θ_f is the ending angle of the ramp in radians, and z_i is the starting z coordinate in mm.

Vacuum Sealing

The motion of the FWS is transferred to the vacuum using an edge welded bellows, constructed of AM350 stainless steel. During testing, it was found that the high rates of acceleration caused the initial bellows to oscillate excessively. This was eliminated by selecting a different bellows with a higher spring rate. An external spring helps shift the combined force of the vacuum and bellows spring such that the net force is near zero at the middle of travel and close to opposite at each end.

Motion Parameters

Several theoretical parameters for a peak speed of 3.25 m/s, shown in Table 1, were calculated using the cam equations, moving mass, vacuum force and spring properties. Stress calculations were then performed for the follower pin, which showed a safety factor of over 6 times for yield strength.

Table 1: Theoretical Motion Parameters

Parameter	Value
Max acceleration	118 m/s^2
Max jerk	8640 m/s^3
Max follower pin force	360 N
Max cam torque	7.5 Nm

Scanning Wire

The scanning wires are mounted to an aluminium fork with stainless steel springs to maintain tension. Machined features on the fork set the wires at the correct angles. Initial beam tests have been done using a 50 µm diameter titanium wire. A carbon wire may be tested in the future when measuring higher beam currents is required.

MOTOR CONTROL AND DAQ

The FWS cam is driven by a NEMA 34 stepper motor and powered by a 10 Amp peak, 160 VDC bus, 64 micro-stepping driver. The driver is controlled by a Galil DMC4040 motion controller. To ensure a minimum 3.0 m/s velocity over the 70 mm scanning range, a peak velocity of 3.25 m/s is required. With a 168 mm/rev pitch, this equates to 19.3 rev/s or a 247.6 kHz pulse rate which is within the driver limit of 400 kHz.

The radiation produced when the wires pass through the beam is detected by a BGO scintillator coupled to a PMT. The PMT location was optimized with a FLUKA simulation and in the low energy section is mounted directly in line with the FWS to a stainless steel flange machined to 500 µm thick in the centre.

The wire position is measured with a precision linear potentiometer. The PMT and linear potentiometer signals pass through a signal conditioning module before going to the Struck SIS3302 VME transient recorder.

The EPICS control system is used to set the PMT high voltage level, send motion commands to the Galil motion controller, and capture and process the data from the transient recorder.

ISBN: 978-3-95450-192-2 doi:10.18429/JACoW-IBIC2017-WEPCC19

BENCH TESTS

To evaluate the FWS performance, several bench tests were performed at various stages of development.

Speed Tests

The linear potentiometer used for the position signal was connected to an oscilloscope to verify the actual speed matched the target speed. The highest reliable peak speed was 3.25 m/s, while speeds higher than this were possible, they would occasionally stall the stepper motor. During testing it was found that a mechanical resonance occurs in the range of speeds from approximately 0.2 m/s to 0.4 m/s. This range will be avoided during operation.

Wire Tests

High acceleration rates may cause distortion of the wire straightness. A short exposure camera triggered by the motion controller was used to capture images of the wire at 3.25 m/s. In fact, wire distortions were observed as shown in Fig. 3, and these were later eliminated by implementing changes to the wire mounting and tensioning.

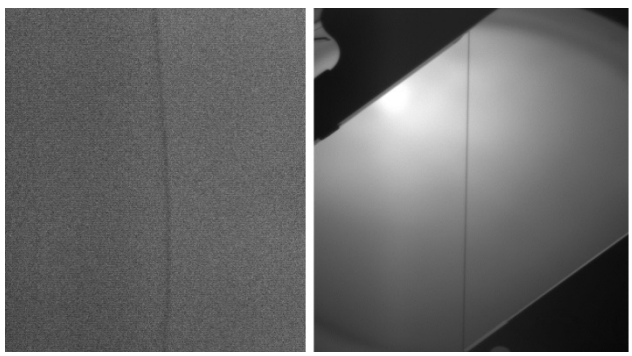

Figure 3: Wire at 3.25 m/s: distorted (left), straight (right).

To verify the linearity of motion, a long exposure capture at 3 m/s of the target shown in Fig. 4 was performed. The multiple holes of the target follow a linear path and overlap with no visible non-linear deviations though the entire motion.

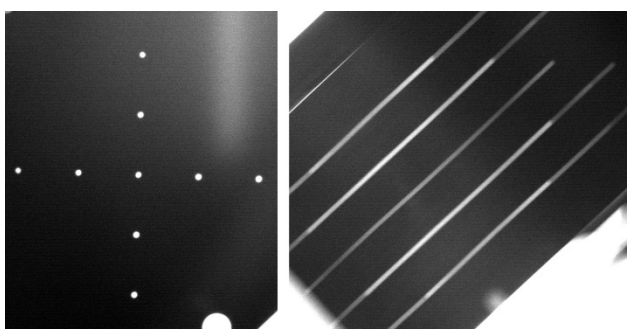

Figure 4: Target at rest (left), and at 3 m/s (right).

BEAM TESTS

Initial beam tests were performed on a FWS installed in the low energy section of the electron LINAC. During the test, 10 µs electron beam pulses at 300 keV were available at a 1 kHz rate with a peak current of ~100 µA; therefore the FWS was run in slow mode at 0.075 m/s with the acquisition system synchronized to the beam pulses.

To check the FWS response, the beam was steered around its nominal trajectory (Fig. 5) and the beam size was varied using the upstream solenoid (Fig. 6).

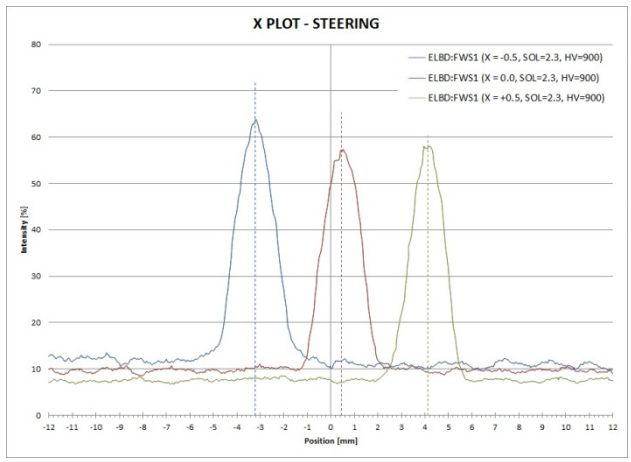

Figure 5: X axis steering changes.

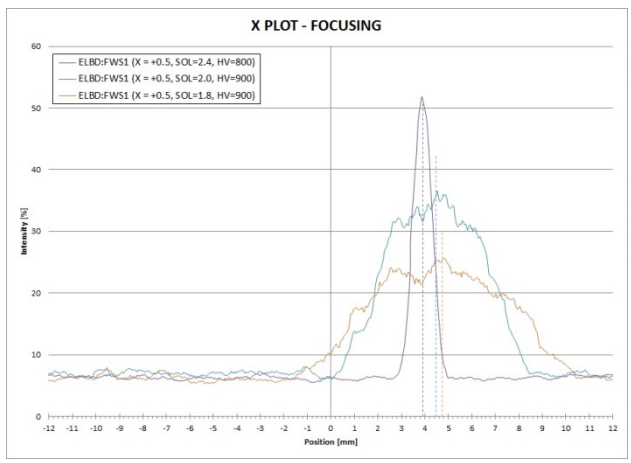

Figure 6: X axis intensity changes.

CONCLUSION

A FWS for the TRIUMF electron LINAC which met the goal of 3 m/s over a 70 mm scan was successfully designed and tested.

REFERENCES

[1] L. Merminga et al., "ARIEL: TRIUMF's Advanced Rare Isotope Laboratory," *Proc. IPAC'11*, San Sebastian, Spain, September 2011, WEOBA01, p. 1917 (2011)

[2] V. Verzilov et al., "Status of beam diagnostic systems for TRIUMF electron linac", *Proceedings of IBIC 2013*, TUPC06, Oxford, UK, 2013, p.361

[3] V. Verzilov, "E-linac wire scanner specifications," unpublished.

[4] B. Dehning et al., "Vacuum Actuator and Controller Design for a Fast Wire Scanner," *Proc. 2012 Beam Instrumentation Workshop*, Newport News, VA, USA, Apr. 2012, TUPG029, pp. 195-197.

[5] U. Hahn et al., "Wire scanner system for FLASH at DESY," Nucl. Instr. Meth., vol. 592, pp. 189-196, 2008.

ISBN: 978-3-95450-192-2 doi:10.18429/JACoW-IBIC2017-WEPCC20

RF DEFLECTOR BASED MEASUREMENTS OF THE CORRELATIONS BETWEEN VERTICAL AND LONGITUDINAL PLANES AT ELI–NP–GBS ELECTRON LINAC

L. Sabato*, University of Sannio, Benevento, Italy
P. Arpaia, A. Liccardo, University of Naples Federico II, Napoli, Italy
A. Giribono, A. Mostacci, L. Palumbo, University of Rome La Sapienza, Roma, Italy
C. Vaccarezza, A. Variola, INFN/LNF, Frascati (Roma), Italy
A. Cianchi, University of Rome Tor Vergata, Rome, Italy

Abstract

The correlations between vertical and longitudinal planes at the Radio Frequency Deflector (RFD) entrance can be introduced by misalignments of accelerating sections or quadrupoles upstream of the RFD. These correlations are undesired effects and they can affect the RFD based bunch length measurements in high–brightness electron LINAC. In this paper, an RFD based measurement technique for vertical and longitudinal planes is proposed. The basic idea is to obtain information about the correlations between vertical and longitudinal planes from vertical spot size measurements varying the RFD phase, because they add contributions on this quantity. In particular, considering a small RFD phase range centred in 0 or π rad, the correlations between the particle longitudinal positions and the vertical plane are constant with the deflecting voltage phase, on the contrary, the correlations between the particle energies and the vertical plane vary linearly with the deflecting voltage phase. The simulations are carried out by means of ELEctron Generation ANd Tracking (ELEGANT) code in the case of the Gamma Beam System (GBS) at the Extreme Light Infrastructure–Nuclear Physics (ELI–NP).

INTRODUCTION

RFD or Transverse Deflecting Structure (TDS) [1] are very common in high–brightness LINACs in order to measure the ultra–short electron bunch length since they allow to achieve very good resolutions, lower than other state–of–the–art measurements, such Electro Optical Sampling [2]: at SLAC [3, 4], at SPARC_LAB [5, 6], at DESY [7], at MIT PSFC [8], and so on. An RFD provides a transverse kick to the electron bunch introducing a relationship between the bunch longitudinal dimension and the bunch vertical dimension at a screen, placed after the RFD. Therefore, the electron bunch length can be obtained through vertical spot size measurements on a screen, placed after the RFD [9, 10], after an appropriate calibration measuring the vertical bunch centroid varying the deflecting voltage phase [11].

The correlations between vertical and longitudinal planes at the RFD entrance can be introduced by misalignments of accelerating sections or quadrupoles upstream of the RFD [12]. These correlations are undesired effects and they can affect the bunch length measurements based on the usage of the RFD in high–brightness electron LINAC. The contribution of strong correlations between vertical and longitudinal are not taken into account by means of the standard bunch length measurement technique [4, 5, 11] and, therefore, they can be sources of systematic error. On the other hand, the variations of the squared value of vertical spot size due to these correlations can be used in order to take information about them. In this paper, a measurement technique for the correlations between the vertical and the longitudinal planes by means of an RFD is proposed. First of all, the theory behind the working principle is explained in section **BASIC IDEA**. Secondly, every step of the proposed measurement technique is detailed (section **MODEL OF MEASUREMENT PRODUCTION**) and, then, the simulation results are compared with the theoretical predictions (section **NUMERICAL RESULTS**). The simulations are carried out by means of ELEGANT code [13] in the case of GBS at ELI–NP facility [14].

BASIC IDEA

Modelling the L_{RFD}–long RFD as a $L_{RFD}/2$–long drift space, a vertical kicker, and another $L_{RFD}/2$–long drift space [15, 16], and assuming *(i)* the particle energy can be written in Taylor series stopped at first order around the particle energy average $\langle E \rangle$, and *(ii)* considering an RFD phase range small and centred in 0 rad (or π rad), the contribution of the correlations between longitudinal and vertical planes on the squared value of the vertical spot size at screen after the RFD is:

$$cor_{l_0 v_0}(\varphi) = 2K_{cal}(0) cor_{t_0 v_0} - 2\frac{K_{cal}(0)}{2\pi f_{RF}} cor_{\delta_0 v_0} \varphi, \quad (1)$$

where f_{RF} and φ are the deflecting voltage frequency and phase, respectively, t_0 is the particle longitudinal position in seconds when the bunch centroid is at RFD centre, $\delta_0 = (E_0 - \langle E_0 \rangle)/\langle E_0 \rangle$, E_0 is the particle energy, $cor_{t_0 v_0}$ and $cor_{\delta_0 v_0}$ are *(i)* the correlation term between the particle longitudinal positions and the vertical plane and *(ii)* the correlation term between the particle energies and the vertical plane, respectively:

$$cor_{t_0 v_0} = \sigma_{y_0 t_0} + L\sigma_{y'_0 t_0}, \quad (2)$$

$$cor_{\delta_0 v_0} = \sigma_{y_0 \delta_0} + L\sigma_{y'_0 \delta_0}, \quad (3)$$

* luca.sabato@unisannio.it

ISBN: 978-3-95450-192-2 doi:10.18429/JACoW-IBIC2017-WEPCC20

where y_0 and y'_0 are the particle vertical position and divergence, respectively, $\sigma_{y_0 t_0}$ and $\sigma_{y'_0 t_0}$ are *(i)* the covariance between the particle vertical and longitudinal positions and the covariance *(i)* between the particle vertical divergences and longitudinal positions, respectively, $\sigma_{y_0 \delta_0}$ and $\sigma_{y'_0 \delta_0}$ are *(i)* the covariances between the particle vertical positions and energies and *(ii)* between the particle vertical divergences and energies, respectively, L is the distance between RFD centre and the screen, and $K_{cal}(\varphi)$ is the calibration factor [11, 15]:

$$K_{cal}(\varphi) = 2\pi f_{RF} L C_{RFD0a} cos\,(\varphi), \tag{4}$$

where $C_{RFD0a} = V_t / \langle E_0 \rangle$ and V_t is the deflecting voltage amplitude. The calibration factor can be calculated through vertical bunch centroid measurements at the screen varying RFD phase in a small range centred in 0 rad (π rad) [11, 17]:

$$K_{cal} = 2\pi f_{RF} p, \tag{5}$$

where p is the slope of the vertical bunch centroid versus deflecting voltage phase. This RFD model neglects the induced energy chirp and energy spread to the bunch. Actually, the TM–like deflecting modes of the cavity has a non–zero derivative of the longitudinal electric field on axis and the deflecting voltage is directly related to the longitudinal electric field gradient through the Panofsky–Wenzel theorem inducing an energy chirp and spread to the bunch [11, 18].

The contribution of strong correlations between vertical and longitudinal are undesired effects for the standard bunch length measurement technique and, therefore, they can be sources of systematic error. On the other hand, the variations of the squared value of vertical spot size due to these correlations can be used in order to take information about them. First of all, these contributions have to be isolated from the contributions of the vertical spot size at the screen with RFD on: *(i)* the vertical spot size at the screen with RFD off, *(ii)* the bunch length term, *(iii)* the energy chirp term, and *(iv)* the energy spread term [19]. The idea is based on this property: for the deflecting voltage phases φ and $\varphi + \pi$, all the terms do not change their values, but the correlation contributions change sign and, on the contrary, the other terms do not change their signs. For these reasons the correlation contributions can be obtained by means of the following equation:

$$\begin{aligned} cor_{l_0 v_0}(\varphi) &= \frac{\sigma^2_{y_s}(\varphi) - \sigma^2_{y_s}(\varphi + \pi)}{2} = \\ &= 2K_{cal}(0) cor_{t_0 v_0} - 2\frac{K_{cal}(0)}{2\pi f_{RF}} cor_{\delta_0 v_0} \varphi, \end{aligned} \tag{6}$$

where σ_{y_s} is the vertical spot size at screen with RFD on. Secondly, the information about the correlations can be found by means of a linear fit: the slope depends on the correlations between the particle energies and the vertical plane, and the intercept is related to the correlations between the particle longitudinal positions and the vertical plane (see 6):

$$p_{cor} = -\frac{K_{cal}(0)}{\pi f_{RF}} cor_{\delta_0 v_0}, \qquad cor_{\delta_0 v_0, m} = -\frac{\pi f_{RF}}{K_{cal}(0)} p_{cor}; \tag{7}$$

$$q_{cor} = 2K_{cal}(0) cor_{t_0 v_0}, \qquad cor_{t_0 v_0, m} = \frac{q_{cor}}{2K_{cal}(0)}. \tag{8}$$

MODEL OF MEASUREMENT PRODUCTION

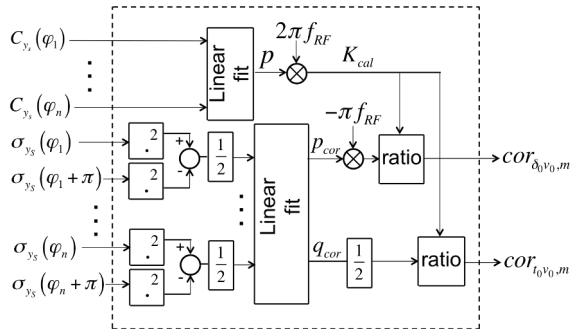

Figure 1: Model of measurement production.

From the considerations of section **BASIC IDEA**, the model of measurement production in Fig. 1 for the correlations between vertical and longitudinal planes can be thought. The model relies on two main stages: the measurements and the data processing. The former stage consists of the following operations:

1. measurements of the vertical bunch centroid at screen for different values of the deflecting voltage phase φ_i in a small range centred in 0 rad (or π rad): $C_{y_s}(\varphi_i)$;

2. measurements of the vertical spot size at screen varying the deflecting voltage phase φ_i in a small range centred in 0 rad: $\sigma_{y_s}(\varphi_i)$;

3. measurements of the vertical spot size at screen for the deflecting voltage phase $\varphi_i + \pi$: $\sigma_{y_s}(\varphi_i + \pi)$.

The data processing stage consists of the following steps:

1. estimation of the slope p of the plot vertical bunch centroid at screen versus φ by means of a linear fit, and then calculate the calibration factor K_{cal} by multiplying the deflecting voltage angular frequency by the slope p (5);

2. estimation of the half of differences between the squared values of the vertical spot sizes $\sigma_{y_s}(\varphi_i)$ and $\sigma_{y_s}(\varphi_i + \pi)$ (from 6): $cor_{l_0 v_0}(\varphi_i)$;

3. evaluation of the correlation term *(i)* between the particle energies and the vertical plane $cor_{\delta_0 v_0, m}$ and *(ii)* between the particle longitudinal positions and the vertical plane $cor_{t_0 v_0, m}$ from (7) and (8), respectively.

ISBN: 978-3-95450-192-2 doi:10.18429/JACoW-IBIC2017-WEPCC20

NUMERICAL RESULTS

Case Study

ELI–NP is one of the pillars of the ELI European project dedicated to high–level research on ultra–high intensity laser, laser–matter interaction, and secondary sources [20]. The GBS at ELI–NP will be an advanced source of up to 20 MeV gamma rays based on Compton back–scattering (i.e. collision of an intense high power laser beam and a high brightness electron beam with maximum kinetic energy of about 720 MeV [14]) in Romania. The GBS electron LINAC can run at a maximum repetition rate of 100 Hz [21], and, therefore, the specifications on the requested spectral density (1×10^4 photon/(eV s)) cannot be achieved with single bunch collisions at room temperature [14]. The final optimization foresees multiple bunch collisions, with trains of 32 electron bunches, 1 ps in length, with a repetition period of 16 ns, distributed along a 500 ns RF pulse. The laser pulse should collide with all the electron bunches in the RF pulse before being dumped, therefore the RF LINAC has to provide bunches in each train equally spaced for recirculating the laser pulse in a suitable device [14]. Moreover, the electron bunch length must be tuned according to the laser bunch length. Consequently, the measurement of the properties of the single bunch and the whole train of bunches is a crucial task for beam diagnostic [22].

Simulation Condition

A bunch composed of 50,000 particles with a charge of 250 pC was tracked by means of ELEGANT code from the RFD to the screen of GBS electron LINAC, placed between the first and the second C–band accelerating section of GBS electron LINAC [14]. The distance between RFD centre and the screen L is 1.1380 m. The deflecting voltage amplitude V_t and frequency are 1 MeV and 2.856 GHz, respectively. The GBS electron LINAC bunch parameters of vertical and longitudinal planes at RFD entrance are (in RMS): σ_y =356 μm, $\sigma_{y'}$ =60.1 μrad, $\sigma_{yy'}$ =−19.6 mm μrad, $\langle E \rangle$ =118 MeV, σ_t =0.912 ps, and $\sigma_{t\delta}$ =5.33 fs.

It is useful to introduce the correlation coefficient in order to quantify the correlations between the vertical and the longitudinal planes:

$$r_{hk} = \frac{\sigma_{hk}}{\sigma_h \sigma_k}. \quad (9)$$

The correlation coefficient quantifies how much two bunch parameters are correlated: when $r_{hk} = 0$ the bunch parameters h and k are not correlated, when $r_{hk} = |1|$ they are strongly correlated ($r_{hk} = -1$ negative correlated and $r_{hk} = 1$ positive correlated) [23]. The correlation factors at RFD entrance used in the simulations are: *(i)* between particle longitudinal positions and the vertical plane $r_{yt} = 0.107$ and $r_{y't} = 0.290$, and *(ii)* between particle energies and the vertical plane $r_{y\delta} = 0.103$ and $r_{y'\delta} = 0.277$. They can be introduced by the misalignments of the first accelerating section and the first quadrupole upstream of the RFD of −2 mm.

Correlation Measurements

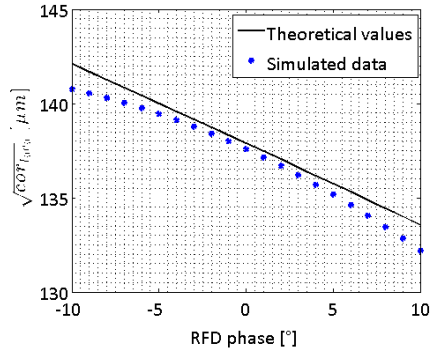

Figure 2: $\sqrt{cor_{l0v0}}$ versus deflecting voltage phase. Simulated data in blue stars (i.e. the square root of the half of the difference of squared vertical spot size measurements at screen with deflecting voltage phase φ and $\varphi + \pi$), and theoretical values (1) in black line.

The assumption of a constant calibration factor in a range of 20° centred in 0° (or 180°) is well–satisfied for the case study [19]. In Fig. 2, $\sqrt{cor_{l0v0}}$ versus deflecting voltage phase is plotted (simulated data in blue stars, i.e. the square root of the half of the difference of squared vertical spot size measurements at screen with deflecting voltage phase φ and $\varphi + \pi$, and theoretical values (1) in black line). In this scenario, the contributions of the correlations between vertical and longitudinal planes on the vertical spot size are in the order of hundreds of micron. The correlation measurements are: $cor_{\delta_0 v_0, m}$ = (0.348 ± 0.011) μm and $cor_{t_0 v_0, m}$ = (54.41 ± 0.06) μm *ps* (the uncertainties take into account only the uncertainties due to the linear fits), with a relative error (i.e. the difference between true and measured values over true value) of the order of 3%.

CONCLUSIONS

In this paper, an RFD based measurement technique for vertical and longitudinal planes is proposed. The basic idea is to obtain information about the correlations between vertical and longitudinal planes from vertical spot size measurements varying the RFD phase, because they add contributions on this quantity. The simulations are carried out by means of ELEGANT code in the case of GBS at ELI–NP facility. In this case study, strong correlations at RFD entrance between vertical and longitudinal planes are introduced in order to add a significant contribution to the vertical spot size at screen: between particle longitudinal positions and vertical plane $r_{yt} = 0.107$ and $r_{y't} = 0.290$, and between particle energies and vertical plane $r_{y\delta} = 0.103$ and $r_{y'\delta} = 0.277$. They can be introduced by the misalignments of the first accelerating section and the first quadrupole upstream of the RFD of −2 mm. The correlation measurements are: $cor_{\delta_0 v_0, m}$ = (0.348 ± 0.011) μm and

ISBN: 978-3-95450-192-2 doi:10.18429/JACoW-IBIC2017-WEPCC20

$cor_{t_0 v_0, m} = (54.41 \pm 0.06)$ μm ps (the uncertainties take into account only the uncertainties due to the linear fits), with a relative error (i.e. the difference between true and measured values over true value) of the order of 3%.

REFERENCES

[1] A. Cianchi *et al.*, "Observations and Diagnostics in High Brightness Beams", *Nuclear Instruments and Methods in Physics Research Section A: Accelerators, Spectrometers, Detectors and Associated Equipment*, vol. 829, pp. 343–347, 2016.

[2] R. Pompili *et al.*, "First Single–Shot and Non–Intercepting Longitudinal Bunch Diagnostics for Comb–Like Beam by Means of Electro–Optic Sampling", *Nuclear Instruments and Methods in Physics Research Section A: Accelerators, Spectrometers, Detectors and Associated Equipment*, vol. 740, pp. 216–221, 2014.

[3] R. Akre, L. Bentson, P. Emma, and P. Krejcik, "A Transverse RF Deflecting Structure for Bunch Length and Phase Space Diagnostics", in *Proc. of Particle Accelerator Conference (PAC), 2001*, pp. 2353–2355.

[4] R. Akre, L. Bentson, P. Emma, and Krejcik, "Bunch Length Measurements Using a Transverse RF Deflecting Structure in the SLAC LINAC" , in *Proc. of European Particle Accelerator Conference (EPAC), Paris, France, 2002*, pp. 682–685.

[5] D. Alesini *et al.*, "RF Deflector Design and Measurements for the Longitudinal and Transverse Phase Space Characterization at SPARC" ,*Nuclear Instruments and Methods in Physics Research Section A: Accelerators, Spectrometers, Detectors and Associated Equipment*, vol. 568, no. 2, pp. 488–502, 2006.

[6] D. Filippetto *et al.*, "Phase Space Analysis of Velocity Bunched Beams", *Physical Review Special Topics-Accelerators and Beams*, vol. 14, no. 9, p. 092804, 2011.

[7] M. Hüning *et al.*, "Observation of Femtosecond Bunch Length Using a Transverse Deflecting Structure", in *Proc. of the 27th International Free Electron Laser Conference (FEL), Stanford, CA, USA, 2005*.

[8] J. Haimson, "Longitudinal Phase Space Measurements of Short Electron Bunches Using a 17 GHz Circularly Polarized Beam Deflector", in *AIP Conference Proceedings*, vol. 737. AIP, 2004, pp. 95–108.

[9] R. H. Miller, R. F. Koontz, and D. D. Tsang, "The SLAC Injector", *IEEE Transactions on Nuclear Science*, vol. 12, no. 3, pp. 804–808, 1965.

[10] X. J. Wang, "Producing and Measuring Small Electron Bunches", in *Proc. of Particle Accelerator Conference (PAC), New York, USA.*, 1999, pp. 229–233.

[11] D. Alesini *et al.*, "Sliced Beam Parameter Measurements", in *Proc. of DIPAC, Basel, Switzerland*, 2009.

[12] P. Emma, J. Frisch, and P. Krejcik, "A Transverse RF Deflecting Structure for Bunch Length and Phase Space Diagnostics", *LCLS Technical Note*, vol. 12, 2000.

[13] M. Borland, "Elegant: A flexible sdds-compliant code for accelerator simulation", Argonne National Lab., IL (US), Tech. Rep., 2000.

[14] O. Adriani *et al.*, "Technical design report eurogammas proposal for the eli-np gamma beam system", *arXiv preprint arXiv:1407.3669*, 2014.

[15] L. Sabato, P. Arpaia, A. Giribono, A. Liccardo, A. Mostacci, L. Palumbo, C. Vaccarezza, and A. Variola, "Effects of Energy Chirp on Bunch Length Measurement in Linear Accelerator Beams", *Measurement Science and Technology*, vol. 28, no. 8, p. 084002, 2017. [Online]. Available: https://doi.org/10.1088/1361-6501/aa6c8a

[16] A. Cianchi, "Observations and Diagnostics in High Bbrightness Beams", in *Proc. of CERN Accelerator School (CAS), Intensity Limitations in Particle Beams, Geneva, Switzerland*, November 2015.

[17] L. Sabato, D. Alesini, P. Arpaia, A. Giribono, A. Liccardo, A. Mostacci, P. L, C. Vaccarezza, and V. A, "Metrological Characterization of the Bunch Length System Measurement of the ELI–NP Electron LINAC", in *Proc. of 14th IMEKO TC10, Milan, Italy, June 2016*, pp. 203–208.

[18] C. Behrens *et al.*, "Measurement and Control of the Longitudinal Phase Space at High–Gain Free–Electron Lasers", in *Proc. of 33rd International Free Electron Laser Conference, Shanghai, China, 2011*.

[19] L. Sabato, P. Arpaia, A. Liccardo, A. Mostacci, L. Palumbo, and A. Variola, "Energy Chirp Measurements by Means of an RF Deflector: a Case Study the Gamma Beam Source LINAC at ELI-NP", in *Proc. of International Particle Accelerator Conference (IPAC'17), Copenhagen, Denmark, 14–19 May, 2017*. Geneva, Switzerland: JACoW, 2017, paper MOPAB059, pp. 242–245.

[20] C. A. Ur *et al.*, "The ELI–NP Facility for Nuclear Physics", *Nuclear Instruments and Methods in Physics Research Section B: Beam Interactions with Materials and Atoms*, vol. 355, pp. 198–202, 2015.

[21] A. Bacci *et al.*, "Electron LINAC Design to Drive Bright Compton Back–Sscattering Gamma–Ray Sources", *Journal of Applied Physics*, vol. 113, no. 19, p. 194508, 2013.

[22] A. Cianchi *et al.*, "Six–Dimensional Measurements of Trains of High Brightness Electron Bunches", *Physical Review Special Topics–Accelerators and Beams*, vol. 18, no. 8, p. 082804, 2015.

[23] F. L. Coolidge, *Statistics: A Gentle Introduction*. Sage Publications, 2012.

ISBN: 978-3-95450-192-2 doi:10.18429/JACoW-IBIC2017-WEPCC21

BEAM SIZE MONITOR BASED ON MULTI-SILT INTERFEROMETER AT SSRF*

B.Gao†[1], Y.B. Leng‡, J.Chen, H.J.Chen[1], K.R.Ye
Shanghai Institute of Applied Physics, Chinese Academy of Sciences, Shanghai 201800, China
[1]also at University of Chinese Academy of Sciences, Beijing 100049, China

Abstract

Double-silt synchrotron radiation interferometer is a common and useful tool to measure transverse beam size around the world. In order to satisfy the requirement of high speed measurement and improve the accuracy of BSM (beam size monitor), multi-silt interferometers have been designed and tested at SSRF. Multi-silt mask pattern has characteristics of high flux throughput and high SNR of the interferogram, which is very useful at high-speed beam size measurement. This technique has a relative complex algorithm to deconvolve the result image and figure out the beam size. Principle of the multi-silt SR interferometer, mask design and experiment will be present detailed in this paper.

INTRODUCTION

The emittance of an electron beam,which is inversely proportional to the brilliance of the synchrotron radiation, is one of the most important characteristics of a storage ring operated as a synchrotron light source. To monitor degradation of the emittance, which could be caused by beam instabilities or ion-trapping phenomena, it is necessary to observe the transverse profile of the electron beam in real time. Third-generation synchrotron light sources such as the SSRF storage ring are designed to achieve low emittance and a small emittance-coupling ratio. To measure the small beam size in few tens micro meters level is very necessary. Visible light interferometer, developed by T. Mitsuhashi [1] has high resolution in beam size measurement, which has been used in different facilities around the world. However, each method has advantages but also limitations, Double-silt synchrotron radiation interferometer is limited at high speed measurement. A novel approach was proposed to satisfy the requirement of high speed measurement. Multi-silt mask pattern has characteristics of high flux throughput and high SNR of the interferogram, which is very useful at high-speed beam size measurement. A prototype 3-silt mask has been designed and test at SSRF.

DOUBLE-SILT INTERFEROMETER AT SSRF

The arrangement of double-silt interferometer at SSRF is shown in Fig. 1. The measuring interferogram is fitted by the intensity distribution of the form. The image analysis system works extracting the orthogonal profile, centre position, and least square fit to evaluate the beam sizes. The 800Mb/s interface enables full frame rate and even more cameras on the same bus. The IEEE-1394b cable with jack screws allows a more secure connection to the camera. 12-bit A/D converter, Via external trigger, software trigger (on same bus), This equipment has been tested and found to comply with the limits for a Class A digital device, have good linearity It provide reasonable protection against harmful interference when the equipment is operated in experimental environment.

After all environments and system calibration, Interferometer is good enough for the measurement of a few micro meters small beam size [2]. But the data refresh rate is 2Hz, which is not able to meet the demand of high speed measurement.

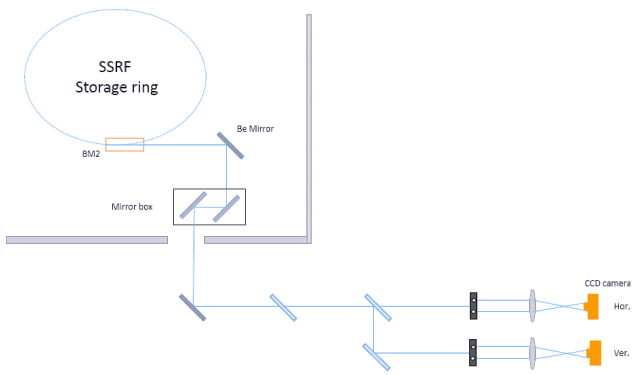

Figure 1: Layout of double-silt interferometer at SSRF.

MULTI-SILT INTERFEROMETER

The N-slit interferometer was first applied in the generation and measurement of complex interference patterns [3]. A demo beam size monitor(BSM) based on multi-silt interferometer has been proposed and developed for high speed measurements at SSRF. Multi-silt mask has characteristics of high flux throughput. A 3 silts mask for use at SSRF has been installed for demo tests, intercepting the synchrotron radiation fan at the location of an existing double-silt interferometer. In order to verify the performance of Multi-silt interferometer, images have been observerd through both double-silt and 3-silt mask using same CCD camera for a variety of beam size at same exposure times. For simplicity of demo experiments, 3-silt masks have been produced for beam size measurements.The beam size can be controlled via adjustment of the emittance coupling ratio. Figure 2 shows the prototype 3-silt mask installed at SSRF.

* Work supported by National Natural Science Foundation of China (No.11375255)
† gaobo@sinap.ac.cn
‡ leng@sinap.ac.cn

ISBN: 978-3-95450-192-2 doi:10.18429/JACoW-IBIC2017-WEPCC21

Arrangement of SR 3-silt interferometer at SSRF is shown in Fig. 3.

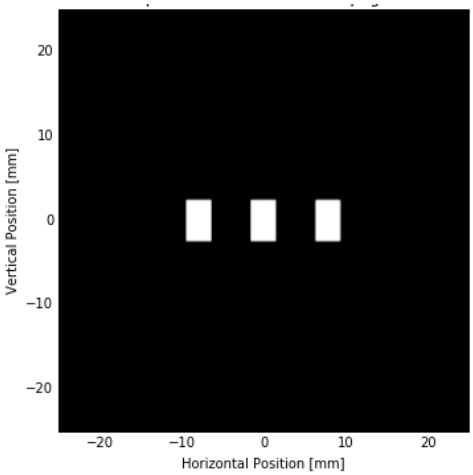

Figure 2: The mask design. Silt width: 3 mm, Pitch: 5 mm.

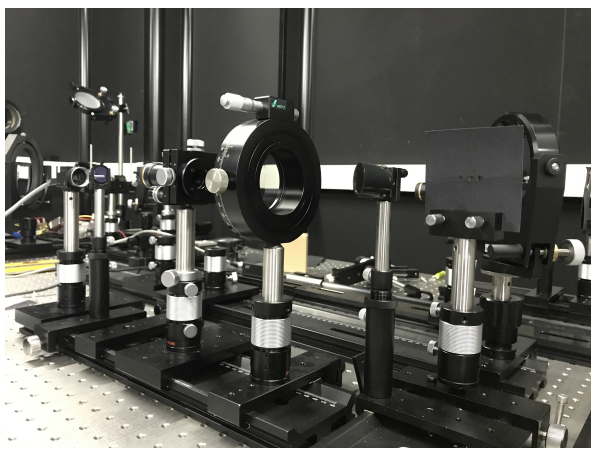

Figure 3: Arrangement of SR 3-silt interferometer at SSRF.

COMPARISONS OF 3-SILT AND DOUBLE-SILT INTERFEROMETER

Double-silt interferometers are currently relied upon to give an accurate beam size measurement at SSRF. Images observerd through both double-silt and 3-silt mask using same CCD camera at same exposure times can be compared. Figure 4 shows image and profile observed through double-silt mask. Figure 5 shows image and profile observed through 3-silt mask.

The results shows the peak intensity of the three-slit interference is twice that of double-slit interference, and the light intensity concentrated in the two main peaks.

For double-slit interferometer, the formula to calculate beam size is shown as Eq. (1). λ is the wave length,D is preparation of double slits,γ is spatial coherence. The coherence is measured by Levenberg–Marquardt fitting of intensity distribution of interference fringe and the other parameters can be measured by simple way. The disadvantage is we need to measure the valley of the interference fringe, which can not satisfy the high speed measurement. In order to overcome this limit, we prefer to find a new way to calculate the beam size. We found the beam size can be measured from first and second peaks intensity of 3-silt interference fringe(shows on Fig. 5).

$$\sigma = \frac{\lambda R}{\pi D}\sqrt{-\frac{ln\gamma}{2}} \quad (1)$$

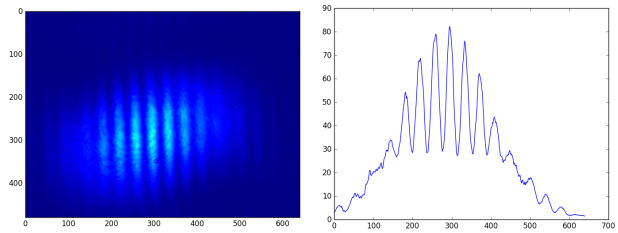

Figure 4: Double-silt interference fringe at SSRF.

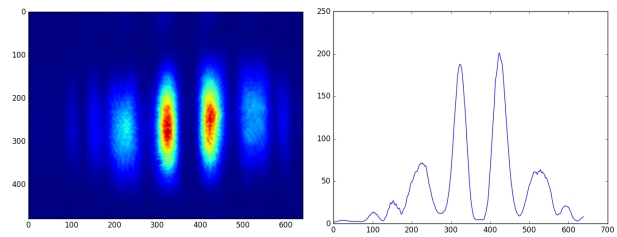

Figure 5: 3-silt interference fringe at SSRF.

COMMISSIONING AND FIRST BEAM SIZE MEASUREMENT OF 3-SILT INTERFERENCE

In order to verify the usability and reliability of 3-silt interference, beam-based calibration method had been developed in the SSRF storage ring. By varying the beam size, at the source point and observing images of the synchrotron radiation through the 3-silt using a CCD camera. The experiment was carried out in a horizontal plane with 500 electron beam bunches, while the current was around 200 mA. The beam size of the source point was changed by modifying the power supply current,I_{Q5}, of the 5th set of the quadrupoles. As we know, the beam size could be described as Eq. (2).

$$S_i^2 = \beta_i \epsilon_i + \left(\eta_i \sigma_{epsilon}\right)^2 \quad (2)$$

where S_i is the beam size in the horizontal or vertical plane, respectively, (i=x,y), β_i and ϵ_i are the betatron and dispersion functions at the source point and in the corresponding plane; and η_i and σ_ϵ are the emittance and the relative energy spread of the electron beam.

The detected flux seen at each detector pixel for different beam size shown as Fig. 6.

The image at the CCD camera shows the characteristic interference pattern difference of the different beam size.

ISBN: 978-3-95450-192-2 doi:10.18429/JACoW-IBIC2017-WEPCC21

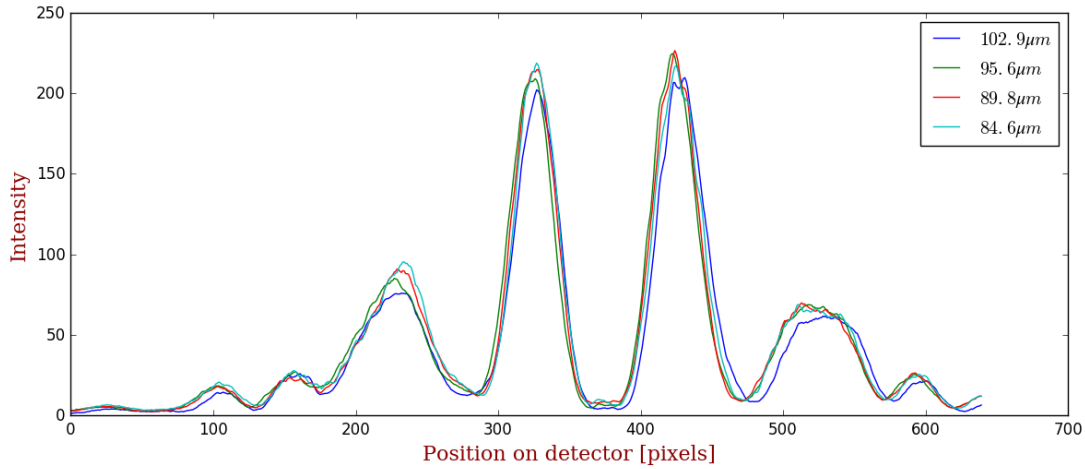

Figure 6: The detected profile of 3-silt interference for different beam sizes.

The maximum intensity of the pattern is defined as I_1 , while the second maximum intensity of the pattern is defined as I_2. I_1,I_2 and the ratio of the (I_1 - I_2) and I_1 depends on the Horizontal source size(Horizontal width of the electron beam, σ_x), as shown in Figs. 7, 8 and 9. The result shows

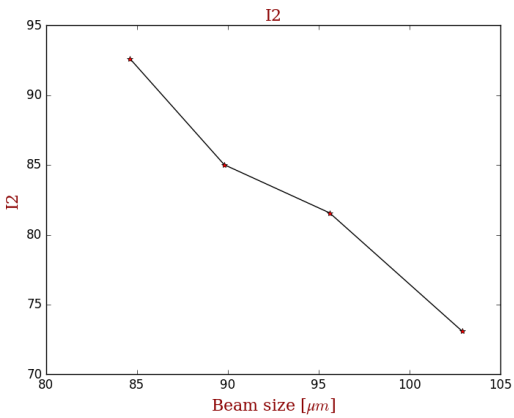

Figure 7: I_1 as a function of beam size.

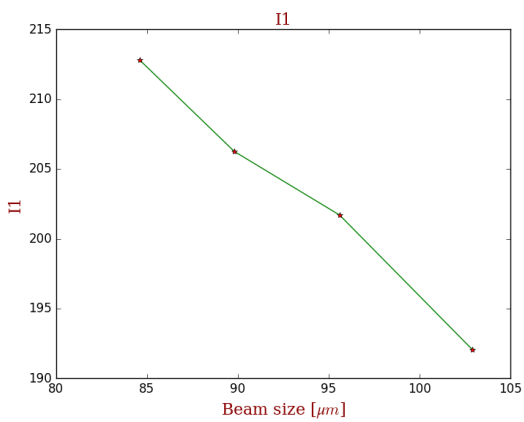

Figure 8: I_2 as a function of beam size.

I_1,I_2 is related to beam size. In order to eliminate the effect of beam current on the intensity of the pattern, the ratio of the (I_1 - I_2) and I_1 was choosed to measured the beam size.

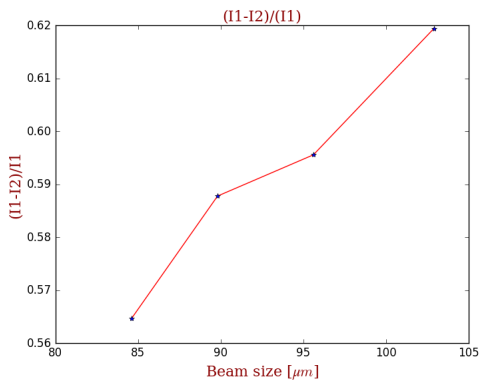

Figure 9: The ratio of (I_1 - I_2) and I1 as a function of beam size.

CONCLUSION

The 3-silt interferometer measurements of beam size shows the ratio of (I_1 - I_2) and I_1 is as a function of source size. Compared with double-silt I_2 is similar with the maximum intensity of the double-silt pattern, and the I_1 is twice of it. In 3-silt interference beam size monitor, we only need to observe 4 detector points, all of this 4 points has high intensity, and can be used for high speed measurement.

In the future, we prefer to use machine learning method and theoretical formula derivation to optimize the beam size extracting algorithm.

REFERENCES

[1] T. Mitsuhashi *et al.*, "Spatial coherency of the synchrotron radiation at the visible light region and its application for the electron beam profile measurement", in *Proc. PAC'97*, 1997, vol. 1, pp. 766-768.

[2] J. Chen *et al.*, "The Synchrotron Radiation Diagnostic Line at SSRF", in *Proc IBIC'12*, Tsukuba, Japan, Oct, 2012, paper MOPB70, pp. 232-236.

[3] F. J. Duarte *et al.*, "Quantum mechanical description of N-slit interference phenomena", in *International Conference on Lasers'88*, McLean, USA, Dec, 1988, paper MOPB70, pp. 42-47.

ISBN: 978-3-95450-192-2 doi:10.18429/JACoW-IBIC2017-WEPCF01

BEAM CHARGE MEASUREMENT USING THE METHOD OF DOUBLE-CAVITY MIXING *

J. Chen, Y.B. Leng†, L.W. Lai, R.X. Yuan, N. Zhang, S.S. Cao
SSRF, SINAP, Shanghai, China

Abstract

The measurement of beam charge is a fundamental requirement to all particle accelerators facility. In this paper, using the TM010 mode of the cavity BPM to measure the beam charge will be introduced. The data processing methods including harmonic analysis, time domain analysis and principle component analysis (PCA) are used and compared in evaluating the resolution of the beam charge. On the basis of this, the results of the evaluation at a ultra-low charge are also given and indicates the superiority of the cavity probe in the measurement of lower beam charge. In addition, the use of double-cavity mixing method to measure the beam charge will be proposed as well.

INTRODUCTION

Beam charge is a fundamental parameter for the particle accelerator facility; therefore, the beam current detector is a very important diagnostic means. There exist many methods such as various types of current transformers (CT), faraday cup (FC), etc.

In addition to that, using the sum signal of the beam position monitor (BPM) four electrodes and the TM010 mode of the cavity BPM can also to achieve the relative measurement of the beam charge. Using the reference cavity of the CBPM to measure the beam charge will be discussed in this paper. Based on this, the method of double cavity mixing to measure beam charge will be proposed and the result indicating that this method can achieve a higher beam charge resolution.

PRINCIPLE OF THE MEASURMENT

For a cylindrical pill-box cavity, when the beam source runs along the z-axis, the bunch does not lose energy in the transverse electric field of the TE mode. However, because of the longitudinal electric field of the TM mode, the bunch loses energy in the longitudinal electric field excited by itself and effectively induces the excitation mode. Therefore, only the TM modes are excited and the amplitude is determined by the bunch energy that is lost. Considering the asymmetric characteristics of TM110 dipole mode which has a strong linear dependencies to the beam offset and the beam charge, whereas TM010 monopole mode unaffected by the beam offset but it is proportional to the bunch charge and bunch length. Electric fields of the TM010 and TM110 mode are shown in Fig. 1.

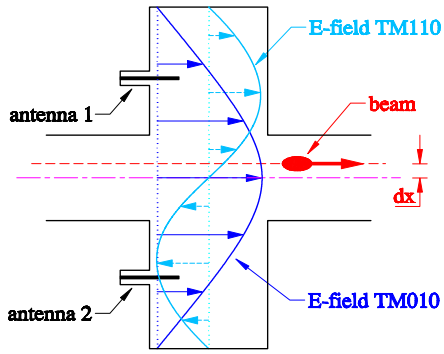

Figure 1: Electric fields of the TM010 and TM110 mode.

According to this characteristic, the beam charge can be measured using the TM010 mode of the cavity BPM. The TM010 mode signal coupled from the cavity can be expressed by Eq. (1):

$$V_p^{010} = \frac{q\omega_{010}}{2} * \sqrt{\frac{Z}{Q_{ext}^{010}} * \frac{2LT^2}{\varepsilon\omega_{010}\pi a^2 J_1^2(\chi_{01})}} * J_0\left(\frac{\chi_{01}}{a}\rho\right) * e^{-\frac{t}{\tau_{010}}} * \sin(\omega_{010}t + \varphi) \quad (1)$$

where the q is the beam charge we want to get, J_1 is the first-order Bessel function of the first kind, ω_{010} is the resonant angular frequency of the TM010 mode, χ_{01} is the first root of $J_0(\rho) = 0$ and a is the cavity radius. Since $J_0(\frac{\chi_{01}}{a}\rho)$ is appropriately equal to 1 when ρ is small. Thus, when the beam deviates from the electric centre within a small range, the signal amplitude is independent of the beam offset but dependent on the beam charge and the beam length. If we assume that the beam length is constant during the measurement process, the coupled signal strength is related to the beam charge only and proportional to it [1].

MIXING WITH LOCAL OSCILLATOR

For the beam experiment in Dalian Coherent Light Source (DCLS) [2], the reference cavities of the cavity BPM are used to measure the beam charge. The system diagram is illustrated in Fig. 2.

*Work supported by National Natural Science Foundation of China (No.11575282No.11305253)
†lengyongbing@sinap.ac.cn

ISBN: 978-3-95450-192-2 doi:10.18429/JACoW-IBIC2017-WEPCF01

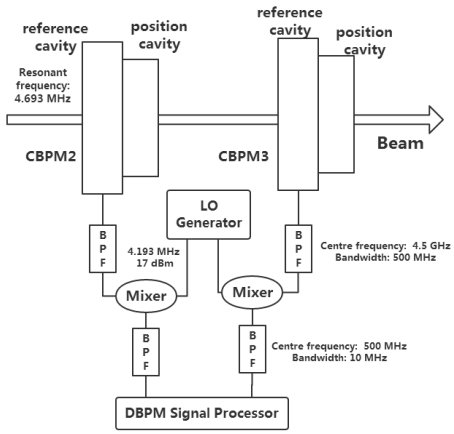

Figure 2: System diagram of using cavity BPM to measure the beam charge.

A sinusoidal signal of 4.193 GHz is generated by a local oscillator and mixed with the reference cavity signal. Since the amplitude of the LO signal is a constant value and irrespective of the beam charge, the amplitude of the signal after down-conversion is proportional to the beam charge.

To verify that the amplitude of the reference cavity signal is independent of the beam position, CBPM2 was fixed as a reference and moved CBPM3 by a stepping platform. Due to the limitation of the platform, the dynamic range was controlled within ±400 um. The relationship between the normalized amplitude and the beam position was shown in Fig. 3.

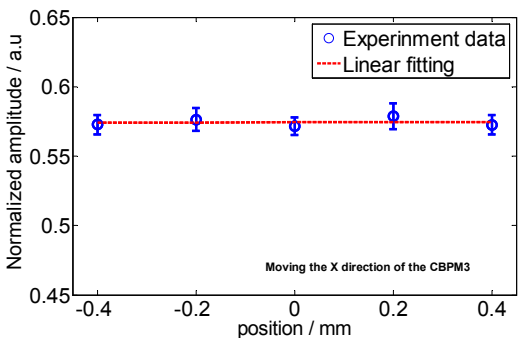

Figure 3: Dependence of the cavity signal amplitude (beam charge measurement) and the beam position.

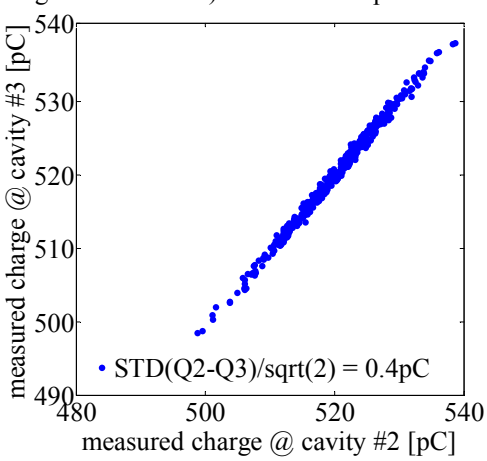

Figure 4: Evaluation results of beam charge resolution using cavity BPM2 and cavity BPM3.

Fig. 4 show the evaluation results of beam charge resolution using the cavity BPM2 and cavity BPM3 when the beam charge is about 500 pC. The relative resolution is about 0.08% using the method mixing with the LO signal, compared with the charge resolution about 1% for the ICT, which indicates the higher performance.

Change the charge of the beam so as to evaluate the relative resolution of the measuring system at different charge levels. For the data processing methods, different methods including Fast Fourier Transform (FFT), Hilbert transform and Principal Component Analysis (PCA) are be used to compare. The evaluation results are illustrated in Fig. 5.

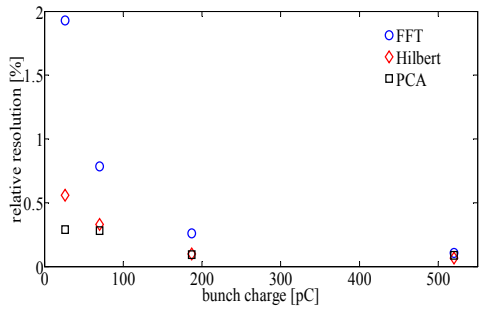

Figure 5: Comparison results of relative beam charge resolution using different data process methods.

The results show that the relative resolution results obtained by these three data processing methods are similar at higher charge levels but PCA method exhibits a superiority at a lower beam charge conditions.

To further verify that the CBPM can still work better in the ultra-low charge conditions, we designed an experiment scheme to obtain an ultra-low charge environment by extending into a profile. And the beam loss factor of 0.67 between CBPM6 and CBPM7 was measured. Predicting the Q7 value using the Q6 measured value combined with the K_{loss} to evaluate the resolution. Figs. 6, 7 and 8 show the results using the data processing method of FFT, Hilbert transform and PCA methods, respectively.

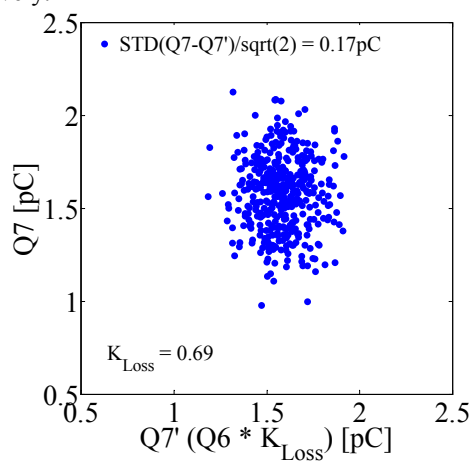

Figure 6: Evaluation of the resolution under ultra-low charge using the FFT method.

ISBN: 978-3-95450-192-2 doi:10.18429/JACoW-IBIC2017-WEPCF01

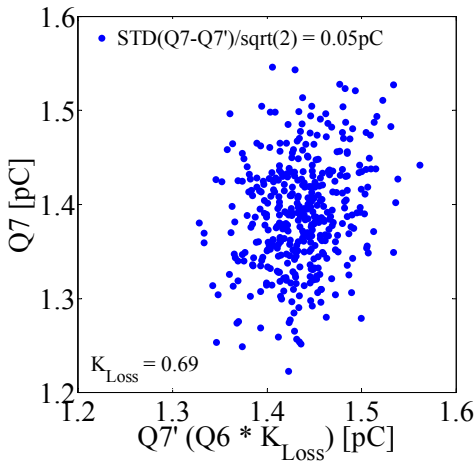

Figure 7: Evaluation of the resolution under ultra-low charge using the Hilbert transform method.

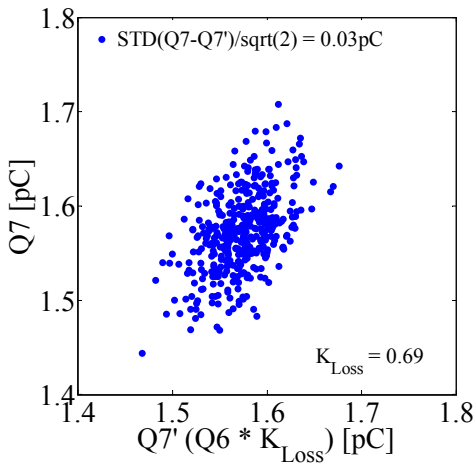

Figure 8: Evaluation of the resolution under ultra-low charge using the PCA method.

The results also show that PCA method has obvious advantages in data processing at lower charge. At ultra-low charge about 1.5 pC, the resolution can also achieved 30 fC which indicates the superiority of the cavity probe in the measurement of ultra-low beam charge.

EVALUATED BY DOUBLE-CAVITY MIXING METHOD

Based on the mixing of the cavity with the LO, a method of double-cavity mixing was proposed. Since the amplitude of the cavity TM010 mode is proportional to the beam charge, the IF signal obtained by double-cavity mixing is proportional to the square of the beam charge theoretically. The advantages of the double-cavity mixing method is that it does not need to provide an external LO and the signals are related to the beam. In addition, a square relationship related to the beam charge is introduced, it can improve the resolution of the square root of 2 times theoretically.

The schematic diagram shown in Fig. 9 is to verify the relation between beam charge and the amplitude of double-cavity mixing. The cavity signal mix with the LO as the real beam charge to compare the results of double-cavity mixing.

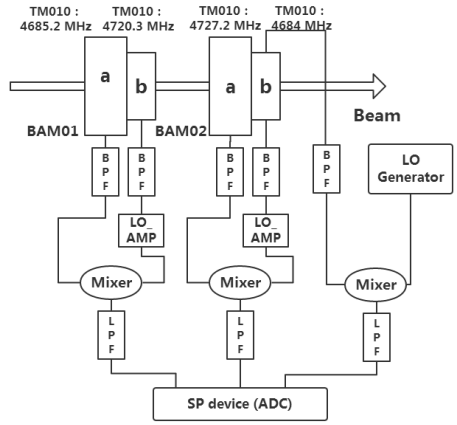

Figure 9: Diagram of the double-cavity mixing.

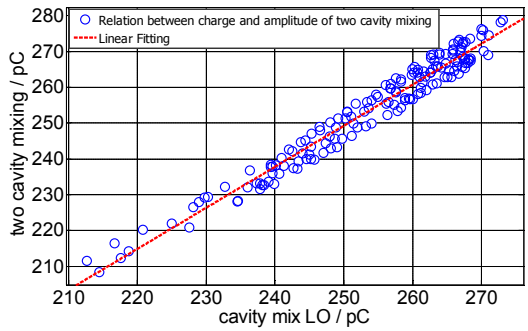

Figure 10: Relation between beam charge and the root of the amplitude of double-cavity mixing.

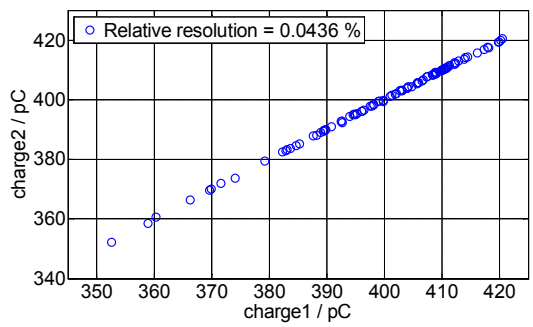

Figure 11: Relative resolution result using the method of double-cavity mixing when the charge is about 400 pC.

The relationship between the beam charge (cavity mixed with LO) and the root of the amplitude of double-cavity mixing was shown in Fig. 10. The results prove that the amplitude of double-cavity mixing is proportional to the square of the beam charge. Using this method we also evaluate the relative resolution of 0.0436% when the charge is about 400 pC (Fig. 11).

CONCLUSION

According to the principle that the signal amplitude of the cavity TM010 mode is proportional to the beam charge, the method mixing with the LO signal was used and get the relative resolution is about 0.08% when the beam charge is about 500 pC. In addition, double-cavity mixing method to evaluate the beam charge was proposed

ISBN: 978-3-95450-192-2 doi:10.18429/JACoW-IBIC2017-WEPCF01

and preliminary experiment also has been down which can get the relative resolution of 0.0436% when the charge is about 400 pC. All of which demonstrate the superiority of Cavity BPM in beam charge measurement.

REFERENCES

[1] M. Stadler *et al*., "Beam test results of undulator cavity BPM electronics for the European XFEL", in *Proc. IBIC'12*, Tsukuba, Japan, Oct. 2012, paper TUPA27, pp. 404-408.

[2] J. Chen *et al*., "Cavity BPM for DCLS", in *Proc. IBIC'16*, Barcelona, Spain, Sep 2016, paper WEPG18, pp. 661-664.

ISBN: 978-3-95450-192-2 doi:10.18429/JACoW-IBIC2017-WEPCF02

A STUDY ON THE RESOLUTION OF BUNCH LENGTH MEASUREMENT SYSTEM USING HARMONIC METHOD*

Q. Wang, B. G. Sun†, Q. Luo‡
NSRL, University of Science and Technology of China, Hefei 230029, China
Y. B. Leng, B. Gao[1]
Shanghai Institute of Applied Physics, Chinese Academy of Sciences, Shanghai 201800, China
[1]also at University of Chinese Academy of Sciences, Beijing 100049, China

Abstract

Harmonic method is very useful when we try to obtain the bunch length, while its resolution is always influenced by many factors. In this paper, the relations between resolution and working frequencies of two cavities are given by mathematical deduction. The laws of resolution change caused by some decisive factors such as beam position, working frequency, electromagnetic mode and probe position are obtained through simulation on computer. An improved measurement method utilizing TM020 mode is presented based on the theory above. The simulation results show that the improved method can enhance the resolution capability of the bunch length monitor and these analyses can provide references for the design of cavity bunch length monitor.

INTRODUCTION

Harmonic method is used to quantify the bunch length with RF pick-up. The RF pick-ups for linacs are usually cavities. The monitors consisting of the cavities have been constructed to measure the bunch length in the CLIC (Compact Linear Collider) Test Facility (CTF) at CERN [1] and the BEPCII [2]. The electromagnetic fields can be induced when the beam passes through the cavity, and the monitor achieves its function by picking up information about bunch length contained in the electromagnetic fields. It has many advantages such as simple structure, wide application rage, and high signal-to-noise ratio. But the resolution of the cavity bunch length monitor is seriously limited by the system signal-to-noise ratio (SNR) [3, 4]. In this paper, the relationship between resolution and SNR is deduced primarily and then the factors which make an impact on the system SNR is analyzed. Finally, an improved measurement method utilizing TM020 mode is proposed.

THEORETICAL ANALYSIS

Cavity bunch length monitor is usually composed of two cavities with different working frequencies. The schematic is shown in Fig. 1.

When a Gaussian bunch passed through the center of the vacuum chamber, the oscillating electromagnetic fields could be excited in the cavities. The power of the field can be written as [2]

$$\begin{cases} P_1 = [I_0 \exp(-\dfrac{\omega_1^2\sigma_\tau^2}{2})]^2 R_1 \\ P_2 = [I_0 \exp(-\dfrac{\omega_2^2\sigma_\tau^2}{2})]^2 R_2 \end{cases} \quad (1)$$

Where the subscripts stand for the cavities' serial number, σ_τ is the bunch length, I_0 is pulse current, ω is resonance frequency of the mode, and R is cavity shunt impedance. The σ_τ and I_0 are quantified by solving this two simultaneous power equations. I_0 is eliminated and the equation is derived as follows

$$\sigma_\tau{}^2 = \frac{1}{\omega_2^2 - \omega_1^2} \ln \frac{P_1 R_2}{P_2 R_1} \quad (2)$$

Take the derivative of both sides,

$$2\sigma_\tau \Delta\sigma_\tau = \frac{1}{\omega_2^2 - \omega_1^2}\left(\frac{\Delta P_1}{P_1} - \frac{\Delta P_2}{P_2}\right) \quad (3)$$

is easily shown. The resolution of the system can be expressed as

$$\Delta\sigma_\tau = \frac{(10^{-SNR/10})}{4\pi^2(f_2^2 - f_1^2)\sigma_\tau} \quad (4)$$

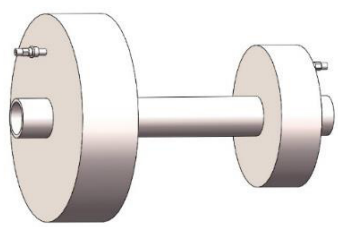

Figure 1: The schematic diagram of cavity bunch length monitor.

From the Eq. (4), it can be seen that the resolution depends on the system SNR and the difference of the square of working frequencies. As far as actual cavity is concerned, without regard to the electronics noise, the decisive factor affecting the resolution is beam position. When passing through the cavity with a position offset, the bunch will

* Supported by The National Key Research and Development Program of China (Grant No. 2016YFA0401900, 2016YFA0401903), the National Science Foundation of China (Grant No. 11575181, 11375178) and the Fundamental Research Funds for the Central Universities (WK2310000046).
† Corresponding author (email: bgsun@ustc.edu.cn)
‡ Corresponding author (email: luoqing@ustc.edu.cn)

ISBN: 978-3-95450-192-2 doi:10.18429/JACoW-IBIC2017-WEPCF02

excite dipole modes such as TM110. These modes may make an impact on the output signals and reduce SNR. The output signals in time domain and in frequency domain are shown in Fig. 2 and Fig. 3, respectively.

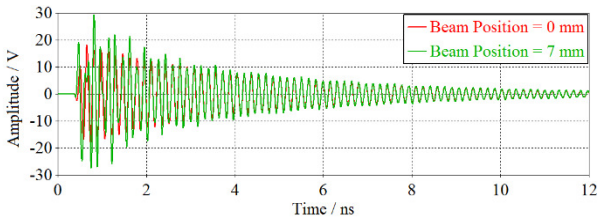

Figure 2: The output signal in time domain.

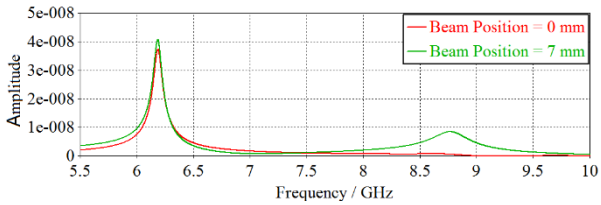

Figure 3: The output signal in frequency domain.

It can be seen that the position offset leads to amplitude changing of the output signal. In the following sections, the amplitude deviation owing to the position offset is regarded as noise. Based on this description, the system SNR and resolution are analyzed.

SIMULATION

The Influence of Beam Position

The cavity bunch length monitor is modeled and loaded with virtual beam in CST. The bunch length is 10 ps and the beam position ranges from 0 mm to 7 mm. The device consists of two cavities. The first one is the reference cavity that works at TM010 mode with 0.476 GHz. The second one is the main bunch length cavity that works at TM010 mode as well. The simulations are performed using main cavities with different working frequencies. Figure 4 shows how the relative errors of the output amplitudes vary with beam positions. In accordance with the amplitudes, the SNR and the resolutions are calculated. They are shown in Fig. 5 and Fig. 6.

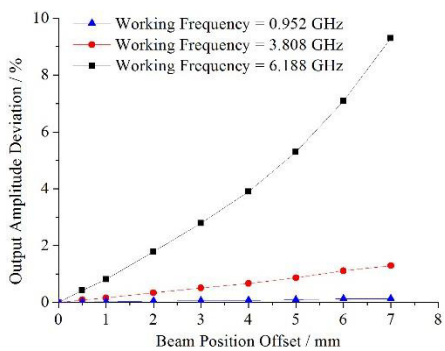

Figure 4: Output amplitude deviations vary with beam position offsets.

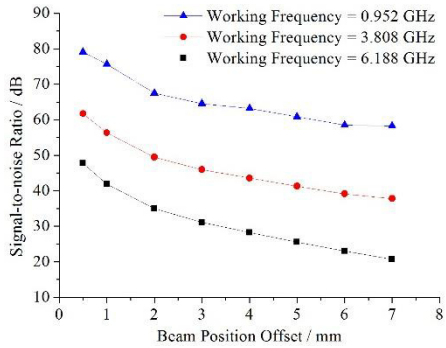

Figure 5: SNRs vary with beam position offsets.

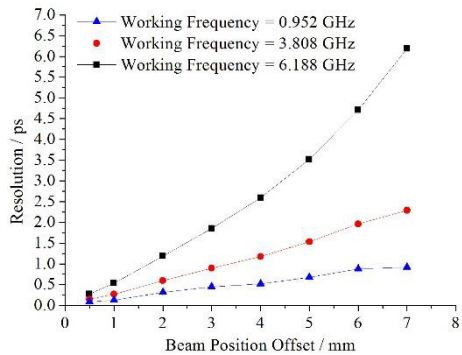

Figure 6: Resolutions vary with beam position offsets.

From the above diagrams, we can clearly figure out that the father away the beam sets from the axis of the cavity, the greater the deviation is. It follows that the SNR and the resolution decline. In the actual accelerator, the beam position is about 1 mm generally, and it will have a negative effect on the resolution. Therefore, the situation still needs optimization.

The Influence of Working Frequency

The extent of the output amplitude deviation due to the beam position also depends on the working frequency of the main cavity. A series of simulations in CST are performed. Keep the reference cavity resonating at 0.476 GHz and change the working frequency of main cavity. The simulation results of output amplitude deviation, SNR and resolution are shown in Fig. 7, Fig. 8 and Fig. 9.

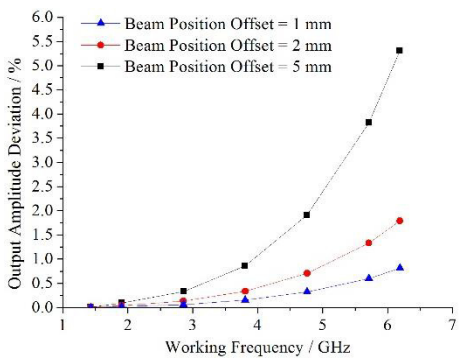

Figure 7: Output amplitude deviations vary with working frequencies.

ISBN: 978-3-95450-192-2 doi:10.18429/JACoW-IBIC2017-WEPCF02

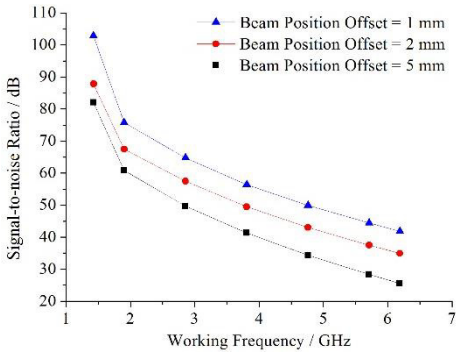

Figure 8: SNRs vary with working frequencies.

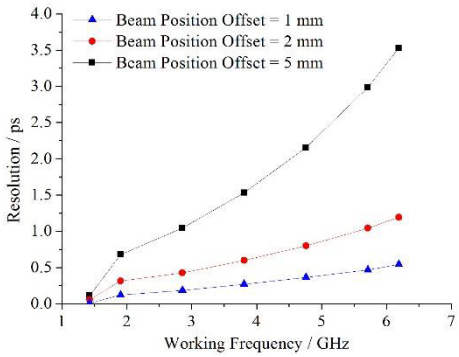

Figure 9: Resolutions vary with working frequencies.

The graphs indicate that the same beam position will introduce greater noise if working frequency is higher. According to the Eq. (4), although increase f_2 can enlarge the difference of the square of working frequencies, the SNR will decline sharply. The situation also needs optimization.

Improved Method and Simulation

To solve the above problems, an improved bunch length measurement method based on TM020 mode cavity is proposed. Comparing with TM010 mode, TM020 mode can be excited in larger cavity whose quality factor Q is higher. In frequency domain, the signal bandwidth Δf can be described as [5]

$$\Delta f = \frac{f_0}{Q_0} \tag{10}$$

Where f_0 is the resonant frequency. Smaller Δf is preferred because it means the interference from dipole modes existing in the cavity such as TM110 can be reduced.

The cavities which resonate at 3.808 GHz and 6.188 GHz with TM020 mode and TM010 mode are designed respectively in CST. The bunch with different position are loaded and the simulation results are shown in Fig. 10, Fig. 11 and Fig. 12.

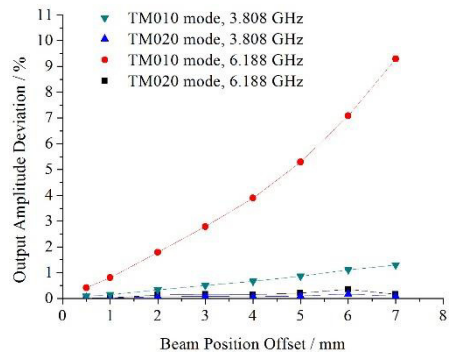

Figure 10: Output amplitude deviations vary with beam position offsets.

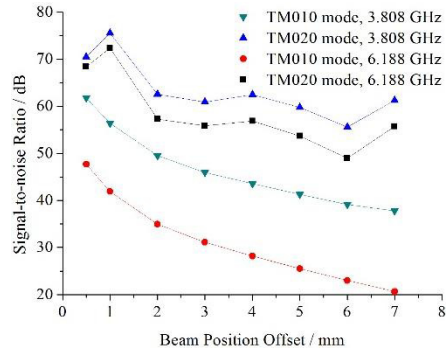

Figure 11: SNRs vary with beam position offsets.

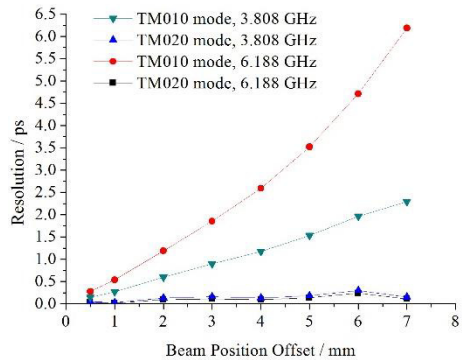

Figure 12: Resolutions vary with beam position offsets.

According to the graphs, it can be seen that using TM020 mode is able to obtain the high SNR and the high resolution compared with the traditional cavity with TM010 mode.

CONCLUSION

In this paper, the main influencing factors of cavity bunch length monitor resolution are analyzed. A series of simulations based on CST have been done and we can find that the SNR depends on the beam position and the working frequency of the eigenmode. To further optimize the performance of the device, an improved method using the cavity that resonates with TM020 mode is proposed. The simulation results prove that this improved method enhances the resolution capability effectively.

REFERENCES

[1] H. H. Braun and C. Martinez, in *Proc. EPAC'1998*, pp. 1559-1561.

ISBN: 978-3-95450-192-2 doi:10.18429/JACoW-IBIC2017-WEPCF02

[2] Y. Y. Cui *et al.*, "Bunch length measurement in BEPCII linac by harmonic method," *High Power Laser and Particle Beams*, vol. 17, no. 12, pp. 1901-1904, Dec. 2015.

[3] Z. C. Chen, W. M. Zhou, Y. B. Leng, L. Y. Yu and R. X. Yuan, "Subpicosecond Beam Length Measurement Study Based on The TM010 Mode," *Phys. Rev. ST Accel. Beams*, vol. 16, p. 072801, Jul. 2013.

[4] R. X. Yuan, W. M. Zhou, L. Y. Yu, Y. B. Leng, in *Proc. IBIC'12*, pp. 162-164.

[5] D. M. Pozar, Microwave *Engineering Fourth Edition*. Amherst, MA, USA: John Wiley & Sons Press, 2012.

ISBN: 978-3-95450-192-2 doi:10.18429/JACoW-IBIC2017-WEPCF04

THE SE-CpFM DETECTOR FOR THE CRYSTAL-ASSISTED EXTRACTION AT CERN-SPS

F.M Addesa*, G. Cavoto, F. Iacoangeli, INFN Sezione di Roma, Rome, Italy
S.Montesano, W. Scandale, CERN, 1211 Geneva 23, Switzerland
L. Burmistrov, S. Dubos, V. Puill, A. Stocchi, LAL, Orsay, France

Abstract

The UA9 experiment at CERN-SPS investigates the manipulation of high energy hadron beams using bent silicon crystals since 2009. Monitoring and characterization of channeled beams in the high energy accelerators environment ideally requires in-vacuum and radiation hard detectors. For this purpose the Cherenkov detector for proton Flux Measurement (CpFM) was designed and developed. It features a fused silica bar in the beam pipe vacuum which intercepts charged particles and generates Cherenkov light. In this contribution the SE-CpFM (Slow Extraction CpFM) detector is described in detail. It has been installed in early 2016 in the TT20 extraction line of SPS to study the feasibility of the crystal-assisted extraction from the SPS. Before the installation the detector has been fully characterized in 2015, during the UA9 data taking in the H8-SPS extraction line with 180 GeV pions. The single particle detection efficiency and the photoelectron yield per proton have been estimated and are shown in this contribution.

INTRODUCTION

Presently the SPS accelerator provides the beam for Fixed Target physics in the North Area (NA) using a slow resonant process and through electrostatic septa (ZSs). The main problematic issue of the resonant slow extraction process regards the small fraction of the beam that is unavoidably lost on the ZS wires. These losses produce both limitation to the delivered beam intensity and a strong activation of the SPS. Bent crystal technology applied in different configurations [1] offers promising solutions for the losses issue in the SPS LSS2 extraction region.

The UA9 experiment [2–7] and the CERN Accelerator Beam Transfer group are working together to demonstrate the feasibility of a crystal-assisted slow extraction toward the NA of the SPS. As a first step, a "proof of principle" experimental campaign started in 2016 during dedicated Machine Development (MD) sessions of the SPS and it is still ongoing. In this frame the installation of the SE-CpFM was needed to detect and measure the crystal-assisted extracted beam flux directly in the TT20 extraction line (Fig.1).

THE CHERENKOV DETECTOR FOR PROTON FLUX MEASUREMENTS

A "proof of principle" experiment basically consists of a very low intensity and bunched extraction from the SPS to the TT20 extraction line. The halo of a low intensity LHC-type bunch ($\sim 1.6 \times 10^{10}$) is extracted at each turn (every 23 μsec) from the circulating beam by a bent crystal located in the UA9 experimental area in LSS5 [8] and then reaches, with the right phase advance, the ZS through a closed orbit bump [9]. The flux of protons expected on the detector in TT20 ranges from 1 up to about 200 protons per turn (from 10^5 up to 10^7 p/s). Such a low flux doesn't allow to use the standard SPS instrumentation like for example BCTs (Beam Current Transformer [10]). During its collimation tests, the UA9 experiment uses to deal with a proton flux of the same order and since 2014 a Cherenkov detector (CpFM, **C**herenkov detector for **p**roton **F**lux **M**easurement) has been installed in LSS5 to measure the proton flux extracted by crystals [11, 12]. Therefore to design the SE-CpFM (**S**low **E**xtraction-CpFM) we started from the CpFM concept using the experience collected by UA9.

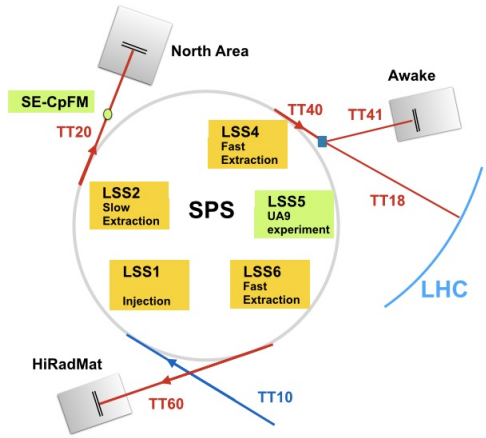

Figure 1: Conceptual sketch of the injection and extraction lines of the SPS.

SE-CpFM Requirements & Layout

The SE-CpFM detector has been devised as an ultra-fast and high resolution proton flux monitor. It has to provide the measurement of the extracted beam directly inside the beam pipe vacuum of the TT20 line, discriminating the signals coming from different proton bunches in case of multibunch beam in the SPS, with a 25 ns bunch spacing. The sensitive part of the detector is located in the beam pipe vacuum in order not to deteriorate the resolution of the flux measurement, avoiding the interaction of the protons with the vacuum-air interface. All the design choices are explained in details in [11, 12]. They were lead by the need to get very high performances matching at the same time the

* francesca.maria.Addesa@cern.ch

ISBN: 978-3-95450-192-2 doi:10.18429/JACoW-IBIC2017-WEPCF04

environmental specifications, especially concerning vacuum and the high radiation field. A conceptual sketch of the SE-

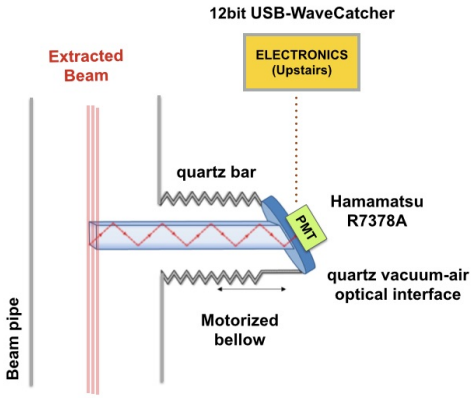

Figure 2: Conceptual sketch of the SE-CpFM.

CpFM is shown in Fig. 2. The sensitive element consists in a synthetic quartz bar ($5 \times 10 \times 300\,mm^3$, 5 mm in the beam direction) acting both as Cherenkov radiator and light guide. When a relativistic charge particle crosses the bar it produces Cherenkov light that is transported by internal reflection to the other end of the bar. To transmit the light signal outside the beam pipe a standard quartz viewport has been used. The light is collected by a R7378A Hamamatsu PMT directly and mechanically coupled to the viewport. The PMT signal is carried upstairs by a low attenuation cable and readout by an ultra fast analog memory [13]. The bar can gradually approach the extracted beam through a movable bellow on which the viewport is mounted. To maximize the light yield of the detector we decide not to install the 4 m quartz fiber bundle used to bring the light signal 1 m away from the pipe in the case of the LSS5-CpFM. The bundle was indeed responsible for a strong reduction of the light yield per proton. Instead we kept the same bar and viewport geometry (inclined at 47°) of the LSS5-CpFM to speed up the production of the tank hosting the detector and to have the possibility to easily add the bundle in case the PMT got damaged by radiation too fast.

THE SE-CPFM DETECTOR CHARACTERIZATION TEST

The whole SE-CpFM detector chain was assembled and characterized in May 2015 with a 180 GeV pion beam in the SPS-H8 extraction line, located in the SPS-North Area, during a beam test campaign of the UA9 experiment. The energy of the pions allows us to consider the results of the characterization test the same as in the case of a proton beam, being the production of Cherenkov light sensitive just to the β and to the charge of the particle. The pion beam intensity was $2 - 5 \times 10^5$ pions delivered in a 4.5 sec long spill; this means one proton delivered every 10 - 20 μs. The beam size at the SE-CpFM bar position was 2 mm in the horizontal axis and 10 mm in the vertical axis.

Test Layout

The setup layout is shown in Fig. 3. During the UA9 beam tests in H8 two experimental areas are available: Area 128 and, 50 m downstream, Area 138. The tank of the SE-CpFM was installed in Area 138 , aligned in the vertical axis (Y) with the center of the beam pipe. To align the detector with respect to the horizontal axis (X), the motorized bellow has been used. In order to perform the SE-CpFM efficiency measurement, a very light and efficient counter system was attached directly to the tank. The counter is a little bar of scintillator material sized in Y and Z ($10\,mm \times 5\,mm$) as the SE-CpFM bar, 30 mm long and readout by two silicon photomultipliers (SiPMs) on both sides. The counter was positioned to get the maximum overlapping surface with the detector bar. The signals were carried to the readout electronics (located upstairs) by 40 m long cables, a normal coaxial cable for the SipM signals and a low attenuation cable for the SE-CpFM PMT. The DAQ system was performed by the 8-channels USB-WC [13], operated at the sampling frequency of 3.2 GHz. To trigger all the system and therefore to open the 320 ns acquisition window of the USB-WC, the main trigger of the UA9 experiment has been used. This trigger is located in Area 128 and it consists of a $4\,cm \times 4\,cm$ plastic scintillator coupled to a PMT.

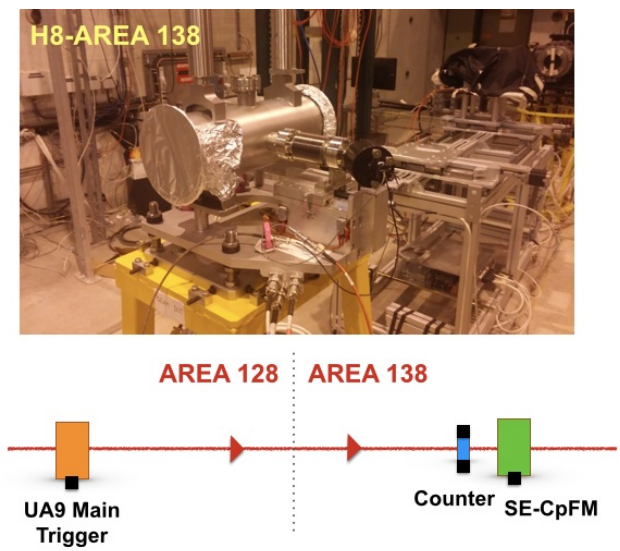

Figure 3: SE-CpFM characterization test layout.

Test Results

The main task of the characterization test was to measure two important operational factors: the SE-CpFM single proton efficiency and the single proton calibration factor, essential to count the number of extracted protons in TT20. The efficiency measurement was performed using both the little scintillator counter and the UA9 main trigger. The DAQ system was triggered by the UA9 upstream detector and the signal of the SE-CpFM, the two signals of the counter and the UA9 trigger signal were digitized by the USB-WC. Moreover the USB-WC is able to deliver for each event and for each

ISBN: 978-3-95450-192-2 doi:10.18429/JACoW-IBIC2017-WEPCF04

channel the measurement of some signal parameters such as peak time, amplitude and charge. This USB-WC feature was used for the off-line signal analysis. The good events, namely the events corresponding to real pions, were selected off-line with several cuts on the signal of the SE-CpFM:

- Pedestal cut: to remove "empty" events, i.e. events in which there is just electronic noise or baseline oscillations.
- Time cut: stringent cut on the peak time calculated from the peak time of one SiPM signal (Leading edge time SE-CpFM signal - Leading edge time SiPM1).
- Counter cut: depending on the amplitude of both SiPM signals of the counter. Only SE-CpFM events were selected for which both signals of the SiPMs correspond to a real event.

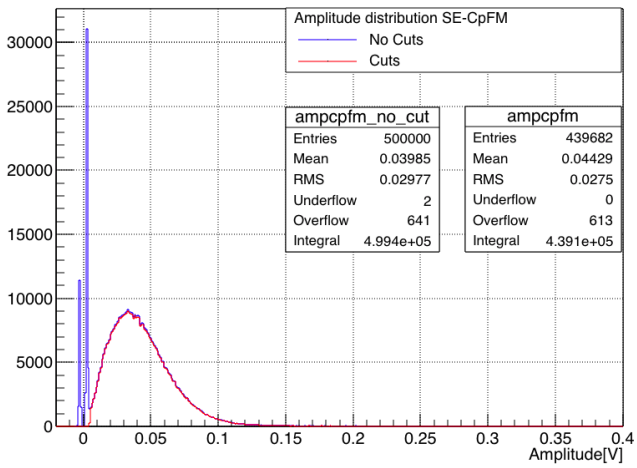

Figure 4: SE-CpFM single proton amplitude distribution with (red) and without (blue) applied cuts.

Figure 4 shows the SE-CpFM amplitude distribution with and without the applied cuts. The single proton efficiency is computed as the ratio between the number of pions measured by the CpFM (plot with cuts) and the number of pions selected by the counter. Considering a systematic error ($\pm 1\ mm$) on the vertical alignment of the SE-CpFM bar with respect to the little counter, the efficiency value has been estimated as:

$$\epsilon = 94 \pm 4.5\%$$

The photoelectron yield per single proton of the detector was obtained by the amplitude distribution, dividing by the amplitude of a single photoelectron event. The latter was extrapolated from a background measurement performed with the LSS5-CpFM PMT in SPS. The PMT of the LSS5 CpFM belongs to the same series of the SE-CpFM PMT but the gain can easily fluctuate from a PMT to another one of the same series. We evaluated that the effect of the PMT gain fluctuations on the photoelectron yield is of the order

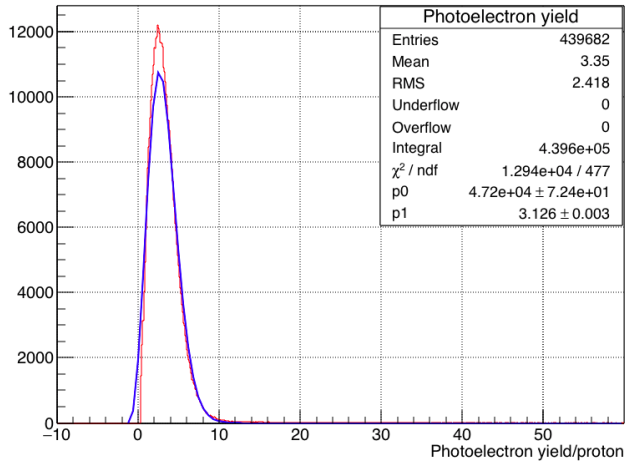

Figure 5: SE-CpFM Photoelectron yield per proton.

of 10%. The photoelectron yield distribution is shown in Fig. 5 together with the poissonian fit applied; the result is the estimation of the calibration factor of the detector:

$$ph.e\ yield = 3.1 \pm 0.3$$

CONCLUSION

A new concept of in-vacuum Cherenkov detector has been selected to perform the proton flux measurement in the first crystal-assisted slow extraction experiments at CERN-SPS. The SE-CpFM has been developed starting from the LSS5-CpFM detector, devoted to the same kind of measurements in the frame of the UA9 experiment, but with improved performances in term of efficiency and photoelectron yield. To characterize the whole detector chain, in May 2015 the detector has been tested with a 180 GeV pion beam, in the SPS-H8 line. The in-beam test campaign has shown a very good performance of the SE-CpFM. The efficiency was indeed evaluated to be $\epsilon = 94 \pm 4.5\%$ and the photoelectron yield per proton, mainly due to the bundle remotion, improved by a factor 5 with respect to the LSS5-CpFM detector changing from 0.63 (as masured in [14]) to 3.1 ph.e per proton.

The SE-CpFM was installed in the TT20 extraction line during the 2015 SPS winter shutdown and its commissioning is still ongoing. In October 2016, the detector has has been fundamental to prove the crystal-assisted proton extraction at the SPS (see Fig. 4 and 6 of [9]).

ACKNOWLEDGEMENT

The authors would like to thank the other members of the UA9 Collaboration, the CERN EN/STI, EN/EA, BE/OP, BE/RF, TE/VSC groups for the support during the design, the construction and the tests of the detector. This work has been partially supported by the ERC CoG CRYS- BEAM G.A. 615089.

ISBN: 978-3-95450-192-2 doi:10.18429/JACoW-IBIC2017-WEPCF04

REFERENCES

[1] W. Scandale, *Bent crystals in particle accelerators*, Seminar at the 19th ABT Engineering Forum, CERN, Geneva, 28th November 2014.

[2] The UA9 Experiment, http://ua9.web.cern.ch

[3] W. Scandale *et al.*, "First results on the SPS beam collimation with bent crystals", *Physics Letters B*, vol. 692, no. 2, pp. 78–82, Jul. 2010.

[4] W. Scandale *et al.*, 'Comparative results on collimation of the SPS beam of protons and Pb ions with bent crystals", *Physics Letters B*, vol. 703, no. 5, pp. 547–515, Jun. 2011.

[5] W. Scandale *et al.*, "Strong reduction of the off-momentum halo in crystal assisted collimation of the SPS beam", *Physics Letters B*, vol. 714, no. 2–5, pp. 231–236, Jul. 2013.

[6] W. Scandale *et al.*,"Optimization of the crystal assisted collimation of the SPS beam", *Physics Letters B*, vol. 726, no. 1–3, pp. 182–186, Aug. 2013.

[7] W. Scandale *et al.*,"Observation of strong leakage reduction in crystal assisted collimation of the SPS beam", *Physics Letters B*, vol. 748, pp. 451–454, Jul. 2015.

[8] S. Montesano and W. Scandale, "Apparatus And Experimental Procedures To Test Crystal Collimation", in *Proc. IPAC'12*, New Orleans, Louisiana, USA, paper THEPPB011, pp. 3254–3256.

[9] M.A. Fraser et al., *Experimental results of crystal-assisted slow extraction at the SPS*, IPAC 2017, Copenaghen, Denmark, 2017.

[10] M. Gasior et al., *Introduction to Beam Instrumentation and Diagnostics*, In proceedings of the CERN Accelerator School (CAS 2013), Trondheim, Norway, 2013

[11] V. Puill et al., *The CpFM, an in-vacuum Cherenkov beam monitor for UA9 at SPS*, JINST, Vol. 12, P04029, 2017.

[12] S. Montesano et al., *The Cherenkov Detector for Proton Flux Measurement (CpFM) in the UA9 Experiment*, IBIC 2016, Barcelona, Spain, 2016.

[13] D.Breton *et al*, "The WaveCatcher family of SCA-based 12-bit 3.2-GS/s fast digitizers", in *proceedings of IEEE Real Time 2014*, Nara, Japan.

[14] L. Butrmistrov *et al.*, "Test of full size Cherenkov detector for proton Flux Measurements", *NIM A*, vol. 787, pp. 173–175, Dec. 2014.

ISBN: 978-3-95450-192-2 doi:10.18429/JACoW-IBIC2017-WEPCF05

LOW FIELD NMR PROBE COMMISSIONING IN LEReC ENERGY SPECTROMETER*

T. Miller†, M. Blaskiewicz, A. Fedotov, D. M. Gassner, J. Kewisch, M. Minty, S. Seletskiy, H. Song, P. Thieberger, P. Wanderer, BNL, Upton, NY, USA
R. Boucher[1], C. Germain, JC. Germain, CAYLAR SAS, Villebon-sur-Yvette, FRANCE
[1]also at POLYTECH, Paris-Sud University, Orsay, FRANCE

Abstract

Low Energy RHIC electron Cooling (LEReC) [1] is planned during a 7.7 – 20 GeV/u run with Au^{+79} starting in 2019 (typically 200 GeV/n center-of-mass), to explore the existence and location of the QCD critical point. An electron accelerator for LEReC is being constructed to provide a beam to cool both the "blue" and "yellow" RHIC ion beams by co-propagating a 30 – 50 mA electron beam of 1.6 – 2.7 MeV. For effective cooling of the ion beam, the electron and ion beam energies must be matched with 10^{-4} accuracy. As the energy of the RHIC ion beam can be known to $< 1\times10^{-4}$ [2], the absolute energy of the electron beam can also be found to 10^{-4} accuracy with energy matching techniques. A 180° bend transport magnet will be used as an energy spectrometer for the electron beam providing fields in the range of 180 – 325 gauss. A Nuclear Magnetic Resonance (NMR) gaussmeter has been customized to measure the field in the magnet and tested to as low as 143 gauss with an accuracy of 50 milligauss and a noise floor of < 10 milligauss. The concept of the magnetic spectrometer with details and commissioning performance of the NMR instrument are presented in this paper.

INTRODUCTION

As the commissioning phase of the LEReC gun test beam line [3] finishes in August 2017, work continues through the RHIC shutdown to complete the construction of the beam transport, diagnostic beam line, cooling sections and high power dump sections of LEReC. Specifically, in preparation of implementing a magnetic energy spectrometer for the electron beam using the 180° dipole magnet in the cooling section, field mapping of the magnet, using integrated Hall and NMR sensors, approaches completion; while efforts to implement remote control of the NMR sensor and the magnet power supply continue in parallel. After field mapping, the dipole will be assembled on a stand with Beam Position Monitors (BPM) and Profile Monitors (PM). These are combined into Hybrid Horizontal-BPM + PM (HyPM) [4] devices that will provide calibrated on-line beam position measurement as part of the spectrometer.

The foremost challenge of the spectrometer, and the field mapping, was an absolute field measurement at the low operating field value of 196 Gauss (for 1.6 MeV operation). Most of the NMR probes available today are for the magnetic fields above ~430 Gauss, and making the NMR for the low field range of 180 Gauss – 350 Gauss is very challenging. This was accomplished by R&D efforts at CAYLAR [5] to fine-tune their model NMR20 Nuclear Magnetic Resonance (NMR) Gaussmeter for a low field range. The adapted NMR20 was acceptance tested to perform over 146 – 561 Gauss.

Energy Matching

For successful e-beam cooling of the RHIC beam, the energies of the two beams must be matched with an accuracy of 10^{-4}. Several steps of energy matching will be employed to approach the proper electron beam energy, as illustrated in Fig. 1. In order to get the electron beam energy to such a precise energy, the electron energy will be initially set to within 5% of the ion beam energy by adjusting the RF voltage and then to within 0.3% with feedback from the magnetic spectrometer. Observing recombination monitors [4], finer e-beam energies to within 0.1% will be attained; where the recombination rate will be maximized with further alignment and scanning of the RF phase. By observing the ion beam Schottky spectrum while further adjusting the beam position and RF phase, the final e-beam energy will be set to match to within 0.01%, required for cooling.

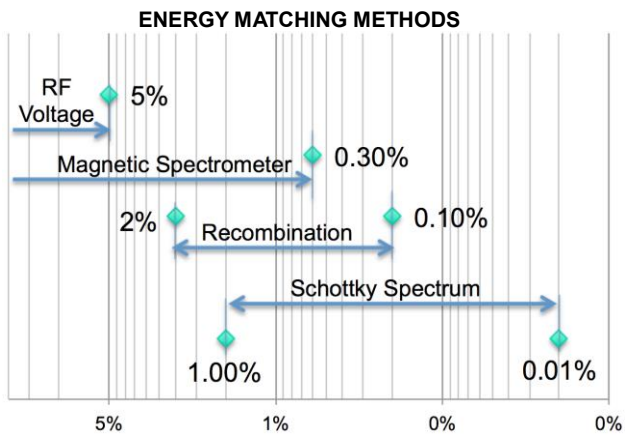

Figure 1: Several methods of energy matching will be employed as a strategy to reach the requirement for cooling. Each method spans a different range of energy matching precision.

MAGNETIC SPECTROMETER

The spectrometer is composed of the 180° dipole magnet and three BPMs [6], as shown in Fig. 2. The 180° dipole magnet design parameters are shown in Table 1 below. The magnet design was tailored for its role as a bending magnet but will be measured for use as a sensitive low field spectrometer magnet.

* Work supported by BSA under DOE contract DE-AC02-98CH10886
† tmiller@bnl.gov

ISBN: 978-3-95450-192-2 doi:10.18429/JACoW-IBIC2017-WEPCF05

Table 1: 180° Dipole Magnet Parameters

Parameter	Value	Units
Operating Field	196 – 318	Gauss
Nominal current	2.7 – 4.2	A
Maximum current	7.3	A
Coil resistance (65°C)	5.5	Ω
Coil Inductance	3.6	H
Number of turns	298	
Pole face	50 x 110	cm
Gap	10	cm
Core material	1005 Low Carbon Steel	

The spectrometer is designed for parallel beam entry and exit, and has a bending radius of $\rho_0 = 0.35$ m. The radius of beam curvature through the magnet varies as a function of beam energy and results in a horizontal beam displacement at the exit. This displacement is an indication of the absolute beam energy.

The first BPM along with the horizontal BPM in the first HyPM will be used to measure the beam entry position and angle. The two horizontal BPMs in the HyPM's will be used to measure the horizontal displacement. At the heart of the spectrometer is the measurement of the absolute magnetic field. This is measured by the permanently mounted NMR probe in the gap of the magnet. Together with the integral of the field map through the beam trajectory, the NMR reading is combined with the beam displacement from the BPMs to give the absolute beam energy.

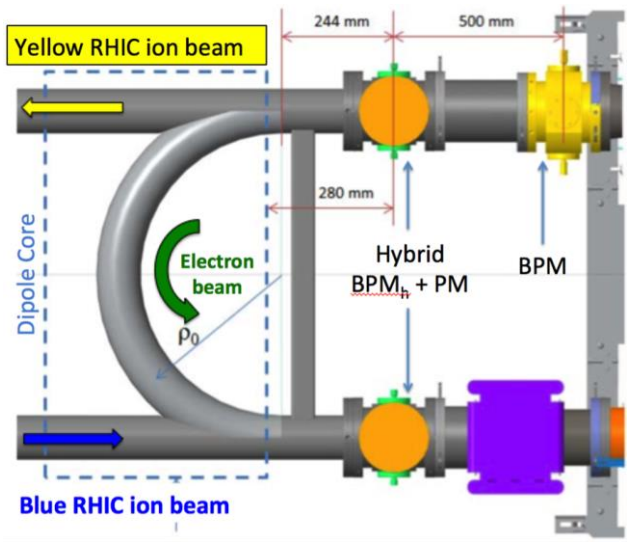

Figure 2: Layout of the magnetic spectrometer.

Accuracy Study

A study was made of the expected precision with which the energy of the beam can be measured [7]. It was found that using the hard edge approximation, the error in measured energy would be too large. Thus to measure real beam energy with a required accuracy of 0.1%, a proper Taylor expansion of the exact expression for magnetic rigidity was performed, resulting in equation (1) below.

$$x_{out} = -x_{in} - 2\rho_0 \frac{E_0+mc^2}{E_0+2mc2}\delta \quad (1)$$

The horizontal beam displacement, given by x_{out} - x_{in} in Eq. (1), is shown in the diagram of Fig. 3. The absolute error of the BPM readings includes the accuracy of the BPM alignment, one with respect to the other and with respect to the dipole, and the reading accuracy per se.

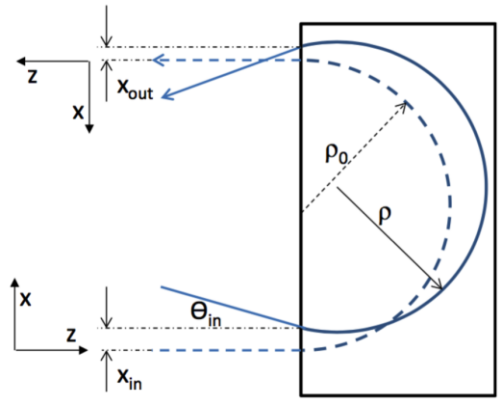

Figure 3: Beam trajectory and angles defined. Bending radius $\rho_0 = 0.35$ m.

Given the accuracy of the magnetic field measurement setting of 0.1%, and the absolute error of the BPM readings to be 0.1mm, then a worst-case accuracy of the energy measurement, at 1.6 MeV, was found to be $\delta = 2\text{x}10^{-3}$. For a case of relaxed BPM measurement/setting error of 0.5 mm, a resulting $\delta = 5\text{x}10^{-3}$ was found.

Possible accuracy errors were included in a simulation, including those for the magnetic probe, dipole current, field quality, ambient magnetic field, and beam trajectory errors. These were included in such a fashion that the total resulting measurement error was maximized. Simulating a 5%-off-energy beam trajectory in the dipole and calculating the measured energy according to Eq. (1), a real beam energy accuracy of $2.6\text{x}10^{-3}$ was found, and of $6.7\text{x}10^{-3}$ in the worst case.

MAGNETIC MEASUREMENTS

Received at the end of 2016, the 180° dipole magnet was staged in the Magnet Division at BNL for field mapping. A customized low-field gaussmeter probe was purchased and mounted on a two-axis motion scanning system to move the probe through the beam trajectory and log the field data for both a Hall sensor and an NMR sensor. The servo-motors with linear optical position encoders are controlled by a LabView based program that also collects field data from the gaussmeter and builds a data map. Figure 5 shows such a map containing five arcs across spanning an area ±20 mm on either side of the 130 cm beam trajectory through the magnet.

The design field value from simulation is shown as the red curve in Fig. 6; where the black curve shows the mapped field along the central arc (radius $\rho_0 = 0.35$ m) in the mid-plane. The mapped data was taken at 318 Gauss

ISBN: 978-3-95450-192-2 doi:10.18429/JACoW-IBIC2017-WEPCF05

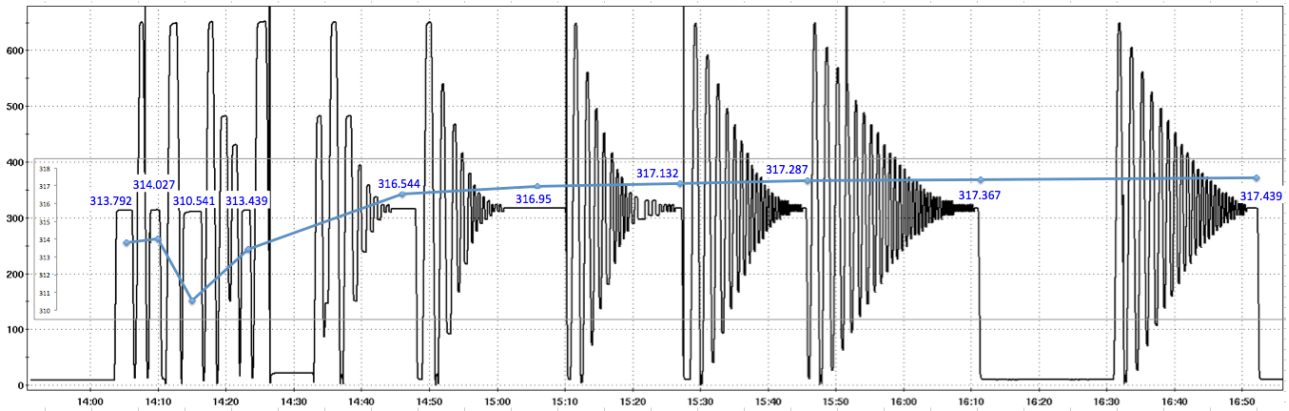

Figure 4: Plot of field measurement (Gauss) vs time. Results of hysteresis loop cycling optimization study. Final value around operating field approaches the field value with residual fields eliminated.

(for 2.6 MeV) and scaled down to 196 Gauss (for 1.6 MeV). Comparing the two field data sets, the fringe field is lower than expected and the central pole field is higher with some non-uniformity.

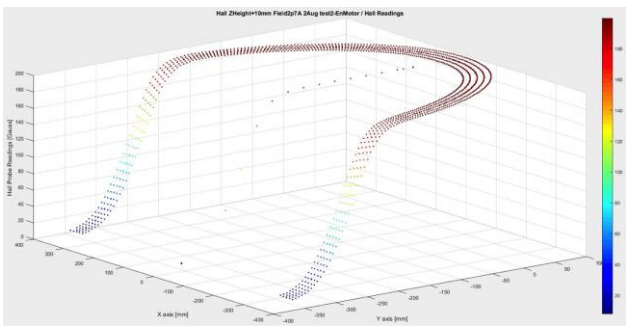

Figure 5: Plot Hall probe measurement of field at 2.7A.

The field measurement must be very repeatable to have confidence that its value or distribution does not change during operation. In order to ensure repeatability, all residual magnetism must be removed from the iron core so that the current applied to the coils can determine the field. To ensure this, a hysteresis cycle is made by cycling the current before measurements are made.

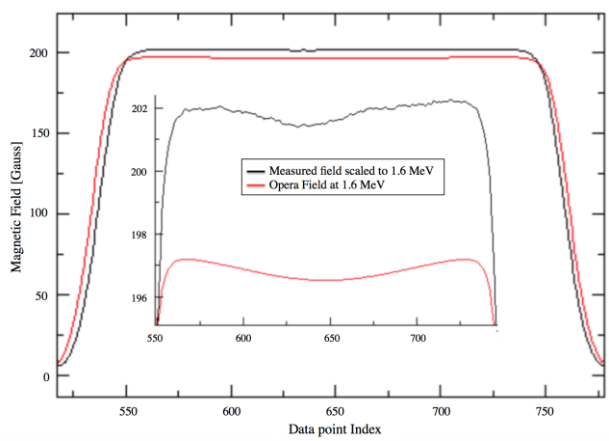

Figure 6: Plot of the design field versus the mapped field through the central beam trajectory.

Hysteresis Cycle

With such a low field magnet, small non-uniform residual fields can alter the total integrated field of the magnet. Thus, development time was spent to perfect a hysteresis cycle to eliminate residual fields in the steel core. As we cannot know what the absolute field value should be, we started with a simple ramp to the operating point that leaves a residual field and followed with multiple bipolar cycles around the operating point with an exponential taper to the envelope, as shown in Fig. 4. As the residual field is eliminated more and more, the final value approaches the ideal, as shown by the curve of final values in Fig. 4. The last curve with 48 cycles is deemed sufficient as it reaches a final value within < 1 milligauss of the former cycle.

Further investigation of the effect of the envelope was made by analysing the final value after a linear, exponential, and linear + exponential curves, as shown in Fig. 7. The results show final values from all three that are within ± 10 milligauss of one another. Thus, no further optimization was deemed necessary.

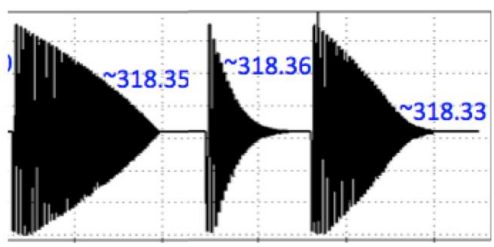

Figure 7: Plot of field measurement (Gauss) vs time. Comparison of hysteresis loop shape. Left to right: linear, exponential, and linear + exponential.

A final hysteresis cycle type was adopted based on the last cycle in Fig. 7. This loop runs for 28 min with a 0.4 A/sec ramp rate, with an amplitude of ±4.2A around the operating point. There will be several operating points, spanning 196 – 318 Gauss (1.6 – 2.7 MeV). The cycle is composed of steps of power supply current (mA), alternating about the operational value within an envelope defined by and exponential function (2) where K is some

ISBN: 978-3-95450-192-2 doi:10.18429/JACoW-IBIC2017-WEPCF05

$$\pm Ke^{cn}|_{n=0-24} \quad (2)$$

value between 2.6 A – 4.2 A, c = 0.075, and with a 20 second hold time at each value. The hysteresis cycle is run each time the magnet is set to a new operating point to ensure a repeatable absolute magnetic field. This was applied to the magnet field mapping techniques carried out and will be used during the operation of the magnet as a spectrometer in LEReC.

INSTRUMENTATION

The instrumentation required to implement the magnetic spectrometer relies heavily on the gaussmeter to assure a known dipole field. This works in conjunction with the BPM's and two HyPM's to realize the spectrometer.

NMR Gaussmeter

In order to have an absolute magnetic field measurement, for the spectrometer and to perform full field mapping (including the fringe field), a combination NMR + Hall type gaussmeter was chosen.

It is a property of atomic nuclei with a non-zero spin to align with a magnetic field applied to it. When the right amount of energy is supplied, a tilting of their spin is induced in the opposite direction. Nuclear Magnetic Resonance (NMR) occurs when a radio-frequency (RF) field applied to a sample, having just the right frequency called the Larmor frequency, induces this spin-flip. The energy difference between the aligned and counter-aligned nuclear states depends linearly on the strength of the magnetic field. The ratio between the resonant frequency and the magnetic field strength is a physical constant called the gyromagnetic ratio (γ). In the case of the proton (hydrogen nucleus) this is equal to $\gamma p/2\pi$ = 42.5774806 MHz per Tesla.

The NMR20 Gaussmeter, developed by CAYLAR [5], uses a probe containing a sample of a material consisting of many chains of hydrogen atoms. By exciting this sample with an RF field from a controlled oscillator, and measuring the sample's response, the resonance frequency of the sample can be locked onto and tracked. This measured resonant frequency precisely determines the magnetic field in which the probe sits. The absolute precision of the measurement of the magnetic field is on the order of 10e-6. The relative precision pertains to the frequency measurement; which in the NMR20 Gaussmeter is ten times better – on the order of 10^{-7}.

This version of the NMR20 is a unique model made for the low field requirement of LEReC. A main design challenge was the extension of the sample from the electronics by 40cm to remove the electronics from the higher radiation area in the beam horizontal plane.

Since the magnetic field to be measured in the LEReC 180° dipole is lower than usual, the nuclei in the sample are weakly aligned with the magnetic field, which induces a weak NMR response. To increase the response to obtain a usable signal, a sample of size greater than those used usually was developed to increase the number of atoms participating in the NMR. The electronics of the probe were also modified to improve the signal-to-noise ratio of the NMR signal allowing better detection and therefore a better stability of the measurement.

A preamplifier will be located near the probe installed in the 180° magnet in the RHIC tunnel. The preamplifier splits the NMR signal into an HF narrow-band signal for measuring the NMR frequency and a LF wide-band signal for detecting the resonance lock. A low pass filter was also added to the HF input of the gaussmeter to prevent high frequency signals from interfering with the measurement in the lower frequency range in this low-field application.

We tested the NMR20 in "Manual" mode where the resonance peak is searched for with course and fine adjustment potentiometers. A "Hall Tracking" mode was used during field mapping to limit the "Automatic" mode's peak search to ±5% of the Hall field reading while varying the field level during the hysteresis cycles. Once the probe is permanently mounted in the 180° dipole magnet, the "Digital" mode will be used with the reference field set according to the expected energy to limit the "Automatic" mode's peak search to ±5% of the operating field value. For remote control and monitoring, the gaussmeter includes Ethernet and RS232 connectivity. Custom controls software was written to interface with the NMR20 via Ethernet.

Acceptance testing of the NMR20 was performed with the 180° dipole magnet with the 100 m long cable bundle to simulate actual conditions. Automatic detection and lock onto the NMR signal was achieved over a field range of 146 – 561 Gauss, which is much better than the project requirements of 180 – 350 Gauss.

DIPOLE FIELD REGULATION

In order to stabilize the magnetic field over long periods of time, a software based feedback loop, shown in Fig. 8, will be implemented to correct the magnet power supply current in small increments based on NMR field measurements collected a 1-Hz rate. Gaussian statistics are used to extract the exact field measurement where the long-term change is buried in the noise among measurements.

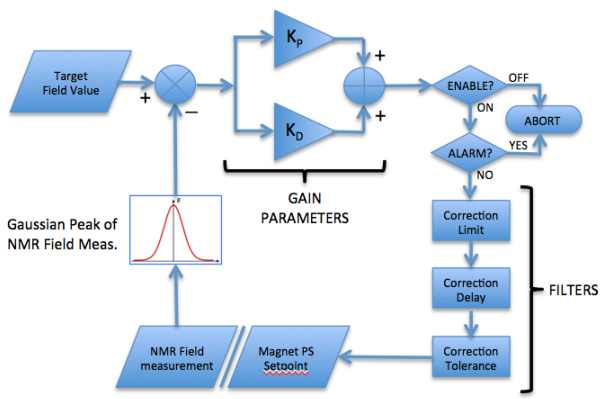

Figure 8: Software based regulation loop.

The peak of the Gaussian, accumulated over an adjustable period of several minutes, is compared to a target value. When the difference surpasses an adjustable dependant

ISBN: 978-3-95450-192-2 doi:10.18429/JACoW-IBIC2017-WEPCF05

variable tolerance, a correction is applied to the power supply setpoint based on a proportional-differential gain. A minimum delay between corrections can be set to limit the rate of correction. The applied correction can be limited by a maximum correction step to filter out responses to possible system failures.

The regulation loop is aborted if the power supply is turned off, the correction value exceeds a predefined limit, or the power supply setpoint is changed by another process. Status values for these conditions are reported along with the difference between target and measurement as status conditions.

STATUS AND CONCLUSION

After the 180° magnet field measurements are complete in September of this year, the magnet will be installed in the RHIC tunnel along with its associated instrumentation and the beam line will be closed by December 2017. The field regulation will be tested with the magnet, power supply and gaussmeter in their final installed places. Eight-hour stability tests will be run on the magnetic field with and without the software feedback loop for comparison.

The full LEReC accelerator is scheduled to be installed by January 2018. All accelerator systems and electron beam transport will be commissioned thereafter in preparation for electron-cooling of Au ions in RHIC in 2019.

ACKNOWLEDGMENTS

The authors would like to acknowledge the contributions and support from W. Fischer and J. Tuozzolo, members of the Superconducting Magnet Division, especially P. Joshi, members of the Controls Group, especially P. Harvey, J. Jamilkowski, and J. Morris, as well as members of the Accelerator Components & Instrumentation Group, especially A. Curcio, D. Lehn, and J. Renta, as well as members of the Mechanical Design Group, especially K. Hamdi.

REFERENCES

[1] A. Fedotov *et al.*, "Bunched Beam Electron Cooler for Low-Energy RHIC Operation", in *Proc. NA-PAC'13*, Pasadena, CA, USA, Sept. 2013, paper TUOAA1.

[2] M. Blaskiewicz, "Dead Reckoning Energy in RHIC", private communication, Sept. 2016.

[3] T. Miller, *et al.*, "LEReC Instrumentation Design & Construction", in *Proc. IBIC'16,* Barcelona, Spain, Sept. 2016, paper TUPG35.

[4] T. Miller, *et al.*, "Multifunction Instrument Designs with Low Impedance Structures for Profile Energy, and Emittance Measurements for LEReC at BNL", in *Proc. IBIC'15*, Melbourne, Australia, Sept. 2015, paper TUPB007.

[5] CAYLAR Scientific Instrumentation, Villebon-sur-Yvette, FRANCE, https://www.caylar.net

[6] Z. Sorrell, P. Cerniglia, R. Hulsart, R. Michnoff, "Beam Position Monitors for LEReC", in *Proc. IBIC'16*, Barcelona, Spain, Sept. 2016, paper MOPG08.

[7] S. Seletskiy, "How to Measure Energy of LEReC EEcgron Beam with Magnetic Spectrometer", Collider-Accelerator Dept., BNL, Upton, NY, USA, C-A/AP /562, BNL-112105-2016-IR, April 2016.

ISBN: 978-3-95450-192-2 doi:10.18429/JACoW-IBIC2017-WEPCF06

R&D PROGRESS ON PRECISION CURRENT MONITORING AND CALIBRATION SYSTEMS FOR THE APS UPGRADE UNIPOLAR MAGNET POWER SUPPLIES*

R. Keane#, J. Carwardine, B. Deriy, T. Fors, J. Wang,
Argonne National Laboratory, Lemont, IL

Abstract

The APS Upgrade storage ring multi-bend acromat lattice uses 1000 individually-powered multi-pole magnets operating at current levels to ~260 A. Requirements for power-supply stability, repeatibility and reproducibility are of the order of 10 ppm. MBA SR quad magn et and Q-bend dipole magnet current regulation will require a higher level of accuracy, precision, stability, and independent control than existing APS systems. In order to meet these requirements, the upgrade will include the installation of 1000 new unipolar power supplies. To monitor and ensure the performance of the power supplies, an independent precision current measurement system is under development, based on a commercially available DCCT sensor. An in-situ calibration system is also required that will maintain the ensemble accuracy of the measurement system and magnet-to-magnet relative calibration by providing precise known calibration current to each of the 1000 DCCTs distributed around the 1100-meter ring. R&D on the in-situ cross-calibration scheme is being performed using a network of 6-8 full-spec DCCTs. This paper discusses the proposed approach, and results and lessons from the R&D program.

INTRODUCTION

Figure 1 shows the conceptual design of the external precision current measurement and calibration system. An interface chassis will provide connections for six DCCTs and will house the current-to-voltage converting circuitry and ADC required to produce a digital current reading. Each power supply cabinet will contain one interface chassis; approximately 200 chassis will be needed for the entire system. The raw digital data is sent to the Power Supply Controller (PSC) through an SPI link, and will be available to the system over Ethernet. A calibration circuit will also be housed in the interface chassis to allow in-situ calibrations of each DCCT through built-in calibration windings. Calibration factors will be applied in the PSC FPGA, or in software, to provide calibrated current read-outs. Calibration will be fully automated and performed remotely, at intervals to be determined by data gathered during further performance testing on the preliminary design hardware.

* Work supported by the U.S. Department of Energy, Office of Science, Office of Basic Energy Sciences, under Contract No. DE-AC02-06CH11357.
#keane@anl.gov

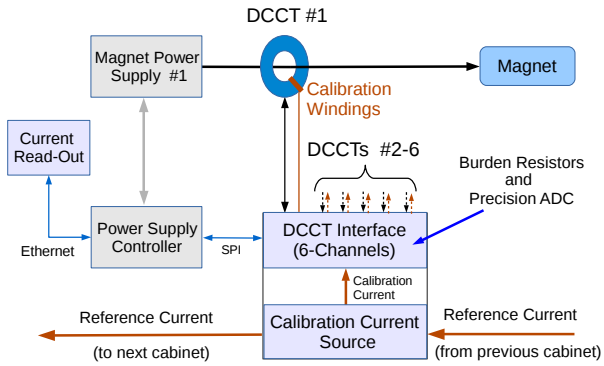

Figure 1: Current measurement and calibration system.

CURRENT MEASUREMENT SYSTEM

DCCT Current Sensor and Burden Resistor

DCCT technology is considered the standard for high-precision current measurement[1], and is capable of very high levels of accuracy, precision and stability. The DCCT is an active, non-interrupting device that produces an output current proportional to the primary DC current. The DCCT under investigation (DaniSence DS200CLSA- 1000) uses a 1:500 ratio, i.e. a 200 A primary current results in a 400 mA secondary output current. This DCCT model has excellent stability and linearity specifications, and includes a built-in calibration winding of 1000 turns. The secondary current is converted to a voltage using a precision burden resistor, and read-out by a precision voltmeter or ADC. Some DCCT models incorporate the burden resistor in the internal circuitry to provide a direct voltage output. Performance of the DCCT system depends strongly on burden resistor performance, so using an external burden resistor allows for better control of the resistor parameters and environmental conditions, particularly thermal conditions. Figure 2 shows the basic components of a DCCT-based current measurement channel.

ISBN: 978-3-95450-192-2 doi:10.18429/JACoW-IBIC2017-WEPCF06

Early R&D for the ADC circuit was conducted separately from the analog components (DCCT and burden resistor). For lab testing of the analog components, a Keysight 3458A DMM along with a multiplex switch was used to digitize the current readings in place of the ADC.

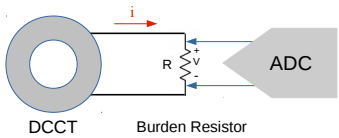

Figure 2: Basic components of a current measurement channel.

CALIBRATION SYSTEM

The current reference is a commercial variable current source that provides a low-noise, stable current from 0 to +/- 110 mA (Krohn-Hite model 523). The voltage output is limited to 110 VDC. Since the calibration winding impedance in the DCCT is on the order of 30 ohms for the unit under investigation, direct (in-series) calibration is limited to a few dozen DCCTs at a time using the instrument directly. A second limitation is the maximum output current of 110 mA. The magnet current specification of 260 A needs a full-scale measurement capability of at least this value, which requires 260 mA into the 1000x calibration winding in the DCCT in order to calibrate at the operating point.

Precision Local Current Source

In order to produce the ~300 mA needed to calibrate over the full range of the measurement system, the 110 mA source needs to be increased by a factor of three. This is achieved using a scheme adopted from NSLS-II [2] and shown in Figure 3. Current is driven through the calibration winding of the DCCT in a local current loop fed from a (non-precision) DC power supply that is regulated using a nulling circuit and additional DCCT, whose calibration winding is fed from the KH523 precision source. A similar circuit was built and tested successfully as a 10 A source during the early stages of R&D.

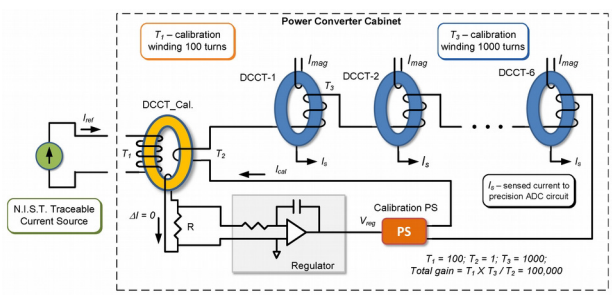

Figure 3: Precision local current source circuit.

Calibration Standards and Traceability

Per manufacturer specifications, the KH523 precision current source must be periodically calibrated using a NIST-traceable precision resistor (Krohn-Hite Model PCR100) and a calibrated NIST-traceable Keysight 3458A DMM. Stability specifications of the KH523 current source, PCR100 resistor, and 3458A DMM are listed in Tables 1-3. The limited time stability of the KH523 requires frequent re-calibration to the transfer sources in order to maintain accuracy over time. This method allows for in-place calibration of the KH525 current source.

Table 1: KH523 Current Source Specifications

Resolution	Stability (24 Hrs)	Max. Output
10 nA	± 2 ppm typ.	110 mA, 110 V

Table 2: PCR100 Calibration Resistor Specifications

Initial Accuracy	Stability (1 Year)	Max. Current
± 0.5 ppm	± 2 ppm typ. ± 6 ppm max.	110 mA

Table 3: Keysight 3458A-004 DVM Specifications

Transfer Accuracy	Accuracy (90 days)	Accuracy (1 Year)
± 0.55 ppm	2.7 ppm	4 ppm

Calibration Reference Current Distribution

A common calibration reference current for all 1000 channels is highly desirable in order to maintain channel-to-channel accuracy. This will require routing the reference current over distances of hundreds of meters. Testing was performed on the KH523 current source to determine its performance over long cable runs. The test set-up consisted of a KH523 sourcing 100 mA through twisted-pair cable to a 100 ohm precision resistor (Krohn-Hite PCR100). The voltage across the resistor was read with a Keysight 3458A DVM. A short, direct run of 4 feet was used as the baseline. Then, the same current was routed through 1600 feet of cable, then though the calibration windings of 4 DCCTs and an additional 100 ohm resistor. Voltage readings were again taken across the PCR100 resistor. The results are shown in Figure 4, and indicate an insignificant effect from the long cable run. The 16 ppm offset in the plotted data is due to the calibration resistor actual value deviation from the nominal 100 ohms.

ISBN: 978-3-95450-192-2 doi:10.18429/JACoW-IBIC2017-WEPCF06

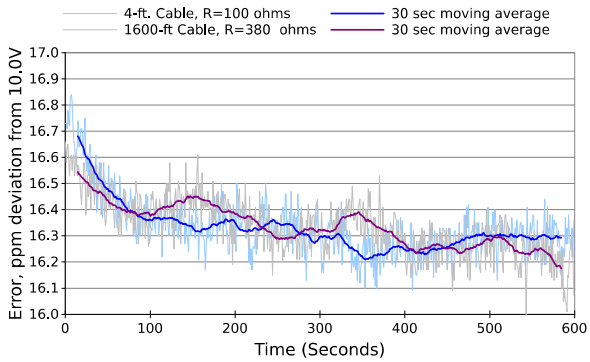

Figure 4: Reference current measurement for short and long current paths.

Full Range Calibration Test

Initially, the magnet current specification was around 190 A, which would have required a full scale range of 200 A. Testing was performed to determine limitations of linear regression calibration over the entire measurement range of 0 to 200 A using the 1000-turn calibration winding in the DCCT. For this test, 200 mA calibration current was achieved by combining the outputs of two KH523 instruments in parallel through a resistor network. After calibration, the DCCTs were used to measure a common primary current from a 200 A power supply, in order to compare the calibrated readings between units (see Figure 5).

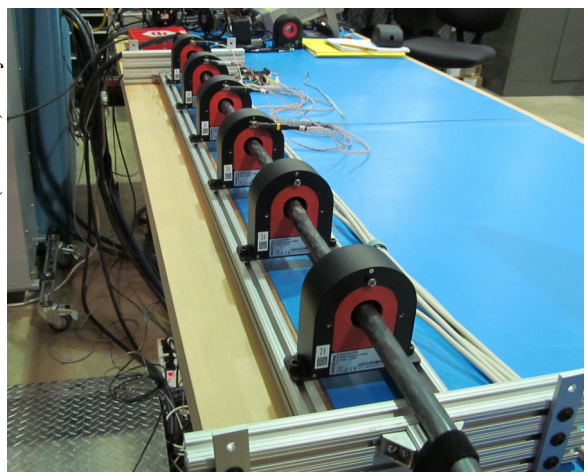

Figure 5: DCCT evaluation with common primary current.

Test results indicated that a single linear calibration over the full range was not adequate; linearity errors were over 10 ppm at the lower end on the scale. A four-zone calibration (50 A per zone), with separate gain-offset pairs for each zone, worked very well for four DCCTs. The results of common primary current measurements for the four DCCTs after the four-zone calibration are plotted in Figure 6, and show agreement within ~3 ppm at all currents. The test also revealed that 2 DCCTs showed unacceptable differences (10-20 ppm) when reading the common primary current after calibration.

These two units were returned to the vendor for evaluation. Consistent agreement between current readings through the primary and calibration windings is a critical requirement, and this issue needs to be examined further.

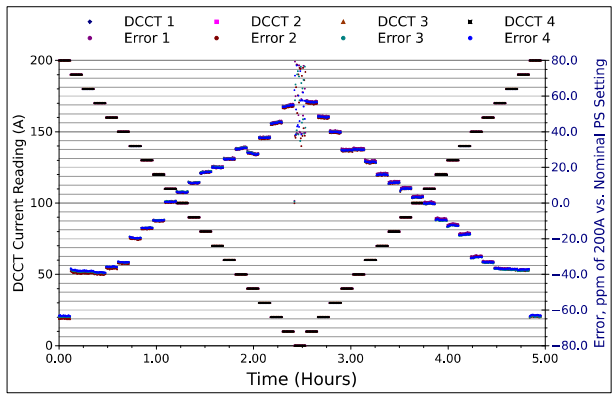

Figure 6: Common primary current from PS measured by four DCCTs after four-zone linear calibration, and the error vs. nominal power supply current setting.

CONCLUSION

Components and processes for a precision current measurement system that will meet better than 10 ppm accuracy and precision have been identified and demonstrated. Sub-5 ppm performance appears possible, but will be challenging and require careful attention to component selection, temperature control, and calibration methods and schedule. The preliminary design is underway for a DCCT interface chassis that will include a custom ADC circuit and temperature-controlled burden resistors, along with a calibration current source and digital interface to the PSC.

Several schemes have been investigated to calibrate all 1000 DCCTs in-situ to a common reference current. R&D results demonstrate that the reference current source under investigation (Krohn-Hite Model 523) can distribute current over the longs lengths necessary. One concern was the lack of agreement between calibration winding and primary current response for two of the six DCCTs examined; this could be an anomaly or a systematic issue. Work to develop a fully automatic, remote calibration system continues.

REFERENCES

[1] M. Cerqueira Bastos, "High Precision Current Measurement for Power Converters", in *Proceedings of the CAS-CERN Accelerator School: Power Converters,* Baden, Switzerland, May 2014.

[2] G. Ganetis, private communication, June 2015.

ISBN: 978-3-95450-192-2 doi:10.18429/JACoW-IBIC2017-WEPCF07

CRYOGENIC CURRENT COMPARATORS FOR 150 mm BEAMLINE DIAMETER*

V. Tympel†, Th. Stoehlker[1, 2], Helmholtz Institut Jena, 07743 Jena, Germany
F. Kurian[1], M. Schwickert[1], T. Sieber[1]
R. Neubert, F. Schmidl, P. Seidel, Institute of Solid State Physics, 07743 Jena, Germany
M. Schmelz, R. Stolz, Leibniz Institute of Photonic Technology IPHT, 07745 Jena, Germany
V. Zakosarenko, Supracon AG, 07751 Jena, Germany
[1]also at GSI Helmholtzzentrum für Schwerionenforschung, 64291 Darmstadt, Germany
[2]also at Institute for Optics and Quantum Electronics, 07743 Jena, Germany

Abstract

New versions of Cryogenic Current Comparator (CCC) sensors with eXtended Dimensions (CCC-XD) for beamline diameters of up to 150 mm – necessary for the planned Facility for Antiproton and Ion Research (FAIR) at GSI (Gesellschaft für Schwerionenforschung) – have been realized. These non-destructive charged particle beam monitoring systems are able to measure intensities in the nA-range with a white noise level below 5 pA/√(Hz). The systems are sensitive from DC to several hundred kilohertz and can be linked up in a traceable way with national and international ampere-standards.

In its present design, the base body consists of a highly-permeable, nano-crystalline core optimized for low-temperatures (ready for superfluid He-II applications) [1] and a niobium shielding/pickup-coil unit. The flexible SQUID (Superconducting Quantum Interference Device) - cartridge allows tuning for application. Three cartridge versions (direct, balanced and enhanced) are presented, discussed and results of electrical laboratory measurements of the noise behaviour and the frequency response are given.

OPERATION PRINCIPLE

The key to measure the beam intensity non-destructively is to measure the magnetic field component created by the charged particle. The main parts of a CCC are shown in Fig. 1.

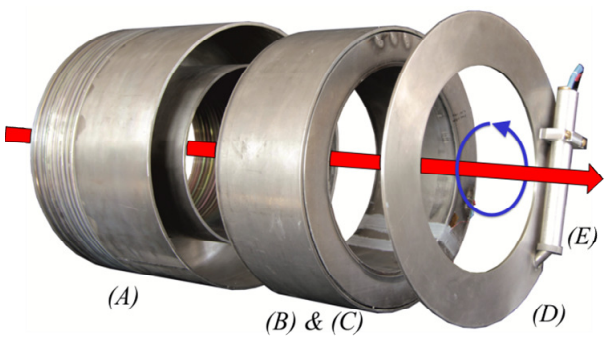

Figure 1: Exploded view of classical meander design CCC as used at CERN; red: charged particle beam; blue: magnetic field, courtesy of R. Geithner.

* Work supported by the BMBF, project number 05P15SJRBA.
† volker.tympel@uni-jena.de

(A) Superconducting Meander Shielding

This shielding separates the concentric magnetic field component created by the charged particle from the interference created by surroundings. Two long coaxial tubes – shorted by a complex meander structure – act as a filter [2, 3]. The meander structure has no electrical connection between both parts and creates a frequency-independent parasitic capacity C_m in the nF-range. For the CCC-XD shielding – consisting of about approximately 65 kg niobium – the measured parasitic capacity is about 40 nF.

(B) Flux Concentrator

A special, highly-permeable, nano-crystalline core – optimized for low-temperature applications – concentrates the magnetic field at the end of the tubes. In cooperation with MAGNETEC GmbH the GSI328plus core was developed and used for CCC-XD [4].

(C) Superconducting Pickup Coil

A full faced, one-turn, superconducting pickup coil covers the flux concentrator and creates a frequency-dependent inductance L_{pu} in the range of (10 to 100) µH at a temperature of 4 K. The pickup coil inductance of the CCC-XD is about 80 µH at 4.2 K and 1 kHz.

(D) Top Cover

A superconductive connection between both parts of the meander shielding tubes completes the shielding and also creates a full faced, one-turn frequency-dependent coupling coil inductance L_m – similar to the pickup coil. This inductance and the parasitic capacity C_m produce a LC-resonator which can be simulated for example with LTspice.

(E) SQUID-Cartridge

The cartridge includes the SQUID as the current meter and additional components like the matching transformer for inductance coupling.

Benefit of Superconductivity

The superconductivity with Meissner effect, Josephson effect and the flux quantization are necessary to realize shielding, DC-transformer and an extreme high sensitive current meter [5].

ISBN: 978-3-95450-192-2 doi:10.18429/JACoW-IBIC2017-WEPCF07

EVOLUTION OF CCCs

The development of CCCs for beam instrumentation started in the 90s. The first systems (1996 at GSI and 2009 for BESSY) were Pb-based. The current running system at CERN-AD and the new larger CCC-XD for GSI/FAIR are Nb-based. Optimization is still in progress and the new designs and materials are under investigation [2]. The CCC-XD sensor as shown in Fig. 2 – manufactured in classical radial meander design – is now ready and the first lab measurements with different SQUID-cartridge versions are done.

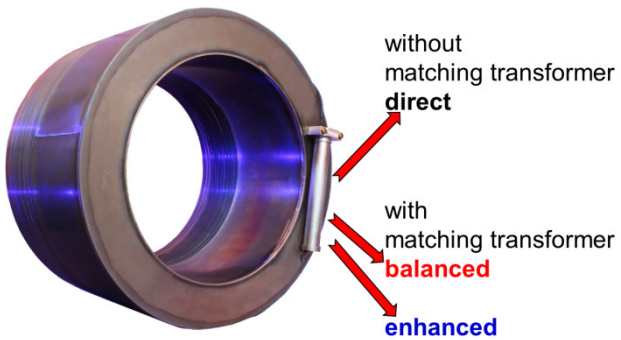

Figure 2: CCC-XD and the three different types of SQUID-cartridge configurations.

SPICE Electronic Simulations

A task of system understanding and application optimization is the electronic design of the SQUID-cartridge. Usually a balanced matching transformer (MT) is used coupling the high inductance pickup coil with the low inductance SQUID input coil [6]. Figure 3 shows a circuit diagram of the balanced MT-version, but also versions without MT or with MT and a higher current magnification. So, the MT influences the additional current magnification and the frequency response as shown in Fig. 4.

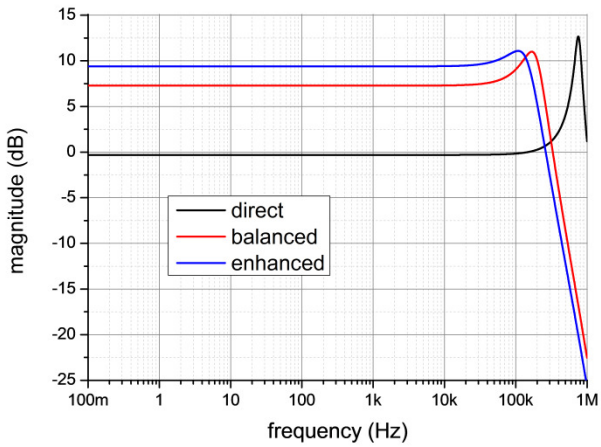

Figure 4: LTspice simulation of amplitude frequency responses. Black (direct): resonance peak at 760 kHz, red (balanced): resonance peak at 170 kHz, blue (enhanced): resonance peak at 115 kHz.

Using L_sR_s inductance measurements of the GSI328plus published in [1] and calculated into the L_pR_s model suitable for higher frequencies it is possible to calculate the LC-resonator frequencies of the cartridge versions. Measurements of the balanced version should have a small resonance peak at 170 kHz and the direct version should have a clear peak about 760 kHz.

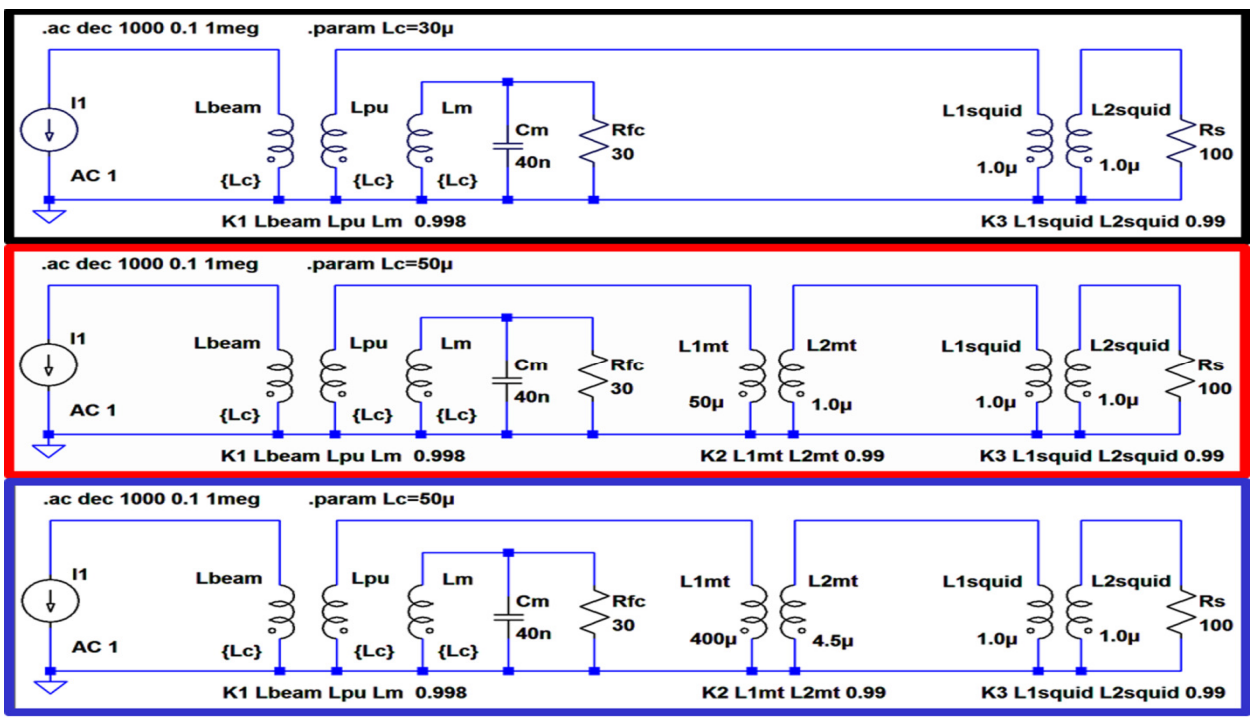

Figure 3: CCC-XD LTspice circuit diagram of the three cartridge versions. Top: direct without MT, middle: balanced with MT and inductance matching, down: enhanced with matching transformer and a higher current magnification.

ISBN: 978-3-95450-192-2 doi:10.18429/JACoW-IBIC2017-WEPCF07

THE CCC-XD FOR GSI/FAIR

The first measurements are done in a wide-necked cryostat inside and outside a magnetic shielded chamber in a lab environment. A wire with an electrical current flow is simulating the charged particle beam if necessary.

Noise Measurement

Figure 5 shows that the white and 1/f input noises of the direct and balanced version are nearly identical and dominated by the core noise which is ten times or more above the SQUID noise. It also shows that there are interference problems between 5 Hz and 100 Hz and that the acoustical noise within the magnetic shielded chamber is not helpful. Clearly visible are – expected by the simulation – resonance peaks measured at 170 kHz (balanced version) and 770 kHz (direct version).

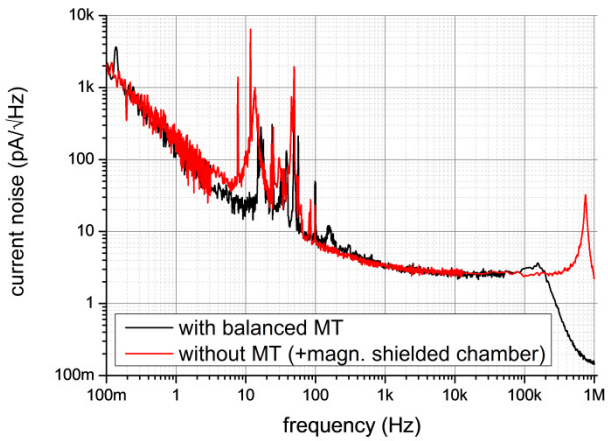

Figure 5: CCC-XD noise measurement, red: direct version with resonance peak at 770 kHz, black: balanced version with resonance peak at 170 kHz.

Sinus Signal Measurement

The small-signal response of the CCC-XD system shows a strong correlation between the signal response and the noise (see Fig. 6). The small-signal frequency bandwidth is about 200 kHz without data processing and it should be feasible to achieve 1 MHz with data processing.

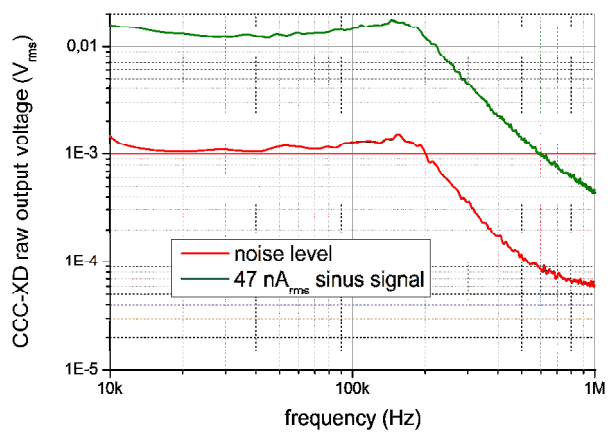

Figure 6: Small-signal response compered to noise level.

The large-signal response (slew-rate) achieved 0.16 µA/µs for the balanced version and 0.32 µA/µs for the direct version at 200 kHz.

Pulse Signal Measurement

Especially the pulse signal response is important for the application in a beamline. Figure 7 shows that in a low-frequency application – like a storage ring with signal integration – it is possible to detect pulses of a few nanoamperes. The used analogue 10 kHz low-pass filter enables the detection of very low-level pulses. Unfortunately the slew rate is also dominated by the low-pass and is reduced to only about 16 pA/µs.

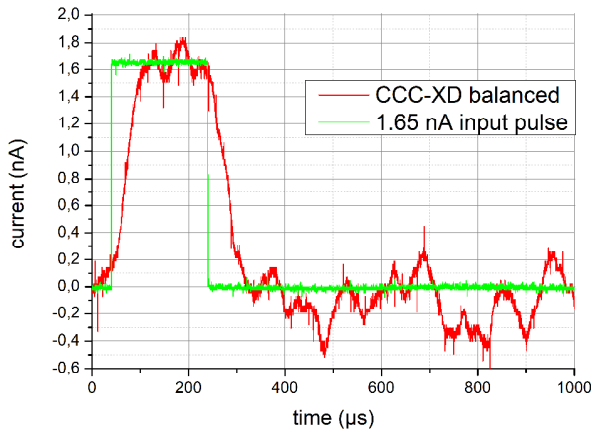

Figure 7: Balanced system response (red) of a low-level 200 µs pulse signal (green), without digital data processing, an analogue 10 kHz low-pass filter is used.

In the case that the full bandwidth is necessary – like in an accelerator line or trigger application – the pulse level should be greater than 5 nA as shown in Fig. 8. Certainly the full CCC-XD slew rate is available again. The source of the lower slew rate for the last 25% is currently under investigation.

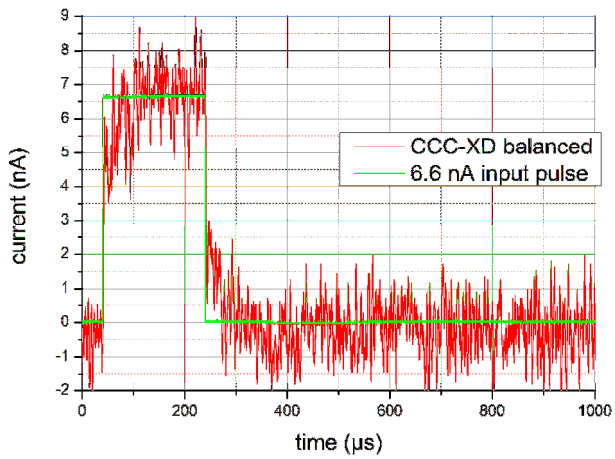

Figure 8: Balanced system response (red) of a low-level 200 µs pulse signal (green), without digital data processing, the full bandwidth of 200 kHz is used.

ISBN: 978-3-95450-192-2 doi:10.18429/JACoW-IBIC2017-WEPCF07

CONCLUSION

We showed that CCC with lager inner diameter can be manufactured. The CCC-XD sensor has been tested in a lab environment and is ready for the integration into its own new beamline-cryostat. Using electronic circuit simulation software it is possible to forecast the frequency response of the complex CCC-system part: beam coil, meander resonator, pickup coil, matching transformer and SQUID input coil. The matching transformer can be used to generate additional current magnification. For the CCC-XD the usable magnification starts at 0.98 (direct version) and ends at 3.7 (enhanced version). Because of dominating core noise the additional magnification is currently not important and it is possible to use a balanced version (magnification 2.8) and a moderate bandwidth of 200 kHz.

ACKNOWLEDGEMENT

We thank the staff of company MAGNETEC GmbH for cooperation developing the special core materials. Furthermore, we thank G. Sobisch and his staff from JOSCH Strahlschweißtechnik GmbH for the excellent manufacturing of the complex niobium CCC-body and R. Geithner for furnishing of the exploded view raw image.

REFERENCES

[1] V. Tympel *et al.*, "The next generation of Cryogenic Current Comparator for Beam Monitoring," in *Proc. IBIC'16*, Barcelona, Spain, Sep. 2016, paper TUPG43, pp. 441-444.

[2] F. Kurian, "Cryogenic current comparators for precise ion beam current measurements," Ph.D. thesis, Dept. Phys., University of Frankfurt, Frankfurt, Germany, 2015.

[3] T. Sieber *et al.*, "Optimization of the Cryogenic Current Comparator (CCC) for Beam Intensity Measurement," presented at IBIC'17, Grand Rapids, MI, USA, Aug. 2017, paper TH2AB03, this conference.

[4] Magnetec, http://www.magnetec.de

[5] W. Vodel, R. Geithner and P. Seidel, "SQUID-Based Cryogenic Current Comparators," in *Applied Superconductivity Handbook on Devices and Applications Volume 2*, P. Seidel, Ed. Weinheim, Germany: Wiley-VCH, 2015, pp. 1096-1110.

[6] R. Geithner, "Optimierung eines kryogenen Stromkomparators für den Einsatz als Strahlmonitor," Ph.D. thesis, Dept. Phys., F. Schiller University Jena, Jena, Germany, 2013.

ISBN: 978-3-95450-192-2 doi:10.18429/JACoW-IBIC2017-WEPCF08

BEAM EXTRACTION BY THE LASER CHARGE EXCHANGE METHOD USING THE 3-MEV LINAC IN J-PARC*

H. Takei†, K. Hirano, and Shin-ichiro Meigo, J-PARC Center, Japan Atomic Energy Agency, Tokai, Ibaraki, JAPAN
K. Tsutsumi, Nippon Advanced Technology Co., Ltd., Tokai, Ibaraki, Japan

Abstract

The Accelerator-driven System (ADS) is one of the candidates for transmuting long-lived nuclides, such as minor actinide (MA), produced by nuclear reactors. For efficient transmutation of the MA, a precise prediction of neutronics of ADS is required. In order to obtain the neutronics data for the ADS, the Japan Proton Accelerator Research Complex (J-PARC) has a plan to build the Transmutation Physics Experimental Facility (TEF-P), in which a 400-MeV negative proton (H^-) beam will be delivered from the J-PARC linac. Since the TEF-P requires a stable proton beam with a power of less than 10 W, a stable and meticulous beam extraction method is required to extract a small amount of the proton beam from the high power beam using 250 kW. To fulfil this requirement, the Laser Charge Exchange (LCE) method has been developed. The LCE strips the electron of the H^- beam and neutral protons will separate at the bending magnet in the proton beam transport. To demonstrate the charge exchange of the H^-, a LCE experiment was conducted using a linac with energy of 3 MeV in J-PARC. As a result of the experiment, a charge-exchanged H^+ beam with a power of 7.99±0.22 W equivalent was obtained under the J-PARC linac beam condition, and this value almost satisfied the power requirement of the proton beam for the TEF-P.

INTRODUCTION

The Accelerator-driven System (ADS) is one of candidates for transmuting long-lived nuclides such as minor actinide (MA) produced by nuclear reactors [1]. For the efficient transmutation of MA, precise prediction of the neutronic performance of ADS is required. In order to obtain the neutronics data for the ADS, the Japan Proton Accelerator Research Complex (J-PARC) has a plan to build the Transmutation Physics Experimental Facility (TEF-P) [2], one of the two buildings of the Transmutation Experimental Facility (TEF) [3]. The critical assembly installed in the TEF-P, which is a small and low power reactor, operates below 500 W to prevent excessive radio-activation. To perform the experiments at the TEF-P with such reactor power, with an effective neutron multiplication factor (k_{eff}) of around 0.97, the incident proton beam power must be less than 10 W. Because the J-PARC accelerators focus on much higher beam power, a low power proton beam extraction device of high reliability is indispensable.

The development of a laser charge exchange (LCE) technique for extraction of the low power proton beam from the high power proton beam is now underway. The LCE technique was originally developed to measure the proton beam profile [4] and applied to the beam forming device [5]. To apply the LCE technique to the beam extraction device for the TEF-P, it is important to evaluate the efficiency of conversion to the low power proton beam and the long-term power stability of the low power proton beam in order to keep the thermal power of the assembly constant. Thus, a LCE experiment to measure the power of the low power proton beam was conducted using a linac with energy of 3 MeV in J-PARC. As already mentioned the preliminary results of the LCE experiment [6], the latest results are presented in this paper.

LCE DEVICE IN THE MAGNETIC FIELD

Figure 1 illustrates the concept of the LCE device for the TEF-P [7]. When a laser beam is injected into a negative proton (H^-) beam with energy of 400 MeV from the J-PARC linac, the charge of the H^- beam crossed with the laser beam becomes neutral (H^0). Here, the remaining H^- beam is introduced to the lead-bismuth spallation target in the ADS Target Test Facility (TEF-T) [3], other building of the TEF.

Since the outer electron of the H^- is very weakly bound to the atom, it can easily be stripped by a laser light in the wavelength range of 800~1100 nm as shown in Fig.2 [8].

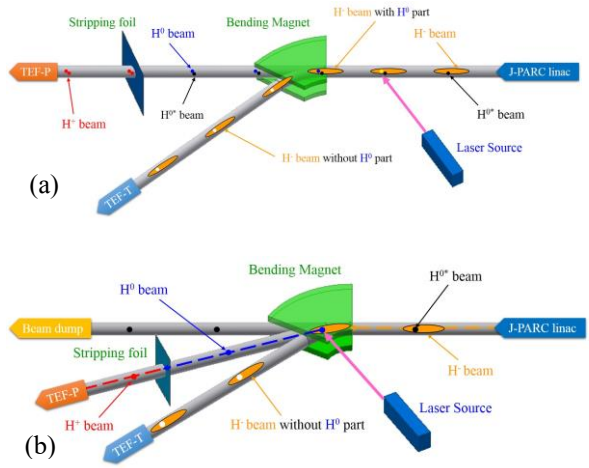

Figure 1: Conceptual diagram of the LCE device for TEF-P. For (a), the laser light is injected in the straight section of the H^- beam line. On the other hand, for (b), the laser light is injected in the bending section of the magnet. The neutralized proton due to interaction by the laser light is written as "H^{0*}", and the pre-neutralized proton due to interaction by the remaining gas in accelerator tubes is written as "H^{0*}".

* This paper summarizes results obtained with the Subsidy for Research and Development on Nuclear Transmutation Technology.
† takei.hayanori@jaea.go.jp

ISBN: 978-3-95450-192-2 doi:10.18429/JACoW-IBIC2017-WEPCF08

These H^0 protons do not sense the magnetic field of a bending magnet, and are completely separated from the remaining H^- beam at the exit of the bending magnet. However, it is well-known that pre-neutralized H^0 particles are produced by collision with the remaining gas in accelerator tubes and are transported with the main proton beam. When we apply the LCE technique to the H^- beam with the pre-neutralized protons, it becomes impossible to predict the total power of the extracted beam.

To eliminate the pre-neutralized protons, we were trying to perform laser injection and beam bending simultaneously in one magnet [7]. When the laser is injected in the magnetic field of the bending magnet, the pre-neutralized proton goes straight along the beam inlet direction and can be separated from the clean low power proton beam at the exit of the bending magnet. The charge-exchanged H^0 beam reaches the stripping foil. After passing the stripping foil, the H^0 beam is converted to a positive proton (H^+) beam and then delivered to the TEF-P target. A material with a low melting temperature will be used as the stripping foil to avoid high power beam injection to the TEF-P target. Hereafter, the low power H^+ beam extracted from the high power H^- beam by using this LCE strategy is referred to as "the stripped H^+ beam."

Figure 2 shows the photoneutralization cross-section of H^- ions as a function of photon wavelength in the centre-of-mass frame. We chose a fundamental wavelength of 1064 nm from the commercial Nd:YAG laser because this wavelength is near the peak of the photoneutralization cross-section of H^- ions. Even taking the Lorentz contraction effect into consideration, the photoneutralization cross-section for the H^- beam with energy of 400 MeV using the fundamental wavelength of Nd:YAG laser is almost the same as that for the stationary H^- ions using the 1064-nm laser light. On the other hand, the Lorentz contraction effect of the collision with the 3-MeV H^- beam and the 1064-nm laser light is insignificant. It is possible to experimentally estimate the conversion efficiency of the LCE for the TEF-P from the results of the LCE experiment with the 3-MeV linac.

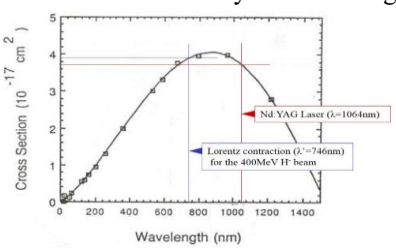

Figure 2: Cross section for H^- photoneutralization as a function of photon wavelength in the centre-of-mass frame [8]. The blue line shows the Lorentz contraction for the H^- beam with 400 MeV.

Table 1: Specifications of the H^- Beam for the J-PARC Linac and the 3-MeV Linac

	J-PARC linac	3-MeV linac
Energy (MeV)	400	3
Maximum beam current (A)	5.0×10^{-2}	3.0×10^{-2}
Macropulse length (s)	5.0×10^{-4}	2.0×10^{-4}
Repetition rate (Hz)	25	25
Maximum beam power (W)	2.5×10^{5}	4.5×10^{2}
RF Frequency (MHz)	324	324
Beam power for a micro-bunch (W)	1.57	6.95×10^{-3}

Table 1 describes the specifications of the H^- beam for the J-PARC linac and the 3-MeV linac. Here, the 3-MeV linac has two operational modes. Specifications for one of these two modes, *i.e.* the LCE experiment mode, are represented in this table. Based on theoretical considerations [9], the outer electrons of the H^- ions can be stripped with an efficiency of almost 100% by using a commercial Nd:YAG laser having a pulse power of a few joules. Therefore, it is expected that a stripped H^+ beam with a power of 1.57 W can be obtained from a micro-bunch of the H^- beam delivered from the J-PARC linac.

LCE EXPERIMENT

Experimental Devices

At J-PARC, a linac with energy of 3 MeV has been constructed for the development of accelerator components such as beam scrapers, bunch shape monitors, laser profile monitors, and so on. This linac consists of an H^- ion source, a low energy beam transport, a radio frequency quadrupole (RFQ) linac, a medium energy beam transport, and beam dumps. For further details about these devices, see ref. [10]. Hereafter, the linac with energy of 3 MeV is referred to as "the 3-MeV linac."

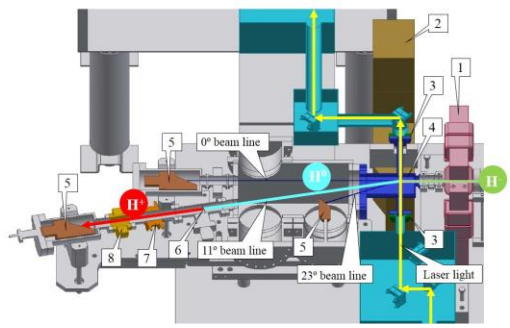

Figure 3: Schematic View of the LCE devices (1-quadrupole magnet, 2-bending magnet, 3-quartz viewing port, 4-vacuum chamber, 5-beam dump, 6-stripping foil, 7-BPM, 8-SCT).

Table 2: Specifications of the Nd:YAG Laser and the He-Ne Laser

	Nd:YAG laser	He-Ne laser
Operation mode	Pulsed	Continuous Wave
Wavelength (m)	1.064×10^{-6}	6.328×10^{-7}
Pulse width (s)	$(5\sim9)\times10^{-9}$	--
Pulse energy (J)	1.6	--
Pulse repetition rate (Hz)	25	--
Power (W)	40	2.0×10^{-2}

ISBN: 978-3-95450-192-2 doi:10.18429/JACoW-IBIC2017-WEPCF08

As shown in Fig. 3, the proton beam line consists of three quadrupole magnets which have a steering function, a bending magnet, a beam position monitor (BPM), beam current monitors, and beam dumps. The LCE devices were installed at the end of the proton beam line. That is, the titanium vacuum chamber was located between two magnetic poles of the bending magnet, in which the H^- beam collided with the Nd:YAG laser light at a near right angle. Two quartz viewing ports were fitted to the vacuum chamber. The commercial high power Q-switched Nd:YAG laser was located on an anti-vibration table. Table 2 describes the specifications of the Nd:YAG laser. The laser light was reflected by ten plane mirrors and transmitted through one quartz viewing port from the laser main body to the collision point. This optical path length was 4.25 m. After the collision with the H^- beam, the laser light was propagated to the termination point in the light-blocking box used for the laser light diagnostics. During the propagation, which was 3.16 m in length, there were five reflections by the plane mirror and one transmission through the quartz viewing port.

In this light-blocking box, three types of diagnostics for the Nd:YAG laser light were located. The first was a laser power meter to measure and absorb the laser light, the second was a photon beam profiler to measure the profile and the position of the laser light, and the third was a biplanar phototube to measure the time structure of the laser light.

To keep the H^+ beam power constant over longer periods, it was important to keep the position of the Nd:YAG laser light at the collision point constant. However, it was difficult to adjust the position of the invisible laser pulse of the Nd:YAG laser. Therefore, the visible laser light from the commercial He-Ne laser was used as a guide beam. The specifications of the He-Ne laser are also described in Table 2.

The trajectory of the H^- beam from the RFQ was bent by the bending magnet with a deflection angle of 23º, and transported to the beam dump provided in the most downstream part of the 23º beam line. As the Nd:YAG laser light was injected in the centre of the magnetic pole of the bending magnet, the H^0 beam was transported to the beam line with the deflection angle of 11.5º and introduced to the stripping foil. Hereafter, this beam line is referred to as "the 11º beam line." The H^0 beam was converted to the H^+ beam by passing the stripping foil. From the upstream to the downstream of the 11º beam line, a BPM, a slow current transformer (SCT), and a Faraday cup (FC) serving as a beam dump were positioned. These instructions are a typical implementation of the requirements.

Experimental Method

In FY2016, a LCE experiment to measure the power and its stability of the stripped H^+ beam was conducted using the H^- beam derived from the 3-MeV linac.

First, the position of the H^- beam was measured by the BPM without exciting the bending magnet, and the trajectory of the H^- beam was adjusted by using steering magnets so that the H^- beam was passed through the centre position of the BPM. Beam width and emittance of the H^- beam were obtained with the beam emittance monitor placed 0.3 m downstream of the quadrupole magnet by using Q scan technique. As a result of the measurement, the root-mean-square (RMS) width in the vertical and horizontal direction (σ_v, σ_h) at the collision point was estimated as about 1.7 and 3.7 mm, respectively.

After exciting the bending magnet, the H^- beam was transported to the 23º beam dump and collided with the Nd:YAG laser light. Then, the deflection angle of the H^- beam was decided by fine-tuning the magnetic field strength of the bending magnet so that the stripped H^+ beam was passed through the centre position of the BPM located in the 11º beam line. By using beam current monitors such as SCT and FC, the current amount of the stripped H^+ beam was measured.

Figures 4 and 5 show the photon profile located near the collision point. The origin O in the Fig. 4 represents the centroid of the photon profile. From this figure, it can be seen that the vertical RMS-radius of the Nd:YAG laser light could be estimated as 2.1 mm at the collision point with the H^- beam. Therefore, from the viewpoint of the vertical direction for the H^- beam, the narrow H^- beam collided with the wide Nd:YAG laser light.

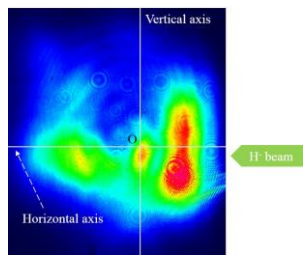

Figure 4: Two-dimensional photon profile for the Nd:YAG laser near the collision point with the H^- beam.

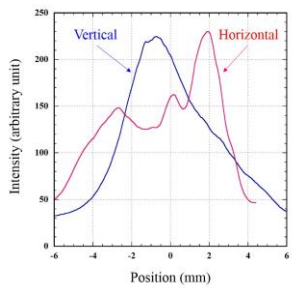

Figure 5: Intensity distributions of the Nd:YAG laser light near the collision point with the H^- beam.

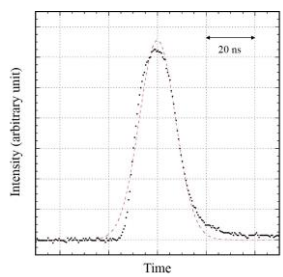

Figure 6: Time structure of the Nd:YAG laser light at the termination point.

ISBN: 978-3-95450-192-2 doi:10.18429/JACoW-IBIC2017-WEPCF08

In addition, the Nd:YAG laser power was set to 64% of the rated output power (25.6 W, 1.0 J/pulse) to protect the quartz viewing port. The power of the Nd:YAG laser light gradually decreased until it reached the collision point due to the reflection by 10 plane mirrors and the transmission through a quartz viewing ports, and the laser power at the collision point was 23.5 W. Consequently, the total transmittance was estimated as 92%. The energy density per unit area for the Nd:YAG laser light injected to the quartz viewing port was estimated as 3.7 J/cm^2, which was lower than the damage threshold for the Nd:YAG laser (10 J/cm^2).

Figure 6 shows the time structure of the Nd:YAG laser light. From this figure, the time spread with a power of 23.5 W was estimated as 7.43 ns (1σ). It was obvious that a pulse of the Nd:YAG laser light collided with the 6.0 micro-bunches of the H$^-$ beam. Therefore, a stripped H$^+$ beam with a power of 9.5 W equivalent could be obtained under the assumption that the conversion efficiency for each micro-bunch of the H$^-$ beam was 100%.

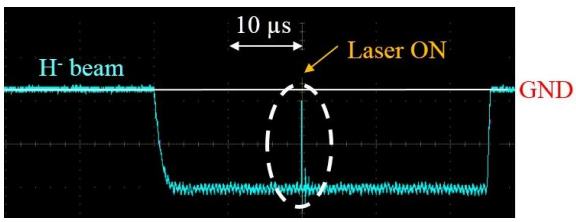

Figure 7: Current waveform of the H$^-$ beam observed at the 23º beam dump.

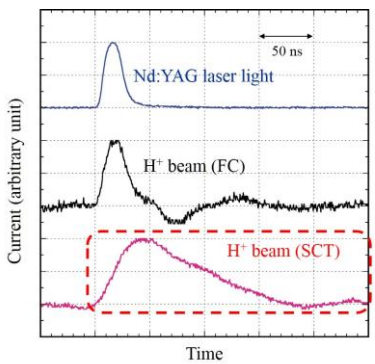

Figure 8: Current waveform of the H$^+$ beam observed at the 23º beam dump.

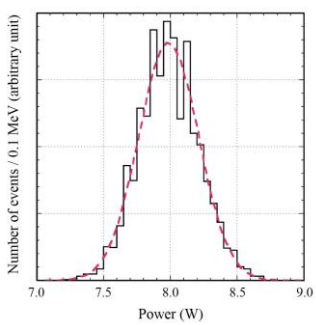

Figure 9: Current waveform of the H$^+$ beam observed at the 23º beam dump.

Preliminary Results

The light-blue broken line in Fig. 7 represents the current waveform of the H$^-$ beam observed at the 23º beam dump. This light-blue current waveform represents a single macropulse, and the rapid rise and fall part surrounded by the white dotted circle is due to the lack of the H$^-$ beam caused by the LCE. This lack was observed from the first shot of the Nd:YAG laser light after beginning the LCE experiment, and then we confirmed the collision between the H$^-$ beam and the Nd:YAG laser light. Figure 8 shows the pulse waveform of the Nd:YAG laser light observed at the biplanar phototube and the H$^+$ beam observed at the FC and SCT of the 11º beam line. From the figure, it can be seen that the pulse waveform of the H$^+$ beam was obtained after the laser light, and the power of the H$^+$ beam was 0.0359 W from the time integral of the H$^+$ beam current inside the dotted-red rectangle. If the laser light from this Nd:YAG laser system collided with the H$^-$ beam delivered from the J-PARC linac, a stripped H$^+$ beam with a power of 7.99 W would be obtained from the following equation.

$$0.0359\ (W) \times \frac{400\ (MeV)}{3\ (MeV)} \times \frac{50\ (mA)}{30\ (mA)} = 7.99\ (W) \qquad (1)$$

This value almost satisfied the power requirement (less than 10 W) of the proton beam for the TEF-P.

Figure 9 shows the power distribution of the stripped H$^+$ beam observed at the SCT. Here, the value of the horizontal axis represents the converted power under the J-PARC linac beam condition. By the approximation of the standard normal distribution, the power spread of the stripped H$^+$ beam was estimated as 0.22 W (1σ).

CONCLUSION

For the extraction of the low power H$^+$ beam (less than 10 W) from the high power H$^-$ beam (400 MeV, 250 kW) by the LCE technique, the LCE experiment to measure the power and its stability of the stripped H$^+$ beam was conducted using the H$^-$ beam from the 3-MeV linac in J-PARC. As a result of this experiment, the stripped H$^+$ beam with a power of 7.99±0.22 W equivalent was obtained under the J-PARC linac beam condition, and this value almost satisfied the power requirement (less than 10 W) of the proton beam for the TEF-P.

REFERENCES

[1] K. Tsujimoto *et al.*, "Feasibility of Lead-Bismuth-Cooled Accelerator-Driven System for Minor-Actinide Transmutation", *Nucl. Tech.*, vol. 161, pp. 315-328, 2008.

[2] H. Oigawa *et al.*, "Conceptual Design of Transmutation Experimental Facility", in *Proc. Int. Conf. on back-end of the fuel cycle: from research to solutions (Global 2001)*, Paris, France, 2001.

[3] F. Maekawa and Transmutation Experimental Facility Design Team, "J-PARC Transmutation Experimental Facility Program", submitted for publication.

[4] Y. Liu *et al.*, "Laser wire beam profile monitor in the spallation neutron source (SNS) superconducting linac", *Nucl. Instr. Meth.*, vol. A612, pp. 241-253, 2010.

ISBN: 978-3-95450-192-2 doi:10.18429/JACoW-IBIC2017-WEPCF08

[5] D.E. Johnson *et al.*, in *Proc. 6th Int. Particle Accelerator Conf. (IPAC2015)*, VA, USA, May 3-8, 2015, paper WEPTY028.

[6] H. Takei *et al.*, "Present Status of the Laser Charge Exchange Test Using the 3-MeV Linac in J-PARC", in *Proc. 5th Int. Beam Instrumentation Conf. (IBIC'16)*, Barcelona, Spain, Sep. 2016, paper WEPG45, pp. 737-740.

[7] S. Meigo, "Conceptual design of proton beam transport system for ADS facilities at J-PARC", *J. Nucl. Mater.*, vol. 450, pp. 8-15, 2014.

[8] John T. Broad and William P. Reinhardt, "One- and two-electron photoejection from H^- : A multichannel J-matrix calculation", *Phys. Rev.*, vol. A14, pp. 2159-2173, 1976.

[9] S. Meigo *et al.*, "A Feasibility Study of H^- Beam Extraction Technique Using YAG Laser", JAERI, Tokai, Ibaraki, JAPAN, Rep. JAERI-Tech 2002-095, Dec. 2002, (in Japanese).

[10] K. Hirano *et al.*, "Development of beam scrapers using a 3-MeV linac at J-PARC", in *Proc. 13th Annual Meeting of Particle Accelerator Society of Japan*, Chiba, Aug. 2016, paper MOP005, (in Japanese).

ISBN: 978-3-95450-192-2 doi:10.18429/JACoW-IBIC2017-WEPCF09

THE OPTIMIZATION DESIGN AND OUTPUT CHARACTERISTIC ANALYSIS OF IONIZATION CHAMBER DOSE MONITOR IN HUST-PTF*

H.D. Guo, P. Tan†, X. Liu, X.Y. Li, Y.J. Lin, Y.C. Yu, Y.Y.Hu
State Key Laboratory of Advanced Electromagnetic Engineering and Technology,
School of Electrical and Electronic Engineering,Huazhong University of Science and Technology,
Wuhan 430074, China

Abstract

An air parallel-plate ion chamber, which acts as a dose monitor for the beam delivery system in Huazhong University of Science and Technology Proton Therapy Facility (HUST-PTF), is designed as a redundant twin ionization chamber in order to meet the security requirements. In this paper, the characteristics of the designed ionization chamber are studied by using Boag theory and Monte Carlo simulation. Geant4 and SRIM are applied to simulate the energy loss and gain of 70-230MeV proton beam in parallel-plate ionization chamber. The influences of different sensitive regions and different gases on the performance of proton beam are discussed, moreover the structure of ionization chamber is optimized. According to the theory of Boag, the collection efficiencies of ionization chamber under different bias are calculated. The results show that the secondary particle collection efficiency of ionization chamber can reach above 99% when the air gap of ionization chamber is 5mm and bias voltage is above 100V. By the calculated gain of the ionization chamber, the output current of the detector can reach the order of 10nA when the proton beam intensity is 0.1nA.

INTRODUCTION

Nowadays, proton therapy facility is one of the most effective radiation therapy methods for cancers which use the Bragg peak characteristic of proton to achieve the precise irradiation of the tumor. The proton beam is tested with a dose detector in the nozzle before treating the patient, to ensure the efficacy of the treatment and the patient's safety. An air ionization chamber is used as a dose detector in Huazhong University of Science and Technology Proton Therapy Facility（HUST-PTF）.

The ionization chamber is composed of the cathode plate, the anode plate and the filling gas between the plates. When a proton beam passes through the gas, it disassociates the gas molecules, producing positive ions and electrons. Under the action of electric field, the positive ions move to the cathode while electrons move to the anode, and the secondary particles collected on cathode plate or anode plate reflect the magnitude of the beam current. The charge collected on the electrode plate is amplified and processed by peripheral electronics to obtain the dose of the proton beam.

In this paper, the structure and principle of plate ionization chamber are introduced. The energy loss and gain of different energy proton beams in ionization chamber are calculated by using the Monte Carlo software SRIM [1] and Geant4 [2]. According to Boag theory [3], the collection efficiency of ionization chamber under different bias voltages is calculated.

STRUCTURE AND PRINCIPLE OF PLATE IONIZATION CHAMBER

The structure of plate ionization chamber in HUST-PTF is shown in Fig. 1. The chamber consists of two windows, two cathode plates, an anode plate, and filling gas between plates. The entrance window acts as a seal and supports the ionization chamber. The material for the electrode background and window is Polyimide [4], with a thickness of 10μm. Polyimide has the characteristics of strong radiation resistance, high mechanical strength and high penetrability, and it has little influence on the beam. The gaps between the plates is filled with air, which is the sensitive volume of the ionization chamber. In order to meet the security requirements, the chamber is designed as a redundant twin ionization chamber.

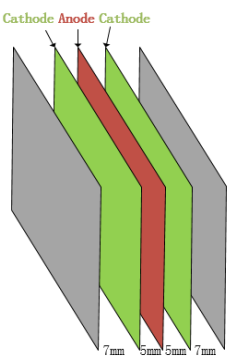

Figure 1: The structure of plate ionization chamber.

When the high-energy proton beam passes through the ionization chamber, the gas molecule is ionized. Due to the composite effect, the secondary particle produced by ionization cannot completely move to the electrode. With the increase of the bias voltage of the anode plate, the positive ions and electrons produced by the proton beam and the ionization of the air are completely collected and saturated. The principle of the ionization chamber is presented in Fig. 2.

* Work supported by the Fundamental Research Funds for the Central Universities (2014TS146), and by National Key R&D Plan (2016YFC0105308).
† Corresponding author, tanping@mail.hust.edu.cn

ISBN: 978-3-95450-192-2 doi:10.18429/JACoW-IBIC2017-WEPCF09

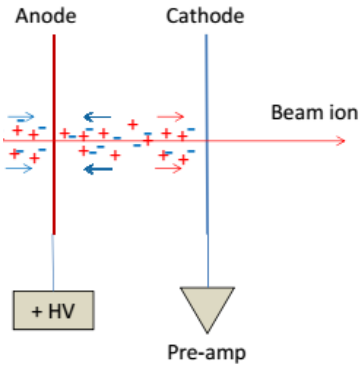

Figure 2: The principle of the ionization chamber.

ENERGY LOSS IN IONIZATION CHAMBER

The energy of the proton beam determines the depth of the Bragg peak, the energy loss of proton beam will affect the beam quality and destroy the therapeutic effect. The energy loss of the 70-230MeV proton beam in the ionization chamber is simulated by using SRIM and Geant4,In the simulations, the state of the gas is 1 atmospheric pressure, 20℃,ρ=1.205g/L, proton number is 20000.The results are listed in Table 1.

Table 1: The Energy Loss of Beam in Ionization Chamber

Proton Energy /MeV	Energy Loss/MeV		Percentage of Initial Energy (%)	
	Geant4	SRIM	Geant4	SRIM
70	0.0224	0.0241	0.032	0.034
100	0.0171	0.0186	0.017	0.019
150	0.0124	0.0139	0.008	0.009
200	0.0104	0.0118	0.005	0.006
230	0.0093	0.0105	0.004	0.005

The energy loss of the 70-230MeV proton beam passing through the ionization chamber is less than 0.032% of the initial energy, meets the treatment requirements. The larger the proton beam energy, the smaller the influence on the beam performance.

GAIN OF PROTON IN IONIZATION CHAMBER

The gain of proton in ionization chamber is the proportional relation between secondary particles and the initial particles. The average ionization energy of protons in air is W=34eV [5]. The energy loss of ionization of a single proton in the air is obtained by simulation, and the number of secondary particles produced by ionization is calculated according to formula (1).The number of secondary particles is the gain.

$$N = \frac{\Delta E}{W} \tag{1}$$

The energy loss of charged particles passing through the target material is divided into two parts: 1. energy loss of inelastic collisions with the nuclear electron of the target atoms (energy loss of ionization); 2.energy loss of elastic collisions with the target nuclei. For high-energy protons, the energy loss is mainly the first part, and the second part is negligible [6]. The energy loss of the 70-230MeV proton in the ionization chamber can be approximately equal to the energy loss of ionization.

Using software SRIM and Geant4 simulation to calculate the gain of 70-230mev proton beam in 5mm air. The results are shown in Fig. 3.

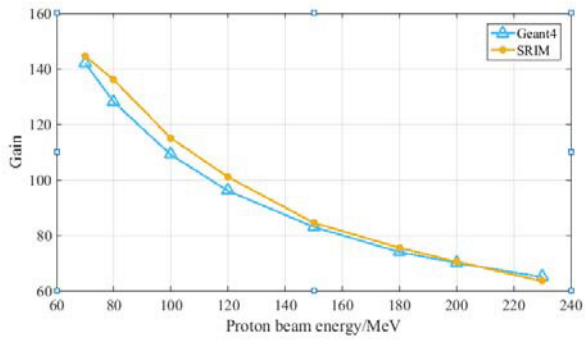

Figure 3: The gain of beam in ionization chamber.

The lower the energy of the proton beam, the greater the gain in the ionization chamber, and the gain of the 70-230MeV proton beam in the ionization chamber is 63-145.The gain in different air states can be obtained by the calibration formula.

$$G_1 = G_0 \times \frac{P_0}{P_1} \times \frac{T_1}{T_0} \tag{2}$$

COLLECTION EFFCIENCY OF IONIZATION CHAMBER

Because of the composite effect, the secondary particle produced by ionization cannot completely move to the electrode. According to Boag theory [3], the collection efficiency of ionization chamber under different bias voltage is calculated.

$$f = \frac{1}{1+\xi^2} \tag{3}$$

$$\xi = m \bullet d^2 \bullet \rho^{1/2} / V \tag{4}$$

Which d is plate spacing, V is bias voltage, ρ is density of air, m is the correction factor of air temperature and air

ISBN: 978-3-95450-192-2 doi:10.18429/JACoW-IBIC2017-WEPCF09

pressure (for dry air m = 36.7 + 2.2). The results are presented in Fig. 4.

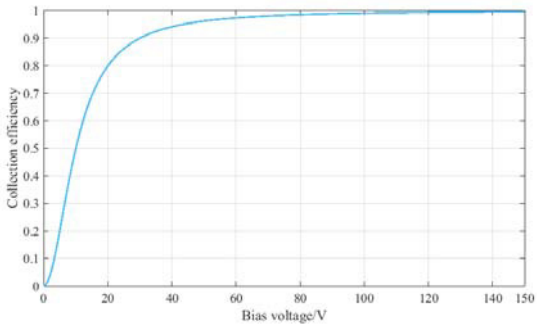

Figure 4: The collection efficiency of secondary particles.

For the 5mm air gap, the collection efficiency of secondary particles is over 99% when the bias voltage of the plate exceeds 100V.

CONCLUSION

The output characteristics of the ionization chamber is simulated and studied, the results show that the energy loss of proton beam 70-230MeV through the ionization chamber is less than 0.05%, when the air gap of two parallel plate ionization chamber are respectively 5mm, bias voltage is above 100V, the collection efficiency of secondary particles in ionization chamber can reach above 99%.The gain of the 70-230MeV proton beam in the ionization chamber is 63-145,the output current of the detector can reach the order of 10nA when the proton beam intensity is 0.1nA.

REFERENCE

[1] M. Pavloviče *et al*., "Supporting routines for the SRIM code", *Nucl. Instr. Meth.*, vol. 257, pp. 601-604, 2007.

[2] S. Agostinelliae *et al.*, "Geant4—a simulation toolkit", *Nucl. Instr. Meth.*, vol. 506, pp. 250-303, 2003.

[3] BOAG J W. "Ionization chamber", in *Radiation dosimetry*, New York, USA: Press Academic, 1968.

[4] Polyimide, https://en.wikipedia.org/wiki/Polyimide

[5] Dan T.L.Jones, "The w-value in air for proton therapy beams", *Rad.Phys.Chem*, vol. 75, pp. 541-550, 2006.

[6] Xu Junkui, "The transmission of medical heavy ions beam was simulated by Geant4 ", Ph.D. Lanzhou University, China, 2009.

ISBN: 978-3-95450-192-2 doi:10.18429/JACoW-IBIC2017-WEPCF11

A PRELIMINARY STUDY OF A CURRENT TRANSFORMER BASED ON TMR SENSOR*

Ying Zhao, Yaoyao Du, Jun He, Lin Wang, Ijanshe Cao
Institute of High Energy Physics CAS, Beijing, China

Abstract

As Tunnel Magneto Resistance (TMR) sensor reaches high resolution and low noise, a new principle CT based on TMR sensor is developed. Simulations and other methods for improving the resolution and accuracy are done .The linearity and bandwidth of the sensor are test in the lab.

INTRODUCTION

A TMR (Tunnel Magneto Resistance) is a new generation of magnetic sensor devices after Holzer devices, AMR (anisotropic magneto resistance) and GMR (giant magneto resistance). TMR has low power consumption; high sensitivity and temperature drift characteristics. In the current sensor, the use of TMR instead of Holzer device can significantly improve the sensitivity of the current sensor, which can significantly improve the sensitivity and temperature characteristics of the current sensor.

Dowaytech has developed a TMR sensor, which has better temperature stability compared with higher sensitivity, lower power consumption and better linearity [1].

Based on the GSI's experiment [1], a new current transformer has been developed in IHEP.

BASIC DESIGN

The basic design of the TMR current transformer is something like clamp ammeter. Beam pass through a magnetic ring with a gap, a TMR sensor is put in a gap of the ring. The output of the sensor changes with the beam current.

A TMR's principle is based on tunnel effect of MTJs (magnetic tunnelling junctions). General MTJs is like a sandwich that consists of ferromagnetic layer, nonmagnetic insulating layer and ferromagnetic layer. The magnetization direction of the two ferromagnetic layer changes when the external magnetic field varies, which cause the tunnelling resistance changes. The resistances' change breaks the balance of the MJTs Bridge, and the bridge's output is linear relation with the magnetic field.

Early TMR sensor performance is limited by the sensitivity and background noise, Figure 1. As the advance of manufacture, the sensor now can measure very low field and reach high resolution for the background noise can be reduced to Pico Tesla. The typical parameter and spectral curve of the background noise with frequency of the sensors is shown in Table 1 [2].

Table 1: TMR9002 Parameter(temperature 25° C)

Parameter	Data
sensitivity	100mV/V/Oe
nonlinearity	1%Fs
noise	150pt/ √ Hz
V_{offset}	15mV/V
hysteresis	0.1Oe

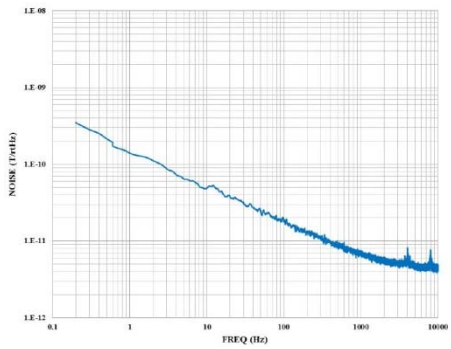

Figure 1: Background noise of TMR9002.

A high permeability nanocrystal soft material is chosen for the magnetic core, the primary μ_r is about 2e+5 and the coercive force is low. When the air gap meets the following requirements：g/a<0.2,g/b<0.2, Figure 2, the filled in the gap is approximate uniform [3].The B_g and H_g of the gap can be calculated as follow:

$$B = I/r[(2\pi - \theta)/\mu_r + \theta/\mu_0]$$

$$B \approx \mu_0 I/d$$

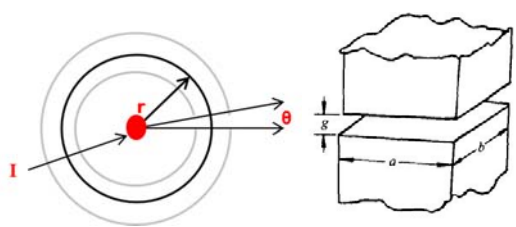

Figure 2: Calculate the B_g of the gap.

B is proportional to μ_0 and inversely proportional to the gap length when μ_r is much greater than μ_0. The dynamic range of TMR can be pre-estimated.

In this case, TMR9002 is chosen for the first prototype. For the extra power supply is needed and it is related to the sensitivity of the sensor. In first type of the electron-

* Work supported Key Laboratory of Particle Acceleration Physics & Technology,

ISBN: 978-3-95450-192-2 doi:10.18429/JACoW-IBIC2017-WEPCF11

ics, the ps and output are integrated for stale and minimum the noise. .The structure of current transformer and the electronics is shown as below in Figure 3.

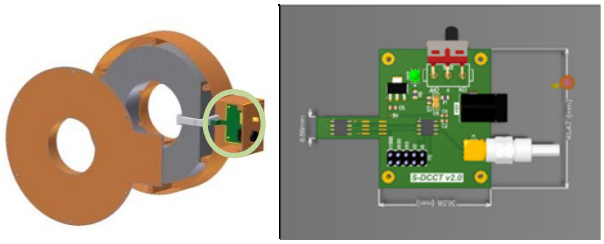

Figure 3: The structure of current transformer (right) and electronics of the TMR (left).

SIMULATION

Different from common magneto resistive device, TMR9002 is X axial sensitivity and SOP8 package, Figure 4. The effective area is quite small and the sensor's position in the gap is important for the measurement accu-racy. So simulation of the magnetic field in the gap has been done first.

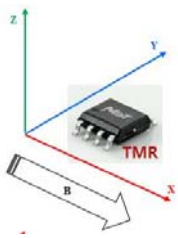

Figure 4: Sensitivity axial of TMR9002.

The CST [4] is used for the gap field simulation. From 0.1mA to 10mA DC current is set in the model as the beam current. In the first type of the core, the gap sectional area is a rectangle, as the result shows that smaller gap gives better distribution of field, but most of the magnetic lines of flux are at the edge of the gap. It makes poor efficiency of the magnetism gathering and the TMR sensor's position becomes critical. Lots of methods have been discussed. One of these is cutting off part of the sectional area. The simulation results are in Figure 5 and Table 5. The results shows that the thickness of the core is not involved too much of the gap field. The gap's width is one of the reasons of the inhomogeneous distribution of the gap field. All the cores without cut shows the deformed edge and weak field. The #4 core is cut off a regular part from the gap side, shows stronger and better field distribution in the gap.

Table2: The Parameter of the Simulation Core

No.	OD mm	ID mm	GAP mm	Specific
1	80	120	10	NA
2	80	120	8	NA
3	80	160	8	NA
4	80	160	8	cut

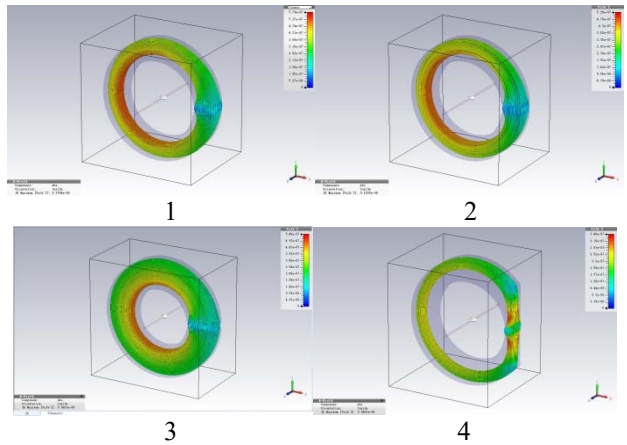

Figure 5: The simulation results.

TEST RESULTS

The first version of TMR current sensor has been test in the lab. The test plan is: a copper wire on a platform which used to fix the magnetic core and sensor is connected to the signal source and an oscilloscope or a voltmeter. Take the wire which is passing through the core as the beam. Different core is used in this experiment for finding a proper one. As the manufacture of the cut-off core is hard, it does not include in the first test.

The results shows, when gap is 8mm, the linearity of the sensor is satisfy and the coefficient of determination is R^2=0.9997 while the gap is 10mm, the R^2= 0.997 with some measurement point has greater deviation, Figure 6. The results trend fit the simulation.

During the test, one of the cores shows hysteresis effect that makes the offset is big. The difference may cause by the manufacture of these cores should be notice.

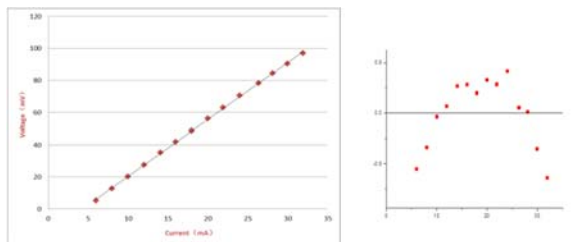

Gap=8mm

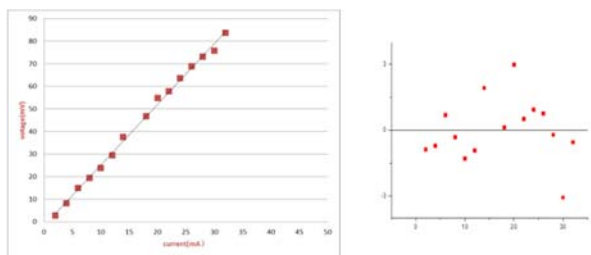

Gap=10mm

Figure 6: Different cores .linearity test result (left) and standard deviation (right).

ISBN: 978-3-95450-192-2 doi:10.18429/JACoW-IBIC2017-WEPCF11

The system bandwidth is related to the TMR's bandwidth, output circuit and the magnetic core. For the TMR is a magnetic device, the response is in tens of microsec-onds even milliseconds. A typical response of the stand-ard square wave shows about 50μs rise time, Figure 7.

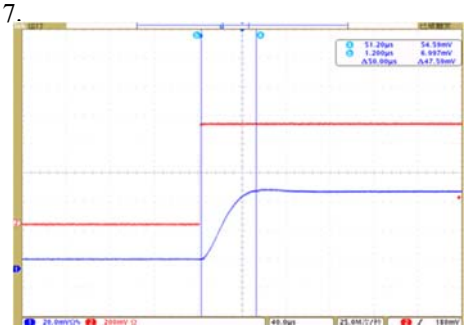

Figure 7: TMR current sensor's response (blue) of standard square wave (red).

CONCLUSION AND NEXT TO DO

The TMR current sensor preliminary test shows good linearity, but the shielding and mechanical support needs to be improved.

The dynamic measurement range of TMR is restricted by the saturation field. In this test, beyond 40mA the sensor works in a bad region. If the magnetic field is beyond a certain value, the TMR sensor will work in a nonlinear region. Limited by the manufacturing process, enlarge the good working region and keep the good resolution at the same time is quite difficult. That's the key point limit the current sensor's range. Two TMR sensors can reach the demand, but the details should be carefully considered.

Although the temperature drift is better than other magnetic sensor devices, the influence of the ambient temperature should be notice too. As the drift of the output induced by temperature is calculate. The chip impedance change from 6300 to 6000Ohm when the temperature changes and the shift of output signal is 0-0.5mV. So the complex environment needs further consideration.

REFERENCES

[1] E. Soliman, *et al.*, "Sensor studies for dc current transformer application", *IBIC'14*, Monterey, CA, USA, Sep 2014, paper WEPF31, pp. 624-628.

[2] Dowaytech, http://www.dowaytech.com

[3] Jibin.Zou, Baoting.Liu, Magnetic circuit and magnetic field, Harbin, China: Harbin Press, 1998.

[4] CST manual, http://www.CST.com

ISBN: 978-3-95450-192-2 doi:10.18429/JACoW-IBIC2017-WEPWC01

OPTICAL BEAM LOSS MONITOR FOR RF CAVITY CHARACTERISATION*

A. Alexandrova†[1], E. N. del Busto, L. Devlin[1], M. Kastriotou[2], V. Tzoganis[1], C. P. Welsch[1],
University of Liverpool, Liverpool, UK
A. Brynes[1], F. Jackson[1], D. J. Scott[1] STFC Daresbury Laboratory, Warrington, UK
E. Effinger, E. B. Holzer, CERN, Geneva, Switzerland
[1]also at Cockcroft Institute, Warrington, UK
[2]also at CERN, Geneva, Switzerland

Abstract

Beam Loss Monitors (BLMs) based on optical fibres have been under development for many years as an alternative solution to commonly used methods, such as ionisation chambers. Optical BLMs (oBLMs) maintain standard BLM functionality but can also be used for machine and personal protection. They can be implemented over the entire beam line providing excellent position and time resolution, while being insensitive to radiation induced damage. This contribution describes how oBLMs can also assist in the characterisation of RF cavities during commissioning and operation. It first presents the design principle of highly compact monitors and the underpinning theory for particle loss detection, before discussing data obtained in experimental tests at the electron accelerator CLARA. It then shows how a 4-channel oBLM can be applied for efficient cavity monitoring. Finally, the results are put into a broader context underlying the application potential in accelerators and light sources.

INTRODUCTION

Optical fibre-based beam loss monitors (oBLMs) have been developed as a comprehensive low-cost solution for beam loss detection in an accelerator [1]. An oBLM system consists of one or more fibres running along a beamline with fast photodetectors at the end of the fibre. The front end readout electronics convert the light signals to electrical pulses followed by high-speed analogue-to-digital converters. The operating principle of an oBLM is based on Cherenkov radiation emitted as a result of a charged particle crossing the fibre. This charged particle originates from beam losses which occur when the charged particle beam impinges on any obstacles along the accelerator, including the beampipe itself. For electrons, the threshold energy to produce Cherenkov radiation in a quartz fibre is 175 keV. The oBLM system is completely insensitive to magnetic fields, so it can be installed inside a magnet, or close to it, without any restrictions. When compared with standard beam loss monitoring methods, an oBLM can monitor the entire beamline and localise the losses with a resolution of up to 10 cm instead of detecting losses only at specific locations. Moreover, on-line oBLM systems can be integrated with the machine and personnel protection systems of an accelerator reducing the probability of losses not being detected early and thus ensuring safer operation.

CLARA (Compact Linear Accelerator for Research and Applications) is a Free-Electron-Laser (FEL) test facility under construction at Daresbury Laboratory [2]. CLARA is based on a 250 MeV electron linac capable of producing short, high-brightness electron bunches. The CLARA front end, on which the oBLM system has been installed, consists of a 2.5 cell RF photocathode gun, and a 2 m S-band (2998.5 MHz) accelerating structure.

For the CLARA front end, in the area marked in Fig. 1 by red lines, four oBLM units have been installed, using two different types of fibres: 600 µm and 400 µm core. Two types of different core fibres provide different sensitivities to ensure the detection of a range of beam loss intensities. Combining four sensors instead of one, oBLMs can collect more information on losses and on their origin, including the estimation of the deviation from the 'golden orbit'. Additionally, four oBLMs allow the reliability of each oBLM system to be cross-checked. Moreover, this configuration allows the potential of localising the losses regarding the symmetry of the beampipe to be thoroughly explored. As can be seen from the marked locations on Fig. 1, fibres are installed in the locations of south, north, west and east of the pipe. The photodetectors installed at the fibre ends are silicon photomultipliers (SiPMs), which are an array of avalanche photodiodes operating in Geiger mode. SiPMs are insensitive to magnetic fields, unlike standard photomultiplier technology and so they do not require additional shielding. This allows for compact installation behind the gun without impeding other systems. Each SiPM, four in total connected to each fibre end, is biased from a custom made power supply to just above the Geiger-breakdown voltage of 70 V, and the charge produced in each SiPM is collected by a transimpedance amplifier and converted to a voltage signal [3].

LINAC CONDITIONING: LOADED AND UNLOADED RF STRUCTURE

Imperfections on the RF cavity surface can cause the field emission of electrons [4]. A travelling RF wave can accelerate these electrons up to energies of tens of MeV, depending on the available distance for the electrons to travel, the accelerating gradient and the RF phase. When colliding with the

* Work supported by STFC Cockcroft Institute core Grant No. ST/G008248/1
† A.Alexandrova@liverpool.ac.uk

ISBN: 978-3-95450-192-2 doi:10.18429/JACoW-IBIC2017-WEPWC01

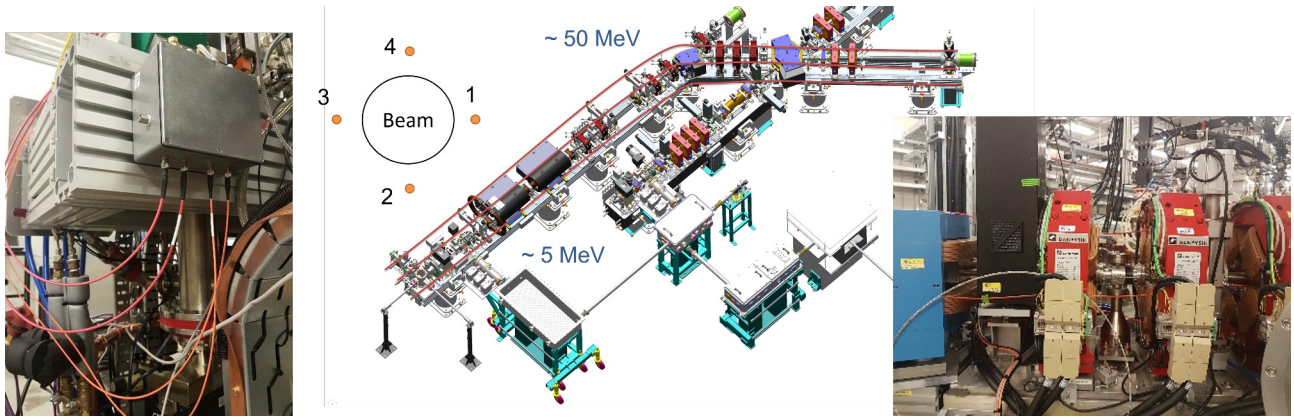

Figure 1: Fibres of oBLM (red line) on CLARA front end to VELA spectrometer line [2]. The inner picture demonstrates the location of four fibres with respect to the beampipe. oBLMs are located at the front end of the beamline therefore the sensors are located upstream. The inner photographs show the oBLM box (left corner) and the fibre locations along the beamline (right corner).

wall, these high energy electrons cause secondary showers, which can be detected by the oBLMs. With sufficiently high fields at certain locations of the cavity, electric breakdown or sparks can appear, caused by field emission. The current due to field emission has been shown to be proportional to the electric field on the surface of the cavity. As a beam propagates through the RF cavity, its field changes due to the charges that are induced on the wall of the cavity [4]. To compensate for this, high output power is applied to the accelerating structure. The unloaded effects can be studied when RF power is provided into the structure without the beam present. Conditioning of RF cavities – gradually ramping the input power and RF pulse length – is a necessary procedure to ensure that the design specifications have been met. During this procedure, breakdowns must be monitored in order to ensure that no damage to the cavity or the klystron occurs. During the breakdown, the input power can be reflected off the RF cavity which can lead to the damage of the klystron and windows. This can be monitored by observing spikes in vacuum activity or in the power reflected back from the cavity. We have measured the response of the oBLM sensors (see Fig. 2) to the RF input parameters and vacuum activity in CLARA. The Inverted Magnetron Gauge (IMG) that is located close to the linac provides the pressure readings which are then returned to the control system for monitoring. The data from IMG are shown by green lines, demonstrating vacuum activity. The input power, which is sent to the RF cavity, is shown by an orange line. The oBLM sensor is installed along the whole structure in four positions, and data has been taken during conditioning of the CLARA Phase 1 linac. The breakdown and oBLM measurements are presented for the unloaded case. The data presented in Fig. 2 shows the charge measured by the silicon photomultipliers, which detects the Cherenkov light propagating in the fibre, according to:

$$Q = \frac{1}{R_L} \int_{t_0}^{t_1} (V_{mes} - V_{off}) dt, \qquad (1)$$

where $R_L = 50\,\Omega$ is the load, V_{mes} is the measured amplitude within the integration interval (t_0, t_1) and V_{off} is the offset mean value of the oBLM sensor without any activity in the accelerator.

The measured total collected charge is plotted together with other measurements from the control system to cross-check the oBLMs signals. The cavity input power and the collected signal from the oBLM sensors show a correlation, in which the increase in the input power changes proportionally with the absolute signal. As the accelerating gradient of a cavity depends on the input power, an increase in power causes a greater number of primary particles to arise due to field emission in the structure. Along with this, the increase in gradient can cause some of the dark current to gain higher energy. Both of these effects lead to larger particle showers, which are then detected by the oBLMs. The rapid increase in the signal of the oBLMs demonstrates the increasing electron field emission and can be used as an indicator of potential breakdown (see Fig. 2 a). Another source of evidence for breakdown is spikes in vacuum activity. A higher level of dark current, which leads to sparking, breaks the vacuum, leading to increased pressure, which can be picked up by the oBLM system, see the spike in pressure and oBLM signal in Fig. 2 b). Currently, the reflected power from the cavity is being used to monitor the RF breakdown. Moreover, any obstacle introduced into the beamline should lead to a change in the oBLM signal, which is demonstrated in Fig. 2 c). At the moment, our sensors are digitised through an oscilloscope before being recorded in our control system with the other measured signals, meaning that the measurements are not fully synchronised. Direct digitisation of the oBLM signals will soon be integrated into the control system, allowing single beam loss events to be captured at rates of up to 100 Hz, meaning that it may be possible to isolate individual beam loss events at high repetition rates.

Figure 3 shows the signal obtained during the dark current studies during conditioning of the RF photo-injector gun. The response of the oBLM signal to variations in the RF

ISBN: 978-3-95450-192-2 doi:10.18429/JACoW-IBIC2017-WEPWC01

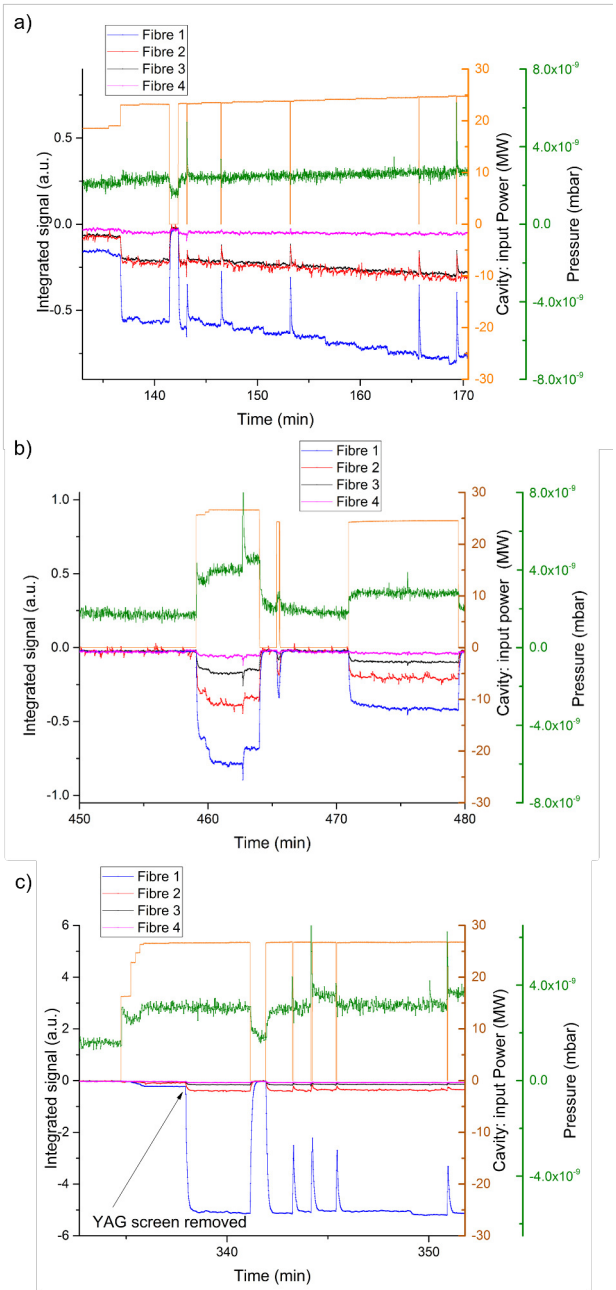

Figure 2: Integrated oBLMs signals (see Eq. 1) from all 4 fibres is presented by blue, red, black and purple lines for the detectors 1, 2, 3 and 4 respectively (see Fig. 1 for the location of the fibres) together with input power (orange line) and measured by IMG pressure (green line). The integrated oBLM signals follow the shape of the cavity input power, see graph a). From graph b) it can be seen that oBLM signals can detect the pressure spikes. Graph c) shows the change of the amplitude of the integrated signals when the obstacle is introduced into the beamline. The collected signal has increased by an order of the magnitude.

pulse length has been measured. An RF pulse of 10 MW power was sent to the cavity, and the pulse width was varied from 3.0 µs to 2.0 µs. The increase in field emission with the RF pulse length can be seen clearly. Figure 4 shows the correlation of the oBLM signal with the signal from the Wall Current Monitor.

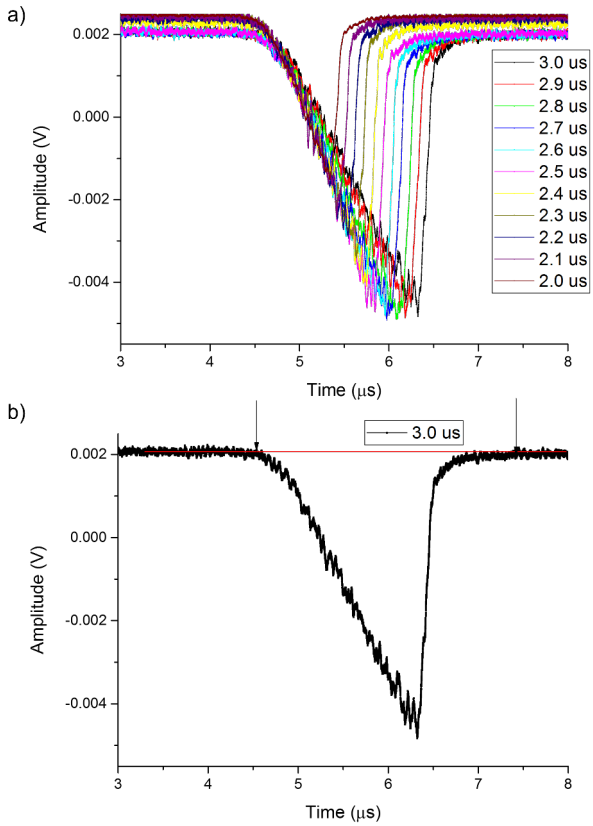

Figure 3: oBLMs signals from one channel for different RF pulses length is presented by different colours on top graph. The RF pulse was varied within 3.0 µs to 2.0 µs. From graph a) it can be seen that the oBLMs signal follows the shape of the pulse and its length can be reconstructed from the oBLM signal. Graph b) shows the oBLM signal which was obtain for 3.0 µs pulse.

CONCLUSION

The oBLM has proven itself as a useful tool which can be used during the conditioning of the RF structures by detecting dark current. This contribution has demonstrated that an oBLM can function as a cavity monitor to monitor the dark current appearing within the linacs and can, as such, provide further information into the sources of RF breakdown. Measurements presented in this contribution were obtained parasitically during the commissioning stage. As we have qualitatively demonstrated the potential of the oBLM systems, a comprehensive and quantitative study in the localisation of the main sources of dark current is planned. The oBLM as a beam loss monitor will also be tested during laser-induced beam commissioning.

Ensuring that losses are kept to a minimum is a crucial part of effective machine operation and the advances we

ISBN: 978-3-95450-192-2 doi:10.18429/JACoW-IBIC2017-WEPWC01

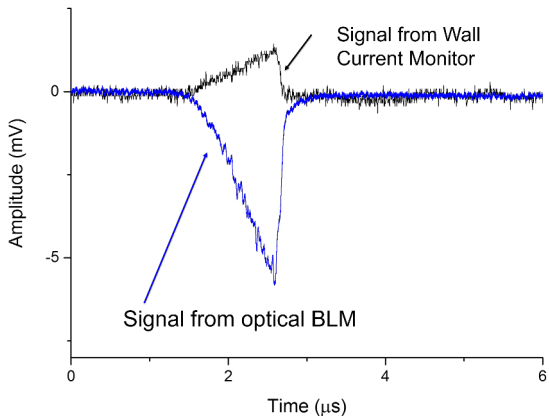

Figure 4: Graph demonstrates measurements which were taken by oBLM (blue signal) and by the Wall Current Monitor (black signal), and their correlation is clear.

have made in this area will ensure that any future UK FEL will benefit from the coverage of the accelerator we are able to deliver and at a cheaper price compared to standard technology. When applied to an FEL, an oBLM system could be particularly advantageous in undulator regions, since the system is not sensitive to magnetic fields and synchrotron radiation and should be able to provide the information about the properties of the propagating beam and intra-beam dynamics.

ACKNOWLEDGEMENT

The authors would like to thank the CLARA team for the opportunity to perform studies at the accelerator, with special thanks to Deepa Angal-Kalinin for supporting the idea of testing oBLMs on CLARA. Many thanks to Steve Buckley for helping to ensure the smooth process of oBLMs installation and ASTEC Drawing department for providing high-resolution pictures of CLARA, and to Chris Edmonds, Bruno Muratori and the CLARA team for fruitful discussions over the subject.

REFERENCES

[1] M. Kastriotou *et al.*, in *Physics Procedia'15*, pp. 21–28.

[2] J. A Clarke *et al.*, "CLARA conceptual design report", *Journal of Instrumentation*, vol. 9, pp. T05001, 2014.

[3] D-Beam ltd, http://www.d-beam.co.uk.

[4] T. P. Wangler, "Microwave Topics for Linacs", in *RF Linear accelerators*, John Wiley & Sons, USA: 2008, pp. 156–164.

ISBN: 978-3-95450-192-2 doi:10.18429/JACoW-IBIC2017-WEPWC02

CONSTRUCTION OF A MOBILE IRRADIATION INSTRUMENT FOR THE VERIFICATION OF THE CERN LHC BEAM LOSS MONITORING SYSTEM

D. Gudkov, V. Grishin, R. Veness, C. Zamantzas, CERN, Geneva, Switzerland

Abstract

The strategy for machine protection and quench prevention of the super-conducting elements of the Large Hadron Collider (LHC) at the European Organisation for Nuclear Research (CERN) is heavily reliant on its beam loss monitoring (BLM) system. This is one of the most complex and large-scale beam instrumentation systems deployed anywhere in the world.

In order to augment the system's dependability and verify the correct connection of each of the approximately 4000 detectors distributed around the 27 km LHC ring to its assigned channel in the electronic system, a mobile irradiation instrument has been designed and built. This instrument can be easily and safely transported along the LHC tunnel and imitate a localised beam loss at each BLM detector.

This paper describes the concept of the instrument, its engineering design, the safety measures included and recent upgrades. Possible future improvements of the device are also considered.

INTRODUCTION

There are approximately 4000 beam loss detectors using the ionization chamber principle installed next to areas where losses can take place in the LHC [1]. It is necessary to periodically verify the connection to the corresponding channels of the electronic system and the signal quality of all detectors. The purpose of the mobile irradiation device is to mimic a beam loss at a given detector using a ^{137}Cs radioactive source, and in so doing verify the complete detection chain for that particular channel. The instrument described here is designed to safely transport the ^{137}Cs radioactive source along the tunnel inside a lead safety container and then to perform the required tests. The equipment functions by pushing the compact radioactive source out from its lead safety container towards a defined end position located several millimetres from an ionization chamber and then to pull it back into the container after the tests are complete. The operators manipulate the device remotely, always remaining at least 5 meters from the radioactive source such that the dose rate does not exceed 1.5 µSv/h. The instruments currently used for BLM system validation have several reliability and safety issues related to the electromechanical system that lead to an increased risk of unnecessary radiation exposure for operators. The new device is therefore designed to be highly reliable during operation to avoid any requirement for human intervention close to the radioactive source

As this validation process is normally conducted as close as possible to the end of machine shutdowns, the transportation and manipulation of the source should be fast and easy.

ELECTRO-MECHANICAL DESIGN

The instrument consists of a metal box trolley with dimensions 1000 mm x 600 mm x 800 mm with all the equipment located inside for safe transportation along the tunnel, that can be towed by a standard LHC electric car. Figure 1 shows the general view of the instrument (opened). In order to safely transport the radioactive source a lead safety container is required. The thickness of the lead must be at least 100 mm to provide sufficient shielding from the source to the outer surface of the container, such that the dose rate on the surface does not exceed 2.5 µSv/h [2]. The radioactive source is attached to the end of a long, ny-

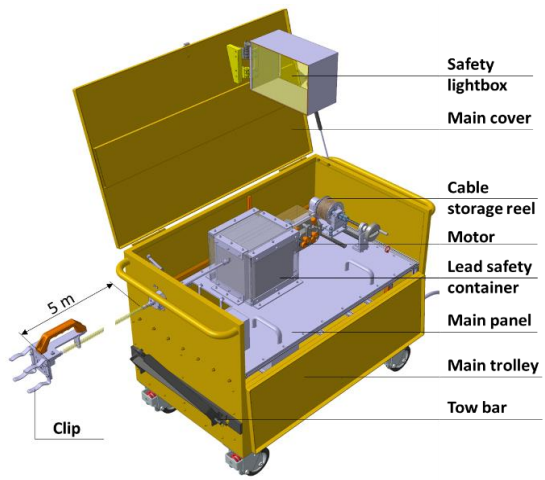

Figure 1: General view of the mobile irradiation instrument.

lon-coated steel cable stored on a reel. This cable is pushed by electric motor rollers through a 5 m long hose. Nylon coating helps to reduce friction between the cable and the hose to ensure low motor loads. It also protects the cable from possible mechanical damage. The hose is connected at one end to the lead safety container and at the other to a clip which is clamped on the detector under verification. When the source arrives at its end position inside the clip it activates an end-switch and the motor stops automatically. It is not then possible to push the source further. When the source is retracted to its home position it activates another end-switch located outside the lead safety container, again automatically stopping the motor.

The cable is stored on a compact reel that houses up to 5.6 m of cable. The reel has an auto-return spring mechanism that will retract the source back into the lead safety container in case of electric motor failure.

The irradiation instrument clip can be easily attached to the BLM thanks to spring-type clamps. These clamps pro-

ISBN: 978-3-95450-192-2 doi:10.18429/JACoW-IBIC2017-WEPWC02

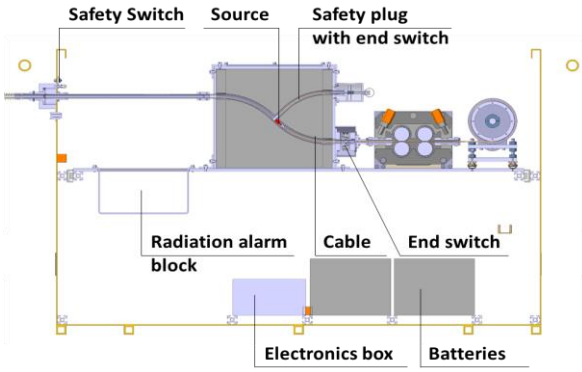

Figure 3: Irradiation instrument cross-section. The batteries and electronics box are located below the main panel. This panel can be extracted for battery replacement or electronic system maintenance.

vide a reliable fixation of the clip on the detector and a precise orientation of the source towards the detector's central axis.

As some detectors are mounted in unusual orientations or positions, the clip can revolve around the hose axis thanks to a swivel connection (Figure 2), to allow comfortable handling of the clip in case of difficult access.

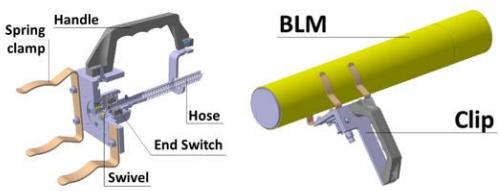

Figure 2: Detailed view of clip (left) and clip fixed on BLM (right).

There are several safety measures included to avoid unsafe extraction of the radioactive source from the lead safety container:

- A safety lightbox with an illuminated sign "IRRADIATION IN PROGRESS. LEAVE IMMEDIATELY" switches on when the main cover is opened to signal that the intervention involving the radioactive source is ongoing.
- A safety plug creates a physical block in case of accidental activation of the system. This device is shown in Figure 3. It is extracted manually by the operator before launching the test. After the test is finished and the source back in the lead container the plug is reinserted.
- A safety switch on the side of the metal box trolley creates an interlock when the hose is not connected to the pipe coming from the lead safety container. The remote control is blocked and the user cannot operate the instrument if this interlock is active.
- An electrical wire connecting the clip end-switches and to the electronics box is fixed on the hose. The end connector of this wire needs to be plugged into the connector on the trolley to activate the control panel.
- An audible radiation alarm is activated when the source is out of the lead safety container.

DESCRIPTION OF OPERATION

The BLM system validation (Figure 4) is performed as follows:

- The box trolley is parked close to the detector under test
- The main cover of the trolley is opened
- The clip is fixed on the detector
- All safety switches are deactivated
  - Hose is connected to the container; electrical wire on the hose is connected to the electronics box
  - Safety plug is extracted
- The operator moves a minimum of 5 m away from the detector with the remote control panel
- The motor is activated and the source moves through the hose towards the BLM
- An audible radiation alarm is activated indicating that the operator should stay at a safe distance from the source.
- The source generates an ionisation current in the detector which the detector transforms into an electrical signal
- The signal is read by the operator in the control room and system levels and interconnections are verified
- The source is moved back to the lead safety container.
- The audible radiation alarm stops several second after the source is safely in its container, indicating that the operator can approach the trolley.
- The safety plug is re-inserted and the main cover closed.
- The trolley is moved to the next BLM

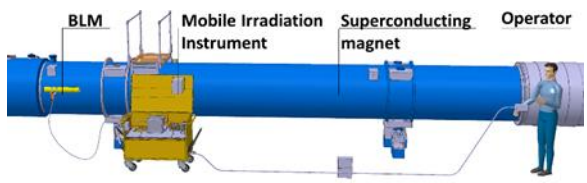

Figure 4: Instrument in operation.

RESULTS OF ELECTROMECHANICAL TESTS WITHOUT RADIOACTIVE SOURCE

To minimise human exposure to radiation it is very important to avoid mechanical problems when the radioactive source is outside its lead safety container. To reduce the time required for the interventions it is also important to avoid mechanical problems during the transport of the mobile irradiation instrument through the tunnel or when setting-up the device. Dedicated testing has therefore been performed in order to debug the mechanism and verify its reliability. Tests were performed using a dummy part with the same geometry as the radioactive source.

ISBN: 978-3-95450-192-2 doi:10.18429/JACoW-IBIC2017-WEPWC02

As two irradiation instruments are planned to be used in parallel for the entire BLM system validation in the LHC it was necessary to prove that each mechanism can perform a specified 2500 full cycles without maintenance or failure (corresponding to over half the total number of BLMs) to ensure complete system validation without instrument maintenance. A special test bench was built in order to make continuous, automatic, in-out tests. 4000 cycles were performed without any mechanical or operational issues.

RESULTS OF TESTS WITH RADIOACTIVE SOURCE

The test set-up with source is shown in Figure 5.

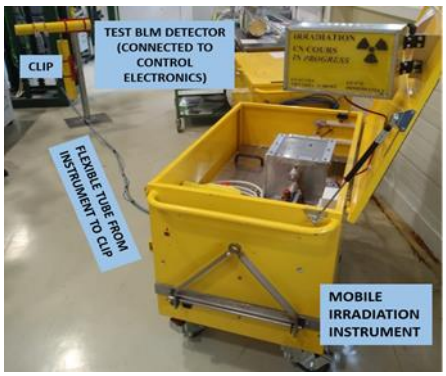

Figure 5: Test set-up with radioactive source.

These tests showed that the source could be brought to the same position with good repeatability with signal variations of less than 4% during 30 in-out cycles. The signal obtained during the test exceeded the intentionally injected electronic offset current of ~10 pA (used to ensure that the electronics chain is always functional) by a factor of 3, hence giving a clear loss signal [3] and allowing the complete detector chain to be considered operational. The radiation level in the area of the instrument operator remained acceptable at below ~0.8 μSv/h.

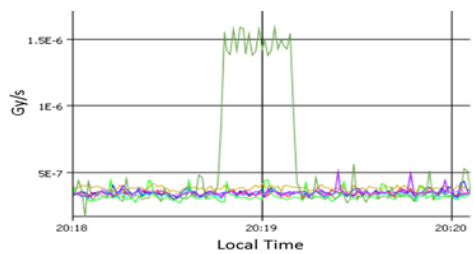

Figure 6: Signal profile showing that the BLM detector is fully operational.

A graphical representation of the signal obtained by the BLM detector in real time is shown in Figure 6. The operators should observe the signal during approximately 25 s to conclude that the monitor fully functional.

FUTURE IMPROVEMENTS OF THE INSTRUMENT AND PROCEDURE

The mobile irradiation of BLM monitors in the LHC involves human operators that have to work in the vicinity of a dangerous ^{137}Cs radioactive source. The average time required to check 1 detector from arrival of the trolley to departure is about 4 minutes. It is therefore quite time consuming to check all the 4000 LHC BLMs using this push-pull cable solution. In addition, the instrument requires regular maintenance of the electromechanical system.

The LHC tunnel is equipped with a monorail system, that could also be used for transporting a mobile radioactive source using a robotic train. Such a train already exists for remote observation and survey in the LHC [4].

A two degrees of freedom manipulator installed on the monorail module could in future house a radioactive source, allowing the BLM detectors to be inspected one-by-one fully remotely from the main LHC control room. This would allow the entire system check to be performed without any human presence in the tunnel hence reducing the integrated dose to operators. The concept of such a system is shown in Figure 7. The telescopic arm in its retracted state is compact enough to allow the train pass throughout the LHC tunnel, while the extended arm would allow validation of BLM detectors on both sides of the magnet cryostats.

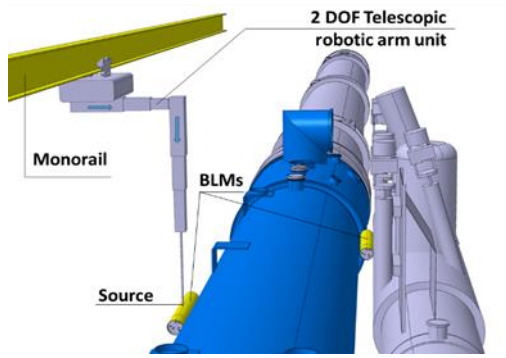

Figure 7 : Possible monorail mobile irradiation instrument.

SUMMARY

A mobile irradiation instrument for validating the LHC BLM system has been designed, produced, assembled and successfully tested. All the electromechanical problems that existed in previous generations of such instruments have been resolved. In addition, several new safety measures have been implemented to significantly reduce the risks of accidental radiation exposure for operators.

New design features have also been added to simplify the manipulation of the instrument components, so reducing the overall time necessary for BLM system validation.

The considered irradiation instrument fulfils all requirements and be used for all future BLM system validation. An alternative, fully remote solution, further reducing the risk of accidental exposure and reducing intervention times is being considered as a future upgrade.

ISBN: 978-3-95450-192-2 doi:10.18429/JACoW-IBIC2017-WEPWC02

REFERENCES

[1] E. B. Holzer *et al.*, "Commissioning and optimization of the LHC BLM System", CERN-BE-2010-031, 2010.
[2] EDMS 907174: Safety manual for special use of a radioactive source: BLM test/calibration for LHC commissioning - 4240-4241RP -137Cs.
[3] A. Marsili, Identification of LHC beam loss mechanism: a deterministic treatment of loss patterns. Universite Paris Sud - Paris XI, 2012.
[4] C. Pralavorio, "TIM, le robot du tunnel du LHC", http://cds.cern.ch/record/2235913 , 2016.

ISBN: 978-3-95450-192-2 doi:10.18429/JACoW-IBIC2017-WEPWC03

IONIZATION CHAMBERS AS BEAM LOSS MONITORS FOR ESS LINEAR ACCELERATOR

V. Grishin, European Spallation Source ERIC, Lund, Sweden
B. Dehning, CERN, Geneva, Switzerland
A. Koshelev, A. Larionov, V. Seleznev, M. Sleptsov, Institute for High Energy Physics, Protvino, Russia

Abstract

The European Spallation Source (ESS) to be under construction in Lund, Sweden, will provide a highest average intensity beam from a 5 MW superconducting proton linear accelerator to produce spallation neutrons. A serious problem for high current accelerators is the high density of the beam, which is able to destroy the equipment, to make a quench of super conductive magnets.
Loss of even a small fraction of this intense beam would result in high radiation and destruction of the equipment. The Beam Loss Monitor (BLM) system must be sensitive to different level of losses in different accelerator locations. BLM system protection should limit the losses to a level which ensures hands-on-maintenance or intervention. From another side, the BLM system should be sensitive enough to enable machine fine tuning and machine studies with help of BLM signals, including mobile detectors.

The main ESS beam loss detector type is ionization chamber (icBLM). The detector is originally designed for CERN LHC and 4250 monitors were produced in 2006-2008, now widely used in almost all accelerators at CERN (figure 1), in IHEP (Protvino, Russia). In 2014-2017 a new production of 830 icBLM was performed to replenish spares for LHC and to make series for ESS, GSI. The requirements, design, testing and layout for ESS accelerator are presented.

INTRODUCTION

Parallel plate gas ionization chambers developed by CERN for LHC [1] and manufactured and tested at the Institute for High Energy Physics (IHEP) in Protvino, Russia, are chosen as beam loss detectors for the ESS linear accelerator due to their fast response, no gain variation (with possible exception of the target region), the robustness against aging, large dynamic range 10^8 (pA-mA), the little maintenance required.

Figure 1: icBLM at LHC.

The icBLM have a fast reaction time, which implies a detector gas with high ion mobility. The 99.9999 % nitrogen filled at 1.1 bar detector is permanently sealed inside a stainless-steel cylinder. Should a leak occur in a detector and air enter the chamber, the detection properties would not change severely as air consist 79% of nitrogen, therefore not leading to system immediate failure. In systematic system testing with a radioactive source, a lower signal due to lower gas pressure will be detected. The composition of the chambers gas is very important so as this is the only component in the icBLM which is not remotely monitored.

The icBLM is very sturdy, offering a good radiation hardness. The consistent, long-term (20 years of operation) high quality of icBLM requires materials testing and various tests during and after production in IHEP, after reception at CERN and ESS. IHEP designed and built the UHV production stand [2], shown in figure 2.

Figure 2: IHEP production stand.

DETECTORS PRODUCTION

The detectors active zone consists of 61 parallel electrodes with a 5.75 mm distance between electrodes in the ionization chambers produced in 2008 (ic08). The gap between electrodes in the ionization chambers produced in 2017 (ic17) is reduced to 5.71 every 2 electrodes, keeping the same spacer length. The electrodes are indeed made of a 0.5 mm thick aluminium in ic08 and 0.54 mm thick aluminium in ic17 (figure 3). The gap between electrodes is built to reduce the drift path and the recombination probability of the ions and electrons, and hence to get the requested linearity.

ISBN: 978-3-95450-192-2 doi:10.18429/JACoW-IBIC2017-WEPWC03

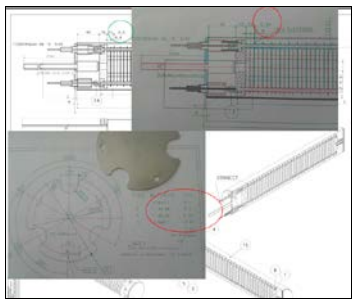

Figure 3: Al electrodes design.

Each signal electrodes are surrounded by two bias electrodes maintained at 1500 V in normal operation. The assembly is attached to the stainless-steel cylinder via two very high resistivity ceramics (Al_2O_3) plates, the electrodes are connected by two ceramics feedthroughs. Feedthroughs testing is done at CERN after reception and in IHEP just before chambers assembly (figure 4). The acceptance criteria for leakage current is set below 1 pA at 2000 V.

Figure 4: Only 15 feedthroughs out of 1700 pieces are not accepted.

The dynamic range of an ionization chamber is defined by its lowest and highest current signals. It is limited by leakage current through the ceramics insulator, which should be less than 1 pA for lowest signals and by saturation due to space charge for highest signals which is the in mA range.

The space charge effect is caused by the large number of positive ions, which drift to the signal electrode much slower then electrons. At a given dose rate, the field created by these ions is so high, that it starts screening the bias voltage between the electrodes and a gap without field is created. The ions located in the gap are usually lost by recombination or diffusion, which lowers the response of the detector (saturation). It should be noted that the ionization chambers in the LHC BLM system will not have signal filters, so the input of the electronics will be saturated before the space charge effects could occur.

The ceramics insulator is the key component of icBLM, limiting the lower end of its dynamic range. In ic08 monitors, ceramics insulators are from SCT, France. No degradation has been observed over 10 years of operation at LHC. In ic17, ceramics insulators are from Friatec Germany. Various investigations on ic17 ceramics insulators include vacuum, chemical, electrical, cleaning, heating tests (figure 5). These tests lead to improve the quality of the ceramics from a first "red" type to a "white" type. Both material types are used in ic17 detectors.

Figure 5: Ceramics test in vacuum.

The thickness of the stainless steel outer cylinder is 2 mm, its length is 483 mm. In ic17 monitors the cylinders are cut by 1.5 mm on both sides. The bottom and the top cover are 5 mm thick. The covers, feedthroughs and the copper pumping tube are welded in argon inert atmosphere (TIG). The quality of the welding is a critical aspect during production, it is therefore tested in vacuum.

Aging depends on the quality of materials to high radiation (ceramics, feedthroughs). To avoid radiation aging (electronegative gases, organic compounds), a strict cleaning procedure for the chambers is followed. Impurity levels due to thermal and radiation induced desorption are estimated to stay in the ppm range. No organic material is present, neither in the production process (pumping, baking, filling) of the detectors, not in the detectors themselves. Standardized test samples analysed at CERN periodically helped to check the cleaning performance. For example, the conclusions of X-ray photoelectron spectroscopy (XPS) from 2016-12-13 is following: "From the point of view of carbon contamination, the stainless steel and aluminum samples are considered UHV compatible. But high amount of Si is observed on all the samples. The latter is very likely coming from NGL 17/40 which contains sodium metasilicates. Probably rinsing was insufficient to eliminate the silicates from the cleaning detergent bath".

The various tests were performed at IHEP before, during and after the production to verify the quality of chambers. All welds including heads are He leak tested (figure 6).

Figure 6: "Head" after welding.

Additional tests have been performed on ic17 chambers, including the test of each ceramics insulators before assembly. The quality of the production has been contin-

ISBN: 978-3-95450-192-2 doi:10.18429/JACoW-IBIC2017-WEPWC03

uously controlled and recorded from the vacuum stand, from the leakage current measurements of the components, from the tests of the assembled monitors. All data was logged into CERN's Manufacturing and Test Folders database [3], shown in figure 7.

Figure 7: Data for each icBLM in MTF.

To stabilize the high voltage a low pass filter, R=1 MOhm and C=0.047 µF is mounted on the HV input (figure 8).

Figure 8: HV low pass filter.

The icBLM connectors are 5 kV HV, series SHV and coaxial, series BNC. The connectors insulating material is chosen to resist to an ionizing dose of up to 10 mGy. The insulator in ic08 chambers is PEEK, the one in ic17 is Polystyrene. The 2 insulators have similar properties in radioactive dose, the only difference is temperature limit.

After transport of the monitors to CERN by lorry, reception and calibration tests were performed at CERNs gamma irradiation facility GIF++ (figure 9).

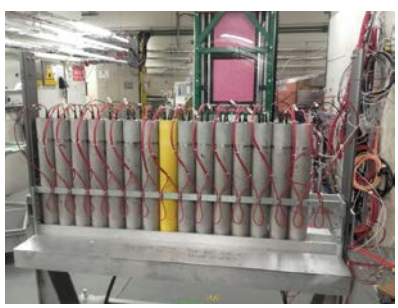

Figure 9: Test set-up at GIF++.

For each ic17 detector the tests consisted of leakage current and radioactive source induced signal measurements (figure 10). 14 tested monitors were placed in a special support at 2.8 m transverse to the flux of the radioactive source, the geometry leading to a difference in flux of +/- 5% between the 14 monitors. One ic08 monitor is in the centre of the set-up as a reference during the measurements.

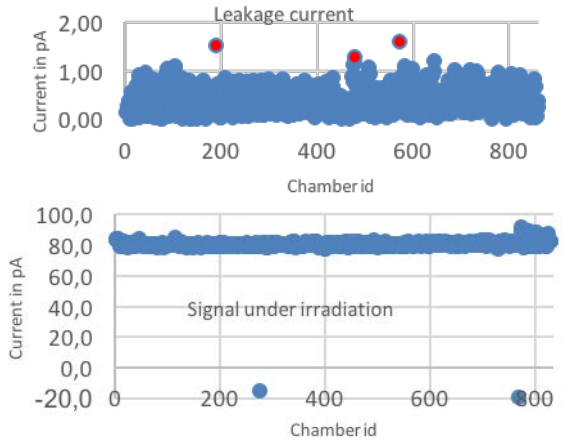

Figure 10: 830 icBLM tests results.

Calibration tests are performed in mixed fields at HiRadMat in order to obtain irradiation conditions as close as possible to operational accelerator dose. These tests allow a comparison between ic08 and ic17 chambers, for which tests are ongoing (figure 11).

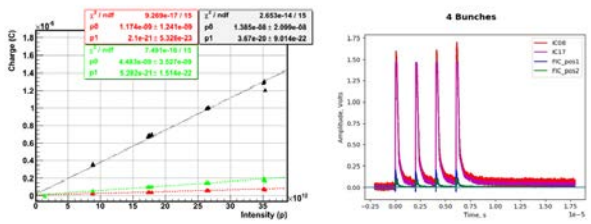

Figure 11: HiRadMat calibration results, 2015 (ic08) and 2017 (ic08 and ic17).

After acceptance test at GIF++ each accepted detector was insulated and shipped to ESS and GSI (figure 12).

Figure 12: Insulation of icBLM.

icBLM at ESS

285 detectors were received at ESS in July 2017 and are now under reception and calibration tests (figure 13).

ISBN: 978-3-95450-192-2 doi:10.18429/JACoW-IBIC2017-WEPWC03

Figure 13: icBLM at ESS.

icBLM detectors positions in the ESS LINAC are chosen in accordance with maximum beam loss locations, to minimize crosstalk and to allow full coverage without blind spots. For diagnostic use, the detector layout (figure 14) should also allow determination of the loss origin [4].

LINAC section	Number of ionization chambers	Comment
DTL	5	1 per Tank
Spokes	52	
Medium Beta	36	
High Beta	84	
HEBT	45	3 per q-pair
Dog leg	21 2	3 per q-pair 1 per dipole
A2T	15	
Dump line	6	
Total	266	

Figure 14: icBLM layout at ESS

Detectors will be installed outside cryostats and will have a mounting flexibility option (figure 15).
Normal operational 1 W/m proton beam loss was considered in the detectors locations determination. This was derived from hands-on maintenance criteria for high intensity proton machines and was adopted at ESS as a maximum allowable operational beam loss.

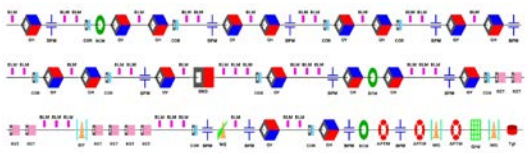

Figure 15: Synoptic installation layout, ESS LINAC A2T sector.

CONCLUSION

830 nitrogen filled ionization chambers have been produced in 2014-2017 at IHEP for the ESS, GSI and LHC beam loss monitoring system, following a first production in 2006-2008 with modifications. These chambers are the main beam loss detector for ESS linear accelerator but need further tests, analysis and simulation.

ACKNOWLEDGEMENT

We thank Andreas Jansson , Thomas Shea, Clement Derrez, who provided support at ESS.

We would like to thank Jean-Marc Malzacker, Christos Zamantzas, Eva Barbara Holzer, Ewald Effinger from CERN for help.

We thank Adrian Fabich, Eduardo Nebot Del Busto, Tatiana Medvedeva for HiRadMat tests.

REFERENCES

[1] E. B. Holzer *et al.*, IEEE NSS-MIC '05, Puerto Rico, CERN-AB-2006-009 BI, 2005.

[2] V. Assanov *et al.*, "Facility for vacuum cleaning and filling of the ionization chambers (beam loss monitors)", *Engineering Physics* in Russian, No.3 2007.

[3] E. B. Holzer *et al.*, EPAC'08, Genoa, Italy, CERN-AB-2008-054 BI, 2008.

[4] ESS Technical Design Report, ESS-2013-001 APR 2013

ISBN: 978-3-95450-192-2 doi:10.18429/JACoW-IBIC2017-WEPWC07

BEAM TRIP DIAGNOSTICS FOR THE TPS

C. Y. Liao, C. Y. Wu, Y. S. Cheng, C. H. Huang, K. H. Hu, K. T. Hsu
NSRRC, Hsinchu 30076, Taiwan

Abstract

The Taiwan Photon Source (TPS) is available to users since March 2016. A beam trip diagnostic system is used as an important tool to analyze the cause of beam trip events since the beginning of 2017. The main function of the system is to record relevant signals when the stored beam is suddenly lost. In the past few months, some useful features have been added, such as capturing trigger signals for pulsers, power line voltage, and auto generated beam trip reports. A detailed system architecture, implementation and progress will be summarized in this report.

INTRODUCTION

The Taiwan Photon Source (TPS) is a low emittance, high brightness synchrotron light source, located in Hsinchu, Taiwan. After commissioning [1], the TPS became available for user service in September 2016. During oper-ation, inevitably there will be unexpected beam trips due to subsystem failure or other abnormal circumstances. In or-der to find out the reason for such an event, a beam trip diagnostic system is developed to serve as an important tool for beam trip analysis. In the past few months, some useful features have been added, such as capture of the pulser trigger signals in case of spontaneous firing of the pulser, capturing the 3-phase power line voltage for power quality monitoring, auto generated beam trip reports, and web-based interface allowing for a quick review of the trip event through the web browser. The main system features are: Generate a trigger signal to subsystems when the stored beam current is lost abnormally; Record relevant signals when a beam trip occurs; View the report from the GUI tool or web browser to analyze each event for cause and effect. Reliability and availability of the TPS operation improved dramatically with the help of this beam trip di-agnostics.

SYSTEM DESCRIPTION

The architecture of the TPS beam trip diagnostic system is shown in Fig. 1. A trigger signal is generated through the beam trip detector when the stored beam current suddenly drops. This trigger is sent to many places (here to the data acquisition system) through an evented-based timing system (EVG/EVR) [2]. The data recorders will be updated on receiving this trigger. After a few seconds delay, all data from the recorders and subsystem parameters of interest will be saved through a PV access. The probable cause of the event will be analyzed by the program and identified by a simple description. Then, a beam trip report will be generated and saved as a web page. After that, operators can access and analyze the event data from the viewer GUI or web browser at any time.

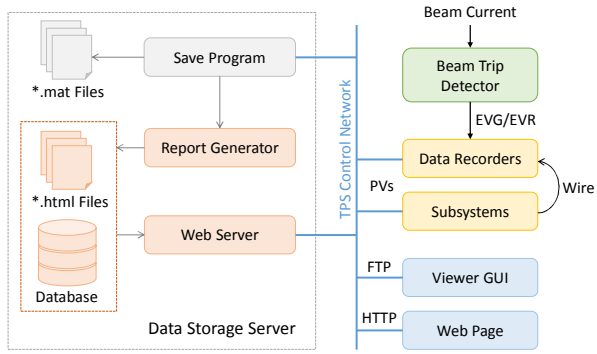

Figure 1: Schematic layout of the TPS beam trip diagnostic system.

Beam Trip Detection and Trip Trigger Generation

A beam trip detector is configured to generate a beam trip trigger signal, when the stored beam current drops abnormally more than 25 mA within 0.1 milliseconds (configurable). This trigger signal is broadcast via the event-based timing system to all data acquisition nodes (BPM platforms and data recorders) to synchronize the data captured. So far, known possible causes for the stored beam trip include: RF system trips, BPM orbit and angle interlock, vacuum interlock, front-end interlock, and abnormal firing of the injection pulse magnets.

Data Recorder

The TPS BPM system [3] provides turn-by-turn orbit post-mortem data which can be used to analyze beam positions during the trip event. In addition, several EPICS embedded standalone data recorders support distributed data acquisition capability to collect data from different subsystems. The quantity and parameters of the data recorders are shown in Table 1. Each data recorder has eight input channels with two types of configurations. These recorders provide waveform type signals which can be captured by many subsystems, including the storage ring beam orbit, machine protection system (MPS), RF and pulsed magnet system. In addition to these signals, some subsystem parameter set values need to be logged when an event occurs. The data to be saved are compiled in Table 2.

Table 1: List of Data Recorder Units used in TPS

Device	BPM platform	Data recorder (8ch)	
Quantity	173	4	1
Sampling rate (kHz)	~578	100	50,000
Time span (ms)	~17.28	100	6
Data length (point)	10,000	10,000	300,000

ISBN: 978-3-95450-192-2 doi:10.18429/JACoW-IBIC2017-WEPWC07

Table 2: List of Saved Post-mortem Data

Group	Signals	Description
Beam signals	Ib, Orbit	Stored beam current and turn-by-turn orbit data
RF signals	Pr, Pf, GV, RC	RF system parameters: forward power, reflect power, gap voltage, and ready-chain signal
Interlock signals	BPM, Vacuum, Frontend, Beamline, Safety	Subsystem interlocks to shutdown the RF system
Pulser	Kickers	SR injection kicker waveform with trigger signal
Machine parameters	Set values	Subsystem parameters, alarm list
Power line	L1, L2, L3	3-phase voltage
Seismic signals	X, Y, Z	Up-down, north-south, and west-east acceleration (in planning)

Data Storage Server

The data storage server is used to automatically store post-mortem data, and provides FTP and web services for viewer GUI and web page access. A capture program, written in Matlab, is running in the background of the server and can detect an event by monitoring BPM post-mortem PV changes. When an event occurs, a two-step saving process starts, one is to save currently subsystem set parameters without delay, the other is to wait a few seconds for the data recorders to get ready, followed by PV channel access to store data as a Matlab file format (*.mat).

The save program also performs a simple timing analysis of the recorded signals in order to give possible event identification, such as a trip caused by a kicker or by other subsystems. The report generator program is used to generate an html file format report and writes the event description to the database for web page access.

Viewer GUI

The viewer GUI is designed to list and plot beam trip events and the graphic user interface is developed with the Matlab guide tool as shown in Fig. 2. It can list the beam trip event with a simple note and provide a signal list check box to select for display the desired data, which can be downloaded from the server using the FTP. Some of the subsystem interlocks, like the BPM orbit (position and angle), vacuum, front-end and beam line interlocks need to shut down the RF system for machine protection. Figure 3 shows that the vacuum interlock is active during 400 mA operation. The RF system is shut down within a few milliseconds. Finally, the BPM position interlock is active.

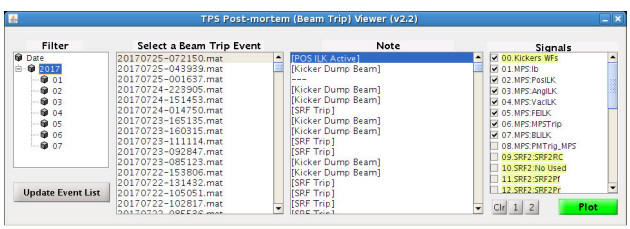

Figure 2: Main page of viewer graph user interface.

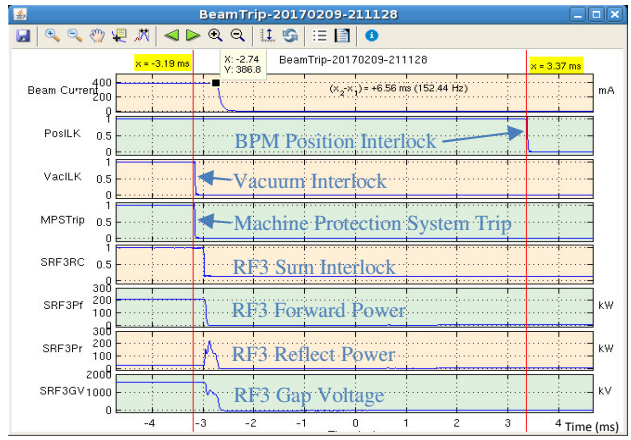

Figure 3: Plot page of vacuum interlock event. A customized toolbar can provide simple data adjustment functions.

Website Interface

The website of the beam trip report is designed to list and view beam trip events. The main page is developed with the Python/Django tool as shown in Fig. 4. It can list a beam trip event similar to the viewer GUI, but only the prepared report can be read. As shown in Fig. 5, the report is generated from the report generator immediately or from the viewer GUI later (regenerate). This web-based interface is useful to quickly review a trip event by any device through the web browser.

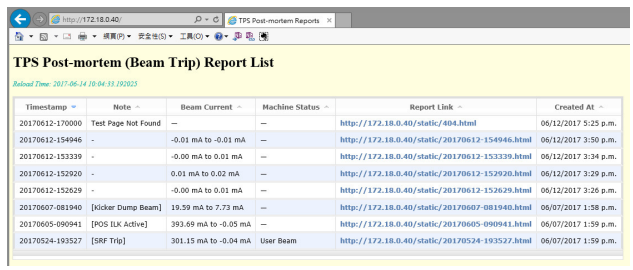

Figure 4: Web interface of TPS beam trip report list.

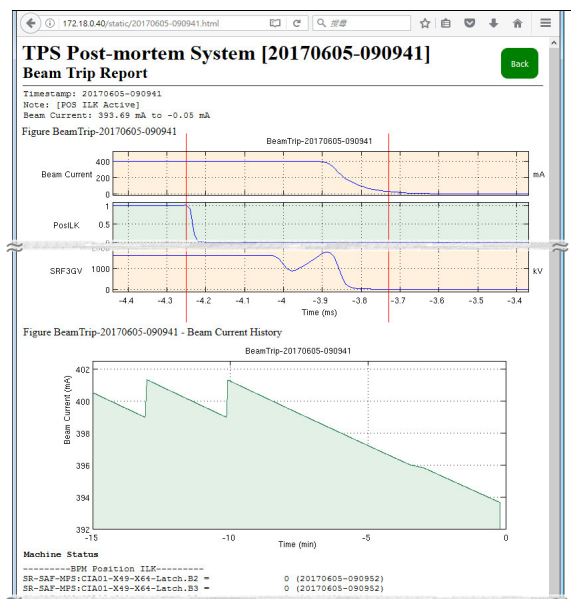

Figure 5: Web page of beam trip report.

ISBN: 978-3-95450-192-2 doi:10.18429/JACoW-IBIC2017-WEPWC07

SPONTANEOUS PULSER FIRING

So far, typical beam trip events include RF trips, subsystem interlock trips, and spontaneous kicker firings. Sev-eral trip scenarios can be found in reference [4]. The 4-channel / 5 MHz sampling rate oscilloscope is replaced with an 8-channel / 50 MHz sampling rate data recorder for data acquisition to understand the spontaneous pulser firing problem. These 8 channels are used to capture the current waveforms of the four kickers and the four trigger signals generated from the control system. It is clear that under normal circumstances, the current waveforms and the trigger signals of the four kickers should exist at the same time, as shown in Fig. 6. This design can be used to determine pulser miss or spontaneous firings, which are caused by the system or spontaneously.

There have been a few beam events caused by spontaneous kicker firing when injection is not active. Some kickers were unexpectedly triggered without trigger signal, causing an instant loss of the electron beam, as shown in Fig. 7. The K1, K3, K4 spontaneously fire although no trigger signal could be observed. In a number of spontaneous firing events similar situations were observed, pointing to spontaneous kicker firing due to noise interference rather than from the trigger control system. In order to solve the possible noise interference, the improvement scheme proposed at present is to use a fiber link instead of copper wires to transmit the trigger signal, hoping to reduce noise pickup.

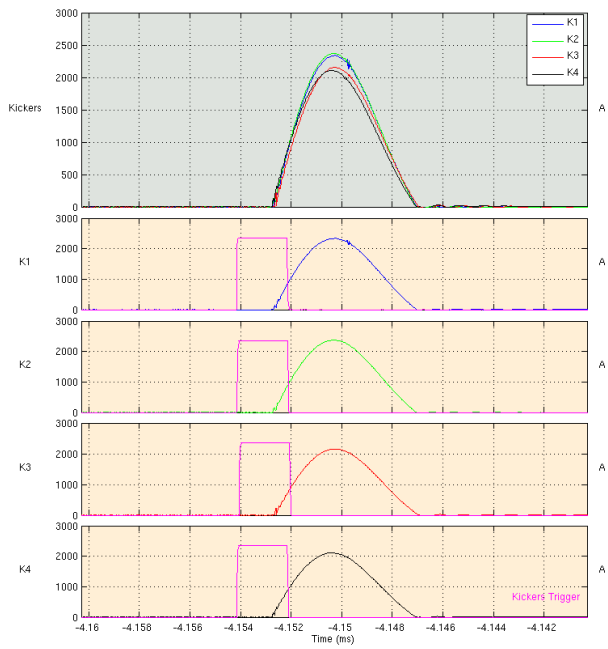

Figure 6: Kicker waveforms (K1: blue, K2: green, K3: red, K4: black) with trigger signals (pink) during normal operation (dump beam).

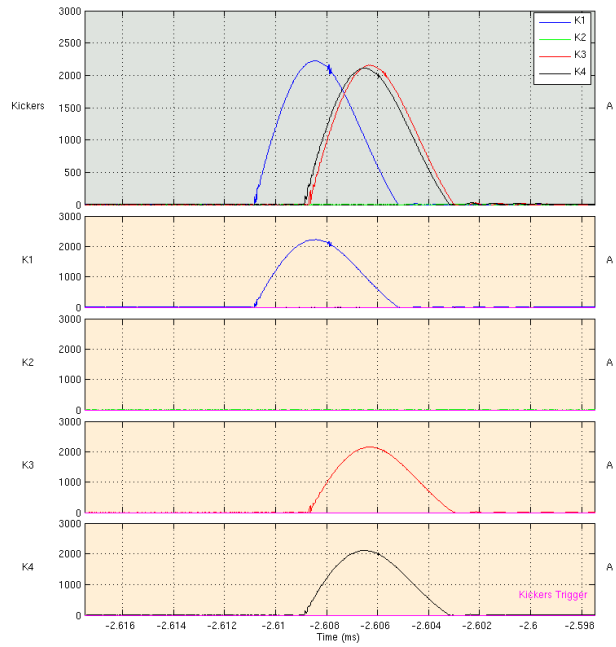

Figure 7: Kicker waveforms (K1: blue, K2: green, K3: red, K4: black) without trigger signals (pink) during spontaneous fired kickers K1, K3, and K4 while the K2 is misfired causing a beam trip.

SUMMARY

A beam trip diagnostics for the TPS is an important tool to analyze the cause of beam trip events during normal operation. The main function of the system is to record relevant signals when the stored beam is suddenly lost abnormally. Some features have been implemented such as: capture of the pulser trigger signals to diagnose miss firings, capturing 3-phase power line voltage for power transient monitoring, auto generated beam trip reports, and web-based interface for quick analysis of trip events through the web browser.

REFERENCES

[1] C. C. Kuo *et al.*, "Commissioning of the Taiwan Photon Source", in *Proc. IPAC'2015*, paper TUXC3, Richmond, VA, USA.

[2] C. Y. Wu *et al.*, "Status of the TPS Timing System", in *Proc. ICALEPCS'2013*, paper THPPC109, San Francisco, CA, USA.

[3] P. C. Chiu *et al.*, "Commissioning of BPM System for the TPS Project", in *Proc. IBIC'2015*, paper TUPB068, Melbourne, Australia.

[4] C. Y. Liao *et al.*, "Post-Mortem System for the Taiwan Photon Source", in *Proc. IPAC'2017*, paper MOPAB125, Copenhagen, Denmark.

ISBN: 978-3-95450-192-2 doi:10.18429/JACoW-IBIC2017-WEPWC09

NEW SCINTILLATION TYPE BEAM LOSS MONITOR TO DETECT SPOT AREA BEAM LOSSES IN THE J-PARC RCS

M. Yoshimoto†, H. Harada, S. Kato, M. Kinsho, K. Okabe
J-PARC, JAEA, Tokai, Ibaraki, Japan

Abstract

In the J-PARC RCS, a large fraction of our effort has been concentrated on reducing and managing beam losses to achieve 1MW high power proton beam operation. Standard beam loss monitor (BLM), which is installed outside of the magnet in every cell of beam optics and detect the beam loss at wide area in each cell, is insufficient to investigate finer beam loss mechanism in the ring. Thus we developed new scintillation type BLM to detect the spot area beam losses on the vacuum chamber inside the magnet. The new BLM isolates a photomultiplier (PMT) from a plastic scintillator, and connects it with optical fibres. Because small plastic scintillator is set on the vacuum chamber directly, it has capability to have high sensitivity for a beam loss at localized spot area. On the other hand, the PMT can precisely be operated without being affected by a magnetic field because it can be kept keeping away from the magnet. In this paper, we report the detail of the performance of the new BLM.

INTRODUCTION

The 3-GeV Rapid Cycling Synchrotron (RCS) of the Japan Proton Accelerator Research Complex (J-PARC) accelerates protons from 400MeV to 3GeV kinetic energy at 25 Hz repetition rate. The average beam current is 0.333 mA and the design beam power is 1 MW. The RCS has two functions as a proton driver for neutron/muon production at the Material and Life science experimental Facility (MLF) and as a booster of the Main Ring synchrotron (MR) for the Hadron experimental facility (HD) and Neutrino experimental facility (NU) [1].

The most important issue in achieving such a MW-class high power routine beam operation is to keep machine activations within a permissible level, that is, to preserve a better hands-on maintenance environment. Therefore we adopt the ring collimator system to remove the beam halo and to localize the beam loss at the collimator area [2]. In addition, a large fraction of our effort has been concentrated on reducing and managing beam losses, in the J-PARC RCS. As a result, we have successfully achieved acceptable low-loss 1-MW beam acceleration [3]. Until now, the highest radio-activation area confines to an injection section, and then the beam loss localization by using the ring collimator is functioned. On the other hand, we surveyed residual doses on the vacuum ducts along the ring and mapped residual dose distributions in detail. The detailed dose distributions give key information about sources and mechanisms of the beam losses [4]. To move on the next step, we developed a new beam loss monitors (BLM) to detect the spot area beam loss, especially in the magnet. This paper presents details of the new BLM.

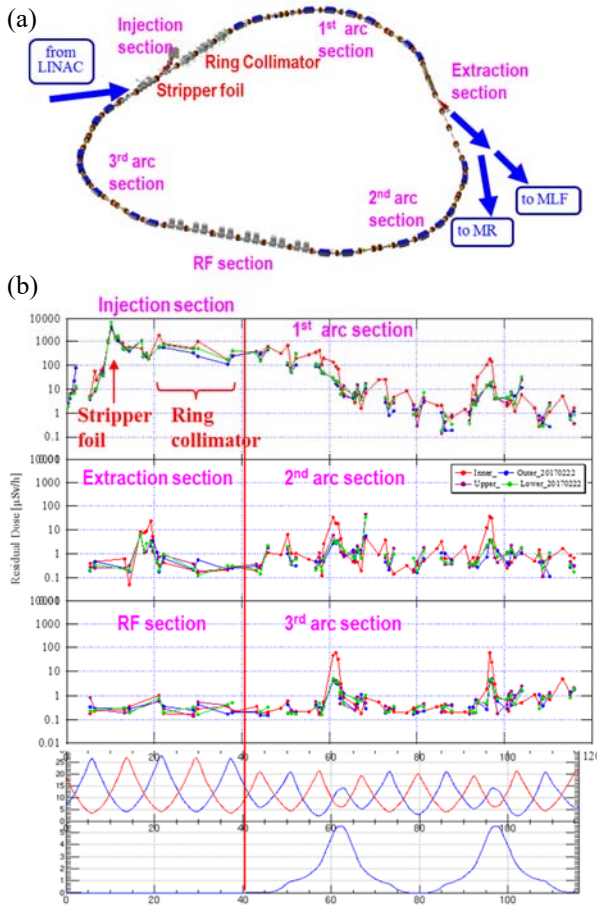

Figure 1: Schematic view of the RCS ring and measured residual dose distributions along the ring.

RESIDUAL DOSE SURVEY AND BEAM LOSS DETECT

Residual Dose Distribution along the Ring

Figure 1 shows the schematic view of the RCS ring and a typical surveying and mapping result of the residual dose distributions along the ring. The residual doses are measured by using the Geiger–Muller (GM) counter. We contact it on a surface of a vacuum duct because the sensitivity to the radio-activation at the contacted local spot can be enhanced drastically. In order to obtain the detailed distribution, we measure the residual dose on inner, .outer, upper, and lower sides of the vacuum duct at upstream and downstream of all magnets.

† yoshimoto.masahiro@jaea.go.jp

ISBN: 978-3-95450-192-2 doi:10.18429/JACoW-IBIC2017-WEPWC09

At first sight, the highest radio-activation area confines to an injection section, especially, an immediate vicinity of a 1st stripper foil and the ring collimator the ring collimator region. The high radio-activation around the stripper foil is caused secondary particles generated from the foil due to the nuclear reaction by hitting the beam into the foil [5-6]. This cause is not the beam losses in general, and then it cannot be disappeared intrinsically as long as a charge exchange multi turn beam injection scheme with the stripper foil is adopted. But it is possible to reduce the secondary particles from the foil. A key parameter to reduce them is "foil hitting rate [3]" that is defined as a ratio of total number of foil hitting particles to number of injecting particles. From the simulation results, "foil hitting rate" can be reduce drastically by expanding the injection painting area and optimizing the stripper foil width and foil irradiation position. Indeed, we can prove experimentally that the residual dose around the foil decreases corresponding to the "foil hitting rate" [7].

The residual doses at the other section extremely small compared with those at the injection section. However up closer examination, it has some specific structure according the lattice structure. The RCS has a threefold symmetric lattice which partitions into 27 FODO cells. Three cells in each straight section and six cells in each arc section. Measured residual doses are plotted in each symmetric lattice. These arranged and detailed dose distributions give key information about sources and mechanisms of the beam losses as follows: momentum spread at the dispersion peak points, leakage particles which are scattered by the primary collimator but not absorbed by the next secondary collimators, dispersion leakage into the straight section, and so on [4].

Beam Losses Measurement System

The detailed residual dose distribution mapping gives important information about the beam losses. In order to investigate more accurate loss mechanism, the detailed beam losses mapping are also required. That is, we need to detect the spot area beam losses, but it is not that easy.

In the J-PARC RCS, proportional counter-type beam loss monitors (P-BLMs) are adopted to detect ionizing radiations due to the beam losses because they use mainly in the interlock system for machine protection. The 90 units of P-BLMs are installed along the ring and beam lines. Basically, only two are placed for every cell in the ring and are set under the steering magnets or quadrupole magnets. This beam loss measurement system by using the P-BLM works very well with a view of the observation of the significant level of the beam loss at wide area. But, it is unsatisfactory with a view of the detailed beam loss mapping; because number of the measurement point is small and above all it cannot detect the spot area beam loss.

DEVELOPMENT OF NEW S-BLM TO DETECT THE SPOT AREA BEAM LOSS

One of useful methods to detect the spot area beam loss is proposed as follows: a small sensor is adopted and is set on the vacuum duct directly to enhance the sensitivity to the ionizing radiation from generated by the local spot area beam loss [4]. The J-PARC RCS adopted a small scintillator type BLM (small S-BLM) which is simply assembled a small plastic scintillator (EJ212: Eljen Technology [8], 20x20x50mm) and a small PMT (H11934-100-10MD: HAMAMATSU [9]). And we proved experimentally that the small S-BLM can be detected the local spot area beam losses during the beam operation. Moreover, it can detect the gamma ray from the local spot area of the radio-activated vacuum duct after the beam stop. This small S-BLM has a high potential advantage. At the same time but the usage has the following restriction; it cannot be used in a magnetic field because a signal gain of the PMT is drifted by the magnetic field. One solution is isolating the PMT from the small scintillator, and then connecting between them by an optical fibre. Here, it is named "Optical Fibre joined S-BLM (OF-SBLM).

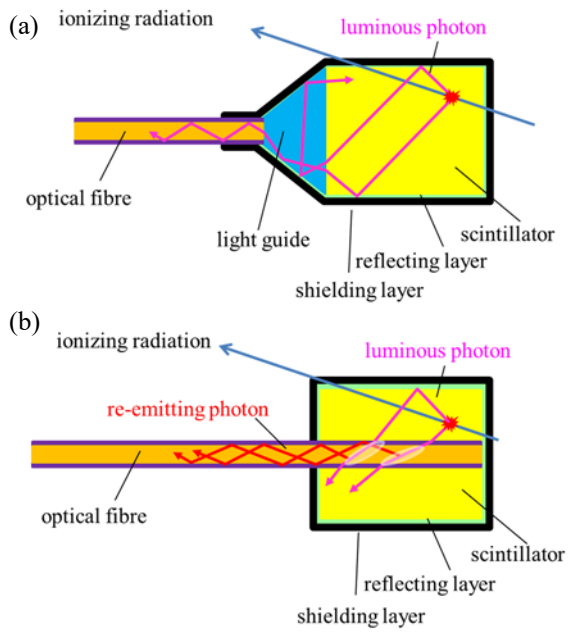

Figure 2: Schematic diagram of the two types design structure for the optical fibre joined S-BLM.

Design of Optical Fibre Joined S-BLM

A most important issue of the OF-SBLM is how to improve photon transmission efficiency from the scintillator to the optical fibre. Thus following two connection and transmission methods (see in Figure 2) were reviewed at the start of the design of the OF-SBLM. In generally, when the ionizing radiation irradiate into the plastic scintillator, that luminescent materials absorb the radiation energy and re-emit the absorbed energy in the form of light. One method is for this luminous photon to transport into the optical fibre directly by using the light guide as shown in Figure 2(a). The tapered light guide concentrates and leads the photo into the edge face of the optical fibre. However the

ISBN: 978-3-95450-192-2 doi:10.18429/JACoW-IBIC2017-WEPWC09

photon transmission efficiency is not be expected to improve because of low photo-condensing efficiency and transmission loss at the boundary surface between the light guide and optical fibre. The other method is for photons to transport indirectly by using a wavelength shifting type optical fibre (WLS fibre) as shown in Figure 2(b). The WLS fibre absorbs the luminous photons, re-emits new photos with shifted wavelength, and finally transmits the re-emitting photons pass through the fibre. Emission peak wavelength of the EJ212 plastic scintillator is 423nm. Thus we adopt Y11 Kuraray [10] WLS fibre which works as a blue to green shifter (emission peak: 476nm, absorption peak: 430nm). In order to increase the number of the incoming luminous photons into the WLS fibre, we made five holes in the plastic scintillator and stuck the five fibres into the holes as shown in Figure 3(a). Diameter of the Y-11 fibre is 1mm and fibre length is 3.5m. After sticking, the scintillator is wrapped by aluminium foil for reflecting layer and over-wrapped by black tape for shielding layer. Five WLS fibres are bundled into a shielding tube together.

On the other hand, the Y-11 fibre also emits a scintillation photon by the incoming ionizing radiation. This dark photon works as an offset noise to the PMT. In order to cancel an influence of the dark photons, a pair of the OF-SBLMs, where one has the scintillator head and the other does not have the scintillator, are assembled as shown in Figure 3(b). A correct value of the local spot area beam loss is obtained by taking a difference between the two PMT signals.

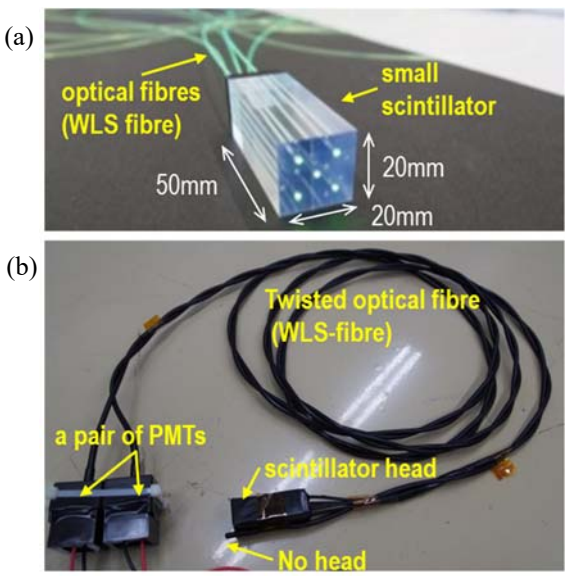

Figure 3: Assembly work of the optical fibre joined S-BLM.

Performance Confirming Test

To confirm the performance of the OF-SBLM, it was compared with the small S-BLM. The two type BLMs were set in the same place on the vacuum duct, which are located at downstream of the ring collimators and has fully separated distance from the magnets.

Performance confirming test was carried out under following two conditions (a) during the beam operation and (b) after the beam stop. During the beam operation, the beam losses due to the leakage particles from the ring collimator are occurred at the measurement spot. In this case, waveform signals are acquired by the digital oscilloscope with a 50 ohm termination because every turn by turn beam loss signal can be detected. After the beam stop, gamma ray generated at the radio-activate vacuum duct can be detected by the scintillator. Thus relative dose level can be estimated and then its decay curve can be obtained by counting the gamma ray continually. In our case, the PMT signals are measured by the digital oscilloscope with 1 M ohm termination and the acquired data during 20 msec are taken an average. And this evaluation process repeats for every 2 sec to obtain the decay curve.

Experimental results summarized in Figure 4. Red plots indicate the small S-BLM signals and blue ones are the OF-SBLM signals. In both conditions, two BLM signals agree very well with each other. Therefore it can be verify that the OF-SBLM can perform as good as the small S-BLM. Namely, it has high sensitivity of spot area beam loss, finer time structure of the beam loss can be measured, and residual dose at the spot area can be evaluated to detect the gamma ray.

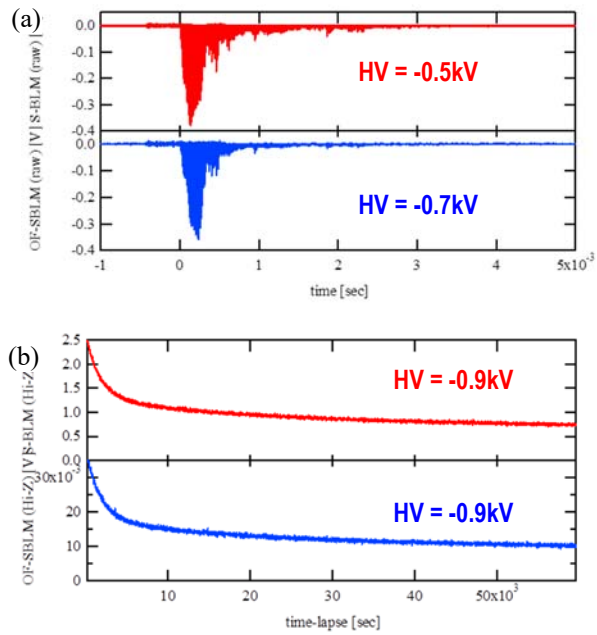

Figure 4: Experimental results to compare the OF-SBLM and small S-BLM. (a) Beam loss waveforms obtained during the beam operation. (b) Relative residual dose decay curves obtained after the beam stop.

Advanced Application of OF-SBLM

In the present, the highest residual doses are observed around the stripper foil. The cause is not the standard beam loss but the secondary particles are produced by nuclear reactions at the stripper foil. Furthermore, it is understand

ISBN: 978-3-95450-192-2 doi:10.18429/JACoW-IBIC2017-WEPWC09

that "foil hitting rate" is the key parameter to reduce these highest dose. The OF-SBLM has a great advantage to enhance the sensitivity the secondary particle detection being influenced by the shift bump magnets. Thus we try to measure the secondary particle from the stripper foil and evaluate the "foil hitting rate". The RCS can choose between circulating mode and one path mode by switching the beam extraction magnets. In the one path mode, only injecting beam hits into the foil. On the other hand, both injecting and circulating beam hits during the beam injection period in the circulating mode. The "foil hitting rate" can be evaluated by comparing with both measured signals in two modes. For preparation, the PMT was replaced with a large PMT (H6410: HAMAMATSU [11]) to increase the dynamic range.

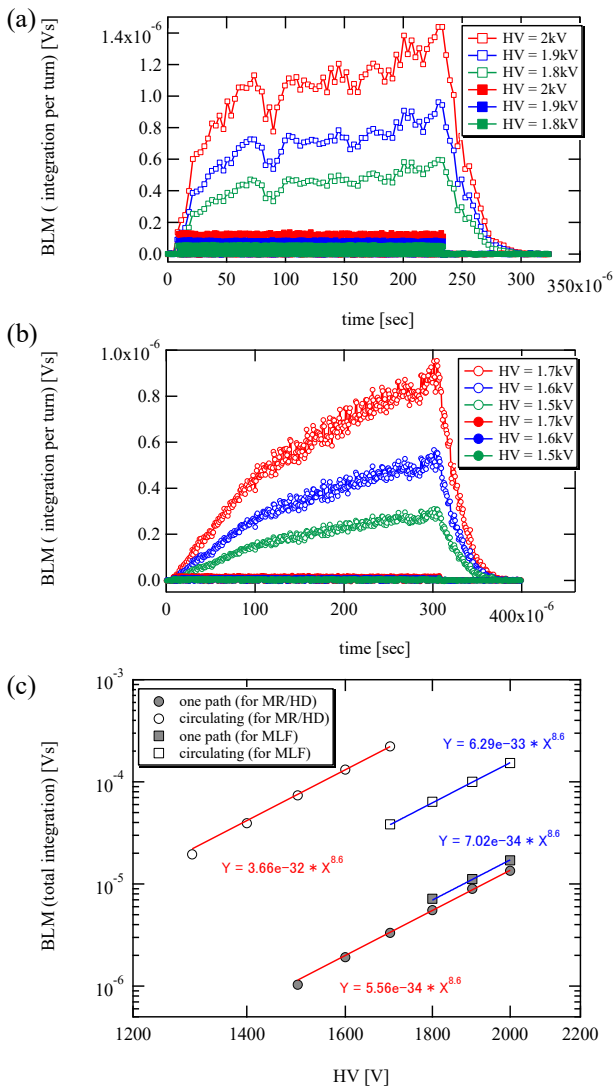

Figure 5: (a) Measurement of the secondary particles from the stripper foil in both one path mode and circulating mode for MLF user operation. (b) Secondary particles measurement for MR/HD user operation. (c) High voltage dependence of the secondary particle measurements.

Beam experiments were carried out in following two user operations; (a) for MLF user (225μs, 200 π/200π-Anti.) and (b) for MR/HD user (300μs, 50 π/50 π-Cor.). Figure 5(a) and (b) shows the turn by turn OF-SBLM signals plots in both one path mode and circulating mode respectively. These signal levels between in one path mode and in circulating mode are markedly different. Thus we have to consider the OF-SBLM (especially the PMT) with saturation in their response or signal buried in a noise, even if the PMT has an enough wide dynamic range. Figure 5(c) shows high voltage dependence of the secondary particle measurements. All plots follow the power-law profile, and each power index obtained by fitting is 8.6 in common. Then it is certain that the OF-SBLM responds without saturation and without being buried in the noise. By comparing the fitting coefficients, the "foil fitting rate" can be estimated directly. It is 8.95 for MLF user operation and 65.8 for MR/HD user operation. Calculating estimation value by using the particle simulation including a space charge effect is 6.3 and 70 respectively. There are a few differences between the measured and calculated values, and it may be caused by slightly varying some conditions. However we can prove the OF-SBLM to have the great advantage for finer tuning to mitigate the beam losses still more.

SUMMARY

Residual dose distributions along the ring are measured by using the GM survey meter, and these detailed dose distributions suggest the various beam loss mechanism. To detect the local spot area beam losses, the optical fibre joined S-BLM is developed. Key technique to improve photon transmission efficiency from the scintillator to the optical fibre is using the wavelength shifting fibre and stricking it into the scintillator. We verify experimentally that OF-SBLM has capability to detect the spot area beam losses without being influenced by the magnetic field. Furthermore, it demonstrates to detect the secondary particles from the stripper foil and evaluate the "foil hitting rate" experimentally.

REFERENCES

[1] High-intensity Proton Accelerator Project Team, JAERI Report No. JAERI-Tech 2003-044 and KEK Report No. 2002-13.

[2] K. Yamamoto, "Efficiency simulations for the beam collimation system of the Japan Proton Accelerator Research Complex rapid-cycling synchrotron", PRST-AB 11, 123501 (2008).

[3] H. Hotchi *et al.*, "Achievement of a low-loss 1-MW beam operation in the 3-GeV rapid cycling synchrotron of the Japan Proton Accelerator Research Complex", PRST-AB 20, 060402 (2017).

[4] M. Yoshimoto *et al.*, "Relation between signals of the beam loss monitors and residual radiation in the J-PARC RCS", *Proc. of IBIC'16*, Bar et al., "Barcelona, Spain (2016), WEPG22.

ISBN: 978-3-95450-192-2 doi:10.18429/JACoW-IBIC2017-WEPWC09

[5] M. Yoshimoto *et al.*, "Maintenance of radio-activated stripper foils in the 3 GeV RCS of J-PARC", JRNC, 3, 305 (2015), PP 865-873.
[6] E. Yamakawa *et al.*, "Measurements and PHITS Monte Carlo Estimations of Residual Activities Induced by the 181 MeV Proton Beam in the Injection Area at J-PARC RCS Ring", JPS Conf. Proc. 8, 012017 (2015).
[7] M. Yoshimoto *et al.*, "Radio-activation caused by secondary particles due to nuclear reactions at the stripper foil in the J-PARC RCS", *Proc. of IPAC'17*, Copenhagen, Denmark (2017), TUPVA093.
[8] Plastic scintillator: EJ212, Eljen Technology, http://www.eljentechnology.com/products/plastic-scintillators/ej-200-ej-204-ej-208-ej-212.
[9] Photomultiplier tube: H11934-100-10MD, HAMAMATSU, https://www.hamamatsu.com/resources/pdf/etd/R11265U_H11934_TPMH1336E.pdf.
[10] Wavelength Shifting Fibers, Y-11(200), Kuraray, http://kuraraypsf.jp/psf/ws.html.
[11] Photomultiplier tube: H11934-100-10MD, HAMAMATSU, https://www.hamamatsu.com/us/en/product/alpha/P/3002/H6410/index.html.

ISBN: 978-3-95450-192-2 doi:10.18429/JACoW-IBIC2017-WEPWC10

BEAM LOSS MONITORING SYSTEM FOR THE RARE ISOTOPE SCIENCE PROJECT*

Yoolim Cheon, Changkyu Sung, Kookjin Moon,
Chulun Choi, Dongnyung Choe, Moses Chung†, UNIST, Ulsan 44919, Korea
Yeonsei Chung‡, Gidong Kim, Hyung Joo Woo, IBS, Daejeon 34047, Korea
Chanmi Kim, Korea University, Sejong 30019, Korea

Abstract

A heavy ion accelerator facility called RAON is being constructed in Korea to produce various rare isotopes for the Rare Isotope Science Project (RISP). This facility is designed to use both In-flight Fragment (IF) and Isotope Separation On-Line (ISOL) techniques in order to provide a wide variety of RI beams for nuclear physics experiments. One of the biggest challenges in operating such a high beam power facility (~400 kW) is to monitor beam loss accurately and to execute the machine protection system reasonably quickly whenever necessary. In this work, we report the conceptual design of the RAON beam loss monitoring system. Monte Carlo simulations using MCNPX code have been performed to generate radiation dose maps for 1 W/m losses of proton and uranium beams. The required machine protection time has been estimated from the yield time of the stainless steel beam line components including the beam grazing angle dependence. Types of the detectors have been determined based on the radiation levels of the gammas and neutrons, and the minimum sensitivity and response time requirements.

INTRODUCTION

The RISP project [1] will be composed of a 70 kW proton cyclotron as a low-power ISOL driver, an 18 MeV/u linac for ISOL post-accelerator and a 200 MeV/u main linac for high-power ISOL and IFF driver. The main driver linac named RAON will accelerate all elements up to uranium with beam power up to 400 kW. To maximize the average currents of the primary beam on target, continuous wave (CW) operation is preferred, and therefore superconducting RF (SCRF) technology has been adopted for the linac design. One of the biggest challenges in operating such a high beam power facility (~400 kW) is to monitor beam loss accurately and to execute the machine protection system (MPS) reasonably quickly whenever necessary.

The role of the dedicated beam loss monitors (BLMs) includes 1) to protect beam line components from fast or irregular beam losses, 2) to minimize activation of the components for maintenance, and 3) to provide information for beam tuning and optimization. The BLM should provide the amount of beam loss, beam loss location, and fast interlock signal to inhibit the beam. The (preliminary) requirements of the RAON BLM system are summarized as follows:

- It should detect beam losses not only from proton beam, but also from heavier ion beams such Oxygen and uranium ion beams.
- It should have a high dynamic range to cover both slow (<1 W/m level) and fast (significant fraction of total beam power) beam losses.
- It should provide the interlock signal within $< 15\mu s$ (overall MPS time would be $< 35\mu s$).

MPS REQUIREMENTS

It has been known that the yield stress of the beam line components (copper, stainless-steel, or niobium etc.) indeed determines the maximum allowable beam injection time, which is given by [2–6]

$$T_{\max} \approx \frac{4\pi}{\sqrt{3}} \frac{\sigma_x \sigma_y}{I} \frac{\rho C_v}{\alpha E} \sigma_m \frac{1}{R_{ave}}, \quad (1)$$

where $\sigma_x(\sigma_y)$ is the rms beam radius in $x(y)$-direction, I is the beam current in pps, ρ is the mass density of the material, C_v is the specific heat, α is the coefficient of linear expansion, E is the Young's modulus, σ_m is the yield strength, and R_{ave} is the average stopping power of the Bragg curve which is estimated from the SRIM code. Because the stopping power of a heavy ion beam is a few ten times larger than proton or electron beams, a fast response of the MPS (faster than the material damage time) is even more important in heavy ion machines.

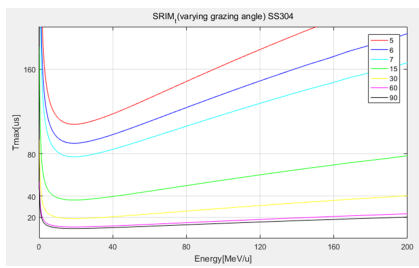

Figure 1: The maximum allowable injection time depends on the incidence angle (~2 orders of magnitude difference).

The required response time strongly depends on incident angle of the beam (θ) as well. Figure 1 shows $T_{\max}$ for the case of uranium beam injecting into stainless-steel (SS) along the RISP linac (see the linac structure in Fig. 2). For incident angles larger than 60 degrees, the damage may happen in less than 20 μs, which is beyond the capability of

* Work supported by the National Research Foundation of Korea (Grants No. NRF-2017M7A1A1019375 and No. NRF-2017M1A7A1A02016413).
† mchung@unist.ac.kr
‡ yschung@ibs.re.kr

ISBN: 978-3-95450-192-2 doi:10.18429/JACoW-IBIC2017-WEPWC10

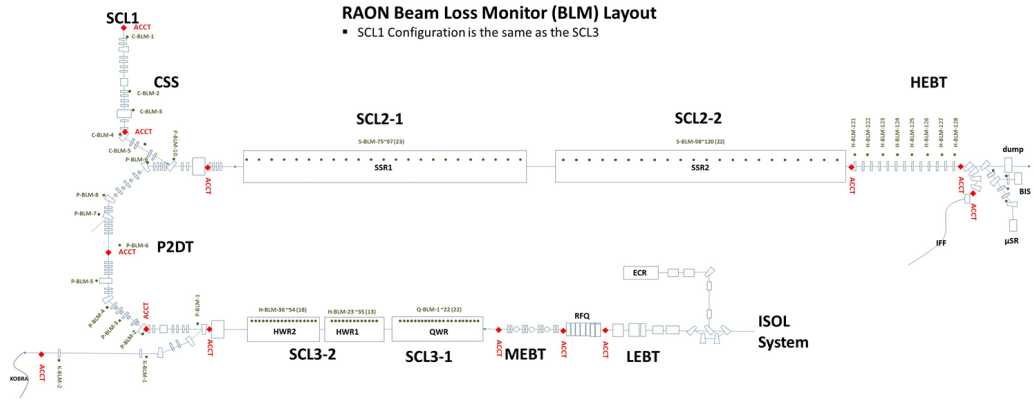

Figure 2: Layout of the RAON beam loss monitoring system. Green dots indicate BLMs while red diamonds ACCTs.

the RISP MPS. The 90 degree angle is the worst case which makes the maximum damage on the components. Nevertheless, such case can occur very rarely, for example only when objects (e.g., gate valve) are in the beam line or beam hits the bellows. In most cases, it is expected that the incident angle is small enough that the response time of $\sim 35\mu s$ would be reasonable.

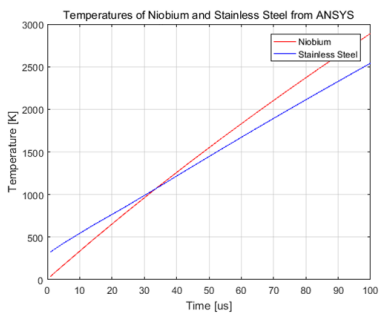

Figure 3: Thermal analysis on Nb and SS by ANSYS with uranium beam of 1-mm rms radius, Gaussian profile, and 90 degree grazing angle.

An ANSYS thermal analysis suggests that indeed the SS yield happens faster than the melting of SS and Nb (see Fig. 3). Temperature rise in a short time is mainly determined by beam deposited power density, and specific heat of the material. Melting times of SS and Nb are $\sim$ 46 μs and $\sim$ 69 μs, respectively, which are longer than the overall MPS time requirement of $\sim$ 35 μs.

LAYOUT OF THE RAON BLM SYSTEM

A preliminary layout of the RAON BLM system is illustrated in Fig. 2. In the superconducting linac sections, one BLM per warm section (i.e., near the quadrupole doublet) will be installed. In the bending sections [post linac to driver linac transport (P2DT) and charge stripper section (CSS)], BLMs will be installed around the possible beam loss points, such as collimators, bending magnets, etc. Currently, total 182 BLMs are planned.

Before and after the sections where a beam transport monitoring is critical, AC-coupled current transformers (ACCTs) are planned to be installed. The signal difference by two ACCTs makes an alarm signal for machine protection. This differential beam current monitor (DBCM) networks will be used as a primary MPS input for fast beam losses.

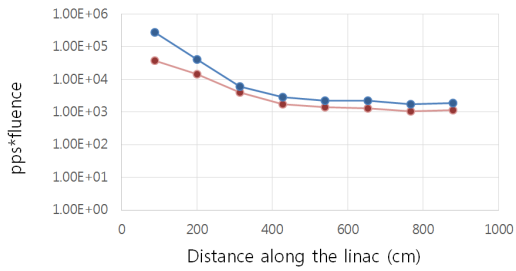

Figure 4: Neutron flux along the position of the doublets for the case of a point loss in the doublet with 3 mrad incidence angle and 1 W of total beam loss. An uranium beam of 200 MeV/u is used in this calculation. Case 1(2) corresponds to the detector position inside(outside) the doublet.

FAST LOSS SCENARIO

Due to the lack of complete list of beam loss patterns, some strategy is needed to determine the number of detectors and their locations [6]. The TRACK simulations indicate that most localized losses occur in the quadrupoles (except the slit), in which the beam size is largest. Therefore, as a default, we decided to place one BLM per one quadrupole doublets in the warm sections. To see the basic characteristics of the fast losses, we perform Monte-Carlo simulations (MCMPX) for point losses in the quadrupoles with 3 mrad incidence angle and 1 W of total beam loss. Figure 4 implies that the neutron flux is sufficiently localized that one might tell at which doublet the beam loss occurs. As a future work, we will increase the incidence angle to the "worst case angle" to do fine-tuning of the BLM locations, following ESS's approach.

ISBN: 978-3-95450-192-2 doi:10.18429/JACoW-IBIC2017-WEPWC10

Table 1: Beam Energy Variation along the Superconducting Linac Sections of the RAON

	QWR	HWR1	HWR2	SSR1	SSR2
Uranium	0.5~2.6 MeV/u	2.6~6 MeV/u	6~18.5 MeV/u	18~56.3 MeV/u	56.3~210.4 MeV/u
Proton	0.5~7.5 MeV/u	7.5~34.2 MeV/u	34.2~87.4 MeV/u	87.4~222 MeV/u	222~600 MeV/u

RADIATION SIMULATIONS

To estimate the radiation doses from 1 W/m level of slow losses, we carried out the MCNPX (Version 2.7.0) Monte-Carlo simulations. A line source with particle flux equivalent to 1 W/m is assumed. The incident angle is set 90 degrees. Average doses are calculated on cylindrical detectors located outside the cryomodules. The geometry inputs for the MCNPX simulations are semi-realistic, i.e., the structures themselves are made bulky without minor details, but material densities and masses are close to the real values (see Fig. 5).

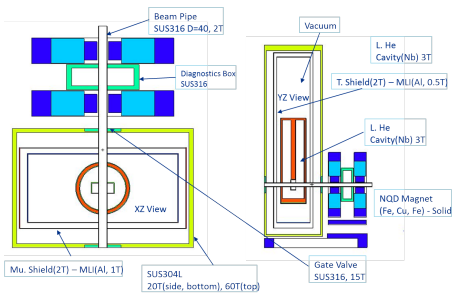

Figure 5: An example of the geometry used for the MCNPX simulations. Shown here is the QWR section.

The normalized (by 1 W/m) neutron flux (#/cm^2/s) and gamma dose (rad/hr) are shown in Figs. 6 and 7, respectively as functions of beam energy. The energy variations of the proton and uranium beams along the superconducting linacs are summarized in Table 1. We note that for a given beam energy per nucleon, radiations induced by heavy ions are much weaker than those induced by protons. We also note that the neutron generation is negligible when the beam energy is less than 10 MeV/u. From Figs. 6 and 7, we expect that beam loss monitoring for the uranium beam in the low energy linac sections would be extremely challenging.

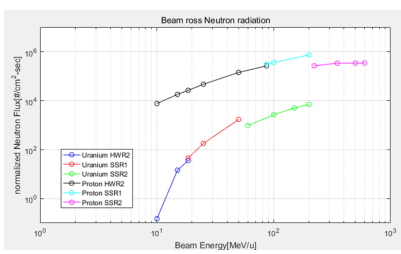

Figure 6: Neutron flux versus beam energy for 1 W/m loss.

As shown in Figs. 8 and 9, the neutron energy spectrum becomes wider as beam energy goes higher while the gamma energy spectrum has more or less a fixed range.

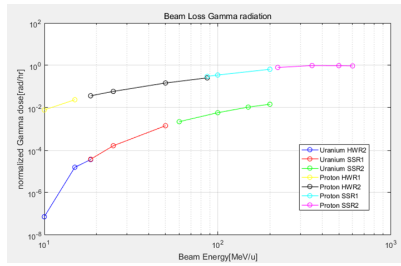

Figure 7: Gamma does versus beam energy for 1 W/m loss.

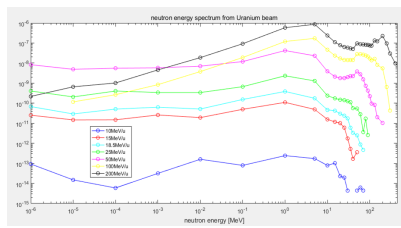

Figure 8: Neutron fluence from a single uranium beam ion.

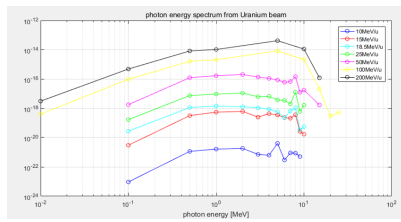

Figure 9: Gamma fluence from a single uranium beam ion.

CAVITY X-RAY ISSUES

Not only from the beam losses in the beam pipe but also from the bremsstrahlung of field-emitted electrons inside the cavity, significant photon radiation can be made. Estimation of the maximum X-ray dose for each linac section is summarized in Table 2. This cavity X-ray indeed acts as a background noise for the BLM detectors, and can exceed the beam loss signal particularly for heavy ions in the low energy sections [7, 8]. As shown in Fig. 10, most X-ray energy lies below 1 MeV for low energy linacs. Therefore, we may use lead to shield low energy photons (< 1 MeV) to separate gamma radiation generated by the beam loss from the cavity X-ray background.

BLM DETECTORS

For low energy, we consider plastic detectors (PD, plastic scintillators + PMTs) because they are fast and have high efficiency for fast neutrons and high energy gamma rays [9–11]. For higher energies, ionization chambers (IC), which almost all accelerators in the world are equipped with, will

ISBN: 978-3-95450-192-2 doi:10.18429/JACoW-IBIC2017-WEPWC10

Table 2: Estimation of the Maximum X-ray Dose for each Linac Section

	QWR	HWR1	HWR2	SSR1	SSR2
Accelerating voltage (MV)	1.1	1.4	1.4	2.3	4.1
Maximum head load (W)	1.6	2.7	2.7	4.5	8
Maximum field emission flux (#/sec)	9.1E+12	1.2E+13	1.2E+13	1.2E+13	1.2E+13
Maximum dose (rad/hr)	3.75E-02	4.97E-02	4.97E-02	5.04E-02	5.03E-02

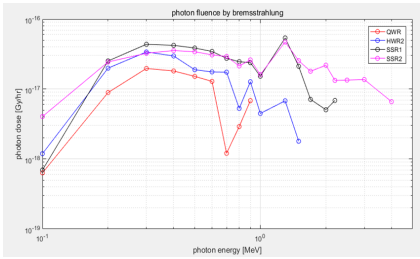

Figure 10: Cavity X-ray energy spectrum.

Table 3: Target Radiation and Particle Species for each BLM Detector

	IC	PD	HRD	ACCT
QWR	N/A	N/A	Beam ions	EM fields
HWR1	N/A	γ	Beam ions	EM fields
HWR2	N/A	γ, n	Beam ions	EM fields
SSR1	γ	γ, n	Beam ions	EM fields
SSR2	γ	γ, n	Beam ions	EM fields

be a better solution in terms of cost and maintenance. The strategy for the RAON BLM systems is summarized in Table 3. For low energy sections (QWR and HWRs), beam loss monitoring by secondaries will be very difficult, thus an interceptive device called Halo Ring Detector (HRD) [7, 8] is also under preparation.

For the scintillator material, we consider BC-408 (or EJ-200). This organic plastic is less sensitive to low energy X-ray, and interacts with fast neutrons (>50 keV) through (n,p) scattering. For 1000 g of BC-408, the sensitivity of the scintillation detector is [9, 10]

$$S_{scint} \approx 140 \left[\frac{\mathrm{C}}{\mathrm{rad}}\right] \times \varepsilon_{coll}, \quad (2)$$

where ε_{coll} is the efficiency of collector or light guide. Here, we assume the light output $R_s = 0.1$ photon/eV and the PMT gain is 7×10^5. The detection efficiency of BC-408 to fast neutrons can be calculated based on np-scattering cross-section for 5 cm-long BC-408 plastic scintillator, which is parameterized as [12]

$$DE = -0.142 \ln(E_n) + 0.5247, \quad (3)$$

where E_n is the neutron energy in MeV. For 1 liter (1000 cm^3) argon filled ionization chamber at 1 atm, the sensitivity is [9, 10]

$$S_{ion} \approx 638 \left[\frac{\mathrm{nC}}{\mathrm{rad}}\right]. \quad (4)$$

Coupled with radiation simulations, we can estimate the actual signal levels of IC, PD, and HRD in each linac section, which is in progress and will be reported elsewhere. Design and fabrication of the prototype detectors are also underway (see Fig. 11).

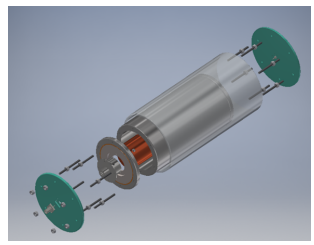

Figure 11: Preliminary 3D drawing of the coaxial ionization chamber.

REFERENCES

[1] RISP web page, http://www.risp.re.kr.

[2] R. E. Shafer, "How Long a SNS Beam Pulse Would Damage a Copper Accelerating Structure?", SNS Technical Note (2001).

[3] C. Sibley, "Machine Protection Stratiges for High Power Accelerators", *Proceedings of the 2013 Particle Accelerator Conference*, Portland, Oregon, USA (2003).

[4] H. Takei *et al.*, *Journal of NUCLEAR SCIENCE and TECHNOLOGY*, Vol. 42, No. 12, p. 1032–1039 (December 2005).

[5] Y. Zhang *et al.*, "Analysis of Beam Damage to FRIB Driver Linac", *Proceedings of SRF2011*, Chicago, IL, USA (2011).

[6] I. Dolenc Kittelmann *et al.*, "Simulations and Detector Technologies for the Beam Loss Monitoring System at the ESS Linac", *Proceedings of HB2016*, Malmö, Sweden (2016).

[7] Z. Liu *et al.*, "Beam Loss Monitor System for the Low-Energy Heavy-Ion FRIB Accelerator", *Proceedings of IBIC2013*, Oxford, UK (2013).

[8] Z. Liu *et al.*, "Collimation Design and Beam Loss Detection at FRIB", *Proceedings of HB2016*, Malmö, Sweden (2016).

[9] K. Wittenburg, "Beam Loss Monitors", CAS2008: Specialised Beam Diagnostics School, Dourdan, France (2008).

[10] K. Wittenburg, "Beam Loss Monitors: Overview of BLM Technology", 3rd oPAC Topical Workshop on Beam Diagnostics, Vienna (2014).

[11] F. Negoita, Private Communications (2017).

[12] J. Va'vra *et al.*,"Neutron Beam Line at SLAC", SLAC-TN-14-026 (2014).

ISBN: 978-3-95450-192-2 doi:10.18429/JACoW-IBIC2017-TH1AB1

FIELD EMISSION IN SRF ACCELERATORS: INSTRUMENTED MEASUREMENTS FOR ITS UNDERSTANDING AND MITIGATION*

R. L. Geng†, A. Freyberger, R. Legg, R. Suleiman, JLAB, Newport News, VA, USA
A. S. Fisher, SLAC, Menlo Park, CA, USA

Abstract

Several new accelerator projects are adopting superconducting RF (SRF) technology. When accelerating SRF cavities maintain high RF gradients, field emission, the emission of electrons from cavity walls, can occur and may impact operational cavity gradient, radiological environment via activated components, and reliability. In this talk, we will discuss instrumented measurements of field emission from the two 1.1 GeV superconducting continuous wave (CW) linacs in CEBAF. The goal is to improve the understanding of field emission sources originating from cryomodule production, installation and operation. Such basic knowledge is needed in guiding field emission control, mitigation, and reduction toward high gradient and reliable operation of superconducting accelerators.

INTRODUCTION

Field emission (FE) is a well-known phenomenon in both normal conducting and superconducting RF cavities. Its impact to SRF cavities is far more profound owing to the fact that the surface power dissipation in SRF cavities is smaller by many orders of magnitude as compared to their normal-conducting counterparts. Therefore, there is significant interest in its understanding and control for SRF accelerator design, construction and operation.

Despite the continued progress in understanding and control of FE over decades, the challenge remains as the specification of operation gradients has been on the rise too. By using today's state-of-the-art cavity surface processing and assembly techniques, FE is controlled satisfactorily in qualified individual cavities. This has been demonstrated in SRF accelerator projects requiring large numbers of multi-cell cavities prepared and assembled in laboratories as well as in industry [1,2]. However, preserving the cavity performance from qualification testing of individual cavities to SRF cryomodule operation with beam remains an issue of interest. One cause for cavity performance loss is the degradation of FE onset and this has provoked lots of recent discussions [3].

It is generally believed that the current understanding of the basic physics of FE in SRF cavities is adequate [4-6]. The challenge lies largely in the engineering aspects of controlling *field emitter input or activation* over the course of constructing, shipping, commissioning and operating the SRF cavities at an increasingly complex level of cryomodules, segments, and linacs. In such a situation, opportunities for learning and improving are rather scarce because of limited number of large-scale SRF projects and yet a closed loop is required to allow understanding and testing. Fortunately, some recently completed SRF projects, such as CEBAF 12 GeV upgrade and E-XFEL, have provided new opportunities. Looking forward, several new accelerator projects are adopting SRF technology, such as ESS, FRIB, LCLS-II etc., one may anticipate a continued progress in our understanding and mitigation of FE in SRF accelerators. In this paper, we present our instrumented measurements of FE from the two 1.1 GeV superconducting CW linacs in CEBAF. This work is based on and an extension of the previous work in our effort of FE understanding for its ultimate control, in particular for large scale CW SRF accelerators [7].

FE THEORETICAL AND PRACTICAL

FE Theory

The original theory of FE was developed by Fowler and Nordheim [8]. It describes electron emission in electric fields at the interface of a metal and a vacuum based on the quantum mechanical tunnelling process. The potential barrier at the interface prevents electrons in the metal from escaping. The work function ϕ, a material dependent property, is the measure of this barrier. ϕ = 3-5 eV for most metals. When no external electric field is applied to the metal surface, electrons in the metal are confined as they are at the Fermi energy level which is below the vacuum energy level by an amount of the work function and the thickness of the potential barrier is infinite. An external electric field applied to the metal surface E_s deforms the original rectangular potential barrier of infinite thickness into a triangular barrier of finite thickness, thus permitting electron tunnelling with finite probability. The salient result of the FN theory is that the FE current density j_{FN} rises exponentially with an increasing electric field: $j_{FN}=(AE_s^2/\phi)\exp(-B\phi^{3/2}/E_s)$, where A and B are constants.

The agreement between experimental results and the FN theory is quite satisfactory provided the surface electric field E_s is replaced by $\beta_{FN}E_s$, where β_{FN} is the field enhancement factor [9,10]. E_s and β_{FN} are typically in the range of 10-100 MV/m and 50-1000, respectively in SRF cavities. Besides β_{FN}, the effective emitting area A_e is a parameter useful for fitting the total FE current $I_{FN}=j_{FN}A_e$ against the FN law.

FE in SRF Cavities

The estimated time for an electron to tunnel through the potential barrier is on the order of fs, orders of magnitude smaller than the ns RF period for typical SRF applications

* Authored by Jefferson Science Associates, LLC under U.S. DOE Contract No. DE-AC05-06OR23177. The U.S. Government retains a non-exclusive, paid-up, irrevocable, world-wide license to publish or reproduce this manuscript for U.S. Government purposes.
† geng@jlab.org

ISBN: 978-3-95450-192-2 doi:10.18429/JACoW-IBIC2017-TH1AB1

[11]. Therefore, the FE process in SRF cavities can be regarded as instantaneous. It then follows that the RF FE current $I_{FN}(t)$ at the emitting site is periodic as the emission is permitted only when the instantaneous local field is pointed toward the surface. Consequently, electrons are field emitted in pulsed mode with a repetition rate identical to the frequency of the RF field in the cavity.

Figure 1 shows two hypothetical FE scenarios in a 7-cell 1.5 GHz CEBAF 12 GeV upgrade SRF cavity with an acceleration gradient E_a=15 MV/m. The upper graph depicts trajectories of electrons emitted from a site close to the iris between the 3rd & 4th cavity cell. Due to the finite spread in the emission phase, electrons emitted from the same point trace out a family of trajectories. Electrons gain energy from the EM field. Some get lost as they hit cavity walls but some survive and reach the borders of the simulation (vertical line at both ends). Those striking the wall give up their gained energy predominantly in the form of heat. Bremsstrahlung X-rays are created as well. Those surviving from wall hitting then export themselves into the neighbouring cavity in case of a string of cavities being laid in tandem (such as in a cryomodule). The lower graph depicts trajectories with the emitting site slightly moved away from the site in the upper graph.

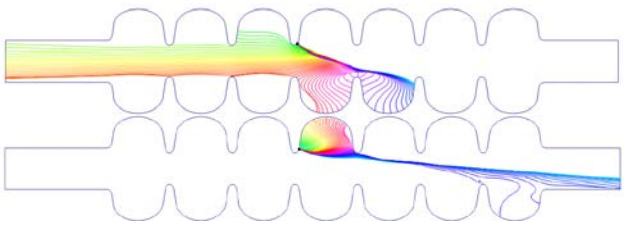

Figure 1: Family of trajectories for electrons emitted from two slightly separated emitting sites in a 7-cell 1.5 GHz CEBAF 12 GeV upgrade SRF cavity at E_a = 15 MV/m.

It is noteworthy that as illustrated in Fig. 1 that, depending on the exact location of the emitting site, FE electrons can export themselves into either the upstream cavity or downstream cavity. The exported electrons can gain significant energy (scales as E_aL, where L is the separation between the emitting site and the export plane) arising from phase synchronization. In principle, electrons emitted from the end cells can gain the full RF voltage. When the emitting site is further moved away from the iris, most FE electrons will get lost in the mid-cell.

It should be mentioned that, on a theoretical ground, due to the existence of an energy gap, a small difference in the FE current is predicted when a metal makes a transition from its superconducting state to normal conducting state. However, no difference of practical significance has been experimentally measured [12]. In addition, as will be shown later, FE in SRF cavities is mostly originated from foreign particulates adhering to niobium surfaces. Therefore, superconductivity does not impose any special concern in view of FE. However, SRF cavities must work at cryogenic temperatures. The cold cavity surface cryopumps residual gas molecules. These adsorbed species do have strong influence in FE behaviours under some circumstances. This point will be touched upon later.

Field Emitters

As a result of past studies, the present view is such that FE in SRF cavities is originated from *localized sites* on the inner cavity surface. The predominant source emitters are microscopic particulates adhering to the inner cavity surface, chemical residuals, and geometrical flaws [13].

Some of the particulate field emitters are introduced by the necessary chemical surface processing which transforms the raw inner surface of an as-built cavity into a high quality working surface able to hold high surface electromagnetic fields. Although the post chemistry ultrasonic cleaning and high pressure water rising remove most particulates and flush them out of the cavity, some may still remain due to either a stronger particle-surface adherence force or varying distribution of the dislodging force delivered to the location where a particle resides.

Other particulate field emitters are introduced through the cavity opening ports onto the cavity surface, at a time beyond the completion of final cleaning, from external sources. Examples are airborne particulates, debris generated from handling, tooling, flange jointing, gasket crashing, gate valve actuating, ion pump starting and operating etc. To minimize this *field emitter input*, SRF cavities are assembled in large-sized high-quality Class 10 (ISO 4) cleanliness clean rooms into cavity strings; critical assembly steps are done with the opening port facing down; cavity strings are evacuated slowly etc. These equipment and procedures reduce particulate input by lowering either the number of external source particles or the chance of external particulates being transported into the cavity. Particulate transportation can be enabled by gravitational pull or mechanical energization (shocking impact at cavity bodies, turbulent flow in vacuum ducts etc.).

For illustration, Fig. 2 shows a typical stainless steel particulate that was collected from a CEBAF-type 5-cell niobium SRF cavity after service for beam operation [14].

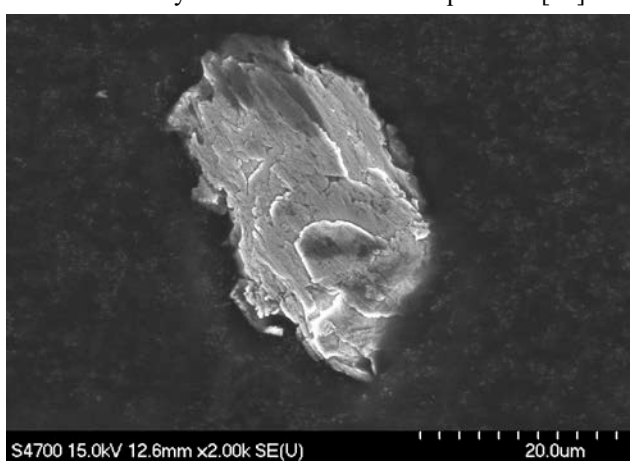

Figure 2: A typical stainless-steel particulate collected from a CEBAF-type 5-cell niobium SRF cavity.

Geometrical flaw field emitters, such as protrusions and scratches, are still encountered but their occurrence is significantly lower than particulate field emitters in modern cavities. This may be a result of broadly adopted elec-

ISBN: 978-3-95450-192-2 doi:10.18429/JACoW-IBIC2017-TH1AB1

tropolishing surface processing which gives a smooth surface and is particularly effective in reducing sharp protruding tips in the iris regions of SRF cavities. In addition, FE caused by a geometrical flaw tends to be stable and insensitive to additional cleaning such as repeated high pressure water rinse [15]. As a result, cavities strongly affected by this kind of field emitters are likely rejected from further string assembly and will not make it to the accelerator (of course such cavities can be repaired and may be used afterwards still). In the context of this talk, we will not discuss this kind of field emitters any further.

FE Instrumentation

In the past, several kinds of instrumentation have been successfully used for studying FE in SRF cavities in laboratory testing studies [16].

- **Temperature monitoring/mapping**: temperature sensors (carbon resistors) attached to the outer surface of a cavity immersed in liquid helium bath detect heat deposited by FE electrons [17-19].
- **Electron detecting**: Metal probes inserted into the cavity space or RF antenna probes, positively biased, collect FE electrons [17,18,20].
- **X-ray monitoring/mapping**: radiation sensors or detectors (photodiodes, ionization chambers, NaI scintillators) placed in liquid helium bath near a cavity or in the air outside Dewar detect intensities and energy spectrums of Bremsstrahlung X-rays induced by FE [4,20,21]. Arrays of detectors (rotating or fixed) near cavity walls detect simultaneously to reconstruct X-ray intensity 3D map [18,21,22]. Detectors traveling on a linear rail trace out X-ray intensity 1D distribution [23].
- **X-ray photography**: "pin hole camera" placed outside of testing Dewars image the X-ray intensity 2D distribution on a film [24,25] .
- **Optical imaging**: cameras with line-of-sight view of the cavity inner space image luminous spots arising from light emission at FE emitting site or luminous objects in the vacuum space [26,27].

These FE instrumentation played a key role in understanding the basics of FE in SRF cavities, such as establishing the exponential nature of FE consistent with the FN law, establishing the point-like nature of field emitters, identifying the locations of field emitter sites when the data are analysed in conjunction with the computer-aided calculations of electron trajectories.

Degradation of FE Onset from Vertical Test to Cryomodule Placement in Tunnel

It is common practice across SRF testing facilities to monitor FE by detecting Bremsstrahlung X-rays with detectors placed outside of Dewars for vertical testing of individual cavities or outside of cryomodules for cryomodule testing. A useful figure of merit is the FE onset, the accelerating gradient at which the first FE induced X-ray being detected. Degradation in the FE onset from vertical qualification testing of a cavity to its verification testing in a cryomodule has been observed. Further degradation may be observed as well at the point of cryomodule commissioning test in the accelerator tunnel. This issue of FE onset degradation has attracted broad international interest for its understanding and mitigation [3]. It is commonly believed this degradation is caused by *particulate input* onto the cavity surface arising from handling and assembly of components beyond the final cavity acceptance test, therefore such degradation might be preventable, or at least can be reduced, by executing strict handling and assembly procedures.

It has been recognized that improved FE instrumentation is needed for understanding the FE onset degradation from cavity vertical testing to cryomodule placement in accelerator tunnels. Presently there are variations in X-ray detector types, cavity-detector distances, materials between the cavity and the detector etc. across SRF facilities, and even within the same facility. This situation leaves ambiguity in quantifying the FE onset degradation or for comparing the degradation among multiple facilities.

An effort has been made recently at JLab by placing a permanent photodiode (Hamamatsu S12230-1 PIN diode) next to each cavity in a cryomodule [28]. In total, 16 diodes were placed in that cryomodule, one each at each end of the eight 7-cell cavities contained (see Fig. 3). The vertical testing of each cavity was instrumented with the same kind of photodiode maintaining the same spatial relationship with respect to the cavity. This effort was aimed to improve the certainty in judging the FE onset degradation from cavity vertical testing to verification testing in a cryomodule at various checking points. These permanent photodiodes might be useful for FE instrumentation during routine beam operations. A test is presently being conducted by instrumenting LCLS-II cryomodules with an optical fiber based X-ray detection system. By maintaining a fixed spatial arrangement with respect to the cavity string contained in a cryomodule, this system leads to a site-independent measurement of FE, permitting comparisons between testing facilities at JLab and FNAL. The optical fiber is expected to be used in SLAC tunnel for beam loss detection and FE detection as well.

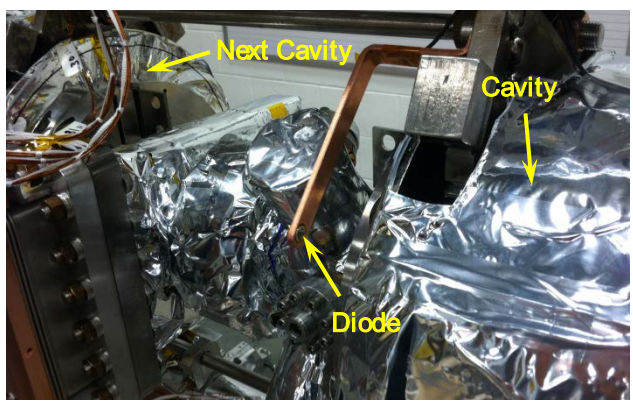

Figure 3: A photodiode placed next to a cavity permanently for FE instrumentation in a CEBAF-type cryomodule.

FE IN SRF ACCELERATORS

FE in SRF accelerators may have impacts to the accelerator energy reach, reliability and maintainability. We will

ISBN: 978-3-95450-192-2 doi:10.18429/JACoW-IBIC2017-TH1AB1

limit the discussion on large scale CW SRF linacs with a focus on the 12 GeV CEBAF. However, many aspects to be discussed may be relevant to other kind of SRF systems such as pulsed SRF linacs, in particular those linacs adopting the CEBAF-type cryomodule topology (SNS, ESS).

Presently, CEBAF consists of two 1.1 GeV SRF linacs [29]. Each linac consists of 20 original CEBAF cryomodules (each provides a nominal acceleration voltage of 20 or 50 MV, dubbed as C20 or C50) plus 5 upgrade cryomodules (nominal voltage 100 MV, C100). In total, 418 multicell cavities are presently installed in CEBAF.

FE Impact to CEBAF Operation

Several aspects must be considered to properly understand the implication and impact of FE to CEBAF:

- FE electrons may affect ceramic windows in RF input couplers causing fast trips as was understood for C20 cryomodules.
- Field emitted electrons may be captured and exported out of the source cavity. These electrons may propagate into other cryomodules and gain increasingly larger energies, resulting in steep radiation damage.
- Cold cavities are open to the vacuum spaces of warm beamline components, resulting in a continued *gas input* into the cavity. The frozen gases may activate new field emitters or enhance FE of existing field emitters arising from the resonant tunnelling effect [4,30,31]. Particulates may be generated from movement of beamline components such as cycling of gate valves. This may lead to *particulate input* into cavities directly or enabled by other mechanism [7].
- The accelerator must be operated at required beam energies and simultaneously with required beam reliability. Pushing the accelerating gradient for higher beam energies may decrease the system reliability when FE is present because of the exponential field dependence of FE.

To improve our understanding of these aspects, several tests have been carried out at CEBAF since January 2016 with instrumented measurements of FE at various zones with various types of radiation detectors.

Propagation of Field Emitted Electrons

Several tests were performed in different zones to study propagation of field emitted electrons. Tests done in the injector zones 0L03 (C20 cryomodule) and 0L04 (C100 cryomodule) were instrumented with an SNS-type fast beam loss monitor (plastic scintillator + PMT by Bridgeport, model R2D-FBLM-138) attached to the downstream endplate of cryomodule in zone 0L04 (see Fig. 4). This detector was operated in the pulse counting mode with an exiting DAQ system. The X-ray count rate was less than 10 Hz with zone 0L04 on and operated at nominal gradients while leaving zone 0L03 off, indicating no detectable FE from 0L04. The count rate went to 10^4 Hz by turning zone 0L03 on at nominal gradients while leaving zone 0L04 off, indicating FE sources being present in 0L03. This count rate went up to 10^6 Hz when zone 0L04 was turned on while maintaining 0L03 on. This experiment shows that electrons field emitted from zone 0L03 were propagated into zone 0L04.

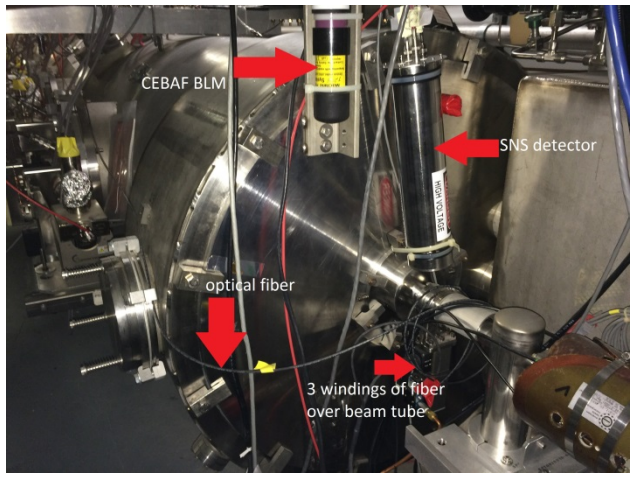

Figure 4: FE testing in CEBAF injector zones 0L03 & 0L04 with a SNS-type detector attached to the downstream endplate of the cryomodule in zone 0L04.

A set of tests was performed in zones 1L25 and 1L26 (both C100 cryomodules) of the North Linac with four high dose rate ion chambers placed adjacent to cryomodules [32]. It was found that FE electrons can be accelerated up and downstream in the C100s between cryomodules. Radiation levels produced by the transmitted electrons go as the ratio of their energy.

An interesting observation was made on November 11, 2016 as shown in Fig. 5. Two ion chambers (one each upstream 1L25 & 1L26) both reacted to gradient changes in zone 1L11, 12 & 13. Gradient scanning at zone 1L22 had no impact. All other cryomodules in North Linac were at nominal gradients. This observation seems to indicate that FE electrons are propagated over a remarkable long distance (> 100 m) passing multiple (15) cryomodules.

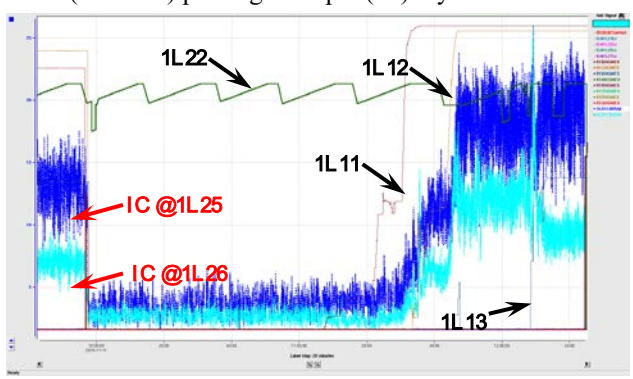

Figure 5: Ion chambers (IC) at zone 1L25 & 1L26 react to sum module gradients at zone 1L11, 12 & 13.

Now that it is known that field emitted electrons can be exported out of the source cavity in either direction and be propagated into near or even far cryomodules, we may come up with some general guide lines for FE mitigation.

- It is useful to know which cavity is a FE source cavity. Turn its gradient down.

ISBN: 978-3-95450-192-2 doi:10.18429/JACoW-IBIC2017-TH1AB1

- It is useful to preferentially place FE-free cryomodules upstream of a linac and heavy FE cryomodules downstream.
- It is useful to choose a set of inter-cavity spacing and inter-cryomodule spacing such that the backward propagation of field emitted electrons can be reduced (the forward propagation cannot be mitigated by this technique due to requirement for the main electron beam).

Due to the exponential field dependence of FE, tuning the source cavity gradient can have a major effect. For example, one FE test in zone 1L25 & 1L26 with ion chamber monitors shows that radiation levels are changed by 50% when a 3% change in gradient made.

The lost gradient due to lowering the source cavity can be restored by raising the gradient of FE-free cavities. A proof-of-principle test of this *gradient re-distribution for reducing FE radiation* was done in zone 0L03 & 0L04 as shown in Fig. 6. By scanning the individual cavities contained in 0L03 & 0L04, two FE source cavities were identified, 0L03-3 & -7. By lowering the gradient of each of them by 3 MV/m and raising the gradient of two FE-free cavities (0L03-5 & -6) by 3 MV/m, the FE induced X-ray count rated was reduced from 6×10^5 to less than 10 Hz with the integrated acceleration voltage still preserved.

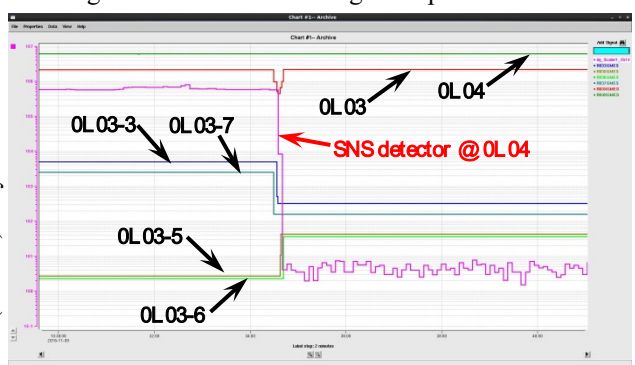

Figure 6: Reducing FE X-rays by gradient re-distribution.

FE Turn-On Event and Possible Trigger

As described in [33], it has been found out recently that many permanent beam loss monitors (BLMs) are sensitive to FE induced radiation. A CEBAF BLM is a PMT (Burle 931B) built into a hosing made of ABS plastics [34]. Its working mechanism is scintillation and Cherenkov radiation in the glass envelope of the tube. Nearly each cryomodule in CEBAF has a BLM attached to its upstream endplate. Figure 7 shows an example at zone 0L04. A pattern was found that a BLM has a preferential sensitivity to radiation induced by FE originating from cavities contained in its upstream cryomodule. As their signals are archived together with other machine data such as cavity gradients, beamline vacuum levels, a possibility arises in using their signals for long term monitoring of FE in each module in CEBAF. Aided by the ion chambers mentioned in previous section, a crude calibration was carried out permitting a rough estimation of the radiation dose rate [33].

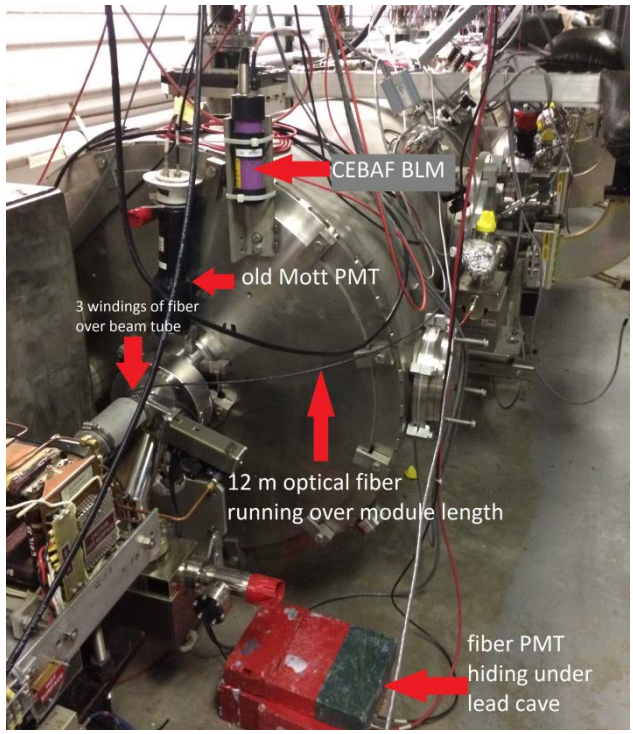

Figure 7: A CEBAF BLM (purple tube in the upper center of the photograph) attached to the upstream endplate of the cryomodule 0L04.

Here we give one example of exploiting BLMs for detecting a giant FE turn-on event. Figure 8 shows the sum gradient of cryomodule 2L26 and the signal of the sensitive BLM (in this case the BLM attached to the downstream endplate of the cryomodule at zone 2L26) for the period of December 1 – 16, 2016. The trend of the BLM signal tracks that of the sum gradient, indicating the sensitivity. This correlation was broken around 5:25 on December 13, 2016. The radiation dose rate jumped up from 1 to 10^4 R/h, indicating a giant FE turn-on.

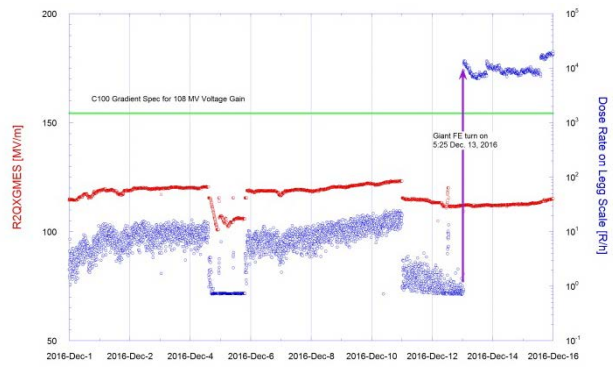

Figure 8: Jump in radiation signal (blue) of the BLM sensitive to FE originated from the cryomodule at zone 2L26, indicating a FE turn-on. The sum gradient in red.

An analysis of this event was carried out, suggesting this FE turn-on was probably triggered by frozen gases. A detailed view of the BLM raw signal for a ~ 14 minute period is shown in Fig. 9.

ISBN: 978-3-95450-192-2 doi:10.18429/JACoW-IBIC2017-TH1AB1

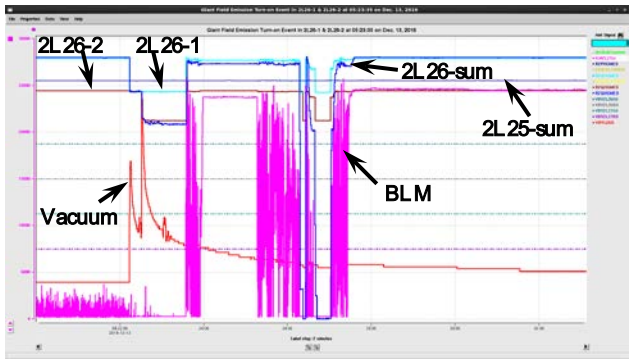

Figure 9: FE turn-on event in cryomodule at zone 2L26. FE induced radiation is reflected by the BLM signal.

The event began with the collapse of the gradient of cavity 2L26-1 at 05:22:13 (the CEBAF beam was lost at his instant) and collapse of the gradient of 2L26-2 17s later. Other cavities were stable. Each gradient collapse was accompanied with a jump in the beamline vacuum pressure (from 2×10^{-9} to 4×10^{-8}, then to 2×10^{-7} torr) measured by the ion pump attached to the warm beamline immediate upstream of cavity 2L26-1. When both collapsed gradients were brought back at 05:23:35, the radiation level saw a large jump. Thereafter, the gradients of cavity 2L26-1 & -2 collapsed two more times (which also triggered gradient collapse in other 2L26 cavities) and the radiation levels were quite noisy while the sum gradient was restored. Finally, at 05:27:31, both the cavity gradients and the beamline vacuum pressure restored to their pre-event levels, but the radiation level stayed at a high level. The CEBAF beam was restored shortly after. It is noted that 2L26 is the last cryomodule in South Linac and the sum gradient in the upstream cryomodule was stable over the course of the entire event. Although we cannot rule out other explanation with regard to the trigger of this FE turn-on event, the most likely one is the following: gas molecules released from cold surfaces arising from gradient collapse in cavity 2L26-1 & -2 re-condensed onto some field emitters initially field emitting mildly. The newly condensed gas molecules significantly enhanced the FE due to the resonant tunnelling effect [4,30,31].

It should be mentioned that the sudden FE turn-on event documented above is not uncommon at all as revealed by comprehensive analyses of the BLM signals for all C100 cryomodules where sensitive BLMs exist for the period from October 2014 to February 2017. Correlation between FE turn-on and beamline vacuum pressure bursts is observed in other cryomodules such as in 1L23.

In the meantime, a beneficial effect is also observable in which the BLM signal decreases slowly with time over the period of accelerator operation for physics programs, indicating gradual weakening of active field emitters. Such an effect is consistent with the ordinary “RF processing effect” of field emitters [10].

It should also be mentioned that "abrupt changes" in the slope of FN fitting for the inverse of trip interval observed in original CEBAF cavities were interpreted as changes in FE and it was speculated that adsorbed gases caused those changes [35,36].

Given what we have recently learned on the FE behaviors in C100 cavities directly measured by CEBAF BLMs since 2014, it appears that the frozen gases may indeed play some role in activating new field emitters in cavities placed in the CEBAF tunnel. A recent analysis of frozen gases condensed onto cold surfaces of C100 cavities revealed that H_2 alone can accumulate up to 3 monolayers in the worst case while in most case H_2 accumulates at a rate faster than expected [37].

In view of the available evidence and our current understanding of FE in CEBAF cavities enabled by FE instrumentation, one can expect FE reduction by reducing gas input into SRF cavities, in particular C100 cavities. Until a method is found for removing particulate field emitters, frozen gas removal should be aggressively pursued to check if degradation in the FE onset can be reversed. This includes not only helium processing cold cavities but also room temperature warmup of cryomodules and an improved beamline vacuum system.

Testing Optical Fiber and Diamond Detectors

As mentioned earlier, new detectors are of interest to us. For this reason, testing of a radiation resistant optical fiber and two types of diamond detectors (Cividec B2 & B4) was carried out at CEBAF in January 2017. One each diamond detector was placed up and downstream of the cryomodule at zone 1L26 in North Linac. A 12-m long optical fiber was laid across the 8-m long cryomodule. At both ends, the fiber made three turns around the beampipe. Figure 10 shows the upstream view of the cryomodule. The optical fiber was later on further tested in the injector at zone 0L04 as can be seen in Fig. 4 & 7.

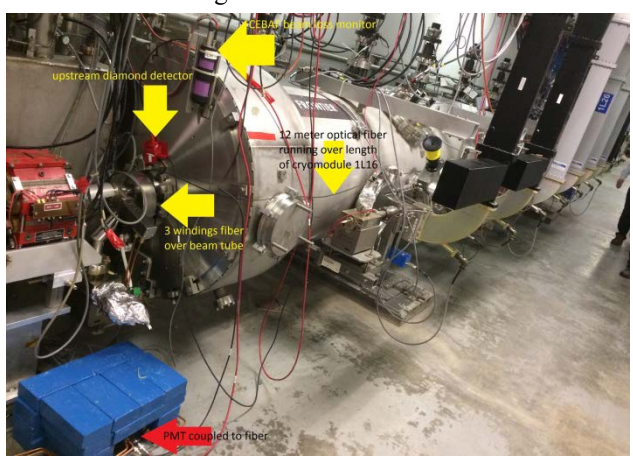

Figure 10: Upstream view of the C100 cryomodule at zone 1L26. The upstream diamond detector, optical fiber and its PMT hidden in a cave made of lead bricks are visible as well as the CEBAF BLM.

Compared to the BLMs and diamonds, the fiber was significantly more sensitive to signals from the interior cavities of cryomodule at zone 1L26, and less sensitive to crosstalk from cryomodule at zone 1L25. This is consistent with its location, draped along the full length of the tank, which should make it sensitive to all cavities, but much less sensitive to the neighbouring cryomodule.

ISBN: 978-3-95450-192-2 doi:10.18429/JACoW-IBIC2017-TH1AB1

CONCLUSIONS

In this talk, we have discussed instrumented measurements of FE from the two 1.1 GeV superconducting CW linacs in CEBAF. Although the effort is still in its early stage, the initial results have shed new lights in our understanding of the unique aspects of FE in an operational SRF linac. Some guidelines are given for field emission reduction and mitigation. New detectors have been tested and an optical fiber emerges as a useful alternative for its sensitivity to inner cavities in a cryomodule.

Future developments are needed in testing radiation hard detectors both for X-ray intensity and energy spectrum measurements, 3D X-ray mapping or imaging for field emitter localization in conjunction with computer simulation of FE electron movement, FE monitoring with permanent detectors placed at individual cavities in cryomodules for optimizing accelerator beam operation at high energy gain and simultaneously low radiation production and low trip rate. It seems that much understanding and benefit can be gained by equipping cryomodules with FE sensors from the design phase of cryomodules. This will permit continued diagnostic of FE over the full course of cryomodule assembly, installation and operation and ultimately lead to high gradient and reliable operation of superconducting accelerators.

ACKNOWLEDGMENT

RLG is indebted to Sasha Zhukov of ORNL for loaning a SNS beam loss monitor. He also wants to thank Tommy Michaelides for help in providing technical information of the CEBAF beam loss monitors.

REFERENCES

[1] A. Burrill et al., "SRF cavity performance overview for the 12 GeV upgrade," *in Proc. IPAC'12*, New Orleans, LA, USA pp.2423-2425 (2012).

[2] D. Reschke et al., "Performance in the vertical test of the 832 nine-cell 1.3 GHz cavities for the European x-ray free electron laser," Phys. Rev. Accel. Beams 20, 042004(2017).

[3] See talks presented at the 2017 TESLA Technology Collaboration (TTC), Working Group 2: Performance Degradation, Cure, Beamline Quality. https://indico.fnal.gov/conferenceTimeTable.py?confId=12662#20170221

[4] H. A. Schwettman, J. P. Turneaure, R. F. Waites, M. Jimenez, "Radiofrequency field-emission studies. II" initial experimental results," Appl. Phys. 45 (1974) 914.

[5] J. Knobloch, H. Padamsee, Part. Accel. "The science and technology of superconducting cavities for accelerators," (1996) 53.

[6] A. Navitski *et al.,* "Field emitter activation on cleaned crystalline niobium surfaces relevant for superconducting rf technology," *Phys. Rev. Spec. Topic – Accel. and Beams*, vol. 16 p. 112001, 2013.

[7] R. L. Geng, "Status of the Short-pulse x-ray project at the advance photon source," Proc. *IPAC'16* pp. 3198-3201 (2016).

[8] R. H. Fowler and L. Nordheim, "Electron Emission in Intense Electric Fields," *Proc. R. Soc. Lond.* A119 (1928) 173.

[9] R. J. Noer, Appl. Phys. A 28 (1982)1.

[10] See Ch. 12, H. Padamsee, J. Knobloch, T. Hays, "RF superconductivity for accelerators," John Wiley & Sons, (1998).

[11] B. Bonin, Proc. CERN Accelerator School. CERN 96-03 (1996)221.

[12] R. Klein and L.B. Leder, "Field emission from niobium in the normal and superconducting states," *Phys. Rev.,* vol. 124, p. 1050, 1961.

[13] D. Reschke, "Cleanliness Techniques," *Proc. SRF2005* pp.71-77 (2005).

[14] R. L. Geng et al., "Nature and implication of found actual particulates on the inner surface of cavities in a full-scale cryomodule previously operated with beam" *Proc. SRF2015,* MOPB035, pp.164-168 (2015).

[15] R. L. Geng, T. Goodman, Jefferson Lab internal report, JLAB-TN-11-006 (2011).

[16] P. Kneisel, Jefferson Lab internal report, JLAB-TN-11-006 (2011).

[17] K. Yoshida, M. Yoshioka, and J. Halbritter, "Measurements of superconducting niobium cavities at 700 MHz", *IEEE Trans. Nucl. Sci.,* vol. NS-26, p. 4114, 1979.

[18] Ph. Bernard *et al*., "Experiments with the CERN superconducting 500 MHz cavity," *Nucl. Inst. Meth*, vol. 190, p. 257, 1981.

[19] J. Knobloch, "Metamathematical extensibility in type theory," Ph.D Thesis, Cornell University (1987).

[20] Sh. Noguchi, Y. Kojima, and J. Halbritter, "Measurement of a superconducting 500 MHz Nb cavity in the TM010-Mode," *Nucl. Instr. Meth.* vol. 179, p. 205, 1981.

[21] Y. M. Li *et al*., "Research on field emission and dark current in ILC cavities," in *Proc. SRF2013*, Paris, France, Sept. 2013, pp. 392-397.

[22] Q. S. Shu *et al*., "Experience in design, construction and application of a rotating T-R mapping system in superfluid He for TESLA 9-cell cavities," in *Proc. SRF1995*, Gif-sur-Yvette, France 1995, pp. 523-527.

[23] S. Musser *et al*., "X-Ray imaging of superconducting RF cavities," in *Proc. SRF2005*, Ithaca, NY, USA, July 2005, pp. 295-299.

[24] I. Ben-Zvi, J. F. Crawford, J. P. Turneaure, "Electron multiplication in cavities," *IEEE Trans. Nucl. Sci.,* vol. NS-20, p. 54, 1973.

[25] T. Grimm *et al.*, "Superconducting RF activities at NSCL," in *Proc. SRF2001*, Tsukuba, Japan, Sept. 2001, pp. 86-90.

[26] W. Bayer *et al*., *Nucl. Instr. Meth.* A 575(2007)321.

[27] P. L. Anthony *et al., Nucl. Instr. Meth*. A 612(2009)1.

[28] R. L. Geng *et al*., "First attempt at cavity x-ray detection in a CEBAF cryomodule for field emission monitoring," in *Proc. IPAC'15.* WEPWI012, pp. 3515-3517 (2015).

[29] A. Freyberger, "Commissioning and operation of 12 GeV CEBAF," MOXGB2, *Proc. IPAC'15* pp. 1-5 (2015).

[30] C. B. Duke and M. E. Alferieff, "Field Emission through Atoms Adsorbed on a Metal Surface," *J. Chem. Phys.,* vol. 46, p. 923, 1967.

[31] J. W. Gadzuk and E.W. Plummer, "Field Emission Energy Distribution (FEED)," *Rev. Mod. Phys.*, vol. 45, p. 487, 1973.

[32] R. Legg, Jefferson Lab internal report, JLAB-TN-16-034 (2016).

[33] R. L. Geng, Jefferson Lab internal report, JLAB-TN-17-030 (2017).

[34] J. Perry et al., "The CEBAF beam loss sensors," *Proc, PAC1993*, Pp 2184-2186 (1993).

[35] J. Benesch, arXiv:physics/0606141, "Field Emission in CEBAF's Superconducting RF cavities and implications for future accelerators" https://arxiv.org/ abs/physics/0606141

ISBN: 978-3-95450-192-2 doi:10.18429/JACoW-IBIC2017-TH1AB1

[36] J. Benesch, arXiv:1502.06877 “A longitudinal study of field emission in CEBAF's SRF cavities 1995-2015" https://arxiv.org/abs/1502.06877
[37] R. L. Geng, Jefferson Lab internal report, JLAB-TN-17-027 (2017).

ISBN: 978-3-95450-192-2 doi:10.18429/JACoW-IBIC2017-TH1AB2

BEAM CONTAINMENT AND MACHINE PROTECTION FOR LCLS-2*

Alan S. Fisher†, Christine Clarke, Clive Field, Josef Frisch, Ryan Herbst,
Ruslan Kadyrov, Bobby McKee, Feng Tao, James Welch,
SLAC National Accelerator Laboratory, Menlo Park, California 94027, USA

Abstract

The first km of the 3-km SLAC linac is being replaced by LCLS-2, a superconducting linac with continuous RF and a maximum beam rate of 1 MHz. The beam will have an energy of 4 GeV and a maximum power of 250 kW, with an upgrade to 8 GeV and 1.2 MW in planning. The beam will be transported through the accelerator tunnel, passing over the future 1-km FACET-2 and the existing 1-km LCLS linacs, both using normal-conducting copper cavities at repetition rates of up to 30 and 120 Hz respectively. The LCLS and LCLS-2 beams will continue together through the Beam Transport Hall to two new undulators, for hard and soft x rays. Kickers will direct individual pulses to either undulator or to a dump. The high power in the beam and potentially in field emission necessitates integrating losses over 500 ms but responding within 0.1 ms. A capacitor for integration and a comparator for the threshold give a simple and robust approach over a wide dynamic range. We plan both long loss monitors covering regions of typically 100 m and point monitors. In regions with two or more beamlines, the system will attempt to determine the line that caused a loss, so that only one is shut off.

INTRODUCTION

LCLS, LCLS-2, and FACET-2

The LCLS x-ray free-electron laser (FEL) at SLAC National Accelerator Laboratory began operation in 2009 [1] using the third kilometre of SLAC's 3-km linear accelerator. It retains the original 2856-MHz copper linac, but with a 1.6-cell copper radio-frequency (RF) photocathode gun at 2856 MHz. Both are pulsed at 120 Hz.

LCLS-2 [2] will replace the first km of the copper linac, removed one year ago, with a superconducting linac using continuous RF at 1300 MHz. Laser pulses at rates of up to 1 MHz will emit electrons from a normal-conducting photocathode gun with 186-MHz (1300/7) continuous RF. Operation will begin at an electron energy of 4 GeV and a maximum beam power of 250 kW. Upgrades will raise the beam energy to 8 GeV and the power to 1.2 MW, as shown in Table 1. This high beam power demands fast but accurate response to beam losses.

The middle km of the linac tunnel will be occupied by FACET-2, a user facility mainly for advanced acceleration studies [3]. The LCLS-2 beam will bypass both FACET-2 and LCLS in a transport line suspended from the tunnel ceiling and only 125 cm from the two linac beams, which may make it difficult at times to determine unambiguously the source of a loss signal.

* SLAC is supported by the U.S. Department of Energy under contract DE-AC02-76SF00515.
† afisher@slac.stanford.edu

Table 1: Parameters for LCLS and LCLS-2

Parameter	LCLS	LCLS-2
Electron energy	15 GeV	4 (later 8) GeV
Bunch charge	20 to 250 pC	20 to 300 pC
Beam power	450 W	**0.25 (later 1.2) MW**
Gun frequency	2856 MHz	185.7 MHz
Linac frequency	2856 MHz	1300 MHz
RF pulse rate	120 Hz	Continuous
e^- bunch rate	120 Hz	92.9 (later 929) kHz
Photon energy	0.2 to 12 keV	1 to 15 (later 25) keV

Safety Systems for Beam Loss

SLAC uses a three-tier protection system. The highest, the Personnel Protection System (PPS), prevents unsafe machine access. The Beam Containment System (BCS) stops the accelerator if a loss of beam current or radiation from beam loss indicates possible harm to people or to safety devices like protection collimators. It must be robust and simple, with no knowledge of bunch timing and no software. As safety systems, both have rigorous configuration control. The Machine Protection System (MPS) is more flexible. When triggered—for example, by high losses, the insertion of an obstacle such as a valve, an excessive temperature—MPS can insert a beam stop, lower the beam rate, block the photocathode laser, or halt the beam. Recovery from an MPS event is faster than from a BCS trip, and so its thresholds are set lower.

LCLS-2 beam-loss detectors will serve three purposes: BCS, MPS, and beam diagnostics. Losses below the trip thresholds will provide diagnostic information to operators for tuning the machine and locating high-loss points to avoid or recover from a rate limit or trip.

Trip specifications vary with the tunnel depth and other shielding and are given in joules of beam loss within an integration time of 500 ms. BCS thresholds range from 500 to 17.5 J. MPS thresholds are generally set 10 times lower. This loss can arrive in a fast burst of lost photocurrent or slowly over the full integration time. The repetition rate of the losses can be at any beam rate from 10 Hz to 1 MHz; a full loss of 1-Hz beam is permitted for tuning. Field emission (dark current) from the gun or linac may generate loss in every RF period (Table 1) and would appear as a DC signal in the loss detectors.

LCLS BEAM-LOSS MONITORS

BCS and MPS at SLAC have long used ionization chambers. A Protection Ion Chamber (PIC), an array of interleaved circular parallel plates, is placed at each expected loss point. A long ionization chamber (LION)

ISBN: 978-3-95450-192-2 doi:10.18429/JACoW-IBIC2017-TH1AB2

using a gas-dielectric Heliax coaxial cable (nominal 1⅝ inch) runs parallel to the beam to cover an extended region. The performance of these detectors for the high-power LCLS-2 beam is problematic due to the slow transit time of ions (>1 ms). An earlier study of loss detection for LCLS-2 [4] showed that ion accumulation can fully screen the electric field in a field-free "dead zone" growing from the positive electrode. That report presented initial tests of the alternative detectors discussed below.

LCLS-2 LONG BEAM-LOSS MONITORS

Optical Fibres

In place of LIONs, we have investigated Cherenkov emission in a radiation-hard optical fibre, FBP600660710 from the Polymicro division of Molex. This high-OH^- quartz fibre has a 600-µm-diameter core, a 660-µm cladding, and a 2-mm-diameter outer protective jacket of black polyurethane. Short fibres of this family were tested to 1.25 Grad for use at CERN in the CMS detector's end cap [5,6]. Using the study's parameterization of attenuation as a function of wavelength and dose, we computed the attenuation in a 100-m fibre at LCLS-2. The calculation made the conservative assumption that a 10-m length of this fibre is constantly irradiated without tripping; the other 90 m remains unexposed. A FLUKA simulation [7] of the radiation field converts lost beam power to dose rate. A constant 50-J loss in 500 ms, the linac's MPS limit, corresponds to 25 Mrad/yr at a distance of 50 cm.

Choice of Wavelength

Figure 1 plots attenuation in a 100-m fibre as a function of wavelength for doses up to 25 Mrad. For a reasonably uniform response, we set the criterion that a loss at the end of the fibre far from the light detector should be no more than 3 dB below a loss at the near end, after irradiation. The longer wavelengths are clearly preferable before exposure and far better after the maximum dose.

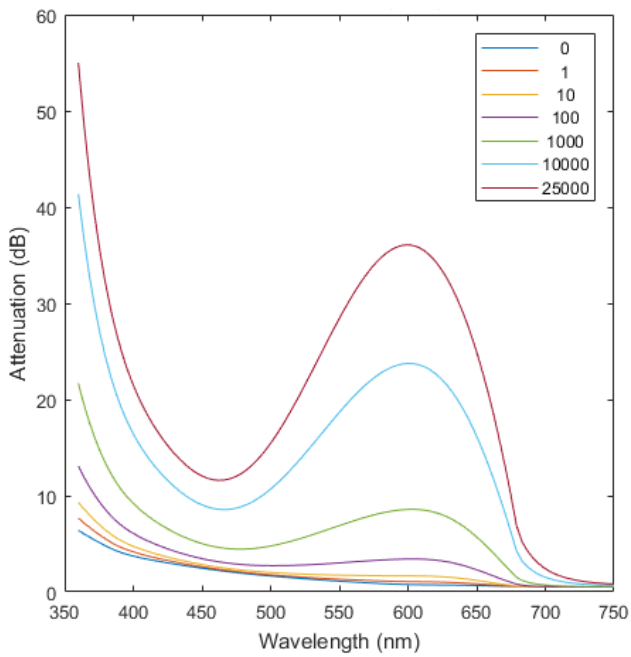

Figure 1: Calculated attenuation in a 100-m-long fibre vs. wavelength, for various radiation doses (krad) to 10 m.

Cherenkov emission is blue, since its intensity $dI/dxd\omega$ is proportional to ω. However, the signal at 700 nm can be adequate since detectors respond to the photon flux $dN/dxd\omega$, which is flat with frequency (although, in terms of wavelength, $dN/dxd\lambda \sim \lambda^{-2}$).

The photocathode work function in a red-sensitive photomultiplier (PMT) is low. This increases dark current, which should be limited to 1 nA for sensitivity to field emission from the gun and linac. Cooling from 20 to 0°C reduces dark current by a factor of 9 in a multialkali PMT [8]; above 10°C, the change is exponential, 0.67 dB/°C. We are testing Hamamatsu's H7422P-40, a PMT module with a GaAsP photocathode having a 30% quantum efficiency at 700 nm, and housed in an enclosure with a Peltier (thermoelectric) cooler holding a 0°C temperature.

A red long-wave-pass or band-pass filter makes the integrated signal largely independent of dose (although reducing the total signal). Figure 2 plots dose vs. the Cherenkov emission combined with the response of the fibre, PMT and filter, integrated over wavelength. An additional point indicates the loss for a fibre of negligible length without radiation, for comparison to 100 m. The long-pass filter doubles the band-pass signal and drops by less than the desired factor of 2 even at the highest dose.

Location of the Photomultiplier

Cherenkov light couples into fibre modes travelling in both directions. Each end of the fibre offers advantages as the PMT location. If electrons passing the start ($z = 0$) of a

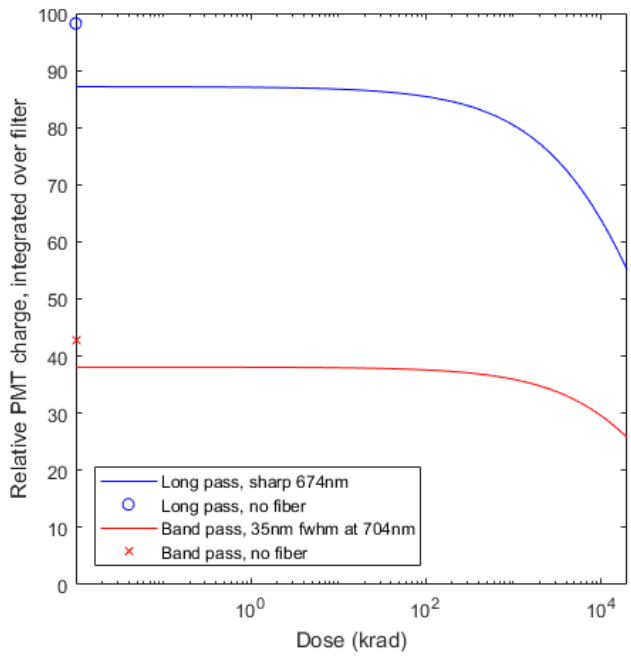

Figure 2: Cherenkov emission integrated over the PMT response and the band of a red filter for a 100-m fibre. Before 10 m of the fibre is irradiated over 10 m, the attenuation is about 10% compared to a fibre of negligible length, and is maintained until the dose exceeds 100 krad.

ISBN: 978-3-95450-192-2 doi:10.18429/JACoW-IBIC2017-TH1AB2

fibre of length L at $t = 0$ are lost at z, the upstream signal (at PMT1) reaches z = 0 at $t_u(z) = (1+n)z/c$, where the refractive index $n \approx 1.5$. The downstream signal (PMT2) arrives at L at $t_d(z) = (1-n)z/c+Ln/c$. Two losses a distance Δz apart produce PMT signals separated by $\Delta t_u = (1+n)\Delta z/c \approx 2.5\Delta z/c$ and $\Delta t_d = (1-n)\Delta z/c \approx -0.5\Delta z/c$. The signals arrive at PMT2 in reverse order and closer by a factor of 5. This compression could simply rescale the time axis, but z resolution can be degraded by cable dispersion, PMT rise time or digitizer bandwidth.

The counter argument to placing the PMT at the upstream end is that the beam-loss shower is stronger in the forward direction: more Cherenkov light should couple into a fibre mode travelling downstream. Determining this effect by computation requires precise models of both the shower and the capture of Cherenkov light. Instead, we measured the effect using a PMT at each end of a 155-m fibre. Blue-sensitive PMTs (Hamamatsu R7400U-06), also allowed us to compare the measured and calculation attenuation, since the loss is higher over this distance.

Corrector magnets steered the beam into the beampipe to generate losses at various distances from a beam stopper at the downstream end. Loss signals (Fig. 3) at the PMTs show changes in both arrival time and amplitude. Figure 4 plots the signal ratio PMT1/PMT2. As the loss shifts downstream, the attenuation grows at PMT1 and drops at PMT2, doubling the attenuation (30 dB/km vs. 5 dB/km at 700 nm). A calculation using only the wavelength dependence of Cherenkov light, fibre and PMT determines the slope of the blue line. Its offset, chosen to fit the measurements, gives a backward/forward signal ratio of 27%. This is a convincing reason to put the PMTs at the downstream end. The upstream end will have an LED for periodic fibre testing and calibration, both to verify that the system is working (a "heartbeat") and to monitor the slow decrease in transmission with radiation.

Transverse Pattern of the Loss Shower

The transverse directionality of the loss shower was also tested. The fibre discussed above runs directly on the beampipe; in a different region, a 100-m fibre was placed 125 cm away from the beam. For both, we found little difference in the loss signals when steering the beam to the left, right, up and down, demonstrating that full coverage does not need multiple fibres. However, we will install two fibres in most places, for redundancy.

Each fibre will be installed in a metal conduit attached to the tunnel wall or to beamline supports. Each end will go an additional 15 m to a rack above the tunnel. This layout protects the fibre from mechanical damage, avoids long cables, prevents radiation damage to the PMT and LED, and makes it possible to install a replacement fibre without tunnel access. Each interface chassis will have two PMTs and two LEDs to receive four fibres.

LCLS-2 POINT BEAM-LOSS MONITORS

Diamond Detectors

We plan to use Cividec diamond detectors [9] in place of PICs as point loss monitors. The B2 polycrystalline type will be suitable for most locations. An earlier test [4] comparing diamonds to PICs showed that the diamond signals are faster and much less noisy. Diamonds also offer a dynamic range of 10^6. The PIC's dynamic range is limited by ion accumulation [4] and by an internal voltage divider providing an offset on the signal output to verify that the −300-V bias is present. The offset would blind the detector to small but steady field-emission losses.

We are investigating two concepts to verify the functionality of the diamonds without this offset. Ultraviolet with $\lambda < 225$ nm produces electron-hole pairs in diamond. The Cividec detector case has an opening over one side of the 8×8×0.5-mm^3 diamond chip, intended for calibration with an α-particle emitter through a 1-mm-diameter region without metallization. This allows a xenon flashlamp with a quartz envelope to produce a UV heartbeat (like the LED and fibre), as demonstrated in a test with a large xenon lamp. We will test a smaller Hamamatsu xenon lamp coupled to a UV-transmitting fibre that can be placed directly over the 1-mm circle.

The alternative is a voltage divider to monitor the 500-V bias. A fault would result from disconnecting either the bias or a dual connector grouping the monitor with the output signal. Although not as comprehensive as the UV

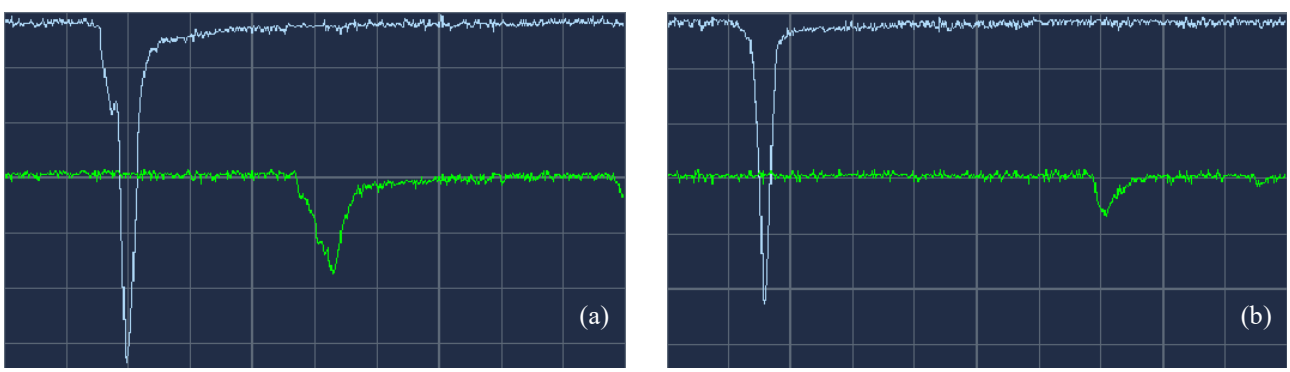

Figure 3: Signals from PMT1 (green trace, upstream end of fibre), and PMT2 (blue, downstream end); 200 ns/div and 1 V/div into 50 Ω. The loss points are (a) 82 m and (b) 39 m upstream of the beam stop at the downstream end. As the loss moves downstream, the peak decreases in amplitude and moves rightward for PMT1, but increases and moves leftward for PMT2. Relative to PMT1, the pulse widths and peak separations of PMT 2 are compressed by a factor of 5.

ISBN: 978-3-95450-192-2 doi:10.18429/JACoW-IBIC2017-TH1AB2

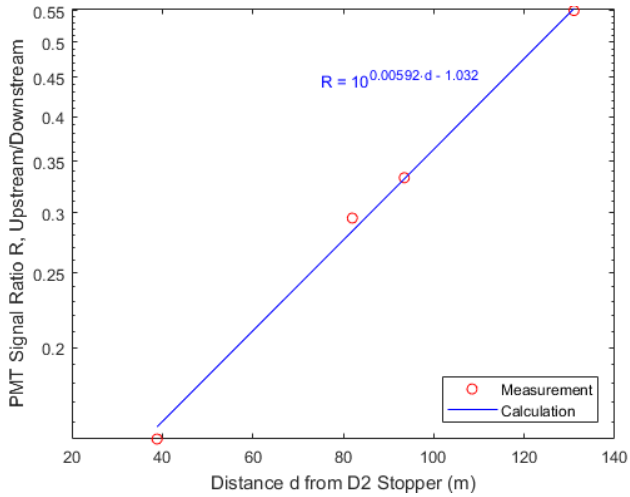

Figure 4: PMT1/PMT2 ratio. The calculated slope comes only from the properties of the Cherenkov light, fibre and PMT. The vertical offset, from a fit to the measurements, determined that the signal from the backward loss shower was 27% of the forward signal.

test, it is simpler and finds the most likely failure modes.

We rejected a third heartbeat idea—modulating the bias to produce a signal across the diamond's 10-pF capacitance—because the signal would be much too small at frequencies passed by the 500-ms filter discussed below.

SIGNAL PROCESSING

The charge in a single 1.3-GHz period of dark current can be as small as 10 aC; a single pulse of photocurrent may contain 250 pC. Digitizing pulse-by-pulse demands an unreasonable dynamic range. Instead, the PMT current will go to a filter, in which a capacitor integrates the low-frequency charge and a large parallel resistor provides the required 500-ms time constant. A comparator will trip the beam if the capacitor voltage exceeds the threshold. A buffer amplifier will pass this voltage to MPS. A second buffer will send high frequencies, needed for loss localization, to a waveform digitizer. Because the PMT will be in the chassis with the filter, cable capacitance will not alter the filter's behaviour.

The diamond must be in the tunnel at the loss point, and so requires a long cable. The diamond current will also be integrated on a capacitor. Cable capacitance is not a problem for low frequencies, and high frequencies are unnecessary without loss localization. The cable's leakage must be well below the large parallel load resistor giving the 500-ms time constant. This concern can be addressed with a low-leakage dielectric, such as solid polyethylene, or with triaxial cable in which the inner shield is driven to match the voltage on the centre conductor.

FIELD-EMISSION TEST ON CEBAF

In January 2017, a 12-m fibre and diamond detectors were tested with field emission from the last cryomodule (1L26, a high-gradient C100) of the CEBAF north linac, in collaboration with Rongli Geng of Jefferson Lab [10]. RF was on for the full linac, without photocurrent. The

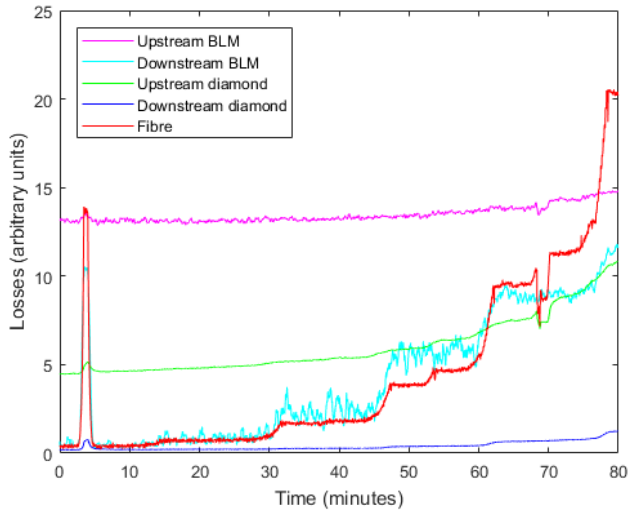

Figure 5: Losses from field-emission at CEBAF.

fibre was draped along the length of the 10-m module; a high-radiation (B4) diamond and a CEBAF scintillating beam-loss monitor (BLM) were at each end. In Fig. 5, as the field gradients in the 8 cavities of 1L26 were stepped sequentially by 1 MeV/m, the upstream BLM and diamond were dominated by losses from the previous module (1L25), but the fibre responded only to 1L26 and was sensitive to losses from the interior cavities. It showed strong growth in field emission from cavity 7 at the highest gradients and highlighted an upward spike from cavity 7 at $t = 4$ and a drop-out of cavity 3 at $t = 68$.

REFERENCES

[1] P. Emma *et al.*, "First lasing and operation of an ångstrom-wavelength free-electron laser", Nature Photonics **4** (2010) 641.

[2] LCLS-II Final Design Report, LCLSII-1.1-DR-0251-R0, 2105-11-22.

[3] FACET-II Conceptual Design, 2015-09-02.

[4] Alan S. Fisher, Clive Field, Ludovic Nicolas, "Evaluating Beam-Loss Detectors for LCLS-2", in *Proc. Int. Beam Instrumentation Conf.*, Barcelona, Spain, Sept. 2016, 678.

[5] K. Cankoçak *et al.*, "Radiation-hardness measurements of high OH^- content quartz fibres irradiated with 24-GeV protons up to 1.25 Grad", Nucl. Instrum. Methods A **585** (2008) 20.

[6] I. Dumanoglu *et al.*, "Radiation-hardness studies of high OH^- content quartz fibres irradiated with 500-MeV electrons", Nucl. Instrum. Methods A **490** (2002) 444.

[7] M. Santana Leitner, "Fluence to dose conversion E-curves for silicon and polyethylene. A FLUKA user-routine to convert fluence into energy deposition in small radiation sensitive accelerator components", SLAC Radiation Physics Note RP-14-20, example 3, dose near a stopper.

[8] Hamamatsu measurement of an H11901P-01 PMT module.

[9] CIVIDEC, https://cividec.at/

[10] R.L. Geng, A. Freyberger, R. Legg, R. Suleiman, A.S. Fisher, "Field Emission in SRF Accelerators: Instrumented Measurements for its Understanding and Mitigation," presented at IBIC'17, Grand Rapids, MI, USA, Aug. 2017, paper TH1AB1.

ISBN: 978-3-95450-192-2 doi:10.18429/JACoW-IBIC2017-TH1AB3

BEAM LOSS MONITORS FOR ENERGY MEASUREMENTS IN DIAMOND LIGHT SOURCE

N. Vitoratou*, P. Karataev
John Adams Institute at Royal Holloway, University of London, Egham, UK
G. Rehm, Diamond Light Source, Oxfordshire, UK

Abstract

Resonant Spin Depolarization is a high precision technique for beam energy measurement employed in the Diamond Light Source storage ring. The relation between spin tune and beam energy can be used to determine the energy of a transversely polarized beam. Vertical oscillations excite the beam at frequencies that match the fractional part of the spin tune and the beam loss rate is used to monitor the beam depolarization. However, the standard procedure of these measurements is intrusive and not compatible with user operation of a light source. The Advanced Resonant Spin Depolarization (AdReSD) project aims to extend and improve the method with the goal of making the measurements compatible with the user operation, for instance by acting only on a small fraction of the stored beam. As a first step, we are investigating the beam loss monitors that will be used to detect beam depolarization. The material, location and optimal geometry of the detector to capture the largest fraction of the radiation footprint resulting from beam losses are studied. Results and designs are presented and future work is discussed.

INTRODUCTION AND MOTIVATION

Diamond Light Source is a 3 GeV, 561m circumference synchrotron light source in operation since 2007. The precise energy of the stored beam has been measured in 2011 [1], and at an infrequent rate thereafter.

More recently, motivation was given to an increased rate of measurements to check for correlation with photon energy fluctuations. Ultimately, this lead to the project presented here, which aims to determine the stored beam energy precisely and at the same time in a way that is not interfering with ongoing 'user operations'.

RESONANT SPIN DEPOLARIZATION

Beam Polarization

The spin of electrons in a storage ring will start to be randomly oriented after injection. The spin vector of individual electrons will develop an overall polarization due to spin flip radiation emission according to the Sokolov - Ternov effect. The spin will gradually align antiparallel with the main guide field of the bending magnets leading to a polarization build up that is given by the equation [2] :

$$P(t) = P_0(1 - e^{t/\tau_0}) \quad (1)$$

where the maximum polarization for an ideal flat storage ring without field errors is $P_0 = 8/5\sqrt{(3)} = 0.9238$ and the time constant of the exponential build-up process is:

$$\tau_0 = [\frac{5\sqrt{3}}{8}\frac{e^2\hbar\gamma^5}{m^2c^2\rho^3}]^{-1} \quad (2)$$

For Diamond Light Source, considering the depolarizing effects for a non-ideal ring, the polarization time has been calculated 27.7 minutes with a maximum polarization of 85.4 % [1]

Spin Precession

The spin precession frequency for a light source storage ring where there are no significant solenoid magnetic fields, nor transverse electric fields, is described by:

$$\Omega_z = \omega_0(1 + \alpha\gamma) \quad (3)$$

where ω_0 is the revolution frequency, α the gyromagnetic anomaly and γ the relativistic factor. The product $\alpha\gamma$ is the number of revolutions the spin vector makes about the vertical axis in one revolution of the storage ring defined as the spin tune. Since α and ω_0 are known, the beam energy can be calculated.

In order to measure the spin tune and calculate the energy of the beam, a polarized beam is needed. The beam is then excited by a horizontal magnetic field produced using a vertical stripline. The magnetic field is set to oscillate at a frequency f_{dep} which matches the fractional part of the spin tune:

$$f_{dep} = (\alpha\gamma - k) \cdot f_{rev} \quad (4)$$

where k is the integer part of the spin tune. When the horizontal excitation frequency is in resonance with the spin tune, the spin-vector is tilted away from the vertical axis by a small amount in successive revolutions of the storage ring, gradually reducing the beam polarization. This is were the term Resonant Spin Depolarization (RSD) has its origin.

Touschek Scattering

Touschek effect is a Möller scattering collision process between two electrons of the bunch. The collision can transfer momentum from transverse to longitudinal motion, and both the electrons can exceed the longitudinal acceptance, in which case they are lost. The scattering cross section is spin dependent hence the particle loss rate depends on the beam polarization.

For a stored beam with equal current in several bunches the bunch population $N(t)$ is proportional to the current $I(t)$

* Niki.Vitoratou.2016@live.rhul.ac.uk

ISBN: 978-3-95450-192-2 doi:10.18429/JACoW-IBIC2017-TH1AB3

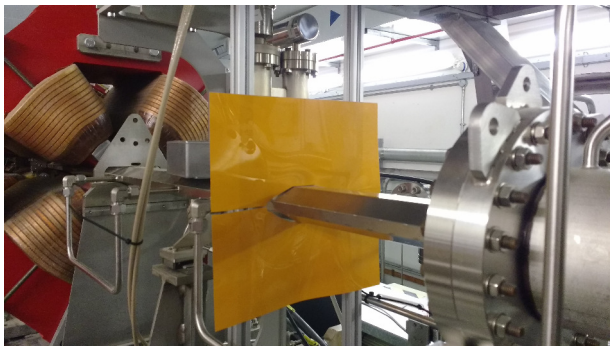

Figure 1: Radiochromic film installed in the storage ring of Diamond Light Source.

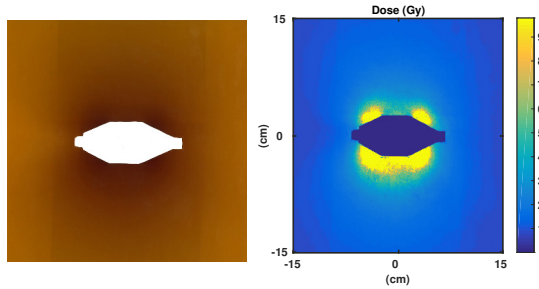

Figure 2: The darkening of radiochromic film after one week of exposure in the storage ring beam and the calculated absorbed dose by the film. The film is used as a dosimeter to measure the radiation in the tested area.

and the normalized loss rate R_{norm} can be written :

$$R_{norm} = \frac{1}{I(t)^2}\frac{dN}{dt} \propto f_1 + f_2 P(t)^2 \qquad (5)$$

where the functions f_1 and f_2 can be treated for a given measurement as constants [3]. A partial depolarization will result in a reduction of the polarization level and consequently in a rise of the normalized loss rate since the constant f_2 is a negative number [4].

RADIATION FOOTPRINT

A beam loss monitor is going to be required for detecting the particles lost as a result of Touschek events and recording the consequential partial depolarization of the beam.

The detectors are located one meter downstream the vertical and horizontal collimator where the losses are generally high in comparison to other areas of the storage ring. The physical aperture of the beam is small, and the Touschek particles that get lost, hit the scrapers creating electromagnetic showers.

These charged shower particles are going later to be detected and counted by the beam loss monitors. Thus, the radiation around the beam pipe is studied to position the detectors under investigation in a location where the radiation is equally distributed. In addition this study will contribute to the future detector design geometry that is optimal for capturing the highest fraction of the lost particles.

A radiochromic film is used to evaluate the radiation footprint in the area of interest. Radiochromic film RTQA2 [5] is typically used for testing radiotherapy sources and commissioning therapy equipment. However, the dynamic range of the film also works in the storage ring of Diamond Light Source, with a source beam of 3 GeV electrons. The radiochromic film consists of a single or double layer of radiation-sensitive organic microcrystal monomers on a thin polyester base with a transparent coating. The darkness of the film increases with the absorbed dose, and no processing is required to develop the image.

A film of dimensions 30 cm×30 cm had been cut, formed to fit around the beam pipe and exposed for one week to the electron beam, see Fig. 1. The film darkening is shown in the Fig. 2. The exposed radiochromic film was scanned, and the dose along the film was calculated using a calibration formula that was given by the manufacturer.

The radiation is high close to the beam pipe and starts to fade just a few cm further out. The horizontal collimator causes the dark shadow vertically in the film and set limits of an area that should sensibly be covered by a detector. The asymmetry of the results above and below the beam pipe might be related a misalignments of the vertical collimator set which was discovered independently. However, a second film is going to be installed in order to investigate further this assumption after the alignment of the collimator set.

BEAM LOSS MONITOR SETUP

Detection of light produced by scintillators or Cerenkov radiators is one of the most common method of monitoring beam losses. Three beam loss monitors using light detection were tested. The performance of polymethyl methacrylate (PMMA, commonly known as acrylic glass) that is used as the detector of the beam loss monitors in Diamond was compared with the performance of the organic plastic scintillator EJ204 [6] and fused quartz used as a Cherenkov radiator . The Scintillator EJ204 has high efficiency, high speed with decay time of 1.8 ns, attenuation length of 160 cm and wavelength that matches with the bialkali photocathode of the attached photomultiplier. The Cherenkov radiators outputs light instantaneous with continuous spectrum without interacting with background low energy x-rays making the fused silica detector a good candidate for this study.

The three materials are shaped in a rod of 15 cm length and 3 cm diameter and attached with the same model of photomultiplier (Electron Tubes ET 9126). The monitors were installed in the storage ring 1 m downstream of the horizontal collimator set. They were positioned about 2 cm above the beam pipe where the radiation distribution is in the same level according to the radiochromic film results. A sheet of lead 1.3 mm thick is used to protect the detectors from background ionizing radiation.

ISBN: 978-3-95450-192-2 doi:10.18429/JACoW-IBIC2017-TH1AB3

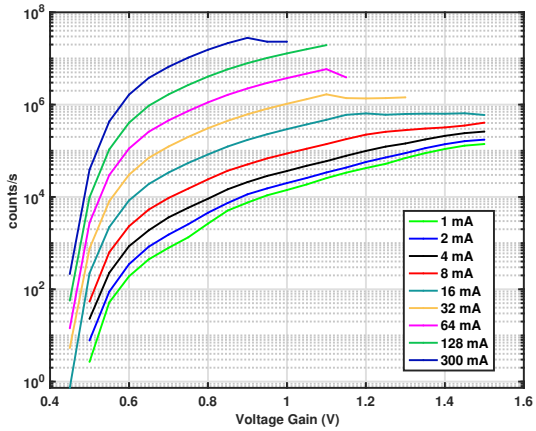

Figure 3: The count rate vs the voltage gain of the photomultiplier is presented for various beam currents. The different beam currents are illustrated by different colours. The saturation of the photomultiplier is observed for lower voltage gains as the beam current increases.

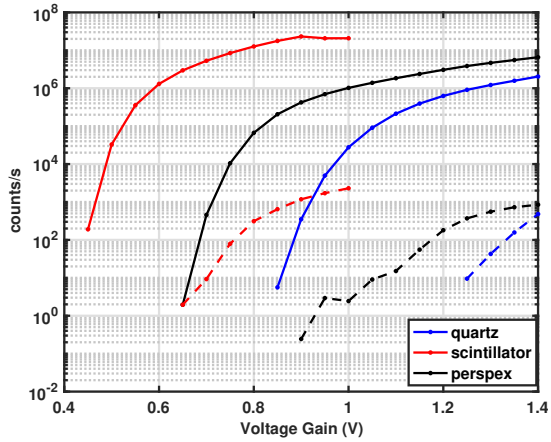

Figure 4: The comparison of the three detectors for 300 mA beam current is shown with the solid lines. The same scan was repeated to measure the background and is presented with dashed lines. The dynamic range of the detectors reduces for higher voltage gains because of the high bakcground events.

Signal Acquisition

The detectors were connected with a commercial acquisition instrument (Instrumentation Technologies Libera BLM [7]) with two hardware interfaces. Four coaxial connectors are used for signal input and four RJ-25 connectors for power suppling and voltage gain control. The instrument is set with low impedance input of 50 Ω for short individual pulses. The input signals are sampled at fixed ADC sampling clock with frequency 125 MHz. The ADC data is continuously monitored for negative peak value and when it exceeds the threshold value a counter increments by one. The threshold counter value was set to ≈1% of the 14-bit resolution ADC amplitude in order to avoid false triggers from electronic noise. The counter readout rate is set to 10 S/s.

RESULTS

Performance of Scintillator EJ204

The first results from the three beam loss monitors showed a problem of the scintillator EJ-204 for high loss rates as associated with high stored beam current, indicating that the high amount of light that is produced had damaged the attached photomultiplier tube. Using a new photomultiplier the performance of scintillator EJ204 was studied for different loss rates as produced increasing stored beam currents.

Starting with low beam current, the count rate was recorded while sweeping the voltage gain, as it is shown in Fig. 3. At 16 mA beam current, the photomultiplier started to saturate. As the beam current increases and the beam losses increase with the square of the stored beam current for a Touschek dominated beam, saturation was observed for increasingly lower voltages gains. Using this test, the maximum voltage gain for operation with the user beam of 300 mA was quantified, avoiding the saturation and any risk of damage of the photomultiplier tube.

Comparison of Materials

Comparing the three detector materials the scintillator EJ204 gives the highest count rate even with lower voltage gain operation of the photomultiplier, as it is illustrated in Fig. 4. For comparison, the count rate of the detectors was also measured while there was no beam in the storage ring revealing that the scintillator and perspex count a high number of background events.

These background counts reduce the dynamic range of the detectors for higher voltage gain operation. We thus chose the voltage gain of the photomultiplier tube at an operating point where the background count rate is at a comparatively low rate of 10 counts/s, which should optimize the dynamic range. Further studies are going to be conducted to examine if a higher thickness of lead could improve the performance of the detectors eliminating the background counts.

Detector Performance in RSD

The performance of the three detectors was studied for energy measurements using resonant spin depolarization technique. A depolarization event was recorded by the three detectors as it is presented in Fig.5, and the results were analyzed. As a first step, the beam losses were normalized by the square of the beam current in order to retrieve information for the beam polarization. The rise of the normalized beam losses indicates a partial depolarization of the beam.

As it is shown in the Table 1, the count rate of scintillator is higher that the other three detectors. The expected relative error was calculated by the formula:

$$RE = \frac{\sqrt{\overline{counts}}}{\overline{counts}} \quad (6)$$

ISBN: 978-3-95450-192-2 doi:10.18429/JACoW-IBIC2017-TH1AB3

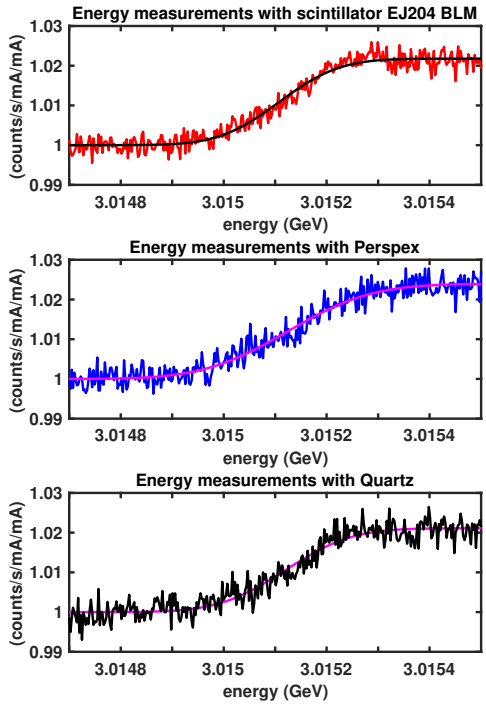

Figure 5: The performance of the three detectors recording a depolarization event. The beam losses are normalized with the square of the beam current. The count rate increases by the same amount for the three detectors. An error function fit calculates the energy of the beam and the width of the depolarization resonance.

Table 1: Measured Count Rates for Investigated Materials

material	counts/s	RE
EJ204	18 10^5	0.7 10^{-3}
Perspex	5.9 10^5	1.3 10^{-3}
Quartz	4.1 10^5	1.6 10^{-3}

Where $\overline{counts}$ is the mean value of the measured counts. According to Poisson statistics for counting events the error is calculated by the square root of the number of counts. The expected error is calculated to be lower for the material with the highest count rate.

The data after the depolarization were normalized with the data before to compare the counting response of the detectors in the increase of the beam losses due to depolarization. An error function fit calculates the width of the resonance and the results are shown in Table 2 . The standard deviation (std) of the difference between the data and the fit is evaluated, including the confidence intervals. This is used as a criterion to estimate the agreement between the fit and the data and to assess the precision of the results by the fit. The calculated std is found to be higher than the expected error indicating that improvements in the counting system should be considered to reach higher accuracy. This analysis confirms that high number of counts gives better measurement accuracy.

Table 2: Calculated Parameters for Investigated Materials

material	rise	width	std
EJ204	2.2 %	92.4 keV	(1.8± 0.2) 10^{-3}
Perspex	2.3 %	128.6 keV	(2.3± 0.24) 10^{-3}
Quartz	2.1 %	101.9 keV	(2.4± 0.26) 10^{-3}

AdReSD PROJECT AND DETECTOR DESIGN

The Advanced Resonant Spin Depolarization (AdReSD) project aims to improve the technique of energy measurements and optimize it in order to be compatible with operation of Diamond Light Source with beam line users. Different aspects of this project are studied regarding the measurements method, the parameters of the beam that can be influenced and the beam loss monitor design.

The energy measurements are based on the excitation of the beam at different frequencies. This process could cause an increase in the vertical beam size due to coupling resonances. In order to preserve the beam size and to minimize the impact on beam parameters, the AdReSD project is going to excite only a small fraction of the beam, leaving the rest of the bunches unaffected. Once the energy information has been determined from the first group of bunches, the next group will be used for excitation and depolarization. In this way, the energy measurements can be continuous without the need of waiting time for beam polarization.

This type of measurements will require a beam loss monitor that can capture the highest fraction of lost particles. The design of the detector will include four identical blocks that will be positioned around the beam pipe as it is shown in Fig. 6. Their dimensions will be decided based on the radiation footprint results and light guides will be used to connect the detectors with the photomultipliers. The four detector setup will allow us to test the depolarization detection by coincidence counting based on the principle that Touschek particles lose and gain an equal amount of momentum when they scatter [8]. In addition, the setup offers the option of summing up the counts from all the detectors. These two methods that aim to optimize the detection of the depolarization will be compared.

CONCLUSIONS AND FUTURE WORK

The AdReSD project has been introduced, and different features of the project have been discussed. The comparison of three different detectors revealed that the scintillator EJ-204 is the most efficient in terms of photon output for a given lost particle flux. However, further investigation is needed to counteract the background counts, and higher thickness of the lead sheet will be considered to resolve the problem.

The objective for a high number of counts will lead to better measurement accuracy. For this reason, different count-

ISBN: 978-3-95450-192-2 doi:10.18429/JACoW-IBIC2017-TH1AB3

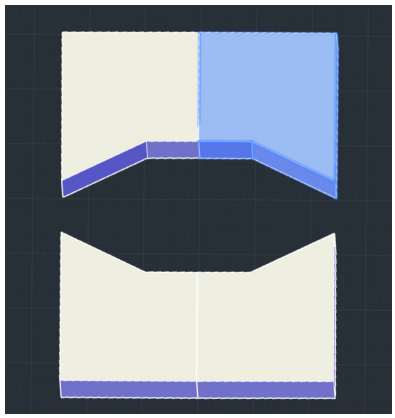

Figure 6: Future design of the beam loss monitor for the AdReSD project. Four block identical with the highlighted blue one will surround the beam pipe and capture the highest fraction of the beam losses.

ing methods for avoiding pile up problems are going to be implemented. In the end, the counts rates from the four future detectors are going to be used for testing the coincidence counting by losses due to depolarization events.

In conclusion, the design of the detector based on the radiation footprint results will be manufactured, and further details of the AdReSD project are going to be studied as soon as the detector setup is installed.

ACKNOWLEDGMENT

I would like to thank Richard Fielder and Ian Martin for their helpful advice on implementing the energy measurements and the Beam Diagnostics group at Diamond Light Source for their interesting ideas and inputs.

REFERENCES

[1] I.P.S. Martin, M. Apollonio, R.T. Fielder, G. Rehm, and R. Bartolini, "Energy measurements with resonant spin depolarisation at Diamond," in *Proc. of IPAC'11*, pages 1404–1406, 2011.

[2] J.D. Jackson,"On understanding spin-flip synchrotron radiation and the transverse polarization of electrons in storage rings," *Reviews of Modern Physics*, 48(3):417–433, 1976.

[3] K. P. Wootton, M. J. Boland, W. J. Corbett, X. Huang, G. S. Leblanc, M. Lundin, H. P. Panopoulos, J. A. Safranek, Y. R E Tan, G. N. Taylor, K. Tian, and R. P. Rassool, "Storage ring lattice calibration using resonant spin depolarization," *Physical Review Special Topics - Accelerators and Beams*, 16(7):1–13, 2013.

[4] S. R. Mane, Yu M. Shatunov, and K. Yokoya, "Spin-polarized charged particle beams in high-energy accelerators," *Reports on Progress in Physics*, 68(9):1997–2265, 2005.

[5] Gafchromic RTQA2 Film, `http://www.gafchromic.com`

[6] Eljen Technology, `http://www.eljentechnology.com`

[7] Instrumentation Technologies, Beam Loss Monitor readout electronics, `http://www.i-tech.si`

[8] Kay Wittenburg, "Beam Loss Monitoring and Control, " in *Proc. EPAC*, 2002.

ISBN: 978-3-95450-192-2 doi:10.18429/JACoW-IBIC2017-TH1AB4

STATUS OF THE BNL LEReC MACHINE PROTECTION SYSTEM*

S. Seletskiy†, Z. Altinbas, D. Bruno, M. Costanzo, A. Fedotov, D. M. Gassner, X. Gu, L. Hammons, J. Hock, P. Inacker, J. Jamilkowski, D. Kayran, J. Kewisch, C. Liu, K. Mernick, T. Miller, M. Minty, M. Paniccia, W. Pekrul, I. Pinayev, V. Ptitsyn, K. Smith, Y. Than, P. Thieberger, J. Tuozzolo, W. Xu, Z. Zhao
BNL, Upton, USA

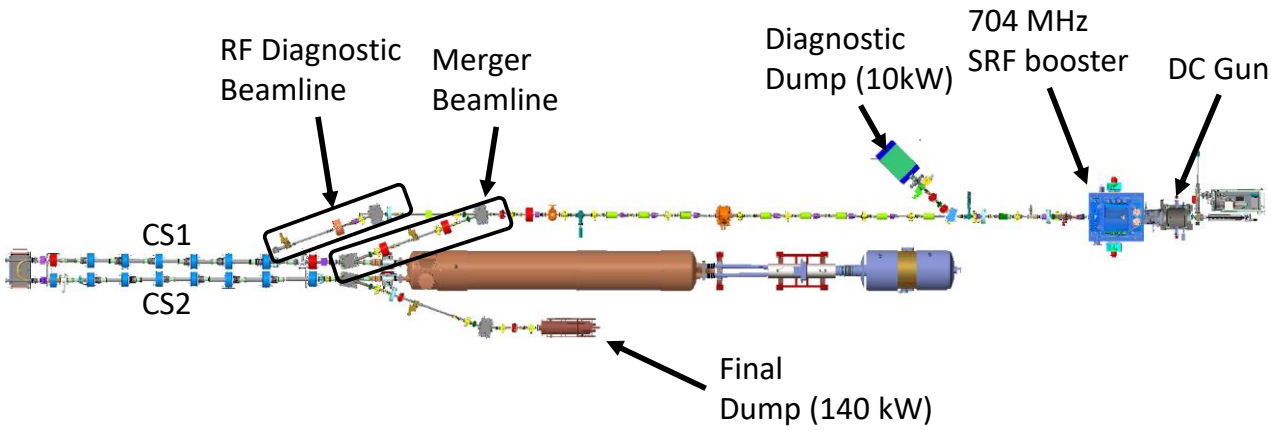

Figure 1: LEReC layout.

Abstract

The low energy RHIC Electron Cooler (LEReC) will be operating with 1.6-2.6 MeV electron beams having up to 140 kW power. It was determined that the missteered electron beam can damage the vacuum chamber and in-vacuum components within 40 us. We protect our accelerator against such a catastrophic scenario by a dedicated machine protection system (MPS). In this paper we describe the current status of the LEReC MPS design. We share our recent experience in commissioning and operation of the scaled down MPS used for the LEReC gun test beamline and discuss the status of the MPS designed for the commissioning of the full LEReC facility planned for next year.

LEREC LAYOUT AND PARAMETERS

The LEReC accelerator [1] consists of the 400 keV DC photo-gun followed by the 1.2-2.2 MeV SRF Booster, the transport line, the merger that brings the beam to the two cooling sections (CS1 and CS2) and the cooling sections followed by the 140 kW dump. The LEReC also includes two dedicated diagnostic beamlines: the low-power beamline capable of accepting 10 kW beam and the RF diagnostic beamline.

The LEReC layout is schematically shown in Fig. 1.

The LEReC beam train consists of 9 MHz macro-bunches. Each macro-bunch (MB) consists of N_b=30 bunches repeated with 704 MHz frequency. The length of each bunch at the cathode is 80 ps. The charge per bunch (Q_b) can be as high as 200 pC.

We will have the ability to work with macro-bunch trains of various length (Δt), various number of macro-bunches per train (N_{mb}), and various time delay (T) between the trains.

In addition to baseline operational modes listed in Table 1 the LEReC might also be operated with CW 704 MHz beam of 85 mA (at 1.6 MeV) and 68 mA (at 2 MeV).

The LEReC beam modes and their use are summarized in Table 1.

Table 1: LEReC Beam Modes

Beam Modes	Goals
Low Current Mode (LCM) N_b = 30; N_{mb} = 1; T = 1 s Q_b = 30 – 200 pC	Optics commissioning; Rough RF settings; Emittance measurement
RF Studies Mode (RFSM) N_b = 10,15,20,25,30; $\Delta t \leq$ 250 us; T = 1s – 5s; $Q_b \leq$ 200 pC	RF fine-tuning. Study beam longitudinal phase space.
Transition Mode (TM) N_b = 30; $\Delta t = T$; $Q_b \leq$ 200pC	Transition from LCM to HCM with gradual adjustment of Q_b.
High current Mode (HCM) N_b = 30; $\Delta t = T$; Q_b = 130 – 200 pC	Getting nominal e-beam parameters in the CS.
CW Mode (CWM) 704 MHz CW; Q_b = 95 – 120 pC	Alternative to HCM.

* Work supported by Brookhaven Science Associates, LLC under Contract No. DE-AC02-98CH10886 with the U.S. Dept. of Energy.
† seletskiy@bnl.gov

ISBN: 978-3-95450-192-2 doi:10.18429/JACoW-IBIC2017-TH1AB4

MPS OVERVIEW

MPS Parameters

The LEReC MPS [2, 3] is designed to protect the machine from the damage caused by the loss of electron beam.

We determined the MPS parameters from the studies of tolerable beam losses under various failure scenarios. The main MPS parameters are shown in Table 2.

Table 2: Main MPS Parameters

Parameter	Symbol	Value
Reaction time	t_{react}	40 us
Tolerable routine losses	I_{loss}	1 uA
Current threshold for ultimately safe operation mode (USOM)	I_{USOM}	40 nA

The MPS reaction time was derived under assumption that beam optics studies are performed in LCM only and that in HCM the beam trajectory is locked in some reasonable range and that some magnet power supply currents are locked at operational value.

We assume that the eventual setting for tolerable loss threshold will be found experimentally while I_{loss}=1 uA is an initial setting. The beam current used in such studies must not exceed 600 uA.

In the USOM any operations with the electron beam are allowed. Apparently the LCM is the USOM.

MPS Related Diagnostics

The MPS relies on the numerous LEReC beam diagnostic systems [4].

The MPS utilizes the fast current transformer (FCT) located close to the gun exit to measure the beam current and to determine what beam and equipment manipulations are allowed at the moment. Another device that is planned as a supplement to the FCT is a dedicated photodiode (PD) located at the exit of the laser room.

The output of the LEReC FCT is the measure of the instantaneous beam current while for the MPS purposes we require the instantaneous measurement of an average beam current. To achieve this goal we measure the total charge accumulated in the moving window of 1 s length. This charge defines our current levels for the MPS.

To monitor the beam trajectory the MPS relies on a number of beam position monitors (BPMs) located along the beamline. The BPMs are equipped with fast electronics capable of providing the response within 12 us.

A number of photomultipliers retrofitted with a few feet long optical fibre are planned to be used as beam loss monitors (BLMs) that determine the routine beam losses.

The ion gauges (IG) measuring the vacuum are also the integral part of the MPS. The gun IG plays a special role in machine protection – the MPS is required to trip the gun high voltage power supply (HVPS) when the gun IG readings exceed the predefined limit.

Finally, the MPS is monitoring a number of magnet power supplies (PS) as well as the gun HVPS.

MPS-Laser Interface

The sequence of the laser devices used to shape the pulse trains in the time domain is schematically shown in Fig. 2.

The CW train of laser pulses coming out of the oscillator is chopped into the 9 MHz macro-pulses by the pulse picker - an electro-optic modulator (EOM) with a fast (~1 ns) rise/fall time.

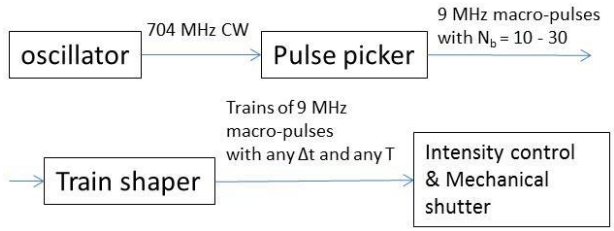

Figure 2: Laser pulse shaping scheme.

The train shaper is a Pockels cell (PC) followed by a half-wave plate (HWP). Depending on the HWP angle the PC either passes the laser pulses through or blocks the laser when the voltage is applied. The first polarization is used to create the trains of macro-bunches of particular length with some repetition rate. The second polarization is used in CWM.

The Intensity Controller consists of the EOM for intensity stabilization and the HWP for intensity limitation. The EOM is used to cut a few percent of laser intensity to smooth the intensity variation. The remotely controlled HWP is used to set the required laser intensity.

During the trips the MPS is blocking the laser beam to the photocathode by removing the high voltage from both the PC and the intensity control EOM and by closing the mechanical shutter.

MPS Logic

The overall MPS schematic is presented in Fig. 3.

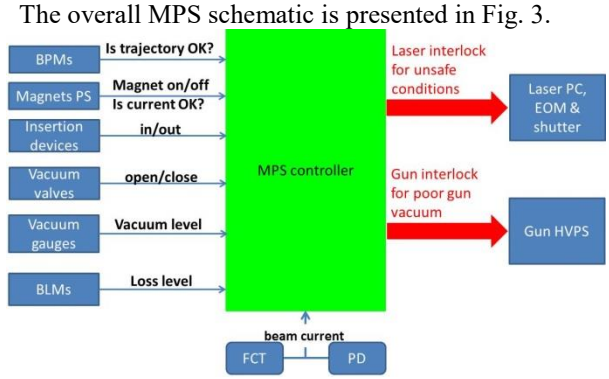

Figure 3: Schematic of LEReC MPS.

The MPS assesses the surface, which the beam is hitting, from the settings of the dipoles and from what insertion devices are inserted into the beamline. These inputs to the MPS are called “qualifiers” and the surface hit by the beam defines the “machine mode” (MM). The operation in each particular MM is allowed below certain current level only.

The actual beam current is calculated from the FCT and the PD readings. The MPS compares the measured beam current to the allowed current level and if the measured

ISBN: 978-3-95450-192-2 doi:10.18429/JACoW-IBIC2017-TH1AB4

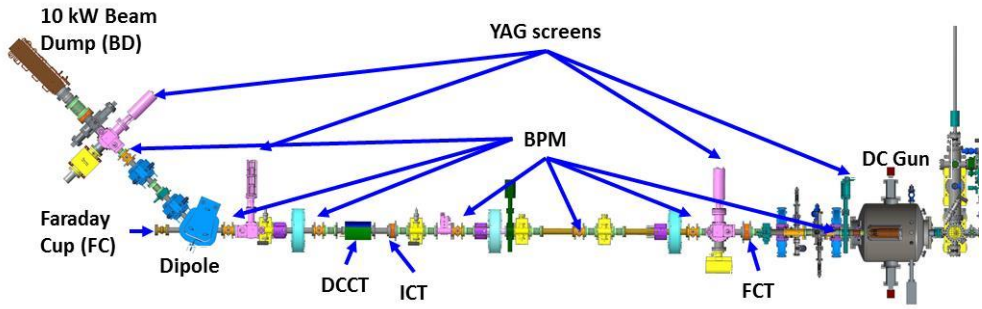

Figure 4: Layout of LEReC gun test.

current exceeds the limit set for the present MM then the MPS interlocks the laser.

Another cause for the MPS to trip the machine above certain current level is the BPM readings or magnet PS readings outside of the allowed range.

Finally, above certain current level the MPS trips the beam if the loss measured by the BLMs is above the I_{loss}.

The MPS allows two additional modes of operation: the "isolation mode" and the "laser alignment mode". In the isolation mode the laser shutter is closed so that the gun and the laser conditioning can be performed independently. The qualifier for this mode is the status of the laser shutter. In the laser alignment mode the gun high voltage (HV) is turned off, so that the laser can be aligned on the cathode. The status of the gun HV is the qualifier for this mode.

MPS EXPERIENCE IN GUN TEST

In April –August of 2017 we performed the LEReC gun test with the gun diagnostic beamline (Fig. 4). The beam energy in this test was 300 - 400 kV with the maximum allowed beam power of 10 kW.

Since the diagnostic beamline included all (with the exception of the RF cavities) essential building blocks of the full LEReC, it was a perfect test bench for the scaled down LEReC MPS.

This MPS has 3 current levels. At the first 40 nA level (I_{USOM}) any beam manipulations as well as inserting any insertion devices is allowed. Faraday Cup (FC) level of up to 50 nA is reserved for sending the beam straight to the flange FC. The beam dump (BD) level is set to 25 mA and corresponds to the maximum beam current allowed on the BD.

The setting of the dipole magnet and the position of insertion devices define the MMs for the gun test MPS.

The rest of the MPS logic is not different from the full scale LEReC logic described above.

MPS Commissioning

The commissioning procedure of the scaled down LEReC MPS consisted of the 3 main blocks.

The integrated system test consisted of checking the interaction between the MPS controller, the MPS diagnostic subsystems, the laser, and the gun HVPS.

The second step was the MPS test without the beam. In that step we verified the logic of the MPS controller by emulating various fault conditions and observing the laser interlocks.

In the final step we commissioned the entire integrated LEReC MPS with electron beam. Working in the LCM we successively adjusted the FC and BD current levels to the level below the current measured by the FCT, created all possible beam faults and observed the expected machine trips.

The scaled down MPS was successfully commissioned with the aid of dedicated software that allowed us to communicate to the MPS controller and the MPS related diagnostic systems. The screenshot of the software GUI is shown in Fig. 5.

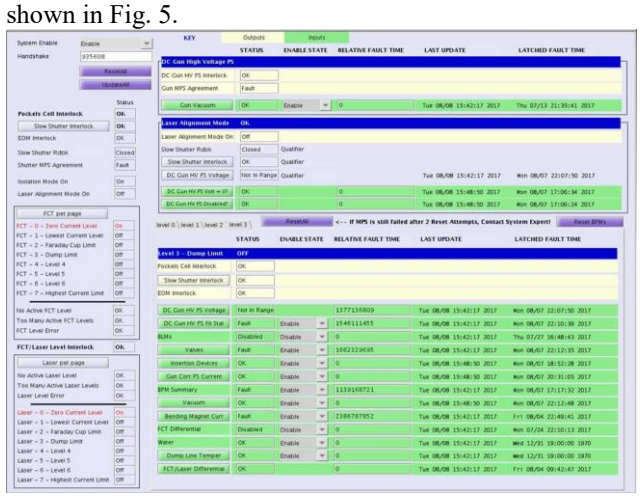

Figure 5: MPS software GUI.

Experience with MPS Diagnostics

We started beam operations in the LCM. The FCT immediately started detecting the e-beam and reporting respective beam current level to the MPS. Figure 6 shows raw FCT signal on the scope under typical operational conditions.

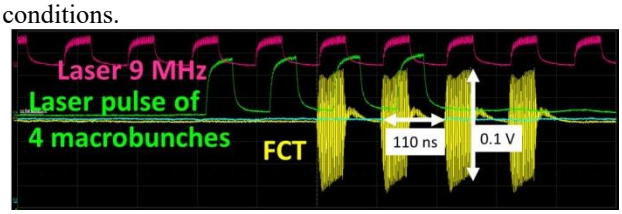

Figure 6: Raw FCT signal for the pulse of 4 MBs.

The FCT was pre-calibrated on the test bench with the pulse generator. The final calibration of the processed FCT signal was performed with the beam.

ISBN: 978-3-95450-192-2 doi:10.18429/JACoW-IBIC2017-TH1AB4

We compared FCT readings to the readings of the FCs and the well-calibrated Integrated Current Transformer (ICT) for various electron charges per bunch and various numbers of MBs.

Figure 7 shows comparison of the calibrated FCT output to beam charge measured by the BD FC. Transport efficiency was set to 100% for this measurement.

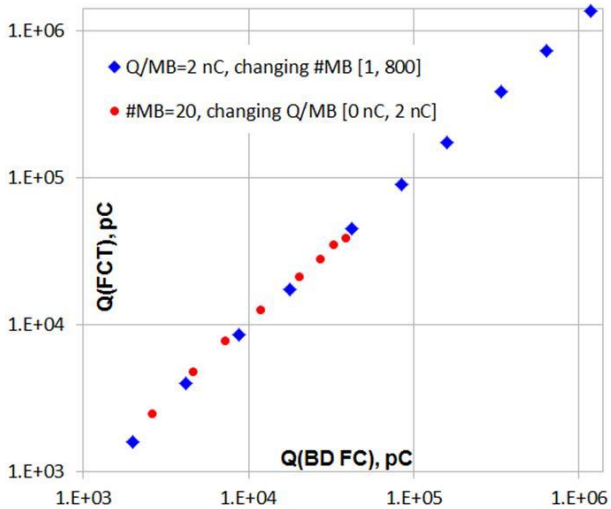

Figure 7: FCT vs BD FC for varying number of MBs at Q=2 nC/MB and for 20 MBs with varying Q/MB.

During commissioning we determined that due to the beam loading inside the gun and the slow HVPS regulation loop the only feasible way of switching to CW mode was increasing beam current from zero level. Since the FCT processing scheme doesn't detect any beam charge less than ~0.5 pC/bunch, we made a decision to always set the MPS to the high current level prior to switching to CW operations. Based on our experience we might make it a permanent automated feature of our MPS for 2018 run.

The BPMs proved to be an extremely useful part of the MPS. After commissioning BPMs both in the pulsed and in the CW modes they have been reliably interlocking the MPS whenever the beam trajectory was moved out of the allowed range. Noticeably, the BPMs were interlocking the MPS because of trajectory change along the train of macrobunches due to the beam loading in the gun. Figure 8 shows the readings of the BPM in dispersive region when beam loading is happening along the train of 50000 MBs and when the gun HVPS regulation loop is malfunctioning in CW mode. Such behaviour causes the respective BPM to trip the MPS when the position of any macrobunch is outside of the allowed range.

The vacuum gauges, readback of the magnets PS currents and readback of position of various insertion devices demonstrated proper and reliable interaction with the MPS during the whole 2017 run. Figure 9 gives an example of the LEReC trip in CW mode due to the BD vacuum exceeding the low limit set for low current operation.

While BLMs interaction with the MPS was fully commissioned and BLMs showed good sensitivity to the direct losses of the beam in pulsed mode, tests of BLMs in the CW mode were limited in time due to schedule pressure. The final integration of BLMs into the MPS will be performed during 2018 run.

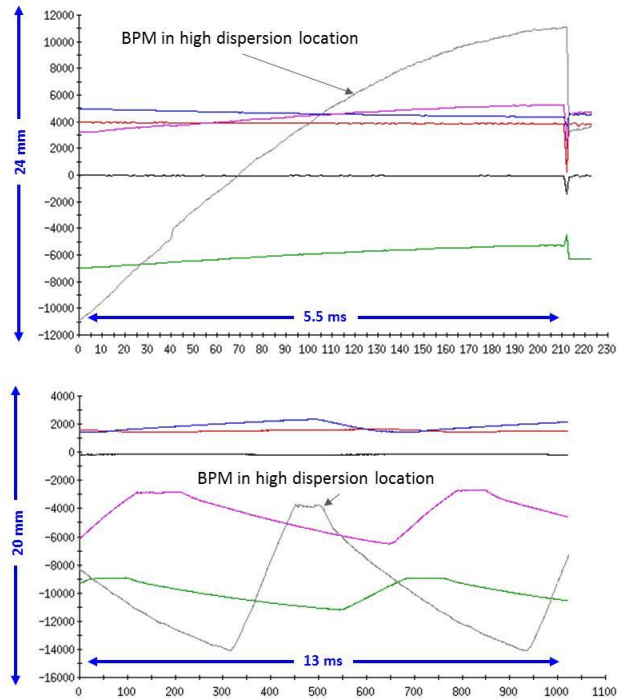

Figure 8: BPMs readings when the beam loading is happening along the train of 50000 MBs with 60 pC/MB (upper plot) and when the gun HVPS regulation loop is malfunctioning in CWM at 2.8 mA current (lower plot).

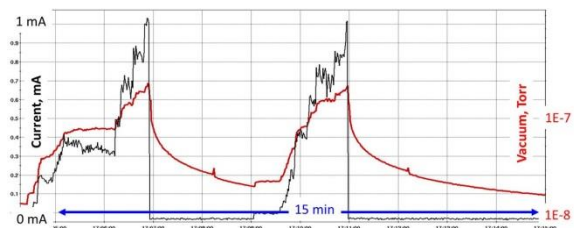

Figure 9: Two MPS vacuum trips during CW operations.

CONCLUSION

We described the design of the Machine Protection System for the Low Energy RHIC Electron Cooling accelerator.

The scaled down MPS was successfully commissioned and utilized in operation of the LEReC gun test.

Presently we are expanding the commissioned system to include all the components necessary for the commissioning of the full LEReC in 2018.

REFERENCES

[1] A. Fedotov *et al.*, WEA4CO05, NAPAC16, 2016.

[2] S. Seletskiy *et al.*, WEPG19, IBIC16, Barcelona, 2016.

[3] S. Seletskiy *et al.*, BNL-113798-2017-IR, 2017.

[4] T. Miller *et al.*, TUPG35, IBIC16, Barcelona, 2016.

ISBN: 978-3-95450-192-2 doi:10.18429/JACoW-IBIC2017-TH2AB1

MINIMIZING ERRANT BEAM AT THE SPALLATION NEUTRON SOURCE*

C. Peters, W. Blokland, A. Justice, T. Southern, Spallation Neutron Source, Oak Ridge National Laboratory, Oak Ridge, TN, 37831, USA

Abstract

Since beginning neutron production operation in 2006 at the Spallation Neutron Source (SNS), one of the goals for the Accelerator Operations group has been to minimize beam trips. The beam trips which occur with the highest frequency are due to errant beam in the Super Conducting Linac (SCL). The process of minimizing the amount of errant beam and the frequency of faults will be described.

DESCRIPTION OF THE SNS LINAC

The linear accelerator at the SNS consists of (in order of beam acceleration) an H^- Ion Source (H^-IS), Low Energy Beam Transport (LEBT) which contains an electrostatic beam chopper (LEBT chopper), Radio Frequency Quadrupole (RFQ), Medium Energy Beam Transport (MEBT), Drift Tube Linac (DTL), Coupled Cavity Linac (CCL), Medium Beta Super Conducting Linac (MB SCL) (3 cavities per cryomodule), and High Beta Super Conducting Linac (HB SCL) (4 cavities per cryomodule). The fundamental RF frequency in the RFQ-DTL is 402.5 MHz, and 805 MHz for the CCL-SCL.

The SCL is physically the longest accelerating component of the linac, and also performs the majority of the beam acceleration. The nominal beam energy for the current SNS linac is 1 GeV, and the energy acceleration by the SCL is from 186 MeV to the design 1 GeV. Of the 96 RF structures used for accelerating, 81 are superconducting [1].

All systems (H^-IS and RF) are pulsed at a 60 Hz repetition rate for approximately 1 millisecond, for a duty factor of about 6%. Figure 1 shows the linac arrangement and relative lengths of the different structures.

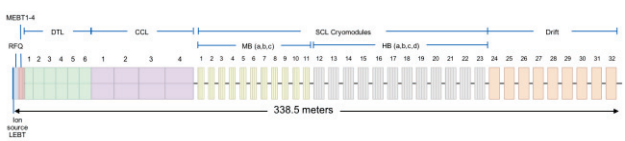

Figure 1: Ion source through SCL schematic.

*This manuscript has been authored by UT-Battelle, LLC under Contract No. DE-AC05-00OR22725 with the U.S. Department of Energy. The United States Government retains and the publisher, by accepting the article for publication, acknowledges that the United States Government retains a non-exclusive, paid-up, irrevocable, worldwide license to publish or reproduce the published form of this manuscript, or allow others to do so, for United States Government purposes. The Department of Energy will provide public access to these results of federally sponsored research in accordance with the DOE Public Access Plan (http://energy.gov/downloads/doe-public-access-plan).

ERRANT BEAM AND BEAM TRIPS

Errant beam is the resulting beam produced by malfunctioning accelerator equipment. When a glitch occurs, this errant beam does not transport through the accelerator properly (see Fig. 2). This beam typically triggers the Machine Protection System (MPS) to stop beam acceleration resulting in what is termed a beam trip. In general, errant beam trips typically take only a few seconds to reset. Occasionally errant beam events induce an SCL RF cavity trip which can take a few minutes to recover. If the frequency of errant beam trips is high enough, it can reduce the overall 60 Hz beam even with the relatively quick recovery.

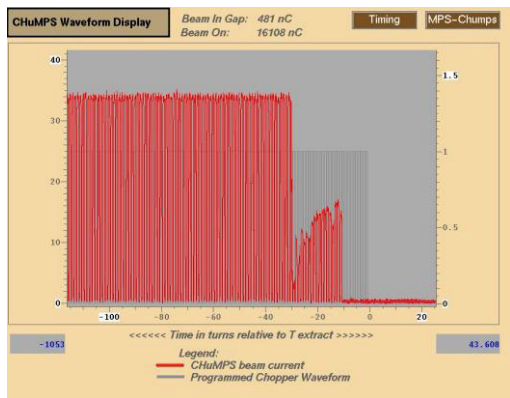

Figure 2: Example of LEBT high voltage malfunction.

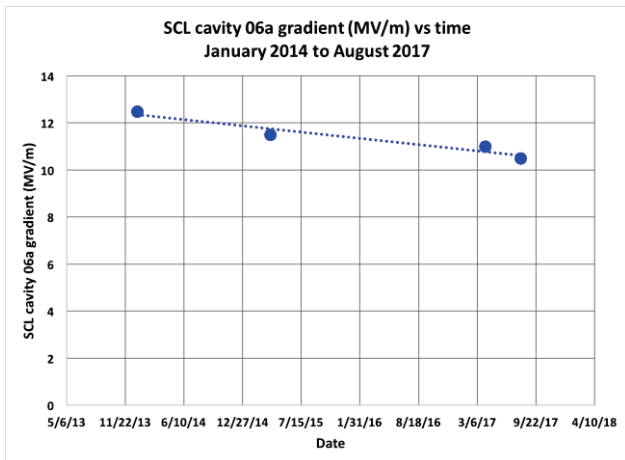

Figure 3: SCL cavity 06a gradient is declining at about 0.6 MV/m per year even with reduced errant beam frequency.

Additionally, repeated errant beam events over weeks, months, and years degrade SCL cavity performance [2,3]. Degradation of cavity performance means that over time

ISBN: 978-3-95450-192-2 doi:10.18429/JACoW-IBIC2017-TH2AB1

cavity gradients must be reduced in order to minimize SCL cavity trips and maintain high availability. Sensitive cavities can lose 5% in gradient per year (see Fig. 3).

Experience has shown that the need to reduce gradients does not occur for the entire SCL. There are particular sections of the SCL that get hit by errant beam. The sections hit are determined by a particular DTL or CCL RF cavity that faults. The problematic areas are SCL cryomodules 2, 3, 6, 7, 12, 16, 19, and 20 (there are currently 23 cryomodules installed). This amounts to about one-third of the total SCL cavities needing gradient reduction over time, which is significant.

The above information is degradation due to abrupt beam losses from DTL or CCL RF faults, but there are additional beam loss issues that contribute to the need to reduce SCL cavity gradients. Beam halo and protons introduced from the ion source can also impact SCL cavity availability, these issues are less typical, and will not be discussed within this paper.

What becomes important when discussing beam trips and errant beam are the fast field decay times for the normal conducting RF structures and the particular structure position along the linac.

The fast field decay times mean that almost immediately the beam energy is incorrect and beam will not transport to the target without massive beam loss in the SCL. However, in the SCL the field decay times are on the order of 250 microseconds so SCL cavity faults typically do not cause massive beam loss as the MPS can respond fast enough to prevent large beam loss even as the field decays. Only if there is an arc within the SCL RF system does the trip cause beam loss since the field decay is on the order of a few microseconds when an arc occurs.

When discussing position along the linac, earlier structures produce less beam loss in the SCL. For example, the DTL is broken up into six segments (DTL1-DTL6), and the CCL is broken up into four segments (CCL1-CCL4). The first cavity (DTL1) accelerates the beam from 2.5 to 7.5 MeV. If a fault occurs in DTL1, in only a few microseconds the field will be too low to provide the appropriate beam energy to properly accelerate the beam downstream. Because the structure is early in the linac (low beam energy) the beam does not transport very far. In fact, in this case the beam doesn't transport beyond DTL2.

For the case of a DTL1 fault the beam does not transport to the SCL, but beginning with cavities DTL2 and DTL3 beam loss occurs in the SCL during an RF fault. The amount of beam that actually transports to the SCL is too small to be detected with a beam current or position monitor. The effect on SCL cavity operation is minimal. However, beginning with DTL4 there is significant beam lost in the SCL during a fault.

BEAM DELIVERY AT SNS AND THE MACHINE PROTECTION SYSTEM (MPS)

In order to properly describe the process of errant beam a description of beam delivery is necessary. As stated above, all of the systems in the linac are always being pulsed at 60 Hz (both H^-IS and RF). When the beam is "off" the beam is just not being accelerated beyond the RFQ. The timing system changes the H^-IS pulse to either align with the RF or be delayed to a time after the RF pulse has occurred. The system that determines whether beam is allowed to be accelerated is the MPS [4].

The MPS turns off the beam if an equipment malfunction occurs. It takes 15-20 microseconds to turn off the beam upon receipt of the malfunction by the MPS. The following is the process of how the beam is turned off. There are two types of MPS faults: Fast Protect Auto-Reset (FPAR) and Fast Protect Latch (FPL).

MPS FPAR

When an FPAR fault is detected, the H^-IS timing gate is turned off (the H^-IS decay time is about 20 microseconds), the RFQ timing gate is turned off (it only takes about 1 microsecond for the RFQ field to decay enough to not transport beam), and the LEBT chopper chops all of the beam (no beam enters the RFQ) for 20 microseconds (the response time is about 1 microsecond). While the MPS is faulted the H^-IS timing gate remains delayed with respect to the RFQ and the RFQ is turned back on. When the fault condition clears the H^-IS trigger gate delay is removed and the beam pulse is synchronized with the RFQ (and all other RF systems). This is all automatic. This particular fault protection is typically used for fast response systems such as Beam Loss Monitors (BLMs) or Low-Level RF High-power Protection Modules (HPMs).

MPS FPAR Chatter Fault

One additional feature within the FPAR is the ability to add a chatter fault feature. This means that if a certain rate of faults is reached the MPS will hold the beam off (H^-IS gate remains delayed) until an operator intervenes to reset the fault condition. This feature is important when discussing errant beam and beam trips.

MPS FPL

When an FPL fault is detected, the machine response is the same as the FPAR above except the H^-IS trigger gate delay remains delayed until an operator intervenes to restart the beam. When beam is re-enabled the H^-IS trigger gate delay is removed and the beam pulse is synchronized with the RFQ (and all other RF systems). The FPL fault is typically a pre-beam MPS check to verify the machine is ready for beam. This particular fault protection is typically used for slower response systems such as magnet power supplies or longer recovery time equipment such as High Power RF (HPRF) power supplies.

ISBN: 978-3-95450-192-2 doi:10.18429/JACoW-IBIC2017-TH2AB1

BEAM INSTRUMENTATION THAT DETECT ERRANT BEAM

The beam instrumentation equipment used to detect errant beam are the BLM system [5] (both BLMs and Neutron Detectors (NDs)), Beam Current Monitors [6] (BCMs), and Beam Position Monitors [7] (BPMs).

BLMs

The BLM system (BLMs and NDs) is extremely sensitive for beam loss detection, and has been the most reliable for detection of errant beam.

The NDs are used in the DTL as they are more sensitive at lower energy (the BLMs are not sensitive at energies below 87 MeV). The NDs are a scintillator detector with a Photomultiplier Tube (PMT) surrounded by a thin layer of lead and a thicker layer of polyethylene. It is relatively rare to see an ND fault during an errant beam event, but they are useful for beam loss tuning for slower losses (over hours or days) that result in elevated activation levels over time. The NDs are connected to the MPS as an FPAR fault. They have a chatter fault setting (described above) of 2 faults in 60 beam cycles.

The BLMs are the main device used for beam loss detection in the CCL and all downstream segments. The BLMs are simple ionization chambers filled with Argon, and are very sensitive for localized beam loss detection at energies above 87 MeV. To gain further sensitivity in the SCL, the BLMs were moved directly onto the beam pipe in the warm sections between cryomodules. Other areas of the accelerator have BLM placement approximately 30 cm above the beamline. All BLMs are also connected to the MPS as an FPAR fault. In the CCL and downstream of the SCL the BLMs have a chatter fault setting of 2 faults in 60 beam cycles. In the SCL, however, the BLMs have a chatter fault setting of 1 fault in 60 beam cycles. This means that any time an SCL BLM trips it must be reset by operators before the MPS allows beam to be accelerated. This was done to eliminate the possibility of instances where errant beam faults occur in consecutive beam pulses. During early beam operations (2006 to 2012) this was highly probable due to the high fault rate for DTL and CCL cavities, but since that time RF faults have been reduced so the probability is quite low. Even with reduced RF fault rates the SCL BLM chatter fault setting remains at 1 in 60 beam cycles.

BCMs

BCMs are calibrated current transformers used for measuring beam charge through the accelerator. There were ten BCMs initially installed in the linac. Of those ten only eight are still installed. Two of the BCMs installed near the CCL were damaged by field emitted electrons from the CCL cavities, and have been removed (see Fig. 4).

Currently, there are two MEBT BCMs, and six DTL BCMs installed. The 6 DTL BCMs are installed within the DTL RF cavities and have had significant noise issues. The signals need significant conditioning in order to provide accurate beam current measurements. These BCMs are not used (see Fig. 5). The most reliable are the two in the MEBT, but only one of those has been highly reliable, also due to noise issues (see Fig. 5). The two BCMs in the MEBT are used for a Differential Beam Current Monitor (DBCM) system to protect against beam loss in the MEBT.

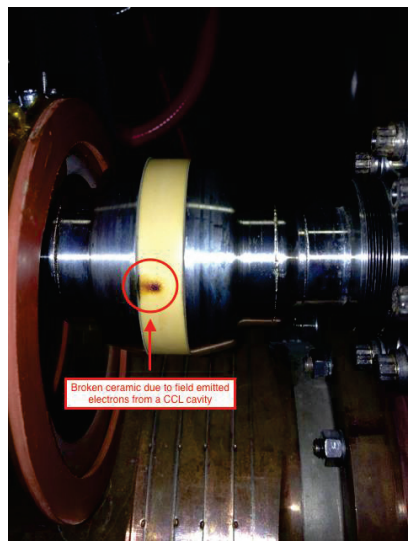

Figure 4: Picture of CCL BCM after being damaged by field emitted electrons.

Figure 5: Example BCM waveforms showing a noisy signal in the MEBT, and that DTL BCMs are not used.

BPMs

BPMs are used for measurement of beam position, phase, and also an uncalibrated measurement of beam current. The actual BPM beamline structure has been highly reliable, but the computers and software to relay this information to the control room has not. The BPM computers must be rebooted daily in order for reliable

ISBN: 978-3-95450-192-2 doi:10.18429/JACoW-IBIC2017-TH2AB1

measurements. However, with different data processing now in the process of deployment the systems are highly reliable.

There are currently two BPMs used for errant beam detection. Both are used as a current measurement. One system is at the beginning of the MEBT, and it is connected to the MPS as an FPL. It looks for abnormal beam from the RFQ (see Fig. 2). The other BPM used is in the beginning of the CCL and is part of the SCL DBCM system.

The issue with using BPMs for current measurement is that they are not easy to calibrate by themselves and sensitivity to RF changes. Pairing a BCM with the BPM for detecting losses allows calibration of the BPM signal. The DBCM is such a system. The sum signal of the BPM pick-up plates is filtered and amplified with a log-amplifier to detect the RF power of the beam. The signal is then processed by the DBCM's FPGA to produce a current signal. Because the DBCM has access to the calibrated BCM signal, the two signals are compared, in situ, to calculate the calibration coefficients for the BPM signal.

DETECTING ERRANT BEAM USING THE SCL DBCM

Initially, during early years of neutron production, the only indication of errant beam was faulting SCL BLMs. Much time was spent trying to understand what was causing errant beam. RF cavities were faulting, but the faulting was not linked directly to SCL BLM faults. Operations used RF fault rates to make adjustments to RF cavities to reduce cavity faults which in turn reduced errant beam [8]. However, there were not clear indicators that individual RF cavities were causing the SCL BLM trips. As the SCL cavity performance continued to degrade it was determined that more detailed investigation was needed.

The decision was made to measure the amount of beam lost in the SCL during an RF fault. The initial DBCM used existing hardware and software. A BCM in the beginning of the CCL, and one downstream of the linac in the High Energy Beam Transport (HEBT) line were used for determining beam loss. The system was first used only as a diagnostic. If the charges on the two BCMs differed by a settable level the system would trigger and save the two BCM waveforms to a file server. These data were easily viewable, and it was determined that the MPS was working properly turning the beam off in the predicted 15-20 microseconds.

Since it was understood that losing 15-20 microseconds causes degradation in the SCL the goal became to try to turn off the beam faster than the normal MPS if the DBCM system detected beam loss. The next-generation SCL DBCM system [9] was created for this purpose. The DBCM system is able to turn off the beam in about 8 microseconds (see Fig. 6). This DBCM system sends out two fault signals. One fault goes to the normal MPS, which turns off the beam in the normal 15-20 microseconds. The other fault signal goes directly to the LEBT chopper controller, which begins chopping all of the beam before it enters the RFQ. The system does this until the normal MPS can truncate the H^- IS and RFQ pulses and prevent beam acceleration. The direct connection to the LEBT chopper reduces the beam turn off time.

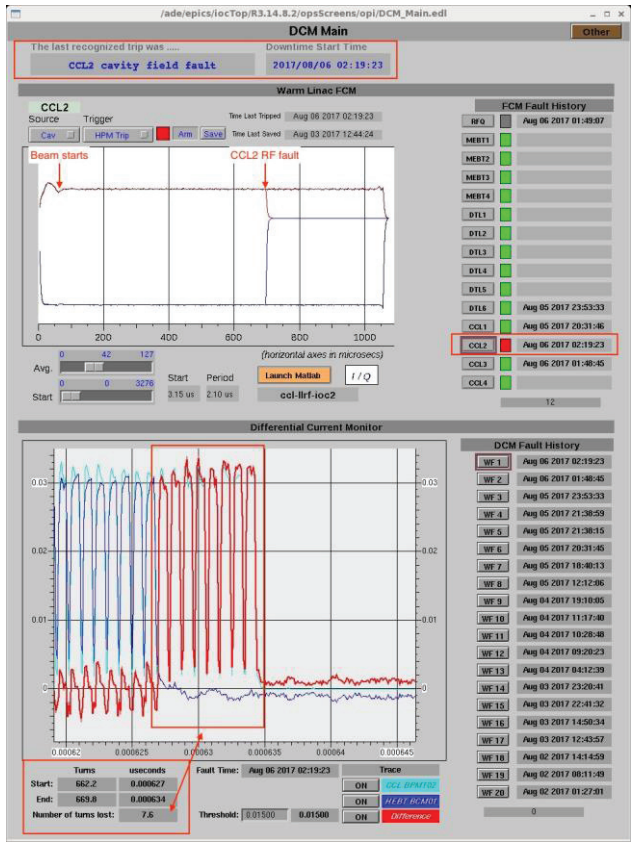

Figure 6: Example errant beam EPICS screen. It shows the particular cavity that faulted with a timestamp (gets counted and archived), the beam profile upstream and downstream of the SCL, and the time during the beam pulse when beam started being lost along with the time it took to turn off the beam. Operators know what happened immediately after a beam trip.

The goal of the DBCM was to reduce the amount of beam lost during an errant beam event and the system does this reliably. However, the 8 microsecond turn off time does not eliminate SCL cavity degradation. Even with the reduced amount of beam being lost in the SCL the cavity gradients still need to be lowered over time. For example, during extended maintenance periods (1 month or more) the Central Helium Liquefier (CHL) raises the SCL cavity temperature from 2 to 4 K, to reduce electricity cost. When the cavities are again cooled from 4 to 2 K after maintenance periods the first errant beam pulse (even with reduced beam turn off time) will cause SCL cavities to fault off. After a few errant beam pulses the cavities begin to "condition", and will no longer fault during an errant beam event. Even with this conditioning effect the probability of an SCL cavity trip during errant beam event is never zero.

ISBN: 978-3-95450-192-2 doi:10.18429/JACoW-IBIC2017-TH2AB1

RECORDING ERRANT BEAM FREQUENCY

From the beginning of neutron production operation in 2006, the beam downtimes have been recorded manually by operators. The first step in reducing machine downtime is to record any significant downtimes to look for trends, and fix any equipment that cause downtime. The downtime recording system is completely manual. The system is web-based with a nearly complete selectable list of equipment with entries available for fault description and fault length. The time structure for recording is broken down into tenths of hours. If a downtime is greater than 3 minutes then it is considered a 0.1 hour downtime and recorded by operators. Conversely, downtimes shorter than 3 minutes are not recorded in the downtime recording system. In this way, the short downtimes taking only a few seconds to recover are not recorded into the system for statistics information. In the case of errant beam this is problematic, because the longer downtimes due to errant beam take weeks or longer to develop.

In order to better understand the different beam trips (focusing on short trips) and study fault trends an automated downtime recording system was developed. The system detects when the beam is not at the nominal 60 Hz repetition rate and starts counting the time when the beam is not at 60 Hz as downtime. When the beam returns to 60 Hz repetition rate the system bins and counts the downtime analyzing beam trips in real-time. The system also detects and counts errant beam faults to specific RF cavities (see Fig. 6). These data are archived, plotted (see Fig. 7), and discussed weekly with the Machine Health Report (MHR). The MHR is a list of equipment issues for the latest run period. It is used to examine all beam trips to try to find the causes. Analysis is done by the machine specialist to determine the cause and fix for the issue. At weekly meetings, these issues are discussed and solutions are found to be implemented during the next maintenance opportunity.

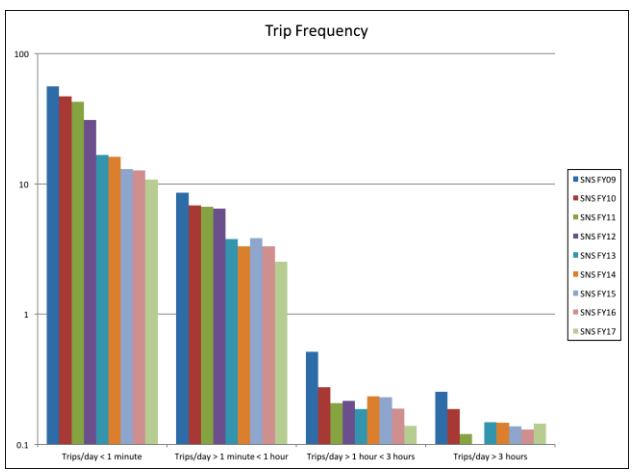

Figure 7: Trips per day for varying beam downtime bins. In most cases the trend is fewer trips per day.

REDUCING NORMAL CONDUCTING RF FAULTS

Warm linac RF faults during the beam pulse are the main cause for errant beam in the SCL. As stated earlier the RF cavities that cause significant beam loss in the SCL are cavities DTL4, 5, 6, and CCL1, 2, 3, and 4. That means 7 cavities pulsing at 60 Hz 24 hours per day or 36,288,000 pulses per day with a goal of 0 faults. It is not an easily achievable goal.

The method to reduce RF faults was the same used to reduce the longer recorded downtimes. The systems faulting the most were investigated first. As those issues were resolved the next system faulting was investigated. Luckily many of the cavities have had similar issues so once a particular issue is understood there are significant drops in fault rates in a short time.

Each RF system was broken down into cavity tank and RF coupler issues, LLRF issues, and HPRF issues.

Eliminating Cavity Fill Faults

The LLRF Field Control Module (FCM) is able to save RF waveforms during a cavity fault that can be viewed quickly and easily in the central control room. The waveforms are the cavity field, forward power to the cavity (downstream of the RF circulator), reflected power from the cavity, and LLRF output to the klystron. The important piece of information that the waveforms provide is the time during the RF pulse when the fault occurred. Based on the time of the fault during the RF pulse there are different methods used to correct the issue. If the RF faulted during the cavity fill then the way the cavity is filled can be adjusted (see Fig. 8).

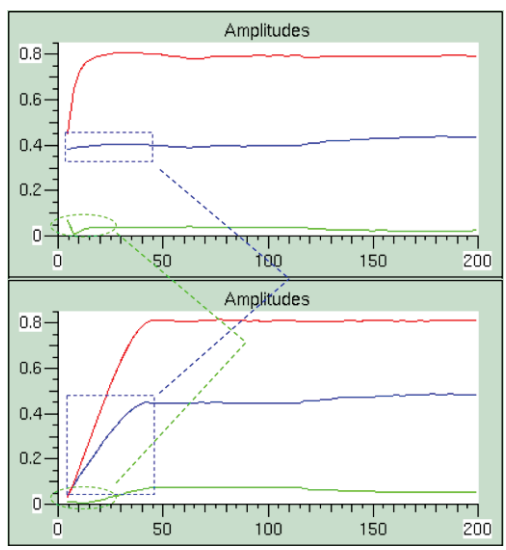

Figure 8: Y-axis is arbitrary FCM field units and x-axis is time in microseconds. Red is cavity field waveform, blue is cavity forward power waveform, green is cavity reflected power waveform. Changing the forward power fill from constant (top image) to a slower linear ramp (bottom image) changed the reflected power structure during the fill and reduced RF faults.

ISBN: 978-3-95450-192-2 doi:10.18429/JACoW-IBIC2017-TH2AB1

Instead of a constant forward power to fill a cavity the forward power can be linearly ramped. Doing this during the transition from a traveling wave to a standing wave reduced RF fault frequency. However, these faults are occurring before beam is entering the cavity and do not produce errant beam. For some of the cavities these changes appear to have helped to reduce some portion of RF faults occurring during the beam pulse as well. Perhaps the vacuum environment caused by faults during the fill contributed to an increase faults later in the RF pulse.

In addition to the adjustment with different forward power filling schemes, changing the resonant frequency of cavities also reduced fill time faults [8] (see Fig. 9).

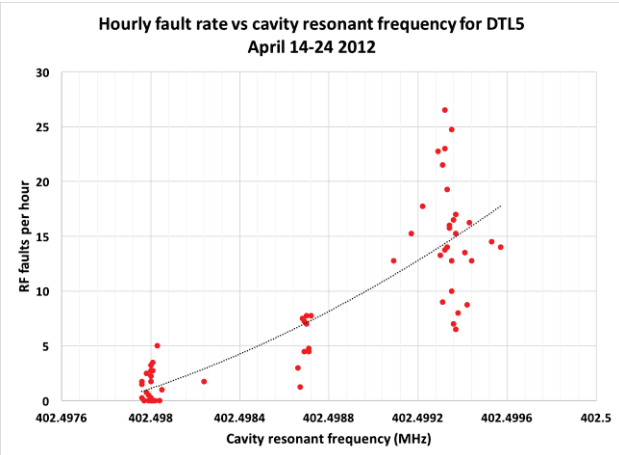

Figure 9: The plot shows the DTL5 hourly fault rate versus cavity resonant frequency during a 10 day period in April 2012. Decreasing the cavity frequency from 402.500 MHz to 402.498 MHz significantly reduced the fault rate.

Changing the temperature of the RF structure changed the resonant frequency of the structure. This was done to try to mimic the effect seen by changing the RF fill method. The reflected power waveform during the fill is affected by the change in resonant frequency. The variable monitored to determine whether a change was good was the vacuum reading near the RF window. As the resonant frequency was changed the window vacuum reading decreased. For DTL cavities running with a negative resonance error (higher reflected power over the majority of the RF pulse) reduced window vacuum levels correlated with a reduced RF fault frequency. For one normal conducting cavity at a time the resonant frequency was changed while monitoring RF fault rates (not necessarily errant beam fault rates). The resonant frequency adjustments made were the main decrease in errant beam faults during early 2012.

Vacuum System Improvement

The vacuum system for the DTL and CCL initially consisted of only capture pumping. Each DTL tank was pumped with 3 ion pumps, and each RF coupler with a Non-Evaporable Getter (NEG) pump. Each CCL tank was pumped with 10 ion pumps, and each RF coupler with a NEG pump. For the DTL there were a total of 18 ion pumps and 6 NEG pumps, and in the CCL there were a total of 40 ion pumps and 8 NEG pumps. Over time the pumping speed of the pumps was not sufficient to maintain proper vacuum levels, and the pumps were bursting inducing errant beam faults and causing significant downtime.

When the DTL RF cavities are energized the structures heat up. When the RF is turned off the different parts of the structure cool at different rates. This differential cooling causes large bursts of air into the structure, and previously the ion pumps were unable to maintain vacuum below interlock levels ($1x10^{-6}$ Torr). The pump down after turning RF off required the structure to reach thermal equilibrium (30-45 minutes) before the vacuum system could maintain levels below the interlock. Eventually Turbo-Molecular Pump (TMP) carts were added to DTL tanks 2-6 for additional pumping speed to eliminate the need to wait for thermal equilibrium.

In addition to the large vacuum bursts requiring additional pumping the NEG pumps on all windows would burst periodically causing the LLRF HPM to interlock the LLRF causing errant beam. Preventative maintenance was done to regenerate the NEG pumps regularly which eliminated the periodic bursts.

The vacuum systems for the DTL and CCL have now both been upgraded to replace all of the ion pumps and NEG pumps with TMPs. There are now 24 TMPs for the DTL, and 32 TMPs for the CCL. Since the upgrade downtimes from the DTL and CCL structures have been eliminated. The overall accelerator availability has increased by a few percent.

Change in RF Conditioning Procedure Reduced Field Emission

The initial version of the RF conditioning procedure for the normal conducting RF was a two-step process to first condition the cavity and then to condition the RF window. The theory was that to condition the window the RF power needed to be increased to beam loading levels. In order to achieve these levels the RF field in the structure was increased to significantly higher levels than required to properly accelerate the beam. Field emission is an exponential process with voltage so increasing the field to reach beam loaded forward power levels created a large increase in the amount of field-emitted electrons. These electrons would hit equipment in or near the cavity heating them to the point where material was released into the vacuum system. This part of the RF procedure actually caused a constant contamination issue each run as the conditioning process was always done after extended maintenance periods.

After an RF window was damaged in 2015 while performing RF conditioning the decision was made to no longer do RF conditioning at beam loaded levels. Since that time x-ray readings from field emitted electrons have dropped significantly, and they continue to decay at a

ISBN: 978-3-95450-192-2 doi:10.18429/JACoW-IBIC2017-TH2AB1

slow pace. It takes months to years for the decay to occur (see Fig. 10).

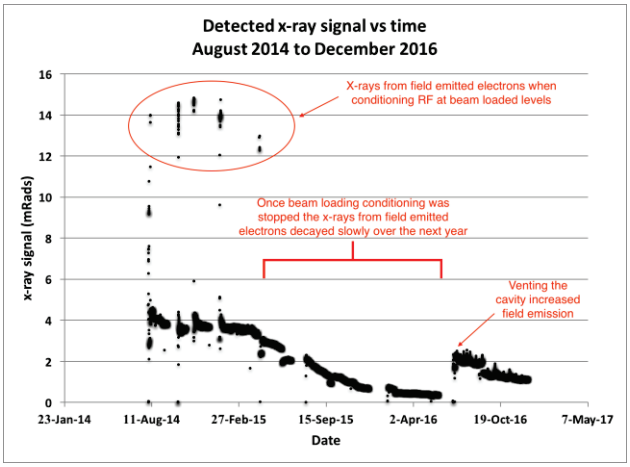

Figure 10: Detected x-rays from field emitted electrons versus time. After removing beam loading conditioning levels from the RF conditioning procedure the amount of field emitted electrons decreased significantly.

Reduction in Normal Conducting RF Fields

In late 2016 the errant beam frequency increased at the beginning of a run. Investigation found that the RF power calibration for the normal conducting RF changed. Fields were incorrect and were higher than they needed to be to accelerate the beam with minimal beam loss. The fields were accidentally increased due to a change in calibration.

The fields in the normal conducting RF were decreased to nominal levels and the beam losses tuned by hand. The thought was then to further reduce RF fields and attempt to properly accelerate the beam and also maintain beam losses at minimal levels. Cavity fields in the normal conducting linac were reduced by up to 5%, and beam losses have not increased. RF cavity faults and consequently errant beam faults have been further reduced.

HPRF Klystron Instabilities

In addition to all of the cavity issues the HPRF system is another cause for errant beam in the SCL. In 2016, after further reducing RF faults, there was a significant increase in errant beam faults for a specific RF cavity in the CCL. By the process of elimination the cause was narrowed down to the HPRF system. An oscilloscope was added to the system that triggered with a LLRF HPM fault. The issue was found to be instability with the klystron. This issue remains, and studies continue to try to further understand how to alleviate the issue without making significant changes to the klystron.

LLRF False Fault Detection

The only issue of note was the installation of arc detector circuits in the DTL and CCL that were too sensitive. The circuits detected arcs even with no RF on in the system. The DTL cards were replaced many years ago, but the sensitive CCL cards remained. From 2015-2017 ~65% (681 out of 1044) of the errant beam faults from the normal conducting linac came from the CCL. These false arc detections are a significant portion of these faults (about 25%). The arcs are detected at all times (during or outside of the RF pulse) so there was a 6% (duty factor) chance of the false arc detection to turn off RF during the beam pulse and cause errant beam (BLM trips).

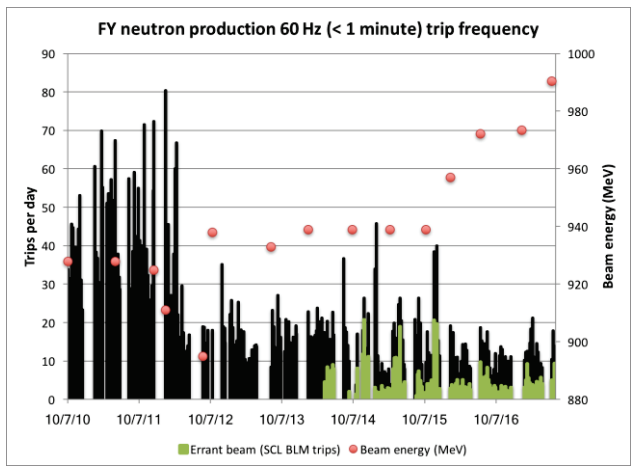

Figure 11: Week by week trip statistics for faults taking less than 1 minute to recover from 2010 until now. Errant beam trip frequency is shown in green.

CONCLUSION

Errant beam events may seem to not be a significant issue because recovery from these events typically only takes a few seconds. However, repeated errant beam events do cause degradation of SCL cavities with the need to reduce gradients to maintain high availability.

In order to reduce the impact of errant beam the amount of beam lost during an event and the frequency of events have been significantly reduced (see Fig. 11). This has slowed the need to continually reduce cavity gradients and allowed SRF personnel to implement techniques to restore previously degraded cavities and actually improve cavity performance by increasing maximum gradients.

ACKNOWLEDGMENT

The authors would like to thank SNS Accelerator Operators for diligently recording errant beam data in the electronic logbook. Additionally, they would like to specifically thank Sang-Ho Kim and Mike Plum, for fruitful discussions about RF systems and fault mechanisms.

ISBN: 978-3-95450-192-2 doi:10.18429/JACoW-IBIC2017-TH2AB1

REFERENCES

[1] S. Henderson *et al.*, "The Spallation Neutron Source accelerator system design", Nucl. Inst. Meth. Vol. A763, pp. 610-673, 2014.

[2] S. Kim *et al.*, "The status of the Superconducting Linac and SRF Activities at the SNS", 16th international conference on RF superconductivity, Sep 23-27, Paris, 2013.

[3] M. Plum, "High Power Operation of SNS SC Linac", in Proc. Linear Accelerator Conference (LINAC'16), East Lansing, MI, USA, 2016, p. 348.

[4] C. Sibley III *et al.*, "The SNS Machine Protection System: Early Commissioning Results and Future Plans", PAC'05, Knoxville, TN, May 16-20, 2005, p. 1727-1729.

[5] D. Gassner *et al.*, "Spallation Neutron Source Beam Loss Monitor System", PAC'03, Portland, OR, May 12-16, 2003.

[6] M. Kesselman, "Spallation Neutron Source Beam Current Monitor Electronics", PAC'01, Chicago, IL, June 18-22, 2001.

[7] J. Power, J. O'Hara, S. Kurennoy, M. Plum and M. Stettler, "Beam Position Monitors for the SNS LINAC", PAC'01, Chicago, June 2001, p. 1375.

[8] C. Peters *et al.*, "Superconducting Radio Frequency Cavity Degradation due to Errant Beam", in Proc. Int. Particle Accelerator Conference (IPAC'15), Richmond, VA, USA, 2015, p. 805.

[9] W. Blokland, "A New Differential and Errant Beam Current Monitor for the SNS Accelerator", IBIC 2013, Oxford, Sep 16-19 2013.

ISBN: 978-3-95450-192-2 doi:10.18429/JACoW-IBIC2017-TH2AB2

BUNCH-BY-BUNCH BEAM LENGTH MEASUREMENT USING TWO-FREQUENCY SYSTEM AT SSRF*

H. J. Chen†,1, L. W. Duan, Y. B. Leng‡, B. Gao[1], L. W. Lai, N. Zhang
Shanghai Institute of Applied Physics, Chinese Academy of Sciences, Shanghai, China
[1]also at University of Chinese Academy of Sciences, Beijing, China

Abstract

A Two-frequency method has been implemented for bunch length measurement at Shanghai Synchrotron Radiation Facility (SSRF). It is based on the information from two harmonic frequencies of Flourier Transformation of longitudinal charge distribution. We select 500MHz and 3GHz as working frequency and the system consists of power splitters, band-pass filters and a mixer. Raw data are acquired by a digital oscilloscope and analyzed by MATLAB code. The system has been calibrated by Steak Camera in single-bunch experiment environment with bunch charge from 0.23nC to 6.05nC. The paper also shows bunch length synchronous oscillation phenomenon during injection period.

INTRODUCTION

Shanghai Synchrotron Radiation Facility (SSRF) is a third-generation light source facility in Shanghai ,China, which has been operating about 8 years. With the second phase construction and more inserts in storage ring, the longitudinal instabilities will raise up including bunch-length diversity. Moreover, bunch length should be regulated within appropriate ranges for high brilliance pulses producing, which leads it as an important factor of overall beam performance.

Bunch length is now precisely measured by Streak Camera in SSRF with bunch-by-bunch capability and resolution of 2 ps [1]. However, the data reputation rate of Streak Camera is low about 2 Hz, and it requires complicated optical structures. A two-frequency system for bunch-by-bunch bunch length measurement has been implemented in SSRF for real-time measurement and data analysis of SSRF daily operation.

The two-frequency method picks up longitudinal distribution information from Beam Position Monitors (BPMs).The bunch length could be calculated through the intensity radio at two harmonic frequencies of Fourier component in Gaussian longitudinal charge distribution.It is a indirectly way in Frequency domain and had been used for average bunch length measurement at CERN with a resolution about 0.7 ps [2].Bunch-by-bunch data acquisition and analysis techniques have been developed at SSRF for many years with successfully implemented for position measurement [4] [5].It could also applied for the two-frequency system to approach bunch-by-bunch results.

* Work supported by National Natural Science Foundation of China (No. 11375255 and No. 11375254)
† chenhanjiao@sinap.ac.cn
‡ Corresponding author:lengyongbing@sinap.ac.cn

Two harmonic frequency detection point is selected as 500 MHz and 3 GHz in the two-frequency system. It employs radio-frequency (RF) electronics, a high sampling rate and multi channels oscilloscope as data acquisition module. Data analysis is under Matlab environment. In this paper, we will discuss the principle, system setup, system calibration using Streak Camera and bunch length synchronous oscillation phenomenon during injection period.

PRINCIPLES

A typical bunch longitudinal charge distribution is Gaussian and its Fourier component of m_i-th harmonic is given as:

$$V(m_i\omega_0) = 2V_0 exp\ -\frac{m_i^2\omega_0^2\sigma_0^2}{2} \quad (1)$$

where ω_0 is the RF frequency 499.654 MHz of SSRF, V_0 is the DC component, σ_0 is the bunch length considered as a constant at one time. Hence, the σ could be obtained with voltage radio between two different harmonic frequency points as follows:

$$\sigma = \sqrt{\frac{2}{m_2^2\omega_0^2 - m_1^2\omega_0^2} ln\left(\frac{KV_1(m_1\omega_0)}{V_2(m_2\omega_0)}\right)} \quad (2)$$

where V_1 and V_2 are experimental measured value at two m_i-th harmonic frequencies, m_2 is larger than m_1 and K is a coefficient calculated by two-frequency results. To calculate the resolution of bunch length σ, we could get the equation as follows:

$$\frac{\Delta\sigma}{\sigma} \simeq \frac{\sqrt{2}}{\left|m_1^2 - m_2^2\right|\omega_0^2\sigma^2}\left[\left(\frac{\Delta V_1}{V_1}\right)^2 + \left(\frac{\Delta V_2}{V_2}\right)^2\right] \quad (3)$$

The $\Delta V/V$ is equal to the signal-to-noise ratios(SNR)of V_1 and V_2 signal, which are close enough at most occasions. From Eq. (3), the resolution of bunch length will suffer a severe enlargement when the two frequencies are too close: $\left|m_1^2 - m_2^2\right| \to 0$. As RF components bandwidth limitation, m_1=1 and m_2=6 (about 500 MHz and 3 GHz) are selected for this application.

SYSTEM SETUP

The two-frequency bunch-by-bunch bunch length measurement system is comprised of RF conditioning module, time module and real-time oscilloscope acquisition module, the detail block diagram is shown in Figure 1.

The signal from BPM button is divided into two channels by a two-way zero-degree power splitter. One channel passes

ISBN: 978-3-95450-192-2 doi:10.18429/JACoW-IBIC2017-TH2AB2

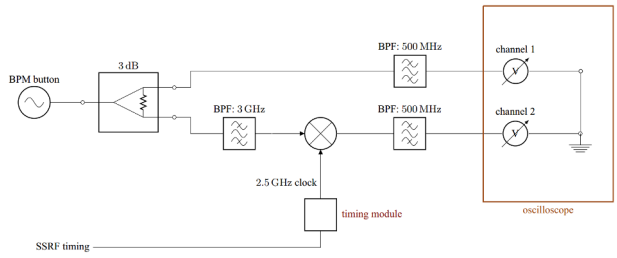

Figure 1: Block diagram of two-frequency bunch length measurement system [3].

through a 500 MHz band-pass-filter (BPF) as one working frequency. On the another channel, the raw signal meets a 3 GHz BPF, which picks up the 6-th harmonic frequency as working frequency. A mixer with 2.5 GHz local oscillator (LO) from clock module transport the 3 GHz signal to a intermediate frequency of 500 MHz for bandwidth limitation acquisition of oscilloscope. After the same 500 MHz BPF, it is acquired by the oscilloscope with the first channel at the same trigger. Time delay between channels are strictly correction by oscilloscope deskew function. The photograph of RF electronics are shown in Figure 2.

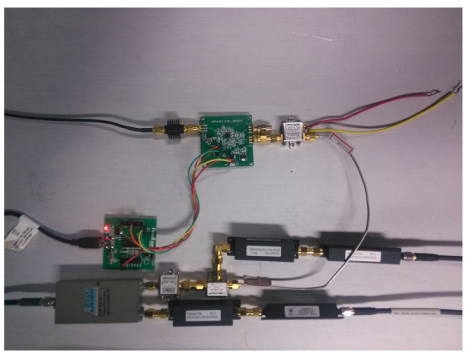

Figure 2: The photograph of RF electronics [3].

CALIBRATION IN SINGLE-BUNCH PATTERN

Equation Correction with Bandwidth Effect

The bunch length calculation equation in Eq. (2) is derived in ideal two dot frequency environment. Actually, the RF bandwidth in electronic are inevitable, which contributes a constant offset. The equation is corrected below as Eq. (4) and following calibration will be based on it.

$$\sigma = \frac{2}{m_2^2\omega_0^2 - m_1^2\omega_0^2} ln \left(K_1 \frac{V_1}{V_2} + K_2 \right) \qquad (4)$$

The variables in Eq. (4) V_1/V_2 is considered as an entirety as R_{12} for simply calculation and coefficients K_1 and K_2 fitting.

Bunch Length Results from Streak Camera

Streak Camera is a usual absolute bunch length measurement method with resolution of about 2 ps and regarded as the reference in our application.In the experiment, the bunch charge enhances from 0.23 nC to 6.05 nC, which is covered the SSRF operating status and up to a high unstable level. The typical four results from Streak Camera at four different currents is shown in Figure 3. The relationship between bunch charge and bunch length is shown in Figure 4. From the bunch length enhanced performance along bunch charge raised up by Streak Camera results in Figure 4, we have a 2-order Polynomial equation below 1 nC bunch charge and a linear equation upon 1 nC. It offers a wide range and precise reference for the two-frequency method calibration.

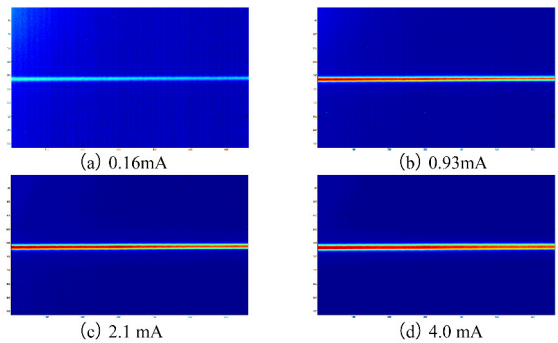

Figure 3: Typical bunch length measured results from Streak Camera.

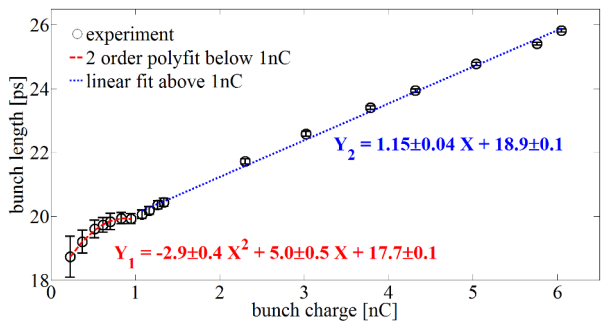

Figure 4: Relationship between bunch charge and bunch length from Streak Camera.

The Two-Frequency Method Calibration Results

The coefficient R_{12} mentioned before could be reckoned by linear fitting between calculated R_{12} and measured R_{12}. The calculated R_{12} comes from truth bunch length value by Streak Camera and the two-frequency method offers the measured R_{12}. Figure 5 presents the relationship and the fitting equation for K_1 and K_2 in Eq.4.

With the calibrated coefficient K_1 and K_2, the two-frequency method also offers absolute bunch length value and could be able to compare with Streak Camera result to evaluate its performance. Figure 6 presents the comparison diagram between this two methods at different bunch charge conditions.

ISBN: 978-3-95450-192-2 doi:10.18429/JACoW-IBIC2017-TH2AB2

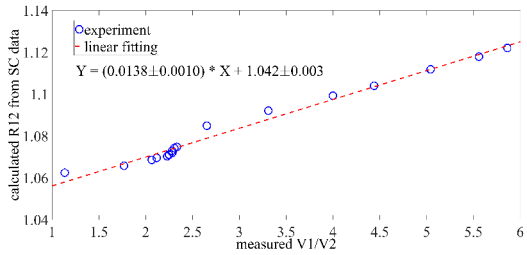

Figure 5: Systemic coefficient calibration.

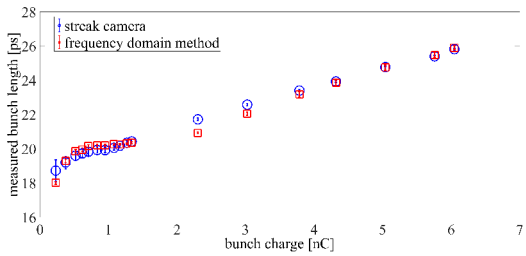

Figure 6: Comparison of bunch length measuring performance between Streak Camera and two-frequency method.

From Figure 6, the two group results keep agreeable generally, even at low charge domain, the two-frequency method shows less deviation than Streak Camera, which demonstrates that Eq. (4) is correct and two-frequency method has the capability of bunch length measurement.

BUNCH LENGTH OSCILLATION DURING INJECTION

There are two kinds of damping oscillation after bunch injection, the betatron oscillation coming from the the timing mismatch of kickers and the synchronous oscillation due to the phase mismatch of the refilled charge, which is combining with the stored charge and a small injected charge. The injected charge oscillate around the stored charge in longitudinal plane, which induces a corresponding bunch length oscillation detected by the two-frequency system. And theoretically, the oscillation frequency will be double of the storage ring synchrotron frequency as phase of injected charge beyond or behind stored charge all contributes bunch length enhanced. Figure 7 shows the behaviors about the betatron oscillation and synchronous oscillation.

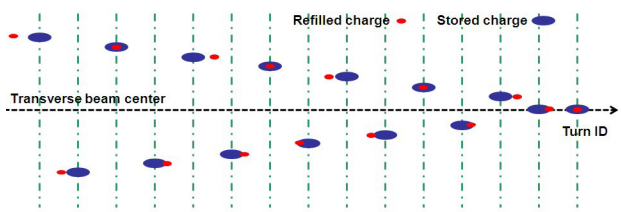

Figure 7: Schematic of two oscillations behaviors after bunch injection [3].

Figure 8 presents bunch length changes in turns after injection contributed by the synchronous oscillation as the blue plots. As a reference, the stored bunch is plotted as well by the red line to demonstrate a stable bunch length status.

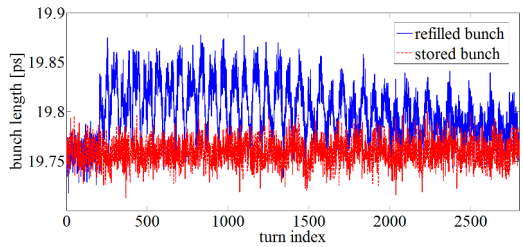

Figure 8: Bunch length changes in turn after injection.

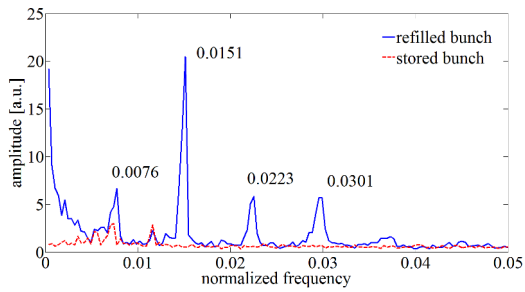

Figure 9: Frequency spectrum of bunch lengths during injection of refilled bunches.

In Figure 8, the bunch length suddenly jumps to a high value, then recover to normal length with damping in thousands turns.We analysis the frequency spectrum of refilled bunch and stored bunch in Figure 9. It could be figured out the synchronous oscillation frequency of SSRF storage ring about 0.0076, and a huge peak at the 2nd harmonic about 0.0151 in Figure 9, which demonstrates our description in Figure 7 about the two oscillation behaviors.

CONCLUSION

The two-frequency method for bunch-by-bunch bunch length measurement has been implemented in SSRF, and successfully calibrated by Streak Camera. The calibration experiments also demonstrates its authenticity and excel-lent resolution in low bunch charge situations. The bunch length oscillations research during injection based on the two-frequency also proves its capabilities in bunch-by-bunch studies. Furthermore, the system will be used for beam loss moment study and other beam phenomenons, or will be served as on-line equipment for real-time bunch length monitoring.

REFERENCES

[1] J. Chen *et al.*, "Bunch length measurement with streak camera at SSRF storage ring", in *Proc. IBIC'13*, Oxford, UK, Sep 2013, paper TUPC43, pp. 478–480.

[2] H. H. Braun, and C. Martinez, "Non-Intercepting Bunch Length Monitor for Picosecond Electron Bunches", in *Proc. EPAC'98*, Stockholm, Sweden, Jun 1998, pp. 1159–1561.

ISBN: 978-3-95450-192-2 doi:10.18429/JACoW-IBIC2017-TH2AB2

[3] L. W. Duan *et al.*, "Injection transient study using a two-frequency bunch length measurement system at the SSRF", *Nucl. Sci. Tech.*, vol. 28, no. 93, p. 1-6, May. 2017.

[4] Y. Yang *et al.*, "Development of the bunch-by-bunch beam position acquisition system based on BEEcube", *Nucl. Sci. Tech.*, vol. 27, no. 47, p. 1-6, April. 2016.

[5] Y. B. Leng *et al.*, "Bunch by Bunch DBPM Processor Development and Preliminary Experiment in SSRF", in *Proc. IPAC'15*, Richmond, VA, USA, May 2015, paper MOPTY022, pp. 984–986.

ISBN: 978-3-95450-192-2 doi:10.18429/JACoW-IBIC2017-TH2AB3

OPTIMIZATION OF THE CRYOGENIC CURRENT COMPARATOR (CCC) FOR BEAM INTENSITY MEASUREMENT*

T. Sieber[1†], H. De Gersem[7], J. Golm[3], M. Fernandes[2, 8], R. Jones[2], P. Kowina[1], F. Kurian[1], N. Marsic[7], R. Neubert[3], H. Reeg[1], M. Schmelz[6], F. Schmidl[3], M. Schwickert[1], P. Seidel[3], L. Soby[2], T. Stoehlker[1,4,5], R. Stolz[6], J. Tan[2], G. Tranquille[2], V. Tympel[5], C.P. Welsch[8], V. Zakosarenko[6]
[1]GSI Helmholtz Center for Heavy Ion Research, Darmstadt, Germany
[2]CERN European Organization for Nuclear Research, Geneva, Switzerland
[3]Institute for Solid State Physics, Friedrich-Schiller-University Jena, Germany
[4]Institute for Optics and Quantum Electronics, Friedrich-Schiller-University Jena, Germany
[5]HIJ, Helmholtz-Institute Jena, Germany
[6]IPHT, Leibniz Institute of Photonic Technology, Jena
[7]TEMF, Institute for Theory of Electromagnetic Fields, Technical University, Darmstadt
[8]University of Liverpool, Liverpool

Abstract

Triggered by the need for nA current measurement of slow extracted beams and in the storage rings at FAIR and CERN, the idea of the CCC as a current transformer has been revitalized during the last ten years. Compared to the first prototype, developed at GSI in the 90s, the second generation of CCCs is based on the possibility of detailed simulation of superconducting magnetic shielding properties, new nanocrystalline materials for the magnetic ring-cores and on superior commercially available SQUID systems. In 2014, nA resolution measurements at 2 kHz bandwidth demonstrated the possibility of spill analysis at slow extracted beams from GSI SIS18. In the following year, the first stand-alone CCC system, including a cryostat with separate He liquefier, started operation in the CERN AD. Although the existing systems show outstanding current resolution, their cost efficiency and robustness, as well as noise- and vibration sensitivity can still be improved, which is subject of ongoing research.

In this paper, recent results of our CCC tests are shown and future developments are discussed.

INTRODUCTION

Beam intensity measurement with a Cryogenic Current Comparator is based on the detection of the azimuthal magnetic field of the particle beam. This field is measured by using a pickup coil wound around a high permeability ring core which acts as a flux concentrator, an arrangement which ensures efficient coupling of the azimuthal magnetic field to the pickup. The signal from the pickup coil is fed (via a transformer for impedance matching) to a dc SQUID (Superconducting Quantum Interference Device) current sensor, which is operated in a compensation circuit, using a so called Flux Locked Loop (FLL) electronics [1]. In order to suppress disturbing magnetic noise from external fields, the pickup coil and ring core are embedded in a superconducting meander-shaped magnetic shield, providing attenuation of non-azimuthal field components of < -100 dB. Figure 1 shows the currently used arrangement, originally developed at the PTB (Physikalisch-Technische Bundesanstalt) [2].

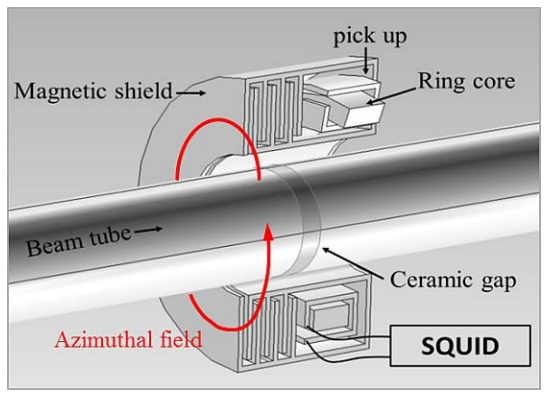

Figure 1: Principle of the CCC, shielding with radial meanders.

Following earlier work by Grohmann, Kuchnir and Peters et al. [2, 3, 4], the most recent and also most detailed investigations of the practical aspects of CCC operation in accelerators were performed in 2014 at GSI in a SIS18 extraction beamline, and in the CERN Antiproton Decelerator, where a CCC started its operation in 2015. Both systems were/are equipped with state of the art commercial SQUID systems (Magnicon© [5] and Supracon© [6] SQUIDs respectively).

While the GSI CCC basically consisted of a prior GSI prototype, equipped with a lead shielding and a VITROVAC© ring core, housed in a comparatively simple high vacuum cryostat, the AD CCC represents the first stand-alone device (including a UHV beam tube and a He reliquefier), which has been extensively optimized with respect to mechanical vibrations and slew rate limitations. For the pickup coil, a different material of the ring core was chosen, since a study at Jena University concluded that the so called NANOPERM© material had a more

* Work supported by the BMBF under contract No. 05P15SJRBA
† T.Sieber@gsi.de

ISBN: 978-3-95450-192-2 doi:10.18429/JACoW-IBIC2017-TH2AB3

stable permeability in the given temperature and frequency range [7]. The magnetic shielding was made from Niobium. The same materials were chosen for the new CCC system for FAIR, which is currently under construction.

Both systems gave significant input for the next steps of optimization with respect to current resolution, system robustness and last but not least system costs. For illustration, Figures 2 and 3 show measurements, which have been performed with the CCC systems in the SIS18 HEBT and in the AD.

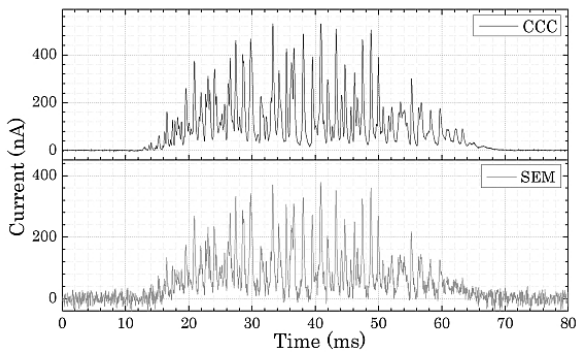

Figure 2: Spill analysis at GSI SIS18, using the CCC (upper) and a SEM foil in comparison (lower).

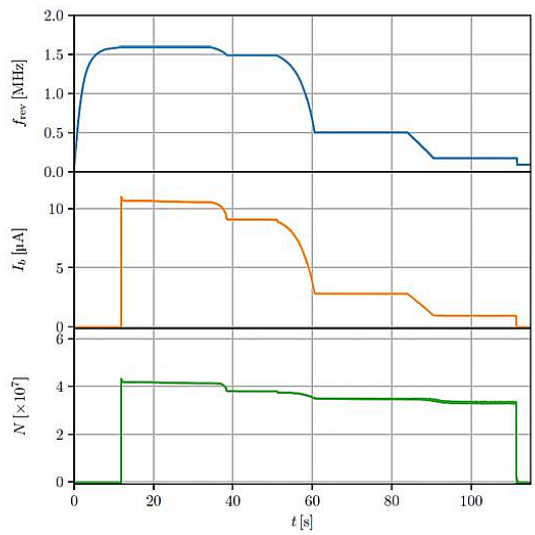

Figure 3: Deceleration cycle of the CERN AD. Revolution frequency (upper), beam intensity measured with CCC (middle) and corresponding particle numbers (lower).

SYSTEM NOISE

Figure 4 shows the input current noise spectrum of the new Nb CCC for FAIR measured in a magnetically shielded room in comparison to a twin system made of Pb. The noise figure is typical for all CCC systems showing basically three different slopes (marked in red) in the range below 1 kHz and excessive noise bursts between 10 Hz and 100 Hz. While the noise at extremely low frequencies ≤ 0.5 Hz probably derives from vibrations of the building (and underlines the necessity of best possible vibrational damping), there is some evidence that the second slope (1 Hz - 10 Hz) besides the 1/f noise is caused by the SQUID itself. However, the main subject of investigation is currently the excessive noise between 10 Hz and 100 Hz. Candidates for this contribution are microphony and/or noise in the magnetic core and mechanical vibrations of the magnetic shielding as well. Both effects are currently investigated by numerical calculations (see below). Concerning the contribution from the ring-core, tests with a coreless alternative CCC design are currently in progress to allow for comparison with the current design. Besides this work, a new shielding geometry proposed by IPHT Jena [8], as depicted in Figure 5, may improve the shielding factor and reduce the fabrication efforts.

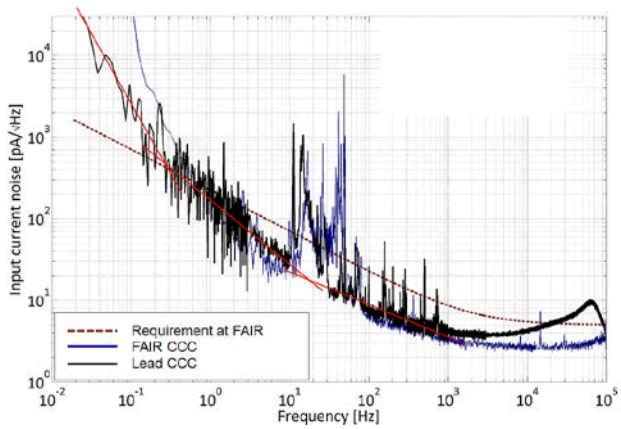

Figure 4: Noise spectrum taken from the FAIR Nb CCC in comparison to a Pb system.

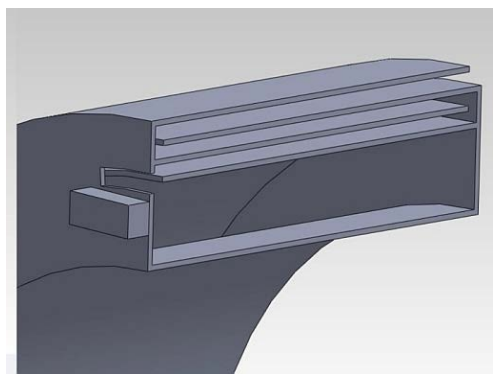

Figure 5: Alternative shielding geometry with axial meanders.

In this design, the meanders are oriented in axial direction, the SQUID is directly connected to the inner part of the shielding, which becomes therefore pickup coil and shielding at the same time. First tests look promising with respect to shielding efficiency and noise reduction below 100 Hz, but further investigations are required. Since this new pickup coil has a much smaller inductance than the former design with ferromagnetic core, it can only work effectively in connection with a new generation of low input inductance SQUID current sensors [9]. Therefore the tests are also expected to deliver valuable

ISBN: 978-3-95450-192-2 doi:10.18429/JACoW-IBIC2017-TH2AB3

information concerning noise contribution of the SQUIDs.

Besides the intrinsic noise in Figure 4, operation in AD shows that there is also influence from well-known external sources, like mechanical vibrations of the pulsed-tube cooler and the magnetic cycles of the ring. Since these disturbances are periodic and identical, they are comparatively unproblematic and can be subtracted software-wise from the signal.

TEMPERATURE DRIFT

A significant zero drift of the CCC output in dependence on the He pressure/temperature was observed during offline campaigns at GSI and later verified in laboratory measurements at Jena and in the AD. To disentangle temperature and pressure effects, an 'anti-cryostat' was built at Jena to vary one quantity independent from the other [10]. Inductance measurements with this device could finally reduce the effect to a temperature dependence of the pickup inductance. Figure 6 shows the dependence of the inductance of a small sample of NANOPERM© cores on temperature and pressure.

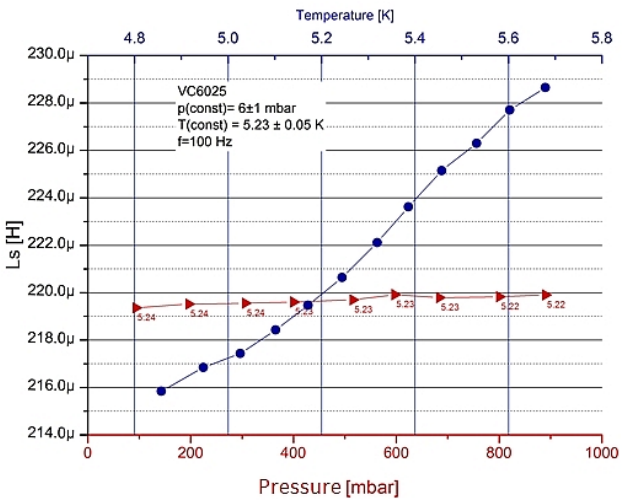

Figure 6: Inductance measurement with the 'anti-cryostat'.

The measured drifts with the CCC systems were in the range of 20 - 40 nA/mK, the effect seems to be slightly smaller for the VITROVAC© material. This is (regarding the desired nA resolution of the devices) a dramatically high value, on the other hand, the real temperature changes (within relevant time intervals) are far below 1 mK, once the cryostat has reached thermal equilibrium. Nonetheless, low frequency pressure fluctuations from recovery lines and He boil-off will have influence on long term measurements, which gives another reason for investigation of coreless CCCs.

NUMERICAL SIMUALTIONS

Numerical simulations (Comsol Multiphysics©, CST EM Studio©) have been performed in the first place to scale the attenuation factor of the GSI prototype shielding to larger CCC dimensions. This resulted in the XD- (eXtremely large Dimensions) CCC for FAIR, which has an inner/outer diameter of 250/350 mm (to cope with the 150 mm beam tubes at FAIR) and a length of 240 mm (resulting from four additional meanders, necessary to maintain the required shielding factor at the larger inner diameter) [11]. Recent calculations have been performed to compare the properties of the two competing 'radial' and 'axial' shielding geometries [12]. Since the required Nb mass and welding efforts are a significant cost-factor of the total system, the required Nb volume at a given attenuation factor has been calculated (see Figure 7). It has been shown that the shielding volume can be decreased by using 1. a large number of short meanders in the radial case; 2. a small number of long meanders in the axial case.

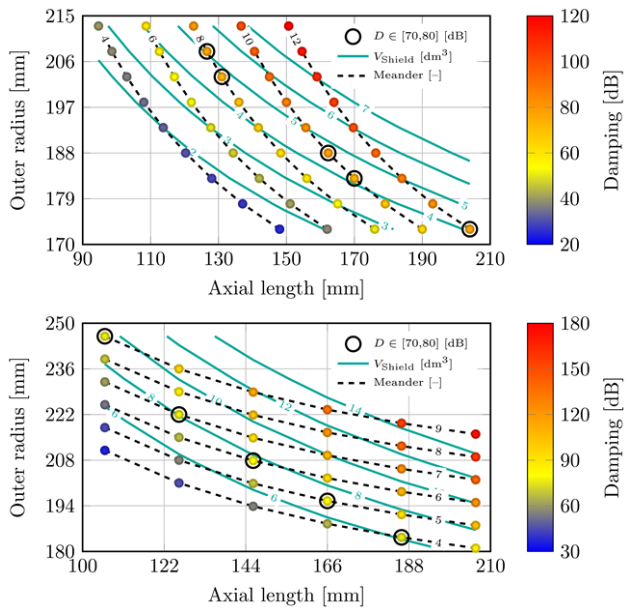

Figure 7: Niobium shielding volume for a -75 ±5 dB attenuation (encircled dots). Upper: Radial meanders. Lower: Axial meanders.

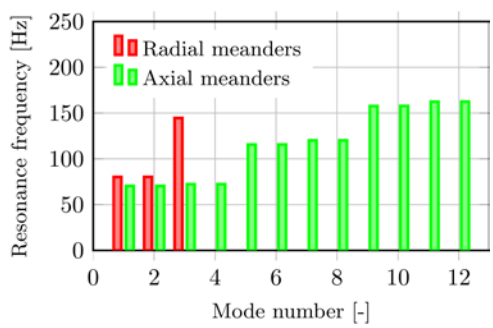

Figure 8: Mechanical eigenfrequencies of radial and axial magnetic shieldings up to 200 Hz. Both shields exhibit a -75 ±5 dB attenuation.

Using the ANSYS© software package, simulations were performed to analyze the mechanical eigenmodes of the shielding. The eigenmode spectrum shown in Figure 8 points to some of the resonances in the noise spectrum in

ISBN: 978-3-95450-192-2 doi:10.18429/JACoW-IBIC2017-TH2AB3

Figure 4 and raises the question how the shielding itself can be designed to be more stiff - a subject which is also related to material choice.

In parallel to the analysis of the shielding, a ANSYS©-model of the FAIR CCC cryostat [13] has been developed. Figure 9 shows the mechanical design. The new cryostat will be installed in CRYRING at first, to check its cryogenics properties, to support the experimental program in CRYRING and to serve at the same time as a test bench for further CCC development. Although this cryostat will be - compared to the AD CCC - a mechanically simple system with the suspension wires of the He container fixed straight in the corners of the insulation vacuum chamber, we plan to check - and if necessary iteratively improve - its vibration behavior, avoiding mechanical resonances close to 50 Hz and higher harmonics in the final design.

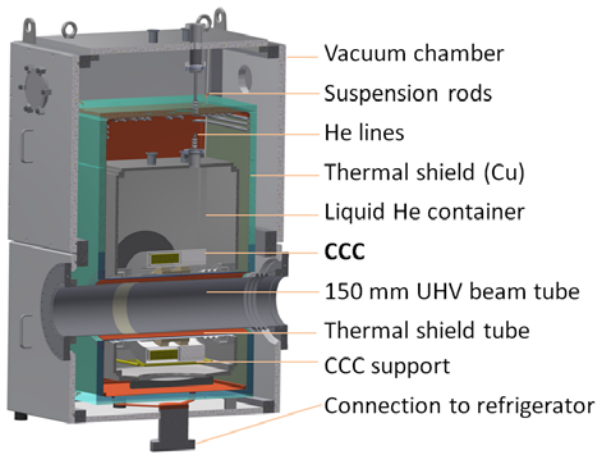

Figure 9: Design of the cryostat for the FAIR CCC.

LEAD VS NIOBIUM

The first magnetic shieldings at PTB and GSI were made from lead. Problems with the machining due to toxicity, the expectation of mechanical instability at larger dimensions and the higher critical temperature led to the choice of Nb as material for the shieldings for AD and FAIR. Recently, the discussion about materials has been relaunched - not only because of the exorbitant costs of large Nb shieldings compared to Pb, but also because Pb, as a superconductor type 1, has superior properties concerning elimination of trapped flux. Since also the problem of mechanical stability can be solved by using alloys of higher rigidity, it is planned as a next step to install a twin of the FAIR CCC made of lead in the beamline to compare the properties of the two systems.

SUMMARY AND OUTLOOK

Despite the excellent performance of the CCC in measuring currents in the nA range, there is still room for improvement of the device. Investigations are on the way covering basically all components of the CCC to reduce its intrinsic noise and to increase system robustness and cost effectiveness.

After the new CCC for FAIR has been completed and tested in the laboratory in 2017, the cryostat will be completed in mid-2018. Besides its function in the FAIR beamlines, this cryostat has been designed as a test bench for CCC development in CRYRING until the startup of FAIR. Due to its comparatively compact design and (expected) low costs, the cryostat might also be an alternative for a possible CCC in ELENA. In CRYRING, it will offer the opportunity to check the major part of the above mentioned points experimentally. In addition, there are already new proposals for further development, like CCCs with a second SQUID for reference as well as SQUID systems for enhanced dynamic range and single particle detection in resonant mode.

REFERENCES

[1] F. Kurian, Cryogenic Current Comparators for precise Ion Beam Current Measurements", PhD thesis, University of Frankfurt, Germany, 2015
[2] K. Grohmann, H. D. Hahlbohm, D. Hechtfischer, and H. Lübbig, "Field attenuation as the underlying principle of cryocurrent comparators 2. Ring cavity elements", Cryogenics, vol. 16, no. 10, pp. 601–605, 1976.
[3] M. Kuchnir, J. McCarthy and P. Rapidis, "SQUID based beam current meter", in IEEE Transactions on Magnetics, vol. 21, no. 2, pp. 997-999, Mar 1985.
[4] A. Peters *et al.*, "A Cryogenic Current Comparator for the absolute Measurement of nA Beams", AIP Conf. Proc. 451 pp.163-180 (1998).
[5] Magnicon GmbH, http://www.magnicon.com
[6] Supracon, http://www.supracon.com
[7] R. Geithner *et al.*, "Cryogenic Current Comparators for Storage Rings and Accelerators", Proc. IBIC'15. Melbourne, Australia
[8] R. Stolz *et al.*, paper in preparation
[9] M. Schmelz *et al.*, "A new family of field-stable and highly sensitive SQUID current sensors based on sub-micrometer cross-type Josephson junctions", Supercond. Sci. Technol. 30 (7), 74010 (2017)
[10] J. Golm, Master thesis in preparation, Institut of Solid State Physics, FSU Jena
[11] V. Tympel *et al.*, "Cryogenic Current Comparators for 150 mm beamline diameter", Proc. IBIC'17
[12] N. Marsic *et al.*, "Analytical and numerical performance analysis of a Cryogenic current comparator", Proc. IPAC'17, Copenhagen, Denmark
[13] T. Sieber *et al.*, "Optimization Studies for an advanced Cryogenic Current Comparator (CCC) system for FAIR", Proc. IBIC'16, Barcelona, Spain

ISBN: 978-3-95450-192-2

List of Authors

Bold papercodes indicate primary authors; ~~crossed out~~ papercodes indicate 'no submission'

ISBN: 978-3-95450-192-2

ISBN: 978-3-95450-192-2

ISBN: 978-3-95450-192-2

ISBN: 978-3-95450-192-2

ISBN: 978-3-95450-192-2

ISBN: 978-3-95450-192-2

ISBN: 978-3-95450-192-2

ISBN: 978-3-95450-192-2

Institutes List

ALBA-CELLS Synchrotron
Cerdanyola del Vallès, Spain
- Alvarez, M.
- Benedetti, G.
- Iriso, U.
- Nosych, A.A.
- Olmos, A.
- Rodriguez, X.I.
- Torino, L.

ANL
Argonne, Illinois, USA
- Arnold, N.D.
- Berenc, T.G.
- Brill, A.R.
- Bui, H.
- Carwardine, J.
- Decker, G.
- Deriy, B.
- Emery, L.
- Fors, T.
- Harkay, K.C.
- Kallakuri, P.S.
- Keane, R.T.
- Kelly, M.P.
- Lill, R.M.
- Nolen, J.A.
- Paskvan, D.R.
- Pietryla, A.F.
- Sereno, N.
- Shoaf, S.E.
- Stillwell, B.K.
- Sun, X.
- Veseli, S.
- Wang, J.
- Wienands, U.
- Xu, S.

ASCo
Clayton, Victoria, Australia
- Boland, M.J.
- Dowd, R.T.

BINP SB RAS
Novosibirsk, Russia
- Anchugov, O.
- Krutikhin, S.A.
- Meshkov, O.I.

BINP
Novosibirsk, Russia
- Dorokhov, V.L.

BNL
Upton, Long Island, New York, USA
- Altinbas, Z.
- Blaskiewicz, M.
- Blednykh, A.
- Bruno, D.
- Costanzo, M.R.
- Fedotov, A.V.
- Fedurin, M.G.
- Fischer, W.
- Gassner, D.M.
- Gu, X.
- Ha, K.
- Hammons, L.R.
- Hock, J.
- Hseuh, H.-C.
- Inacker, P.
- Jamilkowski, J.P.
- Jing, Y.C.
- Kayran, D.
- Kewisch, J.
- Litvinenko, V.
- Liu, C.
- Luo, Y.
- Mernick, K.
- Miller, T.A.
- Minty, M.G.
- Palmer, M.A.
- Paniccia, M.C.
- Pekrul, W.E.
- Pinayev, I.
- Pogorelsky, I.
- Ptitsyn, V.
- Seletskiy, S.
- Shih, K.
- Smaluk, V.V.
- Smedley, J.
- Smith, K.S.
- Song, H.
- Swinson, C.
- Than, R.
- Thieberger, P.
- Tian, Y.
- Tuozzolo, J.E.
- Wanderer, P.
- Wang, G.
- Xu, W.
- Yang, X.
- Zhao, Z.

Case Western Reserve University, Center for Synchrotron Biosciences
Upton, New York, USA
- Bohon, J.

Caylar Scientific Instrumentation
Villebon-sur-Yvette, France
- Boucher, R.B.
- Germain, C.

ISBN: 978-3-95450-192-2

- Germain, J-C.

CEA/IRFU
Gif-sur-Yvette, France
- Marroncle, J.
- Segui, L.

CEA
Gif-sur-Yvette, France
- Papaevangelou, T.

CERN
Geneva, Switzerland
- Alexopoulos, A.
- Allica, J.C.A.
- Andersson, P.
- Andreazza, W.
- Angoletta, M.E.
- Barrios Diaz, E.
- Barros Marin, M.
- Barschel, C.
- Bjorkqvist, O.
- Bjørsvik, E.R.
- Boccardi, A.
- Bodart, D.
- Bogey, T.B.
- Bracco, C.
- Bravin, E.
- Bregliozzi, G.
- Burger, S.
- Chritin, N.
- Dehning, B.
- del Busto, E.N.
- Effinger, E.
- Emery, J.
- Fernandes, M.F.
- Ferro-Luzzi, M.
- Focker, G.J.
- Garattini, M.
- Garcia, L.
- Giovannozzi, M.
- Gonzalez, J.L.
- Grishin, V.
- Gudkov, D.
- Guidoboni, G.
- Holzer, E.B.
- Höfle, W.
- Jacobsson, R.
- Jaussi, M.
- Jensen, L.K.
- Jones, O.R.
- Jones, R.J.
- Kain, V.
- Kastriotou, M.
- Krupa, M.
- Lefèvre, T.
- Levens, T.E.
- Magagnin, P.
- Marqversen, O.
- Matev, R.
- Medina, D.
- Mikulec, B.
- Molendijk, J.C.
- Montesano, S.
- Navarro Fernandez, A.
- Pospisil, J.
- Rihl, M.N.
- Roncarolo, F.
- Ruffieux, R.
- Salustino Guimaraes, V.
- Sanchez-Quesada, J.
- Scandale, W.
- Schneider, G.
- Sirvent, J.L.
- Søby, L.
- Storey, J.W.
- Tan, J.
- Tassan-Viol, J.
- Trad, G.
- Tranquille, G.
- Veness, R.
- Vlachos, S.
- Wendt, M.
- Würkner, B.
- Zamantzas, C.

CFEL
Hamburg, Germany
- Kärtner, F.X.

Cockcroft Institute
Warrington, Cheshire, United Kingdom
- Alexandrova, A.S.
- del Busto, E.N.
- Devlin, L.J.
- Jackson, F.
- Kastriotou, M.
- Scott, D.J.
- Tzoganis, V.
- Welsch, C.P.
- Zhang, H.D.

Cosylab
Ljubljana, Slovenia
- Vintar, R.

CSNS
Guangdong Province, People's Republic of China
- Huang, W.L.
- Peng, J.
- Qiu, R.Y.
- Sun, J.L.
- Yang, T.

D-Pace
Nelson, British Columbia, Canada

ISBN: 978-3-95450-192-2

- Dehnel, M.P.
- Potkins, D.E.

DESY
Hamburg, Germany
- Beutner, B.
- Butkowski, Ł.
- Fröhlich, L.
- Gerth, C.
- Hensler, O.
- Hierholzer, M.
- Hoffmann, M.
- Killenberg, M.
- Lipka, D.
- Obier, F.
- Schlarb, H.
- Schmidt, Ch.
- Scholz, M.
- Sydlo, C.
- Vilcins, S.
- Yan, M.

Dimtel
San Jose, USA
- Teytelman, D.

DLS
Oxfordshire, United Kingdom
- Rehm, G.
- Vitoratou, N.

Elettra-Sincrotrone Trieste S.C.p.A.
Basovizza, Italy
- Bassanese, S.
- Brajnik, G.
- Cautero, G.
- De Monte, R.
- Ferianis, M.
- Grulja, S.
- Penco, G.
- Roussel, E.
- Veronese, M.

EPFL
Lausanne, Switzerland
- Bay, A.
- Blanc, F.
- Gianì, S.
- Girard, O.
- Haefeli, G.J.
- Hopchev, P.
- Kuonen, A.
- Nakada, T.
- Schneider, O.
- Tobin, M.
- Veyrat, Q.D.
- Xu, Z.

ESS Bilbao
Zamudio, Spain
- Bustinduy, I.

ESS
Lund, Sweden
- Baron, R.A.
- Cheymol, B.
- Grandsaert, T.J.
- Grishin, V.
- Hassanzadegan, H.
- Jansson, A.
- Kittelmann, I.
- Kocevar, H.
- Molloy, S.
- Shea, T.J.
- Thomas, C.A.

FBK
Trento, Italy
- BORGHI„ G.
- Boscardin, M.
- Ronchin, S.

Fermilab
Batavia, Illinois, USA
- Alvarez, M.L.
- Crawford, D.J.
- Eddy, N.
- Fellenz, B.J.
- Fitzgerald, J.
- Lumpkin, A.H.
- Lundberg, C.E.
- Prieto, P.S.
- Scarpine, V.E.
- Thangaraj, J.C.T.
- Thurman-Keup, R.M.
- Warner, A.
- Zagel, J.R.
- Zorzetti, S.Z.

FRIB
East Lansing, USA
- Ao, H.
- Beher, S.
- Bultman, N.K.
- Casagrande, F.
- Chen, J.
- Cogan, S.
- Compton, C.
- Dalesio, L.R.
- Davidson, K.D.
- Facco, A.
- Feyzi, F.
- Ganni, V.
- Ganshyn, A.
- Gibson, P.E.
- Glasmacher, T.
- Hao, Y.

ISBN: 978-3-95450-192-2

- Hodges, L.
- Holland, K.
- Hseuh, H.-C.
- Hussain, A.
- Ikegami, M.
- Jones, S.
- Laxdal, R.E.
- LeTourneau, J.
- Lidia, S.M.
- Lund, S.M.
- Machicoane, G.
- Malloch, I.M.
- Marti, F.
- Maruta, T.
- Miller, S.J.
- Morris, D.G.
- Nolen, J.A.
- Omitto, D.O.
- Ostroumov, P.N.
- Popielarski, J.T.
- Popielarski, L.
- Pozdeyev, G.
- Ren, H.T.
- Russo, T.
- Saito, K.
- Shane, R.
- Stanley, S.
- Tatsumoto, H.
- Webber, R.C.
- Wei, J.
- Xu, T.
- Yamazaki, Y.
- Yoshimoto, T.
- Zhao, Q.

FSU Jena
Jena, Germany
- Golm, J.
- Neubert, R.
- Schmidl, F.
- Seidel, P.
- Tympel, V.

FZJ
Jülich, Germany
- Bekman, I.
- Böhme, C.
- Kamerdzhiev, V.
- Lorentz, B.
- Simon, M.
- Weidemann, C.

GSI
Darmstadt, Germany
- Forck, P.
- Kowina, P.
- Kurian, F.
- Pietraszko, J.
- Reeg, H.
- Sapinski, M.
- Schwickert, M.
- Sieber, T.
- Singh, R.
- Stöhlker, T.
- Udrea, S.
- Vilsmeier, D.M.

HIJ
Jena, Germany
- Stöhlker, T.

Huazhong University of Science and Technology, State Key Laboratory of Advanced Electromagnetic Engineering and Technology,
Hubei, People's Republic of China
- Chen, W.
- Liu, X.

HUST
Wuhan, People's Republic of China
- Chen, Q.S.
- Guo, H.D.
- Hu, Y.Y.
- Li, X.Y.
- Lin, Y.J.
- Liu, X.
- Qin, B.
- Tan, P.
- Tang, K.
- Yu, Y.

HZB
Berlin, Germany
- Atkinson, T.
- Goslawski, P.
- Jankowiak, A.
- Malyutin, D.
- Matveenko, A.N.
- Ries, M.

HZDR
Dresden, Germany
- Arnold, A.
- Kuntzsch, M.
- Lu, P.N.
- Murcek, P.
- Schurig, R.
- Steinbrück, R.
- Teichert, J.
- Vennekate, H.
- Xiang, R.

I-Tech
Solkan, Slovenia
- Baricevic, B.B.
- Cargnelutti, M.

ISBN: 978-3-95450-192-2

IBS
Daejeon, Republic of Korea
- Chung, Y.S.
- Kim, G.D.
- Woo, H.J.

IFIC
Valencia, Spain
- Marco-Hernandez, R.

IHEP
Beijing, People's Republic of China
- Cao, J.S.
- Du, Y.Y.
- Fu, S.
- He, J.
- Koshelev, A.V.
- Larionov, A.
- Li, F.
- Li, P.
- Ma, H.Z.
- Meng, M.
- Seleznev, V.S.
- Sleptsov, M.
- Sui, Y.F.
- Tian, J.M.
- Wang, L.
- Wang, S.
- Xu, T.G.
- Xu, Zh.H.
- Ye, Q.
- Yu, L.
- Yue, J.H.
- Zeng, L.
- Zhao, J.X.
- Zhao, Y.
- Zhou, J.S. Zhou.

Imperial College of Science and Technology, Department of Physics
London, United Kingdom
- Garattini, M.

INFN-Roma1
Rome, Italy
- Castorina, G.

INFN-Roma
Roma, Italy
- Addesa, F.M.
- Cavoto, G.
- Cortis, D.
- Iacoangeli, F.
- Marongiu, M.
- Mostacci, A.

INFN/LNF
Frascati (Roma), Italy
- Chiadroni, E.
- Cioeta, F.
- Di Pirro, G.
- Franzini, G.
- Pellegrini, D.
- Shpakov, V.
- Spataro, B.
- Stella, A.
- Vaccarezza, C.
- Variola, A.

INFN/LNL
Legnaro (PD), Italy
- Facco, A.
- Poggi, M.

IOM-CNR
Trieste, Italy
- Dal Zilio, S.
- Greco, S.
- Lazzarino, M.

IOQ
Jena, Germany
- Stöhlker, T.

IPHT
Jena, Germany
- Schmelz, M.
- Stolz, R.

ISDE
Moscow, Russia
- Chubunov, P.A.
- Protopopov, G.A.

J-PARC, KEK & JAEA
Ibaraki-ken, Japan
- Koseki, T.
- Kuboki, H.
- Satou, K.
- Toyama, T.

JAEA/J-PARC
Tokai-Mura, Naka-Gun, Ibaraki-Ken, Japan
- Harada, H.
- Hayashi, N.
- Hirano, K.
- Kato, S.
- Kinsho, M.
- Meigo, S.I.
- Miura, A.
- Okabe, K.
- Saha, P.K.

ISBN: 978-3-95450-192-2

- Takei, H.
- Tamura, F.
- Yoshimoto, M.

JAI
Egham, Surrey, United Kingdom
- Bashforth, S.E.
- Boorman, G.E.
- Bosco, A.
- Gibson, S.M.
- Karataev, P.
- Vitoratou, N.

JINR
Dubna, Moscow Region, Russia
- Mitrofanov, S.V.
- Skuratov, V.A.
- Teterev, Yu.G.

JLab
Newport News, Virginia, USA
- Dixon, K.
- Freyberger, A.
- Geng, R.L.
- Legg, R.A.
- Suleiman, R.
- Wiseman, M.

KEK
Ibaraki, Japan
- Akai, K.
- Ezura, E.
- Honda, T.
- Hosoyama, K.
- Ikeda, H.
- Kobayashi, A.
- Kobayashi, T.
- Koiso, H.
- Kuboki, H.
- Mitsuhashi, T.M.
- Morita, A.
- Nakanishi, K.
- Nishiwaki, M.
- Obina, T.
- Ohnishi, Y.
- Okada, M.
- Sagehashi, H.
- Satou, K.
- Sugimoto, H.
- Sugiyama, Y.
- Tadano, M.
- Takai, R.
- Tejima, M.
- Tobiyama, M.
- Toyama, T.
- Yoshii, M.
- Yoshimoto, S.I.

KIT
Eggenstein-Leopoldshafen, Germany
- Balzer, B.M.
- Blomley, E.
- Brosi, M.
- Bründermann, E.
- Caselle, M.
- Funkner, S.
- Kehrer, B.
- Müller, A.-S.
- Nasse, M.J.
- Niehues, G.
- Patil, M.M.
- Rota, L.
- Ruprecht, R.
- Schmelzer, T.
- Schuh, M.
- Schwarz, M.
- Schönfeldt, P.
- Steinmann, J.L.
- Walter, S.W.
- Weber, M.
- Yan, M.

Korea University
Seoul, Republic of Korea
- Kim, C.

Kyoto University
Kyoto, Japan
- Ichikawa, A.
- Nakamura, K.G.
- Nakaya, T.
- Uno, W.

LAL
Orsay, France
- Burmistrov, L.
- Dubos, S.
- Puill, V.
- Stocchi, A.

LBNL
Berkeley, California, USA
- Byrd, J.M.
- Prestemon, S.

LNLS
Campinas, Brazil
- Marques, S.R.

Lund University
Lund, Sweden
- Johansson, A.J.

ISBN: 978-3-95450-192-2

MPI-P
München, Germany
- Martyanov, M.

Naples University Federico II, Science and Technology Pole
Napoli, Italy
- Arpaia, P.
- Liccardo, A.

Natural Science LLC
Naperville, USA
- Kasper, P.H.
- Lumpkin, A.H.

Natural Science, LLC
Big Rock, USA
- Cathey, D.
- Cullen, G.
- Nelson, J.
- Warner, A.

NERS-UM
Ann Arbor, Michigan, USA
- Kubley, T.
- Toader, O.F.

Nippon Advanced Technology Co., Ltd.
Tokai, Japan
- Tsutsumi, K.

Northern Illinois Univerity
DeKalb, Illinois, USA
- Chattopadhyay, S.

Northern Illinois University
DeKalb, Illinois, USA
- Freemire, B.T.
- Mihalcea, D.
- Piot, P.
- Szustkowski, S.
- Wang, J.

NSCL
East Lansing, Michigan, USA
- Richard, C.J.
- Wong, C.Y.

NSRRC
Hsinchu, Taiwan
- Chan, C.K.
- Chang, C.-C.
- Chen, M.L.
- Cheng, Y.-S.
- Chiu, P.C.
- Chou, P.J.
- Chuang, J. -Y.
- Ho, H.C.
- Hsiao, Y.M.
- Hsu, K.H.
- Hsu, K.T.
- Hu, K.H.
- Huang, C.H.
- Huang, D.-G.
- Kuan, C.K.
- Lai, W.Y.
- Liao, C.Y.
- Lin, C.J.
- Lin, Y.Z.
- Perng, S.Y.
- Sheng, I.C.
- Tseng, T.C.
- Wang, H.S.
- Wu, C.Y.

ORNL RAD
Oak Ridge, Tennessee, USA
- Peters, C.C.
- Southern, T.B.

ORNL
Oak Ridge, Tennessee, USA
- Aleksandrov, A.V.
- Blokland, W.
- Justice, T.A.

PAL
Pohang, Kyungbuk, Republic of Korea
- Hong, J.H.
- Kang, H.-S.
- Kim, C.
- Ko, I.S.
- Lee, S.J.
- Shin, D.C.

PhLAM/CERCLA
Villeneuve d'Ascq Cedex, France
- Bielawski, S.
- Le Parquier, M.

PhLAM/CERLA
Villeneuve d'Ascq, France
- Evain, C.
- Szwaj, C.

PSI
Villigen PSI, Switzerland
- Alarcon, A.D.
- Arsov, V.R.
- Baldinger, M.
- Baldinger, R.
- Bednarzik, M.
- Bonderer, G.
- Borrelli, S.

ISBN: 978-3-95450-192-2

- Buechi, F.
- Chevtsov, P.
- Dach, M.
- David, Ch.
- Dehler, M.M.
- Ditter, R.
- Engeler, D.
- Ferrari, E.
- Frei, F.
- Gloor, M.
- Gobbo, A.
- Guzenko, V.
- Heimgartner, P.
- Heiniger, M.
- Hiller, N.
- Hunziker, S.
- Ischebeck, R.
- Kaiser, M.G.
- Keil, B.
- Koprek, W.
- Kramert, R.
- Llorente Sancho, D.
- Löhl, F.
- Malatesta, A.
- Marcellini, F.
- Marinkovic, G.
- Moser, M.
- Orlandi, G.L.
- Ozkan Loch, C.
- Pollet, P.
- Rippstein, B.
- Roggli, M.
- Rohrer, M.
- Romann, A.
- Schlott, V.
- Stadler, M.
- Treyer, D.M.

RAS/INR
Moscow, Russia
- Feschenko, A.
- Gavrilov, S.A.
- Reinhardt-Nickoulin, P.I.
- Titov, A.I.

Research School of Physics and Engineering, Australian National University
Canberra, Australian Capitol Territory, Australia
- Lobanov, N.R.

Rome University La Sapienza
Roma, Italy
- Mostacci, A.
- Palumbo, L.

Royal Holloway, University of London
Surrey, United Kingdom
- Arteche, A.
- Boorman, G.E.
- Bosco, A.
- Gibson, S.M.
- Karataev, P.
- Levasseur, S.
- Vitoratou, N.

RWTH
Aachen, Germany
- Greim, R.
- Karpinski, W.
- Schael, S.
- Schultz von Dratzig, A.
- Schwering, G.
- Wlochal, M.

Sapienza University of Rome
Rome, Italy
- Giribono, A.
- Mostacci, A.
- Palumbo, L.
- Pompili, M.

SBU
Stony Brook, New York, USA
- Ding, W.
- Muller, E.M.
- Shih, K.
- Zhou, T.

SESAME
Allan, Jordan
- Al-Mohammad, H.
- Manukyan, K.

SINAP
Shanghai, People's Republic of China
- Cao, S.S.
- Chen, H.J.
- Chen, J.
- Duan, L.W.
- Gao, B.
- Lai, L.W.
- Leng, Y.B.
- Shen, T.J.
- Yan, Y.B.
- Ye, K.R.
- Yu, L.Y.
- Yuan, R.X.

SLAC
Menlo Park, California, USA
- Carranza, E.
- Chen, A.
- Clarke, C.I.
- Condamoor, S.
- Corbett, W.J.
- Dusatko, J.E.
- Field, R.C.

ISBN: 978-3-95450-192-2

- Fisher, A.S.
- Fox, J.D.
- Frisch, J.C.
- Green, S.Z.
- Herbst, R.T.
- Hogan, M.J.
- Kadyrov, R.A.
- Krejcik, P.
- Lipkowitz, N.
- McKee, B.D.
- O'Shea, B.D.
- Rivetta, C.H.
- Tao, F.
- Welch, J.J.
- White, G.R.
- Xu, B.
- Yakimenko, V.
- Yocky, G.

Sokendai
Ibaraki, Japan
- Hirosawa, K.

SOLEIL
Gif-sur-Yvette, France
- Brubach, J.B.
- Manceron, L.
- Roy, P.
- Tordeux, M.-A.

SSRF
Shanghai, People's Republic of China
- Chen, F.Z.
- Lai, L.W.
- Leng, Y.B.
- Wu, T.
- Yu, L.Y.
- Yuan, R.X.
- Zhang, N.
- Zhou, Y.M.

Stanford University
Stanford, California, USA
- Turgut, O.

STFC/DL/ASTeC
Daresbury, Warrington, Cheshire, United Kingdom
- Brynes, A.D.
- Jackson, F.
- Scott, D.J.

STFC/DL
Daresbury, Warrington, Cheshire, United Kingdom
- Aden, P.

STFC/RAL/ISIS
Chilton, Didcot, Oxon, United Kingdom
- Harryman, D.M.
- Pertica, A.
- Posthuma de Boer, D.W.
- Wilcox, C.C.

Supracon AG
Jena, Germany
- Zakosarenko, V.

TEMF, TU Darmstadt
Darmstadt, Germany
- De Gersem, H.
- Marsic, N.

The University of Liverpool
Liverpool, United Kingdom
- del Busto, E.N.
- Devlin, L.J.
- Kastriotou, M.
- Tzoganis, V.
- Welsch, C.P.

THM
Friedberg, Germany
- Mattiello, S.
- Penirschke, A.

TRIUMF, Canada's National Laboratory for Particle and Nuclear Physics
Vancouver, Canada
- Dirksen, P.E.
- Laxdal, R.E.
- Lenckowski, M.
- Rawnsley, W.R.
- Rowe, M.
- Verzilov, V.A.

TU Darmstadt
Darmstadt, Germany
- Arnold, M.
- Bahlo, T.
- Galatyuk, T.
- Pforr, J.
- Pietralla, N.
- Rost, A.
- Schließmann, F.

TU Dresden
Dresden, Germany
- Iatrou, C.P.
- Rahm, J.

U. Sannio
Benevento, Italy
- Sabato, L.

ISBN: 978-3-95450-192-2

UAB-IFAE
Barcelona, Spain
- Boix Gargallo, J.

UMAN
Manchester, United Kingdom
- Bertsche, W.
- Sandberg, H.

UNIST
Ulsan, Republic of Korea
- Cheon, Y.L.
- Choe, D.
- Choi, C.U.
- Chung, M.
- Moon, K.
- Sung, C.K.

United Rocket and Space Corporation, Institute of Space Device Engineering
Moscow, Russia
- Anashin, V.S.

University of Chinese Academy of Sciences
Beijing, People's Republic of China
- Gao, B.

University of Oslo
Oslo, Norway
- Adli, E.

University Paris Sud
Orsay, France
- Boucher, R.B.

Università di Roma II Tor Vergata
Roma, Italy
- Cianchi, A.

Universität Bern, Institute of Applied Physics
Bern, Switzerland
- Feurer, T.
- Hayati, M.
- Ollmann, Z.
- Tarkeshian, R.

USTC/NSRL
Hefei, Anhui, People's Republic of China
- Luo, Q.
- Sun, B.G.
- Wang, Q.

UTK
Knoxville, Tennessee, USA
- Garcia, F.G.

Warsaw University of Technology, Institute of Electronic Systems
Warsaw, Poland
- Grzegrzolka, M.G.
- Rutkowski, I.